LOAN DOCUMENT

PHOTOGRAPH THIS SHEET

AD-A263 418

DTIC ACCESSION NUMBER

LEVEL

1

INVENTORY

AFOSR TR 93 0180

DOCUMENT IDENTIFICATION

Apr 92

DISTRIBUTION STATEMENT

Approved for public release
Distribution Unlimited

DISTRIBUTION STATEMENT

HANDLE WITH CARE

ACCESSION FOR
NTIS GRA&I
DTIC TRAC
UNANNOUNCED
JUSTIFICATION

BY
DISTRIBUTION/
AVAILABILITY CODES

DISTRIBUTION	AVAILABILITY AND/OR SPECIAL
A-1	

DISTRIBUTION STAMP

DTIC
ELECTE
APR 23 1993
S C D

DATE ACCESSIONED

DTIC QUALITY INSPECTED

DATE RETURNED

DEFENSE TECHNICAL INFORMATION CENTER

9308382

810 78

DATE RECEIVED IN DTIC

REGISTERED OR CERTIFIED NUMBER

PHOTOGRAPH THIS SHEET AND RETURN TO DTIC-FDAC

DTIC FORM 70A JAN 90

DOCUMENT PROCESSING SHEET

PREVIOUS EDITIONS MAY BE USED UNTIL STOCK IS EXHAUSTED.

LOAN DOCUMENT

93 4 20 022

AD-A263 418



9

Moustakas
Pankove
Hamakawa
EDITORS

VOLUME 242

Wide Band Gap Semiconductors

VOLUME 242

Wide Band Gap Semiconductors

EDITORS
T.D. Moustakas
J.I. Pankove
Y. Hamakawa

REPORT DOCUMENTATION PAGE

Form Approved
OMB No. 0704-0188

Public reporting burden for this collection of information is estimated to average 1 hour per response, including the time for reviewing instructions, searching existing data sources, gathering and maintaining the data needed, and completing and reviewing the collection of information. Send comments regarding this burden estimate or any other aspect of this collection of information, including suggestions for reducing this burden, to Washington Headquarters Services, Directorate for Information Operations and Reports, 1215 Jefferson Davis Highway, Suite 1204, Arlington, VA 22202-4302, and to the Office of Management and Budget, Paperwork Reduction Project (0704-0188), Washington, DC 20503.

1. AGENCY USE ONLY (Leave blank)	2. REPORT DATE	3. REPORT TYPE AND DATES COVERED
		Final Report 15 Sep 91 - 14 Sep 92

4. TITLE AND SUBTITLE
1991 MRS SYMPOSIUM ON WIDE BAND-GAP SEMICONDUCTORS

5. FUNDING NUMBERS
2306/B1

6. AUTHOR(S)
Dr John Ballance

AFOSR-TR- [illegible] 80

7. PERFORMING ORGANIZATION NAME(S) AND ADDRESS(ES)
MATERIALS RESEARCH SOCIETY
9800 MC KNIGHT ROAD
PITTSBURGH PA 15237-6005

8. PERFORMING ORGANIZATION REPORT NUMBER

9. SPONSORING/MONITORING AGENCY NAME(S) AND ADDRESS(ES)
AFOSR/NE
110 DUNCAN AVENUE, SUITE B115
BOLLING AFB, DC 20332-0001

10. SPONSORING/MONITORING AGENCY REPORT NUMBER
AFOSR-91-0411

11. SUPPLEMENTARY NOTES

12a. DISTRIBUTION/AVAILABILITY STATEMENT
UNLIMITED

12b. DISTRIBUTION CODE

13. ABSTRACT (Maximum 200 words)

The Following Symposium was held:

Thin Films: Stresses and Mechanical Properties III

Advanced III-V compound semiconductor growth, processing and devices

Wide Band-Gap Semiconductors

14. SUBJECT TERMS

15. NUMBER OF PAGES

16. PRICE CODE

17. SECURITY CLASSIFICATION OF REPORT	18. SECURITY CLASSIFICATION OF THIS PAGE	19. SECURITY CLASSIFICATION OF ABSTRACT	20. LIMITATION OF ABSTRACT
UNCLASSIFIED	UNCLASSIFIED	UNCLASSIFIED	UL

MATERIALS RESEARCH SOCIETY SYMPOSIUM PROCEEDINGS VOLUME 242

Wide Band Gap Semiconductors

Symposium held December 2-6, 1991, Boston, Massachusetts, U.S.A.

EDITORS:

T.D. Moustakas
Boston University, Boston, Massachusetts, U.S.A.

J.I. Pankove
University of Colorado, Boulder, Colorado, U.S.A.

Y. Hamakawa
Osaka University, Toyonaka, Osaka, Japan

MRS MATERIALS RESEARCH SOCIETY
Pittsburgh, Pennsylvania

This work was supported by the Air Force Office of Scientific Research, Air Force Systems Command, USAF, under Grant Number AFOSR 91-0411.

This work relates to Department of Navy Grant N00014-92-J-1001 issued by the Office of Naval Research. The United States Government has a royalty-free license throughout the world in all copyrightable material contained herein.

Single article reprints from this publication are available through
University Microfilms Inc., 300 North Zeeb Road, Ann Arbor, Michigan 48106

CODEN: MRSPDH

Copyright 1992 by Materials Research Society.
All rights reserved.

This book has been registered with Copyright Clearance Center, Inc. For further information, please contact the Copyright Clearance Center, Salem, Massachusetts.

Published by:

Materials Research Society
9800 McKnight Road
Pittsburgh, Pennsylvania 15237
Telephone (412) 367-3003
Fax (412) 367-4373

Library of Congress Cataloging in Publication Data

Wide band gap semiconductors / editors, T.D. Moustakas, J.I. Pankove, Y. Hamakawa.

p. cm. — (Materials Research Society symposium proceedings, ISSN 0272-9172 ; v. 242)
Includes bibliographical references.
ISBN 1-55899-136-0
1. Wide gap semiconductors—Congresses. 2. Diamond thin films—Congresses. 3. Silicon carbide—Congresses. I. Moustakas, T.D. II. Pankove, Jacques I., 1922- . III. Hamakawa, Yashihiro, 1932- . IV. Series: Materials Research Society symposium proceedings : v. 242.
QC611.8.W53.W52 1992 92-10834
621.3815'2—dc20 CIP

Manufactured in the United States of America

Contents

PREFACE xiii

ACKNOWLEDGMENTS xv

MATERIALS RESEARCH SOCIETY SYMPOSIUM PROCEEDINGS xvi

PART I: DIAMOND GROWTH

*THEORETICAL STUDIES OF DIAMOND SURFACE CHEMISTRY AND DIAMOND-METAL INTERFACES 3
W.E. Pickett, M.R. Pederson, K.A. Jackson, and S.C. Erwin

*GROWTH TECHNIQUE FOR LARGE AREA MOSAIC DIAMOND FILMS 13
R.W. Pryor, M.W. Geis, and H.R. Clark

*CHEMICAL VAPOR DEPOSITION OF DIAMOND FILMS USING WATER: ALCOHOL:ORGANIC-ACID SOLUTIONS 23
R.A. Rudder, J.B. Posthill, G.C. Hudson, D.P. Malta, R.E. Thomas, R.J. Markunas, T.P. Humphreys, and R.J. Nemanich

REMOTE ECR PLASMA DEPOSITION OF DIAMOND THIN FILMS FROM WATER-METHANOL MIXTURES 31
R.K. Singh, D. Gilbert, R. Tellshow, R. Koba, R. Ochoa, J.H. Simmons, P.H. Holloway, J. Rodgers, and K. Buckle

DEPOSITION OF FLAME GROWN DIAMOND FILMS IN A CONTROLLED ATMOSPHERE 37
Kathleen Doverspike, James E. Butler, and Jaime A. Freitas, Jr.

SEQUENTIAL GROWTH OF HIGH QUALITY DIAMOND FILMS FROM HYDROCARBON AND HYDROGEN GASES 43
Darin S. Olson, Michael A. Kelly, Sanjiv Kapoor, and Stig B. Hagstrom

DIAMOND GROWTH FROM SPUTTERED ATOMIC CARBON AND HYDROGEN GAS 51
Michael A. Kelly, Sanjiv Kapoor, Darin S. Olson, and Stig B. Hagstrom

THE CVD DIAMOND NUCLEATION MECHANISM ON Si OVERLAID WITH sp^2 CARBON 57
Pehr E. Pehrsson, John Glesener, and Arthur A. Morrish

AN INVESTIGATION INTO THE USE OF A DIFFUSION BARRIER IN THE MICROWAVE PLASMA ASSISTED CHEMICAL VAPOR DEPOSITION OF DIAMOND ON IRON BASED SUBSTRATES 63
Paul S. Weiser, S. Prawer, A. Hoffman, R. Manory, P.J.K. Paterson, and S-A. Stuart

SELECTIVE NUCLEATION OF DIAMOND CRYSTALS ON THE APEX OF SILICON PYRAMIDS 69
R. Ramesham and C. Ellis

EFFECT OF LASER IRRADIATION ON CARBON-IMPLANTED COPPER SUBSTRATES 79
Rajiv K. Singh and John Viatella

*Invited Paper

PART II: ELECTRONIC PROPERTIES OF DIAMOND AND RELATED DEVICES

*DIAMOND AS A MATERIAL IN SOLID STATE ELECTRONICS 87
Victor S. Vavilov

*INVESTIGATION OF CVD-GROWN DIAMOND BY CATHODOLUMINESCENCE IN TEM 97
R.J. Graham

FLUORINE ATOM ADDITION TO THE DIAMOND (111) SURFACE 109
Andrew Freedman, Gary N. Robinson, and Charter D. Stinespring

STM STUDY OF DIAMOND(001) SURFACE 115
Takashi Tsuno, Takahiro Imai, Yoshiki Nishibayashi, and Naoji Fujimori

CHARACTERIZATION OF THE Si/DIAMOND INTERFACE 121
K.E. Williams, J.S. Speck, and M.D. Drory

ELECTRONIC STRUCTURE OF N-V CENTERS AND TERAHERTZ SPECTROSCOPY OF DIAMOND 127
D.A. Redman, Q. Shu, S.W. Brown, A. Lenef, Y. Liu, J. Whitaker, S.C. Rand, S. Satoh, K. Tsuji, and S. Yazu

ELECTRICAL PROPERTIES OF FINE GRAIN COMPOSITE CARBON FILMS 133
Hsiung Chen and R.O. Dillon

OPTICAL EVIDENCE OF REDUCTION OF RADIATIVE DEFECTS IN DIAMOND FILMS GROWN BY ACETYLENE-OXYGEN FLAMES 139
J.A. Freitas, Jr., U. Strom, K. Doverspike, C.M. Marks, and K.A. Snail

ELECTRONIC DEVICE FABRICATION USING ELECTRON CYCLOTRON RESONANCE ETCHING OF BORON DOPED HOMOEPITAXIAL DIAMOND FILMS 145
S.A. Grot, R.A. Ditizio, G.Sh. Gildenblat, A.R. Badzian, and S.J. Fonash

TANTALUM AND TANTALUM SILICIDE HIGH TEMPERATURE RECTIFYING CONTACTS ON TYPE IIB NATURAL DIAMOND 151
Scott R. Sahaida and Dale G. Thompson

ELECTRICAL PROPERTIES OF SCHOTTKY JUNCTIONS ON HOMOEPITAXIAL FLAME GROWN DIAMOND 161
J.W. Glesener, A.A. Morrish, and K.A. Snail

POLYCRYSTALLINE DIAMOND FILM RESISTORS 165
L.M. Edwards and J.L. Davidson

THE MODIFICATION OF THE ABRASION RESISTANCE OF TYPE IIa (110) DIAMOND USING CARBON AND NITROGEN IMPLANTATION 171
Gregory C. Anderson, Steven Prawer, and Peter N. Johnston

PART III: II-VI COMPOUNDS

*STOICHIOMETRY CONTROL OF COMPOUND SEMICONDUCTORS 179
Jun-Ichi Nishizawa, Ken Suto, and Yutaka Oyama

*INITIAL STAGES OF GROWTH OF ZnSe ON Si 191
R.D. Bringans, D.K. Biegelsen, L.-E. Swartz, F.A. Ponce, and J.C. Tramontana

*Invited Paper

THE MBE GROWTH OF WIDEGAP II-VI INJECTION LASERS AND LEDs 203
W. Xie, D.C. Grillo, M. Kobayashi, R.L. Gunshor, H. Jeon, J. Ding, A.V. Nurmikko, G.C. Hua, and N. Otsuka

ALLOY DEPENDENT PROPERTIES OF EXCITONS AND DEEP ACCEPTORS IN CdZnTe VOLUME CRYSTALS 209
B.K. Meyer, D.M. Hofmann, K. Oettinger, W. Stadler, Al.L. Efros, M. Salk, and K.W. Benz

CHARACTERIZATION OF ZnS LAYERS GROWN BY MOCVD FOR THIN FILM ELECTROLUMINESCENCE (TFEL) DEVICES 215
J.E. Yu, K.S. Jones, J. Fang, P.H. Holloway, B. Pathangey, E. Bretschneider, and T.J. Anderson

GROWTH AND CHARACTERIZATION OF ZnSe/ZnCdSe DIODE STRUCTURES ON (In,Ga)As BUFFER LAYERS 221
G.C. Hua, N. Otsuka, W. Xie, D.C. Grillo, M. Kobayashi, and R.L. Gunshor

MBE GROWTH AND PROPERTIES OF WIDE BAND-GAP II-VI STRAINED-LAYER SUPERLATTICE 227
Hailong Wang, Jie Cui, Aidong Shen, Liang Xu, Yunliang Chen, and Yuhua Shen

IN-SITU SPECTROSCOPIC ELLIPSOMETRY APPLIED TO ZnSe AND ZnCdSe GROWTH PROCESS IN ORGANOMETALLIC VAPOR PHASE EPITAXY 237
J. Iacoponi, I.B. Bhat, B. Johs, and J.A. Woollam

GROWTH OF EPITAXIAL ZnS FILMS BY PULSED-LASER ABLATION 243
J.W. McCamy, D.H. Lowndes, J.D. Budai, B.C. Chakoumakos, and R.A. Zuhr

SYNTHESIS, STRUCTURAL AND OPTICAL CHARACTERIZATION OF ZINC CHALCOGENIDES IN NOVEL SOLID STATE HOSTS 249
Kelly L. Moran, Andrew W. Ott, Thurman E. Gier, William T.A. Harrison, Hellmut Eckert, and Galen D. Stucky

EXCIMER LASER MELTING OF MBE-ZnSe 255
Nallan C. Padmapani, G.-J. Yi, G.F. Neumark, Z. Lu, C.C. Chang, and M.C. Tamargo

CHARACTERISTICS OF ZnSe LAYERS GROWN ON Zn-STABILIZED AND Se-STABILIZED GaAs SUBSTRATES 261
S. Akram, H. Ehsani, I.B. Bhat, and S.K. Ghandhi

OPTICAL TRANSITIONS ON CdS/CdTe CVD HETEROSTRUCTURES 267
Claude Boemare and M.H. Nazare

VAPOR-PHASE GROWTH OF EPITAXIAL AND BULK ZnSe 273
W.L. Ahlgren, S. Sen, S.M. Johnson, W.H. Konkel, J.A. Vigil, and R.P. Ruth

OMVPE GROWTH OF ZnSe UTILIZING ZINC AMIDES AS SOURCE COMPOUNDS: RELEVANCE TO THE PRODUCTION OF p-TYPE MATERIAL 281
William S. Rees, Jr., David M. Green, Timothy J. Anderson, and Eric Bretschneider

HIGH RESOLUTION PHOTOLUMINESCENCE OF EDGE AND NEAR-EDGE CdTe 287
M.C. Carmo and M.J. Soares

HIGH QUALITY EPITAXIAL FILMS OF ZnSe AND ZnSe/ZnS STRAINED LAYER SUPERLATTICES GROWN BY M[illegible]'D 293
Chungdee Pong, R.C. DeMattei, and R.S. Feigelson

THE APPLICATION OF LAMMA-1000 TO THE ELEMENTAL ANALYSIS OF CdTe COMPOUND 299
A.I. Belogorokhov and A.Yu. Khar'kovsky

OPTICAL STUDY OF THE CdTe CRYSTALS IN FAR INFRARED REGION AT TEMPERATURES (5-500)K 303
A.I. Belogorokhov

PART IV: THEORY OF WIDE BAND-GAP SEMICONDUCTORS

*SELF-COMPENSATION AND DOPING PROBLEMS IN ZnSe 311
David B. Laks and Chris G. Van de Walle

*THEORY OF DOPING OF DIAMOND 323
J. Bernholc, S.A. Kajihara, and A. Antonelli

*QUASI-EQUILIBRIUM NUCLEATION AND GROWTH OF DIAMOND AND CUBIC BORON-NITRIDE 335
Y. Bar-Yam, T. Lei, T.D. Moustakas, D.C. Allan, and M.P. Teter

FIRST-PRINCIPLES INVESTIGATIONS OF ACCEPTORS IN ZnSe 349
Chris G. Van de Walle and D.B. Laks

INTERSTITIAL IMPURITIES IN WURTZITE VS. ZINCBLENDE SEMICONDUCTORS: THE CASE OF H IN SiC 355
M.A. Roberson and S.K. Estreicher

POTENTIAL ENERGY SURFACES AND STABILITY OF O IN ELEMENTAL AND COMPOUND SEMICONDUCTORS 361
S.K. Estreicher, M.A. Roberson, C.H. Chu, and J. Solinsky

A COMPARISON OF THE WURTZITE AND ZINCBLENDE BAND STRUCTURES FOR SiC, AlN AND GaN 367
W.R.L. Lambrecht and B. Segall

ON THE BURSTEIN-MOSS SHIFT IN QUANTUM CONFINED WIDE-BAND GAP SEMICONDUCTORS 373
Kamakhya P. Ghatak and Badal De

THE EINSTEIN RELATION IN SUPERLATTICES OF WIDE-BAND GAP SEMICONDUCTORS UNDER CROSS-FIELD CONFIGURATION 377
Kamakhya P. Ghatak and Badal De

PART V: III-V NITRIDES AND OTHER III-V COMPOUNDS

*CONDUCTIVITY CONTROL OF AlGaN, FABRICATION OF AlGaN/GaN MULTI-HETEROSTRUCTURE AND THEIR APPLICATION TO UV/BLUE LIGHT EMITTING DEVICES 383
I. Akasaki and H. Amano

*OPTICAL AND ELECTRONIC PROPERTIES OF THE NITRIDES OF INDIUM, GALLIUM AND ALUMINIUM AND THE INFLUENCE OF NATIVE DEFECTS 395
T.L. Tansley and R.J. Egan

*Invited Paper

*SYSTEMATIC STUDIES ON MAGNETRON-SPUTTERED INDIUM NITRIDE 409
W.A. Bryden, S.A. Ecelberger, J.S. Morgan, T.O. Poehler, and T.J. Kistenmacher

CHARACTERIZATION OF $Al_xGa_{1-x}N$ GROWN BY MOCVD AT LOW TEMPERATURES 421
Z.J. Yu, B.S. Sywe, and J.H. Edgar

A COMPARATIVE STUDY OF GaN FILMS GROWN ON DIFFERENT FACES OF SAPPHIRE BY ECR-ASSISTED MBE 427
T.D. Moustakas, R.J. Molnar, T. Lei, G. Menon, and C.R. Eddy Jr

A COMPARATIVE STUDY OF GaN EPITAXY ON Si(001) AND Si(111) SUBSTRATES 433
T. Lei and T.D. Moustakas

GROWTH DEPENDENCE OF THICKNESS, MORPHOLOGY AND ELECTRICAL TRANSPORT OF InN OVERLAYERS ON AlN-NUCLEATED (00.1) SAPPHIRE 441
T.J. Kistenmacher, S.A. Ecelberger, and W.A. Bryden

LOW TEMPERATURE PREPARATION OF GALLIUM NITRIDE THIN FILMS 445
Roy G. Gordon, David M. Hoffman, and Umar Riaz

AN INVESTIGATION OF LIGHT INDUCED DEFECTS IN ALUMINUM NITRIDE CERAMICS 451
J.H. Harris and R.A. Youngman

CRYSTALLINE GROWTH OF WURTZITE GaN ON (111) GaAs 457
J. Ross, M. Rubin, and T.K. Gustafson

EPITAXIAL GROWTH OF AlN ON 3C-SiC AND Al_2O_3 SUBSTRATES 463
B.S. Sywe, Z.J. Yu, and J.H. Edgar

STRUCTURAL CHARACTERIZATION AND RAMAN SCATTERING OF EPITAXIAL ALUMINUM NITRIDE THIN FILMS ON Si(111) 469
W.J. Meng, T.A. Perry, J. Heremans, and Y.T. Cheng

TEM STUDY OF DISLOCATIONS IN PLASTICALLY DEFORMED AlN 475
V. Audurier, J.L. Demenet, and J. Rabier

TEMPERATURE DEPENDENCE OF OPTICAL PROPERTIES OF AlAs, STUDIED BY *IN SITU* SPECTROSCOPIC ELLIPSOMETRY 481
Huade Yao, Paul G. Snyder, Kathleen Stair, and Thomas Bird

MOMBE GROWTH OF GaP AND ITS EFFICIENT PHOTOENHANCEMENT AT LOW TEMPERATURES 487
Masahiro Yoshimoto, Tsuzumi Tsuji, Atsushi Kajimoto, and Hiroyuki Matsunami

PART VI: SILICON CARBIDE

*PROGRESS IN SILICON CARBIDE SEMICONDUCTOR TECHNOLOGY 495
J.A. Powell, P.G. Neudeck, L.G. Matus, and J.B. Petit

*THE ORIGIN OF POLYTYPES IN SiC AND ZnS 507
Volker Heine, C. Cheng, G.E. Engel, and R.J. Needs

EPITAXIAL MONOCRYSTALLINE SiC FILMS GROWN ON Si BY LOW-PRESSURE CHEMICAL VAPOR DEPOSITION AT 750°C 519
I. Golecki, F. Reidinger, and J. Marti

*Invited Paper

EVALUATION OF SILICON CARBIDE FORMED WITH A SINGLE PRECURSOR OF Di-tert BUTYSILANE 525
Sing-Pin Tay, J.P. Ellul, Susan B. Hewitt, N.G. Tarr, and A.R. Boothroyd

STRESS-INDU[illegible]D POLYTYPIC TRANSFORMATION IN SiC 531
J.W. Yang, T. Suzuki, P. Pirouz, J.A. Powell, and T. Iseki

EFFECT OF CARBONIZATION GAS PRECURSOR ON THE HETEROEPITAXIAL GROWTH OF SiC-ON-Si BY RTCVD 537
A.J. Steckl and J.P. Li

PREPARATION AND CHARACTERIZATION OF 3C-SiC HETEROEPITAXIAL LAYERS ON *Si*(111) 543
Mitsugu Yamanaka and Keiko Ikoma

CHARACTERIZATION OF SILICON CARBIDE THIN FILMS DEPOSITED BY LASER ABLATION ON [001] AND [111] SILICON WAFERS 549
L. Rimai, R. Ager, E.M. Logothetis, W.H. Weber, and J. Hangas

HETERO-EPITAXIAL GROWTH OF SiC FILMS BY CVD FROM SILANE, METHANE, PROPANE, AND HYDROGEN MIXTURES 555
B. Bahavar, M.I. Chaudhry, and R.J. McCluskey

ELECTRICAL PROPERTIES OF THERMALLY GROWN SiO_2-SiC *INTERFACES* 561
Nitya N. Singh, A. Rys, and A.U. Ahmed

ELECTRICAL AND CHEMICAL CHARACTERIZATION OF CONTACTS TO SILICON CARBIDE 567
Jeremy B. Petit and Mary V. Zeller

HIGH TEMPERATURE OHMIC CONTACTS FOR n-TYPE β-SiC SENSORS 573
J.S. Shor, R.A. Weber, L.G. Provost, D. Goldstein, and A.D. Kurtz

PART VII: BORON NITRIDE AND OTHER BORON COMPOUNDS

*HETEROEPITAXIAL GROWTH OF CUBIC BORON NITRIDE ON SILICON 585
G.L. Doll, T.A. Perry, J.A. Sell, C.A. Taylor, and R. Clarke

PULSED EXCIMER LASER ABLATION DEPOSITION OF BORON NITRIDE ON Si (100) SUBSTRATES 593
T.A. Friedmann, K.F. McCarty, E.J. Klaus, D. Boehme, W.M. Clift, H.A. Johnsen, M.J. Mills, D.K. Ottesen, and R.H. Stulen

GROWTH OF TETRAHEDRAL PHASES OF BORON NITRIDE THIN FILMS BY REACTIVE SPUTTERING 599
T.D. Moustakas, T. Lei, R.J. Molnar, C. Fountzoulas, and E.J. Oles

EPR INVESTIGATION OF DEFECTS IN BORON NITRIDE THIN FILMS 605
M. Fanciulli and T.D. Moustakas

ESR CHARACTERISTICS OF CUBIC BORON NITRIDE CRYSTALS 613
Fangqing Zhang and Guanghua Chen

THE EFFECTS OF SUBSTRATE BIAS AND Si DOPING ON THE PROPERTIES OF RF SPUTTERED BN FILMS 617
P.K. Banerjee, J.S. Kim, B. Chatterjee, M. Platek, and S.S. Mitra

*Invited Paper

SUBMILLIMETER OPTICAL PROPERTIES OF HEXAGONAL BORON NITRIDE 623
A.J. Gatesman, R.H. Giles, and J. Waldman

THERMOELECTRIC PROPERTIES OF BORON AND BORON PHOSPHIDE FILMS 629
Y. Kumashiro, T. Yokoyama, J. Nakamura, K. Matsuda, H. Yoshida, and J. Takahashi

CHARACTERIZATION OF BORON CARBIDE FILMS FORMED BY PECVD 637
John Mazurowski, Sunwoo Lee, G. Ramseyer, and P.A. Dowben

MODELING OF THE FORMATION OF BORON CARBIDE PARTICLES IN AN AEROSOL FLOW REACTOR 643
Yun Xiong, Sotiris E. Pratsinis, and Alan W. Weimer

PART VIII: AMORPHOUS AND MICRO-CRYSTALLINE SEMICONDUCTORS

*AMORPHOUS AND MICROCRYSTALLINE SiC AS NEW SYNTHETIC WIDE GAP SEMICONDUCTORS 651
Y. Hamakawa and H. Okamoto

*HIGH-QUALITY AMORPHOUS SILICON CARBIDE PREPARED BY A NEW FABRICATION METHOD FOR A WINDOW P-LAYER OF SOLAR CELLS 663
K. Ninomiya, H. Haku, H. Tarui, N. Nakamura, M. Tanaka, K. Wakisaka, S. Tsuda, H. Nishiwaki, S. Nakano, and Y. Kuwano

DOPED AMORPHOUS AND MICROCRYSTALLINE SILICON CARBIDE AS WIDE BAND-GAP MATERIAL 675
F. Demichelis, C.F. Pirri, E. Tresso, and P. Rava

WIDE-GAP POLYSILANE PRODUCED BY PLASMA-ENHANCED CVD AT CRYOGENIC TEMPERATURES 681
S. Miyazaki, H. Shin, K. Okamoto, and M. Hirose

OPTICALLY INDUCED PARAMAGNETISM IN AMORPHOUS HYDROGENATED SILICON NITRIDE THIN FILMS 687
W.L. Warren, J. Kanicki, F.C. Rong, W.R. Buchwald, and M. Harmatz

STRUCTURE, CHARACTERISTICS, AND THE APPLICATION OF PHOSPHORUS DOPED HYDROGENATED MICROCRYSTALLINE SILICON 693
S.J. Jeng, D.E. Kotecki, J. Kanicki, C.C. Parks, and J. Tien

ELECTRICAL AND OPTICAL PROPERTIES OF OXYGENATED MICROCRYSTALLINE SILICON (mc-Si:O:H) 699
M. Faraji, Sunil Gokhale, S.M. Chaudhari, M.G. Takwale, and S.V. Ghaisas

PART IX: CHALCOPYRITES, OXIDES, AND HALIDES

*LATTICE-MATCHED HETEROEPITAXY OF WIDE GAP TERNARY COMPOUND SEMICONDUCTORS 707
Klaus J. Bachmann

*OBSERVATION OF GAS FLOW PATTERNS IN A CVD REACTOR FOR WIDE BAND GAP SEMICONDUCTOR THIN FILM DEPOSITION 721
Kinya Atsumi, Yoshiki Ueno, Tadashi Hattori, and Yoshihiro Hamakawa

*Invited Paper

ELECTRONIC TRANSITION-RELATED OPTICAL ABSORPTION IN VANADIA FILMS 731
Nada M. Abuhadba and Carolyn R. Aita

PHASE MAPPING SPUTTER DEPOSITED WIDE BAND-GAP METAL OXIDES 737
C.R. Aita, R.C. Lee, C.-K. Kwok, and E.A. Kolawa

CHEMICAL VAPOR DEPOSITION OF HIGHLY TRANSPARENT AND CONDUCTIVE BORON DOPED ZINC OXIDE THIN FILMS 743
Jinhua Hu and Roy G. Gordon

ZnO ON Si_3N_4 BIMORPHS WITH LARGE DEFLECTIONS 749
Wai-Shing Choi and Jan G. Smits

INFLUENCE OF SUBSTRATE TEMPERATURE ON TIN OXIDE THIN FILMS DEPOSITED BY ELECTRON BEAM EVAPORATION TECHNIQUE 755
S.M. Rozati, S. Mirzapour, M.G. Takwale, B.R. Marathe, and V.G. Bhide

NANOMETER SIZE LEAD IODIDE PARTICLES 761
Vivek Mehrotra, Eric Rodeghiero, Jens W. Otto, and Emmanuel P. Giannelis

EFFECTS OF CONTACT MATERIALS ON THE THERMALLY STIMULATED CURRENT SPECTRA OF MERCURIC IODIDE 767
X.J. Bao, T.E. Schlesinger, R.B. James, A.Y. Cheng, C. Ortale, and L. van den Berg

OPTICAL AND MAGNETIC RESONANCE INVESTIGATIONS OF MERCURIC IODIDE CRYSTALS 773
B.K. Meyer, D.M. Hofmann, J. Eckstein, and K.W. Benz

EFFECTS OF REACTIVE SPUTTERING PARAMETERS ON THE GROWTH AND PROPERTIES OF ACOUSTOOPTIC ZnO FILMS 779
E. Jacobsohn and D. Shechtman

AUTHOR INDEX 785

SUBJECT INDEX 789

Preface

It has been two years since MRS had a symposium devoted to wide band gap semiconductors (mostly diamond and SiC). The 1991 MRS Fall Meeting was the first time that the entire spectrum of wide band gap semiconductors was covered at an MRS meeting. Wide band gap semiconductors are under intense study because of their potential applications in photonic devices in the visible and ultraviolet part of the electromagnetic spectrum, and devices for high temperature, high frequency and high power electronics. Additionally, due to their unique mechanical, thermal, optical, chemical, and electronic properties many wide band gap semiconductors are anticipated to find applications in thermoelectric, electrooptic, piezoelectric and acoustooptic devices as well as protective coatings, hard coatings and heat sinks.

Material systems covered in this symposium include diamond, II-VI compounds, III-V nitrides, silicon carbide, boron compounds, amorphous and microcrystalline semiconductors, chalcopyrites, oxides and halides. The various papers addressed recent experimental and theoretical developments. They covered issues related to crystal growth (bulk and thin films), structure and microstructure, defects, doping, optoelectronic properties and device applications. A theoretical session was dedicated to identifying common themes in the heteroepitaxy and the role of defects in doping, compensation and phase stability of this unique class of materials. Important experimental milestones included the demonstrations of bright blue injection luminescence at room temperatures from junctions based on III-V nitrides and a similar result from multiple quantum wells in a ZnSe double heterojunction at liquid nitrogen temperatures.

Theodore D. Moustakas
Jacques I. Pankove
Yoshihiro Hamakawa

April 1992

Acknowledgments

The editors wish to express their appreciation to the Air Force Office of Scientific Research, Office of Naval Research, National Renewable Energy Laboratory, ASTeX Corp., Bandgap Technology Corp., EMCORE Corp., Kennametal Inc., Nippondenso Corp., and Sanyo Electric Company, Ltd., who provided financial support for this symposium.

Many thanks are also due to the chairs of the individual sessions, to the reviewers of the articles, and to the speakers of the invited and contributed papers.

Finally, we acknowledge the invaluable assistance of Kenny Glotfelty and of members of the MRS headquarters in the organization of the Symposium as well as the editing of these proceedings.

Volume 219—Amorphous Silicon Technology—1991, A. Madan, Y. Hamakawa, M. Thompson, P.C. Taylor, P.G. LeComber, 1991, ISBN: 1-55899-113-1

Volume 220—Silicon Molecular Beam Epitaxy, 1991, J.C. Bean, E.H.C. Parker, S. Iyer, Y. Shiraki, E. Kasper, K. Wang, 1991, ISBN: 1-55899-114-X

Volume 221—Heteroepitaxy of Dissimilar Materials, R.F.C. Farrow, J.P. Harbison, P.S. Peercy, A. Zangwill, 1991, ISBN: 1-55899-115-8

Volume 222—Atomic Layer Growth and Processing, Y. Aoyagi, P.D. Dapkus, T.F. Kuech, 1991, ISBN: 1-55899-116-6

Volume 223—Low Energy Ion Beam and Plasma Modification of Materials, J.M.E. Harper, K. Miyake, J.R. McNeil, S.M. Gorbatkin, 1991, ISBN: 1-55899-117-4

Volume 224—Rapid Thermal and Integrated Processing, M.L. Green, J.C. Gelpey, J. Wortman, R. Singh, 1991, ISBN: 1-55899-118-2

Volume 225—Materials Reliability Issues in Microelectronics, J.R. Lloyd, P.S Ho, C.T. Sah, F. Yost, 1991, ISBN: 1-55899-119-0

Volume 226—Mechanical Behavior of Materials and Structures in Microelectronics, E. Suhir, R.C. Cammarata, D.D.L. Chung, 1991, ISBN: 1-55899-120-4

Volume 227—High Temperature Polymers for Microelectronics, D.Y. Yoon, D.T. Grubb, I. Mita, 1991, ISBN: 1-55899-121-2

Volume 228—Materials for Optical Information Processing, C. Warde, J. Stamatoff, W. Wang, 1991, ISBN: 1-55899-122-0

Volume 229—Structure/Property Relationships for Metal/Metal Interfaces, A.D Romig, D.E. Fowler, P.D. Bristowe, 1991, ISBN: 1-55899-123-9

Volume 230—Phase Transformation Kinetics in Thin Films, M. Chen, M. Thompson, R. Schwarz, M. Libera, 1991, ISBN: 1-55899-124-7

Volume 231—Magnetic Thin Films, Multilayers and Surfaces, H. Hopster, S.S.P. Parkin, G. Prinz, J.-P. Renard, T. Shinjo, W. Zinn, 1991, ISBN: 1-55899-125-5

Volume 232—Magnetic Materials: Microstructure and Properties, T. Suzuki, Y. Sugita, B.M. Clemens, D.E. Laughlin, K. Ouchi, 1991, ISBN: 1-55899-126-3

Volume 233—Synthesis/Characterization and Novel Applications of Molecular Sieve Materials, R.L. Bedard, T. Bein, M.E. Davis, J. Garces, V.A. Maroni, G.D. Stucky, 1991, ISBN: 1-55899-127-1

Volume 234—Modern Perspectives on Thermoelectrics and Related Materials, D.D. Allred, G. Slack, C. Vining, 1991, ISBN: 1-55899-128-X

Volume 235—Phase Formation and Modification by Beam-Solid Interactions, G.S. Was, L.E. Rehn, D. Follstaedt, 1992, ISBN: 1-55899-129-8

Volume 236—Photons and Low Energy Particles in Surface Processing, C Ashby, J.H. Brannon, S. Pang, 1992, ISBN: 1-55899-130-1

Volume 237—Interface Dynamics and Growth, K.S. Liang, M.P. Anderson, R.F. Bruinsma, G. Scoles, 1992, ISBN: 1-55899-131-X

me 238—Structure and Properties of Interfaces in Materials, W.A.T. Clark, C.L. Briant, U. Dahmen, 1992, ISBN: 1-55899-132-8

MATERIALS RESEARCH SOCIETY SYMPOSIUM PROCEEDINGS

Volume 239—Thin Films: Stresses and Mechanical Properties III, W.D. Nix, J.C. Bravman, E. Arzt, L.B. Freund, 1992, ISBN: 1-55899-133-6

Volume 240—Advanced III-V Compound Semiconductor Growth, Processing and Devices, S.J. Pearton, D.K. Sadana, J.M. Zavada, 1992, ISBN: 1-55899-134-4

Volume 241—Low Temperature (LT) GaAs and Related Materials, G.L. Witt, R. Calawa, U. Mishra, E. Weber, 1992, ISBN: 1-55899-135-2

Volume 242—Wide Ban-Gap Semiconductors, T.D. Moustakas, J.I. Pankove, Y. Hamakawa, 1992, ISBN: 1-55899-136-0

Volume 243—Ferroelectric Thin Films II, A.I. Kingon, E.R. Myers, B. Tuttle, 1992, ISBN: 1-55899-137-9

Volume 244—Optical Waveguide Materials, M.M. Broer, H. Kawazoe, G.H. Sigel, R.Th. Kersten, 1992, ISBN: 1-55899-138-7

Volume 245—Advanced Cementitious Systems: Mechanisms and Properties, F.P. Glasser, P.L. Pratt, T.O. Mason, J.F. Young, G.J. McCarthy, 1992, ISBN: 1-55899-139-5

Volume 246—Shape-Memory Materials and Phenomena—Fundamental Aspects and Applications, C.T. Liu, M. Wuttig, K. Otsuka, H. Kunsmann, 1992, ISBN: 1-55899-140-9

Volume 247—Electrical, Optical, and Magnetic Properties of Organic Solid State Materials, L.Y. Chiang, A.F. Garito, D.J. Sandman, 1992, ISBN: 1-55899-141-7

Volume 248—Complex Fluids, D. Weitz, E.Sirota, T. Witten, J. Israelachvili, 1992, ISBN: 1-55899-142-5

Volume 249—Synthesis and Processing of Ceramics: Scientific Issues, W.E. Rhine, T.M. Shaw, R.J. Gottschall, Y. Chen, 1992, ISBN: 1-55899-143-3

Volume 250—Chemical Vapor Deposition of Refractory Metals and Ceramics II, T.M. Besman, B.M. Gallois, J. Warren, 1992, ISBN: 1-55899-144-1

Volume 251—Pressure Effects on Materials Processing and Design, K. Ishizaki, E. Hodge, 1992, ISBN: 1-55899-145-X

Volume 252—Tissue-Inducing Biomaterials, M. Flanagan, L. Cima, E. Ron, 1992, ISBN: 1-55899-146-8

Volume 253—Applications of Multiple Scattering Theory to Materials Science, W.H. Butler, P.H. Dederichs, A. Gonis, R. Weaver, 1992, ISBN: 1-55899-147-6

Volume 254—Specimen Preparation for Transmission Electron Microscopy of Materials III, R. Anderson, J. Bravman, B. Tracy, 1992, ISBN: 1-55899-148-4

Volume 255—Hierarchically Structured Materials, I.A. Aksay, E. Baer, M. Sarikaya, D.A. Tirrell, 1992, ISBN: 1-55899-149-2

Volume 256—Light Emission from Silicon, S.S. Iyer, L.T. Canham, R.T. Collins, 1992, ISBN: 1-55899-150-6

Prior Materials Research Society Symposium Proceedings available by contacting Materials Research Society.

PART I

Diamond Growth

THEORETICAL STUDIES OF DIAMOND SURFACE CHEMISTRY AND DIAMOND-METAL INTERFACES

W. E. PICKETT,* M. R. PEDERSON,* K. A. JACKSON,# AND S. C. ERWIN+

* Complex Systems Theory Branch, Code 4692, Naval Research Laboratory, Washington Dc 20375-5000
# Department of Physics, Central Michigan University, Mt. Pleasant MI 48859
+ Department of Physics, University of Pennsylvania, Philadelphia PA 19104

ABSTRACT

Advances in diamond film growth have prompted us to study the interfaces involved in this process: the interface with the substrate, and the growth interface with the ambient hydrocarbon vapor. Carbon chemistry lies at the heart of the properties of both interfaces, and much of the relevant chemistry is not well understood. We report here the energies involved in some idealized chemical processes that may be important in the growth process. Results (Schottky barriers, interface energies) for diamond/metal interfaces are also reported, and the especially unusual diamond/nickel results we have recently obtained are discussed in some detail.

INTRODUCTION

In the process of diamond growth [1] as well as in applications, there are two interfaces of importance. The interface with the substrate, which strongly influences the nucleation density and hence the film morphology, ultimately determines the electrical and thermal properties of an electronic or thermal management application. The interface with the hydrocarbon vapor is where the growth takes place, and has been the subject of considerable attention, both experimental and theoretical. In this article we address some recent theoretical advances in understanding a few of the aspects of both of these interfaces. Of course, actual applications will also be strongly influenced by the bulk properties of the diamond material; this is a topic that we do not address in this paper.

The recent advancements in calculations of materials properties have been highlighted in MRS proceedings [1], which demonstrate that many properties can be predicted (often from first principles methods) and great improvements in the understanding of the microscopic processes have resulted. It is natural, and important, that these methods be applied to emerging fields of science and technology, such as diamond and other wide bandgap insulators (the subject of this symposium) or, for example, the novel fullerene materials discussed elsewhere at this conference. In this paper we address diamond properties, which involves an understanding of the chemistry of carbon at the most basic level.

Mat. Res. Soc. Symp. Proc. Vol. 242. © 1992 Materials Research Society

Basic principles and concepts

Since the recent surge in growth of diamond films, much progress has been made, but the growth of near-perfect diamond monoliths that will be necessary for many optoelectronic applications is still somewhere in the future. In light of the commonplace fabrication and application of silicon chips for two decades, the question arises: in what way(s) is diamond so different from silicon (or germanium, for that matter)? There must be important differences; after all, life is based on hydrocarbons and not on hydrosilicons, in spite of the abundance of available silicon!

In many ways C is similar to Si. Carbon is isovalent with silicon, it forms the same semiconducting tetrahedrally bonded crystal structure, and their bulk electronic band structures are isomorphic, with both materials possessing indirect bandgaps with the conduction band minimum about 75% of the way along the <100> direction to the Brillouin zone (BZ) boundary. In fact, the band structure of diamond is virtually that of silicon stretched by a factor of two: the valence bandwidth is ~24 eV compared to silicon's 12 eV, and the direct bandgap throughout the BZ is approximately twice the 3.5-5 eV Si value [2]. Because the electronic gap is indirect rather than direct, the factor-of-two difference in direct gaps translates into a factor of five difference, 5.5 eV vs. 1.17 eV, in electronic gap and therefore a considerable difference in their electronic properties.

Many of the ways in which diamond differs from silicon are directly related to the reasons it is pursued for technological purposes: it is much harder and more resilient at high temperatures, it is transparent to higher frequencies, its thermal conductivity is much higher, its atomic density is the highest of any common solid. These differences derive at the most basic level from two differences between the C and Si atoms: their sizes, and the characteristics of their s and p valence states. The valence wavefunctions peak in C around two-thirds of the radius of the corresponding peaks in Si; this accounts for the lattice constant of diamond being only 2/3 that of Si (and an atomic density nearly 3.5 times greater).

In addition to the size difference, the s and p valence states bear a different relationship in the two atoms: in C there are no core p states for the valence p state to be orthogonal to, and as a result the p wavefunction shares more strongly the same region of space with the s wavefunction compared to the case in Si, where the p wavefunction peaks noticeably beyond the s wavefunction. In addition, Papaconstantopoulos' tight-binding fits [3] to diamond and Si indicate that the s and p on-site energies are relatively closer in energy (after being scaled down by the factor of two) in diamond than in Si. These two differences would seem to make for a more ideal sp^3 hybrid bond in diamond; whether or not this is the fundamental reason, the diamond bond strength is considerably greater than in Si.

The diamond covalent bond strength, and its large atomic density, and small atomic mass all contribute to its properties, and particularly to its nucleation and growth. Their interrelationships are undoubtedly complicated and certainly are not well understood at present. Perhaps keeping some of these basic properties in mind can help us in understanding the interface behavior of diamond as it is steadily revealed by experiment and by calculation.

Numerical Electronic Structure Studies

Below we provide some results and analysis of density functional calculations carried out in the local (spin) density approximation (LDA). This highly successful calculational method has been reviewed in detail elsewhere [4], and our specific methods of calculation [5-7] have also been described previously. We only note that all calculations have been carried out with full potential (no shape approximations) self-consistent methods, since this factor is very important in dealing with the low symmetry situations encountered at surfaces and interfaces. The results for chemical processes at the diamond "surface" have in fact been obtained using carbon clusters [8] in which dangling bonds at the cluster edges are capped off by hydrogen atoms. This procedure removes the dangling bond states from the gap regions and restores the carbon atoms to a more-or-less bulk diamond environment. An example of such a cluster is shown in Fig.1. The results for the diamond-metal interfaces are obtained with the superlattice geometry [4], as is almost always the case in such theoretical studies.

HYDROCARBON PROCESSES AT THE DIAMOND SURFACE

Rather little is known at present about the microscopic processes governing diamond nucleation and growth, but models have been suggested that provide at least straw men to be confronted. Tsuda et al. [9] laid out a mechanism that relies primarily on the addition of methyl radicals to the (111) surface, and assumes that the methyl-terminated surface is energetically stable. Frenklach and Spear [10] have suggested a model that depends on the addition of acetylene molecules to the diamond surface. Harris [11] has introduced a model based on methyl radical adsorption on the (110) surface. Yarbrough [12] has provided enlightening discussions of these models and of the additional factors that arise in the growth process. In light of the difficulty in observing chemical processes at the diamond surface (especially in the presence of a plasma) these models require theoretical studies of elementary chemical reactions at the diamond surface to ascertain whether they are viable possibilities. We have obtained results for a number of these situations, some of which we review here.

Adsorption of methyl species

Adsorption of a methyl radical CH_3 onto a dangling bond on the diamond (111) surface results in a calculated bond length of 2.92 a.u., within 1% of the (calculated and experimental) C-C spacing in diamond, and a binding energy of 4.5 eV. Evidently this is a perfectly placed, tetrahedrally bonded C atom ideally suited to continuing the diamond surface. However, the umbrella-like structure of three H atoms comes into play as more methyl radicals are considered.

When we allow a second methyl radical to bond to a dangling bond next to the first adsorption site, steric repulsion between the neighboring H umbrellas occurs. We calculate the difference in energy between two isolated adsorbed methyls and two neighboring methyls (substantially relaxed but not completely so) to be 0.7 eV; this is (an upper limit to) the energy of steric repulsion. Compared to the (calculated) C-C bond energy of 4.5 eV, this is a rather small price to pay, if it is one of few process-

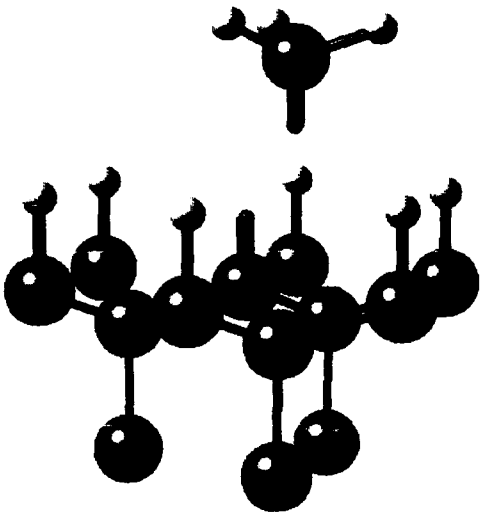


Figure 1. An example of a cluster used to study the adsorption of a methyl radical (above) on a diamond (111) surface. Large balls denote carbon atoms; small balls indicate hydrogen. For clarity, many bond-capping hydrogens at the edges and bottom of the cluster have not been shown.

es available. Therefore we expect neighboring adsorbed methyls on the (111) surface to be an energetically allowed configuration.

We next considered the situation of three adjacent methyl groups. Allowing the nine H atoms of the three umbrella to relax (within the constraint of C_{3v} symmetry) leads to a steric repulsion of 3.65 eV (again an upper bound), primarily due to a triangle of three H atoms spaced at a distance of 2.6 a.u. For such a configuration, it would require only about 1 eV to break a C-C bond and liberate a methyl radical from the surface, or conversely, only 1 eV would be gained by adsorbing the third methyl group in the presence of the other two and a neighboring dangling bond. Since H abstraction reactions {$CH_4 + H \rightarrow CH_3 + H_2$} are believed to involve 0.5-0.7 eV [13] and occur often, islands of three methyl groups should disappear quickly if they form. Even worse (for this model of diamond growth), reactions in which H would replace one of the three methyl groups would be exothermic. These considerations lead us to expect that triplets of methyl groups on the diamond surface will not be a likely enough occurrence to lead to, or even allow, diamond growth.

Acetylinic species at the diamond surface

It requires considerably more energy (1.3 eV by our calculations, 0.9 eV is the experimental value) to break a C-H bond in acetylene than in methane, assuming H_2 to be the result in both cases. This result suggests, in agreement with experimental

population analyses, that the concentration of acetylinic radicals in the vapor is considerably less than that of methyl radicals. However, since diamond growth is a difficult process to nucleate and is often slow, allowing the possibility that low concentration species may be important, we have investigated some acetylinic chemical processes.

For an acetylene radical bonded to a dangling bond on the (111) surface, the bond length is calculated to be 2.76 a.u., 5% smaller than the bond length in diamond. Apart from the "double bond" character suggested by the bond length, this process leads to an extra C atom that, although not precisely in place to replicate a diamond lattice, is bonded to one C atom and is available for further chemical processes.

Frenklach and Spear [10] have argued the importance of the acetylene molecule, which is expected to react strongly with a dangling bond. In fact, their mechanism invokes the binding in such a situation, which is not an foregone conclusion. It is not easy to simulate this interaction in full generality, but we have studied two related reactions. First we allowed the interaction of an acetylene molecule with a dangling bond (simulated in this case by a methyl radical). If the acetylene is constrained to be rigid, the reaction is repulsive, but if the intra-acetylene C-C length is allowed to adjust binding will occur, but it is very weak.

Secondly, we were able, using newly developed numerical algorithms that calculate the forces on atoms, to allow the three C atoms and the two acetylene H atoms to relax as the chemical interaction proceeded. Substantial relaxation occurred; one acetylene C bonded to the dangling bond carbon atom (at a distance 2.87 a.u. very close to bulk diamond), and the acetylene assumed a vinyl-like bent configuration with a chemically active site on the other acetylinic C. The binding energy was calculated to be 1.9 eV. Geometrically, the resulting configuration appears to be favorable for further processes that could extend a diamond lattice.

Improved energies with generalized-gradient LDA.

Although we have not emphasized it above, LDA-based calculations tend to overestimate molecular binding energies by roughly 10% to perhaps 20%. For many purposes, such as the idealized studies described above, this overbinding is not disastrous. As studies get more realistic however, this inaccuracy could be a problem and even a limitation of the method.

Fortunately, a microscopically based extension using not only the value of the density $n(\underline{r})$ to obtain the exchange-correlation potential $v_{xc}(\underline{r})$ but the gradient $dn(\underline{r})/d\underline{r}$ as well, has been introduced by Langreth and Mehl [14], extended by Perdew and Wang [15], and recently perfected by Perdew [16]. The result has been shown, by the extensive collaboration of Perdew et al. [17], to give a very considerable improvement in the predicted energies of atoms, molecules, surfaces, and solids. These references should be consulted for further information about the methods and general results.

For the present purposes, the important implications arise from the calculations by Pederson and Jackson on small hydrocarbon molecules that are reported in [17]. The results, shown in Table I, demonstrate that energies of hydrocarbon molecules are vastly improved, by a factor of six, by the gradient corrections,

TABLE I

Comparison of the calculated atomization energies (in eV) of five hydrocarbon molecules, in Hartree-Fock (HF), local spin density (LSD), and generalized gradient (GG) local spin density calculations, compared with the experimental (EXP) values (with zero-point vibrational energy removed). Also shown is the RMS error per bond for the seven molecules, which is improved with GG by a factor of six over the LSD result. The density functional calculations were performed using a basis of 18s, 9p, and 4d even-tempered Gaussians on each atom (65 basis functions per atom). The experimental numbers are from Clementi and Chakravarty (reference given below).

Molecule	# of bonds	HF	LSD	GG	EXP
H_2	1	3.63	4.89	4.55	4.75
C_2 (AFM)	1	0.73	7.51	6.55	6.36
C_2H_2	3	13.00	20.02	18.09	17.69
CH_4	4	14.39	20.09	18.33	18.40
C_2H_4	5	18.71	27.51	24.92	24.65
C_2H_6	7	24.16	34.48	31.24	31.22
C_6H_6	12	45.19	68.42	61.34	59.67
RMS error / bond		2.40	0.67	0.10	---

Experimental reference:
E. Clementi and S. J. Chakravarty, J. Chem. Phys. 93, 2591 (1990).

TABLE II

Table II. Theoretical interface energies, defined as the energy for the interfacial system minus the bulk energies for the corresponding number of C and Ni atoms, for both (111) and (100) interfaces and both "atop" and "in-hollow" geometries. The predicted Schottky barrier heights (SBH) are also given.

Interface and geometry	Interface energy (eV)	SBH (eV)
(111) in-hollow	1.06	0.84
(111) atop	0.97	0.0
(100) in-hollow	1.92	0.92
(100) atop	1.03	0.0

and that the energies are approaching chemical accuracy, with RMS errors of 0.1 eV per bond. Although the gradient corrected functional has not yet been applied to chemical processes at the diamond surface because of it novelty, its application can be done readily in any future calculations. It appears that very accurate energies for such interactions can now be obtained.

THE DIAMOND-NICKEL INTERFACE

An important application of diamond films could be as Schottky barriers in electronic components that are more stable in high power, high temperature applications than are currently available Schottky systems. Even for applications of diamond films as wear-resistant coatings or thermal diffusers, a knowledge of the diamond-metal interface properties is important. As a first step in understanding diamond-metal interfaces, we have carried out detailed studies [5,7,18,19] of the diamond-nickel interface.

Nickel was chosen [5] for a combination of reasons: (1) its lattice constant is within 1.5% of that of diamond, making the lattice-matched case that we can treat a realistic model; (2) it is not a carbide former, so the abrupt interface idealization that we study is a reasonable candidate for fabrication; (3) the Fermi level within the d-bands, and the magnetism, make Ni a potentially much richer material for unusual applications than, for example, the non-magnetic, sp-band metal Cu, which also satisfies the previous two qualities. In addition, we have been encouraged by experimental attempts to grow diamond epitaxially on Ni [20-22]. Because the exchange splitting in Ni is an order of magnitude smaller than the band gap of diamond we have neglected it in our calculations up to this time.

We have completed thorough self-consistent calculations for abrupt (100) and (111) interfaces. Growth of diamond films on nickel up to the present time probably have not resulted in abrupt interface [21] (perhaps there is not yet <u>any</u> abrupt interface involving diamond), but high quality polycrystalline diamond films have been grown [20]. However, there seems to be no reason why Ni or other metals could not be deposited on clean diamond surfaces to produce abrupt interfaces. For both (100) and (111) interfaces, we have treated two possibilities for C-Ni bonding configurations at the interface: one in which the C atom at the interface is kept four-fold coordinated, emphasizing covalent tetrahedral bonding, and one in which the C atom is more highly coordinated, more consistent with a metallic type of bonding. We refer to these as "atop" and "in-hollow" geometrical configurations, respectively. In all cases the energy has been minimized with respect to the most important structural parameter, the distance between the C and Ni layers at the interface.

<u>Interface energies and stability</u>

Our results can be stated succinctly: for both (100) and (111) interfaces the "atop" geometry, in which covalent tetrahedral configurations are emphasized, is energetically more stable than the metallic "in-hollow" geometry. This strongly suggests that satisfying the C atom's dangling-bond states at the interface is an important consideration. At the onset this result was not at all obvious. Certainly it should be important to attend to the dangling bond states if possible, but it is not clear that Ni can do so in any case: these dangling bonds are the

result of a strong covalent mixture of the C s and p states which in bulk diamond are spread over an occupied valence band region 24 eV wide, while Ni has primarily d states (with some s admixture) spread only over 4 eV below the Fermi level E_f. Therefore it could be the case that the dangling bonds cannot be accommodated regardless of how the adjacent Ni layer is positioned. Whatever the reasons, and they are difficult to determine uniquely, the tetrahedrally coordinated C atom at the interface is found to be preferred. The interfaces energies for both interfaces and for both geometries are given in Table II.

Schottky barrier heights

Our predicted Schottky barrier heights for all four cases are also presented in Table II. The Schottky barrier discussed here is the separation of the Ni Fermi level and the diamond valence band maximum, which is the intrinsic barrier to conduction in p-type diamond. The interfaces are ohmic (barrier height of less than 0.1 eV) for both cases in which tetrahedral coordination of the C atom at the interface is enforced. The Schottky barrier heights are ~0.9 eV for the more metallically coordinated interfaces.

These results are quite unusual in two ways. First, the prediction of an intrinsic ohmic barrier is unexpected, since in the considerable variety of local density calculations of Schottky barrier heights for Si, Ge, GaAs, and a few other semiconductors the barrier height is always (to our knowledge) a significant fraction of the band gap of the semiconductor. The complete vanishing of the barrier height indicates that diamond is displaying novel barrier formation behavior not found previously in studies on abrupt interfaces.

Secondly, the difference in barrier heights of nearly 1 eV between the high and low coordination geometries is also unanticipated. Although the number of Schottky systems in which the geometry has been varied is relatively few, again we are unaware of such a considerable dependence on the character of the bonding across the interface. Together with the vanishing of the Schottky barrier for the tetrahedral coordination, this result suggests novel bonding behavior is occurring at the diamond-nickel interface. We have also obtained similar results for Cu and for Al instead of Ni (in less extensive calculations), so the peculiarity seems to be associated with the diamond itself.

To address the basis of this behavior we have studied the interface band structure in some detail, as well as that of an ideal (i.e. unrelaxed and unreconstructed) (111) diamond surface. For the surface the dangling bonds give rise to a partially occupied surface band that fixed the Fermi level 1 eV above the valence band maximum. The corresponding interface bands, presented and discussed at more length in Ref. [19], strongly mix with Ni 3d states near the Fermi level, producing a pair of interface bands that are near or in the gap.

The upper band is unoccupied and does not influence the results. The lower band is partially occupied, however, and is energetically lower for the tetrahedral geometry than for the inhollow geometry, much as a bonding combination would be. This lowering of the active interface band results in the lowering of the Schottky barrier height and likely is a strong influence in the energetic stabilization of the tetrahedrally coordinated interface.

The electronic structure of these novel diamond-metal interfaces has been [18], or will be [19], discussed elsewhere. However, this short discussion should make clear that the diamond Schottky barrier is presenting us with an exciting scientific questions as well as posing an important technological problem.

SUMMARY AND ACKNOWLEDGMENTS

We have presented only a selection of our recent results to provide an indication of how careful numerical computation, often in combination with experimental results and suggestions, is contributing to the understanding of systems involving diamond and other wide band gap materials.

We thank J. P. Perdew for helpful discussions, insights, and computer subroutines for the GGA portion of this paper. This work has been supported by the SDIO Innovative Science and Technology Program through the Office of Naval Research, Contract No. N00014-91-WR-24138. Calculations were performed on the IBM 3090 at the Cornell National Supercomputer Facility as well on U.S. Navy supercomputers.

REFERENCES

[1] Collections of papers are available in J. Mater. Res. 11, (1990); Diamond, Boron Nitride, Silicon Carbide and Related Wide Bandgap Semiconductors, edited by J. T. Glass, R. Messier, and N. Fujimore (Materials Research Society, Pittsburgh, 1990); Technology Update on Diamond Films, edited by R. P. H. Chang, D. Nelson, and A. Hiraki (Materials Research Society, Pittsburgh, 1989).
[2] See, for example, W. E. Pickett and C. S. Wang, Phys. Rev. B30, 4719 (1984).
[3] D. A. Papaconstantopoulos, Handbook of the Band Structure of Elemental Solids (Plenum, New York, 1986), pp. 227-233.
[4] R. O. Jones and O. Gunnarsson, Rev. Mod. Phys. 61, 689 (1989).
[5] S. C. Erwin and W. E. Pickett, Phys. Rev. B41, 9756 (1990).
[6] M. R. Pederson, K. A. Jackson, and W. E. Pickett, Phys. Rev. B44, 3891 (1991).
[7] S. C. Erwin and W. E. Pickett, Surf. Coatings Technol. 47, 487 (1991).
[8] M. R. Pederson, K. A. Jackson, and W. E. Pickett, in Proceedings of the 2nd International Conference on the New Diamond Science and Technology, edited by R. Messier and J. Glass, MRS International Conference Proceedings (Materials Research Society, Pittsburgh, 1991).
[9] M. Tsuda, M. Nakajima, and S. Oikawa, J. Am. Chem. Soc. 108, 5780 (1986); Jpn. J. Appl. Phys. 26, L527 (1987).
[10] M. Frenklach and K. E. Spear, J. Mater. Res. 3, 133 (1988); D. Huang, M. Frenklach, and M. Maroncelli, J. Phys. Chem. 92, 6379 (1988).
[11] S. J. Harris, Appl. Phys. Lett. 56, 2296 (1990); S. J. Harris, D. N. Belton, and R. J. Blint, New Diamond Science and Technology, edited by R. Messier and J. Glass (Materials Research Society, Pittsburgh, 1991), pp.277-290.
[12] W. Yarbrough, J. Vac. Sci. Technol. A 9, 1145 (1991); W. A. Yarbrough, Diamond Optics IV, edited by S. Holly and A. Feldman, (SPIE, 1991).

[13] S. P. Walch, J. Chem. Phys. 72, 4932 (1980); M. J. Kurylo, G. A. Hollinden, and R. B. Timmons, J. Chem. Phys. 52, 1773 (1070).
[14] D. C. Langreth and M. J. Mehl, Phys. Rev. B28, 1809 (1983).
[15] J. P. Perdew and Y. Wang, Phys. Rev. B33, 8800 (1986); J. P. Perdew, Phys. Rev. B33, 8822 (1986),(E) B34, 7406 (1986).
[16] J. P. Perdew, in Proceedings of the 21st Annual International Symposium "Electronic Structure of Solids," edited by P. Ziesche (Nova Science, in press); Phys. Rev. B (in press).
[17] J. P. Perdew, J. A. Chevary, S. H. Vosko, K. A. Jackson, M. R. Pederson, D. J. Singh, and C. Fiolhais, Phys. Rev. B (in press).
[18] S. C. Erwin and W. E. Pickett, Superlattices and Microstructures 7, 335 (1990).
[19] S. C. Erwin and W. E. Pickett, submitted to Solid State Commun.
[20] Y. H. Lee, K. J. Bachmann, J. T. Glass, Y. M. LeGrice, and R. J. Nemanich, Appl. Phys. Lett. 57, 1916 (1990).
[21] D. N. Belton and Schmeig, J. Appl. Phys. 66, 4224 (1989).
[21] R. A. Rudder et al., in Diamond Optics, edited by A. Feldman and S. Holly (SPIE, 1989).

GROWTH TECHNIQUE FOR LARGE AREA MOSAIC DIAMOND FILMS†

R. W. Pryor,* M. W. Geis,** and H. R. Clark**
* Institute for Manufacturing Research, Wayne State University, Detroit, MI 48201
** Lincoln Laboratory, Massachusetts Institute of Technology, Lexington, MA 02173

ABSTRACT

A new technique has been developed to grow semiconductor grade diamond substrates with dimensions comparable to those of currently available Si wafers. Previously, the synthetic single crystal diamond that could be grown measured only a few millimeters across, compared with single crystal Si substrates which typically are 10 to 15 cm in diameter. In the technique described, an array of features is first etched in a Si substrate. The shape of the features matches that of inexpensive, synthetic faceted diamond seeds. A diamond mosaic is then formed by allowing the diamond seeds to settle out of a slurry onto the substrate, where they become fixed and oriented in the etched features. For the experiments reported, the mosaic consists of seeds ~ 100 μm across on 100 μm centers. A mosaic film is obtained by chemical vapor deposition of homoepitaxial diamond until the individual seeds grow together. Although these films contain low angle (<1°) grain boundaries, smooth, continuous diamond films have been obtained with electronic properties substantially better than those of polycrystalline diamond films and equivalent to those of homoepitaxial single crystal diamond films. The influence of growth conditions and seeding procedures on the crystallographic and electronic properties of these mosaic diamond films is discussed.

INTRODUCTION

The ability to fabricate diamond has been the elusive goal of scientific researchers and their alchemist predecessors for over 2000 years [1]. Numerous different techniques have been tried, with little success [2]. Only within the last 50 years, with the discovery of various high pressure techniques [3,4], has it at last been possible to reproducibly fabricate single crystal diamond materials. The materials that result from these processes can be of excellent quality, in some cases better than natural diamonds [5]. The synthetic diamonds are quite small, however, usually much less than 1 cm in their largest dimension and typically in the range of a few micrometers to less than a millimeter. Such diamonds are generally fabricated for use as abrasives in industrial materials processing applications.

---

† This work was sponsored by the Michigan Research Excellence Fund through the Institute for Manufacturing Research at Wayne State University and by SDIO/OST through the Office of Naval Research.

During the last half century, researchers have also sought to fabricate diamond materials using low pressure processes [6,7], and some limited success has been realized. Research during the last 10 to 15 years has resulted in the ability to fabricate small area polycrystalline diamond films and subsequently the capability of making large area polycrystalline thin films by several different methods [8]. Even though these polycrystalline thin film diamond materials have been achieved only recently, they are no longer just laboratory curiosities. Such films have become interesting and valuable materials in the early stages of a broad applications development phase.

To be able to use the properties of diamond to the maximum extent, methods need to be developed to facilitate the growth of large area, single crystal diamond sheets. Such sheets would allow utilization of the high thermal conductivity, great mechanical strength, and unique electronic properties of diamond. The work reported here, which addresses only a small aspect of diamond properties, is one such attempt. It is the result of a focused research effort in diamond materials development directed toward microelectronics applications. The work emphasizes the development of semiconductor grade diamond for application in the new area of high speed, high power diamond microelectronics. The materials being developed will also have spin-off applications in the area of thermal management of conventional semiconductor device materials, such as Si and GaAs, and in mechanical applications areas. Indeed, the new large area mosaic diamond materials discussed here are near single crystal quality and will be potentially usable in many new applications areas.

SUBSTRATE PREPARATION

Mosaic diamond films are made from small, inexpensive (about $1 per carat) diamond abrasive crystals fixed on a patterned Si substrate. The first major step in the preparation of the substrate is to photolithographically pattern an etch mask onto the (100) surface of a Si wafer. To do this, the outer surface of the Si wafer is thermally oxidized to a depth of 100 nm. A layer of photoresist is then applied to the oxidized, polished side and exposed to form an array of squares (Fig. 1). In this case, the squares are initially sized so that the final etched pits are 90 μm square on 100 μm centers. It is important to size the apertures in the photoresist to allow for the undercut of the SiO_2 mask during etching. The SiO_2 mask layer is then patterned through the resist (Fig. 2) using an appropriate etchant, such as HF or BHF.

The Si wafer is selectively etched through the oxide mask on the Si (100) surface by immersing the wafer in a solution of either 10% $(CH_3)_4NOH$ or 25% KOH (by weight) in water at 90 °C [9] (Fig. 3). Over a period of several hours, tetrahedral pits are formed in the volume of the Si wafer. The wafer is then removed from the selective etching solution, and the SiO_2 mask layer is stripped off with an HF solution.

At this point, a decision needs to be made whether or not to add a diamond nucleation inhibition layer to the Si wafer surface. Such a layer must be considered because of the differential nucleation and growth of diamond during the growth phase. If the conditions in the reactor and at the surface of the mosaic wafer are appropriate, diamond growth will occur on both the mosaic of seeds and on the patterned wafer between the seeds. On the seeds, the growth is homoepitaxial as is desired. On the wafer, however, the growth is polycrystalline and can obstruct the formation of clean, low angle grain boundaries as the seeds expand to closure.

The rate at which the polycrystalline diamond phase nucleates on the patterned Si wafer surface is highly dependent on the nature of the surface, the specific preparatory steps used prior to the diamond growth, and the initial and sustained

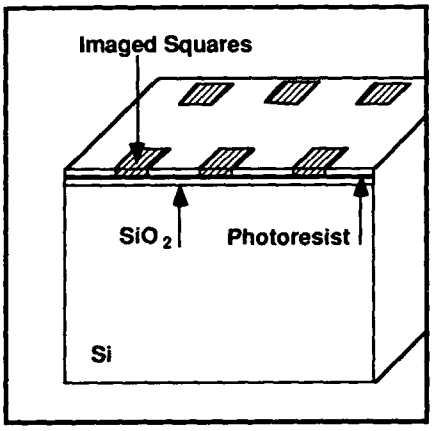


Fig. 1 Photolithographic Array Formation

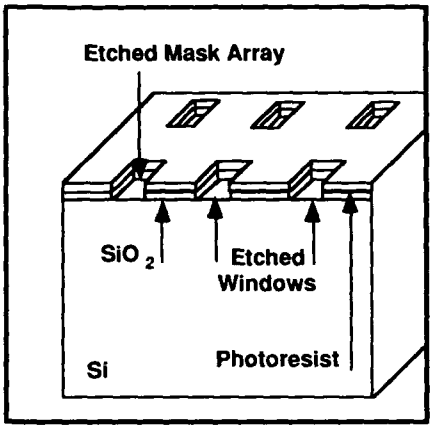


Fig. 2 Etched SiO_2 Mask

conditions experienced by the mosaic substrate in the growth reactor. Here, we describe two fundamentally different, but complementary, technologies [10,11] for the growth of mosaic diamond materials. The technology developed at MIT Lincoln Laboratory uses a hot filament chemical vapor deposition (HFCVD) system [12]. The technology developed in the Institute for Manufacturing Research at Wayne State University, based on a microwave approach, uses a microwave plasma enhanced chemical vapor deposition (MPECVD) system. The details of the MPECVD system are discussed elsewhere [13].

In the HFCVD system, at least one set of conditions exists where the homoepitaxial diamond growth on the seeds is faster than the growth of the polycrystalline diamond on the patterned Si wafer. This results in the homoepitaxial diamond material on the seeds overgrowing the polycrystalline diamond on the wafer and eventually forming a continuous, near single crystal diamond film.

In the MPECVD system, a different approach has been adopted. With the prevailing growth conditions in the MPECVD reactor, the homoepitaxial diamond forms on the seeds at a rate comparable to that of the polycrystalline diamond on the wafer between the seeds. If the polycrystalline diamond is allowed to nucleate and grow freely, the homoepitaxial diamond formation on the seeds is limited in extent by the polycrystalline diamond formation on the wafer. The solution to this problem was found in some earlier selective nucleation studies [14]. In these studies, oxidation and plasma cleaning of the Si wafer surface before the diamond deposition were found to significantly reduce the number of spurious polycrystalline diamond nuclei that form on the Si surface. The nucleation suppression is accomplished by the application of a 100 nm layer of thermal oxide to the unseeded substrate after the formation of the etched tetrahedral pits (Fig. 4) and prior to seeding.

The diamond seeds used in this process are small abrasive grains that are readily available [15] for industrial materials processing applications. At this time the role of diamond seed quality is still being determined, and will probably need to be a major consideration in the future for the formation of thick diamond materials for

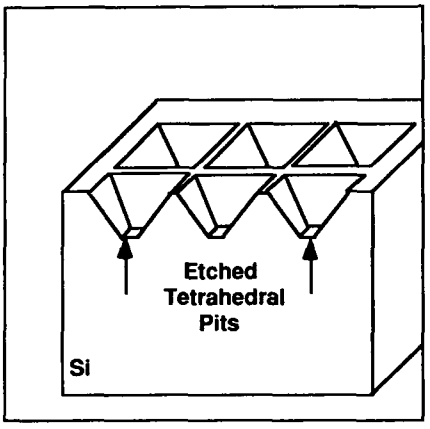


Fig. 3 Etched Tetrahedral Pits

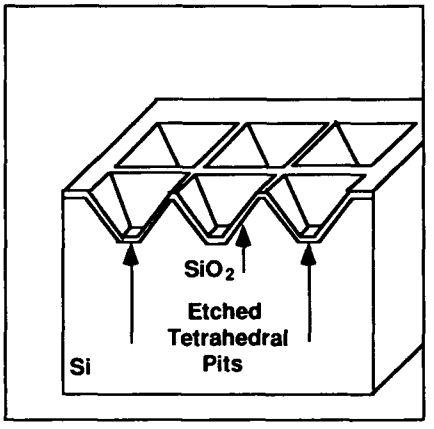


Fig. 4 Oxidized Patterned Substrate

thermal or optical applications. For current microelectronics applications research, where the initial growth to planarity forms a diamond substrate and the active layers (a few micrometers thick) are deposited on top of that growth, it is not a major factor.

For the present research, the diamond seeds are sorted by size and shape, selecting those that are ~ 100 μm on an edge and as close to octahedral (truncated octahedra) as possible. The seeds are cleaned in hot (350 to 400 °C) $NaNO_3$ for 10 min, immersed in a concentrated solution of HF and HNO_3 for another 10 min, and then rinsed in deionized water and acetone and dried. The seeds are then suspended in a slurry using hot H_2SO_4, concentrated HF, or an organic solvent and 0.01% novolac polymer. The polymer acts as a glue to fix the well-faceted seeds in the pits. (For additional details on this process, see reference 9.)

A batch of slurry can be reused. After a few seeding runs, however, the grains should be recleaned and a new slurry made. Residual seeds from a slurry should be reexamined for shape, since the best formed octahedra tend to be selected out in the seeding process and only the less well shaped seeds remain. After the seeding and before the new diamond growth, the wafer is baked at 350 °C and then cleaned either in an oxygen plasma at 15 mTorr or by reactive ion etching for a few minutes. Figure 5 shows a schematic drawing of an oxidized seeded substrate. Figure 6 shows a scanning electron micrograph (SEM) of an oxidized seeded substrate, in which both empty and seeded tetrahedral pits can be seen.

SEED ALIGNMENT

The successful fabrication of near single crystal quality diamond materials using the large area mosaic diamond technique depends initially on three factors: the shape of the seeds and the accuracy of the rotational and the axial (vertical) seed orientation after placement. For well-faceted seeds, the rotational alignment error between the (311) plane of the etched Si substrate and the (311) planes of the diamond seeds, as determined by x-ray diffraction measurements, is typically on the

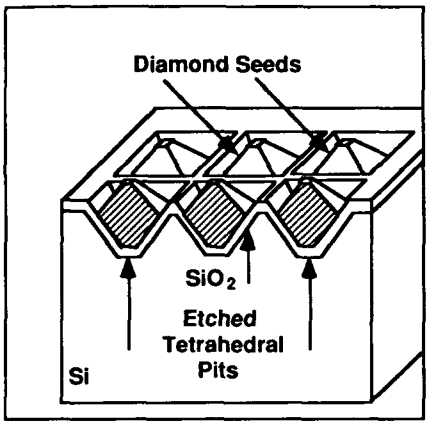


Fig. 5 Schematic of Oxidized, Seeded Mosaic Diamond Substrate

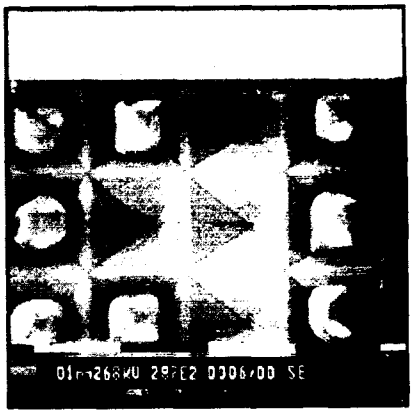


Fig. 6 SEM of Oxidized, Seeded Mosaic Diamond Substrate

order of 1° or less (Fig. 7). The axial orientation alignment error for the diamond seeds has also been determined by x-ray diffraction studies and found to be typically on the order of 0.5° or less (Fig. 8).

MPECVD GROWTH

The large area diamond seeded mosaic substrates used in this work were prepared by the above described technique at Lincoln Laboratory with the collaboration of Wayne State University. The homoepitaxial diamond growth on the substrates was performed at Wayne State University using MPECVD. For successful large area, near single crystal diamond sheet growth, modifications needed to be made to the as received MPECVD equipment [11], and new process parameters and techniques needed to be developed. The initial MPECVD diamond reactor [16] is shown schematically in Fig. 9. This system was modified by the Wayne State University diamond laboratory to enhance the initial polycrystalline diamond deposition capability. A modification was made to allow the system to utilize multiple gases (e.g., H_2, CH_4, O_2, and CO) simultaneously. In addition, the susceptor assembly was remodeled to improve deposition uniformity and reproducibility by incorporating a biasable refractory metal susceptor shield (Fig. 10). The shield shrouds the susceptor and prevents erosion of the susceptor material by reactive gases in the chamber. It also ensures that the composition of the desired reactive gases is not altered by gaseous erosion products generated by the susceptor. A major potential source of reactive gas contamination, undesirable trace materials in the susceptor, is thus eliminated.

The seeded substrates are inserted into the reactor substantially as received from Lincoln Laboratory. The reactor is pumped down, and the substrate temperature is raised to 900 °C, where it is held for the duration of the process. After pump-down of the reactor chamber, a substrate is prepared for diamond growth. This preparation starts with a 30 min, 900 sccm H_2 plasma etch, at a pressure of 25 Torr and a power

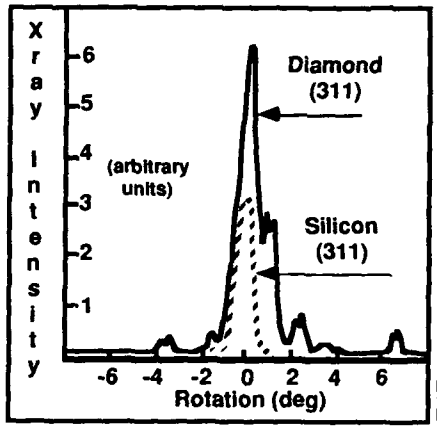


Fig. 7 Rotational Alignment of Seeds and Substrate

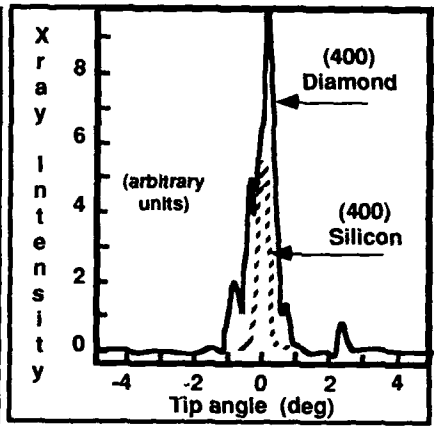


Fig. 8 Axial Alignment (Tip Angle) of Seeds and Substrate

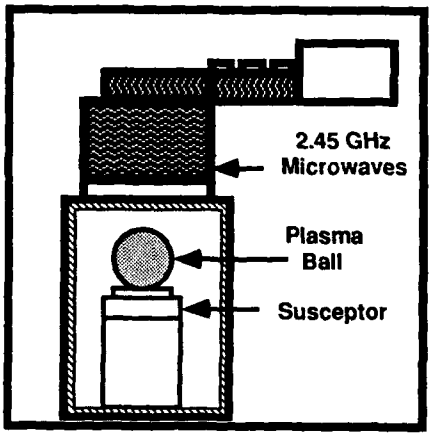


Fig. 9 MPECVD Diamond Deposition System

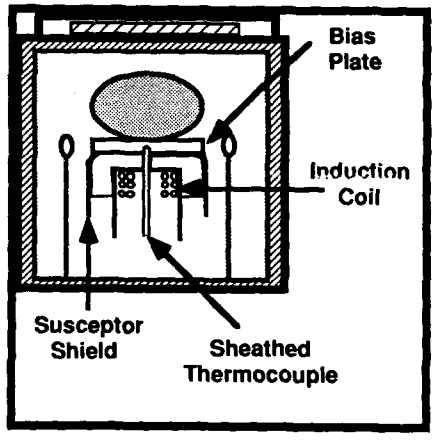


Fig. 10 Modified MPECVD Diamond Deposition System Showing Susceptor Detail

level of 1 kW. The H_2 etch is used to clean off any residual contamination on the substrate, and it has been observed to significantly reduce the number of nucleation sites available for the formation of polycrystalline diamond. Next, the seeded substrate receives a 25 min, 400 W plasma substrate passivation treatment in a gas mix comprising 25 sccm O_2, 50 sccm H_2, and 2000 sccm Ar, at a pressure of 25 Torr. This passivation treatment reoxidizes the Si surface and cleans any residual contamination off the diamond seeds.

Once the sample has been prepared in the reactor, the next step in the growth of a large area mosaic diamond sheet is to alter the reactor gas mix to yield new homoepitaxial diamond growth (111) on the octahedral diamond seeds. In early experimentation, both at Lincoln Laboratory and Wayne State University, it was found that the best mix for growth of polycrystalline diamond also grew polycrystalline diamond all over the seeded substrates. The best polycrystalline diamond grown at Wayne State University in the MPECVD system was on a diamond-bombarded Si substrate at 900 °C with a gas mix of 990 sccm H_2 and 10 sccm CH_4, at a pressure of 45 Torr and a power of 1.5 kW. In order to grow homoepitaxial diamond without the polycrystalline diamond, however, the gas mix had to be changed significantly. The best large area mosaic diamond grown thus far was with 900 sccm H_2,12 sccm CH_4, and 4.5 sccm O_2, at a pressure of 50 Torr and a power of 1.5 kW. In addition, it has been found necessary to periodically refresh the diamond nucleation inhibition layer by using a 15 min, 400 W plasma substrate passivation treatment in a gas mix comprising 25 sccm O_2, 50 sccm H_2, and 2000 sccm Ar, at a pressure of 25 Torr. Currently, this is done about once every 8 h, which is adequate but not necessarily optimal. Deviation from these nominal values significantly alters the character and morphology of the diamond material grown, both on the diamond seeds and on the Si substrate. A detailed presentation of the nature of the changes and their analysis will be the subject of a future paper.

DIAMOND MATERIALS ANALYSIS

The large area mosaic diamond materials grown at both Lincoln Laboratory and Wayne State University have been analyzed by various techniques. The results presented here should be considered preliminary, since the deposition processes at both facilities are currently the subject of active research. At present, because of the competing mechanisms within the reactor that tend to favor the growth of polycrystalline and/or nondiamond materials, the reproducibility of the growth process for large specimens is difficult, which has resulted in a limited number of high-quality samples. The largest specimen to date was grown at Lincoln Laboratory by HFCVD. It is approximately 1 x 2 x 0.025 cm and was obtained by the following technique. First, ~ 100 μm of diamond were grown on a seeded substrate. The Si portion of the seeded substrate was then etched away in a solution containing HF and HNO_3. After etching and cleaning, an additional 150 μm of homoepitaxial diamond was grown on the side previously covered by the Si substrate. This process completely buried the original seeds and resulted in a smooth specimen with a local surface roughness of a few micrometers.

Transmission x-ray diffraction topographic analysis for the above sample was done at Lincoln Laboratory using the (040) diamond crystal planes (Fig. 11). A portion of the sample was analyzed in a system with a 0.06° angle of acceptance and compared with a contiguous polycrystalline region in the same specimen (Fig. 12). Regions of the sample where the diamond (100) plane is within the acceptance angle show on the topograph as very dark. Regions in which angle of the (100) plane exceeds the acceptance angle, but deviates by less than a few tenths of a degree, show as darkened. Within the limits of resolution of this analysis, no major difference could be found between the measurements for the HFCVD large area mosaic diamond sample and those that would be expected for comparable single crystal diamond.

The morphology of the large area mosaic diamond material analyzed above, which was grown in the HFCVD system, is similar to that of material grown by MPECVD. Both materials appear smooth and uniform, with a local surface roughness

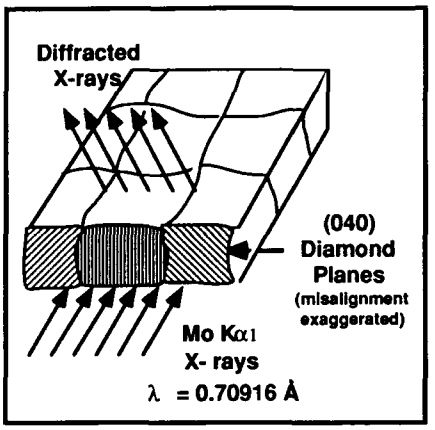


Fig.11 Configuration Schematic of Transmission X-ray Diffraction Topograph

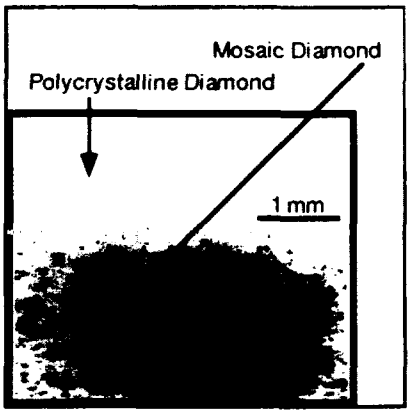


Fig. 12 Transmission X-ray Diffraction Topograph of HFCVD Mosaic Diamond



Fig. 13 SEM of MPECVD Mosaic Diamond

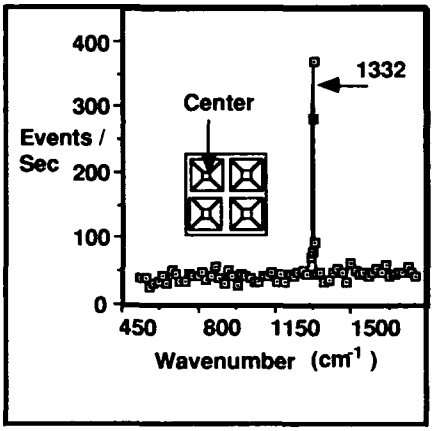


Fig. 14 Raman Spectrum of MPECVD Mosaic Diamond (Center)

of a few micrometers. In SEM images, it is difficult to find the grain boundaries in the mosaic diamond, unless one looks in the region of a missing seed. In the SEM of a T-shaped void in MPECVD-grown diamond, shown in Fig. 13, it can be seen that the material grows into the region of the missing seeds. The thickness of this sample is ~ 150 μm. If the growth process were continued, the voids at the location of missing seeds would eventually become filled.

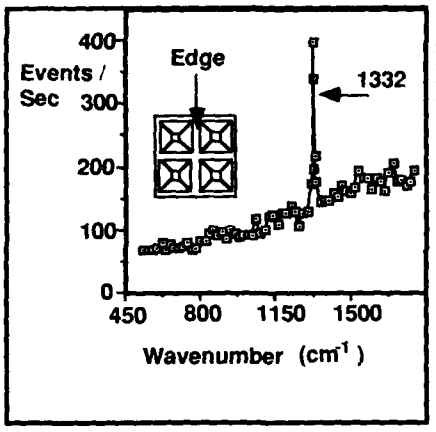


Fig. 15 Raman Spectrum of MPECVD Mosaic Diamond (Edge)

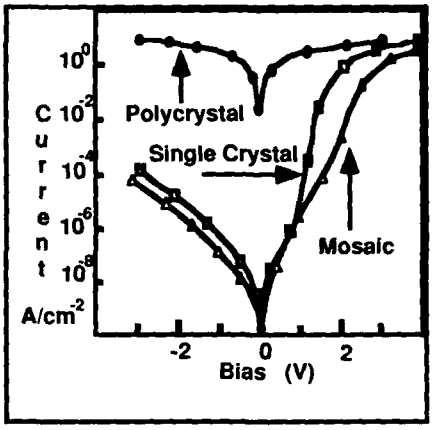


Fig. 16 Device Curves for HFCVD Mosaic Diamond

The microfocus Raman technique [17] has been used to analyze the mosaic diamond material grown in the MPECVD system. Measurements were made in regions corresponding to the nominal axis of a diamond seed (center) (Fig. 14) and to the space between the seeds (edge) (Fig. 15). Both Raman spectra show a well-defined peak at 1332 cm^{-1} and no additional peaks, such as those corresponding to amorphous or graphitic materials. The Raman spectrum for the diamond material grown at the boundary between seeds (Fig. 15) does show, however, an increased background photoluminescence, as might be expected in a region of higher disorder. Raman analysis of recently grown mosaic diamond shows a spectrum similar in quality and amplitude to that of natural diamond.

An additional method for testing the quality of large area mosaic diamond materials is by fabrication of microelectronic devices. At Lincoln Laboratory, diodes have been fabricated using polycrystalline, mosaic, and single crystal diamond (Fig. 16). Based on the initial results, the mosaic diamond and the single crystal diamond devices show comparable performance. The polycrystalline diamond diodes, however, consistently shorted.

SUMMARY AND CONCLUSIONS

A new method has been developed for the fabrication of large area diamond materials, in which small diamond seed crystals are oriented on an etched substrate and then grown together into a large, near single crystal quality diamond sheet. X-ray and Raman analyses of materials grown by this technique show that large area mosaic diamond can be comparable in quality to natural diamond. Initial microelectronic devices fabricated with the materials support this conclusion.

REFERENCES

1. G. Davies, *Diamond* (Hilger, Bristol, England, 1984), p. 2.

2. *Ibid.*, Chap. 4.

3. R. J. Wedlake, in *Properties of Diamond*, ed. J. E. Field (Academic, London,1979), p. 501.

4. F. P. Bundy, H. T. Hall, H. M. Strong, and R. H. Wentorf, Nature **176**, 51 (1955).

5. T. R. Anthony, W. F. Banholzer, J. F. Fleischer, L. Wei, P. K. Kuo, R. L. Thomas, and R. W. Pryor, Phys. Rev. B **42**, 1104 (1990).

6. B. V. Derjaguin and D. V. Fedosev, *Diamonds Wrought by Man* (State Mutual, New York, 1985), p. 45.

7. J. C. Angus and C. C. Hayman, Science **241**, 913 (1988).

8. J. D. Venables, *Status and Applications of Diamond and Diamond-Like Materials: An Emerging Technology* (National Academy, Washington, D.C., 1990), Vol. NMAB-445, Chap. 2.

9. M. W. Geis, H. I. Smith, A. Argoitia, J. Angus, G. H. M. Ma, J. T. Glass, J. Butler, C. J. Robinson, and R. Pryor, Appl. Phys. Lett. **58**, 2485 (1991).

10. M. W. Geis, patents pending.

11. R. W. Pryor, patents pending.

12. M. W. Geis, Proc. IEEE **79**, 669 (1991).

13. R. W. Pryor, R. L. Thomas, P. K. Kuo, and L. D. Favro, Proc. SPIE **1146**, 68 (1989).

14. R. W. Pryor, unpublished.

15. Available from General Electric and De Beers or their representatives.

16. The original MPECVD system was an AsTex Model HPMM, Applied Science and Technology, Inc., Woburn, MA 01801.

17. R. W. Pryor, P. K. Kuo, L. Wei, and R. L. Thomas, *Proceedings of the Sixteenth Annual Review of Progress in Quantitative NDE*, ed. D. O Thompson and D. E. Chimenti (Plenum, New York, 1989), p. 1123.

Chemical Vapor Deposition of Diamond Films Using Water:Alcohol:Organic-Acid Solutions

R.A. Rudder, J.B. Posthill, G.C. Hudson, D.P. Malta, R.E. Thomas, and R.J. Markunas, T.P. Humphreys[†] and R.J. Nemanich[†]

Research Triangle Institute, Research Triangle Park, NC 27709-2194

[†] Dept. of Physics, North Carolina State University, Raleigh, NC 27695-8202

ABSTRACT

A low pressure chemical vapor deposition technique using water-alcohol vapors has been developed for the deposition of polycrystalline diamond films and homoepitaxial diamond films. The technique uses a low pressure (0.50 - 1.00 Torr) rf-induction plasma to effectively dissociate the water vapor into atomic hydrogen and OH. Alcohol vapors admitted into the chamber with the water vapor provide the carbon balance to produce diamond growth. At 1.00 Torr, high quality diamond growth occurs with a gas phase concentration of water approximately equal to 47% for methanol, 66% for ethanol, and 83% for isopropanol. A reduction in the critical power necessary to magnetically couple to the plasma gas is achieved through the addition of acetic acid to the water:alcohol solution. The lower input power allows lower temperature diamond growth. Currently, diamond depositions using water:methanol:acetic-acid are occurring as low as 300 °C with only about 500 W power input to the 50 mm diameter plasma tube.

INTRODUCTION

To date, diamond films produced by chemical vapor deposition techniques have been grown principally using heavy dilution of organic gasses with molecular hydrogen.[1-12] The role of molecular hydrogen to the process is manifold, but the dissociation of molecular hydrogen into a high fraction of atomic hydrogen is critical to diamond stabilization and growth. A plethora of techniques have been applied to create concentrations of atomic hydrogen sufficient for high quality diamond growth. Typically, these techniques involve a high-temperature region (hot-filament, oxy-acetylene torch, microwave plasma, dc arc discharges, etc.) wherein high dissociations of molecular hydrogen is feasible. Some workers have avoided the use of molecular hydrogen by using source gasses rich in oxygen.[8-10] Other workers have augmented the molecular hydrogen with small percentages of water.[11-12] We report here on a low pressure rf-inductive plasma-assisted chemical vapor deposition technique for the growth of diamond which uses water not molecular hydrogen as a process gas stabilizing diamond growth. Atomic hydrogen necessary for diamond growth (in this process) is supplied from plasma-dissociation of water and alcohol vapors. Unlike previous work, addition of water to the alcohol is necessary to produce well-facetted diamond growth in this low pressure rf-plasma technique.[9] Furthermore, it has been observed that addition of acetic acid to this CVD process enables diamond growth to occur at reduced rf power levels and consequently at lower substrate temperatures.

EXPERIMENTAL APPARATUS AND APPROACH

A description of the chemical vapor deposition system used in this work has been previously reported.[13-14] The system produces diamond from both traditional H_2 - CH_4 mixtures as well as the water:alcohol:organic-acid solutions. The system consists of a 50 mm id plasma

tube appended to a standard six-way cross. A radio frequency (13.56 MHz) induction coil couples power from the rf power supply into the plasma discharge. Samples are located on a graphite carrier located immediately underneath the induction plasma. The rf excitation induces currents in the graphite susceptor which serve to heat the sample. Samples are introduced into the vacuum system via a vacuum load-lock which isolates the main chamber. The gasses (water, alcohol, acetic-acid) are introduced into the chamber through a leak valve on a storage tank which contains solutions of the water/alcohol or water/acetic-acid alcohol. Vapors above the liquid are pumped from the storage tank into the growth chamber. The vapor pressure of the constituents above the liquic should be a produce of their molar concentration and their respective vapor pressures. Water and alcohol solutions at room temperature have sufficient vapor pressures to supply a low pressure discharge (~ 10 Torr). High pressure operations might require the liquid solutions to maintained at an elevated temperature. For the growths reported here, vapors from various volumetric mixtures have been evaluated for diamond growth. The leak rate into the growth chamber from the solutions results in a loss of ~ 0.2 cc min from the liquid solutions. While there will be some depletion of the higher vapor pressure component, the practice of mixing allows a convenient method for evaluating different ratios of water-to-alcohol without the necessity of a gas manifold.

Samples are introduced to the growth system through a vacuum load lock. Prior to insertion, samples have been subjected to a diamond abrasive treatment with 1 μm diamond paste to enhance nucleation. Diamond growth proceeds by initiating a rf induction plasma with sufficient power to magnetically couple to the gas. J. Amorrim et al.[15] have shown that rf coils couple to the plasma gas at low power levels through *E*-field coupling. At higher power levels, the rf coil couples power to the plasma gas through *B*-field coupling. The *B*-field coupling is characterized by an intense plasma luminescence from a region of high density electrons, ~ 10^{12} cm^{-3}. The *E*-field coupling at lower powers results only in a low density plasma, ~ 10^{10} cm^{-3} with weak plasma luminescence. Introduction of water vapor alone to a low pressure (1.0 Torr) rf inductive discharge results in intense atomic H emission. The water plasma has a characteristic red color associated with atomic H emission at 656 nm. OH emission lines are clearly visible but not as dominant as the atomic H emission lines. One thus observes that water discharges are capable of generating ample atomic H along with OH from the water dissociation. Atomic O lines, if pevent in the emission spectrum, are minor and have not been identified at this time. Addition of alcohol to the water plasma changes the color of the plasma emission to a bluer spectrum as CH and CO emissions are observed along with the atomic hydrogen Balmer lines.

EXPERIMENTAL RESULTS

A. Water:alcohol results

We have previously reported the growth of polycrystalline diamond films using water/methanol, water/ethanol, or water/isopropanol mixtures.[16] In that work, the vapor mixture entered the deposition system and diffused from the main chamber into the plasma tube. The vapors were not admitted into the system through the plasma gas feed. For this work, the storage bottle containing the liquid solutions was located on the plasma gas feed. Various water-alcohol mixtures were used to determine the effect of the C/O ratio on diamond growth. Figure 1 shows SEM micrographs from samples deposited at 1.0 Torr from volumetric water-methanol mixtures ranging from 80% methanol to 33% methanol. The results for 80% methanol produce poorly faceted diamond. These results contrast remarkably from the work

by Buck et al. and Bachmann et al. in a microwave discharge at higher pressures using 100% methanol. In that work, high quality diamond was obtained from only methanol. In this work, water addition to the methanol is critical to the formation of well-faceted crystalline diamond. As observed in Figure 1, the quality of diamond growth increases as the methanol volumetric concentration is reduced. At 33% methanol in the water solution, well-faceted diamond growth is observed. From the respective vapor pressures of water and methanol at 20 °C, we estimate the vapor pressures of water and methanol to be 11.7 and 31.5 Torr, respectively, above the 33% methanol mixture. Using these vapor pressures, one calculates the C/C+O, the O/O+H, and the H/C+H ratios to be 0.42, 0.22, and 0.83, respectively. According to the deposition phase diagram of Bachmann, the low C/C+O ratio of 0.42 should result in no diamond growth. Nonetheless, this oxygen rich ratio is necessary for diamond growth in this system. As noted in the Bachmann work, actual gas phase concentrations may vary due to interactions of the plasma with the carbonaceous walls of the reactor. In this case, the reactions of the water-vapor plasma with the graphite susceptor undoubtedly increase the carbon concentrations in the gas phase. The graphite susceptor has been observed to be etched by the water-alcohol discharges at a rate of 25/h.

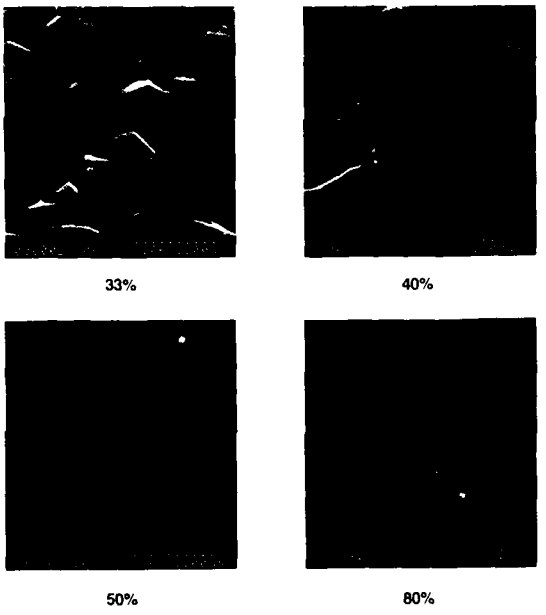


Figure 1. SEM micrographs from diamond films deposited from various volumetric concentrations.

B. Acetic-acid:water:methanol results

It was observed that diamond growth from the water-alcohol solutions required less rf power than diamond growth from more traditional H_2/CH_4. The lower rf power most likely was a consequence of the water-methanol have lower ionization potentials than the H_2 - CH_4. Water, for instance, has an ionization potential of 12.61 eV as compared to an ionization potential of 15.43 eV for H_2. Methanol, for instance, has an ionization potential of 10.84 eV as compared to an ionization potential of 12.64 eV for CH_4. The lower ionization potentials permit lower rf power levels to be applied for sufficient plasma ionization. Correspondingly, we have observed that the addition of organic acids to the water solutions substantially reduces the critical power necessary to magnetically couple to the plasma gas. It is suspected that these organic molecules have even lower ionization potentials than water.

As a consequence, diamond growth in the low-pressure rf-induction plasma can be evaluated at lower substrate temperatures (through reduction in the induced current in the graphite sample carrier). Figure 2 shows SEM micrographs of diamond films deposited at 0.50 Torr using a volumetric mixture of 2:2:1 acetic-acid:water:methanol. The sample temperature

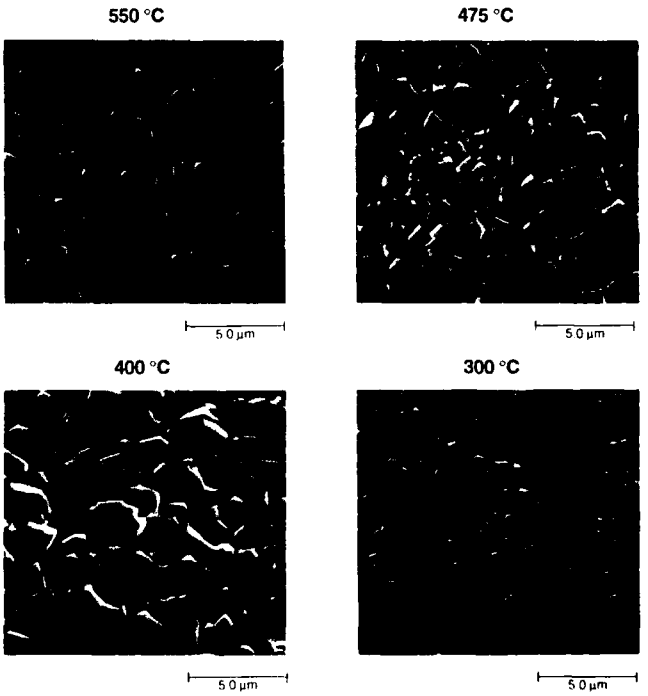


Figure 2. SEM micrographs from diamond films deposited at different temperatures using acetic-acid:water:methanol (2:2:1).

is reduced from one sample to the next by the reduction in rf applied power. The growths at all temperatures show well-faceted diamond polyhedra. There appears to be no severe degradation of the film properties despite the $\sim$ 300 °C reduction in growth temperature. An assessment of the crystalline quality of the films as measured from the full width half maximum of the 1332 cm^{-1} phonon line would tend to indicate that higher quality growth was achieved between 300-400 °C than at higher temperatures. Raman spectra for the films grown at 300 and 400 °C are shown in Figure 3. All these films showed an amorphous carbon component at 1500 cm^{-1}. The reduction in applied power did reduce the deposition rate. The film deposited at 575 °C grew at a linear rate of 6000 Å/hr while the film deposited at 300 °C grew at a linear rate of 2000 Å/hr.

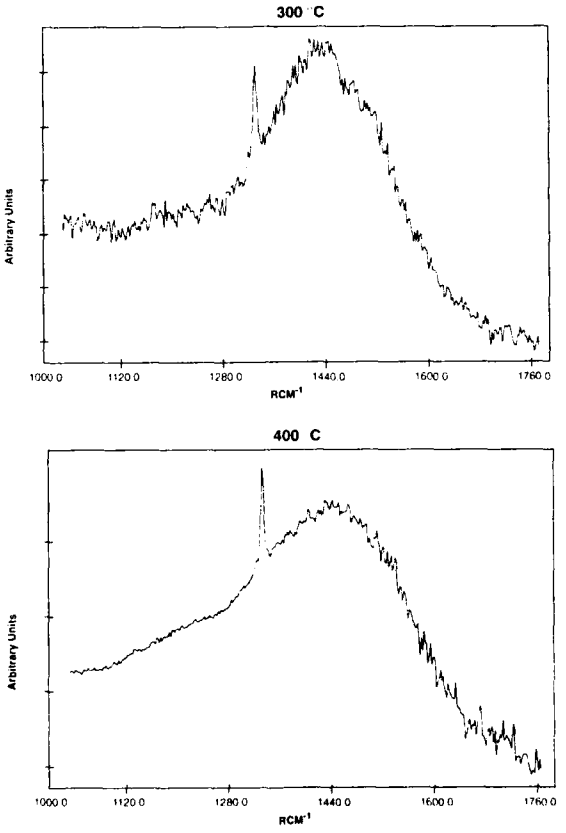


Figure 3. Raman spectra from the films deposited with acetic-acid:water:methanol at 300 and 400 °C.

DISCUSSION

The growth of diamond is undoubtedly facilitated in the low-pressure rf-induction plasma by the high electron density achieved when at a critical power the coupling changes from *E*-field to *B*-field coupling. In this work, we have replaced molecular hydrogen and methane with various mixtures of water, alcohols, and organic acids. The vapor discharges from the water-based solutions are easily ionized in the rf plasma owing to lower ionization potentials for the water, alcohol, and acetic acid molecules. As a consequence, lower power levels are necessary for a *B*-field coupling.

Once the *B*-field coupling occurs, the high electron density and high electron temperature allows atomization of the parent molecules. Atoms and free radicals of both graphite etchant species such as H and OH and carbon-containing radicals are present at the diamond growth surface. Dissociation of those species will depend directly on the bond strengths. If one compares bond-strengths for the various molecules and radical species used in this work, a number of interesting observations are apparent. First, the H-OH bond (5.2 eV) is not significantly weaker than the H-H bond (4.5 eV). Thus, the high generation of atomic hydrogen from water discharges is probably a consequence of the lower ionization potential and a larger cross-section for electron-impact dissociation. Second, the bond strengths for H-liberation for a radical such as CH_2O—H (1.3 eV) from the methanol has a significantly lower dissociation energy than the parent CH_3O—H (4.9 eV) molecule. The CH_2O—H dissociation energy is also significantly lower than any of the energies for methane, methyl, or methylene dissociation. One would expect that electron energies in the plasma sufficient to dissociate hydrogen from the methyl group on methanol would be more than sufficient to dissociate the CH_2O—H bond. And third, the lowest dissociation energies for H- liberation are found for the carboxyl radical COO-H (0.5 eV) These radicals are contained on the organic acid and halogenated organic acid groups. It is the dissociation of this bond that gives the acidity to water solutions containing these organic molecules. One would expect then that, besides the lower ionization potential offered by the addition of the organic acid molecules to the plasma discharge, the organic acids would readily release H atoms to the plasma gas. The organic acid group behaves as graphite solvent in this process. To date, we have not been successful in depositing diamond from solutions of exclusively water and acetic acid. Concentrations of acetic acid in excess of 80% in water solution have not been evaluated. For the concentrations of acetic acid that we are using for the low temperature diamond growth 2:2:1 (acetic-acid:water:methanol), the primary roles of the organic acid group are (1) to promote ionization in the rf induction coil and (2) to contribute H atoms to the growth process.

We have previously been discussing mechanisms by which the water-based processes promote diamond growth in low-pressure rf-induction plasmas. These mechanisms have all been concerned with H- atom generation. At low pressures, diffusion of H atoms to walls and recombination of H atoms on the walls limit the steady-state population of H atoms. The steady state population being the difference of the generation and loss rates. The water-based processed (besides producing higher generation rates per unit power than the molecular-hydrogen based processes) may also significantly reduce the loss rates at low pressure. Water passivation of tube walls in flowing afterglow hydrogen discharges has been used to reduce wall recombination. Water vapor (integral to the diamond growth in this work) would continuously passivate the reactor walls. Indeed, it might be possible to maintain the reactor walls at a temperature low enough to condense multiple layers of water on the plasma tube walls. The water condensate would serve to buffer the wall materials from the extremely aggressive plasma environment. In addition to wall passivation, the water-based process may also reduce loss

rates by permitting H^+ complexing with neutral H_2O water molecules. The hydronium ion H_3O^+ as in acidic-water solutions should remain highly reactive, yet complexed so as to retard rapid diffusion to the plasma walls. It, thus, seems plausible that the water-based processes for diamond growth can enhance diamond growth both by permitting higher generation rates of active species and by reducing loss mechanisms.

CONCLUSION

A low pressure chemical vapor deposition technique using water-alcohol vapors has been developed for the deposition of polycrystalline diamond films and homoepitaxial diamond films. The technique uses a low pressure (0.50 - 1.00 Torr) rf-induction plasma to effectively dissociate the water vapor into atomic hydrogen and OH. Alcohol vapors admitted into the chamber with the water vapor provide the carbon balance to produce diamond growth. Unlike previous results obtained from microwave sources using only methanol or Ar/methanol mixtures, the rf-induction source grows poor quality diamond unless water vapor is admitted. At 1.00 Torr, high quality diamond growth occurs with a gas phase concentration of water approximately equal to 47% for methanol, 66% for ethanol, and 83% for isopropanol. In the operation of the rf induction plasma, there exists a critical power level at which the coupling to the plasma changes from *E*-field coupling to *B*-field coupling. The *B*-field coupling has been shown in Ar plasmas to produce about two orders of magnitude increase in the electron density. We have observed that the critical power to achieve *B*-field coupling is substantially lower for the water-based processes as compared to the traditional molecular hydrogen-based processes. Furthermore, reduction in the critical power necessary to *B*-field couple is achieved through the addition of acetic acid to the water:alcohol solution. The water-alcohol vapors permit diamond growth to occur at lower power levels as compared to the H_2/CH_4 discharges. The lower input power level required in turn reduces substrate-carrier inductive heating and allows lower temperature diamond growth. Currently, diamond depositions using water:methanol:acetic-acid are occurring as low as 300° C with only about 500 W power input to the 50 mm diameter plasma tube.

ACKNOWLEDGEMENTS

The authors would like to acknowledge the support of this work by SDIO/IST through the ONR Contact No. N0014-86-C0460. The authors would also like to thank R. Durkee, S. Ammons, and D. Brooks for their outstanding technical support of this work.

REFERENCES

1. B. Derjaguin and V. Fedoseev, Russ. Chem. Rev. 39, 783 (1970).
2. B.V. Spitsyn, L.L. Bouilov, and B.V. Derjaguin, J. Cryst. Growth 52, 219 (1981).
3. S. Matsumoto, Y. Sato, M. Kamo, and N. Setaka, Jpn. J. Appl. Phys. 21, 183 (1982).
4. Y. Hirose and Y. Teresawa, Jpn. J. Appl. Phys. 25, L51 (1986).
5. M. Kamo, Y. Sato, S. Matsumoto, and N. Setaka, J. Cryst. Growth 62, 642 (1983).
6. L.M. Hanssen, W.A. Carrington, J.E. Butler, and K.A. Snail, Mater. Letters 7, 289 (1988).
7. G. Janssen, W.J.P. Van Enckevort, J.J.D. Schaminee, W. Vollenberg, L.J. Giling, M. Seal, J. Cryst. Growth 104, 752 (1990).
8. Peter K. Bachmann, Dieter Leers, and Hans Lydtin, Diamond and Related Materials 1, 1 (1991).

9. M. Buck, T.J. Chuang, J.H. Kaufman, and H. Seki, Mat. Res. Soc. Symp. Proc. 162, 97 (1990).

10. C.F. Chen, T. M. Hon and C.L. Lin, presented at 18th Int. Conf. on Metallurgical Coatings and Thin Films (ICMCTF), San Diego, CA, April 23, 1991.

11. Yukio Saito, Kouji Sato, Hideaki Tanaka, Kazunori Fujita, Shinpei Matuda, J. Mater. Sci. 23, 842 (1988).

12. Yukio Saito, Kouji Sato, Kenichi Gomi, Hiroshi Miyadera, J. Mater. Sci. 25, 1246 (1990).

13. R.A. Rudder, G.C. Hudson, R.C. Hendry, R.E. Thomas, J.B. Posthill, and R.J. Markunas, "Applications of Diamond Films and Related Materials", Materials Science Monograph 73, 395 (1991).

14. R.A. Rudder, G.C. Hudson, J.B. Posthill, R.E. Thomas, and R.J. Markunas, Appl. Phys. Lett 59, 791 (1991).

15. J. Amorim, H.S. Maciel, and J.P. Sudano, J. Vac. Sci, Technol. B9, 362 (1991).

16. R.A. Rudder, G.C. Hudson, J.B. Posthill, R.E. Thomas, R.C. Hendry, D.P. Malta, R.J. Markunas, T.P. Humphreys, and R.J. Nemanich, to appear Jan 20, 1992 in Appl. Phys. Lett.

REMOTE ECR PLASMA DEPOSITION OF DIAMOND THIN FILMS FROM WATER-METHANOL MIXTURES

R. K. SINGH, D. GILBERT, R. TELLSHOW, R. KOBA*, R. OCHOA, J. H. SIMMONS, P. H. HOLLOWAY, J. RODGERS** AND K. BUCKLE**

University of Florida, Department of Materials Science and Engineering, Gainesville, FL 32611

* Plasma-Therm I.P. Inc,.St. Petersburg, FL

** University of South Florida, Department of Electrical Engineering, Tampa, FL

ABSTRACT

We have applied an electron cyclotron resonance technique to deposit diamond thin films on various substrates under remote plasma, low temperature (600°C) and low pressure (60 mTorr) conditions. Diamond films were grown on different substrates (silicon, molybdenum) with varying concentrations of precursor gases (methanol and water). A positive substrate bias (50 to 60 V) was found to be essential for the growth of diamond films onto substrates positioned 16 cm below the ECR plasma. The films were characterized by Raman, X-ray diffraction and scanning electron microscopy for microstructure, phase purity and chemical bonding characteristics. The effect of various processing parameters including gas pressure, gas composition, substrate temperature and bias have also been analyzed.

INTRODUCTION

Most diamond CVD methods (microwave, dc and rf plasma, hot filament) can be termed "thermal" since the gas mixtures are heated to temperatures over 2000K. [1,2] At these temperatures, the input gases (such as CH_4, O_2 and H_2) decompose thermally, thereby forming active species for diamond growth. The various techniques differ on the type and intensity of other excitation phenomena, (e.g., electron impact ionization and dissociation [3], photon absorption and emission) which operate concurrently with thermal excitation of the gas mixture. In contrast, low pressure and highly ionized plasmas which rely on electron impact for dissociation and ionization can be generated by electron cyclotron resonance (ECR) conditions. This occurs when the microwave energy is coupled with the resonant frequency of the electrons in the presence of a magnetic field. True electron cyclotron resonance cannot occur above 10 mTorr (1.3Pa) due to the limited mean free path of electrons in the plasma, but significant magnetic field confinement and enhancement of a plasma has been observed at pressures as high as 100 mTorr [4]. An ECR plasma typically has a very high electron temperature (e.g., >22,000K) a relatively cool ion temperature (typically 10% of the electron temperature) and neutrals that are typically < 500K. In an ECR plasma, the generation of the species necessary for diamond growth must proceed predominantly by non-thermal mechanisms such as electron-induced dissociation and ionization. ECR plasmas offer several potential advantages as a means to deposit diamond thin films. Since the neutral gas temperature is nearly the same as the temperature of the chamber walls, and the pressures are in the molecular flow regime, it is relatively easy to generate a uniform distribution of activated gas species over a large area. Secondly, the low pressure of the plasma may enable the generation of activated species remote from the substrate surface, i.e, enabling downstream processing in order to coat large areas.

Magnetically enhanced microwave PECVD of diamond was first reported by A. Hiraki et. al. [4, 5] who employed a magnetic mirror ECR design in which two electromagnets were used to couple a static B field to a microwave field. They also reported a significant increase in deposition rate of diamond films using a source gas mixture of methanol and helium. Recently, Eddy et. al. [6] also reported the growth of diamond films at low pressures using CO and hydrogen gas mixtures.

In this paper, we report remote plasma growth of diamond thin films using water plus methanol mixtures. The avoidance of H_2 as a source gas was based on the high H-H bond strength (104 kcal/mol) and the small size of the H_2 molecule, which make plasma-induced dissociation into atomic H highly endothermic. Recently, workers at Research Triangle Institute have also reported the deposition of diamond films from alcohol and water mixtures using a rf

plasma system. [7] The use of H_2O instead of H_2 enabled a reduction in the substrate temperature necessary for rapid diamond growth. The OH group is speculated to perform a similar function to atomic hydrogen, i.e stabilization of the diamond phase and /or preferred etching of graphite and graphite precursors. The use of H_2O instead of H_2 as a source gas also has many practical advantages, e.g. H_2O is cheaper and safer to handle than H_2.

EXPERIMENTAL

Experiments were performed in a Plasma-Therm BECR-6 system at the University of Florida (UF) and in a prototype BECR-6 system at the University of South Florida (USF). A photo of the BECR-6 system is shown in Figure 1. Two rings of rare-earth permanent magnets (10 magnets/ring) are mounted on the exterior of a 6" I.D. by 6" long ECR module. The magnetic field at the pole face of each magnet is approximately 3 kGauss. Cusp-shaped zones of 875 G field are generated inside the vacuum chamber. A turnstile coupler is used to direct 2.45 GHz microwave field through a silica vacuum/microwave window at the top of the ECR module. At pressures below 150 mTorr, the coupling of the magnetic field to the electrons in the microwave plasma is strong enough to position the center of the plasma within the two rings of magnets. At pressures below 10 mTorr, electron cyclotron resonance occurs along the cusp-shaped surfaces where the magnetic field strength equals 875 G. The source gas mixture was methanol and water. Methanol was injected in a ring positioned beneath the base of the ECR chamber, while water was injected from the top. Substrates were placed on a heated platen which was electrically isolated to enable dc biasing. and were positioned 8 to 20 cm downstream from the ECR zone. A positive bias of 50 to 60 V was found to be essential for diamond thin films. The substrates used for growth experiments were Si and Mo plates scratched with submicron diamond powder and then ultrasonically washed in methanol.

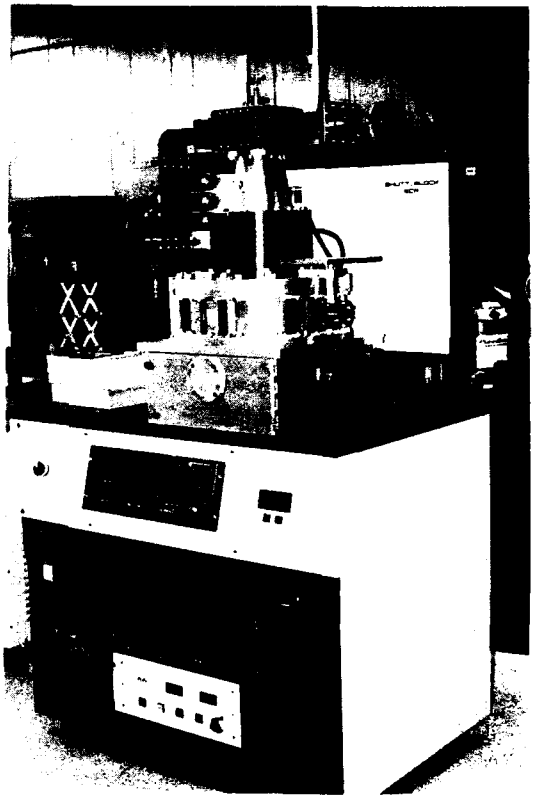


Figure 1 Photograph of Plasma-Therm BECR-6 system.

RESULTS AND DISCUSSION

Figure 2 shows the surface topography of the diamond film deposited using a methanol to water ratio of 20:1. During the deposition process, the substrate temperature was kept between 500°C and 600°C, while the total pressure in the chamber was 60 mTorr. It was found that a positive substrate bias (50 to 60 V) was necessary for remote diamond film growth. Under these conditions, a secondary discharge glow was observed at the substrate, presumably due to electron impact of the gas species arriving from the ECR plasma. The average dc current density measured during the experiment was between 20 - 40 mA/cm^2. The stabilization of the diamond phase under remote plasma conditions depends strongly on the positive substrate bias, which is believed to repel the positively charged ionic species in the plasma as well as generate diamond precursor gas species at the substrate surface.

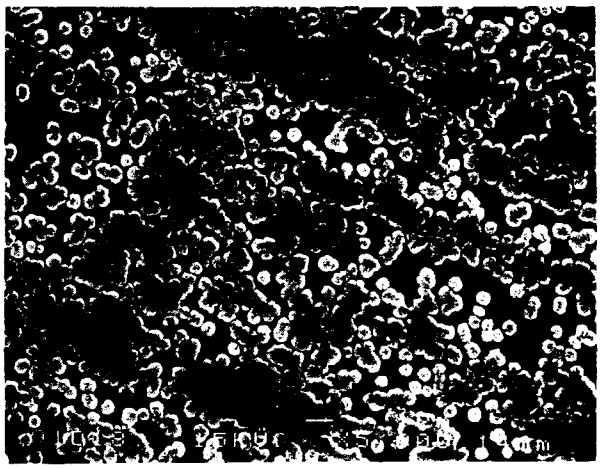


Figure 2 SEM micrograph of diamond film deposited using a methanol to water ratio of 20:1.

The film consists of crystallites of approximately 0.4 to 0.6 μm in size; the average growth rate was 40 to 50 nm an hour. Higher magnification of this diamond film shows a "cauliflower" type structure observed due to multiple nucleation of the diamond phase. The corresponding Raman spectra of this film, (Figure 3), exhibits a diamond peak at 1334 cm^{-1} and a broad spectrum from 1450-1550 cm^{-1} suggesting the presence of sp^2 bonded carbon in the form of graphite, amorphous carbon or a combination of both. The full width at half maximum (FWHM) of the diamond peak is approximately 12 cm^{-1} which is considerably greater than that of natural diamond (FWHM -1.8 -2 cm^{-1}.) This widening of the peak can be attributed to small grain size of the material or formation of a highly defective material.

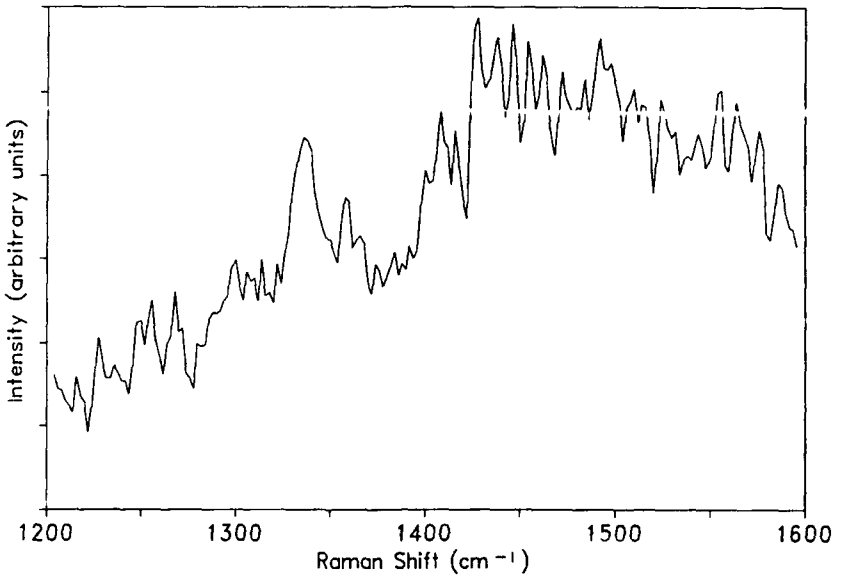


Figure 3 Raman spectra of diamond film deposited using methanol to water ratio of 20:1.

Figure 4 shows a SEM micrograph of a film nucleated for 1 hr at 60 mTorr with methanol to water ratio of 20:1 and then deposited for 15 hr with methanol to water ratio of 5:1. Other conditions for deposition were the same as the earlier film. A nearly continuous film is formed composed of many fine crystallites thus resulting in smooth coverage of the substrate. The corresponding Raman spectrum of the film is shown in Figure 5 which also shows a relatively broad diamond peak at 1334 cm^{-1}, and a weak sp^2 bonded peak . It was observed decreasing the methanol to water ratio of 3:1 resulted in etching of the substrate instead of deposition.

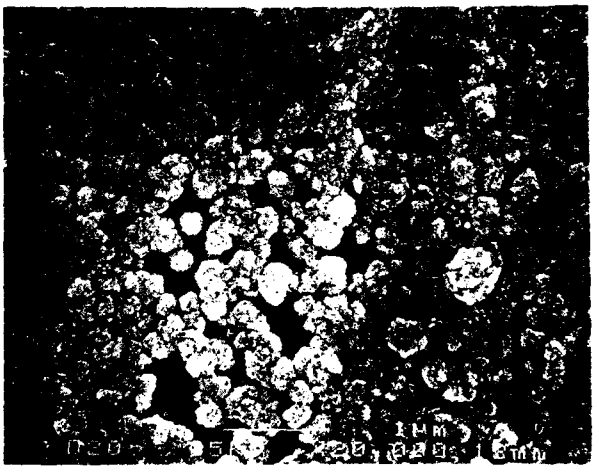


Figure 4 SEM micrograph of diamond film deposited using water to methanol ratio of 5:1.

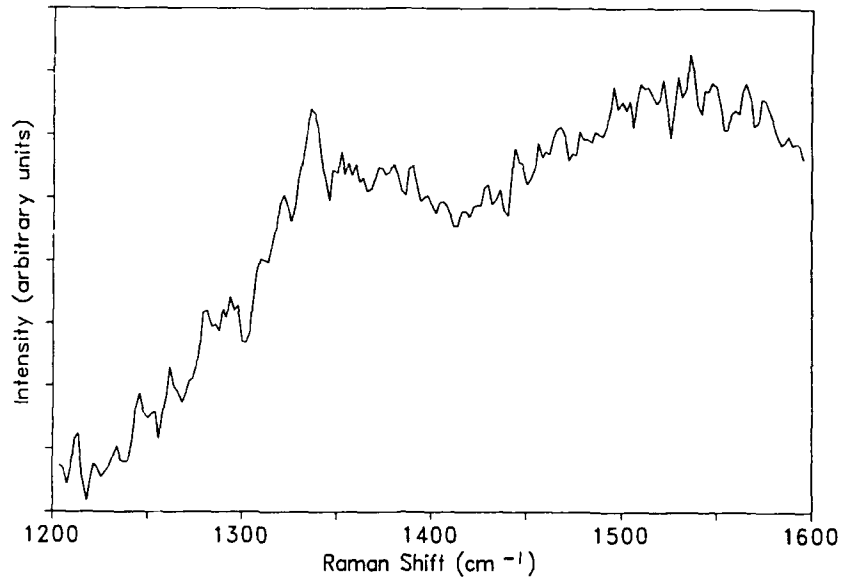


Figure 5 Raman spectra of diamond film deposited using water to methanol ratio of 5:1.

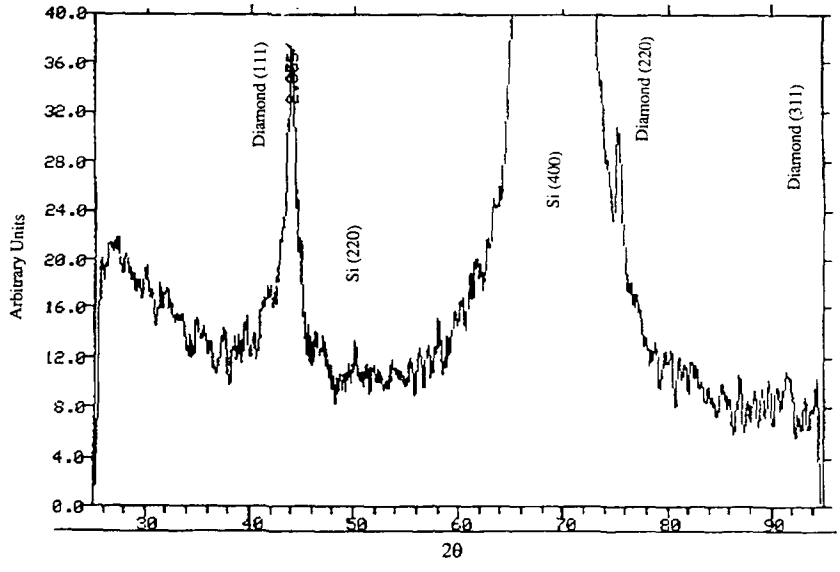


Figure 6 X-ray diffraction spectrum of diamond film deposited using water to methanol ratio 10:1.

Figure 6 shows a X-ray diffraction pattern of a film on silicon substrate deposited with methanol to water ratio of approximately 10 :1. This film was deposited at 25 mTorr and about 7 cm below the ECR zone. This X-ray spectra shows the presence of diamond peaks corresponding to the (111), (220) and (311) planes. The intensities of the peaks are in agreement with their structure factor, thus confirming that the film is randomly oriented. The diffraction peaks are also broadened due to the defective nature of the film.

SUMMARY

In conclusion, we have fabricated diamond films under remote plasma, low temperature and low pressure conditions using methanol and water as input species. Randomly oriented diamond films have been fabricated with varying ratios of methanol to water (20:1 to 5:1). At lower concentrations of methanol, etching of the substrate is observed. It is expected that with further optimization of the processing variables large area continuous diamond films can be fabricated by this method at temperatures below 600°C.

REFERENCES

1. P. K. Bachmann, D. Leers and H. Lydtin, Diamond and Related Materials 1, 1 (1991).
2. J. A. Thorton, in Deposition Technologies for Films and Coatings, edited by R. F. Bunshah, Noyes Publishing, (1982) p. 23.
3. L. S. Plano, D. A. Stevenson and J. R. Carruthers, in Diamond Materials, edited by A. J. Purdes, et al.,The Electrochemical Society, Pennington, NJ, Vol. 91-8 (1991) p.290.
4. J. Wei, H. Kawarada, J. Suzuki, K. Yanagihara, K. Numata, and A. Hiraki, in Diamond and Diamond-like Films, edited by Dismukes, et al., Electrochemical Society, Pennington, NJ, vol 89-12, (1989) p. 393.
5. A. Hiraki, H. Kawarada, J. Wei, J. S. Ma and J. Suzuki, in Diamond Optics III, SPIE Proc. Vol. 1325, edited by Feldman and Holly, SPIE, Bellingham, WA (1990) p.74.
6. C. R. Eddy, D. Youchison and B. D. Sartwell, Surface and Coatings Technology, 48, 69 (1991)
7. R. A. Rudder, G. C. Hudson, J. B. Posthill, R. E. Thomas, R.C. Hendry, D. P. Malta, R. J. Markunas, T. P. Humpreys and R. J. Nemanich, Appl. Phys. Lett., January (1991).

DEPOSITION OF FLAME GROWN DIAMOND FILMS IN A CONTROLLED ATMOSPHERE

Kathleen Doverspike*, James E. Butler**, and Jaime A. Freitas, Jr.***
* Naval Research Laboratory, Code 6861, Washington, D.C. 20375-5000
**Naval Research Laboratory, Code6174, Washington, D.C. 20375-5000
***Sachs/Freeman Assoc. Inc. Landover,MD 20785-5396

ABSTRACT

Polycrystalline diamond films were synthesized both by using an open atmosphere combustion flame, and also using a combustion flame in an enclosed chamber. By operating the pre-mixed oxy-acetylene torch in a chamber, we were able to vary the atmosphere around the flame in a controlled manner and study the effects on the diamond films. Varying the atmosphere around the flame is of interest to control the incorporation of unwanted gases, such as room air, and to obtain finer control over the flame properties. We report on the properties of films grown in the open atmosphere and in the chamber with oxygen and argon.

Introduction

The combustion flame technique has been demonstrated at several laboratories to be a viable technique to obtain high quality diamond films with a high growth rate (>100μm/hr)[1-10]. In this paper, we report on the growth of free standing polycrystalline diamond films grown by the combustion process using an oxy-acetylene torch in the open atmosphere, and in an enclosed chamber where the environment can be controlled. Diamond growth using an oxy-acetylene torch occurs in the fuel rich acetylene feather just outside the primary flame front. The torch is a premixed design, where oxygen and acetylene are combined in the mixing chamber and then burn near the primary flame front (inner cone) where temperatures can reach up to about 3300K[11]. The overall combustion reaction at the inner cone is [12]:

$$C_2H_2 + O_2 \rightarrow 2CO + H_2 \qquad (1)$$

with many reactive intermediates (eg. H, OH, C_2,and C_2H) involved in the overall reaction. If the torch is run in a fuel rich mode, the unburnt hydrocarbons, reactive intermediates, CO, and H_2 form a region (feather) bounded by another flame front caused by oxygen diffusion from the surrounding atmosphere. Although the oxygen and acetylene gases are premixed in the torch, the outer regions of the feather can be described as a diffusion flame because of the oxygen diffusion from the atmosphere. When the torch is operated in the open atmosphere, there is an ample supply of room air available for diffusion into the flame fully oxidizing the combustion products to CO_2 and H_2O in the outer region. Fourier transform infrared spectroscopy has shown that the feather region contains a large concentration of CO and the outer part of the feather and the outer region of the flame contain an appreciable amount of OH, H_2O and CO_2[13]. Laser-induced fluorescence and mass spectrometry have shown the feather region also contains an appreciable amount of nitrogen[12]. This indicates that the atmospheric air not only oxidizes the combustion products in the outer region, but does indeed diffuse into the feather region.

Since environmental gases around the flame diffuse into the area of the flame where diamond growth occurs, these environmental gases are an important variable that warrants further attention. Varying the atmosphere around the flame is also a method of controlling the incorporation of unwanted dopants, such as nitrogen, and of obtaining a finer control over the flame properties. In the present paper, we will discuss films that were made (A) in the open atmosphere, (B) in the enclosed chamber using argon as the auxiliary gas, and (C) in the enclosed chamber using oxygen as the auxiliary gas.

Mat. Res. Soc. Symp. Proc. Vol. 242. © 1992 Materials Research Society

Experimental

All of the diamond films were synthesized using a premixed oxy-acetylene welding torch with a nozzle diameter of 1.17 mm. The flow rates of the oxygen and acetylene(99.6%) were controlled by mass flow controllers with the total flow rate being held constant at 7 SLM. The films were grown on molybdenum screws that were placed in a threaded hole in a water-cooled copper block. The temperature of the screw was controlled by the depth of penetration into the copper block and was monitored by using a two-color pyrometer. The temperature of the films that will be discussed was 900°C (±20°). In order to enhance the nucleation, the surface of the molybdenum screw was polished with 600 mesh silicon carbide followed by 1 μm diamond paste, and then ultrasonically cleaned in acetone and methanol. Because of the large difference in the thermal expansion of diamond and molybdenum, the film delaminates as the substrate cools. All the samples discussed in this paper were thus free standing diamond films.

A similar apparatus to that described above was placed in an enclosed chamber in order to control the atmosphere around the flame. Prior to lighting the torch, the chamber was evacuated to approximately 1 torr and then backfilled with the auxiliary gas, either argon or oxygen. An exhaust valve was opened during the growth process, so the experiments were done at slightly above atmospheric pressure.

Micro-Raman analysis was performed using the 514.5 nm line of an argon ion laser and a spatial resolution of less than 1 μm[14]. The Raman line width measurements were performed in the photoluminescence apparatus using a 488.0 nm line with a laser spot size of about 100 μm[15]. The photoluminescence experiments were carried out at 6K in a Janis supervaritemp cryostat. Scanning electron microscopy (SEM) was performed on these samples using a Cambridge S200 instrument.

RESULTS

Results are reported on three types of samples grown in (A) the open atmosphere, (B) the enclosed chamber using argon as the auxiliary gas, and (C) the enclosed chamber using oxygen as the auxiliary gas. Sample A was grown using an oxy-acetylene torch operating in the open atmosphere with an O_2/C_2H_2 ratio of 1.04. Sample B was grown using an oxy-acetylene torch operating in an enclosed chamber with an O_2/C_2H_2 ratio of 1.10 and an argon flow of 5 SLM. Sample C was grown with an O_2/C_2H_2 ratio of 1.03 and an oxygen flow of 7 SLM. Just prior to ending the growth of sample C, the auxiliary flow was changed to argon while the sample cooled down to room temperature. A fourth sample was grown using the same sample conditions as sample C, but when this experiment was terminated, the auxiliary oxygen continued to flow. Therefore, the substrate cooled from 900°C to room temperature (about 2 minutes) in an atmosphere containing a large concentration of oxygen. The total flow rate through the torch for all of these samples was held constant at 7 SLM. The growth time for each of the samples was 60 minutes, while the temperature of the substrate, measured with a two-color pyrometer, was approximately 900°C(±20°).

The crystallite morphology of the films can be seen in the SEM micrographs of Figure 1a-d. Micro-Raman spectra of samples A, B, and C are shown in Figure 2a-c, while Figure 3a,b show the photoluminescence spectra of sample A and sample C.

The shape of the feather in an argon environment was very long and slender, drastically different from the rounded appearance in the open atmosphere. For a given position in the flame, the temperature of the substrate also appears to be affected by the environmental gases. We have also observed that no water vapor condenses in the chamber in an argon atmosphere, but in an oxygen atmosphere, water is seen condensing on the walls of the chamber.

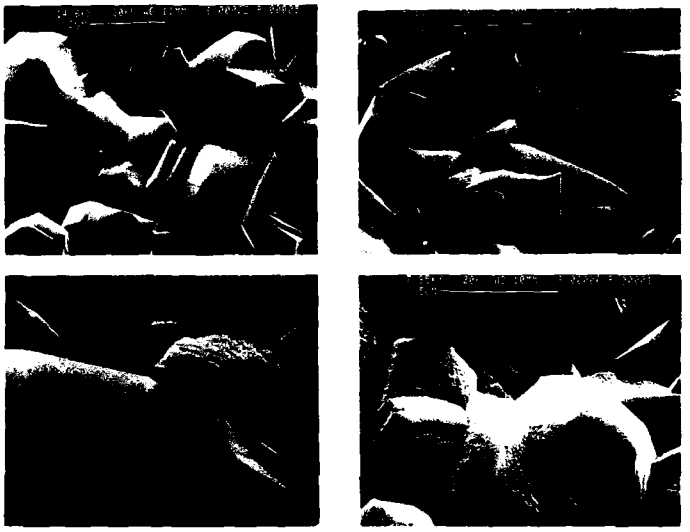


Figure 1. Morphology of films grown in various atmospheres (a,upper left) open atmosphere, (b,lower left) argon atmosphere, (c,upper right) oxygen atmosphere (cooled in argon), and (d,lower right) oxygen atmosphere (cooled in oxygen).

DISCUSSION

The temperature in various parts of the acetylene feather has been shown to be between 2200 and 3000K with a substrate in place[13]. We have found that the temperature of the substrate in the feather is lower in an argon atmosphere, and can easily be varied over a 100K range by changing the environmental gases, without varying the depth of penetration of the substrate into the water-cooled copper block. The lower temperature in an argon atmosphere is not unexpected, since there is no additional oxygen to promote the further combustion of the unburnt fuel, and thus, less heat is provided by the flame. In an argon atmosphere where the only source of oxygen is through the torch, a slightly higher oxygen/acetylene ratio was used to attain similar growth as compared to an oxygen atmosphere. The feather is essentially starved of oxygen in an argon atmosphere that would normally diffuse into the flame and burn with the excess fuel creating a secondary flame front. Therefore, the feather is not bound by this secondary flame front in an argon atmosphere and only a small increase in the acetylene flow rate is needed to extend the slender feather several inches. In the open atmosphere, small increases in the acetylene increased the length of the feather very gradually. Since diamond growth occurs in this feather region, the composition of the environmental gases is important.

Assuming complete efficient combustion, from the equation

$$C_2H_2 + 5/2O_2 \rightarrow 2CO_2 + H_2O \qquad (2)$$

and an O_2/C_2H_2 ratio of approximately 1, then the flow rate of additional oxygen in the chamber should be about 3/2 the flow rate of C_2H_2 through the torch in order to

obtain the fully oxidized combustion products. We see evidence of this visually, by water condensing on the walls of the chamber when sufficient oxygen is present.

The well crystallized faces, typical of growth in the open atmosphere, is shown in Figure 1a. An interesting feature of the film grown in argon is the smooth (100) faces shown in Figure 1b. This is not unexpected, since growth can occur on the (100) face one atom at a time resulting in a smooth face, whereas growth on faces such as the (111) face often proceeds by a step mechanism[16]. Although the smooth (100) faces is not surprising in general, it is interesting that this is so clearly seen in the flame grown polycrystalline samples when there is a decreased oxygen content in the environment.

The morphology of the sample grown in 100% oxygen and cooled primarily in argon is shown in Figure 1c. The grains are much smaller (1 μm) in the outside region and show a micro-Raman spectra similar to 2c. This may be related to an increased concentration of atomic O and OH expected in the outer region of the flame. OH, and to a lesser extent atomic O have been thought to be very effective etchants of various forms of carbon[17]. This is in contrast to the outer edge in the atmospheric grown films where the quality of the diamond is lower possibly due to the increased incorporation of nitrogen[14]. In the past, this has been attributed to a high entrainment of room air (mostly nitrogen) in the outer part of the flame causing the decreased quality of diamond in the outer region of the film[18].

Figure 1d shows the morphology of a film grown in 100% oxygen and allowed to cool in an oxygen environment. Many pits are evident on the grains, and we believe they are most likely a result of etching by oxygen species after the flame was extinguished. This indicates that not only is graphite and amorphous carbon being etched, but the diamond faces show signs of considerable etching. It is interesting that some grains indicate preferential etching with fewer pits being seen on the (100) face which is known to be the slowest etched face in both natural and synthetic diamond[19].

As can be seen in the micro-Raman spectra in Figure 2a the films grown in the open atmosphere show no signs of graphitic or amorphous carbon. The films grown in the chamber with 100% oxygen (Figure 2c) also indicate high quality diamond, although there may be a small amount of amorphous carbon present in these films. Although we have been successful in growing diamond in an argon atmosphere, the quality of the diamond film decreases (Figure 2b). The broad band centered around 1500cm^{-1} is indicative of amorphous carbon, and the background fluorescence is also much larger, which indicates a larger number of defects in the sample. It appears that the oxygen entrainment into the feather region plays an important role in suppressing the formation of amorphous carbon in the films. The Raman line width was measured with a laser spot size of 100 μm in order to get an indication of the overall quality of the film including intergranular regions. The Raman full width half maximum (FWHM), a measure of the crystalline quality, was found to be 4.7 cm^{-1} for the film grown in oxygen and slightly wider, 7.0 cm^{-1}, for the film grown in argon.

Photoluminescence spectroscopy can also be used to monitor the quality of the film by examining the diamond 1st order phonon line shape, and the zero phonon line and phonon replicas of defect bands[15]. Shown in Figure 3a,b are the photoluminescence spectra of a film grown in the open atmosphere and with 100% oxygen in the chamber. In Figure 3a the line at 2.16 eV (d) is believed to be due to a double vacancy-nitrogen complex[20], while the line at 1.95 eV (c) is from a vacancy-nitrogen pair[21] and the line labeled(a) is a nitrogen complex band[20]. The band labeled b is the diamond 1st order phonon line, while b* is indicative of a small amount of graphite present in this sample. The broad band labeled f is due to the spectrometer response when this sample was measured. For the film grown in the chamber (Figure3b) we see no evidence of the nitrogen defect bands, which indicates that we have reduced the defects associated with nitrogen when we operate in the enclosed chamber and control the environmental gases. There was some evidence of nitrogen defect bands (although still smaller in intensity than the open atmosphere films) in other samples that were grown in the chamber, and may be related to impurities in the gases used (oxygen, acetylene or argon).

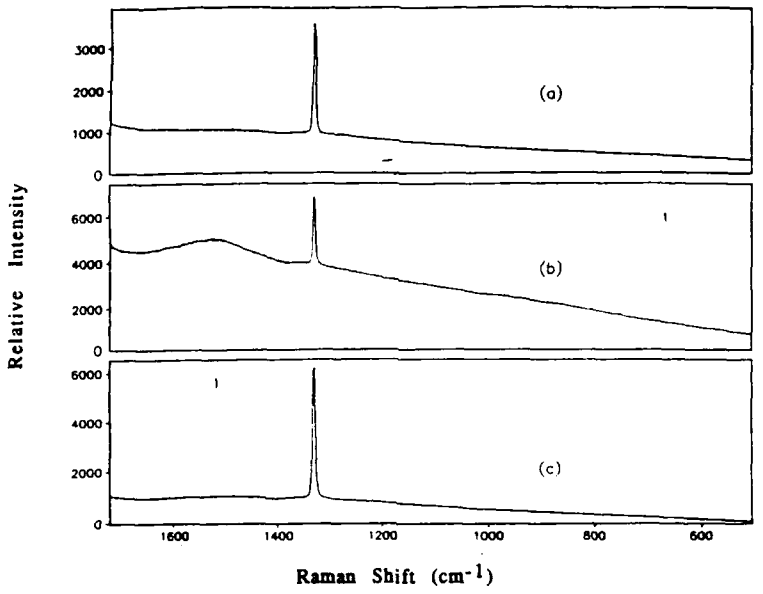


Figure 2. Micro-Raman of films grown in (a) open atmosphere, (b) an argon atmosphere, (c) an oxygen atmosphere.

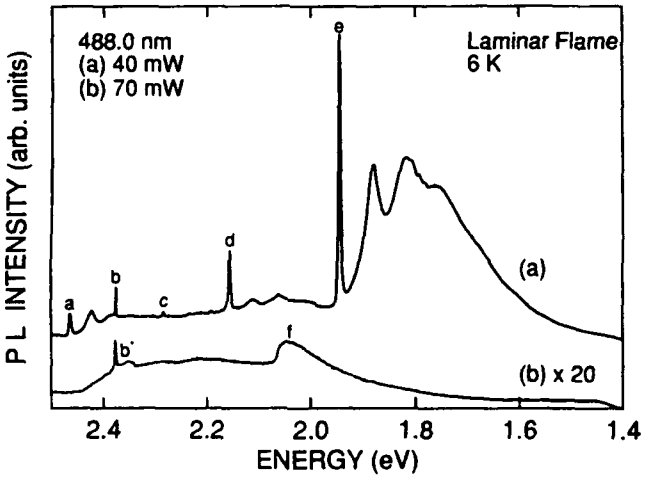


Figure 3. Photoluminescence spectra of films grown in (a) open atmosphere, (b) an oxygen atmosphere

CONCLUSION

In this paper, we have demonstrated the growth of polycrystalline free standing diamond films using a pre-mixed oxy-acetylene torch in an enclosed chamber. We have demonstrated some of the effects that the atmosphere has not only on the flame, but also on the quality and the morphology of the diamond films. When the torch is the only source of oxygen, the films show an increased amount of amorphous carbon present. When the atmosphere is primarily oxygen, the quality of the film is much better even to the outer edge of the film. We have also shown the drastic etching effect that is observed when the films are allowed to cool to room temperature in an oxygenated atmosphere. The photoluminescence results also indicate that there may also be a reduction in the incorporation of nitrogen in the films by controlling the atmosphere around the flame.

ACKNOWLEDGEMENTS

We would like to acknowledge D.J.Vestyck,Jr. for the micro-Raman analysis and D.K.Gaskill for some helpful discussions. This work was partially supported by the Office of Naval Research.

REFERENCES

1. Y.Hirose and N.Kondo, Program and Book of Abstracts, Japan Applied Physics 1988 Spring Meeting, March 29,1988,p.95.
2. L.M.Hanssen, W.A.Carrington, J.E.Butler and K.A.Snail, Mat. Lett. 7, 289 (1988).
3. Y.Hirose, Proc. 1stIntl. Conf. on the New Diamond Science and Technology, Tokyo, Japan, Oct 24/26, 1988.
4. K.A.Snail, L.M.Hanssen, W.A.Carrington, D.B.Oakes, and J.E.Butler, Proc. 1stIntl. Conf. on the New Diamond Science and Technology, Tokyo, Japan, Oct 24/26, 1988.
5. W.Yarbrough, M.A.Stewart and J.A.Cooper, Surf. and Coat. Tech. 39/40, 241 (1989).
6. P.Kosky and D.S.McAtee, Mat. Lett. 8, 369 (1989).
7. L.M.Hannssen, W.A.Carrington, J.E.Butler and K.A.Snail, Mat. Lett., 7 (7,8), 289 (1988).
8. Y.Tzeng, C.Cutshaw, R.Phillips, T.Srivinyunon, A.Ibrahimand B.H.Loo, Appl. Phys. Lett. 56,(2),134 (1990).
9. M.A.Cappelli and P.H.Paul, J.Appl.Phys. 67(5), 2596 (1990).
10. K.V.Ravi, C.A.Koch, H.S.Hu and A.Joshi, J. Mater. Res., 5 (11), 2356 (1990).
11. A.G.Gaydon and H.G.Wolfard, Flames: Their Structure, Radiation, and Temperature., 4thed. (Chapman and Hall, New York,1979).
12. Y.Matsui, A.Yuuki, M.Saharaand Y.Hirose, Jap. J. Appl. Phys. 28(9),1718 (1989).
13. P.W.Morrison,Jr., J.E.Cosgrove, J.R.Markham and P.R.Solomon, New Diamond Science and Technology, edited by R.Messier, J.T.Glass, J.E.Butler and R.Roy (Mater. Res. Soc. Proc., Pittsburgh, PA 1991) pp. 219-224.
14. D.B.Oakes, J.E.Butler, K.A.Snail, W.A.Carrington, L.M.Hanssen, J. Appl. Phys. 69(4)1991.
15. J.A.Freitas, J.E.Butler, U.Strom, J. Mater. Res. 5 (11), 2502 (1990).
16. R.E.Clausing, L.Heatherly, E.D.Specht and K.L.More, New Diamond Science and Technology , edited by R.Messier, J.T.Glass, J.E.Butler and R.Roy (Mater. Res. Soc. Proc., Pittsburgh, PA 1991) pp. 575- 580.
17. S.J.Harris and A.Weiner, Appl. Phys. Lett. 55 (21), 2179 (1989)
18. J.A.Freitas,Jr., U.Strom, J.E.Butler and K.A.Snail, New Diamond Science and Technology , edited by R.Messier, J.T.Glass, J.E.Butler and R.Roy (Mater. Res. Soc. Proc., Pittsburgh, PA 1991) pp. 723-728.
19. K.Tankala and T.Debroy, New Diamond Science and Technology , edited by R.Messier, J.T.Glass, J.E.Butler and R.Roy (Mater. Res. Soc. Proc., Pittsburgh, PA 1991) pp. 827-831.
20. J.Walker, Rep. Prog. Phys. 42, 1605 (1979).
21. G.Davies and M.F.Hamer, Proc. R. Soc. London A 348, 285(1976).

SEQUENTIAL GROWTH OF HIGH QUALITY DIAMOND FILMS FROM HYDROCARBON AND HYDROGEN GASES.

DARIN S. OLSON, MICHAEL A. KELLY, SANJIV KAPOOR, AND STIG B. HAGSTROM
Department of Materials Science and Engineering, Stanford University, Stanford CA.

ABSTRACT

We have constructed a novel, sequential DC glow and hot filament CVD reactor, to study the influence of single parameters on the deposition of diamond thin films. This reactor is capable of growing diamond films, with independent excitation of hydrogen and methane. This is achieved by the sequential exposure of the substrate to spatially separated, chemically independent, plasma regions of hydrogen, and methane in helium. The substrate is mounted on a rotating plate above the gas sources at a variable distance, typically 0.5 - 2 mm. The plate is radiantly heated from behind to a desired temperature up to 1300 K. Using the sequential deposition chamber we have been able to deposit good quality diamond up to 8% methane in helium, without the presence of oxygen, by separating a source of atomic hydrogen and a source of methane. These experiments show that methane and atomic hydrogen do not need to be present simultaneously to grow diamond. Our results further indicate that the primary critical parameter for both quality and growth rate, in hot filament deposition of diamond, is the concentration of atomic hydrogen in the system.

INTRODUCTION

Dramatic advances in the field of the synthesis of diamond films and related materials have occurred in the last few years. The major driving forces behind these efforts are the unique and extraordinary material properties of diamond for technical applications in a large number of fields. However, there are many stumbling blocks before the wide spread application of diamond material can be accomplished. A major hindrance is the poor understanding of the mechanisms of nucleation and growth of diamond, the interaction between the diamond film and the substrate, and the ability to grow large single crystals which can be suitably doped.

The objective of our research is to develop an understanding of the governing kinetic parameters behind the nucleation and growth of diamond. Because of the many species present in applied diamond synthesis techniques, the actual deposition process is complex and poorly understood[1-3]. Attempts to elucidate the mechanisms of nucleation and growth have primarily focused on gas phase precursors, which might form sp^3 bonds on the growing surface[4,5]. The complex gas phase chemistry has also precluded *in situ* measurements and detailed comparison with suggested growth models[6,7]. By separating the deposition process into several sequential steps, our aim is to identify the most critical deposition parameters to reach an understanding of the basic phenomena behind the deposition process.

We have therefore constructed a novel type of sequential CVD reactor in which the substrate can be serially exposed to four independently controlled gas sources. Thus, the role of each species can be isolated and individually modified, to vary deposition parameters such as growth rate and film quality. We are able to expose the substrate to a sequence of hydrogen, carbon, oxygen, and inert gas sources, with independent control of parameters such as excitation and concentration. This control allows, for instance, an increase in the concentration of atomic hydrogen without changing or influencing other deposition parameters. In conventional CVD reactors, and in the newer alternating chemistry reactors[8], a change of a process parameter such as a change in the excitation of one species would lead to a change in the excitation of other species present. Our results indicate that a critical parameter in hot filament deposition of diamond is the bombardment of the growing surface by atomic hydrogen.

REACTOR DESIGN AND PERFORMANCE.

The basic principles behind the design of the sequential deposition system is shown in Figure 1. The apparatus is mounted in a diffusion pumped bell jar vacuum system having a base pressure lower than 2×10^{-7} Torr. The reactor consists of four gas emitter assemblies, each about one inch in diameter, electrically insulated from the substrate. Gases are supplied to each

emitter station at a rate high enough to insure that intermixing between the emitters is minimal and does not influence the growth process. The substrate is mounted on a rotating plate facing the gas excitation sources at a variable distance, typically 0.5 - 2 mm. The plate is heated from behind up to a temperature of 1300 K by a tungsten filament.

Gases flowing through the emitter heads can be excited by a variety of means, such as hot filament, DC glow, and RF radiation, however, this paper will only be concerned with excitation of gases by hot filaments.

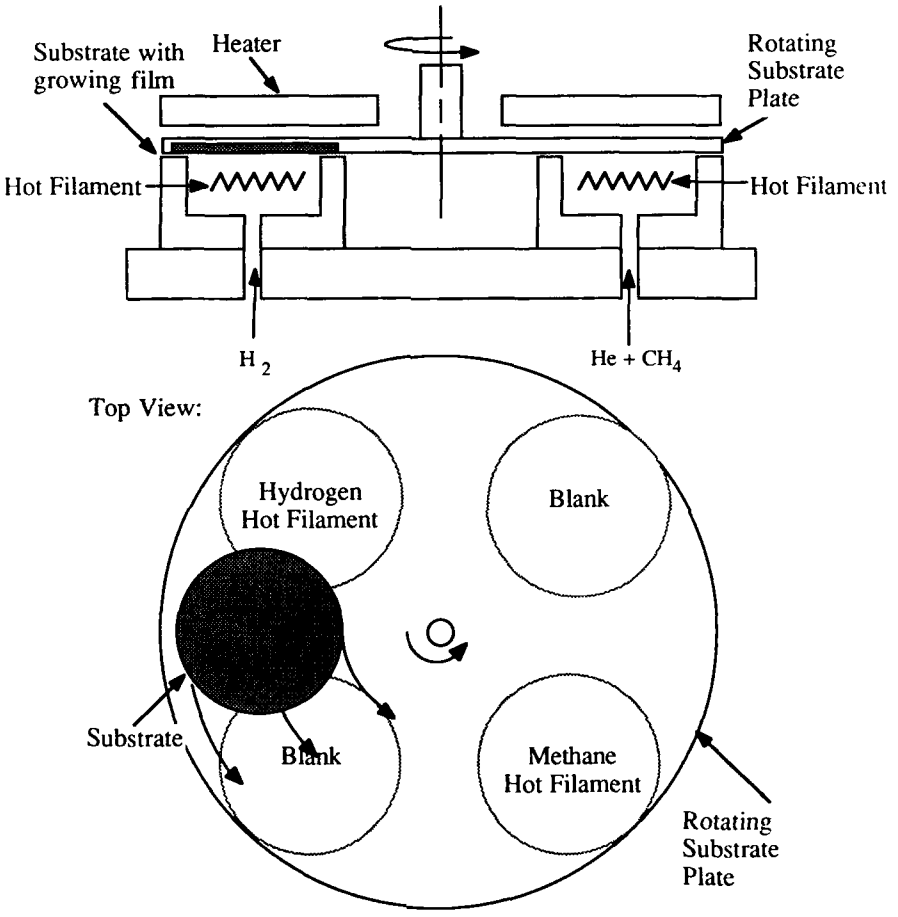


Figure 1: Side View and Top View of Sequential CVD reactor.

One of the major concerns with the separation of the gases into different plasmas is the level of cross-contamination i.e. the flow of gas from one emitter into the active region of another emitter. Cross-contamination was measured under deposition conditions by mass spectrometer sampling of each plasma region. Figure 2 shows the level of cross-contamination of helium in the hydrogen emitter as a function of the gas flow rate of helium and hydrogen through each emitter. The data shows that the cross-contamination can be made arbitrarily low by increasing the flow rates through the emitters. Allowing the level of cross-contamination to

reach 20% has not been observed to effect growth rate or morphology but may have a secondary influence on film nucleation density and incubation time.

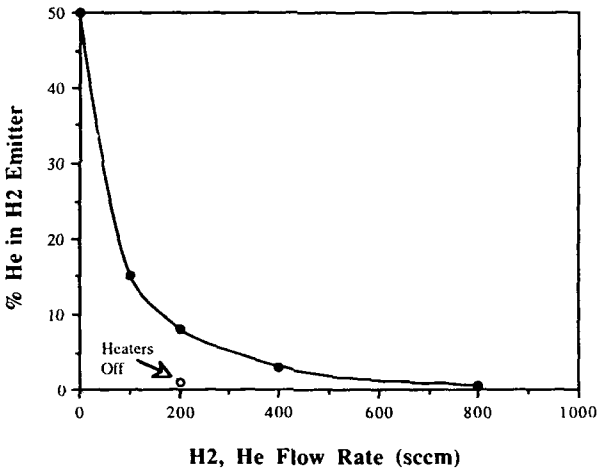


Figure 2. The measured level of cross-contamination in the hydrogen emitter under the following deposition conditions: hydrogen filament temperature 2500 K, substrate temperature 1100 K, substrate disk rotation at 200 RPM, chamber pressure of 30 Torr, and 200 sccm of argon flowing through the blank emitters.

To further illustrate that minimal cross-contamination is occurring a film was grown with the substrate stationary over the hydrogen emitter but otherwise under conditions identical to the growth of a very thick film with rotation. The result was a film two orders of magnitude thinner than in the rotating case. This film consisted of very small, < 0.1μm, individual particles of material only near the edges of the substrate. This is contrasted to the sequential, rotating, case which, under identical conditions, deposited a 1 μm thick fully agglomerated film made up of particles greater then 1 μm is size well faceted with facet features ~1 μm in size.

ROLE OF ATOMIC HYDROGEN

To investigate the role of atomic hydrogen in the deposition of diamond a series of films were deposited by sequential deposition at different concentrations of atomic hydrogen by changing the temperature of the filament in the hydrogen emitter. All other deposition conditions were held constant. Films were deposited on scratched <100> silicon wafers at a substrate temperature of 1060 to 1080 K. The total deposition time was 10 hours, resulting in a total exposure to each excitation source of 69 minutes.

The amount of atomic hydrogen can be estimated by assuming that the filament loses power by radiation, conduction, and dissociation of hydrogen molecules. Observing the characteristics of the filament in helium instead of hydrogen, the radiative and conductive components can be measured, and by allowing for the difference in thermal conductivities of the two gases, the power losses excluding hydrogen dissociation can be calculated. From this, an estimate of the power consumed to dissociate hydrogen molecules, and hence a relative measure of the atomic hydrogen concentration can be made.

Table I contains the deposition conditions data for all of the films presented here. Included in this data is the estimated atomic hydrogen bombardment per atomic site on the surface, per exposure of the substrate to the hydrogen emitter.

TABLE I

Deposition conditions of eleven samples. Including estimated atomic hydrogen bombardment.

Film #	% CH_4	CH_4 fil. T(K)	H_2 fil. T(K)	[H] (estimated).
1	4	2050	1780	300
2	4	2050	2030	450
3	4	2050	2070	480
4	4	2050	2240	660
5	4	2050	2250	660
6	4	2050	2310	840
7	4	1500	1910	360
8	4	1500	2000	450
9	4	1500	2160	540
10	8	2050	2000	450
11	8	2050	2220	600

Figure 3 shows SEM micrographs and Raman spectra of diamond films deposited under identical conditions, except that the flux of atomic hydrogen was changed, film numbers 1, 4, and 6 in Table I.. The conditions for the depositions were 4% methane in helium with a filament temperature of 2050 K. Pure hydrogen was supplied to the opposite emitter stand with filament temperatures set at 1800 K to 2300 K. The substrate was kept at 1100 K, as determined by optical pyrometry and rotated at 200 RPM. As can be seen, the increase in the quality of the deposited film at increased atomic hydrogen flux is quite evident in the improved morphology of the films. The Raman spectra for the three films, clearly shows the improved quality with increasing hydrogen flux. The Raman spectrum of the first film shows a large sp^2 carbon peak at 1550 cm^{-1} and no sp^3 diamond peak at 1332 cm^{-1}. The second film, deposited at a higher hydrogen flux, shows a decreased 1550 cm^{-1} peak and a clear peak at 1332 cm^{-1}. Finally, the third film shows a very sharp 1332 cm^{-1} peak with very little sp^2 content and a low level of photoluminescence background. With the current levels of concentration of atomic hydrogen we are able to generate, we have been able to deposit good quality diamond films with up to 8% methane in helium. Figure 4 shows the SEM micrograph and Raman spectra of two films (sample numbers 10 and 11) deposited with 8% methane in helium. The first film is clearly not diamond while the second is diamond of medium quality. The cause of the unique surface morphology of sample number 11 is not readily apparent. All the samples in Table I exhibit an increasing film quality as measured by Raman spectroscopy as a function of increased atomic hydrogen concentration. This improvement is expected since hydrogen has long been known to be an etchant of sp^2 defects in diamond films[1-3].

We note that the growth rate is increasing linearly with atomic hydrogen concentration. Figure 5 shows the thickness of the deposited films as a function of the temperature of the hydrogen filament, for the samples listed in Table I. Film thicknesses were determined by Rutherford backscattering (RBS), for films < 1 μm, and cross-sectional SEM for thicker films. Clearly, increasing the temperature of the hydrogen filament at constant methane concentration and filament temperature, increased the thickness of the deposited film. Additionally, increasing the supply of carbon, by increasing the temperature of the methane filament, also increased the thickness of the deposited film. Increasing the carbon content by increasing the amount of methane in the source gas seems to have a mixed effect. Increasing the methane concentration resulted in a decreased growth rate at low hydrogen concentration and an increased growth rate at high hydrogen concentrations. If one assumes that the increased growth rate at constant carbon conditions is due to an increase in atomic hydrogen this effect could be explained by two growth mechanisms.

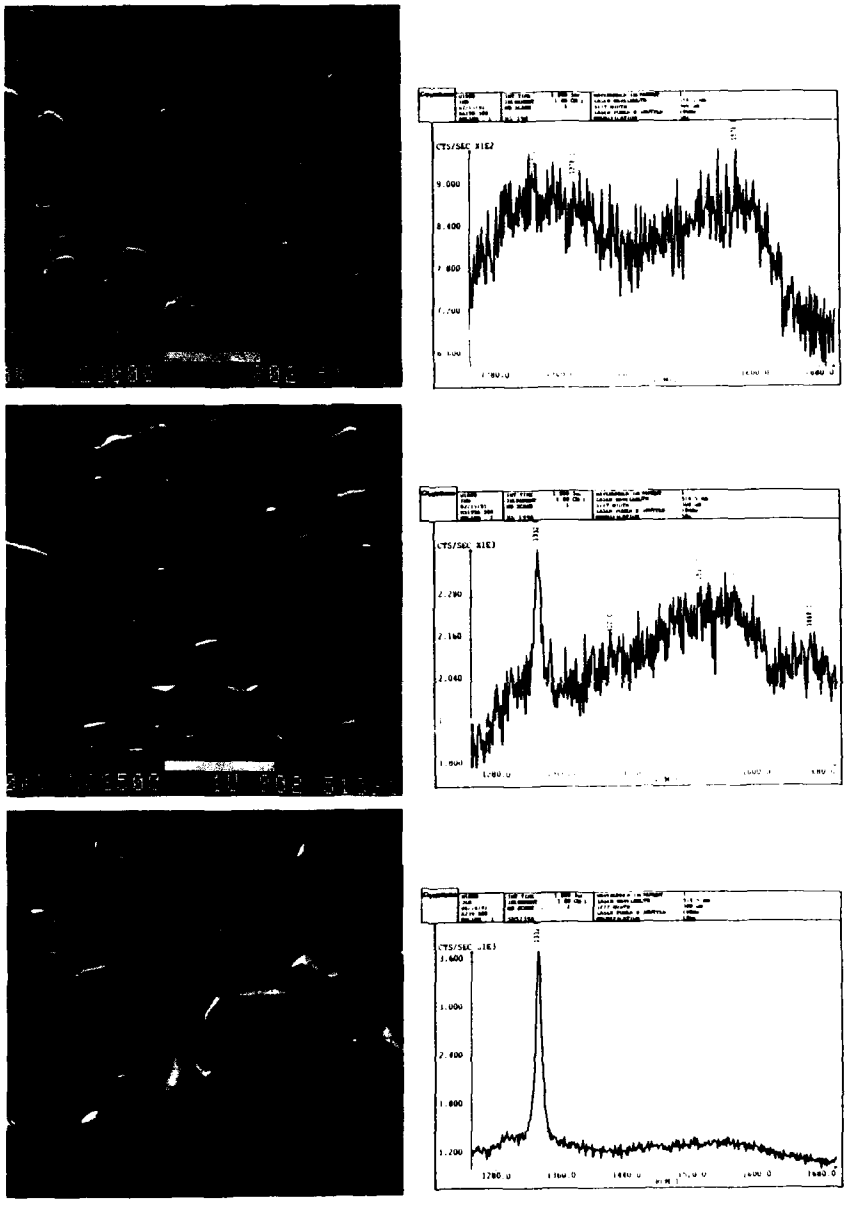


Figure 3: SEM micrographs and Raman spectra of diamond films deposited under identical conditions, except that the flux of atomic hydrogen was changed, film numbers 1, 4, and 6 in Table I. Hydrogen filament temperatures were 1780, 2240, and 2310 (K) respectively.

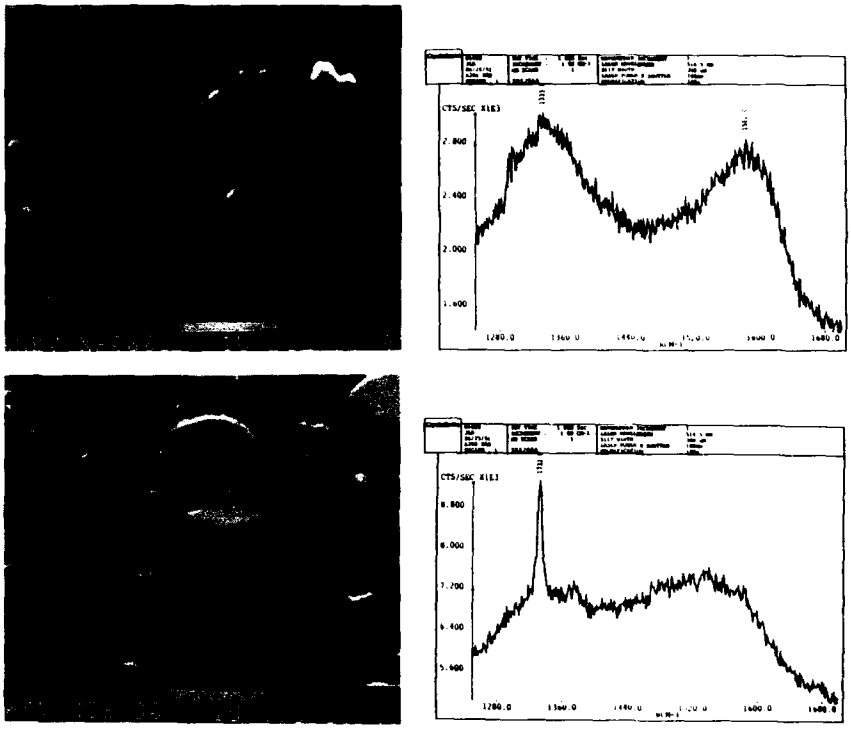


Figure 4: SEM micrographs and Raman spectra of diamond films deposited under identical conditions, except that the flux of atomic hydrogen was changed, film numbers 10, and 11 in Table I. Hydrogen filament temperatures were 2000, and 2220 (K) respectively.

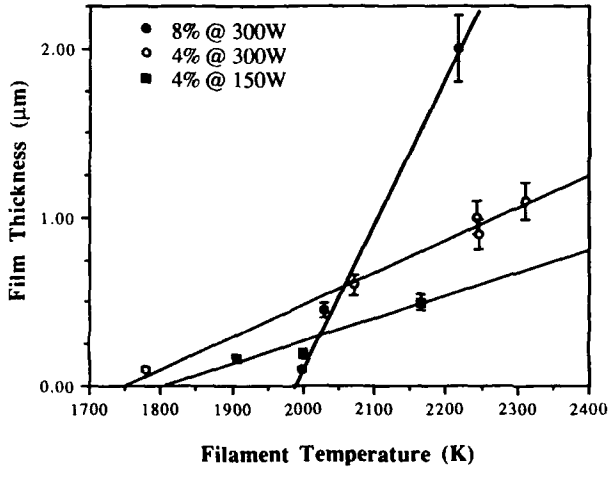


Figure 5. Film thickness as a function of the temperature of the hydrogen filament.

Carbon may be deposited on the surface in three ways; (i) as a non-diamond film on top of the growing diamond, (ii) as individual carbon atoms bonded or chemi-sorbed to the diamond surface, or (iii) carbon may deposit directly as diamond, (this seems sterically possible for the <100> face, but less so for the <111> face). If carbon is deposited as a non-diamond phase in the methane emitter, it could be etched off by the atomic hydrogen, enter the gas phase, collide with the surface of the substrate, and be redeposited as diamond. Increasing the concentration of atomic hydrogen might increase the probability of the redeposition reaction thus increasing the film growth rate. If the carbon is deposited as diamond or as individual carbon atoms on the diamond surface in the methane area, the increased growth rate might be explained by an increase in the reactivity of the diamond surface with increased atomic hydrogen flux. This increased reactivity could be due to several mechanisms; (i) fewer sp^2 defects on the surface, allowing faster surface diffusion and higher ledge velocities, (ii) a higher surface diffusion rate due to increased collisions of atomic hydrogen with adsorbed carbon, or (iii) a higher concentration of surface ledges necessary for growth, due to the roughening of the diamond surface by atomic hydrogen. These mechanisms need further study to explain the results.

CONCLUSIONS

By using the novel design of the sequential CVD reactor we have been able to demonstrate the growth of high quality diamond films by separating a hydrocarbon gas, methane, and an atomic hydrogen source. By applying differential pumping concepts we have shown that the cross-contamination between the gases in the four emitters can be minimized to have a negligible influence on the experiments.

Our results with separated hydrocarbon and atomic hydrogen, produced by hot filament technique, indicate that high quality diamond films can be grown at hydrocarbon concentrations as high as 8% methane in a helium carrier gas.

The growth rate is a linear function of the flux of atomic hydrogen for the levels we have been able to achieve. However, as the competing etching rate starts to increase with higher atomic hydrogen fluxes a tapering off of the growth rate is anticipated.

The most important conclusion we draw from our experiments is the demonstration of the importance of surface reactions for the formation of diamond films as compared to gas phase reactions. Although we do not want to preclude the significance of gas phase reactions, we believe that the crucial reactions occur between atomic hydrogen and carbon containing species on the growing surface. This is also confirmed by a parallel experiment in our sequential reactor where the substrate is sequentially exposed to atomic carbon, supplied by sputtering a graphite target, and atomic hydrogen, resulting in an excellent quality diamond film[9].

ACKNOWLEDGEMENTS.

We appreciate fruitful discussions with Professor Jan-Otto Carlson, Uppsala University, regarding the CVD processes; Dr. K. V. Ravi, Lockheed, on alternating chemistry processes; Dr. Michael Pinneo and Crystallume for characterization of films by Raman spectroscopy and discussion of those results, Professor Piero Pianetta on synchrotron radiation studies, and other discussions with members of the Stanford diamond community. This work was supported by the Center for Materials Research at Stanford University, with funding from the National Science Foundation.

REFERENCES

1. W. A. Yarbrough and R. Messier, Science, **247**, 688 (1990).
2. J. C Angus, C. C. Hayman Science, **241**, 913 (1988).
3. A. R. Badzian, R. C. DeVries, Mat. Res. Bull., **23**, 385 (1988).
4. S. J. Harris, L. R. Martin, J. Mater. Res., **5**, 2313 (1990).
5. F. G. Celii, J. E. Butler, New Diamond Science and Technology, MRS Int. Conf. Proc., 201 (1991).
6. S. J. Harris, Appl. Phys. Lett., **56**, 2298 (1990)
7. M. Tsuda, M Nakajima, S Oikawa, J. Am. Chem. Soc., **108**, 5780 (1986).
8. K. V. Ravi, A. Joshi, Appl. Phys. Lett., **58** (3), 246 (1991)
9. D. Olson, M. A. Kelly, S. Kapoor, S. B. Hagstrom, presented at 1991 MRS Fall Meeting, Boston, MA, December 5 1991.

DIAMOND GROWTH FROM SPUTTERED ATOMIC CARBON AND HYDROGEN GAS.

MICHAEL A. KELLY, SANJIV KAPOOR, DARIN S. OLSON, AND STIG B. HAGSTROM
Department of Materials Science and Engineering, Stanford University, Stanford CA 94305

ABSTRACT

Diamond thin films were grown on a scratched silicon crystal surface by a novel CVD technique. The heated substrate, mounted on a rotating platform, was exposed to a bombardment of sputtered carbon atoms, from a graphite target in a helium plasma, and subsequently bombarded by atomic hydrogen generated by a hot tungsten filament. The resulting diamond films were characterized by Raman spectroscopy and SEM. The SEM images indicate highly faceted diamond crystals and the Raman spectra show a single narrow peak characteristic of pure diamond with no graphitic component. The effective growth rate is about 0.5 microns per hour of exposure time. The novel sequential CVD reactor is described and possible growth mechanisms are discussed.

INTRODUCTION

The wide interest in low pressure CVD diamond films has been prompted by the unique material properties of diamond. Mixtures of hydrogen and hydrocarbon gases have been used extensively for synthesis [1-3]. Attention has focused on the gas phase precursors involved in the growth of the diamond film [4,5]. The understanding of nucleation and growth processes has been impeded by the complex and poorly understood gas phase chemistry. The operating pressure complicates *in situ* diagnostics thus impeding direct verification of proposed growth models [6,7].

In an attempt to understand the diamond deposition process we have constructed a novel sequential reactor which has four isolated gas sources. The chemistry and excitation of each source can be independently varied. This permits, for example, an increase in the amount of atomic hydrogen independent of the amount of carbon incident on the substrate. The substrate is rotated over the sources, being exposed to each source sequentially. The exposure time to each source is in the millisecond range shorter than other approaches to alternating chemistry [8]. Thus, deposition parameters such as growth rate and film quality can be correlated to single chemical species and some indication of the importance of certain growth processes involved is also possible.

We present here the deposition of diamond by a simple chemistry. A scratched silicon substrate is exposed first to a sputtered flux of atomic carbon from a graphite target in a helium plasma, and subsequently to a flux of atomic hydrogen, generated by exposing hydrogen to a hot tungsten filament. Our results indicate that a critical parameter influencing film thickness (growth rate) and film quality (sp^3 content) is the flux of atomic hydrogen bombarding the growing surface.

REACTOR DESCRIPTION AND PERFORMANCE.

The basic design of the sequential CVD system is shown in Figure 1. The sources are mounted in a bell jar which can be evacuated to 2×10^{-7} Torr using a diffusion pump. Four gas emitter assemblies are available, each one inch in diameter. Cross-contamination between any two sources can be made arbitrarily small by flowing gases at a high rate, typically several hundred sccm. The substrate was mounted on a rotating plate facing the gas excitation sources with a nominal separation distance of 0.5 mm from each gas source. A tungsten heater filament located behind the rotating plate is responsible for heating the substrate up to a temperature of 1300K.

Gases flowing through the sources can be excited by different means, including hot filament, DC glow, and RF radiation. However, this paper only addresses experiments involving the excitation of hydrogen gas by hot filament in one emitter, and the sputtering of

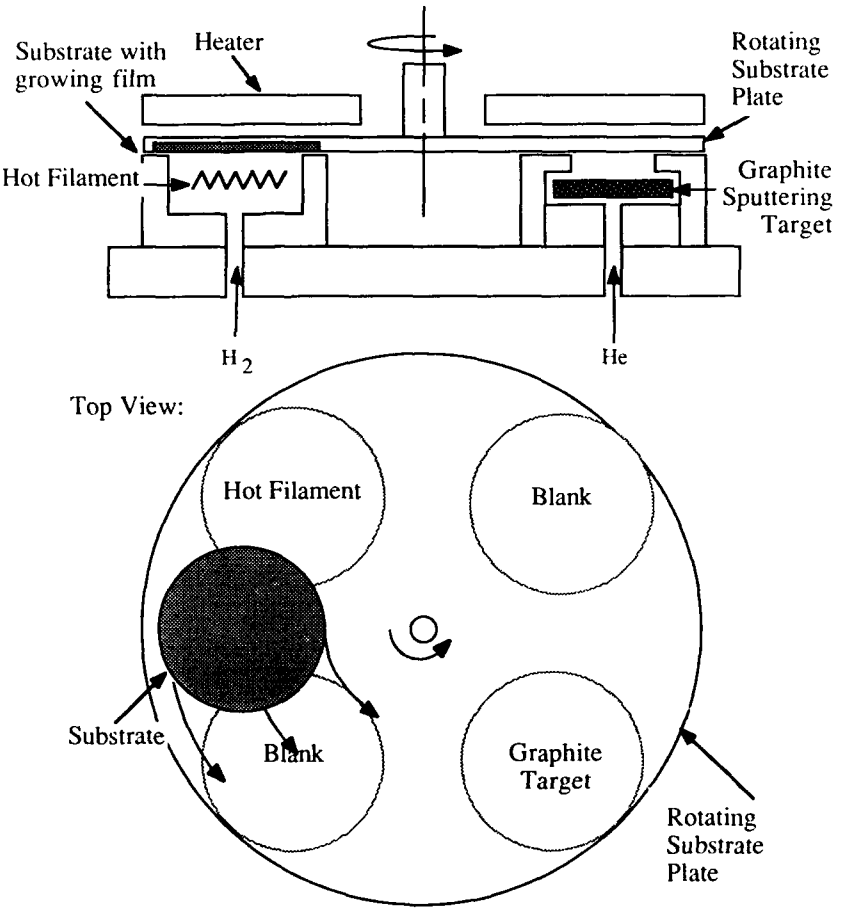


Figure 1: Side View and Top View of Sequential CVD reactor.

carbon in another emitter. The hydrogen emitter utilizes a 0.03" diameter tungsten filament to produce atomic hydrogen; the carbon emitter has a graphite electrode which acts as a sputtering target to produce atomic carbon. Helium is used as the sputtering gas in a DC glow discharge. The reactor was operated with equal flow rate in the two emitters.

A parameter of interest is the cross-contamination of the sources i.e. the flow of gas from one emitter into the active region of another emitter. In order to achieve isolation between the sources it is imperative that the cross-contamination be reduced to an acceptable level. For these experiments it should not be able to account for the growth of diamond films. The cross-contamination can be made arbitrarily small by increasing the gas flow rate through each emitter. Figure 2 shows the level of cross-contamination of helium in the hydrogen emitter as a function of the gas flow rate through each emitter, measured under deposition conditions by mass spectrometer sampling of the hydrogen emitter. The data shows that the cross-contamination can be made arbitrarily low by increasing the flow rate. The data in Figure 2 were obtained with a slightly altered geometry as compared to the geometry used for deposition in that the distance between the rotating plate and the sources was somewhat smaller. We believe that this does not

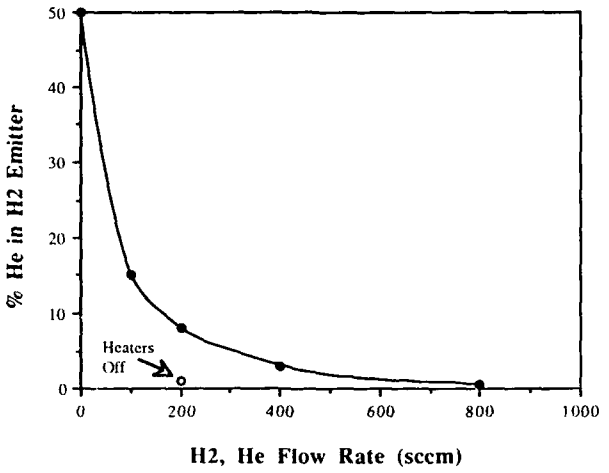


Figure 2. The measured level of cross-contamination in the hydrogen emitter under the following deposition conditions: hydrogen filament temperature 2500 K, substrate temperature 1100 K, substrate disk rotation at 200 RPM, chamber pressure of 30 Torr, and 200 sccm of argon flowing through the blank emitters.

affect our experiments.

Using this reactor, high quality diamond films were deposited with 200 sccm of He flowing through the carbon emitter and 200 sccm of hydrogen in the hot filament emitter. To illustrate that hydrogen contamination of the carbon source is not responsible for diamond growth, growth of a film was attempted with the filament in the hydrogen emitter off. The resulting film was graphitic with no diamond content. Carbon diffusion into the hydrogen emitter could also account for diamond growth. To evaluate this possibility a separate experiment was carried out wherein 8 sccm of methane and 192 sccm He flowed through the helium emitter, with the DC glow discharge turned off, and 200 sccm H_2 flowed over a hot tungsten filament through the opposite emitter. In a standard 10 hour run no film was deposited despite the total amount of gas phase carbon present being over an order of magnitude higher than the the total amount of carbon sputtered in other experiments where high quality diamond films were formed. We therefore conclude that gas phase transport of carbon to the hydrogen emitter, or hydrogen to the carbon emitter, cannot account for the growth of diamond films.

RESULTS AND DISCUSSION

Carbon films were grown under three separate conditions. The power supplied to the hydrogen filament was varied resulting in different filament temperature and atomic hydrogen flux to the substrate. The glow discharge for the carbon emitter was maintained at 550 V and 150 mA for each of these experiments. All the other experimental conditions were held constant for each experiment. Scratched (100) silicon wafers were used as substrates. Substrate temperature was held at 1070K (+/- 5%) as measured by a single wavelength optical pyrometer. The total deposition pressure was 10 Torr and the substrate was rotated at 200 RPM, resulting in an effective exposure of 69 minutes to each source for a 10 hour run.

In the first experiment, no power was supplied to the filament in the hydrogen emitter. A graphitic film was formed on the substrate, as expected. The mass of the film was compared with the weight loss of the cathode, showing that 22% of the carbon sputtered from the cathode

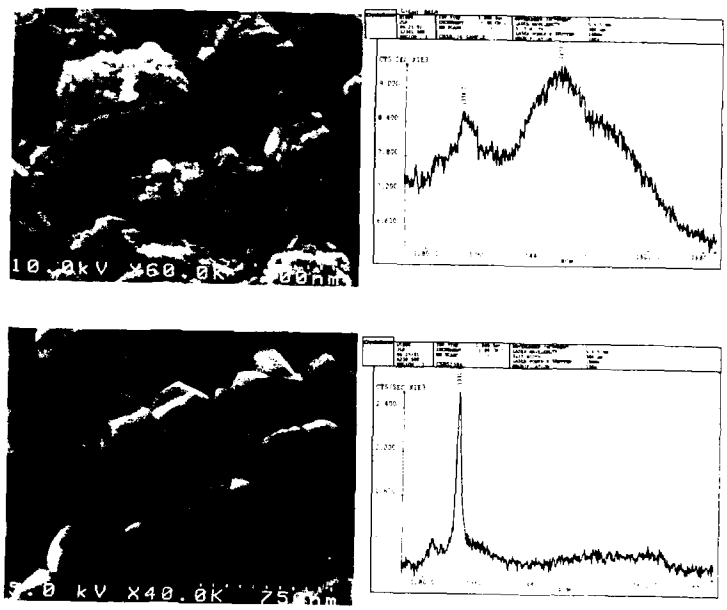


Figure 3: SEM micrographs and Raman spectra of diamond films deposited under identical conditions, except that the flux of atomic hydrogen was changed,. Hydrogen filament temperatures were 2320 K and 2560 K respectively.

was deposited on the substrate. From the measured weight of the film, the total amount of carbon deposited, in monolayers per exposure, was calculated (see Table I). In the next two experiments the power supplied to the filament in the hydrogen emitter was increased to 445W and 730W, respectively. The increased power supply results in an increased flux of atomic hydrogen incident on the substrate.

Figure 3 shows SEM micrographs and Raman spectra of these two films . As can be seen, the increase in the quality of the deposited film at increased atomic hydrogen flux is quite evident in the improved morphology of the films. The Raman spectrum of the first film shows a large sp^2 carbon peak at 1550 cm^{-1} and a small broad sp^3 diamond peak at 1332 cm^{-1}. The second film, deposited at a higher hydrogen flux, shows a decreased 1550 cm^{-1} peak, a clear peak at 1332 cm^{-1}, and a low level of photoluminescence background. The improvement in film quality with atomic hydrogen is expected since hydrogen has long been known to be an etcher of sp^2 defects in diamond films [1-3].

Table I contains the deposition conditions data for all of the films presented here. The amount of atomic hydrogen is estimated by assuming that the filament dissipates power by radiation, conduction, and dissociation of hydrogen molecules. Observing the characteristics of the filament in helium instead of hydrogen, the radiative and conductive components can be measured, and by allowing for the difference in thermal conductivities of the two gases, the

TABLE I

Deposition conditions of two samples. The estimated atomic hydrogen flux per atomic site on the surface, per exposure of the substrate to the hydrogen emitter, [H], is also included .

Film #	Total Carbon Sputtered(mg)	Monolayers carbon per exposure	H_2 fil. T(K)	[H] . (est.)	Film Thickness(μ)	Power to H_2 emitter
1	151	0.35	2320	800	.3	445
2	189	0.44	2560	1700	.45	730

power losses excluding hydrogen dissociation can be calculated. To attain the same filament temperatures reported for the two samples described in Table 1 with helium present instead of hydrogen, 260W and 375W were required, respectively. A model which considered radiation and conduction from the filament geometry in the emitter predicted these powers to within +/- 5%. Using the same model, but with a thermal conductivity appropriate to hydrogen, the power required to heat the filament to the appropriate temperatures was calculated to be 315W and 440W, respectively. The difference, 130W and 290W respectively, was assumed to be required to dissociate the hydrogen. It was further assumed that approximately 25% of the atomic hydrogen is incident on the substrate.

Film thicknesses were determined by cross-sectional SEM. We note that the growth rate is increasing with atomic hydrogen concentration. This trend matches the results of a parallel experiment where the carbon was supplied by methane passed over a hot filament [9].

The observed growth of diamond films cannot be accounted for by the cross-contamination of the sources as explained earlier. Thus we believe the carbon atoms deposited by the carbon source are converted to the diamond phase in one of the two emitters by one or more surface reactions. The large hydrogen flux required may be necessary to induce surface reactions needed to promote sp^3 bonding. The increased thickness with hydrogen flux could be explained due to an increased roughening of the surface and/or due to an increase in the diffusion rate of surface species enabling a faster incorporation of these into the growing diamond film. An alternate mechanism is also possible wherein volatile carbon species are desorbed from the surface modified in the gas phase and readsorbed onto the growing film. This possibility can be ruled out if subsequent experiments show that it is possible to grow at lower pressures since the probability of readsorption would be decreased.

CONCLUSIONS

By using the novel design of the sequential CVD reactor we have demonstrated the growth of high quality diamond films by sequential exposure to a carbon source of sputtered graphite, and an atomic hydrogen source, without supplying a hydrocarbon gas. Experimentally we have verified that the cross-contamination between the gases in the sources was minimized to have a negligible influence on the experiments.

The growth rate of the deposited films was observed to increase with the flux of atomic hydrogen. This is in confirmation with a parallel experiment in our sequential reactor where the substrate is sequentially exposed to carbon, supplied by heating methane, and atomic hydrogen [9].

Based on this work we propose that the growth of diamond films in the sequential CVD reactor is primarily governed by surface reactions. The necessity of gas phase precursors can be precluded unless a complex process is operating wherein surface species are desorbed, modified in the gas phase and then redeposited.

The role of atomic hydrogen was studied directly by using the process of sequential CVD. The atomic hydrogen flux was independently varied for a given flux of carbon. Diamond content in the deposited films and film quality scaled directly with the amount of atomic hydrogen in the hydrogen emitter. The increase in growth rate with atomic hydrogen could be due to an increase in surface roughening and/or due to an increased mobility of surface species.

ACKNOWLEDGEMENTS.

We appreciate fruitful discussions with Professor Jan-Otto Carlson, Uppsala University, regarding the CVD processes; Dr. K. V. Ravi, Lockheed, on alternating chemistry processes; Dr. Michael Pinneo and Crystallume for characterization of films by Raman spectroscopy and discussion of those results, Professor Piero Pianetta on synchrotron radiation studies, and other discussions with members of the Stanford diamond community. This work was supported by the Center for Materials Research at Stanford University, with funding from the National Science Foundation.

REFERENCES

1. W. A. Yarbrough and R. Messier, Science, **247**, 688 (1990).
2. J. C Angus, C. C. Hayman Science, **241**, 913 (1988).
3. A. R. Badzian, R. C. DeVries, Mat. Res. Bull., **23**, 385 (1988).
4. S. J. Harris, L. R. Martin, J. Mater. Res., **5**, 2313 (1990).
5. F. G. Celii, J. E. Butler, New Diamond Science and Technology, MRS Int. Conf. Proc., 201 (1991).
6. S. J. Harris, Appl. Phys. Lett., **56**, 2298 (1990)
7. M. Tsuda, M Nakajima, S Oikawa, J. Am. Chem. Soc., **108**, 5780 (1986).
8. K. V. Ravi, A. Joshi, Appl. Phys. Lett., **58** (3), 246 (1991)
9. D. Olson, M. A. Kelly, S. Kapoor, S. B. Hagstrom, presented at 1991 MRS Fall Meeting, Boston, MA, December 2 1991.

THE CVD DIAMOND NUCLEATION MECHANISM ON Si OVERLAID WITH sp^2 CARBON

PEHR E. PEHRSSON, JOHN GLESENER*, AND ARTHUR A. MORRISH**
Chemistry Division, Naval Research Laboratory, Washington, D.C. 20375-5000
*ONT Post-Doctoral Fellow, Naval Research Laboratory
**Optical Sciences Division, Naval Research Laboratory

ABSTRACT

Rudder et al. [1] observed heavy (>10^9 cm^{-2}) diamond nucleation on unscratched Si wafers overlaid with carbon fibers during CVD growth. We demonstrate that the nucleation occurs on the edges of etch pits and carbon-rich particles resulting from reaction between the fibers and the substrate. Both the etch pits and the particles satisfy what we consider to be two necessary conditions for 'spontaneous' nucleation; a carbon-saturated surface and high energy sites (unsatisfied valencies) at edges and steps.

Introduction

Scratching with diamond or SiC grit increases diamond nucleation density on many substrates from roughly 10^4 cm^{-2} up to 10^{11} cm^{-2} [2],[3],[4] but is not useful for heteroepitaxy or single-crystal growth because the nucleation events and subsequent crystal growth usually occur randomly with respect to each other. In this work, we use carbon fibers to increase diamond nucleation on unscratched Si substrates during growth in a hot-filament reactor, as has been done previously in an RF reactor [1]. We use the results to identify and elucidate some of the factors involved in diamond nucleation.

Experimental:

Samples were prepared by placing carbon fibers directly on Si substrates for various periods of time in a hot-filament reactor. Ni, Cu, and Ta substrates were also used for comparison. The fibers (Aesar, 99.5% pure, 8 μm diameter), were polyacrylonitrile (PAN) fibers carbonized at high temperature to yield principally graphitic carbon. The Si was Si(100), n-type, doped with $2x10^{-17}$ cm^{-3} Sb. The fibers were laid across the substrates, sometimes secured by tabs of metal or other pieces of Si, and appeared to contact the substrate for much of their length.

The samples were exposed to a hot-filament environment of 1% CH_4 in H_2, at a substrate temperature of 850-925°C, as measured with a thermocouple attached to the sample mount. The Re filament temperature was 2150°C, as measured with an optical two-color pyrometer. The gas flow rate was 100 sccm and the chamber pressure was 40 Torr. The growth times ranged from 15 minutes to 4 hours. Si substrates overlaid with carbon fibers were also heated under vacuum or Ar, or in atomic hydrogen alone at 900°C for 30-240 minutes before growth under standard conditions.

Following growth, the samples were analyzed using optical and

scanning electron microscopy (SEM), microRaman scattering, and the scanning Auger microprobe (SAM). Some samples were analyzed and then reinserted into the reactor for further growth.

Results:

Diamond crystals grew on the substrate in straight lines, apparently originating at the fiber/substrates junction and were connected by 50-500 nm debris trails, as seen in Figure 1a-b. The facetted particles were confirmed to be diamond on the basis of the 1332 cm^{-1} diamond Raman phonon. Debris trails and diamond crystals were observed after 15 minutes of growth. Very heavy nucleation densities (>10^9 cm^{-2}, normalized to the trail area) occurred on some of these trails exposed for >1 hour, so that the crystals formed a continuous 1-dimensional line. We observed some variability in the crystal density, which we attribute to poor fiber/substrate contact or inadequate substrate temperature control. The crystals were larger (≈1 μm) than we have previously observed for such short growths, indicating early nucleation and/or a high growth rate. They were also uniformly sized, suggesting simultaneous nucleation at many points, or self-limiting growth [5].

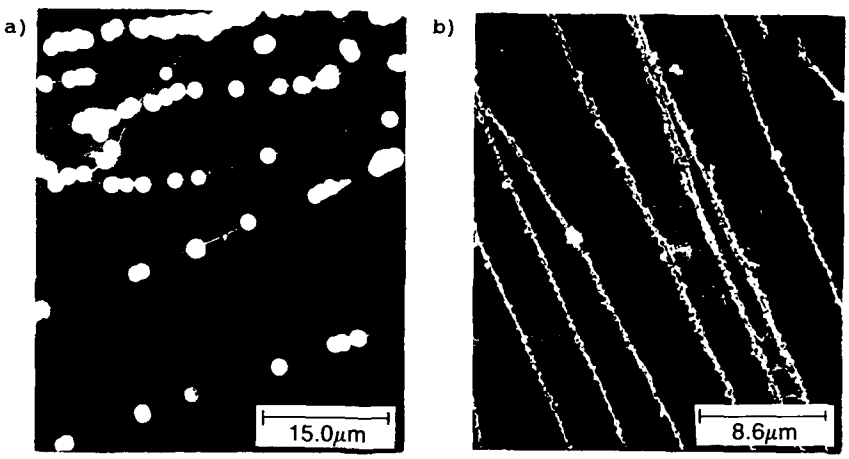


Figure 1a: Scanning electron micrographs (2kX) of diamond crystals and trails left after exposing an unscratched Si(100) wafer overlaid with carbon fibers to hot filament diamond growth for 4 hours; a) magnification=2000x; and b) magnification =6000x.

The debris composing the trails generally consisted of very fine (<50 nm) particles on top of the Si substrate, however as seen in Figure 2a, some of the trails were actually 'trenches' composed of coalesced etch pits in the Si substrate. The diamond crystals originated on the debris particles or on the trench edges.

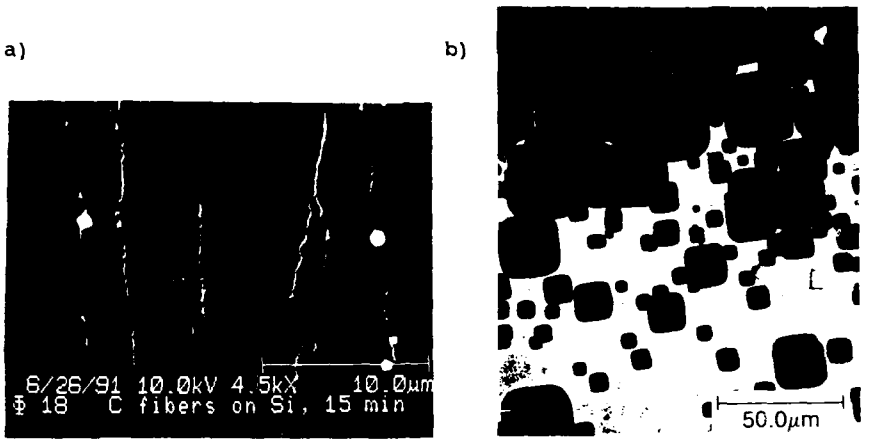


Figure 2: Scanning electron micrograph of features on unscratched Si substrates overlaid with carbon fibers and exposed to the hot filament diamond growth environment (1% CH_4/H_2): a) etch pits formed under the fibers after 15 minutes (4.5kX); and b) etch pits formed at 925°C away from the fibers (600x).

Some of the samples which had been exposed for 15 minutes were examined and then grown on again for an additional three hours after the carbon fibers were removed. The debris trails from the initial 15-minute exposure continued to nucleate diamond.

Samples heated under vacuum or Ar had 'fluffy' black carbon over much of their surfaces, although the fibers occupied only a narrow area in the sample center. Neither the area directly under the fibers, nor the rest of the surface had well-defined etch pits or diamond crystals. The debris trails on samples heated under atomic hydrogen appeared identical to those on regular samples.

The scanning Auger microprobe (SAM) revealed that the debris trails and etch pits had elevated C/Si ratios compared to the surrounding substrate. The C-KLL lineshape was graphitic [6], with a possible silicon carbide component. The Si-LMM lineshape contained elemental, oxidized and possibly carbidic contributions. The high-intensity electron beam altered the carbon lineshape and reduced the surface oxygen. Only C, Si, and O were found in the trails, with one exception. Auger examination of the carbon fibers before and after growth revealed no contaminants, indicating that contaminants were not involved in the nucleation process.

Some samples, inadvertantly heated to >900°C under growth conditions, developed large numbers of oriented, square etch pits, seen in Figure 2b. The pits were very rough, with labyrinthine ledges and pits. The C/Si ratios were elevated in the outer regions of the pits, similar to the fiber trails, but dropped towards the center. The Auger lineshapes were stable and carbidic.

Discussion:

It appears that diamond nucleation occurs on both the etch pit edges and the small particles of carbon-rich debris regions directly underlying the fibers. Both satisfy the criteria of carbon saturation and large numbers of edge sites. Most diamond crystals originated on debris since etch pits occurred less frequently on most of the samples.

The nucleation enhancement could be due to either gas phase nucleation or to reaction of carbon with the substrate to form a surface nucleation site. We support the latter interpretation since nucleation continues on the trails even when the fibers are removed 15 minutes into the growth, and therefore cannot act as a carbon reservoir or otherwise alter the gas-phase chemistry. It is unclear whether the carbon reaches the surface via a solid-state reaction at the fiber/substrate point of contact or is gasified and transported to the surface. However, the narrowness of the debris trails is consistent with a direct, solid-state reaction between the fiber and substrate. Stable carbon species move throughout the system via diffusion, bouyancy and convection effects, exceeding the observed 50-500 nm thickness of the debris trails [7]. Under Ar or vacuum the carbon from the fibers vaporized and redeposited on the substrate, but was apparently not re-evaporated, possibly due to a temperature difference. A fiber in proximity to the substrate could partally shield it from the atomic hydrogen flux and increase the carbon flux from the fiber to the substrate. Carbon species could be stabilized there and ultimately develop into carbidic and/or graphitic debris particles and nuclei, while carbon deposited elsewhere was etched by the atomic hydrogen, as demonstrated in the SAM results showing a sharp carbon gradient in the substrate when the fibers are heated under atomic hydrogen alone. The balance between the carbon flux (whether from a solid carbon reservoir or the gas phase) and etching by atomic hydrogen or oxygen probably controls the development of nucleating features.

Nucleation enhancement could also occur if Si gasifies from the substrate, then re-deposits on the fibers and converts to SiC particles which nucleate diamond. However, the narrowness of the crystal lines on the substrate seems to exclude this mechanism. Furthermore, examination of the fibers after growth revealed evidence of only low density diamond nucleation.

Yang [8] observed that single crystal Si(001) developed large numbers of square etch pits when coated with low levels of carbon and then heated to 950°C or above in vacuum. The square pits resemble those formed on our Si samples described above, suggesting a common mechanism responsible for their formation.

CVD diamond nucleation probably occurs in two ways; 1) homo- or heteronucleation on fragments of the scratching material left embedded in the substrate (the principal nucleation mechanism on diamond-scratched Si substrates), or 2) spontaneous formation on appropriate substrate surface features and defects. Recent HRTEM micrographs [2] confirm diamond fragment transfer to Si substrates during ultrasonication in a diamond suspension, and subsequent growth of the fragments into regularly-facetted diamond crystals during CVD. However, heavy nucleation can also be initiated by non-diamond materials under proper conditions, such as controlled

rubbing of a sapphire stylus across a Si substrate before growth [9]. Specific stylus-induced damage, especially fine cracks and sharp, small-diameter Si debris, clearly enhances diamond nucleation. Such debris possesses two characteristics which we believe are necessary for spontaneous (i.e. non-epitaxial) nucleation; 1) a high surface to volume ratio leading to rapid carbon saturation; and 2) sharp edges with high-energy sites for bonding and stabilization of nucleating species. The carbon-saturated zone retards further carbon diffusion into the substrate bulk, so the substrate surface carbon concentration rises [10]. Diamond nucleation may originate in random, fluctuating aggregations of carbon on the substrate surface, which survive long enough to grow by carbon addition into stable nuclei. Such sub-critical radius nuclei are by definition thermodynamically unstable [11], especially in the etching diamond growth environment, and the stability and density of such species might be increased by higher surface carbon concentrations. In addition, sharp edges and defects contain unsatisfied valencies (dangling bonds) which could stabilize nucleating species. Suggested nucleating species include molecular analogs of the various diamond crystal morphologies [12],[13], and cyclohexane [14].

Both a carbon-saturated substrate and appropriate surface features, must **simultaneously** be present for non-homo-epitaxial nucleation. Even carbon-saturated surfaces such as single crystal SiC [15] or basal plane graphite [16] nucleate poorly compared to diamond-scratched Si or graphite edge planes.

The nucleating high energy sites may not be on the initial substrate. For example, SiC develops a graphitic carbon layer at high temperatures due to preferential Si evaporation, and sharp features on the SiC surface might develop such a layer more rapidly than bulk SiC. The resulting graphite edge sites could nucleate directly by providing an appropriate site to stabilize diamond or could in turn stabilize hydrocarbons or other species which then nucleate diamond. Other substrates such as Ni [17] and Pt [18] develop graphitic carbon and hydrocarbon layers prior to diamond growth. Diamond nucleation may increased when etching by appropriate levels of atomic hydrogen or oxygen increases the number of graphite edge sites. However, high levels of oxygen in the feedgas suppress formation of the graphite and hydrocarbon layers, and ultimately inhibit diamond nucleation on Pt [19].

Conclusions We have demonstrated dense CVD diamond nucleation on unscratched substrates overlaid with carbon fibers and exposed to a hot filament growth environment. The nucleation occurs on etch pits and SiC debris particles created by reactions between the Si substrate and the carbon fibers. The results are consistent with other observations of nucleation on unscratched substrates exhibiting carbon-saturation and sharp-edged surface features.

Acknowledgements We thank Ron Rudder for alerting us to nucleation enhancement by carbon fibers, Dan Vestyk for taking the Raman spectra, and Wally Yarbrough for useful discussions about nucleation on SiC. John Glesener acknowledges the Office of Naval Technology for financial support in their post-doctoral program.

Bibliography:

1. R. Rudder, private communication, 5/91

2. P.E. Pehrsson, F.G. Celii, J.E. Butler, in R. Davis (ed.), Diamond Films and Coatings, 1991, in press

3. S. Iijima, Y. Aikawa, K. Baba, Appl. Phys. Lett., 57(25), 2646 (1990)

4. S. Yugo, T. Kimura, H. Kanai, Science and Technology of the New Diamond, (ed. S. Saito, O. Fukunaga, M. Yoshikawa), Proc. of 1st Intl. Conf. on New Diamond Science and Tech., (1991)

5. A.B. Harker, J.D. DeNatale, J. Mater. Res., 5(4), 818 (1990)

9. P.G. Lurie, J.M. Wilson, Surface Science, 65, 476 (1977)

7. T. Debroy, K. Tankala, W.A. Yarbrough, R. Messier, J. Appl. Phys., 68(5), 2424 (1990)

8. Y. Yang, E.D. Williams, J. Vac. Sci. Tech. A, 8(3), 2481 (1990)

9. P. E. Pehrsson, A. A. Morrish, J. Glesener, presented at the Int. Conf. on Met. Coatings and Thin Films, San Diego, Ca., 1991 (manuscript in preparation)

10. P.O. Joffreau, R. Haubner, B. Lux, J. Ref. Hard Metals, 186 (1988)

11. R. Kern, G. LeLay, J.J. Metois, Current Topics in Materials Science, 3, 135 (1979)

12. S. Matsumoto, Y. Matsui, J. Mater. Sci., 18, 1785 (1983)

13. J.C. Angus, F.A. Buck, M. Sunkara, MRS Bull., 38 (Oct., 1989)

14. J.C. Angus, personal communication, (1991)

15. R.F. Davis, J.T. Glass, G. Lucovsky, K.J. Bachmann, R.J. Trew, R.J. Nemanich, Annual Report: School of Engineering, N.C. State Univ., Raleigh, N.C., (1988)

16. J.C. Angus, Proceedings, 2nd Intl. Sym. on Diamond Materials, The Electrochem. Soc., Washington, D.C., May, 1991, in press

17. D.N. Belton, S.J. Schmieg, J. Appl. Phys., 66(9), 4223 (1989)

18. D.N. Belton, S.J. Schmeig, J. Vac. Sci. Tech. A, 8(3), 2353 (1990)

19. D.N. Belton, S.J. Schmeig, J. Appl. Phys., 69(5), 3032 (1991)

AN INVESTIGATION INTO THE USE OF A DIFFUSION BARRIER IN THE MICROWAVE PLASMA ASSISTED CHEMICAL VAPOR DEPOSITION OF DIAMOND ON IRON BASED SUBSTRATES.

PAUL S. WEISER[1], S. PRAWER[1], A. HOFFMAN[2], R. MANORY[3], P.J.K. PATERSON[4] and S-A. STUART[4],
[1]School of Physics, University of Melbourne, Parkville, Victoria 3052, Australia.
[2]Australian Nuclear Science and Technology Organization, PMB 1, Menai, NSW 2234.
[3]Metallurgical Engineering, [4]Department of Applied Physics,
Royal Melbourne Institute of Technology, GPO Box 2476V, Melbourne, Victoria, 3001, Australia.

ABSTRACT

The growth of CVD diamond onto iron based substrates is complicated by preferential soot formation and carbon diffusion into the substrate, leading to poor quality films and poor adhesion. One strategy to overcome these problems is the use of thin film barrier layers between the Fe substrate and the growing diamond film. The present investigation reports the growth of diamond films on Fe substrates coated with thin films of TiN. The effectiveness of the TiN layers in inhibiting C diffusion into the Fe substrate was investigated by Auger measurements of the C distribution within the TiN layer, through the interface and into the substrate both before and after diamond deposition.

The results show that a layer of TiN only 250Å thick is sufficient to inhibit soot formation and C diffusion into the Fe bulk, as well as providing nucleation sites for CVD diamond growth.

INTRODUCTION

The growth of Chemically Vapour Deposited Diamond on many substrates, including tool materials (cemented carbide, SiAlON, SiC and Tungsten cutting tips) has been extensively studied in recent times [1-5]. Despite this the deposition of diamond on Fe based tools remains comparatively unreported and is poorly understood. Some authors [6,7] have commented that it is difficult to grow diamond on Fe. The factors which have been suggested to mitigate against good quality diamond growth on Fe (as compared to other metals such as Tungsten), are (i) soot formation on the surface presumably due to the catalytic effect of the Fe substrate, and (ii) the diffusion of C into the Fe bulk. The latter may also lead to embrittlement of the Fe substrate.

The presence of a suitable barrier layer on the Fe substrate may well overcome some or all of the above problems. In this study we report the effect of thin TiN layers on the nucleation and growth of diamond on Fe substrates. TiN was chosen because (i) it is extensively used as a hard-coating on steel and cemented carbide tools and (ii) it is known to be very effective as a diffusion barrier [8,9]. Herein, we show that the presence of even a very thin film of TiN on the Fe surface does indeed inhibit soot formation on the surface and the diffusion of C into the Fe bulk.

EXPERIMENT

The substrates were cut from a piece of magnet iron as plates of dimension 10 x 10 x 0.7 mm^3. Auger spectroscopy revealed C ($\leq$5 at. %) and Si (~12 at. %) as the only impurities to within the sensitivity of the Auger technique (2 at. % in these samples). The samples were mechanically polished to a 0.5μm diamond paste finish and then ultrasonically cleaned in acetone and ethanol. Using a TENCOR ALPHASTEP 250 profiler it was found that the typical surface roughness was ~0.3μm.

Reactive Magnetron Sputtering was used to deposit thin TiN films 250, 500 and 1000Å thick. A mask was used to shield half the specimen from the TiN deposition leaving half of the sample uncoated. These samples were used to investigate the effect of the TiN as a diffusion barrier.

For studies of the CVD diamond growth as a function of time, thick (1.4μm) TiN films were deposited using a commercial electron beam coating unit. The mask used for these specimens

was slightly displaced from the substrate leading to seepage of the TiN film creating a graded interface of varying thickness of TiN. No CVD diamond growth occurred in the region of the thick TiN. However, growth did occur in the region of the substrate in which the film thickness was about 700Å; it is growth on this section of the TiN film which is reported herein as the time series reported in figure 3.

The CVD diamond deposition system consists of an Evanson Cavity encasing a 1" vertical quartz tube containing the reactant gases (methane/hydrogen mix), which are excited using a frequency of 2.45 GHz [10]. Prior to insertion in the CVD system, TiN coated specimens were again thoroughly cleaned in acetone and ethanol. The deposition parameters used were Pressure - 30 Torr; Flow Rate - 100 sccm; CH_4/H_2 - 1:99 and Temperature - 900^{0}C. For studies of diamond growth as a function of time, deposition times of 7½, 15, 30, 60, 120, 240, and 360 minutes were used. Temperature was measured using an optical pyrometer.

Auger Electron Spectroscopy (AES) was used to investigate the near surface region (~20Å) and the composition as a function of depth of the substrates before and after CVD diamond deposition. The measurements were performed with a Varian Cylindrical Mirror Analyser (CMA) with a coaxial electron gun. The sputtering was via Argon ion bombardment with an ion energy of 2keV and a current of 90nA into a spot approximately 100μm in diameter. The Auger line shape provides clear signatures for different allotropes of carbon [11] and for carbides. These signatures have been used to gain qualitative information about the nature of the bonding in the films. The concentration of an element X was estimated by

$$\frac{I_x/S_x}{\sum_{\text{all elements}} I_x/S_x}$$

where I_x is the peak to peak intensity of the Auger line and S_x is the sensitivity factor [12]. The sensitivity factors used were 0.14, 0.2, 0.34 and 0.29 for C, Fe, Ti and Si respectively. Micro-Raman spectra were taken using the 488nm excitation line of an Argon ion laser with a spot size of 1-2μm and resolution of 6cm^{-1}.

RESULTS

Figure 1 is an SEM micrograph of the TiN/Fe interface region after 7½ minutes of CVD diamond deposition and Figure 2 shows a similar region after 2 hours of growth. In each case region (a) is the portion of the sample which has been TiN coated (250 Å) and region (b) is the uncoated Fe surface. After only 7½ minutes a continuous film has formed on the Fe, whilst there is no growth on the TiN. The thickness of the film was measured by surface profilometry to be 0.4 μm. The material is soft and can be easily scratched by the profilometer stylus at loads ≥9mg. After 2 hours (Fig. 2) particles have formed on both the coated (250Å TiN) and uncoated surfaces, but the particles on the Fe have grown on top of the thick film which has formed in the first few minutes of growth. Interestingly, the maximum nucleation density on the TiN coated portion of the sample occurred at the TiN/Fe interface where the TiN is very thin. This probably suggests that the deposited TiN is causing smoothing of the diamond abraded surface and the optimum thickness suitable for diamond growth on TiN coated Fe may be less than the 250Å used in the present study. After 6 hours of growth (not shown) the diamond particles coalesce to form a continuous film on both the TiN and Fe substrates.

Further insight into the evolution of the CVD diamond particles was provided by Auger spectroscopy. The inset to Figure 3 shows the C(KLL) Auger line shapes for graphite (a), amorphous carbon (b) and diamond (c). One way of parameterizing these signatures is to extract the ratio G=1000*(A/B) (see inset, figure 3). The values of G for diamond, amorphous carbon, glassy carbon and highly oriented pyrolytic graphite are -20±10, 40±10, 110±10 and 210±10 respectively. Hence, the larger G, the larger the graphitic component of the material. Figure 3 plots this G parameter as a function of growth time for both the uncoated and TiN coated portions of the sample. For the uncoated area there is a clear change in the G parameter after 2 hours of growth which corresponds to the appearance of the small particles shown in Figure 2. By contrast on TiN there is a dramatic change in the G parameter after only one hour of growth. The line shape is characteristic of diamond.

Raman spectra (Figure 4) taken after one and two hours of growth are consistent with the above trends. After one hour there is clear evidence of diamond growth on TiN, whilst the growth on Fe appears to be graphitic. After two hours diamond particles can be found on both

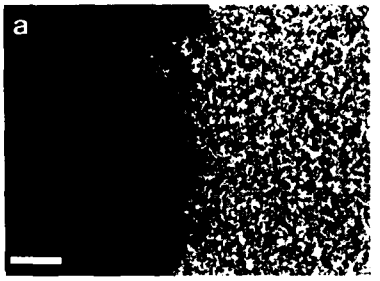


Figure 1 - SEM micrograph of the (a) TiN (250Å) and (b) Fe interface after 7½min. of CVD diamond deposition. The scale-marker represents 10μm.

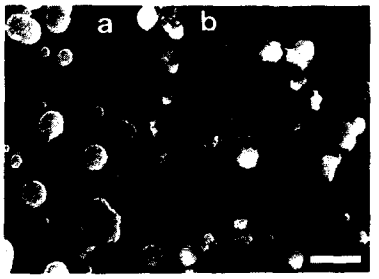


Figure 2 - SEM micrograph of the (a) TiN (250Å) and (b) Fe interface after 2 hours of CVD diamond deposition. The scale-marker represents 10μm.

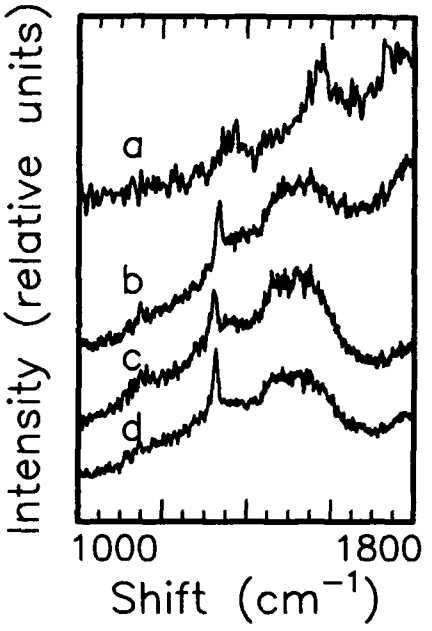


Figure 4 - Micro-Raman Spectra of the growth on (a) Fe and (b) TiN (700Å) after 1 hr. of CVD diamond deposition and (c) Fe and (d) TiN (500Å) after 2 hours of CVD.

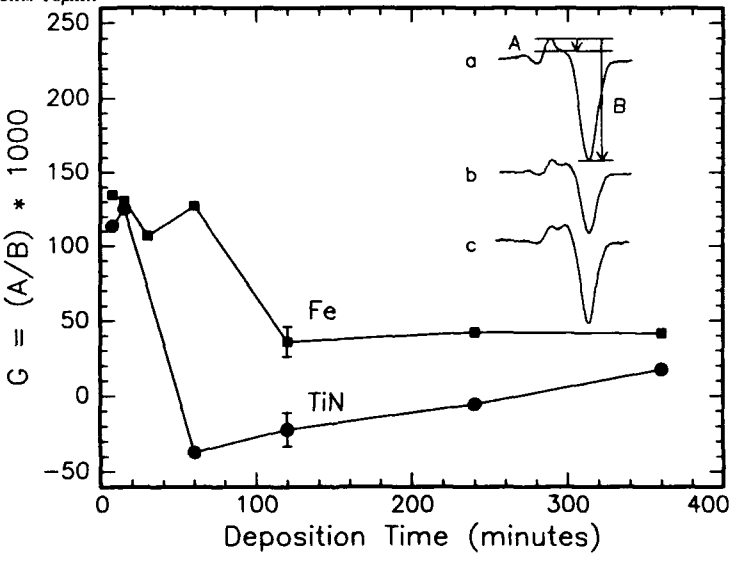


Figure 3 - The G parameter as a function of Deposition Times for Fe and TiN (700Å). The inset shows the line shapes of the three carbon allotropes observed and how the A/B ratio is measured.

TiN and Fe. However, it must be noted that the diamond particles on Fe grow on top of a thick layer of soot. Whilst micro-Raman measurements are spatially selective the Auger measurements sample both the soot and the particles. Hence the G parameter is somewhat greater for the deposit on Fe than on TiN.

Figure 5 displays an Auger Depth Sputter Profile of the uncoated Fe substrate after 7½ min. CVD deposition time. It shows that a sputter time of 175 minutes is required to obtain the pre-CVD carbon concentration within the iron (C ≤5 at. %). The depth of the sputter crater was estimated by profilometry to be approximately 1μm. From these measurements it is clear that there has been considerable diffusion of the carbon into the Fe. Surprisingly, there is up to 30 at % Fe at the surface, indicating that the soot formation may also involve diffusion of Fe into the carbon layer.

The inset (a) to figure 5 shows the Auger lineshape of the carbon close to the surface which is typical of graphitic carbon with the satellite peak at ~30eV to the left of the main peak at 272 eV. As the Fe concentration increases deeper into the sample the C(KLL) lineshape (b) shows evidence of the presence of carbidic carbon (presumably Fe_3C) with the emergence of two more satellite peaks displaced 11 and 19eV to the left of the 272 eV peak. The observed lineshape however does not appear to be one of pure carbide since it is asymmetric. This suggests that the layer is a mixture of graphitic and carbidic carbons at this depth. The line shape becomes increasingly carbidic as one sputters even deeper into the film. However, once the C level reaches that observed in the virgin Fe samples, the line shape once again appears to be graphitic.

Figure 6 shows an AES depth profile of the portion of the sample coated with 250Å of TiN on Fe after 7½ min. of CVD diamond deposition. Estimation of the N content of TiN films is complicated by the overlap of the N(KLL) and Ti(LMM) transitions. Based on the method described in ref. [13], we estimated that the Ti/N ratio was about 1:1. However, this procedure is fraught with errors and for the depth profile we have plotted only the relative Ti, Fe and C concentrations. The sputter profile shown in Figure 6 is very similar to that obtained from depth profiling of the TiN layer prior to CVD deposition. In particular there is no increase in the C concentration underneath the TiN layer following exposure to the CVD plasma. The inset to Figure 6 shows the line shape of the carbon in the TiN layer, which is characteristic of a carbide (presumably TiC), which is present both before and after CVD deposition and is presumably attributable to contamination in the TiN magnetron sputter system. Comparison of Figures 5 and 6 convincingly shows that the TiN has been very effective as a barrier against diffusion of C into the Fe substrate. Similar results were obtained after 2 hours of CVD deposition.

DISCUSSION

1. Growth on uncoated Fe: In the very early stages of exposure to CVD diamond conditions a thick film forms on the Fe substrate. This film is graphitic in nature as has been confirmed by both Raman and Auger measurements. However, despite the fact that the film is of the order of 0.4μm thick after only 7½ minutes of diamond deposition, a considerable amount of Fe is present on the surface. It is not clear whether this is due to Fe diffusing up through the deposited layer or due to the formation of a complicated mixture of Fe_3C and graphite. The equilibrium phase diagram for Fe/C [14] (which is, of-course, not strictly applicable for the non-equilibrium conditions present in the microwave plasma) shows the possibility of a mixture of Fe_3C and graphite at 900^{o}C at high carbon concentrations, above 25 at. %. On the other hand, because our AES analysis is performed at room temperature, we cannot distinguish between carbide formed at 900^{o}C or upon decomposition of austenite into ferrite and Fe_3C during normal cooling. Formation of such a mixture, possibly concomitant with swelling, is consistent with our observations of both carbidic and graphitic carbons in this layer, although the possibility of diffusion of Fe to the surface cannot be discounted.

After 2 hours of exposure to CVD conditions, diamond particles nucleate and grow upon this layer, culminating in the formation of continuous films for deposition times in excess of 6 hours. The appearance of the diamond particles after 2 hours of growth suggests that there may be a critical thickness of graphite necessary to shield the incoming precursor gases from the catalytic surface effects of the iron. However, another possibility is that the Fe concentration at the surface is detrimental for diamond growth, and that diamond will only nucleate once the concentration of Fe has fallen below a certain critical value.

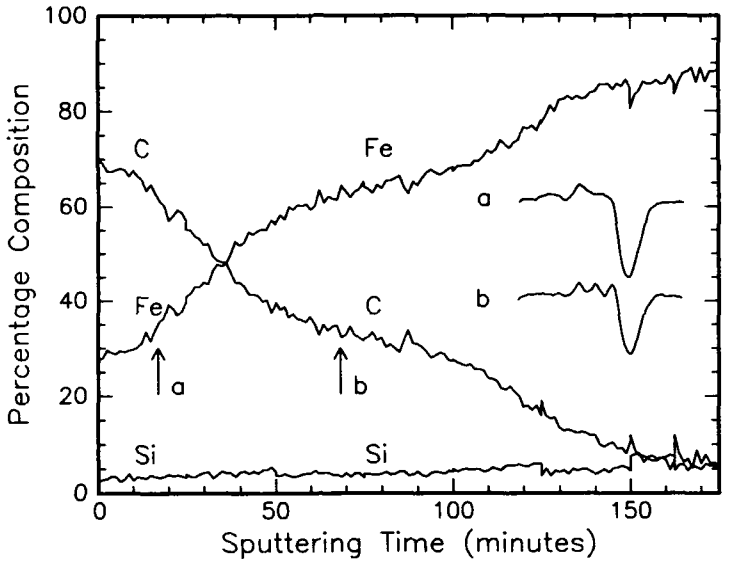


Figure 5 - Auger Depth Profile of the uncoated Fe substrate after 7½min. CVD deposition time. The inset shows the two C(KLL) line shapes observed within the sputter profile ((a) graphitic and (b) graphitic/carbidic carbon).

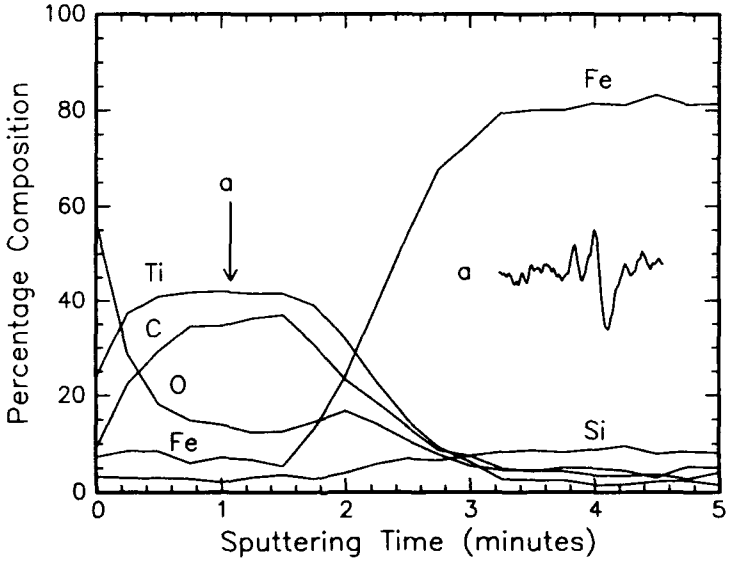


Figure 6 - Auger Depth Profile of an Fe sample coated with 250Å of TiN after 7½min. of CVD diamond deposition. The inset (a) shows the carbidic nature of the C(KLL) line shape within the TiN.

2. Diffusion of C into Fe: Under the plasma conditions in our CVD apparatus, significant diffusion of C into Fe was observed (1μm penetration in 7½ min.). However, we note that the plasma contains a very small overall amount of carbon (CH_4:H_2 = 1:99). This large diffusion rate, despite the low concentration of C is attributable to plasma enhancement of diffusion as has also been observed in the case of DC plasma immersion of steels in methane [15].

3. TiN as a diffusion barrier: In the absence of any TiN coating C diffuses deep into the Fe substrate. The presence of even a thin layer of 250Å of TiN is remarkably effective at inhibiting this diffusion, and no increase in the C concentration in the Fe is observed following exposure to the CVD plasma. At present, the combined effect of the nucleation density and deposition time yield only individual particles. Hence, no qualitative assessment of the diamond adhesion to the TiN can be made at this time. The increase in nucleation density close to the TiN/Fe interface indicates that the optimum thickness of TiN for diamond deposition may be even thinner than 250Å.

CONCLUSION

The growth of CVD diamond on Fe in a microwave plasma is complicated by the formation of a thick graphitic film on the surface during the first few minutes of exposure to the plasma. During this time considerable diffusion of C into the Fe substrate occurs. A thin coating of TiN (250Å) on the Fe was found to inhibit the formation of the graphitic layer and prevent C diffusion into the Fe. For longer deposition times (≥2 hours) diamond nucleates and grows on both the TiN and on this thick graphitic layer. The results show that TiN is very effective as a diffusion barrier for diamond deposition on Fe, as well as a surface upon which good quality diamond will nucleate and grow.

ACKNOWLEDGMENTS

The authors would like to acknowledge the support of the APIRA award held by PSW in conjunction with the support of CRA- Advanced Technical Development. We would also like to thank Peter Jewsbury and Chris Townsend of Materials Research Laboratory (Defence Science and Technology Organization). The assistance of Terry Mernagh (The Bureau of Mineral Resources, Canberra) with the Raman measurements is gratefully acknowledged.

REFERENCES

1. K.E. Spear, J. Am. Ceram. Soc., 72(2), 171-91 (1989).
2. N. Kikucki et al, Mater. Sci. & Eng., A105/6 (1988), 525-534.
3. R.C. M^{c}Cune et al in Thin Films: Stresses and Mechanical Properties (Mater. Res. Soc. Symp. Proc. 130, Pittsburgh, PA.) pp. 261-266.
4. S. Jahanmir et al, Wear, 133, 73-81, (1989).
5. N. Kikucki et al, JP 61/97194, May 1986, 5pp.
6. T.P. Ong and R.P.H. Chang, Appl. Phys. Lett., 58(4), 28 Jan. 1991.
7. P.O. Joffreau et al, J. Ref. Hard Metals, 7, 186 (1988).
8. R. Manory, Surf. Eng., 3(3), p. 233, (1987).
9. J.O. Olowolafe et al, Appl. Phys. Lett., 57(13), 24 Sept. 1990.
10. S. Prawer et al, J. Appl. Phys., 69(4), pp. 6625, 1 May. 1991.
11. A. Hoffman et al, Nucl. Instrum. & Meth. in Phys. Res., B51 (1990), pp. 226-231.
12. L.E. Davies et al, Handbook of Auger Electron Spectroscopy (Physical Electronics Industries, Edina, 1976).
13. M.Y. Al Jaroudi et al, Thin Solid Films, 195(1991), p. 63.
14. O. Kubbaschewski, Iron-Binary Phase Diagrams, (Springer-Verlag, Berlin, 1982), p.24.
15. W.L. Grube et al, Metallurgical Transactions A, 9A, Oct. 1978, p. 1421.

SELECTIVE NUCLEATION OF DIAMOND CRYSTALS ON THE APEX OF SILICON PYRAMIDS

R. RAMESHAM and C. ELLIS
Electrical Engineering Department
Alabama Microelectronics Science and Technology Center
Auburn University, AL 36849-5201

ABSTRACT:

Diamond crystals have been selectively grown on the apex of anisotropically chemically etched silicon pyramids. A novel process sequence is developed which exposes patterned sharp apex of silicon pyramids surrounded by thermally grown silicon dioxide to a high pressure microwave plasma-assisted chemical vapor deposition (HPMACVD) process where the reactant feed gases are methane and hydrogen. Nucleation rate of diamond is very high on the sharp edge of a silicon mesa structure or an apex of a silicon pyramid as anticipated. Selective growth of diamond particles on the apex of silicon pyramids fabricated using various approaches were analyzed by scanning electron microscopy.

INTRODUCTION:

Mirror-smooth finished silicon surfaces have a very low nucleation density for diamond growth. Scratching or damaging the silicon surfaces using a diamond paste has substantially enhanced the nucleation density of diamond growth by several orders of magnitude [1-3]. Hirabayashi et. al., have treated the damaged silicon surface with Ar^+ ion beams prior to the diamond growth studies to achieve the selective diamond growth [4]. Ar^+ ion beam scanning over the damaged silicon surface has minimized the scratch density by rounding off the sharp edges of damage performed by ultrasonic agitation in ethyl alcohol solvent containing diamond particles. Our work resulted selective diamond growth over silicon surface by using thermal oxidation of damaged silicon surface using a silicon nitride mask to minimize the sharp edges by rounding off in the undesired (oxide grown) diamond growth areas [5-7]. Do the above observations indicate that the sharp edges are active sites or very low free energy sites for nucleation of diamond growth ? We have considered the above results as a guideline and assumed the apex of anisotropically etched silicon pyramids as a nucleation site for diamond growth. If an apex of a pyramid is a nucleation site for diamond growth it should in principle have a high growth rate. Figure 1a is a scanning electron micrograph of diamond particles grown on chemically etched silicon mesa structure (diamond deposition time: ~5.75 hrs). It is vivid from the micrograph that the diamond tend to nucleate on the sharp edge of a silicon mesa. The apparent area of the sharp edge is considerably smaller than the apparent flat surface area of the silicon in the micrograph. But, approximately 50% of the diamond nucleation has occurred on the sharp edge irrespective of the lower area ratio. Figure 1b shows an SEM of diamond particles grown on an inverted silicon mesa structure. It is clear from the micrograph that the diamond nucleation is minimum on the sharp edges in an inverted mesa and this could be due to minimum flux density of reactants. This paper delineates the process flow steps to grow diamond particles selectively on the apices of anisotropically etched silicon pyramids fabricated with and without diamond paste treatment prior to the fabrication of pyramids to substantiate the idea of a tendency of diamond nucleation on the sharp edges.

EXPERIMENTAL DETAILS:

A commercially available high pressure microwave plasma-assisted (HPMA) chemical vapor deposition (CVD) system (ASTeX, Inc., Cambridge, MA) was used in our experiments to grow diamond crystals. The typical deposition parameters were as follows: substrate temperature = 900-950°C, methane flow rate = 3.6 SCCM, hydrogen flow rate = 500 SCCM, deposition pressure = 45 Torr, forward power = 1200 watts, and reflected power = <40 watts. The schematic diagram and the process details on diamond deposition are described elsewhere [5-7].

Silicon wafers were processed using the following procedures to obtain selective growth of diamond crystals on the apex of silicon pyramids.

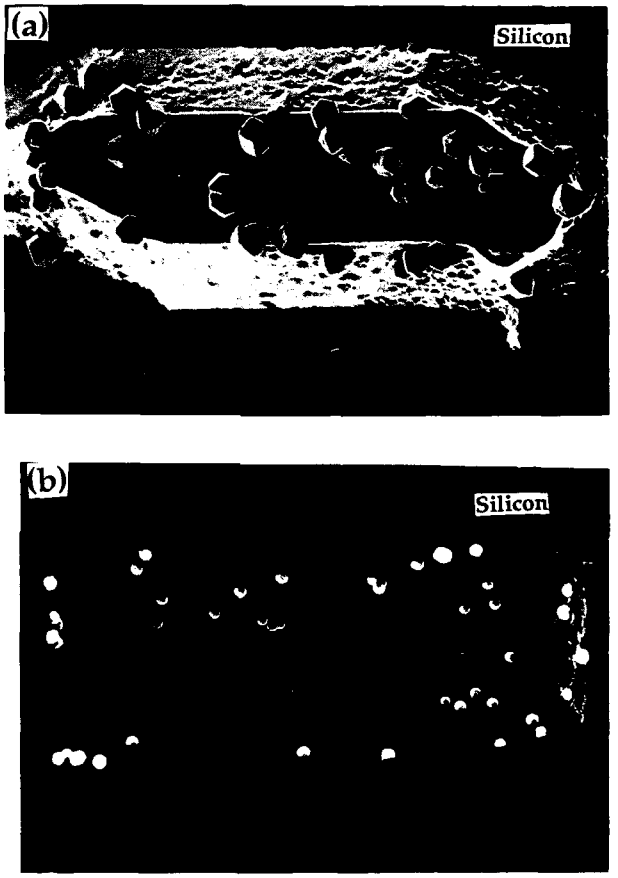


Figure 1. Scanning electron micrographs of the diamond particles grown on a **(a)** vertical mesa and **(b)** an inverted mesa structures of silicon.

(a). Starting substrates were p- or n-type mirror-smooth finished silicon wafers with a resistivity of < 20 Ω-cm. Silicon wafers were chemically cleaned and thermally oxidized using pyrogenic steam at 1000°C for 10 hrs to a silicon dioxide thickness of 1.1 ± 0.1 μm. The silicon dioxide was then patterned with a positive mask of 60 μm side squares using conventional photolithography. The sample was hard baked with photoresist and the silicon dioxide was chemically etched in buffered oxide etch (1 part HF + 6 parts NH_4F) solution. The silicon was anisotropically etched in a solution of KOH + H_2O (2:1) at 60-70°C until (30-50 minutes) the silicon dioxide mask squares fall off to eventually form silicon pyramids by undercutting [8]. Figure 2a shows a scanning electron micrograph of the typical morphology of the fabricated silicon pyramids. Figure 2b is a magnified view of some pyramids in figure 2a (apex diameter: ~2 μm). Some of the pyramids were fabricated by etching the silicon dioxide mask just before the masks tip-off from the substrate (Fig. 2c) using a buffered oxide etch to achieve flat apex and scratch free pyramids. Figure 2d shows scanning electron micrograph of the typical morphology of a silicon pyramids fabricated after etching the oxide mask (apex diameter: ~10-12 μm).

(b). Starting substrates were p- or n-type mirror-smooth finished silicon wafers with a resistivity of < 20 Ω-cm. Silicon wafers were manually scratched on one side using a diamond paste consisting of 0.25 μm mean particle size. The wafer was then chemically cleaned and the silicon nitride was deposited by low pressure chemical vapor deposition (LPCVD) using dichlorosilane and ammonia at 800°C to a thickness of 0.16 μm. The silicon nitride was then photolithographically patterned using a positive mask of 60 μm side squares and plasma etched in a SF_6 + O_2 (7:1) mixture of gases and the photoresist was then removed with acetone. Silicon was anisotropically etched in a KOH + H_2O (2:1) solution at 60-70°C for 30 - 50 minutes [8]. Undercutting of the silicon nitride was monitored closely and the etching of silicon was stopped just before the silicon nitride squares tip off from the apex of silicon pyramids. The typical morphology of the silicon pyramid with a silicon nitride mask by scanning electron micrograph is as shown in fig. 2c. The etched silicon wafer was carefully chemically cleaned and thermally oxidized in a pyrogenic steam at 1000°C for 10 hrs to form a silicon dioxide thickness of 1.1 ± 0.1 μm. The wafer was then immersed in buffered oxide etch for 60 sec to remove a thin layer of oxide formed on the silicon nitride mask. The silicon nitride was then chemically completely etched in hot (~180°C) phosphoric acid. Finally, the wafer was cooled to room temperature, washed with running DI water, rinsed with acetone, and nitrogen dried. The typical morphology of the silicon pyramids fabricated is shown in the fig. 2e by SEM. This approach clearly yields the nucleation site or scratched site and/or an activation site for diamond growth which is, apparently, the apex of anisotropically etched silicon pyramid and the remaining area is oxidized to hinder the growth of diamond. Surface damage or scratching can in fact may be seen on an apex of 1,2, and 3 labeled pyramids in scanning electron micrograph of fig. 2e and also a pyramid (#4) with a sharp apex. Process description for selective growth of diamond on the apex of silicon pyramid is shown in fig. 3 to supplement the above details.

RESULTS and DISCUSSION:

Figure 4a, b, and c show the scanning electron micrographs of diamond grown on the apex of the silicon pyramids shown in fig. 2a fabricated using the procedure delineated in the process (a). Figure 4b is the magnification of a few pyramids in figure 4a. Figure 4c is the magnification of a single pyramid in figure 4a and also the zooming of the apex of the same pyramid is shown in figure 4c. Diamond deposition time was ~5.75 hours. These micrographs show that the diamond is not only grown on the apex of the pyramids but also in the other area. Nucleation density is apparently high on the apex when compared with the other area of the pyramid or the other surface of the silicon substrate. Zooming of the apex in figure 4c clearly denotes the high nucleation rate of diamond particles on the apex of the pyramids. One may even closely observe the high nucleation rate of diamond particles on all the apexes in figure 4a and b. The substrate was not damaged with diamond paste prior to the fabrication of pyramids to eliminate the doubt of residual diamond particles. Therefore, this suggests that the sharp edges are still activation sites for diamond nucleation and this observation is in accordance with results recently reported in [9,10].

Figure 4d is a scanning electron micrograph of the diamond particles grown on the flat apex of silicon pyramids fabricated using the process (a). High nucleation rate of diamond particles is still present on the apex and also several particles on the undesired area (diamond deposition time: ~3.5 hrs). Edge of the flat apex of silicon pyramid still retains high diamond nucleation rate with several particles



Figure 2. Scanning electron micrographs of **(a)** silicon pyramids, **(b)** magnified apexes, **(c)** silicon nitride or silicon dioxide mask, **(d)** apex after etching the mask, **(e)** patterned Si apex surrounded by oxide.

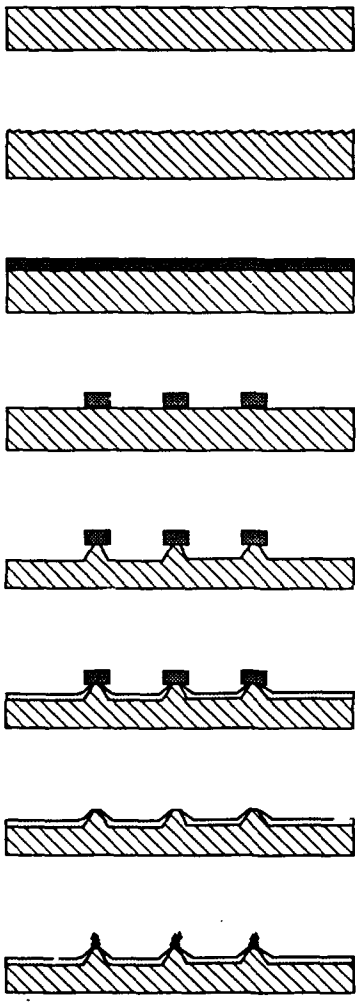


Figure 3. Schematic diagram of process flow steps for the selective growth of diamond crystals on the apex of anisotropically etched silicon pyramids.

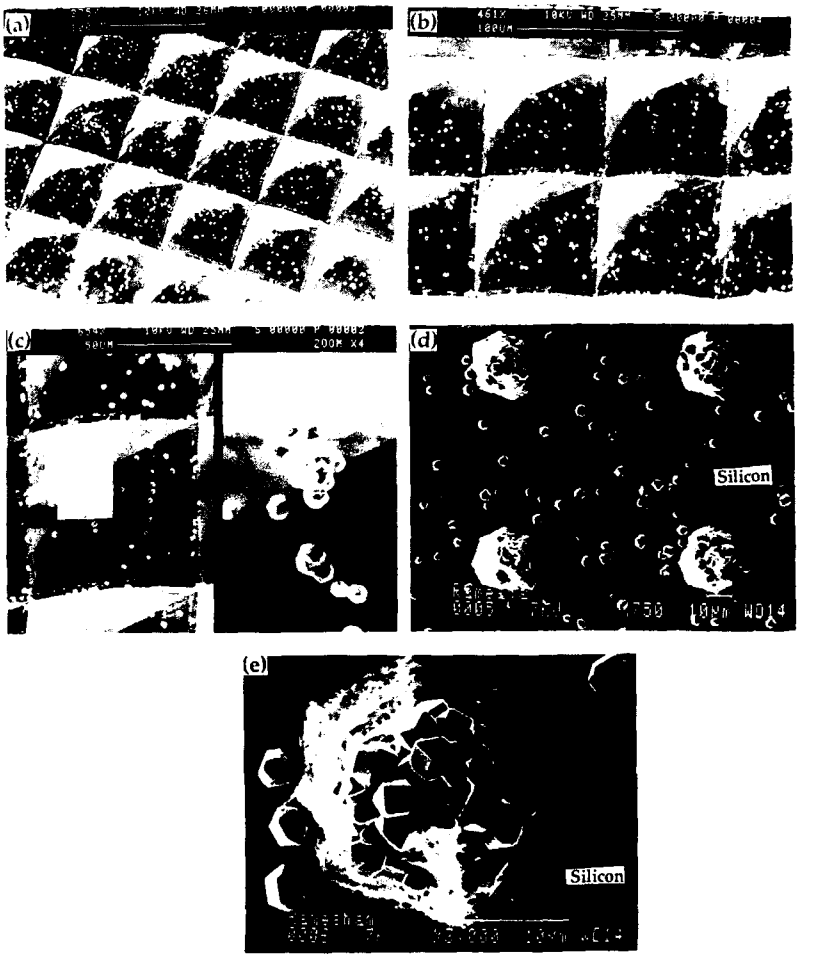


Figure 4. Scanning electron micrographs of diamond growth on **(a)** sharp silicon pyramids, **(b)** magnified view of (a), **(c)** magnified view of single pyramid in (a) and also zooming of an apex of pyramid in (c), **(d)** growth of diamond on flat apex of silicon pyramids, and **(e)** a magnified view of single pyramid in (d).

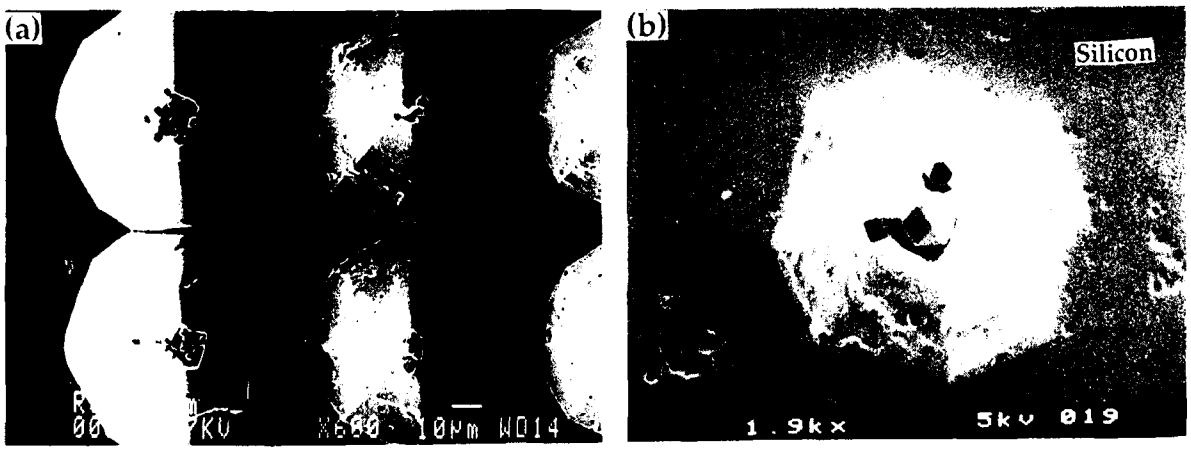


Figure 5. Scanning electron micrographs of as-grown diamond particles on **(a)** the apex of anisotropically etched silicon pyramids and **(b)** magnified view of a single pyramid with diamond particles.

and that may clearly be seen in the magnified view of a single pyramid shown in fig. 4e by SEM. Process (a) did yield the high diamond nucleation on the apex of silicon pyramids and also some deposits in the undesired areas. To avoid the problem of growth on undesired areas we employed the process (b). Figure 5 is a scanning electron micrograph of selectively grown diamond crystals only on the apex of anisotropically etched silicon pyramids (deposition time: ~2 hrs). Figure 5b is magnified view of the diamond particles on an apex of a single pyramid [11]. This result suggests that the oxidation has suppressed the growth of diamond in the undesired area as we observed earlier [5-7]. Furthermore, optical observation showed that the chemically etched silicon has higher nucleation density than the mirror-smooth finished silicon surface but lower than the apex of a silicon pyramid or sharp edges of silicon mesa structures. Scratching is eliminated in the process (b) to test whether diamond can selectively be grown on the apex of a silicon pyramid. Deposition time was increased in order to grow diamond only on the apex of silicon pyramid.

Diamond is harder and more wear resistant than silicon. A sharper tip may be produced using the above delineated selective growth of diamond crystal on an apex of a silicon pyramid. The tip of the bare silicon pyramid is softer than the diamond crystal grown on the apex of a silicon pyramid. Adhesive strength of diamond particles to the apex of the silicon pyramid may be enhanced by fabricating flat apexes. Diamond grown on silicon pyramids may have use as scanning tunneling microscopy tips, electrical probe tips (doped-diamond crystals) [7,12], for micro indentation, etc.

In summary, a process flow is developed to grow diamond crystals selectively only on the apex of anisotropically chemically etched silicon pyramids using either silicon nitride or silicon dioxide layers. We have made an experimental observation that the sharp edges of a mesa structure fabricated on a silicon surface or an apex of a silicon pyramids fabricated using a scratched silicon substrate with diamond paste or unscratched substrate yielded a high diamond nucleation. Unscratched silicon substrates do not have any residual diamond particles to act as nucleation sites for diamond growth, but could still result diamond nucleation based on a sharp apex of a silicon pyramid. Our observations support the mechanism such as high diamond nucleation on the surface texture with sharp points or edges etc. Furthermore, evaluation of nucleation density of diamond growth on various fabricated surface textures of silicon is under progress.

ACKNOWLEDGMENTS:

This work was supported in part by the Strategic Defense Initiative Organization's Office (SDIO/TNI) through Navy contract #N60921-91-C-0078 with the Naval Surface Warfare Center, and in part by the Alabama Microelectronics Science and Technology Center. Thanks are due to Mr. Camil Raad for his help in etching the silicon.

REFERENCES:

1. K. Mitsuda, Y. Kojima, T. Yoshida, and K. Akashi, J. Mater. Sci., 22, 1557 (1987).

2. S. Yugo, T. Kimura, H. Kanai, and Y. Adachi, "Growth of diamond films by plasma CVD," pp. 327-332 in Novel Refractory Semiconductors," edited by D. Emin, T.L. Aselage, and C. Wood, Materials Research Society, Pittsburgh, PA, 1987.

3. C.P. Chang, D.L. Flamm, D.E. Ibbotson, and J.A. Mucha, J. Appl. Phys., 63, 1744 (1988).

4. K. Hirabayashi, Y. Taniguchi, O. Takamatsu, T. Ikeda, K. Ikoma, and N.I. Kurihara, Appl. Phys. Lett., 53, 1815 (1988).

5. J.L. Davidson, C. Ellis, and R. Ramesham, J. Electron. Mater., 18, 711 (1989).

6. R. Ramesham, T. Roppel, C. Ellis, D.A. Jaworske, and W. Baugh, J. Mater. Res., 6, 1278 (1991).

7. R. Ramesham, T. Roppel, B.F. Hajek, C. Ellis, and B.H. Loo, "Selective growth of boron-doped polycrystalline diamond thin films," Proc. 2nd Int. Conf. on New Diamond Science and Technology,, Edited by R. Messier, J.T. Glass, J.E. Butler, and R. Roy, Washington, DC (Mater. Res. Soc., Pittsburgh, PA), p. 943 (1991).

8. K.E. Bean, "Semiconductor Materials and Process Technology Handbook," Edited by G.E. McGuire (Noyes Publications, Park Ridge, NJ) Chap. 4, P. 126.

9. P.A. Denning and D.A. Stevenson, "Influence of substrate preparation upon the nucleation of diamond thin films," Proc. 2nd Intl. Conf. on New Diamond Science and Technology, Edited by R. Messier, J.T. Glass, J.E.

Butler, and R. Roy, Washington, DC (Mat. Res. Soc., Pittsburgh, PA), p.403 (1991)

10. P.A. Denning and D.A. Stevenson, "Influence of substrate topography on the nucleation of diamond thin films," Proc. 1st Intl. Conf. on the Applications of Diamond Films and Related Materials, Edited by Y. Tzeng, M. Yoshikawa, M. Murakawas, and A. Feldman, Auburn, AL, Aug 17-22, 1991 (Materials Science Monographs, 73, Elsevier, Amsterdam), p. 383.

11. R. Ramesham, Communicated at the Spring Electrochemical Society Meeting, Washington, DC, May 5-10, 1991.

12. T.W. Kenny, S.W. Waltman, J.K. Reynolds, and W.J. Kaiser, Appl. Phys. Lett., 58, 100 (1991).

EFFECT OF LASER IRRADIATION ON CARBON-IMPLANTED COPPER SUBSTRATES

RAJIV K. SINGH AND JOHN VIATELLA

Department of Materials Science and Engineering, University of Florida, Gainesville, FL 32611-2066

ABSTRACT

We have analyzed the non-equilibrium thermal effects of pulsed nanosecond lasers on carbon-implanted copper substrates. The thermal effects of pulsed nanosecond lasers were simulated by numerically solving the heat flow equation and taking into account the phase changes which occur at the surface of the irradiated solid. Intense pulsed laser irradiation induces rapid heating at the near surface resulting in melting, followed by rapid quenching of the melt phase. The effect of laser variables (energy density, etc.) on the maximum melt depth, melt-in and solidification velocities and transient temperature profiles have been computed. Maximum melt depths and the surface temperatures were found to increase approximately in a linear manner with pulse energy density. Extremely high average solidification velocities (20-45 m/sec) were calculated which may give rise to solute trapping and other non-equilibrium segregation effects. The change in laser-irradiated characteristics of copper substrates as a result of carbon-ion implantation is also discussed.

INTRODUCTION

Pulsed laser irradiation provides a unique method for near surface modification, in which surface layers can be rapidly heated and melted, kept in the molten state for short times and rapidly solidified to preserve desired microstructures[1-5]. A recent report by Narayan et. al. [1] shows that pulsed laser irradiation on carbon-implanted copper substrates can lead to formation of the metastable diamond phase in the near surface regions. It has been shown that during the molten state, dopant can redistribute itself much more rapidly because the diffusivity of the dopant is many orders of magnitude higher in the liquid phase compared to the solid phase [5]. The segregation coefficient under non-equilibrium conditions depends on the type of impurity (substitutional or interstitial), solidification velocity and the orientation of the substrate. Thus, it is extremely important to understand and determine the non-equilibrium parameters and transient interface velocities and temperatures existing during the laser interaction process. The nanosecond time scales encountered in the laser-solid interaction process makes it very difficult to experimentally determine the transient thermal effects. Theoretical techniques, based on numerical calculations, have been adopted to predict the effects of lasers on solids. In this paper, we analyze and compute the effects of laser variables (energy density, etc) on the maximum melt depths, melt-in and solidification velocities of carbon-doped copper substrates.[6]

THEORY

The heating and melting effects of pulsed laser irradiation on materials constitute a three dimensional heat flow problem [2-4]. However in nanosecond laser processing regimes, the short thermal diffusion distances and the large dimensions of the laser beam limit the thermal gradients parallel to the surface to many orders of magnitude less than the thermal gradients perpendicular to the surface, thus essentially making it a one-dimensional heat flow problem. Although the heat flow is one dimensional in nature, the presence of a moving solid-liquid interface, temperature dependent thermal and optical properties of the irradiated solid, and time dependent laser pulse energy make the exact solutions extremely difficult. Thus, numerical techniques like finite difference methods have to be applied to obtain satisfactory results. In this problem we have employed a very rapid and accurate implicit finite difference scheme, SLIM (Simulation of Laser Interaction with Materials), developed by Singh et. al [7] to determine the thermal history of the targets after intense laser irradiation. This method is based upon a higher order finite difference calculation and is not restricted by any stability criterion, thereby allowing faster convergence to the exact solution [8]. The temperature dependent optical and thermal properties as well as the temporal variation in the laser intensity can be taken into account in this formulation. Finite difference equations have been set-up for accurate determination of

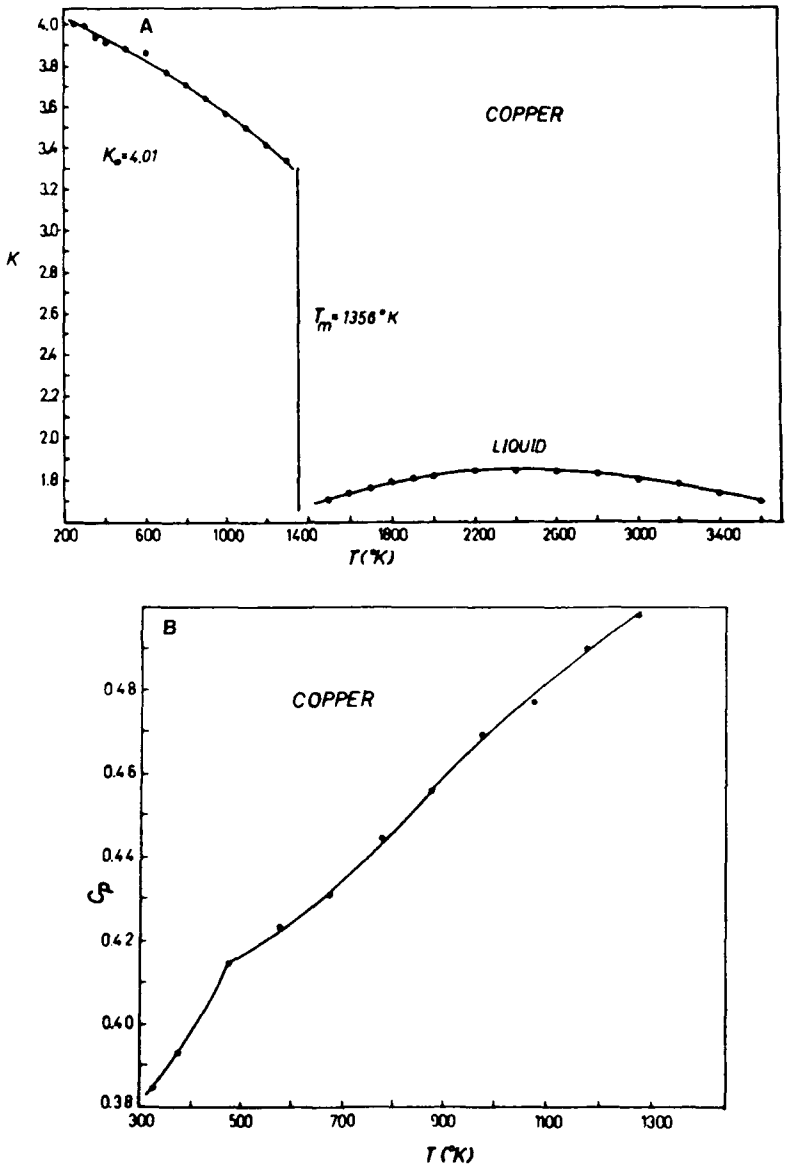


Fig. 1(a) Thermal Conductivity K and (b) specific heat capacity C_p per unit mass of pure copper used in calculations. [Adapted from reference 9]

temperature gradients at the interface which control melt-in and solidification velocities.

The temperature at any point inside the substrate T(x,t) during laser irradiation is controlled by the heat flow equation given by

$$\rho(T)\, C_p(T) \frac{\partial T(x,t)}{\partial t} = \frac{\partial}{\partial x}\left[K(T)\frac{\partial T(x,t)}{\partial x}\right] + (1-R(T))\, I_o(t)\, \alpha(T)\, e^{-\alpha(T)x}$$

where x refers to the direction perpendicular to the plane of the substrate, and t refers to the time. The terms $\rho(T)$ and $C_p(T)$ refer to the temperature dependent density and heat capacity per unit mass of the material. R(T) and α (T) are the reflectivity and absorption coefficient of the target. The time dependent laser intensity striking the surface $I_o(t)$, is dictated by the energy density, duration and the shape of the laser pulse. The velocity of the planar liquid-solid interface is determined by energy balance consideration which is expressed as

$$L\frac{dS}{dt} = K_l\left|\frac{\partial T}{\partial x}\right|_{x=S} - K_s\left|\frac{\partial T}{\partial x}\right|_{x=S}$$

where K_s and K_l are the thermal conductivities of solid and liquid copper at the interface, respectively, L is the latent heat of fusion, and dS/dt is the velocity of the melt interface.

Figure 1 (a) and (b) show the thermal conductivity and specific heat capacity values of pure copper as a function of temperature. Copper possesses a very high thermal conductivity which decreases steadily with increasing temperature, followed by a sharp decrease upon melting of the material. The specific heat capacity per unit volume increases with increasing temperature and has been assumed to be a constant in the liquid phase. It is expected that the thermal properties of copper will change due to carbon ion implantation, especially near the projected range, R_p, (600-800 Å from the surface) of carbon ions. However, as a first approximation we have assumed that the properties of carbon-doped copper substrates are independent of the implantation process. Even if this approximation is not fully valid, the calculated thermal effects are expected to be similar except shift in the absolute energy density scales. It must however be noted that the high-dose ion implantation of carbon may induce formation of high melting point graphitic phase in the vicinity of R_p. This may lead the formation and propagation of two melting interfaces: one initiating from the surface and terminating near R_p, and other initiating at the vicinity of R_p and propagating into the bulk of the substrate. Another possibility is the decrease in thermal conductivity of the implanted layer which can substantially increase the surface temperatures during melting of the material. The input data used in the calculations has been listed elsewhere. [6].The high frequency of the excimer laser (XeCl, KrF, and ArF) photons allow excellent coupling of the laser energy with solid copper . However upon melting, liquid metals display a sudden increase in the reflectivities. We have assumed a value of 0.73 for liquid reflectivity of copper for our calculations

RESULTS AND DISCUSSION

Fig. 2 shows the melt depth of copper as a function of time after laser irradiation with 30 nanosecond pulses having energy densities between 2.5 and 4.5 J/cm^2.The maximum melt depth occurs approximately at the end of the laser pulse. After the termination of the laser pulse, the melt front recedes back to the surface as some heat energy is dissipated into the bulk of the material. The slope of the curves gives the value of the melt-in and the solidification velocities. The maximum melt depth increases with energy density and changes from 2200Å at at 2.5 J/cm^2 to 8800Å at 4.5 J/cm^2. Maximum melt depths are both a function of pulse duration and energy density and increase approximately linearly with energy density.

Another important aspect of understanding the nature of laser-solid interactions is the transient temperature profiles during intense laser irradiation of the substrate. Fig. 3 shows the transient surface temperature as a function of time for copper substrates irradiated with 30 nanosecond excimer laser pulses with energy densities corresponding to 2.5, 3.5 and 4.5 J/cm^2, respectively. The figure shows that the surface temperature rises rapidly until it reaches the melting point of the material, where it pauses momentarily due to reduced coupling of the laser energy. The rise in liquid phase temperature is slower than the solid phase temperature rise, because a part of the laser energy is absorbed as latent heat. On cooling, the surface temperature

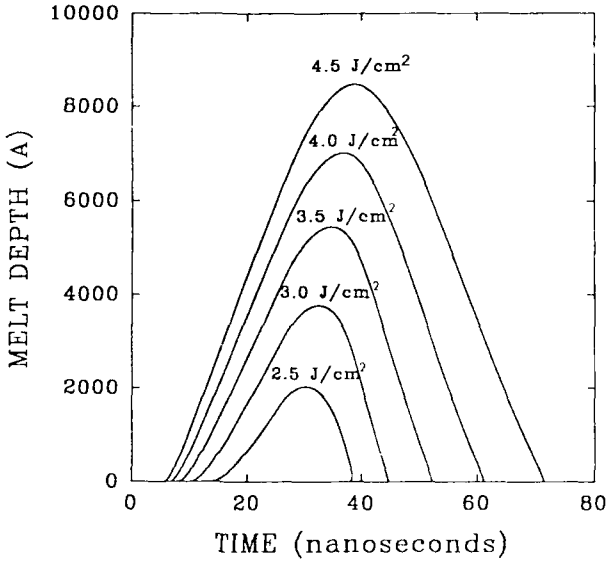


Fig. 2 Position of solid-liquid interface as a function of time for copper substrates irradiated with 30 nanosecond laser pulses with varying energy densities:(i) 2.5 J/cm^2, (ii) 3.0 J/cm^2, (iii) 3.5 J/cm^2, (iv) 4.0 J/cm^2 and (v) 4.5 J/cm^2,

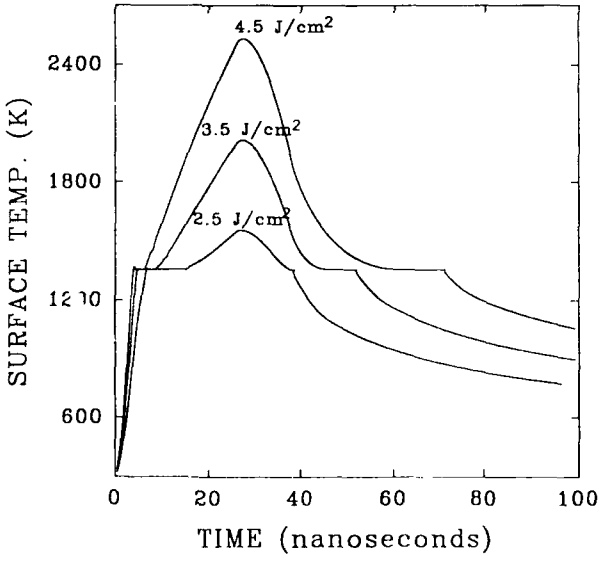


Fig. 3 Surface temperature as a function of time for 30 nanosecond trapezoidal laser pulses irradiated on copper substrates with different energy densities (i) 2.5 J/cm^2, (ii) 3.5 J/cm^2 and (iii) 4.5 J/cm^2.

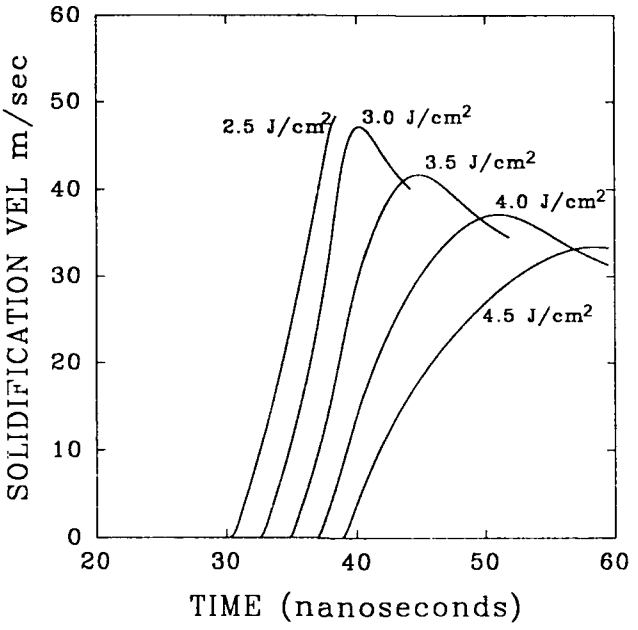


Fig. 4 Transient solidification velocities as a function of time for laser irradiated copper substrates. The substrate is irradiated with 30 nanosecond excimer laser pulses.

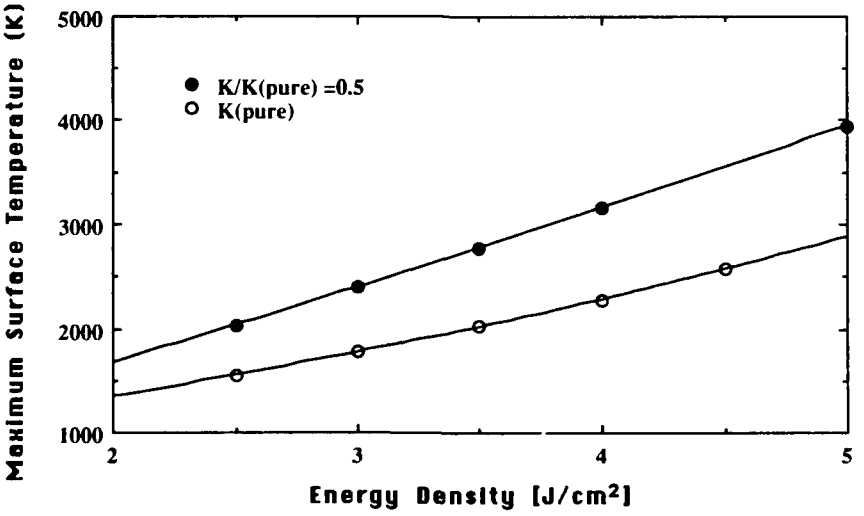


Fig. 5. Maximum surface temperature attained on carbon-implanted copper substrates when thermal conductivity of the near surface regions is (i) equal to pure value and (ii) half of the pure value

drops to the melting point and remains there until the melt interface recedes to the surface. The maximum surface temperature increases from 1550 K at 2.5 J/cm^2 to 2500 K at 4.5 J/cm^2. Much higher surface temperatures can be induced in the near surface regions if the thermal conductivity of the near-surface is reduced by ion implantation.

The solidification velocity is another important parameter that can be controlled by varying the laser parameters. Fig. 4 shows the transient solidification velocity for copper substrates irradiated with 30 nanosecond lasers pulses with energy densities corresponding to 2.5, 3.0, 3.5, 4.0 and 4.5 J/cm^2, respectively. Solidification during laser irradiation takes place via rapid quenching and dissipation of the heat by the bulk. As the liquid gradients become negligible after the termination of the laser pulse, solidification velocities attain a maximum value which decreases very slowly with time. The very high thermal conductivities of solid copper phases is responsible for the extremely high maximum transient interface velocities which are in the range of 40 to 50 metres per second. It has been shown that.the average solidification velocity does not vary strongly with energy density but is strongly affected by the duration of the laser pulse. If the pulse duration of the laser is increased from 15 to 50 nanoseconds, the average solidification values decreases from 40 to 25 meters per second. The extremely high solidification velocities may lead to stabilization of metastable phases.

All the calculations shown above are based on properties of pure copper. As mentioned earlier, the properties of copper, especially near the surface regions may change drastically with carbon implantation. Graphite may be present in a crystalline or an amorphous state. It is well known that melting points of amorphous materials are depressed in the amorphous state [11]. Another possible change induced by the implantation process is the lowering of thermal conductivity of the material. The decrease in thermal conductivity of copper will depend on the defect density in the surface layer. To understand the effect of reduced thermal conductivity, we have simulated laser irradiation of copper whose thermal conductivity at the near surface regions has been reduced by a factor of two. Fig 5 shows the maximum surface temperature induced on copper possessing half the thermal conductivity of the pure material. These films were irradiated with 30 nanosecond laser pulses. For comparison, values obtained from irradiation of pure copper substrates have also been shown. It is clearly seen that for a constant energy density, much higher surface temperature value are attained when surface regions have lower thermal conductivity. Maximum surface temperatures can be as high as 3500 -4000 K on the copper surface. At these temperatures, transformation of graphite may be possible. However, more experimental information is required to fully understand this phenomena.

In conclusion, the laser induced thermal effects on carbon-doped copper substrates have been modelled. The melt depths and the surface temperatures scale approximately linearly with energy density. Very high solidification velocities are induced after intense nanosecond laser irradiation of carbon-doped copper substrates Non-equilibrium laser melting and solidification, thus provides very high temperature and extremely rapid solidification velocities which may produce important transformation effects. .However, more experimental information is presently required to fully model the effect of pulsed laser irradiation on carbon-implanted copper substrates.

REFERENCES

1. J. Narayan, V. P. Godbole and C. W. White, Science, **252**,416 (1991)
2. P. Baeri,S. Campisano, G. Foti, and R. Rimini, J. Appl. Phys. **50**,788 (1979)
3. R.F. Wood and G. E. Giles, Phys. Rev B, **23**, 2923 (1981)
4. R.K. Singh and J. Narayan, Materials Science and Engr. **B3**,217 (1989)
5. C. W. White, in Pulsed Laser processing of Semiconductors , Eds. R.F. Wood, C. W. White and R. T. Young, Academic Press NY 1984 pg.44
6. R. K. Singh, Appl. Phys. Lett. **59**, 2115 (1991)
7. SLIM is a commercially available,personal computer based simulation routine developed by R.K. Singh and J. Viatella at the University of Florida. For more information please contact the authors. at (904)392 -1032
8. R.D. Richtmeyer, Difference methods for initial value problems, Interscience" NY 1957
9. Y. S. Touloukian (Eds), Thermophysical properties of Matter, IFI Plenum Press, NY (1970)
10. M. F. Von Allmen, in Physical processes in Laser-Materials Interactions, M. Bertolotti Eds. Plenum press, N.Y. 1982,pg. 49 (1959)
11. See for example, "Laser-solid interactions " editors J. Narayan et. al. MRS,Vol 13, 1984

PART II

Electronic Properties of Diamond and Related Devices

DIAMOND AS A MATERIAL IN SOLID STATE ELECTRONICS

Victor S.Vavilov
P.N.Lebedev Institute of Physics, USSR,117924, Leninsky Prospect 53, Moscow, USSR

1. Abstract

Present state of the work devoted to the control of properties of diamond is analyzed, with emphasis on the results obtained in USSR, including the data on ion implantation and several types of devices. Future possibilities of the work with single crystals, films and diamond ceramics are discussed and typical difficulties indicated.

2. Introduction. I shall mainly speak about the work done in USSR; as the research of diamond is international, it is most proper to mention the fundamental book edited by Field [1]; I shall abstain from repeating our results discussed earlier [2]. Several authors have compared the properties of diamond to those of other wide band gap semiconductors [3,4,5]. Optimistic picture shown in Fig. 1 represents, of course, ideal material, far above real objects at the disposal of an experimenter or technologist. Only best natural crystals (very rare) and best synthetic ones, grown, for instance by G.E. [1] are in some respects, near to it. So, diamond remained exotic for many years. Recently, due to the development of diamond films deposition processes in USSR, Japan, USA, UK and other countries, the attitude towards diamond is changing rapidly. Future work on diamond films can go on only on the basis of present knowledge, including highly developed theory [1] and experimental data obtained on natural and synthetic bulk crystals. In mid-fifties, in USSR Vereschagin developed the technique of producing large quantities of small industrial crystals. At present much larger single crystals are grown in Moscow and Kiev [3]. Epitaxial films on single crystal substrate, including boron-doped semiconductivity ones, were also grown [6],[2]. At present, most papers describe polycrystalline diamond films [7]. The atomic C-H-O phase diagram presented by Bachmann in [7] systematizes the results given in 70 publications describing low pressure CVD techniques of diamond deposition. In Fig. 2, main features of various types of diamond as a material are presented.

3. The doping of diamond. Doping of man-made single crystals by boron has been repeatedly reported [1.8.9]. The authors working in Kiev have grown boron-doped crystals of various sizes [10]. Small cubic crystals of uniform dimensions were successfully used as thermistors. The authors of [11], who also obtained p-type crystals, have reported on N-type crystals doped by phosphorus. The depth of the donor levels, as well as data on electrons' mobility have not been indicated. According to the calculations of Bernholz & oth [12], P atoms should be shallow donors, but their equilibrium

Paramter	Si	β-SiC	Diamond
E_g,ev, 300K	1.12	2.4	5.48
V_{max} cm/sec	10^7	2×10^7	2.4×10^7
E_{max} V/sec	3×10^5	3×10^6	2.2×10^7
$\mu_e\ cm^2/V - sec$	1350	1000	2400
$\mu_h\ cm^2/V - sec$	480	60	2100
$kW/cm - K$	1.4	2.8	20
T_θ,K	650	1200	2000

Fig. 1 The main parameters of Diamond, as compared to Si and SiC.

General Description	Geometry (size, area)	Inpurities; Typical defects	Carriers' mobilites $cm^2/V - sec$
Natural Diamond	Usaully $\approx$ 5mm and less hard to cut and polish	N in complexes, Transition metals some crystals nearly perfect	μ_e up to 2400 μ_h up to 2100 (300K)
Synthetic crystals of Diamond	Largest > 6mm very expensive small-cheap	Atomic N; Metal inclusion (easily detected)	same as in Natural large crystals can nearly perfect
Epitaxial Layers of Diamond	Dependable data only on orientated diamond substrate	can be very clean successfully doped by B	$\mu_h \approx 1000$
Polycrystal-line films of Diamond	Various substrates Si, metals area over $100cm^2$	can be doped in growth. ceramics special case	
Diamond like Carbon films	any area		mobility must low (<10)

Fig. 2 Diamond in its present various forms as a material for research and applications.

solubility must be very small. It is well known that atomic nitrogen is a deep down in diamond and does not supply free electrons [13]. No positive results of impurities' introduction by thermal diffusion into diamond are known to me. There exists, in principle, a possibility of transmutation doping of diamond, as (γ,n) reaction produces B^{11} nuclei from C^{12}; no published data are at my disposal.

4. Ion implantation into diamond. Long ago we obtained indirect evidence that natural insulating diamond exhibits electron conductivity after bombardment by 40 keV C^+ ions [14]. In 1982, Prins produced N-type regions in transistor-type structures on natural P-type diamond [15]. According to our data, conductivity disappeared after annealing at 700-800°C.

At present, we use systematically a 350 keV HVEE accelerator for our work; the ranges of ions and their straggling were calculated for random orientation with an error of +10%. We were involved in experiments of typically semiconductor physics aims; besides [1], we often used the data analyzed in a book edited in 1986 in USSR [16]. As one knows, diamond constitutes a metastable form of carbon and can amorphize or graphitize (graphite is stable). Fortunately, we found that for ion fluxes below certain limit, the diamond lattice recovers after annealing in vacuum. The maximum flux depends on the mass of that ion and the temperature of crystal. In a special case of sit ions implantation at large fluxes, cubic SiC is produced [18].

Implantation of B^+ ions. Boron is a most appropriate "shallow" (E_v +0.37 eV) acceptor dopant in diamond. Most of the implanted atoms occupy substitutional sits. The depth of penetration of the unchanneled ions for energies in the range up to 350 keV is large enough; recently, on the initiative of A.M.Zaitsev, a series of experiments was conducted with much higher energies, over 1 MeV [19]. In this case, buries layers of semiconducting diamond can be formed. By using a programmed implantation exposure, one can increase the concentration of boron acceptors near the surface, thus forming a pp^+ junction; p^+ regions are metallized without difficulty and ohmic contacts to p-type regions present no problem now.

5. The technique of analysis of the geometry of impurity distribution. The most direct method is, of course, secondary ions mass spectrometry (SIMS), which is systematically used by us for the boron-implanted and other samples, in the cases where impurity concentration was high enough. Some of the results were presented in [13], and I shall mention recent data later, when Li donors shall be discussed.

Other methods, including, of course, Hall effect and conductivity measurements, are often based on the analysis of cathodoluminescence (CL) spectra, which is typical for a wide field of experiments with ion-implanted crystals [20], [21].

Due to the large band gap of diamond (5,48 eV) CL was used by us; I have not seen yet publications, including photoluminescence data obtained for band-to band excitation of diamond. Besides the possibility of local excitation by focused electron beam, the depth of electrons' penetration can be easily changed, as it is a function of their energy. As it

was mentioned above, the volume and area of electron spot near the surface of the sample can be made very small [19,20].

6. The possibilities and limitations of luminescence spectra studies. Luminescence data contribute to the studies of ion implantation problems; on the other hand, implantation, regarded as a method of doping, permits to introduce into a solid (in our case, diamond) a wide variety of impurities [21], [22]. As one can see, for instance, in Fig. 3, the CL spectra, observed in a convenient region of photon energies, show narrow "zero-phonon" lines and related "Phonon ladders". Many narrow lines observed in unimplanted natural diamond were analyzed and interpreted, for instance, by Clark and Mitchell in UK [1]; their work has an exceptional value for those who work now on ion-implanted crystals. However, narrow lines correspond to so called "in the center" transitions, when the photon is estimated as a result of the relaxation of the system of strongly localized states [23]. Thus, these transitions do not include allowed bands of diamond and one has to use additional evidence, such as the changes of spectra after annealing to obtain results important for semiconductor physics. Of course, the studies of CL are very far from completion; one of the examples which seems to be worth mentioning is a non-trivial fact that free vacancies, which produce the well known GR1 narrow line at 741 nm, are generated as a result of irradiation by rather low energy electrons (6 - 10 keV) [24]. This range of energies is very much below the threshold of impact point defects' generation, which was estimated by palmer [25] to be near to 200 keV. At present, one cannot decide whether the vacancy is detached from some complex, or some mechanism in the electronic sub-system is leading to Frenkel pair generation [26]. According to the interpretation of my colleagues in Minsk, based on the analysis of narrow lines in CL spectra of diamond implanted by He^+ and Ne^+ ions, the atoms of these elements exhibit chemical activity due to extremely high hydrostatic pressure of the order of 10^6 bar in dense surrounding of carbon atoms in diamond lattice [27].

Besides narrow spectral lines, both CL spectra and luminescence spectra of structures on diamond including P-N junctions or Schottky barriers, broader bands of intensive electroluminescence were observed by E.A.Konorova, V.F.Sergienko & oth, with the extrinsic quantum yield about 4% [13]. Maximum intensity corresponded to the blue-green region, thus, band to impurity transition.

7. Lithium as a donor in ion-implanted diamond. Those who are involved in the development of semiconductor devices know that both in Ge and Si, Li behaves as a highly mobile interstitial impurity and is a very shallow donor. Long time before modern technique of calculations of atoms' migration and their energy spectrum was developed, we began experimenting with lithium-implanted natural diamond crystals. At present, the main facts are as follows:

1. The mobility of implanted Li atoms due to their diffusion is many orders of magnitude lower than in Si and Ge, but diffusion has been observed after annealing at temperature over 1000°C.

Fig. 3
Temp of anneling indicated

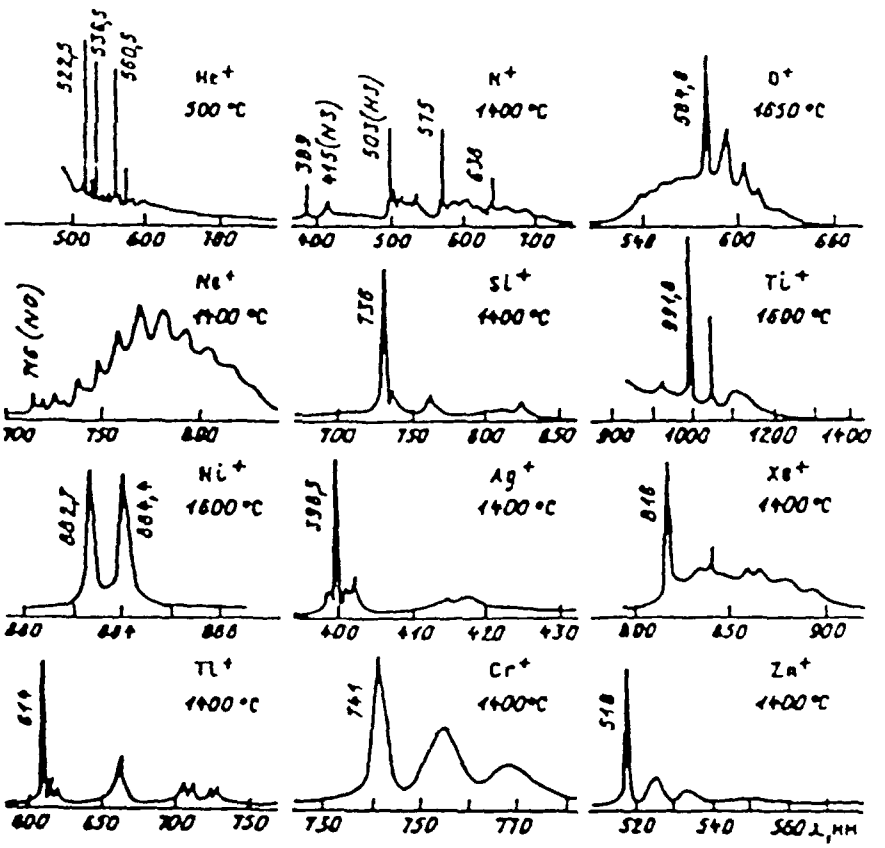


Fig. 3 Cathodoluminescence spectra of natural diamond implanted with several impurities.

2. The maximum concentration of electrons in the conduction band is observed in a layer lying deeper in the sample than the maximum of Li atoms' distribution. This was observed directly by (n, γ) reaction method [28].

3. Lithium implantation results in generation of shallow (Ec-0.1) ev donors. Electrons in the conduction band have high mobility (about 1000 $cm^2 v^{-1} sec^{-1}$) [13,29]. These facts correspond to recent calculations by Bernholz and oth [12].

4. The "average efficiency "of Li as a donor is much smaller than that of B atoms as acceptors. Thus it was suggested [13] that the majority of Li atoms can occupy substitutional sites where they are inactive electrically.

Phosphorus as a donor. We have reported on rectifying junctions produced by implantation of P^+ ions [2]. Experiments in this direction were not continued; there is some evidence that diamond film grown from plasma in presence of P_2O_5 have shown electron conductivity; the Hall mobility reported by the author was near to 50 $cm^2 v^{-1} sec^{-1}$ [30].

8. Some applications of Diamond in Electronics.

a) Diamond heat sinks: Their advantages and importance were recognized early enough [1]. At present they are produced both from natural and synthetic crystals in many places including Moscow and Kiev [3,4]. The stage of diamond films' technology when these films shall simultaneously have high heat conductivity, stability and good adhesion on suitable substrates will be, most probably, a crucial step, but it may require several years of hard work. A simple and dependable method of direct determination of heat conductivity was developed by Zezin Soth in Moscow [31].

b) Diamond particle counters and dosimeters were developed in P.N.Lebedev Institute by E.A.Konorova and S.F.Kozlov [32]. The authors of [32] used injecting contacts produced by ion implantation, and at present there is a series production of diamond counters and dosimeters in Riga [33].

c) There were several cases when transistor action was achieved in diamond structures of various geometry. Besides [15] and a useful discussion in a review by Kvaskov and Tkachenko [34], according to my opinion, the results, published recently by Melnikov, Zaitzev and oth, deserve attention [35]. Using standard photolitography technique, they have produced matrixes of inpolar field effects transistors on natural diamond samples.

d) Other types of electronics devices: Already in 1979, A.Tager published well founded estimates showing that diamond is, in principle, an excellent material for JMPATT's (avalanche diodes) [36]. Later, a group in P.N.Lebedev Institute by using ion milling technique and ion implantation has prepared a series of Read-type diodes, some of which had typical avalanche-type V-J characteristics.

e) Diamond containing ceramics. According to a recent publication by Rotner brothers [37], diamond ceramics, produced by baking pellets made of small inexpensive crystals at a pressure of 7-8 GPa and a temperature of 2000°C, a dense material having high electric resistivity is produced. After illumination of the surface of ceramics by sharply focused intense laser beam, very stable conductive strips were

produced. They were shown to consist of a phase of amorphous carbon (not graphite); the electrical resistance of such strips could be varied in wide range, and the process was quite reproducible.

Conclusions. One can see, that our work and the work of my colleagues in USSR, to which I paid most attention, was mainly concerned with the properties and processes in bulk crystals. We have now also large area diamond films at our disposal; one of the proofs that they are really diamond films are their CL spectra. Of course, we shall try ion implantation in the nearest future.

The technology of diamond films deposition is economically profitable already, and one should expect a rapid development. According to the considerations of D-r Buckley-Golder, "strategic window" for diamond electronics)see Fig. 4) shall begin to close about 1995 in the field of basic concepts (deposition, epitaxy, multilayers) and the next step (technology options, such as contacts, lithography, etching) shall occupy 1997 to 2000 AD.

Fig 4.
THE STRATEGIC WIDOW FOR DIAMOND ELECTRONICS

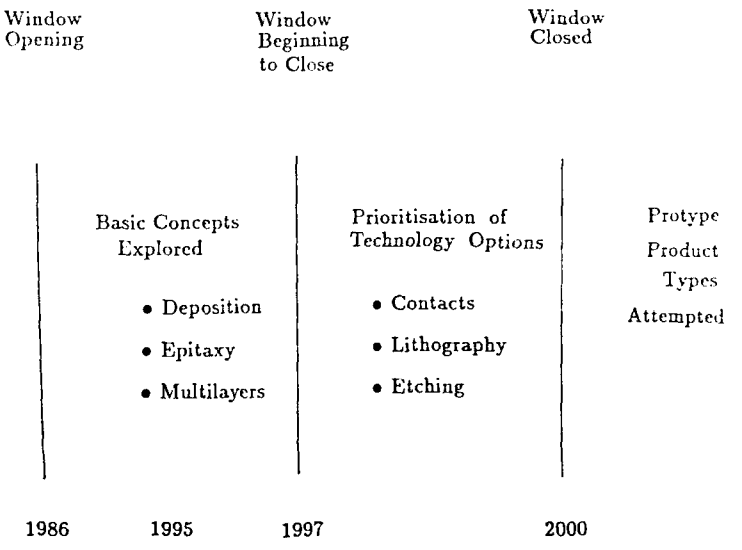


Fig. 4 The strategic window for Diamond Electronics [5].

10. Acknowledgements. The author expresses his gratitude to his colleagues in P.N.Lebedev Institute of Physics, Byelorussian State University and Institute of Superhard Materials in Kiev, especially A.A.Gippius, V.F.,Sergienko, S.F.Kozlov, A.M.Zaitzev and A.G.Gontar for valuable discussions. He is indebted to Dr. Bellamy in AERE Harwell for reprints of the works of Diamond group there. Special thanks are due to Professor Herrmann Grimmeiss of Lund University, Sweden, in whose laboratory this review was prepared.

11. References

1. The Properties if Diamond, Oxford University Press (1979) ed. by J.Field.

2. V.S.Vavilov "Semiconducting Diamond Phys. St. Solidi (a) 31, 11 (1975).

3. Diamond in Electronic Technology Express edition, ed. V.B.Kvaskov. Moscow, Energoatomizdat (1990) in Russian.

4. Perspec ives of the uses of diamond in electronics and electronic technology (In Russian) - Abstracts of the All-Union Conf., Moscow, Energoatomizdat (1991), in Russian.

5. Diamond Electronics, J.M.Buckley-Golder AEA Technology, Harwell, UK, 1990. Gorkam Advanced Materials (Europe) Ltd.

6. A.E.Alexenko and oth, Doklady 223, N 2, p. 334 (1977).

7. See, for instance the new monthly journal "Diamond and Related Materials" Vol. 1, N 1, Aug. 15 (1991).Edited by Elzevier Amsterdam-London-New York.

8. R.M.Chrenko, Phys. Rev. B7, 4560 (1973).

9. G.H.Glover, Solid State Electronics 16, 973 (1973)

10. See [3] page 57, N.V.Novikov, A.G.Gontar. On the use of synthetic diamond in electronics.

11. See [4] page 30, V.A.Laptev & oth. The uses of simple crystals of semiconductivity diamond of p- and N-types as sensors. In Russian.

12. J.Bernholz & oth. Abstract of papers of 20th Int.Conf. on Semiconductor Physics, Thessaloniki, 1990. Page 610.

13. V.S.Vavilov, A.A.Gippius, E.A.Konorova "Electronic and Optical Pressure in Diamond" book, in Russian, Moscow, ed. "Nauka" (1985).

14. V.S.Vavilov, M.J.Gusseva, E.A.Konorova, V.V.Krasnopevtsev, V.F.Sergienko and V.V.Titov. Fiz. Tv. Tela (Sov. Phys. Solid State 8, 1964 (1966).

15. J.F.Prins, Appl. Phys. Lett. (1982). V.41, N 10, p.950-952.

16. G.B.Bokiy and oth. "Natural and Synthetic Diamonds", book, in Russian, Ed. by Shafranovsky, Moscow, Nauka, 1986, in Russian.

17. P.Backmann, see [7], page 1.

18. J.P.Akimchenko and oth, Fiz. Tech. Poluprovodnikov 7, 972 (1973).

19. A.M.Zaitsev, see [3], page 211. Ion implantation into semiconductors with superstrong covalent bonding (in Russian).

20. V.S.Vavilov "Some physical aspects of ion implantation", a review, Sov. Phys. Usp. 28 (2) Feb. 1985, p.196-206.

21. A.A.Gippius, V.S.Vavilov "Luminescence studies of ion-implanted structures in semiconductors", Proc. of 4 Panhellenic Conference on Solid State Physics, Greece, Athens, (1988) p.58-84.

22. A.A.Gippius, V.S.Vavilov, A.M.Zaitsev, V.V.Ushakov, Proc. of the second USSR-USA seminar on ion implantation (1979) p.19-23, in Russian.
23. J.Pankove, Optical Processes in Semiconductors, Dover Publications Inc. NY (1975)
24. A.M.Zaitsev, V.S.Vavilov, A.A.Gippius "Subthreshold defects' generation in natural diamond, Fiz. i Tech. Poluprovodnikov, V16, N 3, p. 397-403 (1982) (in Russian).
25. D.W.Palmer. Inst. Phys. Conf. Series Vol 31, Chapter 1, p. 144 (1977).
26. V.S.Vavilov, A.E.Kiv, O.R.Niyazova "The mechanisms of defects' generation and migration in semiconductors" (book), Ed. "Nauka" Moscow (1981), in Russian.
27. V.D.Tkachev, A.M.Zaitsev, V.V.Tkachev. Fizika i Technika Poluprovodnikov, 19, N 5, 949-951 (1985).
28. B.V.Zatolokin and oth. Proc. of All-Union Conf. "Physics of Alloy Production by Ion Implantation Gorky, 1972, Ed. by Gorky Univ. Press, p. 47 (in Russian).
29. V.S.Vavilov, E.B.Stepanova, see 4, page 52. Photoelectric Properties of ion-implanted structures on natural diamond (in Russian).
30. H.Okano & oth. Appl. Phys. A51, 344-346 (1990).
31. P.B.Zezin, T.V.Khrabrova, Yu.A.Konzevoi, A.B.Tychomirov, see [4], p.89.
32. E.A.Konorova, S.F.Kozlov "Diamond detector of nuclear radiations. Fiz. i Tech. Poluprovodnikov V4, N 10, p. 1865-1871 (1970) in Russian. See also USSR patent N 224697 (1968).
33. V.S.Khrunov and oth. "The technology of diamond detectors of ionizing radiation", see [4] p.20.
34. V.I.Tkachenko, V.B.Kvaskov. Electronic devices based on diamond, a review, see [3], p.22-33, in Russian.
35. A.A.Melnikov, A.M.Zaitsev and oth. Semiconducting p-type structures on natural diamond. See [3] p.228 (in Russian).
36. A.S.Tager, in a book "Problems of physics and technology of wide band gap semiconductors". Proc. of AllUnion Conf., Leningrad 1979.
37. Yu.M.Rotnor, S.M.Rotner "Polycrystalline diamond in the technology of solid state electronics" See [3] pages 187-210 (in Russian).

INVESTIGATION OF CVD-GROWN DIAMOND BY CATHODOLUMINESCENCE IN TEM

R.J. GRAHAM
Center for Solid State Science, Arizona State University, Tempe, AZ 85287-1704

ABSTRACT

High resolution cathodoluminescence (CL) spectroscopy and imaging have been performed in transmission electron microscopy (TEM) to analyze defects and impurities in polycrystalline diamond films grown by chemical vapor deposition (CVD) using a variety of gas mixtures, and oxyacetylene combustion flame synthesis (CFS). The combination of CL and TEM allows a direct correlation of film microstructure with the electronic structure due to defects. The CL was found to be very nonuniformly distributed on a submicron scale reflecting different spatial distributions of N, B and Si impurities and their correlations with microstructure. Band A CL due to closely-spaced donor-acceptor (D-A) pairs was correlated with dislocations in both CVD-grown and CFS material whereas band A from widely-separated D-A pairs was uniformly distributed in the films. CL from several different N-related point-type defects was observed and found to depend on the growth gases used, although no correlation with microstructure has been observed so far. A di-Si interstitial impurity, believed to arise from the Si substrate and reactor walls, was not correlated with any microstructure but varied greatly in concentration from grain to grain and from film to film. In addition, both highly faulted and defect-free grains were found to emit no visible CL due to mid gap states.

INTRODUCTION

The synthesis of diamond films by low pressure techniques such as chemical vapor deposition (CVD) is currently receiving much attention, as evidenced by the appearance of several new journals and whole sections of existing journals devoted entirely to diamond. The intrinsic properties of diamond such as hardness, optical transparency and high carrier mobility, promise potential applications of diamond films in wear-resistant coatings, and as optical and electronic materials. However, current attempts at heteroepitaxial growth, usually on Si substrates, have resulted in heterogeneous polycrystalline films containing many defects and impurities. One of the goals of such growth methods must be the control of the formation of these inhomogeneities, especially if potential optical and electronic applications are to be realized. Characterization of these inhomogeneities is therefore important in two respects. First, it is necessary to identify these defects and assess their impact on the microstructure and electronic structure of the material. Second, it is desirable to understand and control the formation of these defects so that potential applications of this material can be realized successfully.

Since the films are polycrystalline and inhomogeneous, it is clearly necessary to characterize them at high spatial resolution. While transmission electron microscopy (TEM) can be used to observe the microstructure, this and allied techniques, such as electron energy loss spectroscopy, can only provide limited information on the electronic nature of the material. Secondary ion mass spectrometry can detect low levels of impurities but gives no

Mat. Res. Soc. Symp. Proc. Vol. 242. 1992 Materials Research Society

information on their effect on the electronic structure. On the other hand, cathodoluminescence (CL) spectroscopy and imaging have been used successfully for this purpose, since defects and impurities often introduce states within the 5.5 eV diamond band gap which give rise to CL in the readily detectable visible spectral region. However, such studies have all been performed in a scanning electron microscope (SEM), usually with limited spatial resolution. This is especially true when thick, as-grown films with a rough surface morphology are studied because it becomes difficult to deduce reliably the exact origin of CL within the films.

The analytical technique used in this work is spectrally and spatially resolved CL performed in TEM, rather than SEM, and this has a number of useful advantages. The most significant of these is the simultaneous correlation of CL emission, resulting from the electronic structure associated with defects and impurities, with details of the specimen microstructure, such as the presence of dislocations. In addition, use of thinned electron transparent samples enhances the spatial resolution compared with SEM CL.

EXPERIMENTAL

TEM CL technique

Experiments were performed in a Philips EM400T analytical electron microscope equipped with high-resolution TEM CL system, the full details of which may be found elsewhere[1,2]. The system includes a grating spectrometer (Spex 0.22m Minimate) for spectral acquisition and a cooled RCA C31034 photomultiplier detector covering a 250-900nm spectral range. None of the spectra shown here was corrected for system response and the spectral resolution was 2nm throughout except where stated otherwise. The acquisition of digital panchromatic or monochromatic CL images was achieved using a STEM attachment and a multichannel analyzer. A liquid nitrogen-cooled stage was used to give a specimen temperature of about 90K. The electron probe size ranged from 30μm, for large area spectral acquisitions from weakly luminescing material, to 0.2μm for most high resolution spectral and image acquisitions at a beam voltage of 120kV.

Growth details

Polycrystalline diamond films 1-10μm thick, grown by filament-assisted (FA) and rf plasma-enhanced (PE) CVD methods were studied.

Material prepared by FACVD was grown from a gas mixture of CH_4 (2% vol.) and hydrogen using a tungsten filament operated at 1800°C on a roughened Si (100) substrate which was positively biassed relative to the filament. Full details of the growth process are given elsewhere [3,4]. The specimens investigated were prepared under two different conditions: (a) pressure = 15 Torr, substrate temperature ~ 750°C; (b) pressure = 30 Torr, substrate temperature ~ 950°C.

PECVD-grown films were prepared on roughened Si (100) substrates using a variety of gas compositions and conditions as follows: (a) 1%CH_4, 99%H_2, pressure = 5.0 Torr, temperature ~ 650°C; (b) 2%CO, 98%H_2, pressure = 3.0 Torr, temperature ~ 630°C; (c) 8%CF_4, 92%H_2, pressure = 5.0 Torr, temperature ~ 820°C; (d) 20%CH_3OH, 40%CH_3COOH, 40%H_2O, pressure = 1.0 Torr, temperature ~600°C. Growth of the film from dilute CF_4 was achieved on unroughened Si substrate and is described in more detail elsewhere[5]. An additional film was grown using 2%CO/98%H_2 at a temperature of ~ 725°C on R-plane ($10\bar{1}2$) sapphire to examine the effect of the substrate on the presence of impurities and defects.

Diamond films grown by oxyacetylene combustion flame synthesis (CFS) were also studied. Material consisting of [100] oriented single crystals aggregated into a film 300-500μm in thickness was grown by allowing an oxyacetylene torch, operated in a slightly acetylene-rich mode, to impinge on to a molybdenum substrate maintained at ~1000°C[6].

Specimen preparation

The thicker CVD-grown films were removed from the substrate by dissolving the Si with a mixture of HF and HNO_3 and mounted on 3 mm copper slot grids. The substrate of the thinner films was retained for support but was mechanically dimpled. These specimens were then thinned for TEM CL by milling with 5 keV Ar^+ ions at 77K to perforation. Especially in the case of the thicker films, the very uneven surface morphology resulted in specimens with highly variable thickness but also many holes surrounded by electron transparent regions.

Due the large thickness and extremely uneven surface of the films grown by combustion flame synthesis, specimens of this material were prepared by crushing in an agate pestle and mortar under isopropanol to produce thin electron transparent cleaved flakes.

RESULTS

CL spectra

Figure 1 shows CL spectra acquired from relatively large regions (10-20μm diameter) of various diamond films. The principal spectral features are summarised in table I and have all been observed previously to varying extents in diamond films grown by low pressure methods[7-17].

The band at 415-436nm, known as band A, is due to closely-spaced donor-acceptor (D-A) pairs[18]. The donor is believed to be a substitutional aggregate containing an even number (probably two) of nitrogen atoms and the acceptor is boron[19]. The broad bands at 470-607nm are probably also band A but are due to widely-separated D-A pairs. It is also possible that these are phonon sidebands of zero phonon lines at higher energy, which are unresolved in highly strained material. The 575nm band arises from a center probably consisting of a single nitrogen atom and one or more vacancies[11,20]. The uncorrected weak 387.8nm peak is identified as the 388.8nm (3.188eV) emission due to either an interstitial nitrogen or nitrogen-interstitial carbon complex and the peak at 532-534nm is probably similarly due to a nitrogen-vacancy-related complex[8-10]; both identities have been recently discussed[11]. The narrow peak at about 738nm is the same, within experimental error, as that observed previously in CVD-grown diamond and is attributed to di-Si interstitial impurities[8,12,21]. The origins of the emissions at 356-365nm, 484nm and 514nm are unknown at present but may also be nitrogen-related. The energies of the emissions were generally independent of substrate type (Si or sapphire) for the dilute CO-grown material however the 738nm peak was considerably more intense when the substrate was Si.

Correlation of CL with microstructure

Correlations of CL with microstructure fall into two groups. In relatively large-grained (greater than 1μm) material where a limited amount of non-diamond carbon is also present, the CL intensity was usually intense enough to permit a direct correlation of monochromatic CL

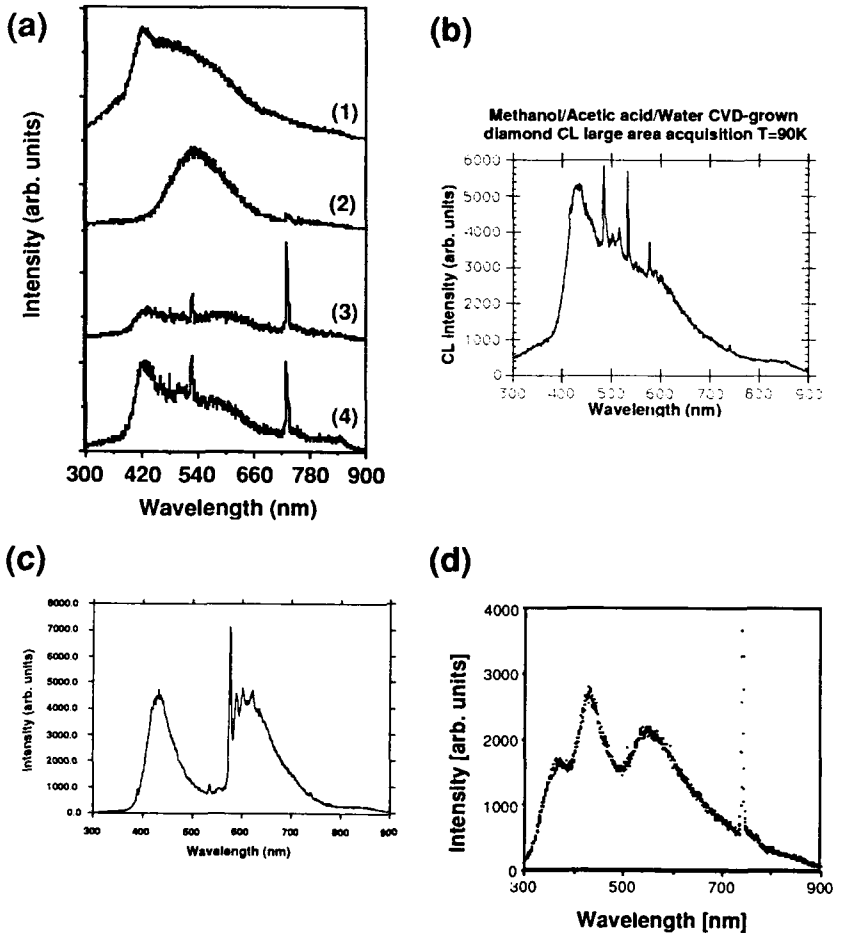


Figure 1. CL spectra acquired from large areas (10-30μm) of various diamond films: **(a)** PECVD-grown (1) 1%CH_4, 99%H_2, pressure = 5.0 Torr, temperature ~ 650°C on Si (100); (2) 8%CF_4, 92%H_2, pressure = 5.0 Torr, temperature ~ 820°C on Si (100); (3) 2%CO, 98%H_2, pressure = 3.0 Torr, temperature ~ 630°C on Si (100); (4) 2%CO, 98%H_2, pressure = 3.0 Torr, temperature ~ 725°C on R-plane ($10\bar{1}2$) sapphire; **(b)** PECVD-grown methanol/acetic acid/water mixture on Si (100); **(c)** CFS diamond film on Mo; **(d)** FACVD-grown 2%CH_4, 99%H_2, pressure = 15 Torr, temperature ~ 750°C on Si (100).

Table I. CL emissions detected in this work, listed in ascending wavelength and grouped in similar type (energy, narrow peak or broad band) with corresponding growth methods/conditions and impurity or defect responsible. MAW = Methanol, Acetic acid, Water (20%CH_3OH, 40%CH_3COOH, 40%H_2O). All substrate material was Si (except CFS films where Mo was used).

CL EMISSION	GROWTH CONDITIONS	IMPURITY/DEFECT
356±1nm (3.48±0.01eV)	FACVD 2%H_2 30 Torr/950°C	Unknown, unique to
365±1nm (3.40±0.01eV)	FACVD 2%H_2 15 Torr/750°C	CVD-grown diamond?
387.8±0.5nm (3.196±0.004eV)	CFS O_2/C_2H_2 1000°C	Interstit. N or N-interstit. C complex
415±1nm (2.99±0.01eV)	FACVD 2%H_2 30 Torr/950°C	Closely-spaced
428±1nm (2.90±0.01eV)	FACVD 2%H_2 15 Torr/750°C	donor-acceptor
	PECVD 1%H_2 5 Torr/650°C	(D-A) pairs. D is
431±1nm (2.88±0.01eV)	CFS O_2/C_2H_2 1000°C	even number (2?) of
	PECVD MAW 1 Torr/600°C	nitrogen atoms, A
436±1nm (2.84±0.01eV)	PECVD 2%CO 3 Torr/630°C	is boron.
483±1nm (2.566±0.005eV)	PECVD MAW 1 Torr/600°C	Unknown
484±1nm (2.561±0.005eV)	PECVD 2%CO 3 Torr/630°C	
514±1nm (2.412±0.004eV)	PECVD MAW 1 Torr/600°C	Unknown
532±1nm (2.330±0.004eV)	CFS O_2/C_2H_2 1000°C	Nitrogen-vacancy-
	PECVD MAW 1 Torr/600°C	related complex
534±1nm (2.321±0.004eV)	PECVD 2%CO 3 Torr/630°C	
575±0.5nm (2.156±0.002eV)	CFS O_2/C_2H_2 1000°C	Single nitrogen + 1
	PECVD MAW 1 Torr/600°C	or more vacancies
470±1nm (2.637±0.005eV)	PECVD 1%H_2 5 Torr/650°C	Widely-separated
540±1nm (2.295±0.004eV)	PECVD 8%CF_4 5 Torr/820°C	D-A pairs, or
551±1nm (2.250±0.004eV)	FACVD 2%H_2 15 Torr/750°C	unresolved phonon
577±1nm (2.149±0.004eV)	FACVD 2%H_2 30 Torr/950°C	sidebands of higher
607±1nm (2.042±0.003eV)	PECVD 2%CO 3 Torr/630°C	energy zero phonon emissions.
737.6±0.5nm (1.680±0.001eV)	CFS O_2/C_2H_2 1000°C	Di-silicon
737.8±0.5nm (1.680±0.001eV)	PECVD 2%CO 3 Torr/630°C	interstitial defect
	PECVD 8%CF_4 5 Torr/820°C	(or N-modified
738.2±0.5nm (1.679±0.001eV)	PECVD MAW 1 Torr/600°C	version of GR1?)
738.7±0.5nm (1.679±0.001eV)	FACVD 2%H_2 15 Torr/750°C	

mapping with specimen microstructure. In smaller-grained or less luminescent material only a general correlation with overall microstructure was possible.

(i) direct correlation

Material grown by FACVD using dilute CH_4 at 15 Torr/750°C was found to suitable for CL/TEM correlation[7]. Figure 2 shows monochromatic CL images of thin film diamond using the closely-spaced D-A pair and di-Si interstitial CL emissions. The images have distinctly different intensity distributions with the D-A emission more "spotty" and the di-Si defect emission often reflecting the long narrow microstructure of the grains in this material.

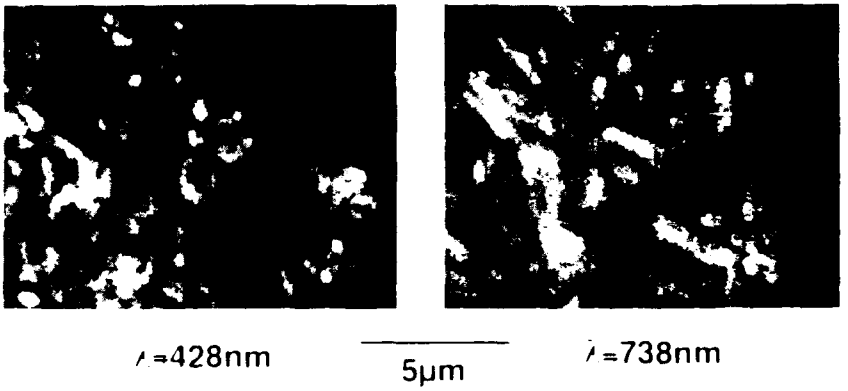


Figure 2. Monochromatic CL images showing closely-spaced D-A (λ=428nm) and di-Si (λ=738nm) impurity distributions in FACVD-grown material (15 Torr/750°C).

These images were acquired from material too thick for TEM imaging, however figure 3 shows CL spectra acquired from three adjacent thin grains. This shows that the closely-spaced D-A emission is correlated with the presence of dislocations and that the defect-free grain is emitting no CL within the detectable range. Further observations confirmed this correlation and while the di-Si defect emission was found to vary greatly from grain to grain, it was not correlated with any particular microstructure. Other emissions at about 360nm (origin unknown) and 550nm (widely-separated D-A pairs) were much more uniformly distributed throughout the films. Both highly defective and defect-free regions of the films were found to emit no observable CL. In the former case non-radiative carrier recombination is probably the cause. In the latter case, the absence of extensive diffuse scatter in convergent beam electron diffraction (CBED) patterns acquired from such grains suggests a low degree of static disorder and so these grains may be defect-free, having no states in the band gap.

A direct correlation was also possible in the CFS diamond[17]. Figure 4 shows the microstructure and CL spectra from two particles. Again, closely-spaced D-A pairs are correlated with dislocations. The other dominant emission from this material is at 575nm and is attributed to a defect probably consisting of a single nitrogen atom and one or more vacancies[11,20]. This emission is not correlated with any microstructure and so this point-type defect appears to be dispersed throughout apparently fault-free material. Here also, D-A emission is absent when dislocations are absent.

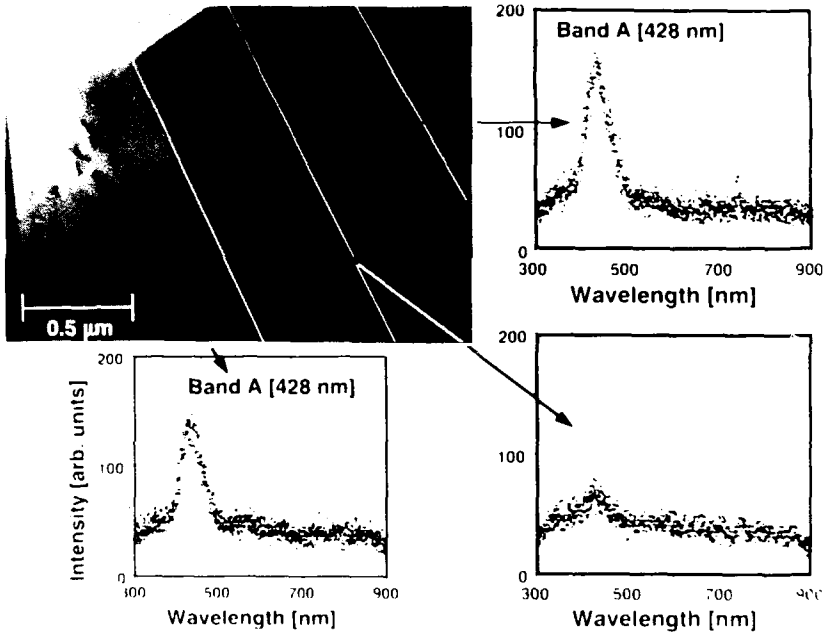


Figure 3. TEM image showing defect-free grain and grains with dislocations on either side (grain boundaries are highlighted in white). CL spectra acquired from each grain, using an astigmatic, elongated probe, show blue band A emission due to closely-spaced D-A pairs correlated with dislocations and little CL from the defect-free grain.

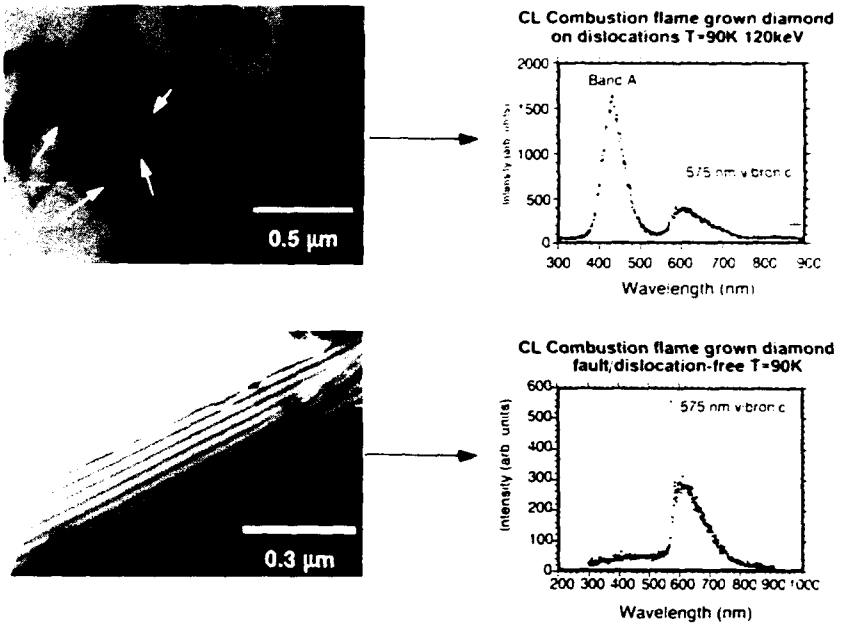


Figure 4. TEM images and CL spectra from fragments of CFS diamond. Crystal containing dislocations (arrowed) gives strong D-A related emission whereas fault-free material has no D-A CL and only the vibronic emission with zero phonon line (ZPL) at 575nm due to a single nitrogen atom + vacancy(ies). (The small dark particles in the TEM images are non-luminescent debris from the agate pestle and mortar used to crush the CFS diamond films).

Thin regions of the methanol/acetic acid/water (MAW) PECVD-grown diamond also permitted a direct correlation. The CL spectrum from this material is particulary rich in different emissions (fig. 1). and figure 5 shows CL images using the four most intense emissions from the same (mostly thick) region of specimen. Some of the intensity variations are attributable to a non-uniform thickness but other independent variations clearly exist. This suggests that although the same impurity, nitrogen, is responsible for at least three of these emissions, the various forms of the nitrogen-related defects are distributed differently. Extensive twinning and stacking faults were often observed in this material and preliminary observations indicate that closely-spaced D-A emission is also correlated with the presence of these defects. Work is in hand to detect any correlation of the other nitrogen-related defects with the microstructure.

(ii) indirect correlation

For material grown from dilute CH_4, CO and CF_4 by PECVD, only a general indirect CL/TEM correlation was attempted[16]. All specimens, except the CF_4-grown films, showed closely-spaced D-A pair band A emission. Although this has been specifically correlated with

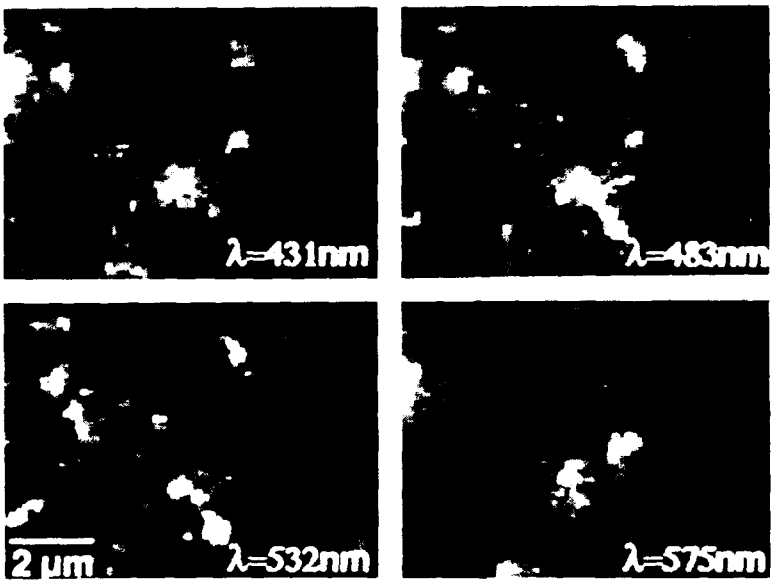


Figure 5. Monochromatic CL images from the methanol/acetic acid/water mixture PECVD-grown films using the emissions indicated. At least three of these emissions are believed to be due to nitrogen as a number of different defect structures. Some of the intensity variations are due to specimen thickness variations but other differences in the distribution of the various CL emissions also exist. This indicates that the spatial distribution of each of the various nitrogen-related defects in the film is different.

dislocations and, in one case, stacking faults/microtwins, other defects, e.g. non-diamond inclusions, could potentially allow D-A pairs to exist in varying degrees of proximity. This may account for the extremely broad band A observed in the CH_4-grown material where such defects in single crystals abound and to a lesser extent the CO-grown film on sapphire. However, if the density of other defects becomes too high resulting in poor crystallinity, increased non-radiative recombination reduces the overall CL intensity, as seen in the CO-grown films. Significantly, the CF_4-grown material was the least defective at a microscopic level, i.e. excluding microtwins, and showed no such band due to closely-spaced D-A pairs. All films showed some degree of band A due to widely-separated D-A pairs normally seen in synthetic diamond. In the CF_4-grown films this was the only peak of any significant intensity and the slightly higher peak energy, 2.3eV compared with about 2.1eV for the CO-grown films, suggests either a difference in impurity concentration or smaller mean D-A pair separation.

DISCUSSION

For band A emission, a Coulombic contribution in the recombination energy, which depends on the mean separation of the D-A pairs, results in band A peaking in the 400-480 nm (3.0-2.6 eV) blue range for closely-spaced pairs and in the 500-560 nm (2.5-2.2 eV) green range for more distant pairs. Blue band A luminescence is normally associated with natural diamonds where it is thought that closely-spaced D-A pairs evolve by diffusion of the impurities at elevated temperatures over millions of years. In contrast, green band A emission is emitted from synthetic diamond where the rapid growth process has "frozen" the impurities at relatively widely spaced sites within the lattice. In our present observations on low pressure-grown diamond[7,16,17], we have observed that in fact blue band A in the 415-431nm range is directly correlated with the presence of dislocations and in one case, also stacking faults or twins. A similar observation was made on natural type IIb diamonds[2]. Presumably, closely-spaced D-A pairs are incorporated in the dislocations during growth, and although the atomic structure of such a system is unknown, a one-dimensional D-A pair model has been suggested[2]. In the FACVD-grown material the relatively uniform distribution of green band A CL at 551 nm due to widely-separated D-A pairs, indicate that these centers are fairly homogeneously dispersed throughout the film. Nitrogen is presumably a contaminant of the source gases and vacuum system, although high purity gases were used in most of the growths. No attempt was made to remove nitrogen dissolved in the MAW components and it is worth noting that the various nitrogen-related CL emissions were fairly intense in this material. In the CFS diamond, the combustion was carried out in air and so the abundance of nitrogen-related defects is not surprising either. Boron may exist as an impurity in the CVD reactor components and in the FACVD-grown material, the Si substrate was B-doped. The presence of boron has been confirmed in some material by SIMS[16]. The origin of boron in the CFS material is more difficult to explain. Moreover, apparently B only exists as an acceptor in this material at the dislocations and not in unfaulted crystal (fig. 4). This leads one to question the identity of B as the acceptor and tentatively speculate that instead some atomic arrangement at the dislocation exists with an acceptor-like electronic structure.

Several other nitrogen-related CL emissions have been observed but none so far correlated with any particular microstructure although they are sometimes non-uniformly distributed.

The origin of the peak at about 738nm deserves some discussion since at least two different centers are known to cause emission close to this energy. The GR1 emission, due to the neutral vacancy defect, occurs at 1.673eV[19]. Another peak at 1.685eV has been attributed to a di-Si interstitial defect[8,22] and, more recently, peaks at 1.680eV and 1.681eV

have been attributed to the same defect[7,12,15,16,21]. Annealing studies and experiments with substrates other than Si[15,16,21], which is often used in CVD diamond growth and believed to be a major source of Si impurity, would seem to confirm that Si is involved in this defect. In addition, glass reactor components are also possible sources of Si. However, in the case of CFS diamond, there is no obvious source of Si impurity. It therefore seems questionable that the di-Si defect is responsible for the observed peak in that material and so the GR1 defect could be considered as a possible cause. Although the presence of stress can shift the GR1 energy by several meV, the full width at half maximum (FWHM) of the 738nm peaks seen here is only 7meV compared with 25meV as apparently observed for GR1[11]. The effect of stress and the possible influence of nitrogen on GR1 is discussed in more detail elsewhere[17]. In FACVD-grown material, no correlation of di-Si impurity with microstructure or any other CL emission was observed. The defect appears to vary in concentration from grain to grain but is relatively homogeneous within a single grain.

To date, most low pressure diamond growth has been carried out using dilute hydrocarbons. It seems that the presence of other atomic species, such as O in CO and the MAW mixture, and F in CF_4 does not introduce any optically active impurity or defect states not previously observed in dilute CH_4-grown CVD diamond.

Finally, it is worth briefly discussing the absence of CL from those grains which are apparently defect-free. It would appear that such grains contain very low levels of impurities and do not therefore emit CL in the visible spectrum but rather in the UV close to the band gap which is not detectable with our current system. Such CL has been observed from CVD-grown diamond[9] but no correlation with microstructure was possible in the work reported. It is interesting to note that defect-free grains often occur adjacent to those containing many defects and may result from different nucleation processes.

CONCLUSION

TEM CL has been used to correlate electronic structure due to defects and impurities with microstructure in a variety of low pressure-grown diamond films at high spatial resolution. The CL spectra from the various films exhibit emissions common to one another but the form of the spectra vary considerably from material to material. The films are very inhomogeneous on a submicron scale with the impurity and defect content varying greatly from grain to grain. Grains with many defects are often found adjacent to defect-free grains of high purity. The dominant impurity is nitrogen which is present in a variety of defect forms in the diamond lattice. Closely-spaced D-A pairs have been directly correlated with dislocations and in one case stacking faults and twins. Interstitial silicon is incorporated in many films and, like other point defect-type nitrogen impurities, has not been correlated with any particular microstructure. In addition, nitrogen may be playing a role in the growth process. Certainly it is associated with major faults in diamond grown by a variety of low pressure methods, but whether it simply segregates to the defects or in fact is their cause is not known. This question and the reasons for the nucleation of these defect-free grains is the subject of continuing work.

ACKNOWLEDGEMENTS

Thanks are due to a number of people for supplying material and useful discussions; T.D. Moustakas (Boston University), M.M. Disko (Exxon Research & Eng.), J.B. Posthill (Research Triangle Inst.) and K.V. Ravi (Lockheed Research & Dev.). This work was supported by the Facility for High Resolution Electron Microscopy at Arizona State University, supported by NSF grant no. DMR-89-13384.

FLUORINE ATOM ADDITION TO THE DIAMOND (111) SURFACE

ANDREW FREEDMAN, GARY N. ROBINSON AND CHARTER D. STINESPRING[a]
Center for Chemical and Environmental Physics
Aerodyne Research, Inc., 45 Manning Road, Billerica, MA 01821

ABSTRACT

Diamond (111) surfaces with the dehydrogenerated 2x1 reconstruction have been exposed to a beam of atomic fluorine at 300 K. The uptake of fluorine, as measured using X-ray photoelectron spectroscopy, is quite efficient and saturates at a coverage of less than a monolayer. Low energy electron diffraction patterns indicate that fluorine termination of the diamond surface produces a 1x1 bulk-like reconstruction in contrast to the disordered surface produced on the (100) surface.

INTRODUCTION

In order for diamond to become a viable semiconductor material, several large advances in growth techniques must be made. To this date, no verified instances of large scale heteroepitaxy have been reported. This lack of success appears to be due to the propensity (in high pressure reactors) of diamond to nucleate at multiple sites and produce growth of micron-sized crystallites which coalesce into a thin film. In order to grow epitaxial films over large areas, films must be grown two-dimensionally (or in a Frank-Van der Merwe growth mode); this evidently requires a very slow growth rate that would be more relevant to molecular beam epitaxy (MBE) techniques. Furthermore, careful tailoring of films with features having dimensions on the order of a lattice parameter will be required to produce advanced devices such as quantum well structures.

We are attempting to develop an atomic layer epitaxy[1,2] scheme for the deposition of diamond thin films based on the use of halogenated reagents. Such a scheme would involve the use of self-limiting chemical reactions that would provide control of the deposition process on an atomic scale. To this end, we have been investigating the surface chemistry of diamond and graphite substrates with both fluorine and chlorine atoms[3-6].

This paper presents results from experiments involving fluorine atom adsorption on a diamond (111) surface, specifically the dehydrogenated 2x1 reconstruction. Previous work on mono-hydrogenated 1x1 (100) surface, has shown that fluorine atoms adsorb at a saturation level of ≈3/4 of a monolayer forming a disordered carbon monofluorine moiety[3]. The adlayer is stable up to 700 K whereupon fluorine desorbs in some form, although desorption is not complete until a temperature of 1100 K is reached.

EXPERIMENTAL

Studies were performed in an ultrahigh vacuum apparatus comprising a turbomolecular pumped, liquid nitrogen trapped ultrahigh cell (ultimate vacuum - 3 x 10^{-10} Torr) interfaced to an ion/sublimation pumped analysis chamber. The diagnostics available in the analysis chamber are x-ray photoelectron spectroscopy (XPS) and low energy electron diffraction (LEED). The sample is transferred between chambers using a linear motion feedthrough with sample heating(1200 K) and cooling (120 K) capabilities.

---

[a]Present Address: Department of Chemical Engineering, West VirginiaUniversity, Morgantown WV

Mat. Res. Soc. Symp. Proc. Vol. 242. © 1992 Materials Research Society

The 5 x 5 x 0.25 mm type 2A diamond (111) substrate (Dubbeldee Harris) was polished using 0.25 mm diamond grit in oleic acid and rinsed in acetone and ethanol baths in an ultrasonic cleaner to remove any trace of the polishing process. Heating the substrate to ≈ 750 K in vacuum produced a surface devoid of any contaminants as measured by the XPS diagnostic. Bright 1x1 LEED patterns at 150 eV were obtained, indicating the presence of the hydrogenated 1x1 bulk-like reconstruction.[7] Further heating to ≈ 1050 K produced intense 2x2 LEED patterns indicating the formation of the dehydrogenated 2x1 surface. This reconstruction removes the dangling bands (one per surface carbon) by forming surface carbon dimer bonds.

The fluorine atom source has been described in detail elsewhere.[8] Briefly, it consists of a miniature fast flow tube whose output is sampled by a small aperture (40 μm), which produces an atomic or molecular beam. A 5% fluorine in argon gas mixture (2 Torr) flows (500 sccm) through an alumina tube which is surrounded by an Evenson-type microwave discharge cavity, past the aperture, and exhausts through a co-annular passage. Operating the discharge at 70W power produces nearly 100% dissociation of the fluorine. The alumina flow tube is readily passivated and no recombination of F atoms in the gas or on the walls is seen when the beam is sampled by a mass spectrometer.

The XPS analyses were performed using a PHI 15 keV, Mg K_{α} x-ray source and a PHI 15-255 GAR double pass cylindrical mirror electron energy analyzer operated at a pass energy of 25 eV. The analyzer was calibrated using the Au $4f_{7/2}$ peak at 83.8 eV and is accurate to ±0.2 eV. Due to the insulating properties of the diamond sample, significant charging effects were observed. For this reason, all spectra presented here are referenced to the C 1s peak (285.0 eV) of bulk diamond. This peak has a full width at half maximum (FWHM) of 1.4 eV and its assignment is never ambiguous. Fluorine atom concentrations are measured using the F 1s transition at 685.5 eV. The LEED diagnostic is of a reverse view variety (Princeton Scientific Instruments).

RESULTS AND DISCUSSION

Figures 1-3 present data obtained from the dehydrogenated 2x1 reconstruction. In this case, the surface dangling bonds, produced by desorbing the surface hydrogen, are energetically satisfied by forming surface dimer bonds between carbon atoms. Thus fluorine atom addition requires the breaking of the surface dimer bond upon formation of a carbon fluorine bond. Figure 1 presents an F atom uptake curve (measured using the XPS) as a function of exposure to atomic fluorine (1 ML = 1.8 x 10^{15} cm^{-2}). The initial uptake appears to be first order in fluorine atom coverage. The saturation coverage is less than a monolayer as determined from the C 1s spectrum which indicates only partial disappearance of a surface state feature.[3]

Figure 2 presents an artists rendition of the obtained LEED patterns before and after fluorination. Fluorination decreases the intensity of the second order spots indicating that the surface dimers are being broken to form areas of a fluorine terminated 1x1 reconstruction. The second order spots never entirely disappear which is in accordance with the fact that the saturation coverage determined above is less than the monolayer required to totally terminate the surface. Unfortunately, without quantitative information as to the width and relative intensities of the individual spots, it is impossible to determine the relative sizes of the 1x1 and 2x1 domains. This behavior is quite different from that found on the (100) surface where fluorine addition results in a disordered surface. Instead, fluorine atoms on the (111) surface behave in a manner similar to that of hydrogen atoms whose removal and adsorption to form ordered surfaces are quite reversible[7,9]. It is interesting to note, though, that as repeated cycles are attempted with both atomic hydrogen and fluorine, the LEED patterns become generally dimmer indicating some damage to the surface[10].

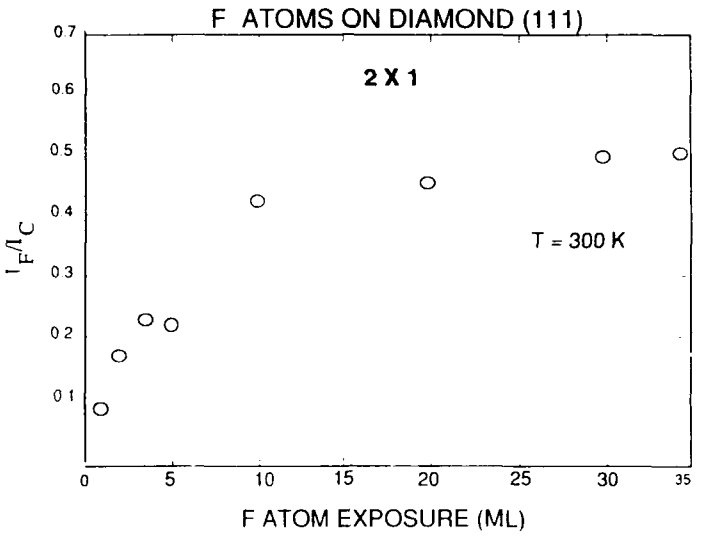


Figure 1. Uptake curve of fluorine as a function of atomic fluorine exposure. The integrated fluorine XPS signal has been normalized to the integrated carbon peak (1 ML = 1.8 x 10^{15} cm^{-2}).

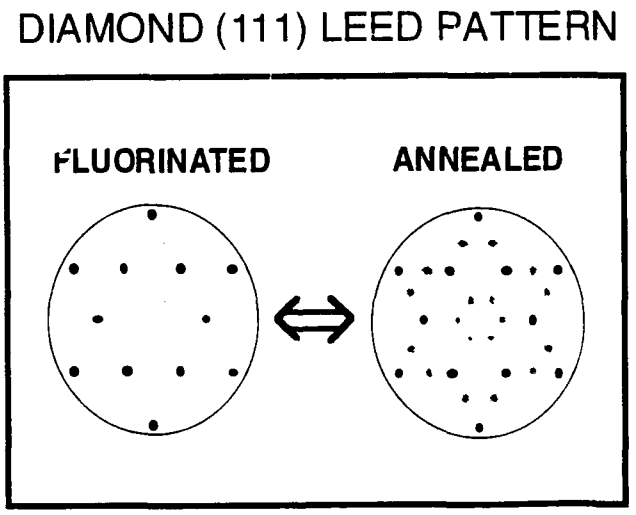


Figure 2. Artist's rendition of LEED patterns obtained at a beam voltage of 150 eV. Note that the second order spots are much less intense after fluorination indicating a partial reconstrution of the 2x1 surface to a 1x1 bulk-like configuration.

Figure 3 presents the relative fluorine coverage as a function of temperature for a (111) surface which has been fluorinated to saturation coverage at room temperature. This thermal behavior is quite similar to that found on the (100) surface, where fluorine desorption also begins at approximately 700 K. We note that the actual fluorine and carbon spectra obtained on both surfaces are virtually identical in shape and structure.

CONCLUSIONS

Fluorine atom adsorption on both the dehydrogenated 2x1 reconstruction of the diamond (111) surface and nonhydrogenated 1x1 bulk-like reconstruction of the diamond (100) surface are found to be quite similar in most respects. Adsorption is efficient and saturation coverages of a carbon monofluoride species of less than a monolayer are found in both cases. Fluorine in some form starts desorbing at ≈700 K, but some fluorine coverage is found up to a temperature of 1100 K. The major difference is that while fluorine addition to the (100) surface produces a disordered adlayer, the 2x1 (111) surface is partially reconstructed to the 1x1 bulk-like reconstruction due to fluorine termination. This result is in accordance with the concept that the (111) surface is less sterically hindered than the (100) surface due to the presence of only one adduct site as compared to two on the (100) surface.

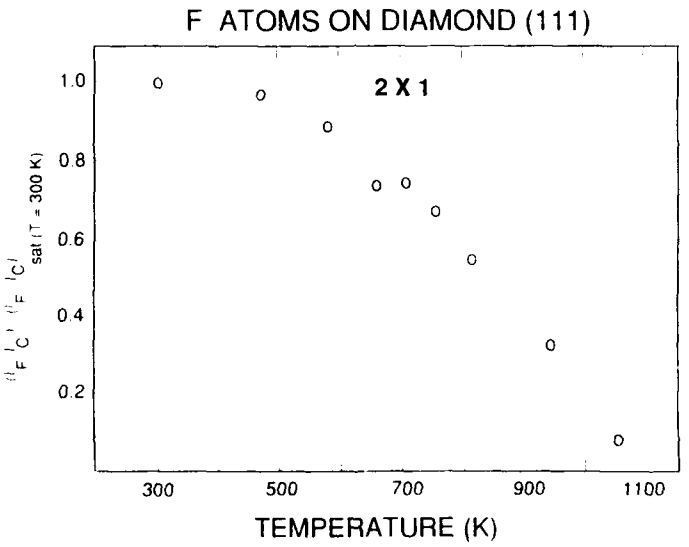


Figure 3. Thermal stability of fluorinated diamond adlayer. The substrate was fluorinated to saturation of 300 K before heating.

ACKNOWLEDGEMENTS

This project has been sponsored by the Strategic Defense Initiative Organization/Innovative Science and Technology (managed by the Office of Naval Research).

REFERENCES

1. T. Suntola and M.J. Antson, US Patent No. 4058430 (1977).

2. M. Pessa, P. Huttenen, and M.A. Herman, J. Appl. Phys. 54, 6047 (1983).

3. A. Freedman and C.D. Stinespring, Appl. Phys. Lett., 57, 1194 (1990).

4. A. Freedman and C.D. Stinespring, MRS Symp. Proc., 204, 571, (1990).

5. A. Freedman and C.D. Stinespring, Proc. of 2nd Int'l Conf. on New Diamond Science and Technology, edited by R. Messier, J.T. Glass, J.E. Butler, and R. Roy (MRS, Pittsburgh, 1991) p. 321-326.

6. A. Freedman and C.D. Stinespring, Proc. of 2nd Int'l Symp.on Diamond Materials (Electrochemical Society) 91-8, 494 (1991).

7. A.V. Hamza, G.D. Kubiak and R.H. Stulen, Surf. Sci. 206, L833 (1988).

8. C.D. Stinespring and A. Freedman, J. Vac. Sci. Technol. A4, 1946 (1986).

9. B.B. Pate, Surf. Sci. 165, 83 (1986).

10. G.D. Kubiak, private communication.

STM STUDY OF DIAMOND(001) SURFACE

Takashi Tsuno, Takahiro Imai, Yoshiki Nishibayashi, and Naoji Fujimori
Itami Research Laboratories, Sumitomo Electric Industries
1-1-1 Koyakita, Itami, Hyogo 664, Japan

ABSTRACT

Undoped and boron-doped diamond epitaxial films were deposited on diamond(001) substrate by micro-wave plasma assisted chemical vapor deposition and their surfaces were studied by scanning tunneling microscopy in air. An atomic order resolution was confirmed for the observation.

For the undoped epitaxial films, which showed 2x1 and 1x2 RHEED patterns, dimer type reconstruction was observed and it was considered that the growth occurs through the dimer row extension. In the case of B-doped films, the dimer reconstruction was also observed. However, 2x2 structure due to the absence of dimer was partially observed.

The effect of boron concentration and methane concentration during epitaxial growth on the surface morphology were also studied. The morphology observed by STM became flatter, as the concentration of B-doping and methane concentration, during growth, increased.

INTRODUCTION

In order to understand the growth mechanism of diamond chemical vapor deposition (CVD), observation of a grown surface is believed to be required. It is very important to control surface atomic structure and morphology for the electronic application of diamonds, especially for B-doped epitaxial films[1]. Shiomi et al.[2] studied the morphology of epitaxially grown diamond surfaces by SEM and optical microscopy (OM) and concluded that the surface roughness caused the poor Schottky property of diamond-metal interfaces.

Scanning tunneling microscopy (STM) is one of the most successful methods for surface analysis, because of its atomic scale spatial resolution. Recently, STM observation studies have been reported for surfaces of diamonds grown by CVD. Most of the trials are for polycrystalline diamonds[3-5]. However, study for well-defined single-crystalline surfaces is desirable in order to resolve fundamental processes. On diamond(001) surfaces, 2x1 and 1x1 structures were reported by LEED and RHEED observation in the case of clean surfaces in UHV[6], hydrogenated surfaces[7] and epitaxially grown surfaces after micro-wave assisted CVD[2]. The authors previously reported on the real space imaging by STM of 2x1[8] and 1x1[9] structures after CVD growth.

Mat. Res. Soc. Symp. Proc. Vol. 242. © 1992 Materials Research Society

EXPERIMENTAL

The undoped epitaxial films were deposited onto diamond(001) substrates using micro-wave plasma assisted CVD, of which the reactant gas consists of methane and hydrogen. In the case of B-doped films, diborane of appropriate concentration was added in reactant gas. The substrates were single crystalline diamonds synthesized under high-pressure and they were cut and mirror-polished. The size of the substrates was 2.0x1.5 mm^2 in area and 0.3 mm in thickness. The substrates were chemically etched by bichromic acid and cleaned by acetone, acid and water prior to deposition. Growth condition was that gas pressure was 40 Torr, micro-wave power was 300 W and temperature of the substrates was measured to be 830°C by optical pyrometry. Methane concentration was mainly 6% with hydrogen flow rate of 100 sccm after the condition reported by Shiomi et al.[2]. Typical thickness of epitaxial layers was 0.8 μm.

After deposition, the samples were taken out of the CVD apparatus and RHEED observation and X-ray photoemission spectroscopy were performed. STM observation was performed in air typically with a tunneling current of 2 nA and tip bias of +0.1 V.

RESULTS AND DISCUSSION

Epitaxially grown surfaces showed sharp RHEED patterns of 2x1 and 1x2 structures. XPS showed no impurities on the surfaces except for small amount of oxygen.

STM observation was found to have an atomic order resolution. A typical image of a diamond(001) surface of undoped epitaxial film is shown in Fig. 1. Patterns of parallel rows can be seen clearly all over the image. The distance between the adjacent rows were found to be 5.0 Å, almost corresponding to twice that of the surface unit, 2.52 Å. This image can be explained by symmetric dimer and hydrogen adsorption.

Figure 2(a) is an image of larger area. As is shown in Fig. 2(b), the Sa steps look straight and Sb steps look rather zig-zag in contrast. (Sa and Sb steps are shown in Fig. 2(c). The notation of steps is after Chadi.[10]) The authors consider that these indicate crystal growth through dimer row extension mainly from Sb steps.



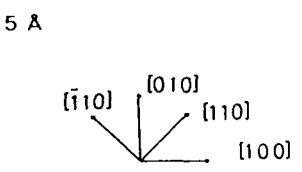


Figure 1
STM image of diamond(001) 2x1 surface with tip bias of 0.1 V and tunneing current of 2 nA.

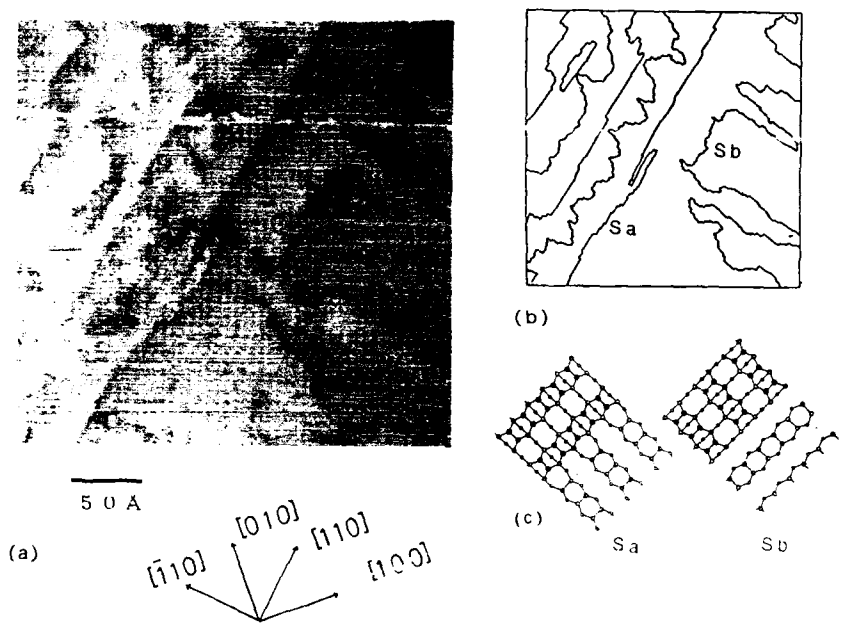


Figure 2
(a) STM image of diamond(001). (b) Outlines of step edges in (a).
(c) Sa and Sb steps of diamond(001) surface

For 2x1 structures of undoped epitaxial surfaces, the dimer atoms were not resolved. However, images of better resolution were successfuly obtained for B-doped films(70ppm), as is shown in Fig. 3. Carbon atoms which form dimers can be observed separately. In the upper right part of the figure, strong contrast (probably corresponding to dangling bond) can be seen. The authors consider that the defect affects the electronic states of dimers and resulted in the resolution of dimer atoms. It is not clear that the defect has any relation to B-doping or not. The distance between dimer atoms was measured to be 1.5 Å, which is one of the shortest interatomic distance ever identified by STM.

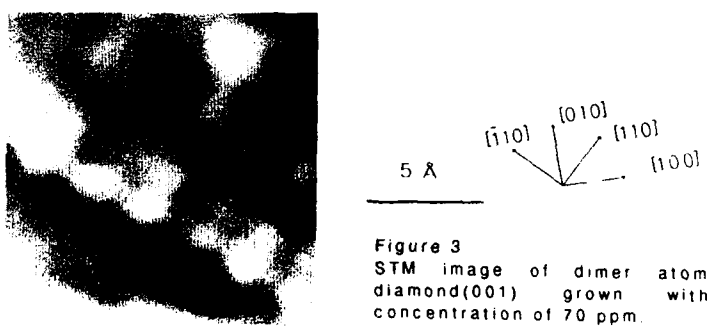


Figure 3
STM image of dimer atoms of diamond(001) grown with B concentration of 70 ppm.

For B-doped films, a structure, which cannot be explained as a simple structure of dimer and hydrogen adsorption, was observed. The image for B-doped film (70ppm) is shown in Fig. 4. An area of apparent 2x2 periodicity is observed and it is considered that dimers are absent periodically and partial 2x2 structure forms. The authors consider the absence of dimer to be caused by the stress in the film due to B-doping.

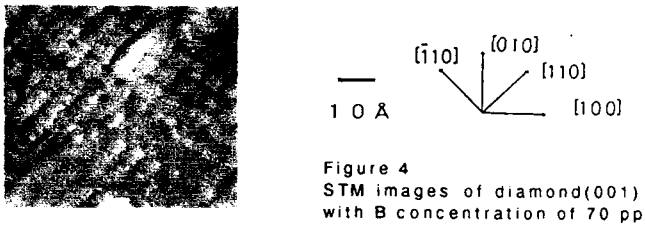


Figure 4
STM images of diamond(001) grown with B concentration of 70 ppm. 2x2 structure can be seen partially.

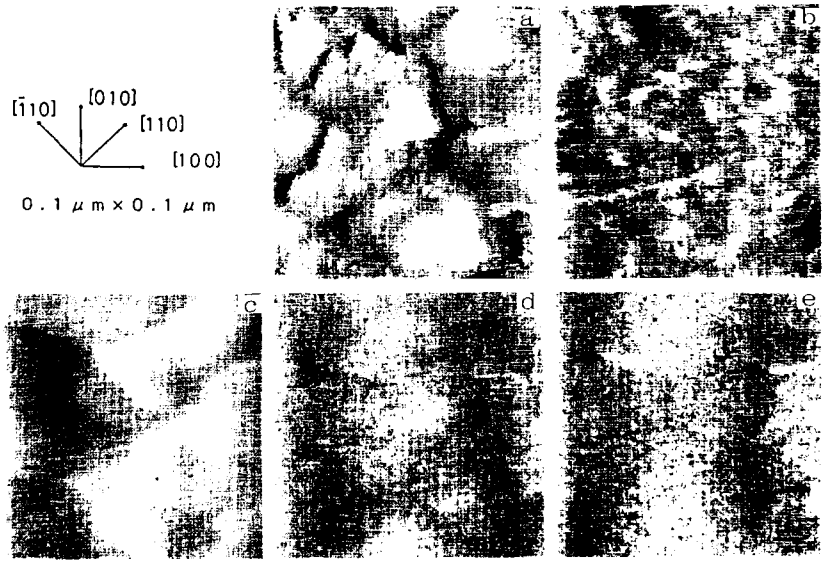


Figure 5
STM images of diamond(001) grown by micro-wave plasma assisted CVD. The results for undoped (a) and B-doped films (b-e) grown with mehane concentration of 6%. B concentration was (b) 3ppm, (c) 20ppm, (d) 70ppm and (e)350ppm.

As the dimer row extension plays important role in the growth of diamond(001), the morphology of the grown surface is probably affected by the absence of dimers. The authors observed larger areas in order to estimate micro-morphology of epitaxial films. The topography in the area of 1000 Å square for grown surface of undoped epitaxial film with 6% of methane concentration is shown in Fig.5(a). The mounds with some hundreds Å in area and 50-100 Å in height are seen. Such mounds are too small for SEM or OM observation. The outline of the mounds were apparently along the [110], or dimer row direction.

Figures 5(b) to 5(d) show the STM images of 1000 Å square for B-doped films, 3, 20, 70, 350 ppm respectively. It is clearly seen from the figures that the doping of B to the films has very strong effect on the surface morphology of epitaxial film. Increasing B concentration makes the surface flatter. The authors consider that the absence of dimers reduced the correlation along the [110] direction and hindered the mound formation.

The similar observation was performed for the effects of methane concentration during CVD growth. The results for methane concentration of 1,2,4,6 and 8 % are shown in Fig. 6(a) to 6(d). In these cases, the difference of surface reconstruction was not clear and other mechanisms should be considered.

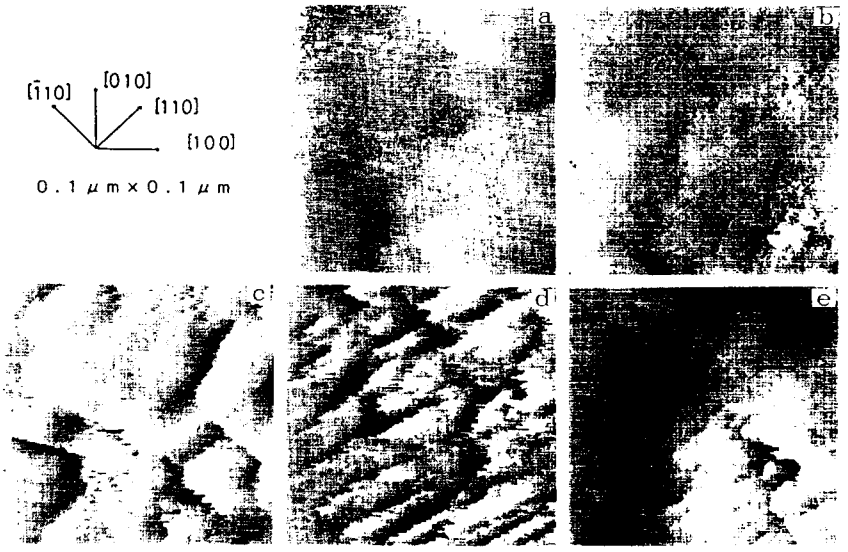


Figure 6
STM images of diamond(001) grown by micro-wave plasma assisted CVD. The results for undoped films grown with methane concentration of
(a) 1%, (b) 2%, (c) 4%, (d) 6% and (e) 8%.

COCNCLUSION

The atomic structure and micro-morphology of diamond(001) surfaces, grown by micro-wave plasma assisted CVD, were observed by STM. The effect of B-doping was admitted to both of them. B-doping makes for an absence of dimers, suggesting the existence of stress in the epitaxial film. B concentration and methane concentration made the surface morphology, observed by STM, change drastically.

Reference

[1] N. Fujimori, T. Ima. and A. Doi, Vacuum 36 99 (1986).
[2] H. Shiomi, K. Tanabe, Y. Nishibayashi and N. Fujimori, Jpn. J. Appl. Phys. 29 34 (1990).
[3] M. P. Everson and M. A. Tamor, J. Vac. Sci. Technol. B9 1570 (1991).
[4] K. F. Turner, B. R. Stoner, L. Bergman, J. T. Glass and R. J. Nemanich, J. Appl. Phys. 69 (1991) 6400.
[5] A. W. Phelps and T. W. Owens, Proc. 2nd Int. Symp. on Diamond Materials, (The Electrochem. Soc., Pennington, 1991), pp.502-509.
[6] P. G. Lurie and J. M. Wilson, Surf. Sci. 65 453 (1977).
[7] A. U. Hamza, G. D. Kubiak and R. H. Stulen, Surf. Sci. 237 35 (1990)
[8] T. Tsuno, T. Imai, Y. Nishibayashi, K. Hamada and N. Fujimori, Jpn. J. Appl. Phys. 30 1063 (1991).
[9] T. Tsuno, T. Imai, Y. Nishibayashi and N. Fujimori, Extended Abstracts (The 52nd Autumn Meeting, 1991, Jpn. Soc. Appl. Phys.), in preparation.
[10] D. J. Chadi, Phys. Rev. Lett. 59 468 (1989).

CHARACTERIZATION OF THE SI/DIAMOND INTERFACE

K. E. Williams and J. S. Speck
Department of Engineering Materials, University of California, Santa Barbara, CA;
M. D. Drory
Crystallume, Menlo Park, CA.

ABSTRACT

Auger spectroscopy is used to determine the bonding states of carbon in the interfacial region between silicon and PECVD diamond films. SiC and sp^2–hybridized carbon are observed. We suggest a possible growth sequence for diamond films to account for the interfacial layer.

INTRODUCTION

Diamond has many attractive properties, which include the highest hardness and room temperature thermal conductivity of any material, an extremely low thermal expansion coefficient, and reasonable electrical insulating properties [1]. As a result of these properties, diamond films have many potential applications as hard coatings and wear surfaces, and in electronic devices. Great interest in these applications has resulted from developments in low pressure diamond synthesis which have allowed polycrystalline diamond films to be produced at linear growth rates of tens to hundreds of microns per hour. Several comprehensive reviews of the field exist [2, 3, 4].

Most electronics applications, however, require further improvements in film quality and smoothness, and in the economics of production. Because CVD is commonly used in silicon and other semiconductor technologies, CVD of smooth diamond films is a focus of current efforts in the field.

The most commonly grown films are of [111] type and display relatively large faceted grains, thereby producing films of considerable surface roughness [2, 3, 4, 5]. Improved properties will clearly require an improved understanding of the nucleation and growth processes involved in diamond film deposition. Belton and Schmieg [6] have examined the silicon/diamond interface by XPS and EELS, and determined that the deposit was a mixture of SiC and diamond. Williams and Glass [7] have, through TEM studies, observed a 50 Å layer of SiC at the diamond/silicon interface. Iijima [8] has examined the growth of diamond particles on substrates seeded with diamond powder, a common practice used to improve the diamond nucleation density, and has determined that diamond grows homoepitaxially on diamond particles which remain embedded in the substrate following the seeding process.

The present study takes advantage of the unique capabilities of Auger electron spectroscopy (AES) to examine both the composition and the chemical bonding of the interfacial region. It has long been known [9] that the fine structure of the Auger spectrum of carbon provides a fingerprint for identification of the form of carbon deposits on a surface. The present paper uses this capability to examine both sides of the diamond/silicon interface and to suggest a growth sequence for CVD diamond films.

EXPERIMENTAL PROCEDURE

Three sets of samples were analyzed for this paper. The first set, referred to as sample A, was grown on an unseeded silicon wafer by plasma enhanced chemical vapor deposition in a

2.45 GHz microwave reactor with 0.5% carbon bearing gases in hydrogen, and a substrate temperature of 755° C. The second set, referred to as sample B, was grown on a silicon wafer which had been abraded with diamond grit under conditions identical to those used for sample A. The third, referred to as sample C, was grown on a seeded Si wafer under similar conditions to the previous samples except with approximately 3% carbon bearing gases.

All three samples were fractured *in situ* in a Perkin Elmer PHI 660 Auger microscope, with an operating pressure of approximately 2×10^{-9} torr. The fracture was accomplished by mounting a thin slice of the sample perpendicular to the surface of a specially grooved sample stage, scribing the backside of the sample at a desired fracture location, and inserting it into the microscope chamber where it was broken by the installed PHI fracture attachment.

Auger spectra were collected from locations on the exposed fracture surfaces and from reference samples of pure SiC, pure natural diamond, pure graphite, and sputtered amorphous carbon. Differences in bonding state are most clearly observable in the derivative (dN(E)/dE) spectra, and are illustrated in Fig. 1. The PHI-MATLAB software package was used to perform a linear least squares fit of the reference spectra to the sample data. We fit to N(E) rather than dN(E)/dE) in order to avoid loss of information due to differentiation. Due to differences in Auger yields from different bonding orbitals, this technique is only semi-quantitative.

Other authors [9] have observed a split peak near 250 eV in diamond, rather than the broad, flat peak shown in Fig. 1. We attribute the difference to damage induced by the electron beam during our relatively prolonged data collection.

Graphite and amorphous carbon produce the least distinctive Auger lineshapes of the four standard materials, as the "shoulder" due to the KL_IL_{II} transition observed near 255 eV becomes less distinct with decreasing graphitic character. For that reason, the terms "sp^2–hybridized carbon" and "carbon" are used here to describe materials having an Auger lineshape with substantial graphitic character, as measured by the fitting routine.

Following Auger analysis, all three samples were examined by SEM to determine the morphology of the fracture surface.

In addition, to determine the likelihood of SiC formation at an existing silicon/diamond interface under growth conditions, silicon powder was mixed with natural diamond powder and reacted in argon at 750° C for four hours. The resulting mixture was analyzed by x-ray diffraction (XRD).

RESULTS

Sample A, grown on an unseeded silicon wafer under the same conditions as the seeded silicon wafer used for sample B, was not a continuous film, as Fig. 2 illustrates. SEM examination showed a smooth surface with small, isolated, diamond grains. The Auger spectra taken from this film were dominated by SiC, with small amounts of sp^2–hybridized carbon (with a graphitic Auger lineshape) also observed.

Upon *in situ* fracture of sample B in the Auger microscope, overhanging diamond "shelves" and underhanging silicon "ledges" were observed. These features are schematically illustrated in Fig. 3, and SEM micrographs of a shelf and a ledge appear in Figs. 4 and 5, respectively.

Figure 4 shows that the undersides of the overhanging diamond shelves are grooved. The damage produced by abrading the silicon substrate is apparently replicated in the growing film. Auger spectra taken from these surfaces showed the presence of SiC and sp^2–hybridized carbon in approximately equal amounts.

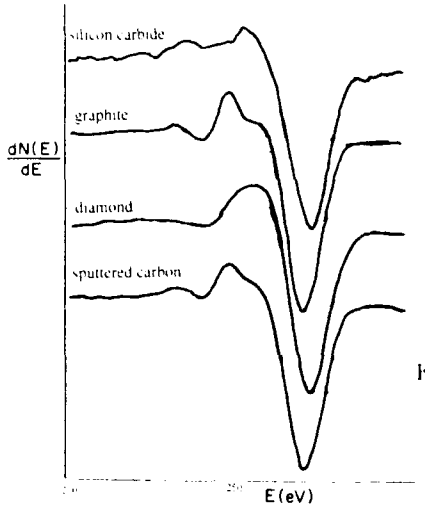


Figure 1: KLL carbon spectra from diamond, graphite, sputtered carbon, and SiC.

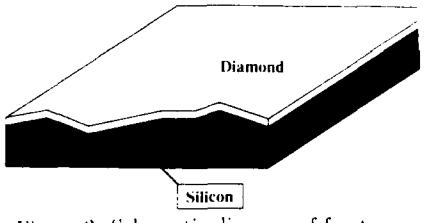


Figure 3: Schematic diagram of fracture surface, samples B and C.

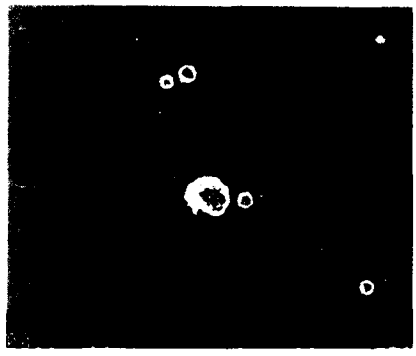


Figure 2: Nucleation of diamond on unseeded silicon wafer, sample A.

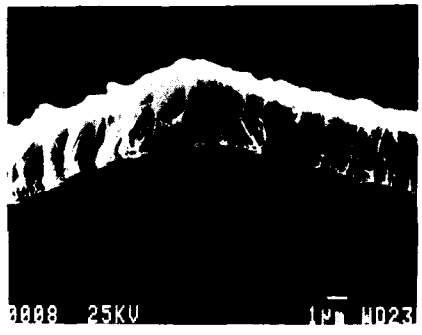


Figure 4: Underside of diamond shelf in sample B.

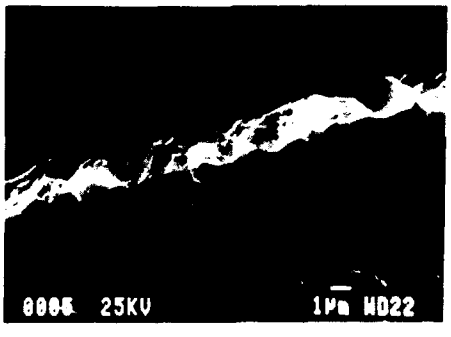


Figure 5: Exposed silicon ledge in sample B.

Figure 5 indicates that a sloping interfacial region is exposed between the substrate and the diamond film. Auger spectra were collected for a series of points in and on both sides of the interfacial region. These spectra show a progression from SiC-dominated material, to a region containing primarily carbon, to the diamond film. Oxygen was also observed in the SiC-dominated region (Fig. 6), but not in the interfacial region, suggesting that the native silicon oxide was still present during the early growth stages. It is worth noting here that Nicalon fibers (amorphous SiC) have been shown to incorporate substantial fractions of oxygen. Since hydrogen is not detectable by AES, it was not possible to measure hydrogen concentration at the interface or elsewhere.

When the shelves and ledges are considered as mating halves of the fracture surface, it appears that fracture of the interface left traces of SiC and carbon on both surfaces. It therefore seems likely that fracture occurred in a transitional region between SiC and the diamond film.

The fracture surface of sample C was somewhat different from that of sample B, as shown in Figs. 7 and 8. In sample C, no clearly delineated interfacial region was visible on silicon ledges. This observation was confirmed by Auger spectra, which showed that SiC and carbon were present in approximately equal quantities on the exposed ledge.

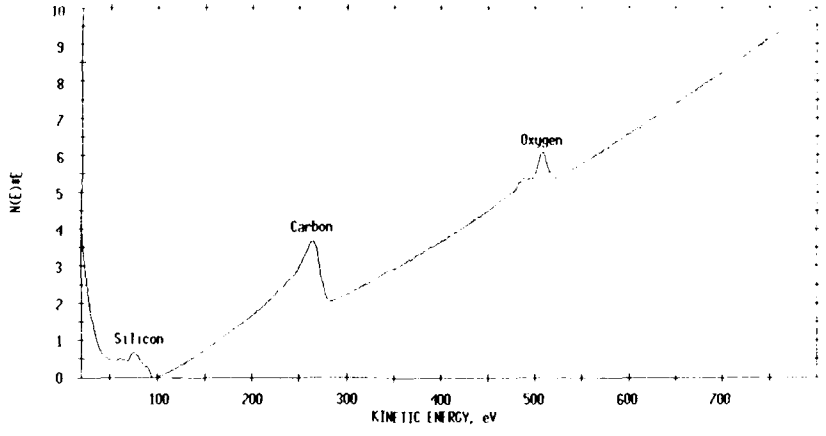


Figure 6: Auger spectra from exposed silicon ledge, sample B.



Figure 7: Underside of diamond shelf in sample C.



Figure 8: Exposed silicon ledge in sample C.

Trace amounts of oxygen were also observed on these ledges, again indicating that some of the native SiO_2 layer was present on the surface. Spectra from the undersides of diamond shelves contained diamond, sp^2–hybridized carbon, and SiC in approximately equal amounts. Since the escape depth for Auger electrons is only on the order of 5 Å [10], these data suggest that, although the transitional interface region was still present in sample C and interfacial fracture occurred in this region, sample C's transition region was substantially reduced relative to sample B's.

It is worth noting that no scratches were visible on the undersides of diamond shelves in Sample C, suggesting that the reduced interfacial region and the reduced interfacial damage are related.

Finally, the mixture of diamond and silicon powder was examined by XRD with Cu Kα radiation both before and after reaction. The diffraction pattern, consisting solely of peaks attributable to silicon or diamond, was unchanged by heat treatment. This indicates that diamond is unlikely to be consumed by silicon carbide formation once diamond has formed on a silicon substrate.

DISCUSSION AND CONCLUSIONS

The AES results clearly demonstrate that the bonding state of carbon changes from SiC-like to sp^2–hybridized to sp^3–hybridized (diamond) across the Si/diamond interface. The Auger results also show that oxygen is present near the Si side of the interface but not near the diamond side. Further efforts will focus on the Si and oxygen lineshapes across the interface in order to identify the oxygen-bearing species in the interfacial region. This will help us better understand the fate of silicon's native oxide during the CVD process.

Several conclusions can be drawn from our results. First, silicon carbide is observed at the diamond/silicon interface in samples B and C, and on the surface of sample A. This carbide must form either by reaction with exposed Si patches; by incorporation of carbon into the SiO_2 layer; by diffusion of Si through the oxide layer; or some combination of these processes. In any case, the rate of growth of a layer AB on a substrate A is proportional to $1/x^2$, where x is the AB layer thickness and hence the diffusion length of A from the substrate through the growing layer. The diffusion length x is in turn proportional to $\sqrt{Dt}$, where D is the diffusion coefficient of A in AB and t is time [11]. So, as the thickness of the SiC layer increases, the rate of SiC growth decreases and eventually becomes negligible. Meanwhile, carbon continues to deposit on the film surface, whether or not Si is present to react with it.

Concurrent with the above process, diamond grows on all three samples. In sample B and C, we note that recent work [8] has shown that diamond particles are embedded in the surface of substrates which have been abraded with diamond powder, and that CVD diamond growth occurs homoepitaxially on these particles.

Therefore, we believe that homoepitaxial diamond growth occurs simultaneously with SiC growth in samples B and C. As the rate of SiC formation decreases, the growing diamond crystallites overgrow the SiC and carbon layers, eventually forming a continuous film. This process is schematically illustrated in Fig. 9.

Finally, we attribute the thin interfacial reaction layer in sample C to the high concentration of carbon bearing gases during growth of this sample. Apparently, for seeded films, the growth rate of diamond is limited by gas phase transport. Hence the diamond grows at an accelerated rate in this sample.

To summarize, we have studied the carbon bonding states in the Si/diamond interfacial region, and have observed SiC and sp^2–hybridized carbon. We suggest that these

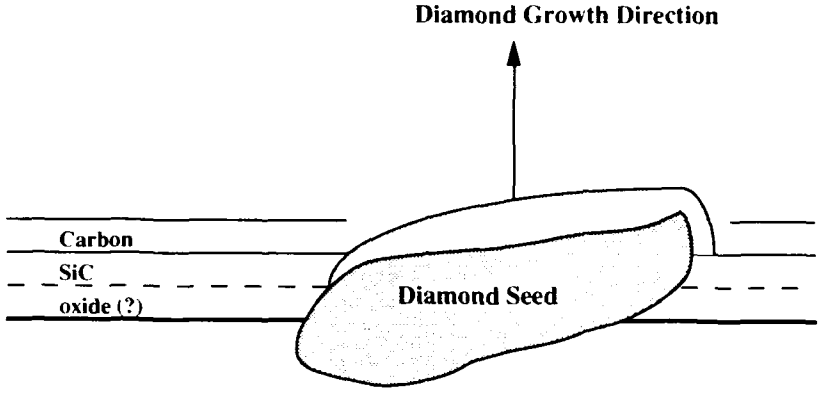


Figure 9: Schematic representation of diamond growth on samples B and C. layers form simultaneously with diamond growth on preexisting nuclei. Further work will concentrate on identification of the silicon and oxygen species in the interfacial region.

ACKNOWLEDGEMENTS

The authors wish to acknowledge helpful discussions with F. F. Lange and P. M. Petroff.

REFERENCES

[1] J.C. Angus, F. A. Buck, M. Sunkara, T. F. Groth, C. C. Hayman, and R. Gat, MRS Bulletin, **1989** (Oct.), 38.

[2] J. C. Angus, *Proc. of Symposium on Diamond and Diamondlike Materials*, 175th Meeting of the Electrochemical Society, Los Angeles, CA, May 8, 1989.

[3] A. R. Badzian and R. C. DeVries, Mater. Res. Bull. **23**, 385 (1988).

[4] W. A. Yarbrough and R. Messier, Science **247**, 688 (1990).

[5] K. Kobashi, K. Nishimura, Y. Kawate, and T. Horiuchi, Phys. Rev. B **38**, 4067 (1988).

[6] D. N. Belton and S. J. Schmieg, J. Vac. Sci. Technol. A **8**, 2353 (1990).

[7] B. E. Williams and J. T. Glass, J. Mater. Res. **4**, 373 (1989).

[8] S. Iijima, Y. Aikawa, K. Baba, J. Mater. Res. **6**, 1491 (1991).

[9] T. W. Haas, J. Y. Grant, and G. J. Dooley III, J. Appl. Phys. **43**, 1853 (1972).

[10] L. C. Feldman and J. W. Mayer, *Fundamentals of Surface and Thin Film Analysis* (North-Holland, New York, 1986), p. 274.

[11] S. Wolf and R. N. Tauber, *Silicon Processing for the VLSI Era*, Vol. 1: Process Technology (Lattice Press, Sunset Beach, 1986), pp 198-242.

ELECTRONIC STRUCTURE OF N-V CENTERS AND TERAHERTZ SPECTROSCOPY OF DIAMOND

D.A. REDMAN*, Q. SHU*, S.W. BROWN*, A. LENEF*, Y. LIU*, J. WHITAKER*, S.C. RAND*, S. SATOH**, K. TSUJI** AND S. YAZU**
*Dept. of EECS, University of Michigan, Ann Arbor, MI 48109-2122
**Sumitomo Electric Industries, Ltd., Itami Research Laboratories, Hyogo, Japan

ABSTRACT

We report an essentially complete characterization of energies and relaxation processes of the lowest seven electronic states of the N-V (nitrogen-vacancy) center in diamond using several different nonlinear laser spectroscopic techniques. We have also applied ultrafast optical techniques to measure dielectric properties of CVD and bulk diamond in the 0.3-1.6 THz range for the first time.

INTRODUCTION

The N-V center with zero phonon absorption at 637 nm is one of the simplest and most studied radiation-induced centers in nitrogen-containing diamond [1]. It was somewhat surprising therefore that Manson and co-workers [2] recently questioned earlier assignments of its electronic states. However, their viewpoint was fully substantiated by subsequent work of Redman et al. [3], who used a combination of EPR and nearly degenerate four-wave mixing spectroscopy to show directly that the ground state was a spin triplet rather than a singlet as suggested earlier by Loubser and Van Wyk [4]. Here we present new results of high resolution optical spectroscopy involving persistent hole-burning, stimulated photon echo and two-beam coupling observations which confirm and extend these findings. Persistent hole-burning was used to determine zero field splittings of the ground and excited triplet states due to spin-spin interactions. Echo techniques with femtosecond pulses revealed quantum beats at oscillation frequencies in agreement with the hole-burning results. These short pulse experiments also characterized fast relaxation processes of the center. Two-beam coupling with frequency-locked dye lasers was used to elucidate slow decay processes.

We have also measured real and imaginary parts of the dielectric tensor for diamond in the Terahertz (THz) frequency regime. Preliminary results reported here were obtained by a precise ultrashort pulse technique [5] applied to bulk single crystals and free-standing CVD polycrystalline films. Broadband bursts of Terahertz radiation were generated by ultrashort optical pulses on a low-temperature-grown GaAs photoconductive dipole antenna, then collimated and passed through the material under study to an identical dipole receiver gated with variable-delay, synchronized pulses from the same laser. CVD diamond crystallite sizes were very much smaller than a wavelength, so these measurements furnish accurate values of refractive index and loss tangent over a broad range of millimeter wavelengths when film thickness is known. These values are the same as would be measured for dielectric constant and conductivity in single crystal diamond films of equivalent density and composition.

EXPERIMENTAL

Sample preparation has been described elsewhere, in reference [3], and there it was shown in a direct manner that the ground state of the N-V center is a spin triplet. Still earlier, uniaxial stress studies [6] showed that the first parity-allowed optical transition is between a ground state of A and an orbitally excited state of E symmetry. Consequently, with the further result from [3] that a metastable state exists between ^{3}A and ^{3}E, the electronic energy level scheme of Fig. 1 is obtained for the center. All states shown are within the gap.

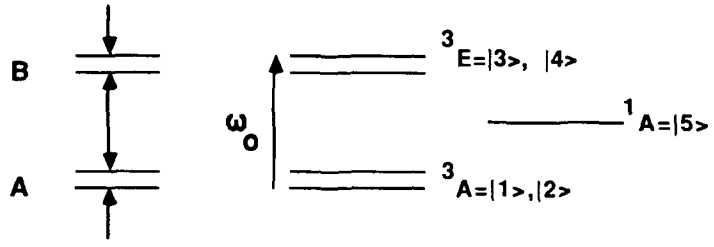


Figure 1. Energy levels of the N-V center in diamond.

Persistent Spectral Hole-Burning

Small spin splittings, such as the one labelled A in Fig.1 between singly and doubly degenerate sub-levels of a triplet orbital state (partly split in zero field by spin-spin interactions), can easily be measured by electron paramagnetic resonance if they occur in ground states. More generally however, both ground and excited state splittings can be measured using various forms of optical hole-burning spectroscopy, which records transmission versus frequency following narrowband laser excitation. Here we first present persistent hole-burning measurements of the splittings A and B depicted in Fig. 1 for the N-V center. We then compare them with quantum beat measurements and in later sub-sections consider relaxation dynamics of the center and Terahertz response.

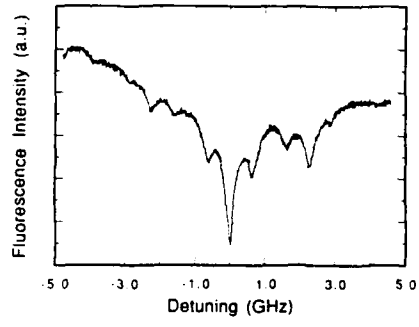


Figure 2. Persistent hole-burning spectrum of the N-V center at 637.87 nm at T=6.5 K.

Optical pumping among the ground and excited spin states of the N-V center was accomplished at liquid helium temperatures with radiation from a cw dye laser tuned to the zero phonon resonance at 637 nm. The re-distribution of population among homogeneous groups of N-V centers within the broad absorption linewidth (hole-burning) was observed by probing absorption changes induced by the pump laser on a fine frequency scale. In our experiments, we observed both transient and persistent changes in absorption in the detuning range 0-10 GHz. Below 70 K, it was possible to observe the spectrum of Fig. 2 after delays of up to an hour by tuning a weak probe beam through the spectral region of the "bleaching" laser. The extraordinary persistence of "satellite" features seen in this spectrum was previously unexplained [7], but all features can now be accounted for by assigning zero field triplet spin splittings of A=2.88 GHz and B=0.65 GHz. That is, all holes appear at frequency shifts of $\pm$A, $\pm$B, $\pm$(A-B), $\pm$(A+B), or $\pm$(A$\pm$2B). The value for A is in excellent agreement with ground state EPR [3,4], whereas B has not been measured previously.

Ultrafast Quantum Beat Spectroscopy

A direct, all-optical method of verifying splittings in the triplet manifolds and of measuring the values of A and B is to observe fluorescence or coherence decay following short pulse excitation. This method relies on preparation of a coherent superposition of the two ^3A and the two ^3E states, and observation of interference between dipole-allowed transitions in subsequent emission of the system. We used cavity-dumped 800 fs pulses from a two-jet, synchronously mode-locked DCM dye laser to excite the N-V center at 637 nm. Two counter-propagating pump pulses mixed with a weak probe pulse within the sample to generate an accumulated 3-pulse echo propagating opposite to the probe and exhibiting the dependence on delay shown in Fig. 3.

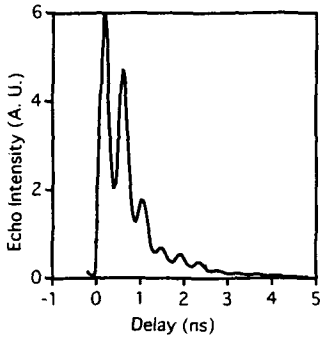


Figure 3. Three-pulse stimulated echo signal versus probe delay for λ=637 nm at T=6.5 K.

The observed oscillations for co-polarized beams occurred at a frequency of 2.2 GHz as determined by FFT analysis. This frequency is in excellent agreement with the difference frequency A-B of the two spin-allowed transitions between the ground and excited state manifolds expected from persistent hole-burning results. Here however, state splittings are implicated directly, without appeal to complex optical pumping and storage processes due to the ultrafast excitation mechanism. Interestingly, signals are also observed for cross-polarized forward pump and probe beams. These signals presumably originate from higher-order coherence among the sub-levels of each manifold. The temporal decay of the quantum beat envelope yields the dephasing time of the ^3E state directly. At 6.5 K this amounts to a few nanoseconds. The population decay time, obtained in separate measurements with delayed backward pump pulses, is 13.3 ns. These are the fast relaxation processes of the N-V center.

Two-beam coupling

Slow decay processes are ordinarily measured by fluorescence or phosphorescence decay experiments. However, if the decay is non-radiative or the wavelength of emission is unknown, frequency-domain techniques like four-wave mixing or two-beam coupling can be very useful.

In Fig. 4 the gain spectrum for a probe wave passing through a bulk single crystal of diamond containing N-V centers illuminated by a strong pump wave is shown. The two beams cross at a small angle in the sample, and spectral variations in the energy transfer between the two beams are well-known to depend sensitively on decay times of internal population dynamics of the center under study [8]. Since the basic relaxation processes within the N-V center have been described previously [3], we can compare the results of two-beam coupling quantitatively with earlier work.

We find that two exponential decay processes are required to describe the observations in Fig. 4. The two-beam coupling spectrum itself is therefore a superposition of in-phase and out-of-phase components of two contributions from distinct dynamical processes. The fitting parameters consist of the corresponding relaxation times t_1 and t_2, and real and imaginary parts of the nonlinear refractive index n_2. The solid curve in the figure is a least squares fit to room temperature data with t_1= 50± 2 ms, t_2= 0.64± .01 ms, and n_2''/n_2'= -1.01± .04 . For comparison with earlier determinations by four-wave mixing (NDFWM), two-beam coupling was also performed at 77 K with the result that t_1= 92± 30 ms, t_2= 1.1± .1 ms, and and n''/n_2'= -0.9± .1. Excellent agreement is obtained for t_2 when compared to the precise NDFWM determination t_2=1.170± .003 ms, whereas t_1 is somewhat shorter than the NDFWM value 265.3± .6 ms. However t_1 from beam coupling does approach the NDFWM value as intensity and chopping duty cycle are reduced. This indicates that the qualitative description of the diamond beam coupling spectrum is excellent and the quantitative comparison with earlier results satisfactory. On this basis the two components t_1 and t_2 in the beam coupling spectrum may be identified as arising from intersystem crossing (^{1}A--> ^{3}A) and spin-lattice relaxation (^{3}A(b)--> ^{3}A(a)) respectively.

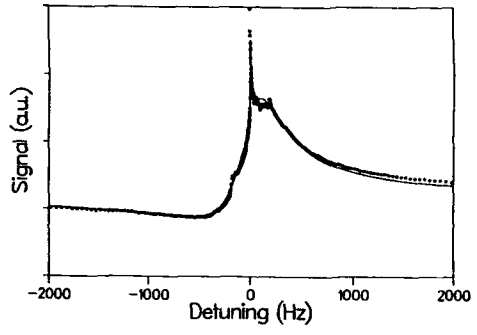


Figure 4. Two-beam coupling signal versus pump-probe detuning. The solid line is a least squares regression based on two-component nonlinear response.

Terahertz spectroscopy

Single cycles of Terahertz radiation of approximately 600 fs duration were generated by 100 fs optical pulses incident on photoconductive antenna structures integrated on GaAs wafers. Collimation was accomplished using a hyper-hemispherical Silicon lens constructed of high resistivity material. Detection relied on a similar arrangement in which the receiver voltage was sampled with 100 femtosecond timing accuracy using optical pulses derived from the same laser. In Fig. 5 the real and imaginary parts of the dielectric constant determined in this way are presented for two nominally undoped, free-standing diamond films of area 1 cm^2 and thicknesses 20 and 60 μm grown by filament-assisted chemical vapor deposition (FACVD).

When losses are dominated by free carrier absorption, the variations in the imaginary index reflect changes in the bulk conductivity versus frequency. Thus, given accurate determinations of film thickness, data such as that in the lower curve of Fig. 5(b) provide an elegant method for characterization of millimeter wave conductivity over a very wide band.

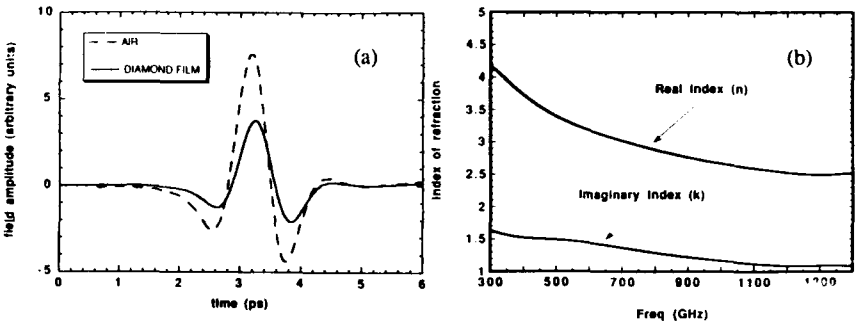


Figure 5. (a) Detected Terahertz pulsed field strengths versus time, with and without a free-standing FACVD diamond film (estimated 20 μm thickness) placed between transmitter and receiver. (b) Refractive index and conductivity of the diamond film derived by preliminary analysis of pulse envelope modulation and phase delay.

The rapid rise in the real index toward lower frequencies evident in Fig.5 is incompletely understood at this time, but is probably due to low frequency electromagnetic resonances associated with dangling bond and impurity spin excitations. Systematic measurements are in progress to correlate these parameters with film morphology, doping and growth conditions as well as to make direct, quantitative comparisons with bulk single crystals.

SUMMARY

Determinations of the electronic structure and dynamics of the lowest seven states of the N-V center in diamond constitute the main results of this work. We have made high resolution observations of the splitting of doubly degenerate and singly degenerate spin states associated with the orbital singlet ground state and the lower component of the orbital doublet excited state, in zero field. Results obtained by persistent hole-burning agree well with those from quantum beat spectroscopy. Evidence [3] for the existence and relaxation rate of a postulated intermediate ^1A state has not been discussed here, but completes our picture of lowest-lying energy states of the center.

Fast population decay, optical dephasing and slow dynamics due to intersystem crossing and spin-lattice relaxation have also been studied. The decay constants associated with each state were determined accurately with a combination of photon echo and beam coupling techniques. Overall, our measurements constitute a rather complete picture of the electronic structure and fundamental relaxation processes of the N-V center. Finally we have presented preliminary measurements of dielectric properties of CVD diamond at Terahertz frequencies using all-optical techniques easily extendable to other widegap semiconductor thin films.

ACKNOWLEDGEMENTS

This research was sponsored in part by a Phoenix Memorial Grant, the Air Force Office of Scientific Research, Sumitomo Electric and the National Science Foundation Science & Technology Center for Ultrafast Optical Science (CUOS) at the University of Michigan under STC PHY 8920108.

REFERENCES

1. C.D. Clark, in The Properties of Diamond, edited by J.E. Field (Academic Press, New York, 1979) pp. 23-77.

2. N.R.S. Reddy, N.B. Manson, and E.R. Krausz, J. Lumin. 38, 46 (1987); E. van Oort, N.B. Manson, and M. Glasbeek, J. Phys. C: Sol. St. Phys. 21, 4385 (1988); N.B. Manson, X.-F He, and P.T.H. Fisk, Opt. Lett. 15, 1094 (1990).

3. D. Redman, S.W. Brown, R.H. Sands and S.C. Rand, Phys. Rev. Lett. 67, 3420(1991).

4. J.H.N. Loubser and J.A. Van Wyk, Diamond Research 11, 4 (1977).

5. M. van Exter, Ch. Fattinger, and D. Grischkowsky, Optics Letters 14, 1128 (1989).

6. G. Davies and M.F. Hammer, Proc. Roy. Soc. (London) A348, 285-298 (1976).

7. P.D. Bloch, W.S. Broklesby, R.T. Harley, and M.J. Henderson, J. de Physique (Coll.) C7, 527 (1985).

8. Y. Silberberg and I. Bar-Joseph, J. Opt. Soc. Am. B1, 662 (1984); M.A. Kramer, W.R. Tompkin, and R.W. Boyd, Physical Review A34, 2026 (1986); I. McMichael, P. Yeh, and P. Beckwith, Optics Letters 13, 500 (1988); S.A. Boothroyd, J. Chrostowski, and M.S. O'Sullivan, J. Opt. Soc. Am. B6, 766 (1989).

ELECTRICAL PROPERTIES OF FINE GRAIN COMPOSITE CARBON FILMS

Hsiung Chen and R. O. Dillon
Electrical Engineering Department and
Center for Microelectronic and Optical Materials Research,
University of Nebraska, Lincoln, NE 68588-0511

ABSTRACT

We have studied the electrical properties of boron doped composite films that consist of diamond and amorphous carbon. These films were deposited by hot filament chemical vapor deposition at a relatively high carbon/hydrogen ratio. The mixture of trimethyl borate vapor, and methane served as a source gas. The composite films had much smoother surfaces than polycrystalline diamond films.

The surface morphology and average roughness were determined by scanning electron microscopy (SEM) and atomic force microscopy (AFM). Raman spectroscopy and x-ray diffraction were used to analyze the structure of the films.

A composite film grown with 4% methane in hydrogen had a higher resistivity than a well faceted diamond film grown at 0.5% methane. In contrast to hydrogenated amorphous carbon films which have a lower resistivity after thermal annealing, the resistivities of composite films increased by a factor of two to ten after 3 hours annealing at 600°C.

INTRODUCTION

The resistivity of diamond and an amorphous sp^2 material are fundamentally different because the electrical conduction mechanism of a crystalline semiconductor is not the same as that of an amorphous semiconductor. An undoped polycrystalline diamond film usually has a resistivity $> 10^8$ ohm-cm [1,2]. However, as the quality of diamond is degraded with a small amount of sp^2 structure, the resistivity becomes less than 10^8 ohm-cm. On the other hand, the resistivity of amorphous carbon films can vary from 10^{-3} to 10^{16} ohm-cm [3,4], depending on the hydrogen concentration and carbon bonding structures.

The purpose of this work is to systematically study the electrical properties of carbon films as a function of carbon sp^2/sp^3 ratio and boron doping level.

EXPERIMENTAL

Semiconducting films made of diamond and amorphous carbon were grown in a hot filament assisted chemical vapor deposition chamber. The deposition conditions were chosen at a typical setting for good diamond growth and the parameters are listed in Table I.

The only two variables are carbon/hydrogen ratio and boron concentration. The growth rate as indicated in the Table I is relatively low. That is because a large distance between hot filament and substrate was used in order to get uniform films over a large area. Trimethyl borate (TMB) was used as doping source. The tungsten filament was carburized prior to film growth and during deposition the temperature was kept at the relatively low temperature of 2000°C in order to minimize metal contamination. Three series of eleven samples were prepared for this study and they are shown in Table II.

The surface morphology and average roughness were determined by scanning electron and atomic force microscopy. The structures of the film were qualitatively studied by Raman spectroscopy and x-ray diffractometry.

Since our substrates were highly doped silicon, 10-20 ohm-cm, free standing films were made by etching off the substrate prior to the resistivity measurement. Resistances

Mat. Res. Soc. Symp. Proc. Vol. 242. © 1992 Materials Research Society

were measured by four point probe from room temperature up to 700°C using a Keithly 224 current source and a 617 electrometer. In addition, W, Al, and Ti point probes were used for studying the metal contacts.

Table I. Experimental parameters.

Tungsten filament temperature	2000°C
Heater temperature	800°C
Estimated substrate surface temp.	850°C - 900°C
Substrate - filament distance	10 mm
Gas flow rate	
CH4 + TMB*	0.5 - 4.0 sccm
H2	99.5 - 96.0 sccm
Total gas flow rate	100 sccm
Total gas pressure	20 torr (26.7 mbar)
Deposition time	20 hours
Growth rate	0.15 - 0.4 μm/h

* TMB = trimethyl borate

Table II. Sample notation, room temperature resistivity, growth rate, and average surface roughness.

	CARBON/HYDROGEN RATIO			
	0.5%	1.0%	2.0%	4.0%
SERIES U UNDOPED	U(0.5)		U(2.0)	U(4.0)
Resistivity (ohm-cm)	4.6×10^4		1.5×10^4	1.2×10^8
SERIES L LIGHTLY DOPED	L(0.5)	L(1.0)	L(2.0)	L(4.0)
Resistivity	510	44	40	7.9×10^3
SERIES H HEAVILY DOPED	H(0.5)	H(1.0)	H(2.0)	H(4.0)
Resistivity	60	7.0	5.6	450
Growth Rate (μm/h)	0.15	0.25	0.40	0.30
RMS Roughness (nm)	182	113	104	13

RESULTS AND DISCUSSION

Surface morphology and structures

Fig. 1 shows the effect of the methane concentration change on the surface morphology. The root mean square roughness measured by AFM is listed in the bottom of

Table II. This data shows that the roughness of diamond films can be reduced by more than an order of magnitude with the addition of an sp^2 phase. The growth rates are 0.15, 0.25, 0.4, and 0.3 μm/h for gas combinations of 0.5%, 1%, 2%, and 4% methane in hydrogen, respectively. The reduced growth rate at 4% methane is possibly due to significant amount of carbon precipitating on the filament during growth. The addition of the TMB vapor for doping in the source gas neither changed the growth rate nor the surface morphology.

The corresponding Raman spectra for different carbon concentrations are shown in Fig. 2. It indicates that the higher the carbon concentration, the broader and weaker the Raman diamond peak. For the film grown at 4% methane, the sp^2 peaks are the dominated features, and the diamond signal is too weak to be identified. Based on these Raman spectra, we conclude that the sp^2/sp^3 ratio of the films increased with a rising methane concentration.

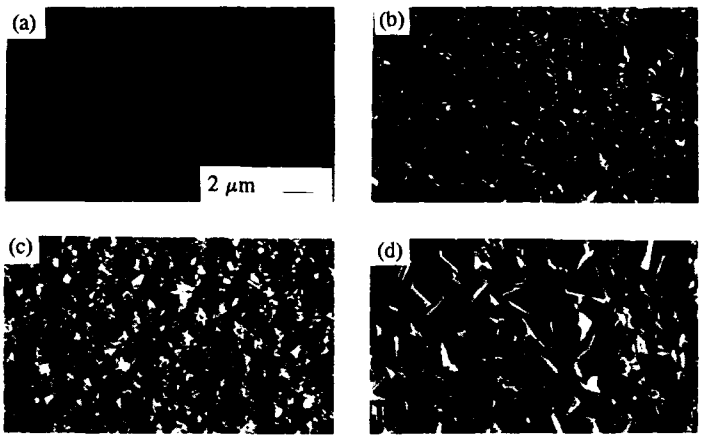


Fig. 1 The surface morphology of diamond films with methane concentrations of (a)4%, (b)2%, (c)1%, and (d) 0.5%. All SEM micrographs were taken at same magnification.

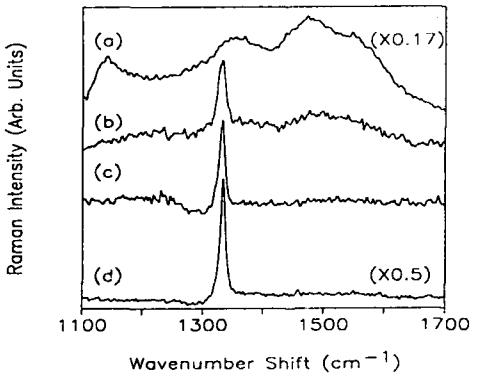


Fig. 2 Raman spectra of diamond films with methane concentrations of (a)4%, (b)2%, (c)1%, (d)0.5%.

X-ray diffraction spectra of samples L(0.5) and L(4.0) are shown in Fig. 3. The broad small peaks of sample L(4.0) are from diamond (111) and (220). This indicates that small-grain diamond is in this film even though it is not identified in the Raman spectrum.

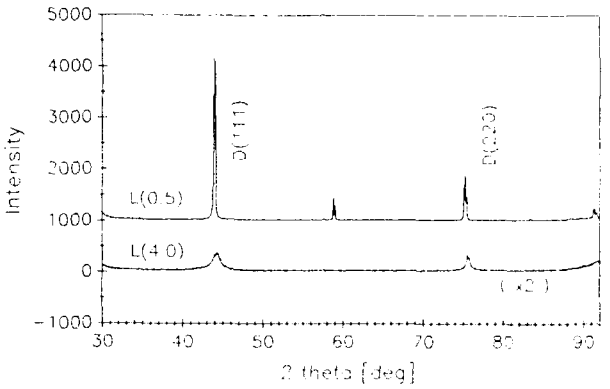


Fig. 3 X-ray diffraction patterns of sample L(0.5) and L(4.0).

Resistivity

Surface contamination can be a serious problem for resistivity measurements [5]. Thus, a low power oxygen plasma was adopted for surface cleaning. The resistances measured before and after cleaning process were the same for all eleven samples. However, on some of our older samples, the plasma cleaning changed the resistance reading by as much as three orders of magnitude.

The room temperature resistivity results in Table II show that a small sp^2 concentration in a diamond film will decrease the resistivity while a large sp^2 concentration will increase it.

Heating can significantly influence electrical properties of the films. Some groups [6,7] reported that the existence of hydrogen in diamond films may lower the resistivity. They found that after annealing at a temperature as low as 400°C, the resistivity increased by a few orders of magnitude. Therefore, we studied the annealing effect. However, after 3 hours annealing at 600°C, our results for all series showed the resistivity only increased by a factor of two to ten. The films with the largest amount of sp^2 component increased the most in resistivity. Thus, in contrast to hydrogenated amorphous carbon, our amorphous carbon dominated film had a higher resistivity after annealing. Fig. 4 shows the resistivity as a function of inverse temperature. The activation energies decreased with increasing boron concentration in agreement with other work [8].

We plan to do further work to understand why the films with the largest sp^2 components have the highest resistivity and largest increase of resistivity upon heating. Perhaps the sp^2 contains very little hydrogen and is therefore very different hydrogenated amorphous carbon. We are planning to work on the distribution and electrical percolation of the sp^2 and sp^3 phases as a function of temperature.

Since there is no natural solid oxide compound for carbon, the composite film with a high resistivity could be used as a passivation layer for the application of diamond electronic devices.

Metal contacts

Fig. 5(a) shows a typical rectifying current-voltage characteristic of a Ti contact on undoped polycrystalline diamond film. For all the boron doped samples, Al, Ti,and W

contacts showed ohmic characteristics and a typical result is shown in Fig 5(b). Besides the effect of doping, small amount of amorphous component on the surface also can enhance the ohmic contact [9,10]. However, our film with the greatest sp^2 content showed a nonlinear I-V characteristic when a large voltage range was used. (see Fig 5(c))

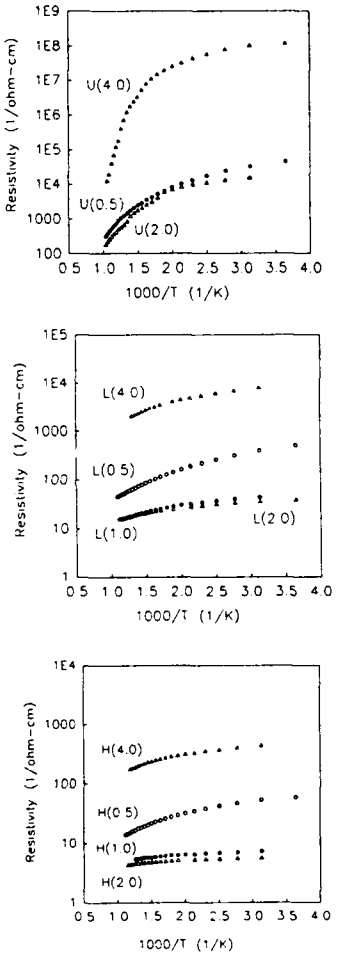


Fig. 4 Resistivity vs. reciprocal temperature.

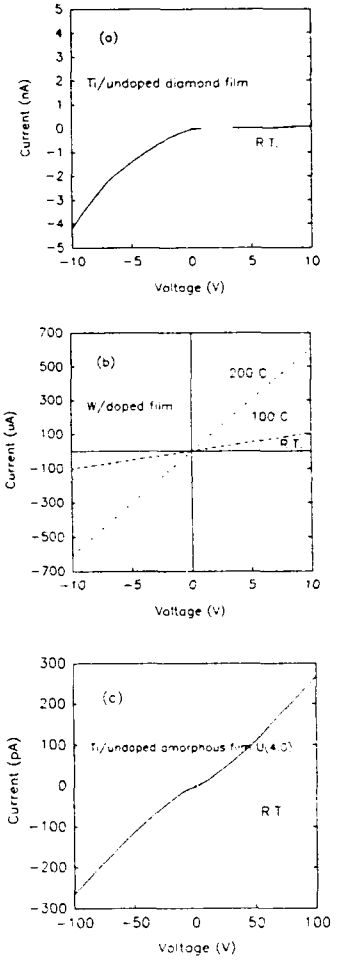


Fig. 5 (a) I-V characteristic of rectifying contact.(Ti on diamond) (b) A typical ohmic I-V characteristic of a doped film. (c) Non-linear I-V characteristic of amorphous carbon film.

SUMMARY

Three series of diamond films with different boron doping level and carbon sp^2/sp^3 ratio have been studied by means of electrical resistivity and metal contacts. It is shown that the electrical resistivity of diamond films can be strongly affected by non-diamond components. In a high purity diamond film, small amount of sp^2 carbon can reduce its resistivity. However, when the amorphous carbon is the dominant component in the film, the resistivity increases drastically, and the increase of resistance caused by annealing is the greatest.

This composite carbon film with a high electrical resistivity can be utilized a passivation layer for diamond thin film devices since there is no natural solid oxide for carbon.

REFERENCES

1 K.V. Ravi and M.I. Landstrass, Proc. First Int. Symp. on Diamond and Diamond-like Films, Vol.89-12, edited by J.P. Dismukes (The Electrochemical Society, Pennington, NJ, 1989), pp 24-37.
2 J. Mort, D. Kuhman, M. Machonkin, M. Morgan, F. Jansen, K. Okumura, Y.M. LeGrice, and R.J. Nemanich, Appl. Phys. Lett. 55(11), 1121 (1989).
3 Th. Frauenheim, U. Stephan, K. Bewilogua, F. Jungnickel, P. Blaudeck, and E. Fromm, Thin Solid Films, 182, 63 (1989), and references therein.
4 D.I. Jones and A.D. Stewart, Phil. Mag., 46(5), 423 (1982).
5 S.A. Grot, G.Sh. Gildenblat, C.W. Hatfield, C.R. Wronski, A.R. Badzian, T. Badzian, R. Messier, IEEEE Electron Dev. Lett. 11, 100 (1990).
6 M.I. Landstrass and K.V. Ravi, Appl. Phys. Lett. 55, 975 (1989).
7 S. Albin and L. Watkins, Appl.Phys. Lett 56, 1454 (1990).
8 T.B.Kustka, R.O. Dillon and T. Furtak, "Boronated Films Deposited by Radio Frequency Plasma", Diamond and Diamond-Like films and Coatings, (Proceedings of the NATO-Advanced Study Institute), edited by R.E. Clausing, L.L. Horton, J.C. Angus and P. Koidl, NATO-ASI Series, B: Physics, Vol. 266, Plenum, New York, in print.
9 J.F.Prins, Appl. Phys. Lett. 41, 950 (1982).
10 M.W. Geis, M.Rothschild, R.R. Kunz, R.L. Aggarwall, K.F. Wall, C.D. Parker, K.A. McIntosh, N.N. Efremow, J.J. Zayhowski, D.J. Ehrlich, and J.E. Butler, Appl. Phys. Lett. 55, 2295 (1989).

OPTICAL EVIDENCE OF REDUCTION OF RADIATIVE DEFECTS IN DIAMOND FILMS GROWN BY ACETYLENE-OXYGEN FLAMES

J.A. Freitas, Jr.*, U. Strom, K. Doverspike, C.M. Marks** and K.A. Snail
Naval Research Laboratory, Washington, DC 20375-5000
*Sachs/Freeman Associates Inc., Landover, MD 20785-5396
**NRC Postdoctoral Fellow

ABSTRACT

Raman scattering and photoluminescence spectroscopies have been used to characterize polycrystalline diamond films deposited on molybdenum substrates by laminar and turbulent premixed oxygen-acetylene flames in air. Samples deposited under laminar flame conditions are characterized by a high degree of incorporation of nitrogen-vacancy complexes. However, samples deposited with a turbulent flame show a significant decrease in the concentration of these defects and a reduction of the amorphous carbon film component.

INTRODUCTION

One of the most challenging problems in diamond film research has been the growth of high quality, monocrystalline films on a heterogeneous substrate. Solution of the problem requires an improved understanding of the nucleation and growth mechanism, which in turn may depend on the details of the deposition technique.

Combustion assisted chemical vapor deposition (CACVD) in open atmosphere has attracted the attention of many research groups because the instrumental simplicity and high growth rate (1,2). One of the basic problems with this technique, other than the polycrystallinity of the films, is the undesirable incorporation of nitrogen impurities during the film deposition (3,4). Recently, Snail et al. (5) have reported the synthetization of polycrystalline films in a turbulent flame with very low levels of incorporation of nitrogen impurities. These results are very important since they allow the possibility of the study of in situ doping.

In this work we report a comparative study of polycrystalline films deposited in molybdenum substrates using laminar and turbulent premixed oxygen-acetylene flames in air. Low and high resolution room temperature Raman scattering (RS) experiments were used to evaluate the film quality. Low temperature photoluminescence (PL) experiments were performed to monitor the incorporation of nitrogen and nitrogen-vacancy complexes.

EXPERIMENTAL TECHNIQUE

We have examined free-standing films deposited on molybdenum substrates by CACVD, in the laminar and turbulent flame regimes. The film deposition was performed in ambient air using a commercial oxygen-acetylene brazing torch with 1.17 mm and 1.85 mm diameter orifice tips for laminar (1) and turbulent (5) flame conditions, respectively. High purity oxygen (99.99%) and acetylene (99.6%) were used as source gases, with the acetylene passing through an activated charcoal trap to remove residual acetone (6). For the samples ex-

amined in this work the ratio (R_f) of the oxygen-acetylene flow varied from 1.017 to 1.080. The substrates were positioned in the feather about 1-2 mm from the primary flame front, and adjusted so as to maintain a surface temperature ~ 900°C. The substrate temperature was adjusted by varying the fraction of the length by which a 3/8" threaded molybdenum rod was inserted into a threaded hole in the water cooled copper substrate mount (2). The substrate temperature, during the growth, was monitored with a two-color infrared pyrometer. The films deposited under laminar flame conditions are nearly transparent in the center, degrading to a gray-brown color at the edges, with crystallite size varying from sub-micron to a few microns. Similar morphology was observed in films deposited with flames in the turbulent regime, except for the absence of the colored rings. An observed decrease of the film growth rate under turbulent conditions by a factor of two or three, may be associated with simultaneous etching (5).

The RS measurements were carried out at room temperature. The 514.5 nm and 488.0 nm argon ion laser lines provided between 10 and 100 mW of laser power with the laser spot size of approximately 150-200 μm. The scattered light was dispersed by a scanning double grating spectrometer with 85 cm focal length and a built in spatial filter to increase the straight light rejection. The analyzed scattered light was detected by a GaAs photomultiplier tube, operated in a photon counting mode.

The PL measurements were performed with the sample at 5-6 K, by means of a liquid and/or continuous gas flow He cryostat. The sample temperature was monitored by a solid state sensor located in the copper sample holder, and its temperature was stabilized by a temperature controller with sensitivity of ±0.1 K. We have used the UV and blue (351.1 nm, 457.9 nm, 476.5 nm and 488.0 nm) argon ion laser lines to excite the defects in our sample, however we will present only results with the 488.0 nm (2.54 eV) laser line. The light emitted by the samples was dispersed and analyzed by the same experimental set-up as was used for the RS experiment.

RESULTS AND DISCUSSION

The low temperature PL spectra of two films deposited in the laminar flame regime are presented in Fig. 1. The spectrum (a) is from a sample grown with R_f = 1.017 and substrate temperature (T_S) varying between 885 and 915°C. The spectrum (b) was obtain from a sample grown with R_f = 1.031 and T_S = 890°C. Both spectra are similar in regard to the overall shape of PL spectrum and the number of observed defect PL bands. Differences in the spectra include the reduction of the zero phonon line (ZPL) linewidth (reduced by 4 to 5 times), in spectrum (b), and the relative intensity between the Raman peaks associated with the diamond and the amorphous carbon (a-C) content. The gradual increase in the spectral intensity observed on the high energy side of both spectra are due to laser Raleigh scattering. The peak "1" at 2.465 eV is the ZPL of the H3 center, which may be associated with a single vacancy (V) complexing with a nitrogen (N) cluster (N-V-N?) (7). The peak "2" at 2.375 eV is the first order TO/LO phonon, and the first broad shoulder on its low energy side is the phonon associated with the a-C film content. Two other features, clearly observed in spectrum (b), are the small peaks at 2.282 eV ("3") and 2.156 eV ("4"). The first feature has not been correlated with any defect previously observed in natural diamond, and the second feature is the 575 nm center which has been tentatively assigned to a nitrogen-vacancy complex (V-N-V?) (7). The most intense peak ("5") in the spectra is the ZPL at 1.946 eV (637 nm center) which has been assigned to a single nitrogen-vacancy pair (N-V) (7,8).

Fig. 2 shows the first order low resolution Raman spectra of the same samples analyzed on Fig. 1. High resolution measurements (bandpass ~ ±0.25 cm^{-1}), carried out on these

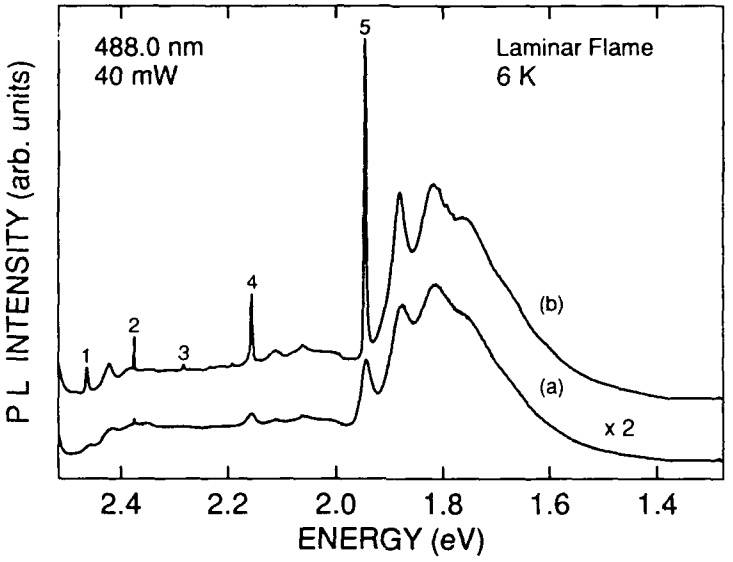


Fig. 1. Photoluminescence spectra obtained at 6K from two CACVD films deposited in the laminar flame regime. The peaks "1,3, and 4" are due to nitrogen-vacancy complexes. The peak "2" is the first order diamond phonon, and the peak "3" is an unidentified center. The spectra (a) and (b) have been offset in the vertical axis.

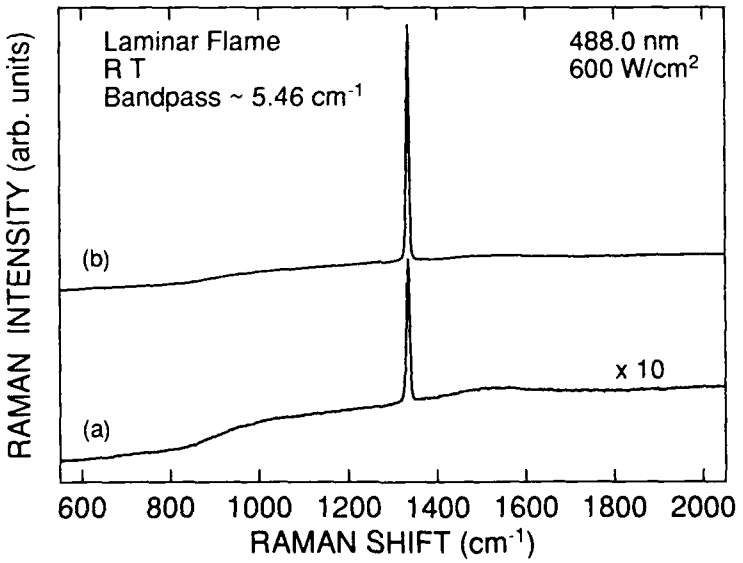


Fig. 2. Low resolution room temperature (RT) Raman spectra of the two films shown in Fig. 1. The phonons are represented as peak "2" in Fig. 1. The spectra (a) and (b) have been offset in the vertical axis.

samples, yield a phonon peak position at 1333.60 cm^{-1} and full width at half maximum (FWHM) of 4.53 cm^{-1} in spectrum (a), and 1333.30 cm^{-1} and FWHM = 2.94 cm^{-1} for the phonon in spectrum (b). In Fig. 2, taking the phonon intensity as reference, we observe a relative reduction of the PL background and the a-C component in this films.

The ~35% reduction of the linewidth of the ZPL and first order phonon lines is correlated with the decrease of the a-C component in the films. This observation is consistent with an increase in the average crystallite size (9) which yields higher quality diamond as well as reduced grain boundary regions, which are the likely location of the a-C deposits(10).

In Fig. 3 is shown the first order low resolution Raman spectrum of a polycrystalline diamond film deposited at T_S = 900°C in a premixed (R_f = 1.08) turbulent oxyacetelene flame. The extremely low PL background and a-C content in this film is noted. High resolution Raman measurements yield a phonon peak position at 1333.30 cm^{-1} and FWHM of 3.00 cm^{-1}. For calibration and comparison, we had performed high resolution RS measurement (bandpass ~ ±0.25 cm^{-1}) in a natural type IIa diamond heat sink. The result is a phonon peak position at 1333.50 cm^{-1} and FWHM of 2.40 cm^{-1}. The agreement (within experimental error) of the phonon peak position for films grown in the laminar and turbulent flame regimes with the type IIa diamond suggests that the films are rather strain free (10). The 25% phonon line broadening observed in the FWHM of our films in comparison with the type IIa diamond seems to be associated with the polycrystalline character of the films, in which grain sizes vary from the submicron level to a few microns. It needs to be emphasized that many crystallites and intergrain regions are probed with the relatively large laser spot size used in the present experiment.

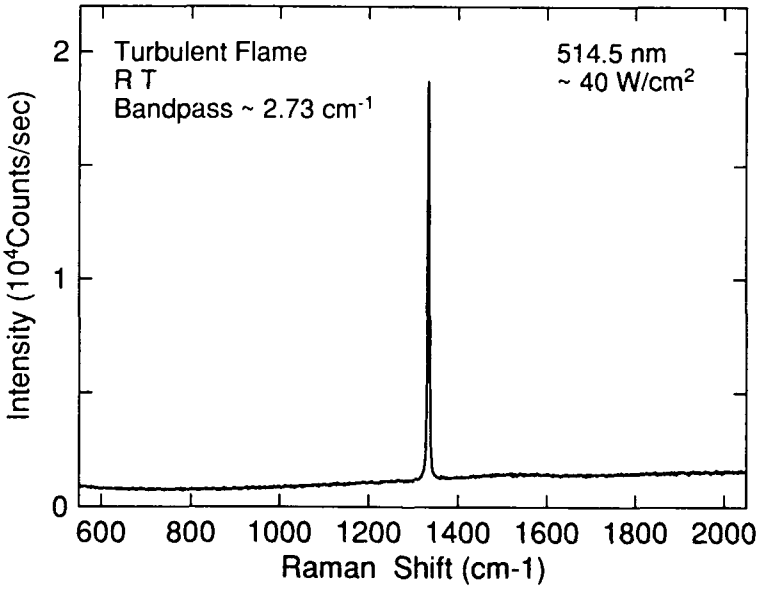


Fig. 3. Low resolution room temperature (RT) Raman spectrum of an CACVD film deposited under turbulent flame condition. The phonon peak position is represented as peak "2" in the PL spectra (Fig. 1. and Fig. 4.)

The low temperature PL spectrum of the film analyzed in Fig. 3 is presented in Fig. 4. This spectrum is quit different from those shown in Fig. 1, since the dominant feature is the

strong first order phonon peak at 2.375 eV. The defect ZPLs and side band phonons are extremely weak, and can be observed only with a high gain scale. The continuous decrease in PL intensity from the begin of the spectrum to 2.48 eV is due to the laser Raleigh scattering. The broad feature between 2.1 and 2.0 eV is probably due to the spectrometer response. The dominant emission of the 637 nm center (N-V) as observed in Fig. 1, has been reduced to a weak band from 1.95 to 1.70 eV, in Fig 4. The regularly spaced small peaks from 1.75 to 1.4 eV are due to interference effects in the film. It is emphasized that the strong PL background dominated by intense side band phonons generally observed in laminar flame deposited samples, has been replaced by a weaker, almost featureless background in the sample deposited under turbulent flame conditions. The weakness of the a-C component observed in the low energy side of the phonon in Fig. 4 is also noted.

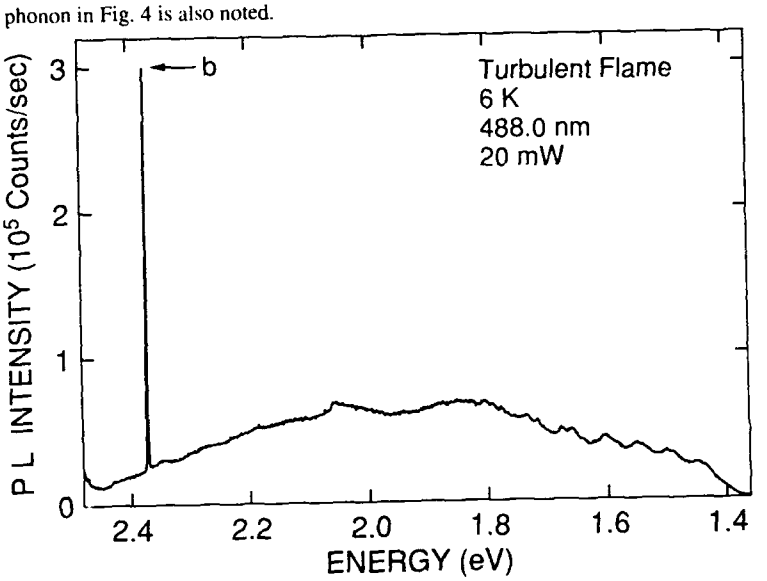


Fig. 4. Low temperature (6 K) photoluminescence spectrum of the CACVD film analyzed in Fig. 3. The peak "2", the first order diamond phonon, is the singly dominant feature observed.

CONCLUDING REMARKS

Low and high resolution RS experiments were successfully carried out on polycrystalline films deposited on molybdenum substrates by CACVD to evaluate the material quality. Although good quality films can be deposited with laminar flames, films deposited in the turbulent flame regime show very low amorphous carbon content and very small PL background. Low temperature PL measurements of films deposited under laminar flame conditions exhibit the presence of strong luminescence bands associated with nitrogen-vacancy complexes probably incorporated during the film deposition (3). PL experiments performed in samples deposited under turbulent flame conditions reveal an extremely low level of nitrogen-vacancy complexes. This result is extremely important because low level of intrinsic impurities and defects are basic requirements to achieve controlled doping.

ACKNOWLEDGMENTS

This work was supported in part by the Office of Naval Research.

REFERENCES

1. L.M. Hanssen, W.A. Carrington, J.E. Butler, and K.A. Snail, Mat. Lett., **7**, 289 (1988).
2. L.M. Hanssen, K.A. Snail, W.A. Carrington, J.E. Buttler, S. Kellog, and D.B. Oakes, Thin Solid Films, **196**, 271 (1991).
3. J.A. Freitas, Jr., J.E. Butler and U. Strom, J. Mater. Res., **5**, 2502 (1990).
4. J.A. Freitas, Jr., U. Strom, J.E. Butler, and K.A. Snail Proc. of The 2nd Intl. Conf. on New Diamond Science and Technology (MRS, Washington, DC September 1990), p. 723.
5. K.A. Snail, C.J. Craigie, R.G. Vardinam, C.M. Marks, and J.A. Freitas, Jr., Proc. of The 2nd Intl. Symp. on Diamond Materials (ECS - 2), Washinton, DC May 1991, vol. 91-8, p. 91.
6. D.C. Manning, Atomic Absorption Newsletter, **7**, 44 (1968)).
7. J. Walker, Rep. Prog. Phys. **42**, 1605 (1979).
8. G. Davies, Rep. Prog. Phys., **44**, 787 (1981).
9. A.T. Collins and S.H. Robertson, J. Mat. Sci. Lett. **4**, 2223 (1971).
10. Y. Sato, C. Hata, T. Ando and M. Kamo, Proc. of The 2nd Intl. Conf. on New Diamond Science and Technology (MRS, Washington, DC September 1990), p. 537.

ELECTRONIC DEVICE FABRICATION USING ELECTRON CYCLOTRON RESONANCE ETCHING OF BORON DOPED HOMOEPITAXIAL DIAMOND FILMS

S.A. GROT[1,2], R.A. DITIZIO[1,3], G.SH. GILDENBLAT[1,2], A.R. BADZIAN[4], AND S.J. FONASH[1,3]
[1]Center for Electronic Materials and Processing
[2]Department of Electrical and Computer Engineering
[3]Department of Engineering Science and Mechanics
[4]Materials Research Laboratory
The Penn State University, University Park, PA 16802

ABSTRACT

We describe the applicability of oxygen based Electron Cyclotron Resonance (ECR) etching of diamond for the purpose of fabricating electronic test structures and recessed gate field effect transistors. Boron doped homoepitaxial diamond films grown in a microwave assisted CVD reactor were used for this study. Etch rates from 8 nm/min up to 0.5 μm/min. were achieved depending on etch parameters.

INTRODUCTION

Diamond, when considered as a semiconductor material has properties that make it attractive for high temperature, high power electronics[1]. To date, processing techniques are limiting the advancement of diamond film electronic devices. Controlled etching is an important processing step for microelectronic device fabrication. However, the chemical inertness and hardness of diamond make it difficult to remove surface layers in a smooth damage-free manner. Several techniques have been investigated for the purpose of etching diamond. For example, ion beam etching[2], reactive ion etching[3], and electron cyclotron resonance (ECR) etching with -500 Volt external bias[4] have all produced uniformly etched structures in diamond. These techniques involve ion energies in excess of those where ion bombardment can result in damage of diamond, which according to Ref. [5] can be as low as 150 eV. Chemical methods of etching diamond such as oxidation of CVD diamond films in oxygen containing ambients[6] resulted in pitting of the diamond surface. In this work we report on the ECR etching of boron doped homoepitaxial diamond film, with ion energies below 50 eV[7,8], for the purpose of electronic applications. This method of etching was used to fabricate test structures, and recessed gate diamond thin-film field effect transistors[9].

EXPERIMENTAL

Boron doped homoepitaxial diamond films were grown on natural type Ia insulating diamond crystals which were cut and polished along the (001) plane. The film was deposited using a microwave plasma assisted CVD apparatus described elsewhere[1]. The growth parameters were as follows : 2.45 GHz, 1.2 kW microwave source; substrate temperature 910°C (as measured by optical pyrometer), and 100 sccm gas flow of 1% CH_4 in H_2 at 80 Torr pressure. Boron doping was achieved by introducing diborane, B_2H_6, into the feed gas. The boron to carbon ratio in the plasma was 0.8 - 7.5 x 10^{-3}. The surface of the diamond film was chemically cleaned in a saturated solution of $(NH_4)_2S_2O_8$ in H_2SO_4 at 200°C and subsequently rinsed using a 1:1 solution of H_2O_2 and NH_4OH at 70°C[10]. This cleaning

procedure was found to be effective in removing the conductive layer which is present on the surface of homoepitaxial diamond film without leaving as much particle contamination as the chromic acid-based clean procedure described in Ref. [11].

Sputter deposited SiO_2 served as the masking material for the etching experiments. The oxide was sputtered in 3 millitorr Ar for 8 minutes, with 150 Watts forward power and no substrate heating. This resulted in an oxide thickness of 100 nm. The SiO_2 was patterned with photolithography to produce a matrix of resistivity measurement bridges.

The ECR plasma system used in these experiments is shown in Fig. 1. The 2.45 GHz ASTEX microwave source was coupled through a tunable waveguide to the reactor chamber. The sample was mounted on an electrically isolated stainless steel stage and inserted into the chamber with the sample surface perpendicular to the gas flow. The reactor chamber was evacuated to $< 10^{-5}$ Torr with a 514 liter/s turbomolecular pump. The reactant gases (O_2 with possible Ar dilution) were then bled into the chamber through separate needle valves. The pressure of the reactant gas(es) was measured with a baratron type pressure gauge. In all the experiments the microwave power was 1000 Watts and typical run times were 10 to 20 minutes. After etching the SiO_2 was stripped in hydrofluoric acid, and etch depth was determined with a profilometer.

RESULTS AND DISCUSSION

In the first etching experiment the sample was inserted in the center of the ECR plasma region, 16.5 cm from the microwave window (see Fig. 1) and the stage was biased at -500 V with respect to the chamber walls. The plasma was struck in 0.4 millitorr of oxygen. In less than 5 mins., the sample and stage were glowing red hot and the diamond was etched at a rate of approximately 0.5 μm/min. These etch conditions were not uniform over the sample area and the etch was excessively high for our applications. Subsequent experiments were all carried out 53 cm downstream from the microwave window. (See Fig. 1) When the sample was positioned in this area, no dependence of the etch rate on substrate bias was observed. (See Fig. 2) When no bias was applied, negative 6.4 V was measured on the substrate during etching. As shown in Fig. 2, the etch rate was widely scattered under

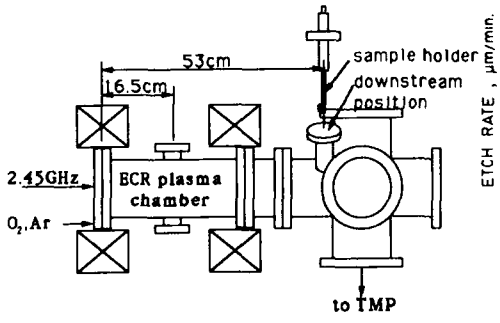


Fig. 1 Schematic drawing of the ECR diamond etching system

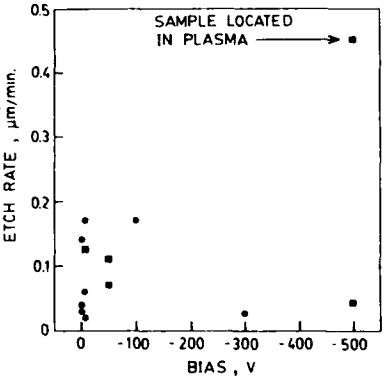


Fig. 2 Etch rate vs. substrate bias with respect to the chamber. • - etch rates for one particular sample.

identical experimental conditions. In order to eliminate the possibility of sample variations being responsible for the observed scatter, identical etching conditions were repeated many times for one particular sample (solid circles, Fig. 2). No explanation can be given at this time for the irreproducible etch rates with pure oxygen plasmas. However if the oxygen is diluted with 2.7 mTorr of argon, then the etch rate drops drastically and becomes more repeatable, see Fig. 3. As a control experiment etching of a diamond film was attempted with argon at 2.7 millitorr as the only reactant gas; no etching was observed.

Typical etched structures are shown in Figs. 4,5. Profilometry measurements of the etched areas indicated a surface roughness of less than 10 nm which is comparable to that of the substrate.

ECR etching is useful in fabricating FETs with boron doped CVD diamond films[1]. It may have an advantage over the selective growth[12] procedure for FET fabrication in that contamination of the growing diamond film from the SiO_2 growth mask is avoided. In order to demonstrate the applicability of ECR plasma etching to diamond film electronics, we have used it to perform spreading resistance measurements. A four-terminal bridge structure, shown in the insert of Fig. 6, was fabricated on the diamond film using ECR

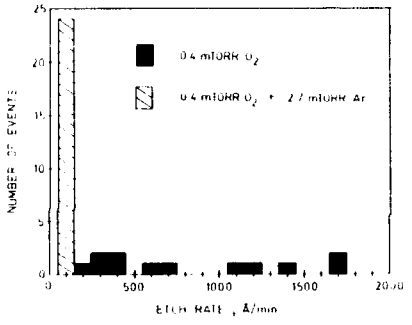


Fig. 3 Histogram showing increased etch rate reproducibility when Ar dilution is used.

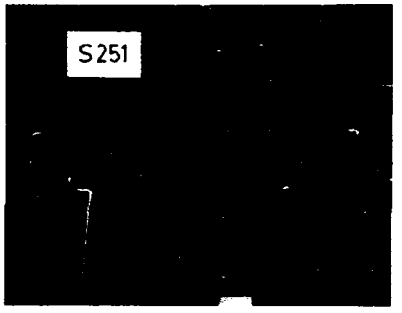


Fig. 4 SEM photograph of cross-hair etched in diamond film.

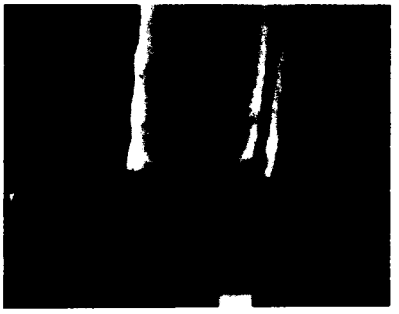


Fig. 5 High magnification (14.3 kX) end-on view of the cross-hair. The diamond substrate surrounding the cross-hair has been exposed using ECR etching.

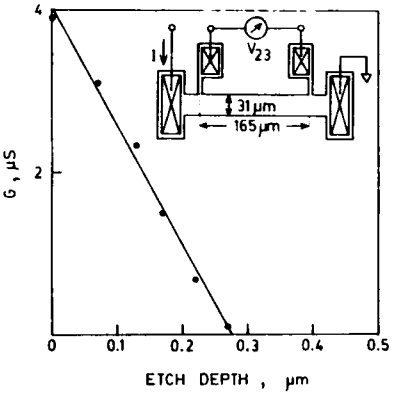


Fig. 6 Conductance of boron doped diamond film as a function of etch depth.

plasma etching so that accurate conductivity measurements could be made. The SiO_2 etch mask was stripped and the contact pads were metallized with a gold / titanium bilayer and annealed to form ohmic contacts as described in Refs. [13,14]. The conductance, $G = I/V_{23}$, (see Fig. 6) measured as a function of etch depth, is shown in Fig. 6. After each 10 min. ECR plasma exposure, the etch depth was measured, and was typically about 80 nm. While etching the first 0.3 μm of the film, the conductance was linearly dependent on the etch depth, indicating that the resistivity of the top 0.3 μm of the diamond film was uniform in resistivity. The average resistivity in this region was determined to be 1.28 Ω•cm from a least squares fit to the first six data points, shown in the insert to Fig. 6. Further etching did not change the conductance indicating that a highly resistive layer, sitting on a more conductive layer, had been reached. However, at a depth of 0.43 μm the conductance decreased further as more diamond was removed, and was essentially zero at a depth of 0.57 μm. The resistivity of the diamond film between a depth of 0.43 μm and 0.57 μm was 364 Ω•cm.

Hall effect measurement bridge test structures were also formed during device isolation etching so that the mobility and carrier concentration of the film could be measured. Figs. 7-9 show the dependence of resistivity, activation energy, carrier concentration, and mobility on the boron to carbon ratio in the feed gas.

The recessed-gate fabrication sequence is shown in Fig. 10. After device isolation etching, an Au (1.25 micron)/Ti (50 nm) bilayer metallization was deposited on the sample. The source/drain regions were protected with photoresist, and the remaining metallization was etched with aqua regia followed by a titanium etch (1:1:50 , $HF:HNO_3:H_2O$). The sample was annealed in N_2 for 15 min. at 480°C in order to form ohmic contacts. The source/drain metallization was used to self align the gate recess etch. The area between the source and drain metal was exposed to the ECR etching conditions described above so that the channel area was etched 170 nm in thickness. The gate insulator was deposited by

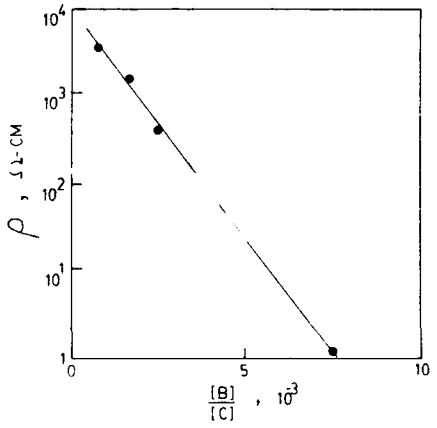


Fig. 7 Diamond film resistivity vs. boron to carbon ratio in the feed gas

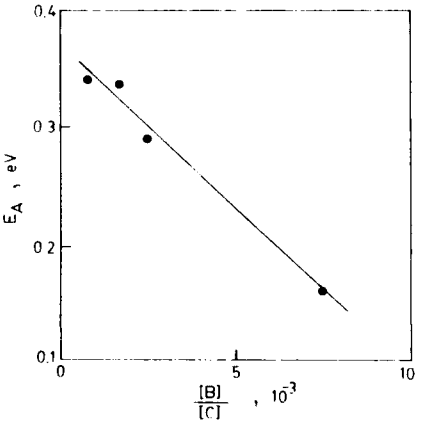


Fig. 8 Thermal activation energy of the diamond film's resistivity vs boron to carbon ratio in the feed gas

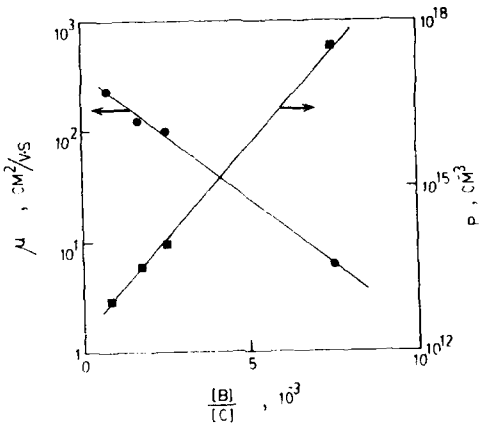


Fig. 9 Hole concentration and mobility vs. boron to carbon ratio.

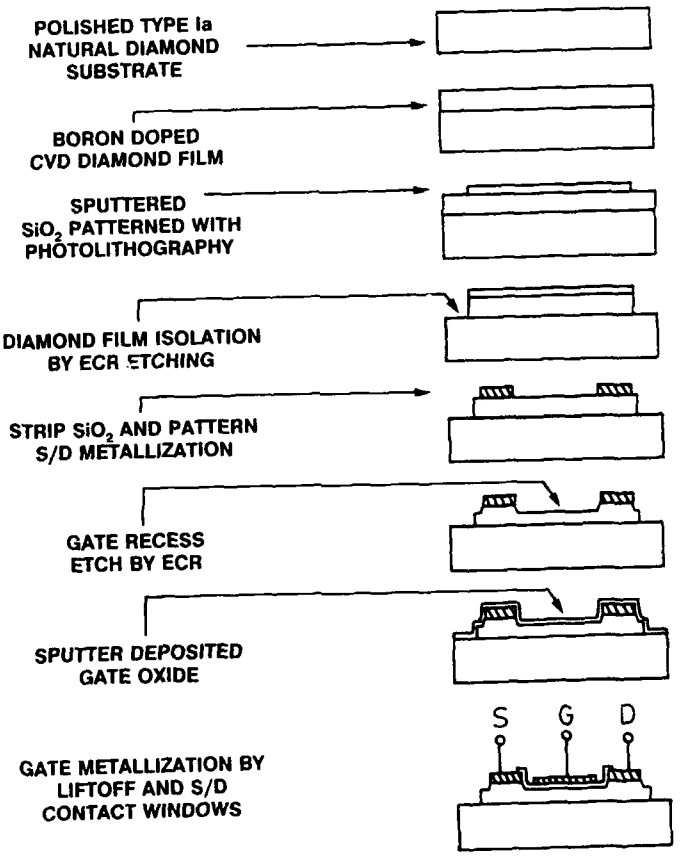


Fig. 10 Fabrication sequence for isolated recessed gate MOSFET's.

sputtering 100 nm of SiO_2 with an Ar (50%) - O_2 (50%) plasma at 350°C at 3.3 mTorr for 70 minutes[15]. Finally the 40 nm gold gate contact was defined by a lift-off method. The channel width and length of the device are 30 and 46 micron, respectively. Further details about the performance of this device are described elsewhere[9].

CONCLUSIONS

Downstream oxygen ECR plasma etching of boron doped homoepitaxial diamond films has been demonstrated. Etch rates from 8 nm/min. to 0.5 μm/min. were achieved. Etch rate dependence on bias was not observed, however, argon dilution resulted in much more reproducible etch rates. This etch technique has been applied to the processing of thin-film diamond electronic devices[9].

ACKNOWLEDGEMENTS

This work was supported in part by the Diamond and Related Materials Consortium and the SDIO/IST through the Office of Naval Research under contract N00014-86-K-0443. The Kurt J. Lesker Company is acknowledged for their support of the SiO_2 sputtering system used in this work.

REFERENCES

1. G.Sh. Gildenblat, S.A. Grot, and A.R. Badzian, Proc. of the IEEE, **79**, 647 (1991).
2. N.N. Efremow, M.W. Geis, D.C. Flanders, G.A. Lincoln, and N.P. Economou, J. Vac. Sci. Technol. B **3**, 416 (1985).
3. G.S. Sandhu and W.K. Chu, Appl. Phys. Lett., **55** 437 (1989).
4. C.P. Beetz, Jr., B.A. Lincoln, B.Y. Lin, and S.H. Tan, in Proc. 2nd, International Conference on New Diamond Science and Technology, Washington DC, Sept. 23-27, 1990, 833 (1991).
5. J.B. Marsh and H.E. Farnsworth, Surface Sci., **1**, 3 (1964).
6. W. Zhu, X.H. Wang, A.R. Badzian, and R. Messier, in Proc. 2nd International Conference on New Diamond Science and Technology, Washington DC, Sept. 23-27, 1990, 821 (1991).
7. M. Matsuoka, and K. Ono, J. Vac. Sci. Technol. A, **6**, 25 (1988).
8. W.M. Holber, and J. Forster, J. Vac. Sci. Technol. A, **8**, 3720 (1990).
9. G.Sh. Gildenblat, S.A. Grot, and A.R. Badzian, presented at The 1991 International Semiconductor Device Research Symposium, Charlottesville, VA, Dec. 4-6, 1991.
10. M.W. Geis, Private communication.
11. S.A. Grot, G.Sh. Gildenblat, C.W. Hatfield, C.R. Wronski, A.R. Badzian, T. Badzian, and R. Messier, IEEE Electron Device Lett., **11**, 100 (1990)
12. S.A. Grot, C.W. Hatfield, G.Sh. Gildenblat, A.R. Badzian, and T. Badzian, Appl. Phys. Lett., **58**, 1542 (1991).
13. G.Sh. Gildenblat, S.A. Grot, C.W. Hatfield, A.R. Badzian, and T. Badzian, IEEE Electron Device Lett., **11**, 371 (1990).
14. K.L. Moazed, R. Nguyen, and J.R. Zeidler, IEEE Electron Device Lett., **9**, 350 (1988).
15. G. Liu, S.J. Fonash, Jap. Appl. Phys., **30**, L269, 1991.

TANTALUM AND TANTALUM SILICIDE HIGH TEMPERATURE RECTIFYING CONTACTS ON TYPE IIB NATURAL DIAMOND

SCOTT R. SAHAIDA AND DALE G. THOMPSON
Kobe Steel USA Inc., Electronic Materials Center, 79 T.W. Alexander Dr., P.O. Box 13608, Research Triangle Park, NC 27709

ABSTRACT

Tantalum and tantalum silicide contacts were investigated as high temperature rectifying contacts on type IIB natural diamond. Tantalum and silicon were co-sputtered using DC and RF planar magnetrons, respectively. Current-voltage measurements of tantalum silicide subjected to various anneals and of pure tantalum contacts were recorded at 50°C intervals up to 400°C which was the desired operating temperature of the rectifying contact. Tantalum contacts to diamond maintained good rectification up to 300°C whereas amorphous tantalum silicide operated well up to 400°C.

INTRODUCTION

Diamond has a very high breakdown voltage, thermal conductivity, and electron saturation velocity, which will make it very useful as the active semiconducting medium for electronic devices operating in severe environments (i.e., high temperature, radiation, corrosive, etc.). In these hostile environments, particularly at high temperatures, the contact metal will limit the usability of the device. The objective of this research is to obtain a stable, high temperature rectifying contact that will adhere to a highly polished diamond surface. Silicides may prove useful as contacts on diamond since they are stable at high temperatures while maintaining the desirable electrical properties of metals. In particular, tantalum silicide was chosen because it has proved useful as a high temperature Schottky contact to GaAs [7,8] but has not yet been investigated as a contact to diamond. Tantalum silicide has also been studied on single crystal, polycrystal, and amorphous silicon [1,3-6]. Two different stoichiometries of tantalum silicide (Ta_5Si_3, and $TaSi_2$) were investigated.

Mat. Res. Soc. Symp. Proc. Vol. 242. © 1992 Materials Research Society

EXPERIMENTAL

To optimize deposition conditions, tantalum and silicon were co-sputtered on 1 cm square polished alumina using DC and RF magnetrons, respectively. Substrates were rotated during deposition to ensure thorough mixing of the components and uniform coverage on the substrates. Sputtering was chosen due to the ease of contact fabrication and high degree of control of alloy composition. Also, contact adhesion was improved (compared to evaporation deposition) due to the momentum of the tantalum and silicon atoms as they deposited upon the diamond surface. Alumina was chosen initally as the substrate for the materials characterizations due to its high temperature stability, lack of silicon, and availability. The atomic ratios of these alloys must be exact since the substrate does not contribute silicon to make up for any deficiencies in stoichiometry as in the case of deposition on silicon. Quantitative energy dispersive spectroscopy (EDS) using a proza correction was used to determine the atomic ratio of silicon to tantalum. Various samples were then annealed in an argon ambient at temperatures ranging from 450°C to 1100°C. X-ray diffraction showed that Ta_5Si_3 was completely formed at 900°C. Since $TaSi_2$ is a higher temperature phase, it was not completely formed at the annealing conditions attempted. X-ray diffraction (XRD) data for other annealing conditions was not conclusive possibly due to the formation of two or more different phases.

Once the proper sputtering parameters were determined, the Ta/Si mixtures were deposited on type IIB natural semiconducting diamond for electrical characterization. A 4mmx4mmx0.25mm sample of (100) diamond (Drukker International) was patterned with 100μm diode dots using a standard photolithography process. Tantalum and silicon were then co-sputtered in the desired atomic ratio to an approximate thickness of 2000Å. The final contact pattern was obtained by lifting off the excess material. In addition, 100μm tantalum contacts were DC magnetron sputtered onto type IIB semiconducting natural diamond for comparison to the silicide samples.

Current-voltage measurements were made before and after annealing using a high temperature probe station with a Hewlett-Packard semiconductor parameter analyzer. I-V measurements were made on each composition after annealing at 500°C and later at 900°C in 200mTorr of argon for one hour. It was desirable that tantalum/silicon remain rectifying at 400°C, thus a 500°C anneal proved sufficient for stabilization of the contact. The higher temperature anneal, 900°C, was the

temperature needed to completely transform the mixture into a silicide as determined by initial annealing experiments of tantalum/silicon mixtures on alumina. Current-voltage measurements were made from room temperature to 400°C at 50°C intervals and then remeasured at room temperature to confirm contact stability.

RESULTS/DISCUSSION

$TaSi_2$ Contacts

Figure 1a is a plot of the room temperature I-V characteristics of the as-deposited amorphous $TaSi_2$ contacts on type IIB natural diamond. As is evident from this graph, at room temperature $TaSi_2$ is a very good rectifying contact with less than 10pA reverse leakage current and no breakdown up to 100V which is the highest voltage that the probes could deliver. Current-voltage measurements were then made at 50°C intervals up to 400°C. The contact remained rectifying at all temperatures, but the leakage current increased and the breakdown voltage decreased with increasing temperature. Figure 1b is a plot of the I-V characteristics for a 100μm amorphous $TaSi_2$ contact measured at 400°C. After cooling the contact to room temperature the I-V characteristics were remeasured and the rectifying characteristics had noticeably degraded. Leakage current at 100V increased from a few picoamps to 600nA. A summary of the temperature dependence of reverse leakage current versus temperature is shown in Figure 2.

After measuring the I-V data for the as-deposited $TaSi_2$, the sample was annealed at 500°C in an Ar ambient for one hour. Annealing had a detrimental effect on the rectifying characteristics of the contact. Leakage current at all temperatures was higher than for the as-deposited contact. The I-V characteristics of the tantalum disilicide at 400°C, interestingly, are nearly identical to those of titanium disilicide at the same temperature [5]. The increase in reverse leakage current from annealing is most likely due to the nature of the silicide/diamond interface. For the as-deposited material there is an abrupt interface with little or no intermixing of the tantalum and silicon atoms with the diamond substrate. As the

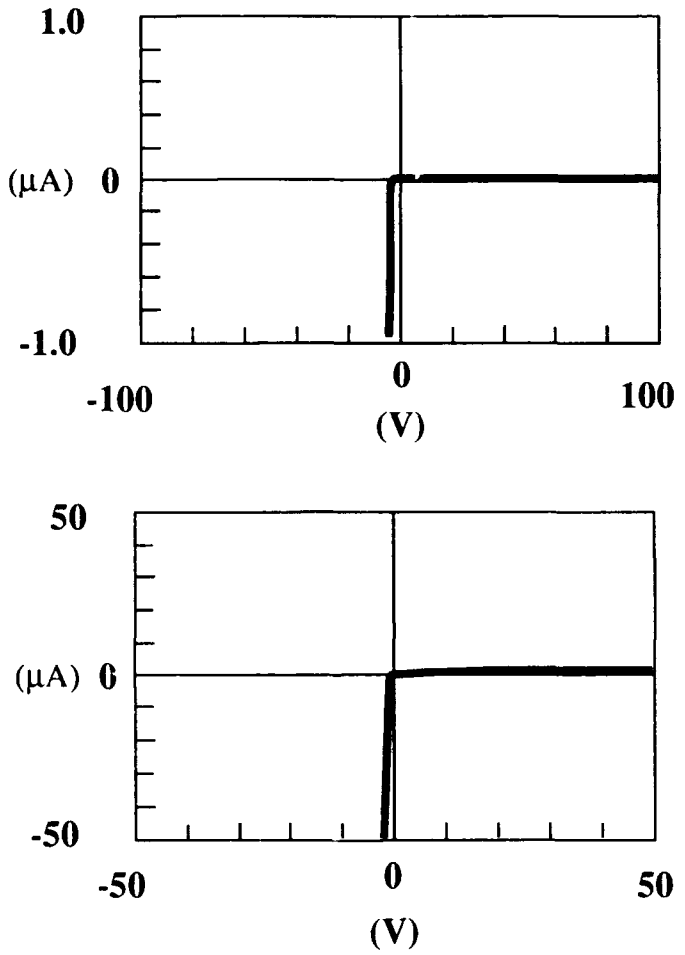


Figure 1. (a) Room temperature current -voltage data for $TaSi_2$, and (b) current-voltage characteristics for $TaSi_2$ at 400°C.

sample is annealed the interface becomes less well-defined which may degrade the rectifying characteristics of the contact. The interface reaction is very complicated since tantalum can form a carbide as well as a silicide. No interface

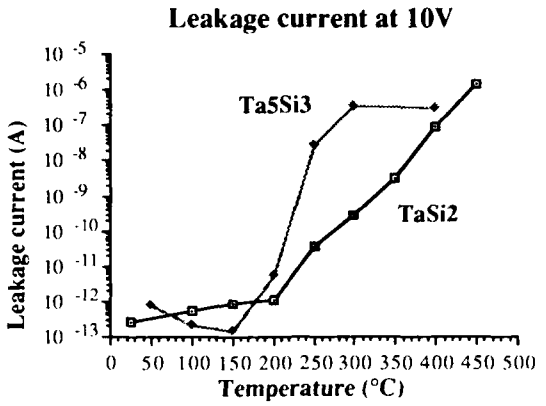


Figure 2. Leakage current versus temperature at 10 volts for $TaSi_2$ and Ta_5Si_3.

studies were carried out due to the minimal availability of suitable substrates and the difficulty in preparing cross-sectional specimens.

Finally, the contact was annealed at 900°C in an Ar ambient for one hour, slowly cooled to 450°C and then removed from the furnace. Before measuring I-V characteristics the surface graphite was removed from the sample since graphite forms when diamond is heated above 800°C. A boiling, saturated solution of CrO_3 in H_2SO_4 was used to remove any surface graphite that could contribute to leakage current. There was a slight improvement of the rectifying characteristics of the contact after the etch. The contact remained rectifying after this anneal and etching treatment although the leakage current at 10V was considerable up to 400°C, measuring 69μA.

After completing the high temperature anneal, it was very difficult to remove the contact metallization from the diamond. A solution of HF, HNO_3, and HCl in a 1:1:2 ratio was used to etch the silicide. However, even after this etch a translucent layer remained. This layer is believed to be silicon carbide, but no analysis was performed. If SiC is formed as the annealing temperature is increased, then the diamond/silicide interface becomes diffuse as silicon and carbon atoms mix. This could explain why rectification degrades with higher annealing temperatures.

Ta_5Si_3 Contacts

Ta_5Si_3 was deposited on type IIB semiconducting natural diamond in the same manner as tantalum disilicide. As-deposited amorphous Ta_5Si_3 exhibited rectifying characteristics up to 400°C as shown in Figure 3a and b . Leakage

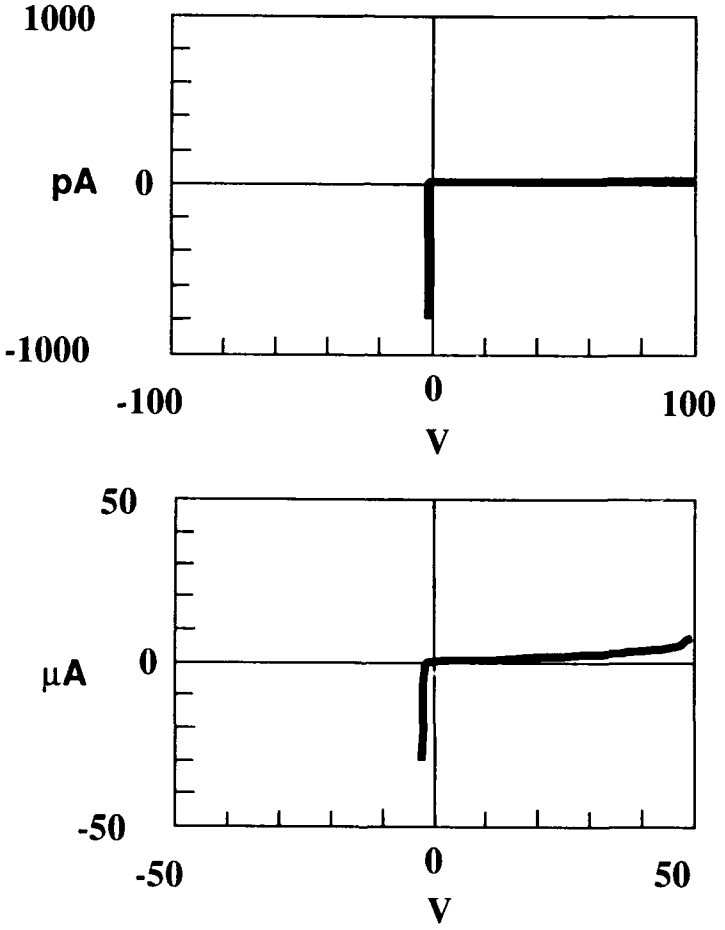


Figure 3. (a) Room temperature current-voltage data for Ta5Si3, and (b) curent-voltage characteristics for Ta5Si3 at 400°C.

current at 10V versus operating temperature is plotted in Figure 2 and shows that Ta_5Si_3 is slightly inferior to $TaSi_2$ in the higher temperature regime. Although Ta_5Si_3 had a higher leakage current than $TaSi_2$ at 400°C, it was more stable because I-V characteristics were unchanged upon cooling to room temperature. Also, leakage current for Ta_5Si_3 levels out from 300°C to 400°C while for $TaSi_2$ it is steadily increasing. As in the case of $TaSi_2$ contacts, annealing degraded the rectifying characteristics of the Ta_5Si_3 contacts. Annealing at 900°C in Ar ambient for one hour degraded the rectifying characteristics.

Tantalum Contacts

Pure tantalum contacts were sputtered onto the type IIB diamond as described earlier. Tantalum was an excellent rectifying contact to diamond up to 300°C as depicted in Figure 4. However, upon heating the diamond to 400°C the tantalum contacts buckled as shown in Figure 5 and rectification was severely degraded, Figure 6. The reverse leakage current at 50V increased from 182nA at 300°C to

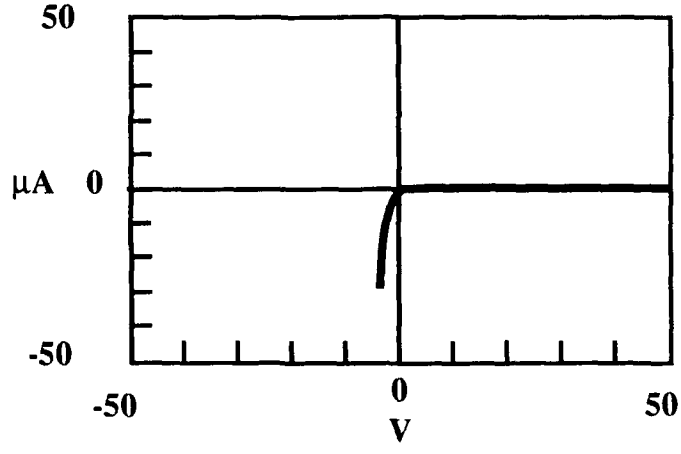


Figure 4. 300°C current-voltage characteristics of 100μm tantalum contact.

3.56mA at 400°C. This is most probably due to the large thermal expansion difference between diamond and tantalum. Diamond is 1.18×10^{-6} $(C°)^{-1}$ and

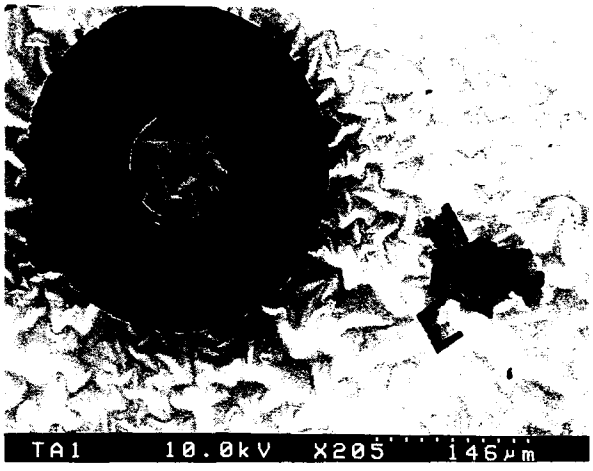


Figure 5. Scanning Electron Micrograph of pure tantalum after annealing at 400°C. The tantalum has buckled due, probably, to differences in thermal expansion coefficients between Ta and diamond.

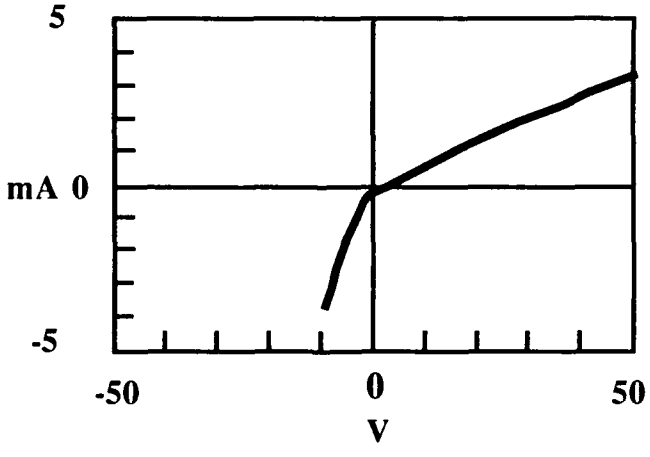


Figure 6. I-V data for Ta contact taken at 400°C

tantalum is 6.5×10^{-6} $(C°)^{-1}$. When silicon is added to tantalum the contact is much more stable at higher temperatures and buckling of the film is not observed up to 400°C; hence, the amorphous silicide contact remains rectifying at higher temperatures. Since the coefficient of thermal expansion for silicon is closer to diamond, $3.0 \times 10^{-6} (C°)^{-1}$, it is likely that the silicon dispersed throughout the tantalum prevents sufficient stress from building at the diamond/contact interface for separation to occur.

CONCLUSIONS

Tantalum and tantalum silicide contacts have been deposited on type IIB natural semiconducting diamond. Amorphous $TaSi_2$ and Ta_5Si_3 remain rectifying up to 400°C. However, Ta_5Si_3 is more stable than $TaSi_2$ after cycling through a high temperature measurement. Annealing of the silicide contacts increases the reverse leakage current due to the tantalum, silicon, carbon interdiffusion and interface reactions. Tantalum retains excellent rectifying characteristics up to 300°C, but functions poorly at higher temperatures due to adhesion problems.

ACKNOWLEDGEMENTS

The authors would like to thank K. Das, J. Tassitino, and A. Tessmer for their assistance with processing the contacts and the rest of the Kobe Steel USA Inc., Electronic Materials Center whose support is greatly appreciated.

REFERENCES

1. D.B. Fraser, S. Murarka, A. Tretola, A. Sinha, J. Vac. Sci. Technol., 18 (2), 345-348 (1981).

2. T.P Humphreys, J. LaBrasca, R. Nemanich, Electronics Letters, 27 (17), 1515-1516 (1991).

3. C.P. Lee, T. Liu, T.Lei, S. Wu, J. Appl. Phys., 65 (2), 642-645 (1989).

4. S.P. Murarka, Silicides for VLSI Applications, (Academic Press, Inc., Orlando, Florida, 1983).

5. S.P. Murarka, D. Fraser, J. Appl. Phys. 51 (3), 1593-1598 (1979).

6. V.L. Teal, S. Murarka, J. Appl. Phys., 61 (11), 5038-5046 (1987).

7. W.F Tseng, B. Zhang, D. Scott, S. Lau, A. Christou, B. Wilkins, IEEE Electron Device Letters EDL-4 (7), 207-209 (1983).

8. G.H. Whipple, M. Thompson, A. Kulkarni, J. Appl. Phys., 64 (5), 2519-2522 (1988).

Electrical properties of Schottky junctions on homoepitaxial flame grown diamond.

J.W. Glesener, A.A. Morrish, and K.A. Snail
Optical Sciences Division, Naval Research Laboratory, Code 6522, Washington, DC 20375-5000

Abstract:

Schottky diodes were fabricated from boron doped diamond grown in a turbulent flame. The substrates used were type IIa diamond (100) crystals 1.5 mm in diameter and .25 mm thick. A p/p+ structure was deposited using the p+ layer as an ohmic contact. Current-voltage (I-V) and capacitance-voltage (C-V) measurements were made on the finished devices. An ideality factor of 1.8 was obtained from the I-V characteristics. Doping levels from C-V measurements indicate an acceptor concentration on the order of $5 \times 10^{17}/cm^3$.

Diamond has several properties that make it a unique semiconductor. These include a wide band gap, high carrier mobility, hardness, a large thermal conductivity and chemical inertness.

Many groups have reported results of Schottky junctions fabricated on CVD diamond.[1,2,3,4,5] This report will present results of the electrical characterization of homoepitaxial diamond synthesized in a turbulent flame.

The growth setup consisted of an oxygen-acetylene torch, flow controllers, and water cooled substrate holder. Two bubblers containing a methanol/boric acid mixture were used. A small fraction of the total acetylene flow was diverted through the bubblers using mass flow controllers. One bubbler contained a solution of boric acid for deposition of the p^+ layer and the solution in the second bubbler was diluted by a factor of 500 for growing a p layer. The gas flow ratio was 8.48/8.00/0.050 lpm for O_2/C_2H_2/bubbler respectively. These flow rates were selected in order to operate the oxygen-acetylene flame in the turbulent regime, since recent results have shown that high quality diamond is grown, if the flame is turbulent[6]. Details of the growth setup

Mat. Res. Soc. Symp. Proc. Vol. 242. 1992 Materials Research Society

have been presented elsewhere[7]. The growth process used a clean diamond substrate brazed to a Mo screw. The p^+ layer was grown first followed by the lighter doped layer referred to as p. Switching from the p^+ bubbler to the p bubbler during growth was accomplished without affecting the O_2/C_2H_2 ratio. The substrate temperature was maintained at 1220 C +/- 20 C. After completion of the growth the resultant crystal was separated from the Mo screw and cleaned in aqua regia for 10 minutes, immersed into a chromic acid/sulfuric acid mixture at 150 C and finally placed in a H_2O_2/NH_3OH solution. The substrate was rinsed in water after each chemical bath. After cleaning, aluminum Schottky contacts were evaporated onto the samples. An evaporation mask was used and the contact area was 1.0×10^{-3} cm^2. Upon completion of the evaporation, the samples were characterized using I-V and C-V measurements. Contact to a sample was made with a prober for the Al dot and using the p^+ layer as an ohmic contact. The p/p^+ structure had a total thickness of 22 microns of which 1 micron was attributed to the p layer. This was ascertained from the relative growth times of each layer. Current device yields are low and are subject to continuing improvement.

The I-V measurements are shown in Fig. 1.

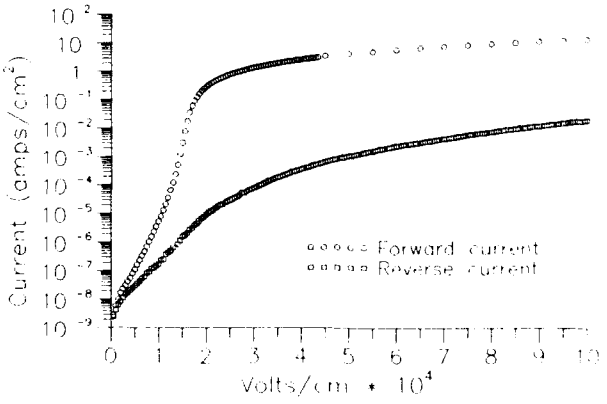


Fig. 1 I-V curve of S/N 112-4 at 300 K.

A least squares fit of the forward conduction characteristics was done using the expression for a Schottky diode with a bulk series resistance[8] R,

$$I=I_s e^{q(V-IR)/nkT}$$

where n is the ideality factor and I_s the saturation current. The ideality factor was found to be 1.9 and the bulk resistance 650 ohms. Ref. 2 reported an ideality factor of 1.8 and a result of 1.85 is reported in Ref. 3. From results on Schottky junctions on other semiconductors, the literature suggests three possible causes for high ideality factors,[9] an insulating (oxide) layer, cleavage steps at the contact interface, or high doping levels. Given the differences in growth methods and surface preparation between this work and refs. 2 and 3, and the chemical inertness of the diamond surface, the first possibility would seem to be ruled out. The second possibility is tied to surface carbon diffusion and the nature of the surface step structure produced in the diamond growth process. Finally, because nitrogen compensation in CVD diamond is relatively high and metallic-like conductivity is seen for boron levels on the order of $10^{20}/cm^3$, the amount of boron needed to overcome compensation narrows the available doping range in CVD diamond. High ideality factors might have a more fundamental cause other than just poor contact fabrication or a variance in fabrication procedures. Also, the bulk resistance of Schottky junctions on diamond reported in the literature can make it difficult to compare I-V results because a high bulk resistance would tend to mask the "true" reverse characteristics.

C-V measurements are shown in Fig. 2.

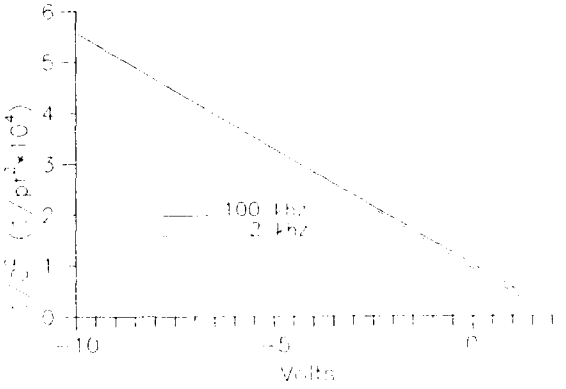


Fig. 2. $1/C^2$ vs. voltage at two different frequencies, S/N 112-4.

Two different methods were used in measuring the capacitance. Lock-in amplifier techniques were used to measure the imaginary

part of the AC impedance as a function of voltage for the 2 khz measurements and a Keithley model 590 capacitance-voltage meter was used in the 100khz measurements. The Keithley C-V instrument can make capacitance measurements assuming a parallel or serial R-C circuit as the electrical model for a Schottky diode. The variance in the capacitance from assuming either a parallel or serial R-C circuit is less than .5% over the range of capacitances reported here. From ref. 8, the smallness of this difference was found to be a necessary criterium in defining when the influence of the conductance on the measurements was minimal. This criterium is adopted here. The acceptor concentration obtained from the slope of the line in Fig. 2 was 5 x $10^{17}/cm^3$. It is unclear what influence the ideality factor has on diamond C-V characteristics.

In conclusion, Schottky junctions were fabricated to investigate the electrical properties of diamond grown in a turbulent flame, demonstrating that this material has potential for electronic applications. Further work is required to raise the device yields and further explore the growth parameter space available. One of us (J.W.G) would like to gratefully acknowledge that this work was carried out while holding an Office of Naval Technology postdoctoral fellowship.

REFERENCES

1. S. Matsumoto, Y. Sato, U. Kamo, and N. Setaka, Jpn. J. Appl. Phys. 1.21, 1183 (1982).

2. M.C. Hicks, C.R. Wronski, S.A. Grot, G. Sh. Gildenblat, A.R. Badzian, T. Badzian, and R. Messier, J. Appl. Phys. 65, 2139 (1989).

3. D.G. Jeng, H.S. Tuan, R.F. Salat, and G.J. Fricano, J. Appl. Phys. 68, 5902 (1991).

4. M.W. Geis, D.D. Rathman, D.J. Ehrlich, R.A. Murphy, and W.T. Lindley, IEEE Electron. Device Lett. 8, 341 (1987).

5. H. Shiomi,H. Nakahata, T. Imai, Y. Nishibayashi, and N. Fujimori, Jpn. J. Appl. Phys. 28, 758 (1989).

6. K.A. Snail and C. Craigie, Appl. Phys. Lett. 58, 1 (1991).

7. J.W. Glesener, A.A. Morrish, and K.A. Snail, J. Appl. Phys. 70, 5144 (1991).

8. N. Newman, M. van Schifgaarde, T. Kendelwicz, M.D. Williams, and W.E. Spicer, Phys. Rev. B, 33, 1146 (1986).

9. H.K. Henisch, Semiconductor Contacts, (Oxford, New York, 1989), and references therein.

POLYCRYSTALLINE DIAMOND FILM RESISTORS

L. M. Edwards and J. L. Davidson
Department of Electrical Engineering, Vanderbilt University, Nashville, TN

ABSTRACT

The technology to fabricate polycrystalline diamond film resistors has been initiated using modified thick film patterning techniques and *in situ* solid source doping.

Doping of polycrystalline diamond films in microwave plasma CVD systems has been achieved historically through use of diborane gas, which may contaminate the deposition system causing all diamond films thereafter to be doped p-type. We have attempted noncontaminating *in situ* doping utilizing two solid source dopants, and have met with preliminary success.

The more effective source (B_2O_3) produces a fairly even dopant concentration across the substrate, with sheet resistances ranging from 800 ohms per square to 4500 ohms per square. The other source (BN) showed significant doping in a narrow band surrounding the source, but the doping concentration decreased rapidly with distance from the source. Films grown afterwards with no doping were evaluated through resistance measurements; no evidence of doping contamination was observed.

INTRODUCTION

Polycrystalline diamond films (PDF) have been shown to have many of the same properties as natural diamond, and therefore possess material properties that are desirable in semiconductor electronic use [1]. These are of particular interest for high temperature and high power applications [2]. Undoped diamond is an electrical insulator [3], yet has a high thermal conductivity [4]. Diamond also possesses a low thermal coefficient of expansion [5,6], and high electron and hole mobilities in single crystal material [7].

CVD diamond doping has been accomplished with diborane gas [8], which may contaminate the growth chamber [9]. This work examines *in situ* doping of polycrystalline diamond films utilizing solid sources. We have investigated two sources, and found that one produces a fairly even dopant concentration across the substrate, while the other provides doping only in a narrow band in immediate proximity to the source. Data will be presented only from the more effective source.

EXPERIMENTAL PROCEDURE

Polycrystalline diamond films are grown using a microwave plasma CVD system developed by ASTEX, Inc., Woburn, MA, which is installed at Vanderbilt. Typical deposition conditions were 40 torr pressure, 850 °C, flow rate of 500 sccm hydrogen and 3.5 sccm methane, microwave power 1500 watts, and twenty hours deposition. Silicon samples were prepared by abrading selections of 1" × 1" silicon wafer with 0.25 micron diamond paste. Aluminum nitride samples were cut to 1" × 1" size from stock. Table I

describes the particulars of each sample investigated, and also indicates whether an undoped diamond layer is present. The dopant source is boron oxide (B_2O_3) in wafer form obtained from Owen-Illinois. Other work [12] has indicated such material may dope PDF.

Electrical properties were measured utilizing a fixed spacing four point tungsten carbide probe which was connected to a current source and voltage meter. Measurements were also taken with an HP 4145B parameter analyzer utilizing both the four point probe described above and four separate tungsten probes. The latter measurement points utilized silver contacts placed on the diamond as well as direct diamond contact.

Resistivity, (ρ), can be determined through four point probe measurements, where

$$\rho = \frac{\pi\, t}{\ln 2}\ \frac{V}{I}\ \Omega\text{-}m \quad for \quad s \gg t \tag{1}$$

where s is the probe spacing and t is the film thickness. For a p-type material, the carrier property description of resistivity is

$$\rho = [q\ \mu_p\ p]^{-1} \tag{2}$$

where q is electronic charge, μ_p is hole mobility, and p is carrier concentration. Sheet resistance is determined through use of Van der Pauw's method [10]. For a symmetrical structure, sheet resistance is defined as

$$R_S = \rho / t = \frac{\pi}{\ln 2}\ \frac{V}{I} \tag{3}$$

where t is the thickness of the doped layer. Sheet resistance is designated in ohms per square, and the geometry of the resistor defines the resistance.

RESULTS

Figure 1 shows a cross section of sample A. The doped layer of diamond can be visually distinguished from the undoped layer. The underlying substrate is silicon.

A composite of sheet resistance profiles for all samples is shown in Figure 2, with the results for sample B shown separately in Figure 3. These measurements were taken with the four point probe method described above, using a current source and voltage meter. Each point is an average over a range of 0.5 mA to 25 mA. The doping sources for samples A and B were new wafers from separate manufacturer lots; the source used in sample C had been utilized in two previous depositions and may have been dopant depleted or blocked by surface coatings. Due to the geometry of sample A, the profile was taken in a base orientation only, which is the initial measurement reference orientation. The center value is 1810 Ω/square with a variance of ±21%. Sample B has a center value of 800 Ω/square, with variance of ±42% in the base orientation and ±5% in a ninety degree rotation. Sample C shows a center value of 3900 Ω/square, with a variance of ±23% in the base orientation and ±17% in a ninety degree rotation.

Table I. -- Sample Parameters

	Sample A	Sample B	Sample C
Substrate	Silicon	Aluminum Nitride	Aluminum Nitride
Undoped Diamond Base	Yes	Yes	No
Comments	Sample was originally a 1" × 1" square, edges were broken away to isolate the doped layer and provide thickness samples	Sample printed with isolation ring, base layer of undoped diamond deposited for growth purposes	Sample was unaltered except for sizing.



Figure 1. Cross section of doped diamond film grown on undoped diamond film.

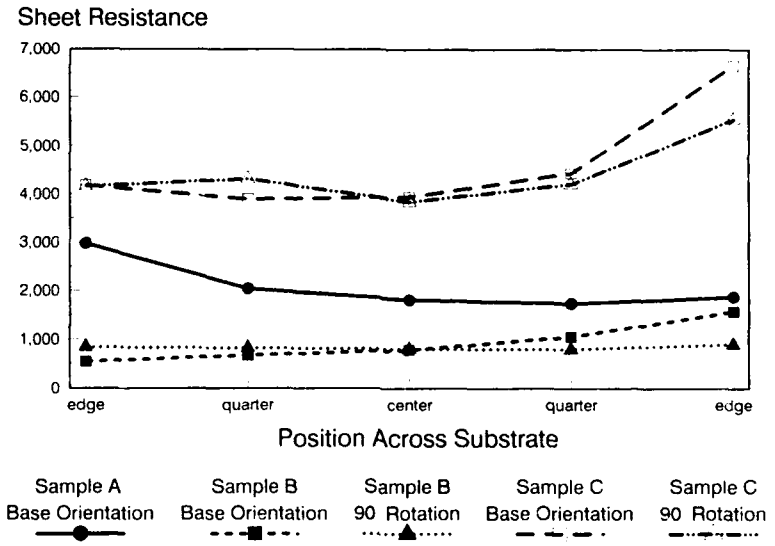


Figure 2. Composite of sheet resistance profiles across each sample.

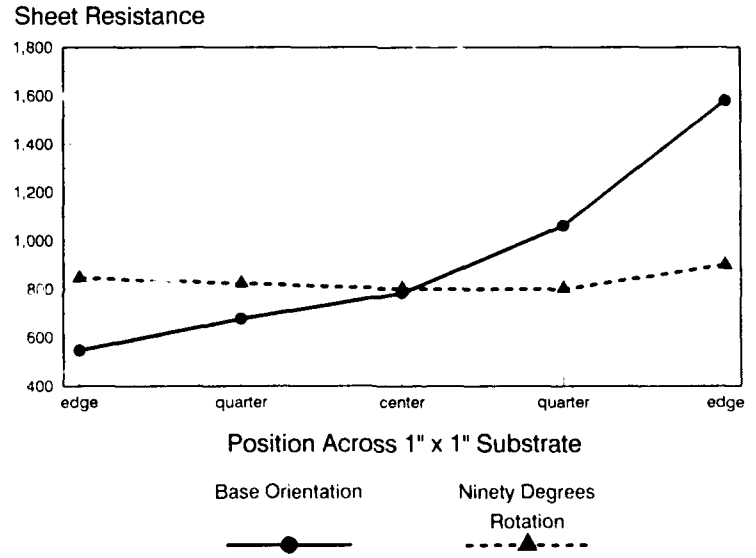


Figure 3. Sheet resistance profiles for sample B.

DISCUSSION

Sample B shows the smallest variation, and is therefore presumed to have the most uniform doping concentration of these samples. The sheet resistance profile across the surface is the most uniform of the samples. Based on growth rate, the thickness of the doped layer is assumed to be approximately ten microns, and the resistivity estimated to be 0.8 Ω-cm. From the resistivity equation for p-type doped material (Equation 2), the mobility-carrier concentration product is 7.8×10^{18} [V-cm-s]$^{-1}$. Depending on the dopant concentration and activated carrier concentration, the mobility can be estimated for PDF. For example, if N_A were 10^{20}/cm^3 and an active carrier concentration at room temperature were 0.2% [11], mobility would be estimated at 40 cm^2/V-s. SIMS analyses are in process.

SUMMARY

A minimum variance of ±5%, best case from center across a 1" × 1" sample has been observed in solid source doped CVD polycrystalline diamond film. The sheet resistance profiles observed provide an initial characterization of this doping method, and may be utilized to further refine the process.

In situ solid source doping has been shown to be effective in CVD polycrystalline diamond film. Subsequent films are found to be undoped as determined by resistance measurements. These results, in conjunction with ongoing application of modified thick film hybrid technology, may yield PDF resistors configurationally similar to traditional thick film resistors and materially compatible with microelectronic technology.

ACKNOWLEDGEMENTS

We would like to acknowledge invaluable processing assistance by Mick Howell. This work is supported in part by AVS, Tennessee Valley Chapter; the ISHM Educational Foundation; and the NASA Center for the Commercial Development of Space. Aluminum nitride substrates were provided by Stellar Industries, Leominster, MA.

REFERENCES

[1] K. Shenai and B. J. Baliga, "Diamond: A Semiconductor for High-Temperature and High-Power Electronics," in *Proceedings of the First International Symposium on Diamond and Diamond-Like Films, The Electrochemical Society* 89-12, 405 (1989).

[2] Davidson, J. L., L. Edwards and D. Feather, "Diamond as an Active Microelectronic Device," presentation to *JTC/ISHM Advanced Materials Technology Symposium*, Dallas TX (April 1991).

[3] S. Albin and L. Watkins, *IEEE Electron Device Letters* 11, 159 (1990).

[4] H. Shiomi, H. Nakahata, T. Imai, Y. Nishibayashi and N. Fujimori, *Japanese Journal of Applied Physics* 28, 758 (1989).

[5] A. B. Harker, *R&D Magazine* March, 84 (1990).

[6] M. Bernstein, *Lasers & Optronics* April, 57 (1991).
[7] M. Geis, D. D. Rathman, D. J. Ehrlich, R. A. Murphy and W. T. Lindley, *IEEE Electron Device Letters* EDL-8, 341 (1987).
[8] N. Fujimoro, T. Imai and A. Doi, *Vacuum* 36, 99 (1986).
[9] M. I. Landstrass, D. Moyer, S. Yokata and M. A. Plano, "Boron-Doped and Undoped Diamond/Silicon Heterostructure Applications," *Second International Conference on the New Diamond Science and Technology*, Washington DC (1990).
[10] R. C. Jaeger, *Introduction to Microelectronic Fabrication. Modular Series on Solid State Devices, Vol. V.* (Addison-Wesley 1988).
[11] A. T. Collins, *Semiconductor Science and Technology* 4, 605 (1989).
[12] Ramesham, R., T. Roppel, B. F. Hajek, C. Ellis and B. H. Loo, "Selective Growth of Boron-Doped Polycrystalline Diamond Thin Films," *Second International Conference on the New Diamond Science and Technology*, Washington DC (1990).

THE MODIFICATION OF THE ABRASION RESISTANCE OF TYPE IIa (110) DIAMOND USING CARBON AND NITROGEN IMPLANTATION.

GREGORY C. ANDERSON*, STEVEN PRAWER** and PETER N. JOHNSTON*.
*Department of Applied Physics and Microelectronics and Materials Technology Centre, Royal Melbourne Institute of Technology, G.P.O Box 2476V, Melbourne, Victoria, 3001, AUSTRALIA.
**School of Physics, University of Melbourne, Parkville, Victoria, 3052, AUSTRALIA.

ABSTRACT

The modification of the wear properties of type IIa diamond following ion implantation with 100 keV carbon and nitrogen has been studied at implantation temperatures of 150 and 470 K. Abrasion testing using low load multiple pass scratch testing with a Rockwell diamond indenter has shown a decrease in wear resistance. Microstructural modifications resulting from ion implantation have been assessed using Channeling Rutherford Backscattering Spectroscopy (C-RBS). No correlation was found between the presence of ion beam induced point defects (as measured by C-RBS) and the increase in wear. There are no obvious wear rate differences observed for nitrogen or carbon implantation.

INTRODUCTION

Diamond is believed to wear by a process of microcleavage[1] in which microscopic surface irregularities are broken off from the surface of the diamond along (111) cleavage planes thus exposing further surface roughness to enable abrasion to occur. The abrasion resistance and hardness of diamond varies considerably between different stones and between Type I and Type II diamonds[2]. Natural Type I diamonds containing high concentrations of nitrogen are known to be considerably harder[3] than Type II stones. Hartley[4] implanted diamond cutting tools with carbon and nitrogen to a total dose of $3x10^{15}$ ions.cm^{-2}. These results suggested that nitrogen implantation produced enhanced wear resistance, whilst carbon implantation did not. From these results Hartley postulated that nitrogen implantation to synthesize Type I diamond behavior may improve the wear resistance of diamond.

In the present study carbon and nitrogen have been implanted in order to test this hypothesis. Carbon implants were used to study the effect of ion beam induced damage on wear behavior, in the absence of any chemical effect. The results were then compared to those involving nitrogen implantation at similar energies. Since the knock-on damage due to nitrogen and carbon (both at 100 keV) is very similar, any differences on the wear behavior between these two implant species can be attributed to the chemical effect of nitrogen. Hence by comparing nitrogen and carbon implantations Hartley's postulate can be tested.

Previous work by our group[5] has concentrated on studying the effect of high temperature (1070 K) ion implantation on the wear properties of natural, industrial quality, Type Ia diamonds. This early work returned positive results in favour of ion beam induced wear reduction. However variations in behavior between samples and indeed, different regions on the one sample, has made the acquisition of a reproducible data set difficult. The current study uses optically flat, polished, inclusion free, oriented (110) Type IIa diamond windows (3.0 x 3.0 x 0.25 mm^3) supplied by Drukkers Corp. of Amsterdam. The flatness and uniformity of these samples provides a consistent sample set for the investigation.

The implantation temperatures of 150 and 470 K were chosen so as to assess the effect of the mobility of ion beam induced defects on wear behavior. At implantation temperatures above 800 K both vacancies and interstitials are believed to be mobile in diamond. In the temperature range from 300 to 800 K interstitials are the predominant mobile defect, while below 300 K there is no defect mobility[6]. Thus at 150 K, at least for moderate doses, complex defect structures are less likely to be formed. For implantation at 470 K, recombination of vacancies and interstitials is expected to occur and more complex extended defects may also form.

The aim of this study was to determine the implantation parameters which lead to an increase in wear resistance. All results obtained with type IIa samples show a reduction in wear resistance, but analysis of these results still provides useful information with regard to the modification of the wear properties of diamond.

EXPERIMENTAL

Implantation was performed using a Whickham 200 keV Ion Implanter. All implants were performed using an acceleration voltage of 100 keV with a beam current of approximately 0.3 $\mu A.cm^{-2}$. The flat face (110) of each sample was divided into three regions (Figure 1). The middle strip was masked while the other regions were implanted with doses of 10^{14} ions.cm^{-2} and 2.5 x 10^{15} ions.cm^{-2}. The masked strip provided a reference unimplanted area.

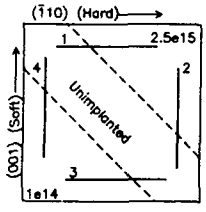


Figure 1. Diagram of a sample showing the two implanted areas separated by an unimplanted strip. The lines marked 1 to 4 indicate approximate positions of the scratch tests.

Implantation doses were chosen with reference to surface resistivity measurements on carbon implanted diamond[8] (Figure 2). Conductivity is very sensitive to microstructural modifications, and these measurements show three distinct implantation dose regimes, $D < D_1$, $D_1 < D < D_2$ and $D > D_2$ which characterize the ion beam induced damage For $D < D_1$ a build up of point defects occurs while the diamond remains essentially single crystal. For $D_1 < D < D_2$ partial amorphization or graphitisation may occur. For $D > D_2$ the formation of semicontinous pathways between conducting graphitic regions within the diamond occurs, approaching complete graphitization as the dose is increased. The doses chosen for this study are shown in Figure 2, which also shows the values of D_1 and D_2 for each implant temperature. For both 150 K and 470 K implant temperatures, the low dose implant of $1x10^{14}$ ions.cm^{-2} is less than D_1 and should thus create only localized point defects within the sample. Similarly, the high dose $2.5x10^{15}$ ions.cm^{-2} implant is just below D_2 and should create partial amorphisation of the implanted region while avoiding complete graphitisation.

Wear testing has been conducted using the technique of low load, multiple pass scratch testing. All scratch tests have been performed with an applied load of 0.98N. The indenter used for the scratch tests was a Rockwell diamond indenter with a tip radius of 0.200 mm. During testing the indenter was aligned with the hard (110) direction being presented to the sample. Care was taken to ensure that the face of the sample to be tested was horizontal and that the indenter axis was normal to the diamond surface. The sample was scratch tested in the hard (1̄10) direction for 200,000 passes and in the soft (100) direction for 1200 passes. The length of each scratch is approximately 2 mm and the relative speed of the indenter was approximately 2.8 $mm.s^{-1}$. The duration of the scratch tests was chosen to try and obtain a groove approximately 1000Å deep which corresponds roughly with the damage peak due to implantation.

After scratch testing, surface profilometry was performed using a Tencor Instruments Alpha Step 250. Surface profilometry across the wear track allows the depth, width and shape of the resulting scratch to be determined. Prior to surface profilometry the samples were first cleaned in nitric acid to remove any debris from scratch testing and then ultrasonically cleaned in methanol. Five or more of surface profiles were taken across the length of each wear track in both the unimplanted and implanted regions. The average depth and cross-sectional area of each wear track in the implanted and unimplanted regions was then calculated from these measurements. The latter, when divided by the number of passes, allows the average wear rate to be determined in $Å^2$/pass[8].

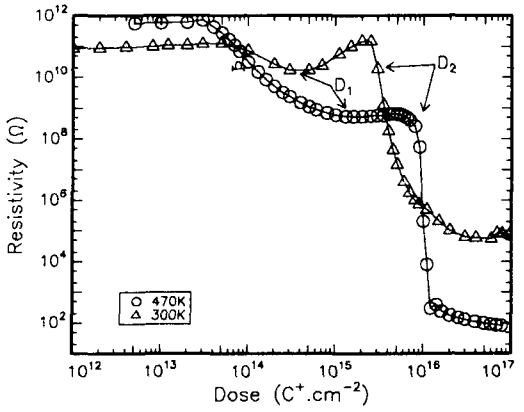


Figure 2. The surface conductivity curves of 100 keV C^+ implanted diamond for implant temperatures of 300 and 470 K. The doses chosen in this study and the temperature dependant doses D_1 and D_2 are shown.

The microstructural modifications which have occurred as a result of ion implantation were monitored using Channeling Rutherford Backscattering Spectrometry (C-RBS). A 1.46 MeV alpha particle analyzing beam was used with the spot size on target approximately 300μm in diameter.

RESULTS AND DISCUSSION

Figure 3 shows typical surface profilometry results for both the hard ($\bar{1}10$) direction after 200,000 passes and the soft (100) direction after 1200 passes. The wear track in the hard direction is in general broader than that in the soft direction. Tables I and II summarize the result of the profilometry measurements for all of the samples studied. Table I tabulates the results for the soft (100) direction and Table II, the results for the hard ($\bar{1}10$) directions. In both tables the absolute wear rates are tabulated, together with a value of the wear rate in the implanted region compared to that in the unimplanted diamond in the same wear track. For completeness Tables I and II also list the relative depth of the wear track, being the depth of the scratch in the implanted region divided by the depth in the unimplanted region.

Implant Dose & Species (cm^{-2})	Implant Temp (K)	Wear Rate (1000Å^2/pass) Unimplanted	Implanted	Relative Wear Rate	Relative Depth
$1x10^{14}C^+$	150	57±13	114±23	2.0±0.9	1.4±0.4
"	470	16±2.5	20±6.7	1.3±0.6	1.1±0.3
$2.5x10^{15}C^+$	150	46±16	88±16	1.9±1.0	1.4±0.3
"	470	78±15	150±6.7	2.0±0.5	1.7±0.3
$1x10^{14}N^+$	150	100±32	110±2.5	1.0±0.3	1.8±0.3
"	470	96±9.2	130±48	1.3±0.6	1.1±0.3
$2.5x10^{15}N^+$	150	75±27	110±17	1.5±0.7	1.8±0.5
"	470	87±7.5	210±23	2.5±0.5	2.1±0.5

Table I. Profilometry results for the (100) (soft) direction showing the relative depth and wear rates of the implanted region. A relative value > 1 shows an increase in the measured value in the implanted area, as compared to the unimplanted area. The large errors are due to fluctuations in the wear track profile as a function of distance along the scratch.

Implant Dose & Species (cm^{-2})	Implant Temp (K)	Wear Rate ($Å^2$/pass) Unimplanted	Implanted	Relative Wear Rate	Relative Depth
$1x10^{14}C^+$	150	230±45	270±58	1.2±0.5	1.2±0.1
"	470	210±20	340±45	1.7±0.4	1.1±0.3
$2.5x10^{15}C^+$	150	1500±120	2500±340	1.7±0.4	5.1±1.3
"	470	360±150	690±290	1.9±1.6	2.4±1.1
$1x10^{14}N^+$	150	710±170	1600±200	2.2±0.8	2.7±0.5
"	470	420±76	2400±160	5.7±1.4	4.4±0.5
$2.5x10^{15}N^+$	150	710±170	4300±150	6.0±1.6	5.3±1.2
"	470	470±140	1300±160	2.7±1.1	3.1±0.9

Table II. Profilometry results for the ($\bar{1}10$) (hard) direction showing the relative depth and wear rates of the implanted region. As in Table I the large errors are due to fluctuations in the wear track profile as a function of distance along the scratch.

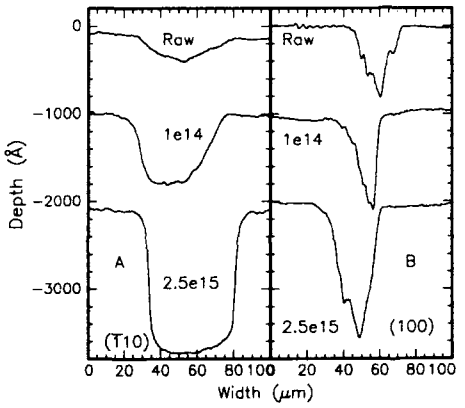


Figure 3. Typical cross-sectional profiles of the wear tracks obtained from scratch testing showing (a) Wear track in the hard ($\bar{1}10$) direction (470 K nitrogen) and (b) Wear track in the soft (100) direction (150 K nitrogen).

The profilometry results show no obvious differences in wear rate modification between carbon and nitrogen implantation except perhaps that the ion beam induced increase in wear for the hard direction is greater for nitrogen than for carbon implants. In particular, Hartley's[4] result reporting increased wear resistance for nitrogen implants cannot be confirmed. However we note that this may be due to the differing implantation conditions used. Hartley implanted $1x10^{15}$ ions.cm^{-2} at room temperature using a multiple energy implant at energies of 300, 200 and 100 keV to obtain a total dose of $3x10^{15}$ ions.cm^{-2}, whereas the single energy 100 keV $2.5x10^{15}$ ions.cm^{-2} implants used in this study will result in a narrower more highly damaged layer within the diamond.

The C-RBS spectra for the high dose implants are shown in Figure 4. The low dose spectra have not been included as these show very little damage, if any, as compared to the unimplanted diamond. Figure 4a shows the C-RBS spectra for nitrogen implantation at both 150 K and 470 K, while figure 4b shows the equivalent spectra resulting from carbon implantation.

Both carbon and nitrogen implantation at 150 K show the measured yield (χ_{min}) at the implant damage peak to approach the random yield, suggesting almost complete amorphisation of the implanted layer. The differences in the C-RBS spectra between the two species are consistent with TRIM[9] calculations which show nitrogen creating a slightly broader, taller damage peak than carbon implants. The predominant implant induced defect structures are point defects as little dechanneling is visible behind the damage peak, which would be expected from more complex defect structures.

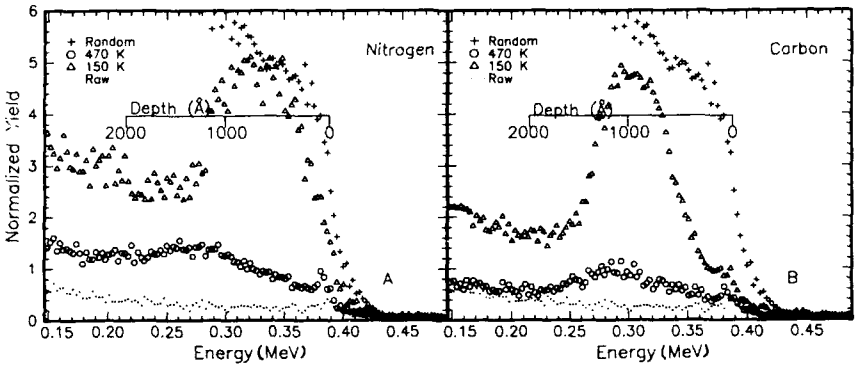


Figure 4. C-RBS spectra obtained from the $2.5x10^{15}$ ions.cm^{-2} implants using (a) 100 keV nitrogen implantation, and (b) 100 keV carbon implantation. The effect of temperature on point defect concentration is clearly visible.

The 470 K spectra of both carbon and nitrogen show much less ion beam induced damage with a χ_{min} of approximately 20% at the damage peak for both implant species as compared to the 150K spectra. This suggests that a high proportion of the ion-beam induced point defects have been annealed out due to the higher implant temperature. The C-RBS spectra of the 470K nitrogen implant also shows enhanced dechanneling behind the damage peak which suggests the presence of extended defects. This enhanced dechanneling is not present in the 470K carbon spectra.

Despite the large differences between the 150K and 470K C-RBS spectra there is no apparent temperature dependence on the wear rate. Similarly, both low and high dose implants result in similar wear rate modifications, despite the large difference in point defect concentration. This suggests that the presence of point defects is not implicated in the macroscopic wear behaviour. It also suggests that very little ion-beam induced damage is required to produce wear rate modifications. The presence of extended defects in the 470K nitrogen implant also appears to have little effect on the wear behaviour when compared to the 470K carbon implant. Thus other defects which are not visible in C-RBS analysis must be responsible for the observed changes in wear behavior.

CONCLUSION

Ion implantation at doses of $1x10^{14}$ and $2.5x10^{15}$ ions.cm^{-2} at temperatures of 150 and 470 K shows no obvious trend in modifying the wear rate despite large differences in the C-RBS spectra. This suggests that both point defects have little role in defining the ion-beam induced wear behavior. In particular, there are no obvious wear rate differences observed for nitrogen or carbon implantation.

The effect of ion implantation on the wear rate is different for hard (110) and soft (100) directions. There is a tendency for the ($\bar{1}$10) direction to show a dose dependency which is not always the case in the (100) direction.

ACKNOWLEDGEMENTS

The authors are grateful for the assistance of R. Kalish and V. Richter in performing some of the implants used in this study.

The assistance of A. Saint for undertaking analyses on the ion microprobe at the Microanalytical Research Centre, University of Melbourne is gratefully acknowledged.

REFERENCES

1. E.M. Wilks, and J. Wilks, J. Phys. D 5, 1902 (1972).

2. R.M. Chrenko, and H.M. Strong, Physical Properties of Diamond (G.E Technical Information Series, 1975).

3. T. Evans, Contemporary Physics, 17 (1), 45-70, (1976).

4. N.E.W. Hartley, Metastable Materials by Ion Implantation, Materials Research Society Papers, Edited by S.T. Picraux and W.J. Choyke, (Elsevier Science Publishing Co, 1982), p295.

5. G.C. Anderson and S. Prawer, Surface Modification Technology III, ed. T.S. Sudarshan & D.G. Bahat, Pub. The Minerals, Metals and Materials Society, 1990, p37.

6. J. F. Prins, Phys. Rev. B38, 5576 (1988).

7. S. Prawer, A. Hoffman and R. Kalish, App. Phys. Letts., 57, 1990, p2187.

8. M. Seal, Science and Technology of Industrial Diamonds, Proc. Int. Ind. Diamond Conf., Oxford, 1966, Vol I: Science, p145.

9. J.P. Biersack, G.Cuomo and J.F. Ziegler, TRIM, Copyright (1990); J.F. Zeigler, J.P. Biersack and U. Littmark, The Stopping and Range of Ions in Solids (Pergamon, New York, 1985).

PART III

II-VI Compounds

STOICHIOMETRY CONTROL OF COMPOUND SEMICONDUCTORS

JUN-ICHI NISHIZAWA*, KEN SUTO** and YUTAKA OYAMA***
*Tohoku University, Katahira Aoba-ku, Sendai 980 Japan
**Faculty of Engineering, Tohoku University, Aramaki Aoba-ku, Sendai 980 Japan
***Semiconductor Research Institute, Semiconductor Research Foundation, Kawauchi Aoba-ku, Sendai 980 Japan

ABSTRACT

Vapor pressure control technology is successfully applied to the bulk crystal growth, epitaxial growth and diffusion process of ZnSe crystals. Surface morphology and the crystal quality are investigated by the optical microscope and the X-ray double crystal diffractometry as the function of the growth temperature and the applying Zn vapor pressure. The cathode luminescence is also measured to evaluate the optical properties and the effect of low temperature growth and the application of Zn vapor pressure are demonstrated. *p*-type ZnSe crystals are grown from the Se solution with group I_a element as a dopant under controlled Zn vapor pressure. *p-n* junction diodes are also prepared by the Ga diffusion from Zn solution under Se vapor pressure. Emission spectra from the *p-n* junction and its Zn and Se vapor pressure dependencies are also presented.

INTRODUCTION

The most important factor to be controlled in compound semiconductor crystals is the deviation from the stoichiometric composition. Starting from the investigation of iron-pyrite[1], we have carried out the annealing experiments of various III-V compound semiconductor crystals[2] under controlled vapor pressure of group V elements. Crystallographic, electrical and optical evaluation have led to the crucial conclusion that the nearly perfect crystals with stoichiometric composition could be obtained under a specific vapor pressure (optimum vapor pressure)[3]. Later, some experimental studies were carried out at another laboratory and good coincidence could be obtained with our results[4]. Temperature dependence of the optimum vapor pressure was also determined. The vapor pressure control technology has been successfully applied to the liquid phase epitaxial growth of GaAs[5] and GaP[6] from the Ga solution in combination with the temperature difference method (TDM-CVP). It has been shown that there has been also the optimum vapor pressure to improve the crystal qualities. Vapor pressure control technology has been applied to the bulk crystal growth of Czochralski-grown GaAs[7] and zone melting InP[8]. It has been shown that the application of vapor pressure is also effective to control the deviation from the stoichiometric composition of compound semiconductor crystals and to reduce the dislocation density in commercially available GaAs ingots.

In order to clarify the mechanism of the vapor pressure control technology, the theoretical analysis was also carried out on the basis of the extension of the conventional chemical potential equilibrium through three phases. Our experimental results of the phase diagram in Ga-As system can be successfully explained by taking into account the change of the saturated solubility in the solution under controlled vapor pressure[9], resulting in that the deviation from the stoichiometric composition can be controlled by the application of the vapor pressure.

Mat. Res. Soc. Symp. Proc. Vol. 242. 1992 Materials Research Society

II-VI compound semiconductors including ZnSe crystals are the promising material for light emitting devices with short wavelength. Recently, ZnSe semiconductor laser has been reported to operate at liquid nitrogen temperature. In wide gap II-VI compounds such as ZnSe, both Zn and Se show high vapor pressure, resulting in that various sorts of defects are easily introduced during crystal growth and other thermal processes. Therefore, high quality ZnSe crystals with *p*-type conduction have not been easily obtained for a long time. We have applied the vapor pressure control technology to the bulk crystal growth, epitaxial growth and fabrication of *p-n* junction with the blue light emission of 480nm[10].

In order to reduce the residual defects and impurities, lower growth temperature will be expected in epitaxial growth. This paper reports the results of liquid phase epitaxial ZnSe crystals grown by the TDM-CVP using Se solution under Zn vapor pressure at relatively low growth temperature. Change of the surface morphology and the cathode luminescence spectra are presented as a function of the growth temperature and the applying Zn vapor pressure. Doping characteristics are also shown in view of the controlled Zn vapor pressure[11].

EXPERIMENTAL

Figure 1 is a schematic drawing of the epitaxial growth system and the temperature distribution of the furnace. Due to the differences of the specific gravity of ZnSe and Se, the source material (ZnSe) was maintained above the molten Se solution by a narrow portion of the quartz ampoule (8mmϕ , 50-80mm length). The temperature of the source material is maintained 1-3°C higher than that of the ZnSe substrate. ZnSe substrates used were {111} oriented and also grown by the TDM-CVP at 1050°C. Crystal quality of the substrate materials were evaluated by the X-ray double crystal diffractometry and the full width at half maximum (FWHM) of the X-ray rocking curve was less than 100 second of arc.

p-n junction was fabricated by the Ga diffusion under controlled Se vapor pressure into the *p*-type ZnSe crystals grown by the TDM-CVP. p-type ZnSe crystals were grown from the Se solution with group I_a elements as a dopant impurity under controlled Zn vapor pressure. In order to obtain the diffused layer with the thickness of 5~7μm, typical diffusion temperature and time used were 740°C and 1h respectively.

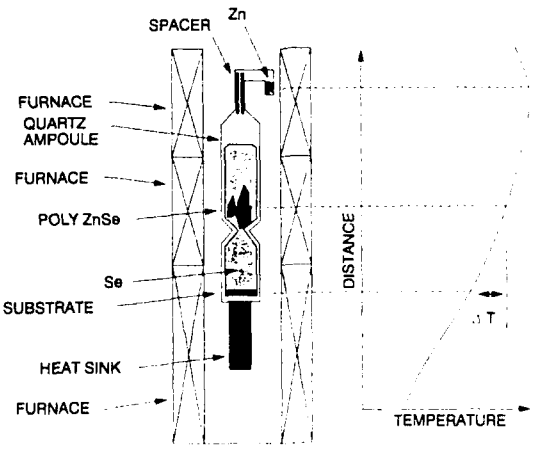


Fig.1
Schematic draw of the epitaxial growth system.

Nomarski interference microscopy analysis was applied to inspect the surface morphology of the epitaxial layers. Cathode luminescence (CL) measurements were carried out using the electron probe microanalyzer modified to collect the luminescent light at 77K. Accelerating voltage and beam current used were 25kV and 94μA respectively. Beam diameter was about 5μm. The luminescence was analyzed by the grating monochromator and detected by the S-20 type photomultiplier. Emission spectra from the *p-n* junction were also obtained at various measurement temperatures ranging 77~300K.

The Hall measurements were made by the Van-der Pauw method. For fabricating the ohmic contact, Au was evaporated followed by the heating up to 250°C for 10 min. in an Ar atmosphere.

RESULTS AND DISCUSSION

Surface morphology

Figure 2 shows the optical micrographs of the epitaxial layers and the cleaved surface of intentionally-undoped ZnSe crystals grown on the (111) oriented substrates at 750~950°C without excess Zn vapor pressure. Island growth was shown on the crystal surface when grown below 750°C perhaps due to the low solubility and surface migration distance. When crystal growth was carried out at 850~950°C, the islands were spreading and becoming larger. Consequently, single crystals could be epitaxially grown with smooth surface at the growth temperature of 950°C.

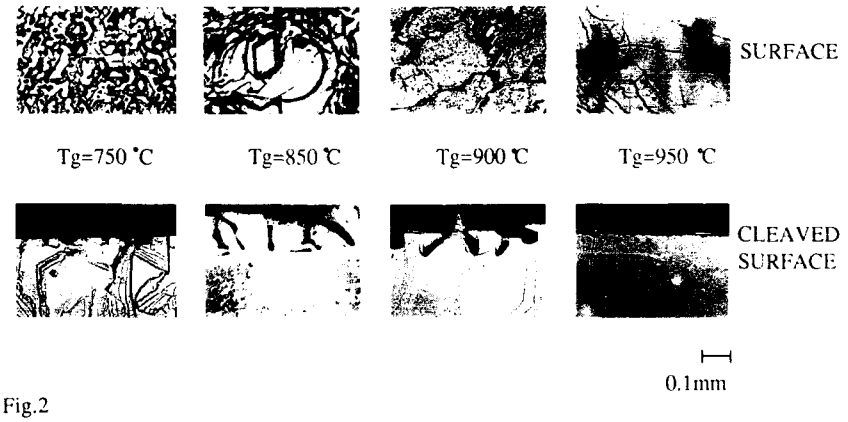


Fig.2
Surface morphology and the cleaved surface of the epitaxially grown intentionally-undoped ZnSe crystals.

Crystallographic properties

In order to investigate the crystallographic properties, X-ray double crystal diffractometry analysis was applied to the ZnSe epitaxial layers. (111) oriented HB grown GaAs crystal was used as the 1st crystal and the X-ray rocking curve was measured using the Cukα_1 radiation and the $(333)_s$-$(333)_s$ symmetrical configuration. Therefore, the FWHM of

the X-ray rocking curve reflects the irregularity of the crystal lattice plane. Figure 3 shows the FWHM of the X-ray rocking curve obtained from the ZnSe epitaxial layers as a function of growth temperature of the substrate materials. The growth temperatures of the epitaxial layers were in the range 850~950°C. In Fig.3, some of the samples grown at 850 and 900°C show multi-peaks of the X-ray rocking curve due to the existence of misoriented island growth region. In those cases, FWHM corresponds to the total width of the X-ray rocking curve. As shown in Fig.3, crystal perfection of the epitaxial layer was shown to be superior to that of the substrate.

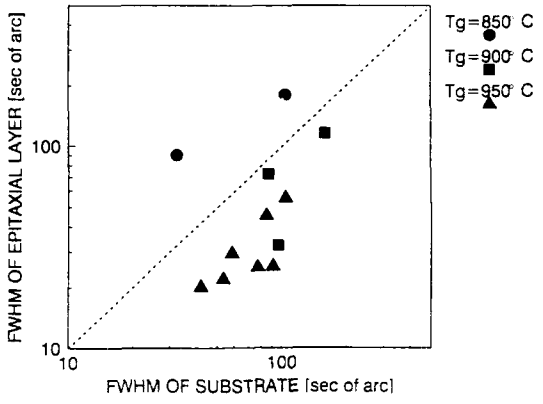


Fig.3
FWHM of the epitaxial layers as a function of that of substrate materials. FWHM was measured by the X-ray double crystal diffractometry using $(333)_s$-$(333)_s$ symmetrical configuration.

Cathode luminescence investigation

Figure 4 shows the cathode luminescence (CL) spectrum of the intentionally-undoped epitaxial ZnSe grown at 900°C. The electron beam was focused onto the single domain of the epitaxial layer. The CL spectrum shows three peaks as shown in Fig.4. 2.773 and 2.696eV CL peaks correspond to the exciton emission (EX) and the donor-acceptor pair emission (DA) respectively. DA pair emission peak was shown to be followed by the phonon replicas with 30meV intervals. A weak emission band relating with the deep levels could be also detected at around 2.48eV. Whereas, no other deep level-related emissions could be detected in the longer wavelength region.

Figure 5 shows the CL spectra of the epitaxial layers grown at various growth temperatures. For comparison, the CL spectrum of the substrate material before growth was also shown. It is clearly shown that the intensity of the EX emission decreases with increasing of the growth temperature. On the contrary, the intensity of the DA pair emission increases with increasing the growth temperature. In view of the enhancement of the EX emission intensity, these experimental results confirm that the lower growth temperature improves the crystal quality. It is also shown that the deep level-related CL emission at around 2.4eV could be scarcely detected in the epitaxial growth layer.

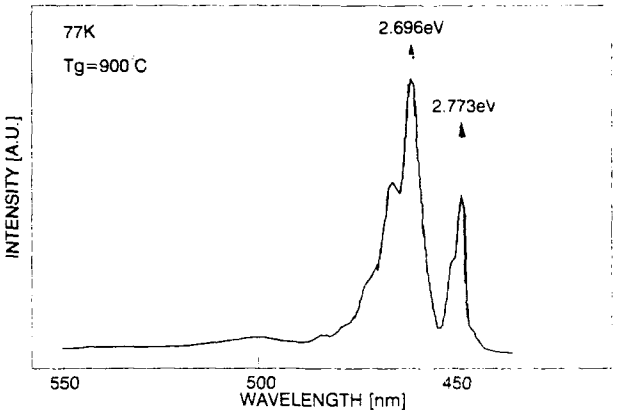


Fig.4
Cathode luminescence spectra of intentionally-undoped ZnSe epitaxial layers grown at 900°C without application of Zn vapor pressure.

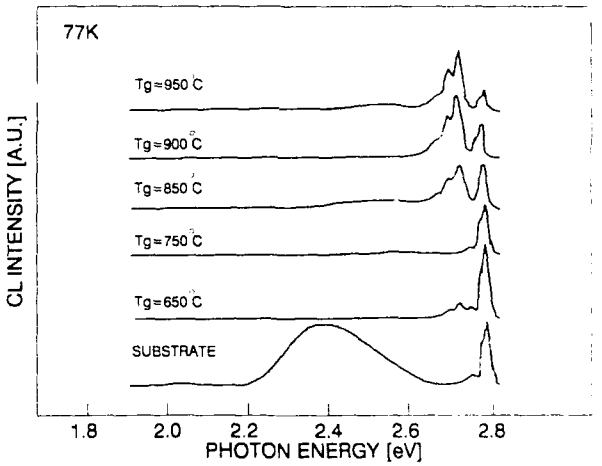


Fig.5
Cathode luminescence spectra of intentionally-undoped ZnSe epitaxial layers grown at various growth temperatures without application of Zn vapor pressure.

Next, we show the Zn vapor pressure dependencies of the CL spectra. Figure 6 shows the CL spectra of the epitaxial layers grown under the various controlled Zn vapor pressure. In all samples, the EX emission intensity dominates over that of the DA pair emission. On the contrary, DA pair emission intensity was shown to be larger than that of the EX emission in the epitaxial ZnSe crystals grown without applying Zn vapor pressure. Therefore, it is concluded that the application of Zn vapor pressure during epitaxial growth is effective to reduce some sorts of point defects which prevent the formation of excitons in the crystals.

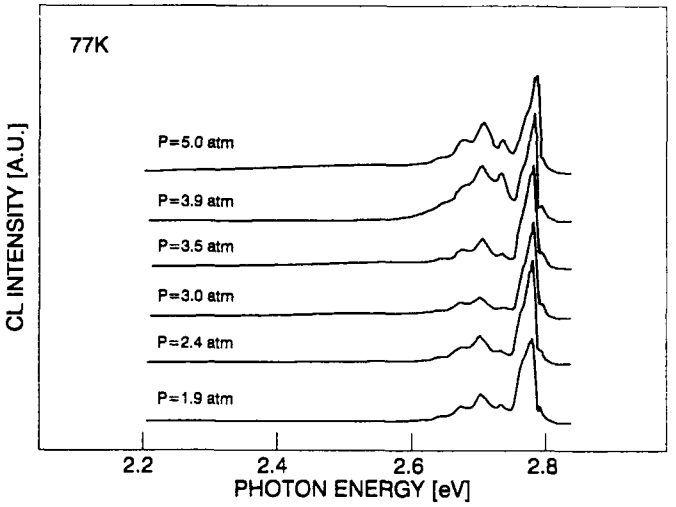


Fig.6
Cathode luminescence spectra of intentionally-undoped ZnSe epitaxial layers grown under various Zn vapor pressure. Growth temperature was 950°C.

Figure 7 shows the intensity ratio of the CL emission attributable for the EX (2.773eV) and DA pair emission (2.696eV) as a function of the applying Zn vapor pressure. It is shown that the relative EX emission intensity shows its maximum at a specific Zn vapor pressure of ~3.0 atm.

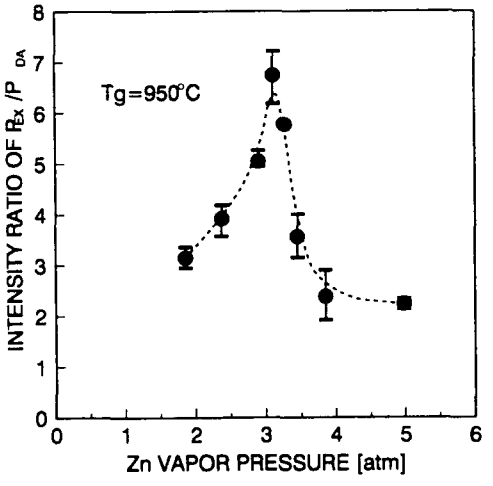


Fig.7
Relation between the applying Zn vapor pressure and the emission intensity ratio of the exciton (EX) emission peak at 2.773eV to the donor-acceptor (DA) pair emission peak at 2.696eV.

Figure 8 shows the CL spectra of the epitaxially-grown ZnSe crystals doped with Au, Na and Li. Dopant materials used were metal gold, Na_2Se, Li_2Se and $Li_2SO_4{\cdot}H_2O$ respectively. Experimental results obtained were rather complicated. When the Na_2Se and Li_2Se doped ZnSe crystals were epitaxially grown without Zn vapor pressure, the EX emission decreased drastically. However, application of 3.0 atm Zn vapor pressure enhances the CL intensity of the EX emission, meaning that the formation of the point defects associated with the deviation of the stoichiometric composition should be reduced. In the Au-doped ZnSe crystals, the intensity of the deep level-related CL emission (2.2~2.3eV) was also shown to be reduced by applying specific Zn vapor pressure of 3 atm. Therefore, it is concluded that the Zn vapor pressure control is shown to be effective to control the deviation from the stoichiometric composition of ZnSe crystals.

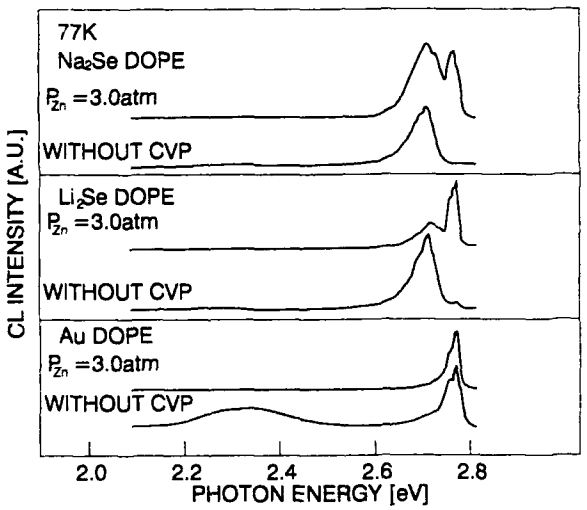


Fig.8
The effect of the applying Zn vapor pressure on the cathode luminescence spectra of epitaxial layers doped with Au, Na_2Se, Li_2Se and $Li_2SO_4{\cdot}H_2O$.

Doping characteristics

Zn vapor pressure control during ZnSe epitaxial growth was also shown to be effective in the doping characteristics. When ZnSe crystals were grown without application of Zn vapor pressure from the Se solution with acceptor impurities, only the insulating materials could be obtained. However, epitaxial growth was carried out under controlled Zn vapor pressure, p-type ZnSe crystals could be obtained with the hole carrier concentration ranging 8×10^{13}~3×10^{17} cm^{-3} at room temperature. Acceptor impurities used were Na_2Se, $Li_2SO4{\cdot}H_2O$ and Li_2Se. The highest hole carrier concentration was obtained when Na_2Se was used as acceptor impurity with 2.5 mole% or less in the Se solution. Table 1 summarizes the results of the Hall effect measurements at room temperature. It is noticeable to say that the mobility of the Li-doped ZnSe epitaxial layer shows considerable higher than that obtained from the theoretical calculations[13].

Table 1 Results of the Hall effect measurements at room temperature

DOPANT	mole % in Se solution	conduction type	carrier concentration [cm^{-3}]	Hall mobility [cm^2/V sec]	Resistivity [ohm cm]
Na_2Se	1-3E2	p	2E16-3E17	4-90	2-90
$Li_2SO_4 H_2O$	3E2	p	6E15	300	60
Li_2Se	3E2	p	8E13	450	3

GROWTH TEMPERATURE = 950°C
Zn VAPOR PRESSURE = 3.0 atm.

Blue light emission from the *p-n* junction prepared by diffusion under controlled Se vapor pressure

Figure 9 shows the typical emission spectra from the *p-n* junction measured at various temperatures ranging 77~300K. Sample used was grown under not-optimized Zn vapor pressure. The emission spectra show two sorts of emission lines associated with the gap energy (P_{edge}) and the deep levels (P_{deep}). The emission of the P_{deep} was very weak in most diodes at temperatures below 172K. The emission intensity of the P_{edge} decreased at higher temperatures above 280K. Figure 10 shows the temperature dependencies of the emission wavelength of the P_{edge} and the P_{deep}. The emission lines associated with the deep levels are classified into three sorts according to the emission wavelength (A,B,C). The energy of emission line B is the same as that of self-activated defects[12]. The temperature dependencies of the peak energies determine the activation energy for energy shift to be 55meV for the Pedge and 38meV for the peak C.

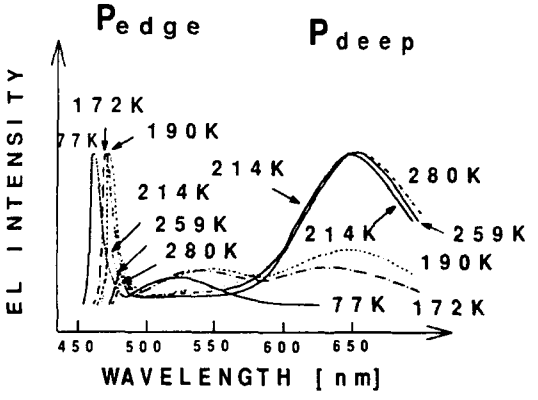


Fig.9
Typical emission spectra from the *p-n* junction measured at various temperatures ranging 77~300K. Sample used was grown under not-optimized Zn vapor pressure.

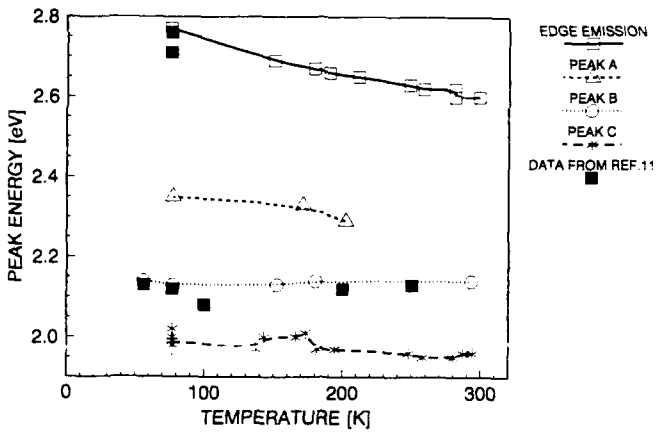


Fig.10
Temperature dependencies of the peak energy of the P_{edge} and P_{deep} obtained from the *p-n* junction. ■ shows the data from ref.12.

Vapor pressure dependencies of the emission spectra from the *p-n* junction

Figure 11 shows the relation between the intensity ration of P_{deep} to P_{edge} from the *p-n* junction and applied Zn vapor pressure. The intensity ratio shows its minimum at a specific Zn vapor pressure. Especially, the specified sample grown under the optimum Zn vapor pressure shows almost only a single emission line of 2.7eV (~460nm) at 77K without any deep level-related emissions. Figure 12 shows the Zn vapor pressure dependencies of the emission intensity of the P_{edge}. The emission intensity of the P_{edge} shows its maximum also at a specific Zn vapor pressure.

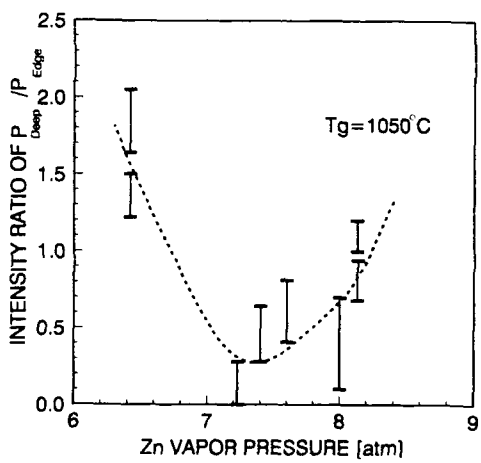


Fig.11
Relation between the intensity ration of P_{deep} to P_{edge} and applied Zn vapor pressure.

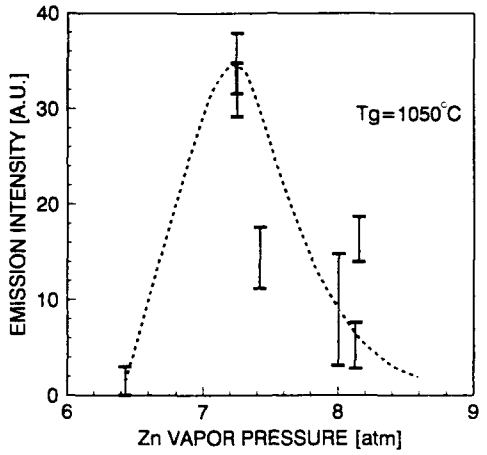


Fig.12
Zn vapor pressure dependencies of the emission intensity of the P_{edge} from the *p-n* junction.

Next, we show the effects of diffusion conditions on the emission characteristics. The Ga diffusion was carried out in the Zn solution under the controlled Se vapor pressure. All samples used were grown under the optimum Zn vapor pressure of 7.2atm at 1050°C. Figure 13 and 14 show the Se vapor pressure dependencies of the emission intensity measured at room temperature. As shown in Fig.13, the intensity ratio of the P_{deep} to P_{edge} shows minimum at a specific Se vapor pressure applied during the diffusion process. In addition, the emission intensity of the P_{edge} shows maximum at almost the same specific Se vapor pressure.

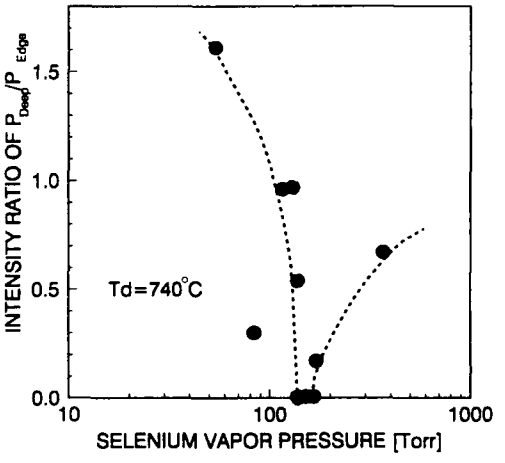


Fig.13
Effect of the Se vapor pressure during Ga diffusion from the Zn solution on the emission intensity ratio of P_{deep} to P_{edge} of the *p-n* junction measured at nominal room temperature.

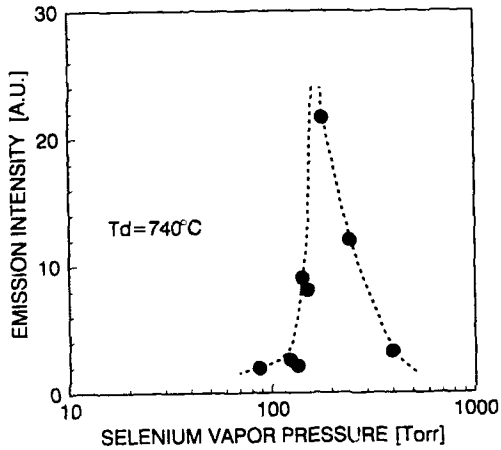


Fig.14
Effect of the Se vapor pressure during Ga diffusion from the Zn solution on the emission intensity of P_{edge} of the *p-n* junction measured at nominal room temperature.

Therefore, it is concluded that the formation of deep levels will be also controlled by the application of the Se vapor pressure during Ga diffusion process. Figure 15 shows the emission spectrum at room temperature obtained from the *p-n* junction grown under the optimum Zn vapor pressure followed by the Ga-diffusion process under the optimum Se vapor pressure. Even at room temperature, a pure blue light emission was obtained at 480nm with a half width of 7nm without any deep level-related emissions. The brightness of this sample was 2mcd at the driving current of 2mA.

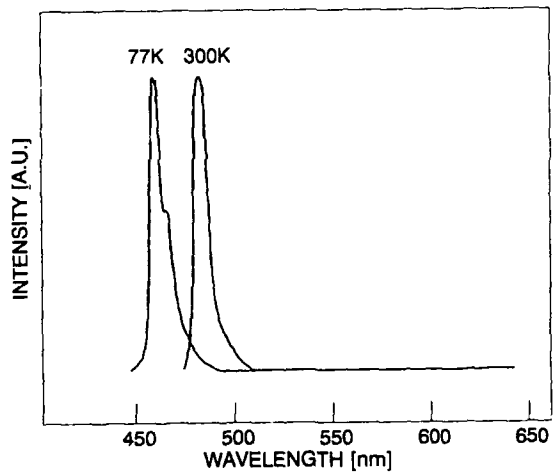


Fig.15
Emission spectra from the ZnSe *p-n* junctions measured at 77K and 300K.

References

[1] Y.Watanabe, J.Nishizawa and I.Sunagawa, Kagaku (Iwanami), 21(3), 140-141 (1951)

[2] H.Otsuka, K.Ishida and J.Nishizawa, Jpn. J. Appl. Phys., 8, 632 (1969)

[3] J.Nishizawa, H.Otsuka, S.Yamakoshi and K.Ishida, Jpn. J. Appl. Phys., 13, 46 (1974)

[4] J.M.Parsey, Jr., Y.Nanishi, J.Lagowski and H.C.Gatos, J. Electrochem. Soc., 128, 937 (1981)

[5] J.Nishizawa, Y.Okuno and H.Tadano, J. Crystal Growth, 31, 215 (1975)

[6] J.Nishizawa and Y.Okuno, IEEE Trans. Electron. Device ED-22, 716 (1975)

[7] K.Tomizawa, K.Sassa, Y.Shimanuki and J.Nishizawa, J. Electrochem. Soc., 131, 2394 (1984)

[8] J.Nishizawa, Solid State Materials, edited by S.Radhakrishna and A.Daud (Narosa Publishing House, New Delhi, 1991) p.279

[9] J.Nishizawa, Y.Okuno and K.Suto, Japan Annual Reviews in Electronics, Computers & Telecommunications (JARECT), vol.19, Semiconductor Technologies, (1986) OHMSHA and North Holland, p.p. 17-80 (1986)

[10] J.Nishizawa, K.Ito, Y.Okuno and F.Sakurai, J. Appl. Phys., 57(6), 2210 (1985)

[11] F.Sakurai, K.Suto and J.Nishizawa, J. Crystal Growth, 112, 153 (1991)

[12] M.Yamaguchi, A.Yamamoto and M.Kondo, J. Appl. Phys., 48, 196 (1977)

[13] H.E.Ruda, J. Appl. Phys., 59, 3516 (1986)

INITIAL STAGES OF GROWTH OF ZnSe ON Si.

R. D. BRINGANS, D. K. BIEGELSEN, L.-E. SWARTZ, F. A. PONCE and J. C. TRAMONTANA
Xerox Palo Alto Research Center, 3333 Coyote Hill Road, Palo Alto, CA 94304

ABSTRACT

Zinc selenide films have been grown heteroepitaxially on Si(100) substrates by molecular beam epitaxy. The initial stages of growth are dominated by the reaction of Se and Si atoms to form the compound $SiSe_2$. The compound formation disrupts epitaxy, and several growth methods which avoid this are described and compared. We find that room temperature deposition plus solid phase epitaxy does not lead to significant $SiSe_x$ formation and yields uniformly thick films which are misoriented with respect to the substrate and contain large regions of twinned ZnSe. The use of an As monolayer on the Si surface before the start of ZnSe growth allows good ZnSe epitaxy without any Si-Se reaction or any misorientation. ZnSe films have also been used as interlayers for GaAs growth on Si. This has allowed us to obtain uniform GaAs films at thicknesses which typically manifest a coalesced island morphology for GaAs grown directly on Si.

INTRODUCTION

Heteroepitaxy of compound semiconductors on Si substrates is a promising method of combining the best properties of both materials. A great deal of work has been carried out for GaAs heteroepitaxy on Si. In this paper, on the other hand, we will examine the related case of the growth of ZnSe on Si. ZnSe is of interest for optical devices because of its large direct band gap, but it is the main purpose of this paper to use the ZnSe-on-Si system to understand more about general questions of heteroepitaxy on Si.

Several effects make the growth of compound semiconductors on Si difficult to achieve successfully. These may include one or more of the following: (i) lattice mismatch which gives rise to dislocations at the interface or in the film, (ii) different thermal coefficients of expansion, which can lead to the introduction of stress during cooldown from the growth temperature, (iii) the formation of passivating layers which have very low surface free energy and thus inhibit the bonding between the substrate and overlayer, thereby leading to island formation and (iv) reaction between atoms from the substrate and the overlayer. We begin by considering the growth of the first few monolayers of the overlayer. The very early stages of growth of GaAs on Si, for example, are dominated by the passivating effect of an As monolayer on the Si substrate. This occurs because a monolayer of As can bond to either the Si(111) or Si(100) surface so that all of the Si and As atoms near the surface are fully coordinated. The surface formed is therefore highly unreactive. In principle a fully coordinated monolayer of Se could also form on Si(100) in an analagous manner so that passivation and island

Mat. Res. Soc. Symp. Proc. Vol. 242. © 1992 Materials Research Society

formation would also take place for ZnSe-on-Si growth. We find, however, that it is the reaction between Si and Se to form an amorphous compound that is the major effect in this case.

After giving some experimental details, we will describe the bonding of Se to the Si surface and discuss the chemical reaction that is found to take place. In the subsequent sections the growth of ZnSe using several growth techniques will be discussed and finally we will present some results for the use of ZnSe as an interlayer between GaAs and Si.

EXPERIMENTAL DETAILS

Unless otherwise noted, the silicon wafers used as substrates had their surfaces tilted by 4 degrees from the (100) plane (the surface normal being tilted by 4 degrees towards [0-11]). A thin, protective oxide was grown on these (0.01 ohm-cm, n-type) silicon substrates as described elsewhere [1]. After introduction into ultra high vacuum, the oxide was thermally desorbed and the surface cleanliness and order was determined by x-ray photoemission (XPS) or Auger spectroscopy (AES) and low energy electron diffraction (LEED). The ZnSe and GaAs films were grown in situ by molecular beam epitaxy (MBE), using a compound ZnSe source and elemental As and Ga sources, respectively. An electrochemical Se cell was used when Se alone was required. The resulting films were characterized in situ with AES, XPS and LEED. Prior to standard sample thinning for the transmission electron microscopy (TEM) studies, an amorphous Si layer was deposited over the films.

INTERACTION OF Se WITH Si

The unreconstructed Si(100) surface has two dangling bonds per surface atom and is therefore energetically very unstable. On the clean surface, adjacent atoms pair up to form dimers so that the number of dangling bonds is reduced to one per surface atom. If each of these atoms is replaced with an As atom then the extra valence electron in an As atom replaces the dangling bond with a lone pair. Moreover, the energy level of the dangling bond is lowered from midgap down into the valence band. Therefore a Si(100) surface covered with a monolayer of As-As dimers is fully coordinated. This is found to be the case in practice and leads to a very unreactive surface [2]. Se atoms have two extra valence electrons compared with Si and thus it is possible in principle to fully coordinate the un-dimerized Si(100) surface with a monolayer of Se as is shown schematically in Fig. 1. The two dangling bonds that were present are replaced with two non-reactive lone pairs. An arrangement such as this is found to occur for S atoms on Ge(100) surfaces [3], but we have found that this is difficult, if not impossible, to achieve for Se on Si(100). Experiments utilizing soft x-ray core level spectroscopy (SXPS) found that thick films of Se would react with Si to form a thick layer of $SiSe_2$ [4,5]. This is a compound analagous to SiO_2 and appears to be a stable product when Se comes into contact with Si. Results of the SXPS from refs 4 and 5 are given in Fig. 1 where the Si core level is shown for (a) a thick film of Se that was deposited at room temperature (RT) onto an on-axis Si(100) substrate and then annealed at a temperature of 300 °C and (b) the same film after annealing at 550

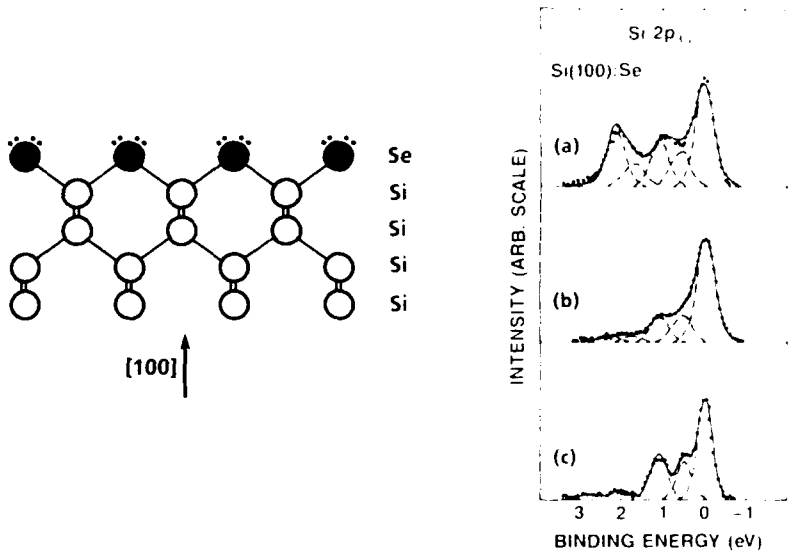


Figure 1. Schematic atomic structure of the ideal Se-terminated Si(100) surface and photoemission core level spectra for (a) a film of Se that was deposited on Si at RT and annealed at 300 °C, (b) the same film after annealing at 550 °C and (c) a ZnSe film which was annealed until all of the Zn but not all of the Se was desorbed (from ref. 5).

°C. Both spectra can be fitted with a bulk Si peak and 4 chemically-shifted peaks with separations of δ, 2δ, 3δ and 4δ from the bulk peak where $\delta = 0.53$ eV, the shifts being to higher binding energies. This is consistent with an ensemble of Si atoms being bonded to 1, 2, 3 or 4 Se atoms (bonding to four Se atoms corresponds to the compound $SiSe_2$). After the 550 °C anneal, the majority of the chemically shifted intensity is in the first two peaks. This also is found to be the case for a ZnSe film deposited on Si and then annealed so that all of the Zn, but not all of the Se is re-evaporated [Fig. 1(c)]. For a monolayer of Se to be bonded to Si(100) as shown in the schematic structure in Fig. 1, only the 2δ chemical shift should be present in the SXPS spectra and the presence of a 1δ chemical shift indicates that the surface is not fully passivated. This result and other subsequent Se deposition methods have failed to achieve a well ordered Se-terminated surface. At low substrate temperatures, the surface is fully covered and disordered and at higher surface temperatures the surface cannot be fully covered. Presumably this is due to the competition between surface ordering and the etching of the surface which takes place via the evolution of the volatile SiSe molecule [6]. It should also be noted that ordered layers of S do not occur on Si(100) [7] whereas they have been obtained for S on Ge(100) [3]. This again implicates the reactivity of Si with group VI atoms and the existence of volatile SiSe, SiS (and SiO) molecules.

We will show in the following sections that the interaction of Se with the Si substrate also dominates the initial stages of ZnSe growth on Si.

GROWTH OF ZnSe ON Si AT ELEVATED TEMPERATURES

Early results found that ZnSe could be grown epitaxially on Si with MBE by carefully controlling the Zn to Se flux ratio at the substrate [8,9]. Park and Mar [9] found that the best results could be obtained by slowly ramping up the Se flux while holding the Zn flux constant. In the absence of any Se flux the sticking coefficient of Zn on the surface was found to be zero at the substrate temperature of 330 °C that was used. It was concluded that the growth must be initiated at a slow rate *AND* that the flux of Zn should be greater than the Se flux at the initiation [9]. Epitaxial growth presumably occurred because the excess of Zn atoms prevented the Se and Si atoms from reaching one another and forming $SiSe_2$.

When both Se and Zn are supplied to the surface at the onset of growth, the reactivity between Si and Se dominates. This is shown in Fig 2 where the Si 2p core level spectra for ZnSe deposited on Si at both RT and 300 °C are contrasted to those for GaAs deposited on Si at elevated temperature We see large chemical shifts in the ZnSe-on-Si case which are indicative of the $SiSe_x$ formation, especially for the 300 °C deposition. A TEM image for a thick film whose growth was initiated at 300 °C is shown in Fig. 3. This figure, and other images of the same film, show the presence of a 70 nm amorphous film directly on top of the Si substrate and a polycrystalline film above that. The SXPS results [4,5] suggest that the thick amorphous film observed consists of $SiSe_x$. The small ~ 5 to 7 nm

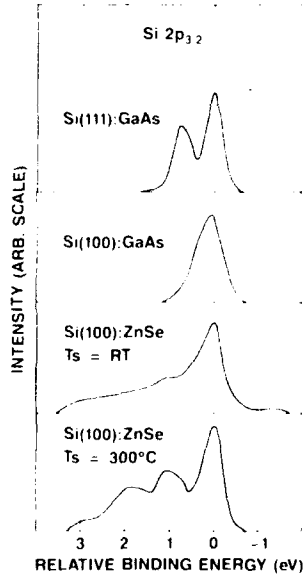


Figure 2. Comparison between the Si 2p photoemission core level spectra for GaAs on Si and ZnSe on Si (from ref. 5). The increased reactivity of ZnSe with Si compared to GaAs-on-Si is shown by the presence of large chemical shifts corresponding to Si atoms bonded to 4 Se atoms.

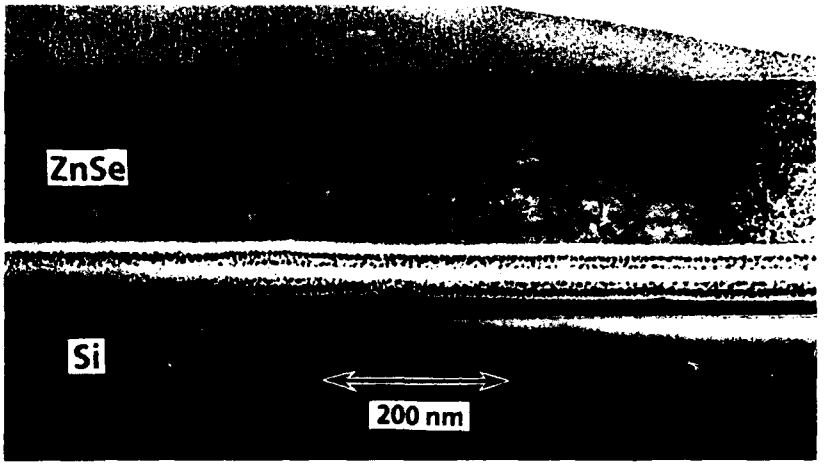


Figure 3. TEM cross section ([011] projection) of a ZnSe film deposited on Si at 300 °C. An amorphous Si film has been evaporated onto the ZnSe layer to provide protection during TEM thinning.

inclusions that can be seen within the amorphous layer are likely to be small Zn or ZnSe crystals. The transition between the amorphous, reacted layer and the polycrystalline ZnSe layer is likely to occur once silicon atoms are unable to diffuse fast enough to the surface or once Se atoms are unable to diffuse fast enough to the interface. We would thus expect the thickness of the amorphous layer to be very sensitive to growth rate and substrate temperature. We note that other films grown in this temperature regime also show reaction between the Si substrate and the ZnSe overlayer.

ZnSe FILMS ON Si BY ROOM TEMPERATURE DEPOSITION AND SOLID PHASE EPITAXY

On the basis of the results presented in the previous section, some method to limit the degree of reactivity between Si and Se is necessary. Lowering the substrate temperature during deposition is one possibility. Subsequent annealing and crystallization may then take place without large numbers of Se atoms being able to reach the Si because the Se atoms are tied down by bonding to Zn atoms.

A series of ZnSe films was grown by room temperature deposition followed by solid phase epitaxy (SPE) [10]. It was found using LEED and TEM that annealing films for 2 minutes at 500 °C gave crystalline films without any significant reaction between the ZnSe and the Si substrate. Annealing at 600 °C did cause a reaction to take place. A cross section TEM image of a 50 nm ZnSe film on Si(100) is presented in Fig 4. There is no evidence for the formation of an amorphous layer between the Si and the ZnSe. The ZnSe film also has a characteristic orientation relative to the substrate. The inset in Fig. 4 shows the electron diffraction pattern that was obtained from the same

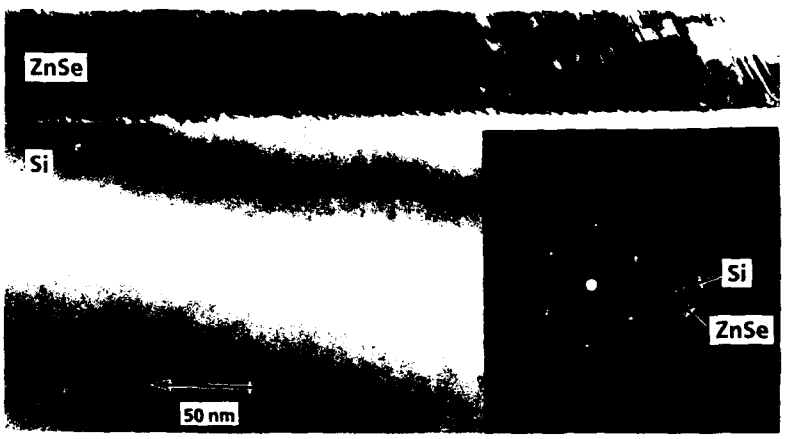


Figure 4. (a) TEM cross section in the, [011] projection, of a ZnSe film deposited on Si at room temperature and then annealed for 2 minutes at 500 °C. The [100] vector for the substrate is 4° from the interface normal and has a component towards the right of the figure. The inset is an electron diffraction pattern of the same area.

area of the interface. Several conclusions can be drawn from the figure: (i) the film is uniform in thickness; (ii) the diffraction pattern shows that the ZnSe crystal is tilted with respect to the Si substrate; and (iii) a large number of crystal defects tilting from the lower right to the upper left are seen. The misorientation angle was measured for a number of films deposited in the same manner and was found to be $5° \pm 1°$ with the same orientation sense relative to the surface offcut in all cases. A film grown on a 1.5° offcut substrate also had a 4° misorientation showing that the misorientation was insensitive to the offcut angle. Tilts have been seen in many heteroepitaxial systems grown on off-cut substrates, but no simple models for their origin seem to explain all of the present data. Lattice mismatch is not the only important parameter. This can be seen dramatically by comparing results for GaAs on Si substrates with similar offcut angles to those in this study. Although GaAs-on-Si has close to the same mismatch (~4%) as ZnSe on Si, (i) the tilts are in the opposite direction to those found here (i.e. the [100] vector of the ZnSe is tilted *towards* the surface normal for GaAs-on-Si and *away from* the normal for ZnSe-on-Si) and (ii) the tilts have a magnitude in the range of 0 to 0.3° [11-14] for GaAs-on-Si, which is much smaller than the value of $5° \pm 1°$ that we have measured in our RT deposited and SPE ZnSe-on-Si films. We also note that ZnSe grown on 4° off-axis Ge(100) [15] (lattice mismatch ~0.2%) has a tilt of 0.5° in the same direction as our results for ZnSe on Si. As we discuss later, we believe that the tilt for ZnSe on Si is related to the presence of small areas of $SiSe_x$.

High resolution images [10,16] revealed a large number (around 50% of the total cross-sectional area) of twinned areas all of which were oriented on only one of the two possible sets of {111} planes imaged in the [011] direction. Fig 5 (a) shows the orientation of the twinned regions relative to the interface. A similar result has been seen recently for GaAs-on-Si where, at large distances from the interface, a predominance of one of the sets of planes over the other was found [17,18]. There are several differences between the observations we have made and those in the GaAs-on-Si case. There was no misorientation observed for GaAs-on-Si and the ratio of the majority to minority stacking faults was 10:1 for GaAs-on-Si and is at least 200:1 in our case where we have not observed any minority orientations in any of our films.

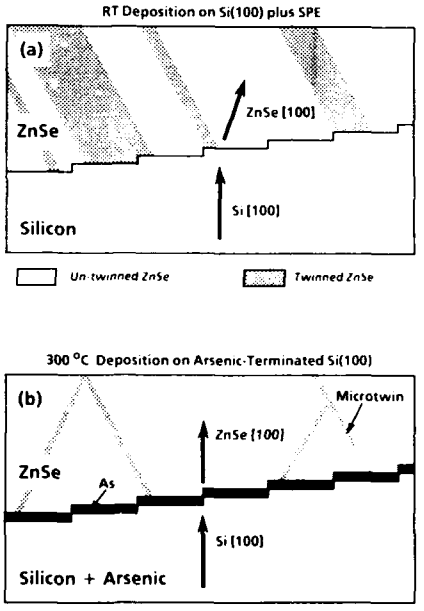


Figure 5. Schematic cross-section, in a [011] projection, showing the relative orientations of the ZnSe and Si crystals, the stacking faults and the interface for (a) a film deposited on Si(100) at room temperature and then annealed at 500 °C for 2 min and (b) a film deposited on arsenic-terminated Si(100) at 300 °C.

ZnSe FILMS GROWN ON ARSENIC - TERMINATED Si

Following a suggestion by Chadi [19], we have grown ZnSe films on As-terminated Si(100). The advantage of this approach is that a monolayer of As at the interface between Si and ZnSe allows all of the Si, As, Zn and Se atoms to be fully coordinated. This structure is shown schematically in Fig. 6. When As is bonded to Si(100) it has bonds to two Si atoms, contributing two electrons and having three electrons left over for bonding to the next layer. This is the same as Se in bulk ZnSe

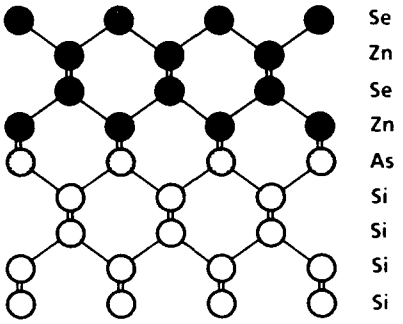


Figure 6. Schematic atomic structure for ZnSe grown on arsenic-terminated Si(100) [19].

which contributes three electrons to bonds to the Zn layer below it and three electrons to bonds to the Zn layer above. A Si(100) surface with a layer of As therefore appears qualitatively the same to a Zn atom as does a Se layer terminating bulk ZnSe. Bonding between Si and ZnSe exclusively via bonds between Si and Zn atoms or via bonds between Si and Se atoms cannot fully coordinate all of the atoms in the system.

A second and related advantage of using As-terminated Si(100) as the substrate is that the As monolayer prevents the direct interaction of Si and Se to form Si-Se compounds. Because As monolayers are stable up to temperatures of 750 °C it is possible to grow ZnSe on Si(100):As at the

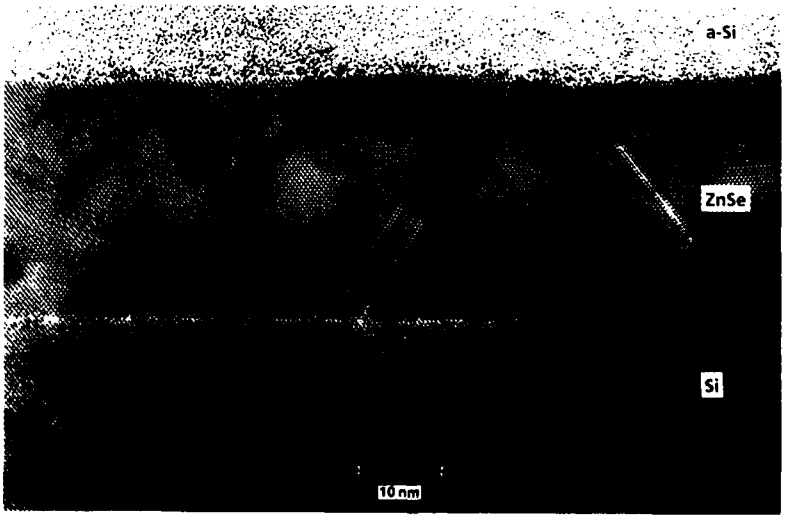


Figure 7. TEM cross section in the, [011] projection, of a ZnSe film deposited on arsenic-terminated Si at 300 °C. The [100] vector for the substrate is 4° from the interface normal and has a component towards the right of the figure. The inset is a schematic atomic structure of the interface region.

preferred growth temperature for ZnSe homoepitaxy of around 300 °C. In Fig. 7, we show a TEM image of a ZnSe film grown at 300 °C on Si(100):As. The film can be seen to be very uniform in thickness and there is no evidence of any reaction to form an amorphous layer at the interface. In contrast to the ZnSe films formed by RT deposition on clean Si(100) plus SPE, no large twinned regions are observed in this image or for any of the other films that we have grown on Si(100):As. This contrast is summarized in Fig 5.

COMPARISON OF GROWTH METHODS

The dominant effect in the initial stages of growth of ZnSe on Si is the tendency of Si and Se to react with one another to form $SiSe_2$. We have shown that growth at the ZnSe homoepitaxial temperatures of around 300 °C is not viable if both Se and Zn atoms can reach the clean Si surface. Successful growth methods have to overcome this tendency. One approach is to force the first monolayer bonded to the Si surface to be Zn as was shown to work for thick films [9]. The problem with this method is that a ...Si-Si-Zn-Se-Zn-Se... layer sequence does not fully coordinate the interface atoms and leads to a dipole at the interface. It is possible that intermixing between Si and Zn can overcome this effect (in analogy to the effects that have been proposed for the GaAs on Si case[20]), but any intermixing will probably allow partial formation of $SiSe_x$. The difference between the ZnSe crystal structures obtained for growth at RT on clean Si(100) plus SPE and the growth on As-terminated Si(100) at 300 °C which are summarized in Fig 5 indicates that partial formation of $SiSe_x$ is also occurring for the RT plus SPE case. This is suggested by the partial loss of epitaxy (crystal misorientation and the presence of large regions of twinned ZnSe) for RT deposition on Si(100) plus SPE. (We note that RT deposition plus SPE for growth on As-terminated Si(100) gives the same results as deposition at 300 °C on Si(100):As showing that it is the presence of the As layer that makes the difference and not the SPE mechanism). Analysis of the twinned regions shows that the (111) planes make a small angle with the interface plane if the ZnSe is misoriented in the direction that is observed. We have therefore proposed [16] that the misorientation plus the twinning are a result of ZnSe nucleating with a (111) plane close to the interface in regions where there is sufficient reaction between Si and Se to disrupt epitaxy.

ZnSe AS AN INTERLAYER BETWEEN GaAs ON Si.

The ZnSe films produced by deposition on Si(100):As are particularly uniform and are therefore of considerable promise as interlayers between Si and GaAs. The use of a ZnSe interlayer has been proposed [21,10] because it has two advantages over direct growth of GaAs on Si. ZnSe is softer than either GaAs or Si (the Knoop hardnesses for Si, GaAs and ZnSe are 1150, 750 and 150 respectively). This suggests that it is possible that dislocations can be forced to reside in the interlayer instead of propagating into the GaAs film, and that dislocations in the GaAs can be squeezed out into the ZnSe layer by thermal cycling sequences. The second advantage is that ZnSe films with uniform thickness can be grown on Si at thicknesses where GaAs films grown directly on Si are dominated by island formation and coalescence. The ZnSe therefore serves initially as a good template for GaAs growth (the lattice constants and thermal expansion coefficients of GaAs and

ZnSe are comparable compared with their differences to those of Si) and then after the GaAs is grown the ZnSe serves as a sink for dislocations.

The use of a thick (0.5 μm) ZnSe film as in interlayer in metal organic chemical vapor deposition (MOCVD) growth of GaAs-on-Si has been described recently [22] and the authors of that study found that the resulting GaAs was of better quality than control samples in which no ZnSe layer was present. Here, we examine the growth modes of very thin layers. The use of thin layers has the advantage that a dislocation net can be kept very close to the substrate. We will show that very uniform films of ZnSe and GaAs with a combined thickness of around 0.1 μm can be grown on Si.

GaAs growth on ZnSe is considerably more difficult than the much-studied inverse growth of ZnSe on GaAs because the optimum temperature for GaAs growth is high compared with that (~300 °C) used for ZnSe MBE. Nevertheless, epitaxial growth of GaAs on high quality ZnSe layers (epitaxially grown on GaAs substrates) has been achieved recently [23-25]. In the case of ZnSe as an interlayer between Si and GaAs, we wish to keep the ZnSe layer on Si as thin as possible and therefore the growth of GaAs must occur on a surface that is not yet completely smooth. Growth at temperatures above about 300 °C was found to cause island formation of the GaAs and, on the other hand, deposition at RT followed by SPE gave a mixture of epitaxial and polycrystalline GaAs. For GaAs films thicker than some minimum value, we have found that by slowly ramping the temperature during growth good quality overlayers can be obtained. The TEM image in Fig. 8. is

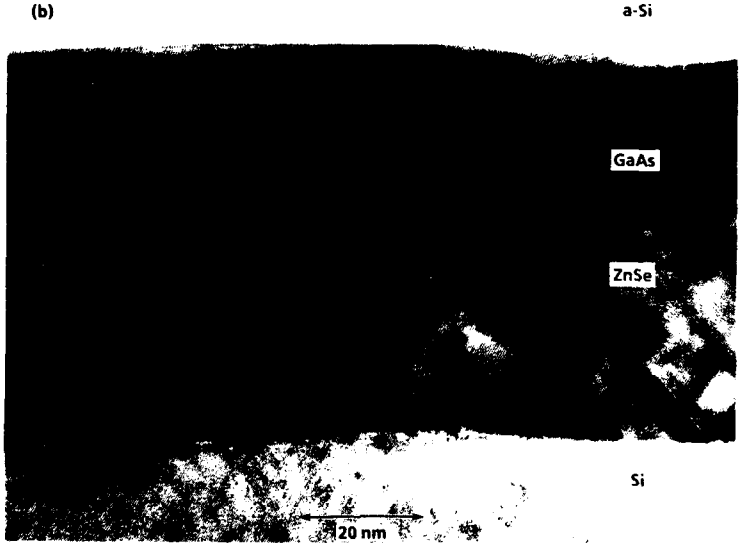


Figure 8. TEM cross section in the, [011] projection, of a ZnSe interlayer deposited on arsenic-terminated Si at 300 °C and a GaAs film grown onto this interlayer as discussed in the text.

from a GaAs film that was deposited at temperatures between 190 °C and 500 °C. Specifically, after the ZnSe film was grown at 300 °C on Si(100):As, the substrate was held at 300 °C while the As and Ga sources were warmed up, then the substrate temperature was dropped to 190 °C. The GaAs was grown for 3 minutes at each of the temperatures in the sequence: 190, 225, 250, 300, 350, 400, 450 and 500 °C.

The TEM image shows that the GaAs film is epitaxial with respect to the ZnSe interlayer and to the Si substrate. It has a relatively uniform thickness with good surface morphology. There is no evidence of growth via island formation and coalescence and the interface between the ZnSe and the GaAs is rather featureless. The major defects present in the ZnSe interlayer are microtwins and some of these terminate at the ZnSe-GaAs interface and others propagate into the GaAs film.

CONCLUSIONS

We have shown that thin uniform films of ZnSe can be grown on Si(100) either by RT deposition plus SPE or by deposition at 300 °C onto an arsenic-terminated Si(100) surface. In the latter case the ZnSe crystal quality is superior. We have also presented results for the use of these ZnSe films as interlayers for the growth of GaAs on Si. We found that good uniform GaAs films could be formed at thicknesses where GaAs grown directly onto Si is usually affected by island formation.

REFERENCES

1. *B. S. Krusor, D. K. Biegelsen, R. D. Yingling and J. R. Abelson, J. Vac. Sci. and Technol.*, **B7**, 129 (1989).
2. R. I. G. Uhrberg, R. D. Bringans, R. Z. Bachrach and J. E. Northrup, Phys. Rev. Lett., **56**, 520, (1986).
3. T. Weser, A. Bogen, B. Konrad, R. D. Schnell, C. A. Schug and W. Steinmann, Phys. Rev. B, **35**, 8184, 1987.
4. R. D. Bringans and M. A. Olmstead, Phys. Rev. B, **39**, 12985, (1989).
5. R. D. Bringans and M. A. Olmstead, J. Vac. Sci and Technol., **B7**, 1232 (1989).
6. See, for example, the discussion about the growth of CdS on Si in D. B. Holt, Thin Solid Films, **24**, 1 (1974)
7. T. Weser, A. Bogen, B. Konrad, R. D. Schnell, C. A. Schug, and W. Steinmann, in Proceedings of the 20th Int. Conf. on the Physics of Semiconductors, Stockholm, Engström, O., ed., World Scientific, Singapore, 1987 p. 97.
8. N. Mino, M. Kobayashi, M. Konagi and K. Takahashi, J. Appl. Phys., **58**, 793 (1985).
9. R. M. Park and H. A. Mar, Appl. Phys. Lett.,**48**, 529, (1986).
10. R. D. Bringans, D. K. Biegelsen, F. A. Ponce, L.-E. Swartz, J. C. Tramontana, Mat. Res. Soc. Symp. Proc. **198**, 195 (1990).
11. J. W. Lee, J. P. Salano, R. P. Gale and J. C. C. Fan, Mat. Res. Soc. Proc., **91**, 33, (1987).
12. T. Yao, Y. Okada, H. Kawanami, S. Matsui, A. Imagawa and K. Ishida, Mat. Res. Soc. Proc., 91, **63**, (1987).
13. S. K. Ghandi and J. E. Ayers, Appl. Phys. Lett.,**53**, 1204, (1988).
14. J. Varrio, A. Salokatve, H. Asonen, M. Hovinen, M. Pessa, K. Ishida and H. Katajima, Mat. Res. Soc. Proc., **116**, 91, (1988).
15. J. Kleiman, R. M. Park and H. A. Mar, J. Appl. Phys, **64**, 1201, (1988).
16. R. D. Bringans, D. K. Biegelsen, F. A. Ponce, L.-E. Swartz, J. C. Tramontana, to be published.
17. K. C. Rajkumar, A. Madhukar, J. K. Liu and F. J. Grunthaner, Appl. Phys. Lett., **56**, 1160, (1990).

18. P. Lao, W. C. Tang, K. C. Rajkumar, A. Madhukar, J. K. Liu and F. J. Grunthaner, J. Appl. Phys., 67, 6445 (1990).
19. D. J. Chadi, to be published.
20. W. A. Harrison, E. A. Kraut, J. R. Waldrop and R. W. Grant, Phys. Rev. B, 18, 4402 (1978).
21. D. K. Biegelsen, U.S. patent 4,935,385, "Method of forming heterostructures having intermediate buffer films with low plastic deformation threshold for lattice mismatched heteroepitaxy", (1990).
22. M. K. Lee, R. H. Horng, D. S. Wuu and P. C. Chen, Appl. Phys. Lett., 59, 207, (1991).
23. M. C. Tamargo, J. L. de Miguel, F. S. Turco, B. J. Skromme, M. H. Meynadier, R. E. Nahory, D. M. Hwang and H. H. Farrell, SPIE vol. 1037, p 73, Monitoring and Control of Plasma-Enhanced Processing of Semiconductors (1988), Society of Photo-Optical Instrumentation Engineers, Box 10, Bellingham, WA 98227.
24. M. C. Tamargo, J. L. de Miguel, F. S. Turco, B. J. Skromme, D. M. Hwang, R. E. Nahory and H. H. Farrell, in "Growth and Optical Properties of Wide-Gap II-VI low dimensional Semiconductors", T. C. McGill, C. M. Sotomayor Torres and W. Gebhart, eds (Plenum Publishing Corp, 1989) p239.
25. N. Kobayashi and Y. Horikoshi, Japn. J. Appl. Phys, 29, L236, (1990).

THE MBE GROWTH OF WIDEGAP II-VI INJECTION LASERS AND LEDs

W. XIE*, D.C. GRILLO*, M. KOBAYASHI*, R.L. GUNSHOR*, H. JEON**, J. DING**, A.V. NURMIKKO**, G.C. HUA***, and N. OTSUKA***
*School of Electrical Engineering, Purdue University, West Lafayette, IN 47907
**Division of Engineering and Department of Physics, Brown University, Providence, RI 02912
***School of Materials Engineering, Purdue University, West Lafayette, IN 47907

ABSTRACT

Striking progress in the development of II-VI semiconductor heterostructures, coupled with seminal advances in doping, has very recently led to the first demonstration of blue and blue/green diode lasers operating from cryogenic to room temperature. The active region in these devices was based on the (Zn,Cd)Se/ZnSe multiple quantum wells (MQW) which had earlier been actively studied as a candidate for laser medium by optical pumping techniques. We report on the performance of such MQW diode lasers with emphasis on structural versatility in terms of preparation on both p-type and n-type GaAs substrates, and where sulfur is or is not incorporated for blue/green color lasing. In this work we have obtained pulsed, high power, high quantum efficiency laser emission up to near room temperature conditions. Efficient LED devices are described which operate in the blue (494nm) at room temperature.

Recently, Park et al [1] and Ohkawa et al [2], have reported significant levels of p-doping in ZnSe using a nitrogen plasma source. The use of the nitrogen plasma source has since resulted in the realization of pn junction light emitting devices operating in the blue and blue/green portion of the spectrum such as pulsed lasers (3M [3] and Brown/Purdue [4,5]) and light emitting diode (LED) structures (Park et al [1], Purdue/Brown [6,7], Matsushita et al [8]).

The several types of laser and LED structures described in this paper include devices fabricated both with and without alloys containing sulfur. Schematic device structures are shown in Fig. 1. The ZnSe-based structures have ZnSe/(Zn,Cd)Se multiple quantum wells (MQW) inserted in a ZnSe p-n homojunction, while the Zn(S,Se)-based structures consist of Zn(S,Se)/(Zn,Cd)Se MQWs placed in a p-n homojunction formed from Zn(S,Se) layers. The Zn(S,Se)-based structures have essentially the same device configuration as the ZnSe-based configurations, except ZnSe was replaced by Zn(S,Se) with a S mole fraction of about 7%. ((In,Ga)As buffer layer is replaced by GaAs layer.) For lasing, the waveguiding is provided by the index difference between the MQW region and the adjacent binary or S-containing alloy. In an additional configuration (ZnSe-Zn(S,Se)-based structures), the ZnSe/Zn(Cd,Se) MQW region is positioned within a ZnSe region which is itself bounded by Zn(S,Se) "cladding" layers. Optical

Mat. Res. Soc. Symp. Proc. Vol. 242. © 1992 Materials Research Society

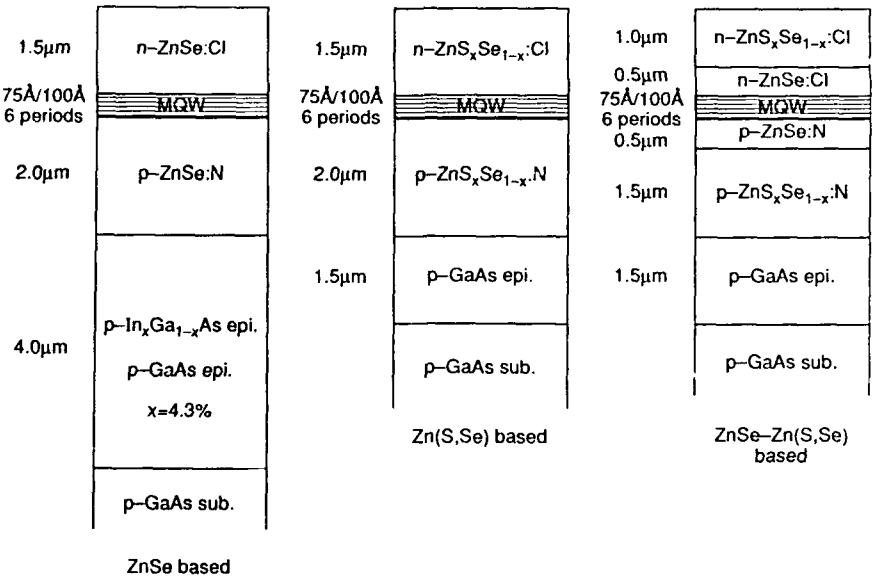


Figure 1 Schematic device structures used in this study

confinement calculations suggest that the main role of the cladding layers is the formation of a "reservoir" for carriers. Photoluminescence measurements of (Zn,Cd)Se epilayers were used to determine the Cd fraction [9]. Dislocations in all laser and LED device structures can be dramatically reduced by growing the II-VI active region on an appropriate III-V buffer layer, and in the case of the structures containing sulfur, by correct choice of the S fraction. Additional details of the microstructural analysis is included elsewhere in these proceedings [10].

All the samples were grown in a Perkin Elmer MBE system providing separate growth chambers for the II-VI and III-V epilayer growth. Devices were grown on both n and p-doped GaAs substrates. In the case of those ZnSe-based laser and LED structures, a 4μm thick (In,Ga)As buffer layer was grown at a substrate temperature of 520°C. The (In,Ga)As layers were doped n-type using PbTe [11], or p-type using Be. For the structures employing Zn(S,Se) layers, a 1.5μm GaAs buffer layer was grown (at 580°C for p-type, and 520°C for n-type) using the same dopant sources as for the (In,Ga)As. The III-V buffer layers were transferred to the II-VI growth chamber under ultra high vacuum. The II-VI structures were nucleated at 240-245°C. Elemental sources were used for Zn, Se, and Cd; the Zn(S,Se) layers were grown using a ZnS compound source in combination with appropriate Se and Zn fluxes [12,13]. The Zn, Se, and Cd source materials were supplied by Osaka Asahi; the ZnS material was provided by Sumitomo Electric. A $ZnCl_2$ source [14-16] was used for n-doping. The various flux ratios were measured using a crystal monitor placed at the substrate position. An Oxford Applied Research plasma source was used for the nitrogen doping[1,2].

{400} and {511} x-ray diffraction peaks are used to evaluate

the tetragonal distortion of the (In,Ga)As buffer layers; the lattice mismatch was only partially relaxed by misfit dislocations despite the fact that the thickness of the buffer layers was far greater than the theoretically predicted critical thickness. In cross-sectional TEM images of the (In,Ga)As epilayers, evidence of threading dislocations was found only in the regions close to the (In,Ga)As/GaAs interfaces. Plan-view imaging revealed dislocation densities in the upper parts of the (In,Ga)As buffer layers to be in the range of 10^5 cm^{-2} or lower. The dislocation densities estimated from the ZnSe-based II-VI regions grown on $In_{0.043}Ga_{0.957}As$ buffer layers were found to be in the lower range of 10^6 cm^{-2}. For the ZnSe-Zn(S,Se)-based structures, the TEM images indicated an estimated dislocation density of 10^6 cm^{-2} in the Zn(S,Se) layers, while the dislocation densities in the MQW optical gain regions were estimated at 10^7 cm^{-2}.

The Zn(S,Se)-based structures were grown with a sulfur fraction of 7%. X-ray rocking curves were obtained using a four crystal Si monochrometer. The full widths at half maxima (FWHM) of {400} x-ray diffraction peaks obtained from the $ZnS_{0.07}Se_{0.93}$ layers ranged between 20 and 55 arcsec. These values are unusually narrow for such compounds [13], but are consistent with the lack of dislocations observed in transmission electron microscopy (TEM) imaging; images of all observed areas show that the Zn(S,Se)/GaAs interfaces are free from misfit dislocations, indicating that the entire II-VI epilayer remains pseudomorphic to the GaAs buffer layer.

Previous optical studies of (Zn,Cd)Se/ZnSe quantum well structures indicated that the injection emission from both the laser and LED structures originated from the (Zn,Cd)Se MQW region [17]. The turn-on voltage (V_T) for forward conduction, typically 5 volts, but as low as about 3 volts, was found to be coincident with the observation of incoherent light emission emanating from the cleaved facets with a spectrum typical of the photoluminescence observed from the (Zn,Cd)Se quantum wells. We note that the turn on voltage for the devices having a p^+-ZnSe top layer was somewhat higher (typically ≈12 V); the difference is likely due to a larger potential barrier at the Au-contact. Although laser operation is similar for both polarities of a specific structure, the LED operation of devices formed on p-GaAs are found to be somewhat brighter than those grown on n-GaAs; the difference is attributable to the difficulty of forming an ohmic contact to p-ZnSe.

Laser device configurations (with or without S) consisted of 600 μm to 1mm long cleaved resonator structures having 20-40 μm wide stripe electrodes at the top. Indium was usually evaporated as the contact for those structures having an n^+-ZnSe top layer; gold was used to contact the p-type top layers. The structures having a Cl-doped top layer exhibit a substantial current spreading, especially at T=77 K (and below); these laser structures were fabricated in a mesa configuration. Laser emission from both the mesa and the broad area devices (the former grown on p-III-V and the latter on n-III-V epilayers, respectively) was obtained under pulsed excitation. The current pulse duration was varied from 100 to 500 nsec, with duty cycles ranging from 10^{-4} to $5x10^{-2}$. It is important to emphasize that lasing was obtained from each of the different devices

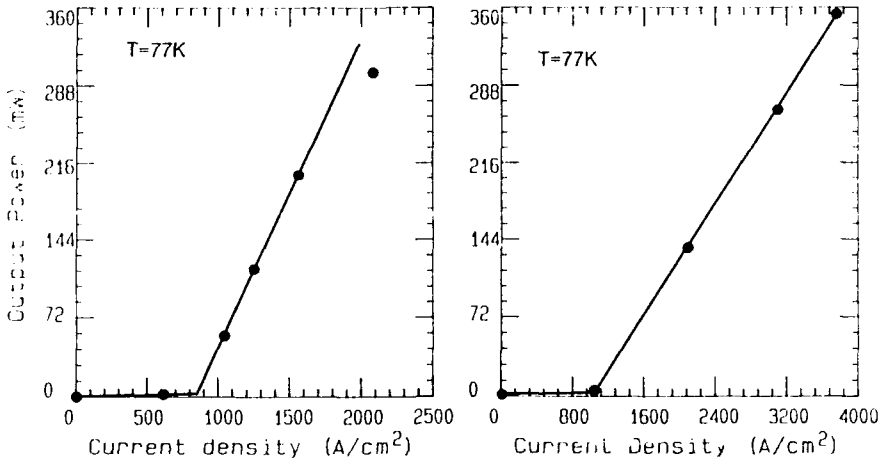


Figure 2. The figure shows the output power per (uncoated) facet as a function of injected current density for typical laser devices of both polarities at T=77K. The left one is grown on a p-type GaAs substrate, while the right one is grown on an n-type GaAs substrate.

configurations discussed in this paper, and for structures grown on both n and p-type substrates.

Figure 2 shows the output power per (uncoated) facet as a function of injected current density for typical ZnSe-Zn(S,Se) based laser devices of both polarities at T=77K. The threshold current densities for the two polarities is similar, approximately 850 A/cm^2. The differential quantum efficiency of both device polarities is rather similar and equals approximately $n_{ext} \approx 28\%$ per facet. The quantum efficiency decreases with increased temperature. At this time, the laser devices have been perated up to 250K with uncoated facets.

LED devices emitting in the blue (494nm) at room temperature were prepared by cleaving the Zn(S,Se)-based heterostructures into 2x2 mm^2 pieces which were contacted by a small indium dot ($\approx$ 500 μm in diameter). The room temperature spectrum of the Zn(S,Se) device is shown in Figure 3. Lateral transport was found to be quite effective in the present heterostructures, as was the case for previously reported display devices [18] so that LED emission over the entire front surface of the devices was uniformly visible. The optical power was measured with a optical power meter, and represents total emission in the forward 2π steradian solid angle through the entire n-Zn(S,Se) surface. The voltage applied across the entire device corresponding to the highest light output power (P = 120 μW) was V_A = 20V; however it is probable that most of this voltage is needed to overcome the built-in contact barriers in order to achieve adequate initial

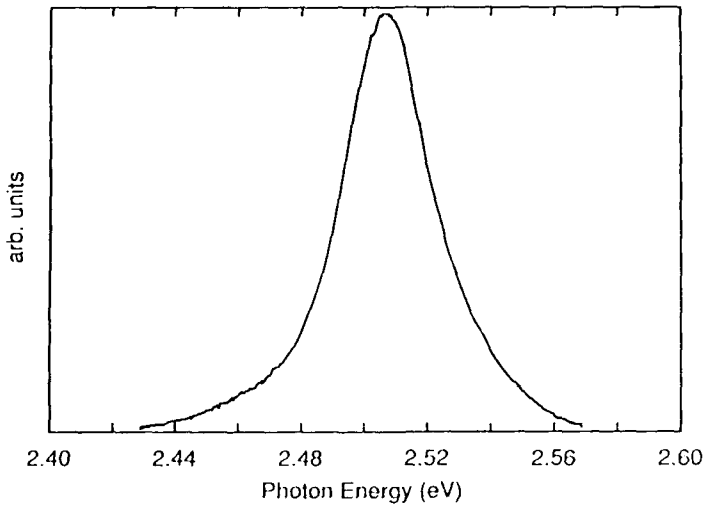


Figure 3. Room temperature electroluminescence spectrum of the Zn(S,Se) based LED.

current flow. Considerable improvement in the overall quantum efficiency can thus be anticipated when such contact problems are solved. Nonetheless, the powers are sufficient to suggest the importance of such (Zn,Cd)Se/Zn(S,Se) QW LEDs for display applications. (In the case of the ZnSe-based structures, the emission wavelengths is about 5080Å in the blue-green at room temperature.)

The authors would like to acknowledge the assistance of S. Ogino, H. Iwata, D. Li, Y. Fan, and D.A. Lubelski in the growth of the structures and M. Vaziri for assistance in Hall evaluations of Cl-doped ZnSe. The research was supported by DARPA/ONR URI grant 218-25015, and AFOSR grant AFOSR-89-0438.

References

1. R.M. Park, M.B. Troffer, C.M. Rouleau, J.M. DePuydt and M.A. Alaase, Appl. Phys. Lett. **57**, 2127 (1990).
2. K. Ohkawa, T. Karasawa, T. Mitsuyu, Japan J. of Appl. Phys. **30**, L152 (1991).
3. M. Haase, J. Qiu, J.M. DePuydt, and H. Cheng, Appl. Phys. Lett. **59**, 1273 (1991).
4. H. Jeon, J. Ding, W. Xie, D.C. Grillo, W. Patterson, M. Kobayashi, R.L. Gunshor, and A.V. Nurmikko, Appl. Phys. Lett. **59**, Dec. 1991
5. H. Jeon, J. Ding, A.V. Nurmikko, W. Xie, D.C. Grillo, M. Kobayashi, and R.L. Gunshor,to be published.
6. W. Xie, D.C. Grillo, R.L. Gunshor, M. Kobayashi, G.C. Hua, N.

Otsuka, H. Jeon, J. Ding, and A.V. Nurmikko, Appl. Phys. Lett. **60**, Jan. 27, 1992.
7. W. Xie, D.C. Grillo, R.L. Gunshor, M. Kobayashi, H. Jeon, J. Ding, A.V. Nurmikko, G.C. Hua, and N. Otsuka, (to be published)
8. T. Mitsuyu, K. Ohkawa, and O. Yamazaki, (to be published).
9. N. Samarth, H. Luo, J.K. Furdyna, R.G. Alonso, Y.R. Lee, A.K. Ramdas, S.B. Qadri, N. Otsuka, Appl. Phys. Lett. **56**(12), 1163 (1990).
10. N. Otsuka, G.C. Hua, W.Xie, D.C. Grillo, M. Kobayashi, and R.L. Gunshor (to be published elsewhere in this volume).
11 S. M. Newstead, T.M. Kerr, and C.E.C. Wood, J. Appl. Phys. **66**, 4184 (1989).
12. N. Matsumura, M. Tsubokura, J. Saraie, and Y. Yodogawa, J. Crystal Growth **86**, 311 (1988)
13. N. Matsumura, M. Tsubokura, K. Miyagawa, N. Nakamura, and J. Saraie, J. Crystal Growth **99**, 446 (1990)
14. K. Ohkawa, T. Mitsuyu, and O. Yamazaki, J. Appl. Phys. **62**, 3216 (1987).
15 H. Cheng, J. DePuydt, J. Potts and M. Haase, J. Cryst. Growth **95**, 512 (1988).
16. S. Hwang, J. Ren, K.A. Bowers, J. W. Cook, Jr., and J.F. Schetzina, Mater. Res. Soc. Symp. Proc. **161**, 133 (1990).
17. J. Ding, N. Pelekanos, A.V. Nurmikko, H. Luo, N. Samarth, J. Furdyna, Appl. Phys. Lett. **57**, 2885 (1990).
18. H. Jeon, J. Ding, A.V. Nurmikko, W. Xie, M. Kobayashi, and R.L. Gunshor, Appl. Phys. Lett. **60**, Jan. 13, 1992.

ALLOY DEPENDENT PROPERTIES OF EXCITONS AND DEEP ACCEPTORS IN CdZnTe VOLUME CRYSTALS

B. K. MEYER, D. M. HOFMANN, K. OETTINGER, W. STADLER, Al. L. EFROS, M. SALK[+] and K. W. BENZ[+]
Physik - Department E 16, Technische Universität München, James Franck Str., D - 8046 Garching, Germany
[+]Kristallographisches Institut, Universität Freiburg, Hebelstr. 25, D - 7800 Freiburg, Germany

ABSTRACT

$Cd_{1-x}Zn_xTe$ crystals grown by the travelling heater methode (THM) have been investigated by low temperature photoluminescence (PL). The excitonic energy gap as a function of the alloy composition was determined for the complete range of x = 0 to x = 1. The composition dependent broadening of the neutral acceptor bound exciton (A^oX) line was measured and compared to theoretical calculations. The Donor - Acceptor pair luminescence in the crystals is a superposition of recombinations due to residual Cu acceptors and A - centers (anion vacancy - donor pairs).

1. INTRODUCTION

The ternary II - VI compound semiconductors are direct energy gap materials with potential applications for optoelectronic devices. For $Cd_{1-x}Zn_xTe$ the energy gap is tunable from 1.5 to 2.3 eV at room temperature [1], for x = 0 and x = 1, respectively. However, applications are strongly limited up to now by severe selfcompensation mechanisms acting in the wide gap materials. It is thought to be the reason why ZnTe grows only p-type. CdTe on the other hand can be obtained p- or n-type by doping. It is therefore an interesting task to study the ternary compound $Cd_{1-x}Zn_xTe$ in view of its optical properties in order to characterize crystal quality and to study the radiative relaxation in the material. One interesting aspect is that the excitonic recombination in the ternaries show line broadening effects caused by the statistical cation (Zn, Cd) fluctuations [2].
Our investigation reports on low temperature PL results obtained in THM grown $Cd_{1-x}Zn_xTe$ crystals for the complete composition range of x = 0 to x = 1. The excitonic line broadening effects due to the alloy fluctuations have been studied in detail. The results are discussed in the framework of existing theories taking into account the detailed nature of the neutral acceptor bound exciton and considering the conduction/valence band offset between CdTe and ZnTe. The Donor - Acceptor pair recombination which causes in CdTe the prominent 1.42 eV PL band [3] has been investigated as a function of the alloy composition. The results show that the involved acceptors, Cu and A - centers, have similar properties over the complete composition range from CdTe to ZnTe.

2. EXPERIMENTAL DETAILS

The $Cd_{1-x}Zn_xTe$ crystals were grown from a CdTe seed in a Te zone with a ZnTe reservoire at 800 °C with a rate of 3mm/d. As starting materials CdTe and ZnTe from melt - and gasphase- growth were used, respectively. The undoped crystals contained as residual impurities mainly Li, P, Cu, Ag and Fe. Details of the THM growth furnace are described elsewhere [4]. By this

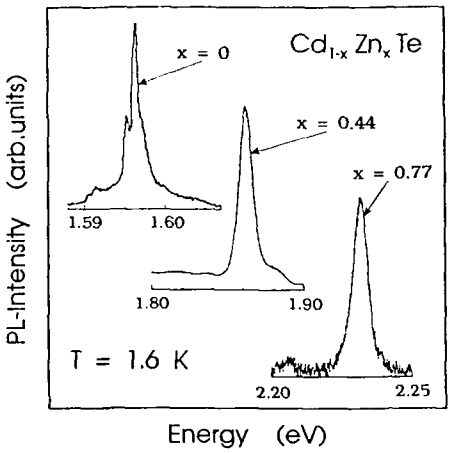


Fig. 1 :
Typical photoluminescence spectra of the excitonic regime in $Cd_{1-x}Zn_xTe$ crystals for different compositions x

technique crystals covering the complete x range are obtained in one boule. The composition of the $Cd_{1-x}Zn_xTe$ crystals was determined by dispersive analysis of x rays (EDAX), giving the x-values with an accuracy of better than 1%.
High resolution PL measurements were carried out in 90 degree geometry with the sample in contact to superfluid He at temperatures below 2 K. The PL was excited by the 514 nm line of an Ar^+ ion laser with excitation powers of less than 200 mW (unfocused beam). The PL light was analysed by 1 m double monochromator with a spectral resolution of 1 Å. For the detection a photomultiplier with S1 response or a LN_2 cooled Ge detector was used.

3. EXPERIMENTAL RESULTS AND DISKUSSION

3.1 Excitonic recombination

The excitonic band gap as well as the exciton linewidths as a function of x, were determined from PL measurements. Typical PL spectra of our samples are presented in fig.1. In the binary compound CdTe (fig. 2a) the acceptor bound exciton luminesence lines (A^oX) are found in the range from 1.591 to 1.580 eV. At higher energies weak structures due to the donor bound (D^oX) and free (X) excitons are also visible [5]. The strong A^oX lines arise from the presence of Copper, usually one of the dominant residual contaminants in volume grown CdTe and ZnTe [6] (see below). The neutral Cu bound exciton dominates in the excitonic recombinations of both binary systems. Since the Cu diffusion oefficents in both compounds are very similar, we expect that the Cu concentration differ not very muc also in the alloy samples [7]. We therefore assume that the excitonic recombination in CdZnTe is also due to the A^0X recombination of Cu. The shift of the energetic position of the A^oX lines as a function of the alloy composition x is given in fig 2a. by the full circles. The data of fig. 2a have been used to calculate the excitonic band gap variation (E_{A^oX}). The drawn line represents the best fit, with the result:

$$E(_{A^oX}) = 1.589 + (0.65\pm0.01)x + (0.19\pm0.02)x^2 \quad \text{for } T=1.6\ K. \qquad (1)$$

The obtained parameters are similar to those of previous calculations, where, however no specifications about the origin of the lines has been given [8]. In addition to the energy shift a significant broadening of the A^oX line was observed in the alloys. The linewidth amounts to 1.3 meV in

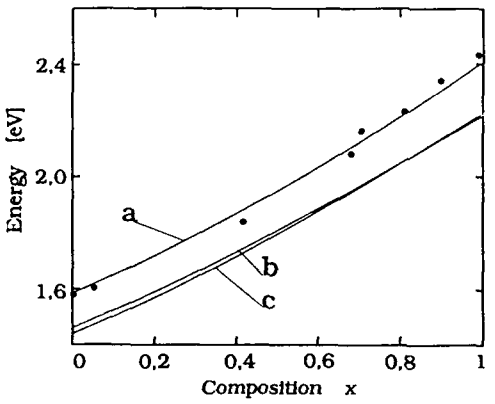


Fig. 2:
Energetic positions as a function of the alloy composition x in $Cd_{1-x}Zn_xTe$:
a) of the copper bound exciton recombination (dots: experimental values, drawn line: calculated)
b) of the A - center DAP band
c) of the Cu DAP band

both binary compounds, whereas a maximum linewidth of 10 meV is obtained for an alloy composition of x = 0.67. In fig.3 the contribution of the binary compounds (1.3 meV) has been substracted.

In the binary compounds the exciton linewidth of the volume crystals was lower by a factor of 4 compared to epitaxially grown material (usually on GaAs substrates). However, linewidths as narrow as 0.1 meV have already been reported in the literature [8,9]. A linewidth of about 10 meV seems to be the lower limit which can be obtained for highly alloyed samples ($0.3 < x < 0.6$) and it seems to be also independent of growth technique used.

Alloy broadening of the excitonic lines is caused by statistical fluctuations in the concentrations of the cations (Zn, Te). Theories describing this behaviour were developed in [2,10]. Assuming a Gaussian line shape, the broadening F of the A^oX exciton line is calculated to be [3]:

$$F(\sigma) = 1/\sqrt{2\pi}\tau \exp(-\sigma^2/2\tau^2) \qquad (2)$$

with σ the variance and τ the broadening parameter which is depends on the type of the electron - hole movement within the A^oX complex. A model for the description of such A^oX complex is the "pseudo-donor" model which proposes, that the two holes of the A^oX complex form a A^+ center with an extension smaller than the electron Bohr radius a_e. In this case, the electron attracted by the A^+ centers moves around the holes as in a hydrogen like atom with a radius $a_e = \epsilon\hbar^2/m_e e^2$ (m_e is the electron effective mass and ϵ the static dielectric constant). The binding energy of this A^oX complex E_{AX} is equal to the sum of the binding energies of the second hole bound to the neutral acceptor E_{2h} and the hydrogen-like donor binding energy $E_e = e^4 m_e/2\hbar^2\epsilon^2$:

$$E_{AX} = E_{2h} + E_e$$

The holes and the electron bound to this complex give independent contributions to the linewidth, because their ranges of movement differ significantly. They can be considered independently. In this case the alloy broadening is given by:

$$\delta E = 2\sqrt{2\ln 2}\,\tau = 2.35 \frac{dE_g}{dx}\left[\frac{x(x-1)}{8\pi K}\right]^{1/2} * \left[\frac{\delta_c}{a_e^{3/2}} + \frac{\delta_v}{a_{2h}^{3/2}}\right]^3 \qquad (3)$$

Where the symbols have the following meanings $K = 4(a_o)^{-3}$ is the cation density, a_o is the lattice constant, δ_c and δ_v are the relative band offsets of the conduction and valence band ($\delta_c = 0.88$ and $\delta_v = 0.12$ [11]) and a_{2h} is the radius of the second hole.

The radius of the second hole bound to the neutral acceptor a_{2h} (i. e. the radius of the A^+ center) is known in two limiting cases. For *deep* acceptors this radius is equal to the radius of the first hole $a_o = \hbar/\sqrt{2m_h E_o}$ [12],

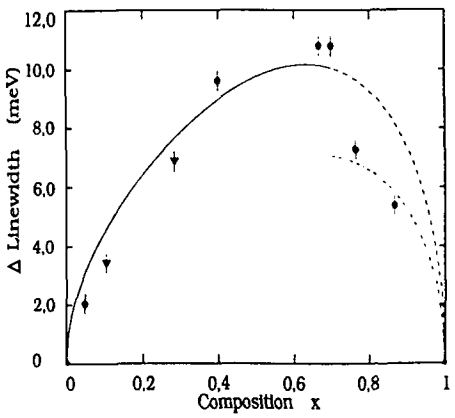


Fig. 3:
Excitonic line broadening as a function of the alloy composition x of $Cd_{1-x}Zn_xTe$ (full circles: experimental values, triangles: values taken from ref. [10], drawn and dashed dotted line : calculations, for details see text)

where E_o is the binding energy of the deep acceptor and m_h is the effective mass for heavy holes. For Cu in CdTe this radius is $a_o \approx 6.6$ Å.
For a *hydrogen* like A^+ center both holes can also occupy one orbit with a radius approximately two times larger ($1/0.483$) compared to the Bohr radius a_{hh} of heavy holes $a_{hh} = \hbar^2\epsilon/m_h e^2$ [13]. In CdTe $2a_{hh}$ is approx. 17.2Å. For our case where the binding energy of the Cu acceptor (E_o = 149 meV) is comparable to the binding enery of the shallow acceptors, E_{hh} = 37.7 meV we use an intermediate approximation $a_h = a_o/0.483 \approx 13.2$ Å.
The electron Bohr radius in equ. 3 depends on the alloy composition x through m_e and the dielectric constant, for which we used linear interpolations between CdTe and ZnTe The drawn line in fig. 3 shows the result of the calculations for the "pseudo donor" model in the alloy system. One can see that it gives good agreement with the experimental data for x up to 0.7. However, the model cannot explain the significant deviation for compositions x > 0.7. Here an abrupt decrease of the linewidth is observed from δE = 9.5 meV at x = 0.7 to δE = 6.0 meV at x = 0.77.
A mechanism which could decrease the expected alloy broadening is clustering of the Zn cations, which might have happen due to the special growth of our samples at high x values. For clusters formed by n Zn cations the alloy broadened linewidth should decrease as $\sqrt{n}$. Including this mechanism in "pseudo - donor" model would require clusters with twice as much Zn ions to explain the experimental data for x > 0.7 (dashed dotted line in fig. 3). Scanning tunneling microscpy investigations are under the way to clarify this point.

3.2 Donor - Acceptor - Pair (DAP) Luminescence

One of the prominent DAP Luminescence bands in CdTe has its peak maximum at 1.42 eV and is is structured by LO phonon replica with 21 meV energy separation (see fig.4). It originates from the recombination of shallow donors and intermediate deep acceptors. The nature of the acceptors involved has been debated widely whether they are due to intrinsic defects or residual impurities. It has been shown that Cu gives rise to a "1.42 eV" luminescence band in CdTe. The Cu acceptor binding energy has been determined to be E_a = 145 meV and the intensity of the PL is given by a Poission distribution:

$$I(n) = e^{-S}(S^n/n!) \qquad (4)$$

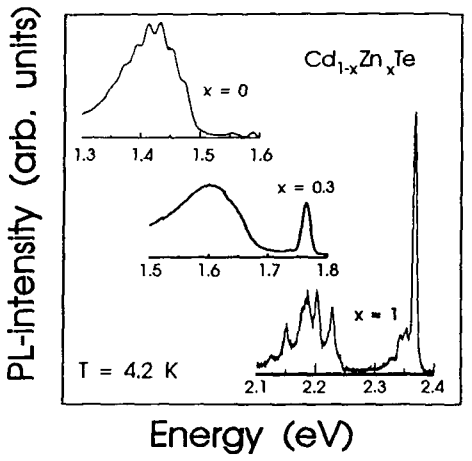


Fig. 4:
Donor - Acceptor - Pair (DAP) luminescence of $Cd_{1-x}Zn_xTe$ crystals for different compositions x

with a Huang-Rhys factor of S = 1.6 [6] and n the numbers of phonons emitted. In a recent study [14] it has been shown that also A - centers, Cd vacancy - donor pairs acting as single acceptors, give rise to a "1.42 eV" PL band in CdTe. The Clorine A - center has a binding energy and Huang Rhys factor of E_a = 120meV and S = 2.2, respectively. A detailed analysis of "1.42 eV" PL lineshape in our CdTe shows that the observed spectrum can be reconstructed by the presence of both defects, Cu and A - centers. For the calculation we assumed a linewidth of 20 meV the Zero Phonon Line (ZPL) and the phonon replicas, the position of the ZPL is given by $E(h\nu) = E_{gap} - E_a - E_d$, neglecting Coulombic effects in undoped material. E_d is the shallow donor binding energy of 14 meV in CdTe.

The DAP band in ZnTe can be reconstructed in a similar way by a superposition of the Cu and A - center spectrum. In this case we used E_d = 17 meV and for the LO phonon energy 26 meV [1]. The lineshape of the ZnTe DAP band of fig.4 is well reconstructed when energies of E_a = 150 meV for the Cu acceptor, and E_a = 160 meV for the A - center were taken. For the Cu acceptor this value is in close agreement to the PL data of ref. [7] (E_a= 149 meV). The binding energy for A - center (Cd vacancy - Al donor) has been determined to be 170 meV from ODMR investigations [15] compared to our value of 160 meV.

In the alloyed samples this analysis is much more complicated because the phonon structure becomes less significant it is completely absent in the composition range from x > 0.2 to x < 0.8 (see fig. 4). However, the observation of a broad DAP band in each of these alloy samples indicates that both defects, Cu and A - centers, are still present. The energy shift of both Cu and A - center DAP bands in the alloy is consistent with our calculations and included in fig. 2.

It should be noted that the binding energy of Cu is almost independent of the host, 145 meV for CdTe and 149 meV for ZnTe, this is expected for 3d transition metal impurities from theory [16]. Whereas the A - center binding energy changes about 25 % from ZnTe to CdTe. Assuming that the Cd - vacancy is the dominating part of the A - center, the wavefunction is set up from the dangling bonds of the Te neighbors. In the undistorted lattice the valence band is set up mainly from the Te 4p - wavefunctions, the energy shift of the vacancy levels is therefore expected to be roughly the same as that of the valence band from one compound to the other. As shown in the previous section the valence band shift amounts to 12% of the total energy gap shift from CdTe to ZnTe. This is only half the value obtained for the A - center but shows the correct trend. The deviation from this simple model

may be partly explained by the more complex nature of the A - center including a nearby donor.

CONCLUSIONS

In conclusion excitonic line broadening has been observed on the copper bound exciton recombination in bulk grown $Cd_{1-x}Zn_xTe$ crystals. The alloy composition dependence is properly described by models taking into account statistical fluctuations of the cation density, the nature of the exciton recombination (pseudo-donor model) and the conduction/valence band offset in this system. The Donor - Acceptor pair luminescence in the crystals is a superposition of recombinations due to residual Cu acceptors and A - centers (anion vacancy - donor pairs). It has been investigated as a function of the alloy composition x.

ACKNOWLEDGEMENT

This investigation was supported by the Deutsche Forschungsgemeinschaft under contract Be 896/3-1.

REFERENCES

[1] Landolt-Börnstein, Neue Serie Band 17, Ed. O. Madelung, M.Schulz, H. Weiss (Springer-Verlag Berlin 1982)
[2] N. N. Ablyazov, M. E. Raikh, and Al. L. Efros, Sov. Phys. Solid State, 25, 199 (1983)
[3] C. B. Norris and C. E. Barnes, Rev. Phys. Appl., 12, 219 (1977)
[4] P. Sikinger, W. Hofer, Dissertation 1990, Freiburg, Germany
[5] J. M. Francou, K. Saminadayar and J. L. Pautrat, Phys. Rev., B 41, 12035 (1990)
[6] E. Molva, J. P. Chamonal and J. L. Pautrat, Phys. Stat. Sol.B, 109, 635 (1983)
[7] E. Molva, J. L. Pautrat, K. Saminadayar, G. Milchberg, and N. Magnea, Phys. Rev. B 30, 3344 (1984)
[8] D. J. Olego, J. P. Faurie, S. Sivanathan, and P. M. Raccah, Appl. Phys. Lett., 47, 1172 (1985)
[9] E. Cohen, R. A. Street, and A. Muranevich, Phys. Rev., B 28, 7115 (1983)
[10] E. F. Schubert et al, Phys. Rev., B 30, 813 (1984)
[11] Tran Minh Duc, C. Hsu, and J. P. Faurie, Phys. Rev. Let. 58, 1127 (1987)
[12] N.S. Averkiev et al, Sov. Phys. Semicond., 13, 96 (1985)
[13] B. L. Gelmont, A. V. Rodin and Al.L.Efros, Sov. Phys. Semicond., 24, 120 (1990)
[14] D. M. Hofmann, P. Omling et al, Materials Science Forum, Vol. 87, (Trans Tech Publ.) p.1235 (1991)
[15] J. Bittebierre and R. T. Cox, Phys. Rev., B 34, 2360 (1986)
[16] J. M. Langer and H. Heinrich, Phys. Rev. Lett., 55, 1414 (1985)

CHARACTERIZATION OF ZnS LAYERS GROWN BY MOCVD FOR THIN FILM ELECTROLUMINESCENCE (TFEL) DEVICES.

J.E. YU*, K.S. JONES*, J. FANG*, P.H. HOLLOWAY*;
B. PATHANGEY†, E. BRETSCHNEIDER†, T.J. ANDERSON†
*Department of Materials Science & Engineering, University of Florida, Gainesville, FL 32611
†Department of Chemical Engineering, University of Florida, Gainesville, FL 32611

ABSTRACT

We have characterized MOCVD grown ZnS layers for thin film electroluminescence (TFEL) devices. Films with thicknesses ranged from several Å to 2 μm were studied by x-ray diffractometry (XRD), cross-sectional transmission electron microscopy (XTEM), high-resolution transmission electron microscopy (HRTEM), and ultraviolet-visible photospectrometry (UVS). From HRTEM micrographs, it was observed that ZnS films consist of a mixture of hexagonal and cubic phases. Correlation of UV absorption spectra with XRD analysis resulted in a method for quantitative determination of the cubic packing fraction of polymorphic ZnS films. The initial ZnS layer (< 1000 Å) deposited on $BaTa_2O_6$ had more hexagonal than cubic phase because of denser crystal defects. However, the fraction of cubic phase increased with the film thickness. In addition to film microstructures, the mean grain size, growth rate, film uniformity, and surface roughness of MOCVD grown ZnS thin films as functions of film thicknesses and substrate te...peratures were also calibrated by XTEM results.

INTRODUCTION

A major obstacle for developing ZnS EL full color flat panel displays is that the insufficient intensity of blue light emission (two orders of magnitude lower than that of red or green emission) [1]. Many studies have been performed in order to improve the intensity of the blue light emission [1-4]. They include, for example, using 1) better electroluminescent impurities, e.g. Tm, rather than Al, Ag, etc.; 2) new growth methods, e.g. ALE or MOCVD, rather than sputtering or e-beam evaporation; 3) alternative host compounds, e.g. CaS or SrS, rather than ZnS; and 4) advanced doping methods, e.g. ion implantation, rather than in-situ doping. One of the possible reasons for poor blue EL emission is the loss of hot electrons to crystal defects within ZnS thin films [5]. In addition, a faint luminescence layer appears to result from an existence of a fine grain regime formed during the initial deposition of the ZnS film on an insulating layer [6,7]. It was also reported that hexagonal ZnS is favorable for electroluminescence centers [8]. Thus, the ability to control and characterize the film microstructure appears essential to improved intensity.

In this study, the structure of ZnS layers grown by MOCVD on insulator/ITO/glass substrates was characterized by a variety of techniques.

EXPERIMENTAL

ZnS Thin Film Growth

A modified Spire Model SPI-MOCVD 450 system was used to grow ZnS thin films on $BaTa_2O_6$/ITO/glass substrates provided by Planar System, Inc.. The growth parameters used in this study are listed below:

- Precursors: diethylzinc (DEZ) and H_2S
- Substrate temperature: 250, 300, 350, and 400 °C
- Growth time: varied from several seconds to 30 min.
- VI / II ratio: 100
- Reactor pressure: 80 Torr

Material Characterization

A Philips ADP 3600 X-ray Diffractometer was used to determine the crystal structure of ZnS films. Since it was found that the ZnS films consist of both cubic and hexagonal regions, the

determination of their crystal structures was difficult. The principal problem is that for every reflection from the cubic phase there exists one or more hexagonal phase with a very similar reflection. A 4-crystal high-resolution XRD system was also tried to distinguish the small difference in interplanar spacings between these crystal structures. However, this did not work due to the low x-ray intensity and the polycrystalline nature of the film. There was a x-ray technique using the intensity that allows one to estimate the cubic fraction [9]. In addition, TEM and HRTEM were used to characterize the microstructures and to calibrate film growth characteristics. A JEOL 200CX TEM and a JEOL 4000FX HRTEM were used. Most of the samples were examined in cross section. The UVS was used to measured the *absorption edge* and therefore the energy gaps of ZnS films from UV absorption spectra. From these results the different phases within the polymorphic ZnS films could be distinguished due to their larger difference in the energy gaps, i.e. 3.54 eV and 3.67 eV for cubic and hexagonal phase at room temperature, respectively [10].

RESULTS AND DISCUSSION

Film Microstructures

1. Polymorphic structure: The first problem encountered in microstructure studies was how to distinguish the different crystal structures in polymorphic ZnS films grown by MOCVD. It had been reported that ZnS films grown by MOCVD using H_2S as the group VI precursor had a cubic structure and, in some cases, a mixture of cubic and hexagonal structures [11,12]. Usually, XRD was the major characterization technique used to identify the film crystal structure. However, it appears to be not possible to distinguish these two similar structures by XRD alone since there are always several hexagonal related diffraction peaks at the same angle as every significant peak of the cubic phase [13,14]. The XRD spectra of different thickness ZnS films grown by MOCVD under the stated conditions are shown in Figure 1 and the possible indices of each peak are listed in Table I. The film thickness of each sample was calibrated by XTEM. It is very difficult to make any conclusion as to the crystal structure of these films since peaks of both structures almost overlap.

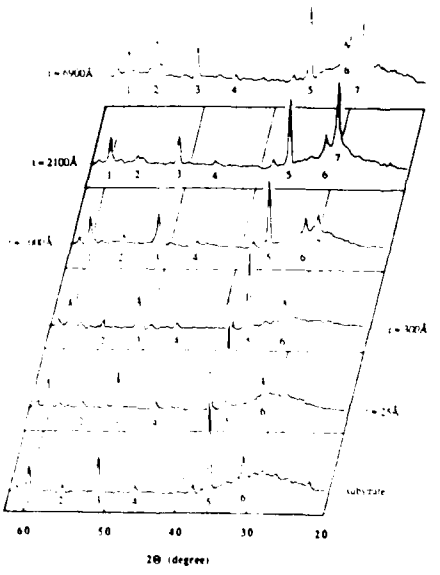


Figure 1 The XRD spectra of different thickness ZnS films grown at 350°C

Table 1 The possible ZnS indices of the major peaks observed in Figure 1

PEAK	d(Å)	$BaTa_2O_6$		3C	2H	4H	6H	8H	10H	9R	15R	21R
1	1.534	622*	—	222	00.4	00.8	00.12	—	—	20.6	20.10	20.14
2	1.631	—	—	311	11.2	11.4	11.6	11.8	11.10	20.3	20.5	20.7
3	1.799	402*	052†	—	—	—	—	—	—	—	11.9	—
4	1.993	—	—	—	—	10.5	—	10.10	—	—	—	—
5	2.542	511*	—	—	—	—	—	—	10.8	—	—	—
6	2.930	430*	410†	—	10.1	10.2	10.3	10.4	10.5	—	—	—
7	3.114	—	—	111	00.2	00.4	00.6	00.8	00.10	10.3	10.5	10.7

Data from JCPDS-ICDD and [9,15]; * Hexagonal; † Orthorhombic

A significant peak (number 7), which could be identified as (111) cubic or (00.1) hexagonal, emerged when the ZnS film was thicker than 1000 Å. When the film became thicker, an additional peak (number 2) became more intense. This peak could be identified as (311) cubic or (11.1) hexagonal. From these direct XRD results, the crystal structure evolution during the initial ZnS growth on $BaTa_2O_6$ was revealed though the crystal structure in term of cubic or hexagonal could not be distinguished unambiguously. As previous discussion, there was a reported method to determine the fraction of each structure using XRD technique. This is based on the fact that the relative ratio of the integrated intensities of hexagonal peaks to that of cubic (111) peak is proportional to their fraction in mixed crystals [9]. Using this technique, we have determined the cubic fraction of ZnS films grown by MOCVD and found it was between 40% to 60% depending upon their thicknesses and growth temperatures. These results were also correlated to the energy gap determination which will be discused later.

The ZnS polytypism could be identified from HRTEM micrographs showing the periodicity of the layer stacking [16]. The multiple stacking periodicity of the closed-packing layers in a MOCVD grown ZnS film was observed (Figure 2). In these HRTEM micrographs, there are regimes of cubic and hexagonal phases, for example, 6H structure.

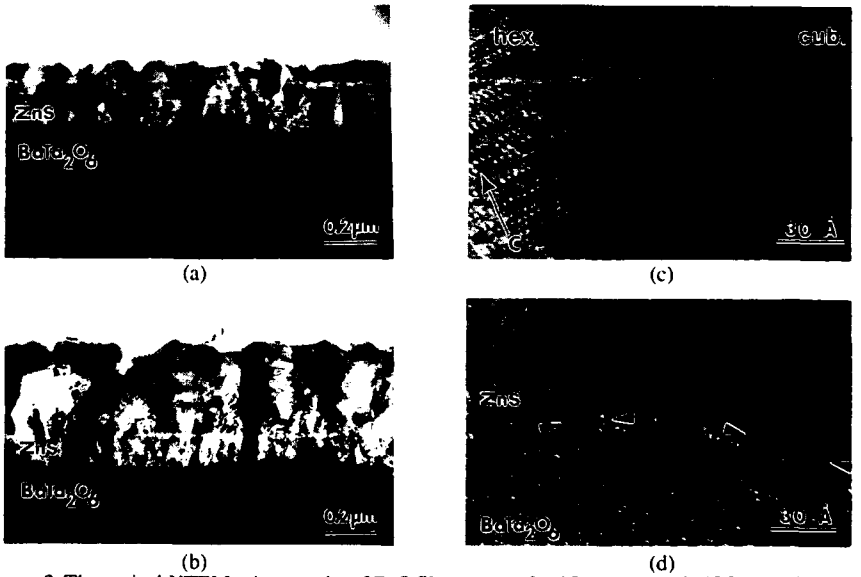


Figure 2 The typical XTEM micrographs of ZnS films grown for 15 min. (a) at 250°C (b) at 300°C and the HRTEM micrographs of (c) the bulk of ZnS films (d) the interface of ZnS/$BaTa_2O_6$

In addition, the polymorphic crystal structures were distinguished from their energy gap measured at room temperature by optical techniques. It was found that the measured absorption edges varied with the mean film thickness. As the mean film thickness increased from 700 Å to 6000 Å, the wavelength of the absorption edge of ZnS films grown at 350°C increased from 333.0 nm to 335.7 nm, respectively. They correspond to a shift of the energy gap from 3.72 eV to 3.69 eV as shown in Figure 3. The measured absorption edges were also affected by film growth temperatures. For films with a similar thickness, for example approximate 2000 Å, the wavelength of the absorption edge of ZnS films increased with the growth temperature.

It was reported that the shift of energy gaps of ZnS films could be related to their *cubic packing fraction*, a ratio of zincblende to wurtzite crystal structure of a mixed material [17-19]. Figure 4 shows the correlated results of the cubic fraction determined by XRD and the energy gap measured by optical *absorption* . This method was not only able to distinguish these different structures in ZnS but also to determine the fraction of each phase in the mixed structure. Based on these measurements, the crystal structure of ZnS films grown by MOCVD increases in the fraction of cubic phase with increasing the film thickness. Also shown are reports by other groups using *reflectance* measurements alone (the determination of cubic fraction not present) on a line drawn between the cubic and hexagonal energy gaps. Although all results show the same tendance, their discrepancy may be due to the different techniques used to measure the bandgap and cubic fraction.

2. Interface: The observation of the fine grain layer of ZnS films in EL thin films is very common [6,20]. This had been attributed to the so called "dead layer" in electroluminescence and one of the causes of higher threshold voltages for luminescent emission. To date for published works MOCVD grown ZnS EL films without a dead layer were grown by using DES or CS_2 as sulfur precursor. However, ZnS thin films grown by using H_2S always had the dead layer [12,20].

A fine grain layer extended from the ZnS/$BaTa_2O_6$ interface up to approximate 1000~2000 Å above which columnar grains became larger (Figure 2a,b). It was interesting that this coincided with the thickness below which no significant preferential orientation, i.e. (111) or (00.1), was observed in the XRD results and all peaks resemble that of the substrate materials. The interface between a ZnS film and an insulating $BaTa_2O_6$ layer had been examined by HRTEM (Figure 2d). It was observed that small regimes (indicated with arrows) of ZnS aligned on preferred orientations of the crystalline $BaTa_2O_6$ indicating some *nucleation* by the insulator. In addition, very fine "clusters" which were slightly misorientated to each others were also observed in some interfacial regions as well as the initial layer. Thus, within the initial ZnS layer deposited on $BaTa_2O_6$ denser crystal defects appear to associate with a higher fraction of hexagonal phase observed.

Growth Characteristics

The growth characteristics were calibrated using cross-sectional TEM micrographs. They include the mean grain size, growth rate, film uniformity, and surface roughness as functions of film thicknesses and substrate temperatures. In the sample grown at 350°C for only 1 second, no ZnS island or layer could be identified on the surface of the $BaTa_2O_6$ substrate. After 5 seconds of growth, small islands about 20~30 Å height and 5~10 Å wide were observed. The separation between islands was approximately 30~100 Å.

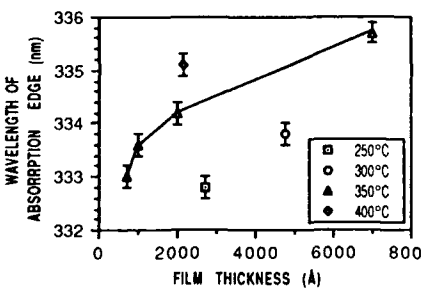


Figure 3 The wavelength of the absorption edge varied with the ZnS film thickness and substrate temperature

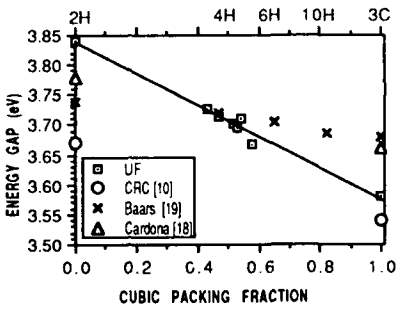


Figure 4 The relationship between the cubic packing fraction and the energy gap of ZnS films

1. Grain size: The mean size of columnar grains increased from approximate 500 Å at the interface up to 3000 Å when the film thickness was greater than 0.7 μm (Figure 5a). The substrate temperature slight affected the mean grain size. In Figure 5b, the mean grain size at the interfacial region did not vary significantly with the substrate temperature. This could be attributed to the effect of the grain size of the insulating $BaTa_2O_6$ substrate layer. The mean grain size at a region about 0.2 μm from the interface was larger than that at the interface and also did not vary significantly with the substrate temperature. However, the grain size distribution as indicated as the error bar was different.

2. Growth rate: The growth rate was determined from Figure 6. It was found that the growth rate was slower during the first two minutes of growth. Subsequently, it became greater slightly. This phenomenon appears to be related to the evolution of the film structures as discussed previously.

3. Film uniformity: Generally, the film thickness varied across an entire sample. This was indicated by the error bar as shown in Figure 6. The thicker films exhibited a greater variation in uniformity. This appears to be due to the facet growth and the greater grain size. The film thickness variation was < ±15 % of the total film thickness.

4. Surface roughness: The surface roughness was measured as the surface peak-to-valley height on average as shown in Figure 7. When a film was thinner than 1000 Å, the surface roughness was smaller than 100 Å. For a thicker ZnS film, the surface roughness increased several fold. Significant surface faceting caused the increased roughness. The surface roughness was about 6~10 % of the total film thickness.

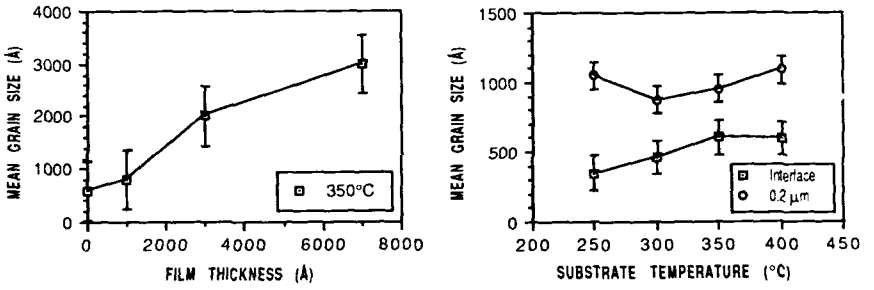


Figure 5 The mean grain size of ZnS films (a) varied with film thicknesses (b) as a function of the substrate temperature

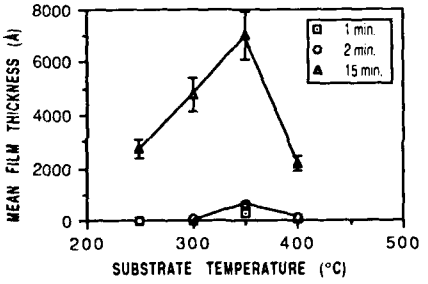


Figure 6 The film thickness as a function of the substrate temperature for films grown for different time periods

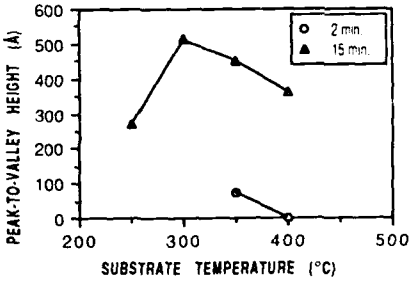


Figure 7 The surface roughness measured as the surface peak-to-valley height for films grown at different temperatures

SUMMARY

In summary, we have presented several results of the structure of the ZnS thin films grown by MOCVD. Multiple characterization techniques, including XRD, TEM, HRTEM,and UVS, have been used to analyze this materials system. From HRTEM micrographs, several different crystal structures, such as 3C, 6H etc., have been observed. It was shown that the cubic packing fraction could be estimated from the relative ratio of the integrated intensities of cubic phase to that of hexagonal phase. The measurements of the room temperature energy gaps of ZnS films by UV absorption provide a more convenient way to identify the polymorphic structures. Correlating the absorption and x-ray measurements made it possible to deduced a linear relationship between the cubic packing fraction and the energy gap of polymorphic ZnS thin films. In addition, the mean grain size, growth rate, film uniformity, and surface roughness of MOCVD grown ZnS films were calibrated using XTEM micrographs. It was found that initially ZnS films grew at a slower rate which increased as the film thickness increased. The nonuniformity and surface roughness also increased with thickness. There was a little dependence of the mean grain size on the growth temperature where as the growth rate was maximized at 350°C.

ACKNOWLEDGMENTS

The authors gratefully acknowledge Planar System, Inc. for providing us TFEL substrates. This work was supported by Florida High Technology and Industry Council.

REFERENCES

1. R. Mach and G.O. Muller, phys. stat. sol. (a) 69, 11 (1982)
2. V.-P. Tanninen, M. Oikkonen, and T. Tuomi, Thin Solid Films 109, 283 (1983)
3. P.J. Dean, phys. stat. sol. (a) 81, 625 (1984)
4. V.V. Ushakov and A.A. Gippius, J. Crystal Growth 101, 458 (1990)
5. Research report of SPIRE Co., FR-60174, 1990
6. H. Venghaus, D. Theis, H. Oppolzer, and S. Schild, J. Appl. Phys. 53(6), 4146 (1982)
7. D. Theis, H. Oppolzer, G. Ebbinghaus, and S. Schild, J. Crystal Growth 63, 47 (1983)
8. T. Buch, phys. stat. sol. (b) 150, 191 (1988)
9. F.G. Smith, American Mineralogist 40, 658 (1955)
10. D. R. Lide ed., HANDBOOK of CHEMICAL AND PHYSICS, 71st ed.(CRC press, Boston 1990), p. E110
11. K. Hirabayashi and O. Koqure, Jpn. J. Appl. Phys. 24(11), 1484 (1985)
12. T. Shibata, K. Hirabayashi, H. Kozawaquchi, and B. Tsjiyama, Jpn. J. Appl. Phys. 26(10), L1664 (1987)
13. T. Matsuoka, J. Kuwata, M. Nishikawa, Y. Fujita, T. Tohda, and A. Abe, Jpn. J. Appl. Phys. 27(4), 592 (1988)
14. S. Takata, T. Minami, T. Miyata, and H. Nanto, J. Crystal Growth 86, 257(1988)
15. H.T. Evans,Jr. and E.T. McKnight, American Mineralogist 44, 1210 (1959)
16. W. Coene, H. Bender, F.C. Lovey, D. van Dyck, and S. Amelinckx, phys. stat. sol. (a) 87, 483 (1985)
17. J.A. Lahtinen and T. Tuomi, J. de Physique C10, 239 (1983)
18. M. Cardona and G. Harbeke, Phys. Rev. 137, 1467 (1965)
19. J.W. Baars in Proc. of the Intern. Conf. on II-VI Semiconducting Compounds, Providence (1967), pp. 631
20. K. Hirabayashi and H. Kozawaguchi, Jpn. J. Appl. Phys. 28(5), 814 (1989)

GROWTH AND CHARACTERIZATION OF ZnSe/ZnCdSe DIODE STRUCTURES ON (In,Ga)As BUFFER LAYERS.

G. C. Hua and N. Otsuka
School of Materials Engineering, Purdue University, West Lafayette, IN 47907

W. Xie, D. C. Grillo, M. Kobayashi and R. L. Gunshor
School of Electrical Engineering, Purdue University, West Lafayette, IN 47907

ABSTRACT

ZnSe/ZnCdSe diode structures were grown on (In,Ga)As buffer layers by molecular beam epitaxy. Lattice distortions and defect distributions in buffer layers and diode structures were examined by X-ray diffraction and transmission electron microscopy. Diode structrues with low dislocation densities were obtained by the growth on tetragonally distorted $In_{0.043}Ga_{0.957}As$ buffer layers, the lattice spacing of which is slightly smaller than that of ZnSe.

ZnSe has long been considered as the leading candidate of materials for development of light emitting devices operating in the blue and green spectrum ranges. Difficulty in obtaining conductive p-type of this material, however, has prevented progress towards the realization of such optoelectronic devices. In the past decade, new low temperature epitaxial growth techniques represented by molecular beam epitaxy (MBE) and metallorganic chemical vapor deposition (MOCVD) have led to the resurgence in the research of ZnSe and other wide gap II-VI semiconductors with the expectation that the advantage of employing these epitaxial growth techniques may enable us to overcome the afore-mentioned material problem. These research efforts have resulted in successful p-doping in ZnSe using a nitrogen plasma source in MBE in the last year [1,2], and very recently have led to the realization of ZnSe based p-n junction light emitting devices such as pulse lasers [3-5] and multiple quantum well light emitting devices [6]. It is expected that these recent developments will open a new stage of the research on wide-gap II-VI semiconductors aimed at their full device applications.

One of the major problems to be solved for further progress towards the development of ZnSe-based devices is the formation of high density defects in epilayers which results from the lattice mismatch between ZnSe and GaAs; GaAs is widely used as a substrate for the growth of ZnSe at present owing to the unavailability of high quality ZnSe bulk single crystals. With the lattice mismatch being 0.25% (room temperature), pseudomorphic ZnSe layers can be grown on a GaAs substrate only up to thicknesses around 2000Å which is too

thin for realistic device structures. In the past several years, a number of methods have been developed for reduction of defect densities in lattice mismatched layered structures of III-V and elemental semiconductors. Direct applications of those methods to II-VI semiconductors, however, may not lead to sucessful control of defect densities because of considerable differences in mechanical properties of these materials from those of III-V and elemental semiconductors. In the present paper, we report an approach for overcoming the problem of the defect formation caused by the lattice mismatch between ZnSe and GaAs. By utilizing a MBE system having separate growth chambers, ZnSe/ZnCdSe diode structures were grown on (In,Ga)As buffer layers. Addition of In to GaAs crystals is known to make the alloy crystals highly resistive to the generation and multiplication of dislocations [7,8]. The (In,Ga)As buffer layers with the proper control of the In mole fraction, therefore, are expected to serve as lattice-matched substrates having very low defect densities for the growth of ZnSe-based structures.

All structures examined in this study were grown in a Perkin Elmer modular MBE system consisting of separate growth chambers for the II-VI and III-V layer growth. (In,Ga)As buffer layers with a thickness of 4μm were grown on (100) GaAs at 520^0C. The In mole fractions in the buffer layers were varied among samples over the range from 4 to 6%. After the buffer layers were transferred to the II-VI growth chamber under ultra-high vacuum, ZnSe diode sturctures with ZnCdSe quantum wells were grown at 240^0C. The total thickness of diode structures are typically 3.5μm. Quantum well structures consist of several layers of ZnCdSe and ZnSe with individual layer thicknesses ranging from 60Å to 100Å. Nitrogen and chlorine were doped in diode structures as acceptors and donors, respectively. Details of growth procedures of these structures are described in a separate report [6].

X-ray rocking curves of diode structures and (In,Ga)As buffer layers were obtained using a four crystal Si monochromator with the Cu K_α radiation. For the examination of buffer layers, diode structures were removed by selective etching. Both (400) and {511} diffraction peaks were recorded in order to determine the lattice spacings in the directions parallel and perpendicular to the interfaces. Full width at half maximum (FWHM) of (400) peaks of (In,Ga)As buffer layers ranges from 100 to 150 seconds. These values are in good agreement with the results of earlier studies which measured FWHM of (In,Ga)As layers grown on GaAs by MBE [9,10]. From the analysis of {511} peaks, the crystal lattices of (In,Ga)As buffer layers were found to be tetragonally distorted, implying that the lattice mismatch at (In,Ga)As/GaAs interfaces are partially relaxed by misfit dislocations. The estimated values of the c/a ratios of tetragonally distorted lattices range from 1.0010 to 1.0012. The In mole fractions in the buffer layers were estimated from measured lattice spacing by taking the tetragonal distortion into account, and assuming a Vegard's relationship. The FWHM of ZnSe in diode structures also range from 100 to 150 seconds. Unlike the (In,Ga)As buffer layers, no significant tetragonal distortion was observed by the analysis of {511} peaks of diode structures.

Defect distributions in the samples were examined by a JEM 2000EX transmission electron microscope (TEM). For the observation, cross-sectional and plan-view specimens were prepared by ion-thinning. Highly developed networks of misfit dislocations were observed at (In,Ga)As/GaAs interfaces of all observed samples. Figure 1 is a cross-sectional bright field image of an

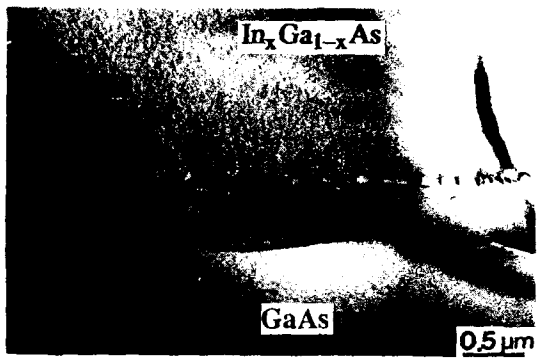


Fig. 1 Cross-sectional bright field image of the $In_{0.054}Ga_{0.946}As$/GaAs interface.

$In_{0.054}Ga_{0.946}As$/GaAs interface. This image was taken by tilting the specimen about the [011] axis, so that misfit dislocations parallel to the [011] axis are seen as short segments in the image. As seen in the cross-sectional image, dislocations have threaded towards the GaAs crystal from the interface, while the interior of the (In,Ga)As buffer layer remains as a dislocation-free crystal. This observation clearly shows the difficulty of generation and multiplication of dislocations in (In,Ga)As crystals. In plan-view images of the buffer layers, no dislocation was observed except for the region close to (In,Ga)As/GaAs interfaces, implying that dislocation densities in the buffer layers are less that 10^5 cm^{-2}. Such low dislocation densities appear to contradict large FWHM of X-ray diffraction peaks obtained from these buffer layers. According to a simplified relationship between FWHM of X-ray diffraction peaks and dislocation densities, the measured FWHM corresponds to dislocation densities in the range of 10^7 cm^{-2} [11], which is significantly greater than the observed densities. One possible explanation for this apparent discrepancy is that the large FWHM results from a nonuniform distribution of elastic strains in the buffer layer which is caused by the large variation of spacing of misfit dislocations at the (In,Ga)As/GaAs interface. A more systematic analysis, however, is necessary to substantiate this explanation.

Figure 2 (a) and (b) are cross-sectional bright field images of ZnSe/(In,Ga)As interfaces with two different In mole fractions in the buffer layers. At the ZnSe/$In_{0.040}Ga_{0.960}As$ interface, closely spaced misfit dislocations are seen, even though the lattice parameter of a bulk (In,Ga)As crystal with the 4.0% In mole fraction exactly matches that of ZnSe at the growth temprature (240°C). (A lattice match occurs at a slightly lower mole fraction, 3.5%, for room temperature because of the difference of thermal

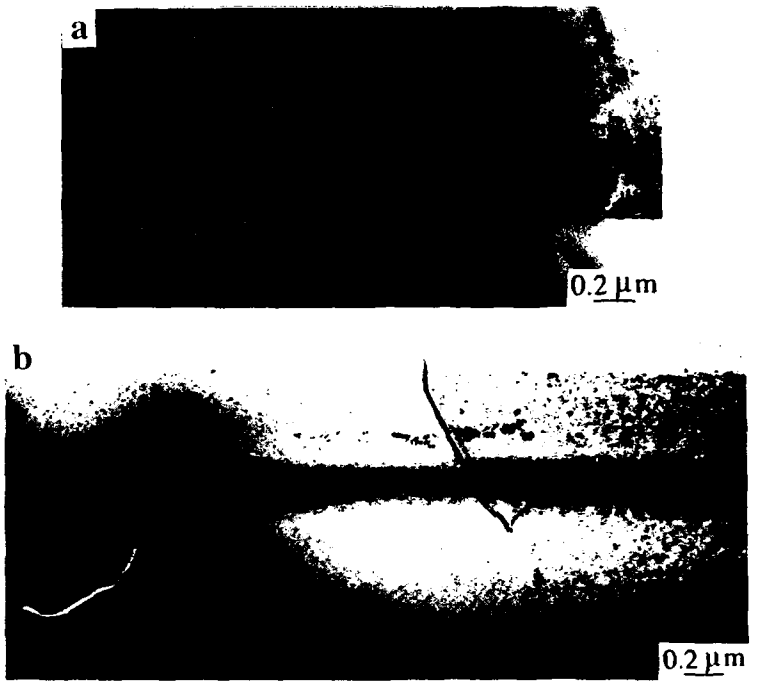


Fig. 2 Cross-sectional bright field image of (a) ZnSe/$In_{0.040}Ga_{0.960}As$ and (b) $In_{0.054}Ga_{0.946}As$ interfaces.

expansion coefficients). The ZnSe/$In_{0.054}Ga_{0.946}As$ interface, on the other hand, appears to be nearly free from arrays of misfit dislocations. In plan-view images, misfit dislocations were observed, but their density is lower than that at the ZnSe/$In_{0.040}Ga_{0.960}As$ interface. These observations imply that the lattice matching is obtained with a higher In mole fraction than that expected from the lattice constants of bulk crystals, and are consistent with the aforementioned results of X-ray diffraction. Although the $In_{0.054}Ga_{0.946}As$ buffer layer with the tetragonal distortion gives rise to close lattice matching with ZnSe at the growth temprature, relatively high density dislocations and stacking faults were observed in diode structures grown on these buffer layers. Many of these defects exist in the region from the middle to the free surface of the diode structures as seen in Fig. 2(b). One possible cause of these defects is the relatively large difference of thermal expansion coefficients between ZnSe and III-V semiconductors; the lattice parameter of ZnSe is slightly smaller than the lattice spacing of the tetragonally distorted $In_{0.054}Ga_{0.946}As$ crystal in the direction parallel to the interface at the growth temperature and further decreases at room temperature, compared to that of the $In_{0.05}Ga_{0.946}As$ crystal, resulting in a large tensile strain.

The best structural quality of diode structures was obtained by the growth on (In,Ga)As buffer layers whose lattice spacings along the interface is

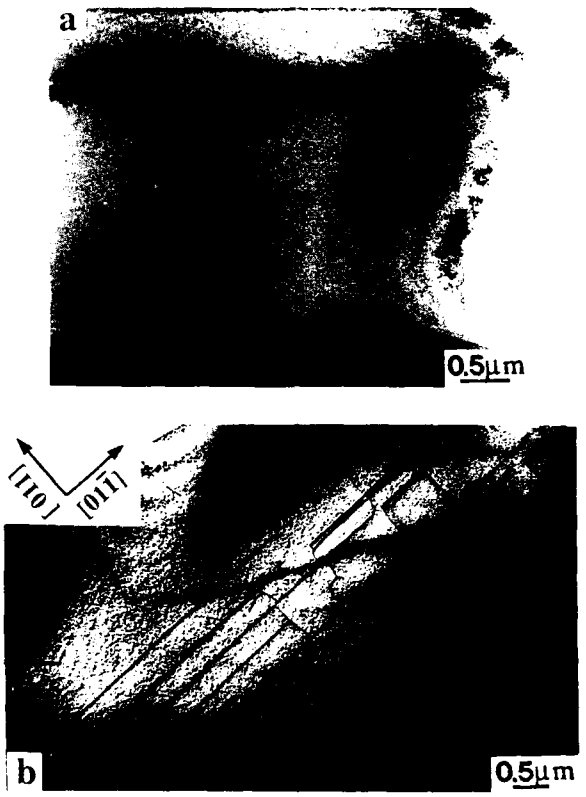


Fig. 3 (a) Cross-sectional bright field image of a ZnSe/ZnCdSe diode structure grown on $In_{0.043}Ga_{0.957}As$, (b) plan-view bright field image of $ZnSe/In_{0.043}Ga_{0.957}As$ interface.

slightly smaller than that of ZnSe, giving rise to compressive strains in diode structures. Figure 3(a)is a cross-sectional bright field image of a diode structure grown on an $In_{0.043}Ga_{0.957}As$ buffer layer. The entire region seen in the image is free from dislocations including the interface. Figure 3(b) is a plan-view bright field image of the $ZnSe/In_{0.043}Ga_{0.957}As$ interface which shows a widely spaced group of misfit dislocations. Densities of threading dislocations in diode structures grown on $In_{0.043}Ga_{0.957}As$ buffer layers are in the lower range of 10^6 cm^{-2}. From these diode structures, highly efficient blue/green electroluminescence [6] and diode laser actions [3] were obtained. The results described above clearly demonstrate the effectiveness of using lattice matched III-V semiconductor alloy buffer layers in reducing defects in ZnSe-based device structures. It is also suggested by the present study that further significant improvement is possible by making precise control of the In mole fraction to obtain stable pseudomorphic layers both at growth temperatures and room temperature.

ACKNOWLEDGEMENTS

The authors gratefully acknowledge the assistance of D. Li, S. Ogino, H. Iwata, Y. Fan, D. A. Lubelski in the growth and characterization of the structures. The research was supported by DARPA/ONR URI grant 218-25015, AFSOR grant AFOSR-89-0438, and the Indiana Corporation for Science and Technology grant P-5058.

REFERENCES

1. R. M. Park, M. B. Troffer, C. M. Rouleau, J. M. DePuydt and M. A. Haase, Appl. Phys. Lett. 57, 2127 (1990).
2. K. Ohkawa, T. Karasawa, T. Mitsuyu, Jap. J. Appl. Phys. 30, L152 (1991).
3. M. Haase, J. Qiu, J. M. DePuydt and H. Cheng, Appl. Phys. Lett. 59, 1273 (1991).
4. H. Jeon, J. Ding, W. Xie, D. C. Grillo, W. Patterson, M. Kobayashi, R. L. Gunshor and A. V. Nurmikko, Appl. Phys. Lett. 59, Dec (1991).
5. H. Jeon, J. Ding, A. V. Nurmikko, W. Xie, D. C. Grillo, M. Kobayashi and R. L. Gunshor, to be published.
6. W. Xie, D. C. Grillo, R. L. Gunshor, M. Kobayashi, G. C. Hua, N. Otsuka, H. Jeon, J. Ding and A. V. Nurmikko, Appl. Phys. Lett. 60, Jan 27 (1992).
7. H. Ehrenreich and J. P. Hirth, Appl. Phys. Lett. 46, 668 (1985).
8. E. D. Bourret, M. B. Tabache, J. W. Beeman, A. G. Elliot and M. Scott, J. Cryst. Growth, 85, 275 (1987).
9. S. Fujita, Y. Nakano, T. Uemura, M. Tabuchi, S. Noda, Y. Takeda and A. Sasaki, J. Cryst. Growth, 95, 224 (1989).
10. D. I. Westwood, D. A. Woolf and R. H. Williams, J. Cryst. Growth, 98, 782 (1989).
11. P. Gay, P. B. Hirsch and A. Kelly, Acta Met. 1, 315 (1953).

MBE GROWTH AND PROPERTIES OF WIDE BAND-GAP II-VI STRAINED-LAYER SUPERLATTICE

HAILONG WANG JIE CUI AIDONG SHEN LIANG XU YUNLIANG CHEN AND YUHUA SHEN
Shanghai Institute of Optics and Fine Mechanics, Academia Sinica
P.O.Box 800-216 Shanghai 201800, P.R.China

ABSTRACT

The $(ZnSe)_8/(ZnS)_8$ strained layer superlattices (SLSs) on (100) GaAs and $(ZnTe)_8/(ZnSe)_8$ SLSs on (100) InP have been grown by molecular beam epitaxy (MBE) and atomic layer epitaxy (ALE). The structural characteristics of these SLSs were investigated in situ RHEED observation, low-angle X-ray diffraction spectra, TED image and AES analysis. The optical properties of the SLSs, such as refractive index of superlattice materials, photoluminescence (PL) spectra, transient PL spectra, Raman spectra, far-infrared reflectivity spectra and Optical nonlinear have been studied.

INTRODUCTION

II-VI wide-gap semiconductor strained-layer superlattice are potential materials for application to optoelectronic devices in the short-wavelength visible region. Recently, major efforts have devoted to realizing blue or green light emitting devices (LED)/laser diode (LD)[1-3] and optical waveguide devices[4]. For the reason, it is important to study structural and optical characteristics of these superlattice materials for getting high-quality devices.

In this paper, we report studies of the structural and optical properties on ZnSe-ZnS and ZnTe-ZnSe SLSs, grown on GaAs and InP substrate by MBE. A lot of results are the first observation at our laboratory.

MBE GROWTH OF ZnSe-ZnS AND ZnTe-ZnSe SLSs

Devices-quality ZnSe-ZnS and ZnTe-ZnSe SLSs have been grown by MBE in Our laboratory. The substrate used were semi-insulating (100) GaAs and high-resistance (100)InP. High purity Zn(6N), S(6N), Se(5N) and Te(6N) were used as source materials. The cell temperature for Zn,S,Te,Se are 250°C,200°C,230°C and 220°C respectively. Vapor pressure of Zn,S,Te,and Se beams at the substrate position are 10^{-7}-10^{-8}Torr range, which were monitored by nude-gauge. Typical beam pressure radio (BPR)Zn/S,Te,Se was taken to be 0.5-1. The growth were carried out at a substrate temperature about 350°C for ZnSe-ZnS SLSs on GaAs substrate and 320°C for ZnTe-ZnSe SLSs on InP substrate, respectively. In this condition, the growth rate is about 30Å/min.

EXPERIMENTAL

The reflective high-energy electron diffraction (RHEED) have been used to monitoring the crystalline and surface smoothness of the grown layers of ZnSe-ZnS and ZnTe-ZnSe SLSs. Auger electron spectroscopy (AES) technique was used for analyzing the depth profile of the epi-layers and interface qualities. We measured low-angle X-ray diffraction in order to determine superlattice periodicity. TEM and TED observation were carried out by using JEM-4000EX transmission electron microscope.

DEC 0 5 1991

Mat. Res. Soc. Symp. Proc. Vol. 242. ©1992 Materials Research Society

We measured refractive index of SLSs, transient PL spectra Raman spectra, far-infrared reflectivity spectra and optical nonlinearity. The optical properties of SLSs have been studied in detail.

RESULTS AND DISCUSSION

Structural characteristics of SLS

Fig.1 shows the RHEED patterns of ZnSe-ZnS and ZnTe-ZnSe superlattices at the end of growth. Long streaky pattern together with Kikuchi lines shows that epi-layer grown is of a high-quality crystalline and smooth surface morphology. This is confirmed by TEM, TED and AES observation (Fig.2, Fig.3 and Fig.4). From Fig.4 you can see that satellite diffraction spots due to the superlattice periodicity are observable on side of the fundamental sports. The satellite sports of four orders along [001] axis were observed, showing that rather smooth interfaces and accurate periodicity were obtained on the superlattices with one period composed of 15Å ZnSe layer and 15Å ZnTe layer. The superlattice period determined from the spacing between satellite and fundamental sports is about 29.6Å.



(a) (b)

Fig.1. RHEED patterns of (a) ZnSe-ZnS SLS
(b) ZnSe-ZnTe SLS

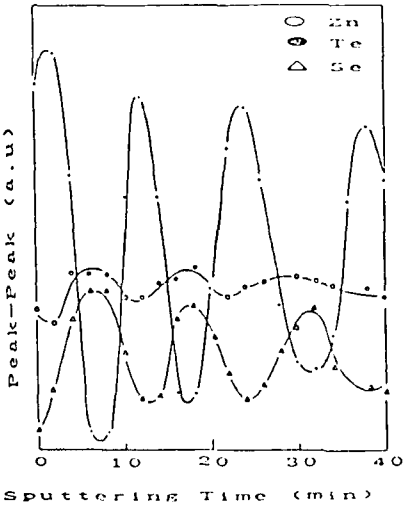


Fig.2. AES analysis profiling of ZnSe-ZnTe SLS.



Fig.3. A (110) cross-sectional image of a superlattice with a structure of ZnSe(29Å)-ZnS(27Å)x100, showing clearly a periodic ZnSe-ZnS layer structure.

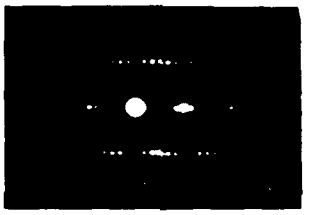


Fig.4. ASTED pattern of a ZnSe(15Å)-ZnTe(15Å) superlattice for [110] electron beam incidence. Four orders of satellite spots due to the periodicity of the superlattice are observed.

Fig.5 shows a typical low-angle X-ray diffraction measurement of ZnSe(20Å)-ZnTe(20Å) SLS grown on InP substrate by ALE. A period of the SLS determined by the Bragg peak was 38Å, which is good agreement with results of counting number of atomic layers.

Optical and spectroscopy properties of SLSs

Refractive index of SLSs

The refractive indices of ZnSe-ZnS and ZnTe-ZnSe SLSs were determined, for the first time, by double-beam reflectance measurements at room temperature[5]. Fig.6 shows the refractive indices of ZnSe-ZnS and ZnTe-ZnSe SLSs vs wavelengths. You can see that a jump occurs at about the photon energy equal to E_1(e-h). This discontinuity cannot be found in the index curves of bulk ZnSe and ZnS materials. Our results show that the difference between the indices of the SLSs and those of their compositional materials are even much large than 20%. This may result from the elastic strain caused by the large lattice mismatch, which shifts the quantized levels for a few hundred meV.

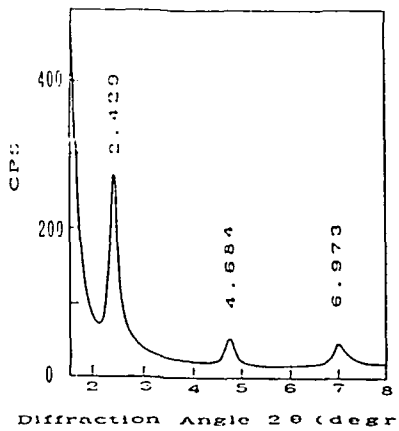


Fig.5. Low angle x-ray diffraction pattern ZnSe-ZnTe SLS sample.

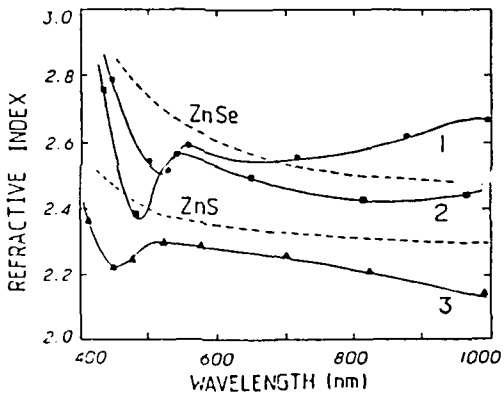


Fig.6. The refractive index dispersion curves for ZnSe-ZnTe and ZnSe-ZnS SLSs: (1) ZnSe-ZnTe (62 Å, 46 Å); (2) ZnSe-ZnTe (59 Å, 39 Å); (3) ZnSe-ZnS (29 Å, 26 Å). The dashed lines show the indices of bulk ZnSe and ZnS.

Time resolved photoluminescence spectra of ZnSe-ZnS SLS

The transient photoluminescence spectra of ZnSe-ZnS SLS was measured at 77K, for the first time.. The typical values of the exciton formation time and decay time of the luminescence due to exciton recombination are 40 ps and 100 ps, respectively. The relationship between the exciton lifetime and well width of the superlattice are shown also.

Fig.7 is an example of transient luminescence due to ground state exciton recombination at 77K in zero external field for the ZnSe-ZnS sample with 13Å ZnSe quantum well width and 12Å ZnS barrier thickness. We also measured the exciton life time for different well width. As fig.8 shows, the luminescence decay time

decrease as well width L_z decreases from 30Å to 10Å. The decrease of life time directly results the recombination enhancement duo to localization, this is a typical 2D quantum well confinement effect[6].

Our measurement indicate that localization is the main fact for affect the exciton lifetime even at the high-temperature of 77K. Because in ZnSe-ZnS SLSs, the exciton binding energy is much large that the Rydberg energy (20meV)[7].

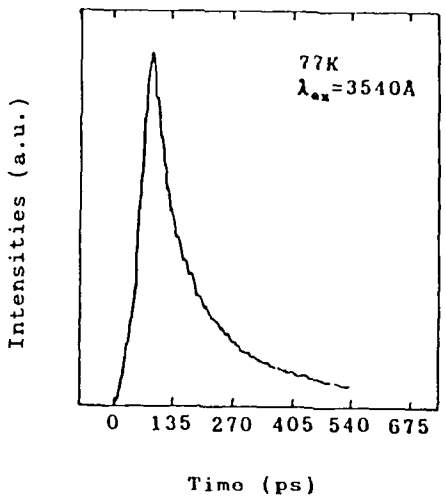


Fig.7. Transient ground state exciton luminescence from the ZnS(12Å)-ZnSe(13Å) SLS.

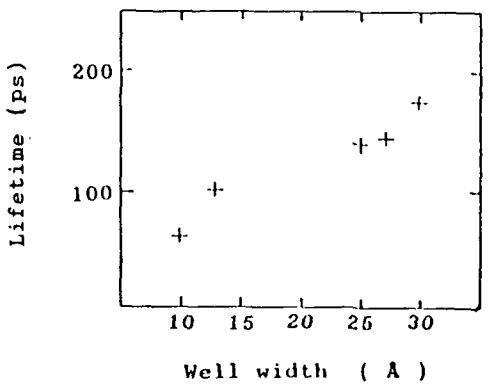


Fig.8. Well width vs exciton lifetime in ZnS-ZnSe SLSs.

Phonon spectra of ZnSe-ZnS and ZnTe-ZnSe SLSs

In this paper, we present our measurement of fold LA phonons in ZnSe-ZnS SLS and confined LO phonon modes in ZnTe-ZnSe. Theoretical analyses include confinement and strain effects are carried out.

Fold LA phonons in ZnSe ZnS SLSs

The samples used is ZnSe-ZnS SLS with 29Å ZnSe layer and 26Å ZnS layer grown on (100) GaAs substrate at 320°C by MBE.

The Raman spectra were excited in back-scattering geometry at room temperature with the 488nm line of an Ar^+ ion laser. Fig.9 shows the low-frequency region of the Raman spectrum for SS-1(ZnSe 29Å, ZnS 26Å). In the region of 10-90 cm^{-1} three doublet lines were clearly observed near 22, 44 and 67cm^{-1}, the separation between the component of doublet is about 5 cm^{-1}. We attribute these newly apparel lines to the scattering from the longitudinal acoustic (LA) phonons folded into the new Brillouin zone, which arises from the additional periodicity of superlattices.

LO phonon modes in ZnTe-ZnSe SLS

The ZnTe-ZnSe SLS samples were grown at 320°C by MBE on (100) InP substrates. The Raman spectra were recorded with Jobin-Yvon laser spectrometer model JY-T800 in back scattering geometry[8]. The measurements were performed at room temperature.

Fig.10 shows the Raman spectrum from the ZnTe-ZnSe sample ZST-3. the thicknesses of ZnTe and ZnSe layer are 29Å and 27Å, respectively. The period was repeated 100 times. Six confined LO_n phonon modes in the ZnSe layer and one confined phonon mode in the ZnTe layer have been observed[9]. We have calculated the confined phonon frequencies by considering the red shifts due to confinement and the shift induced by elastic strain. Table 1 lies the calculated and measured frequencies of the confined LO_n modes in the ZnSe layer.

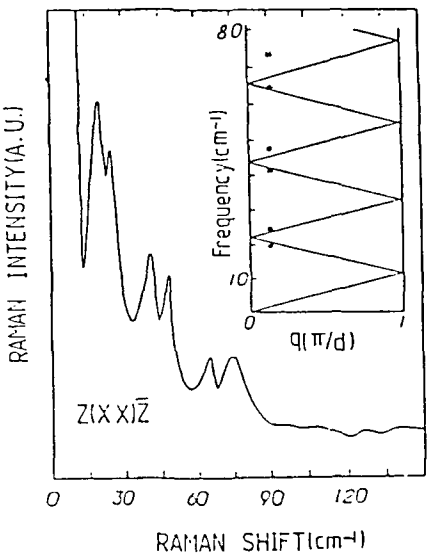


Fig.9 Low-frequency region Raman Spectrum for a ZnSe(29Å)-ZnS(26Å) SLS.

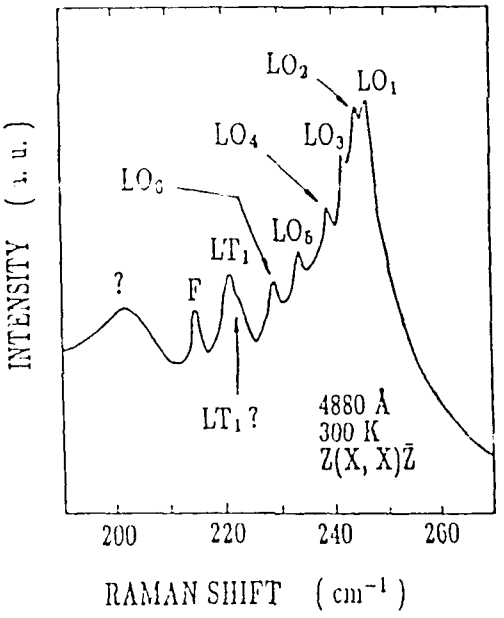


Fig.10. Confined LO_n phonon modes in ZnSe layer of the ZnSe(27Å)-ZnTe(29Å) SLS sample. LT_1 is the confined LO mode in ZnTe layer, the F peak is attributed to folded LO mode and the question mark to interface vibration or ZnSe-like TO mode. X=(1$\bar{1}$0), Y=(110), and Z=(001).

Table 1
Measured and calculated frequencies of confined LO_m modes in ZnSe layer

m	ω_{meas} (cm^{-1})	ω_{cal} (cm^{-1})
1	246	246
2	244	244.5
3	242.5	242.5
4	239	239.2
5	233.5	234.3
6	228.5	229
7		222

Far-infrared reflective spectra of ZnTe-ZnSe SLS.

Far-infrared reflectivity measurement is the simple way to characterize the quality of the microstructures. We have reported, for the first time, the far-infrared reflectivity spectra of II-VI wide-gap compound ZnTe-ZnSe SLSs and determined the phonon parameters by fitting the experimental data with the computer calculated curves.

Fig.11 shows the far-infrared reflectivity spectrum for the sample ZST-22. In the region 150-250 cm^{-1}, there are two peaks near 180 cm^{-1} and 210 cm^{-1} correspond to the ZnTe-like TO and ZnSe-like TO modes, respectively.

Fig.12 shows the fit curve, (*) are the measured data, (—) is the curve calculated. The phonon parameters determined list in Table 2.

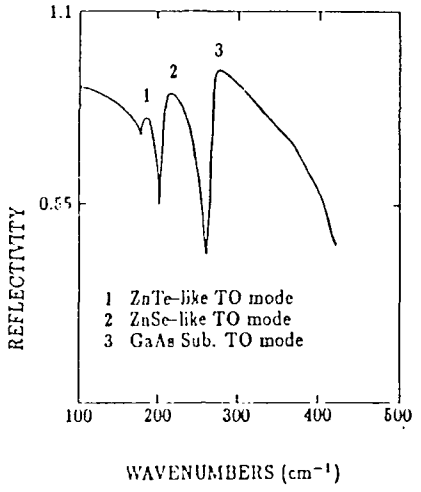


Fig.11.
The measured far-infrared reflectivity spectrum of ZnSe-ZnTe strained-layer superlattice

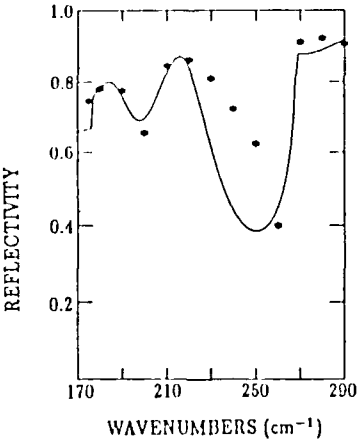


Fig.12.
Measured (*) and fitted (—) far-infrared reflectivity spectrum of the ZnSe-ZnTe SLS sample ZST-22 at 300K.

Table 2
Phonon parameters giving best fit to the measured reflectivity curve for the ZnSe-ZnTe SLS sample (ZST-22).

layer	ϵ_∞	$\omega_{TO}(cm^{-1})$	S	γ	d(Å)
ZnTe	8.3	178.2	4.63	24.7	86
ZnSe	5.8	206.0	1.91	27.4	86
ZnSe buffer	6.0	210.5	1.8	27.0	0.12μ
GaAs sub.	11.5	268.2	5.9	0.46	

ZnSe-ZnS multiple quantum well optical nonlinearity

The multiple quantum well (MQW) wafer was cleaved to a certain size and stuck on polished thin sapphire slice by epoxy resin. A window on a GaAs substrate was opened by using selective etching in order to transparent visible light. A MQW film with flat surface and thicknesses of 1-2μm was obtained on sapphire support. Third harmonic beam of a YAG laser was used as a exciting light source for nonlinearity measurement. Fig.13 shows measured hysteresis loop in the ZnSe-ZnS MQW film. It is shown that the ZnSe-ZnS MQW materials are of apparent optical nonlinearity effects[10].

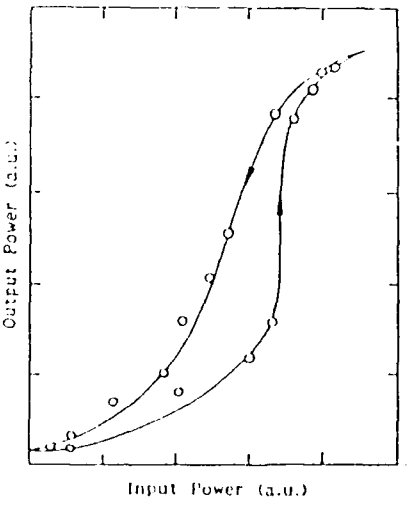


Fig.13. Hysteresis loop of the ZnSe-ZnS MQW étalon.

CONCLUSION

ZnSe-ZnS and ZnTe-ZnSe wide-gap II-VI compound superlattices were grown by MBE and ALE techniques. We have, for the first time, determined refraction indices of the SLSs, exciton lifetime, phonon parameters. We observed the confined LO_m (m=1,2,...6) in the ZnTe-ZnSe SLS, the folded LA phonon modes in ZnSe-ZnS SLS and optical nonlinearity effect in ZnSe-ZnS MQW films.

REFERENCES

[1]. J.Ren, K.A.Bowers *et.al.*, Appl. Phpys. Lett. **57**, 1901 (1990).
[2]. M.KObayashi *et.al.*, J. Appl. Phys. **61**, 1105 (1987).
[3]. M.Kobayashi *et.al.*, Appl. phys. Lett. **48**, 296 (1986).
[4]. Toshiya Yokogawa *et.al.*, Appl. Phys. Lett. **52**, 120 (1988).
[5]. Aidong Shen, Jie Cui *et.al.*, J. Cryst. Growth **111**, 807 (1991).
[6]. E.O.Göbel *et.al.*, Phys. Rew. Lett. **51**, 1588 (1983).
[7]. Londolt-Börnstein Tables Eds. O.Madelung *et.al.*, Vol. 111/17b.
[8]. Z.P.Wang *et.al.*, Solid State Commun. **65**, 661 (1988).
[9]. Jie Cui, Hailong Wang *et.al.*, J. Cryst. Growth **111**, 811(1991).
[10].Hailong Wang,Peihua Qiu *et.al.*, J. Appl. Phys. **68**, 4338(1990).

IN-SITU SPECTROSCOPIC ELLIPSOMETRY APPLIED TO ZnSe AND ZnCdSe GROWTH PROCESS IN ORGANOMETALLIC VAPOR PHASE EPITAXY

J. IACOPONI, I.B. BHAT, B. JOHS* and J.A. WOOLLAM*
Electrical, Computer and Systems Engineering Department, Rensselaer Polytechnic Institute, Troy, New York 12180 and J.A. Woollam Company*, Lincoln, Nebraska 68508

ABSTRACT

Spectroscopic ellipsometry is a well developed technique for studying the semiconductor materials and heterostructures. Here, we have applied this technique to in-situ studies of ZnSe and ZnCdSe growth in a low pressure organometallic vapor phase epitaxy system. The growth of ZnSe on GaAs was studied using a light source in the range 2 to 4 eV, and film thickness of a few tens of angstroms could be monitored by this technique. The band gap and the composition of $Zn_{1-x}Cd_xSe$ could also be measured as a function of real time. It was found that, for a gas phase DMCd composition of 60%, the amount of Cd incorporated in the layers is less than 25%. Spectroscopic ellipsometry is demonstrated to be a valuable technique for in-situ monitoring of semiconductor growth in organometallic vapor phase epitaxy systems.

1. INTRODUCTION

During epitaxy, real time monitoring of the growth process is important in understanding the growth mechanism as well as in controlling the layer thickness, interface smoothness, doping incorporation and layer quality. Reflection high energy electron diffraction (RHEED) is the primary tool used in molecular beam epitaxial (MBE) system for this purpose, but electron beam probes of this type cannot be used in atmospheric or low pressure organometallic vapor phase epitaxial (MOVPE) systems. Recently, many optical monitoring techniques such as reflectance difference spectroscopy [1, 2], spectroscopic reflectometry [3, 4] and spectroscopic ellipsometry [5, 6] have been used to study the growth process in MOMBE and MOVPE systems. Of these, spectroscopic ellipsometry (SE) is the most powerful tool, in the sense that both the surface and bulk processes can be monitored in real time. In-situ analysis by spectroscopic ellipsometry has not been used until recently, because the analysis is computer intensive. Due to the advancement in computer technology and software, data can now be taken in a fraction of a second, so that it can be meaningful in a growth environment.

For ellipsometric studies, a linearly polarized light beam having p- and s-polarization components is incident on a surface. The reflected wave is, in general, elliptically polarized, and its state of polarization is determined using a second polarizer (called an analyzer). The analyzer is rotated mechanically, and the relative intensity of light as a function of analyzer azimuth is measured. We have used an arc lamp as a light source with the output connected by fiber optics to a computer controlled monochromator. The light from the monochromator is directed through a fiber optic cable to a polarizer and then to the sample surface at an angle of approximately 70 degrees to the normal. The signal detected after the analyzer is digitized and a Fourier

analysis is performed. The result is a measurement of the polarization state of the system represented by the complex number [7, 8]

$$\rho = \tan\psi \exp(i\Delta)$$

The data is frequently expressed in terms of ψ and Δ. The value of ρ is related to the value of complex reflection coefficients,

$$\rho = R_p/R_s$$

where R_p and R_s contain information on the properties of the material and the surface. By fitting the experimental reflection results with the theoretical modelling, we can obtain information about the nature of the surface as well as the material composition. The penetration depth is varied by varying the wavelength of the light incident on the sample from 3000$\AA$ to 9000$\AA$. This feature is the most important because a suitable wavelength can be used depending on the material under study. At Rensselaer, we have used this technique to study the growth of ZnSe and $Zn_{1-x}Cd_xSe$ on GaAs for the first time in a low pressure MOVPE system.

2. EXPERIMENTAL SETUP

Figure 1 shows the experimental setup for the SE studies. Our experiments were performed in an r.f. heated, horizontal MOVPE reactor, equipped with a pressure-balanced, vent-run gas system, operating at low pressure. Dimethylcadmium (DMCd), dimethylzinc (DMZn) and dimethylselenium (DMSe) were used as the sources for ZnSe and $Zn_{1-x}Cd_xSe$ growth. Substrates used were (100) GaAs wafers misoriented 2° towards (110). The reactor pressure was maintained at 300 Torr for all the growth experiments. The reaction chamber was a 2" i.d. quartz tube, with 3/4" diameter optical access tubes at two sides so that the incident and the reflected light beams were at approximately 70°C to the sample surface. The windows were 1/4" thick quartz optical flats, mounted so that the incident light passed normal through them. The windows were located away from the growth environment and no visible deposition was observed on them after many runs.

3. RESULTS AND DISCUSSION

We studied ZnSe film growth at 400°C and 500°C with this system. During growth, the ellipsometer continuously acquired data at three different energies, namely 2.07 eV, 2.58 eV and 4.13 eV. Light at the lower energies penetrated the entire ZnSe film and was reflected back from the ZnSe/GaAs interface. This resulted in interference oscillations as the film growth proceeded, which are readily observed in Figs. 2 and 3. From the number of oscillations in the interference pattern, we can estimate the thickness to be 0.75 μm; this has been verified using post growth measurement, by Fourier transform infrared spectroscopy. The use of shorter wavelength light gives higher resolution, which is required to monitor the deposition of thin films. Light at the higher energy could not penetrate the depth of the ZnSe film. The interference oscillations therefore died out, converging to a steady state value after the film became optically thick, as seen in Fig. 4. Figure 5 shows the experimental and the modeled ellipsometric data for a 20 minute growth run of ZnSe on GaAs at 400°C, using this high energy probe. From the ellipsometric data at the growth temperature, the layer parameters were obtained as follows: film thickness = 215 $\AA$, growth rate = 10.9 $\AA$/minute.

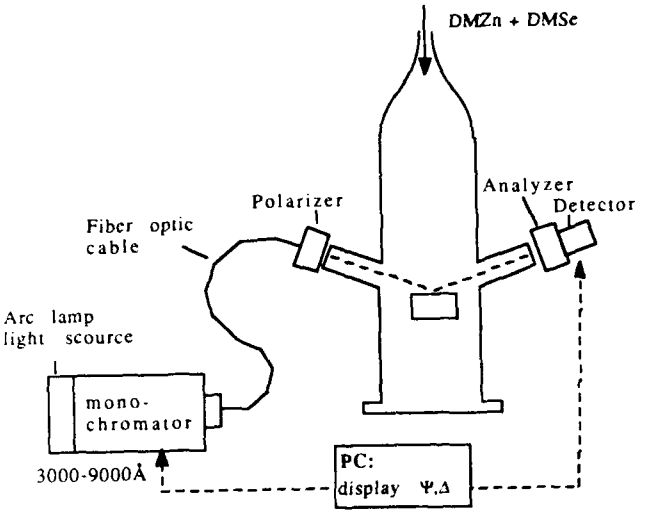


Figure 1. Experimental Setup

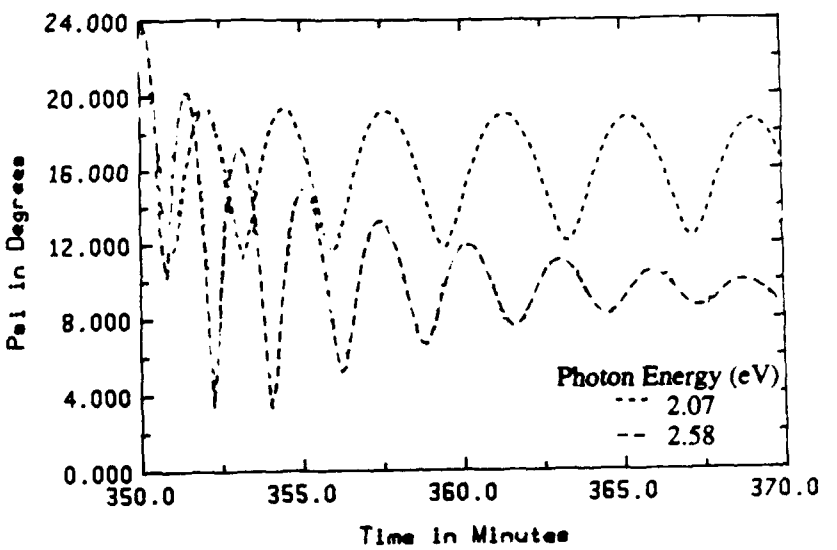


Figure 2. Ψ data of 7633Å ZnSe growth on GaAs (lower energy data).

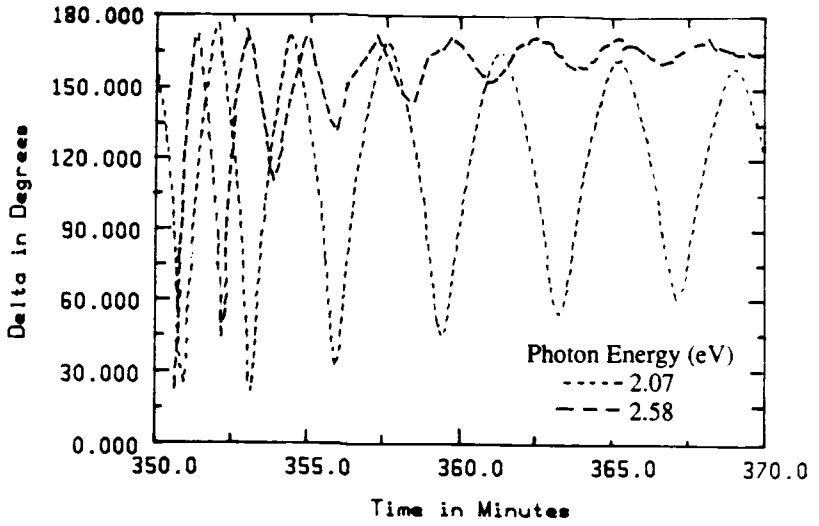


Figure 3. Δ data of 7633Å ZnSe growth on GaAs (lower energy data).

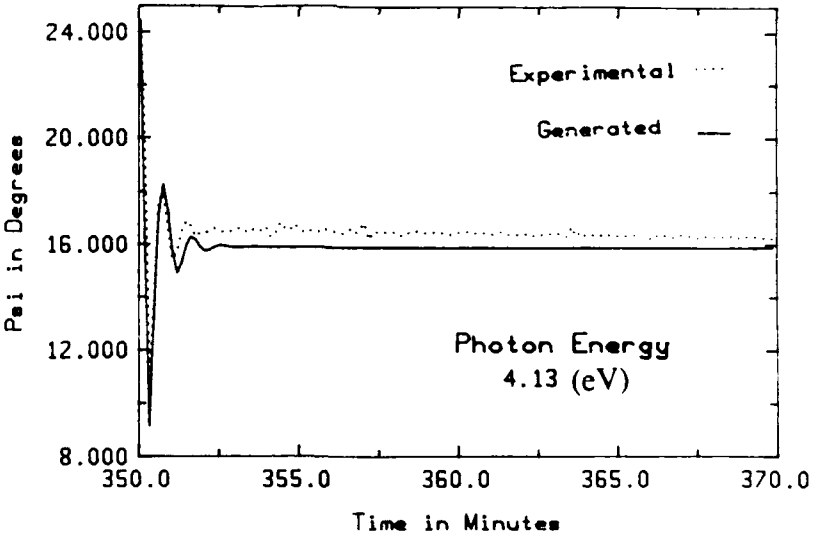


Figure 4. Ψ data, experimental and modeled, of 7633Å ZnSe growth on GaAs (higher energy data).

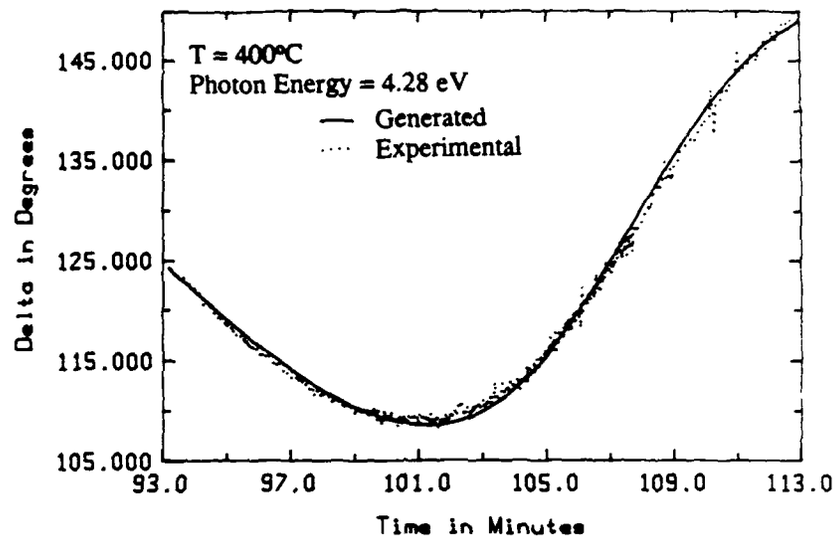


Figure 5. Δ data, experimental and modeled, of thin ZnSe film growth.

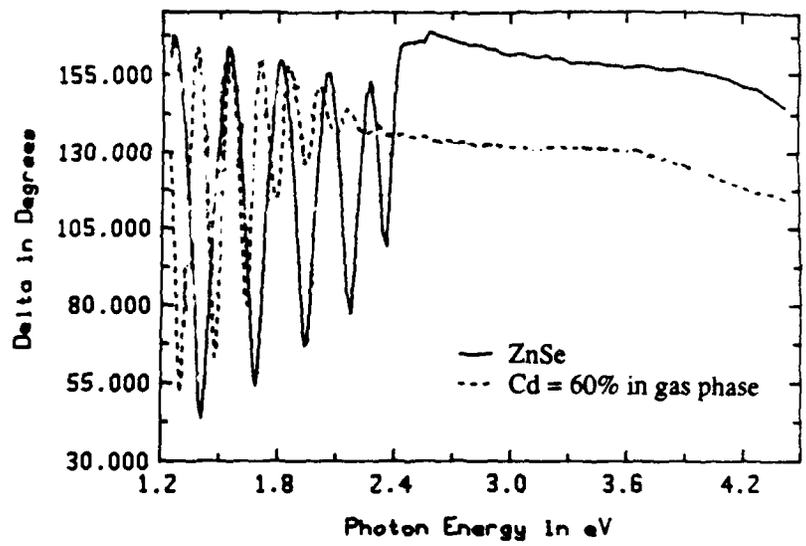


Figure 6. Δ data, $Zn_{1-x}Cd_xSe$ layers resulting from different Cd gas phase concentrations

Another application of spectroscopic ellipsometry is in in-situ monitoring of the composition of ternary compounds. We deposited $Zn_{1-x}Cd_xSe$ on GaAs with varying x values. These growth runs were carried out at 500°C. Figure 6 shows the spectroscopic ellipsometric data after the growth of ZnSe and $Zn_{1-x}Cd_xSe$, taken at the growth temperature. For $Zn_{1-x}Cd_xSe$ growth, the DMCd/DMZn ratio in the gas phase was 3 to 2. For clarity, data for only one $Zn_{1-x}Cd_xSe$ layer are shown. For energy below the band gap, the interference fringe pattern is observed, which gives the layer thickness. For light energy above the band gap, Δ and ψ values give information on the composition. As seen in the figure, the band gap of the layer can be estimated during growth. Even though the gas composition was 60% cadmium, the layer composition was less than 25%. The SE method can thus be used to find the layer composition for a ternary compound during growth. Closed loop control of the composition should be possible after characterization of standard layers.

4. CONCLUSIONS

In conclusion, we have shown that SE method can be used for in-situ monitoring of ZnSe and ZnCdSe growth rate. Layer thickness to tens of angstroms can be controlled for heteroepitaxial layers. The composition of ZnCdSe was also measured during growth and correlated to the gas phase composition. The SE technique can thus be used for the monitoring and control of various epitaxial layers grown in an organometallic epitaxial system.

ACKNOWLEDGEMENT

The authors would like to thank J. Barthel for technical assistance and P. Magilligan for manuscript preparation. This work was carried out on Contract No. DAAH01-90-C-0636 from the U.S. Army Missile Command and also supported by the Defense Advanced Research Projects Agency, under the University Research Initiative Program (N-00014-90-J-1582) administered by the Office of Naval Research. Partial support was also provided by the Philips Corporation. This support is gratefully acknowledged.

REFERENCES

1. E. Colas, D.E. Aspnes, R. Bhat, A.A. Studna, J.P. Harbison, L.T. Florez, M.A. Koza and V.G. Keramidas, J. Crys. Growth, 107, 47 (1991).
2. B.Y. Maa and P.D. Dapkus, Appl. Phys. Lett., 58, 2261 (1991).
3. N. Kobayashi and Y. Horikoshi, Jap. J. Appl. Phys., 29, L702 (1990).
4. N. Kobayashi, T. Makimoto, Y. Yamaguchi and Y. Horikoshi, J. Crys. Growth, 107, 62 (1991).
5. J.B. Theeten, F. Hottier and J. Hallais, J. Crys. Growth, 46, 245 (1979).
6. D.E. Aspnes, W.E. Quinn and S. Gregory, Appl. Phys. Lett., 57, 2707 (1990).
7. R.M.A. Azzam and N.M. Bashara, Ellipsometry and Polarized Light, North-Holland, Amsterdam (1977).
8. K.G. Merkel, P. Snyder, J.A. Woollam, S.A. Alterovitz and A.K. Rai, Jap. J. Appl. Phys., 28, 1118 (1989).

GROWTH OF EPITAXIAL ZnS FILMS BY PULSED-LASER ABLATION

J. W. McCamy,* D. H. Lowndes,† J. D. Budai,† B. C. Chakoumakos,† and R. A. Zuhr,†
* Department of Materials Science and Engineering, The University of Tennessee, Knoxville, TN 37996-1200
† Solid State Division, Oak Ridge National Laboratory, Oak Ridge, TN 37831-6056

ABSTRACT

Pulsed KrF (248nm) laser ablation of a polycrystalline ZnS target has been used to grow high quality, carbon-free, epitaxial ZnS thin films on GaAs(001), GaAs(111), and GaP(001). The films were grown at temperatures of 150–450°C, using a rotating substrate heater and deposition geometry that produces films with highly uniform thickness. X-ray rocking curves are consistent with (111) stacking faults being the dominant defects in the ZnS films grown on GaAs. The estimated stacking fault density is ~6×10^{10} cm^{-3}, comparable to the best MOCVD ZnS films. RBS analysis shows that these defects are located predominantly near the GaAs-ZnS interface. The anisotropy of the ZnS growth rate, between the GaAs(001) and GaAs(111) surfaces, was found to be temperature-dependent.

INTRODUCTION

Zinc sulfide (ZnS) is an attractive optoelectronic material because of its wide direct bandgap (E_g = 3.7 eV, λ_g = 335 nm). Thin, epitaxial ZnS films are especially interesting because of their potential applications for active devices such as blue LEDs or laser diodes [1], and for passive structures such as optical waveguides [2] or index-matching windows in solar cells [3]. The techniques used to grow thin, crystalline ZnS films include physical transport methods (e.g., elemental vapor transport) and metalorganic chemical vapor deposition (MOCVD) [4,5]. The physical transport methods require high growth temperatures of 500–900°C; defect complexes, which may act as carrier trapping centers, are formed at these temperatures [6]. Experience to date with pyrolytic MOCVD shows that the principal problems with this approach are either premature reactions in systems using H_2S and zinc alkyls (e.g., dimethyl- or diethylzinc), or the high temperatures needed to promote many alkyl-alkyl reactions (e.g., dimethylzinc and dimethylsulfur) [6]. In either case, the presence of an alkyl in the reaction poses an inherent problem of carbon incorporation in the film, which may result in film polycrystallinity and formation of carbon defect complexes [7].

Pulsed-laser ablation (PLA) is an attractive alternative deposition method that uses solid, carbon-free sources. While PLA has become widely known recently for growth of epitaxial high-temperature superconductor films, it also can be used to grow epitaxial films of other ceramics [8] as well as both elemental (group IV) [9] and compound (e.g., II-VI) [10] semiconductors. PLA has several principal advantages, including the ability to grade compositionally an epitaxial layer [11]; growth of smooth films when the laser energy density, E_ρ, and the target surface morphology are controlled properly [12]; and, stoichiometric (congruent) transport of material from the ablation target to the substrate surface, when laser beam conditions are correctly adjusted [13]. Several ablation regimes exist, including one in which the constituents are transported as energetic (~several ev) neutrals and ions [14]. In principle, this incident kinetic and/or internal energy can be used to reduce the growth temperature, T_g. However, a well-known disadvantage of PLA film deposition is that the angular distribution of ablated material usually is strongly peaked in the forward direction so that the film thickness varies rapidly with position (~$[\cos \vartheta]^n$, with n ~1.5–10) [15,16]. As shown here, this problem can be overcome by altering the ablation "plume"-substrate geometry, resulting in films with highly uniform thickness.

In this paper we describe the preparation and structural properties of epitaxial ZnS films grown by PLA on GaAs(001) and GaAs(111) substrates, using only moderate substrate temperatures, T_g ~ 300°C, and moderate laser energy densities, E_ρ = 0.2–1.5 J/cm^2. Preliminary results for growth on GaP(001) substrates also are reported. ZnS films with excellent thickness

uniformity were grown by using an offset laser beam geometry together with a rotating substrate heater. The film growth rate was monitored in situ using an optical reflectivity method. An ex situ reflectivity measurement by scanned laser spot was used to accurately determine film thickness uniformity. The film-substrate epitaxial relationship was determined by x-ray diffraction (XRD), using a 4-circle goniometer; the films' crystalline quality (defect density) also was studied by XRD, using a 2-circle goniometer, and by Rutherford backscattering spectrometry (RBS).

FILM DEPOSITION CONDITIONS AND GEOMETRY

Substrates of Cr-doped semi-insulating (SI) GaAs(001) and GaAs(111) were used, with areas of 25–50 mm^2. The substrates were degreased in organic solvents, then etched (15s) in concentrated H_2SO_4. The S-doped (n-type) GaP(001) samples were degreased, then etched (15s) in a Br_2(1%):MeOH solution, followed by an etch (5s) in a HCl:HNO_3 solution. Following this, the substrates were passivated in an $(NH_4)_2S_x$ solution, mounted on the substrate heater, and introduced into the growth chamber (2×10^{-7} Torr base pressure). Immediately prior to film growth, they were heated to 420°C for 3 minutes, then cooled to the growth temperature. It has been reported in MOMBE growth experiments that this passivation/preheat treatment results in a 2×1 reconstruction of the GaAs surface, a reduction of the surface-state density, and allows two-dimensional (2D) nucleation to occur from the beginning of growth [17].

The substrate heater was designed with a pumped Wilson seal to allow the substrate-target separation to be varied while still permitting substrate rotation during growth. The target and substrate faces were vertical and parallel, with coincident rotational centerlines. Substrate-target separations, D_{st}, were maintained at either 5.7 cm or 10.8 cm. At D_{st} = 5.7 cm, film growth was carried out for T_g = 200–400°C, while for D_{st} = 10.8 cm, the temperature range used was T_g = 150–450°C. Growth was carried out in vacuum or in an inert, low-pressure atmosphere of ultra-high purity (99.9999+ %) helium. Growth in helium had little or no effect on film quality, for pressures in the 0–10 mT range. Unless otherwise noted, the films discussed below were grown in an atmosphere of 2 mT He, with D_{st} = 10.8 cm, to a film thickness ~225 nm.

A pulsed KrF (248nm) excimer laser beam (~35 ns FWHM pulse duration) was passed through an aperture and brought to a vertical focus (E_ℓ = 0.2 - 1.5 J/cm^2) on a 2.54 cm-diam polycrystalline ZnS target (Angstrom Sciences; 99.999+ % purity) using a single +500 mm cylindrical lens. The laser beam was incident on the target face at an angle of ~25° from the surface normal, with a horizontal offset L = 0.5–0.7 cm from the rotational centerline. Substrate rotation was maintained such that there were 12.5 laser pulses per revolution.

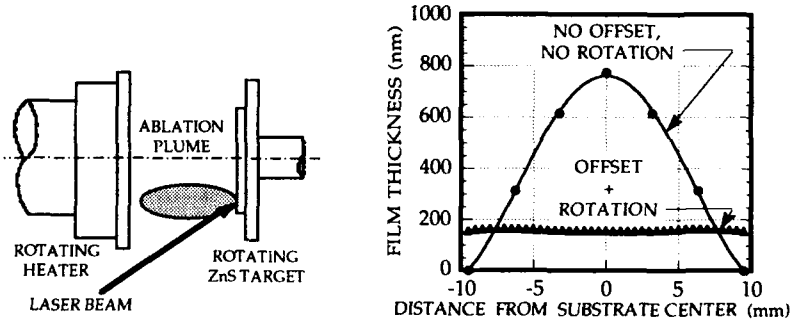


Figure 1. Offset geometry and resulting differences in film thickness uniformity for D_{st} = 5.7 cm, and E_ℓ = 0.35 J/cm^2, with no substrate rotation or offset (1200 shots), and with 12.5 laser shots/rev, and 5 mm laser beam offset (2000 shots).

Figure 1 shows that for D_{st} = 5.7 cm, this offset geometry and pulse rate resulted in films that were completely uniform (±1%) in thickness over areas of ~75 mm^2, and moderately uniform (±3%) over areas of ~300 mm^2. By modeling the film thickness uniformity as a function of D_{st} and L, we found that uniform film thickness can be achieved over much larger areas simply by scaling, i.e., using larger separations and offsets [18]. Thus, although the small size of the ablation target and chamber are constraining factors in the present experiments, these are not fundamental constraints on larger-scale applications of the PLA film-growth method.

RESULTS AND DISCUSSION

The ZnS films appeared smooth and mirrorlike under all deposition conditions; examination by scanning electron microscope (SEM) revealed no surface features or structure at the 50 nm level of resolution.

Epitaxial Alignment

The crystallographic structure of the films was characterized by XRD (Cu Kα) measurements. For growth on GaAs(001), only substrate peaks and strong ZnS(00ℓ) diffraction peaks were observed at all growth temperatures (T_g = 150–450°C) and for E_ℓ = 0.2–1.5 J/cm^2, confirming alignment of the film and substrate (001) axes. Analysis of ZnS growth on GaAs(001) (E_ℓ = 0.35 J/cm^2, D_{st} = 5.7 cm, T_g = 300°C) using a 4-circle goniometer showed that the ZnS[001] and GaAs[001] were aligned to within < 0.2°, and that the in-plane ZnS and GaAs [100] and [010] directions also were aligned, i.e., the ZnS films are fully epitaxial on GaAs(001). The lattice constant, a_o, of the ZnS film was determined to be 5.404 ± 0.003 Å (bulk a_o = 5.406 Å.)

On GaAs(111), similar results were obtained: Only substrate peaks and strong ZnS($\ell\ell\ell$) peaks were observed for all growth temperatures, and the ZnS($\ell\ell\ell$) Kα_1, Kα_2 peaks were easily resolved at all T_g. However, on GaP(001) only a low intensity ZnS(004) peak was observed for T_g > 300°C at E_ℓ = 0.35 J/cm^2. At no temperature could the 2θ peak be resolved into its Kα_1, Kα_2 components. The in-plane alignment has not yet been determined for films grown on the GaAs(111) and GaP(001) substrates.

X-ray Broadening Due to Lattice Defects

The large lattice mismatch between ZnS and GaAs (4.4%), and between ZnS and GaP (0.8%), results in strain and lattice defects that contribute to line broadening in the ZnS XRD peaks. For epitaxial ZnS grown by MOCVD, cross-sectional high-resolution TEM (HRTEM) studies [19] showed that the principal defects were stacking faults, but lattice mismatch did not correlate with the stacking fault density.

Figures 2 and 3 show typical rocking curve line profiles for the ZnS(004) Kα_1 and ZnS(111) Kα_1 peaks, using a 2-circle goniometer. Two superimposed peaks, one narrow and one much broader, were observed for each orientation. The narrow central peak has a FWHM of ~ 0.09°, which is the limit of resolution for this instrument; the width of this peak did not change with growth temperature. However, for both the GaAs(001) and GaAs(111) substrates the width of the second, broad peak was temperature dependent. For the ZnS(004) peak, the rocking curve FWHM decreased as T_g increased, reaching a minimum at T_g ~325°C, then increased at higher growth temperatures (Fig. 4.) For the ZnS(111) peak, the rocking curve FWHM decreased continuously with increasing growth temperature (Fig. 5). At T_g = 300°C, the integrated area intensity ratios of the two peaks, I_{narrow}/I_{broad}, were I_n/I_b(001) ~0.06 and I_n/I_b(111) ~1.08.

The two peaks seen in the rocking curve line profiles are characteristic of a film that contains two distinct types of crystalline material. The broad peak is due to diffraction by strained (or otherwise defective) regions, from which the diffracted amplitude is summed incoherently; the narrow peak originates from regions of coherent addition of diffracted amplitudes. Consequently, for an epitaxial film, the relative intensities of the narrow and broad

peaks provide information about the type of defects present, by the following reasoning. Stacking faults on the (111) planes have little effect on the lattice coherency in the (ℓℓℓ) direction; thus, a narrow rocking curve is obtained. However, lattice planes intersected by stacking faults [e.g., the (00ℓ)] will be offset across the fault by a non-integral multiple of the lattice spacing; this decreases coherency and appears as broadening of the rocking curve. Therefore, the different relative diffraction intensities (I_n/I_b) quoted above for ZnS/GaAs(001) and ZnS/GaAs(111) rocking curve line profiles are consistent with (111) stacking faults being the predominant defects in ZnS films grown by PLA. This is not surprising due to the low (5.4 mJ/m^2 [22]) stacking fault energy of ZnS. The presence of a narrow (001) peak indicates that a region of near-perfect (coherently diffracting) crystalline material exists.

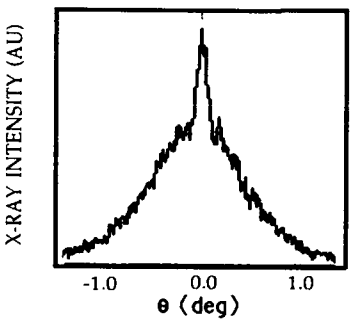


Figure 2. Rocking curve profile for ZnS(004) on GaAs(001)

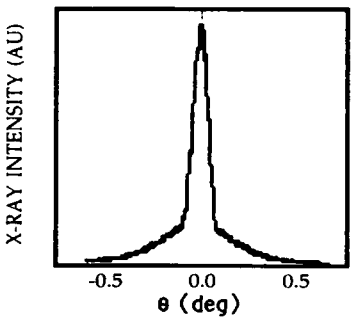


Figure 3. Rocking curve profile for ZnS(111) on GaAs(111)

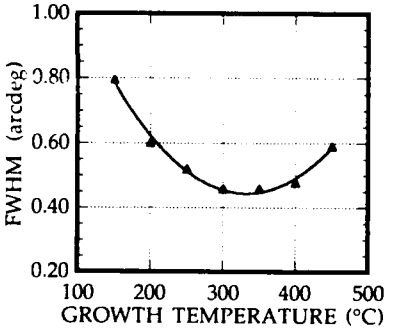


Figure 4. ZnS(004) Kα_1 rocking curve ZnS/GaAs(001), E_ℓ = 0.75 J/cm^2

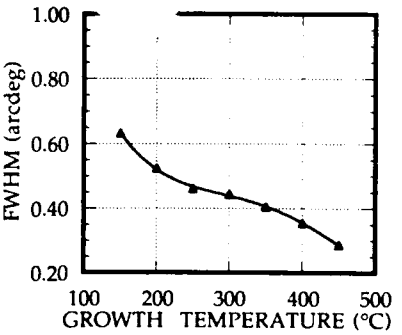


Figure 5. ZnS(004) Kα_1 rocking curve for for ZnS/GaAs(111), E_ℓ = 0.75 J/cm^2

Sebastian and Krishna [20] studied the broadening of the 2θ XRD peaks due to a random distribution of stacking faults in close-packed single crystals, with application specifically to ZnS (treated as two interpenetrating fcc lattices). They found that the FWHM (Δ2θ) of certain 2θ peaks (e.g., (00ℓ) peaks) is related to the stacking fault probability (α) by

$$\Delta 2\theta = (3/\pi)\cos^{-1}[(4Z-Z^2-1)/2Z].$$

For growth faults (no deformation twinning), $Z = (2\alpha\text{-}1)^{-1/2}$. Once α has been determined, the stacking fault density (ρ) can be calculated [21]. Consequently, if the principal defects in PLA-grown ZnS films are stacking faults, as in MOCVD ZnS, then an upper bound for the defect density can be obtained by assuming that all of the observed 2θ broadening is due to stacking faults.

Extensive line broadening of the (00ℓ) 2θ peaks was observed: For $T_g \geq 250°C$, the ZnS(00ℓ) $K\alpha_1$, $K\alpha_2$ peaks were deconvoluted using a Pearson VII function-fitting routine, while for $T_g < 250°$ C the peaks could not be deconvoluted. The $\Delta 2\theta$ of the ZnS(002) $K\alpha_1$ peak reached minimum values of 0.116°, 0.103°, and 0.093° (corrected for instrumental broadening) at T_g's of 300°C, 350°C, and 400°C, respectively. For stacking faults bounded by <112>/6 partial dislocations, the broadening observed here corresponds to a stacking fault density $\rho \sim 6 \times 10^{10}$ cm/cm^3. This value is comparable to the lowest stacking fault densities found by HRTEM examination of high quality MOCVD ZnS films [19].

In contrast to the results obtained for GaAs(001), no temperature-dependent line broadening of the 2θ peaks was observed for growth on GaAs(111). The $\Delta 2\theta$ for the ZnS(111) $K\alpha_1$ peak was 0.035° (corrected for instrumental broadening).

As explained above, the (001) rocking curve (Fig. 2) reveals that both near-perfect (coherently diffracting) and strained or defective (incoherently diffracting) regions are present. The strained/defective region can be located by RBS channeling. The RBS spectrum of a ZnS/GaAs(001) sample in Fig. 6 shows that the minimum yield, X_{min}, from the surface region is much less than from material near the film-substrate interface. (This is most easily seen from the difference in slope of the sulfur peak for the aligned and random spectra.) This indicates that most of the strain and defects are located near the interface, with the uppermost region of the film being near-perfect. This has been confirmed by initial cross-section TEM images.

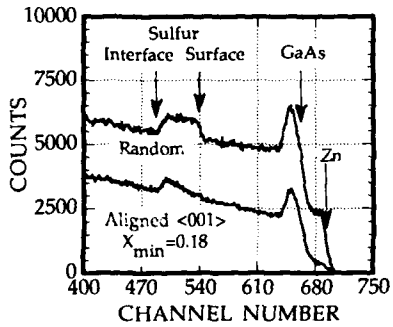


Figure 6. Rutherford backscattering spectra, random and channeling directions, for ZnS/GaAs(001) with T_g = 400°C.

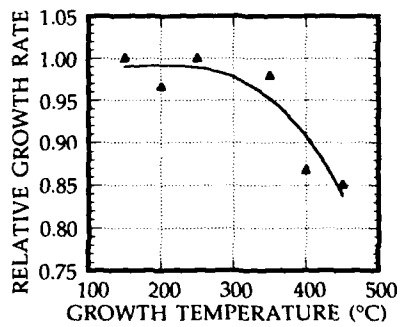


Figure 7. Relative growth rate in comparison for ZnS/GaAs(111) and ZnS/GaAs(001) at various growth temperatures.

Growth Rate: Temperature-Dependent Anisotropy

The ZnS film-growth rate was measured in situ via the interference oscillations in the intensity of a HeNe (633 nm) laser beam reflected from the upper and lower surfaces of the growing film. For $E_\ell = 0.75$ J/cm^2, the growth rates for the ZnS/GaAs(001) films were in the range 1.25–1.82 Å per laser shot, while for ZnS/GaAs(111) the rates were similar, 1.06–1.79 Å per laser shot. The variation in growth rate was found to be small in any particular growth run (<±7%). Since the radial distance of the HeNe probe laser beam from the rotational centerline varied from run to run, absolute growth rates in different runs are not directly comparable. However, because of the relatively large area of uniform deposition, as many as four 36 mm^2 substrates could be mounted in each run, making possible the direct determination of relative growth rates for different pairs of substrate materials, or for substrate surfaces of different

crystallographic orientation, during a single growth run. In this way, it was found that the ZnS growth rate was the same on GaAs(001) and GaP(001) for all T_g, but the growth-rate ratio GR(111)/GR(001) decreased with increasing temperature, as shown in Fig. 7. The different temperature dependences of the (001) and (111) rocking curve widths (Figs. 4 and 5) and of the (001) and (111) growth rates (Fig. 7) probably are related. Adsorption and desorption are competing processes in film growth. Since bond strength is crystal orientation-dependent, the different temperature dependences may arise from different adsorption and/or desorption rates on the (111) and (001) faces. However, these data are insufficient to suggest a detailed mechanism.

CONCLUSION

We have demonstrated that PLA is an attractive method for growth of fully epitaxial ZnS thin films with excellent thickness uniformity. Rocking curve profile data indicates that stacking faults are the predominant defects present in these films; the stacking fault densities are comparable to those found in the best films grown by MOCVD. However, the PLA-grown films have the advantage that they are inherently carbon-free. RBS and TEM analyses show that in films ~220 nm thick, the ~120 nm nearest the GaAs-ZnS interface is highly faulted, but the upper ~100 nm is much less defective. Finally, we find that on GaAs the anisotropy of the ZnS epitaxial growth rate is temperature-dependent.

This research was sponsored by the Division of Materials Sciences, U.S. Department of Energy under contract DE-AC05-84OR21400 with Martin Marietta Energy Systems, Inc.

REFERENCES

1. S. Yamaga, *Jpn. J. Appl. Phys.* **30**, 437 (1991).
2. T. Saitoh, T. Yokogawa, T. Narusawa, *Jpn. J. Appl. Phys.* **30**, 667 (1991).
3. G. A. Landis, J. J. Loferski, R. Beaulieu, P. A. Sekula-Moise, S. M. Vernon, M. B. Spitzer, C. J. Keavney, *IEEE Trans. Elec. Dev.* **37**, 372 (1990).
4. T. Imai, S. Fuke, H. Araki, K. Kuwahara, *J. Cryst. Growth* **94**, 983 (1989).
5. Y. Kawakami, T. Taguchi, A. Hiraki, *J. Vac. Sci. Technol.* B **5**, 1171 (1987).
6. H. Kukimoto, *J. Cryst. Growth* **107**, 637 (1991).
7. K. P. Giapis, K. F. Jensen, J. E. Potts, S. J. Pachuta, *J. Elect. Mater.* **19**, 453 (1990).
8. L. Shi, H. J. Frankena, *Vacuum* **40**, 399 (1990).
9. D. Lubben, S. A. Barnett, K. Suzuki, S. Gorbatkin, J. E. Greene, *J. Vac. Sci. Technol.* B. **3**, 968 (1985).
10. J. J. Dubowski, *Chemitronics* **3**, 66 (1988).
11. J. T. Cheung, E. H. Cirlin, N. Otsuka, *Appl. Phys. Lett.* **53**, 310 (1988).
12. H. Sankur, J. T. Cheung, *Appl. Phys. A* **47**, 271 (1988).
13. J. T. Cheung, H. Sankur, *CRC Critical Reviews in Solid State and Materials Sciences*, **15**, 63 (1988).
14. J. F. Ready, *Effects of High-Power Laser Radiation*. Academic Press, New York, 1971.
15. T. Venkatesan, X. D. Wu, A. Inam, J. B. Wachtman, *Appl. Phys. Lett.* **52**, 1193 (1988).
16. R. E. Muenchausen, K. M. Hubbard, S. Foltyn, R. C. Estler, and N. S. Nogar, *Appl. Phys. Lett.* **56**, 578 (1990).
17. Y. Kawakami, T. Toyoda, Y. Wu, S. Fujita, S. Fujita, *J. Cryst. Growth* **107**, 1072 (1991).
18. J. W. McCamy, D. H. Lowndes, S. Zhu, unpublished
19. J. O. Williams, T. L. Ng, A. C. Wright, B. Cockayne, P. J. Wright, *J. Cryst. Growth* **68**, 237 (1984)
20. M. T. Sebastian, P. Krishna, *Prog. Cryst. Growth Charact.* **14**, 103 (1987)
21. L. F. Vassamillet, *J. Appl. Phys.*, **32**, 778 (1961)
22. Y. M. Tairov, V. F. Tsvetkov, in *Growth and Defect Structures*, Springer-Verlag, New York, 1984
23. S. M. Sze, *Physics of Semiconductor Devices*, John Wiley and Sons, New York, 1969.

SYNTHESIS, STRUCTURAL AND OPTICAL CHARACTERIZATION OF ZINC CHALCOGENIDES IN NOVEL SOLID STATE HOSTS

Kelly L. Moran, Andrew W. Ott, Thurman E. Gier, William T. A. Harrison, Hellmut Eckert and Galen D. Stucky

Department of Chemistry, University of California, Santa Barbara, CA 93106

ABSTRACT

Several series of sodalite analogues of unit cell composition $M_8X_2(TO_2)_{12}$, where M is Zn or Cd, X is a chalcogen, and T is a tetrahedral cation B, or Be in combination with Si or Ge, have been prepared. An M_4X tetrahedron, which is the first coordination sphere of the bulk semiconductor MX, sits at the center of each sodalite cage. These materials have been structurally characterized by solid state ^{77}Se and ^{125}Te MAS NMR and by powder X-ray diffraction. Diffuse reflectance optical absorption spectra are reported for each series. The borates have optical properties similar to the bulk MX whereas the beryllosilicates and germanates exhibit large blue shifts in the absorption spectra.

INTRODUCTION

Zinc and cadmium chalcogenides are used for various electrooptic applications including photoconductors, phosphors, optical waveguides and semiconductor devices. Epitaxial growth of heterostructures has resulted in the fine tuning of electronic properties for specific applications [1] and this is one reason why these materials are exciting candidates for closer examination. Another method for fine tuning semiconducting materials is by cluster size quantization: physically limiting the size of the particles to dimensions below the exciton radius by formation of colloidal suspensions [2] or by inclusion in porous hosts [3]. Size quantization of cadmium chalcogenides has been widely demonstrated in the literature; the products exhibit optical spectra which are blue-shifted from that of bulk CdS [4].

Our approach in this study is to begin with the first coordination sphere of the semiconductor MX and build up an expanded structure of these tetrahedra within a rigid framework. The unit cell structure of a sodalite analogue with composition $M_8X_2(TO_2)_{12}$ is shown in Figure 1, where M is Zn or Cd, X is a chalcogen and T is a tetrahedral atom bonded to bridging oxygens to form the sodalite cage. The M_4X tetrahedron occupies the center of this cage. By varying the cage composition, and hence the cage size, the distance between M_4X clusters and the cage electric field can be varied.

In the borate analogues, in which all of the T atoms are boron, the cages are small enough

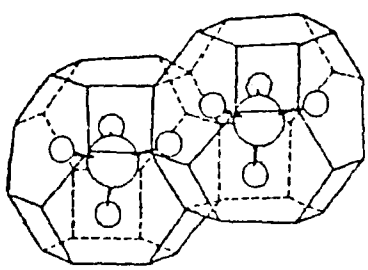


Figure 1. Sodalite unit cell. The central M_4X tetrahedron is represented by the circles and the tetrahedral cage atoms are located at the vertices.

so that the MX bond distance is shorter in the sodalite than in the corresponding bulk material. As reported previously for Zn_4S borate the Zn-S bond length is 2.260(3) Å compared with 2.34 Å in the bulk sphalerite-type ZnS [5]. In the Zn_4S beryllosilicate and beryllogermanate, the Zn-S distances are 2.346(2) and 2.345(3) Å, respectively. Due to the larger cation size in the beryllogermanates, the cage volume is slightly smaller than in the corresponding beryllosilicates. Similar trends are observed with the selenides. The borate cage is too small to accommodate the tellurium anion, however; the zinc and cadmium telluride beryllosilicates and germanates have been prepared.

Here we report the effect on the optical absorption when the central anion is varied in the solid solution series $Zn_8S_xSe_{2-x}(BO_2)_{12}$, the effects of doping sulfur into the oxoborate and oxygen into the sulfoborate, and also present the NMR and optical characterization of the zinc selenide and telluride beryllosilicates and germanates.

EXPERIMENTAL

The sodalite analogues were prepared by solid state synthesis in sealed graphite-coated quartz ampules. Stoichiometric mixtures of the oxides and chalcogenides were ground together, heated under vacuum to *ca.* 500 °C to remove water, evacuated to 10^{-3} Torr and sealed. Each ampule was placed separately inside a loosely fitting #304 stainless steel tube as a secondary containment device in the event of ampule failure. The samples were placed in a muffle furnace and heated to 850 °C for 12 to 24 hours. The recovered powders were stable to oxidation and could be mixed with water and sonicated to remove any residual graphite or broken quartz. Due to the toxic nature of the reactants, especially that of BeO, all sample manipulations were carried out in a N_2 flow-through glovebox fitted into a fume hood.

High resolution powder diffraction data were collected with a Scintag Pad X diffractometer and Rietveld structural analyses were carried out as described previously [6]. ^{125}Te and ^{77}Se Magic Angle Spinning NMR spectra were obtained at 94.7 and 57.3 MHz, respectively, on a General Electric GN-300 spectrometer using a 7-mm MAS probe from Doty Scientific. The spectra were acquired with 90° pulses of length 5 μs for ^{125}Te and 8.5 μs for ^{77}Se. Recycle delays varied from several minutes to two hours. Diffuse reflectance optical absorption spectra were measured with a Cary-14 spectrometer upgraded by On-Line Instrument Systems.

RESULTS

1. The Solid Solution Series $Zn_8S_xSe_{2-x}(BO_2)_{12}$. The effect of varying the central anion was examined in the solid solution series containing S and Se. Optical absorption data for this series are shown in Figure 2. The absorption edge shifts to a higher energy in a systematic fashion as the amount of S relative to Se is increased. At the end points (Zn_8Se_2 borate and Zn_8S_2 borate) the absorption edge is sharp, indicating that the cluster-cluster contact distances are uniform. In the solid solutions, which were shown to be single phase materials by powder XRD, the M_4X tetrahedra are disordered, which is reflected in the broader optical features.

2. Effects of Doping in the $Zn_8O_xS_{2-x}(BO_2)_{12}$ System. Fine tuning of the absorption edge can be accomplished by doping small amounts of sulfur into the zinc oxoborate and oxygen into the sulfoborate, as shown in Figures 3A and 3B. In each of these series the dopant level was small enough that the unit cell size was unchanged.

3. Optical and NMR Characterization of the Beryllosilicates and Germanates. The effect of varying the cage atoms was measured by examining solid solution series of the beryllosilicates and germanates. In Figure 4A are shown the ^{125}Te MAS NMR spectra of Zn_4Te in beryllosilicate and beryllogermanate hosts. The narrow linewidths and absence of spinning sidebands (even at spinning speeds as slow as 1.5 kHz) verify that the central anion resides in a well-defined tetrahedral site with essentially zero chemical shift anisotropy. The chemical shifts, measured relative to CdTe, are -466 ppm for the silicate and -491 ppm for the

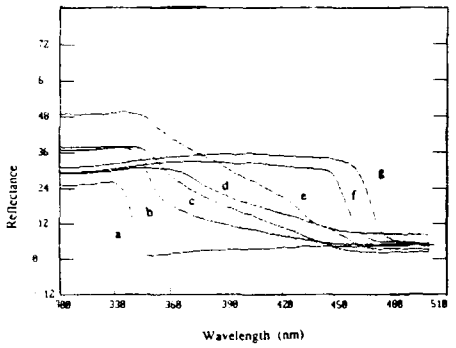


Figure 2. Optical absorption data for the series $Zn_8S_xSe_{2-x}(BO_2)_{12}$, where x = (a) 2.0, (b) 1.8, (c) 1.6, (d) 1.4, (e) 1.5, (f) 1.0, and (g) 0.2.

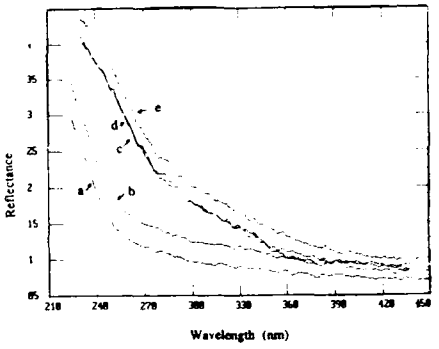


Figure 3A. Effects of doping S into Zinc Oxoborate. $Zn_8O_xS_{2-x}(BO_2)_{12}$, where x = (a) 2.00, (b) 1.98, (c) and (d) 1.97, (e) 1.99. The unit cell constant for these body-centered cubic structures was 7.475(2) Å for each solution.

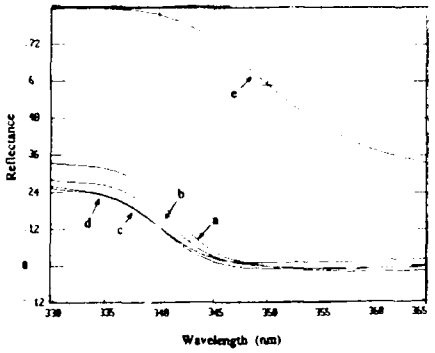


Figure 3B. Effects of doping O into Zinc Sulfoborate. $Zn_8O_xS_{2-x}(BO_2)_{12}$, where x = (a) 0.00, (b) 0.02, (c) 0.06, and (d) 0.10. The curve at (e) is the bulk sphalerite ZnS.

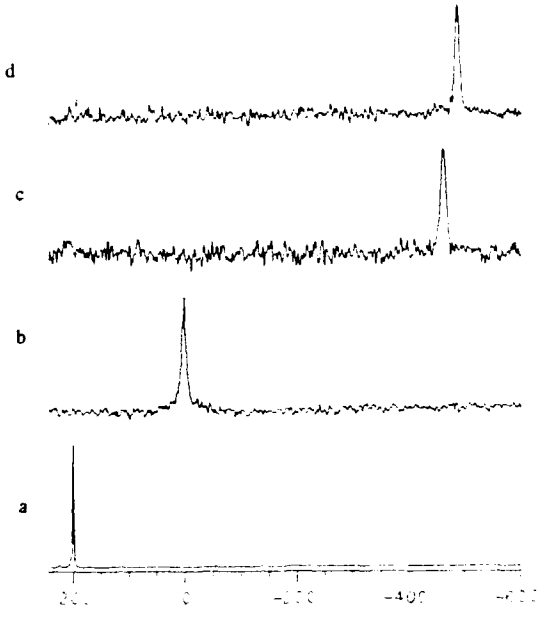


Figure 4A. ^{125}Te MAS NMR spectra of (a) bulk ZnTe, (b) bulk CdTe (reference compound, δ = 0 ppm) (c) $Zn_8Te_2(BeSiO_4)_6$ and (d) $Zn_8Te_2(BeGeO_4)_6$.

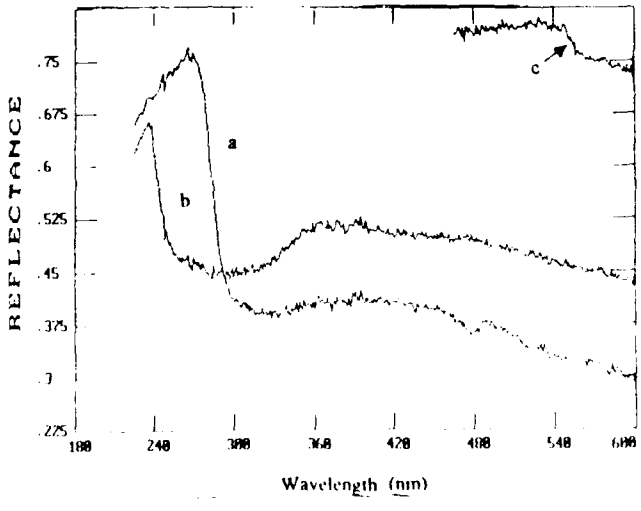


Figure 4B. Optical absorption data of (a) $Zn_8Te_2(BeGeO_4)_6$, (b) $Zn_8Te_2(BeSiO_4)_6$, and (c) bulk ZnTe; the absorption edge is indicated by the arrow.

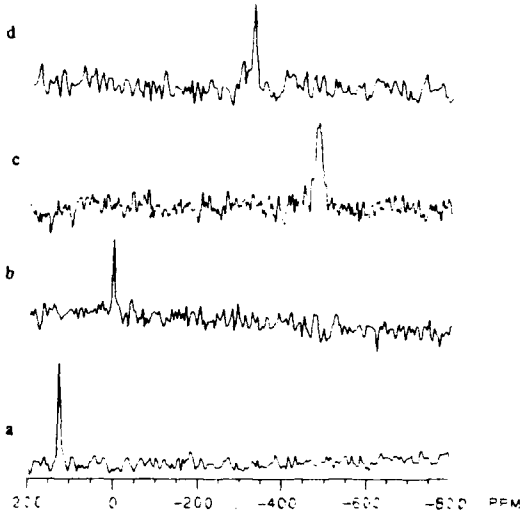


Figure 5A. ^{77}Se MAS NMR spectra of (a) bulk ZnSe, (b) bulk CdSe (reference compound, $\delta = 0$ ppm) (c) $Cd_8Se_2(BeSiO_4)_6$ and (d) $Zn_8Se_2(BO_2)_{12}$.

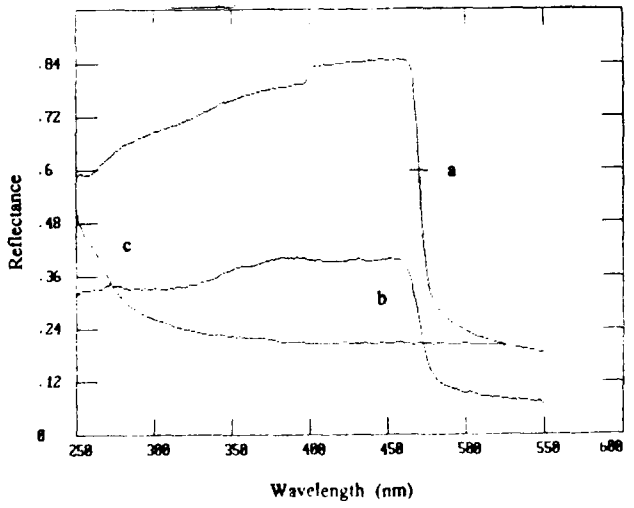


Figure 5B. Optical absorption data of (a) bulk sphalerite ZnSe, (b) $Zn_8Se_2(BO_2)_{12}$, and (c) $Zn_8Se_2(BeSi_{.5}Ge_{.5}O_4)_6$.

germanate, compared with +200 ppm for the parent compound ZnTe. The large upfield shift in both sodalite structures is indicative of a dramatic change in the chemical bonding properties of the central anion. This is expected; essentially the first coordination sphere of the bulk is isolated within the sodalite cage and charge delocalization is restricted primarily to the Zn_4Te tetrahedra. Consistent with these results are the optical spectra, shown in Figure 4B; the large blue shifts relative to the bulk reflect the change in electronic structure.

The analogous selenide system was examined by ^{77}Se MAS NMR and the results are shown in Figure 5A. As in the telluride compounds, the shifts are far upfield from those measured in the bulk semiconductors ZnSe and CdSe. Noteworthy is the observation that the shift difference between the Zn_4Se and Cd_4Se sodalites is approximately the same as that between bulk ZnSe and CdSe.

Also similar to the results obtained for the Te-compounds are the absorption data, shown in Figure 5B. For the $Zn_8Se_2(BeSi_5Ge_5O_4)_6$ compound, the absorption band is dramatically blue-shifted relative to bulk ZnSe. An anomaly seems to appear with the Zn_4Se borate material, however. From the NMR results, the Se bonding state clearly is electronically distinct from the bulk ZnSe and yet the absorption edge is not shifted to any large degree. Thorough "washing" of the Zn_4Se borate to remove any residual bulk ZnSe failed to change significantly the optical absorption [7]. The forced proximity of the Zn_4Se tetrahedra in the borate apparently results in absorption bands close to that of the bulk, despite the fact that the nature of the electronic transitions are very different in the two materials.

DISCUSSION

It has been shown that the optical properties of zinc chalcogenides can be varied by inclusion into the sodalite framework. In the borates, in which the M-X distance is shorter in the sodalite than in the corresponding bulk, the optical properties depend on the constitution of the central tetrahedra. Sharp band edges are observed for end members in a solid solution series and these features broaden slightly as the anion is mixed for single phase materials.

In the beryllosilicates and beryllogermanates, the cage effects dominate the optical spectra. The M-X distances in these materials are comparable to those in the bulk and the tetrahedra are well separated from each other. The exact nature of the optical absorption band in these materials has not yet been assigned; further characterization is in progress.

ACKNOWLEDGEMENTS

Funding for this project was provided by the Division of Materials Research of the National Science Foundation, The NSF Center for Quantized Electronic Structures Science and Technology (QUEST) at UCSB, and the Office of Naval Research.

REFERENCES

1. A. Henglein, Top. Curr. Chem. 143, 113 (1988).
2. A. P. Alivisatos, A. L. Harris, N. J. Levinos, M. L. Steigerwald, L. E. Brus, J. Chem. Phys. 89, 4001 (1988).
3. G. D. Stucky and J. E. MacDougall, Science, 247, 669 (1990).
4. Y. Wang, N. Herron, W. Mahler, A. Suna, J. Opt. Soc. Am. B. 4, 808 (1989).
5. K. L. Moran, W. T. A. Harrison, T. E. Gier, J. E. MacDougall, G. D. Stucky, Mat. Res. Soc. Symp. Proc. 164, 123 (1990).
6. T. E. Gier, W. T. A. Harrison, G. D. Stucky, Angew. Chem, 103, 1191 (1991).
7. From a private communication with Thomas E. Mallouk. The sodalite material is washed for 12 to 24 hours in an aqueous Br_2 solution which has been adjusted to a pH of 6 with bleach. This solution effectively dissolves bulk II-VI compounds.

EXCIMER LASER MELTING OF MBE-ZnSe

NALLAN C. PADMAPANI*, G.-J. YI*, G.F. NEUMARK*, Z. LU**, C.C. CHANG***, M.C. TAMARGO***

*Henry Krumb School of Mines, Columbia University, New York, NY,10027.
**Electrical Engineering Department, Columbia University, New York, NY, 10027.
***Bellcore, Redbank, NJ.

ABSTRACT

It has generally been concluded that good doping in wide-gap semiconductors is best accomplished by non-equilibrium means. Excimer lasers, because of their high intensity and short pulses, are ideal for this. Our earlier laser annealing work on bulk ZnSe resulted in complications due to increased twinning of the sample. Our present work shows that twinning can be eliminated by the use of originally untwinned MBE material. The MBE samples had the additional advantage, over bulk, of a far smoother surface, which simplified the investigation of melting and evaporation. Use of power levels of 10, 20, and 35 MW/cm^2 showed no melting at 10 MW/cm^2, melting and no detectable evaporation at 20 MW/cm^2, and evaporation at 35 MW/cm^2. Combined ion beam cratering and SEM examination showed a depth of the melted layer, at 20 MW/cm^2, of ~ 0.5 μm. Moreover, AES analysis showed minimal decomposition of the 20 MW/cm^2 sample.

1. INTRODUCTION

Wide band gap materials such as ZnSe are of high interest for applications in visible light emitting devices such as diode lasers and display panels. Obtaining bipolar conductivity in such materials has however been a pervasive problem; for ZnSe, the problem has been to obtain adequate p-type conductivity. For years, reports of high conductivity could not be reproduced (see e.g. ref.1). This problem has been alleviated recently, with carrier concentrations of $3*10^{17}$/cm^3, first reported by Park et al.[2], now having been obtained by a number of other groups (e.g. ref.3). Nevertheless, even higher concentrations would be desirable.

Based on an analysis showing low dopant solubilities in wide-gap materials [4], one of us has suggested that non-equilibrium dopant incorporation is required. One approach to this is incorporation via excimer laser melting. This is known to give dopant concentrations above the solubility limit in the case of elemental and III-V compound semiconductors, by increasing the substitutional dopant concentrations and activating the dopant atoms that had been incorporated via other nonequilibrium processes like ion-implantation, MBE etc.[5]. In our prior work [6], we attempted to redistribute the dopant (Na) from the interstitial (donor) site to the substitutional (acceptor) site by using such excimer lasers. This work was carried out on bulk ZnSe, and although it showed some encouraging results, all samples showed appreciably heavier twinning after the laser treatment than before it. Such twinning, based on an analysis of literature by one of us [1], is not satisfactory for either good doping or good device performance. However, all bulk material in that work showed some initial twinning, and in view of the potential benefits of excimer laser processing, we felt that the method should be tried on initially untwinned material, to check whether this would result in good (untwinned) material subsequent to melting. The present work examines this point.

In addition to examining the question of twinning on originally untwinned material (the present samples were grown by MBE - see ref. 7), investigations were carried out to determine that the samples did melt, that there was minimal evaporation, and that there was minimal

surface decomposition (i.e. preferential evaporation of one constituent). In our prior work [6], we did investigate these points. However, although we did obtain good circumstantial evidence on melting and on absence of decomposition, we did not obtain definitive evidence. We thus felt that obtaining further corroborative evidence, on the present better MBE samples, was warranted.

2. EXPERIMENTAL

The samples used were MBE grown, undoped ZnSe on GaAs with a (100) orientation. The ZnSe epilayer was 3μm thick with a mirror smooth surface and good luminescence characteristics. A Lambda Physik EMG 102 MSC excimer laser was used to anneal the samples. The wavelength of the coherent radiation was 308 nm and the pulse duration was ~20 ns. The samples were cleaned with methanol before annealing (the first sample to be annealed was not cleaned, but showed poor results. See section 3). All the samples were mounted on a graphite block and annealed in air (we do not expect any atmospheric contamination during the ultra short laser pulse anneal). The laser spot was focussed by a UV lens to the desired spot size, which was usually in the range of a few square mm. Based on our earlier results on bulk ZnSe[6], we used single laser pulses with intensities in the range of 10-40 MW/cm^2.

An optical Nomarski microscope and a JOEL scanning electron microscope (SEM) were used to observe the surface morphology and to check on possible twinning features on the surface of the sample. A Perkin Elmer 660 Scanning Auger Microscope was also used, which enabled us to obtain both SEM and Auger electron spectroscopy (AES) data. This also had an ion beam attachment, which could mill a crater on the samples. This enabled us to study the near surface layers of the samples by both SEM and Auger spectroscopy. Photoluminescence (PL) measurements were made with a He-Cd laser to observe the changes in luminescence due to laser annealing . For this, the annealed samples were lightly etched with a Br-methanol solution to obtain luminescence data from the sub-surface regions in the annealed region. The etch time was adjusted to remove about 0.1μm. An Alpha-step profilometer, with a depth sensitivity of a few nanometers,was used to measure the surface profile.

3. RESULTS

An important aim of the present work was to investigate the questions of melting, decomposition and evaporation of the samples. There were several reasons for this, given the fact that we had already investigated this for bulk samples. One was, as we mentioned above, that we desired additional corroborative evidence. In addition, the smoother surface of the present samples enabled us to obtain more reliable results, particularly as regards evaporation and melting. These aspects were investigated by the profilometer, SEM and Auger scans.

The laser annealing was carried out at three power levels viz., 10, 20 and 35 MW/cm^2. The 10 MW/cm^2 sample showed no evidence of melting. The profilometer scan was very smooth and showed no detectable change in the profile. Similarly, no change in the surface morphology was seen in the SEM. Also, a crater dug into the surface showed no evidence of melting (see results for 20 MW/cm^2 for comparison). In the case of the sample annealed at 20 MW/cm^2, the profilometer scan (Fig.1) shows a spike at the annealed - unannealed boundary and then the surface is wavy in the annealed zone. The annealed area appears visually dark with a clear boundary between annealed and unannealed regions. Fig.2 shows an SEM picture of a crater milled at the annealed- nonannealed boundary. The dark ellipse on the left is the exposed GaAs substrate at the bottom of the crater. Three layers can be distinguished in the annealed ZnSe: the bottom layer of undisturbed ZnSe, a second grey layer and a top dark layer. The top dark layer

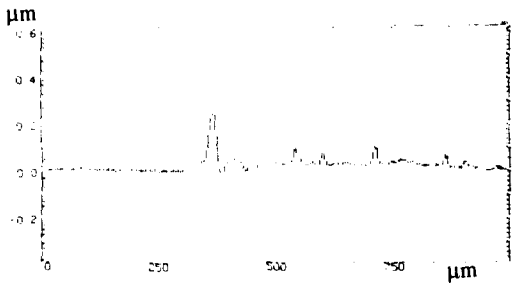


FIG. 1. Profilometer scan of a sample annealed at 20 MW/cm^2. The region to the left of the spike is unannealed and to its right is annealed.

was found to contain carbon, which could have come on to the surface from the graphite sample holder used during our annealing experiments and then diffused into the ZnSe during laser anneal. This layer is about 0.1µm thick. The composition of the second grey layer was analyzed by AES but no impurity could be detected at a concentration within the sensitivity of the AES. The thickness of this layer is about 0.5 µm. This layered structure was not present in the unannealed region of the sample. In addition, Auger surface scans were taken on the annealed and unannealed regions of the sample. The relative intensities of the Zn and Se peaks remained the same before and after the laser annealing. The sample annealed at 35 MW/cm^2 showed evidence of evaporation in the profilometer scans. The surface was visibly degraded with

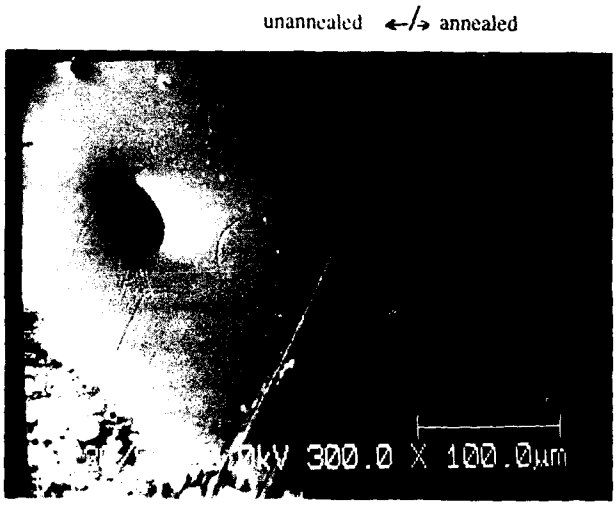


FIG. 2. A 1000X magnification SEM picture of a sample annealed at 20 MW/cm^2. This shows a crater at the unannealed-annealed boundary. The layered structure (see text for details) is visible in the annealed region while it is absent in the unannealed region.

extensive surface ripples and other features. So, no further work was done at and beyond this power level. It is also worth noting that the first sample, which was annealed at 20 MW/cm^2 without cleaning, showed some regions having a parallel line structure, where such lines give a strong indication of twinning (Some particles, presumably dust, were observed on this sample under the SEM; the twinning on this sample could have resulted from stresses caused by the interaction of these dust particles with the laser radiation).

Photoluminescence measurements were taken in the annealed region before etching, and in the unannealed regions before and after etching the sample to a depth of ~ 0.1μm (this should remove the top dark layer contaminated with carbon and expose the underlying grey layer). The PL spectra of the unannealed sample shows strong bound exciton lines (Fig.3). The PL intensity decreased drastically in the annealed region, so much so that we could not see any exciton luminescence. But after etching, the annealed region regained a part of its exciton luminescence (Fig.4). We also see an additional peak at ~2.3eV (indicated by the arrow in Fig.4).

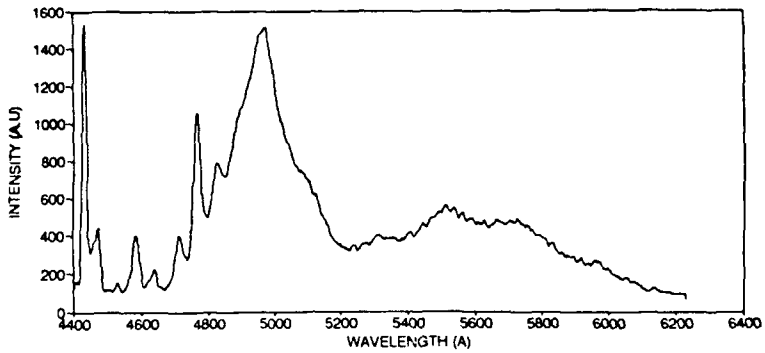


FIG. 3. PL spectrum of an as-grown MBE-ZnSe sample at 9 °K showing strong exciton luminescence.

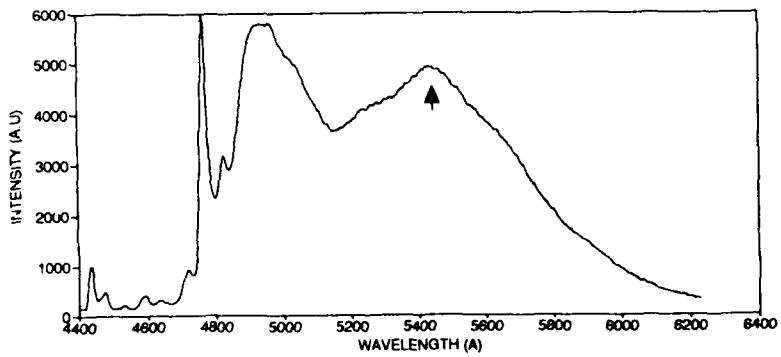


FIG. 4. PL spectrum of the annealed region of a sample annealed at 20 MW/cm^2 after a Br-methanol etch to a depth of 0.1 μm. Note the new peak at ~2.3eV (shown by the arrow). Also, note that the PL intensity was appreciably lower than prior to annealing; the indicated intensity is higher because a wider slit was used.

4. DISCUSSION

The spike at the boundary of the annealed region and the wavy nature of the surface profile (Fig.1) in the annealed region show that the material has melted and flowed. This has also been observed in the laser melting of silicon [8]. The occurrence of the layered structure only in the annealed region (Fig.2) proves that the layers were formed by the laser annealing. Based on the above profilometer and SEM results (Figs.1& 2), there can be no doubt that there was melting of the 20 MW/cm^2 sample. Moreover, based on the profilometer data (Fig.1) it is also apparent that this sample showed either no evaporation or, at most, very minimal evaporation. Regarding decomposition, the fact that the Auger scans showed comparable Zn and Se intensities before and after annealing gives a strong indication of minimal decomposition. It is more difficult to conclude that there is no decomposition, since it some Se (or Zn) were to evaporate, leaving some clumps or balls of Zn (or Se) on the surface, these may not give a strong enough Auger signal to significantly affect the Zn (or Se) peak; however, major decomposition seems unlikely. Moreover, if Zn vacancies were formed, they would be expected to form the well known A center [9], a complex with donors, showing a PL peak at about 2.0eV. This peak was not found in the PL spectra. Even the peak at 2.783eV, which some authors [10,11] have claimed to be formed by Zn vacancies, was not observed in the PL spectra.

In addition to the question of melting, it is also important to determine the depth of the melted layer; it is for instance of interest to see whether the melt depth is adequate to obtain devices such as diode lasers or LEDs. From our cratering work, we have concluded that there is a top layer, with appreciable carbon, of about 0.1 μm and a layer, showing SEM contrast, of about 0.5μm, below that. Since we did not see much carbon on the surface of the as-grown samples, we assume that the top layer resulted from carbon contamination due to some of the laser beam hitting the graphite holder (we are now modifying this part of our set-up). At this time we do not know the cause of the contrast of the lower grey layer, since Auger spectroscopy did not pick up any impurities within its sensitivity range. However it is known that relatively small changes in impurity concentrations can change the contrast in semiconductors [12]. That there is such a change is corroborated by the PL data, which shows a new peak at ~ 2.3 eV, in the annealed region, after etching (it is known that Cu introduces a peak in this range [9]). We therefore feel that we have good indication of a melted layer of ~0.5 μm. thickness. We are conducting further experiments to determine whether the grey layer boundary of Fig. 2. is indeed the melt boundary.

A further important aim of the present work was to investigate the occurrence of twinning after annealing. Based on our SEM and optical microscopy examinations, we saw no evidence of twinning on the cleaned samples. The fact that we did obtain a strong indication of twinning on one sample which was not cleaned, gives us confidence that we would have seen it on the cleaned material if it were there.

5. CONCLUSIONS

In conclusion, we have shown that we can obtain melting, with an adequate layer depth, without capping, with minimal (if any) evaporation and decomposition, of MBE- ZnSe. Moreover, we have also demonstrated laser melting without twinning, on originally untwinned material. The next step will be to attempt improved doping by such laser processing.

ACKNOWLEDGEMENT

This work was supported by NSF grant ECS-89-21159. We would like to thank Prof. Bersohn and Prof. Flynn for lending their laser facilities, and Arun Chattopadhyay and Liedong Zheng of the Department of Chemistry, Columbia University for their help in doing the laser annealing work.

REFERENCES

1. G.F. Neumark, J. Appl. Phys. 65, 4859 (1989).
2. R.M. Park, M.B. Troffer, C.M. Rouleau, J.M. DePuydt and M.A. Haase, Appl. Phys. Lett. 57, 2127 (1990).
3. M.A. Haase, J. Qui, J.M. DePuydt and H. Cheng, Appl. Phys. Lett. 11, 1272 (1991).
4. G.F. Neumark, Phys. Rev. Lett. 62, 1800 (1989).
5. R.T. Young and R.F. Wood, Ann. Rev. Mat. Sci. 12:323-50 (1982).
6. Guan-Jiun Yi, G.F. Neumark, Z. Lu, P.R. Newbury, C.F.Yu, B.J. Fitzpatrick, M. Shone and A. Sicignano, MRS Symp. Proc. 161, 141 (1990). (In this work, we observed, through Auger depth profiling, oxygen in a thin (0.5μm) surface layer, presumably resulting from diffusion during melting; however this result proved to be poorly reproducible).
7. M.C. Tamargo, J.L.DeMiguel, D.M. Hwang, H.H. Farrell, J. Vac. Sci. Tech. B6, 784 (1988).
8. D.H.Auston, J.A. Golovchenko, P.R. Smith, C.M. Surko and T.N. Venkatesan, Appl. Phys. Lett. 33, 539 (1978).
9. G. Jones and J. Woods, J. Lum. 9, 389 (1974).
10. M. Isshiki and K. Masumoto, J. Phys. C: Solid State Phys. 21, 2771 (1988).
11. Shi-Min Huang, Y. Nozue and K. Igaki, Jap. J. App. Phys. 22, L240 (1983).
12. J.I. Goldstein et. al. Scanning Electron Microscopy and X-Ray Microanalysis, p. 162.

CHARACTERISTICS OF ZnSe LAYERS GROWN ON Zn-STABILIZED AND Se-STABILIZED GaAs SUBSTRATES

S. AKRAM, H. EHSANI, I.B. BHAT and S.K. GHANDHI
Electrical, Computer and Systems Engineering Department, Rensselaer Polytechnic Institute, Troy, New York 12180.

ABSTRACT

Organometallic vapor phase epitaxial (OMVPE) growth of ZnSe on GaAs was carried out using dimethylzinc (DMZn) and dimethylselenium (DMSe) as source precursors. The growth of ZnSe can be initiated either by introducing DMZn first (Zn stabilized) or DMSe first (Se stabilized).

A systematic study of this growth initiation step on the properties of ZnSe epilayers was carried out using Photoluminescence (PL) and Double Crystal X-Ray Diffraction (DCD) in order to optimize the ZnSe-GaAs interface. PL and DCD data show a considerable difference in lattice relaxation mechanism between Zn and Se stabilized layers. Se stabilized layers are also seen to be considerably tilted with respect to the substrate. PL properties of Se stabilized layers exhibit strong near band edge emission (NBE) and weak deep level emission such as Y_O, compared to layers grown by Zn stabilization.

INTRODUCTION

ZnSe is a promising material for blue light emitting diodes, lasers and for other optoelectronic applications. Growth of ZnSe on GaAs by MBE [1], OMVPE [2], and ALE [3], has attracted the most attention because of the close lattice match between the two materials.

Unlike III-V systems where growth is always started by first introducing column V precursors and then column III precursors, the growth of ZnSe can be initiated by introduction of either the column II or column VI precursor. These two growth initiation steps are expected to result in different layer properties, as seen in other II-VI systems [4]. In this work, a systematic study of such initial stabilization of the GaAs substrate on the ZnSe layer properties was carried out.

EXPERIMENTAL

The growth of ZnSe was carried out in a low pressure horizontal OMVPE reactor with rf heating. Growth temperatures were in the range 450°C to 525°C and the reactor pressure was 300 torr. The layers were grown on (100) GaAs substrates misoriented 2° towards [110]. DMZn and DMSe were used as the source material. These substrates were degreased using standard solvents and etched in a solution of H_2O:H_2O_2:H_2SO_4 (1:1:5) by volume and dipped in NH_4OH to remove any oxide just before loading into the reactor. Typical partial pressure of

DMZn was 2.0 x10^{-4} atm, while that of DMSe was 3.0 x10^{-4} atm. The total gas flow through the reactor was maintained at 2000 sccm.

Growth was initiated by first introducing DMZn (Zn stabilized) or DMSe (Se stabilized) for 120 seconds, immediately after which the second precursor was introduced to start the growth. The partial pressures used in the growth of ZnSe were the same for stabilization effects. Initial stabilization was carried out for 120 seconds rather than a few seconds generally encountered in a typical reactor in order obtain consistent results.

The PL system consisted of 300mW Argon laser, 3/4m grating spectrometer and a photomultiplier tube with a thermoelectric cooled GaAs photocathode. PL spectra was recorded at 9°K excited by 10mW laser intensity. The X-Ray measurements were made as described in [5].

RESULTS AND DISCUSSION

The lattice mismatch between ZnSe and GaAs is about 0.3% and this lattice mismatch is accommodated by a compressive strain in the epilayer for thicknesses less than the critical thickness h_c (~1500 A°) [6]. As the thickness of the epilayer starts to exceed the critical thickness [7], misfit dislocations are rapidly generated reducing the compressive strain in the ZnSe epilayer. Beyond the critical thickness, the epilayer relaxes and the compressive strain due to lattice mismatch decreases, eventually becoming negligible and the dominant residual strain in the ZnSe epilayer, when cooled to room temperature, is tensile due to the differences in the thermal expansion coefficient for ZnSe and GaAs.

DCD and PL were used to determine the strain and out of plane lattice constant $a_\perp$ of the epilayers as a function of thickness. X-Ray diffraction is a well established technique to measure $a_\perp$ in ZnSe [8]. Similarly PL measurements have been studied in many hetroepitaxial systems including ZnSe - GaAs [9]. The free and bound exciton peak position is a function of strain in the layer.We have used the shift in energy for the heavy hole (E_x^L) as this is stronger and clearly identifiable to measure strain in the layers. From this shift, the in plane strain (e_{11}) was measured by using the following equation [9,10]:

$$\Delta E_x^L = [\, 2a\,(\,C_{11} - C_{12}\,)/\,C_{11} + b\,(\,C_{11} + 2C_{12}\,)/C_{11}\,]\,e_{11}$$

The values used for hydrostatic deformation potential (a) and shear deformation potential (b) are : -a=5.4eV, -b=1.2eV [11] respectively while values used for the elastic stiffness constants were C_{11}= 8.1 x 10^{11} dyn/cm^2 and C_{12}= 4.88 x 10^{11} dyn/cm^2. Figure 1 shows the change in E_x^L position for ZnSe grown on Zn-stabilized and Se stabilized GaAs substrates. Also shown in the figure is the in plane lattice strain in the layer, calculated using the above formula. As can be seen, the residual strain in the two types of layers is found to be different, even though for layers of thickness greater than h_c, both types of layers are expected to be relaxed at the growth temperature and the only strain observed should be due to difference in thermal expansion coefficients.

To confirm the above observation, we have measured the perpendicular lattice constant $a_\perp$ of the layers using DCD, and these (along with the PL) results are plotted in figure 2. Here, it is seen, that for layers grown under Zn stabilized conditions, ZnSe is completely relaxed at the growth temperature beyond 0.5μm. For the Se-stabilized case, the layers are still under compression at growth temperature. Clearly, the lattice relaxation mechanism of layers grown on Zn-stabilized substrates is different from those grown on Se-stabilized substrates.

The full width half maximum (FWHM) value of the x-ray diffraction peak is shown in figure 3 as a function of layer thickness. For layers <1.2μm the FWHM for both Zn and Se stabilized layers are similar. For layers >1.2μm, Zn stabilized layers are seen to have a lower FWHM. ZnSe layers grown with Se stabilization were seen to be tilted with respect to the substrate (figure 4) with a tilt of 440 arc-sec (0.12°) in the <110> direction for a 3.5μm thick layer. The tilt observed on Zn-stabilized layers is within the experimental accuracy of measurement and for all practical purposes these layers are not tilted with respect to the substrate. Earlier reports of ZnSe on GaAs indicated no tilt of the epilayer [12]. Moreover, the tilt of the layer is a function of the layer thickness and hence this is reflected in a higher FWHM for layers grown on Se stabilized surface.

As seen from figure 2, Zn and Se stabilized layers relax differently. Se-stabilized layers are seen to relax much slower. This difference in relaxation rates of Zn and Se stabilized layers is further supported by the difference in tilting of the epilayers for the two cases.

PL from Zn and Se stabilized layers is also considerably different as shown in figure 5. Similar PL was obtained for sample thickness from 0.5 to 3.2μm. Se stabilized layers exhibit strong near band edge (NBE) emission, very weak Y_0 emission, and no I_0^V emission. The Y_0 peak was attributed to dislocations and a strong Y_0 emission reflects a higher optically active dislocation density [13]. The I_0^V peak has also been found to exist in layers with high dislocation densities [14]. These results are consistent with an earlier report of improved PL from tilted ZnSe layers [15]. Differences in growth rates were also observed for Zn and Se stabilized cases, and Se stabilized surfaces exhibited superior morphology. From the above results, it is clear that Zn stabilized layers have a higher dislocation density which shows up as an intense Y_0 peak.

When DMZn is passed over GaAs at 525°C, a surface reaction takes place, probably forming Zn_3As_2 which is volatile leaving atomic gallium on the surface. This may be the source of dislocations on Zn-stabilized layers and the layer relaxes rapidly by forming a high density of dislocations. When DMSe is passed over GaAs, no surface reaction may take place because DMSe is very stable. However, we cannot rule out the possibility of Ga_2Se_3 formation. In fact this interfacial layer is found to be important in obtaining high quality ZnSe layers [16], with good interfacial properties. We believe growth with Se-stabilization results in defect free interface for thin layers and lattice relaxation takes place by glide of 60° dislocations from the surface. This mechanism generally results in tilt of the layer with respect to the substrate.

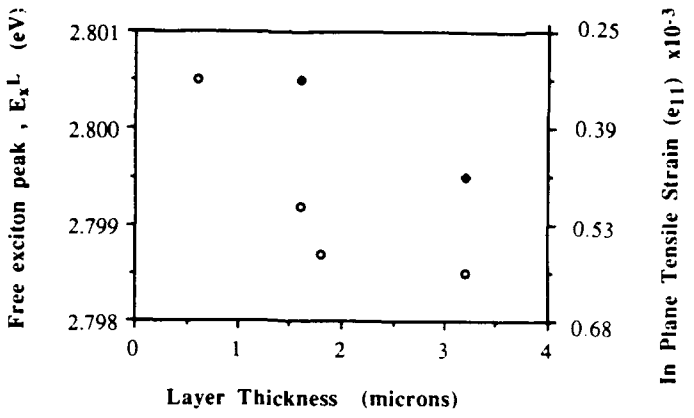


Figure 1. Free Excition (E_x^L) emission and in plane tensile strain (e_{11}) versus layer thickness.
(o Zn Stabilized, • Se Stabilized).

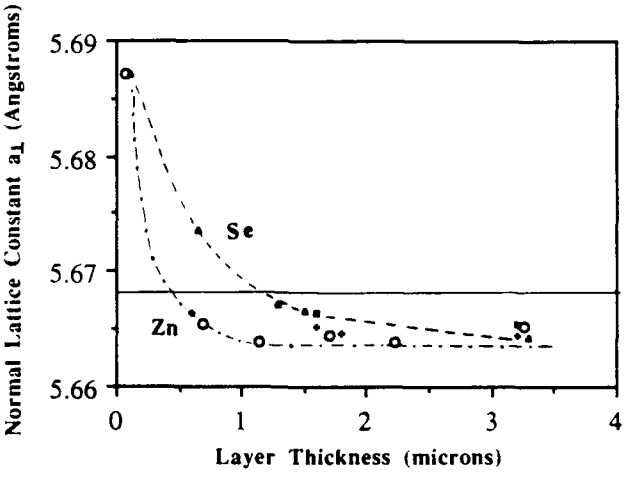


Figure 2. Normal Lattice Constant $a_\perp$ (Angstroms) versus Thickness (microns).
DCD (▪ Se, o Zn), and PL (▪ Se, ▪ Zn).

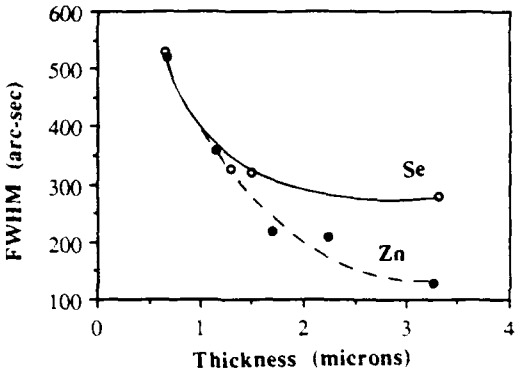


Figure 3. X-ray Diffraction Full Width Half maximum versus Layer Thickness (microns). (o Se Stabilized, • Zn Stabilized).

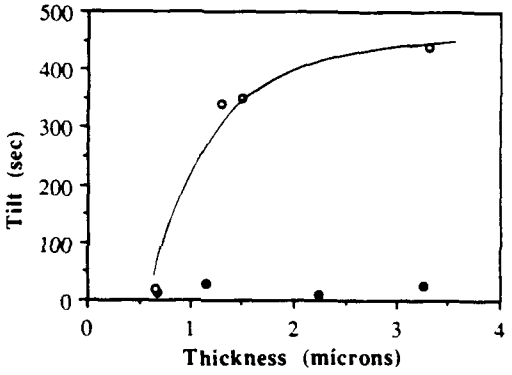


Figure 4. Epilayer Tilt (sec) versus Layer Thickness (microns). (o Se Stabilized, • Zn Stabilized).

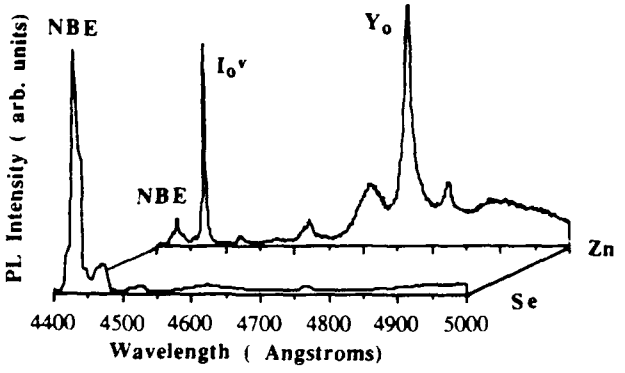


Figure 5. Photoluminescence from Zn and Se stabilized layers.

CONCLUSION

The effect of initial growth stabilization on the ZnSe layer properties is studied. It was found that layers grown on Se stabilized surfaces relax much slower compared to those grown on Zn-stabilized surface. For thickness > 0.5μm, the Zn-stabilized layers are completely relaxed at the growth temperature whereas this is not the case for even 3μm thick Se-stabilized layers. A large network of dislocations generated from the interface could be responsible for this relaxation in Zn-stabilized case. The optical properties of the layers grown by Se-stabilization is superior to the Zn-Stabilized case.

ACKNOWLEDGEMENTS

The authors would like to thank J. Barthel for technical assistance and P. Magilligan for manuscript preparation. This work was supported by the Defense Advanced Research Projects Agency, under the University research Initiative Program (N-00014-90-J-1582) administered by the Office of Naval Research. Partial support was provided by a fellowship from Philips Laboratories. This support is gratefully acknowledged.

REFERENCES

1. J. Depuydt, H. Cheng, J. Potts, T. Smith, S. Mohapatra, J. Appl. Phys. 62, 4756 (1987).
2. W. Stutius, Appl. Phys. Lett. 33, 656 (1978).
3. T. Yao, T. Takeda, Appl. Phys. Lett. 48, 160 (1986).
4. S.K. Ghandhi, N.R. Taskar and I.B. Bhat, Appl. Phys. Lett., 49, 1290 (1986).
5. I.B. Bhat, K. Patel, N.Taskar, J. Ayers, S.K. Ghandhi, J. Crys. Growth, 88, 23 (1988).
6. K.Mohammed, D. Cammack, R. Dalby, P. Newbury, B. Greenburg, J. Petruzzello and R N. Bhargava, Appl. Phys. Lett. 50, 37 (1987).
7. J.W. Matthews and A. E. Blackeslee, J. Crys. Growth, 27, 118 (1974).
8. T. Yao, Y. Okada, S. Matsui, K. Ishida, I. Fujimoto, J. Crys. Growth, 81 , 518 (1987).
9. K. Shahzad, Phys. Rev. B28, 8309 (1988).
10. F.H. Pollak and M. Cardona, Phys Rev. 172, 816 (1968) ; A. Gavini and M. Cardona, Phys. Rev. B1, 672 (1970).
11. A. Blacha, H. Presting, M. Cardona Phys. Status Solid, B126, 11 (1984).
12. E.Yamaguchi, I. Takayasu, T. Minato, M. Kawashima, J. Appl. Phys , 62, 885 (1987).
13. S. Myhajlenko, J. Bastone, H. Hutchinson, J. Steeds, J. Phys C. 17, 6477 (1984).
14. K. Shahzad, J. Petruzello, D. Olego, D Cammack, App.Phys. Lett. 57, 2452 (1990).
15. A. Ohki, N. Shibata, S. Zembutsu, J. Appl. Phys., 64, 694 (1988)
16. D. Li, J. Gonsalves, N. Otsuka, J. Qiu, M. Kobayashi, R. Gunshor, App. Phys. Lett. 57, 449 (1990).

OPTICAL TRANSITIONS ON CdS/CdTe CVD HETEROSTRUCTURES

Claude Boemare and M H Nazare

Departamento de Fisica. Universidade de Aveiro. 3800 Aveiro. PORTUGAL.

ABSTRACT

Wide-band gap II-VI semiconductors have direct bandgaps which cover the energy range from the red to the u-v. This makes such compounds ideal for optoelectronic applications. CdS has a band gap of 2.42 eV and becomes potentially useful for the green region of the spectrum. However, because CdS has a preference to adopt the hexagonal wurtzite structure, epitaxial growth of this semiconductor is complicated. Nevertheless succesful growth or CdS layers onto CdTe is possible. We report a detailed photoluminescence study of CdS/CdTe heterostructures grown by CVD. The CdS layers have high quality hexagonal structure. Luminescence lines are narrow enough and we could detect a splitting ocurring on the excited state of a neutral acceptor bound exciton, at 2.5462 eV.

INTRODUCTION

The fact that wide-band gap II-VI semiconductors have direct bandgaps which cover the visible range makes such compounds potentially suitable for optoelectronic applications like light emitting devices operating in the blue green region of the spectrum. The best example is ZnSe which luminesces very efficiently in the blue. This material also has an almost perfect lattice match to GaAs and high quality strained layers could be grown by different methods. Therefore, the optical properties of heterostructures and of superlattices based on ZnSe have been intensively studied for the last 6-7 years. As a result a blue laser based on ZnSe has recently been reported.

CdS has a band gap of 2.42 eV and becomes potentially useful for the green region of the spectrum. However, because CdS has a preference to adopt the hexagonal wurtzite structure, epitaxial growth of this semiconductor is complicated. Nevertheless succesful growth of CdS layers onto (111)A GaAs by MOCVD [1] and onto CdTe by CVD have been reported [2]. Recently CdS heterostructures have received renewed attention because of the novel features presented by intrinsic Stark superlattices of which CdS/CdSe type II superlattices are striking examples [3].

Growth on to (111) CdTe substrats yields hexagonal CdS of high quality. In

this paper we report the results of a detailed photoluminescence study performed on CdS/CdTe heterostructures grown by CVD.

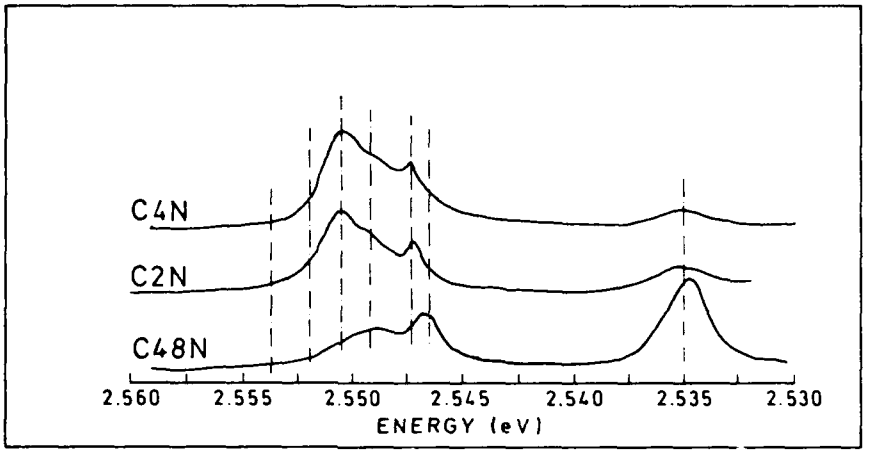


Figure 1: *PL spectra of CdS epilayers of various thicknesses grown on CdTe substracts, recorded* at 4K. Vertical lines indicate, from left to right, the positions of A, $I_{1B'}$, I_3, I_{1B}, I_2, I_5 and I_1

EXPERIMENTAL DETAILS

Single-crystalline CdS epilayers were grown on an (111) oriented CdTe substrate by CVD (Chemical Vapour Deposition). The epilayers thickness ranged from 1 μm up to 48 μm. The growth rate was 2.2 μ h^{-1} at a substrate temperature of 475 C and a source temperature of 800 C. The layers were grown on a Cd face under an hydrogen flux of 18 l h^{-1} in a quartz reactor. The composition of the substrate face, i.e Te or Cd, was determined by chemical attack using a solution 1:1:1 of hydrofluoric acid, nitric acid and methanol. Prior to growth the substrate face was polished mechanicaly until it was a mirror-like and chemicaly etched using a bromethanol solution. The surface of the grown CdS epilayer was also mirror-like, and good crystal quality was confirmed by X-ray mesurements.

Luminescence was excited using the 457 nm line from an Ar ion laser, and was collected at right angles to the axis of excitation. Measurements were made using

SPEX 1701 dispersive monochromator, fitted with a photomultiplier tube. In all cases the sample was mounted with the growth axis parallel to the excitation axis.

RESULTS and DISCUSSION

The valence and conduction bands for wurtzite semiconductors have both maxima and minima at the center of the Brillouin zone, and the associated Bloch functions have p-like and s-like orbital character, respectively. The top three valence bands are split, by the combined effect of both spin-orbit interaction and the action of a noncubic crystal field perturbation,into a Γ_9 and two Γ_7 states. The separations between the top state, Γ_9, and the two Γ_7 states, can be found from the Hamiltonian matrix. This matrix can be set up using the p-functions to represent the valence band states, and has the same form as the energy matrix for the zincblend valence band states under a $\langle 111 \rangle$ uniaxial strain [4,5]. The energies of the two low lying Γ_7 states are, relatively to the Γ_9 state, given by:

$$E = 1/2(\Delta_{so} + \Delta_{cr}) \pm [1/4(\Delta_{so} + \Delta_{cr}^2 - 2/3\Delta_{so}\Delta_{cr}]^{1/2} \qquad (1)$$

In conjunction with the conduction band each valence band gives rise to a series of exciton states, labeled A, B, C by increasing order of energy. A, B and C excitons are all seen polarized with the electric vector of the light perpendicular to the axis of growth, (c axis) but only B and C excitons are seen for parallel polarization [7].

Photoluminescence spectra from CdS layers with a thickness of $2\,\mu$ (sample C2N), $4\,\mu$ (sample C4N) and $48\,\mu$ (sample C48N) are shown in figure 1. In figure 2 the temperature dependence of the luminescence is depicted.

In all spectra we can identify the recombination of free excitons A, as well as excitons bound to neutral acceptors, I_1 and I_5 at 2.5359 eV and 2.5459 eV respectively, to neutral donors, I_2, at 2.5470 eV and to an ionized donor, I_4, at 2.5499 eV (figures 1 and 2) [6,7]. This identification is confirmed by the temperature dependence of all the features. Raising the temperature strongly affects the intensity of the bound exciton lines, I_1 to I_5, relatively to the intensity of the free exciton, A line. At 4 K bound exciton lines dominate the spectrum while at 20 K the situation is reversed. The temperature dependence reflects the diference in binding energy between the exciton to the impurity and the exciton itself.

The energies we measure at 4 K for all the components of the edge recombination, agree, as expected, with the correspondent value measured for bulk CdS, indicating

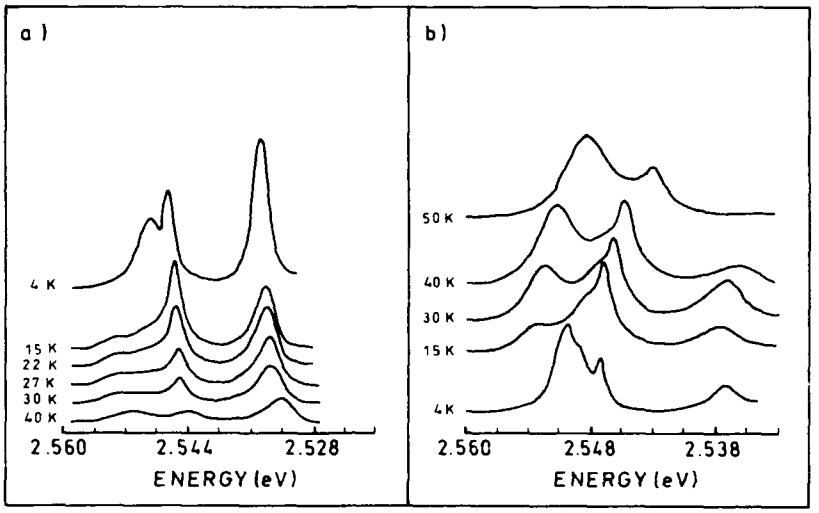


Figure 2: Photoluminescence spectra from samples (a) C2N and (b) C4N at various temperatures

that the thickness of our samples is well above the critical thickness.

We could also observe (figure 3) the states I_{1B} and $I_{1B'}$ arising from the I_1 neutral acceptor state and an exciton formed from a hole in the second valence band. The splitting of 1.5 meV arising from the exchange interaction between the two unlike holes [8].

The A exciton is split by jj coupling into Γ_5 and Γ_6 states. Altough transitions from the Γ_6 state into the fundamental state are forbidden they have been reported to occur (the AΓ6 line in reference [7]). The transition is perhaps made allowed trough mixture with the exciton state originated from the Γ_7 valence band. This transition could be detected in some of our samples (figure 3).

A further splitting was also detected for the I_5 line [6] identified as an exciton recombination at a neutral acceptor (figure 4). The two lines I_5 and I_5', at 2.5464 eV and at 2.5468 eV are separated by an energy of .4 meV and thermalize (figure 4) according to a Boltzmann distribution law.

$$I_5'/I_5 = \alpha \exp(-\Delta E/KT) \qquad (2)$$

We suggest that the splitting may be due to hole-hole interaction. However more work needs to be done before discussing this assignement in more detail.

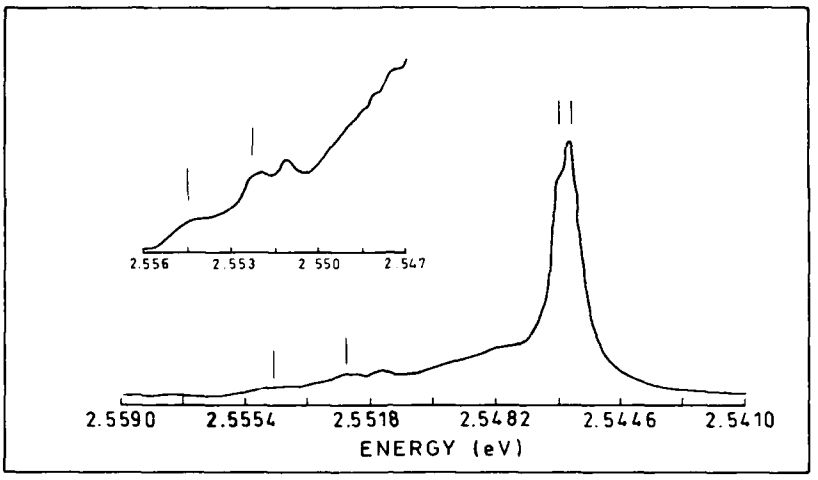


Figure 3: *High temperature (15K) photoluminescence spectrum of a 1μm thick CdS layer. Vertical lines indicate, from left to rigit, AF5, AF6, I_5 and I_5'.*

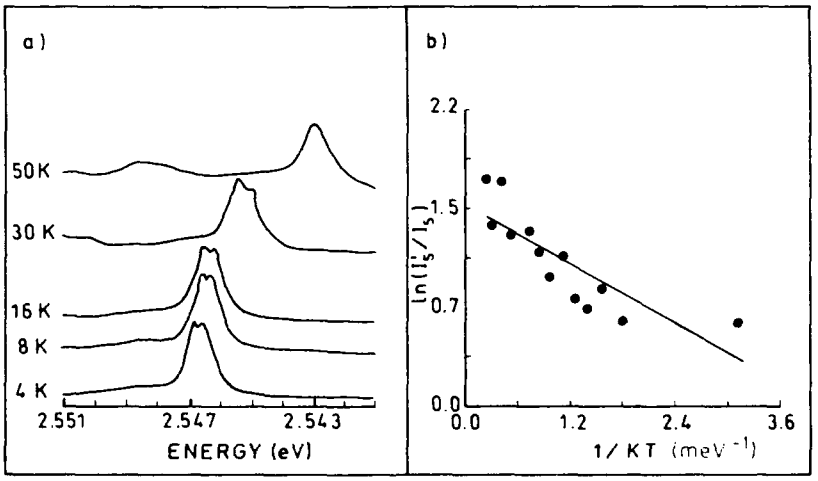


Figure 4: *(a)The I_5 and I_5' lines recorded in PL at different temperatures. (b)Logarithm of the intensity ratio of I_5/I_5' line as a function of reciprocal temperature. Solid line represents Eq. (2) using $\Delta E = 36$meV and $\alpha = 1.5$. These values are the best fit values in a least squares sense.*

CONCLUSIONS

In this paper we have shown that good crystal quality CdS can be grown onto CdTe (111) face by CVD. The quality is demonstrated by the photoluminescence obtained from the samples.

We have also detected a previously unreported zero field splitting of a acceptor bound exciton transition and ascribed it to *jj* coupling. Further work is under way to clarify this point.

ACKNOWLEDGEMENTS

We acknowledge INIC and JNICT (*contract* MPF/114/90) *for financial support*. The work was started as a project for a Master Degree Thesis and one of us (CB) gratefully acknowledges EEC *for a scholarship under the programme* ERASMUS. The samples have been grown at the University of Liège and we acknowledge Ann Sweyllan.

References

1 Halsll M P, Davies J J, Nicholls J E, Cockayne B, Wright P J and Russel G J *1988 J Cryst. Growth* **91** 135

2 Halsll M P, Davies J J, Nicholls J E, Cockayne B, and Wright P J 1991 *J. Lumin.* **48-49**

3 Mancini A M, Lovergine N, De Blasi C and Vasanelli L 1988 *Nuovo Cim.* **10 D** 57-68

4 Langer D W, Euwema R N, Koh Era, and Takao Koda 1970 *Phys. Rev.B* **2** 4005-4022 5 Pikus G E 1964 *Soviet Phys. Solid State* **6** 261-281

6 Reynolds D C and Litton C W 1963 *Phys. Rev.* **132** 1023-1029

7 Thomas D G and Hopfield J J 1962 *Phys. Rev.* **128** 2135-2148

8 Hopfield J J and Thomas D G 1961 *Phys. Rev.* **122** 35-52

VAPOR-PHASE GROWTH OF EPITAXIAL AND BULK ZnSe

W.L. AHLGREN, S. SEN, S.M. JOHNSON, W.H. KONKEL, J.A. VIGIL, AND R.P. RUTH
Santa Barbara Research Center, 75 Coromar Drive, Goleta, CA 93117

ABSTRACT

Epitaxial and bulk ZnSe of good structural perfection have been grown by vapor-phase techniques. Epitaxial undoped ZnSe layers were grown by metal-organic chemical vapor deposition (MOCVD) on GaAs {100} substrates in a horizontal-flow quartz reactor chamber. Conventional pyrolytic growth at 450°C was used, with diethyl zinc (DEZn) and diethyl selenium (DESe) reactants transported in hydrogen carrier gas.

Layers with smooth surface morphology and very good crystal structure were obtained, with no evidence of gas-phase pre-reaction. Sharp electron channeling patterns produced in the scanning electron microscope (SEM) indicated that {100}-oriented ZnSe layers were grown on {100} GaAs surfaces, as expected. X-ray rocking-curve analysis with a silicon four-crystal monochromator gave full-width at half-maximum (FWHM) line widths of 165 to 180 arc-sec for layers 2.5 to 3.0 μm thick, better than values for MOCVD-grown ZnSe/GaAs reported to date in the literature known to us. Cathodoluminescence (CL) imaging in the SEM showed significant defect substructure in the layers, probably due to lattice-misfit dislocations in the interface region. Bright blue CL emission from the layers was observed in the SEM at both 77K and room temperature, indicating the dominance of radiative recombination in the material.

Bulk ZnSe crystals were grown using a physical vapor transport technique. The crystals, a few millimeters on a side, had fully developed crystal facets, predominantly {110}-oriented. X-ray rocking-curve analysis gave FWHM values of about 19 arc-sec, indicating excellent structural perfection.

INTRODUCTION

ZnSe is a material of interest for the production of blue-emitting laser diodes, provided p-type material of high conductivity can be prepared. In recent years, substantial progress has been made toward solving this long-standing problem. P-type doping has now been achieved by MBE, MOMBE, and MOCVD techniques (for MOCVD see Yasuda, Mitsuishi, and Kukimoto [1] and Phat et al. [2]). Low-temperature epitaxial growth (around 350°C) appears to be important. Low growth temperature should (1) minimize point defect formation during growth; (2) aid dopant incorporation during growth; and (3) minimize formation of misfit dislocations during cool-down, due to differences in thermal expansion coefficient between substrate and epitaxial layers. Photo-assisted growth may also be important to achieve high doping levels and low growth temperature.

Choice of substrate for epitaxy is important. GaAs is attractive because of its highly developed technology, ready availability, and close lattice match to ZnSe. Nevertheless, there are potential problems with GaAs as a substrate for ZnSe epitaxy: (1) Ga and As from the substrate may diffuse or be vapor-transported into the II-VI epitaxial layer, unfavorably affecting the electrical properties. (2) Exact lattice-matching of the II-VI epitaxial layer to the GaAs substrate at the growth temperature, although achievable in principle using ZnSSe alloys, may be difficult initially, when II-VI alloy composition and uniformity are not well controlled. Lattice-mismatch will lead to the formation of defects in the epitaxial layers that will unfavorably affect the electrical properties and the long-term stability of devices produced using the material. (3) The lattice parameter of the II-VI epitaxial layer can be exactly matched to that of GaAs at only one temperature because the two materials have different thermal expansion coefficients. Even if the layer is perfectly matched to the substrate at the growth temperature, lattice defects may be generated in the layer when it is cooled to room temperature.

Because of these problems, it is desirable to also have available high-quality ZnSe substrates as an alternative to GaAs.

In this paper we report initial experiments in the growth of both epitaxial and bulk ZnSe by vapor phase techniques. The objective of this preliminary work was to establish a baseline for epitaxial growth of ZnSe on GaAs and for bulk growth of ZnSe.

EPITAXIAL GROWTH OF ZnSe ON GaAs

ZnSe epitaxial layers of good surface morphology and crystal lattice perfection were grown by conventional pyrolytic MOCVD on GaAs substrates. The growth conditions and characteristics of the epitaxial layers are discussed in this section. The results provide a baseline upon which future improvements will be made.

MOCVD Growth Conditions

A horizontal quartz reactor with a tilted graphite susceptor heated from below by a focused quartz-halogen lamp was used. The reactor configuration is shown in Figure 1. Alkyl reactants were chosen for both the zinc and the selenium sources to avoid the gas phase pre-reaction associated with the use of hydrogen selenide. The reactants used were diethyl zinc (DEZn) and diethyl selenium (DESe). This particular combination of reactants has been previously used by Mitsuhashi, Mitsuishi, and Kukimoto [3] A similar system, dimethyl zinc (DMZn) and DESe, has been used by a number of groups, including Mitsuhashi et al.[4] and Giapis et al. [5].

Prior to growth, the GaAs {100} or {100} 2° to ⟨110⟩ substrates were etched in 15:1:1 H_2SO_4:H_2O_2:H_2O solution at 20 to 30°C for 20 seconds, rinsed in DI water and dried with N_2, and then baked in-situ in the reactor, in flowing hydrogen, at 600°C for 15 minutes. The substrate temperature during growth was 450°C. The reactor pressure was 304 Torr (0.4 atm). In the majority of the experiments, the total gas flow was 1.29×10^{-1} mol min^{-1} and the reactant flows were 1.81×10^{-5} mol min^{-1} (DEZn) and 7.27×10^{-5} mol min^{-1}. Thus, the total reactant mol fraction was 7×10^{-4}, and the VI:II reactant ratio was 4.

Growth rates were typically about 0.7 μm h^{-1} (corresponding to a deposition efficiency of 1.6%), and growth runs were typically about 4 hours in duration, leading to layers about 2.5 to 3.0 μm thick. A total of eight growth experiments were carried out. Most layers grown were specular, as shown in Figure 2. There was no direct evidence of gas-phase pre-reaction, such as powdery deposits. The low overall deposition efficiency, however, could be indicative of a competing reaction; alternatively, it may simply reflect inefficient pyrolysis of one of the reactants under the deposition conditions employed, which were not optimized.

Epitaxial Materials Characteristics

The layers were characterized to determine structural perfection, impurity content, and luminescence properties.

Structural Perfection. The layers had good structural perfection, as indicated by their electron channeling patterns and by x-ray rocking-curve analysis. Very sharp electron channeling patterns were obtained in the scanning electron microscope (SEM), showing that epitaxial ZnSe {100} was grown on GaAs {100}. X-ray rocking-curve analysis carried out with a four-crystal Si monochromator and Cu $K\alpha_1$ radiation gave a FWHM in the range 165 to 180 arc-sec, better than available literature reports for ZnSe on GaAs, but still

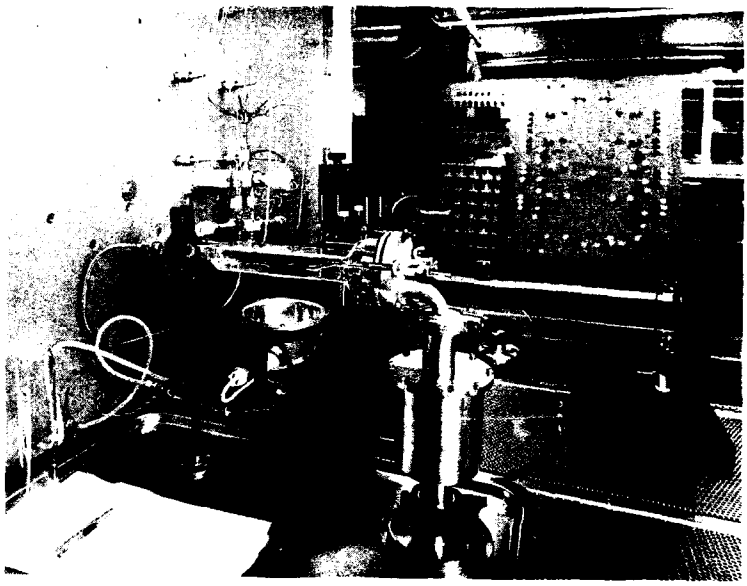


Figure 1. Horizontal growth chamber for pyrolytic MOCVD

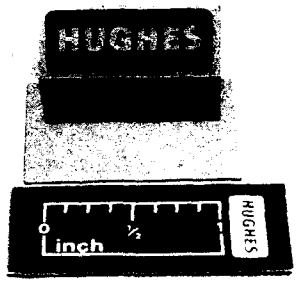
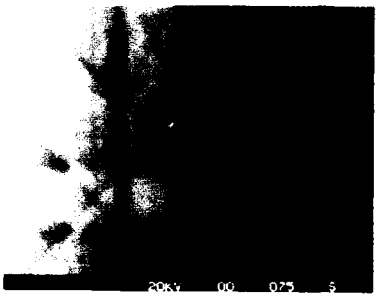
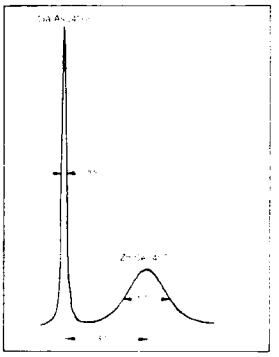


Figure 2. MOCVD-grown ZnSe epitaxial layer, 2.7 μm thick, grown on GaAs (100) substrate

capable of improvement. Typical results are shown in Figure 3. The separation between the ZnSe and GaAs (400) x-ray reflections is somewhat anomalous. A separation in the neighborhood of 300 arc-sec was typically observed, whereas the theoretical separation is 342 arc-sec. This may be indicative of strain or tilt in the epitaxial layer.



(a)



(b)

Figure 3. Lattice-structural perfection of epitaxial ZnSe, 2.7 μm thick, grown on GaAs (100) substrate. (a) Electron-channeling pattern; (b) X-ray rocking curve

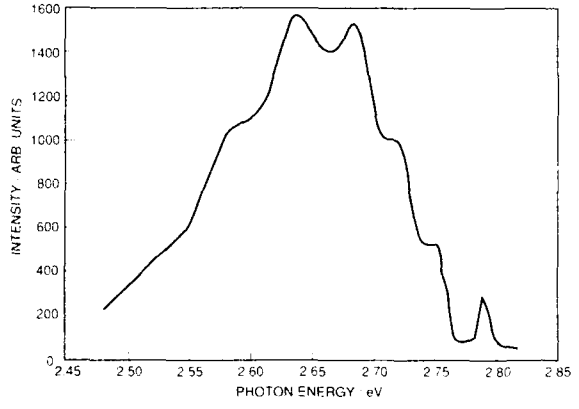
Cathodoluminescence imaging in the SEM showed a substantial defect substructure in the layers, which can tentatively be ascribed to misfit dislocations. These results are consistent with the expectation that structural improvement can be expected by growing $ZnS_{1-y}Se_y$ alloys lattice-matched to GaAs at the growth temperature, as reported in the literature.

Impurity Content. Key to the p-type doping of ZnSe is the production of pure material, free of residual n-type donors, into which acceptor impurities can be introduced in a controlled manner. One of the layers was analyzed first by laser-ionization mass spectrometry (LIMS) and then by secondary-ion mass spectrometry (SIMS). The LIMS analysis indicated that in the main part of the layer, the principal contaminants were Cd and Te, but that in addition the Ga and As concentrations were also high. This suggests that the Cd, Te and the Ga contamination may be associated with Ga droplets that migrate to the GaAs substrate as discussed below. SIMS analysis was carried out with both O_2 and Cs primary beams, and confirmed that Cd, Te, Ga, and As are the primary contaminants. Significant levels of Cl were also found. Significant levels of Cu, C, O, and S were recorded, but these may be due to instrumental background.

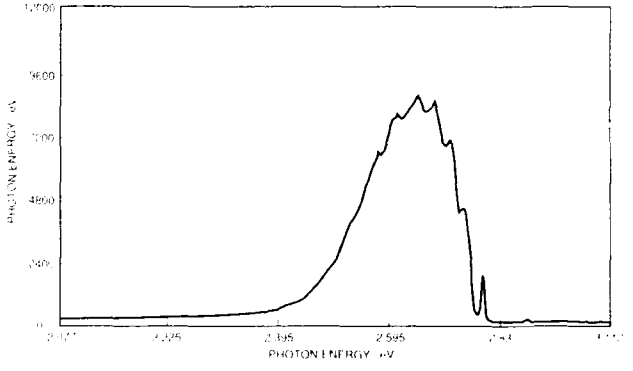
These results suggest that purity improvement can be achieved by taking several steps: (1) Cd and Te contamination comes from shared lines in our II-VI MOCVD system, which is also used to grow HgCdTe. Apparatus modifications have been carried out to minimize this problem in the future. (2) Ga and As contamination may come from the Ga-rich surface of the GaAs substrate annealed under flowing hydrogen at too high a temperature, causing minute Ga droplets (with dissolved As) to form on the surface. These can be eliminated by a lower-temperature, better-controlled anneal of the GaAs substrate. (3) Cl is a well-known contaminant in diethyl zinc, arising from the synthetic route employed. Zinc reactants synthesized by a Cl-free process are now available, and can be used in future work. (4) Further development of analytical techniques, including SIMS, is needed to eliminate possible instrumental background effects and provide adequate quantitation.

Luminescence Properties. Bright blue cathodoluminescence was observed to emanate from the ZnSe layer in the SEM at room temperature and at 77K (brighter at the lower temperature). Spectral analysis of the cathodoluminescence (CL) was carried out at the University of California, Santa Barbara. Photoluminescence (PL) spectra were also measured. The CL and PL spectra, shown in Figure 4, agree well. Note that the CL spectrum was measured at 15K, whereas the PL spectrum was measured at 1.4K. The spectra show a weak peak near the band edge and a strong, broad, sub-bandgap band that may be due to donor-acceptor pair recombination.

Table I is a summary of the ZnSe bandgap at the measurement temperature, from Gumlich, Theis, and Tschierse [6], and of the positions of the observed CL and PL near-edge peaks (the position of a similar peak observed in bulk-grown material, to be described below, is also included). Fine structure in the PL near-edge peak, not visible in Figure 4 but observed at higher resolution, is indicated by entries in the table. The near-edge peaks in the epitaxial ZnSe are believed to be associated with free excitons, which, according



(a)



(b)

Figure 4. Luminescence spectra of ZnSe epitaxial layer. (a) Photoluminescence at 1.4K; (b) Cathodoluminescence at 15K

to the cited reference, have a binding energy of about 0.02eV, consistent with the observations summarized in Table I.

Table I. ZnSe bandgap and near-edge CL and PL data

Temperature/K	1.4	15
ZnSe bandgap/eV	2.82	2.81
Epi ZnSe near-edge PL peaks/eV		
First principal peak	2.790	
Second principal peak	2.793	
High-energy shoulder	2.799	
Epi ZnSe near-edge CL peak/eV		2.79
Bulk ZnSe near-edge CL peaks/eV		
Principal peak		2.781
High-energy shoulder		2.790

BULK GROWTH OF ZnSe

ZnSe crystals were grown by a close-spaced physical vapor transport technique. Single-crystals of small size but excellent structural perfection and good purity (as indicated by luminescence measurements) were obtained. The growth conditions and characteristics of the materials produced are discussed in this section.

Vapor Transport Growth Conditions

The growth technique is illustrated in Figure 5. Stoichiometric proportions of high-purity (6 9s grade) elemental Zn and Se from Osaka/Asahi were pre-reacted and multiply-sublimed in separate ampoules prior to growth. This

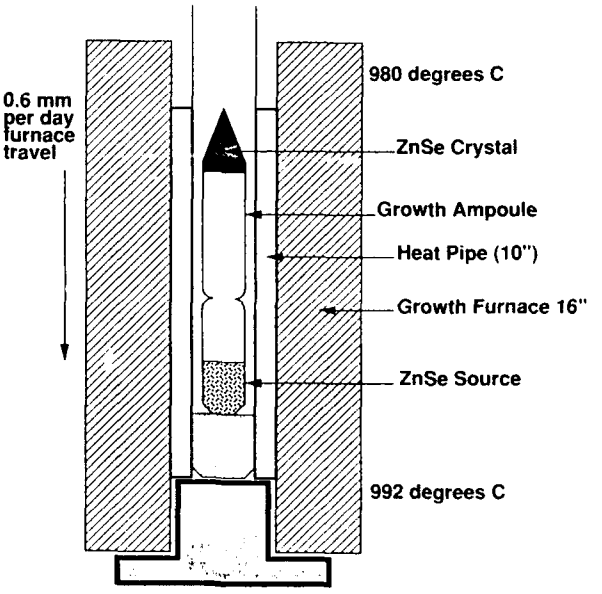


Figure 5. Growth of ZnSe by the close-spaced physical vapor transport technique

results in further purification by separating nonvolatile and low-vapor-pressure impurities from the ZnSe sublimate. To bring about single-crystal growth, the multiply-sublimed polycrystalline ZnSe charge was placed in one end of an evacuated quartz ampoule maintained at 992°C, while the other end of the ampoule was maintained at 980°C, establishing a relatively small temperature gradient of 0.3°C cm^{-1} along the axis of the growth ampoule. The furnace was then slowly translated in the direction pointing from the cooler to the hotter zone. The rate of furnace travel was fixed at 6 mm per day. The single-crystal growth was unseeded. The duration of the growth was approximately four weeks. During the course of the growth, an accidental power failure occurred that interrupted the transport process.

Bulk Materials Characteristics

The crystals grown were a few millimeters on a side. This small single-crystal size is probably due to a growth interruption caused by the power failure that occurred during the experiment. The crystals had fully developed facets, predominantly {110}-oriented. X-ray rocking-curve analysis carried out with a four-crystal Si monochromator gave a FWHM of 19 arc-sec, indicating excellent crystal lattice perfection. Very bright cathodoluminescence was observed. The CL spectrum at 15K is shown in Figure 6. As discussed in connection with Table I, the sharp peak at about 2.78 to 2.79 eV can be associated with free excitons. Phonon replicas at lower energies, separated by about 31 meV, are derived from this peak. The brightness of the free exciton emission indicates excellent crystal lattice perfection, in consonance with the very narrow X-ray rocking curve linewidth observed. There is also a broad, very bright, emission band at lower energies (2.3 to 2.5 eV). The origin of this band is uncertain. Its presence was reflected by the slightly greenish appearance of the as-grown crystals.

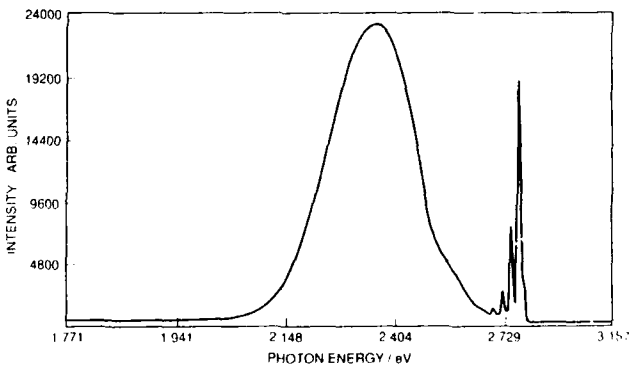


Figure 6. Cathodoluminescence spectrum of bulk ZnSe at 15K

SUMMARY AND CONCLUSION

The results of preliminary experiments in vapor phase growth of ZnSe, both epitaxial and bulk, have been reported. Epitaxial layers and bulk single crystals of good crystal lattice perfection were obtained. Impurities in the epitaxial layers were determined by mass-spectroscopic techniques, and their likely sources identified. The luminescence properties of the materials were studied, and bright emission was observed. Both epitaxial and bulk material give evidence of free excitons at 15K, very strong in the bulk, relatively weak in the epitaxial material. Both also show strong sub-bandgap bands of unknown origin, presumed to related to the presence of impurities and/or point defects.

In addition to eliminating the sources of the principal impurities (Cd, Te, Ga, As, and Cl) observed in the epitaxial material, lowering of the growth temperature from 450°C to around 350°C is deemed important for future efforts to achieve high-conductivity n-type and p-type doping of ZnSe. To achieve this, promising approaches are the use of photo-assisted MOVPE and/or the use of new reactants designed for lower-temperature decomposition while still avoiding gas-phase pre-reaction.

Future work on bulk growth of ZnSe will focus on increasing the single-crystal size while still maintaining excellent crystal lattice perfection. The availability of high-quality large-area ZnSe substrates will aid the development and understanding of high-purity and doped epitaxial ZnSe.

ACKNOWLEDGMENTS

We would like to thank Virginia Harper of SBRC for expert operation of the SEM; Takashi Yasuda and Jim Merz of UCSB for the photoluminescence measurements reported in this paper; and Sid Bhargava and Pierre Petroff, also of UCSB, for the cathodoluminescence measurements.

REFERENCES

1. T. Yasuda, I. Mitsuishi, and H. Kukimoto. "Metalorganic vapor phase epitaxy of low-resistivity p-type ZnSe." Appl. Phys. Lett. *52*, 57-59 (1988).

2. B.A. Khan, N. Taskar, D. Dorman, and K. Shahzad (1991). "P-type conversion of nitrogen-doped ZnSe films grown by MOCVD." Proceedings of the Spring 1991 MRS Meeting (unpublished).

3. H. Mitsuhashi, I. Mitsuishi, and H. Kukimoto. "MOCVD growth of ZnS_xSe_{1-x} epitaxial layers lattice-matched to GaAs using alkyls of Zn, S, and Se." Jap. J. Appl. Phys. *24*, L864-L866 (1985).

4. H. Mitsuhashi, I. Mitsuishi, M. Mizuta, and H. Kukimoto. "Coherent growth of ZnSe on GaAs by MOCVD." Jap. J. Appl. Phys. *24*, L578-L580 (1985).

5. K.P. Giapis, D-C. Lu, D.I. Fotiadis, and K.F. Jensen. "A new reactor system for MOCVD of ZnSe: Modelling and experimental results for growth from dimethyl zinc and diethylselenide." J. Crystal Growth *104*, 629-640 (1990).

6. H.E. Gumlich, D. Theis, and D. Tschierse. "Zinc selenide." In Landolt-Bornstein, New Series, *Vol. 17b*, pp.126-156. Berlin: Springer-Verlag (1982).

OMVPE GROWTH OF ZnSe UTILIZING ZINC AMIDES AS SOURCE COMPOUNDS: RELEVANCE TO THE PRODUCTION OF p-TYPE MATERIAL

WILLIAM S. REES, JR.* AND DAVID M. GREEN

Department of Chemistry and Materials Research and Technology Center, The Florida State University, Tallahassee, FL, 323006-3006 U.S.A.

TIMOTHY J. ANDERSON AND ERIC BRETSCHNEIDER

Department of Chemical Engineering and MICROFABRITECH, University of Florida, Gainesville, FL

ABSTRACT

Growth of ZnSe on GaAs from H_2Se and $Zn[N(TMS)_2]_2$ precursors has been demonstrated. When Et_2Zn is used as the zinc precursor a higher quality deposit is obtained. Results of experiments employing Et_2Zn as the main zinc source with $Zn[N(TMS)_2]_2$ introduced at a dopant level indicate nitrogen has been incorporated. Final thin films were characterized by PL, XRD, SIMS, and Raman.

INTRODUCTION

A recent report by workers from the 3M Company of a ZnSe-based quantum well diode laser operating at 77K in a pulsed mode has motivated researchers to develop methods for producing low resistivity, p-type ZnSe with nitrogen doping. The main interest in this wide band-gap material stems from its potential to operate in the blue end region of the visible spectrum. Several current problems exist in the development of ZnSe-based optoelectronic devices, including the lack of a commercially available lattice-matched substrate material, a suitable cladding material, and a reproducible method for production of low resistivity, p-type material. This last problem is the focus of this report.

The first report of conductive p-type ZnSe grown by MOVPE was in 1988 by Yasuda[2] *et al.* Lithium nitride (Li_3N) was the dopant source in a low pressure reactor utilizing $ZnMe_2$ and $SeEt_2$ precursors. An extremely high doping level of 9×10^{17} cm^{-3}, determined by Hall measurements, was reported. PL measurements suggested lithium was the active acceptor element, although nitrogen could not be excluded. However, this report has not been duplicated by other workers. Yoshikawa[3] *et al.* demonstrated lithium incorporation as an acceptor when cyclopentadienyl lithium (*CpLi*) was used as a source in conjunction with $ZnMe_2$ and $SeMe_2$ at 500°C in an atmospheric pressure MOVPE system. Only PL results were given and the CpLi source is a low vapor pressure solid (like Li_3N) thus making it difficult to control transport rates. More recently workers at Toshiba[4] have demonstrated moderate levels of p-type doping using tertiary-butyllithium (*t*BuLi) as the lithium source and $ZnMe_2$ and $SeMe_2$ as the main element sources. Hall measurements were

Mat. Res. Soc. Symp. Proc. Vol. 242. © 1992 Materials Research Society

performed on both the as-deposited film and the film for which the GaAs substrate was removed. The results of the Hall measurements were nearly identical, indicating minimal p-type conversion of the underlying S. I. GaAs substrate by zinc diffusion.

In addition to lithium doping, marginal success has been achieved with nitrogen doping during MOVPE growth of ZnSe. Stutius[5] first reported the incorporation of nitrogen in MOVPE ZnSe using NH_3 as the dopant source. Similar results were reported more recently by researchers at NTT[6] and Chiba University[7] using NH_3 as the dopant and $ZnEt_2$ and $ZnMe_2/H_2Se$ as the main element precursors. Suemune[8] *et al.* found that films of $ZnS_{0.06}Se_{0.94}$ (lattice matched to GaAs) gave ten times larger PL efficiency than lattice mismatched ZnSe films. In addition, only low resistivity p-type behavior was observed for the lattice matched material (NH_3 dopant source). Researchers at Hitachi[9] have reported successful p-type doping with NH_3 by MOMBE. It was suggested that the efficient incorporation of nitrogen by this technique was due to growth under more zinc-rich conditions. In each of these studies NH_3 was used as the nitrogen acceptor source. Significant incorporation of nitrogen with this source is difficult because of slow thermal decomposition rates at growth temperature, low sticking coefficients, and possible adduct formation with organometallic precursors.

The success reported by the 3M Company was based on achieving significant nitrogen incorporation during MBE growth using a ground state, free radical nitrogen source. This success, and the difficulty in obtaining atomic nitrogen at higher pressures, motivated us to examine alternative precursors. Keeping in mind the need to locate the nitrogen atom specifically on a selenium site in the lattice, we decided to examine precursors which contained a Zn-N bond. Realizing that zinc prefers the native site, an enhancement in site selectivity would occur, *if* the Zn-N bond could be retained during the deposition experiment. The results of our preliminary investigation are presented here.

RESULTS AND DISCUSSION

To have a reliable baseline against which to judge the dopant experiments, nominally undoped ZnSe was grown first. The growth conditions for ZnSe were: GaAs substrate, 2° to nearest (110); 550°C, H_2, 10 minutes (pre-cleaning); 3 slpm (10^{-2} mol fraction) H_2Se; 2 slpm (10^{-4} mol fraction) Et_2Zn; 60°C bubbler temperature (10^{-6} mol fraction) $Zn[N(TMS)_2]_2$; 250 - 450°C substrate temperature; 80 torr reactor pressure; 0.5 μ/h growth rate. A PL spectrum of such nominally undoped material is given (**Fig. 1**). Next, growth utilizing only $Zn[N(Si(CH_3)_3]_2]_2$ as the source of zinc was performed. The purpose of this experiment was two-fold. First, to determine if the zinc amide was a viable transport source for zinc. Second, to ascertain the optimum decomposition temperature for this dopant precursor. XRD (**Fig. 2**) patterns of films grown using Et_2Zn (**A**) and the zinc amide (**B**) are virtually identical, thus indicating the zinc *bis*-amide compound is a good source for deposition of zinc-containing materials. Downstream monitoring of the zinc amide decomposition pattern by capillary sampling/mass spectroscopy (**Fig. 3**) indicated the optimum region of thermal decomposition for this source is ~350°C to maintain the Zn-N bond while eliminating $SiMe_4$.

Figure 1: PL spectrum of ZnSe grown from Et_2Zn and H_2Se.

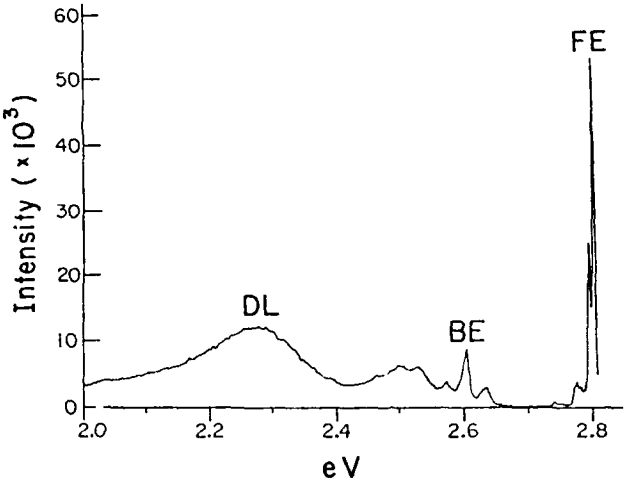


Figure 2: XRD spectra of ZnSe grown from H_2Se and Et_2Zn (A) or H_2Se and $Zn[N(TMS)_2]_2$ (B).

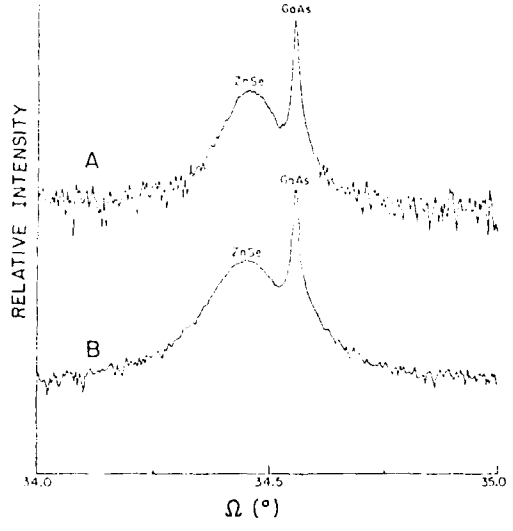


Figure 3: Arbitrary strength of post-substrate mass spectrum signal attributed to the ZnN_2^+ fragment of $Zn[N(TMS)_2]_2$ as a function of substrate temperature.

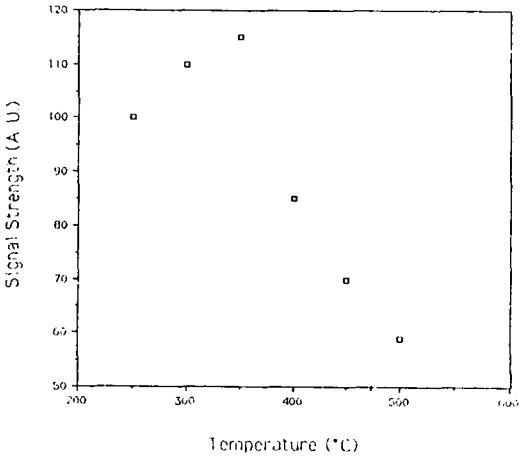
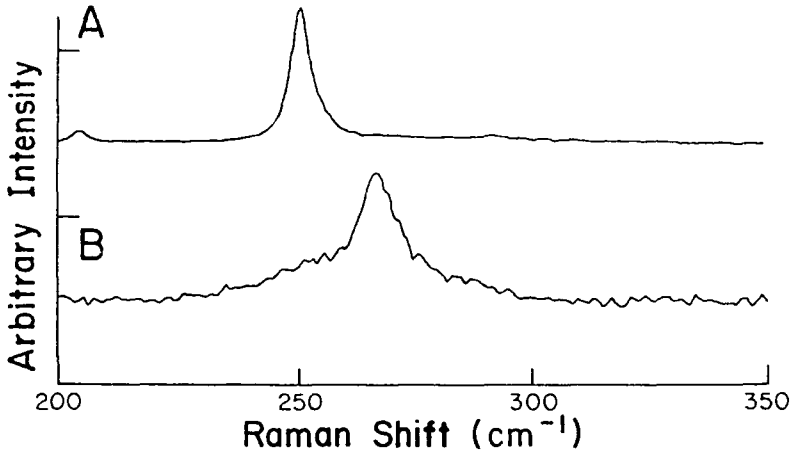


Figure 4: Raman spectra of ZnSe grown from H_2Se and Et_2Zn (A) or H_2Se and $Zn[N(TMS)_2]_2$ (B).



Having thus demonstrated both the capability of growing nominally undoped ZnSe and the viability of $Zn\{N[Si(CH_3)_3]_2\}_2$ as an OMVPE source compound, we directed our efforts at the utilization of this zinc amide as a dopant precursor for growth of p-type films. The basic idea was to enforce retention of the Zn-N bond under growth conditions. Previously, we had shown that gas phase decomposition of the zinc amide proceeded by expulsion of "ZnN."[10] Such an observation conflicts with known bond strengths.[11] Recently, we undertook a computational project aimed at providing some insight into this problem.[12] The bulk of the electron density in the top five occupied molecular orbitals resides in the trimethylsilyl groups, thereby rendering both the Zn-N *and* Si-N bonds somewhat weakened. Also, we have prepared $Zn\{N[C(CH_3)_3Si(CH_3)_3]\}_2$, determined its solid state structure by single crystal x-ray diffraction, and examined both its vapor phase decomposition profile and molecular orbital bonding arrangement.[13] Just like the *bis*-silylamide, the carbido-silylamide exhibits a strong peak in the MS attributable to the parent-(ZnN). The MO scheme for this unsymmetrical metal amide also indicates strong organic fragment bonding at the top of the filled levels. All of these results point to the potential for zinc amides to serve as dopant sources for electronically active nitrogen incorporation to produce p-type ZnSe.

Preliminary SIMS data show a strong peak assigned to SeN, identical to the one observed for ion-implanted (N) pure ZnSe. Raman spectra of nominally undoped films and films grown with $Zn\{N[Si(CH_3)_3]_2\}_2$ as the zinc source show several features of interest (**Fig. 4**). As observed, the intensity decrease of the longitudinal optical phonon frequency at 253 cm^{-1} is coupled to an intensity increase evident at 267 cm^{-1}. **Figure 4A** is a Raman spectrum for a film deposited only from Et_2Zn and H_2Se. Comparable data were observed for higher deposition temperatures. The assignment of the vibration at 267 cm^{-1}, which increases in intensity as the concentration of $Zn\{N(TMS)_2\}_2$ is increased, is attributed to the coupled plasmon LO phonon mode of pure ZnSe. Combining these observations with those of the thermal decomposition studies (**Fig. 3**) suggests an optimum growth temperature from the $Zn\{N[Si(CH_3)_3]_2\}_2$ of 350°C. This was identified as the temperature for maximum production of ZnN. This correlation of flux of species possessing a zinc-nitrogen bond with the observed changes in the Raman spectrum gives confirmation to our suggestion that nitrogen incorporation is occurring in the films. Future work is aimed at obtaining additional supporting evidence for the "designer dopant" approach.

ACKNOWLEDGEMENTS

We thank Dr. Gary McGuire of MCNC for the SIMS measurements and Mr. Dick Roche of FSU for the illustrations.

REFERENCES AND FOOTNOTES

1. Reported at Device Research Conference, Boulder, CO. , 17 - 19 June 1991.
2. Yasuda, T.; Mitsuishi, I.; Kukimoto, H. *Appl. Phys. Lett.*, **1988**, *52*, 57.
3. Yoshikawa, A.; Muto, S.; Yamaga, S.; Kasai, S. *Japan. J. Appl. Phys.*, **1988**, *27*, L260.
4. Yahata, A.; Mitsuhashi, H; Hirahara, K.; Beppu, T. *Japan. J. Appl. Phys.*, **1990**, *29*, L4.
5. Stutius, W. *J. Crystal Growth.*, **1982**, *59*, 1.

6. a. Ohki, A.; Shibita, N.; Ando, K.; Katsui, A. *J. Crystal Growth*, **1988**, *93*, 692.
   b. Ohki, A.; Shibata, N.; Zambutsu, S. *Japan. J. Appl. Phys.*, **1988**, *27*, L909.
7. a. Yoshikawa, A.; Muto, S.; Yamaga, S.; Kasai, H. *J. Crystal Growth*, **1988**, *86*, 279.
   b. Yoshikawa, A.; Muto, S.; Yamaga, S.; Kasai, H. *Japan. J. Appl. Phys.*, **1988**, *27*, 992.
8. Suemune, I.; Yamada, K.; Masato, H.; Kando, T.; Kan, Y.; Yamanishi, M. *Japan. J. Appl. Phys.*, **1988**, *27*, L2195.
9. a. Taike, A.; Migita, M.; Yamamoto, H. *Appl. Phys. Lett.*, **1990**, *56*, 1989.
   b. Migita, M.; Taike, A.; Yamamoto, H. *J. Appl. Phys.*, **1990**, *68*, 880.
10. Rees, Jr., W. S.; Green, D. M.; Anderson, T. J.; Bretschneider, E.; Pathangey, B; Kim, J., accepted in *J. Electronic Materials*, **1992**.
11. See, for example, Huheey, J. E. *Inorganic Chemistry, second edition*, Harper and Row: New York, 1978.
12. Rees, Jr. W. S., unpublished results.
13. Rees, Jr., W. S; Green, D. M.; Hesse, W. "Synthesis and X-ray Diffraction Crystal Structure of $Zn\{N[(C(CH_3)_3)(Si(CH_3)_3)]\}_2$. The First Solid State Characterization of a Homoleptic Zinc Amide," submitted for publication.

HIGH RESOLUTION PHOTOLUMINESCENCE OF EDGE AND NEAR-EDGE CdTe

M.C. Carmo and M.J. Soares
University of Aveiro, Physics Department, 3800 Aveiro, Portugal

ABSTRACT

Among II-VI semiconductors CdTe is the one that can be grown in better crystal quality. However most of the edge and near edge luminescence properties are still to be clarified. CdTe can be obtained in both n and p type and conductivity type conversion is obtained under heat treatment.

In this work we studied the behaviour of a batch of CdTe samples under annealing in different conditions. We observed the growth and destruction of the 1.47 eV band and separated the 1.47 eV and 1.43 eV bands. We also show that these bands are strongly related with the chemical stoichiometry.

INTRODUCTION

Among II-VI semiconductors CdTe has received a great deal of attention partially because of its extensive use as a substrate in HgCdTe infrared detectors among other applications in solar cells, nuclear detectors[1] and the growth of epilayers. It is also an interesting material for use in diluted magnetic superlattices and optoelectronic devices. All these applications are very sensitive on the quality of starting material. Although a great deal of work has already been published few precise results are availabe[2,3,4] and a correct identification of most donor and acceptor levels is still under controversy. This is partially due to the fact that the quality of the crystals available was in general poor and frequently polycrystals were employed. The study of this material is also important from the physical point of view. It is one of the few II-VIs that can be grown in both n and p conductivity type and type conversion can be experimentally induced and monitored, thus providing insight for the true role of intrinsic defects in this process.

EXPERIMENTAL DETAILS

Low temperature (4 - 70 K) photoluminescence was used to study the emission of CdTe crystals. Above gap excitation was achieved either by an argon laser (5145 Å) or with a Xe lamp followed by a monocromator. The luminescence was caught in a 90° geometry, dispersed by a 1700 SPEX machine and detected by a photomultiplier tube with an extended red cathode. The samples were prepared from single CdTe crystals grown by a Bridgman process in different crystals orientations, conductivity and sizes. A batch of more than 30 crystals was available. The samples were cut and mechanically polished or etched. The density of etch pits was in the order of $10^5/cm^2$. Annealing treatments were performed either in open tubes in inert atmosphere or in closed quartz ampoules and excess high purity cadmium overpressure. In all measurements a control sample was kept for monitoring the experimental results.

Mat. Res. Soc. Symp. Proc. Vol. 242. © 1992 Materials Research Society

› GROWN CdTe

Fig. 1 shows the spectrum of CdTe at two different temperatures. It is clearly seen the contribution of 3 acceptors to a donor-acceptor transition and a band-acceptor transition. An impurity bound exciton is also observed at 60 meV from the conduction band edge as measured spectroscopically from the free to bound transition energy

$$h\nu = E_G - E_A + \frac{kT}{2} \qquad (1)$$

and taking the electron temperature as the lattice temperature.

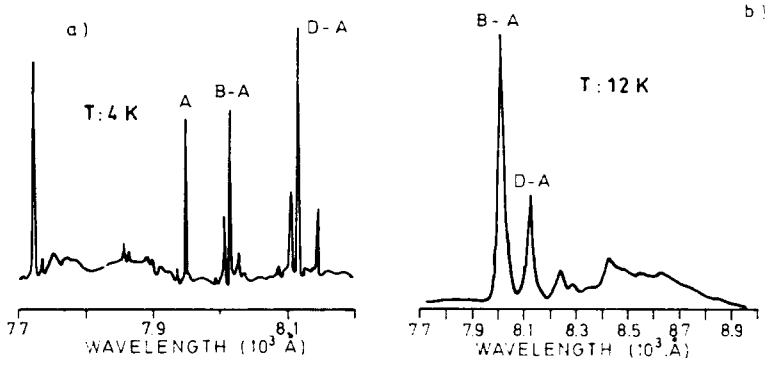


Fig. 1 - Edge luminescence from CdTe
a) 4 K; b) 12 K

At higher temperatures (Fig. 1b) the free to bound transition dominates the spectrum. The energy of the shallow donor can be estimated from the separation of the donor-acceptor band-acceptor transition and the pair mean separation

$$h\nu_{D-A} = h\nu_{B-A} - E_D + \Delta \qquad (2)$$

$$(\Delta = \frac{e^2}{\varepsilon r})$$

as $\sim$ 15 meV. These results are in accordance with previous publications [5,6], apart from the greater detail shown in our low temperature spectrum.

NEAR EDGE LUMINESCENCE

Fig. 2 shows typical 12 K luminescence spectra of p type CdTe samples. The spectral structure shown varies strongly with the resistivity of the sample and within the same sample the face from which the luminescence is colected. Namely the spectra of the same (111) sample with uniform EPD are very different when collected from face A (Cd) and face B (Te). The spectrum is dominated by the donor-acceptor and band-acceptor transitions at 1.54 eV (8061 Å) and 1.55 eV (8024 Å) followed by their phonon side band separated by $\sim$ 21 meV (the LO phonon energy is quoted as 21.3 meV in CdTe). In some samples a line at 1.59 eV normaly identified as an exciton bound to the Cu acceptor [7] is also present. This system is followed by a broad band that can be deconvoluted in two separate bands, one with its stronger intensity at 1.47 eV with a halfwidth of $\sim$ 8 meV and the other peaking at 1.43 eV and $\sim$ 60 meV wide. The zero-phonon lines of these bands

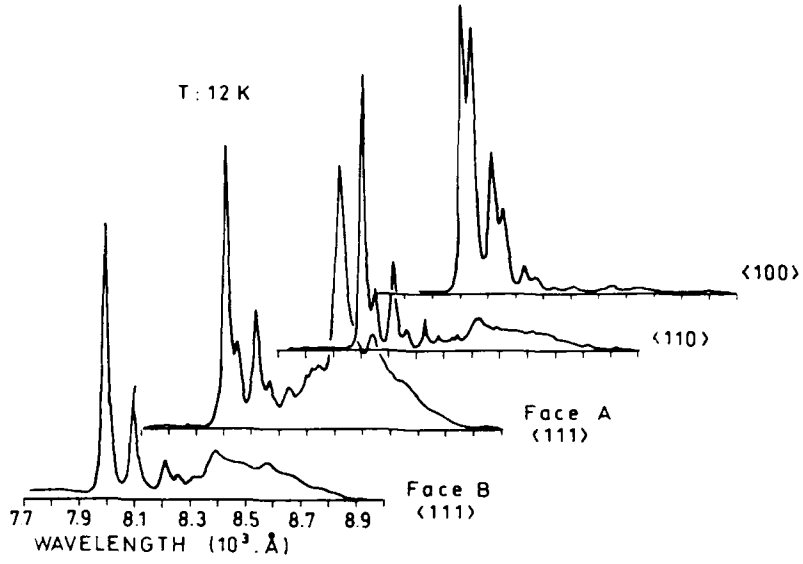


Fig. 2 - Edge and near edge luminescence from as grown CdTe

are not clearly identified. The broad structure of these bands suggests their origin as the spectral convolution of different but closely related defect clusters. This idea is supported by the experimental fact that the phonon structure of the 1.43 eV (8700 Å) band could always be evidenced by selectively exciting some defect clusters by varying the excitation wavelength. The 1.43 eV band has been frequently assigned to a DAP (Donor Acceptor Pair) band[5] while it has recently been argued that the 1.47 eV (8400 Å) band is related with the etch pit dislocation density[8].

HEAT TREATMENTS

Heat treatments of CdTe are of particular importance since the stoichiometry of the crysta' can be overall changed and it is known that higher temperature annealing always results in conversion of CdTe to n conductivity type, although this process is still not completely understood specially due to the fact that the role of the intrinsic defects in the process has been most probably over emphasized.

We have performed a few annealing experiments under different conditions to evaluate the behaviour of the broad near edge luminescence bands. The results are shown in Figs. 3a) and b). The results show that the 1.47 eV band can be created by annealing in an excess cadmium atmosphere. It was also observed that in samples containing the 1.47 eV band at the starting point the annealing of the 1.47 eV band occurs at 300 C in argon atmosphere and only at $\sim$700 C in cadmium atmosphere.

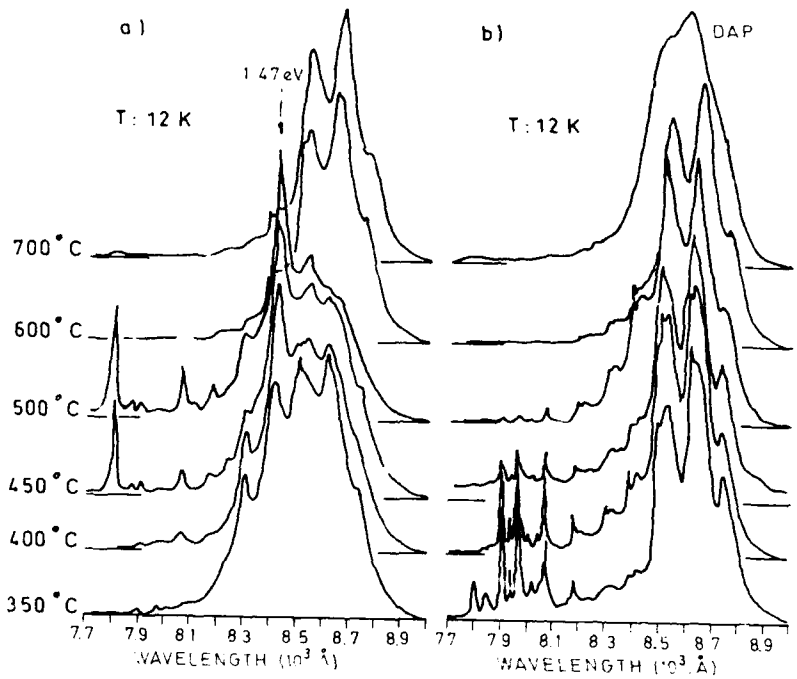


Fig. 3 - Annealing behaviour of near edge broad bands in CdTe a) in Cd overpressure; b) in inert atmosphere

The DAP band grows fast under annealing in argon atmosphere. This could work as an argument in favour of a Cd vacancy related band. But a similar growth is also obtained in an excess cadmium overpressure. In Fig. 4 we show how these two bands can be separated by spectral subtraction. So the presence of the donor species Cd_i does not affect greatly the DAP 1.43 eV band.

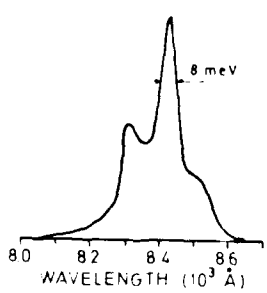


Fig. 4 - The 1.47 eV (8400 Å) band

CONCLUSIONS

We have shown in this paper that the edge and near edge luminescence of CdTe, specially the presence of broad bands is strongly dependent on the chemical stoichiometry, this is specially clear comparing the sistematic differences shown by the spectra of faces A and B of (111) samples. We also were able to create the 1.47 eV band by annealing of a p type crystal in an Cd overpressure environment. This questions the idea that this band is correlated with EPD apart from the fact that these extensive defects could act as good trapping centres for the Cd_i species acting as a donor. The 1.43 eV DAP band could not be correlated with the presence of excess cadmium atoms and so its assignement to intrinsic defects is not obvious. Its annealing behaviour could equally well be interpreted in the basis of the native defects, this would explain the raise of the 1.43 eV band obtained by Taguchi et al[7] near the interface of epilayers CdTe/GaAs.

ACKNOWLEDGMENTS

The authors want to thank JNICT for financial support.

REFERENCES

1. Triboulet et al, Journal of Applied Physics 45 (6), 2759 (1974).
2. Francou et al, Physical Rev. B 41, 12035 (1990).
3. Molva et al, Phys. Status Solidi (b) 109, 635 (1982).
4. Molva et al, Solid State Communic. 48, 955 (1983).
5. Dean, Prog. in Solid State Chemistry 8, 1 (1973)
6. Panosyan, Soviet Physics Solid State (1978).
7. Taguchi et al, Materials Sc. Forum 65, 253 (1990).
8. Babentsov et al, Sov. Phys. Semic. 23, 967 (1990).

HIGH QUALITY EPITAXIAL FILMS OF ZnSe AND ZnSe/ZnS STRAINED LAYER SUPERLATTICES GROWN BY MOCVD

CHUNGDEE PONG, R. C. DeMATTEI*, and R. S. FEIGELSON*
Department of Materials Science and Engineering, Stanford University, CA 94305
*Center for Materials Research, Stanford University, 105 McCullough, Stanford, CA 94305

ABSTRACT

High quality epitaxial films of ZnSe and ZnSe/ZnS strained layer superlattices (SLS) have been grown on (100) GaAs substrates using diethylZinc, dimethylSelenide, diethylSelenide, and propyleneSulfide as reagents in both atmospheric and low pressure environment. This source combination produces the results showing the influence of process conditions, such as reagent flow ratio (f_{VI}/f_{II}) and substrate temperature, on the film stoichiometry, surface morphology, and crystalline quality. Low temperature photoluminescence (PL), Rutherford backscattering spectrometry (RBS), cross-sectional TEM, and x-ray diffraction have been used to characterize the films. Photoluminescence studies at 2.8 K on samples of ZnSe/ZnS strained layer superlattices; 10 periods ZnSe(1.5 nm)/ZnS(8.5 nm), have shown quantum size effect with the peak energy blue-shifted to 3.03 eV with the FWHM=73 meV. Atomic force microscopy (AFM) was applied to study surface morphology of multilayer samples.

INTRODUCTION

In the past decade, the improvements in epitaxial growth of II-VI compounds by MOCVD and MBE techniques [1-4] have generated vivid interests in the application of these materials to optoelectronics devices, i.e., mainly visible laser diodes and non-linear devices like second harmonic generators. Some recent success [5-7] in prototype devices based on superlattices and multiple quantum wells of ZnSe/ZnS, ZnSSe/ZnS, and CdZnSe/ZnS has shown great potential of this family of materials in device applications.

Crystal growth of these materials is still not perfect. The strains between different layers due to lattice mismatch often pose an instability concern. Rough surface morphology is of great concern in the growth of II-VI compounds [1]. The rough growth front causes the usually observed wavy interfaces in II-VI superlattices, which causes the broadening of luminescence emission peak [8-9] and weak x-ray satellite peaks. The present study is focused on the epitaxial growth of stoichiometric film and the influence of process conditions on the surface morphology and interface abruptness.

EXPERIMENTAL

Samples were grown in a horizontal quartz reactor using diethylZinc, dimethylSelenide, diethylSelenide, and propyleneSulfide as reagents in both atmospheric and low pressure environment. The range of growth temperatures varied from 400°C to 475°C. The pressure was kept at 94 torr for the ZnSe/ZnS SLS growth. Reagents were mixed in a fast switching unit before facing the substrate. GaAs substrate was prepared by standard solvent cleaning, then etched for 2 minutes in a mixture of 1 part DI water, 1 part hydrogen peroxide, and 5 parts sulfuric acid. Before growth, substrate was thermally treated at 540°C for 10 minutes in hydrogen environment.

The PL was excited by the UV line of a He-Cd laser and detected with a Spex double monochromator, and the liquid helium dewar temperature was maintained at 2.8 K through pumping. A Picker full-circle single crystal diffractometer was used to obtain x-ray diffraction curve. The alignment of diffractometer was achieved by maximizing the GaAs (400) reflection intensity. Study on small-scale surface morphology used a Nanoscope II by Digital Instruments to scan 1 μm x 1μm area on the sample

RESULTS AND DISCUSSIONS

Growth of ZnSe

PL measurements at 2.8 K of ZnSe layers (Fig. 1 (a)) showed a strong near band edge (NBE) peak at 2.802 eV and relatively weak deep level (DL) emission band between 2.0 and 2.2 eV, which is characteristic of a good quality ZnSe film [10]. The detailed structure of NBE peaks was resolved by performing a narrow PL scan on the same film (Fig. 1 (b)). The peak identities were assigned based on peak energies, which were very close to the values people reported earlier [11-12]. The relatively strong free excitonic peak is at 2.802 eV. The strongest peak at 2.798 eV is due to bound exciton with neutral donor, as neutral donor is shallower in bandgap than neutral acceptor. No transition due to bound exciton with neutral acceptor was observed from this sample. A weak emission peak at 2.787 eV was believed to be associated with bound exciton and ionized acceptor.

The donor-acceptor pair (DAP) is clearly shown on the spectrum with the peak energy of 2.702 eV, and also three phonon replicas associated with it, each of 31 meV [11]. Since no dopants were added during growth, it is believed the donor is associated with Ga_{Zn}, and the acceptor is due to As_{Se} [13]. From this, it is obvious interdiffusion had occurred at the interface between film and substrate, which people observed before [11].

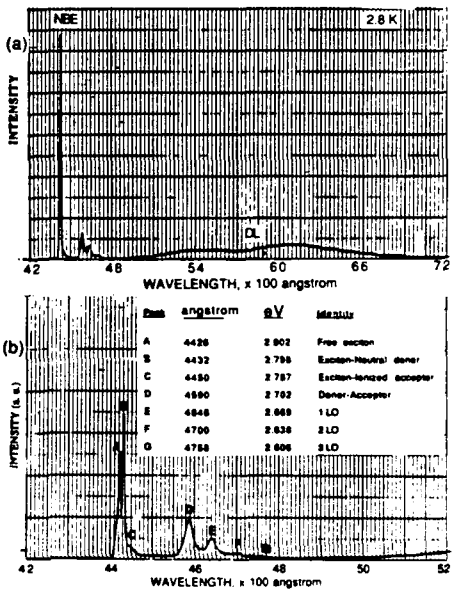


Fig. 1 (a) A photoluminescence spectrum of a good quality ZnSe film showing NBE and DL peaks. (b) Narrow scan of the same film.

The result of Rutherford backscattering spectrometry, Fig. 2, gave a 5.2% minimum yield on the same film, which is lower than the value reported by Ohmi et al. [14]. The x-ray diffraction curve in Fig. 3 of a 400nm-thick film showed a narrow (400) ZnSe film peak and two substrate peaks, indicative of good epitaxy and crystallinity. The FWHM of the ZnSe (400) peak was measured to be 0.1 degree, and the FWHM of the substrate peak was 0.06 degree.

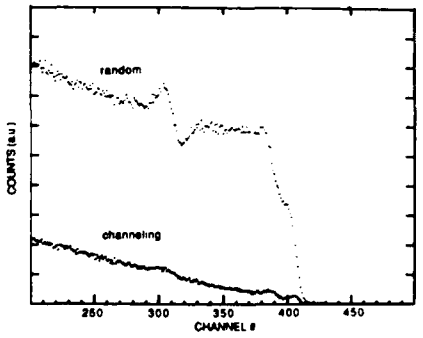


Fig.2 An RBS spectrum gave 5.2% minimum yield of a good quality ZnSe/GaAs.

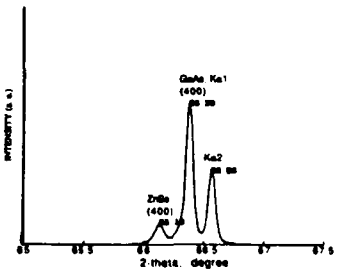


Fig. 3 An x-ray diffraction curve showing ZnSe (400) reflection at 2-theta = 66.13°.

A cross-sectional transmission electron micrograph (Fig. 4) showed coherent growth of ZnSe on the substrate. Some stacking faults appeared in the film and the interface seemed smooth.

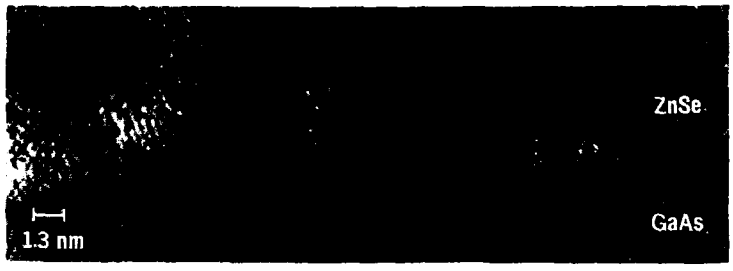


Fig. 4 A transmission electron micrograph showing the cross section of ZnSe grown on (100) GaAs.

The surface morphology of a good quality ZnSe film was usually faceted and textured, and the degree of facetedness depended on f_{Se}/f_{Zn}. The texture was usually toward <011> direction, as also observed by the other researchers [15]. A schematic diagram shown in Fig. 5 (a) was adopted to explain the facet formation on the surface. The scanning electron micrograph in Fig. 5 (b) is a typical cross-sectional view of a crystalline ZnSe film.

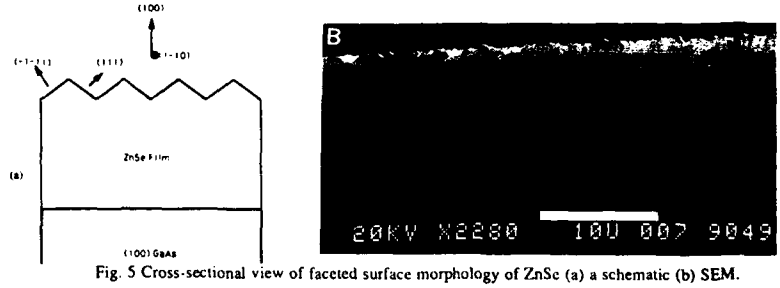


Fig. 5 Cross-sectional view of faceted surface morphology of ZnSe (a) a schematic (b) SEM.

The effect of f_{Se}/f_{Zn} on surface morphology is shown in Figure 6; f_{Se}/f_{Zn}=8 yielded the smoothest surface, while f_{Se}/f_{Zn}=4 yielded the roughest surface among the three samples. It was pondered that since diethylZinc and dimethylSelenide were used as precursors in the film growth, and ethyl molecules decomposed easier than methyl molecules, the Zn atoms left on the growth front quickly settled down due to its lower vapor pressure (larger sticking coefficient) in the growth conditions of small f_{Se}/f_{Zn}, thus enhanced facet formation. The observation of increased growth rates with decreased f_{Se}/f_{Zn} also supports this argument.

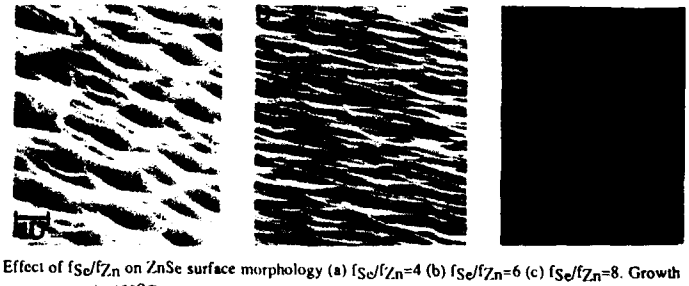


Fig. 6 Effect of f_{Se}/f_{Zn} on ZnSe surface morphology (a) f_{Se}/f_{Zn}=4 (b) f_{Se}/f_{Zn}=6 (c) f_{Se}/f_{Zn}=8. Growth temperature is 450°C.

Growth of ZnSe/ZnS SLS

Low temperature PL measurements performed on ZnSe/ZnS SLS yielded very strong blue emission. A typical luminescence spectrum is shown in Fig. 7(a), which was obtained from a sample of single quantum well grown at 450°C. The peak energy is 3.025 eV and the ZnSe well thickness is estimated to be 1.5 nm [3]. The red shift of peak energy due to increased well thickness is observed in Fig. 7(b), which was obtained from a sample grown at the same conditions as (a), except that the growth time of well layer was increased from 75 sec to 95 sec. The peak energy in (b) is 2.924 eV and the corresponding well thickness is estimated to be 3 nm [3]. The quantum size effect is clearly observed on the two samples.

We also investigated the issue of interface roughness [9] by growing multiple quantum wells (MQW) structures (Fig. 7(c)). There were 10 periods ZnSe (1.5 nm)/ZnS (8.5 nm) in this sample and the growth conditions were the same as (a). The peak energy of (c) is 3.075 eV, but the FWHM is increased from 68.7 meV (in (a)) to 116.8 meV, which is a sign of increased interface roughness between ZnSe and ZnS layers. In order to solve this problem, a brief interruption of the layer growth with group VI overpressure in the growth chamber was applied.

The procedure was that instead of only hydrogen purge between different layer growth, the group VI source continuously flowed for a brief moment after the growth, then followed by pure hydrogen purge. It was in the hope that during the step of flowing group VI source, the interface would be smoothened out. The preliminary result is shown in Fig. 7(d), which was obtained from a sample of 10 periods ZnSe/ZnS with the same growth conditions as (c). The peak energy of this sample is 3.027 eV and the FWHM is 73 meV. And both values are very close to those of the single QW sample (a), which is a very encouraging sign. The origin of fringes on this emission peak is not clear at this moment.

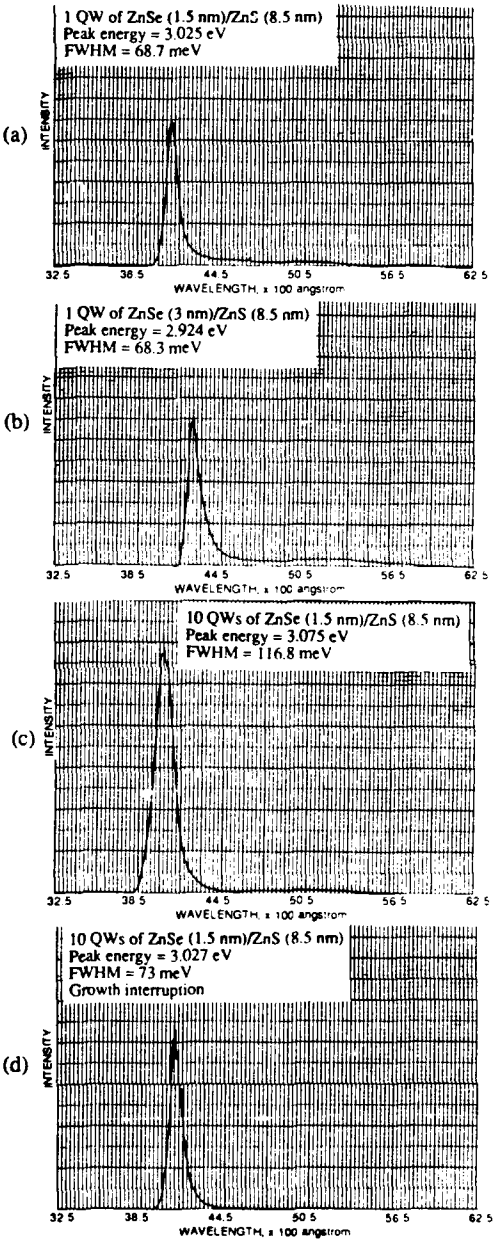


Fig. 7 Low temperature PL showing excitonic emission peaks of 4 cases of ZnSe/ZnS SLS.

Atomic force microscope is a powerful tool to investigate minute changes of surface morphology [16], which are too important information in crystal growth to be neglected. The improvement in morphology is the key to monolithic integration of optoelectronic devices consist of groups IV, III-V, and II-VI semiconductors. Some lineplots of the result are shown in Fig. 8. The scanned area is 1 μm by 1μm. The smoothest surface was (a) among the three samples, which is expected for a single QW sample. Textures or hillocks were appeared on (b) and (c). The influence of growth temperature on surface morphology was also observed.

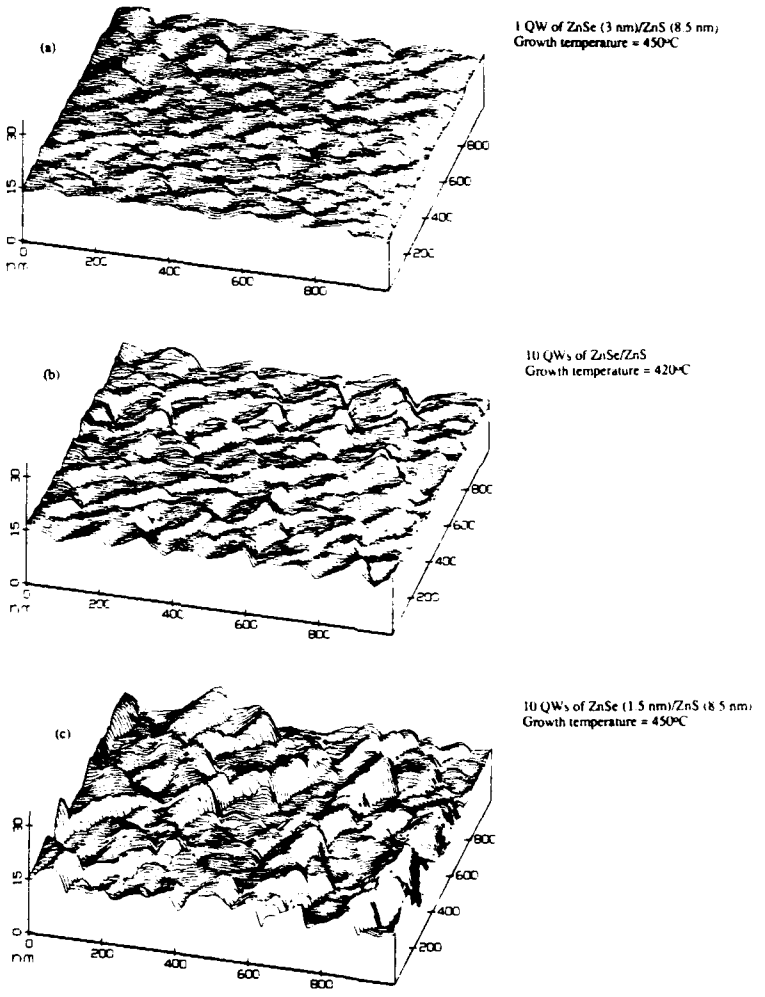


Fig. 8 AFM lineplots of surface morphologies of three cases of ZnSe/ZnS quantum well structures.

CONCLUSIONS

We have investigated the stoichiometric and crystalline properties of epitaxial ZnSe film on GaAs substrate. Interdiffusion between film and substrate was observed. With proper control of group VI to II ratio in the growth process, it is possible to grow smooth films of good quality. The quantum size effect was confirmed on ZnSe/ZnS SLS and the interface abruptness could be improved with growth interruption under the overpressure of group VI source. Atomic force microscopy reveals very small-scale variations of surface morphology, which can give some insight of growth kinetics.

ACKNOWLEDGEMENTS

The authors are indebted to R. Street of Xerox PARC for very valuable discussions and for providing the use of PL instrument. The authors also wish to thank D. Fork (Xerox PARC) and J. Phillips (AT&T Bell Lab.) for the RBS work, and J. Tramontana and F. Ponce of Xerox PARC for the TEM study. This work is supported by NSF-MRL thrust program through CMR at Stanford University.

REFERENCES

1. P. J. Wright, B. Cockayne, P. J. Parbrook, K. P. O'Donnell, and B. Henderson, Semicond. Sci. Technol. 6, A29 (1991).
2. T. Yokogawa, H. Sato, and M. Ogura, J. Appl. Phys. 64 (10), 5201 (1988).
3. T. Yokogawa, T. Saitoh, and T. Narrusawa, Appl. Phys. Lett. 58 (16), 1754 (1991).
4. T. Yokogawa, M. Ogura, and T. Kajiwara, Appl. phys. Lett. 49 (25), 1702 (1986).
5. M. A. Haase, J. Qiu, J. M. DePuydt, and H. Cheng, Appl. Phys. Lett. 59 (11), 1272 (1991).
6. H. Jeon, J. Ding, A. V. Nurmikko, H. Luo, N. Samarth, and J. Furdyna, Appl. Phys. Lett. 59 (11), 1293 (1991).
7. G. Sun, K. Shahzad, J. M. Gaines, and J. B. Khurgin, Appl. Phys. Lett. 59 (3), 310 (1991).
8. D. S. Chemla and D. A. B. Miller, J. Opt. Soc. Am. B 2 (7), 1155 (1985).
9. M. A. Herman, D. Bimberg, and J. Christen, J. Appl. Phys. 70 (2), R1 (1991).
10. P. J. Wright et al., J. Crystal Growth 94, 441 (1989).
11. P. Blanconnier, Thin Solid Films 55, 375 (1978).
12. H. Cheng, J. M. Depuydt, M. Haase, and J. E. Potts, Appl. Phys. Lett. 56 (9), 848 (1990).
13. T. Yao et al., Jpn. J. Appl. Phys. 22 (3), L144.
14. K. Ohmi, I. Suemune, T. Kanda, Y. Kan, and M. Yamanishi, J. Crystal Growth 86, 467 (1988).
15. N. Shibata et al., Jpn. J. Appl. Phys. 26 (8), 1305.
16. R. Howland and M. Kirk, Supercond. Industry, 1991, 25.

THE APPLICATION OF LAMMA-1000 TO THE ELEMENTAL ANALYSIS OF CdTe COMPOUND.

A.I.BELOGOROKHOV, A.Yu.KHAR'KOVSKY,
Institute of Rare Metals, B.Tolmachevsky per., 5, 109017 Moscow, Russia

ABSTRACT

Data from numerous LMMS analysis of specimens of a polished sample of CdTe crystal are treated statistically to estimate the accuracy and reproducibility of quantitative analysis. The data are consistent with the instrument producing a fixed condition in plasma for a given laser power. The plasma chemistry is shown to control the conditions reached in the plasma for a given power.

INTRODUCTION

The aim of current work is to establish methods for dealing with the data relating to major element concentrations in a compound, and to provide some idea of the accuracy and reproducibility achievable. The results are also used to provide an insight into the effects of specimen composition, and hence plasma chemistry, on the behaviour of plasma.

MATERIALS AND METHODS

Two kinds of CdTe crystals, which were as-grown undoped p-type and annealed n-type crystals, used in the present research, were grown from Te-rich melt by the Bridgmen method. Polished 1 x 1 x 0.1 cm^3 samples with resistivity (0.5-2.5) 10^2 Ohm cm, mobility (40-80) $cm^2V^{-1}s^{-1}$ and carrier concentration 10^{15}-10^{18} cm^{-3} at room temperature were used by us. The polished surfaces were [111] faces.

The work was carried out on a Leybold AG LAMMA-1000 instrument. Each specimen was analysed using a series of increasing laser powers with analyses taken at ten locations to reduce variability due to surface roughness.

Peak areas were measured using the LAMMA software, with a correction to allow for electron multiplier saturation at high signal levels [1]. Peak areas of elements were plotted against total area as in Fig.1. The measured percentage could be found from the slope of the line so produced.

RESULTS AND DISCUSSION

Strong correlation was found between the various elemental ion yields (peak areas). This can be shown both by simple error analysis and also by plots of the type shown in Fig. 1. This figure also shows that, at a given power, there is a linear relationship between the elemental area and the total ion yield. It appears that, within experimental error, the measured percentage of any element is constant at each power.

Mat. Res. Soc. Symp. Proc. Vol. 242. © 1992 Materials Research Society

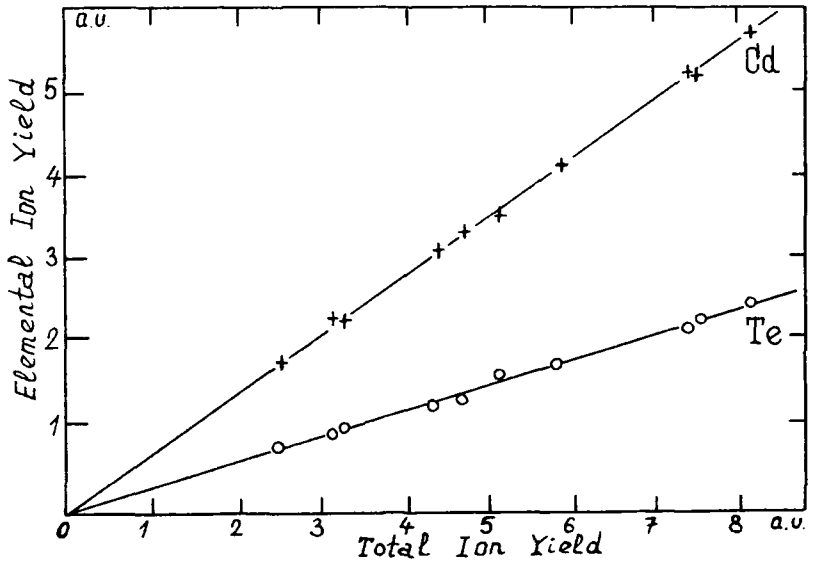


Fig. 1.: Variation in elemental ion yields with total ion yield for the elements in CdTe at a laser power of 3 (respect to threshold power).

The elemental percentages derived from the slopes in such plots (calculated by least-squares analysis) can have standard errors typically 0.5-2%, but can be as low as 0.3%. The error is related to the laser power and hence to total ion yield; larger number of ions improve the statistics. These percentages can be used to establish working curves, and the errors indicate that accurate quantification is possible, provided sufficient results are obtained.

The above measured percentages can also be expressed as correction factors for a given elemental ratio. The correction factor is the multiplicative factor used to correct an ion yield ratio to a concentration ratio.

It has been shown that the temperature is a function of the laser power dencity [2,3], and so it can be assumed that the correction factor depends on laser power [4]. Hence, it appears that a given incident laser power produces a fixed set of plasma conditions.

The variation of the correction factor for CdTe with power is shown in Fig.2. The correction derived from CdTe increases and asymptotically approaches a value close to 0.4 at relatively high powers. Growth of the correction factor with power can be explained by relationship of the ionisation potentials of elements (IP(Cd) is less than IP(Te)). It is snown in Fig.2 that correction factor is constant and far from unity at high laser power. So it can be assumed that plasma conditions (principally the electron temperature and density) are not varied with power and charge-to-neutral ratio for Te is also considerably less then unity.

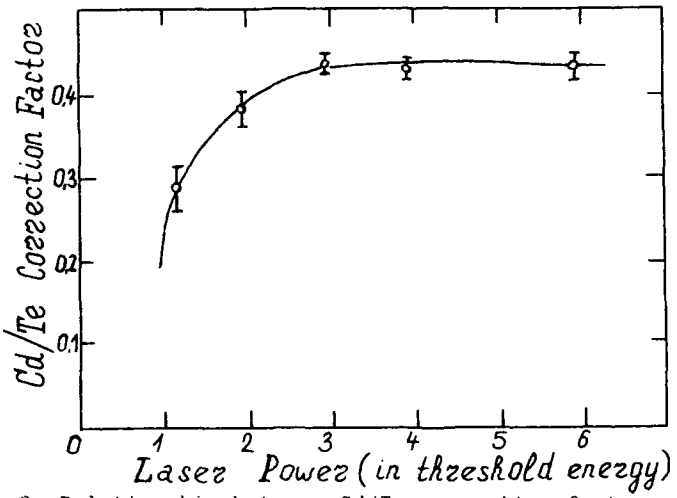


Fig. 2: Relationship between Cd/Te correction factor and laser power for the CdTe.

CONCLUSION

This work shows that, for CdTe investigated, the measured ratio of the elements present is constant for a given incident laser power. This ratio can be measured with accuracy as high as 0.3% standard error, indicating that quantification with good accuracy is possible. The plasma chemistry has a major effect, but only as the plasma conditions produced by a given laser power are altered. However plasma conditions for CdTe slightly vary beginning from some given laser power. The relationship between plasma conditions and elemental ratios is constant.

References

1. D.S. Simons, Int. J. Mass Spectrom. Ion Proc. 55 15 (1983).
2. P.K. Carroll and E.T. Kennedy, Contemp. Phys. 22 61 (1981).
3. J.F. Ready, Effects of High-Power Laser Radiation (Academic Press, New York, 1971).
4. A.Harris and E.R.Wallach in 3rd Intern. LMMS Workshop (Antwerpen, 1986), p.95-99.

OPTICAL STUDY OF THE CdTe CRYSTALS IN FAR INFRARED REGION AT TEMPERATURES (5 - 500)K

A.I.BELOGOROKHOV
Institute of Rare Metals, B.Tolmachevskiy, 5, Moscow 109017, RUSSIA

ABSTRACT

The semiconductors of zinc blend structure are promising candidate materials for numerous experimental and theoretical investigations. In recent years, considerable effort has been made to study the lattice infrared absorption spectrum of II-VI compounds, renewed interest has been taken in CdTe owing to its relatively high electro - optic coefficient in the near infrared. In addition, its nonlinear response to two-phonon absorption in the infrared region is of interest because the material is transparent in this spectral region.

A high quality CdTe bulk crystal is a very promising semiconductor for gamma-ray detectors operating at room temperature [1] and is a technologically important material with applications in solar cells and infrared focal plane technology. In the latter it is an end-point constituent of the HgTe-CdTe alloy system, a commonly used substrate for thin film growth, and a promising passivating overlayer for HgCdTe photodiodes. The electrical properties of CdTe are dependent upon the growth method and chemical impurities. Nominally undoped material is generally insulating (resistivity > 10^7 Ω ·cm) with electrical properties controlled by deep trap levels associated with native defects and defect-impurity complexes. Added dopants may yield low-resistivity n- or p-type material [2].

The CdTe valence band consists of heavy and light holes which are degenerated in the center of Brillouin zone, Γ-point. In this case we can expect a resonant behaviour of dielectric function caused by heavy-light-hole subband transitions V1→V2 within valence band E_V. It takes place in the spectral region corresponding to the crossing V1V2 with Fermi level energy.

The far-infrared transmission (TR) spectra were measured with BRUKER - 113v Fourier-transform spectrometer. The spectral range was from 20 to 5000 cm^{-1} and the resolution was 1 cm^{-1}. The accuracy for determination of the TR coefficient was better than 0,2%. All samples were measured in the temperature range of (4,2 - 500)K. The more interesting was the fenomena taking place at low temperatures when the electron system is almost degenarated but we must take into account the finite charge carrier temperature.

It has been demonstrated that the consideration of the influence of valence band isoenergetic surface corrugation on $\varepsilon(\omega)$ allowed us to discribe the wavelenght dependence of absorption coefficient $\alpha(\omega)$ and to determine the optical effective heavy-hole m^*_{HH} mass.

Mat. Res. Soc. Symp. Proc. Vol. 242. © 1992 Materials Research Society

p-type and annealed n-type crystals, used in this work were grown from Te-rich melt by the Bridgman method. Polished, 1·1·0,1 cm^3 with resistivity (0,5-2,5)·10^2 Ω·cm, mobility (40-80) $cm^2V^{-1}s^{-1}$ and carrier concentration ~10^{15} - 10^{18} cm^{-3} at room temperature were used in this study. The polished surfaces were [111] faces.

Figure 1 shows the result of 5K-temperature optical transmission measurements on the samples studies. Samples with low carrier concentration are more transparent in FIR up to multiphonon absorption. The second sample series have strong intersection in the region (500-2000) cm^{-1}.

It is seen from the figure 2 that, at temperatures T=(5-400)K, all curves of $\alpha_i(\omega,T)$ are crossing practically at one point. At the same time this crossing point has displaced according degenerancy varing. We thus conclude that fact should be associated with the heavy holes - light holes interband absorption which can be calculated according to:

$$\Delta\varepsilon_{inter} = 4\pi e^2\left[\frac{1}{m_2}-\frac{1}{m_1}\right]\sum_K \frac{f(\varepsilon_{K_1})-f(\varepsilon_{K_2})}{\varepsilon_{K_1}(-\varepsilon_{K_2})^2-\omega^2} \qquad (1),$$

where m_1 and m_2 are effective mass of light and heavy holes, correspondently. In the case of the $\hbar\omega \ll E_0$, where E_0 is the characteristic hole energy: E_0=kT in the non-degenerate case (k is the Boltzmann constant) and E_0 is equal Fermi energy E_f in degenerate area the image part of $\varepsilon(\omega)$ can be expressed as:

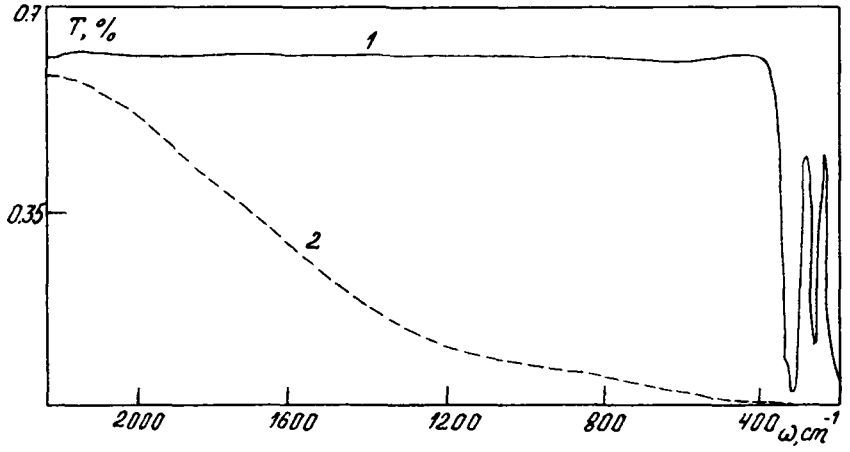


Fig.1. Transmittance spectra of the samples with low (1) and high (2) carrier concentration at 5K temperature.

$$Im\,\varepsilon(\omega) = \frac{\sqrt{2}e^2}{\hbar\sqrt{\hbar\omega}} < I(\Omega)\sqrt{\frac{m_1 m_2}{m_1 - m_2}}\left[f(a) - f(b)\right] > \quad (2)$$

Here $I(\Omega)$ is the integral of wave function overlapping:

$$I(\Omega) = \frac{1}{g^2}\left(\frac{5}{3}\gamma - \frac{2}{3}g^2\right) - \frac{3}{2}\frac{\gamma^2}{g^4}\left\{\sum_i \vec{l}_i^{\,6} - \left(\sum_j \vec{l}_j^{\,4}\right)\right\}, \quad (3)$$

$$\vec{l}_i \equiv \vec{\kappa}/|\vec{\kappa}|,$$

$$g = \sqrt{1 + 3\gamma\left(l_x^2 l_y^2 + l_z^2 l_y^2 + l_z^2 l_x^2\right)},$$

$$\gamma = \left(\gamma_3^2 - \gamma_2^2\right)/\gamma_2^2$$

$\gamma_1, \gamma_2, \gamma_3$ are Luttinger parameters.

Note that if we neglect the valence band corrugation and if $I(\Omega) = 1$ the functional dependence of V1 → V2 absorption coefficient $\alpha_{12}(\omega)$ on T is expressed:

$$\alpha_{12}(\omega) = \frac{e^2\omega^{1/2}}{nch^{3/2}\left(\frac{1}{2m_2} - \frac{1}{2m_1}\right)}\left\{\left[\exp\left(\frac{\hbar\omega}{\kappa T}\cdot\frac{\rho}{1-\rho} - \right.\right.\right. \quad (4)$$

$$\left.\left.\left. - \frac{E_f}{\kappa T}\right) + 1\right]^{-1} - \left[\exp\left(\frac{\hbar\omega}{\kappa T}\cdot\frac{1}{1-\rho} - \frac{E_f}{\kappa T}\right) + 1\right]^{-1}\right\}.$$

Here ω is frequency, $\rho = m_2/m_1$, n is the refractive index. We used the approximation for the dependence of E_f on T given by:

$$E_f(T) = E_{f0}\left[1 - \frac{\pi^2}{12}\left(\frac{\kappa T}{E_{f0}}\right)^2\right] \quad (5)$$

If we take into account that valence band corrugation will lead to essential change of high frequency edge of $Im\,\varepsilon(\omega)$ shape.

On the condition that

$$\hbar\omega \gg \frac{8\kappa T(\gamma_2)(1+\gamma)^{3/2}}{\gamma_1\cdot\gamma}$$

numerical calculation for $Im\,\varepsilon(\omega)$ shows that in the case of the valence band isoenergetic suface corrugation holes are excited from states in the direction of the quasi-momentum corresponding the largest hole masses.

edge.

In Fig.3 are shown the experimental transmission spectra of CdTe sample at various temperatures. In the presentn approach (eq.4) we made numerical calculations using following values of CdTe crystal parameters: P_{cv} =9,0·10^{-6} eV·cm (the matrix element of the V- and C- zones interaction), m^*_{hh}=0,7·m_0, E_{f0} = E_g/25. Here m_0 - is the free electron mass, Eg - is the band gap energy. For the above parameters we got the best fit with experimental spectra. In that temperature interval Fermi level has taken following positions: 65 meV at T=5K till 39 meV at T=405K from the valence band edge. We noted that the spectra crossing point is displaced according variation E_{f0} at (5-400)K. For understanding the nature of that physical phenomenon we must calculate free charge carrier concentration. At 300K we find the heavy hole concentration (HHC) = 2,63 · 10^{18} cm^{-3} and light holes 1,42·10^{17} cm^{-3}; at 78K this values are: HHC=1,53·10^{14} cm^{-3} and 8,80·10^{12} cm^{-3}, correspondently. On the other hand, we can verify the above result using reflectivity spectra and obtained plasma frequency ω_p meaning. It must be equal 66 cm^{-1} and 2 cm^{-1} at T=300K and T=78K, correspodently. From experimental optical reflection spectra we have found ω_p predicted by the theory.

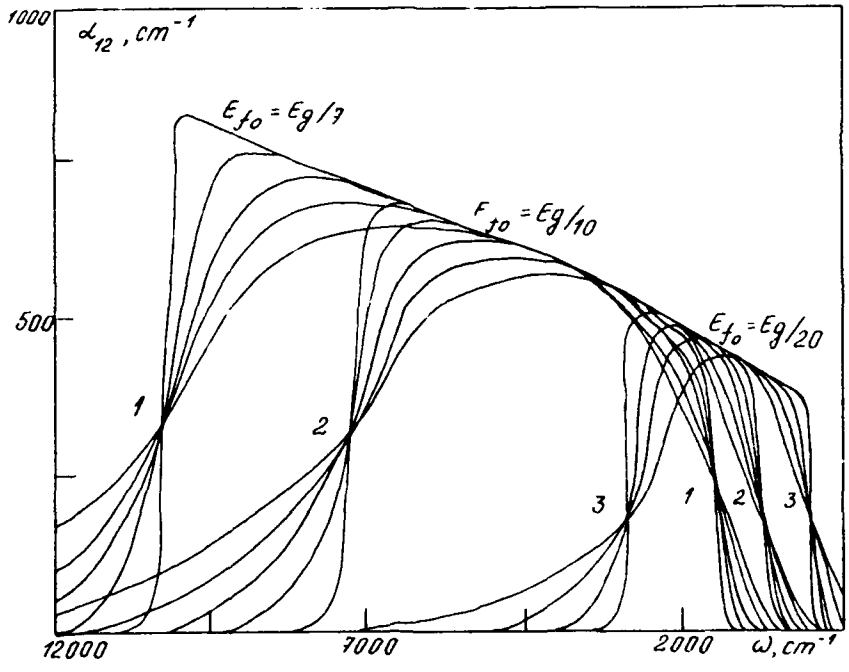


Fig.2. Calculated spectra of V1 V2 absorption at T=5K - 400K.

The theoretical analysis shows that two crossing points

The theoretical analysis shows that two crossing points must exist: the first is described above and the second is within spectral region ω ~350 cm^{-1}. Our calculated results agree quite well with the experimental data from transmittance spectra of some CdTe samples; there are some difficulties in that spectral region because at the same time multiphonon processes take place here. So the obtained calculation results are valid for description the phenomena of far infrared spectral and temperature absorption coefficient dependences of crossing point.

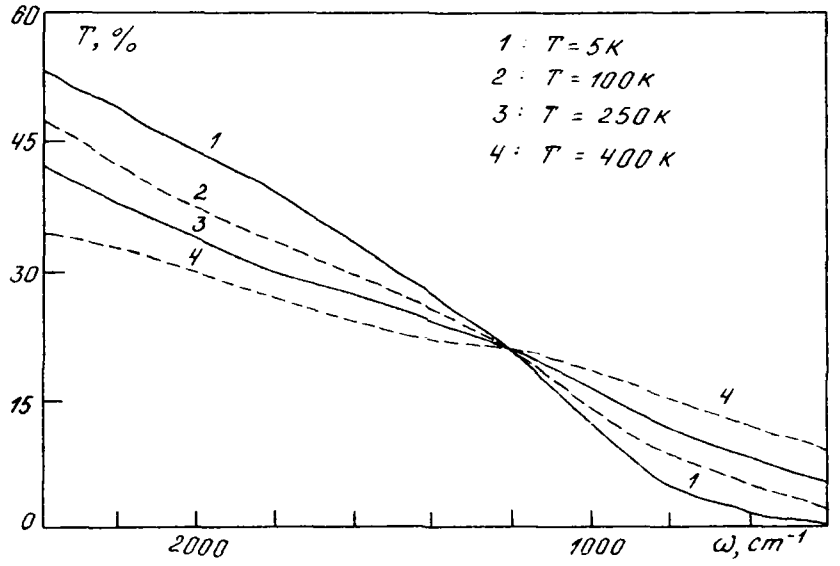


Fig.3.The experimental transmittance spectra of CdTe crystals.

REFERENCES.

1. R.O.Bell, Nucl. Instr. and Meth. 93, 341 (1971)
2. S.Hwang, R.L.Harter, K.A.Harris, N.C.Giles et.al., J.Vac. Sci. Technol. A6, 2821 (1988).

PART IV

Theory of Wide Band-gap Semiconductors

SELF-COMPENSATION AND DOPING PROBLEMS IN ZnSe

David B. Laks* and Chris G. Van de Walle**
* National Renewable Energy Laboratory, Golden, CO 80401
** Philips Laboratories, Briarcliff Manor, NY 10510 USA and
Xerox Palo Alto Research Center, Palo Alto, CA 94304 (present address)

Abstract

We examine native-defect compensation, solubility limits, and dopant self-compensation in ZnSe. Our results are based on a formalism, using first-principles density-functional theory, that treats dopant atoms and native defects on an equal footing. For the case of acceptor doping of ZnSe with Li, we find that compensation due to interstitial Li donors and to native donor defects can be reduced to a tolerable level by carefully adjusting the growth conditions. A more serious impediment to Li doping comes from the solubility limit of Li in ZnSe.

1. Introduction

Wide-band-gap semiconductors have important optoelectronic applications. ZnSe (E_g = 2.6 eV), for example, can be used to make a blue semiconductor laser. Greater use of wide-band-gap materials has been hampered by doping difficulties: very few wide-band-gap semiconductors can be doped both n-type and p-type.[1, 2, 3] For instance, ZnTe and diamond can be doped p-type much more easily than n-type, while other wide-band-gap materials can be readily made n-type but not p-type. In spite of recent reports of well-conducting p-type ZnSe,[4, 5] the causes of the doping problems remain unclear.

In the past, native-defect compensation was the most widely accepted explanation of the doping problems in wide-band-gap semiconductors.[6, 7] According to the native-defect mechanism, when acceptors are added to ZnSe, the dopants are compensated by the spontaneous formation of native donor defects. The energy cost to form the native defects would be offset by the energy gained when electrons are transferred from the donor levels of the native defects to the Fermi level (which is near the valence band in p-type material). If the native donor defect levels are near the conduction band edge, then the energy gained by electron transfer would almost equal the width of the band gap (Fig. 1). Consequently, native defect compensation would become more likely as the band gap is increased. n-type doping of ZnTe and diamond would be compensated by native acceptor defects that transfer their holes to the donor dopants. The appeal of native defect compensation is its universality – it applies to all wide-band-gap materials, all growth methods, and all dopants. Were the native defect picture correct, there would be little room for optimism about the doping of wide-band-gap materials: compensation would be a fundamental thermodynamic process that would be almost impossible to avoid.

We present a theoretical investigation of native-defect compensation in ZnSe. Using first-principles pseudopotentials and density functional theory, we calculate the total energies of all native point defects in ZnSe. The total energies are used to determine defect concentrations as a function of the chemical environment and the Fermi level. We find that only minute concentrations of native defects are induced in stoichiometric p-type ZnSe. Poor control of stoichiometry could lead to significant concentrations of compensating defects. Some of these results were published previously.[8] These results are good news in that they

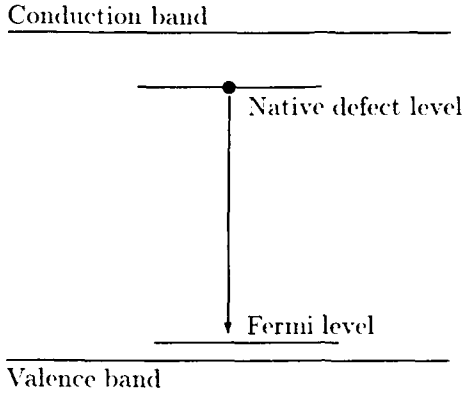


Figure 1: Native defect compensation in a p-type semiconductor. According to the native defect mechanism, native donor defects are formed in wide-band-gap semiconductors. These defects gain back much of their energy of formation by transferring electrons from defect levels near the conduction band to the Fermi level near the valence band. The energy gain due to electron transfer can be of the order of the band-gap energy.

show that it is possible, in principle, to produce well-conducting p-type ZnSe. But they still do not explain why, in practice, it is hard to make p-type ZnSe.

To examine this question, we go beyond the results for native defects in ZnSe and examine the behavior of specific doping systems. We study the doping of ZnSe with Li acceptors, using a formalism that applies our first-principles calculations to both the native defects and the dopant atoms. With this formalism we address three potential problems: (1) compensation of substitutional Li acceptors by interstitial Li donors, (2) compensation by native defects caused by deviations from stoichiometry, and (3) the solubility limits of Li in ZnSe.[3] Our results show that interstitial Li and native defect compensation are not a serious problem when growth conditions are optimized. Solubility limits, however, limit the total Li concentration to the 10^{18}–10^{19} cm^{-3} range.

2. Thermodynamic Formalism

In this section we present a thermodynamic formalism that, using the results of first-principles total-energy calculations, determines defect and dopant concentrations, the Fermi level, and dopant solubilities, as a function of the growth conditions. The concentrations of native defects in a compound semiconductor, and of dopants in any semiconductor, are a function not only of the semiconductor system itself, but also of the surrounding environment. The formalism provides a quantitative way of dealing with these environmental effects. Although we apply it here to the specific case of Li in ZnSe, the formalism is general and can be applied to any dopant and host semiconductor.

The strength of the formalism is that it treats both the native point defects and the dopants on an equal footing. We will give a precise definition of the formation energies for defects and dopants and show how they depend on the chemical environment, using Li

doping of ZnSe as a concrete example. The total energies of both native and dopant defects are calculated using a supercell approach, using separate calculations for each charge state of each defect.

While the total energies of a defect supercell can be calculated directly, determining defect *formation* energies is more complicated. Formation energies depend on the relative abundance of Zn, Se, and Li atoms in the environment. These dependences are handled by introducing the chemical potentials of Zn, Se, and Li: μ_{Zn}, μ_{Se}, and μ_{Li}. The Zn chemical potential is the energy of a reservoir of Zn atoms in equilibrium with the system. Zn atom states with energy more than a few k_BT below μ_{Zn} will be filled, while those more than a few k_BT above μ_{Zn} will be empty. Thus a high value of μ_{Zn} will correspond to a Zn-rich environment, and a low value to a Zn-poor environment. The formation energies of the native defects are also functions of the Zn and Se chemical potentials. For example, raising the Zn chemical potential lowers the formation energies of defects that introduce excess Zn atoms, such as Zn_i and V_{Zn}. The formation energies of Li impurities will be a function of the Li chemical potential, as well. For charged defects, the formation energy will also depend on the Fermi level, E_F, which is the chemical potential for the electrons. It is important to understand that μ_{Zn} and μ_{Se} are not intrinsic properties of ZnSe; their values will change as the environment changes. For example, ZnSe in equilibrium with Zn metal will have a higher μ_{Zn} than ZnSe in equilibrium with bulk Se. However, μ_{Zn} and μ_{Se} are not independent of one another: they are constrained by the condition that, in equilibrium, their sum must equal the total energy of a two-atom unit of perfect ZnSe, $E_{ZnSe} = \mu_{Zn} + \mu_{Se}$. (We use the total energy of a perfect ZnSe cell at T = 0 K for E_{ZnSe}.)

Given the chemical potentials, the formation energy of each native defect is well defined and can be derived from a supercell calculation as follows. The total energy, $E_{tot}(D_i)$, of the i^{th} defect, D_i, is calculated using a supercell containing n_i^{Zn} Zn atoms, n_i^{Se} Se atoms, and n_i^{Li} Li atoms. The defect formation energy, $E_{form}(D_i)$, is then

$$\begin{aligned} E_{form}(D_i) &= E_{tot}(D_i) - n_i^{Zn}\mu_{Zn} - n_i^{Se}\mu_{Se} - n_i^{Li}\mu_{Li} - n_i^e E_F \\ &= \mathcal{E}(D_i) - \Delta n_i \mu_{Zn} - n_i^{Li}\mu_{Li} - n_i^e E_F, \end{aligned} \tag{1}$$

$$\mathcal{E}(D_i) = E_{tot}(D_i) - n_i^{Se} E_{ZnSe}, \quad \Delta n_i = n_i^{Zn} - n_i^{Se}, \tag{2}$$

where n_i^e is the charge state of the defect, and Δn_i is the number of extra Zn atoms that must be added to form the defect (+1 for Zn_i and V_{Se}, -2 for Se_{Zn}, etc.). Here, we treat μ_{Zn} as an independent variable and remove μ_{Se} from the expression for $E_{form}(D_i)$; alternatively, we could treat μ_{Se} as independent and eliminate μ_{Zn}. In terms of its formation energy and entropy, S_i, each defect's equilibrium concentration is

$$[D_i] = N_{sites} e^{S_i/k_B} e^{-E_{form}(D_i)/k_B T}, \tag{3}$$

where N_{sites} is the site concentration for each species, which is 2.2×10^{22} cm^{-3} for ZnSe. The Fermi level is determined by the charge conservation condition:

$$\text{Net charge} = 0 = p - n - \sum_i n_i^e [D_i], \tag{4}$$

where p and n are the hole and electron densities, respectively. The charge conservation equation provides for an indirect interaction between the concentrations of all charged defects through their influence on the Fermi level. For example, a positively charged defect produces extra free electrons that raise the Fermi level; the higher Fermi level, in turn, increases the concentrations of all negatively charged defects and lowers the concentrations of all positively charged defects. Using this prescription, all of the defect formation energies, and hence their concentrations, $[D_i]$, are unique functions of μ_{Zn}, μ_{Li}, and T.

The value of μ_{Zn} also determines the stoichiometry parameter, X:

$$X = \frac{N_{Se} - N_{Zn}}{N_{Se} + N_{Zn}} = \frac{-\sum_i \Delta n_i [D_i]}{2N_{sites}}, \tag{5}$$

where N_{Zn} and N_{Se} are the total numbers of Zn and Se atoms in the crystal. X is positive for Se-rich and negative for Zn-rich. In this equation, X refers only to the contributions to the stoichiometry due to native point defects. Deviations from stoichiometry due to higher dimensional defects, such as surfaces, are not included. Also, dopant atoms do not contribute to X, (i.e., a substitutional dopant atom is counted as if it were the same species as the native atom that it replaces) because the process of substituting a dopant does not necessarily create any native defects. This definition of X means that the value of the stoichiometry parameter measured in experiment will differ from X as defined here if the former is dominated by anything other than the native defects.

The formalism thus far provides us with information about the Fermi level and the concentrations of both native and dopant defects. Thermodynamics also provides limits to the allowed values of the chemical potentials. These limits determine the solubility of the dopant in the host semiconductor.[9] The limits exist because two phases of the same material can exist in equilibrium only if the chemical potential is the same in both phases. Thus, in equilibrium, μ_{Zn} must be the same in both the ZnSe and the external Zn source. The chemical potential of the external Zn source, however, can never exceed the free energy of bulk Zn metal, μ_{Zn}^{bulk}; if it did, the external source would be unstable against the formation of Zn metal. Thus, $\mu_{Zn} \leq \mu_{Zn}^{bulk}$. Similarly, the limit for the Se chemical potential is $\mu_{Se} \leq \mu_{Se}^{bulk}$. As already mentioned, we have the additional constraint that

$$\mu_{Zn} + \mu_{Se} = E_{ZnSe} = \mu_{Zn}^{bulk} + \mu_{Se}^{bulk} + \Delta H_f(ZnSe), \tag{6}$$

where ΔH_f (ZnSe) is the heat of formation of ZnSe (ΔH_f is negative for a stable compound). Combining these three conditions sets the limits for the allowed range of μ_{Zn}:

$$\mu_{Zn}^{min} = \mu_{Zn}^{bulk} + \Delta H_f(ZnSe) \leq \mu_{Zn} \leq \mu_{Zn}^{max} = \mu_{Zn}^{bulk}. \tag{7}$$

The same arguments provide an upper bound for the Li chemical potential: $\mu_{Li} \leq \mu_{Li}^{bulk}$. (Since ZnSe can exist in a Li-free environment, there is no lower bound to the Li potential.) However, a more stringent upper bound for μ_{Li} is found by taking into account all possible compounds that contain Li with either Zn or Se (or both).[9] The actual upper bound is due to the compound Li_2Se, which leads to the condition

$$2\mu_{Li} + \mu_{Se} \leq \mu_{Li_2Se} = 2E_{Li}^{bulk} + \mu_{Se}^{bulk} + \Delta H_f(Li_2Se). \tag{8}$$

This condition on the Li chemical potential limits the maximum Li concentration in ZnSe because it provides a minimum value for the Li dopant formation energy in Eq. (3). Physically, this solubility limit occurs because the configurational entropy for Li impurities in ZnSe depends on the number of Li atoms already present in the crystal; as the total number of Li atoms in the crystal increases from m to $m + 1$, the number of ways to distribute the Li atoms over N sites decreases. This configurational entropy is not included in S_i defined previously. (See Ref. [10] for a fuller discussion of the configurational entropy and how it can be used to derive Eq. (3).) Consequently, the *total* free energy, including the configurational entropy change, for adding one more Li atom to the crystal decreases as the Li concentration increases. By contrast, the free energy of adding one more unit of Li_2Se is independent of the amount of Li_2Se already present (ignoring surface effects). When the total free energy of adding one more Li atom to the ZnSe crystal exceeds the free energy to form Li_2Se, Li_2Se will form instead and the solubility limit is reached.

3. Methods

In this section we describe the theoretical methods used to calculate total energies. First, a word of caution: although the defect formation *energies* calculated here are accurate, with error bars ~ 0.1 eV, the defect *concentrations* derived from them do not attain the same level of accuracy. Because the concentrations depend exponentially on the energies, a 0.1 eV uncertainty in the latter becomes a seven-fold multiplicative factor in the former. This inherent limitation means that our results should be viewed not as precise numerical predictions, but as predictions of the important physical processes and trends.

Our calculations use density-functional theory in the local-density approximation (LDA) and norm-conserving pseudopotentials.[11, 12] Supercells, corresponding to 32 atoms of pure ZnSe, are used to represent the defects. These methods, combined with a plane-wave basis set, have been used very successfully in the past for studies of defects in Si and other semiconductors. The II-VI materials, however, present a problem for these methods: zinc contains a tightly bound set of 3d electrons that cannot be easily represented by a plane-wave basis set. These d electrons may be treated as core states of the pseudopotential, but this results in a very poor description of ZnSe. For example, the lattice constant calculated with a "d-in-the-core" pseudopotential is 5.19 Å compared with the experimental lattice constant of 5.67 Å.

To treat the d electrons as valence states, we use an all-new mixed-basis program, which combines localized functions with the plane waves. The program was carefully optimized, allowing defect calculations in large supercells. We use the Zn 3d pseudo-wave functions as the localized basis functions, and include all plane waves up to a kinetic energy cutoff of 9 Ry. (The eigenvalue problem was solved using an iterative diagonalization scheme.[13]) For our calculations involving Li, we implemented a nonlinear-core correction to the Li pseudopotential.[14] These methods provide a good description of the lattice constant, bulk modulus, and transverse optical phonon frequency of ZnSe (and other materials). Convergence tests were performed for supercell size, the basis set and other calculational parameters, assuring that our results are well-converged.

Density-functional theory used with the LDA consistently predicts band gaps that are too small compared with experiment. For ZnSe, our calculated band-gap is about 1 eV. This band-gap error will affect formation energies of defects that have occupied electron states in the band gap. The band-gap error will not affect our results for p-type material, where the Fermi level is near the valence band edge, because defect states in the gap will be empty and will not contribute to the total energy of the defect.

We use these methods to calculate the formation energies of all native point defects in ZnSe: two types of interstitials (Zn_i and Se_i), two types of vacancies (V_{Zn} and V_{Se}), and two types of antisites (Zn_{Se} and Se_{Zn}). In addition, we calculate the formation energies of Li impurities on the substitutional zinc site (Li_{Zn}) and at five different interstitial sites (Li_i). Of the interstitial sites we examined, the tetrahedral site surrounded by four Se atoms has the lowest energy, and we include only this site when referring to interstitial Li. The total energy of each defect was calculated in each relevant charge state, except for the neutral Li_{Zn}, which contains a hole in a shallow level. (This level merges with the valence band in our finite supercell calculation.) The formation energy for the neutral Li_{Zn} is derived from the calculated value of Li_{Zn} in the -1 charge state, and the experimental transition level of 114 meV.

The formation energy of a defect may be lowered by the relaxation of nearby host atoms from their perfect crystal sites. We calculate relaxation energies explicitly for the dominant native defects in n-type ZnSe, and for the substitutional and interstitial Li defects. For interstitial defects, we relax the first and second nearest-neighbor atoms and also the fourth

nearest neighbors that are bonded directly to the first nearest neighbors. For substitutional defects we relax the first nearest neighbors. All of these relaxations are small: the largest relaxation that we found was 0.2 Å with a relaxation energy of 0.6 eV. For the remaining defects, we assume a relaxation energy of 1 eV; our conclusions remain unchanged even if we allow a 2 eV relaxation energy.

Defect concentrations will also depend on the formation entropy of the defect. In our work we allow a range of 0–10 k_B for the defect formation entropies. By comparison, a recent accurate calculation[15, 16] for the Si self-interstitial found a formation entropy of 5-6 k_B for the ground state. The Si self-interstitial represents an extreme case in that the ground-state configuration has low symmetry, which accounts for half of the formation entropy. It is therefore highly unlikely that the entropies for native defects in ZnSe could be larger than 10 k_B. The results are presented here assuming an entropy of 5 k_B.

We use the same theoretical techniques to calculate the energies of the bulk solid phases of ZnSe, Zn, Se, Li and Li_2Se. We calculate the heat of formation for ZnSe as -1.39 eV, while the experimental value is -1.69 eV.[17] For Li_2Se we find -4.12 eV, compared to the experimental value of -3.96 eV.[17] The deviations are in line with the expected accuracy of the methods and are comparable to those found in other local-density calculations. (Note that the heats of formation are energy differences between solid phases. Cohesive energies, by contrast, are energy differences between isolated atoms and the solid phase. Since the LDA gives worse predictions for the total energies of individual atoms, calculated cohesive energies contain systematic errors which do not occur for heats of formation.) Throughout this work, we will use the theoretical values for the heats of formation.

4. Native Defects

In this section we will answer the question, "Do native defects automatically compensate acceptor doping of ZnSe?". The native defect mechanism is by its very nature generic: it claims that compensation occurs whenever the Fermi level is brought close enough to the valence band edge, irrespective of the dopant. To test this idea, we picture a ZnSe crystal doped with an "ideal" acceptor, by which we mean an acceptor that fixes the Fermi level without changing the crystal in any other way. (In the next section we will examine a real acceptor in ZnSe.) As discussed in Section 2, the external parameters that determine native defect concentrations are the temperature, T, the Zn chemical potential, μ_{Zn}, and the Fermi level, E_F. Throughout this article, we will use $T = 600$ K, the typical temperature for MBE growth of ZnSe. We will use our "ideal" dopant to fix the Fermi level at 0.13 eV above the valence band maximum, corresponding to a net hole concentration of $p = 2.9 \times 10^{18}$ cm^{-3}. Having fixed the temperature and hole concentration in our ideal sample, there is only one external parameter that is still undetermined: the zinc chemical potential, μ_{Zn}, which is determined by the growth environment. (As discussed in Section 2, we could equally well use μ_{Se} as the independent parameter instead of μ_{Zn}, since the two chemical potentials are constrained by $E_{ZnSe} = \mu_{Zn} + \mu_{Se}$.)

Figure 2 shows the concentrations of electrons produced by all native defects in p-type ZnSe, as a function of μ_{Zn}. In the figure μ_{Zn} spans its thermodynamically allowed range from ZnSe in equilibrium with bulk Se on the left, to ZnSe in equilibrium with bulk Zn on the right (Eq. 7). The stoichiometry parameter, X, is determined by μ_{Zn} (Eq. 5). In Fig. 2, $\mu_{Zn} = \mu^s_{Zn}$ corresponds to perfect stoichiometry; all points to the left are Se-rich, and those to the right are Zn-rich. We see that for perfect stoichiometry the concentrations of native defects is negligibly small - 10^7 times smaller than the hole concentration p. For material grown at temperatures higher than 600 K, excess native defects will recombine during cooling, unless the sample is rapidly quenched. (Native defects in ZnSe remain mobile

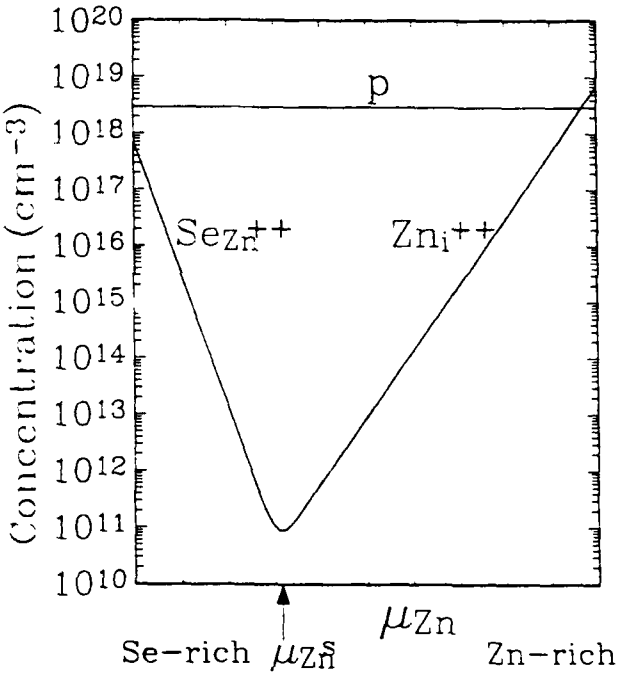


Figure 2: Concentration of electrons produced by all native point defects in p-type ZnSe, with $p = 2.9 \times 10^{18}$ cm^{-3} and $T = 600$ K. Concentrations are shown as a function of the chemical potential μ_{Zn} over its thermodynamically allowed range. The lower limit of μ_{Zn} (left-hand axis) corresponds to ZnSe in equilibrium with bulk Se, the upper limit (right-hand axis) to ZnSe in equilibrium with bulk Zn. The point labelled μ_{Zn}^{s} corresponds to perfectly stoichiometric ZnSe; points to the left are Se-rich, to the right Zn-rich. Se_{Zn}^{++} is the dominant defect on the Se-rich side, and Zn_i^{++} on the Zn-rich side.

even at temperatures of 400 K,[18] so that kinetic barriers do not prevent the attainment of thermal equilibrium.)

Native defect concentrations start to increase as μ_{Zn} deviates from μ_{Zn}^{s}, with Se_{Zn}^{++} the dominant defect for $\mu_{Zn} < \mu_{Zn}^{s}$, and Zn_i^{++} the dominant defect for $\mu_{Zn} > \mu_{Zn}^{s}$. It is clear from the figure that native defect compensation can only occur for extreme values of μ_{Zn}, near the limit where either bulk Zn or bulk Se are formed in the sample. For these extreme cases, the level of compensation by native defects is 20% for μ_{Zn}^{min} and 70% for μ_{Zn}^{max}. (To keep p at 2.9×10^{18}, the ionized acceptor concentration must be increased to 3.6×10^{18} for μ_{Zn}^{min}, and to 9.7×10^{18} for μ_{Zn}^{max}.) Using Eq. (5), we find that the deviation from stoichiometry due to native defects is $X = 2 \times 10^{-5}$ for μ_{Zn}^{min}, and $X = -8 \times 10^{-5}$ for μ_{Zn}^{max}.

These results show clearly that compensation by native defects is not an intrinsic problem for p-type ZnSe. For stoichiometric material native defect concentrations are truly negligible: even when deviations from perfect stoichiometry occur, the level of native-defect compensation is less than 3% over more than 80% of the allowed range of the chemical potential.

Further insight into the relationship between the width of the band gap and native-defect compensation can be gained by comparing the energies of the native defects in ZnSe (E_g = 2.6 eV) and in GaAs (E_g = 1.35 eV). Zhang and Northrup[19] recently calculated the formation energies of native defects in GaAs, using similar theoretical techniques to those used here. Their calculated formation energies for the dominant native defects in p-type GaAs, with the Fermi level at the valence band maximum (first panel of Fig. 2 in Ref. [19]), are −0.25 eV for As_{Ga}^{+++} in the As-rich limit, and 0.55 eV for Ga_i^{3+} in the Ga-rich limit. Our own results for p-type ZnSe are 0.57 eV for Se_{Zn}^{++} in the Se-rich limit, and 0.45 eV for Zn_i^{++} in the Zn-rich limit. The native defect formation energies are no greater in ZnSe than they are in GaAs. We conclude that a wider band gap does not imply more native defects. Also, since GaAs can be doped p-type without compensation by the native defects, the same should be true for ZnSe.

5. Li in ZnSe

Having eliminated native defects as a generic source of compensation in wide band-gap materials, it is fruitful to identify problems associated with specific dopants. We will now examine the case of acceptor doping of ZnSe with Li_{Zn}. Recently, significant progress has been made with Li doping of ZnSe, but the maximum hole concentration attained to date is a few times 10^{17} cm^{-3}.[20] It is unclear what makes Li doping so difficult.

We examine the issue of Li doping using the formalism of Section 2 and the calculated formation energies for the native defects and for interstitial and substitutional Li. The formalism automatically includes all possible defect reactions between Li and the native defects. Furthermore, it includes the effects of the relative abundance of Zn and Se atoms and the solubility limit Li. The results for Li and for other acceptors in ZnSe are discussed in more detail elsewhere.[21]

In the previous section, which dealt with the native defects alone, the two independent parameters were μ_{Zn} and E_F. In this section, where the presence of the Li dopants is considered explicitly, E_F is no longer an independent parameter because it is determined by the charge conservation condition (Eq. 4). Fermi level effects are still important because they allow the charged native defects and Li impurities to affect one another through their mutual effect on E_F. Although we have now eliminated E_F as an independent variable, we must introduce the Li chemical potential, μ_{Li}, as a new second variable. When applying the formalism to Li in ZnSe, we provide as input the values of $\mathcal{E}(D_i)$ for all of the native defects and the Li impurities, and the relevant range of μ_{Zn} and μ_{Li}. In return we get the formation energies and concentrations of each defect and the Fermi level, each as a two-dimensional function of the chemical potentials. Since a vast amount of information is produced, we present only the most relevant quantities.

In Fig. 3(a) and (b), we display contour plots of the total Li concentration, [Li], and the Fermi level. [Li] increases with increasing μ_{Li} because it is more favorable for the Li to dissolve in the semiconductor as the energy of the Li reservoir rises. Also, $[Li_{Zn}]$ increases with *decreasing* μ_{Zn}, which is the energy of the reservoir to which Zn atoms are removed in order to accommodate the Li. The concentration of Li_i, on the other hand, does not depend explicitly on μ_{Zn}. Therefore, for high μ_{Zn} (Zn-rich environment) Li_i is favored relative to Li_{Zn}. The presence of compensating Li_i raises E_F in the upper part of the figure, and makes the material semi-insulating. Compensation by Li_i can be avoided by lowering μ_{Zn}, which favors Li_{Zn} over Li_i. But if μ_{Zn} is lowered too far, the concentration of compensating Se_{Zn}^{++} begins to increase. This is why the Fermi level contours bend back at the bottom of Fig. 3(b). It is only for these very low values of μ_{Zn} that the native defects play an important role. Comparing to Fig. 2, we see that the native defect concentration only becomes significant

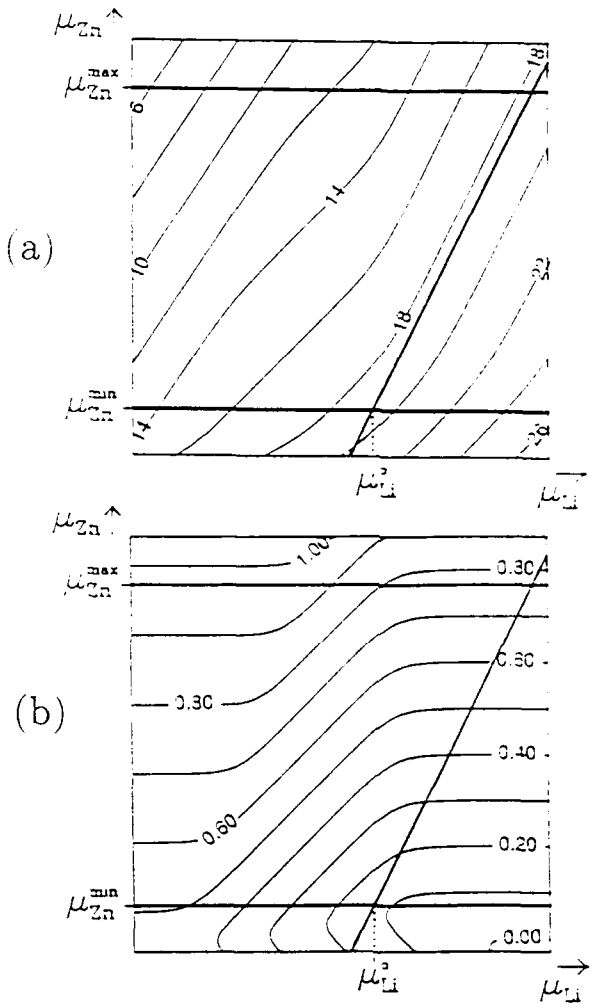


Figure 3: The behavior of Li in ZnSe at 600 K. Results are in the form of contour plots as a function of the Li and Zn chemical potentials, μ_{Zn} and μ_{Li}. Part (a) shows contour lines for $\log_{10}$[Li], where [Li] is the total Li concentration (cm^{-3}), including both Li_{Zn} and Li_i. Part (b) shows the Fermi level contours in units of eV, measured from the valence band maximum. The two solid horizontal lines are the thermodynamic limits of μ_{Zn} due to bulk Zn (μ_{Zn}^{max}) and bulk Se (μ_{Zn}^{min}). The solid slanted line is the limit of μ_{Li} due to Li_2Se.

when μ_{Zn} reaches its thermodynamic limit μ_{Zn}^{min}. (Figure 2 also shows that native defect concentrations will be large for μ_{Zn} near μ_{Zn}^{max}. This, however, applies only when E_F is near the band edge: in Fig. 3 E_F is far from the valence band near $\mu_{Zn} = \mu_{Zn}^{max}$. Consequently, the native defects are not important when μ_{Zn} is high in ZnSe:Li.) We can therefore expect a small amount of compensation due to native defects near the μ_{Zn}^{min} line in the figure. This compensation is not an effect of the native defects themselves, but instead occurs because the Zn chemical potential must be reduced so as to increase [Li_{Zn}] and decrease [Li_i]. If we could find a dopant that could be incorporated without having to push μ_{Zn} to its extreme values, then the native defects would not appear at all.

Figure 3 also shows the thermodynamic limits of the chemical potentials μ_{Zn} and μ_{Li} (Eqs. 7 and 8). These bounds mean that the Li solubility limit in ZnSe is a few times 10^{18} cm^{-3}. The lowest value of E_F (most effect p-type doping) is about 0.13 eV, and occurs near the point labelled μ_{Li}^0 in Fig. 3. In this region there is a small concentration of interstitial Li and compensating native defects. But doping limits imposed by interstitial Li or native defects can be avoided; it is solubility that presents the most stringent limit to Li doping.

6. Summary

In conclusion, we have shown that native defects alone *cannot* be responsible for difficulties in doping ZnSe. Native defect concentrations in MBE-grown stoichiometric ZnSe are too low to compensate. Deviations from stoichiometry in ZnSe *can* produce large numbers of native defects which, however, is also true for GaAs. Therefore native defects produced by deviations from stoichiometry cannot explain why it is so hard to dope ZnSe p-type. Having eliminated native defects as the source of doping problems in ZnSe, we examine specific dopant systems. Doping problems for Li acceptors in ZnSe are caused by limited solubility of Li in ZnSe.

We have greatly benefited from collaborations with G.F. Neumark and S.T. Pantelides. We are very grateful to P. Blöchl for many fruitful suggestions, and for making his unpublished work available to us. We are indebted to D. Vanderbilt for his iterative diagonalization program. We acknowledge helpful conversations with R. Bhargava, J.M. DePuydt, T. Marshall, J. Tersoff, and G.D. Watkins.

References

[1] Y. S. Park and B. K. Shin, in *Topics in Applied Physics* (Springer Verlag, Berlin, 1977), Vol. 17, p. 133.

[2] R. Bhargava, J. Crystal Growth **59**, 15 (1982).

[3] G. F. Neumark, Phys. Rev. Lett. **62**, 1800 (1989).

[4] H. Cheng, J.M. DePuydt, J.E. Potts, and M.A. Haase, J. Crystal Growth **95**, 512 (1989).

[5] R. M. Park *et al.*, Appl. Phys. Lett. **57**, 2127 (1990).

[6] G. Mandel, Phys. Rev. **134**, A1073 (1964).

[7] R. W. Jansen and O. F. Sankey, Phys. Rev. B **39**, 3192 (1989).

[8] D.B. Laks, C.G. Van de Walle, G.F. Neumark, and S.T. Pantelides, Phys. Rev. Lett. **66**, 648 (1991).

[9] F.A. Kröger, *The Chemistry of Imperfect Crystals* (North-Holland, Amsterdam, 1964).

[10] N.W. Ashcroft and N.D. Mermin, *Solid State Physics* (Saunders College, Philadelphia, 1976).

[11] J. Ihm, A. Zunger, and M.L. Cohen, J. Phys. C **12**, 4409 (1979).

[12] G.B. Bachelet, D.R. Hamann, and M. Schlüter, Phys. Rev. B **26**, 4199 (1982).

[13] R. Natarajan and D. Vanderbilt, J. Comput. Phys. **82**, 218 (1989).

[14] S.G. Louie, S. Froyen, and M.L. Cohen, Phys. Rev. B **26**, 1738 (1982).

[15] P.E. Blöchl and S.T. Pantelides, (To be published).

[16] P.E. Blöchl *et al.*, in *Proceedings of Int. Conf. on Physics of Semiconductors* (World Scientific, Thessaloniki, 1990).

[17] *Lange's Handbook of Chemistry*, 13 ed., edited by J.A. Dean (McGraw-Hill, New York).

[18] G.D. Watkins, in *Proceedings of International Conference on Science and Technology of Defect Control in Semiconductors* (Yokohama, 1989).

[19] S.B. Zhang and J.E. Northrup, Phys. Rev. Lett. **67**, 2339 (1991).

[20] M.A. Haase, H. Cheng, J.M. Depuydt, and J.E. Potts, J. Appl. Phys. **67**, 448 (1990).

[21] C.G. Van de Walle and D.B. Laks, these Proceedings.

THEORY OF DOPING OF DIAMOND

J. Bernholc, S. A. Kajihara, and A. Antonelli*
Department of Physics, North Carolina State University
Raleigh, NC 27695-8202

ABSTRACT

Electronic applications of diamond require control over native defects as well as the ability to dope it p- and n-type. B is an excellent p-type dopant, but n-type doping has proven very difficult. Diamond films have also been very difficult to anneal, indicating a high activation energy for self-diffusion. We have investigated the properties of native defects and impurities through large-scale band structure and Car-Parrinello calculations. We indeed find that the activation energy for self-diffusion is very high in the intrinsic material, but it decreases by as much as 3 eV in either p- or n-type material. P, Li, and Na are shallow donors, but their solubilities are too low for incorporation into diamond through in-diffusion. It is energetically favorable for B and N to dissolve in diamond, which explains their prevalence in natural diamond. The calculations explain for the first time the reasons for the distortion of atoms around N from the fully tetrahedral site, as well as why N is a deep rather than a shallow donor. We also consider the effects of simultaneous doping with N and B on the thermodynamic equilibrium between diamond and graphite.

INTRODUCTION

The electronic and optical properties of diamond are determined to a large extent by the number and types of impurities and defects present in the film. For example, shallow impurities control the majority carrier densities and make it display n- or p-type conductivity. Deep impurities, *i.e.*, impurities whose energy levels are far from the conduction and valence band edges, do not determine the carrier density, since their electrons or holes cannot be thermally promoted at room temperature. However, both deep impurities and native defects act as recombination or deep trapping centers, as well as light absorbers. Native defects also govern diffusion and material transport in semiconductors. If the formation energies of na-

* Present address: Department of Physics, Virginia Commonwealth University, Richmond, VA 23284.

Mat. Res. Soc. Symp. Proc. Vol. 242. 1992 Materials Research Society

tive defects are large, diffusion is slow and annealing is very difficult. This is the case for diamond (see below).

Impurities in diamond have not yet been well characterized. The experimental data are sparse [1] and the only impurities that have been studied at substantial length are boron and nitrogen. Boron is a p-type dopant with an energy level at E_{val} + 370 meV. Both natural and synthetic p-type diamond exists, and boron-doped p-type thin films have also been made. However, the making of n-type diamond is much more difficult. Nitrogen, which is a common impurity in diamond, introduces a deep level 1.7 eV below the bottom of the conduction bands. This is very unexpected, because an impurity atom having one more electron than the host atom should be a shallow donor (cf. P in Si). Despite a number of theoretical studies of the properties of N in diamond, the atomic distortions around the N center have not been explained.

The only reports of successful n-type doping of diamond to date [2, 3] involved ion implantation of Li into bulk diamond. Due to the damage caused by the implantation, the quality of the resulting material was relatively poor. Furthermore, most of the n-type conductivity was lost after prolonged annealing [4]. However, Li is the only proven shallow donor in diamond. Since it is an interstitial dopant, it is believed to be a fast diffuser that may need stabilization in high temperature applications by, *e.g.*, complexing.

Although N is a deep donor, its energy level is still ~ 4 eV above the top of the valence band of diamond. A N^+ - B^- pair should thus be bonded by a substantial amount. Since both N and B are highly soluble in diamond (see below), simultaneous doping with N and B could potentially be used to stabilize the diamond phase. We investigate the effects of this doping on the thermodynamic balance between diamond and graphite below.

CALCULATIONS

The calculations use the plane wave pseudopotential method. The native defects and the impurities were embedded in a periodically repeated supercell. Both symmetrized band structure codes and the Car-Parrinello method [5] were used. Calculations with relatively low plane wave cutoffs were possible because of a previously developed soft-core pseudopotential for carbon. In the band structure calculations the supercell size corresponded to 32 atoms. Plane waves up to 14 Ry were included directly, while plane waves up to 26 Ry were included through perturbation theory. Two special k-points in the irreducible part of the Brillouin zone were used for k-space summations. The details of the band structure calculations for the native defects are described in Ref. 6.

Table I. Calculated formation energies of neutral point defects and the saddle point energy for the concerted exchange in diamond [eV].

vacancy	tetrahedral interstitial	<100> split-interstitial	bond-centered interstitial	concerted exchange
7.2	23.6	16.7	15.8	13.2

The Car-Parrinello calculations for isolated impurities were carried out in a 64-atom unit cell. N, Li, Na, and P were considered. The plane wave cutoff was 26 Ry, except for the case of N, where 30 Ry were used. Due to the size of the cell only the Γ point was used. A test for N that utilized the Baldereschi point resulted in a change in the relaxation energy of only 0.1 eV, compared to the Γ point case (see below). For N, Li, and Na, all atoms were relaxed using *ab initio* forces. For substitutional P, radial relaxations were computed for the nearest neighbors, while the relaxations of the more distant neighbors were obtained employing a Keating force field. The details of the calculations are described in Ref. [7].

Because diamond has a relatively small lattice spacing, the non-local parts of the standard Bachelet-Hamann-Schlüter pseudopotentials for Li and Na [8, 9] overlap the bonding region in the diamond lattice. Special, harder pseudopotentials were constructed and it was verified that the results were insensitive to variations in the matching radii of those potentials.

In calculating the formation energies, we have used the computed cohesive energy of diamond [6] and the experimental bulk cohesive energies for the impurities. The solubility of an impurity at a given site is related to the formation energy by the Boltzmann factor, i.e. Solubility $\approx$ Conc. $\times \exp(-E_f/kT)$ [10], where Conc. is the concentration of the site per unit volume.

The calculations involving comparisons between diamond and graphite utilized 64- and 48-atom unit cells for diamond and graphite, respectively. All atoms in the supercells were fully relaxed by *ab initio* forces. In order to increase the accuracy of the comparison we used a slightly harder pseudopotential for diamond, which was previously used in the studies of buckyballs [11]. The plane wave cutoff was 35 Ry for both diamond and graphite.

NATIVE DEFECTS AND SELF-DIFFUSION IN DIAMOND

The energies of the various neutral native defects and the activation energy of the concerted exchange mechanism are quoted in Table I. Clearly, the contributions of other diffusion mechanisms should be negligible under equilibrium conditions. In particular, the formation energies of self-interstitials are very high. This is due to the lack of d-orbitals in diamond (which makes overcoordination unfavorable),

high electronic density, and a large band gap. In the case of the tetrahedral interstitial, which has a doubly occupied level near the bottom of the conduction bands, the formation energy is particularly high. The energies of interstitial impurities are high for similar reasons.

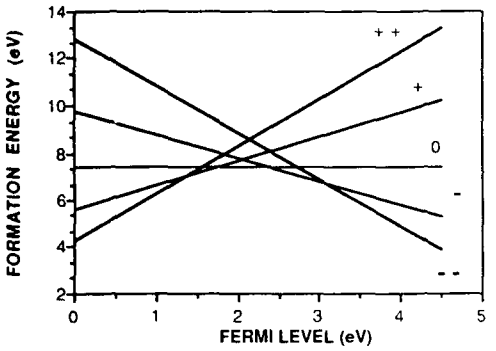


Fig. 1. The formation energy of the carbon vacancy in diamond in its various charge states as a function of the Fermi level.

The migration energy of the vacancy is substantial and ranges from 1.7 to 1.9 eV, depending on its charge state [6]. The activation energy for self-diffusion, which is the sum of the formation and migration energy, is 9.1 eV in intrinsic diamond. However, p- or n-type doping lowers the formation energy of the vacancy by about 3 eV (see fig. 1) thereby leading to enhanced self-diffusion and vacancy-assisted impurity diffusion. It was predicted [6] that doping during growth should thus lead to better annealing of defect structures due to the lowering of the self-diffusion activation energies. This effect was subsequently observed in growth of B-doped thin films on non-diamond [12] and natural diamond substrates [13]. However, the observed enhancement could also be due to an increase in surface diffusivity upon doping, or to surface reactions involving B.

DONOR IMPURITIES

In the present work, P, Li and Na are considered as potential shallow dopants. Since the position of the impurity is critical for its doping action, we have carried out total energy calculations of the impurities at substitutional and interstitial sites. As expected, P prefers the substitutional site whereas Li and Na prefer interstitial positions.

For P, which is larger than C, the nearest neighbors relax radially outward by 0.15 Å, but the carbon-phosphorus bond length is still substantially smaller than the sum of the C and P covalent radii. This is a consequence of the stiffness of the diamond lattice. The P level is shallow, ~0.2 eV below the bottom of the conduc-

tion band. Substitutional P would thus be a good candidate for a shallow donor. However, the calculated formation energy of P, defined as the energy of the P atom in diamond with respect to C and P bulk reservoirs, is 10.4 eV. The equilibrium solubility of P in diamond is thus very low even at high temperatures.

Both Li and Na prefer the tetrahedral interstitial site over the hexagonal interstitial site and are indeed shallow dopants, with their donor levels at ~0.1 and ~0.3 eV below the conduction band minimum. The nearest neighbor radial relaxations at both the tetrahedral and hexagonal sites are outwards and are of course dependent on the size of the dopant atom. At the tetrahedral site they are 0.05 and 0.19 Å for Li and Na, respectively. At the hexagonal site the relaxations are 0.06 and 0.26 Å. The formation energies at the tetrahedral site are 5.5 and 15.3 eV, measured with respect to experimental cohesive energies of bulk Li and Na. Since the relative solubility is given by $\exp(-E_f/kT)$, the solubilities of the shallow interstitial dopants are very low as well.

Three methods are commonly used to incorporate impurities in semiconductors: in-diffusion, doping during growth, and ion implantation. In cases where the formation energy is small, high temperature in-diffusion is often a very convenient alternative. However, due to the very low solubilities of P, Li, and Na, in-diffusion would result in a negligible concentration of dopants. If doping during growth is selected, the impurities will have to be kinetically trapped in diamond, since their energies of formation are very high. The successful doping with B during growth of diamond films by a number of workers is due to the fact that the formation energy of the B substitutional acceptor in diamond is negative (see Table II), which provides a thermodynamic force for its incorporation.

Ion implantation is a particularly viable alternative for impurities with high formation energies. In diamond, ion implantation of impurities has been studied by a number of workers (see, *e.g.*, Ref. 2 and 3). In fact, the only n-type diamond samples to date were made by ion implantation of Li into natural diamond [2]. Further studies of ion implantation were carried out by Braunstein and Kalish [3], who investigated ion implantation of ^{121}Sb, ^{74}Ge, ^{31}P, ^{12}C, and ^{6}Li into hot diamond and found only small variations in ion implantation damage caused by heavy

Table II. Calculated formation energies of neutral impurities in diamond measured relative to the respective bulk reservoirs (diamond and bulk impurities).

boron	-0.5 eV
nitrogen	-0.6 eV
phosphorus	10.4 eV
lithium	5.5 eV
sodium	15.3 eV

and light atoms. More recently, Prins [14] and Sandhu, Swanson, and Chu [15], showed that ion implantation at liquid nitrogen temperature followed by annealing has substantial advantages, because the mobile C self-interstitials are trapped during implantation and do not escape to the surface. The annealed samples turned out to have much better electrical characteristics than the ones implanted at room or elevated temperatures. So far, only ion implantation of B has been successfully achieved, resulting in a p-type diamond. However, in order to provide lattice sites for the substitutional B acceptor, it was necessary also to co-implant C. For interstitial dopants the last step should not be needed, which should lead to less implantation damage. Since Li and Na prefer the interstitial site by a substantial energetic margin, they would not compete with C atoms displaced during the implantation for the vacant substitutional sites. Subsequent annealing should thus result in a better quality material.

The mechanism of impurity diffusion is also important in the consideration of prospective dopants, since diffusion of the impurity to the surface or complexing with structural defects leads to inactivation. For substitutional impurities, Table I suggests that the their diffusion will be dominated by the vacancy mechanism. Since the formation energy of the vacancy varies between 4 and 7 eV (depending on the Fermi level position), and its migration energy is 1.7-1.9 eV, the vacancy-assisted diffusion will have a high activation energy and substitutional impurities should remain stationary even at high temperatures. However, if growth and/or processing of diamond results in injection of vacancies, the activation energy becomes equal to the migration energy. If the substitutional impurity has a high formation energy, segregation is energetically favorable and may occur if vacancies are injected at a high temperature.

The simplest mechanism for the diffusion of interstitial impurities involves jumps between adjacent tetrahedral sites, the saddle point for the motion being the hexagonal site. We carried out studies of this path for both Li and Na. Total energy calculations, which included relaxation of all atoms in the cell at both the tetrahedral and the hexagonal interstitial sites, predict 0.85 and 1.4 eV for the activation energies for Li and Na diffusion, respectively. The low activation energy for Li is in agreement with experimental data [4], since Li-doped samples become deactivated after prolonged annealing. Na, however, has a substantially larger activation energy and should be immobile up to moderate temperatures. It is therefore more suitable than Li for n-type doping of diamond. However, due to the high formation energy of the Na interstitial, Na will have to be introduced into diamond by ion implantation or possibly kinetically trapped during growth.

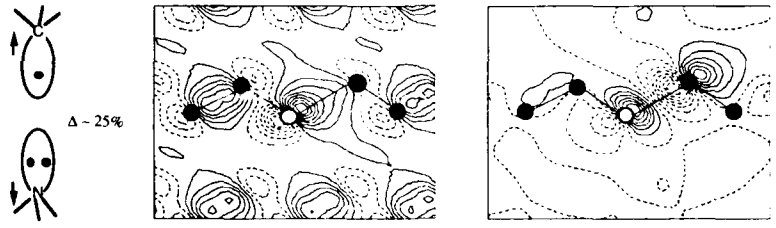


Fig. 2. a) A schematic model of the origin of the distortions around N in diamond. b) Contour plot of the N lone pair state. c) Contour plot of the gap state associated with N in diamond. See text.

NITROGEN IN DIAMOND

Nitrogen is known from EPR data to distort in the ($\bar{1}$, $\bar{1}$, $\bar{1}$) direction. This distortion was first thought to be a result of a Jahn-Teller effect [17, 18, 19] but later work has shown that the state in the gap is non-degenerate [20]. Furthermore, recent cluster calculations [21] revealed that the ideal substitutional N is stable against the displacements of only the N atom in the ($\bar{1}$, $\bar{1}$, $\bar{1}$) direction, showing that N motion is due to a more complicated effect.

Our calculations were started assuming a simple zeroth-order model shown in fig. 2a. The figure shows the N atom forming three bonds with its nearest-neighbor C atoms. This results in the N lone pair state being directed towards the fourth nearest-neighbor C atom. Since the lone pair state is fully occupied and the dangling bond contains one electron, the Pauli repulsion results in *both* the N atom and the (111) C atom moving away from each other.

Car-Parrinello calculations starting from this geometry and utilizing first-principles forces indeed converge to a distorted geometry in which the C – N distance has been lengthened by 25%. However, Table III shows that the radial relaxations and the motion of other atoms are also important, and that both effects contribute an approximately equal amount to the total gain in energy, which is 0.76 eV. The calculated bond lengthening is in good agreement with the values deduced from the EPR data, which range between 10 and 36%.

One should note that the calculated distortion is somewhat similar to the one attributed to the EL2 center in GaAs [22]. For EL2, however, the distorted configuration is metastable and is accessible only following an electronic excitation. For N in diamond, on the other hand, the distorted state is the ground state. Furthermore, our search utilizing equal but opposite displacements of the N and the (111) C

atom did not find any barriers separating the distorted and the undistorted configurations.

In fig. 2b we show the contour plot of the lone pair orbital, which is very near the top of the valence bands and therefore contains a substantial admixture of valence band states. The gap state (fig. 2c), which is occupied by one electron, is an antibonding combination of the lone pair orbital and the carbon dangling bond. It has most of its amplitude on the carbon atom, which is in very good agreement with EPR data. The energy level of this state has dropped from $E_c - 0.7$ eV for undistorted substitutional N to $E_c - 1.5$ eV. The experimentally measured level associated with N in diamond is at $E_c - 1.7$ eV [23].

N - B PAIRS IN DIAMOND AND GRAPHITE

Electron transfer between N and B in diamond releases several eV of energy. Since both N and B have negative formation energies in the dilute limit, heavy doping and possibly even alloying are feasible. This raises a prospect of altering the thermodynamic balance between diamond and graphite by simultaneous doping with nitrogen and boron, since the energetic difference between the two phases is only 0.02 eV per atom. This idea is distantly related to that of Bar-Yam and Moustakas [24], who propose that low pressure growth of thin film diamond is due to a large, non-equilibrium concentration of vacancies, which have a lower formation energy in diamond than in graphite [cf. 6 and 25].

We have carried out calculations for both distant N-B pairs (as far apart as possible given the size of the supercell) and nearest neighbor pairs. Although one could consider very distant pairs by computing separately the formation energies of N^+ and B^-, we chose not to do so, since the treatment of charged states in periodic systems involves additional approximations due to the infinite range of the Coulomb potential. For diamond, the formation energies of the distant and nearest neighbor pairs are calculated to be -4.0 and -5.3 eV, respectively. Since the formation energies of isolated N and B are -0.6 and -0.5 eV, respectively, the charge

Table III. Total energy gains for various distortion modes around substitutional N in diamond using a 64-atom unit cell. For all but the last row only the Γ point was used for k-space sampling. See text.

unrelaxed substitutional N	0.00 eV
full radial relaxation around N	-0.36 eV
distortion of N and C along (111) only	-0.32 eV
distortion of N and C and full relaxation	-0.63 eV
distortion of N and C and full relaxation (Baldereschi point)	-0.76 eV

transfer and bonding effects are sizable for this pair. In graphite, however, these formation energies are even lower, -5.6 and -6.2 eV for the distant and nearest neighbor pairs, respectively. These results indicate thus that simultaneous N and B doping will increase rather than reduce the thermodynamic preference for graphite.

However, before dismissing the above idea, one should point out that the bonding in diamond and graphite is quite different. Also, the respective supercells differ substantially in shape and size. This may affect the accuracy of the calculations and thereby of the above comparison. Other potential sources of error are the plane wave cutoffs, which may have to be even higher if structures with very different bonding properties are compared, and the local density theory. Clearly, more calculations and convergence tests are needed in order to assess the accuracy of the results. There are also experimental indications that N is difficult to incorporate into graphite, possibly for kinetic reasons, which may lead to a preference for the formation of diamond. It may thus still be useful to carry out the appropriate experiments.

SUMMARY AND CONCLUSIONS

The energetics and electronic properties of native defects and impurities in diamond were investigated through large scale band structure and Car-Parrinello calculations. Among the native defects in diamond, it was found that the vacancy has the lowest formation energy, and, as such, governs self-diffusion in diamond. The activation energy for self-diffusion in intrinsic diamond is very high (9.1 eV), which explains the well-known difficulties in annealing diamond during growth and/or processing. However, the formation energy of the vacancy decreases by ~ 3 eV in p- and n-type diamond. Doping during growth (*e.g.*, with B) should thus lead to an increase in self-diffusion and thereby in annealing rates, possibly resulting in a better quality material. This effect was indeed observed in diamond growth on both non-diamond [12] and diamond [13] surfaces.

Our calculations for the potential shallow donors found that Li, Na, and P would dope diamond. As expected, P strongly prefers the substitutional site, while Li and Na are interstitial donors. However, since their solubilities are very low, they cannot be introduced into diamond by in-diffusion, which is an equilibrium process. The alternatives are kinetic trapping during growth or ion implantation. Ion implantation is particularly suitable for interstitial impurities, since no host atoms need to be displaced and co-implantation with C, necessary for substitutional impurities, can be avoided. Ion implantation has already been successful at n-type doping of natural diamond with Li, although the samples lost their n-type conductivity after prolonged annealing. The ion implantation method of Refs. 14 and 15 is

particularly promising, since it minimizes the number of self-interstitials escaping to the surface.

The suitability of a particular shallow dopant is also dependent on its stability at the dopant site. Substitutional impurities are likely to diffuse by the vacancy mechanism, by analogy to the self-diffusion mechanism [6]. Since the activation energy for self-diffusion in diamond is very high, the activation energies for the diffusion of substitutional impurities are also likely to be high. Substitutional impurities would thus be suitable for high temperature applications. For interstitial impurities, interstitial channel diffusion is most likely. For Li and Na, the activation energies for diffusion through this path are 0.85 and 1.4 eV, respectively. Li is therefore a fast diffuser that may become inactive after prolonged annealing or even extended storage. Na-doped samples, however, should remain active up to moderate temperatures.

Nitrogen occupies a distorted substitutional site. The distortion occurs in the (111) direction with the N atom and the (111) C atom moving away from each other. It is due to the interaction of the fully occupied N lone pair with the dangling bond of the (111) C atom. The single electron associated with the center resides in an antibonding orbital formed from the dangling hybrid and the N lone pair. This orbital has most of its amplitude on the C atom. These results provide the first consistent explanation of the properties of the N center, which was first observed and identified by EPR over 20 years ago.

The formation of N-B pairs in diamond results in the release of 3-4 eV of energy. We investigated whether this effect can be used to alter the thermodynamic balance between diamond and graphite at low pressures. Unfortunately, the calculations indicate that the formation energies of these pairs in graphite are even lower. However, additional calculations are needed in order to assess the accuracy of these results, since different sizes and shapes of the supercells, as well as the very different bonding environments in diamond and graphite, may have introduced significant errors. Furthermore, experiments have shown that it is difficult to incorporate N into graphite. It may thus still be worthwhile to test this idea experimentally.

REFERENCES

1. For reviews, see e.g. J. H. N. Loubser and J. A. van Wyk, Rep. Prog. Phys. **41**, 1201 (1978); G. Davies, *ibid.*, **44**, 787 (1981).
2. V. S. Vavilov *et al.*, Sov. Phys. Semicond. **13**, 604 (1979); **13**, 635 (1979).
3. G. Braunstein and R. Kalish, Appl. Phys. Lett. **38**, 416 (1981).
4. V. S. Vavilov, Radiation Effects **37**, 229 (1978).
5. R. Car and M. Parrinello, Phys. Rev. Lett. **55**, 2471 (1985).

6. J. Bernholc, A. Antonelli, T. M. Del Sole, Y. Bar-Yam, and S. T. Pantelides, Phys. Rev. Lett. **61**, 2689 (1988).
7. S. A. Kajihara, A. Antonelli, J. Bernholc, and R. Car, Phys. Rev. Lett. **66**, 2010 (1991).
8. D. R. Hamann, M. Schlüter, and C. Chiang, Phys. Rev. Lett. **53**, 1494 (1979).
9. G. B. Bachelet, D. R. Hamann, and M. Schlüter, Phys. Rev. B **26**, 4199 (1982).
10. C. Kittel and H. Kroemer, *Thermal Physics*, 2nd Edition, Freeman (1980); see also J. Tersoff, Phys. Rev. Lett. **64**, 1757 (1990).
11. Q. Zhang, J.-Y. Yi, and J. Bernholc, Phys. Rev. Lett. **66**, 2633 (1991).
12. A. W. Phelps and R. Koba, *Proc. First Int. Symp. on Diamond and Diamond-Like Films*, Electrochem. Soc. Proc. **89-12**, 38 (1989).
13. M. W. Geis, Bull. Am. Phys. Soc **35**, 702 (1990).
14. J. F. Prins, Phys. Rev. *B* **38**, 5576 (1988); Nuclear Instruments and Methods in Physics Research B **35**, 484 (1988).
15. G. S. Sandhu, M. L. Swanson, and W. K. Chu, Appl. Phys. Lett. **55**, 1397 (1989).
16. W. V. Smith, P. P. Sorokin, I. L. Gelles, and G. J. Lasher, Phys. Rev. **115**, 1546 (1959); C. A. J. Ammerlaan, Inst. Phys. Conf. Ser. **59**, 81 (1981).
17. R. P. Messmer and G. D. Watkins, Phys. Rev. B **7**, 2568 (1973).
18. M. Astier, N. Pottier, and J. C. Bourgoin, Phys. Rev. B **19**, 5265 (1979).
19. A. Mainwood, J. Phys. C: Solid State Physics **12**, 2543 (1979).
20. G. B. Bachelet, B. A. Baraff, and M. Schlüter, Phys. Rev. B **24**, 4736 (1981).
21. K. Jackson, M. R. Pederson, and J. G. Harrison, in *Impurities, Defects and Diffusion in Semiconductors: Bulk and Layered Structures*, edited by D. J. Wolford, J. Bernholc, and E. E. Haller, Mat. Res. Soc. Proc. **163**, 89 (1990).
22. J. Dabrowski and M. Scheffler, Phys. Rev. Lett. **60**, 2183 (1988); D. J. Chadi and K. J. Chang, Phys. Rev. Lett. **60**, 2187 (1988).
23. R. G. Farrer, Solid State Comm. **7**, 685 (1969).
24. Y. Bar-Yam and T. D. Moustakas, Nature **342**, 786 (1989).
25. E. Kaxiras and K. C. Pandey, Phys. Rev. Lett. **61**, 2693 (1988).

QUASI-EQUILIBRIUM NUCLEATION AND GROWTH OF DIAMOND AND CUBIC BORON-NITRIDE

Y. BAR-YAM,* T. LEI,* T. D. MOUSTAKAS,* D. C. ALLAN** AND M. P. TETER**
*ECS, 44 Cummington St., Boston University, Boston MA 02215
**Applied Process Research, SP-PR-2-2 Corning Inc., Corning NY 14830

ABSTRACT

Material growth is an inherently non-equilibrium process. However, thermodynamic considerations often provide important insight into material growth, the structure of grown materials, and process control parameters. In essence, thermodynamic considerations are important when activated processes are either slow or fast on the time scale of the growth. Activated kinetic processes are important when their time scale is the same as that of growth. Realistic *ab-initio* calculations of material structure and dynamics can provide a microscopic understanding of both thermodynamics and the kinetics of material growth. The primary focus of this article is a recently proposed defect-assisted multiple-regrowth stabilization of cubic phases.[1,2] In this theory the incorporation of vacancies at the growth face changes the relative binding energy of cubic versus hexagonal phases so that diamond and cubic boron nitride can nucleate and grow. This theory predicts that diamond nucleation and growth is enhanced under electron rich or positive ion conditions. Experimental results on growth of both diamond and cubic boron nitride that motivate and support theoretical predictions are described. Cubic boron-nitride grows under off-stoichiometric conditions. The nucleation rate of diamond is increased by many orders of magnitude when a flux of electrons impinges upon the surface. Raman line broadening and ESR measurements indicate the presence of significant concentrations of point defects. Predictions and experimental evidence for both n and p type doping will be discussed. *Ab-initio* calculations of key kinetic processes and thermodynamic quantities for diamond and boron nitride growth are described.

INTRODUCTION

The growth of diamond under vapor conditions which are substantially in the stability regime of graphite presents us with a theoretical puzzle. One way to resolve this puzzle is to discuss the growth entirely as a kinetic process. Growth is a non-equilibrium process so equilibrium stability considerations need not apply. However, often equilibrium considerations *do* apply. Thus we choose to take the opposite approach and explain why we should consider that equilibrium considerations may apply to the growth of diamond. Having thus confounded the original mystery a resolution will be proposed in terms of the quasi-equilibrium theory of defect-assisted multiple-regrowth stabilization.[1,2]

KINETICS OF GROWTH AND THERMODYNAMIC EQUILIBRIUM

Growth is an inherently non-equilibrium process. Atoms move from one phase (vapor or plasma) to another (solid). In vapor phase growth of solids the kinetics of growth generically involves several processes:

(a) Atom arrival, controlled by the sticking probability of various vapor species,
(b) Atom motion / diffusion, controlled by the hopping rate on the surface,
(c) Atom removal, controlled by the emission or etching rate of surface atoms.

Despite the kinetic nature of these processes, equilibrium solids often are grown. Generally, the equilibrium solid is simply the lowest energy structure of the material. A first explanation for the growth of equilibrium solids which might be given is the formal reason given for equilibrium in any system: Equilibrium occurs because the kinetics are fast enough to explore the available phase space. Low energy structures grow because kinetics are fast enough to explore all the possible arrangements of atoms. This is not a sufficient answer because materials do not really have the time to explore all of the phase space. If they did have sufficient time, on realistic time scales, then atoms of the same material originally in any arrangement would spontaneously rearrange to form an ideal equilibrium solid if heated to the temperature of growth. In reality, a more limited phase space exploration occurs at the surface during growth. This means that we actually rely for the growth of equilibrium solids upon two other conditions:

(a) Fast surface kinetics compared to growth time.
(b) Surface energetics which are similar to bulk energetics.

While (a) is not necessarily true, it is not surprising since it seems intuitive that atom motion at the surface proceeds faster because of fewer constraints due to fewer bonds. The second statement is more surprising than the first since surface reconstructions occur and the structure and energetics of the surface therefore appear very different from the bulk. However, one or two layers beneath the surface the energetics appear generally to be very similar to the bulk. Step edges are an environment which is more similar to the bulk than the surface itself. The use of island growth by addition of atoms to step edges enables this environment to control the structure of the growing solid.

Finally, while (a) and (b) are necessary, it is also important to note that the growth rate is controlled (typically through the arrival rate of atoms) to limit the growth rate so that the surface kinetics are indeed fast enough to enable sufficient atom motion to give rise to the equilibrium structure. This brings us to a discussion of conventional Ultra-High vacuum MBE growth.

CONVENTIONAL MBE

In conventional Molecular Beam Epitaxy (MBE), materials are grown under ultra-high vacuum, and low temperature. The arrival rate of atoms at the surface is kept low enough to ensure that atoms can migrate along the surface to a surface step and be incorporated.

In this picture there are two fast processes: atom migration on the surface and atom in corporation at a step. These processes are fast enough so that equilibrium considerations apply and high quality low defect concentration "equilibrium" solids can be grown. But it is equally important to recognize that there is a slow process which is characteristic of this type of growth - interlayer mixing of atoms. Because this is a slow process it is possible also to grow non-equilibrium solids in the form of multilayers which are another feature of this type of growth which can be used for technological applications.

This well known example illustrates the importance of both fast and slow processes in characterizing the kinetics of growth. Fast processes enable equilibration and equilibrium solids to grow, while slow processes can either prevent equilibration or equivalently enable non-equilibrium solids to grow. Using this as a guide it is possible to inquire whether there are fast and slow processes which characterize the growth of diamond.

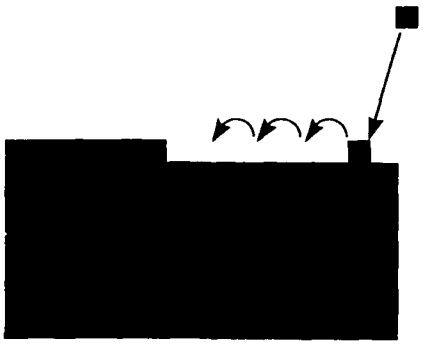


Fig. 1: Illustration of conventional MBE growth where atoms arrive on the surface, stick and move and attach rapidly to surface steps. The rapid process of motion along the surface results in equilibrium within the layer. However, the slow interlayer mixing enables non-equilibrium superlattices to be grown.

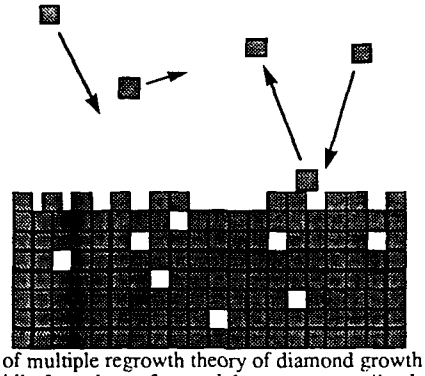


Fig. 2: Illustration of multiple regrowth theory of diamond growth where atoms are added and removed rapidly from the surface and do not move easily along the surface or in the bulk so that many vacancies are to be found in layers of material near the growth face.

DIAMOND GROWTH

The growth of diamond occurs under conditions quite different from conventional MBE. Diamonds are conventionally grown under a hydrogen pressure of 100 torr and a carbon species pressure of 1 torr. In order to develop an understanding of this growth it is important to generally compare the rates of processes which are relevant. It is possible to consider a kinetic picture involving a variety of molecular species, their sticking probabilities and migration rates. However, we begin by considering what processes might be fast or slow in these circumstances so as to simplify the discussion. An indication of the migration rate of carbon atoms may be obtained from bulk calculations in diamond.

Ab-initio theoretical studies by Bernholc et al [3] indicate that migration of atoms in the bulk of diamond occurs by vacancy hopping and requires overcoming a barrier of 1.9eV. This result has also been confirmed by experiment.[4] Using this barrier an estimate of the hopping rate at 1000 C is only about 10^{1+3}/sec. This may be compared with the barrier to vacancy motion in silicon which is 0.3eV. In graphite vacancy motion is only slightly faster. *Ab-initio* calculations[5] give a migration barrier of 1.6eV. While this is only an estimate of the rate at a surface, migration is not a naturally fast process in this system and can be expected to be many orders of magnitude slower than in materials which are typically grown in MBE systems.

The unusual growth conditions however suggest another process to be fast compared to the growth rate. The growth rate of diamond is about 1 μm / Hour, which is 1.5 monolayers/sec. If we were to estimate the growth rate from the flux of carbon species the number should be more like 10^6 monolayers /sec. It is conceivable that only one species of carbon with a relative concentration of 10^{-6} may be active in the growth. However, it is also possible to suggest that many atoms are added and removed from the surface for each atom which eventually remains and is incorporated. This gives rise to the picture of "Multiple-regrowth" where layers are added and etched many times during the growth process. The importance of hydrogen as an etchant (and more recently of oxygen as a low temperature etching agent) in the growth of diamond has already been emphasized by others.[6,7]

This picture of multiple regrowth suggests that layers or areas of either diamond or graphite could grow, and be removed in this process. The active dynamic competition between diamond and graphite would suggest, that the lower energy structure would win.[8] This argument indicates that equilibrium considerations should apply, confounding the original puzzle of the successful non-equilibrium growth of diamond. The observation that both fast and slow processes are present, however, suggests a mechanism for diamond stabilization.

DEFECT STABILIZATION OF CUBIC PHASES

The slow process of atom motion on the surface of diamond and graphite suggests that the growth process of these materials under the multiple regrowth conditions does not result in the same type of surface growth as conventional MBE, instead atoms arrive on the surface and do not

move around to fill in vacancies so that the surface is formed out of only partially completed layers with large concentrations of vacancies. Thus in order to correctly compare the relative stability of diamond and graphite under the growth conditions we have to consider defective diamond and similarly defective graphite. The comparison of these materials proceeds then by using the formula for the formation energy of a solid with a concentration n of vacancies:[9]

$$F = F_B + n F_D \qquad (1)$$

where F_B is the binding energy of the materials with negligible defect concentrations and F_D is the free energy of formation of a vacancy. If we consider that both materials should have roughly comparable vacancy concentrations then, as Fig. 3 indicates, the formation energy of graphite may be raised above that of diamond if the formation energy of vacancies is higher than that of diamond. It is important to recognize that in this picture the slow process of vacancy motion freezes a non-equilibrium concentration of vacancies but the rapid multiple regrowth process enables a direct energetic comparison of defective graphite with the defective diamond.

By comparing two expressions for the formation energy of defective diamond and graphite it may be seen that a transition to diamond will occur if the formation energy of vacancies is smaller in diamond and the number of defects is greater than:

$$n > (F_B(diamond) - F_B(graphite)) / (F_D(graphite) - F_D(diamond)) \qquad (2)$$

Ab-initio calculations of the formation energy of vacancies in diamond[3] 7.2 eV and graphite[5] 7.6 eV yield only a small difference between the formation energy of vacancies in these materials so that diamond with more than 8% vacancies is stable compared with similarly defective graphite. This is a rather large concentration of vacancies. However, since diamond is a insulator the defect in diamond can be charged. The formation energy of charged defects changes with the position of the Fermi energy. Graphite is metallic so the defects can not be charged and their formation energy can not be changed by varying the Fermi energy. Figure 4 indicates how the formation energy of vacancies in diamond and graphite can be compared including the possible variation in Fermi energy of diamond. The formation energy of charged defects varies linearly with a shift in the Fermi energy because the energy of electrons moved to the electron reservoir from the defect are raised by shifting the Fermi energy up or lowered by shifting the Fermi energy down as follows:

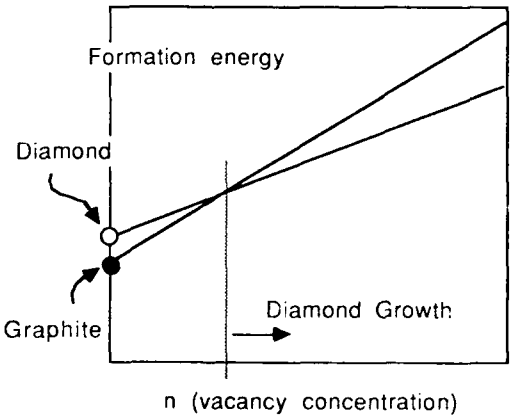


Fig. 3: Illustration of defect stabilization of diamond. The formation energy of diamond and graphite is schematically shown as a function of vacancy concentration. The slope of each line is the formation energy of a vacancy. Due to multiple regrowth a non-equilibrium concentration of vacancies is frozen at the growth face but competition is present between defective diamond and defective graphite. Since the formation energy of vacancies is larger in graphite than in diamond a sufficiently high concentration of vacancies can stabilize the growth of diamond over graphite.

$$F_D(q,\mu)=F_D(q,\mu_0)+q(\mu-\mu_0) \qquad (3)$$

where q is the charge of the defect and μ, μ_0 are the Fermi energy and reference Fermi energy respectively.[10] The second term arises from the energy of the electron added to or taken from the electron reservoir with an energy μ.

Because it is possible to have both positive and negatively charged vacancies, shifting the Fermi energy either up or down lowers the energy of the diamond vacancy relative to the graphite vacancy. For extreme Fermi energy shifts a concentration of less than *one percent* would stabilize diamond over graphite. The growth of diamond is presently performed under electron rich conditions. We can extend our quasi-equilibrium picture to include an effective Fermi energy which describes the electron rich conditions. Thus the comparison of diamond and graphite under current growth conditions should include both a substantial concentration of vacancies and a Fermi energy shift which lowers the energy of negative diamond vacancies.

NUCLEATION AND EPITAXIAL GROWTH

An advantage of the quasi-equilibrium nature of the multiple-regrowth picture is that it accounts both for the nucleation and continued growth of diamond. Kinetic theories which rely heavily on a preexisting diamond surface do not easily generalize to explain nucleation. It is reasonable to assume that homo-epitaxial growth proceeds more easily than the nucleation itself. Thus one would expect a wider range of conditions would be consistent with homo-epitaxial growth than with the nucleation step. Nevertheless the well known instability of diamond surfaces to graphitization suggests that the importance of the diamond surface as a substrate to growth is not as great for the growth as in many other materials. Thus that multiple-regrowth is likely to be important both for nucleation and continued growth under conventional conditions.

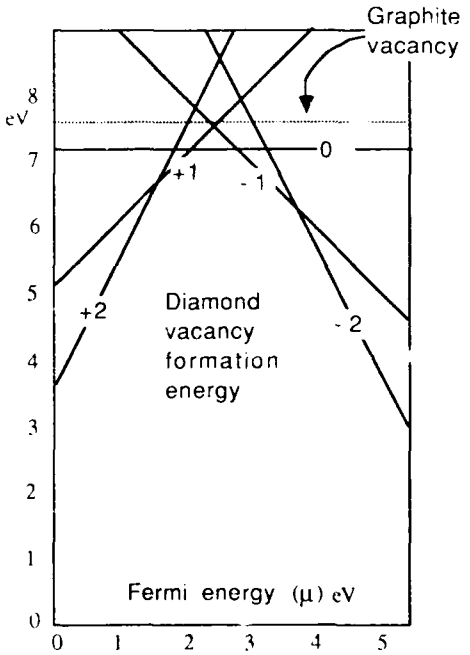


Fig. 4: Vacancy formation energy in diamond as a function of Fermi energy and graphite vacancy formation energy. By varying the Fermi energy it is possible to lower the energy of the diamond vacancy so as to enable the vacancy assisted stabilization of diamond during growth.

Table I: A comparison of conventional MBE growth and Diamond growth. In each case the conditions of growth provide fast and slow processes. The fast processes ensure a high quality single phase material while the slow processes enable quasi-equilibrium solids to grow. In the case of conventional MBE growth layered materials are grown. While under the conditions of diamond growth slow processes stabilize the diamond.

	Conventional MBE	Diamond Growth
Fast processes	Atom migration on surface Atom incorporation at step	Atom addition and removal
Slow processes	Interlayer mixing	Atom migration
Results	High-quality "equilibrium" solids Multilayers (non-equilibrium) Low defect concentrations	Growth of Metastable diamond Polycrystalline growth Residual defect densities

PREDICTIONS OF MULTIPLE REGROWTH VACANCY STABILIZATION

Residual defect concentrations - The theory of multiple regrowth induced vacancy stabilization of diamond simplifies the consideration of the growth parameters for diamond and suggests several predictions which can be compared with experimental results. The first prediction is simply the association of defects with diamond growth. It is important to recognize that defects still move and therefore anneal on the time scale of the complete growth of the film. Only near the active growth face are defects effectively frozen. At the growth face the rate of vacancy motion is slower than the addition and removal of layers. However, far away from the growth face layers are no longer being actively added and removed, and the vacancy moves at a rate which is fast compared to the eventual rate of layer addition. It can therefore move toward grain boundaries or dislocations which act as defect sinks and anneal. However, it may be expected that vacancies will cluster into less mobile aggregates and be found in the eventual diamond. The final concentration of these vacancies or vacancy clusters may be quite sensitive to the temperature of growth (the higher the temperature the more they will anneal), the thickness of the grown film (the longer the growth process the more annealing will occur), the density of grain boundaries and dislocations (the higher the grain boundary or dislocation density the lower the vacancy concentration), or other conditions of growth. The concentration of vacancies would be expected to vary with depth in the grown film with a larger concentration near the surface.

Several experimental results are now consistent with the predictions of this theory. These experiments attempt to observe a correlation between defect concentrations and the growth of high quality diamond films. In conventional growth it would be expected that conditions which lead to higher percentage of diamond in the film would also lead to higher quality - lower defect concentration - diamond. In the defect assisted growth picture, the opposite would be expected since the vacancies are assisting in the stabilization of diamond.

An experiment which tests the association of diamond growth with defects was performed by varying the total pressure of the growth a series of films. The films were found to contain varying concentrations of diamond and graphite. Two measurements on diamond films were performed which can be sensitive to defect concentrations: Raman spectroscopy and ESR measurements. The Raman spectrum[2,11] was found to show that the width of the diamond Raman line increased for films which were of higher diamond purity. The increasing width of the Raman line is consistent with a higher concentration of point defects. The ESR signal provides a quantitative measure of paramagnetic defect centers and is reported by Fanciuli et al.[12] The ESR signal is found to increase dramatically for higher purity diamond films from a concentration of 10^{17} to a concentration of 10^{19} spins per cm^3.

Fermi energy and growth - A second prediction of the multiple-regrowth theory pertains to the role of the Fermi energy shift in the growth. Based on Fig. 5, a prediction is made that the ease of growth of diamond should follow the energy dependence of the vacancies with the effective Fermi energy at the growth face. In its simplest from this means that both positive ion conditions (plasmas containing high concentrations of positive ions) and electron rich conditions should enhance the growth of diamond.

A test of this prediction may be made by controlled addition of electrons by biasing the substrate or using an electron beam. It is important to emphasize that the results which are

achieved further depend on the other conditions of growth. A shift in the Fermi energy which lowers the formation energy of vacancies indicates that diamond with the same concentration of vacancies is now lower in energy and the purity of films will be higher and the nucleation of diamond is easier. However it also indicates that diamond may be grown with fewer vacancies so that conditions of growth may be varied to achieve faster or higher quality diamond growth without lowering the purity of diamond films. The same conditions without the addition of electrons could result in graphitic rather than diamond growth.

Two experimental results have been achieved which are suggestive of the predicted results. Biasing the substrate without changing the conditions has been shown to lead to many orders of magnitude change (e.g. over 10^{10}) in the nucleation rate of diamonds. For typical growth conditions diamond does not nucleate at an experimentally viable rate on polished silicon surfaces, only on roughened surfaces. Under biased conditions which enhance the electron concentration incident on the surface, diamond nucleates on polished silicon substrates.[2,13] This result is obtained by consistent substrate biasing during growth so that the current through the surface is maintained at a constant value throughout the growth. Another experimental result suggests that diamond growth rates may be increased by an order of magnitude when electrons are added to the growth environment.[14]

Another way to vary the Fermi energy of the growth is by doping. A proper consideration of the effect of dopants must include the dopants themselves in the quasi-equilibrium picture. This leads to a separate prediction regarding the conditions for optimal doping.

Doping - A central problem in the growth of diamond is not just achieving high quality solids, but also incorporating dopants in desired quantities. An area of investigation which has not yet been extensively utilized experimentally is the ability of the growth conditions to enhance dopant incorporation by controlling the surface conditions. Generally growth is optimized for the intrinsic material and the parameters are not changed for dopant incorporation. However, it can be shown that control over the effective Fermi energy during growth may have significant impact on dopant incorporation and activity. The energy of dopant incorporation directly depends on the value of the Fermi energy. Consistent with Equation (3), a donor will have its energy of incorporation raised if the Fermi energy is raised. This suggests that for successful dopant incorporation, the Fermi energy during growth should be moved opposite to the direction of desired eventual doping. The Fermi energy should be moved down for n-type doping and up for p-type doping. The temporary Fermi energy shift during growth may be achieved by electron rich conditions for p-type doping or by incident positive ions for n-type doping.

A further complication occurs in many cases where dopants may be incorporated in several different configurations, some active and some inactive or even causing counter doping. In this case the counter Fermi motion during growth also enhances the doping efficiency defined as the ratio of active to total dopant concentration. This enhancement of doping efficiency will survive beyond the time of the growth if the equilibration in the bulk is slow, as it would be in diamond or in many other solids.

These considerations are quite general;[10] however, in diamond growth an experimental result lends support to these qualitative predictions. p-type doping of diamond has been achieved for diamond grown in an electron rich environment. There is no n-type doping which has been achieved for electron-rich environment. It remains to be seen whether n-type doping may be achieved under positive ion conditions. *Ab-initio* calculations relevant to the consideration of doping may be found in the work of Kajihara et al.[15] While these calculations suggest that n-type doping is difficult, the advantage of shifting the Fermi energy may be sufficient to enable the doping to occur.

CUBIC BORON NITRIDE GROWTH

Cubic Boron Nitride, similar to diamond, is unstable to the formation of a graphite-like form of Boron Nitride. It is thus possible to ask whether a similar defect induced stabilization may also apply to the growth of Boron Nitride. An essential difference for BN is that the defect concentration may be controlled by variation of the stoichiometry. Different stoichiometries may be attainable by the control of vapor pressures of gas species under conditions of conventional low pressure MBE growth where surface migration is the dominant "fast" process and sticking coefficients control the rate of growth. The departure from stoichiometry may be used to stabilize growth of the cubic-BN.

In the same spirit as for diamond growth, we begin with the simplest set of assumptions enabling a comparison of off-stoichiometric materials during growth. These are interpreted with the aid of accurate *ab-initio* calculations to provide guidance as to systematic trends which may be

expected in actual growth. Departures from stoichiometry may be considered in two limits: the first assumes that cubic and graphitic materials are in equilibrium and share the same chemical potentials, the second assumes that sticking coefficients which control the off-stoichiometry are approximately similar and thus materials with similar stoichiometries should be compared. We adopt the latter approach. For simplicity, each material is assumed to be in equilibrium internally, so that defect concentrations are determined by equilibrium formation energies. The comparison of material formation energies may then be considered equivalently either in the grand-canonical or canonical ensemble. In the former we would write the free energy per atom of the solid as

$$F = (N(\mathrm{B})\mu_B + N(\mathrm{N})\mu_N)/N = 1/2\,\mu_{BN} + s/2\,(\mu_B - \mu_N) \qquad (4)$$

Where $N(B)$, $N(\mathrm{N})$ are the number of Boron and Nitrogen atoms respectively, N is the total number of atoms and $s=N(B)-N(\mathrm{N})$ measures the stoichiometry. The two expressions in Equation 4 are related by the assumption of equilibrium in the bulk solid so that the sum of N and B chemical potentials is equal to the binding energy of a pair in the solid: $\mu_N+\mu_B=\mu_{BN}$. The other chemical potential adjusts to achieve the desired stoichiometry. The chemical potential may then be thought of as being determined by the formation energy of the defects responsible for the off-stoichiometry. Consequently, the chemical potentials of the two different materials are not the same.

For the purpose of comparison of equal stoichiometry materials we can equivalently consider the more intuitive canonical ensemble and write the difference between the free energies per atom of the two solids by using a reference value for $\mu_B-\mu_N$:

$$F(c\text{-}BN)-F(g\text{-}BN) = 1/2\ (\mu_{BN}(c\text{-}BN)-\mu_{BN}(g\text{-}BN)) + |s|(F_D(c\text{-}BN) - F_D(g\text{-}BN)) \qquad (5)$$

In this expression the defect formation energies appear explicitly but are to be understood as taken for a particular reference chemical potential, and are of the dominant defect which is responsible for the off-stoichiometry. As written it is for defects such as vacancies, where the difference in s of a single defect is ±1. The generalization to antisites where the difference in s of a single defect is ±2 is straightforward. The relative concentrations of vacancies and antisites is established by assuming a chemical potential consistent with the off-stoichiometry.

In order to include the possibility of charged defects, for each material a quasi-equilibrium Fermi energy is assumed. Experimentally, the Fermi energy may often be adjusted for optimal growth using substrate bias or ionic conditions of the plasma at the growth face. Unlike the case of diamond and graphite, both cubic and graphitic BN are insulators. Fermi energy variations and charged defects are present in both materials.

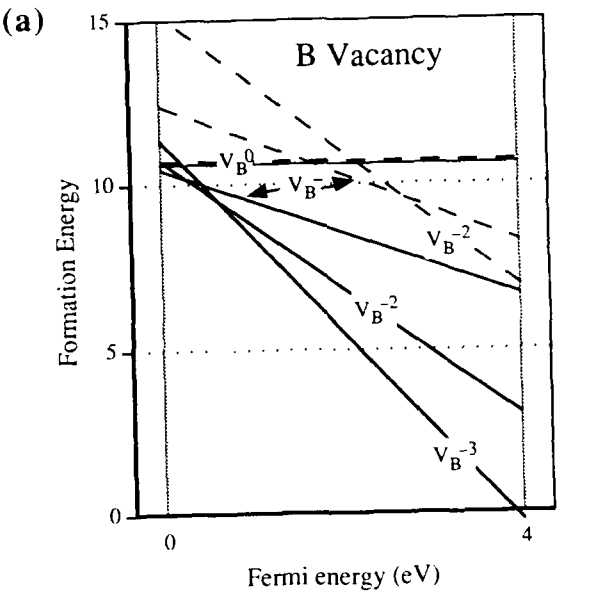
In addressing the defect induced off-stoichiometry in both cubic and graphitic BN, it appears reasonable to neglect interstitials and restrict our attention to vacancies and anti-site defects. This was justified by detailed calculations for the case of diamond which showed a much larger formation energy for interstitial defects.[3]

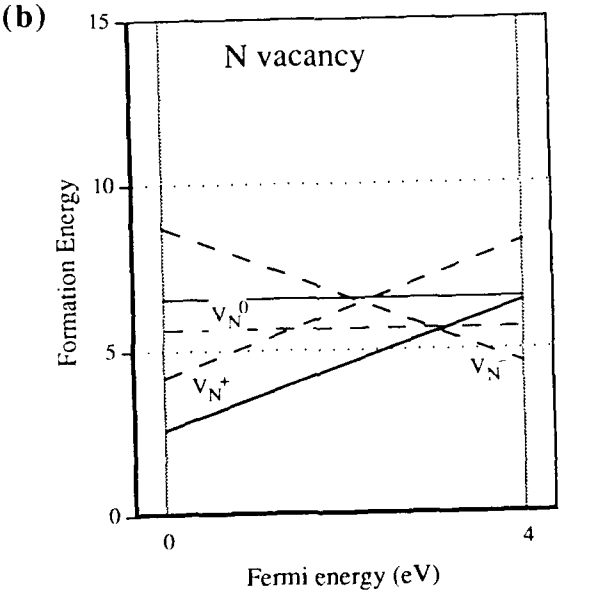
AB-INITIO CALCULATIONS OF DEFECT FORMATION ENERGIES IN BORON NITRIDE

We have performed *ab-initio* theoretical studies of the formation energies of vacancies and anti-site defects in cubic and graphitic BN. The calculations employed the Pseudopotential Local-Density-Functional (LDA) formalism and a recently developed conjugate gradient algorithm.[16] Charged states were considered by using a neutralizing background.[17] The plane wave expansion used has a kinetic energy cutoff of 15 Hartrees. Detailed descriptions of the calculation methodology and results will be presented elsewhere.[18] These theoretical studies parallel experimental work on the growth of BN that are summarized below and are presented separately in greater detail.[19]

In Fig. 5 we show the formation energies of the four defects in both materials as a function of Fermi energy. Consistent with LDA calculations in general, the calculated semiconductor gaps are significantly smaller than experimental ones. The gaps of cubic and graphitic BN are calculated to be similar (3.85eV vs. 4.12eV), so the formation energies for both materials are shown on the same figures. The reference chemical potential of $\mu_B-\mu_N$ is chosen so that μ_B is the chemical potential of metallic boron.

Systematically it may be seen that there are more charge states of the defects in cubic-BN. This means that shifting the Fermi energy is more effective at reducing the formation energy of defects in cubic-BN below those of graphitic-BN. It is interesting to note that for three of four defects, the formation energy of the neutral defect is lower in graphitic material, and for the boron vacancy, they are approximately equal. It is only with the inclusion of the charged defects that lower energy defects in cubic material and defect stabilization is possible.


(a)
B Vacancy
Formation Energy
15
10
5
0
0
4
Fermi energy (eV)
V_B^0
V_B^-
V_B^{-2}
V_B^{-2}
V_B^{-3}


(b)
N vacancy
Formation Energy
15
10
5
0
0
4
Fermi energy (eV)
V_N^0
V_N^+
V_N^-

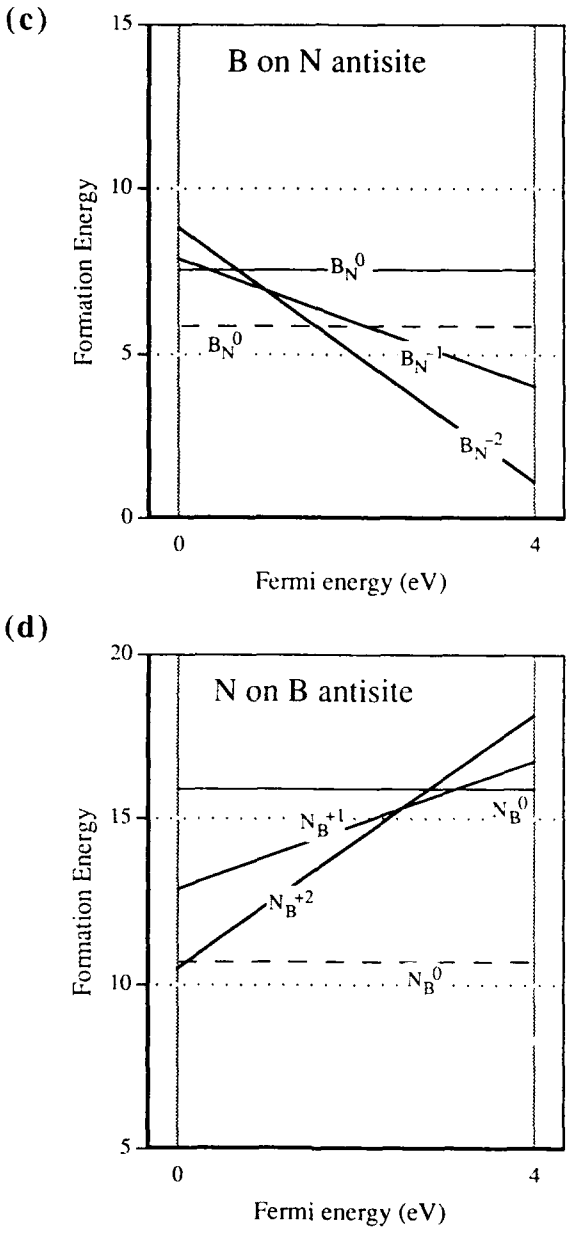


Fig. 5: Defect formation energies in cubic-BN (solid lines) and graphitic-BN (dashed lines) as a function of the the position of the Fermi energy in the gap of each material. The reference chemical potentials are taken to be those appropriate for equilibrium with bulk B metal. The defects shown are. (a) B vacancy, (b) N vacancy, (c) B on N antisite, and (d) N on B antisite.

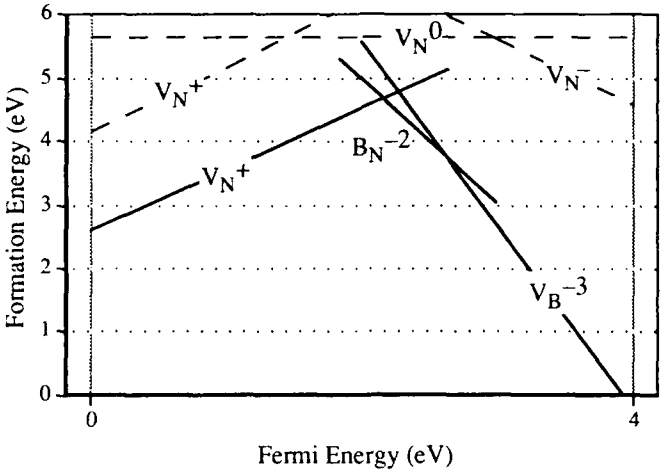


Fig. 6: Minimum energy defects as a function of Fermi energy for cubic-BN (solid line) and graphitic-BN (dashed line). The reference chemical potentials are taken to be those appropriate for equilibrium with bulk B metal. The minimum energy defect and charge state are identified on each line segment. Direct implications for defect induced stabilization of cubic-BN are discussed in the text.

In Fig. 6 we show the minimum energy defects as a function of Fermi energy in the two materials. This figure provides the simplest comparison for our purposes. It may be seen that for all values of the Fermi energy the cubic-BN defects are substantially lower in energy than the graphitic-BN. This suggests that defect induced stabilization is possible for cubic BN. A systematic consideration (Table II) of boron-rich and nitrogen-rich growth for different values of the Fermi energy leads to the following conclusions, most of which may be directly deduced from this figure. For p-type or positive-ion conditions of growth, the defect formation energies predict that stabilization is possible for boron-rich material, with nitrogen vacancies as the dominant defect. Nitrogen rich material is stable in the graphitic structure. On the other hand, under n-type or electron rich conditions of growth defect stabilization is predicted to be possible for nitrogen rich material *and* nitrogen poor material. The dominant defect is the boron vacancy or boron antisite respectively. However, under n-type conditions there is a strong tendency to nitrogen rich material. Even though the reference chemical potential is for boron solid, which would lead to the most boron rich solid in equilibrium, nevertheless, the boron vacancy is still the lowest energy defect in cubic-BN for electron rich conditions. Thus, it is concluded that under p-type conditions boron-rich cubic-BN, and under n-type conditions nitrogen-rich cubic-BN may be stabilized.

Table II: Summary of theoretical predictions for the growth conditions where stabilization of cubic-BN may be possible in the quasi-equilibrium picture. The variation of stoichiometry and the ionic charge of the growth are experimentally tunable parameters. The dominant defect under each conditions is indicated. It is believed from experiment that graphitic-BN is stable in stoichiometric conditions. Experimental growth of boron-rich cubic-BN under positive-ion conditions (*) is described in Table III and the accompanying text. The question mark for boron-rich BN under electron-rich conditions is included to indicate the strong preference of the growth for nitrogen-rich material under electron-rich conditions.

	Boron rich	Stoichiometric	Nitrogen rich
electron rich	? cubic-BN B antisite	graphitic-BN	cubic-BN B vacancy
positive ion	* cubic-BN N vacancy	graphitic-BN	graphitic-BN N antisite

It should be emphasized that the theoretical calculations suggest that the limit of off-stoichiometry which may be achieved in true equilibrium is small. Off-stoichiometric material is generally unstable to phase separation. For a boron rich solid, the limit of boron excess is established by setting the boron chemical potential to the chemical potential of boron solid as is indicated in Figs. 5 and 6. A 1% excess of boron would then require a defect formation energy (either nitrogen vacancy or boron antisite, the difference is not significant) of 0.5 eV. Except possibly for the boron antisite in highly n-type material this condition is not realized. Moreover, in equilibrium, in the bulk, unless an equivalent concentration of dopants is included, the defects are not stable in their charged states since the material must be locally neutral. Two interesting consequences may be inferred. First, that the material may be grown boron-rich only if phase-separation is inhibited by slow atomic migration. Generally, phase-separation is a slow dynamical process so this may not be a concern for nearly stoichiometric material. Equivalently we may say that the effective boron chemical potential may be significantly lower than that of metallic boron before phase separation occurs during growth. Second, following growth, the intrinsic instability to phase separation may play an important role in the stability of cubic-BN. This is particularly true because in otherwise undoped material the defects must become on average neutral and the Fermi energy will shift to the position of the defect-electron-transition raising dramatically the energy of the defects causing the off-stoichiometry. It may be possible that the instability to phase-separation results in material which gradually undergoes phase separation on experimental time scales. It may be possible to overcome this instability to phase separation (or graphitization) of the cubic BN after growth by post processing to restore the stoichiometry of the material. An intriguing though speculative possibility for achieving stoichiometric cubic-BN material is through growth alternately in p-type and n-type conditions resulting in layered boron-rich and nitrogen-rich materials which may interdiffuse to form stoichiometric material.

Finally, it may be mentioned that N vacancies and B vacancies are intrinsic donors and acceptors respectively and thus an effective doping of cubic BN may be achieved only through careful control of stoichiometry. Moreover, the stoichiometry itself may serve, at least in part, for achieving p-type and n-type materials. Material which is nitrogen-rich grown under n-type conditions will be found to be p-type after growth, and conversely for boron-rich material. Limitations to doping efficiencies may be derived from the results described above.

GROWTH OF CUBIC BORON NITRIDE

The experimental growth of cubic BN is reported in detail separately.[19] Preliminary results of the experimental effort were the primary motivation for the theoretical studies described above. Growth of cubic material was performed by sputtering of high-purity (pyrolitic) BN in an argon plasma. The sticking coefficient of nitrogen is much lower than that of boron, so that in a pure argon plasma the film has a B:N ratio of 5:1 and is phase separated into metallic boron and BN. To increase the nitrogen in the film, N_2 gas was added to the plasma and adjusted to achieve optimal growth. The plasma conditions cause the substrate to be negatively biased attracting positive N_2^+ ions from the plasma to the surface and causing an electron depleted surface. This may be taken to correspond to the theoretical discussion of cubic BN growth in a p-type environment.

The conditions of growth and the resulting materials are summarized in Table III. The optimal hardness of the films (3,500 kg/mm^2) was obtained with 10% N_2 pressure in the plasma. Films grown under these conditions were characterized by in-plane X-ray diffraction and electron diffraction as cubic-BN. The hardness of 3,500 kg/mm^2 is consistent with the hardness of synthetic cubic-BN. The B:N ratio of these films was measured directly and found to be between 1.01:1 and 1.02:1. This 1-2% off-stoichiometry is consistent with the results of ESR measurements which find a spin density of $10^{20} \sim 1\%$ of atomic sites.[20] The ESR line shape and g-value measured is consistent with other measurements of nitrogen depleted BN which have been associated with the nitrogen vacancy. When the N_2 pressure is increased to 50% the films become very soft and are stoichiometric to the accuracy of the measurements.

These results appear to be consistent with the theoretical predictions linking the nitrogen vacancy with the off-stoichiometry induced stabilization of cubic-BN under p-type conditions. The observation of spins from the nitrogen vacancy may be understood in detail as follows. During growth the nitrogen vacancy is expected to be positively charged. Once the growth has proceeded and the vacancy is away from the surface, the material must become on average neutral. This occurs through capture by the nitrogen vacancy of electrons. A single electron on a nitrogen vacancy neutralizes the vacancies and is expected to give an ESR signal since it only half occupies a gap state.

Table III: Plasma pressures of N_2 in an argon plasma during BN films and the resultant properties and stoichiometry of BN films. See text and Ref. 18 for details.

N_2 pressure	Film property	Stoichiometry: B:N
0%	phase separation	5:1
10%	cubic-BN (see text)	1.01:1 to 1.02:1
50%	soft like graphite	1:1

The theoretically predicted possibility of cubic-BN growth under electron rich conditions remains to be tested.

This work was supported in part by the National Science Foundation (Grant #DMR-9014370) the Cornell National Supercomputer Center, and by the US-Israel Binational Science Foundation.

REFERENCES:

[1] Y. Bar-Yam and T. D. Moustakas, Nature 342, 786, 14 December 1989
[2] Y. Bar-Yam and T. D. Moustakas, Mater. Res. Soc. Symp. Proc. Vol. 162, 201 (1989)
[3] J. Bernholc, A. Antonelli, T. M. Del Sole, Y. Bar-Yam and S. T. Pantelides, Phys. Rev. Lett. **61**, 2689 (1988)
[4] G. Davies and S. Lawson, private communication.
[5] E. Kaxiras and K. C. Pandey, Phys. Rev. Lett. 60, 2693 (1988)
[6] B. V.Spitsyn, L. L.Bouilov, and B. V. Derjaguin, J. Cryst. Growth 52, 219 (1981)
[7] A.R. Badzian, and R.C. DeVries, Material Research Bulletin 23,181,(1988)
[8] It is possible instead to suggest that the etching process itself is able to stabilize the growth of diamond because graphite etches more easily than diamond. However, once dynamical processes become reversible, fast etching is equivalent to fast growth and slow etching becomes equivalent to slow growth. This is the standard result in equilibrium processes which operate in both directions. It is possible, as in Ref. 7, to construct kinetically consistent arguments for the stabilization of diamond growth by different etching rates if the etching process is different from the atom addition process. Then the production of diamond is directly controlled by the kinetic processes of atom addition and removal from diamond and graphite.
[9] The "entropy of mixing" term is not included in this expression because for non-equilibrium defect densities it is negligible compared to the terms shown, and it is the same for materials with similar concentrations of defects.
[10] Y. Bar-Yam, D. Adler, and J. D. Joannopoulos Phys. Rev. Lett. **57**, 467 (1986); Physics and Applications of Amorphous Semiconductors I, (ed Demichelis, F.)(World Scientific, 1988).p. 1.
[11] R. G. Buckley, T. D. Moustakas, L. Ye and J. Varon, J. of Appl. Phys. 66, 3595 (1989)
[12] M . Fanciulli, and T. D. Moustakas, Diamond and Related Materials (in press) (1992)
[13] T. D. Moustakas in *Proceedings of the 20th Int. Conf. on the Physics of Semiconductors*, (E. M. Anastassakis, and J. D. Joannopoulos eds.) (1990) p. 320
[14] A. Sawabe and T. Inuzuka, Appl. Phys. Lett. 46, 146 (1985)
[15] S. A. Kajihara, A. Antonelli, J. Bernholc and R. Car, Phys. Rev. Lett. 66, 2010 (1991)
[16] M. P. Teter, M. C. Payne, and D. C. Allan, Phys. Rev. B 40, 11357 (1989)
[17] Y. Bar-Yam and J. D. Joannopoulos, Phys. Rev. Lett. 52, 1129 (1984); J. of Electron. Mater. 14a, 261 (1985)
[18] J. Lei, Y. Bar-Yam, D. C. Allan and M. P. Teter (unpublished)
[19] T. D. Moustakas, et. al. (this volume)
[20] M . Fanciulli, and T. D. Moustakas (this volume)

FIRST-PRINCIPLES INVESTIGATIONS OF ACCEPTORS IN ZnSe

CHRIS G. VAN DE WALLE* AND D. B. LAKS**
* Philips Laboratories, North American Philips Corporation, Briarcliff Manor, NY 10510 and Xerox PARC, 3333 Coyote Hill Road, Palo Alto, CA 94304[a]
** National Renewable Energy Laboratory, Golden, CO 80401

ABSTRACT

We present a theoretical formalism to investigate doping efficiencies of impurities in semiconductors, and show results for various acceptor impurities (Li, Na and N) in ZnSe. These results, obtained from first-principles calculations, yield important insights in the mechanisms that govern impurity formation energies and solubilities.

INTRODUCTION

Doping of ZnSe has been the subject of intense investigations for many years. The belief was widely held that p-type doping could not be achieved due to some intrinsic limitation, often attributed to self-compensation by native defects. We have recently shown, based on state-of-the-art first-principles calculations, that under appropriate growth conditions the concentration of native defects in ZnSe is quite low, and will not cause self-compensation.[1] Recent experimental achievements have also conclusively established that p-type doping of ZnSe is indeed feasible.[2-5] However, high doping levels are still hard to obtain, and a comprehensive understanding of the doping difficulties has been lacking.

The theoretical approach presented in this paper shows that two mechanisms play an important role in the doping limitations. *One is a competition* between various configurations that the dopant impurity can assume in the lattice. The second mechanism is a solubility limit, imposed by the coexistence of other phases that can be formed out of the constituents. In this paper we briefly sketch the theoretical approach, and then present detailed results for Li and other impurities. We find that Li suffers from a competition between substitutional and interstitial lattice sites. More importantly, the total solubility is limited by formation of the compound Li_2Se. For Na, we find the solubility to be much lower than for Li, rendering Na useless as a dopant. Nitrogen turns out to be the best candidate among the elements examined here. These results can serve to guide experiments, not only regarding the choice of dopant, but also with respect to establishing optimal growth conditions.

FORMALISM

The equilibrium concentration of an impurity in a semiconductor is given by

$$C = N_{sites}\exp[-\frac{E_{form} - TS_{form}}{kT}]. \quad (1)$$

N_{sites} is the appropriate site concentration, e.g., for substitutional Li (Li_{Zn}) this is the number of Zn sites per unit volume. E_{form} is the formation energy, and S_{form} the formation entropy. The pressure-dependent term in the Gibbs free energy can be neglected for the solid phase. Entropy contributions have been estimated to be small[6]; they also tend to cancel when comparing relative free energies.[7]

The key quantity for determining impurity concentrations is thus the formation energy. Its value must be determined from first-principles total energy calculations. We carry out

these calculations based on density-functional theory, using *ab initio* pseudopotentials, and a mixed basis set to ensure an adequate description of the Zn *d* orbitals.[1,6] A supercell geometry is used, in which the impurity is surrounded by a sufficiently large volume of the host crystal. A general definition of formation energy is given in Eq. (1) of Ref. 1. Here we discuss the specific example of an ionized, substitutional Li atom:

$$E_{form}(Li_{Zn}^{-}) = \mathcal{E}(Li_{Zn}^{-}) - \mu_{Li} + \mu_{Zn} - E_F. \qquad (2)$$

$\mathcal{E}(Li_{Zn}^{-})$ is the calculated energy of a supercell containing the Li_{Zn}^{-} impurity, minus the energy of a reference cell containing the pure bulk semiconductor. μ_{Li} and μ_{Zn} are the chemical potentials of Li and Zn atoms; they represent the energies of the reservoirs with which these atoms are exchanged. E_F is the Fermi level, i.e. the energy of the reservoir delivering the electron that is responsible for the negative charge on the impurity.

Equations similar to Eq. (2) can be written down for all configurations of all impurities to be examined, in their various charge states. In addition, we take all intrinsic point defects into account, thereby ensuring that reactions involving different impurity configurations can take place. For instance, a substitutional Li atom can leave its site and become interstitial, leaving a Zn vacancy behind. This leads to a long list of formation energies for various impurity and defect configurations. The corresponding concentrations are coupled through the condition of charge neutrality, as described in Ref. 1. These concentrations are still a function of the chemical potentials of the constituents; we therefore present our results in the form of contour plots, with μ_{Zn} and μ_{Li} as the variables (as explained above, μ_{Se} is not an independent variable since it is determined by $\mu_{Se} = \mu_{ZnSe} - \mu_{Zn}$). Other details about the formalism are discussed in Ref. 1.

RESULTS

Lithium

Fig. 1 shows some of our results for Li in ZnSe. The *total* concentration of Li impurities is displayed in Fig. 1.a. Not all Li atoms reside on substitutional sites, however. As pointed out by Neumark,[8] Li can also go interstitially, where it behaves as a donor. Our calculations indicate that Li_i^+ has its lowest energy at the T_d site surrounded by Se atoms (T_d^{Se}), which is 0.2 eV lower in energy than the T_d^{Zn} site. Analogous to Eq. (2), we can write down an expression for the formation energy of the interstitial species:

$$E_{form}(Li_i^+) = \mathcal{E}(Li_i^+) - \mu_{Li} + E_F. \qquad (3)$$

The individual concentrations of the substitutional and interstitial species are given in Figs. 1.c and 1.d. Inspection of Eqns. (2) and (3) reveals that the formation energy of the substitutional impurity (acceptor) rises as the Fermi level goes dov n (increasingly p-type material), whereas the formation energy of the interstitial (donor) becomes lower. As the material becomes more p-type, it becomes increasingly favorable to form interstitials. For some limiting position of the Fermi level, the formation energies of the two species actually become equal. It is then impossible to push the Fermi level any lower; indeed, doing so would make the formation energy of interstitials lower than that of substitutionals, thus creating more donors than acceptors, which would push the Fermi level back up. Eqns. (2) and (3) show that this limiting Fermi level position is still a function of the Zn chemical potential, as can be seen in Fig. 1.b: for a given value of μ_{Zn} (along a horizontal line), the Fermi level first decreases as μ_{Li} is increased (increasing Li concentration, mostly as acceptors), until eventually it saturates; at that point, each Li has an equal chance of being incorporated as an interstitial or as a substitutional.

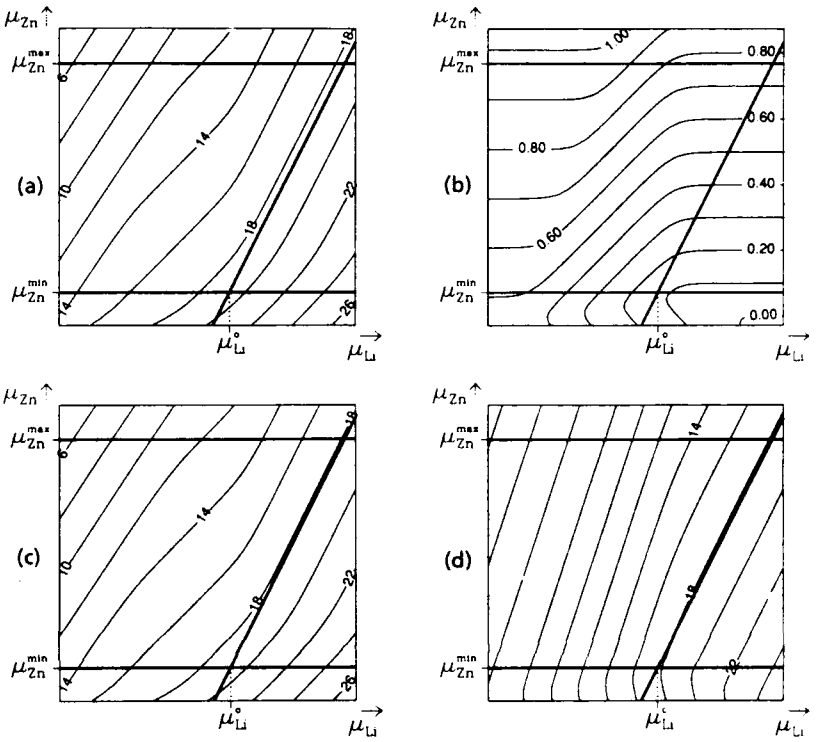


Figure 1: *Contour plots describing the behavior of* Li *impurities in* ZnSe, *at 600 K, as a function of* Zn *and* Li *chemical potentials. Solid lines indicate bounds on* μ_{Zn} *and* μ_{Li} *(see text). (a)* log_{10} [Li], *where* [Li] *is the total Li concentration in* cm^{-3}; *(b) Fermi level (in eV, referred to the top of the valence band); (c)* log_{10} [Li_{Zn}], *the concentration of* Li *on substitutional sites; (d)* log_{10} [Li_i], *the concentration of* Li *on interstitial sites.*

The chemical potentials are subject to strict constraints, imposed by the energies of other phases that can be formed from the constituents.[1] These bounds are indicated by solid lines in Fig. 1. The formation of bulk Zn puts an *upper* bound on μ_{Zn}: $\mu_{Zn}^{max} = \mu_{Zn(bulk)}$. Similarly, formation of bulk Se puts a *lower* bound on μ_{Zn}, since

$$\mu_{Zn} + \mu_{Se} = \mu_{ZnSe} = \mu_{Zn(bulk)} + \mu_{Se(bulk)} + \Delta H_f(ZnSe) \quad (4)$$

where ΔH_f (ZnSe) is the heat of formation of ZnSe (ΔH_f is negative for a stable compound). It follows that $\mu_{Zn}^{min} = \mu_{Zn(bulk)} + \Delta H_f$ (ZnSe). Calculated heats of formation are listed in Table 1.

To find an upper bound on the Li chemical potential, one may consider Li bulk, but it turns out that a much more stringent constraint is imposed by formation of the compound Li_2Se, leading to a bound defined by the equation:

$$2\mu_{Li} + \mu_{Se} = \mu_{Li_2Se} = 2\mu_{Li(bulk)} + \mu_{Se(bulk)} + \Delta H_f(Li_2Se) \quad (5)$$

Table 1: *Theoretical and experimental (Ref. 9) heats of formation (in eV per formula unit) for various materials containing* Zn, Se, Li, Na, *and* N. *Also listed is the minimum formation energy (corresponding to maximum concentration) for the neutral substitutional acceptor in ZnSe, and the corresponding minimum Fermi level position (in eV, referred to the top of the valence band), at 600 K.*

	solubility-limiting compound				
		ΔH_f^{th}	ΔH_f^{exp}	E_F	E_{form}^{min}
ZnSe		-1.39	-1.69		
ZnSe:Li	Li_2Se	-4.12	-3.96	0.13	0.46
ZnSe:Na	Na_2Se	-3.13	-3.54	0.44	1.08
ZnSe:N	Zn_3N_2	-	-0.24	0.09	0.38

The point where this line intersects the lower bound on μ_{Zn} is given by $\mu_{Li}^{o} = \mu_{Li(bulk)} + \frac{1}{2}\Delta H_f(Li_2Se)$. The corresponding formation energy of the *neutral* acceptor, and the self-consistently determined Fermi level are also listed in Table 1.

These contour plots, along with the bounds on the chemical potentials, provide important insights regarding the solubility of Li in ZnSe. Our results indicate that Li incorporation strongly depends on the growth conditions; in particular, the ratio of interstitials to substitutionals can be suppressed by lowering μ_{Zn} (see Figs. 1.c and 1.d). This simultaneously increases the total Li concentration, which reaches its maximum in the lower right-hand corner of the accessible region, where $\mu_{Zn} = \mu_{Zn}^{min}$ and $\mu_{Li} = \mu_{Li}^{o}$. These results are in good agreement with experimental observations on MBE-grown Li-doped samples, in which the Li solubility was found to be limited, and the concentration of Li interstitials varied from sample to sample (indicating the dependence on growth conditions).[10,11]

Sodium

Figure 2 summarizes our results for Na in ZnSe. The qualitative behavior of Na is quite similar to Li: both substitutional and interstitial configurations occur, and the solubility is limited by the formation of the compound Na_2Se. There is a pronounced quantitative difference, however, in the value for the solubility: Fig. 2.a indicates that total Na incorporation is limited to 10^{16} cm^{-3}, i.e. three orders of magnitude lower than Li. These results explain the experimental failure of doping attempts with Na.[12]

Nitrogen

We have found that N does not suffer from the substitutional/interstitial competition associated with the column-I elements. Nitrogen on a substitutional Se site is a shallow acceptor; N on a substitutional Zn site is a donor, but has a very large formation energy. The bounds on the N chemical potential arise in this case from the Zn_3N_2 compound, as well as from N_2 molecules. The contour plots for ZnSe:N (not shown here) indicate that N has the highest solubility of the dopants investigated here. Under optimum growth conditions, the hole concentrations that can be obtained are high enough for useful device applications, making nitrogen the most promising among the dopants studied here.

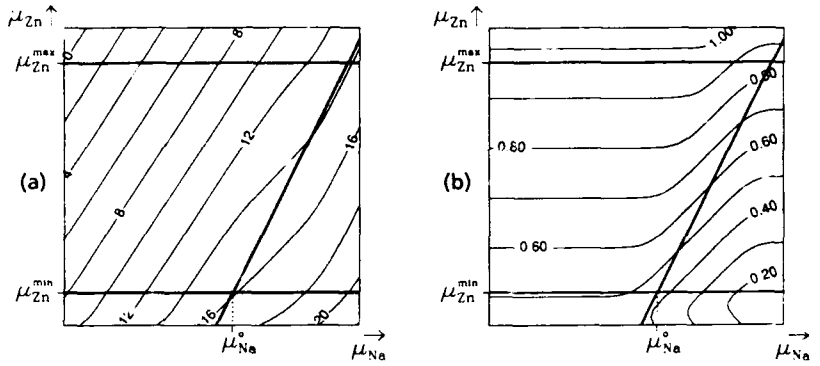


Figure 2: *Contour plots describing the behavior of* Na *impurities in* ZnSe, *at 600 K, as a function of* Zn *and* Na *chemical potentials. Solid lines indicate bounds on* μ_{Zn} *and* μ_{Na} *(see text). (a)* log_{10} [Na], *where* [Na] *is the total Na concentration in* cm^{-3}; *(b) Fermi level (in eV, referred to the top of the valence band); The concentration of* Na_i *is much lower than that of* Na_{Zn} *over the whole of the accessible range.*

CONCLUSION

We have presented a theoretical investigation of acceptor dopants in ZnSe, based upon a thermodynamic formalism and state-of-the-art first-principles calculations. Our results not only provide quantitative information upon impurity incorporation, but can also serve as a guide in exploring optimum growth conditions.

ACKNOWLEDGMENTS

We acknowledge fruitful collaborations with G. F. Neumark and S. T. Pantelides, and discussions with D. A. Cammack, J. Gaines, T. Marshall, R. M. Martin, and J. Tersoff.

REFERENCES

[a] Present address.
[1] D. B. Laks and C. G. Van de Walle, these Proceedings.
[2] R. M. Park, M. B. Troffer, C. M. Rouleau, J. M. DePuydt, and M. A. Haase, Appl. Phys. Lett. **57**, 2127 (1990).
[3] M. A. Haase, H. Cheng, J. M. DePuydt, and J. E. Potts, J. Appl. Phys. **67**, 448 (1990); M. A. Haase, J. M. DePuydt, H. Cheng, and J. E. Potts, Appl. Phys. Lett. **58**, 1173 (1991).
[4] J. Ren, K. A. Bowers, B. Sneed, D. L. Dreifus, J. W. Cook, Jr., J. F. Schetzina, and R. M. Kolbas, Appl. Phys. Lett. **57**, 1901 (1990).
[5] T. Marshall and D. A. Cammack, J. Appl. Phys. **69**, 4149 (1991).
[6] D. B. Laks, C. G. Van de Walle, G. F. Neumark, and S. T. Pantelides, Phys. Rev. Lett. **66**, 648 (1991).
[7] G.-X. Qian, R. M. Martin, and D. J. Chadi, Phys. Rev. B **38**, 7649 (1988); N. Chetty and R. M. Martin, to be published.
[8] G. F. Neumark, J. Appl. Phys. **51**, 3383 (1980).
[9] *Lange's Handbook of Chemistry*, 13th Edition, edited by J. A. Dean, (McGraw-Hill, New York).
[10] M. A. Haase, J. M. DePuydt, H. Cheng, and J. E. Potts, Appl. Phys. Lett. **58**, 1173 (1991).
[11] T. Marshall, C. G. Van de Walle, J. Gaines, and D. Cammack, these Proceedings.
[12] H. Cheng, J. M. DePuydt, J. E. Potts, and M. A. Haase, J. Cryst. Growth **95**, 512 (1989).

INTERSTITIAL IMPURITIES IN WURTZITE VS. ZINCBLENDE SEMICONDUCTORS: THE CASE OF H IN SiC

M.A. ROBERSON AND S.K. ESTREICHER

Physics Department, Texas Tech University, Lubbock, TX 79409-1051.

ABSTRACT

Most compound semiconductors crystallize in the zincblende or the wurtzite structures. In both cases, all the host atoms are tetrahedrally coordinated. However, the two lattices have no high symmetry interstitial sites in common. As a result, the stability, lowest-energy configuration, electronic structures, and barriers for diffusion of interstitial impurities are in general very different. This situation is illustrated here in the case of interstitial H in 3C (zincblende) and 2H (wurtzite) SiC. The results can be used to obtain the properties of H in other hexagonal polytypes, in particular 6H-SiC.

INTRODUCTION

Nearly all the theoretical studies of properties of impurities and defects in semiconductors deal with hosts that crystallize in the diamond or zincblende structures and of those, most of the research focuses on Si and $GaAs$. There is less impetus to conduct similar extensive studies in compounds that have the wurtzite structure. This is due at least in part to the fact that it is often difficult to dope them *both* n- and p-type, i.e., easily make devices with them.

However, as this very symposium suggests, there is an increasing interest in more exotic semiconductors, where "exotic" refers to materials that have extreme properties, such as the ability to withstand high temperatures or large doses of radiation. Further, considerable improvements in the growth and purity of films and single crystals makes these materials more readily available than ever before.

Among these semiconductors, SiC is special because it is found in a large number of polytypes.[1,2] As discussed in Ref. 1, a set of 50 layers of SiC can theoretically crystallize in 93,813,567 different ways, with cubic, hexagonal, rhombohedral, or trigonal structures. Further, many polytypes can be doped n- and p-type.[3]

Although some properties of intrinsic defects have been studied in several wide band-gap semiconductors,[4] little is known about the basic properties of impurities: diffusion of shallow dopants, structure of deep-level impurities, interactions with hydrogen, etc. In most cases, the problems themselves have yet to be clearly formulated. For example, does atomic H passivate shallow acceptors or donors in SiC as it does in Si? Direct extrapolation of the known properties of H in Si or $GaAs$ to materials such as cubic BN or 6H-SiC are not necessarily correct, and there is little doubt that experimental and theoretical studies will bring new and unexpected results.

In this paper, we will briefly discuss the different structures of SiC, the key characteristics of the various interstitial sites, and summarize the results of our calculations for interstitial H in the cubic form of SiC (3C, zincblende, or β-SiC) and in the hexagonal

polytype which is the most different from it (2H, wurtzite, or one of the α-SiC). These results can be used to determine the properties of H in other hexagonal polytypes.

Our calculations were done in large clusters[5,6] near the *ab initio* Hartree-Fock level, with the method of PRDDO.[7] To study 3C-SiC, we used $Si_{22}C_{22}H_{42}$, $Si_{13}C_{13}H_{26}$ and $Si_4C_4H_{18}$ to convince ourselves that cluster size effects are small. For 2H-SiC, we used $Si_{26}C_{26}H_{50}$ and $Si_{24}C_{24}H_{46}$. The smallest cluster that contains all the interstitial sites of 6H-SiC, the most stable of all polytypes, is $Si_{69}C_{69}H_{94}$. This cluster is too large for the current version of the code. However, the properties of H in 6H-SiC can be obtained from our results.

STACKING SEQUENCES AND INTERSTITIAL SITES

The various polytypes of SiC differ by the way the $Si-C$ pairs are stacked along the c-axis (Fig.1). In the familiar zincblende (or 3C) structure, the sequence involves three layers which are repeated periodically ($ABC\,ABC\,ABC\,\ldots$). All the $Si-C$ bond lengths are the same, and the angles are exactly tetrahedral.

In the wurtzite (or 2H) structure, only two layers are repeated ($AB\,AB\,AB\,\ldots$). The $Si-C$ bond length along the stacking direction ($L_{\parallel}$) is not equal to that which is approximately perpendicular to it ($L_{\perp}$), and the angles are not exactly tetrahedral. In the 6H polytype, the basic sequence involves 6 layers ($ABCACB\,ABCACB\,\ldots$).

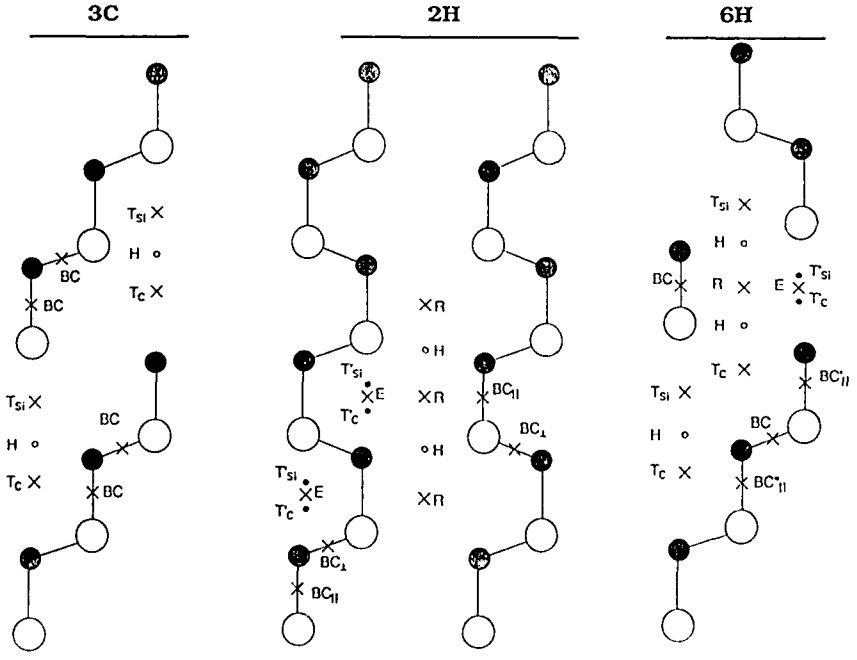


FIGURE 1. Stacking sequences in 3C-, 2H-, and 6H-SiC and high-symmetry interstitial sites (see text). The crosses show the local minima of the potential energy surface for interstitial H, the open circles are saddle points, and the full circles are not stationary points.

The various high-symmetry interstitial sites are shown in Fig.1. The *bond-centered* (BC) sites differ from each other by the amount of relaxation which can be achieved, that is mainly by how much room is available for the bond to expand. The bond-centered site that can stretch the most is $BC_\perp$ in 2H-SiC: The C and Si atoms are 2.32 Å away from the nearest high-symmetry interstitial site (denoted R in Fig.1). Next comes BC (in 3C-SiC), where the C and Si atoms are 1.84 Å away from T sites. Finally, $BC_\parallel$ is the most crowded, with its nearest neighbors (NNs) only 1.23 Å away from T' sites. It can be seen in Fig.1 that intermediate situations are realized in 6H-SiC.

The *tetrahedral interstitial* (T) sites have a subscript which refers to their 4 NNs. The differences between T (in 3C-SiC) and T' (in 2H-SiC) are readily visible in Fig.1. However, in 6H-SiC, there are *two* T_{Si} (and *two* T_C) sites which have the same NNs as the T sites in 3C-SiC, but differ from them by further shells.

The hexagonal polytypes have two interstitial sites with no counterpart in the cubic structure. We labeled them R and E. Finally, the hexagonal interstitial (H) sites are almost identical in all the polytypes. They are near the saddle points of the potential energy surfaces (PES) for light interstitials such as H.

INTERSTITIAL HYDROGEN

In the past ten years, interest in the properties of H in semiconductors has grown enormously.[8] Hydrogen passivates the electrical activity of a number of shallow and deep centers, activates some normally inactive impurities, enhances the diffusivity of interstitial O, and forms a variety of extended complexes which are still poorly understood. Because it is light, H diffuses rather easily. Since the presence of most impurities results in incompletely saturated bonds, H interacts with many defect centers by saturating weak bonds, rearranging the local structure, thus shifting energy levels.

Hydrogen is so active that in fact much less is known about isolated H in the perfect lattice than about complexes such as $\{H, X\}$ pairs, where X is a donor or an acceptor. Much of the experimental information about isolated hydrogen stems from muon spin rotation (μSR) spectroscopy,[9] i.e., the information is about the positive muons, a light isotope of the proton.

Summary of μSR data

At low temperatures, three centers are observed in diamond and silicon, with relative abundances largely independent of the doping.[9] The most abundant center (about 65% of incoming muons) is called normal muonium (Mu) and is characterized by an isotropic hyperfine tensor with a delocalized but still mostly atomic wavefunction. Then comes anomalous muonium (Mu^*), which has a highly anisotropic hyperfine tensor, with most of the unpaired electron localized on two NNs to the muon, and a nearly zero value of the Fermi contact density. In diamond and, to a lesser extent, in Si there is experimental evidence of a $Mu \longrightarrow Mu^*$ transition at higher temperatures, showing that Mu^* is the more stable of the two paramagnetic species. Finally, less than 10% of incoming muons form μ^+, which is not paramagnetic. In Si, both paramagnetic species undergo transitions to μ^+ as the temperature is increased to room temperature, but in diamond, Mu^* is stable (and immobile) up to at least $1,000\,K$.

The basic chemistry of these centers was proposed by Symons and Cox and Symons.[10] The models they proposed for Mu and Mu^* were later confirmed by more rigorous theoretical studies.[11] It is now accepted that Mu corresponds to μ^+e^- located on the average at the T site, and Mu^* to μ^+e^- at a relaxed bond-centered site, with the odd electron in a non-bonding orbital primarily localized on the two NNs to the muon. Finally, μ^+ is Mu^{*+}, the ionized version of bond-centered muonium. However, the possibility of a Mu^- species cannot be ruled out by the available experimental data.

A few μSR experiments[12] were performed in 6H- and 3C-SiC, and the results show qualitative differences between SiC and diamond or Si. First, no Mu^* signal is seen in SiC at any temperature. Then, in 6H-SiC, at low temperatures, the μSR spectrum consists of *three* Mu signals, labeled Mu^{AI}, Mu^{AII}, and Mu^B. At room temperature, Mu^{AI} and Mu^{AII} merge into Mu^A, and only two signals remain. Finally, in 3C-SiC, Mu and μ^+ are present at low temperature, but μ^+ undergoes a transition to Mu as the temperature is increased.

Theoretical predictions

We have calculated the potential energy surface (PES) for H in 3C- and 2H-SiC. At the local minima, both first and second NN atom shells were allowed to relax, and the electronic configurations obtained. Finally, the barriers for diffusion between the various minima were estimated.

Figure 2 shows the relative energies of H at various sites in diamond, Si, 3C-, 2H-, and 6H-SiC. All these values have been obtained with PRDDO in our largest clusters, after relaxation of the first and second NN atoms around H (with the exception of E sites, which are very shallow minima and very high in energy). Figure 3 shows upper limits for the barriers for diffusion of H between the various minima.

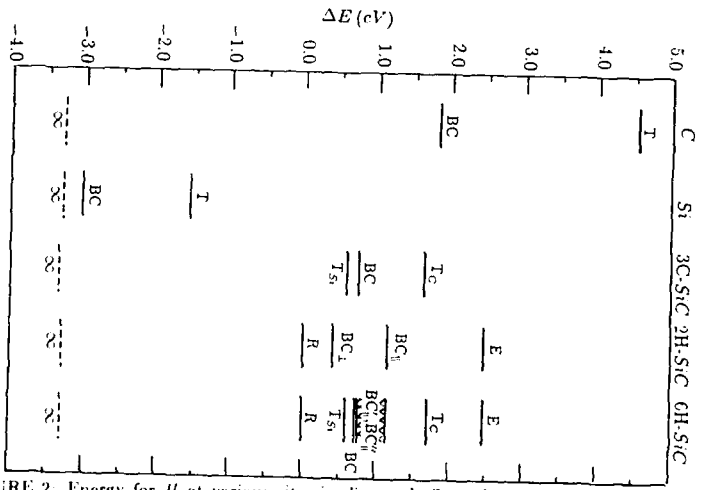


FIGURE 2. Energy for H at various sites in diamond, Si, and 3C-, 2H-, and 6H-SiC. The dashed lines show the energy of the perfect cluster and H far away. The zero of the energy corresponds to H at the B site.

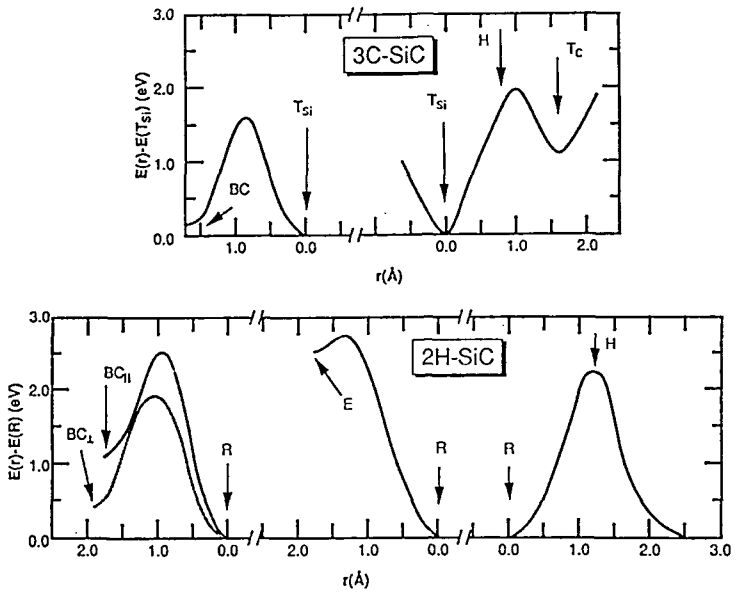


FIGURE 3: Barriers for diffusion for H in 3C- and 2H-SiC.

Discussion

It is clear from Fig.2 that both interstitial sites in Si are much more stable than any site in SiC. Thus, if a SiC film is grown on a Si substrate, interstitial H will not spontaneously diffuse from Si towards SiC, but remain in the Si lattice.

Hydrogen passivation is efficient in Si because H diffuses readily at temperatures at which most $\{X, H\}$ complexes (X = donor or acceptor) are stable. In SiC, the barriers for diffusion of H are very high, which suggests slow diffusion. Thus, unless $\{X, H\}$ pairs are, for some reason, much more stable in SiC than in Si, we expect hydrogen passivation to be quite difficult to achieve in SiC.

While the BC sites are the most stable for H in diamond and Si, they are not the lowest-energy sites in SiC. We propose the following identification of the μSR species.

In the 3C polytype, T_{Si} is preferred, although not by much. The high barrier between BC and T_{Si} suggests that both sites could be populated at low temperatures. Since T_C is much higher in energy, only one Mu signal should be seen, associated with T_{Si}. Mu^* and μ^+ correspond to the BC site. Which of the two is observed may depend on the doping of the sample and other factors. However, at higher temperatures, a $\mu^+ \longrightarrow Mu$ (or $Mu^* \longrightarrow Mu$) conversion should occur.

In 2H-SiC, the R site is the lowest in energy. Adjacent R sites are separated by a high barrier and are far apart. This suggests that H or Mu should be strongly localized there. Some population of $BC_\perp$ is possible at low temperatures, but Mu^* or μ^+ should readily convert to Mu as the temperature is increased. Thus, the μSR spectrum of 2H-SiC should be very simple.

In 6H-SiC, we expect the barriers to be of comparable height to those in the other polytypes of SiC, thus allowing three local minima of the PES to be populated at low

temperatures.[13] R (for Mu^B) and the two slightly inequivalent T_{Si} sites (for Mu^{AI} and Mu^{AII}). A small contribution of the BC site cannot be ruled out, but the corresponding signal should convert to Mu^B at higher temperatures. Rapid thermal diffusion between the two T_{Si} sites could be responsible for the conversion of Mu^{AI} and Mu^{AII} to Mu^A at room temperature.

Acknowledgments

Many thanks to T.L. Estle for conversations about the structure of SiC and for insights into the interpretation of μSR data. This work was supported by the grant D-1126 from the R.A. Welch Foundation and by a grant from the Advanced Technology Program of the State of Texas.

References

1. J. Schlichting, G. Czack, E. Koch-Bienemann, P. Kuhn, and F. Schröder, in *Gmelin Handbook of Inorganic Chemistry*, Suppl. Vol. B2 (Silicon), ed. G.Kirschstein, Springer-Verlag (Berlin, 1984).

2. G. Pensl and R. Helbig, Adv. Sol. St. Phys. **30**, 133 (1990) (*Festkörperprobleme*, ed. U. Rössler, Vieweg, Braunschweig - Germany).

3. See e.g., L.G. Matus, J.A. Powell, and C.S. Salupo, Appl. Phys. Lett. **59**, 1770 (1991).

4. See e.g., Y. Li and P.J. Lin-Chang, Phys. Rev. B **36**, 1130 (1987); C. Wang, J. Bernholc, and R.F. Davis, Phys. Rev. B **38**, 12752 (1988); C.Wang, J.Bernholc, and R.F. Davis (preprint).

5. More details about these calculations can be found in C.H. Chu and S.K. Estreicher, Phys. Rev. B **42**, 9486 (1990), and M.A. Roberson and S.K. Estreicher, Phys. Rev. B **44**, (Nov. 15, 1991).

6. For a discussion of cluster size effects, see S.K. Estreicher, A.K. Ray, J.L. Fry, and D.S. Marynick, Phys. Rev. Lett. **55**, 1976 (1985); **57**, 3301 (1986); S.K. Estreicher, Phys. Rev. B **37**, 858 (1988).

7. T.A. Halgren and W.N. Lipscomb, J. Chem. Phys. **58**, 1569 (1973); D.S. Marynick and W.N. Lipscomb, Proc. Natl. Acad. Sci. (USA) **79**, 1341 (1982). See also T.A. Halgren, D.A. Kleier, J.H. Hall, L.D. Brown, and W.N. Lipscomb, J. Am. Chem. Soc. **100**, 6595 (1978); D.S. Marynick, in *Topics in Physical Organometalic Chemistry*, ed. M.F. Gielen (Freund, London, 1988), p.37.

8. For recent reviews: S.J. Pearton, J.W. Corbett, and T.S. Shi, Appl. Phys. A **43**, 153 (1987); S.J. Pearton, M. Stavola, and J.W. Corbett, Mat. Sci. Forum **38-41**, 25 (1989); *Hydrogen in Semiconductors*, ed. J.I. Pankove and N.M.Johnson (Academic, New York, 1991); U.S. DoE Panel Report on Fundamental Issues in Hydrogen-Defect Interactions (Rev. Mod. Phys., in press).

9. B.D. Patterson, Rev. Mod. Phys. **60**, 69 (1988).

10. M.C.R. Symons, Hyp. Int. **17-19**, 771 (1984); S.F.J. Cox and M.C.R. Symons, Chem. Phys. Lett. **126**, 516 (1986); S.F.J. Cox, J. Phys. C **20**, 3187 (1987).

11. For diamond and silicon: T.L. Estle, S.K. Estreicher, and D.S. Marynick, Hyp. Int. **32**, 637 (1986); for diamond: T.A. Claxton, A. Evans, and M.C.R. Symons, J. Chem. Soc. Faraday Trans. **82**, 2031 (1986); T.L. Estle, S.K. Estreicher, and D.S. Marynick, Phys. Rev. Lett. **58**, 1547 (1987). A detailed study of H in Si, was published by S.K. Estreicher, Phys. Rev. B **36**, 9122 (1987). A comprehensive discussion of H in 6 cubic semiconductors can be found in Ref.5. Other authors have used a variety of theoretical techniques to study H in Si: P. Deak, L.C. Snyder, and J.W. Corbett, Phys. Rev. B **37**, 6887 (1988); P. Deak, L.C. Snyder, J.L. Lindstrom, J.W. Corbett, S.J. Pearton, and A.J. Tavendale, Phys. Lett. A **126**, 427 (1988); G.G. DeLeo and W.B. Fowler, Phys. Rev. B **38**, 7520 (1988); C.G. Van de Walle, Y. Bar-Yam, and S.T. Pantelides, Phys. Rev. Lett. **60**, 2761 (1988); C.G. Van de Walle, P.J.H. Denteneer, Y. Bar-Yam, and S.T. Pantelides, Phys. Rev. B **39**, 10791 (1989); K.J. Chang and D.J. Chadi, Phys. Rev. Lett. **62**, 937 (1989) and Phys. Rev. B **40**, 11644 (1989). The delocalization of the *Mu* wavefunction is discussed in C.G. Van de Walle, Phys. Rev. Lett. **64**, 669 (1990) and in Dj.M. Maric, S. Vogel, P.F. Meier, and S.K. Estreicher, Hyp. Int. **64**, 573 (1990).

12. J.W. Schneider, Hp. Baumeler, H. Keller, R.F. Kiefl, W. Kündig, W. Odermatt, B.D. Patterson, T.L. Estle, S.L. Rudaz, K.W. Blazey, and C. Schwab, Hyp. Int. **32**, 607 (1986); B.D. Patterson, Hp. Baumeler, H. Keller, R.F. Kiefl, W. Kündig, W. Odermatt, J.W. Schneider, W.J. Choyke, T.L. Estle, D.P. Spencer, K.W. Blazey, and I.M. Savic, Hyp. Int. **32**, 625 (1986).

13. This assignment was suggested to us by T.L. Estle.

POTENTIAL ENERGY SURFACES AND STABILITY OF O IN ELEMENTAL AND COMPOUND SEMICONDUCTORS

S.K. ESTREICHER, M.A. ROBERSON, C.H. CHU, and J. SOLINSKY†.
Physics Department, Texas Tech University, Lubbock, TX 79409-1051.

ABSTRACT

Potential energy surfaces and electronic structures of interstial oxygen (O_i) in cubic C, Si, AlP, SiC, and BN have been calculated. The equilibrium site is a bent-bridged bond. In compound semiconductors, O_i has a larger degree of bonding with the most electronegative of the host atoms (P, C, or N) than with the least electronegative one. In addition to the barrier for rotation of O_i about the $<111>$ axis, which does not involve breaking a bond, we calculated the barriers for migration between adjacent bond-centered sites. There are two such barriers in compound semiconductors. In order to estimate the relative stability of O_i in the various hosts, we calculated the energies involved in inserting O_2 into the lattice and dissociating it into two isolated O_i's.

INTRODUCTION

Oxygen is one of the most common impurities in many semiconductors. In Czochralski Si, it can reach concentrations of 10^{18} (cm^{-3}). The properties of oxygen in Si have been studied[1] since the early 1950's. The most stable configuration for isolated interstitial oxygen (O_i) is a bent $Si-O-Si$ bond[2-4] with bond length $Si-O \approx 1.6$ Å and bond angle $\widehat{SiOSi} \approx 160°$. In this configuration, O_i can rotate almost freely about the $<111>$ axis.[3] The barrier for diffusion between adjacent equilibrium sites, which we label bond-centered (BC) for convenience, is 2.56 eV from stress-induced dichroism experiments.[4] Despite this high barrier, O_i becomes mobile around 450 °C, and oxygen-related thermal donors are formed,[5] in addition to other aggregates which are not electrically active. Finally, O is also found at vacancies (A-center[6]). Interstitial oxygen and the A-center in Si have been studied theoretically,[7] but recent work has concentrated on O-related pairs and models for TD formations.[7,8]

In this paper, we report studies of O_i in several group IV and group III-V cubic semiconductors: C (diamond), Si, BP, AlP, SiC, and BN. Our calculations include the equilibrium structures, the barriers for rotation and diffusion, the relative stability of O_i in various hosts, and a search for trends. A similiar investigation[9] of interstitial H in the same six hosts has revealed a number of general features which influence the stability of H in cubic semiconductors.

The calculations were performed in molecular clusters[10] at and near the *ab initio* Hartree-Fock (HF) level. Final geometries were obtained in clusters of the form $OA_{22}B_{22}H_{12}$ using the method of partial retention of diatomic differential overlap[11] (PRDDO). Geometry optimizations involved relaxations of the first and second nearest neighbors (NNs) of O_i. Symmetry constraints were applied to reduce the number of degrees of freedom. The barriers for diffusion were also calculated in smaller clusters at the *ab initio* HF level using split-valence polarized basis sets. A complete report of our results will be published elsewhere.[12]

EQUILIBRIUM STRUCTURES, ROTATION, AND STABILITY

Interstitial oxygen cannot remain at the tetrahedral interstitial (T) site in cubic semiconductors because O_i is an orbital triplet at the T site, and is therefore Jahn-Teller unstable. It moves off-center towards a BC site and strongly binds to the lattice. The equilibrium configuration was obtained by relaxing O_i both parallel and perpendicular to the bond, and allowing its first and second NNs to relax as well. This process was repeated with the O_i oriented at various angles around the $< 111 >$ direction. This not only produced the most stable BC configuration, but also gave the barrier for rotation of oxygen around the axis.

• **Equilibrium Configuration:** In group IV hosts, O_i remains in the plane bisecting the original host-host bond and forms an equally strong bond with its two NNs. In III-V hosts, O_i moves off the bisecting plane and forms a bond with a larger degree of bonding[13] with the most electronegative (ME) of its two NNs, and a bond with a smaller degree of bonding with the least electronegative (LE) one. This is illustrated in figure 1 in the cases of Si and AlP.

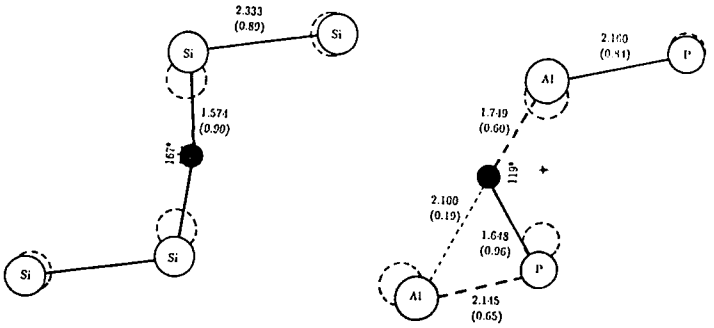


FIGURE 1: Calculated equilibrium configurations for O_i in Si and AlP. In elemental hosts, O_i has a symmetric configuration, while in compounds the degree of bonding to the ME atom is larger. The figure gives the bond lengths (Å), the degrees of bonding, and the O_i bond angle. The dashed circles show the undisturbed locations of the host atoms.

In compound hosts, the puckered bond is oriented in a way that optimizes the overlap between O_i and one of its second NNs: Oxygen is always closest to one of the three second NN host atoms with the largest covalent radius.[14] The calculated[12] dipole moments of O_i are much larger in compound than in elemental semiconductors.

• **Barrier for Rotation:** The barrier for rotation of O_i about the $< 111 >$ axis does not involve breaking a covalent bond, except for the (small) overlap with one of the second NNs to O_i. We obtained this barrier by reoptimizing the geometry (first and second NNs) for various orientations of O_i about the $< 111 >$ axis. This procedure assumes that the lattice has enough time to fully relax as O_i rotates, and therefore tends to underestimate the barrier. The calculated barriers for rotation are shown in figure 2. The barrier heights correlate with the Pauling ionic character[15] of the host.

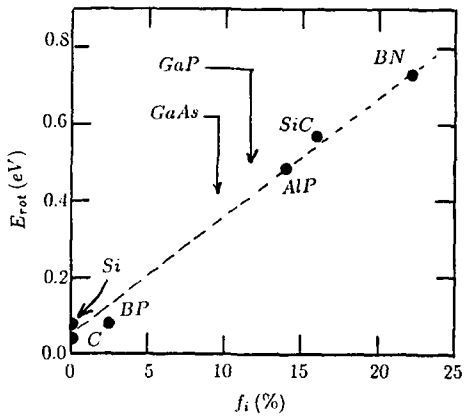


FIGURE 2: Calculated barriers for rotation of O_i about the < 111 > axis as a function of the Pauling ionic character f_i of the host. The arrows show where $GaAs$ and GaP are located on this scale.

• **Relative Stability:** In order to determine the relative stability of O_i in the various hosts, we needed to evaluate the energies relative to a common zero. We defined the reference point as that of free O_2, far outside the undisturbed cluster ("O_2^∞"). Then, we optimized the geometry of the O_2 molecule near the T site in the clusters ("O_2^T"). Finally, we compared these energies to that of two isolated O_i's in the same host. For example, in the case of Si, we compared the following energies: $E_1 = 2E(Si_{44}H_{42}) + E(O_2^\infty)$, $E_2 = E(Si_{44}H_{42}) + E(Si_{44}H_{42} + O_2^T)$, and $E_3 = 2E(Si_{44}H_{42} + O_i)$. Figure 3 shows $E_2 - E_1$ and $E_2 - E_3$ as functions of the lattice constant. For hosts with a small lattice constant, these energy differences depend on the volume available. However, other factors include the strengths of the host atom-O bond, as well as the overall stability of O_2 and of O_i in various hosts. For large lattice constants, these other factors dominate and the trend is lost.

In all cases, O_2^T is unstable. While the $O - O$ bond in O_2^∞ is a double bond, it becomes a single bond when the molecule is inserted into the lattice, at a great cost in energy. Our results are consistent with O_2^T dissociating readily and forming two O_i's in all the hosts.

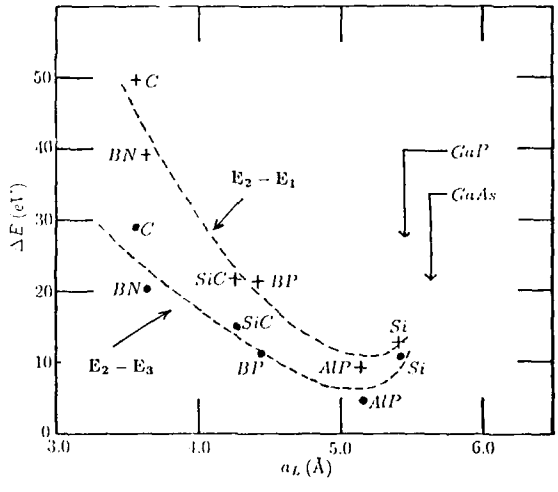


FIGURE 3: Upper curve: $E_2 - E_1$ is the amount of energy needed to insert a free O_2 molecule into the cluster near the T site as a function of the lattice constant a_L.

Lower curve: $E_2 - E_3$ is the energy gained by dissociating O_2 at the T site and forming two isolated O_i's.

BARRIERS FOR DIFFUSION

In compound semiconductors, there are two inequivalent ways for O_i to go from one configuration to another: The diffusion can be described as a rotation about the ME or the LE host atom to which it is attached. Diffusion will result only from overcoming the largest of the two barriers. In our notation, the "A-barrier" refers to O_i moving from one BC site to the next while preserving the $O_i - A$ bond, where A is one of the host atoms. For all the diffusion barriers studied, the atom about which O_i was rotating maintained approximately the same bond distance and degree of bonding with O_i. It is the other bond which affects the barrier height the most.

We experienced a number of difficulties when calculating these barriers. One problem is that the bonds involving O_i are strong, and breaking them costs a lot of energy. At the transition point, the electronic structures are difficult to describe with one-determinant wavefunctions, since stretched or broken bonds involve much more electron correlation than the equilibrium configuration. Further, some of the barriers are very high and very narrow while others involve very large displacements of the atoms. Finally, there are at least 18 degrees of freedom that should be considered when optimizing the transition point geometry. We used symmetry to lower the number of degrees of freedom.

We have painstakingly optimized the geometries at the saddle points with PRDDO, and calculated the barrier heights using closed-shell and unrestricted open-shell wavefunctions (PRDDO), as well as polarized split-valence basis sets (*ab initio* HF). The PRDDO calculations were done in our largest clusters ($OA_{22}B_{22}H_{42}$) and the *ab initio* calculations in $OA_4B_4H_{18}$. Suprisingly, in many cases, the barriers obatined with all three methods were within a few tenths of an eV of each other. In a few cases, however, large discrepencies occured, caused by a dependence on basis set, electron correlation, and/or cluster size. Some of the factors which affect the barriers are the bond strengths[16] between the various atoms involved, the degree to which the bonds are stretched at the saddle points, the distance that O_i actually moves and, if there are broken bonds at the transition point, the stability of odd electrons on the various atoms. We stress that these barriers are the weakest part of our results and should be interpretated with caution.

- **Diamond:** The calculated barrier for diffusion is 3.2 eV with PRDDO and 3.6 eV at the *ab initio* level. At the barrier, the two $C - O$ bonds are stretched by some 25%. The seperation between adjacent BC sites is 0.64 Å. The calculated barrier is only slightly lower than the 3.7 eV of the $C - O$ single bond strength.

- **Si:** The distance O_i has to travel in order to move from one BC site to the next is 1.8 Å, the largest distance of all the hosts we considered. At the transition point, the $Si - O$ bonds are stretched by some 34% and are nearly broken. As a result electron correlation effects are larger at the transition point in Si than in most other hosts, where the bonds are stretched much less. It is therefore not suprising that the barrier for diffusion in Si shows a strong basis set dependence. We found the barrier to be over 4 eV in large clusters with PRDDO, only a little lower than the $Si - O$ bond strength (4.7 eV). If the same geometry is used in smaller clusters with *ab initio* HF and a 6-31G* basis set, the barrier drops to 2.5 eV. However, when second-order Møller-Plesset corrections (MP2) in electron correlation are added, the barrier increases to 2.7 eV.

- **BP:** The $O - B$ and $O - P$ bond strengths are 5.5 eV and 3.9 eV, respectively. The calculated B-barrier is 3.5 eV, with the $O - P$ bonds stretched by 17%. The calculated P-barrier is 3.8 eV and the $B - O$ bonds are stretched by 25%. Both barriers are about the same at the PRDDO and *ab initio* HF levels. The distance between neighboring BC sites is about 1.0 Å for both barriers.

• **AlP:** The bond strengths are $Al-O = 4.6\,eV$ and $P-O = 3.9\,eV$. As in Si, the lattice constant of AlP is large, the distance between BC sites is substantial, and the bonds are nearly broken at the transition point. The barrier height varies again with basis set. Our best estimate is $2.0\,eV$ for the Al-barrier. The P-barrier is still under study.

• **SiC:** The $O-Si$ and $O-C$ bond strengths are $4.9\,eV$ and $3.7\,eV$, repectively. The calculated C-barrier is $4.7\,eV$ and the Si-barrier is about $1.0\,eV$.

• **BN:** The case of BN combines the weakest and strongest oxygen-host bonds: $O-N = 2.1\,eV$, $O-B = 5.47\,eV$, while $B-N$ is intermediate ($4.0\,eV$), the only such occurence for the hosts studied here. Further, O_i is heavier than each of the host atoms. In the lowest-energy configuration, O_i is nearest to a N host atom and strongly overlaps with *two* B atoms. This "BC" configuration is actually almost at the "N-barrier" transition point, and the only barrier for diffusion is the B-barrier. In order to migrate, O_i must first rotate by 60° (which requires over $0.7\,eV$). Then, its configuration changes to a puckered BC bond similiar to configurations found in other hosts. From this configuration, the B-barrier is an additional $1\,eV$.

DISCUSSION

The lowest energy configuration for isolated O_i in cubic C, Si, BP, AlP, SiC, and BN is a puckered BC bond. The bond angle is 167° in Si, and much smaller in the other hosts. The bond puckers oward the second NN to O_i which has the larger covalent radius.

In elemental hosts, O_i is symmetrically located between its two NNs. In compound hosts, O_i has a larger degree of bonding with the ME host atom than with the LE one. The calculated dipole moment of the defect is much larger in compound than in elemental hosts.

The barrier for rotation of O_i increases linearly with the Pauling ionic character of the host, the lowest barriers of rotation corresponding to C and Si.

It costs from about $15\,eV$ to $50\,eV$ to insert an O_2 molecule into the various hosts. The largest amount of energy is required in semiconductors with the shortest lattice constant. Near the T site, the $O-O$ bond is a *single* bond, *not* the double bond characteristic of an O_2 molecule. The energy gained in forming two isolated O_i's is shown in Fig.3. We did *not* investigate the possible combinations involving two O_i's near each other.

Because O_i forms two unequal bonds with the host atoms in compound hosts, there are in general two ways for O_i to go from one BC site to the next, with two different barriers. The calculation of barriers for diffusion of O_i are tricky, in particular when O_i must move by a large distance when going from one BC site to the next. The more the bonds are stretched, the larger the correlation effects, and the more uncertain the result. In Si and AlP, O_i must move by a larger distance than in other hosts. This results in strongly stretched bonds and horrible electronic configurations at the transition point. Our best barrier for the diffusion of O_i in Si is $2.7\,eV$. This number was obtained from *ab initio* calculations with a split-valence basis set followed by MP2 treatments. But even this number may not be that reliable since it was obtained in a small cluster.

Acknowledgements

This work was supported by the Grant D-1126 from the Robert A. Welch Foundation.

References

†Clark Foundation Scholar

1. For reviews, see J.R. Patel, in "*Semiconductor Silicon 1977*", ed. H.R.Huff and E. Sirtl, (Electrochem. Soc. Princeton, 1977), p. 521; L.C. Kimerling, in "*Defects in Semiconductors*" (Elsevier, NY, 1981).

2. W. Kaiser, P.H. Keck, and C.F. Lange, Phys. Rev. **101**, 264 (1956); D.R. Bosomworth, W. Hayes, A.R.L. Spray and G.D. Watkins, Proc. Roy. Soc. (London), Ser. A **317**, 133 (1970).

3. H.J. Hrostowski and B.J. Adler, J. Chem. Phys. **33**, 980 (1960).

4. J.W. Corbett, R.S. McDonald and G.D. Watkins, J. Phys. Chem. Sol. **25**, 873 (1964).

5. See e.g., R.C. Newman, J. Phys. C **18**, L967 (1985).

6. G.D. Watkins and J.W. Corbett, Phys. Rev. **121**, 1001 (1961); J.W. Corbett, G.D. Watkins, R.M. Chrenko, and R.S. McDonald, Phys. Rev. **121**, 1015 (1961).

7. L.C. Snyder, J.W. Corbett, P. Deak, and R. Wu, MRS Symp. Proc. **104**, 179 (1988); J.Plans, G.Diaz, E. Martinez, and F. Yndurain, *ibid.* **35**, 788 (1987); E. Martinez, J. Plans, and F. Yndurain, Phys. Rev. B **36**, 8043 (1987).

8. D.J. Chadi, Phys. Rev. B **41**, 10595 (1990); R. Jones, Semic. Sci. Technol. **5**, 255 (1990); P. Deak, L.C. Snyder, J.W. Corbett, Phys. Rev. Lett. **66**, 747 (1991).

9. C.H. Chu and S.K. Estreicher, Phys. Rev. B **42**, 9486 (1990).

10. S.K. Estreicher, A.K. Ray, J.L. Fry, and D.S. Marynick, Phys. Rev. Lett. **55**, 1976 (1985) and **57**, 3301 (1986); S.K. Estreicher, Phys. Rev. B **37**, 858 (1988).

11. T.A. Halgren and W.N. Lipscomb, J. Chem. Phys. **58**, 1569 (1973); D.S. Marynick and W.N. Lipscomb, Proc. Nat. Acad. Sci. USA **79**, 1341 (1982).

12. S.K. Estreicher, M.A. Roberson, and C.H. Chu, unpublished.

13. D.R. Armstrong, P.G. Perkins, and J.J.P. Stewart, J. Chem. Soc. Dalton Trans. **8**, 838 (1973).

14. J.E. Huheey, "*Inorganic Chemistry*" (Harper & Row, New York, 1983), p. 258.

15. L. Pauling, "*The Chemical Bond*" (Cornell UP, 1967).

16. The bond strengths come from J.C. Bailar, Jr., H.J. Emeléus, R. Nyholm, and A.F. Trotman-Dickenson, "*Comprehensive Inorganic Chemistry*" (Permagon, Oxford, 1973), except the $O-Al$ bond strength: "*Handbook of Chemistry and Physics*", ed. R.C. Weast, (CRC, Boca Raton, 1988).

A COMPARISON OF THE WURTZITE AND ZINCBLENDE BAND STRUCTURES FOR SiC, AlN AND GaN

W. R. L. LAMBRECHT and B. SEGALL
Department of Physics, Case Western Reserve University, Cleveland, OH 44106-7079

ABSTRACT

Total energy and band structure results of linear-muffin-tin orbital calculations *within the* atomic-sphere-approximation are presented for SiC, GaN and AlN in the zincblende and the wurtzite structure. We discuss the origin of the directness or indirectness and the relative magnitudes of the band gaps.

INTRODUCTION

In order to develop applications based on the electronic and optical properties of the promising wide band-gap semiconductors SiC, GaN and AlN, a thorough knowledge of their bulk band-structures and equilibrium properties is required. While some of this information is already available, it appears that there has not yet been a systematic study of the band-structures of this class of materials using the same approach. Such a study, which has the advantage that a uniformly accurate comparison between the various materials and structures can be made, is *presented here.*

An important aspect of these materials is the polymorphism. While SiC has a large number of polytypes, the nitrides GaN and AlN occur naturally only in the wurtzite (WZ) structure. They may, however, be stabilized in the zincblende (ZB) structure by epitaxial growth. While this possibility has already been demonstrated for GaN [1], it is still a challenge for AlN. The only report of *ZB AlN refers to AlN precipitates formed inside an fcc Al matrix* by N-ion implantation [2], obviously a non-equilibrium situation.

For optical applications, the question whether the bandgap is direct or indirect is very important. We will thus pay special attention to this issue.

COMPUTATIONAL METHOD

The underlying computational framework used in this work is the *density functional* theory [3] in the local density approximation (LDA). The linear muffin-tin orbital (LMTO) method [5] is used in the atomic sphere approximation (ASA) with the so-called combined correction.

In order to apply this approach to open structures such as ZB and WZ, so-called empty spheres must be introduced in order to appropriately describe the charge density and wave functions in the interstitial region. In the ZB case, the empty spheres are positioned at the tetrahedral interstitial sites. Equal sphere radii are used on all spheres in order to reduce the overlap between the spheres as much as possible. For the WZ structure, we introduced small empty spheres of radius $s_{E_1} \sim \frac{2}{3} s_A$ (s_A being the atomic sphere radius) in between the atoms along the c-direction and large empty spheres of size $s_{E_2} \sim 1.16 s_A$ in the channel regions. The Brillouin zone summations were converged to < 1 meV accuracy in the total energy results.

RESULTS

Equations of state

In this section, we present our results for the energy as a function of volume, i.e. the equations of state. We used a fit of the calculated results to the Rose-Smith-Ferrante equation of state [6] in

Table I: Equilibrium properties of SiC, AlN, GaN.

		V/molecule(Å^3)	E_c(eV/molecule)	B(MBar)	B'
SiC	ZB	20.2 (20.7[a])	14.1 (12.7[b])	2.3 (2.2[c])	3.8
	WZ	19.9 (20.7[a])	14.6	2.4	3.9
AlN	ZB	20.3	12.6	2.2	3.9
	WZ	20.1 (20.8[a])	13.1 (11.5[b]a)	2.2 (2.1[d])	3.9
GaN	ZB	22.8	9.9	2.0	4.4
	WZ	21.7 (22.6[e])	10.2 (8.9[b])	2.2 (1.9[e])	4.4

Experimental values in parentheses.
a. Wyckoff [7]
b. From enthalpies of formation given in CRC Handbook [8]
c. Carnahan, [9]
d. Wettling and Windscheif [10]
e Gerlich et al. [11]

order to extract the equilibrium volume/molecule, V; the cohesive energy, E_c; the bulk modulus, B; and the pressure derivative, B', of the latter. Table I summarizes the results.

The overall agreement with the experimental values (given in parentheses) is satisfactory. We note that our calculations may slightly overestimate the bulk modulus in the WZ structure because we did not minimize the energy with respect to the c/a ratio and internal degree of freedom u. We did not attempt this since it is well known from work on phonon-distortions in Si [12] that the ASA is not sufficiently accurate for studying the effects of small structural relaxations. The required accuracy can, however, be achieved by means of the full-potential (FP) version [12] of the LMTO-method. We recently carried out FP calculations of cubic SiC in order to determine its elastic constants [13]. Similar work on the nitrides and on the WZ structures is in progress. The above calculations predict the WZ structure to be stable with respect to the ZB in all cases by about 0.2–0.3 eV/atom. Cheng et al.'s work [14], however, indicates that for SiC, the ZB structure is lower in energy than the WZ by ~ 5 meV/atom. For GaN, Muñoz and Kunc [15] using pseudopotential calculations have recently found WZ to be stable with respect to ZB by only 15 meV/atom. To pin down these small structural energy differences, it appears to be essential to go beyond the ASA.

Band structures

To facilitate the comparison between the band structures in the ZB and the WZ structures, we follow the approach of Salehpour and Satpathy [16]. The ZB band structures are thus displayed in a double unit cell along axes in reciprocal space which are relevant for the hexagonal system. We refer to Ref. [16] for a complete discussion of the relationships between the k-points in the two crystal structures. In particular, we note that the point X_{fcc} of ZB lies at 2/3 of the way between the M and L points of the hexagonal Brillouin zone if the c/a ratio is ideal and is here indicated as X. The symmetry labels of the ZB band structures indicated in the Figs. 1-3 are those for the fcc Brillouin zone. The minimum bandgaps are given in Table II.

The overall features of the band structures agree well with previous calculations for SiC [18] and GaN in both structures [19] and for WZ AlN [20]. There are differences, however, in the magnitudes of the band gaps obtained with the earlier empirical pseudopotential calculations [19, 18] in which the gaps were adjusted to experimental data. As is well known, the gaps are underestimated in the LDA Kohn-Sham eigenvalue spectrum. We have calculated a correction to the LDA gap following the approach of Bechstedt and Del Sole [21]. Their method provides essentially a tight-binding estimate of the correction Δ_{GW} to the quasiparticle energy in Hedin's many-body perturbation theory [22]. We see that typically their procedure slightly overestimates the correction. We note that our bandgaps were calculated at the theoretical equilibrium lattice

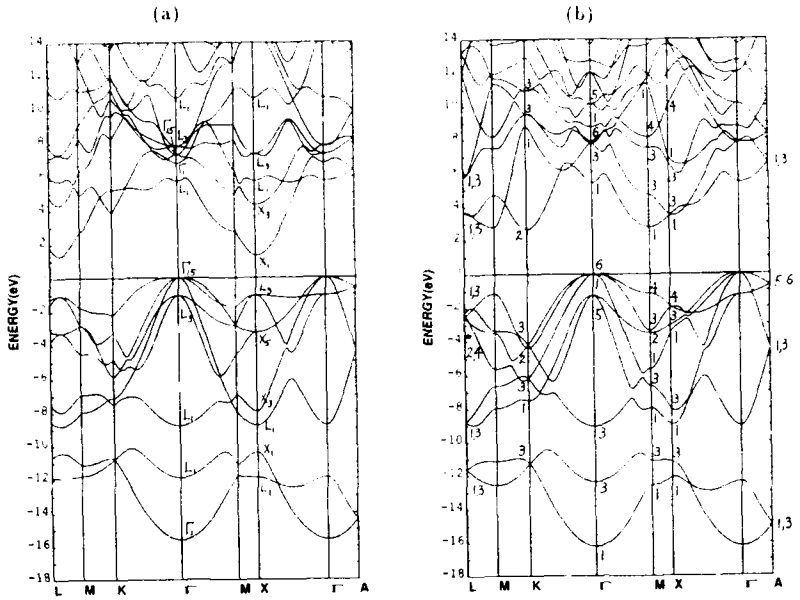


Figure 1: Band structure of SiC in (a) zincblende and (b) wurtzite structure

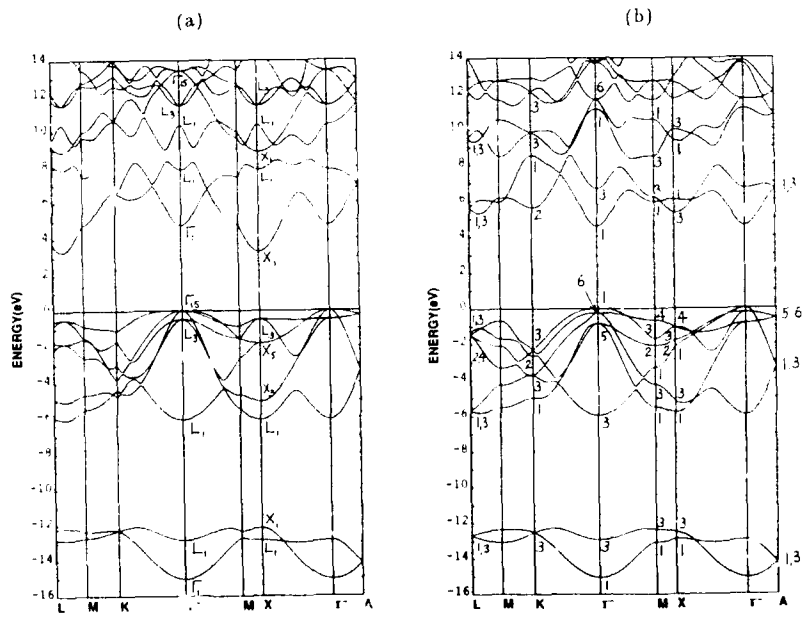


Figure 2: Band structure of AlN in (a) zincblende and (b) wurtzite structure

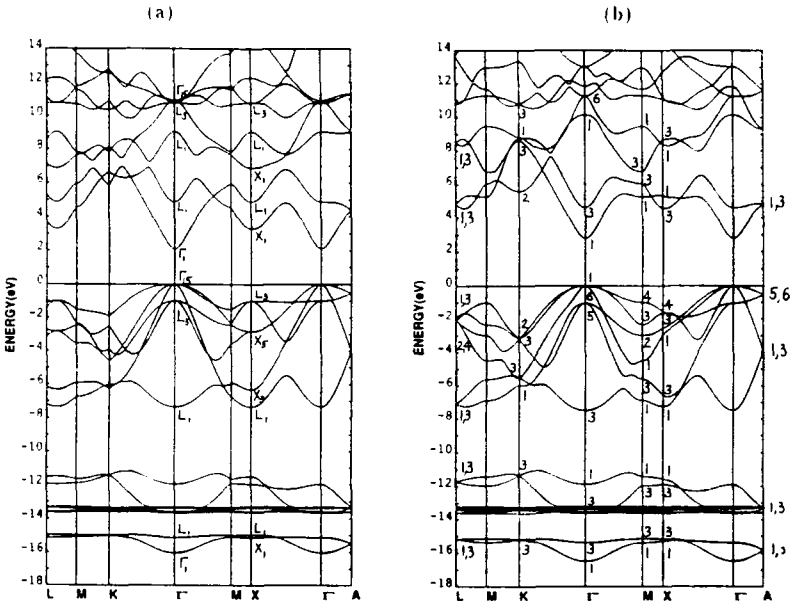


Figure 3: Band structure of GaN in (a) zincblende and (b) wurtzite structure

Table II: Minimum band gaps of SiC, AlN and GaN in zincblende and wurtzite structures (in eV)

		ZB	WZ
SiC		$\Gamma - X$	$\Gamma - K$
	LDA	1.47	2.67
	LDA+Δ_{GW}	2.7	3.9
	Expt.	2.416[a]	3.330[a]
AlN		$\Gamma - X$	$\Gamma - \Gamma$
	LDA	3.32	4.94
	LDA+Δ_{GW}	5.1	6.7
	Expt.		6.28[a]
GaN		$\Gamma - \Gamma$	$\Gamma - \Gamma$
	LDA	2.09	2.75
	LDA+Δ_{GW}	3.6	4.2
	Expt.		3.6[b]

a. Landolt and Börnstein Tables, [17]
b. Bloom et al. [19]

constant using the experimental c/a ratio and the ideal value of u, namely 0.375. This partially explains the discrepancy from Ching and Harmon's value (4.4 eV) for the LDA gap of AlN which was calculated at the slightly larger experimental lattice constant. At the experimental lattice constant and the non-ideal experimental value $u = 0.385$, we obtain 4.6 eV. For GaN, the calculations of Bloom et al. [19] obtained the bandgap for ZB only 0.1 eV lower than that for WZ GaN. They, however, used the same form factors for their pseudopotential calculation, instead of self-consistent quantities for each of the structures.

Next, we consider a number of aspects of the band edges, including the directness or indirectness of the bandgaps. First of all, one may notice that the energy of the X_1^c conduction band minima are lower in ZB than the corresponding states in WZ in all three compounds. This is in part a result of the fact that in ZB the only state of the same X_1 symmetry, with which it can interact, lies quite deep. In a tight-binding picture, the X_1 valence and conduction band states are bonding and antibonding combinations of the anion s-orbital with a cation p-orbital. In WZ, on the other hand, this point has a lower symmetry and the state can interact with several closer lying states. The interaction with the upper valence band states of the same symmetry tends to push the WZ conduction band state to higher energies. There is no interaction with the nearest conduction band state above the minimum because this state has a different symmetry. In addition, the eigenvalues along the $M - L$ axis must approach each other to become degenerate at L on the face of the Brillouin zone, because the spacegroup (C_{6v}^4) is non-symmorphic. This also tends to push up the conduction band edge at X in WZ.

In AlN, the competing level for the conduction band minimum is the Γ_1 state. Thus, that state becomes the conduction band minimum in WZ, and, although it falls just barely below the lowest conduction band state at the X-point, the gap becomes direct. In the case of SiC, however, the Γ_1^c conduction band state is higher in energy relative to the eigenvalues at the other k-points and thus does not become the minimum in WZ. Rather, it is the K-point where the minimum occurs, followed closely (at 0.12 eV higher) by the M-point. This leaves the band gap indirect. The energies of the conduction band minimum at the M-point are practically the same in the ZB and WZ structures, but the K-point is lowered by about 1 eV. The fact that the conduction band minimum changes character because of these symmetry effects, explains why there is a significant difference in band gap (by about 1 eV) between the cubic and hexagonal SiC polytypes.

Finally, we may inquire as to why the Γ_1^c state is relatively high[illegible] (with respect to conduction band states at other k-points) in SiC and lower in GaN compared to AlN. Those facts prevent SiC from becoming direct even in WZ and makes GaN direct even in ZB. The Γ_1^c state is basically an antibonding combination of cation and anion s-orbitals. As such it is quite sensitive to the depth of the potential well near the nucleus. Obviously, Ga, being the atom with the highest atomic number, has the strongest potential at the nucleus. The key factor in the comparison between SiC and AlN is the stronger ionicity of the latter. This is confirmed by a partial wave analysis of the Γ_1^c state which shows a smaller admixture of N 2s in AlN than of C 2s in SiC. Since the cation of these compounds have a larger Z than the anions, the higher cation content in AlN more than compensates for the slightly stronger Si potential at the nucleus.

We note that for GaN, it is important to treat the Ga 3d semicore state as a band state. It overlaps in energy with the N 2s band and hybridizes significantly with it at most k-points except Γ. We found that omission of this state leads to a larger equilibrium lattice constant, and, as a result to a lower bandgap (1.8 eV in the LDA).

Finally, we find that the densities of states (DOS) in the WZ and the ZB structures show systematic differences which are very similar in SiC, AlN and GaN. The valence band DOS is more peaked near the top of the band in WZ. These differences should be observable in XPS or UPS photoemission or in soft X-ray emission spectra of the valence band and may also be identifiable in the CVV (core-valence-valence) Auger electron spectra of these materials. The latter essentially corresponds to an auto-convolution of the valence band density of states. This may be useful for the experimental characterization of the cubic versus the hexagonal structure.

CONCLUSIONS

Using the LMTO-ASA method we have calculated the band structures and equilibrium properties of SiC, AlN and GaN in the zincblende and wurtzite structures. We have discussed the origin of the directness and indirectnes of their bandgaps.

This work was supported by ONR and the N.A.S.A. Lewis Research Center.

REFERENCES

1. W. Seifert and A. Tempel, *Phys. Status Solidi (a)* **23**, K39 (1974).
2. D. Schwabe and W. Mader, in *Proceedings of the European Conference on Advanced Materials and Processes (EUROMAT)*, Aachen, Germany, Nov. 22-24, 1989.
3. P. Hohenberg and W. Kohn, *Phys. Rev.* **136**, B864 (1964); W. Kohn and L. J. Sham, *ibid.* **140**, A1133 (1965).
4. U. von Barth and L. Hedin, J. Phys. C **5**, 1629 (1972).
5. O. K. Andersen, *Phys. Rev. B* **12**, 3060 (1975); O. K. Andersen, O. Jepsen, and M. Šob, in *Electronic Band Structure and its Applications*, edited by M. Yussouff, (Springer, Heidelberg, 1987).
6. J. H. Rose, J. Smith and J. Ferrante, *Phys. Rev. B* **28**, 1835 (1983).
7. R. W. G. Wyckoff, *Crystal Structures*, Second Edition, (Interscience Publishers, New York 1964), Vol. 1.
8. CRC Handbook of Chemistry and Physics, edited by R. C. Weast, (CRC Press, Inc., Boca Raton, FL 1988), 68th Edition.
9. R. D. Carnahan, *J. Am. Ceram. Soc.* **42**, 254 (1959).
10. W. Wettling and J. Windscheif, *Solid. State Commun.* **50**, 33 (1984).
11. D. Gerlich, S. L. Dole and G. A. Slack, *J. Phys. Chem. Solids* **47**, 437 (1986).
12. M. Methfessel, *Phys. Rev. B* **38**, 1537 (1988); M. Methfessel, C. O. Rodriguez, and O. K. Andersen, *Phys. Rev. B* **40**, 2009 (1989).
13. W. R. L. Lambrecht, B. Segall, M. Methfessel, and M. van Schilfgaarde, *Phys. Rev. B* **44**, 3685 (1991).
14. C. Cheng, R. J. Needs, and V. Heine, *J. Phys. C* **21**, 1049 (1988).
15. A. Muñoz and K. Kunc, *Phys. Rev. B* **44**, 10372 (1991).
16. M. R. Salehpour and S. Satpathy, *Phys. Rev. B* **41**, 3048 (1990).
17. *Numerical Data and Functional Relationships in Science and Technology*, edited by O. Madelung, Landolt-Börnstein, New Series, Group III, Vol. 17a (Springer, Berlin, 1982).
18. L. A. Hemstreet and C.Y. Fong, in *Silicon Carbide - 1973*, edited by R. C. Marshall, J. W. Faust, C. Y. Ryan, (University of South Carolina Press, Columbia, SC 1974), p. 284.
19. S. Bloom, G. Harbeke, E. Meier, and I. B. Ortenburger, *Phys. Statuts Solidi (a)* **66**, 161 (1974).
20. W. Y. Ching and B. N. Harmon, *Phys. Rev. B* **34**, 5305 (1986).
21. F. Bechstedt and R. del Sole, *Phys. Rev. B* **38**, 7710 (1988).
22. L. Hedin, *Phys. Rev.* **139**, A796, (1965).

ON THE BURSTEIN-MOSS SHIFT IN QUANTUM CONFINED WIDE-BAND GAP SEMICONDUCTORS

KAMAKHYA P. GHATAK* AND BADAL DE**

* Department of Electronics and Telecommunication Engineering, Faculty of Engineering & Technology, University of Jadavpur, Calcutta 700032, India

** John Brown E and C Inc., 333 Ludlow Street, P.O.Box 1422, Connecticut 06902, USA.

ABSTRACT

We study the Burstein-Moss shift (BMS) in quantum wires and quantum dots of wide-gap semiconductors, taking Ge as an example. It is found that the BMS increases with increasing electron concentration in a ladder like manner. The numerical values of the BMS is greatest in quantum dots and least in quantum wells. The theoretical analysis is in agreement with the experimental results as given elsewhere.

With the advent of FLL, MBE, MOCVD and other experimental techniques, quantum wires (QWs) and quantum dots (QDs) have in the last few years attracted much attention not only for their potential in uncovering new phenomena in material science but also for their interesting device applications. In QWs the motions of the electrons are quantized in the two perpendicular directions in wave vector space and the carriers can move only in the single free direction [1]. In QDs, the dimensions of the quantum well increases from 1D to 3D and the density-of-states function is changed from Heaviside step function to Dirac's delta function [2]. Though considerable work has already been done, nevertheless it appears from the literature that the Burstein-Moss shift (BMS) in such quantum confined wide gap materials has yet to be studied. This is done in what follows, taking Ge as an example of wide gap semiconductors.

The energy spectrum of the conduction electrons in wide gap semiconductors can be expressed [3] as

$$E=(-E_g/2)+(\hbar^2 k_z^2/2m_{\parallel})+[(E_g/2)^2+E_g k_s^2(\hbar^2/2m_{\perp})]^{\frac{1}{2}} \qquad (1)$$

where the notations are defined in the above reference.

The modified electron dispersion law in QWs can be written using (1) as

$$\hbar^2 k_x^2/2m_1 = C(E,n) - (\hbar^2\pi^2/2m_2)(S/d_2)^2 \qquad (2)$$

where $m_1=m_{\perp}$, $C(E,n)=[E(1+\alpha E)-D(n)(1+2\alpha E)+\alpha(D(n))^2]$,

$\alpha = 1/E_g$, $D(n) = (\hbar^2 \pi^2/2m_3)(n/d_1)^2$, $n=1,2,3.....$, $s=1,2,3....$, $m_3 = (3m_{11}m_\perp)(2m_{11}+m_\perp)^{-1}$, $m_2 = (m_\perp + 2m_{11})/3$, and d_1 and d_2 are film thickness along y and z directions respectively. Using (2), the electron concentration per unit length can be expressed as

$$n_{1D} = (g_v\sqrt{2m_1}/\pi\hbar)\sum_{n,s} \langle A_1 + A_2 \rangle \qquad (3)$$

where g_v is the valley degeneracy, $A_1 = \langle C(E_{F1}, n) - (\hbar^2\pi^2/2m_2)(s/d_2)^2 \rangle^{\frac{1}{2}}$, $A_2 = \sum_{r=1}^{k_0} A_{3,1}\langle A_1 \rangle$, $A_{3,t} = 2.(k_BT)^{2r}(1-2^{1-2r})\zeta(2r)\frac{d^{2r}}{dE_{F,t}}\langle A_1 \rangle$, k_B is Boltzmann constant, T is temperature $t = 1$ and 3, r is the set of real positive integer where upper limit is k_0, $\zeta(2r)$ is the Zeta function of order 2r [4] and E_{F1} is the Fermi energy in QW case. The heavy hole energy can be written [5] as

$$E_h = (A - B)k^2 \qquad (4)$$

where the notations are defined in [5]. Therefore the BMS in QWs can be written as

$$\Delta_{1D} = E_{F1} + E_g + E_1 \qquad (5)$$

where $\langle E_1 = (A-B)\pi^2(d_1^{-2}+d_2^{-2})\rangle (A-B)^{-1}(\hbar^2/2m_1) \equiv C(E_1,1) - \frac{\hbar^2\pi^2}{2m_2 d_2^2}$

Similarly the BMS in QDs can be expressed as

$$\Delta_{3D} = E_{F3} + E_g + E_3 \qquad (6)$$

where E_{F3} is the Fermi energy in QDs and can be related through the electron concentration per unit volume as

$$n_{3D} = \langle g_v/d_1d_2d_3 \rangle \sum_{n,t,S} \langle 1+\exp(-g) \rangle^{-1}$$

$g = (k_BT)^{-1}(E_{F3}-E_4)$, $C(E_4,n) = \left[\frac{\hbar^2\pi^2}{2m1}.(t/d_3)^2 + (\hbar^2\pi^2/2m_2)(S/d_2)^2\right]$, $t=1,2,3.....$, d_3 is the film thickness along x-direction and $E_3 = (A-B)\pi^2\langle d_1^{-2} + d_2^{-2} + d_3^{-2}\rangle$

Using the appropriate equations together with the parameters [6] $A = 4.28\,\hbar^2/2m_o$, $B = 0.75\,\hbar^2/2m_o$, $m_\parallel = 1.588\,m_o$, $m_\perp = 0.081\,m_o$, $E_g = 2.2$eV, the normalized BMS in QWs of Ge as a function of electron concentration per unit length has shown in plot a of Fig 1 where the circular plot exhibits the same dependence in accordance with the experimental datas as given elsewhere [6]. The plot b of Fig.1 has been drawn by using the parabolic energy band structures of Ge for the purpose of assessing the

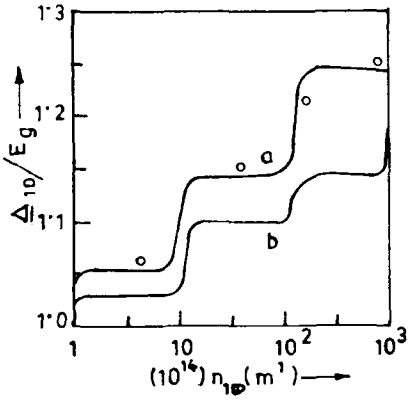


Fig.1 Plot of normalized BMS versus n_{1D} in QWS of Ge in acceptance with (a) generalized band model and (b) parabolic model. The circular plots correspond to experimental results. [$d_1 = d_2 = 40$ nm]

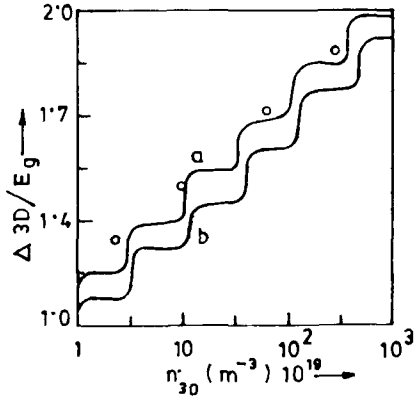


Fig.2. Plot of normalized BMS versus n_{3D} in QDS of Ge in accordance with (a) generalized band model and (b) parabolic model. The circular plots correspond to experimental results. [$d_1 = d_2 = d_3 = 40$ nm]

influence of energy band models. The Fig. 2 exhibits the all cases of Fig. 1 for QDs of Ge.

It appears from both the Figs. that the BMS increases with increasing carrier degeneracy in non-ideal steps for both QWs and QDs of Ge. The numerical values of the BMS are greatest in QDs and the least in QWs. In QDs the width of the steps is smaller and the influence of quantization of band states is immediately apparent from the Figs. Finally we wish to note that though the many-body effects and the influence of surface states and charges should be considered alongwith a self consistent procedure, this simplified analysis exhibits the basic features of BMS in quantum confined wide gap semiconductors and the agreement between the theoretical results and the experimental datas is significant.

1. W.J.Stoopol, L.D. Jackel, E.L.Hu, R.E. Howard, L.A. Fetter, Phys. Rev. Letts. 49, 951 (1982).
2. Y.Arakawa, H.Sakaki, Appl.Phys.Letts.40, 939 (1982).
3. B.Mitra, K.P.Ghatak, Solid State Electronics 32,177(1989).
4. M.Abramowitz, I.A. Stegun, Handbook of Mathematical Functions, NBS Appl. Math series, 55, Washington (D.C.), 1965.
5. N.S.Averkiev, Yu.V.Ilisavsky, V.M.Sternin, Solid State Commun. 52, 17(1984).
6. A.Aronov and I.M.Tsidilkovskii, J.Exp.Theo. Phys. 114, 203 (1991).

THE EINSTEIN RELATION IN SUPERLATTICES OF WIDE-BAND GAP SEMICONDUCTORS UNDER CROSS-FIELD CONFIGURATION

KAMAKHYA P. GHATAK* AND BADAL DE**

Department of Electronics and Telecommunication Engineering, Faculty of Engineering and Technology, University of Jadavpur, Calcutta 700032, India.

John Brown E and C Inc., 333 Ludlow Street, P.O. 1422, Connecticut 06902, USA.

ABSTRACT

In this paper we study the Einstein relation in superlattices of wide-band gap semiconductors under crossfield configuration and the forming materials incorporating spin and broadening of Landau levels. It is found, taking GaAs/AlAs superlattice as an example that the diffusivity-mobility ratio increases with increasing electron concentration and oscillates with inverse quantizing magnetic field due to SdH effect. The theoretical analysis is in agreement with the suggested experimental method of determining the same ratio in degenerate materials having arbitrary dispersion laws.

The semiconductor superlattices (SLs) as originally proposed by Esaki and Tsu, has found wide applications in many new device structures such as photodiodes, transistors, light emitters etc. [1]. Though extensive work has already been done on the various electronic properties of such semiconductor heterostructures, it appears from the literature that the Einstein relation for the diffusivity-mobility ratio of SLs has relatively been less investigated [2]. The connection of the DMR with the velocity autocorrelation function, its relation with the screening length and the various formulation of the DMR has been studied under different physical conditions [3]. In this connection we wish to note that the cross-field configuration is fundamental for classical and quantum transport in solids [4]. In what follows we shall study the Einstein relation in SLs of wide bandgap semiconductors under crossfield configuration, taking GaAs/AlAs SL as an example.

In the presence of a quantizing magnetic field B along the SL direction and the crossed electric field $\vec{E}_o$ along the x-axis, the Hamiltonian H assumes the form

$$H = \hat{p}_x^2/2m^* + (\hat{p}_y - e\hat{Bx})^2/2m^* + E_{os} - E_{ls}\cos(2\pi\hat{p}_z/\hbar k_o) - e\vec{E}_o\hat{x} \qquad (1)$$

hats denote the respective operators and the other notations are defined in [1]. The modified electron energy spectrum for SLs, including spin, reads

$$\epsilon = (n+\tfrac{1}{2})\hbar w_o - e\bar{E}_o p_y/m^* w_o - \frac{e^2\bar{E}_o^{\,2}}{2m^* w_o^{\,2}} + E_{os} - E_{ls}\cos\left(\frac{2\pi k_z}{k_o}\right) \pm \tfrac{1}{2} g_o u_o B \quad (2)$$

where ϵ is the electron energy under cross-field configuration, n, w_o, g_o and u_o are the Landau quantum number, cyclotron frequency, spectroscopic splitting factor at the band edge and the Bohr magneton respectively. Considering only the lowest miniband, since in an actual SL only this miniband is significantly populated at low temperatures where the quantum effects become prominent, the electron statistics can be expressed as

$$n_o = A \sum_{n=0}^{n_{max}} [P(E_o) + Q(E_o)] \quad (2)$$

where $A = m^* w_o E_{11}/e\bar{E}_o \hbar \pi^2 d_o^{\,2}$, $P(E_o) \simeq$ R.p. of $[[1-a_1 + b\,c\,]^{1/2} - \{a_1 - b\,c\}\cos^{-1}(a_1 - bc)]$ - $[1-a_1 + bd_1]^{1/2}$ + $(a_1 - bd_1)\cos^{-1}(a_1 - bd_1)]$ $a_1 = (E_{11})^{-1}[(n+\frac{1}{2})\hbar w_o - E_F - \frac{e^2\bar{E}_o^{\,2}}{2m^* w_o^{\,2}}]$, $E_F = F_o + i\Gamma$, E_o is the fermi energy, $i=\sqrt{-1}$, Γ is broadening parameter, $b = e\bar{E}_o\hbar/m^* w_o E_{11}$, $c = d_1 + eBd_o\hbar^{-1}$, $d_1 = -m^*\bar{E}_o/2B\hbar$, $Q(E_o) = \sum_{\gamma=1}^{t} \nabla_r [P(E_o)]$, r is the set of real positive integers, $\nabla_r = 2(k_B T)^{2r}(1-2^{1-2r})\,\zeta(2r)\frac{d^{2r}}{dE_o^{2r}}$ and $\zeta(2r)$ is the zeta function of order 2r. Since the DMR can, in general be expressed as [3]

$$\frac{D}{\mu} = \frac{1}{e} n_o \Big/ \frac{dn_o}{dE_o}, \quad (4)$$

we can combine (3) and (4) to get the expression of the same ratios in wide gap SL under cross-field configuration as

$$\frac{D}{\mu} = \frac{1}{e}[\sum_{n=0}^{n_{max}} [P(E_o)+Q(E_o)]][\sum_{n=0}^{n_{max}} P'(E_o)+Q'(E_o)]^{-1} \quad (5)$$

where the primes denote the differentiation w.r.t. E_o. For the purpose of comparison, the expressions of n_o and DMR in the corresponding wide gap bulk materials having parabolic energy bands can be expressed under cross-field configuration as

$$n_o = A_1 \sum_{n=0}^{n_{max}} [E(E_o) + S(E_o)] \quad (6)$$

and

$$\frac{D}{\mu} = (e)^{-1} \sum_{n=0}^{n_{max}} R(E_o)+S(E_o)][\sum_{n=0}^{n_{max}} R'(E_o)+S'(E_o)]^{-1} \quad (7)$$

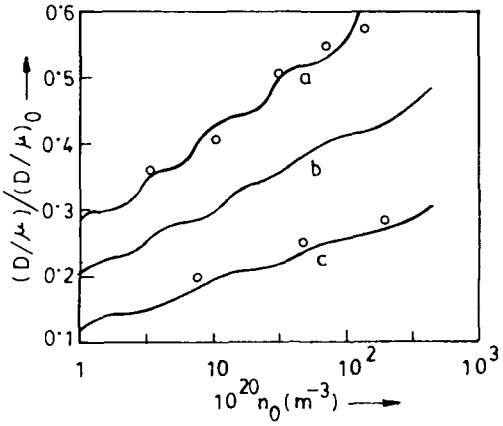


Fig.1. Normalized DMR under cross-field configuration versus n_o in (a) GaAs/AlAs SL, (b) GaAs and (c) AlAs. The circular plots exhibit the experimental suggestion for measuring the DMR in degenerate materials having arbitrary dispersion laws.

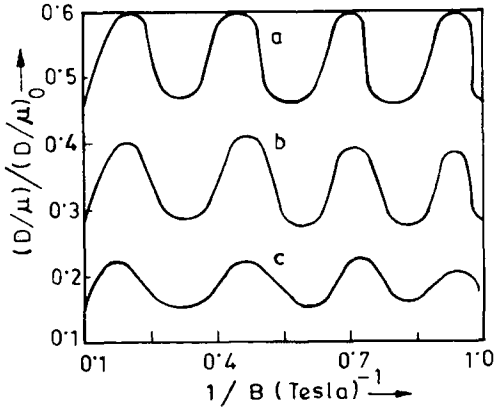


Fig.2. Normalized DMR under cross-field configuration versus 1/B in (a) GaAs/AlAs, (b) GaAs, and (c) AlAs. $(n_o = 10^{20} m^{-3})$

where $A_1 = B\sqrt{2m^*}/3L_x \pi(\hbar^2\bar{E}_o$, L_x is the sample length along x. direction, $R(E_o)$=R.P. of $[(t_1 + gt_2)^{3/2} - (t_1+g_1 t_2)^{3/2}]$, $t_1 = [E_F - (n + \frac{1}{2})\hbar w_o \pm \frac{1}{2} g_o \mu_o B + m^* \bar{E}_{o_t}^2 (2B^2)^{-1}]$, $t_2=\bar{E}_o\hbar/B$, $g=g_1+eBL_x\hbar^{-1}$, $g_1=-m^*\bar{E}_o/2B\hbar$ and $S(E_o) = \sum_{r=1} \nabla_r [R(E_o)]$

In the absence of electric field, spin and broadening, (6) and (7) assume the well-known forms as [5]

$$n_o = N_c\theta \sum_{n=0}^{n_{max}} F_{\frac{1}{2}}(\eta') \qquad (8)$$

$$\frac{D}{\mu} = (k_B T/e) \left[\sum_{n=0}^{n_{max}} F_{-\frac{1}{2}}(\eta')\right] \left[\sum_{n=0}^{n_{max}} F_{\frac{3}{2}}(\eta')\right]^{-1} \qquad (9)$$

where the notations are defined in [6].

Using (3) and (5) and taking the parameters [7] E_{01}=0.05eV, B=1.5 Tesla, E_{11} = 0.01 eV, m*=0.067 m_o, d_o = 6 nm, T=4.2K, Γ = 2.3 x 10^{-4} eV, g_o=2 and $\bar{E}_o=10^4$ V/m as valid for GaAs-AlAs SLs we have plotted the normalized DMR versus n_o as shown in plot a of Fig. 1 in which the plots b and c exhibit the same dependence for GaAs and AlAs, respectively. Taking the same parameters as used in obtaining Fig.1 we have plotted the normalized DMR versus 1/B in all the above mentioned cases in Fig. 2. The thermoelectric power can be written in the present case as $D/\mu = \pi^2 k_B^2 T/3Ge$ where G is the thermoelectric power. By taking the experimental values of G as given elsewhere [8] we have plotted in Fig. 1 the circular points. The DMR oscillates with 1/B due to SdH effect.

Finally, it may be noted that the conclusions made here would be of particular significance in view of the fact that the switching speed and the performance of the semiconductor devices at the device terminals can be related to the DMR [3].

1. B.Mitra, K.P.Ghatak, Phys. Letts.A. 142A, 401 (1989) and the references cited therein.
2. S.N.Biswas, K.P.Ghatak, Proc. of SPIE, 792, 239 (1987).
3. K.P.Ghatak, N.Chattopadhyay, M.Mondal, J.Appl. Phys. 63, 4536 (1988) and the references therein.
4. K.P.Ghatak, M.Mondal, Z.F.Physik B, 69, 471 (1988) and the references therein.
5. P.N.Butcher, A.N.Chakravarti, S.Swaminathan, Phys. Stat. Sol. (a) 25, K47 (1974).
6. B.R.Nag, Electron Transport in Compound Semiconductors, Springer Series in Solid State Sciences 11, 87 (1980).
7. N.Newberger, Electronic Materials, 2, New York, 1971.
8. A. Aronov, J. Exp. Theo. Phys. 103, 401 (1991).

PART V

III-V Nitrides and Other III-V Compounds

CONDUCTIVITY CONTROL OF AlGaN, FABRICATION OF AlGaN/GaN MULTI-HETEROSTRUCTURE AND THEIR APPLICATION TO UV/BLUE LIGHT EMITTING DEVICES

I. AKASAKI AND H. AMANO

Nagoya University, Department of Electronics, Furo-cho
Nagoya 464-01, Japan

Abstract

The method for controlling the electrical properties of n-type GaN and AlGaN have been established. Both GaN and AlGaN films having p-type conduction have been realized for the first time. High quality AlGaN/GaN multi-heterostructure showing clear quantum size effect has been fabricated. P-n junction type UV/blue LED with double heterostructure have been developed for the first time.

1. Introduction

In the last few years, the demand for the fabrication of compact and high-power short wavelength light emitter in the blue, violet and ultraviolet (UV) region, such as light emitting diode (LED) and laser diode (LD) has been increasing. Applications of such devices include a new compact and high-density optical storage system, a new full color display system and a new medical engineering system. For the achievement and fabrication of these new systems, the research and development of semiconductors having large band gaps, the so called wide-gap semiconductors should be necessary.

Aluminum gallium nitride ($Al_xGa_{1-x}N$: $0<x$) as well as gallium nitride (GaN) are the promising candidate as the material for fabrication of such a short wavelength light emitter, because they have direct transition type band structure with the band gap energy from about 3.39eV to 6.2eV at room temperature (RT). In contrast with other III-V compounds such as GaAs and InP, however, it had been fairly difficult to grow high quality epitaxial film with a flat surface free from cracks, because of the large lattice mismatch and the large difference in thermal expansion coefficient between epitaxial film and sapphire substrate.

In 1986, we succeeded to overcome these problems and to grow high quality GaN film with a specular surface free from cracks by the prior deposition of a thin AlN buffer layer in MOVPE growth of GaN. The electrical and optical properties as well as the crystalline quality can be remarkably improved at the same time [1-3]. By using such a GaN film, we achieved the

Mat. Res. Soc. Symp. Proc. Vol. 242. 1992 Materials Research Society

UV stimulated emission at RT by optical pumping for the first time. We achieved also the successful growth of $Al_xGa_{1-x}N$ with x up to 0.4, having smooth surface free from cracks on the sapphire substrate in the same way [3,4].

Silicon was found to act as donor in both GaN and AlGaN, and free electron concentration has been controlled from the undoped level up to mid 10^{18} cm^{-3} to 10^{19} cm^{-3}. It has been well known that undoped GaN shows n-type conduction, and p-type GaN had never been realized. In 1989, we succeeded for the first time to produce p-type GaN [5] and recently p-type AlGaN by low energy electron beam irradiation (LEEBI) treatment of Mg-doped film.

Furthermore, we have succeeded to fabricate AlGaN/GaN multi-heterostructures with good crystalline quality [6], from which quantum size effect has been clearly observed [7]. On the basis of these results, we develop the first p-n junction type UV/blue LEDs with AlGaN/GaN double heterostructure. In this paper, (1) conductivity control of GaN and AlGaN for both n-type and p-type, (2) fabrication and properties of AlGaN/GaN multi-heterostructure and (3) performance of the UV/blue LED consisted of AlGaN/GaN double heterostructure will be described.

2. MOVPE growth of high-quality GaN and AlGaN thin films on the sapphire substrate using AlN buffer layer and their properties

A horizontal type MOVPE reactor operated at an atmospheric pressure was used for the growth of both GaN and AlGaN film. Trimethylgallium (TMGa), trimethylaluminum (TMAl) and ammonia (NH_3, were used as source gases and hydrogen as a carrier gas.

Polished and etched sapphire crystals were used as substrate. The misorientation was less than 1°. In our process, before GaN growth, a thin AlN layer about 50nm thick was deposited at 600°C by feeding TMAl and NH_3 diluted with H_2. Then the temperature was raised to 1050°C, and single crystalline GaN film of several μm thick was grown.

The surface morphology of GaN film could be remarkably improved by the preceding deposition of the AlN as a buffer layer. GaN film with optically flat surface could be grown on the sapphire substrate covered with AlN buffer layer. On the contrary, the island growth occurred in the growth of GaN on the bare sapphire substrate surface.

X-ray rocking curves (XRC) measurement also revealed that GaN grown using the AlN buffer layer has high-quality. The full width at half maximum of the GaN film grown with the AlN layer is about 110 arcsec, which is the narrowest up to date in this material. While, that of the GaN film grown directly on the sapphire substrate is more than 1000 arcsec.

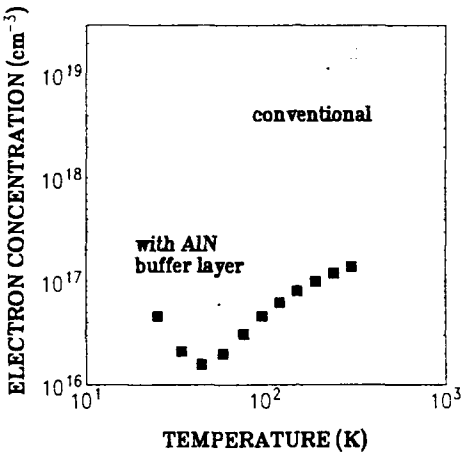


Fig.1(a) Temperature dependence of the electron concentration of undoped GaN film grown using the AlN buffer layer(■) and the GaN film grown directly on the sapphire substrate(□).

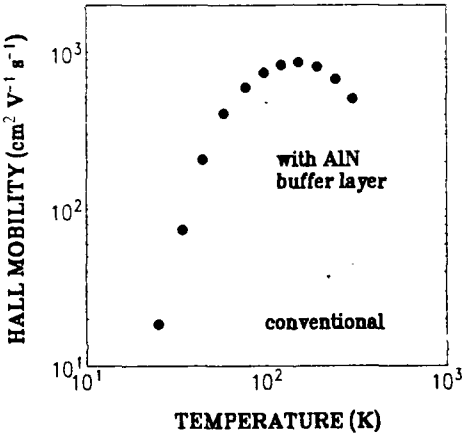


Fig.1(b) Temperature dependence of the Hall mobility of undoped GaN film grown using the AlN buffer layer (●) and the GaN film grown directly on the sapphire substrate(○).

Photoluminescence (PL) measurement also showed that luminescence property of the GaN film can be improved by using AlN buffer layer. In the PL spectrum at 4.2 K of GaN grown with the buffer layer, free exciton line (E_x) and the donor-bound exciton line (I_2) clearly appear, while emission bands in long wavelength region, which may be due to deep-level defects, are scarcely observed. On the other hand, emission bands in long wavelengths dominated in the spectrum of the GaN film grown directly on the sapphire substrate. Therefore, the deep level defects in our GaN film could be reduced.

Figure 1 shows the electrical properties of GaN film measured by Hall effect using van der Pauw method. The GaN film grown with the AlN buffer layer has n-type conductivity with an electron concentration of about 10^{17} cm^{-3} or $8x10^{16}$ cm^{-3} at RT, which is two or three orders of magnitude lower than that of GaN film grown directly on the sapphire substrate. The electron mobility is about 500 $cm^2/V \cdot s$ at RT, which is one order of magnitude higher than that of directly grown film .

All these results (surface morphology, XRC, PL and electrical properties) clearly show that by the preceding deposition of the AlN buffer layer, the electrical and optical properties as well as the crystalline quality of GaN film can be remarkably improved.

The effectiveness of the AlN buffer layer on the improvement of crystalline quality of AlGaN film has recently been proved [3,4], and the role of the buffer layer was discussed elsewhere [2,3].

We have also succeeded in observing the first RT stimulated emission from a GaN film grown using the AlN buffer layer, which was cleaved in a 2 mm stripe and excited by a pulsed nitrogen laser. The threshold power for stimulated emission was found to be around 0.7 MW/cm^2 at RT. The detailed characteristics of this emission was reported elsewhere [8,9].

3. Conductivity control for n-type GaN and AlGaN films

The electron concentrations and resistivities of GaN and AlGaN can be easily controlled by changing silane flow rate. The figure 2(a) shows the results on GaN film, and figure 2(b) for $Al_{0.1}Ga_{0.9}N$ film. In both cases, the linear dependence of electron concentration on the source flow rate can be clearly observed, although only about one third of incorporated silicon is activated. The intensity of cathodoluminescence, which may be due to near band-edge emission increased with the increase of doping level of Si in both GaN and AlGaN films.

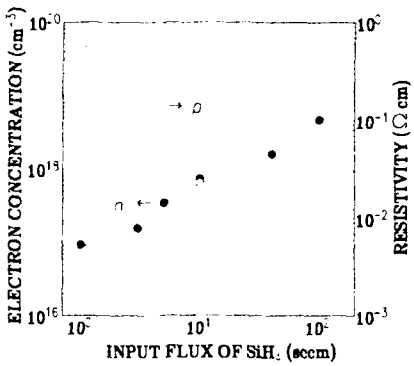


Fig.2(a) Dependence of the electron concentration and resistivity of GaN film at RT on the silane flow rate during growth.

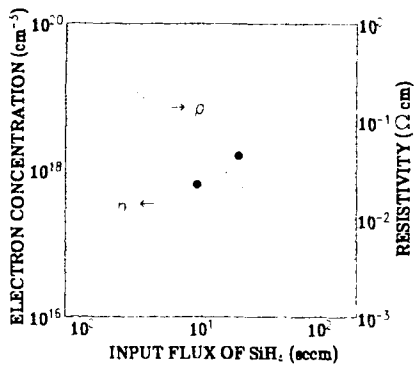


Fig.2(b) Dependence of the electron concentration and resistivity of $Al_{0.1}Ga_{0.9}N$ film at RT on the silane flow rate during growth.

4. Realization of p-type GaN and AlGaN films

Doping of Magnesium (Mg) was carried out during the growth of GaN film by supplying biscycropentadienylmagnesium (Cp_2Mg) as a Mg source gas. Compared to Zn, the vapor pressure of Mg is rather low, and/or the sticking coefficient of Mg at GaN surface is rather high. Therefore, Mg concentration in GaN changed linearly according as the supply flow rate of Cp_2Mg. And, this relationship was almost independent of the substrate temperature [10]. Thus, we can easily obtain the desired Mg concentration and its profile in GaN by controlling the supply flow rate of Cp_2Mg.

It is difficult to determine the type of conductivity of as-grown Mg-doped GaN, because the resistivity is too high (about $10^8\ \Omega \cdot cm$). The Mg-doped GaN tended to become low resistivity by low energy electron beam irradiation treatment. (We call this treatment as LEEBI-treatment for short [5]). And it is rather easy to measure the Hall effect. It was found that the film tends to show p-type conduction by the LEEBI treatment. The treatment condition is summarized in Table 1.

Table 1 LEEBI treatment condition

Accelerating voltage:3~30KV
Emission current:120 μA
Beam spot size:60 μmϕ
Sample temperature :RT

An ohmic contact to the LEEBI treated Mg-doped GaN layer was achieved by depositing Au. RT hole concentration up to about 1.4×10^{17} cm^{-3} could be achieved. Therefore, it can be said that Mg behaves as an acceptor impurity in GaN. For the reason of the change of the electrical properties, we speculate that some interstitial Mg atoms replace Ga atoms at lattice sites by the LEEBI treatment, although the detailed mechanism is not clear at present.

In the PL spectrum at 4.2 K of the Mg-doped GaN with Mg concentration less than $2\times10^{19}cm^{-3}$, D-A pair emission and its LO-phonon replica can be clearly observed. On the contrary, in the spectrum of undoped GaN, D-A pair emission did not appear, and E_x-line and I_2-line appeared. Therefore, the origin of the D-A pair emission is thought to be residual donor (D) and doped Mg acceptor (A). This also shows that Mg acts as an acceptor impurity in GaN.

The activation energy of Mg acceptor was found to be about 155~165meV, which is somewhat shallower than that of Zn (210meV) [11].

As seen in the spectra of Mg-doped GaN with Mg concentration higher than 5×10^{19} cm^{-3}, a strong blue emission appears even at RT. Therefore, it should be emphasized that Mg forms the blue luminescence centers as well as acts as an acceptor in GaN.

By the LEEBI treatment, the intensity is remarkably enhanced keeping the shape of the spectrum. The Enhancement of blue luminescence intensity suggests the increase of Mg-related blue luminescence centers, which may be due to the redistribution of Mg atoms by the LEEBI treatment. The detailed mechanism for such effects of the LEEBI treatment on the electrical and luminescence properties of Mg-doped GaN is not clarified at present.

Figure 3 shows that "the LEEBI effect" really appears in Mg-doped $Al_{0.1}Ga_{0.9}N$ film. The intensity of purple-blue emission becomes about twenty-times stronger than that of as-grown sample.

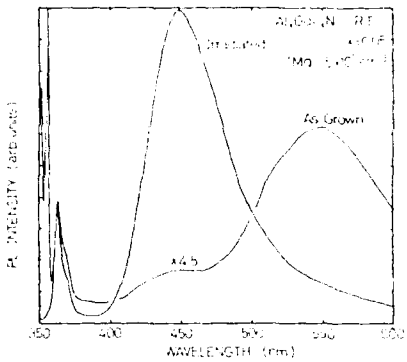


Fig.3 PL spectra of the as-grown AlGaN film and the LEEBI treated AlGaN film.

5. Fabrication of AlGaN/GaN multi-heterostructures and their properties

For the fabrication of AlGaN/GaN heterostructure, we studied widely the growth of AlGaN on GaN film grown on sapphire covered with the AlN buffer layer. As an important result, we found that high quality AlGaN/GaN heterostructure with smooth surface free from cracks can be successfully grown, when the thickness of AlGaN layer is thinner than 0.3 um and its molar fraction of AlN is less than 0.1 [6,7].

Figure 4 shows X-ray rocking curve of (0004) diffraction of $Al_{0.1}Ga_{0.9}N$/GaN layered-structure with thickness 20 nm each. The main GaN peak is associated with the GaN underlayer, and others are with the layered-structure. This experimental result indicated by solid line agrees well with the calculated one, which is shown by broken line. The line width of the zero-order peak is nearly the same as that of the GaN underlayer (that is 2~3 arcmin). This indicates that the crystalline quality of the layered-structure is as good as that of the GaN underlayer.

The PL measurement showed the first observation of the quantum size effect from nitride-based heterostructure. In the relationship between the shift of the emission peak energy and the GaN well width, experimental results are in good agreement with the estimated quantum energy levels, which was calculated using Kronig-Penny model, assuming that $m_e=0.22m_o$ and $m_h=0.8m_o$. Band discontinuities were estimated according to Harrison's model (ΔEc: 168 meV, ΔEv: 12 meV) [12].

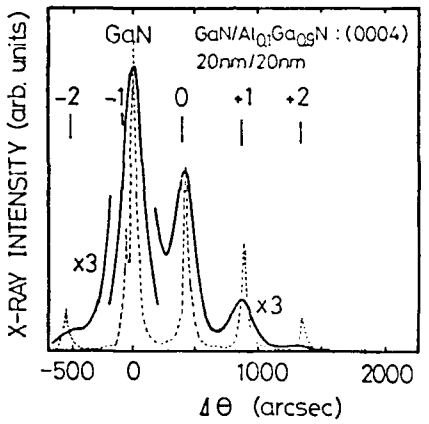


Fig.4 XRC of the AlGaN/GaN multi-heterostructure with each thickness of 20 nm.

6. Development and characteristics of p-n junction type UV/blue light emitting devices with AlGaN/GaN double heterostructures

By using double heterostructure, the threshold power for UV stimulated emission by optical pumping can be decreased markedly about one sixth by carrier confinement as shown in figure 5.

Figure 6 shows the schematic structure of the newly developed p-n junction type AlGaN/GaN double heterostructure diode. Typical DC-EL spectrum at RT observed from the newly developed double heterostructure is shown in figure 7. The blue emission peaking at 423 nm is due to the transition in Mg-related centers in the p-AlGaN layer. And the UV emission peaking at 372 nm is thought to originate from band to band transition in GaN. With the increase of the injection current, the intensity of the latter emission may overcome that of the blue one in the same way of the homo-junction GaN p-n diode [13]. Typical I-V characteristic of these diodes is shown in figure 8. As shown in the figure, large current density of 850 A/cm^2 can be obtained.

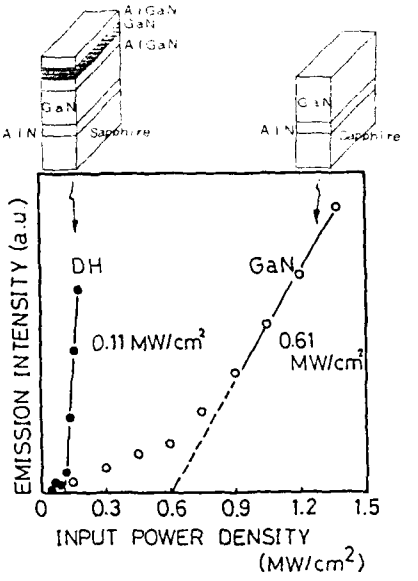


Fig.5 Total output power of AlGaN/GaN double heterostructure and GaN film excited with various power of pulsed nitrogen laser light.

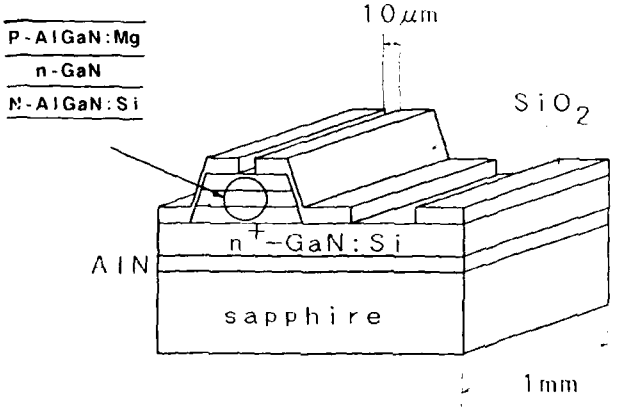


Fig.6 Schematic structure of the newly developed p-n junction AlGaN/GaN double heterostructure.

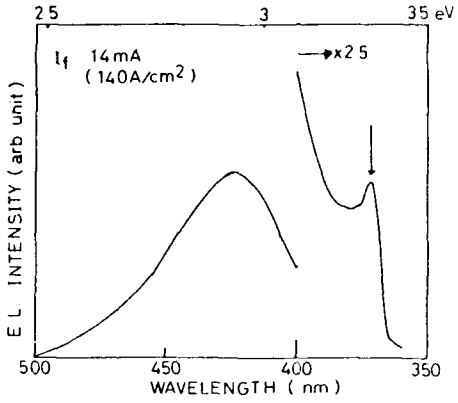


Fig.7 DC-EL spectrum of the newly developed p-n junction AlGaN/GaN double-heterostructure.

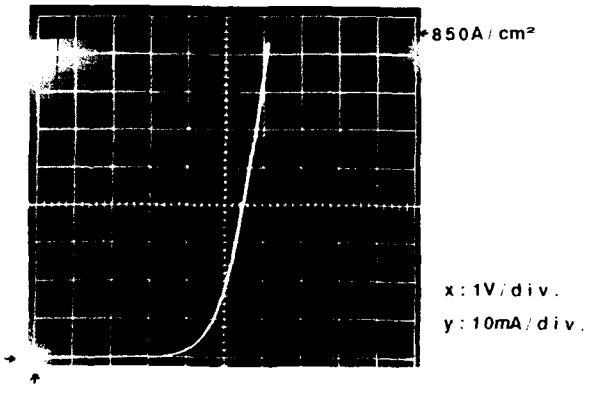


Fig.8 Typical I-V characteristic of the newly developed p-n junction AlGaN/GaN double-heterostructure.

7. Summary

By MOVPE using the AlN buffer layer, crystalline quality as well as the electrical and optical properties of GaN and AlGaN films was remarkably improved. Conductivity control for n-type GaN and AlGaN films has been achieved. Both GaN and AlGaN films having distinct p-type conduction have been realized for the first time (by Mg doping and following LEEBI treatment). High quality AlGaN/GaN multi-heterostructure showing quantum size effect have been fabricated. This is the first time observation of quantum size effect from nitride-based wurtzite-type quantum well structure. P-n junction type UV/blue light emitting devices with AlGaN/GaN double heterostructure have been developed.

Acknowledgment

The authors wish to thank Mr.M.Kito, Mr.H.Murakami and Dr.K.Itoh for preparation of the sample. The authors are also indebted to Prof.K.Hiramatsu and Prof.N.Sawaki for valuable discussions. This work was partly supported by "The Mitsubishi Foundation" and the Grant-in-Aide from the Ministry of Education, Science and Culture of Japan for Scientific Research on Priority Areas "Crystal Growth Mechanism in Atomic Scale".

References

[1]H.Amano, N.Sawaki, I.Akasaki and Y.Toyoda; Appl.Phys.Lett., 48(1986)353.

[2]H.Amano, I.Akasaki, K.Hiramatsu and N.Koide; Thin Solid Films, 1963(1988)415.

[3]I.Akasaki, H.Amano, Y.Koide, K.Hiramatsu and N.Sawaki; J. Cryst.Growth,98(1989)209.

[4]Y.Koide, N.Itoh, K.Itoh, N.Sawaki and I.Akasaki; Jpn.J. Appl.Phys.,27(1988)1156.

[5]H.Amano, M.Kito, K.Hiramatsu Jpn.J.Appl.Phys., 28(1989) L2112.

[6]K.Itoh, K.Hiramatsu, H.Amano and I.Akasaki;J.Cryst.Growth, 104(1990)533.

[7]K.Itoh, T.Kawamoto, H.Amano, K.Hiramatsu and I.Akasaki; Jpn.J.Appl.Phys.,30(1991)1924.

[8]H.Amano, T.Asahi and I.Akasaki; Jpn.J.Appl.Phys.,29(1990) L205.

[9]H.Amano, T.Asahi, M.Kito and I.Akasaki; J.Lumin.,48&49 (1991)889.

[10]H.Amano, M.Kitoh, K.Hiramatsu and I.Akasaki; J. Electrochem.Soc.,137(1990)1639.

[11]I.Akasaki, H.Amano, M.Kito and K.Hiramatsu; J.Lumin.,48&49 (1991)666.
[12]W.A.Harrison; Electronics structure and the properties of Solids,W.H.Freeman and Company, San Francisco(1980)253.
[13]H.Amano, M.Kitoh, K.Hiramatsu and I.Akasaki; Inst.Phys. Conf.Ser.,106(1989)725.

OPTICAL AND ELECTRONIC PROPERTIES OF THE NITRIDES OF INDIUM, GALLIUM AND ALUMINIUM AND THE INFLUENCE OF NATIVE DEFECTS

T.L. Tansley and R.J. Egan
Semiconductor Science & Technology Laboratories
Physics Department, Macquarie University
NSW 2109 Australia

Abstract.

The nitrides of Al, Ga and In are III-V compound semiconductors with properties more closely akin to those of the II-VI system and applications problems of similar type. All three have wide, direct band gaps and relatively light, therefore mobile, electrons. Less encouragingly, native point defects appear to play a significant role in both optical and electronic properties.

Both experiment and theory point to a triplet of donor states associated with the nitrogen vacancy, with deep compensating centres deriving from antisite defects. The ionic radius of the metal then seems to determine the conductivity of as-grown material, indium is reluctant to occupy nitrogen sites while aluminium does so readily and gallium is equivocal. Thus the upper donor level of InN is not depleted and n-type behaviour is always observed, the equivalent level in AlN is always overcompensated and the remaining donor levels are too deep to contribute free electrons at normal temperatures so that the material is consistently insulating. GaN may be n-type or semi-insulating since compensation ratios either side of unity appear to be possible, depending on the method of growth.

In this paper we review the evidence, both optical and electrical, for the existence, nature and energetic location of the four basic point defects in each nitride, noting in particular that all four broad luminescence bands in GaN:Zn can be accounted for by the presence of nitrogen on gallium sites and of nitrogen vacancies.

I. Introduction

The nitrides of the three group III metals Al, Ga and In have received attention varying between the sporadic and the sustained, as specific applications have been promoted, and as a sequence of material growth and processing strategies have emerged.

Indium nitride is an n-type semiconductor with a band gap in pure material of 1.95 eV[1], often Moss-Burstein shifted to about 2.05eV in the more commonly produced samples of high electron concentration[2-6]. The low conduction band density of states responsible for this shift suggests that the conduction electron is light and its mobility therefore high, an inference substantiated in experimental values[7] as high as 4×10^3 cm^2 V^{-1} s^{-1} in relatively poor polycrystalline samples of $n \sim 10^{17}$ cm^{-3}. This combination of wide gap and high electron mobility suggests that useful devices, including those luminescent in the orange spectral region, can be constructed eventually, although we are unaware of any reports of efficient photon-emission or of successful counter-doping of this compound.

The blue electroluminescence characteristic of gallium nitride has been of interest over a number of years[8-13], revived more recently as viable vapour phase epitaxial growth methods have been developed[14-15]. Although direct band-to-band recombination delivers an ultraviolet (365nm) photon of 3.39eV, broad-band emission is found over much of the visible spectrum[16] depending upon a combination of extrinsic influences including choice of dopant and growth method. As-grown material may be semi-insulating or n-type, although doping with magnesium is reported[17,18] to produce genuinely p-type material.

Aluminium nitride, in common with the gallium compound, has attracted interest as a result of both insulating and piezoelectric properties[19]. The band gap is 5.9 eV, although this may be reduced by a few percent if stoichiometry is not maintained, or increased by a similar margin when oxygen is present as the oxynitride[20]. AlN has excellent insulating properties, low dielectric loss and dispersion of permittivity[21], and can be prepared at low temperature on GaAs substrates[22] leading to the possibility of metal-insulator-semiconductor structures entirely within the III-V system[23-25].

Each of these potential applications requires, amongst other factors, an understanding of the nature of native defects in each material and in particular the charge states and energies of electron levels generated by the four residual point defects (metal vacancy V_M, nitrogen vacancy V_N and antisite defects M_N and N_M) likely to persist even under optimal growth conditions. Such states may trap carriers, either presenting a space-charge particularly undesirable in MIS structures or increasing the density of point charges with a consequent degradation of mobility in conductive material. Deep levels, particularly these close to mid-gap offer preferential recombination routes, frequently non-radiative and thus inimical to luminescent devices. Since autocompensation, involving the interaction between dopant atoms and doping-generated point defect compensators, has limited the range of applications of direct wide-gap II-VI compound semiconductors, it is possible that similar interactions may be influential in the III-N system. It is therefore germane to examine the substantial amount of experimental evidence for the existence and nature of point defect levels in these compounds, in the light of theoretical guidance provided by Jenkins and Dow[26].

Since calculated electronic structures show the same commonality of features across all three compounds as do a broader range of properties[27], we remark first, on general theoretical and experimental approaches.

II Theoretical Considerations

II.1 Hydrogenic centres

Where the potential surrounding the defect varies only slowly, an effective mass treatment can be employed. The energy levels are given in terms of the effective Rydberg energy R_H by:

$$E = R_H / n^2 , \quad \text{where } R_H = q^2 m^* / 2(4\pi\varepsilon_r)^2 \hbar^2 \qquad ...(1)$$

This result is valid only for shallow, single donors or acceptors in non-polar semiconductors with spherical constant energy surfaces close to the band extrema. Only the last of these conditions is met in III-N compounds and only the nitrogen vacancy, V_N, is sufficiently shallow in all three to be susceptible to a hydrogenic treatment. Substituting Zq for q for a multiple donor of degeneracy Z extends the model successfully to excited states while underestimating the ground state

energy[26] . Extension to polar materials requires the inclusion of the coupling between electron and optical phonon modes. The collective, polaron, excitation has mass m_p^* given, in the usual nomenclature, by:

$$m_p^* = (1 + \alpha/12)/(1 - \alpha/12) \text{ , where } \alpha = \left(q^2/4\pi\varepsilon_0 h\right)\left(\varepsilon_\infty^{-1} - \varepsilon_s^{-1}\right)/\left(m^*/2\hbar\omega\right)^{1/2} \quad ...(2)$$

Here ε_∞ and ε_s are the high and low frequency relative permittivities respectively.

Table I brings together calculated hydrogenic ground and first excited energies for hydrogenic donors in the III-N compounds and relevant parameters. Equivalent data for GaAs and InP are included for comparison. The correct choice of a value for permittivity, ε_r, in equation 1 is made, following Ridley[28], by observing that $R^*_{H2P} > \hbar\omega_{TO}$ for all three nitrides so that $\varepsilon_r = \varepsilon_\infty$.

The photoionisation process which takes an electron from a neutral hydrogenic donor into a parabolic conduction band is characterised by an absorption coefficient α_H which depends on photon energy $\hbar\omega$ as:

$$\alpha_H \propto \left(\hbar\omega - E_D\right)/(\hbar\omega)^5 \quad ...(3)$$

where E_D is the excitation threshold energy.

Equation (3) represents a narrow absorption peak whose maximum is at an energy $5E_D/4$. In a typical experiment, the threshold is much more sensitive than the peak to thermal broadening, so the latter is used to estimate the former.

In most semiconductors the mobility of a thermally generated free electron is sufficiently insensitive to temperature to allow a direct interpretation of donor depth from temperature dependence of conductivity $\sigma(T)$, since:

$$\sigma(T) = \sigma_0 \exp(-E_D/kT) \quad ...(4)$$

The value of E_D obtained experimentally from equations (3) and (4) may not coincide since the techniques do not measure the same quantity. There may be a significant difference in the strongly polar lattices of the nitrides, for which available experimental data are discussed in section III .

TABLE I Data for modified-hydrogenic calculations

All energies are in meV. Suffixes to Rydberg constants are: 1 and 2, singly and multiply charged donor states; O and P, unmodified and polaron-modified values.

	ε_∞	ε_s	m*/m	$\hbar\omega_{LO}$	$\hbar\omega_{TO}$	R^*_{H1O}	R^*_{H2O}	R^*_{H1P}	R^*_{H2P}	α	m^*_{pol}
InN	8.4	15.3	0.12	89	57	23	90	24	94	0.24	1.04
GaN	5.5	10	0.20	79	70	90	360	97	390	0.48	1.083
AlN	4.7	8.5	0.33	97	82	200	800	216	890	0.65	1.114
GaAs	10.9	13.18	0.067	30	32	5.24	-	5.33	-	0.088	1.015
InP	9.5	12.35	0.08	39	43	7.14	-	7.29	-	0.127	1.021

II.2 Quantum defects and deep levels

Even if core effects cannot be ignored, an effective mass approach may still be appropriate provided a quantum defect ground state wavefunction is used. Here the absorption coefficient, α_Q , for a neutral centre, a deeper occupied donor for example, becomes:

$$\alpha_Q \propto (\hbar w - E_Q)^{3/2} / (\hbar w)^3 \qquad ...(5)$$

A significant feature of this result is that the energy at the absorption peak is twice that at the threshold E_Q .

The energies associated with deep levels, where the effective mass approximation breaks down completely, can be determined using techniques not unlike band structure calculations. Jenkins and Dow[26] and others[29,30] have employed a technique attributed to Hjalmarson et al.[31] in which empirical tight-binding theory is used to determine an effective defect potential V, but the effects of long-range coulombic potentials and charge splitting of the levels are neglected. It is said that uncertainties of a few tenths of an eV result[26], clearly of experimental significance in the case of levels in the proximity of the band edges.

Cross sections for the photoionisation of deep levels depend upon whether the impurity state is $|s>$-like or $|p>$-like. The relevant absorption coefficients take the form:

$$\alpha_{DS} \propto \left(\hbar\omega - E_{DS}\right)^{3/2} / \hbar\omega \qquad (|s>) \qquad ...(6)$$

$$\alpha_{DS} \propto (\hbar\omega - E_{DP})^{1/2} / \hbar\omega \qquad (|p>) \qquad ...(6b)$$

Since; a) deep-level threshold energies are large, by definition, and b) densities of states away from the band extrema cease to be parabolic, the likely range of usefulness of (6) is confined to the vicinity of the experimental absorption edge.

III Experimental Data

In comparison with other III-V compounds, basic data on the optical and electronic properties of InN and AlN are sparse while GaN has been more widely studied. Much of the experimental work has involved polycrystalline thin films with large surface area to volume ratios in which surface states play an important role. Single crystal GaN and AlN have been studied but not specifically for defect properties. Recent advances in deposition of GaN films[15,18,32,33,34], in particular by molecular beam epitaxy (MBE), and metalorganic chemical vapor deposition (MOCVD) may permit the resolution of some of the features of defect behaviour.

In the following discussion of experimental results, data are quoted for material prepared by a variety of techniques, often with little detail reported on either the method or the micromorphology of the product. Since these are crucial to the determination of defect content, it is not possible to speculate in many cases whether the defects ascribed to particular energy levels are plausible. Our previously published results[1,7,27] have all been obtained on radio frequency reactively sputtered (RFRS), polycrystalline films. New results appearing here are from films grown by either RFRS or laser activated chemical vapour deposition (LCVD)[22].

Each of the nitrides is also susceptible to oxygen contamination on exposure to atmosphere. In the case of InN a few surface monolayers are converted to the oxide[35] while absorption bands at 4.45 and 4.95 eV in AlN have been ascribed to oxygen[36]. The problems are most acute in AlN where an oxygen solubility limit of 8% is reported[37] and both the oxide and oxynitride may occur during growth unless strict precautions are taken for the exclusion of the impurity from both deposition system and precursors[20,22].

A survey of the room temperature optical absorption spectra of InN, GaN and AlN in the energy range 40 meV to 6 eV shows the three compounds to have a number of features in common: a) direct band-to-band absorption edges, b) band edge tails and mid-gap absorption features of extrinsic origin and associated with crystal defects, and c) optical phonon absorption structure in the infrared.

Each of the compounds additionally shows at least one electron trap capable of thermal excitation into the conduction band over some temperature range.

Band-to-band absorption in polycrystalline RFRS film samples[27] is typical of direct Γ ($\Gamma_6^v - \Gamma_1^c$ in this case) transitions and yields minimum transition energies of 1.94 eV , 3.40 eV and 5.94 eV for InN , GaN and AlN respectively. The value for InN , which shows a significant Moss-Burstein shift above the low electron concentration limit of 1.89 eV[1] , is for a sample of $n \approx 10^{19}$ cm^{-3}. We now discuss the levels introduced by the native defects in each of the nitrides.

III.I Indium nitride

InN has received very little attention because of the difficulty inherent in the preparation of stoichiometric samples. High mobility material with electron concentrations below 10^{17} cm^{-3} at room temperature has been prepared by RFRS with balanced target nitridation[38]. Figure 1 identifies the five distinguishable energy levels observed in the gap and further includes the result of the hydrogenic calculation from table I and the deep-level calculations of Jenkins and Dow.

A shallow level appears as a shoulder at 50 meV on the 60 meV infrared absorption peak associated with the LO phonon[27]. The threshold energy of 40 meV agrees well with the 45-50 meV thermal activation energy measured in samples with carrier concentration between 7×10^{16} cm^{-3} and 10^{17} cm^{-3} at room temperature[39]. This group of samples reached an exhaustion region below 150 K with n in the range 2.5 to 7 x 10^{16} cm^{-3}. No further variation in concentration was observed down to 25 K, a temperature at which $kT \approx 2$ meV , the absence of carrier freeze-out implying an additional donor-like level very close to , or resonant with, the band edge.

An important feature in the absorption spectrum of InN is a broad band centred at about 0.2eV, and with a full width at half maximum (FWHM) of about 0.25 eV[39], which has been interpreted as either a deeper donor level or a compensating acceptor[26,27,39]. The width of this peak precludes detailed analysis as a strictly hydrogenic state whilst its shallowness suggests that a deep-level approach is equally inappropriate. Excitation thresholds are obtained by plotting the quantity $\alpha^{2/3}(\hbar w)^2$ vs $\hbar\omega$ in accrordance with equation 5 we have found excitation thresholds of 0.155, 0.215 and 0.255 eV in three samples of room temperature electron concentration 5 x 10^{16}, 1 x 10^{18} and 1 x 10^{19} cm^{-3} respectively. The energies of peak absorption, are 0.31, 0.37 and 0.41 eV respectively and threshold and peak energies both increase with electron concentration at a rate compatible with the filling of

conduction band states. The shift in absorption edge indicates a low-concentration limit of about 0.15 eV for the threshold energy.

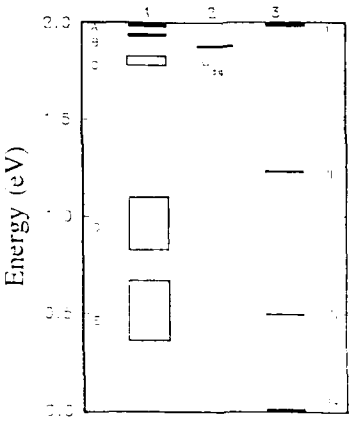


Figure 1 Distribution of defect levels in the band gap of InN. The states in column I are those reported from experimental studies and fall into five groups, A to E. Column 2 shows the result of donor-level calculations in the modified-hydrogenic approximation from Table I. Column 3 data are the electron states calculated in reference 26 for the following defects: I=V_N , II=In_N , III=N_{In} , IV=V_{In} .

Evidence thus points to a relatively deep donor level at about 150 meV below the conduction band with a second level at 40 meV. The energy of the former is close to the predicted hydrogenic ground state for the double donor associated with the nitrogen vacancy and within the range predicted by deep-level calculations[26] Details of its absorption line shape are better described, however, by a quantum-defect analysis intermediate between these two approaches. The shallower level becomes identifiable as elevated by coulomb interaction when the donor is doubly occupied.

The persistence of a significant electron concentration down to temperatures where kT is of the order of 2 meV indicates that the prediction of a third donor level, resonant with the conduction band, is also correct. Finally we note that absorption strength within this band increases with electron, and therefore donor, concentration[39] as the above interpretation would require.

When free carriers are excited in n-InN, charge balance requires $n \approx N_D^-$. However, mobility measurements indicate that ionised impurity scattering involves a component due to charged, compensating acceptors. Compensation ratios N_D^- / N_A^- between about 1.3 and 3 have been inferred[7] . This evidence suggests the involvement of the In_N , V_{In} and N_{In} defects, each of which includes hole states which would be empty (of holes) and therefore carry a negative charge when the fermi level lies close to the conduction band edge. Two absorption features, appearing as longer wavelength tails on the band-to-band absorption edge, can be identified as follows.

In low-doped material, $n < 2 \times 10^{17}$ cm^{-3} plots of α^2 vs $\hbar\omega$ yield straight lines[39] with thresholds E_{DP} between 0.9 and 1.2 eV in accordance with the prediction for E_{DP} |p> like states of equation (6b). The apparent threshold energy varies strongly with electron concentration for this group of samples with the shallowest (0.9 eV) occuring in $n = 2.3 \times 10^{17}$ cm^{-3} material and the deepest (1.2 eV) in our lightest doped sample at $n = 1.1 \times 10^{17}$ cm^{-3}.

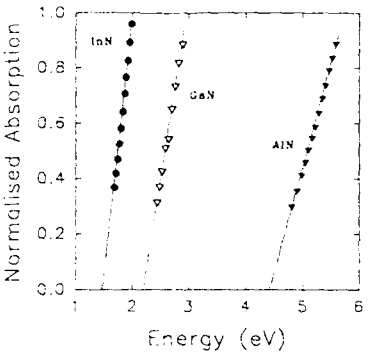


Figure 2 Absorption data for deep levels in InN, GaN and AlN. In accordance with equation 6a, the absorption coefficient α is plotted as $\alpha^{2/3}(\hbar\omega)$ against $\hbar\omega$ and yields threshold energies of about 2/3 E_G in each case.

In higher doped samples, $n > 5 \times 10^{17} cm^{-3}$, an absorption tail with threshold energies between 1.35 and 1.65 eV , and no systematic variation with electron concentration, is observed. This result is obtained from linear plots of $\alpha^{2/3}(\hbar\omega)vs$, $\hbar\omega$, an example with $E_{DS} = 1.5\,eV$ is shown in figure 2 along with similar levels in GaN and AlN, and indicates the involvement of $|s>$ -like states as shown by equation 6a.

These two defect bands may be associated with the calculated[26] In_N levels at about 0.8 eV and deeper N_{In} levels at about 1.5 eV. We note, however, that low electron concentrations are obtained experimentally by increasing nitrogen content in order to minimise V_N donor concentrations, at the same time increasing N_{In} . Similarly, reduced nitrogen concentration yields higher electron concentrations brought about by the increase in V_N while commensurate with this would be an increase in M_N . The experimental 1eV level in low-doped material is therefore more plausibly associated with the presence of N_{In} while the deeper 1.5eV level can be associated with its converse In_N.

III.2 Gallium Nitride

GaN, with a bandgap of 3.4 eV has proven to be rather easier to prepare than InN and a good deal of information on defect levels has been gathered. This is collected with relevant calculated values in figure 3. Shallow donor levels have been reported in GaN with energies 10-40 meV[40-43] (group A) and 110-115 meV[41,43,44] (group B) both from the temperature dependence of carrier concentration and optically. Single reports of miscellaneous energy levels in this region also exist although, in general, their nature has not been posited. Vavilov et al.[45] suggest either impurities or native defects to be responsible for the 110meV level, considering also the possibility of absorption by excitons although these are now known to be considerably shallower. Tansley et al.[27] ascribed these levels to nitrogen vacancies. Thermal activation analysis of their insulating GaN reveals a donor (group C of fig. 3) the depth of which varies between 0.23 eV[43] and 0.39 eV[44] and is generally coincident with a modified hydrogenic estimate of about 0.39 eV (table I). We therefore suggest that the three electron states associated with V_N in GaN are located at about 30 meV, 100 meV and 0.4 eV below the conduction band.

A deep level is observed in thermal activation to be between 0.8 eV and 1.1 eV below the conduction band edge[41,43,44,46] (group D of fig. 3) and has been variously attributed to gallium vacancies or carbon impurities. A better interpretation is that the level represents the nitrogen antisite defect predicted by Jenkins and Dow.

The deep trap (group E of fig. 3) which we observe as a band tail absorption feature[27] has a threshold in the range 2.3-2.7 eV when plotted as an $|s>$like level. An example is included in figure 2. The proximity of the level to the 2.8 eV prediction for Ga_N of Jenkins and Dow suggests a correspondence.

A level at 3.264 eV (F) has been identified[12,,47,48] (by photoluminescence of doped single crystal GaN) to be a result of gallium vacancies and agrees well with the location predicted by Jenkins and Dow.

Much of the detail available from luminescence spectroscopy of GaN is concerned with samples including at least one of: i) heavy doping, ii) high compensation levels and iii) non-ideal crystallinity. It is clear from a survey of the published data that many spectral features are independent of the introduced species and therefore involve native defects.

Edge emission at room temperature and in undoped material is at 365nm (3.39eV), an excitonic photoluminescence peak displaced by about 30meV from the direct band to band transition energy. Study of this feature at lower temperature has furnished much detail on exciton structure in GaN[45,49].

The introduction of zinc as a compensating centre generates a broad blue emission peak centred at about 2.92eV[47], indicating a recombination centre at about 470meV above the valence band. Extinction of this peak at higher temperatures has a dependence suggesting a relaxation energy of about 330meV for this centre acting as a hole trap in thermal exhaustion. Coincidentally, the introduction of phosphorus as an alternative compensator to zinc yields almost identical photon and hole emission energies[51].

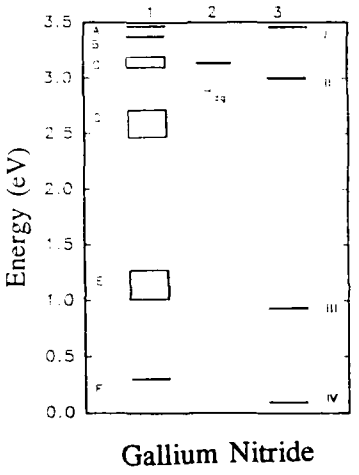


Figure 3 Distribution of defect levels in the band gap of GaN. The states in column I are those reported from experimental studies and fall into six groups A to F. The gallium vacancy, F, at E_G-3.264 eV is often seen in luminescence studies. Column 2 shows the result of donor level calculations in the modified hydrogenic approximation from Table I. Column 3 are the electron states calculated in reference 26 for the following point defects: I=V_N, II=N_{Ga}, III=Ga_N, IV=V_{Ga}.

In addition to the blue peak, GaN:Zn emits broad bands in the green (centred at about 2.6eV), orange-yellow (2.2eV) and red (1.8eV) regions[16,52]. Whilst the 2.6eV band requires Zn (or other similar) compensation, the 2.2eV emission occurs in VPE grown material in which carbon has precipitated[52]. Most significantly, this band has been observed in samples implanted with no less than thirty five atomic species[54] , clear evidence of its defect-related nature. The red emission band is variously reported as centred between 1.65 and 1.85eV, is also certainly defect-related but appears to have some dependence upon the impurity species introduced[54] .

A possible scheme for the involvement of the defects identified in figure 3, and in view of the above discussion, is suggested in figure 4. Band to band emission at 3.39eV (transition I) is superseded by preferential recombination via the compensator when zinc is introduced (II), yielding blue 2.92eV luminescence and locating the zinc level at about E_V+470meV. Since the nonstoichiometric nitrogen vacancy is always likely to present, donor-acceptor recombination is an obvious candidate for green emission (III). A peak centred at 2.56 eV would require V_N to be located about 360meV below the conduction band and this correlates well with both calculated and measured values for donor ground state energy.

The independence of orange-yellow emission (IV) of extrinsic dopants suggests the participation of a defect level at a depth of about 1eV and the experimentally observed centre, which we have suggested is associated with the N_{Ga} antisite defect, (figure 3) is an obvious candidate. Finally, we point out that the energy difference between this centre and those induced by a group of impurities, including P and Zn is about 1.75 eV. The location of this energy within the red emission band leads us to the tentative allocation (V) of red emission to a N_{Ga}- acceptor transition.

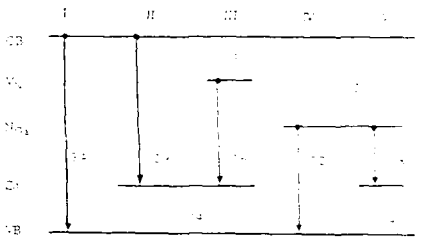


Figure 4 Suggested scheme for the involvement of native defects in the four principal luminescence bands (II:blue, III:green, IV:orange-yellow, V:red) in GaN, either Zn compensated or undoped. The ultraviolet emission (I) is direct band-to-band recombination-emission.

III.3 Aluminium nitride

A surprising volume of information is available on AlN although its popularity stems from its use in tribological and diffusion-resistant coatings rather than its semiconducting properties. Thus while it is relatively simple to prepare, until recently material quality has not been optimised for electronic properties and the values available are many and varied. Those attracting some concensus are collected in figure 5, along with the modified hydrogenic result and the predictions of Jenkins and Dow. Again the range of values reported for the donor excitation falls into three groups at about 170, 500 and 800-1000 meV [12,55,58]. Recently, we have reported a study of thermally activated conductivity in AlN[22], identifying a deep donor level at 790 meV. This agrees surprisingly well with the values predicted from the hydrogenic (800 meV) and deep level (500 and 1000 meV) approaches in view of the shortcomings of each in this energy range. By analogy

with InN and GaN it is therefore reasonable to assume that a donor triplet at about 200 meV, 500 meV and 900 eV is associated with V_N in AlN.

A deeper level with threshold 1.4-1.85 eV[18,19,57,59,60] has been repeatedly observed and can be identified with the calculated level of 1.6 eV for N_{Al}.

Deep level excitations have been observed with a range of thresholds. The band tail absorption analysed in the same way as for InN and GaN is included in figure 2 and has a range of thresholds between 3.4 and 4.5 eV. An example at 4.5 eV is shown, while other workers have reported 3.45 eV[33], 3.1 to 3.7 eV[59] and 4.2 eV[60]. Although the V_{Al} levels are predicted to lie within this range, the similarity of behaviour to the metal antisite defects in InN and GaN suggest that Al_N is responsible.

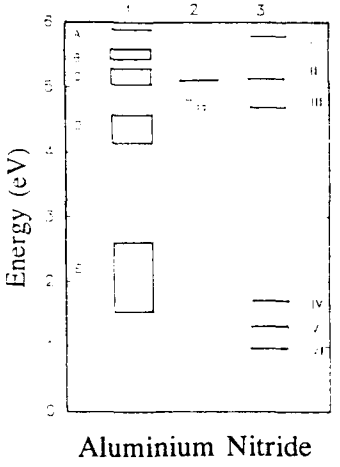


Figure 5 Distribution of deep levels in the band gap of AlN. The states in column 1 are those reported from experimental studies and fall into five groups A to E. Column 2 shows the results of donor level calculations in the modified hydrogenic approximation from Table I. Column 3 data are the electron states calculated in reference 26 for the following point defects: I=V_N, II=V_N, III=N_{Al}, IV=V_{Al}, V=V_{Al}, VI=Al_N.

IV Summary and Conclusions

Median values of experimentally reported defect-related levels in the three group III metal nitrides are brought together in table II. A common feature is the presence of a triplet of shallow, donor-like levels associated with nitrogen vacancies the depth of which increases for lighter occupants of the metal site.

The presence of deeper, compensating antisite defects becomes thermodynamically less probable[27] as the atomic mass difference between gpIII and gpV components increases. Thus InN, with very shallow and uncompensated donors is invariably an n-type semiconductor, while AlN, with a much deeper donor and high compensation levels, is invariably an insulator. GaN lies between these extremes of behaviour, as might be expected from a combination of a donor of moderate depth and some tendency to compensation, and the selection of growth method dictates the conductivity obtainable. It is worth noting that the available level of control in as-grown GaN is commensurate with the much greater effort thus far devoted to it.

TABLE II Probable Assignment of Experimental Data (median values)

Nitride	V_N, donor triplet (meV)			N_M (eV)	M_N (eV)	V_M(eV)	E_G(eV)
InN	0	40	150	1.05	1.5	-	1.89
GaN	30	110	390	0.9	2.3	3.264	3.4
AlN	170	500	900	1.7	4.5	3.8	5.9

Because it is a) heavily occupied and b) sufficiently shallow to have a large optical cross section for excitation to the conduction band, the 150meV donor level in InN provides a significant spectral absorption feature. Examination of this level in quantum-defect terms is fruitful and a revised threshold value[11] is obtained. Threshold energy varies with electron concentration in the conduction band in a way entirely compatible with the band-filling process responsible for the Moss-Burstein shift[36] in optical band gap. A low-electron-concentration limit of 150meV is deduced.

A hydrogenic treatment of donor levels yields results close to those obtained experimentally, surprisingly since both depth and complexity would suggest the approach to be inappropriate.

Deep levels in gallium and aluminium nitrides, in most respects, appear to have the general features predicted by Jenkins and Dow. The location of the N_{Al} antisite defect at about 1.7eV is well substantiated by a number of reports in the range 1.4-1.8eV whilst the N_{Ga} prediction of about 0.45eV is somewhat shallower than experimental data between 0.8 and 0.9 eV. The M_N antisite and V_M vacancy defects all lie within the bottom half of the respective bands and are manifest as absorption tails on direct band to band spectral edges. Here additional information on the $|s\rangle$ or $|p\rangle$ like character of the defect helps in identification.

The gallium vacancy observed in studies of GaN luminescence is at 3.26eV below the conduction band and close to the calculated value of about 3.3eV. The GaN band tail, and $|s\rangle$ like absorption feature with threshold in the 2.2-2.5eV range, can therefore be attributed to the Ga_N antisite defect with some confidence. Similar $|s\rangle$ like features appear in AlN between 3.4 and 4.5eV, a range embracing the predicted V_{Al} antisite defect, while its converse, Al_N, is calculated to lie somewhat deeper at about 5.2eV. Studies of the effect on optical properties of the in-diffusion of excess aluminium strongly suggest that the $|s\rangle$ like feature is associated with Al_N rather than V_{Al}, a view supported by its similarity to GaN.

The situation in InN is less clearly related to the predicted levels for In_N at 0.8eV and N_{In} at 1.5eV. We find, in a large number of reactively sputtered samples which we will call type I, an $|s\rangle$ like level between 1.35 and 1.65eV, experimentally similar to the M_N antisite defect in both gallium and aluminium nitrides and also at about 2/3 bandgap. Present in other samples is a type II feature, rather shallower at 0.9 to 1.2eV and of $|p\rangle$ like character which, if the above allocation is correct, is associated with N_{In}. These allocations are the reverse of the theoretical prediction[26]. Whether a sample is of type I or II depends upon the circumstances of its growth. Type I are typically prepared at higher growth rates and lower nitrogen pressure from less-nitrided targets, conditions which yield high nitrogen vacancies

concentrations evident in high electron densities, ($n>5 \times 10^{17}$ cm^{-3}) and more favourable to the generation of In_N antisite defects. Type II, on the other hand, are grown at lower rates, with higher nitrogen pressures and from fully nitrided targets. These conditions yield low V_N concentrations ($n<2 \times 10^{17}$ cm^{-3}) and are conducive to N_{In} antisite formation. Accordingly we conclude that the levels associated with nitrogen occupancy of indium sites is shallower, at about 1eV, than its converse at about 1.5eV.

Acknowledgements
This work is supported by the Australian Research Council (ARC) and the Australia Telecommunications Research Board (ATERB). Special thanks to coworkers Vincent Chin, Catherine Foley, Corinna Horrigan and Xin Li.

REFERENCES

1) T.L.Tansley and C.P.Foley, J.Appl.Phys. **59**,3241(1986).
2) H.J.Hovel and J.J.Cuomo, Appl.Phys.Lett. **20**,71(1972).
3) J.W.Trainor and K.Rose,J.Electron.Mater. **3**,821(1974).
4) N.Puychecherrier and M.Menoret, Thin Solid Films **36**,141(1976).
5) H.Takeda and T.Hada, Toyama Kogyou Kute Semmon Gakko Kiyo **11**,73(1977).
6) V.A.Tyagai, A.M.Evstigneev, A.N.Krasiko, A.F.Andreeva and V.Ya.Malakhov, Sov.Phys.Semicond. **11**,1257(1977).
7) T.L.Tansley and C.P.Foley, Electron.Lett. **20**,1066(1984).
8) H.G.Grimeiss, R.Groth and J.Maak, Z.Naturforsch. **15a**,799(1960).
9) H.G.Grimeiss and B.Monemar, J.Appl.Phys. **41**,4054(1970).
10) J.I.Pankove, E.A.Miller and J.E.Berkeyheiser, RCA Rev. **32**,383(1971).
11) R.Dingle, K.L.Shakleek, R.F.Leheny and R.B.Zetterstrom, Appl.Phys.Lett. **19**,5(1971).
12) M.Ilegems, R.Dingle and R.A.Logan, J.Appl.Phys. **43**,3797(1972).
13) R.D.Cunningham, R.W.Brander, N.D.Knee and D.K.Wickenden, J.Luminesc. **5**,21(1972).
14) H.Amano, N.Sawaki, I.Akasaki and Y.Toyoda, Appl.Phys.Lett. **48**,353(1986).
15) K.Naniwae, S.Itoh, H.Amano, K.Itoh. K.Hiramatsu and I.Akasaki, J.Cryst.Growth **99**,381(1990).
16) B.Monemar, O.Lagerstedt and H.P.Gislason, J.Appl.Phys. **51**,625(1980).
17) R.Madar, G.Jacob, J.Hallais and R.Fruchart, J.Cryst.Growth **31**,197(1975).
18) Hiroshi Amano, Masahiro Kito, Kazumasa Hiramutsu and Isamu Akasaki Jpn.J.Appl.Phys. **28**,2112(1989).
19) G.A.Cox, D.O.Cummins, K.Kawabe and R.H.Tredgold, J.Phys.Chem.Solids **28**,543(1968).
20) H.Demiryont, L.R.Thompson and G.J.Collins, J.Appl.Phys. **59**,3235(1986).
21) Li Xinjiao, Xu Zechnan, He Zujou, Cao Huazhe, Su Wuda, Chen Zhongcai, Zhon Feng and Wang Erguang, Thin Solid Films, **139**,261(1986).
22) Xin Li and T.L.Tansley, J.Appl.Phys. **68**,5369(1990).
23) M.Mizuta, S.Fujieda, T.Jitsukawa and Y.Matsumoto Inst.Phys.Conf.Ser. **83**,153,(1986).
24) K.Akimoto, I.Hirosawa, J.Mizuki, S.Fujieda, Y.Matsumoto and J.Matsui Jpn.J.Appl.Phys. **27**,L1401(1988).
25) Y.Mochizuki, M.Mizuta, S.Fujieda and Y.Matsumoto, Appl.Phys.Lett. **55**,1318(1989).

26) David W.Jenkins and John D.Dow, Phys.Rev.B. **39**,3317(1989).
27) T.L.Tansley. R.J.Egan and E.C.Horrigan, Thin Solid Films **164**,441(1988).
28) B.K.Ridley in "Quantum Processes in Semiconductors" Clarendon Press, Oxford 2nd edition (1988).
29) W.Y.Hsu, J.D.Dow, D.J.Wolford and B.G.Streetman, Phys.Rev.B **16**,1597(1977).
30) W.A.Harrison, ELectronic Structure and the Properties of Solids (Freeman, San Francisco, 1980).
31) H.P.Hjalmarson, P.Volg, D.J.Wolford and J.D.Dow, Phys.Rev.Lett. **44**,810(1980).
32) M.Asif Khan, J.N.Kuznia, J.M.Van Hove and D.T.Olson, J.Appl.Phys.Lett.58, 526 (1991).
33) T.Lei, M.Fanciulli, R.J. Molnar, T.D.Monstakas, R.J.Graham and J.Scanlon, Appl.Phys.Lett.59, 944 (1991).
34) W.E.Hoke, P.J.Lemonias and D.G.Weir, J.Cryst.Growth, 111, 1024 (1991).
34) C.P.Foley and J.Lyngdal. J.Vac.Sci.Tech.A **5**,1708,(1987).
35) J.Pastrnak and L.Roskovcova, Phys.Stat.Sol. **26**,591(1968).
36) F.S.Ohuchi and R.H.French, J.Vac.Sci.Technol.A. **6**,1695(1988).
37) T.L.Tansley and C.P.Foley, in Proceedings of the Third International Conference on Semi-Insulating III-V Materials, Warm Springs, Oregon, 1984, Edited by J.Blakemore (Shiva, London 1985) pp 497-500.
38) T.L.Tansley and C.P.Foley, J.Appl.Phys. **60**,2092(1986).
39) R.Dingle, D.D.Sell, S.E.Stokovski and M.Ilegems, Phys.Rev.B. **4**,1211(1971).
40) J.I.Pankove, S.Bloom and G.Harbeke, RCA Rev. **36**,163(1975).
41) R.Dingle and M.Ilegems, Sol.State Commun. **9**,175(1971).
42) B.Monemar and O.Lagerstedt, J.Appl.Phys. **50**,6480(1979).
43) J.C. Veseley, M.Shatzkes and P.J.Burkhardt, Phys,Rev.B. **10**,582(1974).
44) V.S.Vavilov, S.I.Makarov, M.V.Chukichev, I.V.Chetverikova, Fiz.Tekh.Poluprov. **13**,2153(1979): English Trans: Sov.Phys.Semicond. **13**,2153 (1979).
45) J.I.Pankove, H.P.Maruska and J.E.Berkeyheiser, Appl.Phys.Lett. **17**,197(1970).
46) M.Ilegems and R.Dingle, J.Appl.Phys. **44**,4234(1973).
47) O.Lagerstedt and B.Monemar, J.Appl.Phys. **45**,2266(1974).
48) B.Monemar, Phys.Rev.B **10**,676(1974).
49) J.I.Pankove, J.E.Berkeyheiser and E.A.Miller, J.Appl.Phys. **45**,1280(1974).
50) Toshio Ogino and Masahuri Aoki, Jpn.J.Appl.Phys. **18**,1049(1979).
51) J.I.Pankove, M.T.Duffy, E.A.Miller and J.E.Berkeyheiser, Luminescence **8**,89(1973).
52) Toshio Ogino and Masahuri Aoki, Jap.J.Appl.Phys. **19**,2395,(1980).
53) J.I.Pankove and J.A.Hutchby, J.Appl.Phys. **47**,5387(1976).
54) J.Edwards, K.Kawabe, G.Stevens and R.H.Tredgold, Sol. State Commun. **3**,99(1965).
55) Mizuho Morita, Kazuo Tsubouchi and Nobou Mikoshiba, Jpn.J.Appl.Phys. **21**,728(1982).
56) Akiko Kobayashi, Otto F.Sankey and John D.Dow, Phys.Rev.B. **28**,946(1983).
57) M.Gautier, J.P.Duraud and C.Le Gressus, Surface Science **178**,201(1986).
58) Jean Lagrenaudie, J.de Chimie Physique **53**,222(1956).
59) R.W.Francis and W.L.Worrell, J.Electrochem.Soc. **123**,430(1976)

SYSTEMATIC STUDIES ON MAGNETRON-SPUTTERED INDIUM NITRIDE

W. A. BRYDEN, S. A. ECELBERGER, J. S. MORGAN,
T. O. POEHLER AND T. J. KISTENMACHER
Applied Physics Laboratory, The Johns Hopkins University, Laurel, MD 20723-6099.

ABSTRACT

Extensive and systematic studies on reactive magnetron sputtering of InN thin films are summarized. The films have been deposited onto several types of substrates, with variations in such process parameters as deposition temperature, partial pressures of reactive and inert gases, sputtering power and gas flows. These films have been characterized by measuring their electrical, optical, structural and morphological properties. It has been shown that epitaxial growth of InN occurs on the basal plane of single-crystal (00.1) sapphire and (001) mica substrates and on the (111) face of cubic substrates such as silicon and zirconia.

Two principal problems currently limit the usefulness of thin films of InN. First, although epitaxy can be attained with the proper choice of substrate type and deposition temperature, the resulting film is an agglomerate of epitaxial grains -- not a single crystal. Second, all magnetron sputtered InN films prepared to date have low mobility and high carrier concentration (likely due to nitrogen vacancies). In an attempt to address these problems, experiments on the growth and characterization of sputtered InN films have been carried out and are discussed here with particular emphasis on seeded heteroepitaxial growth and the effects of film deposition temperature.

For example, it was found early that the growth of InN on the bare surface of several crystalline substrates at growth temperatures near 350°C results in a morphological transition that causes a degradation of semiconducting properties. The predeposition of an AlN seed layer inhibits this morphological transition and stabilizes a relatively high mobility state, but a still too high carrier concentration obtains. Further progress critically depends on optimizing the seeded heteroepitaxial growth technique in conjunction with the achievement of InN films with lower density of nitrogen vacancies.

INTRODUCTION

The Group IIIA nitrides (AlN, GaN and InN) are an isostructural family of semiconductors that hold great promise for optoelectronic applications in the visible and ultraviolet regions of the spectrum owing to their wide, direct bandgaps (6 eV, 3.4 eV and 2 eV respectively). The potential for high efficiency optoelectronic devices based on these semiconductors can be realized by optimizing the growth of each family member, controlling doping type and forming alloys (e.g., $Al_xIn_{1-x}N$) to be used in heterostructures. The growth of InN is particularly important for visible light photonic applications as it is the member of the family with the smallest energy gap. By alloying InN into either AlN or GaN the bandgap can be lowered to the 2-3 eV range, a critical

Mat. Res. Soc. Symp. Proc. Vol. 242. © 1992 Materials Research Society

range for making high efficiency visible light sources and detectors.

The early report [1] of deposition of InN by reactive sputtering with carrier concentration of $7x10^{18}$ cm^{-3} and mobility of 250 cm^2/V sec, followed later by the report [2] of growth of **polycrystalline** films with carrier concentration of 10^{16}-10^{17} cm^{-3} and mobility of ≈4000 cm^2/V sec by reactive rf-diode sputtering pointed out the efficacy of sputtering for the deposition of this semiconductor. Although the semiconducting properties of these films were very promising, the extremely long pre-sputtering and sputtering times, the polycrystalline structure of the films and the glass substrates employed were not compatible with the fabrication of modern devices, including those based on heterostructures and quantum wells. One of the long-range goals of the research reported on here is the preparation of **single crystal** films of InN by reactive magnetron sputtering for the investigation of intrinsic semiconducting properties and for eventual device applications. Unfortunately InN prepared in other laboratories, [3-7] including ours [8] universally has high carrier concentration ≈10^{20} cm^{-3} with concomitant low mobility < 100 cm^2/V sec.

The high carrier concentrations exhibited by InN films are believed to arise from nitrogen vacancies created during the growth process or from unintentional oxygen doping either during growth or following exposure to atmosphere. It is also quite conceivable that these two mechanisms could act cooperatively with the nitrogen vacancies making the material even more susceptible to oxidation. Unfortunately, severe experimental constraints arise from attempting to resolve these concerns. Oxygen must be rigorously excluded from the growth chamber and exposure of the sample to air prior to characterization should be avoided if possible. Also, in order for stoichiometric films to be grown, a high density of atomic nitrogen is necessary at the reaction site and high growth temperatures should be avoided (given the thermal instability of InN).

The difficulties associated with the growth of **single crystal** films of InN arise from this low temperature deposition constraint, the unavailability of bulk single crystals of the semiconductor (due to thermodynamic considerations), and a lack of substrates sufficiently lattice matched to allow unstrained heteroepitaxial growth. In this context, Table 1 presents the variety of substrates employed in our studies along with their calculated lattice mismatch with InN.

Table 1

Substrate	Crystal Face	Lattice Mismatch
Al_2O_3	(00.1)	28.8%
Mica	(001)	17.9%
ZrO_2	(111)	3.0%
Si	(111)	7.8%
GaAs	(111)	11.5%

The approach taken here to optimize the growth and semiconducting properties of InN thin films entails: (1) depositing under a carefully chosen set of process conditions (substrate, temperature, sputtering power, reactive gas mix, etc.); (2) measuring and interpreting the structural, compositional, morphological, electrical and optical properties; and, (3) feeding this information back by altering the process parameters based on the interpreted data. This optimization process develops most intelligently when taking advantage of breakthroughs such as that recently found for

seeded-heteroepitaxial growth of GaN on sapphire [9].

In what follows, the results and interpretations engendered through this approach to the growth of single-crystal InN films are recounted.

EXPERIMENTAL

The magnetron sputtering system used to deposit these films has been previously described. [8] It is built on a liquid nitrogen trapped, diffusion pumped vacuum station capable of pressures on the order of $5x10^{-8}$ Torr with a pumping speed of 2000 l/s. Within the limitations of high vacuum technology, two measures are taken to lower the risk of oxygen contamination of the film during growth; a high efficiency organic resin gas purifier is in the inlet gas line and a Meissner trap, that surrounds the growth area, is maintained at liquid nitrogen temperature while sputtering. Dual magnetron sputtering guns are mounted below a rotatable arm carrying a variable temperature substrate fixture.

One gun is fitted with an indium metal target of purity greater than 99.999% for the deposition of InN. The second gun is used primarily for the deposition of the nucleation and buffer layers employed in seeded heteroepitaxy studies but could also be used for preparing multilayer films. A wide variety of substrates are employed including single-crystals of sapphire, silicon, gallium arsenide, mica and zirconia and amorphous substrates such as glass and fused quartz. Process parameters (such as substrate temperature, sputtering gas pressure and sputtering rate) are varied to optimize growth.

Samples are characterized by the measurement of their structural, compositional, morphological, electrical and optical properties. Microstructure and crystallographic texture are determined by X-ray scattering methods using a Read camera (CrKα radiation), in reflection, and a Buerger precession camera (MoKα radiation),in transmission. Most compositional analysis has been performed using scanning Auger electron spectroscopy. On a coarse scale, film thickness and surface roughness are measured with a stylus profiler. A scanning tunnelling microscope (STM) is employed to determine the micro-topography of the samples which, under favorable conditions, can be related to the grain structure. In addition, textural, structural coherence, and interlayer diffusion measurements are carried out by transmission and scanning electron microscopy. Electrical resistivity and Hall effect are measured over a wide range of temperature (1.4-320 K) and magnetic field (0-7T). Finally, the optical properties of the films measured over a large wavelength range (0.1 μm to 50 μm) using a variety of double beam spectrometers.

RESULTS AND DISCUSSION

The results of a succession of experiments on the growth and characterization of sputtered InN films are discussed here with particular emphasis on seeded heteroepitaxial growth techniques.

Initial Experiments

Initial experiments focused on targeting a set of process parameters that produced characteristic magnetron sputtered InN on amorphous substrates at room temperature. InN films were deposited onto fused quartz substrates with variations in process parameters such as sputtering power, total gas pressure, reactive gas partial pressure. The optimal process conditions that resulted from this procedure are given in Table 2.

Table 2

Sputtering Power	50W at 13.56 MHz
Sputtering Gas	Pure Nitrogen
Sputtering Pressure	$5x10^{-3}$ Torr
Target	Indium Metal
Presputter Time	30 Minutes
Sputtering Time	60 Minutes

These general experimental conditions were used in the following sets of experiments with changes as noted.

Higher Temperature Growth on Fused Quartz and (00.1) Sapphire

The first set of experiments aimed to elucidate the effect of deposition temperature on the properties of InN thin films. A series of InN films were sputtered onto quartz and sapphire substrates at temperatures from 50-600°C [8]. In addition, two different sets of (00.1) oriented sapphire crystals were employed: one had a somewhat rough surface prepared by mechanical polishing; and the second set had a much smoother, chemically polished surface. For all films the carrier concentration had a relatively independent value of $\approx 10^{20}$ cm^{-3}. The temperature dependence of the carrier mobility for samples deposited on the three substrate types are displayed in Figure 1. Films deposited on fused quartz have generally lower mobility, higher carrier concentration and higher resistivity than those on sapphire. The amorphous nature of the substrate leads to material that is strongly c-axis textured but obviously not epitaxial. Presumably this lack of epitaxial growth is responsible for the poorer electrical quality of these samples.

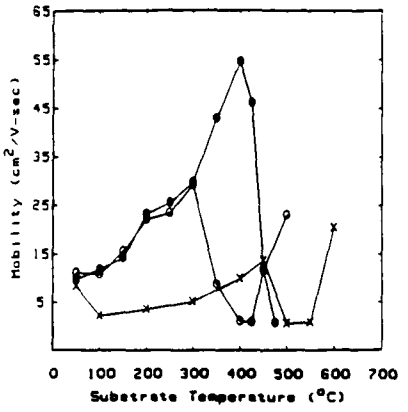


Figure 1 Electrical mobility of InN on quartz(X) and sapphire: chemically polished(●), mechanically polished(O).

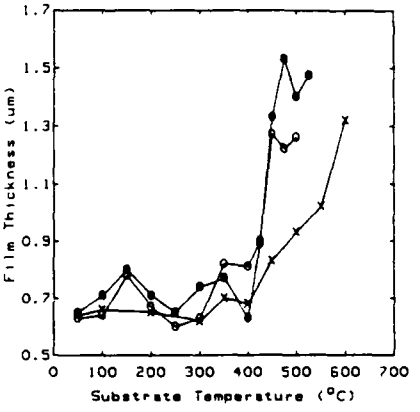


Figure 2 Film thickness of InN deposited onto quartz(X) and sapphire: chemically polished(●), mechanically polished(O).

Films on sapphire show electrical behavior that is strongly deposition temperature dependent. In the low temperature regime the mobility steadily rises, the carrier concentration generally decreases and the resistivity is virtually constant as the temperature is increased. X-Ray diffraction indicates that materials in this regime smoothly change from a mixture of epitaxial and textured grains to complete epitaxy [10]. The film thickness (Figure 2) in this temperature regime is relatively constant and the grain size determined by STM and SEM is slowly increasing with increasing growth temperature.

This behavior is interrupted above 300°C on mechanically polished sapphire and above 400°C on the chemically polished sapphire when the mobility experiences a sharp downturn (Figure 1) concurrent with a steep increase in film resistivity. The mobility falls from a high of 30 cm^2/V-sec on mechanically polished sapphire and 54 cm^2/V-sec on chemically polished sapphire to a low of 1 cm^2/V-sec over a 100 degree interval. The film thickness (Figure 2) and grain size each show a relatively sharp upturn at these transition temperatures.

Extensive studies by SEM, STM and TEM of the temperature dependent microstructure of these InN films have been conducted and results are schematically summarized in Figure 3. Films grown at low temperature are relatively smooth, small grained and physically continuous. X-Ray diffraction studies of the nanostructure in this range indicate that the films are a mixture of c-axis textured and epitaxial grains. As the temperature is raised, the grains grow larger, become completely epitaxially oriented and their physical properties improve. At an intermediate temperature (determined by sample-substrate interactions), the films begin to roughen and start to become physically disconnected. In large measure, the electrical transport properties of these films are determined by the degree of connectivity between grains. As the connectivity decreases, the electronic mobility decreases with it. At high deposition temperature, the grains grow quite large but become isolated. The electrical transport across such a film is extremely limited due to the hopping nature of the conduction.

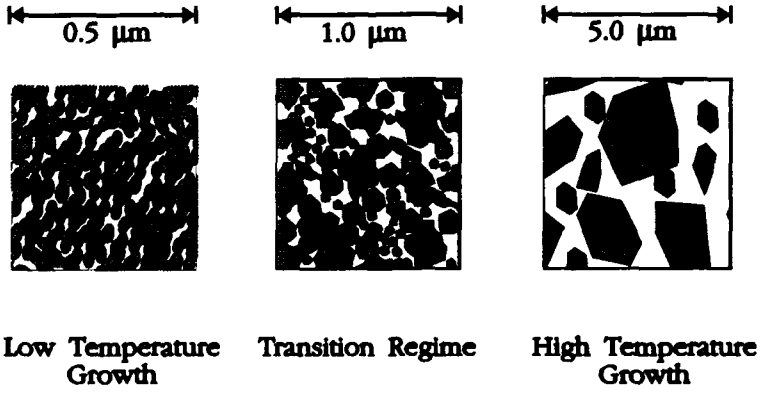


Figure 3 Schematic representation of the growth temperature variation of film morphology for magnetron sputtered InN. Primary data was obtained from SEM, STM and TEM measurements.

Deposition onto the (001) Surface of Mica

The aforementioned study indicated that heteroepitaxial strain and substrate surface finish played a role in determining how the properties of InN were affected by growth temperature. For example the temperature at which the electrical properties sharply deteriorated was clearly dependent upon the surface roughness of the substrate. Following on this recognition, mica was identified as a substrate with a smaller lattice mismatch (see Table 1) and with a nearly atomically smooth surface.

The measured properties of the reactively sputtered InN films grown on the pseudo-hexagonal (001) face of mica as a function of deposition temperature were compared to and contrasted with the properties of InN films deposited onto the (00.1) face of sapphire [12]. Despite the smaller lattice mismatch and smoother surface the physical properties of these films were quite similar to those prepared on sapphire. Similar trends were seen in the electrical transport and morphology with a transition temperature to a low mobility state of 300°C. At higher deposition temperatures (>500 °C), however, the interconnection between grains improves and the high mobility state is reestablished. Unfortunately, the thermal degradation of mica above 550 °C makes this promising result somewhat impractical.

Deposition onto the (111) Face of Cubic Crystals

These results implied that the main cause of the morphological transition in epitaxial InN is due to lattice strain. As evident in Table 1, the (111) face of several cubic substrates have a decidedly lower lattice mismatch with InN than either sapphire or mica.

The structure, morphology, and transport properties of thin films of InN deposited onto the (111) face of several cubic substrates were studied as a function of deposition temperature [13]. In general, the film structure is such that $(00.1)_{InN}$ parallels the (111) plane of the cubic substrate and the in-plane growth coherence parallels the magnitude of the lattice mismatch (Table 1), in that films on GaAs are textured at all growth temperatures, while pseudo heteroepitaxial growth is achieved at elevated deposition temperatures for growth onto Si, and true heteroepitaxy is attained above 300°C for deposition onto ZrO_2. Using the X-ray precession technique the secondary heteroepitaxial relationships between InN and the cubic substrates were found to be $(2\bar{1}.0)_{InN}//(2\bar{2}0)_{cubic}$ or equivalently $(30.0)_{InN}//(4\bar{2}\bar{2})_{cubic}$.

The semiconducting substrates (Si and GaAs) used in this study did not allow the measurement of the electrical properties of the InN films due to the sizable parallel conductance of the substrate. The electrical transport properties of films grown on insulating zirconia were measured and found to be quite similar to those of films deposited on sapphire. The carrier concentration was still $\approx 10^{20}$ cm^{-3}, and the mobility had the same strongly peaked behavior as depicted in Figure 1. The film thickness had the same general dependence on deposition temperature displayed in Figure 2 and morphological investigations identified the same trend displayed in Figure 3 with a transition temperature of 350°C.

Seeded-Heteroepitaxial Growth

Since the (111) face of zirconia has the smallest calculated degree of lattice mismatch with InN of any commonly available substrate (Table 1), it became obvious that other means of achieving single-crystal growth of InN would need to be explored. Recent advances have been made in the techniques of achieving heteroepitaxy -- driven in many cases by the desire to deposit single crystal diamond onto substrates other than natural diamond [14]. These techniques are generally referred to as seeded heteroepitaxy and a particularly germane result for the deposition of InN was the effect

of a thin nucleation layer of AlN on the MOCVD growth of GaN [9]. There it was found that the use of a thin (≈50 nm) AlN nucleation layer yielded GaN single crystal films with optically flat, crack free surfaces. The AlN seed layer serves to provide a supply of nucleation sites with the same heteroepitaxial relationship and to promote lateral growth by decreasing the interfacial free energy between the substrate and growing GaN layer. The resulting film is a "mosaic" single crystal with a carrier concentration decreased by two orders of magnitude and a room temperature mobility increased by one order of magnitude. Given the similarities in the crystal physics of InN and GaN the effects of thin layers of AlN on the magnetron sputtering growth of InN were investigated. Two studies were conducted to assay the effects of a thin nucleation layer of AlN on the magnetron sputtering growth of InN.

Deposition onto a High Temperature Nucleation Layer

A nucleation layer was deposited on the (00.1) face of sapphire by dc sputtering for 30 min. at 900 ^{o}C using a 50/50 mixture of nitrogen and argon [15]. The resulting AlN layer thickness was ≈50 nm. A sequence of InN films at various growth temperatures (50-600 ^{o}C) were deposited onto such a seed layer using magnetron sputtering in a pure nitrogen atmosphere. Full physical characterization of the resulting films was carried out.

Microscopic studies show that at low growth temperatures the agglomerate morphology (average grain size of ≈8.5 nm) of the seeded films is essentially equivalent to that found for films deposited onto bare sapphire. As the substrate temperature is raised, the grain size for the seeded films is nearly temperature independent while that of the single layer film is gradually rising. At intermediate temperatures the grain size of both types of films begins to increase but the increase is much more rapid for the film on bare sapphire. At still higher temperatures, the seeded films remain granular, with the details of grain size and connectivity varying only marginally with deposition temperature. This is in sharp contrast to the morphology of unseeded films, where a large grain structure with significant void area between the grains is evident.

Since the morphology largely determines the physical properties of these films, this contrast has profound effects on the physical properties of the materials. For example, X-ray scattering from these films using the precession method [16] are reiterated here. Films deposited onto the AlN buffer layer consist nearly exclusively of epitaxial grains of InN at all temperatures investigated. In contrast, InN films deposited directly onto the (00.1) surface of sapphire were comprised mainly of textured grains below 200 ^{o}C and became fully epitaxial above this temperature. From variations in the angular dispersion of the $\{11\bar{2}0\}$ X-ray reflection for the two type of films, the following deductions were made: (1) For unseeded films at $T < 200^{o}$C, there is a weak azimuthal correlation between the InN grains and the sapphire substrate; (2) This azimuthal correlation strengthens considerably with the disappearance of textured grains and remains strong until the onset of the morphological transition; and finally, (3) The azimuthal correlation restrengthens at the highest deposition temperatures as the transition progresses and the large grains come to dominate the morphology. By contrast, the films deposited with an AlN seed layer are fairly strongly correlated even at low temperatures --in accord with the observation of solely epitaxial films. This correlation strengthens and remains strong for all such films -- a fact consistent with the relatively unchanging morphology of these films.

In a similar vein, the electrical transport properties are affected by these variations in morphology (Figure 3). While the carrier concentration ($> 10^{20}$ cm^{-3}) remains high for both types of films, the dependence of carrier concentration, electrical resistivity and mobility on deposition temperature differ significantly for the two types

of films. Firstly, the carrier concentration remains relatively constant at low substrate temperatures (<300 ^{o}C) and generally decreases monotonically above this temperature. Secondly, in the range below 200 ^{o}C, the carrier mobility for the epitaxial seeded films is consistently higher than found for the unseeded films which are a mixture of epitaxial and textured grains. Thirdly, the general variation in mobility with deposition temperature is the same for both types of films in the transition temperature regime, 300 ^{o}C < T < 450 ^{o}C. In particular, the mobility slowly rises as the substrate temperature increases up to the point where the grains lose connectivity resulting in a precipitous jump in resistivity and a concomitant sharp drop in mobility.

In addition, it has been shown that the evolution of the physical properties of these seeded films with increased substrate temperature is dominated by subtle changes in the granularity of the film. This is in stark contrast to unseeded films where the physical properties are dominated, at high temperature, by the formation of a large grained morphology with significant intergranular voids. Therefore, the use of a nucleation layer has stabilized the film morphology and muted the rapid degradation of film properties above ≈400 ^{o}C seen here and elsewhere for growth on unseeded substrates. This quite promising result followed from an arbitrary choice of growth conditions for the AlN nucleation layer. A systematic search for optimized seed layer growth condition are discussed next.

Nucleation and Overlayer Growth Temperature Effects

In this study, an investigation of the dependence of film properties on the growth temperatures and growth times of the nucleation layer and the InN overlayer (both sputtered in pure nitrogen) was carried out. The nucleation layer was deposited on the (00.1) face of sapphire by dc sputtering for 7.5-30 min. at temperatures between 100 ^{o}C and 1000 ^{o}C. The resulting AlN layer thickness was between 20 and 80 nm. A sequence of InN films at growth temperatures from 100 ^{o}C to 500 ^{o}C and deposition times between 14 sec. and 6 hours were deposited onto the nucleated sapphire substrate using magnetron sputtering.

A discussion of the results of a fixed deposition temperature with variable time, giving clear evidence of a crossover from a two dimensional to a three dimensional growth mechanism, appears separately. [17] The discussion presented in this paper will focus on the effects of growth temperatures for fixed times for the nucleation and overlayers (15 min. and 60 min. respectively).

The carrier concentrations for these samples remain in the 10^{20} cm^{-3} range. A plot of the mobility of the InN films as a dual function of buffer layer and film growth temperature is shown in Figure 4. At low buffer layer temperatures (<300 ^{o}C), all film growth temperatures result in low mobility. In parallel, at low film growth temperatures, all buffer layer temperatures also result in low mobility films. It is also evident in the plot that for buffer layer growth temperatures ≥300 ^{o}C and for film growth temperatures ≥400 ^{o}C a plateau in mobility is achieved. This plateau extends to at least 500 ^{o}C in film growth temperature and 1000 ^{o}C in buffer layer growth temperature. This is in contrast to films deposited onto the bare surface of any substrate and also in contrast to films deposited onto a seeded (00.1) sapphire substrate where the AlN layer was sputtered in a mixed argon/nitrogen atmosphere. Although the morphology of these seeded films is yet to be completely elucidated, evidence for a crossover from a three-dimensional growth mode to a two-dimensional growth mechanism has been presented [17]. Most importantly for future device applications, the AlN seed layer grown in pure nitrogen has stabilized the InN overlayer to the transition that resulted in the loss of intergrain connectivity and the dramatic drop in electrical mobility for the unseeded films.

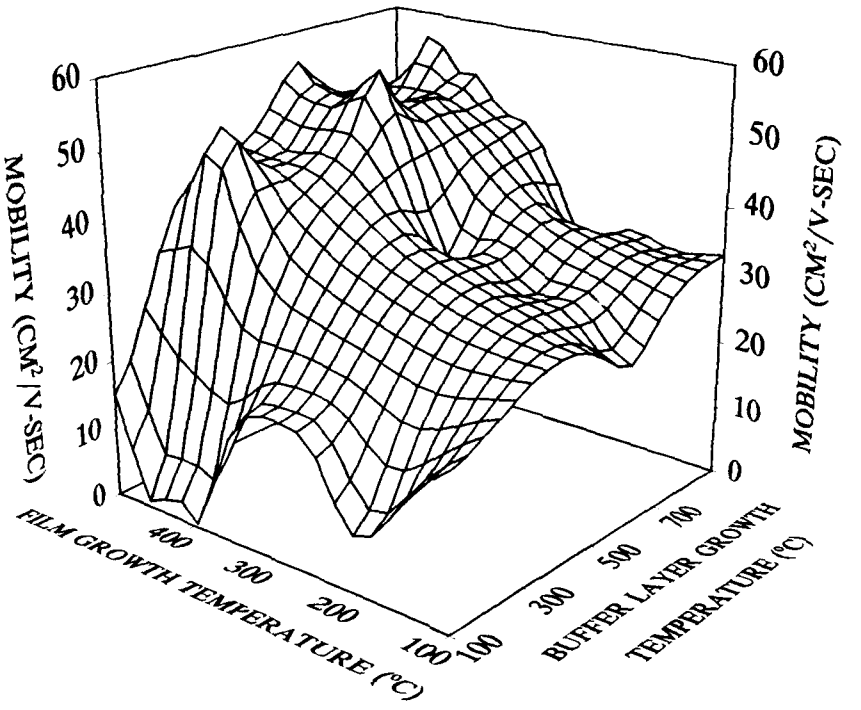


Figure 4 Electrical mobility of InN films deposited onto a seeded (00.1) sapphire substrate as a dual function of seed layer growth temperature and film growth temperature.

Future Directions

Although the seeded heteroepitaxial growth technique has yet to yield extremely high mobility InN films, the effect is clearly positive. The properties of the InN films are quite sensitive to the conditions of nucleation layer growth. Further optimization of the process may indeed lead to films with vastly superior properties, including a significant reduction in carrier concentration (as was found for the seeded MOCVD growth of GaN [9]). In fact, ongoing investigations are focusing on reducing the high concentration of n-type carriers in thin films of InN.

As discussed above, the properties of InN are degraded by the presence of oxygen containing species during growth and the film properties may be further degraded by exposure to air. In order to address these concerns, an ultrahigh vacuum sputtering system, working at base pressures of $5X10^{-11}$ Torr has been constructed. This dual magnetron setup is quite similar to the high vacuum sputtering system employed above with three distinct advantages: (1) The low base pressure and bakeability of the system results in orders of magnitude reduction in background oxygen containing species; (2) The chamber has an integral load-lock assembly that

allows exchange of samples and substrates without breaking vacuum; and, (3) An analysis chamber is available for the *in situ* measurement of temperature dependent electrical resistivity, Hall effect and optical absorption.

Initial experiments in this deposition system have been carried out by reactively sputtering InN under typical process conditions. The electrical transport properties of these films have been measured both *in situ* and *ex situ* and the measurements reveal InN thin films that have the same carrier concentration ($\approx 10^{20}$ cm^{-3}) and mobility (<60 cm^2/V sec as films deposited in the high vacuum system and measured in air [18]. Although these experiments do not completely rule out the possibility of high carrier concentration due to oxygen contamination, the probabilities of nitrogen vacancies as the likely unintentional doping mechanism are considerably enhanced.

As a means of following up on this deduction, additional sources of activated nitrogen species are being introduced into the current sputtering systems hopefully leading to a drop in carrier concentration. Finally, alternate growth techniques with intrinsically higher atomic nitrogen concentrations at the reaction site are being investigated and implemented. In every case, seeded heteroepitaxial growth is considered crucial to the achievement of single-crystal InN thin films of device quality.

ACKNOWLEDGEMENTS

This work was supported in part by the U.S. Department of the Navy under Contract N00039-89-C-5301.

REFERENCES

1. H. J. Hovel and J. J. Cuomo, Appl. Phys. Lett. **20**, 71 (1972).
2. T. L. Tansley and C. P. Foley, Electron. Lett. **20**, 1066 (1984); C. P. Foley and T. L. Tansley, Appl. Surf. Sci. **22/23**, 663 (1985).
3. J. W. Trainor and K. Rose, J. Electr. Mat. **3**, 821 (1974).
4. B. R. Natarajan, A. H. Eltoukhy, J. E. Greene and T. L. Barr, Thin Solid Films **68**, 201 (1979).
5. O. Takai, J. Ebisawa and Y. Hisamatsu, Proc. ICVM **7**, 137 (1982).
6. B. T. Sullivan, R. R. Parsons, K. L. Westra and M. J. Brett, J. Appl. Phys. **64**, 4144 (1988).
7. K. Kubota, Y. Kobayashi and K. Fujimoto, J. Appl. Phys. **66**, 2984 (1989).
8. W. A. Bryden, J. S. Morgan, T. J. Kistenmacher, D. Dayan, R. Fainchtein and T. O. Poehler, Mat. Res. Symp. Proc. **162**, 567 (1990).
9. H. Amano, N. Sawaki, I. Akasaki, and Y. Toyoda, Appl. Phys. Lett. **48**, 415 (1988); H. Amano, I. Akasaki, K. Hiramatsu, N. Koide, and N. Sawaki, Thin Solid Films **163**, 415 (1988); I. Akasaki, H. Amano, Y. Koide, K. Hiramatsu, and N. Sawaki, J. Cryst. Growth **98**, 209 (1989).
10. T. J. Kistenmacher, D. Dayan, R. Fainchtein, W. A. Bryden, J. S. Morgan and T. O. Poehler, Mat. Res. Symp. Proc. **162**, 573 (1990).
11. J. S. Morgan, T. J. Kistenmacher, W. A. Bryden and T. O. Poehler, Mat. Res. Symp. Proc. **162**, 579 (1990).
12. T. J. Kistenmacher, W. A. Bryden, J. S. Morgan, D. Dayan, R. Fainchtein and T. O. Poehler, J. Mater. Res. **6**, 1300 (1991).
13. J. S. Morgan, T. J. Kistenmacher, W. A. Bryden and S. A. Ecelberger, Mat. Res. Soc. Symp. Proc. **202**, 383 (1991).
14. See, for example, J. Narayan, V. P. Godbole, and C. W. White, Science **252**, 416 (1991) and references therein.

15. W. A. Bryden, J. S. Morgan, R. Fainchtein and T. J. Kistenmacher, Thin Solid Films (in press).
16. T. J. Kistenmacher, W. A. Bryden, J. S. Morgan and T. O. Poehler, J. Appl. Phys. **68**, 1541 (1990).
17. T. J. Kistenmacher and W. A. Bryden, Appl. Phys. Lett. **59**, 1844 (1991); T. J. Kistenmacher, S. A. Ecelberger and W. A. Bryden, Mat. Res. Soc. Symp. Proc. (this volume).
18. W. A. Bryden, S. A. Ecelberger and T. J. Kistenmacher (to be published).

CHARACTERIZATION OF $Al_xGa_{1-x}N$ GROWN BY MOCVD AT LOW TEMPERATURES

Z. J. YU, B. S. SYWE, AND J. H. EDGAR
Department of Chemical Engineering, Durland Hall,
Kansas State University, Manhattan, KS 66506

ABSTRACT

The low temperature deposition (400-650° C) of $Al_xGa_{1-x}N$ films by metalorganic chemical vapor deposition (MOCVD) was characterized. Triethylgallium (TEG), trimethylaluminum (TMA), and ammonia (NH_3) served as the precursors and both sapphire and silicon as the substrates with helium as the carrier gas. The deposition was operated at the atmospheric pressure. The crystallinity was improved even at low temperatures when $Al_xGa_{1-x}N$ was grown on a thin buffer layer of AlN at 400° C. With an $Al_xGa_{1-x}N$/AlN layered structure, epitaxial growth of $Al_xGa_{1-x}N$ was obtained at 650° C on sapphire substrates. Auger results showed that the Al fraction x was less than 0.1. X-ray diffraction indicated a strong peak at $2\theta = 34.9$ degrees for the (0002) planes from the film on sapphire substrates. The electron channelling pattern (ECP) of the film produced at 650° C revealed a 6 fold symmetry contrast pattern indicating the epitaxial growth of the film. Photoluminescence (PL) showed a dominant emission at 353 nm for the film on sapphire substrate. Surface morphology examined by SEM was featureless for the film produced at 500° C, while a relatively rough surface can be seen on the film produced at 650° C (5,000x). The band gap was measured as 3.56 eV. The Al mole fraction x in the alloy was observed to be lower than that in the gas phase.

INTRODUCTION

The semiconductor alloy $Al_xGa_{1-x}N$ has a band gap which can be controlled from 3.4 eV to 6.2 eV and it has potential applications in ultraviolet light emitting diodes, detectors, lasers or high temperature electronic devices. MOCVD is one of the most widely employed method for producing $Al_xGa_{1-x}N$ films. The dependence of the energy band gap of the alloy on the Al mole fraction x has been studied[1] and with precise control of x, it is possible to also control the band gap width. To grow an epitaxial layer of $Al_xGa_{1-x}N$ on sapphire substrates, depositions were typically performed in the temperature range between 900° -1150° C[2,3]. Akasaki *et al*[4] has shown that by first depositing an AlN buffer layer at 600° C, the quality of $Al_xGa_{1-x}N$ is greatly improved, but even in this work, the deposition temperature used was in the range of 900° to 1020° C. Based on the results of our previous work on the low temperature deposition of GaN[5], this study was initiated to deposit epitaxial $Al_xGa_{1-x}N$ at lower temperatures.

EXPERIMENTAL

A horizontal atmospheric-pressure reactor was employed to deposit $Al_xGa_{1-x}N$ alloy films. The susceptor surface was tilted about 10° with respect to the incoming gas direction. The deposition temperatures ranged from 400° C to 650° C. The susceptor temperature was measured by a thermocouple. The substrates were Al_2O_3 (0001), Si (100) and Si (111). The gallium and aluminum source gases were triethylgallium (TEG) and trimethylaluminum (TMA). Ammonia served as the nitrogen source and helium as the carrier gas. The total gas flow rate was about 1100 sccm with 13 μmol/min TEG, 5 μmol/min TMA and 20,000 μmol/min NH_3. A mechanical vacuum pump was employed

for evacuating the reactor prior to purging the system with helium after loading the sample before each deposition. The substrates were cleaned by dipping in hydrofluoric acid, rinsing in deionized water, and then blowing dry with filtered nitrogen. The thickness of the films was determined by measuring the mass increase of the samples after deposition with a microgram balance. Scanning electron microscopy (SEM) was used to examine the surface morphology and to make electron channelling patterns (ECP). The film composition was analyzed by Auger electron spectroscopy (AES). X-ray diffraction was used to analyze the crystal structure of the films.

RESULT AND DISCUSSION

An epitaxial film of $Al_XGa_{1-X}N$ was obtained on the sapphire substrate at 650° C after first depositing about 1000 Å of AlN at 400° C. The thickness of the film was about 0.3-0.4 μm after a half hour deposition.

The composition of the epitaxial layer with sapphire as the substrate was analyzed by Auger electron spectroscopy (AES). The AES spectrum is shown in the Fig. 1.

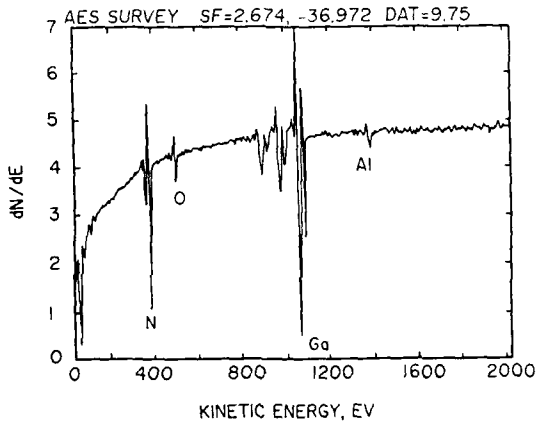


Fig. 1 Auger electron spectrum of $Al_XGa_{1-X}N$ deposited at 650° C on sapphire.

The resulting spectrum shows three main element peaks, corresponding to Al, Ga and N. The calculated average concentrations for three main elements Ga, Al and N are 0.58, 0.06, and 0.33 respectively for the sample. The Al mole fraction x in the alloy is in the vicinity of 0.1. Notice that the ratio of nitrogen to group III elements is lower than stoichiometric material. One possible explanation for this is that the ion sputtering of the film surface, which is a technique to clear the surface contaminations when performing AES, might preferentially remove more nitrogen than gallium or aluminum from the analyzed surface. Besides the three main element peaks, there is a small oxygen (0.03) peak possibly originating from an incomplete purging or an adsorbed gas layer on the film surface. The composition was normally found to be a function of the sample positions on the susceptor. Higher aluminum concentrations were observed for samples set on the leading edge. The difference of the Al fraction x between the gas phase (0.28) and the solid phase (0.1) may indicate different rates of dissociation of the reactants on the surface at low temperatures.

X-ray diffraction was used for crystal structure analysis. The diffraction patterns from films produced at two different temperatures are shown in the Fig. 2. Fig. 2a is for

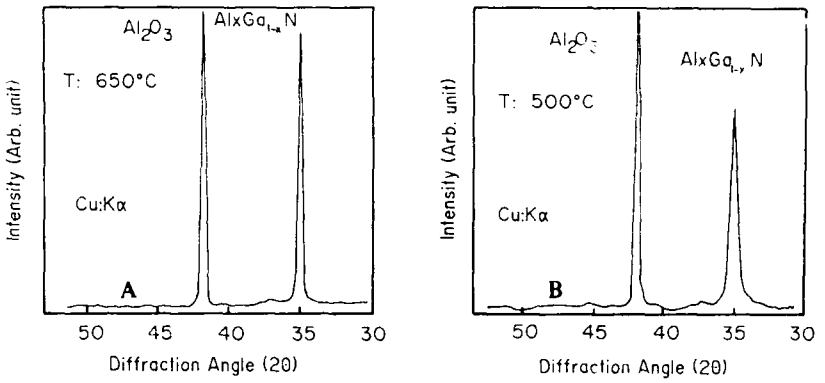


Fig. 2 X-ray diffraction patterns of $Al_xGa_{1-x}N$ deposited at (a) 650° C and (b) 500° C.

the epitaxial film produced at 650° C and Fig. 2b for film produced at 500° C. The (0002) $Al_xGa_{1-x}N$ diffraction peak was detected at a diffraction angle 2θ in the vicinity of 34.9° on both spectra. The (0002) peak intensity for epitaxial film in Fig. 2a is stronger and shaper than the highly oriented crystal film in the Fig. 2b. This peak position is close to the peak position of GaN (34.6°), but was between of the peak positions of (0002) GaN and (0002) AlN. The peak intensity from the film is stronger than that from the substrate for an epitaxial layer. Compared to Koide *et al's*[3] results for an Al fraction of 0.1, the change in the lattice constant is similar with the fraction x in the vicinity of 0.1. Under the same experimental conditions as was used for the film on the sapphire substrate, $Al_xGa_{1-x}N$ alloy films were also deposited on both types of silicon substrates. However, the X-ray diffraction patterns of those films were identified as polycrystalline.

To further examine whether the deposited film was an epitaxial layer, an electron



Fig. 3 Electron Channelling pattern of $Al_xGa_{1-x}N$ on sapphire deposited at 650° C.

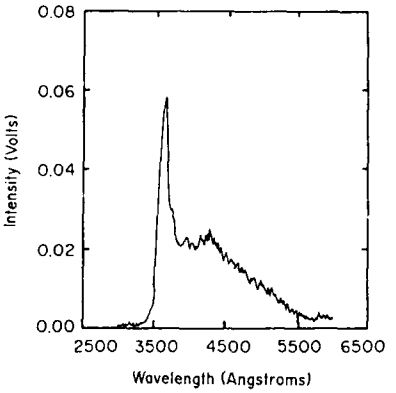


Fig. 4 Photoluminescence spectrum for $Al_xGa_{1-x}N$ on sapphire deposited at 650° C.

channelling pattern was made. If the film is single crystal, when examined under the SEM at very low magnifications, an electron channelling contrast pattern will be observed. Otherwise, for a polycrystalline film, only regular SEM will be seen. The corresponding photograph was shown in the Fig. 3. It showed a six fold symmetry contrast, which is agreement with the X-ray diffraction peak from (0002) crystal planes. For the film deposited at 500° C, no channelling contrast was observed.

Photoluminescence (PL) spectrum was taken for the epitaxial layer as shown in Fig. 4. The dominant emission was observed at 350 nm at a temperature of 15 K. This is the so called I_2 line of $Al_XGa_{1-X}N$, the donor-bound exciton line as previously identified by Khan *et al.*[6] The line width of the peak at half height was about 135 meV.

Optical transmission measurements were made at room temperature on the epitaxial layer. The result is given in Fig. 5. A rough estimation of the band gap for the film is about 3.56 eV. This is similar to Koide *et al's*[1] result for a film with an aluminum fraction x in vicinity of 0.1. It also seems, in some degree, in agreement with the photoluminescence result.

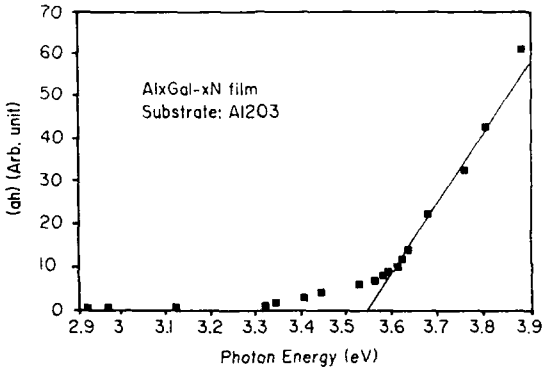


Fig. 5 Optical measurement for $Al_XGa_{1-X}N$ deposited on sapphire at 650° C.

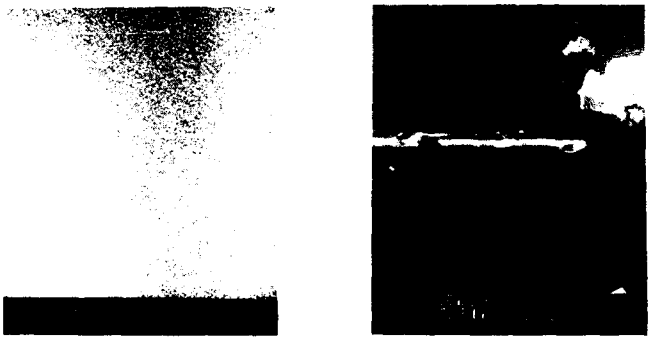


Fig. 6 SEM images of $Al_XGa_{1-X}N$ films deposited at (a) 650° C and (b) 500° C. (5000x).

The surface morphology was examined by scanning electron microscope (SEM). The surface was smooth for films produced at lower temperatures. Fig. 6. gives the photographs of the epitaxial layer and the film produce at 500° C. Small bumps can be seen for the film produced at 650° C under 5,000x.

As originally applied to the deposition of GaN, we tried to deposit $Al_XGa_{1-X}N$ at low temperature in order to promote the heterogeneous reactions. However, low temperatures reduce the surface mobility of the gas molecules adsorbed on the substrate surface. Because the surface decomposed fragments of metalorganic molecules may play a important role in the lower temperature growth of the crystal,[7] this process may be achieved by a mechanism of site-selective incorporation of components into the proper configuration. With source gases introduced separately with a high gas velocity, the growth rate may be reduced because of incomplete gas mixing at the surface. Instead of a higher gas flow rate which is normally used in MOCVD, in this work, a slow gas flow rate was employed. The slow gas velocity provides time for molecules to diffusion and for the gases to mix, and surface adsorption of the reactants may be promoted in such case. The actual $Al_XGa_{1-X}N$ growth rate for this kind of deposition was between 0.5 - 1.3 μm hr.

The deposited films normally turned out to be random oriented polycrystals without a AlN buffer layer. With this buffer layer on either silicon substrate, highly oriented polycrystal films were produced.

CONCLUSIONS

Epitaxial $Al_XGa_{1-X}N$ films can be produced at a temperature of 650° C by MOCVD on sapphire substrates. The growth of this alloy is mainly attributed to the promotion of site selective heterogeneous reactions. No epitaxy was obtained on either type of Si substrate. The difference of the Al fraction x between the gas phase and the solid phase may indicate different rates of decomposition of the reactants on the surface at such temperatures. The growth rate seems moderate even at low temperatures and low gas flow rates. The band gap change is proportional to the concentration of aluminum in the alloy.

ACKNOWLEDGEMENTS

We are grateful to L. Seib for his assistant in x-ray diffraction, Read thin camera and SEM, to Mr. J. B. Petit at the NASA Lewis Research Center for Auger analysis, and to Dr. H. Jiang in the Physics Department, Kansas State University for photoluminescence measurements.

REFERENCES

1. Y. Koide, H. Itoh, M. R . H. Khan, K. Hiramatu, N. Sawaki, and I. Akasaki, J. Appl. Phys. 61, 4540 (1987).
2. M. A. Khan, R. A. Skogman, and R. G. Schulze, Appl. Phys. Lett. 43, 492 (1983).
3. Y. Koide, H. Itoh, N. Sawaki, and I. Akasaki, J. Electrochem. Soc. 133, 1956 (1986).
4. I. Akasaki, H. Amano, Y. Koide,K. Hiramatsu, and N. Sawaki, J. Cryst. Growth 98, 209 (1989).
5. Z. J. Yu, B. S. Sywe, and J. H. Edgar, submitted to J. Electron. Mater.
6. M. R. H. Khan, Y. Koide, H. Itoh, N. Sawaki and I. Akasaki, Solid State Commun. 60, 509 (1986).
7. T. M. Mayer, J. W. Rogers, Jr., and T. A. Michalske, Chem. Mater. 3, 641 (1991).

A COMPARATIVE STUDY OF GaN FILMS GROWN ON DIFFERENT FACES OF SAPPHIRE BY ECR-ASSISTED MBE

T. D. MOUSTAKAS, R. J. MOLNAR, T. LEI, G. MENON AND C. R. EDDY JR.
Molecular Beam Epitaxy Laboratory, Department of Electrical Engineering, Boston University, Boston, MA 02215.

ABSTRACT

GaN films were grown on c-plane (0001), a-plane (1120) and r-plane (1102) sapphire substrates by the ECR-assisted MBE method. The films were grown using a two-step growth process, in which a GaN buffer is grown first at relatively low temperatures and the rest of the film is grown at higher temperatures. RHEED studies indicate that this growth method promotes lateral growth and leads to films with smooth surface morphology. The epitaxial relationship to the substrate, the crystalline quality and the surface morphology were investigated by RHEED, X-ray diffraction and SEM studies.

INTRODUCTION

Recently Electron-Cyclotron-Resonance Microwave Plasma-assisted Molecular Beam Epitaxy (ECR-MBE) has emerged as one of the most versatile methods for the growth of GaN and other III-V nitrides[1-5]. In this method, films are grown at relatively low temperatures under ultrahigh vacuum conditions. This allows for control of the film stoichiometry[6] and reduction of unwanted impurities[7]. Moreover, our group demonstrated that significant improvement in film quality can be attained if film growth takes place in two steps[2,3,5]. In this process, a GaN buffer is grown first at relatively low temperatures and the rest of the film is grown at higher temperatures. Using this method, we have demonstrated the epitaxial stabilization of single crystalline GaN films in the zinc-blende structure on (001) silicon substrates[2,3].

In this paper, we report on a comparative study of GaN films grown on c-plane, a-plane and r-plane sapphire substrates by the ECR-MBE method, using the two-step growth process.

EXPERIMENTAL METHODS

The ECR-MBE method was used for the growth of GaN films on c-plane, a-plane and r-plane sapphire substrates. The details of the deposition method have been published elsewhere[2,3].

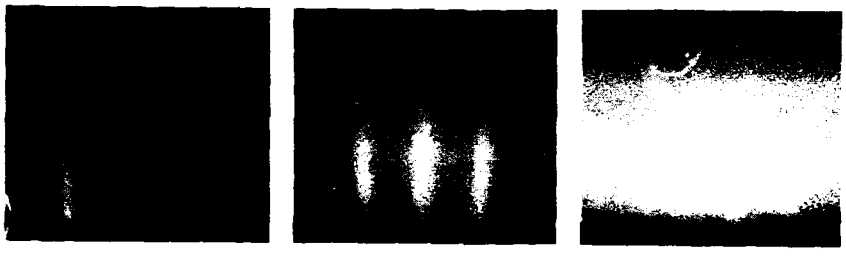
The substrates were subjected to the following cleaning steps, prior to the growth of the GaN films. They were sequentially cleaned in ultrasonic baths of trichloroethylene, acetone and isopropanol for removal of hydrocarbon residues from the surface, etched in $H_3PO_4 : H_2SO_4$ (1:3) for the removal of surface contaminants and mechanical damage due to polishing and finally rinsed in de-ionized water. After these steps the substrates were blown dry with nitrogen, mounted on a molybdenum block and transferred to the introduction chamber of the MBE system. In the preparation chamber, the substrates were heated to $850°C$ for approximately half an hour and then transferred to the growth chamber, where they were subjected to bombardment by a nitrogen plasma for approximately half an hour at $700°C$.

The GaN films were grown in two steps at different temperatures. First, a thin GaN buffer (about 300Å) was grown at $400°C - 500°C$ and then the rest of the film was grown at $600 - 800°C$. The film growth rate was $2000 - 3000 Å/h$ and the overall film thickness was $1 - 2 \mu m$.

The substrate and film structures at various stages of substrate preparation and film growth were assessed by Reflection High Energy Electron Diffraction (RHEED). The epitaxial relationship to the substrate and the crystalline quality of the films were determined from RHEED, $\theta - 2\theta$ XRD and rocking curve studies around the main diffraction peak. The surface morphology was studied by SEM.

EXPERIMENTAL RESULTS AND DISCUSSIONS

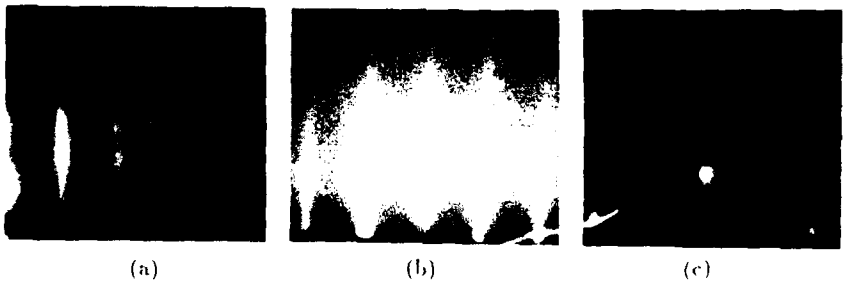
Fig. 1 shows RHEED patterns of the three types of substrates after the exposure to the nitrogen plasma. The data indicate that the surface of the substrates were nitrided and from the diffraction patterns, the lattice constant of the AlN was estimated to be $a = 3.1$Å. Furthermore, the streakiness of the diffraction patterns, in particular those of the c-plane and a-plane sapphire substrates, suggests that the AlN layers are atomically smooth[8].



(a) (b) (c)

Fig. 1 RHEED patterns of the sapphire substrates after exposure to the nitrogen plasma: (a) c-plane, (b) a-plane, (c) r-plane.

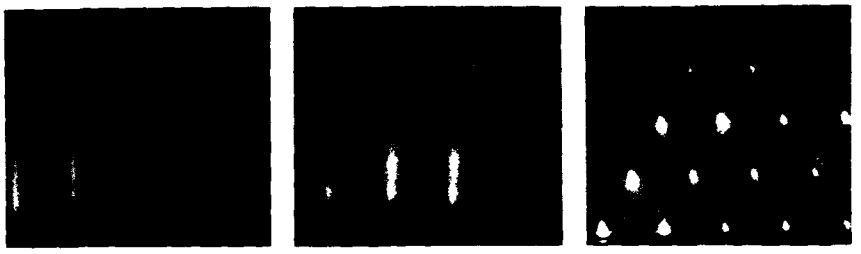
Fig. 2 shows RHEED patterns of the GaN buffer on the three types of substrates. The data indicate that the GaN-buffer is single crystalline on all three types of substrates. The GaN films grown on the c-plane and a-plane sapphire substrates have their c-plane (0001) parallel to the substrates, while the GaN films grown on the r-plane of sapphire have their a-plane (1120) parallel to the substrate. The streakiness of the diffraction patterns of the GaN buffers on the c-plane and a-plane sapphire substrates suggests that the GaN-buffer on these substrates are atomically smooth.



(a) (b) (c)

Fig. 2. RHEED patterns of the GaN-buffer on the various sapphire substrates: (a) c-plane, (b) a-plane, (c) r-plane.

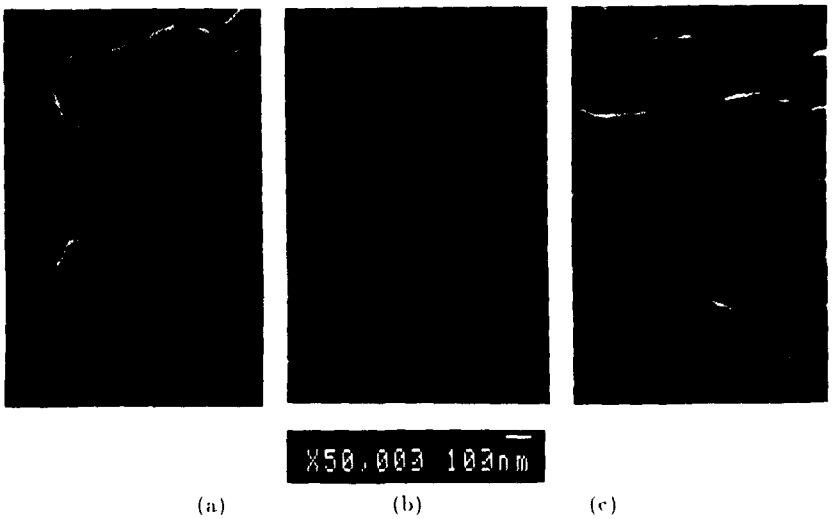
Fig. 3 shows RHEED patterns of the GaN films at the end of each run. These reveal the same epitaxial relationship between GaN films and the substrates as the corresponding GaN buffers discussed in Fig. 2. Also the films on the c-plane and a-plane sapphire substrates are atomically smooth.



(a) (b) (c)

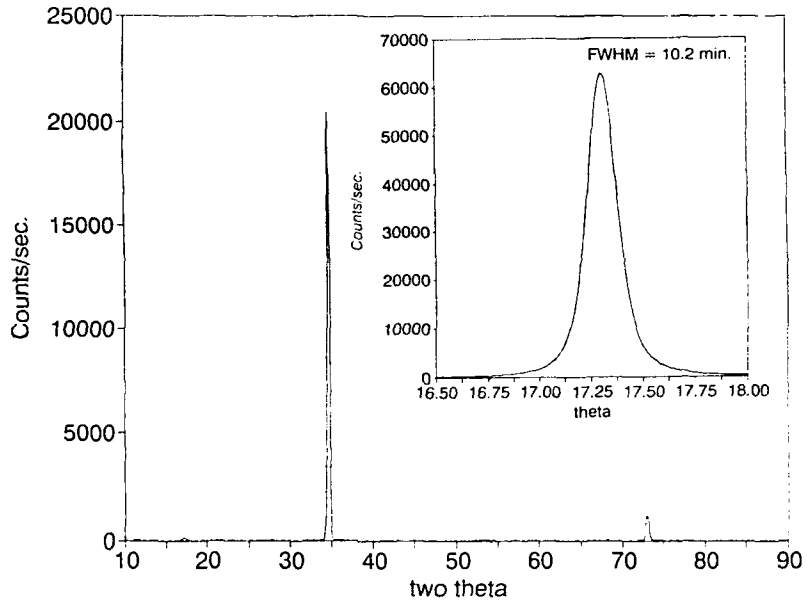
Fig. 3 RHEED patterns of the GaN films after growth on the various sapphire substrates: (a) c-plane, (b) a-plane, (c) r-plane.

Fig. 4 shows the surface morphology of GaN films grown on the three types of the substrates. The films on the a-plane have the smoothest surface morphology. The surface morphology of GaN films on the c-plane consists of interconnected tiles several thousand angstroms in size. The GaN films grown on the r-plane sapphire were found to have roughest surface morphology. The pyramidal surface morphology is related to the fact that the a-plane of GaN is bounded by two prism planes under equilibruim growth condition.

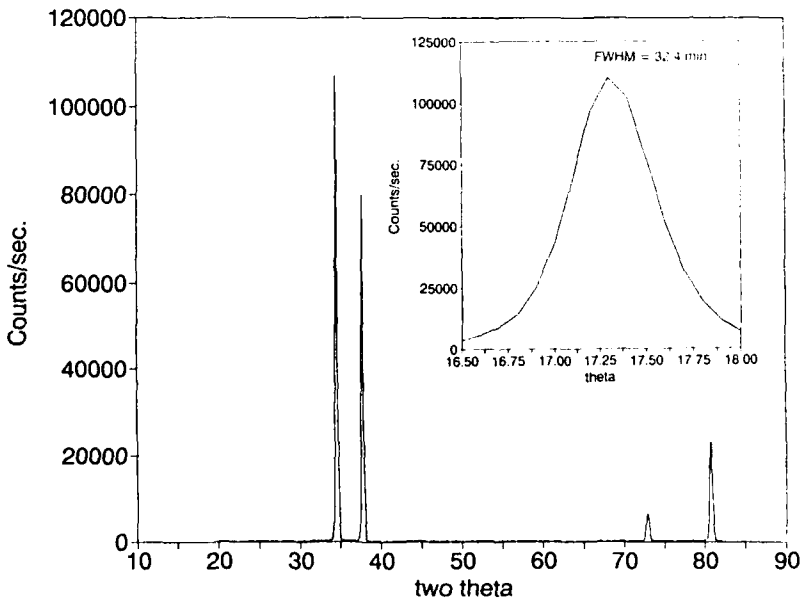


(a) (b) (c)

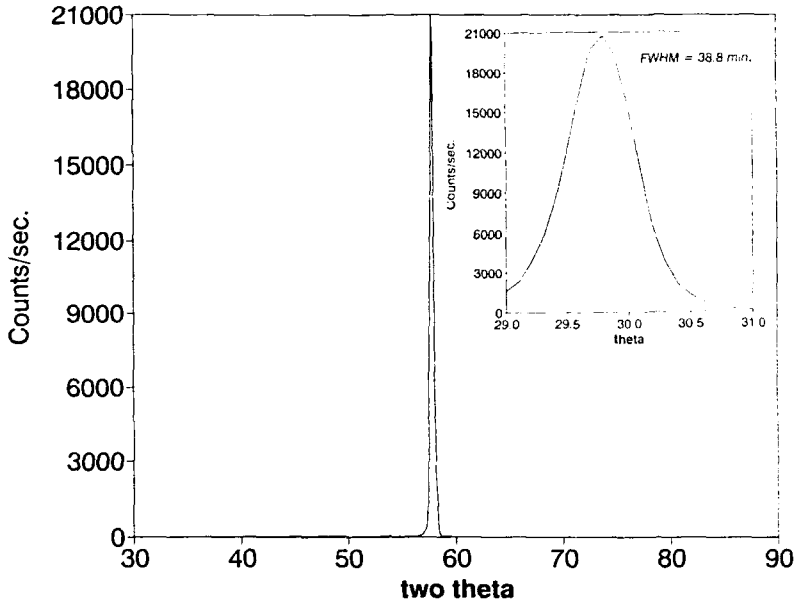
Fig. 4. SEM surface morphology of GaN films grown on various substrates: (a) c-plane, (b) a-plane, (c) r-plane.


25000
20000
15000
10000
5000
0
Counts/sec.
10
20
30
40
50
60
70
80
90
two theta
70000
60000
50000
40000
30000
20000
10000
0
Counts/sec.
FWHM = 10.2 min.
16.50 16.75 17.00 17.25 17.50 17.75 18.00
theta

(a)


120000
100000
80000
60000
40000
20000
0
Counts/sec.
10
20
30
40
50
60
70
80
90
two theta
125000
100000
75000
50000
25000
0
Counts/sec.
16.50 16.75 17.00 17.25 17.50 17.75 18.00
theta

(b)



(c)

Fig. 5 $\theta - 2\theta$ XRD of the GaN film on various sapphire susbtrates:(a) c-plane, (b) a-plane, (c) r-plane. The inserts show the corresponding rocking curves.

Fig. 5 shows the $\theta - 2\theta$ XRD and the θ-rocking curve at the main reflection peak of the GaN films grown on the three types of substrates. The main reflection peak for the GaN films grown on the c-plane and a-plane sapphire substrates occurs at $2\theta = 34.6°$, corresponding to the (0002) reflection. This confirms that films were grown with their c-planes parallel to the substrate. The main diffraction peak of the GaN film on the r-plane of sapphire occurs at $2\theta = 57.8°$ corresponding to the GaN (1120) reflection. This confirms the RHEED study that the a-plane of the GaN film is parallel to the substrate. The rocking curve of the GaN film on the c-plane of sapphire has the smallest width (FWHM=10 min.), indicating that the crystalline quality of these films to be the best.

The epitaxial relationship of the GaN films to the c-plane of sapphire is to be expected. However, the epitaxial relationship of the GaN films on the a-plane and r-planes of sapphire is not obvious. This epitaxial relationship can be accounted for as follows: The a-plane sapphire has a rectangular unit cell with dimensions 12.97Å × 8.23Å, two of which can accomodate a number of unit cells of GaN basal planes as shown in Fig. 6(a). This results in 1.6% lattice mismatch along [0001] of sapphire and 0.6% along [1100] axis of the sapphire substrate. The r-plane of sapphire substrate has a unit cell with dimension 4.75Å × 15.34Å, which accomodate three unit cells of the a-plane of GaN as illustrated in Fig. 6(b). This results in 16% lattice mismatch along the [1120] of sapphire and 1.3% along the [1101] of sapphire.

CONCLUSIONS

GaN films were grown on various crystallographic faces of sapphire by ECR-MBE. The growth process involves the conversion of the sapphire surfaces into AlN by plasma

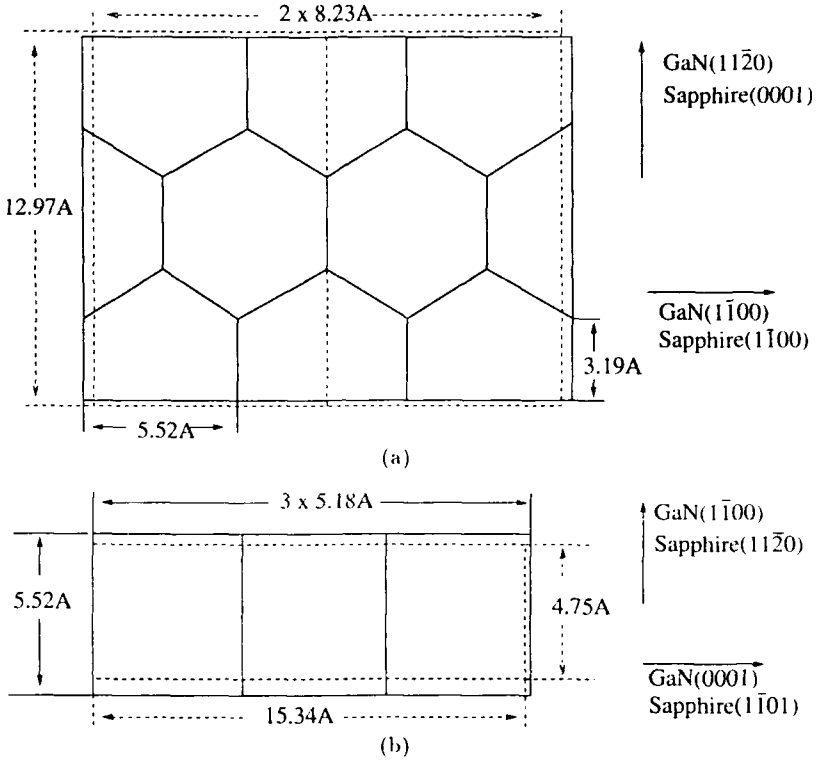


Fig. 6 Epitaxial relationship between GaN and (a) the a-plane of sapphire; (b) the r-plane of sapphire.

nitridation, the growth of a thin GaN buffer at $400 - 500°C$ and the growth of the rest of the film at $600 - 800°C$. RHEED studies indicate that this process of film growth promotes lateral growth and leads to films with smooth surface morphology. The XRD studies indicate that GaN films on the c-plane sapphire have the best crystalline quality. However, the films on the a-plane appear to have the smoothest surface morphology.

REFERENCES

1. M. J. Paisley, Z. Sitar, J. B. Posthil and R. F. Davis, J. Vac. Sci. Tech., 7, 701(1989).
2. T. Lei, M. Fanciulli, R. J. Molnar, T. D. Moustakas, R. J. Graham, and J. Scanlon, Appl. Phys. Lett., 58, 944(1991).
3. T. Lei, T. D. Moustakas, Y. He and S. J. Berkowitz, J. Appl. Phys., 71 (10), May 15(1992).
4. S. Strite, J. Ruan, Z. Li, N. Manning, A. Salvador, H. Chen, D. J. Smith, W. J. Choyke and H. Morkoc, J. Vac. Sci. Technol. B9, 1924 (1991).
5. C. R. Eddy Jr., T. D. Moustakas and J. Scanlon, submitted to J. Appl. Phys.
6. J. I. Pankove, MRS Symposium Proceedings, V162, 515(1990).
7. W. Seifert, R. Franzheld, E. Butter, H. Sobotta, V. Riede, Crystal Res. and Technol., 18, 383(1983).
8. T. D. Moustakas, MRS Bulletin, Vol. XIII, pp. 29 (1988).

A COMPARATIVE STUDY OF GaN EPITAXY ON Si(001) AND SI(111) SUBSTRATES

T. LEI* AND T. D. MOUSTAKAS**
*Department of Physics, Boston University, Boston, MA 02215.
**Department of Electrical Engineering and Department of Physics, Boston University, Boston, MA 02215.

ABSTRACT

Epitaxial GaN films were grown on Si(001) and (111) substrates, using a two-step process. The films on Si(001) are single crystalline having the zincblende strucutrue, while those on Si(111) have the wurtzite structure. The crystalline qualities of the films were studied by X-ray diffraction. While the zincblende GaN has a perfect cubic structure, the wurtzitic GaN on Si(111) has a considerable amount of stacking faults along (0002) direction, which gives rise to significant zincblende component with (111) orientation. Room temperature resistivity for both type of GaN films was found to be larger than 100 $\Omega \cdot cm$. The temperature dependence of th resistivity gives a defect level at 110meV for wurtzitic GaN and 80meV for cubic GaN. Optical studies show that GaN on Si(001) has a gap 3.2eV, and GaN on Si(111) has a gap of 3.4eV at room temperature.

INTRODUCTION

III-V nitrides and in particular GaN have been the subject of intensive studies due to their potential for short wavelength light emitting devices[1,2]. GaN films have been grown by a variety of deposition techniques[1,2], such as Chemical Vapor Deposition, Metal-Organic Chemical Vapor Deposition, Molecular Beam Epitaxy and a number of plasma-assisted processes. A variety of substrates such as silicon, spinel, silicon carbide and various crystallographic orientations of sapphire have been used in these studies. Most of the films grown have the wurtzite structure (α-GaN), with n-type conductivity and high carrier concentration, which is believed to result from nitrogen vacancies. Growth of GaN on foreign substrates is typically three dimensional, which leads to rough surface morphology.

Zincblende GaN(β-GaN), which is the thermodynamically metastable phase of GaN, is hoped to be more amenable to doping than the wurtzitic GaN, since all of the III-V compounds that can be efficiently doped n-type or p-typed are cubic[1]. β-GaN has been epitaxially stabilized on β-SiC and MgO(100) substrates[3,4], which are closely lattice-matched to β-GaN, and on GaAs[5,6] and Si[7,8] substrates, which have significant mismatch to β-GaN.

The growth of GaN on silicon substrates is both a scientifically challenging and a technologically important problem, since it offers the potential to integrate GaN and Si devices. The difficulties are due to the large difference in lattice constant, crystal structure and thermal expansion coefficient. The majority of the work on the growth of GaN on Si(001) or Si(111) reports the growth of polycrystalline or amorphous materials[9-11]. Recently, we demonstrated the growth of single crystalline GaN on Si(001), having the zincblende structure[7,8]. It was reported that single crystalline GaN in the wurtzite structure was grown on Si(111) substrates[9]. However, this conclusion was based on a $\theta - 2\theta$ scan of X-ray diffraction studies which only probe the structural ordering normal to the substrate, and thus can not distinguish single crystalline from well-oriented polycrystalline material.

Mat. Res. Soc. Symp. Proc. Vol. 242. © 1992 Materials Research Society

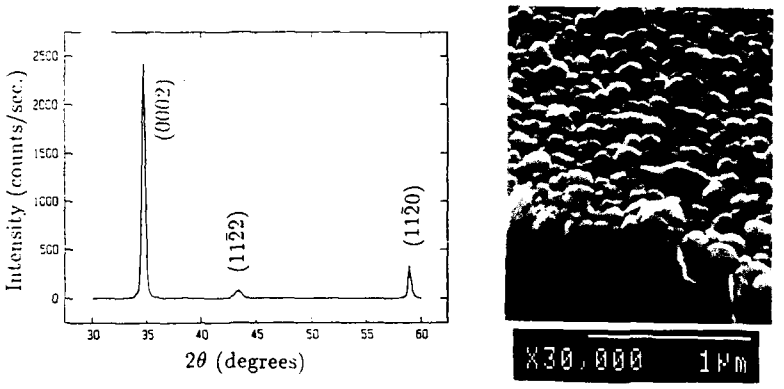
In this paper, we report a comparative study of GaN films grown on Si(001) and Si(111) substrates by ECR assisted MBE. Particular emphasis is placed on studies of the in-plane and out-of-plane crystalline quality of the GaN films.

EXPERIMENTAL METHODS

GaN films were grown using the Electron-Cyclotron-Resonance microwave plasma assisted Molecular Beam Epitaxy (ECR-MBE) method[7,8]. GaN films were studied by Reflection High Energy Electron Diffraction (RHEED), Scanning Electron Microscopy (SEM) and X-ray diffraction (XRD). X-ray diffraction studies were performed using a diffractometer with four-circle geometry[12]. This allows us to perform ϕ-scans at a reflection peak (hkl), corresponding to planes not parallel to the substrate, to probe the in-plane ordering. Additionally, standard $\theta - 2\theta$ scans were performed to probe the ordering normal to the substrate.

GaN films were grown by the one-step or two-step processes as described previously[7,8]. In the one-step process, GaN films were grown onto the substrate held at a fixed temperature, while in the two-step process, a GaN buffer layer of a few hundred angstroms thick is grown first at a low temperature, and the rest of the film is epitaxially grown on this GaN-buffer at higher temperatures.

EXPERIMENTAL RESULTS AND DISCUSSIONS



(a) (b)

Figure 1. (a) XRD of a GaN film grown in one-step on Si(111); (b) SEM surface morphorlogy of the same films.

Growth of GaN on Si(001) and Si(111) by the ECR-MBE method, using the one step growth process, leads to polycrystlline films. The results on Si(001) have been discussed previously[7,8]. Here we discuss the results on the growth of GaN on Si(111). Fig. 1 (a) and (b) show the $\theta - 2\theta$ scan of XRD and SEM surface morphology of a GaN film grown at $600°C$ on Si(111). The data show that the film is polycrystalline, with strong (0002) preferred orientation. The SEM studies reveal that the film has columnar morphology.

In the following we present studies on GaN films grown on Si(001) and Si(111) using the two-step process. The buffer layer, approximately 300Å thick, was grown at $400°C$, and the rest of the film, approximately $1\mu m$ thick, was grown at 600°.

The RHEED patterns, shown in Fig. 2, indicate that GaN films on Si(001) have the zincblende structure with their (001) planes parallel to the substrate, and those on Si(111) have the wurtzite structure, with their (0001) planes parallel to the substrate. The sharpness of the spots indicates good crystalline quality of the film, and the streaking feature of the spots suggests a fairly smooth surface morphology.



(a) (b)

Figure 2. RHEED patterns for (a) a GaN film on Si(001) with [100] electron azimuthal incidence; (b) a GaN film on Si(111) with [1120] electron azimuthal incidence.



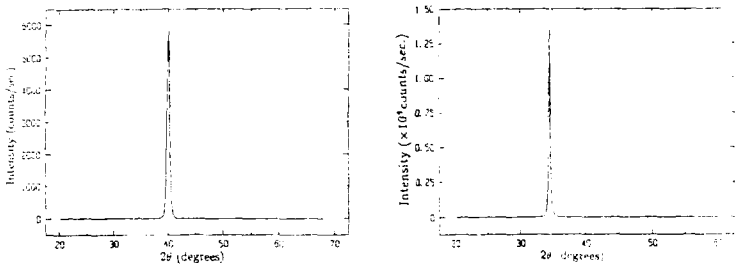
(a) (b)

Figure 3. SEM surface morphology of the two GaN films discussed in Fig. 2. (a) zincblende GaN, (b) wurtzite GaN.

Fig. 3 shows the SEM surface morphology of the GaN films discussed in Fig. 2. The surface of the cubic GaN film consists of many retangular 'tiles', well oriented along [110] direction. The height of these tiles is of the order of 1000Å, which is then characteristic of the film roughness. The front view of the wurzitic GaN film shows

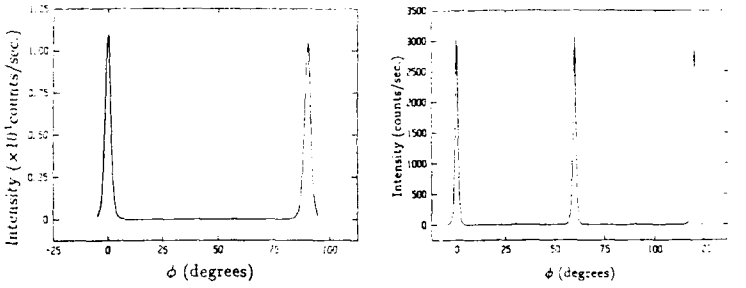
comparable roughness, however, it does not show any particular geometric pattern. The cross-sectional SEM studies did not show any indication of columnar morphology.

Figure 4 shows $\theta - 2\theta$ scans for GaN films on Si(001) and Si(111). The GaN film on Si(001) shows a peak at $2\theta = 40.0°$, which corresponds to (002) reflection of GaN. From these data, the lattice constant was calculated to be 4.50Å. The GaN film on Si(111) shows a peak at 34.6 degrees, which corresponds to (0002) reflection of the wurtzite GaN, therefore, the the c-value for the wurtzite GaN was found to be 5.18Å.



(a) (b)

Figure 4. $\theta - 2\theta$ scans for (a) a zincblende GaN film on Si(001), (b) a wurtzitic GaN film on Si(111).



(a) (b)

Figure 5. ϕ-scan for (a) a zincblende GaN film (b) a wurtzite GaN film.

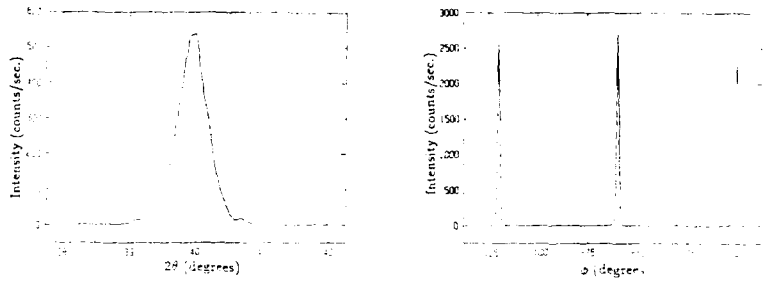
The ϕ-scan for the zincblende GaN was performed at the $(\bar{1}11)$ reflection, and is shown in Fig. 5(a). The data clearly show that the peak repeats itself every 90 degrees, consistent with the cubic symmetry of this material. The FWHM (Full Width at Half Maximum) of these peaks, which measures the in-plane orientational spread, was found to be 2.5 degrees, while the FWHM of the θ-rocking curve at the (002) reflection, which measures the orientational spread perpendicular to the substrate, was found to be 1°[8].

The ϕ-scan for the wurtzitic GaN was performed at the $(1\bar{1}02)$ reflection. Clearly the peak repeats every 60 degrees, consistent with the 3mm symmetry of the rotation

axis. The FWHM is found to be 1.9 degrees, while FWHM of the $\theta - 2\theta$-rocking curve at the (0002) peak is found to be 0.9°

The data of Fig. 5 (a) and (b) indicate that there are no in-plane misoriented domains in both structures, thus further confirms the good crystallinity of GaN films grown by the two-step process on both Si(001) and Si(111) substrates.

The XRD shown in Fig. 4 indicates that while β-GaN may has a very small component of (111) or (0002) oriented domains[7,8], the α-GaN appears to be a perfect single crystal. However, any stacking faults along the growth direction of the GaN film on Si(111) can not be easily detected in the normal $\theta - 2\theta$ scans[13]. Such stacking faults are very common defects in materials with the FCC or HCP structures growing along the (111) and (0002) directions[14]. Such stacking faults, if exist in the wurtzitic GaN films on Si(111), should give rise to a certain amount of cubic GaN component with the (111) planes parallel to the substrate. To explore this possibility, we rotated the sample in such a way that the X-ray diffraction corresponds to the (002) reflection of the zincblende structure, and indeed a peak was detected at $2\theta = 40$ degrees. This is shown in a $\theta - 2\theta$ scan around this peak Fig. 6(a).



(a) (b)

Figure 6. (a) $\theta - 2\theta$ scan at the (002) reflection of cubic GaN grains in a wurtzitic GaN film: (b) ϕ-scan at (111) peak of cubic GaN.

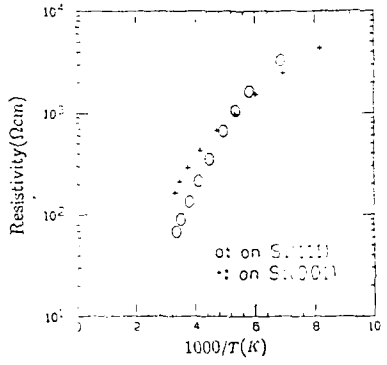


Figure 7. Temperature dependence of the resistivity of GaN films

To obtain a stronger reflection, ϕ-scans on these cubic domains were performed at (111) peak, which is shown in Fig. 6(b). These data reveal a repetition every 60 degrees. Since the (111) axis in the zincblende structure is only a 3-fold rotational axis, *the* $\phi - scan$ should show a repetition every 120° instead of every 60°. Therefore the ϕ-scan of Fig. 6(b) indicates that the cubic domains have two in-plane orientations differing by 60 degrees in ϕ. This can be accounted for if there are two kinds of stacking sequence, namely, ABC... and CBA... sequence. The fact that the peak at $\phi = 60°$ is of comparable intensity to the other two peaks suggests that the two types of stacking sequence occur with an equal probability, as is expected.

The existence of the cubic GaN domains in the wurtzite structure implies the existence of high concentration of stacking faults. This could be due to the fact that the cohesive energies of wurtzite and zincblende GaN are comparable, so that the formation energy of a stacking fault is neglegible. If this is true, then all of the (0002) oriented GaN films have a considerable amount of stacking faults. This is currently being investigated by XRD studies of GaN on (1120) and (0001) sapphire substrate[15]. However, one should not rule out that the high concentration of stacking faults in GaN on Si(111) is related to strain resulting from the large lattice mismatch between GaN and Si, which could lead to reduction of the formation energy of stacking faults due to structural deformation.

Optical studies suggests that the zincblende GaN on Si(001) has a direct band gap $3.2eV$ and wurtzite GaN on Si(111) has a direct band gap $3.4eV$. GaN films on Si(001) and Si(111) have comparable room temperature resistivity, of the order of $100\Omega cm$. The activation energy from the temperature dependence of the resistivity (Figure 7) is approximately $110meV$ for wurtzitic GaN, and $80meV$ for zincblende GaN.

CONCLUSIONS

In conclusion, GaN films were successfully grown on Si(001) and (111) substrates, using the two-step process. The films on Si(001) are single crystalline having the zincblende strucutrue, while those on Si(111) have the wurtzite structure. Although RHEED suggest that the wurtzitic GaN on Si(111) is single crystalline, considerable amount of cubic phase was detected by XRD studies, and was attributed to larger concentration of stacking faults along the growth direction. Both type of GaN films showed comparable electrical properties. The temperature dependence of th resistivity gives a defect level at 110meV for wurtzitic GaN and 80meV for cubic GaN. Optical studies show that they have slight different bandgap.

ACKNOWLEDGMENT

We thank Professor Karl Ludwig for the help with X-ray diffraction and valuable discussions. The work was supported by Bellcore and Exxon Educational Foundation.

REFERENCES

1. J. I. Pankove, MRS Symposium Proceedings, V162, 515(1990).
2. R. F. Davis, Proceedings of the IEEE., V. 79, No. 5, 702(1991); R. F. Davis, Z. Sitar, B. E. Williams, H. S. Kong, H. J. Kim, J. W. Palmour, J. A. Edmond, J. Ryu, J. T. Glass and C. H. Carter, Jr., Mat. Sci. & Eng. B1, 77(1988).
3. M. J. Paisley, Z. Sitar, J. B. Posthil and R. F. Davis, J. Vac. Sci. Tech., 7, 701(1989).
4. R. C. Powell, G. A. Tomasch, Y. W. Kim, J. A. Thornton and J. E. Greene, MRS Symposium Proceedings, V162, 525(1990).

5. M. Mizuta, S. Fujieda, Y. Matsumoto and T. Kawamura, Japanese J. Appl. Phys. 25, L945(1986).
6. S. Strite, J. Ruan, Z. Li, N. Manning, A. Salvador, H. Chen, D. J. Smith, W. J. Choyke and H. Morkoc, J. Vac. Sci. Technol. B9, 1924 (1991).
7. T. Lei, M. Fanciulli, R. J. Molnar, T. D. Moustakas, R. J. Graham, and J. Scanlon, Appl. Phys. Lett., 58, 944(1991).
8. T. Lei, T. D. Moustakas, Y. He and S. J. Berkowitz, J. Appl. Phys., 71 (10), May 15(1992).
9. Y. Morimoto, K. Uchiho and S. Ushio, J. Electrochem. Soc.: Solid-State Sci. and Tech., 120, 1783(1973).
10. E. Butter, G. Fitzi, D. Hirsch, G. Leonhardt, W. Seifert and G. Preschel, Thin Solid Films, 59, 25(1979).
11. Z. Sitar, M. J. Paisley, B. Yan and R. F. Davis, MRS Symposium Proceedings, V162, 537(1990).
12. W. R. Busing and H. A. Levy, Acta Cryst. 22, 4579(1967).
13. B. E. Warren, X-ray diffraction, Addison-Welsley Publ. Company, Inc. (1969).
14. C. Kittle, Introduction to Solid State Physics, John Wiley & Sons, Inc., (1986).
15. T. Lei, K. F. Ludwig Jr. and T. D. Moustakas, to be published.

GROWTH DEPENDENCE OF THICKNESS, MORPHOLOGY AND ELECTRICAL TRANSPORT OF InN OVERLAYERS ON AlN-NUCLEATED (00.1) SAPPHIRE

T. J. KISTENMACHER, S. A. ECELBERGER AND W. A. BRYDEN
Applied Physics Laboratory
The Johns Hopkins University, Laurel, MD 20723-6099

ABSTRACT

The seeded-heteroepitaxial growth, morphology and electrical transport properties of InN overlayers deposited by reactive magnetron sputtering on AlN-nucleated (00.1) sapphire have been investigated. For comparison, InN films were grown directly onto (00.1) sapphire under identical experimental conditions. These unseeded films showed a unimodal growth and were a mixture of textured and broadly heteroepitaxial grains. Low Hall mobility and carrier concentration and high resistivity were typical. In contrast, the AlN-nucleated InN overlayers exhibited a bimodal growth, strongly heteroepitaxial grains, and high Hall mobility. A particularly interesting aspect of the films grown on seeded (00.1) sapphire is the preservation of electrical continuity and high Hall mobility even in the limit of InN overlayers with thicknesses only on the order of 20-40Å.

INTRODUCTION

It is well known [1-2] that as the lattice mismatch for heteroepitaxial systems increases, the film nucleation mechanism changes from the Frank-van der Merwe (layer-by-layer) to either the Stranski-Krastnov or Volmer-Weber (3D island) growth mode. It is also becoming more widely appreciated that seeded heteroepitaxy can alter the choice of growth mechanism and therefore significantly modify dependent physical properties. Very recent examples of the utility of seeded-heteroepitaxial growth include: the deposition of smooth, high mobility films of GaN on AlN-nucleated [3] and self-nucleated (00.1) [4] sapphire; the achievement of heteroepitaxial TiN films on Si(100) via self nucleation [5]; the study of the intrinsic magnetic anisotropy in Co/M (M = Au [6], Pt [7], and Pd [8]) epitaxial superlattices; and, finally, the growth of highly oriented cubic zirconia on (00.1) sapphire [9].

In this report, aspects of our continuing studies [10] on the growth dependence of thickness, morphology and electrical transport for InN films deposited on (00.1) sapphire and AlN-seeded (00.1) sapphire substrates are presented.

EXPERIMENTAL

All films were grown in a magnetron sputter deposition system with a typical base pressure near 5×10^{-8} Torr. The targets were Al or In disks with purity in excess of 99.99% and growth was carried out in 99.999% pure N_2 gas at a pressure of 5 mTorr. The substrates were chemically polished (00.1) sapphire which were degreased and subsequently heated to 900°C in vacuo. For the InN films deposited directly onto (00.1) sapphire, the substrate temperature was then reduced to 400°C, and film growth (rf; 50W) initiated. For the InN films deposited onto AlN-nucleated (00.1) sapphire, the temperature was intermediately reduced to 600°C and an AlN

nucleation layer was dc sputtered (500mA, 325V; 15min, ~400Å), and finally the temperature of the nucleated substrate was reduced to 400°C and the InN overlayer grown.

RESULTS AND DISCUSSION

To establish a framework for discussion, a description of the properties of the InN films deposited directly onto (00.1) sapphire at 400°C is first given. From Figure 1, it can be seen that there is a single, essentially linear dependence of film

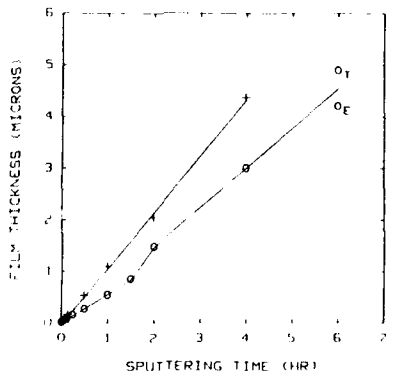


Figure 1. Dependence of film thickness film on sputtering time for InN films grown on (00.1) sapphire (+) and on AlN-nucleated (00.1) sapphire (o).

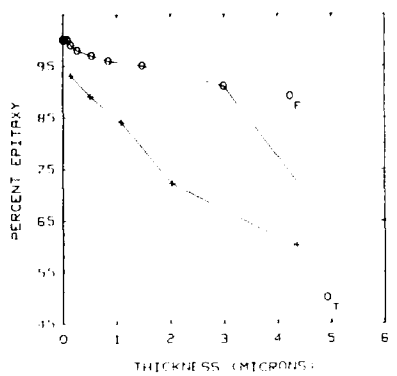


Figure 2. Variation in percent epitaxial grains with film thickness for InN films grown on (00.1) sapphire (+) and on AlN-nucleated (00.1) sapphire (o).

thickness on deposition time. Moreover, these films are a composite of substantial fractions of textured [$(00.1)_{InN}//(00.1)_{sapphire}$] and broadly heteroepitaxial [additionally, $(10.0)_{InN}//(11.0)_{sapphire}$] grains (Figure 2) and show a uniformly poor Hall mobility (Figure 3), low carrier concentration and high resistivity. These results are typical of thin films of InN on (00.1) sapphire having evolved by a 3D island growth mode and comprised of a mosaic of weakly interacting columnar grains.

The rather mundane properties of these InN films on (00.1) sapphire are contrasted by the characteristics of the InN overlayers grown on AlN-seeded (00.1) sapphire. Firstly, the AlN-nucleated InN overlayers are found to be composed almost entirely (Figure 2) of heteroepitaxial grains showing the same heteroepitaxial relationship to the sapphire substrate as for the unnucleated films. Importantly, this heteroepitaxial relationship prevails even from the very thinnest films investigated (~20-40Å) on up to a film thickness of over 3.5μm. At the limit of the thickest films investigated (~4.5μm), the structural and morphological correlations significantly degenerate, and the films are either largely textured (T) or heavily epitaxial (E) and

exhibit significantly different thicknesses (Figure 1) and transport (Figure 3) properties.

Secondly, two distinctive regimes are readily identified for the dependence of overlayer thickness on deposition time, viz. Figure 1. Consistent with these and other data [1-2], the morphology of the InN overlayers on AlN-nucleated (00.1) sapphire in the early time regime likely evolves via a 2D layer-by-layer growth mechanism. For longer deposition times, these results are suggestive of a change in growth mechanism and a likely crossover to a large grain, 3D island mode.

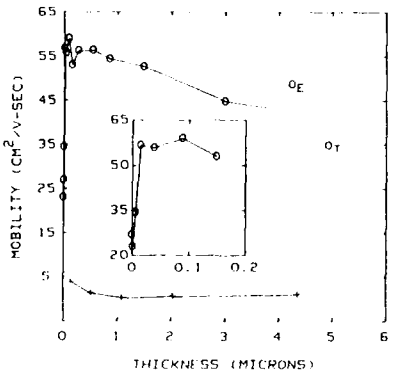


Figure 3. Dependence of Hall mobility on film thickness for InN films grown on (00.1) sapphire (+) and on AlN-nucleated (00.1) sapphire (o).

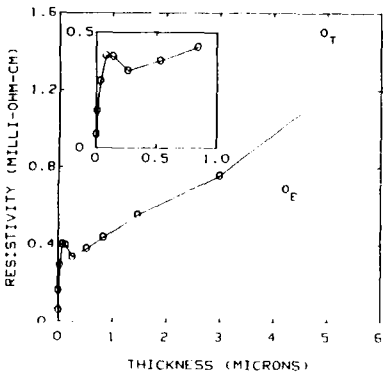


Figure 4. Variation in resistivity with film thickness for InN films grown on AlN-nucleated (00.1) sapphire (o).

Thirdly, the electrical characteristics of these InN overlayers are quite interesting. From an InN film thickness of about 20-40Å to over 3.5μm, Figure 3, Hall mobilities from 25 to 60 cm^2/V-sec are measured. For the thinnest of the InN overlayers studied, electrical continuity is maintained in spite of the fact that the AlN nucleation layer is composed of a high density of small particles (lattice mismatch for AlN and sapphire of 13.2%) and that the thickness (20-40Å) of the InN overlayer is very modest compared to that (400Å) for the insulating AlN-nucleation layer. Finally, the observed variation in Hall mobility with film thickness shown in Figure 3 arises from competing trends in carrier concentration and film resistivity. There is a smooth and rapid reduction in carrier concentration as the importance of misfit dislocations and surface scattering states decreases with increasing distance from the film/nucleation layer/substrate interface. As can be seen in Figure 4, however, there is a sharp rise in film resistivity with increasing InN overlayer thickness, followed by a local maximum (possibly signalling the transformation from heteroepitaxial to homoepitaxial growth), and then a slow rise.

In summary, thin films of InN have been deposited onto (00.1) sapphire and AlN-nucleated (00.1) sapphire by reactive magnetron sputtering. The influence of the AlN

nucleation layer on film thickness, morphology, and transport properties has been shown to be dramatic. For example, the unnucleated films show a single 3D island growth mechanism, while there is a crossover from a 2D layer-by-layer to a 3D island growth mode at a critical film thickness for the AlN-seeded InN overlayers. Lastly, while InN films grown directly onto (00.1) sapphire are a mixture of textured and heteroepitaxial grains and generally exhibit poor transport properties at all film thicknesses, AlN-nucleated overlayers as thin 20-40Å show fully heteroepitaxial growth and quite high electrical mobility.

ACKNOWLEDGMENTS

This work was supported in part by the U.S. Department of the Navy under Contract N00039-89-C-5301.

REFERENCES

1. E. G. Bauer, et al., J. Mater. Res. **5**, 852 (1990).
2. See, for example, R. Kern, G. Le Lay, and J. J. Metois, in Current Topics in Materials Science, E. Kaldis, ed., (North Holland, Amsterdam, 1979), pg. 130.
3. H. Amano, N. Sawaki, I. Akasaki, and Y. Toyoda, Appl. Phys. Lett. **48**, 415 (1988); H. Amano, I. Akasaki, K. Hiramatsu, N. Koide, and N. Sawaki, Thin Solid Films **163**, 415 (1988); I. Akasaki, H. Amano, Y. Koide, K. Hiramatsu, and N. Sawaki, J. Cryst. Growth **98**, 209 (1989).
4. D. K. Wickenden, T. J. Kistenmacher, W. A. Bryden, J. S. Morgan, and A. E. Wickenden, Proc. Mater. Res. Soc, **221**, 167 (1991).
5. C.-H. Choi, L. Hultman, W.-A. Choi, and S. A. Barnett, J. Vac. Sci. Technol. B **9**, 221 (1991).
6. B. N. Engel, C. D. England, R. A. Van Leeuwen, M. H. Wiedmann, and C. M. Falco, Phys. Rev. Lett. **67**, 1910 (1991).
7. C. H. Lee, H. He, F. Lamelas, W. Vavra, C. Uher, and R. Clarke, Phys. Rev. Lett. **62**, 653 (1989).
8. C. H. Lee, R. F. C. Farrow, C. J. Lin, E. E. Marinerom and C. J. Chien, Phys. Rev. B **42**, 11384 (1990).
9. K. T. Miller and F. F. Lange, J. Mater. Res. **6**, 2387 (1991).
10. T. J. Kistenmacher and W. A. Bryden, Appl. Phys. Lett. **59**, 1844 (1991); W. A. Bryden, J. S. Morgan, R. Fainchtein, and T. J. Kistenmacher, Thin Solid Films, in press.

LOW TEMPERATURE PREPARATION OF GALLIUM NITRIDE THIN FILMS

ROY G. GORDON,† DAVID M. HOFFMAN‡ AND UMAR RIAZ†

†Department of Chemistry, Harvard University, 12 Oxford Street, Cambridge, MA 02138
‡Department of Chemistry, University of Houston, Houston, TX 77204

ABSTRACT

Gallium nitride thin films were prepared by atmospheric pressure chemical vapor deposition from hexakis(dimethylamido)digallium, $Ga_2(NMe_2)_6$, and ammonia precursors at substrate temperatures of 100–400 °C with growth rates up to 1000 Å/min. The films were characterized by transmission electron microscopy, X-ray photoelectron spectroscopy, Rutherford backscattering spectrometry and forward recoil spectrometry. The N/Ga ratio varied from 1.05 for films deposited at 400 °C to 1.5 at 100 °C. The hydrogen concentration increased from 10 atom % for films deposited at 400 °C to 24 atom % at 100 °C. Films deposited at 100 °C were amorphous but films deposited at higher temperatures were polycrystalline. Bandgaps of the films varied from 3.8 eV for films deposited at 400 °C to 4.2 eV at 100 °C.

INTRODUCTION

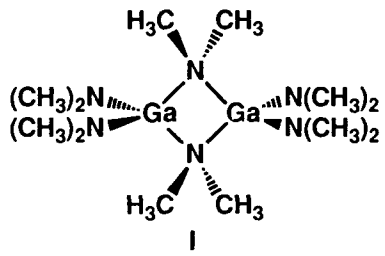
Gallium nitride is a semiconductor with a direct bandgap of 3.4 eV that has potential applications in optoelectronic devices such as light emitting diodes and UV-emitting lasers [1]. Because of its predicted large saturated electron drift velocity, gallium nitride is also a candidate for use in high power, high frequency devices [2]. Alloys of the group III nitrides, such as AlGaN and GaInN, have also been widely studied because of their potential applications in microelectronic and optoelectronic devices [3]. To date, applications of gallium nitride have been limited because most methods of preparation yield conductive *n*-type GaN. The conductivity is attributed to the presence of nitrogen vacancies, which are thought to result because of the high temperatures required in the preparation of GaN films [1].

Chemical vapor deposition (CVD) routes to GaN include the use of gallium metal, hydrogen chloride and ammonia at 800–1200 °C [4], gallium halides and ammonia at 600 °C [5, 6], and gallium alkyl complexes and ammonia at 500–700 °C [7]. Recently, there has been a considerable effort to develop lower temperature physical and chemical vapor deposition routes to GaN. For example, electron cyclotron resonance plasma excited organometallic vapor phase epitaxy has been used to deposit GaN films at 300–400 °C [8]. Lower CVD temperatures have been achieved by use of trimethylgallium and hydrazine (425–960 °C) [9] and the thermal decomposition of diethylgallium azide, $[Et_2Ga(\mu\text{-}N_3)]_3$ (350–450 °C) [10, 11].

We recently demonstrated that polycrystalline gallium nitride thin films deposited from hexakis(dimethylamido)digallium, $Ga_2(NMe_2)_6$ (**I**), and ammonia precursors at 200 °C [12] according to the idealized chemical reaction shown below (eq 1). $Ga_2(NMe_2)_6$ is a moderately air-sensitive solid which melts at 92 °C and sublimes readily under vacuum in the temperature range 70–80 °C [13,14].

$$Ga_2(NMe_2)_6 + 6NH_3 \longrightarrow 2GaN + 6HNMe_2 \qquad (1)$$

Herein we report the extension of the gallium nitride synthesis to include temperatures of deposition in the range 100 to 400 °C.



I

EXPERIMENTAL

General experimental procedures have been described previously [12,15]. Rutherford backscattering and forward recoil spectrometry were performed on a General Ionics Model 4117 spectrometer. A gold-coated piece of Kapton (composition: $C_{22}H_{10}N_2O_5$) was used as the calibration standard in the forward recoil experiments. The transmission electron micrographs and electron diffraction patterns were obtained on a Philips EM420T scanning transmission electron microscope. Transmission spectra were recorded with a Varian 2390 spectrophotometer for samples deposited on quartz. Refractive indexes were measured with a Rudolf Auto-EL ellipsometer for samples deposited on silicon.

RESULTS

Film depositions from $Ga_2(NMe_2)_6$ and ammonia were successfully carried out on silicon, quartz and glass substrates in the temperature range 100–400 °C. At each deposition temperature the highest growth rates of up to 1000 Å/min were obtained when the bubbler assembly containing the precursor and the reactor feed lines for the gallium complex were maintained at 100 and 130 °C, respectively. The films showed good adhesion on all substrates by the adhesive tape criterion and were not visibly affected when placed in concentrated hydrochloric acid for 5 minutes.

The nitrogen to gallium ratio in the films was determined by Rutherford backscattering spectrometry (RBS) for films deposited on silicon. The results are summarized in Table I. In general, the films were nitrogen rich but the amount of excess nitrogen decreased as the temperature of deposition increased. No signals due to carbon or oxygen were observed in the RBS spectra.

Table I. Composition of Gallium Nitride Films

Temperature of Deposition (°C)	N/Ga ratio[a]	H content[b] (atom %)
100	1.50	24
200	1.20	19
300	1.05	14
400	1.05	10

[a] The error in these values is estimated to be ±0.05.
[b] The error in these values is estimated to be ±1%.

Forward recoil spectrometry (FRS) was used to determine the hydrogen content of the films (Figure 1). The content decreased by ≈5 atom % for each 100 °C increase in deposition temperature. The smallest amount of hydrogen (≈10 atom %) was found in the films deposited at 400 °C.

X-ray photoelectron spectra were used to estimate the amount of carbon and oxygen in the films. After sputtering (3-keV Ar^+ sputter gun) into the bulk of the films, no carbon signals were

observed which indicated that the concentration of the carbon was less than 1–2 atom %. None of the films examined had more than 5 atom % oxygen present in the bulk. The binding energy of the Ga 3d peak was 19.4 eV, which is consistent with the value reported previously for GaN [16].

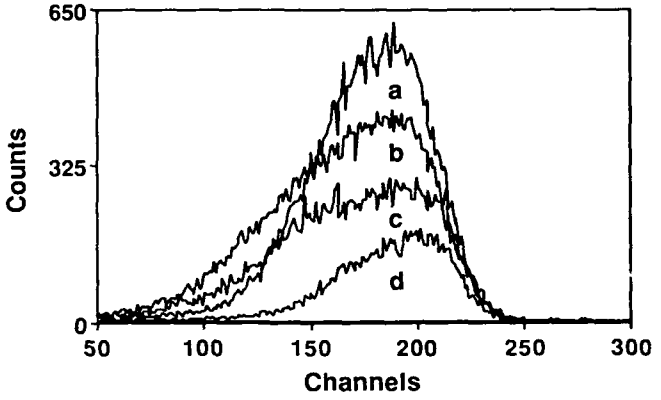


Figure 1. EPS spectra for GaN films deposited on silicon at 100 (a), 200 (b), 300 (c) and 400 (d) °C.

Transmission electron microscopy (TEM) was used to examine the morphology of the films. The films deposited at 100 °C were smooth and featureless and showed a diffuse electron diffraction pattern consistent with an amorphous material. Films deposited at 200, 300 and 400 °C, on the other hand, gave well-defined electron diffraction patterns indicative of a

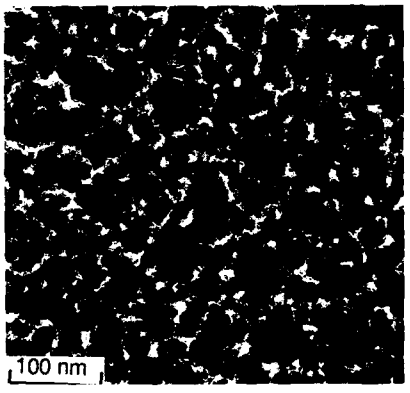


Figure 2: Transmission electron micrograph of a GaN thin film deposited at 400 °C on carbon-coated mica

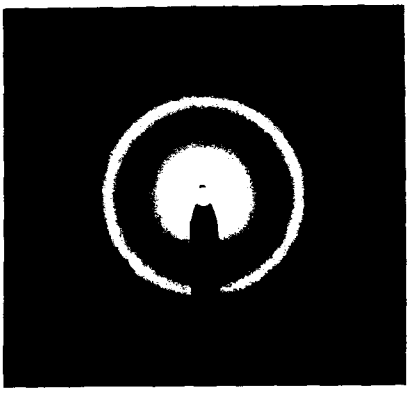


Figure 3: Electron diffraction pattern for a GaN film deposited at 400 °C on carbon-coated mica.

polycrystalline material. The diffraction patterns were consistent with the hexagonal phase of gallium nitride [17]. Micrographs indicated that the films were dense with a crystallite size in the 2–10 nm range. The TEM micrograph and electron diffraction pattern for a film deposited at 400 °C are shown in Figures 2 and 3.

Transmission spectra recorded for films deposited at 100, 200 and 400 °C are shown in Figure 4. The films showed a high transmittance in the visible region. The optical band-gaps of the films were estimated by plotting $h\nu$ vs $(\alpha h\nu)^{1/2}$ where $h\nu$ is the photon energy and α is the absorption coefficient. This procedure revealed that the bandgap decreased as the deposition temperature was increased (Table II) from a value of 4.2 eV for films deposited at 100 °C to 3.8 eV for films deposited at 400 °C. The bandgaps were higher than the value of 3.4 eV reported for single crystal gallium nitride [1].

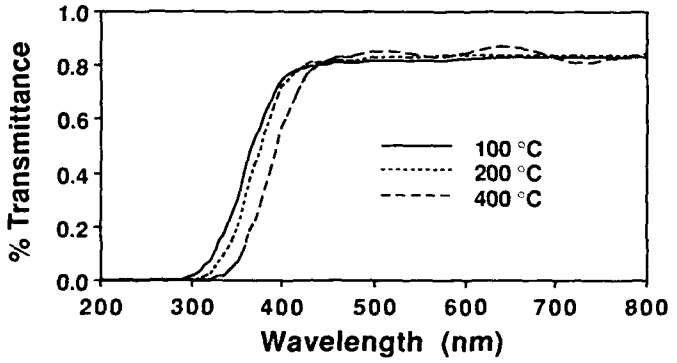


Figure 4. Transmission spectra for gallium nitride films deposited on quartz at 100, 200 and 400 °C.

Table II. Optical Properties for Gallium Nitride Films Deposited on Quartz.

Temperature of Deposition (°C)	Bandgap[a] (eV)	Refractive index
100	4.20	1.86
200	4.10	2.08
300	4.10	2.10
400	3.80	2.17

[a] The error in these values is estimated to be ±0.05.

Refractive indexes of the films were found to increase with deposition temperature. For example, the values were 1.86 at 100 °C and 2.17 at 400 °C. Refractive indexes in the range 2.03-2.5 have been reported for gallium nitride [18]. For all deposition temperatures the films had resistivities greater than 10^8 Ω cm as determined by the four point probe method.

Hexakis(dimethylamido)digallium was also examined as a possible single source precursor to GaN films. In the substrate temperature range 100–300 °C no film deposition was observed from the single-source precursor system on silicon or glass. However, at 400 °C under deposition conditions that were similar to those described above for the dual precursor system, films were obtained on silicon. Analysis of the films by XPS revealed that after sputtering into the bulk of the sample, only strong gallium and weak oxygen signals were observed. No signals attributable to carbon or nitrogen were detected.

DISCUSSION

Hexakis(dimethylamido)digallium and ammonia is a promising precursor system for the low temperature chemical vapor deposition of gallium nitride thin films. Films deposited by this method showed good adhesion, good chemical resistance and had high growth rates.

Films deposited at 100 °C were amorphous with hydrogen concentrations greater than 20 atom % and contained a large excess of nitrogen over the expected GaN stoichiometry. Films deposited at 200–400 °C were polycrystalline (hexagonal). At the higher temperatures, the N:Ga ratio was close to 1 and the hydrogen content was low. Hence, films deposited at 200 °C and higher temperatures can be formulated as GaN containing residual hydrogen.

The refractive index of films deposited at 100 °C was 1.86, which is lower than the value reported for gallium nitride [18]. This is probably due to a lower density of the films, which is perhaps a consequence of the large amount of hydrogen in the films. Films deposited at 200 °C and higher temperatures display refractive indexes close to the reported value. The hydrogen in the films may also account for the discrepancy between the measured bandgaps (3.8–4.0 eV) and the bandgap reported for crystalline gallium nitride (3.4 eV), since the amount of hydrogen and the bandgap both decrease with increasing temperature of deposition.

The deposition of GaN films from $Ga_2(NMe_2)_6$ and NH_3 probably proceeds via $Ga\text{–}NH_2$ and/or Ga=NH containing intermediates. Incomplete decomposition of these putative intermediates may account for the large amount of hydrogen in the films at low temperatures.

CONCLUSIONS

Hexakis(dimethylamido)digallium and ammonia precursors deposited amorphous and polycrystalline gallium nitride films at 100 °C and 200–400 °C, respectively. Because the precursor mixture gave polycrystalline films with low carbon and oxygen contamination, the system warrants further examination. In particular, single crystal films may be accessible if the depositions were carried out over suitable substrates such as sapphire. Also, it may be possible to use the $Ga_2(NMe_2)_6/NH_3$ precursor system in combination with the $Al_2(NMe_2)_6/NH_3$ system, which produced AlN films of similar quality in the same temperature range [19], for the deposition of AlGaN films.

ACKNOWLEDGEMENTS

We are grateful to the National Science Foundation (DMR-8802306) for support of this work. The RBS and FRS spectra were acquired using the Cambridge Accelerator for the Materials Sciences housed in the Harvard Materials Research Laboratory, an NSF funded facility (DMR-86-14003). DMH acknowledges the support of the Robert A. Welch Foundation in the latter stages of this research.

REFERENCES

1. J. I. Pankove, Mater. Res. Soc. Symp. Proc. 162, 515 (1990).
2. R. F. Davis, Z. Sitar, B. E. Williams, H. S. Kong, H. J. Kim, J. W. Palmour, J. A. Edmond, J. Ryu, J. T. Glass, C. H. Carter, Jr., Mat. Sci. Eng. B1, 77 (1988).
3. I. Akasaki, H. Amano, Y. Koide, K. Hiramatsu, N. Sawaki, J. Cryst. Growth 98, 209 (1989).

4. H. P. Maruska, J. J. Tietjen, Appl. Phys. Lett. 15, 327 (1969).
5. P. J. Born, D. S. Robertson, J. Mater. Sci 15, 3003 (1980).
6. T. L. Chu, J. Electrochem. Soc. 118, 1200 (1971).
7. H. M. Manasevit, F. M. Herdmann, W. I. Simpson, J. Electrochem. Soc. 118, 1864 (1971).
8. S. Zembutsu, T. Sasaki, Appl. Phys. Lett. 48, 870 (1986).
9. D. K. Gaskill, N. Bottka, M. C. Lin, J. Cryst. Growth 77, 418 (1986).
10. J. Kouvetakis, D. B. Beach, Chem. Mater. 1, 476 (1989).
11. K. L. Ho, K. F. Jensen, J. W. Hwang, J. F. Evans, W. L. Gladfelter, Mater. Res. Soc. Symp. Proc. 204, 101 (1991).
12. R. G. Gordon, D. M. Hoffman, U. Riaz, Mater. Res. Soc. Symp. Proc. 204, 95 (1991).
13. K. M. Waggoner, M. M. Olmstead, P. P. Power, Polyhedron 9, 257 (1990).
14. H. Noth, P. Konrad, Z. Naturforsh. B. 10, 234 (1955).
15. R. Fix, R. G. Gordon, D. M. Hoffman, Chem. Mater. in press.
16. Practical Surface Analysis, edited by D. Briggs, M.P. Seah (John Wiley, New York, 1983), p. 498.
17. GaN: Index No. 2-1078. Powder Diffraction File, editor-in-chief: W. F. McClune (JCPDS International Centre for Diffraction Data, Swarthmore, PA 19081-2389, USA).
18. H. J. Hovel, J. J. Cuomo, Appl. Phys. Lett. 20, 71 (1972).
19. R. G. Gordon, D. M. Hoffman, U. Riaz, J. Mater. Res. 6, 5 (1991).

AN INVESTIGATION OF LIGHT INDUCED DEFECTS IN ALUMINUM NITRIDE CERAMICS

J.H. HARRIS and R.A. YOUNGMAN
BP Research, Warrensville Research Center, 4440 Warrensville Center Road, Cleveland, OH 44128

ABSTRACT
It has been observed that aluminum nitride (AlN) ceramics exhibit a significant photo-darkening when exposed to UV or X-ray radiation, though the origin of this effect has never been understood. In this study, the optical character of these defects is investigated utilizing a UV-pump, visible-probe arrangement, where very large changes ΔT in the probe transmission T (induced absorption) are observed after excitation ($\Delta T/T \approx 0.60$). These experiments reveal that the photo-darkening is due to the creation of light induced defects, with an energy level deep in the AlN bandgap. Utilizing these results, a light induced defect formation model is proposed which is consistent with the known defect chemistry of this material.

INTRODUCTION- OXYGEN DEFECTS IN ALUMINUM NITRIDE
Oxygen related defects in aluminum nitride (AlN) ceramics have been the subject of numerous studies over the past two decades. This defect, which has been investigated utilizing photoluminescence [1-4], X-ray diffraction [1,5,6], NMR [7], thermal conductivity measurements [1,5,8,9] and electron microscopy [10-13], has been shown to influence phase and polytype formation [13-15], optical properties [1-4,16-18] and thermal conduction [1,5,8,9,19,20] in AlN ceramics and single crystals [1,5].

The earliest comprehensive modelling of the oxygen defect in AlN ceramics, with particular emphasis on its effect on thermal conduction, is the work of Slack [5]. In these studies, Slack proposed that oxygen substitutes for nitrogen in the wurtzite AlN lattice (tetrahedrally coordinated Al and N sites) with the subsequent formation of an aluminum vacancy (V_{Al}) as a charge balancing mechanism. Slack supported this model with the results of X-ray diffraction lattice parameter measurements and thermal conductivity measurements performed on single crystal samples.

Recently, Harris et al. have elaborated on, and extended, the Slack model by illustrating that a transition in the nature of the oxygen related defect occurs for oxygen concentrations above a critical value [1,21]. These workers studied the manifestations of this transition utilizing photoluminescence spectroscopy, X-ray diffraction derived lattice parameter measurements and thermal resistance measurements. In the luminescence experiments, AlN ceramic and single crystal samples with varying oxygen concentrations were excited at 267nm. The results of this experiment, shown in Figure 1 for 273K, indicated a significant shift in the luminescence peak as oxygen concentrations were increased up to 0.75 at.%; whereas above this value the peak became stationary. At this same transition point a significant increase in the luminescence intensity was observed. The nature of this transition is further revealed in the AlN unit cell volume as a function of oxygen content as shown in Figure 2. Note from this figure that the AlN lattice is observed to contract as oxygen is dissolved up to a concentration near 0.75 at. percent (labelled region I), but further oxygen addition re-expands the AlN lattice (region II).

A schematic of the model proposed by Harris et al. to explain their experimental findings is shown in Figure 3. This model contends that at oxygen concentrations below 0.75 at.% (region I), the oxygen defect consists of oxygen substituted on a nitrogen site O_N and an aluminum vacancy V_{Al} (with a ratio $O_N/V_{Al}=3$), as first proposed by Slack [5]. This defect is shown schematically in Figure 3(a). As analyzed by Harris et al., the presence of vacancies on the Al sub-lattice produces the lattice contraction shown in Figure 2 [1]. The thermal conduction modelling performed by these workers also indicates that both O_N and V_{Al} must be charged defects (correlated to each other via a coulomb interaction) [1]. As oxygen concentrations exceed 0.75%, a transition in the oxygen accomodating defect occurs. The region II defect, which forms at the expense of the defect complex of region I ($V_{Al} + O_N$), consists of Al atoms octahedrally bound to an increasing number of oxygen atoms, as shown schematically in Figure 3(b). Thus for each octahedral defect formed, two aluminum vacancies are annihilated. This explains the re-expansion of the AlN lattice, shown in Figure 2, as the oxygen concentration increases in region II. At still higher oxygen concentrations, Harris et al. propose that this

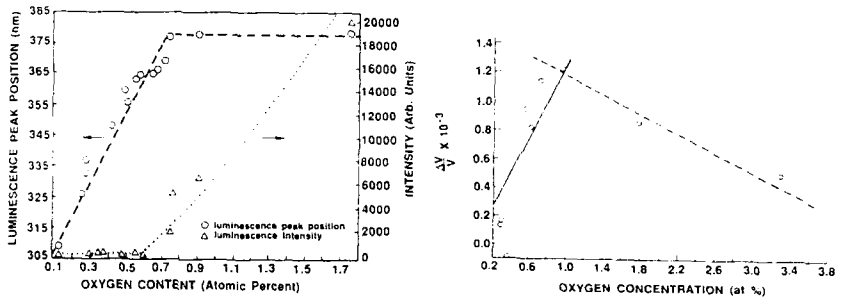


Figure 1: Steady state luminescence peak position and intensity as a function of oxygen concentration in AlN ceramics at 273K.

Figure 2: AlN unit cell volume changes as a function of oxygen concentration (positive ΔV/V indicates contraction).

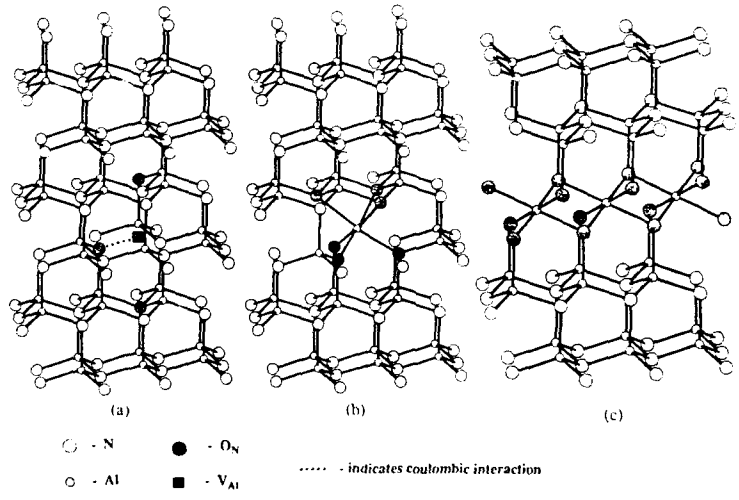


Figure 3: Schematic representation of the oxygen-related defect evolution as a function of oxygen content: (a) isolated aluminum vacancy with associated oxygen; (b) aluminum octahedrally coordinated to oxygen; and (c) extended defect.

octahedrally coordinated Al atom unit can be used as a building block for producing the extended defects frequently observed in AlN ceramics (e.g. stacking faults, inversion domain boundaries) as pictured in Figure 3(c) [1].

It will be the goal of the remaining portion of this paper to show that the defect complex of region I, a (negatively charged) aluminum vacancy coupled to a (positively charged) substituted oxygen atom, may trap photo-excited carriers to populate a meta-stable energy level within the AlN bandgap (E_g=6.2 eV at T=300K). This excited level, which will be investigated via photo-induced absorption spectroscopy, gives rise to a distinct photo-darkening of the AlN sample, as shown in Figure 4.

RESULTS- PHOTO INDUCED ABSORPTION MEASUREMENTS

In order to investigate photo-induced energy levels in AlN ceramics, a photo-induced absorption experiment was undertaken. In this simple experiment, AlN ceramic samples are excited at 252nm utilizing the (filtered) radiation from a Hg(Ar) vapor lamp while the transmission of a probe beam at 441nm (HeCd laser) is monitored. A typical induced absorption trace is shown in Figure 5, where the probe transmission (441nm) is monitored from time t=0 and the UV lamp is activated at $t=t_1$. Note the significant decrease in the probe transmission (photo-induced absorption) observed for $t>t_1$. The dynamics of this effect will be the subject of a future publication [22]. At time $t=t_2$, the UV irradiation is turned off with the probe beam still activated. Note that the probe transmission increases (with time), indicating a probe-induced photo-bleaching of the UV induced center. This photo-bleaching is clearly evident by observing the sample after this experiment, where a light region is observed at the spot where the probe beam was incident, whereas regions uneffected by the probe remain photo-darkened.

The AlN samples utilized in this study were prepared with either a Y_2O_3 sintering aid, which produces AlN with Y-Al-O as a second phase [23], or with a CaO sintering aid, which produces AlN containing no second phase [19]. All samples studied had a grain size ≥2μm and were polished on both sides to a 0.3μm finish.

In Figure 6 is shown the change in the probe transmission due to UV irradiation (ΔT) normalized by the probe transmission before irradiation ($\Delta T/T$), as a function of AlN oxygen content. Also shown in this figure is the change in the AlN unit cell volume as a function of oxygen concentration. Note that as the AlN unit cell volume contracts (indicating formation of aluminum vacancies) the magnitude of the induced absorption effect increases; and as the unit cell re-expands (indicating annihilation of aluminum vacancies), $\Delta T/T$ decreases. In Figure 7 is shown $\Delta T/T$ versus specimen thickness for samples with two different oxygen contents. Note that in both cases there is a significant decrease in $\Delta T/T$ as the samples are thinned. Also notice from this figure that to obtain a fixed value of $\Delta T/T$, thicker samples are required as the oxygen content is decreased.

DISCUSSION- A MODEL FOR PHOTO-EXCITATION OF ALN CERAMICS

The specific experimental findings briefly outlined in Section II may be generalized into a few key observations concerning photo-induced absorption in AlN ceramics. First, and most important, as is evident from Figure 6, the size of the photo-induced absorption effect scales with the concentration of the region I defect ($V_{Al} + O_N$). This result provides direct evidence that this is the defect complex responsible for the observed photo-induced effects. Also, as is evident from the sample thickness dependence shown in Figure 7, for a sample with a fixed concentration of this defect, the magnitude of $\Delta T/T$ depends on the number of V_{Al}+O_N centers excited by the pump. Thus as the thickness of the sample (l) falls below the pump absorption length α^{-1}(pump) ($l<\alpha^{-1}$(pump)), the number of excited centers decreases and a corresponding decrease in $\Delta T/T$ is observed. In addition, the different value of $\Delta T/T$ for given specimen thicknesses for samples with different oxygen concentration (and thus different concentrations of V_{Al} and O_N) indicate the pump absorption length α^{-1}(pump) is proportional to the concentration of V_{Al}, O_N.

Utilizing these results, the following model is constructed for photo-excitation of AlN ceramics. In the unexcited material, the defects O_N, V_{Al} are charged, as has been shown by Harris et al. from considerations of thermal conductivity [1]. Upon UV irradiation, carriers are excited directly from band states and trapped at these (localized) charged sites (which are consequently partially or totally neutralized). This creates a (metastable) energy level within the AlN bandgap, as shown schematically in Figure 8. The direct population of this level by the pump beam explains the dependence of the pump absorption on the concentration of O_N, V_{Al} in a given sample. Photons from the probe beam then de-trap these carriers, elevating them to extended states where radiative recombination processes may occur. Thus after exposure to the probe, the O_N and V_{Al} centers are returned to their

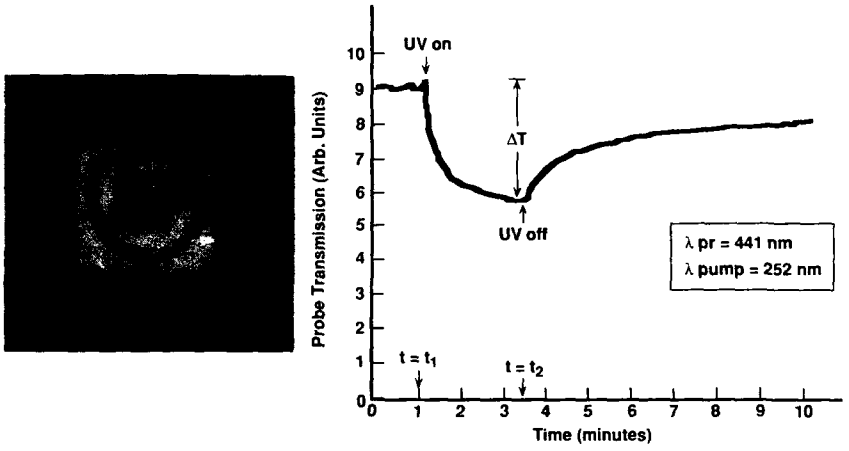


Figure 4: Photograph of AlN ceramic substrate selectively exposed to UV radiation (dark regions).

Figure 5: Typical probe transmission trace showing UV induced absorption ($t_1<t<t_2$) and recovery after UV pump is turned off ($t>t_2$).

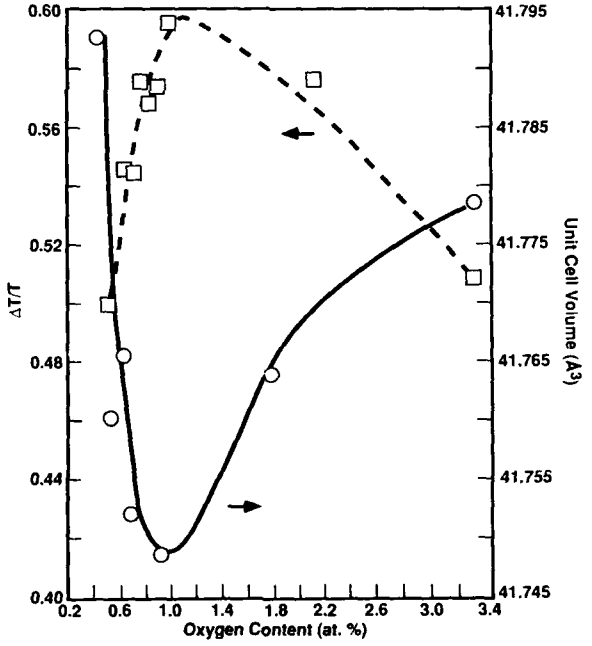


Figure 6: Normalized change in probe transmission ΔT/T as a function of the oxygen content of AlN ceramics. Also shown is the AlN unit cell volume as oxygen concentrations are varied over the same range.

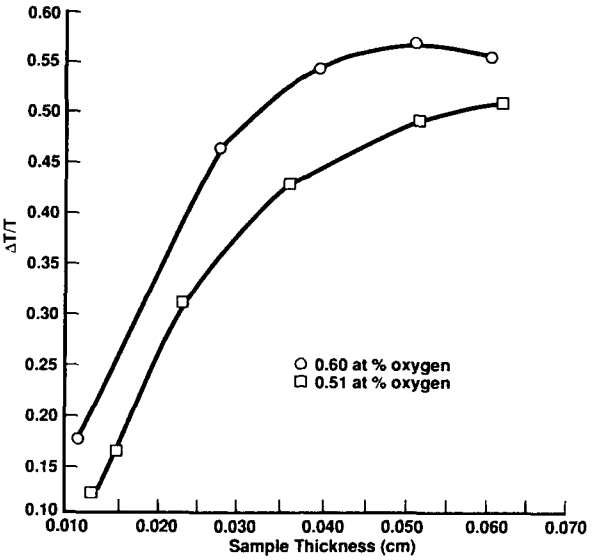


Figure 7: Dependence of induced absorption ΔT/T on sample thickness l for two different oxygen concentrations, 0.60 and 0.51 at.%.

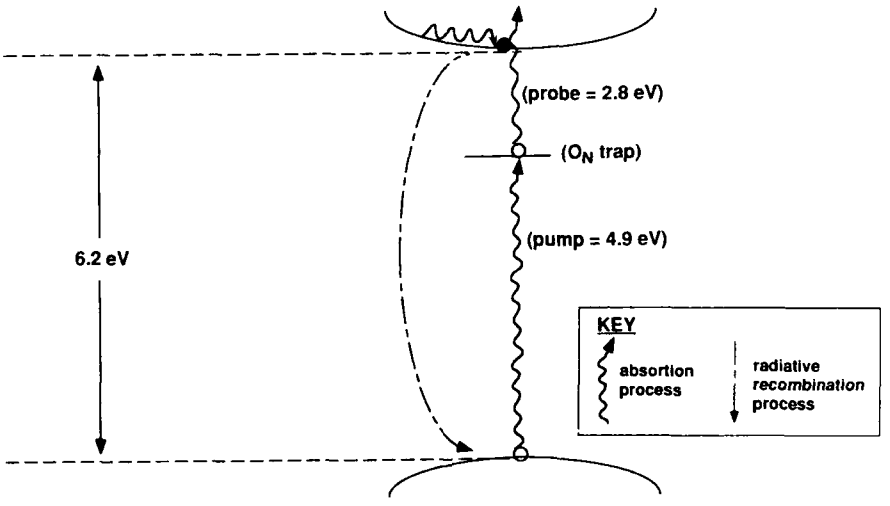


Figure 8: Schematic energy level diagram showning UV pump induced population of trap centers located at O_N, V_{Al} defects, and visible probe de-population of these centers.

original charged state and the metastable energy level created by the pump is annihilated. This explains the observed photo-bleaching effect induced by the probe beam.

Utilizing the thickness dependence of $\Delta T/T$ shown in Figure 7, an approximate value for α^{-1}(pump) can be estimated (for a sample with an oxygen concentration of 0.51 at.%). Using this value, an absorption cross-section for a probe photon with a wavelength of 441nm is estimated to be approximately 2.5×10^{-19} cm^2. The large magnitude of this cross-section indicates a very strong coupling between the incident probe radiation and photo-excited carriers trapped at the $(O_N + V_{Al})$ complex.

CONCLUSIONS

This paper presents the results of photo-induced absorption measurements performed on AlN ceramic samples. The results of these experiments indicate that the defect responsible for the pronounced UV-induced absorption (and hence photo-darkening) of this material is a substitutional impurity, specifically oxygen residing on the nitrogen sub-lattice, in combination with an aluminum vacancy. In the model presented here, absorbed UV radiation causes a transition directly from the ground state to a trapped state at the (charged) defect, producing a meta-stable energy level in the AlN bandgap. Upon absorption of the probe beam, this carrier is de-trapped and elevated to extended states where radiative recombination occurs. Thus the probe beam annihilates the meta-stable energy level created by the pump. This model explains a number of diverse experimental findings, including: the dependence of $\Delta T/T$ on AlN oxygen content, the dependence of $\Delta T/T$ on sample thickness and the observed photo-bleaching effect of the probe beam.

ACKNOWLEDGEMENTS

The authors wish to acknowledge stimulating discussions with Drs. Harvey Scher, William Curtin and Rudy Enck and the skillful technical assistance of Mr. Thomas Nemecek, all from BP Research.

REFERENCES

1. J.H. Harris, R.A. Youngman and R.G. Teller, J. Mater. Res. 5, 1763 (1990).
2. J. Pastrnak, S. Pocesova, and L. Roskovcova, Czech. J. Phys. B24, 1149 (1974).
3. J.H. Harris and R.A. Youngman, in Advanced Packaging Materials, edited by J. Partridge, C-Y. Li, C.J. Chen, and A. Barfknecht (Mater. Res. Soc. Symp. Proc. 167, Pittsburgh, PA, 1990), p. 253.
4. R.A. Youngman and J.H. Harris, J. Am. Ceram. Soc. 73, 3238 (1990).
5. G.A. Slack, J. Phys. Chem. Solids 34, 321 (1973).
6. G.A. Jeffrey, G.S. Parry, and R.L. Mozzi, J. Chem. Phys. 25, 1024 (1956).
7. J. Haas, D. Freude, T. Frohlich, G. Himpel, F. Kerbe, E. Lippmaa, H. Pfeifer, P. Sarv, H. Schafer, and B. Seiffert, Chem. Phys. Lett. 156, 328 (1989).
8. G.A. Slack, R.A. Tanzilli, R.O. Pohl and J.W. Vandersande, J. Phys. Chem. Solids 48, 641 (1987).
9. R.C. Enck and R.D. Harris, in Electronic Packaging Materials, edited by J. Partridge, C-Y. Li, C.J. Chen, and A. Barfknecht (Mater. Res. Soc. Symp. Proc. 167, Pittsburgh PA, 1990), p. 235.
10. R.A. Youngman, J.H. Harris, R.A. Labun and R.J. Graham, ibid, p. 271.
11. S. McKernan and C.B. Carter, ibid, p. 259.
12. A. Westwood and M. Notis, ibid, p. 265.
13. G. Van Tendeloo, K.T. Faber, and G. Thomas, J. Mater. Sci. 18, 525 (1983).
14. S.F. Bartram and G.A. Slack, Acta Cryst. B35, 2281 (1979).
15. J.W. McCauley, K.M. Krishnan, R.S. Rai, G. Thomas, A. Zangville, R.W. Doser, and N.D. Corbin in Ceramic Microstructures '86 edited by J. Pask and A. Evans (Plenum Press, New York, 1988) p.577.
16. S. Pacesova and L. Jastrabik, Czech. J. Phys. B29, 913 (1979).
17. F.S. Ohuchi and R.H. French, J. Vac. Sci, Technol. A6, 1695 (1988).
18. J. Pastrnak, S. Pocesova, and L. Roskovcova, Czech. J. Phys. B24, 1149 (1974).
19. N. Kuramoto, H. Taniguchi, Y. Nurmata and I. Aso, Ygoyo-Kyokai-Shi 93, 41 (1985).
20. A. Virkar, T.B. Jackson and R. Cutler, J. Am. Ceram. Soc. 72, 203 (1989).
21. J. Harris and R.A. Youngman, Proceedings of Symposium N, MRS Meeting, Boston, MA., 1990.
22. J. H. Harris and R.A. Youngman, in preparation.
23. K. Komeya and H. Inoue, Trans. J. Brit. Ceram. Soc. 70, 107 (1971).

CRYSTALLINE GROWTH OF WURTZITE GaN ON (111) GaAs

J. ROSS*, M. RUBIN** AND T.K. GUSTAFSON*
*University of California, Department of Electrical Engineering, Berkeley, CA 94720
**Lawrence Berkeley Laboratory, Berkeley, CA 94720

ABSTRACT

Gallium Nitride films were grown on (111) Gallium Arsenide substrates using reactive rf magnetron sputtering. Despite a 20% lattice mismatch and different crystal structure, wurtzite GaN films grew epitaxially in basal orientation on (111) GaAs substrates. Heteroepitaxy was observed for growth temperatures between 550-600°C. X-ray diffraction patterns revealed (0002) GaN peak with a full-width-half-maximum (FWHM) as narrow as 0.17°. Possible surface reconstructions to explain the epitaxial growth are presented.

INTRODUCTION

Gallium Nitride is a direct wide bandgap semiconductor (3.4 eV) having potential applications for stimulated emission in the blue, violet, and ultra-violet spectral range. Development of GaN devices have been limited by problems in obtaining p-type conduction and convenient substrates for epitaxial growth. Recent reports of p-type conduction [1,2] in Mg doped samples show promise in this area. As seen in Table I, there are no readily available substrates that are lattice matched to GaN in both lattice parameter and thermal expansion coefficient. Sapphire has been frequently used despite a 16% lattice mismatch. Attempts on other substrates include: silicon [3,4], gallium arsenide [3,5,6,7], gallium phosphide [3], and silicon carbide [8]. Aluminum nitride has been used effectively as a thin-film buffer layer on sapphire for improved GaN growth [9]. Table I summarizes the material data for GaN and various substrates. The lattice parameters for the cubic crystals are given as the effective spacing in the (111) plane corresponding to "a" in the wurtzite system for easier comparison.

Table I. Lattice parameters and thermal expansion coefficients of various substrates.

Material	Lattice constant (A)	$\Delta a_{GaN}/\Delta a_{sub}$ (%)	Thermal exp. coef. ($\times 10^{-6}$/K)
GaN	a= 3.189 c= 5.182	---- ----	5.6 7.7
AlN	a= 3.111 c= 4.980	+2.5 ----	5.3 4.2
α-SiC (6H)	a= 3.08 c= 15.11	+3.4 ----	4.2 4.8
Al_2O_3	a= 2.74 c= 12.991	+16.1 ----	7.5 8.5
GaAs (111)	a= 3.997	-20.2	4.8

Despite the large mismatch, GaAs is desirable due to its wide acceptance in the electrooptic industry. Few researchers have used GaAs as a substrate for GaN growth possibly because early comparisons showed sapphire to produce smoother and more oriented GaN films [5]. Recently, the electrical properties of cubic GaN in a S-I-S structure on (100) GaAs grown by modified molecular beam epitaxy has been reported [10]. Concurrent work in Japan, involving the growth of GaN on (111) GaAs by MBE has also shown wurtzite GaN on (111) GaAs [6], however, our material appears to have narrower (0002) GaN x-ray diffraction peaks. GaN is typically grown by chemical vapor deposition (CVD) or modified molecular beam epitaxy (MMBE). Sputter deposition has produced highly resistive GaN films in the past [11], and although it is perhaps not suitable for the growth of minority carrier electronic devices, sputter deposition can be a viable method for the study of GaN growth kinetics and rudimentary GaN devices. In this paper, we report the growth of highly oriented wurtzite GaN films on the (111) face of GaAs. Little strain is observed, but crystalline growth is a sensitive function of temperature. The growth conditions and possible explanations for the heteroepitaxy are detailed. This is the first report of crystalline wurtzite GaN on (111) GaAs by sputter deposition techniques.

EXPERIEMNTAL PROCEDURE

The GaN films were deposited using an US Gun-II 2 inch modular source. The target was pure gallium (99.999999%), held in a stainless steel cup. The GaAs substrates were degreased and etched before deposition in a <111> directional etch of 1 H_20: 5 H_2SO_4: 1 H_2O_2 at 65°C for 2 minutes. The substrates were then rinsed with alcohol and dried before entering the chamber. The chamber was evacuated to less than 10^{-7} Torr, and then backfilled with a mixture of N_2 and Ar gas to 25 mTorr. The substrates were heated to 500-700°C as measured by a thermocouple clamped on the surface of the heating block. As soon as the discharge was ignited, the Ga target liquified and slowly formed a nitrided crust. ENI sources were used to deliver 110 watts of rf (13.56 MHz) power to the 2 inch target. The growth rate was measured by a quartz-crystal oscillator calibrated with a stylus profilometer. Growth rates ranged from 1-5 A/s. After deposition, the substrates were cooled to 200°C in 100% nitrogen atmosphere at 30 mTorr. The choice of deposition parameters for epitaxial growth was partly determined from our earlier work on sapphire substrates [12,13]. Higher partial pressures of nitrogen (25 mTorr) were needed to crystallize GaN on (111)GaAs compared to the sapphire substrates. However, similar nitrogen flow rates (200 sccm) and N_2:Ar ratios (7:3) were used.

RESULTS AND DISCUSSION

The GaN film's crystal orientation was analyzed using a Siemens x-ray diffractometer (CuKα, λ=0.154 nm). For temperatures below 550 °C only mixed phases of GaN were obtained (Figure 1a). In this temperature range, the films were characterized by rough surfaces with numerous defects as seen in Figure 1b. For growth temperatures between 550-600 °C

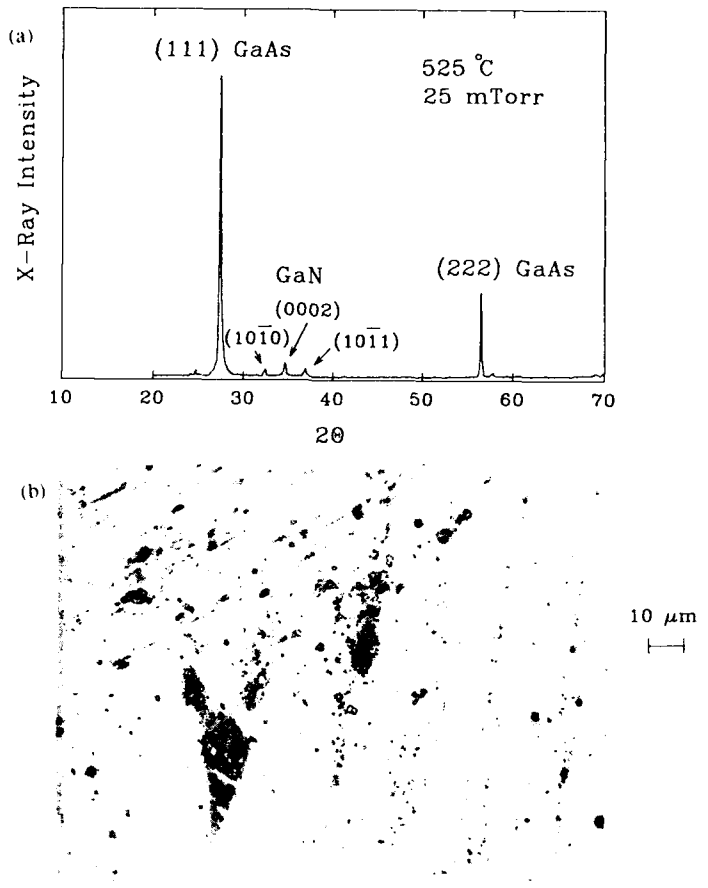


Figure 1(a) X-ray diffraction pattern of GaN film grown at 525°C; and (b) the surface of the film characterized with many defects.

highly oriented basal plane GaN was achieved with much smoother surface morphology. Figures 2a and 2b show the x-ray pattern and the surface morphology of a 200 nm film grown at 580 °C. The FWHM of the (0002) peak is 0.17°. The peak is located at 2θ=34.607° which corresponds to a d-spacing of 2.589 A. The measured (0002) plane spacing is therefore 5.178 A, which agrees well with the theoretical value of 5.182A. Despite the large lattice mismatch, the (0002) planes do not appear appreciably strained. We did not observe any critical thickness phenomen. For films grown under similar conditions, no variation in peak location or width was measured for film thicknesses ranging from 0.05 - 2 μm.

For substrate temperatures greater than 620°C the x-ray diffraction peaks vanished and many films delaminated from the GaAs substrates. We found the delamination could be

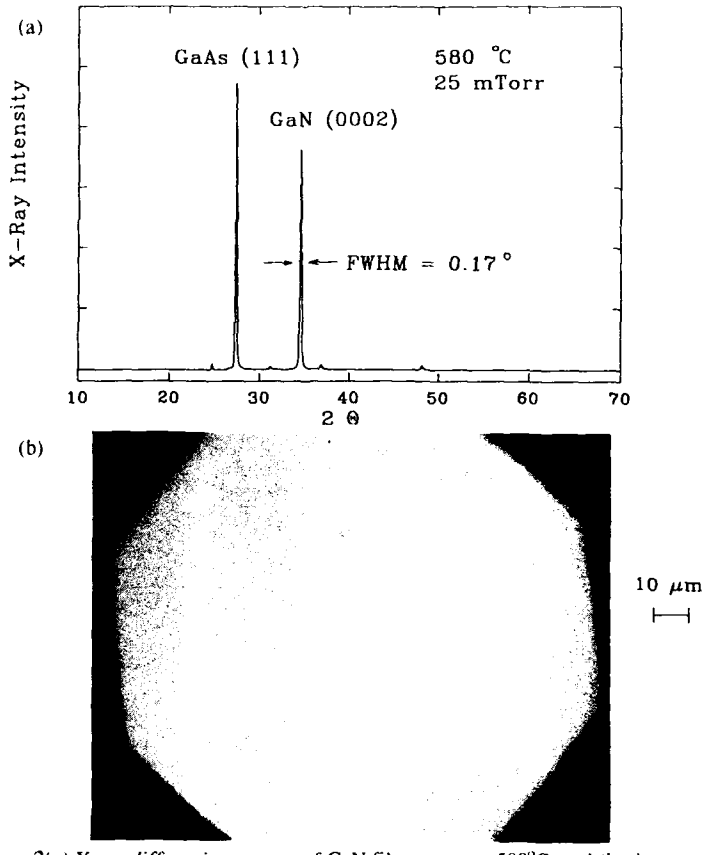


Figure 2(a) X-ray diffracttion pattern of GaN film grown at 580°C; and (b) the smoother surface morphology of this film.

minimized and in some cases eliminated if the films were cooled down slowly from the growth temperature (~100°/hr). Also, no appreciable GaN x-ray peaks were observed at pressures below 20 mTorr. To ensure the x-ray diffraction peak at $2\theta=34.607^{\circ}$ is indeed the (0002) wurtzite phase of GaN and not strained cubic GaN growing in the (111) direction, reflection electron diffraction (RED) was employed. With the beam incident on the (1120) plane, only spots in vertical rows were visible as predicted by theory. Carrier concentrations for these GaN films were all n-type and greater than 2×10^{18} cm^{-3}.

We believe the reason highly oriented wurtzite GaN was obtained on (111) GaAs can be explained by examining the 2-D interface. Figure 3a shows the wurtzite and zinc-blende crystal structures with the <0002> and <111> directions aligned. The only difference between the wurtzite and zinc-blende structures in these directions is the stacking order of the layers. The (111) GaAs face has the identical bond termination as the GaN basal plane substrate would.

The atomic spacing is the only difference between the (0002) GaN and (111) GaAs planes. These similarities were the reason the (111) face of GaAs was chosen over other orientations. Heteroepitaxy on large mismatch systems has been achieved on other material systems when the number of broken bonds is minimized and the 2-D interface lattices have a common superlattice [14,15,16]. The likelihood of epitaxy increases with the number of coincident sites. As seen in Figure 3b, the (0002) GaN and (111) GaAs planes are overlapped. The larger unit cell drawn has a considerably smaller mismatch (4%) between the two materials at room temperature.

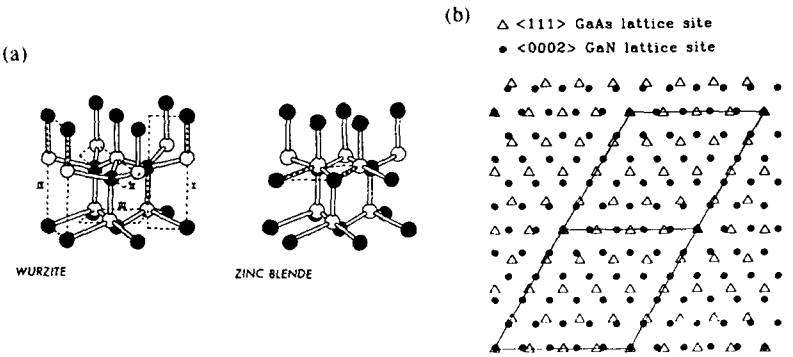


Figure 3(a) Wurtzite and zinc-blende crystal structures oriented with the basal plane and (111) directions aligned; and (b) Overlap of the (111) GaAs and (0002) GaN planes. The larger unit cell represents a 4% mismatch.

CONCLUSIONS

In summary, hexagonal GaN has been grown epitaxially in the basal orientation on the (111) face of GaAs using rf reactive sputter deposition. Phase identification is verified with x-ray diffraction and RED measurements. A narrow temperature regime (550-600°C) is defined which produces highly oriented films with smooth surface morphologies. The differences in the 3-D crytstal structures appear to be less important than the similarities of the 2-D interface for the (0002)GaN/(111) GaAs system.

ACKNOWLEDGEMENTS

We would like to thank Jeff Walker (UCB) for assistance with the RED measurements. Partial support was provided by the U.S. Department of Energy under contract # DE-AC03-76SF00098 and the National Science Foundation # 1-442427-21482. Funding was also provided through a Rockwell International fellowship.

REFERENCES

1. H. Amano, M. Kito, K. Hiramatsu and I. Akasaki, Jpn. J. Appl. Phys., 28, L2112 (1989).
2. S. Nakamura, M. Senoh and T. Mukai, Jpn. J. Appl. Phys., 30, L1708 (1991).
3. Y. Morimoto, K. Uchiho and S. Ushio, J. Electrochemical Society, 120, 1783 (1973).
4. T. Lei, M. Fanciulli, R. Molnar, T. Moustakas, R. Graham and J. Scanlon, Appl. Phys. Lett., 59, 944 (1991).
5. B. Kosicki and D. Kahng, J. Vacuum Science and Tech., 6, 593 (1969).
6. H. Okura, S. Misawa and S. Yoshida, Appl. Phys. Lett., 59, 1058 (1991).
7. M. Mizuta, S. Fujieda, Y. Matsumoto and T. Kawamura, Jpn. J. Appl. Phys., 25, L945 (1986).
8. T. Sasaki and T. Matsuoka, J. Appl. Phys., 64, 4531 (1988).
9. I. Akasaki, H. Amano, Y. Koide, K. Hiramatsu and N. Sawaki, J. Crystal Growth, 98,209 (1989).
10. G. Martin, S. Strite, J. Thorton, H. Morkoc, Appl. Phys. Lett., 58, 2375 (1991).
11. E. Lakshmi, B. Mathur, A. Bhattacharya, and V. Bhargara, Thin Solid Films, 74, 77 (1980).
12. J. Ross, M. Rubin, Mater. Lett., 12, 215 (1991).
13. J. Ross, Masters thesis, University of California Berkeley, 1990.
14. F. LeGoues, M. Liehr, M. Renier and W. Krakow, Philosophical Magazine B, 57, 179 (1988).
15. A. Zur and T. McGill, J. Appl. Phys., 55, 378 (1984).
16. P. Bai, G-R. Yang, L. Lou and T-M. Lu, J. Mater. Res., 5, 989 (1990).

EPITAXIAL GROWTH OF AlN ON 3C-SiC AND Al_2O_3 SUBSTRATES

B. S. SYWE, Z. J. YU, AND J. H. EDGAR
Department of Chemical Engineering, Kansas State University, Manhattan, KS 66506-5102.

ABSTRACT

AlN films were grown on the (100) plane of 3C-SiC/Si and the (0001) plane of Al_2O_3 substrates by metalorganic chemical vapor deposition (MOCVD) using trimethylaluminum (TMA) and ammonia (NH_3) as the precursors. The deposited films were characterized by X-ray diffraction (XRD) and a Read thin film camera. At 1150°C, preferentially oriented polycrystalline AlN films were obtained on both substrates and the crystal structure was wurtzite. The epitaxial relations were $(10\bar{1}0)$AlN//(100)SiC//(100)Si and (0001)AlN// (0001)Al_2O_3. The attempt to grow cubic AlN on 3C-SiC/Si was not successful.

I. INTRODUCTION

Aluminum nitride (AlN) is a wide band gap (Eg=6.2 eV), III-V semiconductor rarely studied in single crystal form. It is a highly refractory ceramic which has potential applications as a substrate material in high performance (high power, high temperature, high speed, and high density) devices because of its unique properties. Among these properties are excellent thermal conductivity, thermal expansion coefficient matching that of Si, good electrical insulation characteristics and nontoxic nature.[1,2] The difficulties associated with producing single crystal AlN are responsible for the limited exploration of its applications in crystalline form. The demonstrated applications include its use as an electrical insulator and circuit passivation in GaAs-based electronic devices,[3,4] and in forming alloys with gallium nitride (GaN) to produce blue and ultraviolet light emitting diodes (LEDs) and lasers.[5,6]

AlN films have been grown by various techniques such as MOCVD,[7-14] sputtering[15] and molecular beam epitaxy (MBE).[16] The most successful epitaxy to date was on sapphire (Al_2O_3) substrates. Because of the large lattice mismatch (13.2%) between AlN and Al_2O_3, the deposited films, though single crystal in nature, contain a large number of crystal defects which degrade their properties.

Recently, two types of silicon carbide (SiC) have become available; the cubic polytype epitaxially deposited on silicon substrates (3C-SiC/Si) and bulk crystals of the hexagonal polytype (6H-SiC). The lattice mismatch between AlN (commonly in the wurtzite structure) and 6H-SiC is less than 1% as would be the mismatch between cubic AlN (should it exist) and cubic SiC.[17] Therefore, SiC would be a superior substrate for AlN epitaxy. MBE of GaN on both SiC substrates (with a lattice mismatch less than 4%) has shown an improvement in crystal quality over that of GaN grown on Al_2O_3 substrate (with a lattice mismatch of 16.1%).[18] Furthermore, GaN grown on cubic SiC also exhibits the cubic structure.[18,19] Based on this information, this work was dedicated to depositing AlN on 3C-SiC/Si, as well as on Al_2O_3 substrates, with the goal of producing cubic AlN on 3C-SiC/Si substrates. Potential applications of epitaxial AlN on SiC include its use as a substrate for GaN epitaxy, or as an alternative insulator (to SiO_2) for SiC based devices.

II. EXPERIMENTAL

AlN was deposited in a standard atmospheric MOCVD system using trimethylaluminum (TMA) and ammonia (NH_3) as the source precursors. The water-cooled quartz reactor was 50 mm in diameter, and in a horizontal configuration. TMA and NH_3, carried by Pd-cell purified hydrogen (H_2), were separately introduced into the reactor to avoid the room-temperature predeposition reaction.[7] The distance between the TMA delivering tube and the susceptor was 10 cm. The susceptor was a graphite electric heater, 60 mm long x 40 mm wide x 1 mm thick, coated with boron nitride. The temperature of substrate was monitored by a type S thermocouple attached underneath the susceptor, and further calibrated by an optical pyrometer to account for the temperature gradient in the thickness of the susceptor.

The 3C-SiC/Si substrates were provided by NASA Lewis Research Center in Cleveland, Ohio. The epitaxial SiC layers were deposited on Si(100) with a two-step CVD process at 1350°C for two minutes, and the resulting thickness was about 1500 Å.[20] The orientation relationship is (100)3C-SiC//(100)Si. The Al_2O_3(0001) substrate was a bulk crystal wafer 20 mm in diameter. In the present work, both 3C-SiC/Si and Al_2O_3 substrates were cleaned by a sequence of trichloroethylene, acetone, methanol, and deionized water, followed by a 49% HF etching. An additional pregrowth etching was applied in a H_2 carrier gas at 1100°C for 15 min to remove any trace of contaminants and produce a surface suitable for epitaxy. AlN was grown at 1150°C with a high flow rate (1500 sccm NH_3, 15 sccm H_2 through TMA bubbler, and 4000 sccm back-up H_2). The resulting growth rate of AlN was 0.4 μm/hr for 3C-SiC/Si and 0.8 μm/hr for Al_2O_3, as determined by examining the mass changes of each sample after deposition. The crystallinity of the grown films were characterized by X-ray diffraction (XRD) with Cu-Kα radiation, and a Read thin film camera.

III. RESULTS AND DISCUSSION

The X-ray diffraction patterns of both AlN/3C-SiC/Si and AlN/Al_2O_3 samples are shown in Figure 1. The thickness of the AlN layer in these samples were about 0.3 μm and 0.6 μm, respectively. As shown in Figure 1, only a single Bragg peak from AlN was detected in both cases, indicating that the AlN films were well oriented. The peak ($2\Theta = 33.0°$) appearing in the AlN/3C-SiC/Si sample corresponds to $(10\bar{1}0)$ diffraction

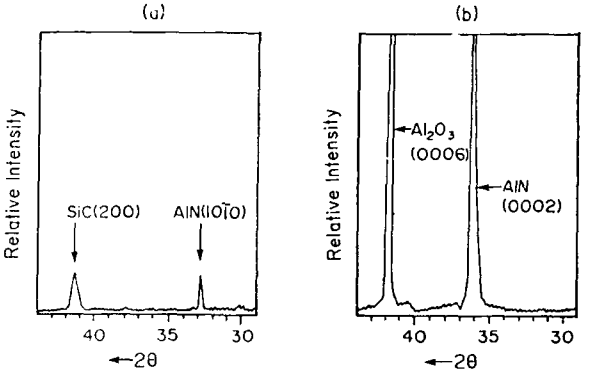


Figure 1. X-ray diffraction patterns for (a) AlN/3C-SiC/Si and (b) AlN/Al_2O_3 samples deposited at 1150°C. The thickness of AlN layers were about 0.3 μm and 0.6 μm, respectively. The Si diffraction peak at $2\Theta = 69.2°$ is not shown in (a).

from AlN, while the peak ($2\Theta=36.1°$) appearing in the AlN/Al_2O_3 sample is due to (0002) diffraction from AlN.[21] These results indicate that wurtzite AlN was grown on 3C-SiC/Si with the c-axis perpendicular to the growth direction. An identical orientation relation was also reported previously in AlN on Si(100).[22] In contrast, AlN grown on Al_2O_3 was oriented with the c-axis parallel to the growth direction, a common observation in literature.[7,8,12]

The crystallinity of the grown AlN films on both substrates was further investigated by a Read thin film camera, which is basically a modified Debye-Scherrer camera with the substrate tilting at an angle to the incident X-ray beam. With an angle of 17°and an exposure time of 5 hours, the diffraction patterns shown in Figures 2 and 3 were obtained. Because the deposited layers were very thin, the intensities from the films were very weak. Figure 2(a) is the Read pattern for a single crystal Si(100) sample without any epilayer. Each spot on the photograph is generated by the constructive diffraction of a particular family of lattice planes. Figure 2(b) reveals some extra spots, generated by the SiC layer

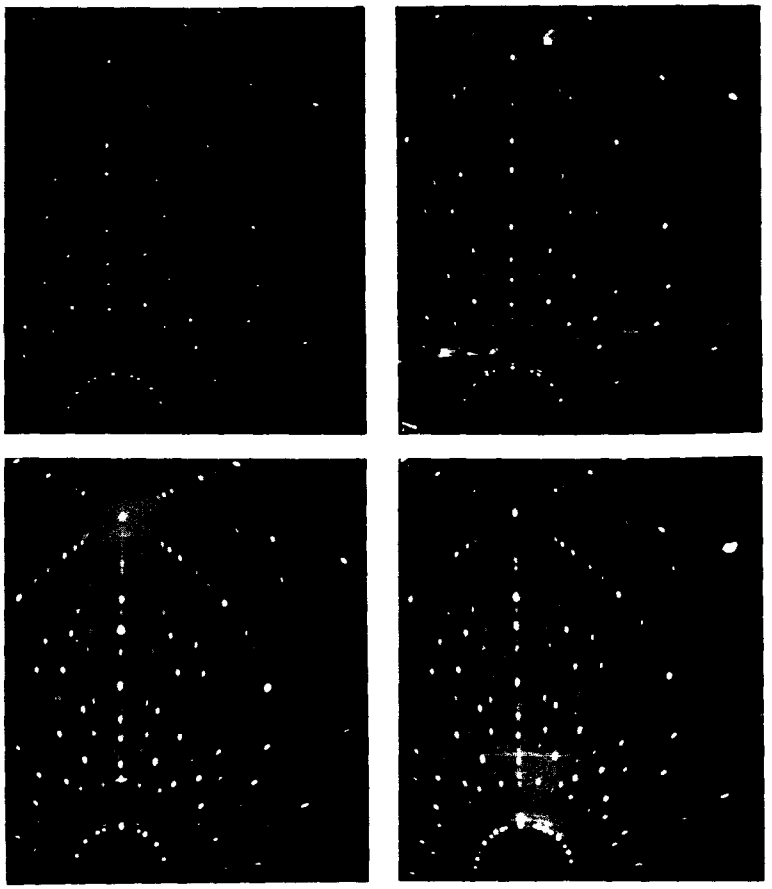


Figure 2. Read camera patterns for (a) Si, (b) 3C-SiC/Si, (c) AlN/3C-SiC/Si, and (d) AlN/Si samples. AlN films were deposited at 1150°C for (c) and 450°C for (d). The tilting angle was 17° and the exposure time was 5 hours for these photographs.

on Si substrate, in the bottom region of the photograph. Figure 2(c) is the Read pattern from the same AlN/3C-SiC/Si sample in Figure 1(a). More spots with streak pattern appear in the bottom region. These segmented spots suggest the AlN layer was preferentially oriented polycrystalline film. If a randomly oriented polycrystalline film were obtained, one would expect seeing rings in the Read pattern. Figure 2(d) gives an example of randomly oriented polycrystalline AlN film, grown at 450°C, on Si(100) substrates. As shown in this photograph, several concentric rings are visible, which reveals the randomly oriented polycrystalline nature of this film.

Figure 3(a) and 3(b) reveal the difference of the Read patterns before and after deposition of AlN on Al_2O_3 substrate. Again using the same sample in Figure 1(b), some extra segmented spots can be easily seen in the bottom of Figure 3(b), suggesting the preferentially oriented nature of the AlN film on the Al_2O_3 substrate. Comparing the Read patterns, Figure 2(c) and 3(b), for the AlN films on both substrates, we can roughly estimate the crystal quality of AlN film on Al_2O_3 is superior to that on 3C-SiC/Si substrate since Figure 2(c) reveals a longer streak pattern for the extra spots from AlN film. This is not surprising anyway, because as a substrate for wurtzite AlN epitaxy, 3C-SiC does not offer any advantage. The lattice mismatch between wurtzite AlN and 3C-SiC is 28.6%, much bigger than 13.2% for AlN and Al_2O_3. At this stage, we are unable to identify the types and densities of the structure defects in these samples. Also, more research is needed to characterize the electrical properties of AlN film on 3C-SiC substrate.

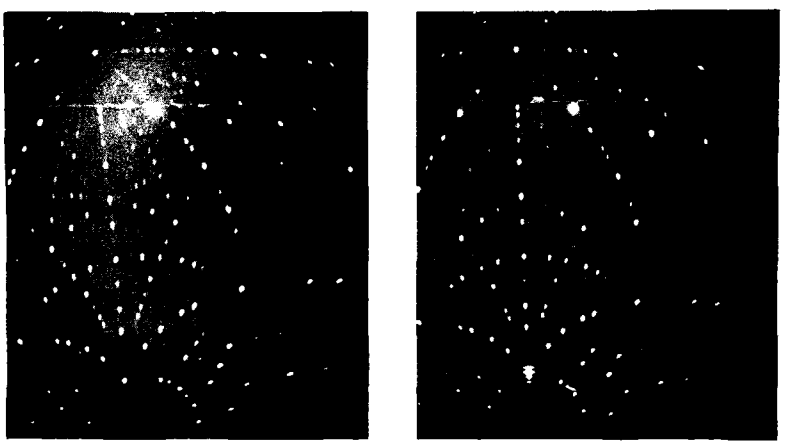


Figure 3. Read camera patterns for (a) Al_2O_3 and (b) AlN/Al_2O_3 samples. The AlN film was deposited at 1150°C. The tilting angle was 17° and the exposure time was 5 hours for these photographs.

IV. CONCLUSIONS

Epitaxial AlN films were grown on both 3C-SiC/Si and Al_2O_3 substrates at 1150°C in a horizontal MOCVD reactor using TMA and NH_3 as the precursors. AlN grown on 3C-SiC/Si reveals the wurtzite structure, as does the AlN on Al_2O_3. The epitaxial relations are $(10\bar{1}0)AlN//(100)SiC//(100)Si$ and $(0001)AlN//(0001)Al_2O_3$. The crystallinity of the AlN films were examined by a Read thin film camera and the result

showed preferentially oriented ploycrystalline AlN films were obtained on both substrates. More research is needed to characterize the crystal defects as well as the properties in these films.

ACKNOWLEDGEMENTS

This research was supported by a grant from the National Science Foundation, Chemical and Thermal System Program, Grant no. CTS-9010061. The supply of 3C-SiC/Si substrates from NASA Lewis Research Center in Cleveland, Ohio, is gratefully acknowledged. The authors would like to thank Mr. L. Seib for his assistance in obtaining X-ray diffraction and Read thin film camera patterns.

REFERENCES

1. W. Werdecker and F. Aldinger, IEEE Trans. Compon., Hybrids, Manuf. Technol. CHMT-7, 399 (1984).
2. H. Takamizawa, T. Kamata, and S. Noguchi, IEEE Trans. Compon., Hybrids, Manuf. Technol. CHMT-8, 247 (1985).
3. S. Fujieda, M. Mizuta, and Y. Matsumoto, Jpn. J. Appl. Phys. 27, L296 (1988).
4. F. Hasegawa, T. Takahashi, K. Kubo, S. Ohnari, Y. Nannichi, and T. Arai, Jpn. J. Appl. Phys. 26, L1448 (1987).
5. I. Akasaki, H. Amano, K. Hiramatsu, and N. Sawaki, Inst. Phys. Conf. Ser. No. 91, 80 (1988).
6. D. K. Gaskill, N. Bottka, and M. C. Lin, J. Cryst. Growth 77, 418 (1986).
7. H. M. Manasevit, F. M. Erdmann, and W. I. Simpson, J. Electrochem. Soc. 118, 1864 (1971).
8. M. T. Duffy, C. C. Wang, G. D. O'Clock, Jr., S. H. McFarlane III, and P. J. Zanzucchi, J. Electron. Mater. 2, 359 (1973).
9. J. K. Liu, K. M. Lakin, and K. L. Wang, J. Appl. Phys. 46, 3703 (1975).
10. U. Rensch and G. Eichhorn, Phys. Stat. Sol. (a) 77, 195 (1983).
11. M. Matloubian and M. Gershenzon, J. Electron. Mater. 14, 633 (1985).
12. M. Morita, N. Uesugi, S. Isogai, K. Tsubouchi, and N. Mikoshiba, Jpn. J. Appl. Phys. 20, 17(1981).
13. M. Morita, S. Isogai, N. Shimizu, K. Tsubouchi, and N. Mikoshiba, Jpn. J. Appl. Phys. 20, L173 (1981).
14. H. Kawakami, K. Sakurai, K. Tsubouchi, and N. Mikoshiba, Jpn. J. Appl. Phys. 27, L161 (1988).
15. W. J. Meng, J. Heremans, and Y. T. Cheng, Appl. Phys. Lett. 59, 2097 (1991).
16. S. Yoshida, S. Misawa, and S. Gonda, J. Vac. Sci. Technol. B1, 250 (1983).
17. M. E. Sherwin and T. J. Drummond, J. Appl. Phys. 69, 8423 (1991).
18. Z. Sitar, M. J. Paisley, B. Yan, and R. F. Davis, Mater. Res. Soc. Symp. Proc. 162, 537 (1990).
19. M. J. Paisley, Z. Sitar, J. B. Posthill, and R. F. Davis, J. Vac. Sci. Technol. A7, 701 (1989).
20. J. A. Powell, L. G. Matus, and M. A. Kuczmarski, J. Electrochem. Soc. 134, 1557 (1987).
21. I. Akasaki and M. Hashimoto, Solid State Commun. 5, 851 (1967).
22. J. H. Edgar, Z. J. Yu, and B. S. Sywe, Thin Solid Films 204, 115 (1991).

STRUCTRUAL CHARACTERIZATION AND RAMAN SCATTERING OF EPITAXIAL ALUMINUM NITRIDE THIN FILMS ON SI(111)

W. J. Meng, T. A. Perry, J. Heremans, Y. T. Cheng
General Motors Research Laboratories, Warren, Michigan 48090

ABSTRACT

Thin films of aluminum nitride were grown epitaxially on Si(111) by ultra-high-vacuum dc magnetron reactive sputter deposition. Epitaxy was achieved at substrate temperatures of 600°C or above. We report results of film characterization by x-ray diffraction, transmission electron microscopy, and Raman scattering.

INTRODUCTION

Heteroepitaxial growth of aluminum nitride (AlN) thin films has potential applications in diverse areas such as surface acoustic wave devices[1], electronic device thermal management[2], and substrate for growth of other refractory metal nitrides[3]. Epitaxial growth of AlN on Si(111) substrates was achieved by chemical vapor deposition at ~1200°C[4] and by reactive sputter deposition at ~1000°C[5]. We recently demonstrated that epitaxial growth of AlN can occur on Si(111) at 600°C or above by reactive sputter deposition under ultra-high-vacuum (UHV) conditions[6]. Here we report results of film characterization. Film-substrate orientational relationship and crystalline quality of AlN films were examined by x-ray diffraction, transmission electron microscopy, and Raman scattering.

EXPERIMENTAL

Reactive sputter deposition of AlN was carried out in an UHV chamber with base pressure ~ 2×10^{-10} Torr[7]. Si substrates were chemically cleaned followed by heating under UHV conditions to ~850°C[8]. Substrate temperature was measured by an optical pyrometer. Growth took place in a mixture of Ar and N_2[7]. Growth was monitored in-situ by an optical interference technique[9]. After growth, films were examined by θ-2θ x-ray diffraction with CuKα radiation, by plan-view and cross-sectional transmission electron microscopy (TEM), and by Raman scattering. Raman spectra were excited by an argon ion laser (4880Å) with an output of 50 mW (line focus, power density ~ 35 W/cm^2) and collected at room temperature.

RESULTS AND DISCUSSION

Results of θ-2θ x-ray diffraction on AlN/Si(111) films are summarized in fig. 1. Figs. 1(a) and 1(b) show the low and high angle diffraction patterns of an AlN film grown at 800°C. The low angle pattern shows regularly spaced interference peaks. Peak

positions θ_m are related to film thickness d by,

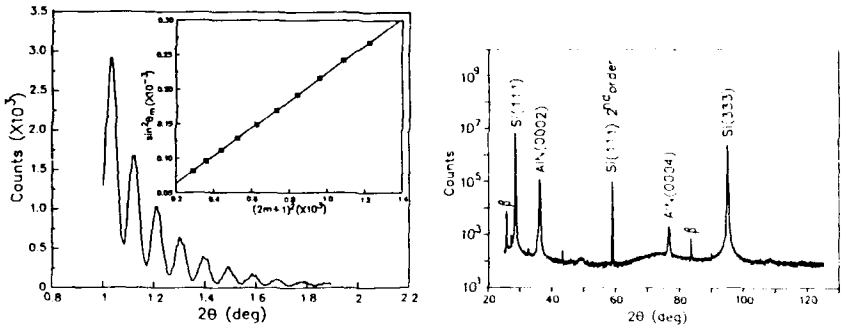
$$sin^2\theta_m - sin^2\theta_0 = (\frac{\lambda}{4d})^2(2m+1)^2, \quad (1)$$

where θ_0 is the angle of total reflection, m is the peak order, and λ is the x-ray wavelength[7]. Least squares analysis of data shown in fig. 1(a) according to eq. (1) yields an AlN thickness of 862Å. The high angle pattern shows expected Si reflections together with AlN (0002) and (0004) reflections. The absence of other AlN reflections indicate complete film texture with AlN[0001]//Si[111].

Results of electron diffraction on AlN/Si(111) films are summarized in fig. 2. Figs. 2(a) and 2(b) show the plan-view and cross-sectional selected area diffraction patterns (SADP), together with indexing, of two AlN films grown at 700 and 800°C, respectively. The AlN film thicknesses were ~450Å. The plan-view SADP was taken from an area with overlapping AlN and Si, and shows simultaneously the Si[111] and AlN[0001] zone axis patterns. Fig. 2(a) shows epitaxy of AlN on Si with AlN[$11\bar{2}0$]//Si[$1\bar{1}0$], in agreement with previous reports[4]. The cross-sectional SADP shows simultaneously the Si[$0\bar{1}1$] and AlN[$2\bar{1}\bar{1}0$] zone axis patterns. The orientational relationship of AlN[0001]//Si[111] and AlN[$0\bar{1}10$]//Si[$\bar{2}11$] shown in fig. 2(b) supports the information shown in figs. 1(b) and 2(a). Taken together, figs. 1 and 2 clearly demonstrates epitaxy of AlN on Si(111). Similar diffraction patterns were obtained from AlN films grown at 800 to 600°C.

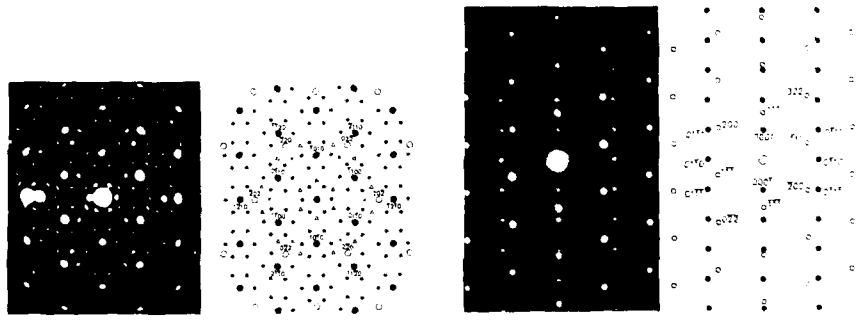
Both the in-plane and c-axis lattice parameters of AlN were measured from data shown in figs. 1 and 2. Fig. 1 gives c=4.968Å and fig. 2 gives a=3.104Å. Both measured values are close to the tabulated bulk values of c=4.975Å and a=3.110Å[10], indicating that no significant strain is present in the AlN films. Several groups of double diffraction spots are present in the plan-view SADP shown in fig. 2(a). The strongest group of double diffraction spots comes from Si{$2\bar{2}0$} and AlN{$11\bar{2}0$} planes (smallest Δg)[6,11]. Plan-view high resolution micrographs, taken with diffraction condition corresponding to that shown in fig. 2(a), is shown in fig. 3. Fig. 3 shows three sets of *parallel* Moire fringes inclined at 60° to one another. Detailed examination shows *threading* dislocations in the film, whose presence is revealed by extra half fringes[6]. Dislocation density was estimated to be $\sim 3 \times 10^{11}/cm^2$. By counting the number of extra half fringes in three directions, the in-plane component of the Burgers vector can be determined to be $\frac{1}{3} < 11\bar{2}0 >$[6]. [$0\bar{1}1$] cross-sectional high resolution micrograph of the AlN/Si(111) interface shows parallel lattice fringes of (111) Si and (0001) AlN extend up to the interface, indicating interface sharpness and the absence of interfacial reaction[6].

While growth at substrate temperatures of 600°C or above resulted in epitaxy, polycrystalline AlN films resulted at lower growth temperatures[6]. Fig. 4(a) shows a plan-view SADP taken from an AlN film grown at 500°C, taken in [0001] orientation. A ring pattern was observed which, nevertheless, showed clear evidence of a remnant single crystal pattern. Thus considerable in-plane alignment still exists. Figs. 4(b) and 4(c) show the dark-field micrograph taken with the remnant ($10\bar{1}0$) spot and the bright-field micrograph, respectively. Fig. 4(b) shows randomly distributed grains, 100 to 200Å in diameter, with similar crystallographic alignment.



(a) (b)

Fig. 1. θ-2θ x-ray diffraction patterns of an AlN grown on Si(111) at 800°C: (a) low angle; (b) high angle.



(a) (b)

Fig. 2. Plan-view and cross-sectional electron diffraction patterns of AlN films on Si(111): (a) plan-view; (b) cross-section.



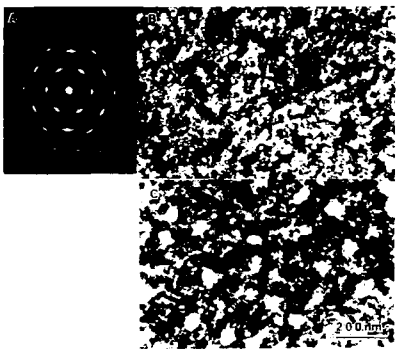
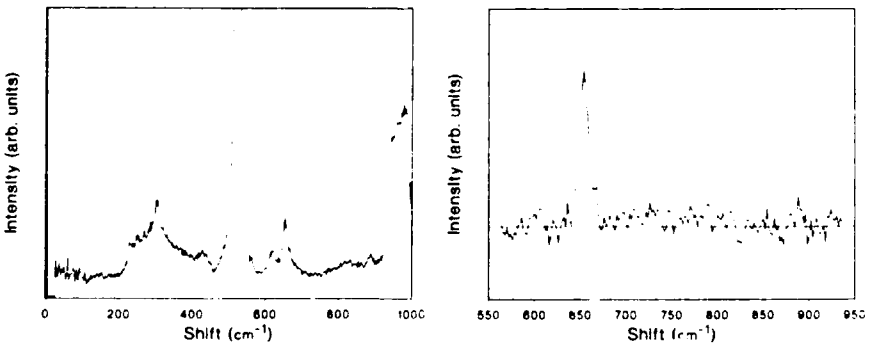


Fig. 3 (upper left). Plan-view high resolution micrograph of overlapping AlN and Si, scale bar = 115Å.

Fig. 4 (upper right). Plan-view TEM examination of an AlN film grown on Si(111) at 500°C: (a) SADP; (b) dark-field; (c) bright field micrograph.



(a) (b)

Fig. 5 Room temperature Raman spectra of a 732 nm thick AlN film grown on Si(111) at 800°C: (a) raw spectrum, (b) substrate background subtracted difference spectrum (line indicates zero)

Epitaxial AlN films of much larger thicknesses were also grown. Taking advantage of the optical transparency of AlN, growth of AlN film was monitored in real time with optical interference using a laser beam. Post growth examination showed single crystal AlN film up to thicknesses of 0.7μm[9]. This thick AlN film was further examined by Raman scattering. The Raman spectrum of a 732 nm AlN film grown on Si(111) at 800°C is shown in fig. 5(a). The spectrum shown is dominated by single and multi-phonon Si features[12]. The broad structures from 200-470 cm^{-1} and about 700 cm^{-1}, and also the small peak at 620 cm^{-1}, are due to multiphonon scattering from the Si substrate. The intense line at 522 cm^{-1} is the zone center Si mode. The peak at 654 cm^{-1} is the only structure in this spectrum attributed to AlN. This is confirmed by taking the difference between fig. 5(a) and the spectrum of the bare Si substrate. The difference spectrum, shown in fig. 5(b), shows the only remaining feature due to scattering of the AlN film. For the spectra shown in fig. 5, the light was incident and scattered along the c-axis of the film (the film growth direction), with the polarizations of the the incident and scattered light parallel {z(x,x)-z}. Rotation of the polarization {z(x,y)-z} yielded a similar spectrum. AlN is known to have three Raman allowed symmetries, A1, E1, and E2[13]. In the backscattering geometry, the E1 modes are silent, and the E2 modes are allowed for both parallel and perpendicular polarizations, the A1 modes should be allowed for parallel and forbidden for perpendicular polarizations. The observed mode at 654 cm^{-1} is close in energy to the E2 mode (655 cm^{-1}) observed by Harman et al.[14]. This mode is quite broad ($\sim$ 17 cm^{-1} FWHM). The broad width of the phonon, the absence of modes associated with A1 symmetry, and the weak nature of the scattering are all consistent with the high defect density in these AlN films.

SUMMARY

Characterization of AlN films grown on Si(111) by UHV reactive sputtering has been accomplished by x-ray diffraction, plan-view and cross-sectional TEM, and Raman scattering. In addition to demonstrating epitaxy at relatively low substrate temperatures ($\geq$ 600°C), the epitaxial AlN films were shown to contain a high density of threading dislocations. Although clear Raman scattering signature from the AlN film is obtained, the relatively broad Raman peak is consistent with high defect density in the AlN film.

REFERENCES

1. S. Yoshida, S. Misawa, Y. Fujii, S. Takada, H. Hayadawa, S. Gonda, and A. Itoh, J. Vac. Sci. Technol. 16, 990 (1979).

2. A. D. Westwood and M. R. Notis, JOM June 1991, p. 10.

3. Y. Koide, N. Itoh, K. Itoh, N. Sawaki, and I. Akasaki, Jpn. J. Appl. Phys. 27, 1156 (1988).

4. M. Morita, S. Isogai, N. Shimizu, K. Tsubouchi, and N. Mikishiba, Jpn. J.

Appl. Phys. 20, L173 (1981).

5. A. J. Noreika, M. H. Francombe, and S. A. Zeitman, NASA Rep. CR-86395, Contract NAS 12-568 (1969).

6. W. J. Meng, J. Heremans, and Y. T. Cheng, Appl. Phys. Lett. 59, 2097 (1991).

7. W. J. Meng, J. A. Sell, and R. A. Waldo, J. Vac. Sci. Technol. A9, 2183 (1991).

8. A. Ishizaka and Y. Shiraki, J. Electrochem. Soc. 133, 666 (1986).

9. J. A. Sell, W. J. Meng, and T. A. Perry, to be published in J. Vac. Sci. Technol. A.

10. T. B. Massalski, Ed., *Binary Alloy Phase Diagrams*, (ASM International, Materials Park, OH, 1990), p. 176.

11. P. Hirsch, A. Howie, R. B. Nicholson, D. W. Pashley, and M. J. Whelan, *Electron Microscopy of Thin Crystals* (R. E. Krieger, Malabar, FL, 1977).

12. P. A. Temple and C. E. Hathaway, Phys. Rev. B7, 3685 (1973).

13. R. Loudon, Adv. Phys. 13, 423 (1964).

14. O. Brafman, G. Lengyel, S. S. Mitra, P. J. Gielisse, J. N. Plendl, and L. C. Mansur, Solid State Comm. 6, 523 (1968).

TEM STUDY OF DISLOCATIONS IN PLASTICALLY DEFORMED AlN

V. AUDURIER, J.L. DEMENET AND J. RABIER
Laboratoire de Métallurgie Physique, U.R.A. 131 CNRS
Faculté des Sciences
86022 Poitiers Cedex, France

ABSTRACT

AlN ceramics were plastically deformed using uniaxial compression under hydrostatic pressure between room temperature (RT) and 800°C. Deformation microstructures have been studied by Transmission Electron Microscopy (TEM) using the weak beam technique. The deformation substructure at RT is characterized by perfect glide loops with 1/3<11$\bar{2}$0> Burgers vector in (0001) elongated in the screw direction. When deformation temperature increases, the screw character is associated to cross slip events and dislocation dipoles are found. In the investigated temperature range, slip of dislocations with 1/3<11$\bar{2}$0> Burgers vector is also evidenced on prismatic planes. Weak beam observations failed to evidence any dislocation splitting. Some of these dislocation properties, similar to those of III-V compound semiconductors, suggest that electronic doping effects could be used to control plastic behaviour of covalent ceramics.

INTRODUCTION

AlN is a III-V compound semiconductor with a wide band-gap (6eV) which crystallizes in the (2H) wurtzite structure. AlN is a prime candidate for VLSI devices substrates since it exhibits excellent thermal conductivity, good electrical insulation characteristics, and a coefficient of thermal expansion matching closely that of silicon in the temperature range 293-473K [1,2]. This is also a ceramic for structural applications at high temperature in inert atmosphere, and as hard coating of aluminum obtained by ion implantation [3]. Furthermore, it is a model material to investigate if the dislocation properties found in III-V compounds are also relevant to wide band-gap covalent ceramics.

Plastic deformation studies of AlN were previously investigated with the aim to obtain a better densification of the ceramic material. Tests conducted at high pressure [4], compaction by explosives (see for example [5,6]) have demonstrated that dislocations are activated. Preliminary results have been reported also on the fine structure of dislocations after deformation at RT [7].

In this context a study of the plastic deformation of AlN, in a low temperature range (RT-800°C), has been undertaken. This paper focuses on the dislocation substructures, studied by TEM, obtained in deformed samples.

EXPERIMENTAL

Sintered AlN samples were obtained from Ceramiques Techniques Desmarquet (Trappes, France). Concentrations of Y_2O_3, used as a sintering additive, ranged from 1% to 20% of the total starting powders. Results presented in this paper are concerned with two concentrations : NA3-19 (1%Y_2O_3) and

NA16-1 (20%Y_2O_3). Samples were sintered one hour at 1700°C. These samples have been characterized at the TEM level before deformation : defects found in sintered AlN grains consist of extended defects and dislocations [8,9].

Plastic deformation of AlN was achieved in a Griggs apparatus [10] set up in an Instron frame which allows to deform brittle solids. Deformation tests have been conducted on AlN from RT up to 800°C under a confining pressure ranging between 0.7 to 1 GPa at a strain rate $\dot{\varepsilon} = 2.10^{-5}\ s^{-1}$, up to permanent strains of 1 to 2%.

Slices were cut from the deformed samples and mechanically polished down to 80 µm. Electron beam transparency was obtained by ion thinning. Thin foils were observed in a JEOL 200 CX electron microscope operating at 200 kV, after evaporating a carbon coating in order to suppress the build up of charges under the electron beam.

RESULTS

Dislocation microstructures after RT deformation

Most of the results on the microstructure of the NA3-19 (1%Y_2O_3) sample has been reported in a previous paper [7]. The three possible Burgers vectors $<11\bar{2}0>$ of the basal plane were observed, together with a strong screw character of the glide loops. Additional observations have been conducted in NA16-1 (20%Y_2O_3) where prismatic glide is also observed. Perfect dislocations of figure 1 lie in the $(\bar{1}100)$ plane. The full glide loop is elongated in the screw direction (Burgers vector $1/3[\bar{1}\bar{1}20]$), showing, as well as in the basal plane, a strong asymetry of dislocation mobility in the prismatic plane. Observations using the weak beam technique fail to resolve any dissociation of the dislocations in the two types of sample and the two different glide planes.

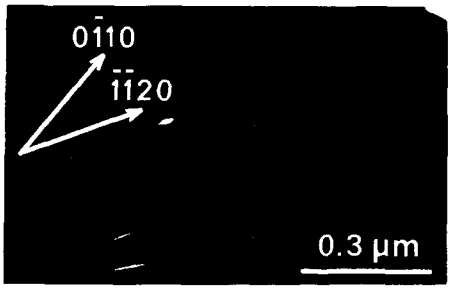


Figure 1. RT deformation (NA16-1). Glide loops in the prismatic plane $1/3[\bar{1}\bar{1}20](\bar{1}100)$. Note the elongation of the loops along the screw direction. Weak beam conditions : $\mathbf{g} = 01\bar{1}0$ (g, 2.8g).

Dislocation microstructures after plastic deformation at 800°C

The deformation was stopped on the sample NA3-19 (1%Y_2O_3) at a stress level of 1020 MPa, roughly a quarter of the stress level obtained at room temperature. Figure 2 shows the microstructure in the basal plane. Dislocations appear locally pinned which leads to cusped segments. This pinning seems to result from cross slip events which can have started at impurities relevant to the sintering process. Numerous dipoles and small loops resulting likely from dipole annihilations are also observed. These features are characteristic of a medium temperature type deformation. However, the screw orientation of dislocations is

the dominant character as shown on figure 3, where two families of dislocations $1/3<11\bar{2}0>$ type are in contrast. These observations indicate that the low mobility of screw segments still remains at 800°C.

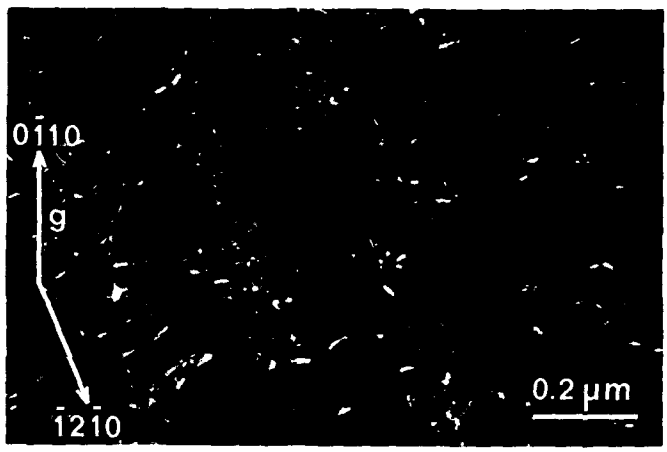


Figure 2. Microstructure after deformation at 800°C (NA3-19). $1/3<11\bar{2}0>$ type dislocations in the basal plane. Weak beam conditions : $g = 0\bar{1}10$ (g, 5.2g).

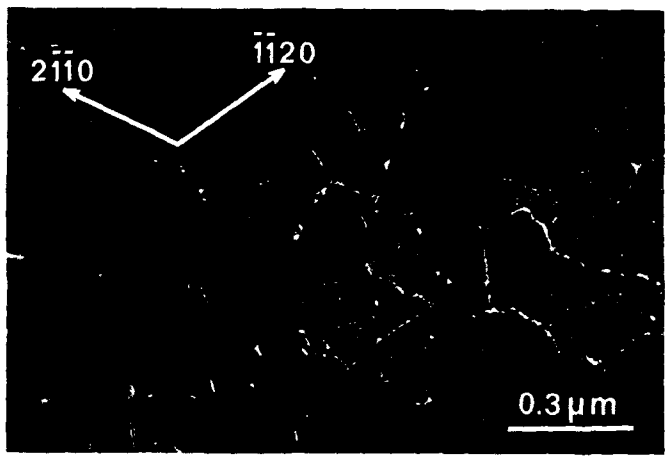


Figure 3. Microstructure after deformation at 800°C (NA3-19). Basal plane. Two families of dislocations in contrast. Weak beam conditions : $g = \bar{1}010$ (g, 5.2g).

In order to check the nature of the cross slip plane, additional observations have been performed in the prismatic plane ($1\bar{1}00$) (fig.4). They reveal a high density of dislocations. These dislocations (Burgers vectors are of $1/3<11\bar{2}0>$ type) can belong either to the basal plane or to a prismatic plane of first kind. This bears witness of a cross slip activity in this plane. Some of the dislocations are oriented in particular orientation: the straight dislocation line arrowed on figure 4 is oriented along [0001] and has a pure edge character. This feature could be explained by a low mobility of the edge segment or by climb of this segment in the prismatic plane of second kind.

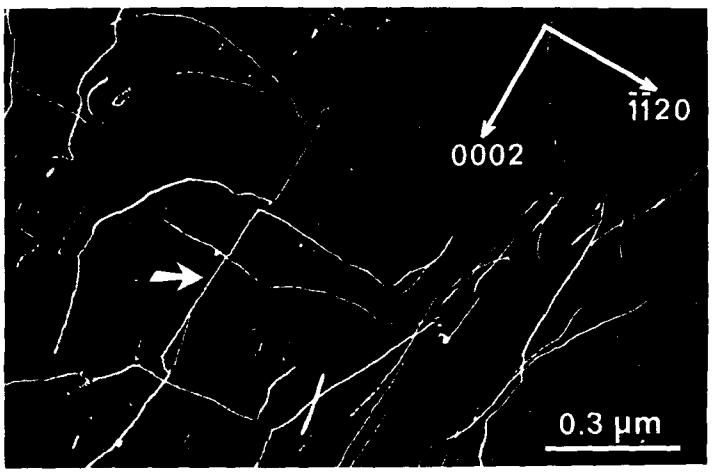


Figure 4. Microstructure after deformation at 800°C (NA3-19). Prismatic plane ($1\bar{1}00$). The dislocation arrowed is a pure edge dislocation. Weak beam conditions : $\mathbf{g} = 11\bar{2}0$ (g, 3.1g).

DISCUSSION

Although plastic deformation of ceramics in the temperature range investigated could be achieved also by grain boundary sliding (not studied here), our observations provide evidence that generation and multiplication of dislocations take a major part in the deformation of AlN between RT and 800°C. Glide occurs on the basal plane with dislocations having $1/3<11\bar{2}0>$ type Burgers vector. When temperature increases, the activity of first kind prismatic planes becomes more and more important, due to an easier activation of cross slip. However, glide on first kind prismatic planes is also observed at RT (fig.1).

An important feature of dislocations induced by plastic deformation is the elongation of dislocations or dislocation loops in the screw direction. This feature is more pronounced at low temperature but still remains after deformation at 800°C, although most of the dislocations having pinning points bow out between these pinning points. The low mobility of screw segments has to be compared to other III-V compounds : after deformation at low temperature, similar behaviour

is observed in GaAs [11], InP [12] and GaSb [13]. In those compounds, deformation is controlled by screw dislocations and when temperature increases the asymetry between non screw and screw characters is less and less important. Another agreement with the microstructure of III-V compounds is that the dislocation segments of glide loops observed in AlN lie along the $<11\bar{2}0>$ directions of the basal plane at RT, showing that dislocations have to overcome a high Peierls potential when moving in this glide plane. Nevertheless, the behaviour of dislocations in AlN differs somehow from other compounds when temperature increases. In fact, the screw orientation remains the dominant character but dislocation lines are not rectilinear. They are cusped and possess numerous pinning points. What is the nature of the pinning points? The stress field due to a screw dislocation does not interact with a spherical impurity, so it is reasonable to assess that pinning points could be associated to point defect clusters.

Another interesting - and more intriguing- point to notice is that no dislocation splitting can be evidenced using the weak beam technique. In elemental (Si, Ge) and III-V compound (GaAs, InP,...) semiconductors, dislocations created by plastic deformation are dissociated at rest and move in this configuration [14]. Under high stress, deformation occurs by the uncorrelated movement of partial dislocations, yielding to large stacking fault ribbon. In our experiments, the engineering applied stress varied from about 1000 MPa (at 800°C) to about 4000 MPa (at RT). The applied stress within the grains is difficult to know since the exact orientation of the observed grains with respect to the compression axis is unknown, moreover part of the deformation can be achieved also by grain boundary sliding. However, it is likely that dislocations, especially at RT, have been submitted to high stresses. No significant dissociation being obtained in our observations suggests that AlN has a high stacking fault energy. Extended nodes, stacking faults and dissociated dislocations have been previously observed in as-grown material leading to low values for the stacking fault energy : from 4 $mJ.m^{-2}$ [15] to 7.5 $mJ.m^{-2}$ [8]. Such stacking fault energy values would have led to a large splitting of $<11\bar{2}0>$ dislocations under the high stresses applied in our experiments. The different behaviour between dislocations created during the sintering process and those created by controlled plastic deformation could be understood by the effect of impurities on stacking fault energy at high temperature on one hand, and on dislocation dynamics during low temperature deformation, on the other hand.

CONCLUSION

Dislocations are responsible for the plastic deformation of sintered AlN between RT and 800°C. Screw segments control deformation in this temperature range. At RT, they are straight and well confined in the Peierls valleys. At 800°C, screw dislocations are cusped and many cross slip events occur. The first kind prismatic plane has been found to be the cross slip plane. Impurity clusters interacting with screw dislocations are suspected to promote the cross slip nucleation. Although large stresses were applied, no dissociation of dislocations created by plastic deformation has been resolved. Other experiments with different impurity concentrations are needed to clarify the cross slip abilities of screw dislocations as well as the splitting mode of dislocations. Finally, microstructures and plastic behaviour of sintered AlN are very similar to those of other III-V compounds. This suggests that mechanical properties of aluminum nitride and covalent ceramics could be improved by electronic doping.

REFERENCES

1. G.A.Slack, J. Phys. Chem. Sol., 34, 321 (1973).
2. W.Werdecker and F.Aldinger, IEEE Trans. on components and manufacturing technology CHMTH7, 4, 399 (1984).
3. M.F.Denanot, J.Delafond and J.Grilhé, Rad. Effects, 88, 145 (1986).
4. H.C.Heard and C.F.Cline, J. of Mater. Sci., 15, 1889 (1980).
5. C.L.Hoenig and C.S.Yust, Ceramic Bulletin, 60, 1175 (1981).
6. E.K.Beauchamp, R.A.Graham and M.J.Carr in Defect Properties and Processing of High-Technology Nonmetallic Materials, edited by J.H.Crawford, Jr., Y.Chen, W.A.Sibley (Mat. Res. Soc. Symp. Proc., 24, 1984) pp. 281-289.
7. M.F.Denanot and J.Rabier, Inst. Phys. Conf. Ser., 100, 439 (1989).
8. M.F.Denanot and J.Rabier, J. of Mater. Sci., 24, 1594 (1989).
9. M.F.Denanot and J.Rabier, Mat. Sci. and Eng. A, 109, 157 (1989).
10. P.Veyssière, J.Rabier, M.Jaulin, J.L.Demenet and J.Castaing, Rev. Phys. Appl., 20, 805 (1985).
11. P.Boivin, J.Rabier and H.Garem, Phil. Mag. A, 61, 647 (1990).
12. P.Gall, J.P.Peyrade, R.Coquillé, F.Reynaud, S.Gabillet and A.Albacete, Acta Met., 35, 143 (1987).
13. M.Omri, thesis, I.N.P.L.Nancy, 1987.
14. H.Alexander, in Dislocations in Solids, 7, edited by F.R.N.Nabarro (Elsevier Science Publishers, 1986) p.113.
15. P.Delavignette, H.B.Kirkpatrick and S.Amelinckx, J. Appl. Phys., 32, 1098 (1961).

TEMPERATURE DEPENDENCE OF OPTICAL PROPERTIES OF AlAs, STUDIED BY *IN SITU* SPECTROSCOPIC ELLIPSOMETRY

HUADE YAO*, PAUL G. SNYDER*, KATHLEEN STAIR**, THOMAS BIRD**
*University of Nebraska, Center for Microelectronic and Optical Materials Research, and Department of Electrical Engineering, Lincoln, NE 68588-0511
**Amoco Research Center, Naperville, IL 60566

ABSTRACT

The dielectric functions $\varepsilon = \varepsilon_1 + i\varepsilon_2$ of AlAs were determined from 1.5 eV to 5.0 eV, by spectroscopic ellipsometry (SE), from room temperature (RT) to ~577 °C in an ultrahigh vacuum (UHV) chamber. Molecular beam epitaxy (MBE)-grown AlAs was covered by a thin GaAs layer, which was passivated by arsenic capping to prevent oxidation. The arsenic cap was desorbed inside the UHV chamber. SE measurements of the *unoxidized* sample were made, at various temperatures. Temperature dependent optical constants of AlAs were obtained by mathematically removing the effects of the GaAs cap and substrate. Quantitative analyses of the variations of critical-point energies with temperature, by using the harmonic oscillator approximation (HOA), indicate that the E_1 and $E_1+\Delta_1$, energies decrease ~350 meV as temperature increases from RT to 500 °C.

INTRODUCTION

AlAs is the binary endpoint of the $Al_xGa_{(1-x)}As$ system, which plays an extremely important role in high-speed electronic and optoelectronic device technologies. The materials in this alloy system are essentially lattice matched over the entire composition range. As x value approaches to 1 (AlAs), sample surfaces become so reactive that the oxide layer can not be removed by wet-chemical etching [1]. Therefore, studies of optical constants (dielectric function $\varepsilon = \varepsilon_1 + i\varepsilon_2$) of AlAs, in the entire visible range, were not complete, especially at elevated temperatures [2,3]. In this paper, we report the results of *in situ* spectroscopic ellipsometric (SE) measurements of dielectric functions ε of AlAs, at elevated temperatures, inside a UHV chamber.

THEORY

Spectroscopic ellipsometry accurately determines the complex ratio $\rho = R_p / R_s$, where R_p and R_S are the reflection coefficients of light polarized parallel to (p) or perpendicular to (s) the plane of incidence. The ratio has been traditionally defined as:

$$\rho = \tan(\psi)e^{i\Delta}, \tag{1}$$

where the values of $\tan(\psi)$ and Δ are the amplitude and phase of the complex ratio. Results of the SE measurements are expressed as $\psi(h\nu_i, \Phi_j)$ and $\Delta(h\nu_i, \Phi_j)$ where

hν is the photon energy and Φ is the external angle of incidence. The ability of measuring the phase changes $\Delta(h\nu_i, \Phi_j)$ in particular gives the ellipsometer great sensitivity to the structural and surface changes of the samples [4].

The pseudodielectric function $<\varepsilon>$ can be obtained from the ellipsometrically measured values of ρ, based on a two-phase model (ambient/substrate) [5]:

$$<\varepsilon> = <\varepsilon_1> + i<\varepsilon_2> = \varepsilon_a\left[\left(\frac{1-\rho}{1+\rho}\right)^2 \sin^2\Phi \tan^2\Phi + \sin^2\Phi\right], \quad (2)$$

regardless of the possible presence of surface overlayers. The ε_a in Eq.(2) represents the ambient dielectric function (i.e., ε_a=1 in vacuum).

If the sample contains multiple layers, the SE data must be numerically fitted. A model is assumed, and $\tan\psi^c(h\nu_i, \Phi_j)$ and $\cos\Delta^c(h\nu_i, \Phi_j)$ are calculated as in Eq. (1) for comparison with the measured values. A regression analysis is used to vary the model parameters (e.g., layer thickness or dielectric function) until the calculated and measured values match as closely as possible. This is done by minimizing the mean square error (MSE) function, defined as:

$$MSE = \frac{1}{N}\sum_{i,j}\left\{\left[\tan\psi(h\nu_i, \Phi_j) - \tan\psi^c(h\nu_i, \Phi_j)\right]^2 + \left[\cos\Delta(h\nu_i, \Phi_j) - \cos\Delta^c(h\nu_i, \Phi_j)\right]^2\right\}. \quad (3)$$

The dielectric response of a solid crystal can be quantum mechanically expressed as a superposition of a set of harmonic oscillators [6-8]. In this study, we found that a six-oscillator model could satisfactorily fit our SE data. therefore, the dielectric function can be written as

$$\varepsilon(E) = 1 + \sum_{k=1}^{h} A_k\left(\frac{1}{E + E_k + i\Gamma_k} - \frac{1}{E - E_k + i\Gamma_k}\right). \quad (4)$$

A detailed discussion of our SE data analysis using this HOA will be presented in a later section of this paper.

EXPERIMENTAL

AlAs of ~5000 Å nominal thickness was grown, by MBE with a Varian Modular Gen II, on semi-insulating GaAs (100) substrate, and covered by a ~20 Å GaAs layer. GaAs substrate temperature was determined as ~680 °C, by using an IRCCN optical pyrometer, and the growth rate was one micron per hour. After finishing the MBE growth, the sample was allowed to cool down to ~20 °C, and then exposed to arsenic pressure at 1.24×10^{-5} torr for 94 minutes. Thus the top GaAs thin layer was passivated by arsenic capping to prevent oxidation.

The sample was installed, after growth, into a UHV chamber, to which a rotating-polarizer spectroscopic ellipsometer was attached. SE measurements were performed through a pair of low-strain fused-quartz windows to minimize the measuring error. This optical system has been described in detail in reference 8.

The sample was heated on a resistor-heater plate, inside the UHV chamber, to ~350 °C. The arsenic cap was desorbed at this temperature, and the surface of the top GaAs layer was monitored by an *in situ* SE measurement near the E_2 energy. An unoxidized, clean top GaAs surface was obtained when the monitored $<\varepsilon_2>$ value reached its maxium [8-11]. Temperatures were controlled and measured by a calibrated k-type thermocouple. The typical base pressure of the UHV was ~1-2x10^{-9} torr and all SE measurements were made without arsenic overpressure.

MEASUREMENTS AND ANALYSIS

Dielectric functions

SE data, measured at RT, from the unoxidized sample surface, were used to determine the layer thicknesses of AlAs and GaAs cap. Peak positions of the dielectric function ε of RT AlAs, which was calculated from our model with different layer thicknesses, were compared with RT dielectric function data from ref. 3. It was found that the actual thicknesses of AlAs and GaAs cap were 5000 Å ± 50 Å and 23 Å ± 2 Å, respectively, by aligning the major peak positions of ε_1 and ε_2 with those from ref. 3 data and the known critical-point positions. Those actual thicknesses are in good agreement with the nominal values. In general, our RT dielectric function data of AlAs are comparable with the data in ref. 3, except our ε_2 peak value in the near E_2 region is slightly lower (ε_2 =~28) than that in ref. 3 (ε_2 = ~30). This is because the peak value of ε_2 in ref. 3 was an assumed value used to determine the surface oxide thickness, while ours was the result from direct measurement of an unoxidized surface.

Dielectric functions of AlAs were obtained by mathematically removing the effects of the GaAs cap and substrate, assuming a four-phase model (ambient/GaAs cap/AlAs/GaAs substrate) with actual thicknesses. Temperature dependent optical constants of GaAs, obtained from our previous studies [8], were used in the model. Dielectric functions ε of AlAs, measured from 1.5-5.0 eV, at the temperatures ranging from RT to 577 °C, are shown in Fig.1. Actual SE measurements were made at increments of ~50 °C. Starting at 500 °C, surface quality was checked by taking RT SE data each time, after measurements were made at the elevated temperatures. It was found that after heating above 500 °C, the GaAs cap surface was slightly roughened. This correlated with a blurred Reflection High Energy Electron Diffraction (RHEED) pattern associated with a dynamic GaAs surface (i.e., arsenic was moving around), seen at ~500 °C, in a UHV chamber without arsenic overpressure. AT ~577 °C, the GaAs cap became thinner and the surface was rougher. This was likely caused by additional congruent evaporation of Ga and As at high temperatures between 577-657 °C [9-12]. Roughening could be approximately modeled as a nondense GaAs layer (i.e., layer containing voids), by using the Bruggeman effective-medium approximation (EMA) [8,13]. Corrections were made mathematically to remove the surface roughening effects at 500 and 577 °C.

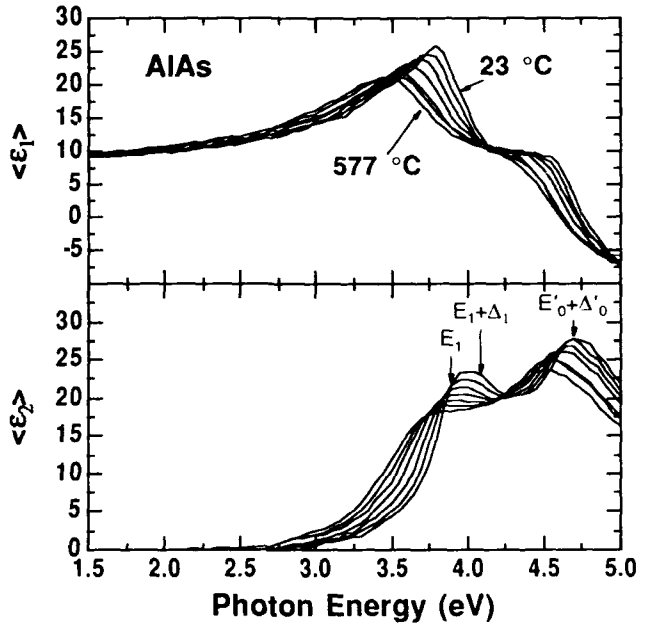


FIG. 1 Representative dielectric functions ε of AlAs at 23, 100, 200, 300, 400, 500, and 577 °C. The 500 and 577 curve have been corrected for surface roughening. The three critical energy positions are marked for RT.

Temperature Dependence of Critical-Point Energies

As shown in Fig. 1, peaks of the dielectric functions of AlAs shift toward lower energy, as temperature increases, indicating an overall shift of the critical-point energies at elevated temperatures. HOA was employed to explore the variations of critical-point energies with temperature. A six-oscillator model, described in Eq. (4), was used to fit the SE data of AlAs, in the range of 3.2-5.0 eV. Among the six oscillators, three represented the major optical transitions E_1, $E_1+\Delta_1$, and $E'_0+\Delta'_0$. One oscillator was used to describe optical transitions between $E_1+\Delta_1$ and $E'_0+\Delta'_0$, and the other two oscillators were employed to include the effects of all transitions above $E'_0+\Delta'_0$ and outside our spectral range.

Fig. 2 shows the results of our HOA fit for the dielectric functions of AlAs at RT and 400 °C, respectively. All the parameters A_k, E_k and Γ_k, of each oscillator were allowed to vary except Γ_6, to minimize the MSE function through a regression analysis. The six-oscillator HOA fit was applied to ε of AlAs at each elevated temperature.

The center energies of the three oscillators, representing three particular optical transitions, correspond to critical points (CP) E_1, $E_1+\Delta_1$, and $E'_0+\Delta'_0$. Temperature dependent variations of the three critical points are shown in Fig. 3.

We can see that as temperature increases from RT to ~500 °C, the E_1 and $E_1+\Delta_1$ energies decrease almost ~350 meV, while the $E'_0+\Delta'_0$ energy decreases only ~140 meV. The deviations of the (CP) energies at 577 °C, we believe, is related with

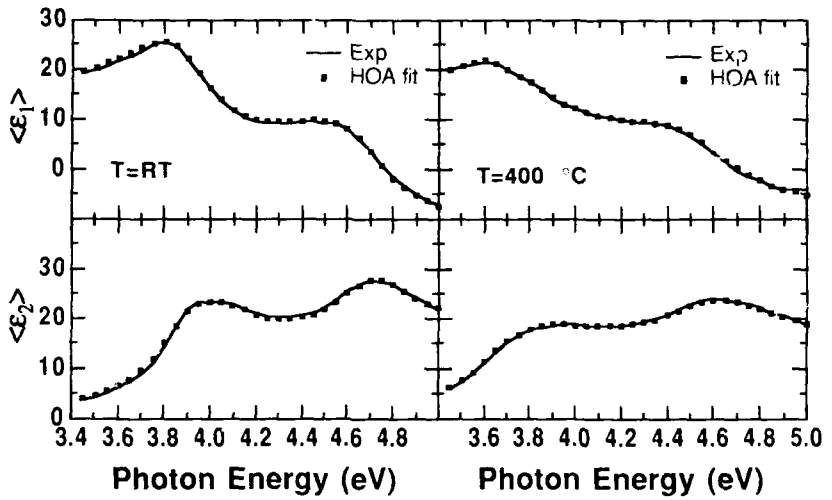


FIG. 2 Six-oscillator HOA fit (dot line) for the dielectric functions of AlAs (solid line) at RT and 400 °C.

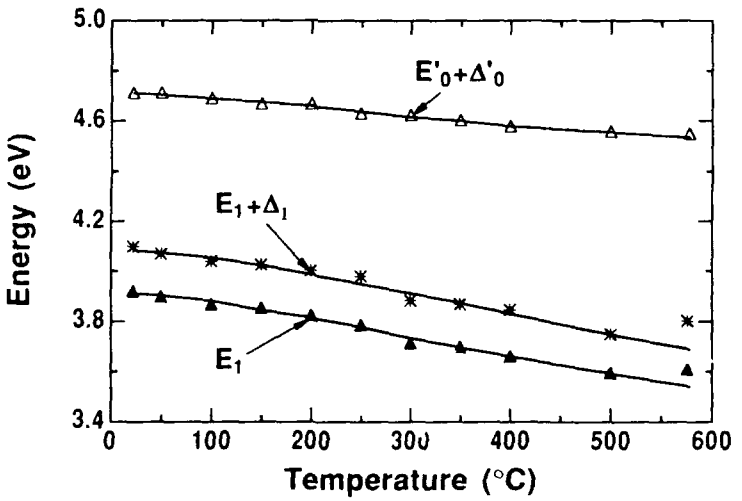


FIG.3 Temperature dependence of CP energies, of AlAs, E_1 (solid triangle), $E_1+\Delta_1$ (asterisk), and $E'_0+\Delta'_0$ (hollow triangle). The solid lines are cubic polynomial fits for each CP energy, from RT to 500 °C.

sample surface degradation at that temperature. The three CP energies at RT in Fig. 3 are in good agreement with values in literature [3]. The error bars for CP energy values, ranging from RT to ~500 °C, were estimated to be ~10 meV.

SUMMARY

We have presented dielectric functions $\varepsilon = \varepsilon_1 + i\varepsilon_2$ of AlAs , measured by *in situ* SE , as functions of temperature. Variations of CP energies with temperature, analyzed by HOA, indicates that E_1, $E_1+\Delta_1$, and $E'_0+\Delta'_0$ energies of AlAs decrease as temperature increases. From RT to 500 °C, E_1 and $E_1+\Delta_1$ energies decrease almost ~350meV.

ACKNOWLEDGMENTS

This work was partially supported by NASA-Lewis Grant NAG-3-154.

REFERENCES

1. D.E. Aspnes, S.M. Kelso, R.A. Logan, and R. Bhat, J. Appl. Phys. **60**, 754 (1986).
2. R.E. Fern and A. Onton, J. Appl. Phys. **42**, 3499 (1971).
3. M. Garriga, P. Lautenschlager, M. Cardona, and K. Ploog, Solid State Commun. **61**, 157 (1987).
4. D.E. Aspnes, in *Properties of Solids-New Developments*, edited by B.O. Saraphin (North-Holland, Amsterdam, 1976) p799.
5. R.M.A. Azzam and N.M. Bashara, *Ellipsometry and Polarized Light*, (North-Holland, Amsterdam, 1977).
6. F. Wooten, *Optical Properties of Solids* (Academic Press, New York, 1972).
7. M. Erman, J.B. Theeten, P. Chambon, S.M. Kelso and D.E. Aspnes, J. Appl. Phys. **56**, 2664 (1984).
8. H.D. Yao, P.G. Snyder, and J.A. Woollam, J. Appl. Phys. **70**, 3261 (1991).
9. H.D. Yao, P.G. Snyder and J.A. Woollam, Proceedings of ICEM-**2**, 501 (1990).
10. H.D. Yao, P.G. Snyder and J.A. Woollam, Mat. Res. Soc. Symp. Proc. **202**, 339 (1991).
11. H.D. Yao and P.G. Snyder, Solid Thin Films (in press, 1991).
12. C.T. Foxon, J.A. Harvey and B.A. Joyce, J. Phys. Chem. Solids **34**,1693 (1973).
13. D.E. Aspnes and J.B. Theeten, Phys. Rev. B **20**, 3292 (1979).

MOMBE GROWTH OF GaP AND ITS EFFICIENT PHOTOENHANCEMENT AT LOW TEMPERATURES

MASAHIRO YOSHIMOTO, TSUZUMI TSUJI, ATSUSHI KAJIMOTO*
AND HIROYUKI MATSUNAMI
Department of Electrical Engineering, Kyoto University, Sakyo,
Kyoto 606-01, Japan
*Nisshin Steel Co. Ltd., 5 Ishizu-nishimachi, Sakai, Osaka 592, Japan

ABSTRACT

GaP epilayers grown at temperatures ranging from 420 to 500℃ had smooth surfaces and streaky RHEED patterns. The decomposition of group-Ⅲ sources of TEGa limits the growth rates of GaP at lower substrate temperatures(<390 ℃). The growth rate of GaP epitaxial layers was efficiently enhanced by N_2-laser irradiation at lower substrate temperatures.

INTRODUCTION

Gallium phosphide (GaP) is widely used for light-emitting diodes (LEDs). The performance of LEDs, however, is limited by its indirect-gap structure, though suitable recombination centers for light emission are utilized. For further improvement in GaP light-emitting devices, heterostructures consisting of GaP/AlP or GaP/GaN have received considerable interest. Metalorganic molecular beam epitaxy (MOMBE) promises to be an attractive technique for Ⅲ-Ⅴ semiconductors, especially for P-based Ⅲ-Ⅴs, owing to its excellent controllability of high vapor-pressure group Ⅴ sources.

In MOMBE without cracking group Ⅲ metalorganics, the decomposition of metalorganics takes place just on a heated substrate. Stagnant layers which govern growth processes in organometallic vapor phase epitaxy (OMVPE) are not formed. Thus, reactions among sources in gas phase are completely removed. Furthermore, the decomposition reaction of metalorganics at the growth surface brings crystal growth governed by surface reactions. Selective epitaxy by modulating the reaction with insulator-masking and/or electron/photon irradiation will be practically achievable in MOMBE. These advantages of MOMBE, however, have been investigated mainly in the epitaxy of As-based Ⅲ-Ⅴ semiconductors [1,2]. Recently, a reduction of carbon in GaAs epilayers [3] and the growth of GaAs epilayers with fine patterns [4] were demonstrated in MOMBE with Ar^+ laser irradiation.

In this paper, we describe the homoepitaxial growth of GaP and the properties of layers grown at appropriate substrate temperatures. The decomposition of group-Ⅲ sources such as triethylgallium (TEGa) is insufficient at lower substrate temperatures. To obtain an abrupt heterojunction with a smooth interface, a reduction of growth temperature is required. Here, we report an enhancement of GaP growth rate at lower substrate temperatures by ultraviolet-light irradiation emitted from a N_2 laser (337nm).

GaP EPITAXY IN MOMBE

The MOMBE system is described elsewhere [5]. Triethylgallium (TEGa) and PH_3 were used in our MOMBE system. The temperature of TEGa was kept constant in a thermostat. The flow rates of TEGa (F_{TEGa}) were precisely controlled between 0.015 and 0.100 SCCM by a mass-flow controller without H_2 as a carrier gas. PH_3 with a flow rate (F_{PH3}) from 0.06 to 1.0 SCCM was

precracked in a thermal cracking cell. In the cell, the cracking efficiency is estimated to be 58 % from the reduction rate in the peak intensity of 34 amu (PH_3) in mass spectrum detected by a quadrupole mass analyzer. The pressure of the production chamber during epitaxy was maintained in the order of 10^{-5} Torr. The substrate temperature was varied between 290 and 500 ℃. GaP with the orientation of (100) or (111) was used as a substrate.

In our previous report [6], it was found that the decomposition of metalorganics limits the growth rate of P-based Ⅲ-Ⅴs (InGaP, GaAlP and InAlP) at low substrate temperatures in MOMBE. Also in GaP epitaxy, the decomposition of TEGa becomes insufficient with an activation energy of 39 kcal/mol below 390℃ as shown in Fig.1. The flow rates of TEGa and PH_3 were kept at 0.020 and 0.20 sccm, respectively. Above 390℃, the decomposition of TEGa showed a saturation limited by the amount of supplied metalorganics. The quality of typical GaP epilayers was examined by reflection high-energy electron diffraction (RHEED) observation and X-ray rocking-curve analysis.

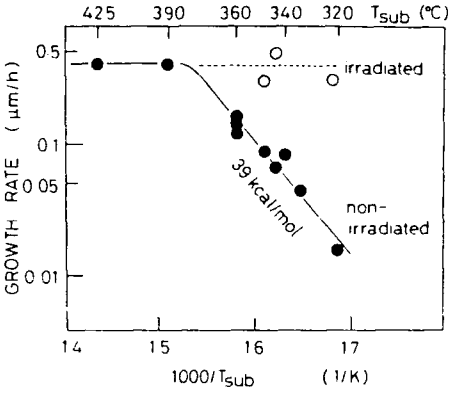


Fig.1. Growth rate of GaP and its photo-irradiation effect. F_{TEGa}=0.020sccm and F_{PH3}=0.20 sccm.

GaP epilayers grown at temperatures ranging from 420 to 500 ℃ had smooth surfaces and streaky RHEED patterns. Figure 2 shows an example of the surface and the RHEED pattern. Full width at half maximum (FWHM) of X-ray

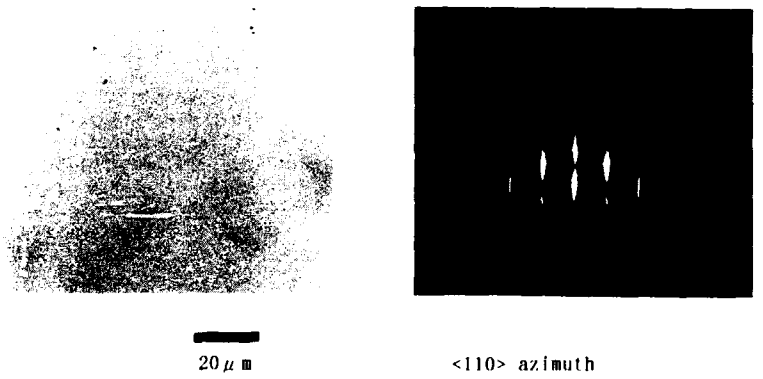


Fig.2. Surface and RHEED pattern of GaP (100) epilayer without photo-irradiation. F_{TEGa}=0.02sccm and F_{PH3}=0.3 sccm. Substrate temperature=420℃.

rocking curves for the epilayers shows as low as 18-22". The undoped epilayers exhibited n-type conduction, and the carrier concentration reached 10^{14} cm^{-3} measured by capacitance-voltage characteristics in a Schottky-diode structure.

PHOTO-IRRADIATION EFFECT IN GaP EPITAXY

Growth enhancement

At lower substrate temperatures, the growth rates of GaP are enhanced with ultraviolet-light (337 nm) emitted from a N_2 laser(pulse operation, repetition rate <20 Hz). Figure 3 shows a thickness profile measured by DekTak 3030 for the epilayer with photo-irradiation. As shown in Fig.1, the growth rate of GaP reaches 0.4 μm/h with photo-irradiation, which is limited by the supply of metalorganics. The flow rate of TEGa and PH_3 was maintained at 0.020 and 0.20 SCCM, respectively.

The growth enhancement increases with the irradiated photon number below $\sim 1 \times 10^{17}$ photons/cm^2pulse (Fig. 4). Above the photon number, the enhancement is saturated at 0.8 μm/h for F_{TEGa}=0.050 sccm. The repetition rate of the N_2 laser was 7Hz. In Fig.4, the saturated value of the growth rate becomes smaller (0.4 μm/h) in the case of F_{TEGa}=0.020sccm.

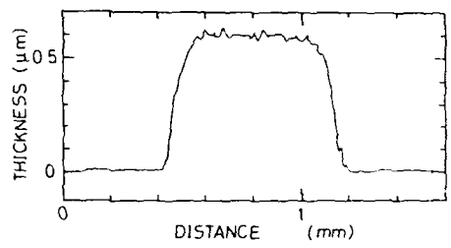


Fig.3. Thickness profile of selectively grown GaP.

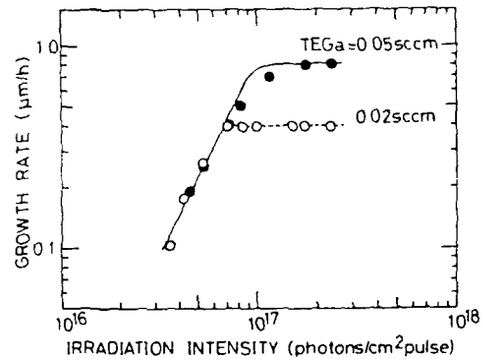


Fig.4. Growth enhancement by photo-irradiation as a function of irradiated photon number. F_{PH3}/F_{TEGa}=10, Substrate temperature=350℃. Repetition rate of N_2 laser=7Hz.

Photochemical effect

In OMVPE growth of GaP [7], the irradiation by an intense ArF excimer laser with a power density of 0.11 J/cm^2 (repetition rate: 50 Hz) enhanced the growth rate. It is noted that the substrate temperature showed an increase of 380 ℃ by the irradiation [8]. Based on the calculation for one-dimensional heat conduction as in ref.[8], a transient increase in the substrate temperature in our experiment

Is 30 ℃ at most. Also, GaP was deposited even at 200 ℃ as shown in Fig.5 with the same value of the growth enhancement at 350 ℃. Thereby, the enhancement of the growth rate by the N_2-laser irradiation is believed to be due to photochemical reactions. Since TEGa shows no absorption for longer wavelengths than 310 nm [9], TEGa has essentially no absorption in gas phase for N_2 laser. Adsorbed Ga metalorganics on a growing surface may absorb the UV-light, which brings the growth enhancement.

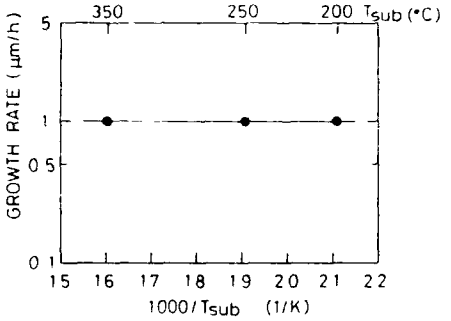


Fig.5. Growth enhancement by photo-irradiation as a function of substrate temperature.
F_{TEGa}=0.020sccm and F_{PH3}=0.20 sccm. Repetition rate of N_2 laser=7Hz. Laser intensity=1x10^{17}photons/cm^{2}pulse.

Efficiency of photo-enhancement

In the optimum case until now, the growth enhancement of 0.8 μm/h was obtained by the irradiation with 1x10^{17} photons/cm^{2}pulse and 1 Hz. The number of Ga atoms deposited on a growing surface is calculated to be 5.4x10^{14} atoms/cm^{2}s from the increased growth rate. If the photo-enhancement efficiency is defined as the ratio of the number of deposited Ga atoms to the irradiating photon number per unit area per unit time, the efficiency is estimated to be around 5x10^{-3}. We also observed an increase in the growth rate of GaP (0.06 μm/h) by Ar$^+$-laser (488nm, 5W/cm^2, CW operation) irradiation. The photo-enhancement efficiency in this case is estimated to be 3x10^{-6}. In MOMBE growth of GaAs using TEGa and AsH_3 [10], the growth rate shows an increase of 0.4 μm/h as a result of irradiation by an Ar$^+$ laser (515 nm, CW operation, ~80mW/cm^2). Here, the photo-enhancement efficiency is also estimated to be in the order of 10^{-6}. The efficiency by N_2-laser irradiation is roughly three orders of magnitude larger than by Ar$^+$-laser irradiation. Hence, the efficiency of the photo-enhancement appears to be affected by the wavelength of irradiating light and/or scheme of photo-irradiation (pulse or CW).

To clarify the reason of efficient photo-enhancement, the wavelength of irradiation light was changed. When the pulsed light (365 nm) emitted from a dye laser (2 Hz, ~6x10^{16} photons/cm^2·pulse) was irradiated on the growing surface with a substrate temperature of 350 ℃ (F_{TEGa}=0.050 SCCM, F_{PH3}=0.5 SCCM), no appreciable enhancement in the growth rate of GaP was observed after 1 hour. Under the same growth condition with N_2-laser irradiation (337 nm, 1.5 Hz, 6x10^{16} photons/cm^2·pulse), a growth enhancement of 1.0 μm/h was achieved. Hence, the efficiency of the photo-enhancement seems affected by the wavelength of irradiated light based on the preliminary result.

CONCLUSIONS

GaP epilayers grown at temperatures ranging 420-500℃ had smooth surfaces and streaky RHEED patterns. The undoped epilayers exhibited n-type conduction, and the carrier concentration reached 10^{14} cm^{-3} measured by the

capacitance-voltage characteristics of a Schottky-diode structure.

The growth rate of GaP was enhanced by ultraviolet-light irradiation emitted from a N_2 laser. The growth rate reached the value limited by the supply of metalorganics. The photo-enhancement efficiency is estimated to be $5x10^{-3}$, which is roughly the three orders of magnitude larger compared with Ar^+-laser irradiation. The enhancement is thought to be due to photochemical reaction on a growing surface.

ACKNOWLEDGMENT

This work was partially supported by The Grant-in-Aid on Priority-Area Research on "Photo-Excited Process", the Ministry of Education, Science and Culture, Japan.

REFERENCES

1. W.T.Tsang, J.Electron.Mater. 15, 235 (1986).
2. M.A.Herman and H.Sitter, Molecular Beam Epitaxy, (Springer, Berlin, 1989) p.16.
3. R.Iga, H.Sugiura, T.Yamada, and K.Wada, Appl.Phys. Lett. 55, 451 (1989).
4. T.Yamada, R.Iga, and H.Sugiura, in Proc. 16th Int. Sympo.GaAs & related Compounds 1989, (IPO, 1990, Bristol) p.213.
5. K.Ozasa, M.Yuri, S.Tanaka and H.Matsunami, J.Appl.Phys. 65, 2711 (1989).
6. K.Ozasa, M.Yuri and H.Matsunami, J.Crystal Growth 102, 31 (1990).
7. U.Sudarsan, N.W.Cody, T.Dosluglu and R.Solanki, Appl.Phys. Let. 55, 738 (1989).
8. U.Sudarsan, and R.Solanki, J. Appl.Phys. 67, 2913 (1990).
9. H.Okabe, M.K.Emadi-babaki, and V.R.McCrary, J. Appl. Phys. 69, 1730 (1991).
10. H.Sugiura, R.Iga, T.Yamada and M.Yamaguchi, Appl.Phys.Let. 54, 335 (1989).

PART VI

Silicon Carbide

PROGRESS IN SILICON CARBIDE SEMICONDUCTOR TECHNOLOGY

J. A. POWELL*, P. G. NEUDECK**, L. G. MATUS*, AND J. B. PETIT***

*NASA Lewis Research Center, 21000 Brookpark Road, Cleveland, OH 44135
**Ohio Aerospace Institute, 2001 Aerospace Parkway, Brook Park, OH 44142
***Sverdrup Technology, Inc., 2001 Aerospace Parkway, Brook Park, OH 44142

ABSTRACT

Silicon carbide semiconductor technology has been advancing rapidly over the last several years. Advances have been made in boule growth, thin film growth, and device fabrication. This paper will review reasons for the renewed interest in SiC, and will review recent developments in both crystal growth and device fabrication.

INTRODUCTION

Interest in SiC as a semiconductor dates back more than thirty years.[1-3] Then, as now, SiC was recognized as having great potential for applications involving high temperature, high radiation, and high frequency. The use of 6H-SiC to fabricate blue light-emitting diodes (LEDs) was also recognized early on. More recently, the potential for high power applications has been receiving more attention. Over the last several decades, the lack of suitable crystal growth processes has hindered its development. The situation has changed over the last few years. Advances in both boule and thin film SiC growth have accelerated the development of this unique semiconductor. For example, high-quality polished 6H-SiC wafers, 25 mm in diameter, are now commercially available. Chemical vapor deposition (CVD) is used to produce multi-layer n- and p-type 6H-SiC device structures. Other new device processes have also contributed to the development of excellent devices. Many of these developments are reviewed in the Proceedings of recent conferences[4,5] and several excellent review articles.[6,7] In this paper, we will discuss SiC properties, crystal growth, and device fabrication with emphasis on developments not covered in previous reviews.

PROPERTIES AND APPLICATIONS

Silicon carbide exhibits a form of one-dimensional polymorphism called polytypism.[6,8] Because of its importance in SiC technology, this structural feature will be described first. The many polytypes of SiC differ from one another only in the stacking sequence of double layers of Si and C atoms. Each successive double layer is stacked on the previous double layer in a close-packed arrangement that allows only three possible relative positions for the double layers. These positions are normally labeled A, B, and C. Depending on the stacking sequence, various structures (i.e. cubic, hexagonal, or rhombohedral) are produced. In the hexagonal frame of reference, the stacking sequence is in the [0001] direction (the c-axis), and the (0001) plane is referred to as the basal plane.

The two most common SiC polytypes are 3C-SiC with the sequence ABC... (or ACB...) and 6H-SiC with the stacking sequence ABCACB... The 3C polytype, also known as ß-SiC, is the only polytype with a cubic structure. All of the others are known as α-SiC; 6H is the most common and has a hexagonal structure. The number-letter designation of the polytypes denotes the number of double layers in a polytype repeat sequence and the structure of the polytype, respectively. Because of the polar nature of SiC bonds at the basal plane, the (0001) surfaces of 6H and the {111} surfaces of 3C are terminated with either Si atoms

(a Si face), or C atoms (a C face). In discussions that follow, the tilt angle of a vicinal (0001) SiC surface is the angle between the actual surface and the (0001) plane.

Properties

An appreciation of the potential of SiC can be gained by examining Table I, which is a comparison of its properties with those of diamond and GaP (two other contenders for high temperature applications) and with those of the two most common commercially available semiconductors, Si and GaAs. In the SiC column of the table, if a property of 6H differs from 3C, it is listed within parentheses. The maximum operating temperature was calculated relative to that of Si by assuming a maximum for Si of 300°C and multiplying this temperature (expressed in K) by the ratio of bandgaps. The maximum for diamond is imposed by a phase change.

Silicon carbide does not melt at any reasonable pressure, but does sublime at temperatures greater than 1800°C. Below 1500°C, its physical stability is excellent and its stability in an oxidizing atmosphere gives it an edge over diamond. We believe that long term stability at high temperatures will be a problem with the more common III-V compounds, such as GaAs and GaP. Thus, SiC has a significant advantage where long-term reliable operation at elevated temperatures is a requirement.

Table I. Comparison of Semiconductors

Property	Si	GaAs	GaP	3C SiC (6H SiC)	Diamond
Bandgap (eV) at 300 K	1.1	1.4	2.3	2.2 (2.9)	5.5
Maximum operating temperature (°C)	300	460	925	873 (1240)	1100(?)
Melting point (°C)	1420	1238	1470	Sublimes > 1800	Phase change
Physical stability	Good	Fair	Fair	Excellent	Very good
Electron mobility R.T., $cm^2/V-s$	1400	8500	350	1000 (600)	2200
Hole mobility R.T., $cm^2/V-s$	600	400	100	40	1600
Breakdown voltage E_b, 10^6 V/cm	.3	.4	—	4	10
Thermal conductivity σ_T, W/cm-°C	1.5	.5	.8	5	20
Sat. elec. drift vel. v(sat), 10^7 cm/s	1	2	—	2.5	2.7
Dielectric const., K	11.8	12.8	11.1	9.7	5.5
Relative Z_J	1	7	—	1100	8100
Relative Z_K	1	.5	—	6	32

Johnson: $Z_J \propto E_b^2 v^2(sat)$ Keyes: $Z_K \propto \sigma_T [v(sat)/K]^{1/2}$

The room temperature electron and hole mobility of SiC at low electric fields does not compare as favorably as the other properties but is acceptable for most applications. For high temperature power applications, the advantages of SiC and diamond are the result of their much higher values of breakdown voltage and thermal conductivity.

Silicon carbide (and diamond) also have great potential for high frequency devices. Two figures of merit for semiconductors for high frequency operation are the Johnson (Z_J)[9] and Keyes (Z_K).[10] Relative values (to that of Si) for these quantities are shown in Table I and illustrate the high potential of SiC and diamond.

Applications

Initial commercial SiC devices have been blue LEDs.[11] Mass production of these products has brought prices down to moderate levels. High voltage diodes for operation up to 350°C are also available, and other devices are under development.

We expect that there will be important applications for SiC devices in the aerospace industry. Sensors, control electronics, and power electronics that can operate at temperatures up to 600°C, and beyond, are required. For example, in advanced turbine engines, many actuators for mechanical components will be required throughout the engine. Using electric actuators instead of traditional hydraulic or pneumatic actuators has many advantages; however, electric actuators will require sensors and power electronics in ambient temperatures up to 600°C. Another example is power electronics for space power systems. For reduced weight, it is highly desirable that the power electronics operate at elevated temperatures, and sometimes also in a high radiation environment.

Component reliability is a key issue in all applications, and in particular for aerospace applications. Failure can lead to expensive, and possibly tragic, consequences. Because of its chemical stability and ceramic-like character, we believe that the potential reliability of semiconductor devices and sensors fabricated from SiC will be much higher than that obtainable from any other semiconductor material. This reliability advantage should hold for all operating temperatures.

Other applications for SiC include: electronics for deep well drilling operations, microwave power devices for radar systems, sensors for the nuclear power industry, automobiles, etc.

CRYSTAL GROWTH

Since SiC does not melt at reasonable pressures, most bulk crystal growth approaches have involved the sublimation of polycrystalline SiC. Until recently, nearly all SiC semiconductor research was carried out using small irregular α-SiC crystals that were sublimation grown by either the industrial Acheson process,[12] or the Lely process.[13] Examples of Lely crystals are shown in Fig. 1. These crystals were not only small, but they frequently contained heterojunctions due to a multiple polytype structure. They were not suitable substrates for commercial device production. Because of this lack of suitable substrates, interest in SiC waned in the 1970s. During the last decade, progress in both bulk and thin film growth processes have revived the prospects for SiC semiconductor technology.

Boule Growth

The growth of bulk SiC single crystals is a key element of the rapidly developing SiC semiconductor technology. Tairov and Tsvetkov[14,15] established the

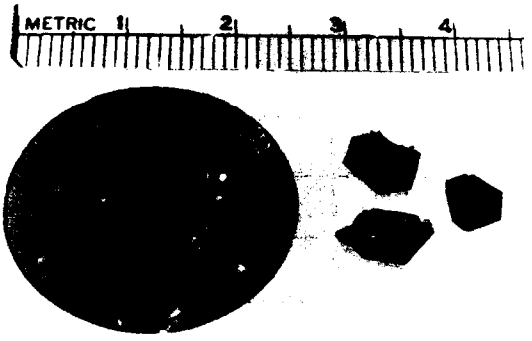


Fig. 1. Cree wafer and Lely crystals.

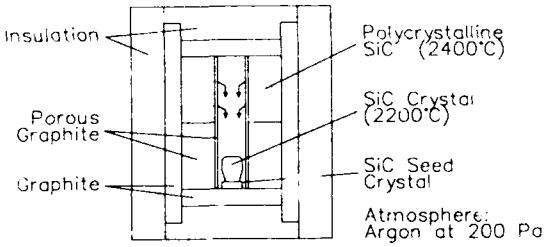


Fig. 2. Growth chamber for the modified sublimation process.

basic principles of a "modified sublimation" bulk growth process in the late 1970s. Although other research groups were somewhat slow in adopting this process, it is now being developed by many labs throughout the world.[16-19]

The basic elements of the modified sublimation process are shown in Fig. 2, which is a schematic diagram of the configuration used by Ziegler et al.[16] Nucleation takes place on a SiC seed crystal located at one end of a cylindrical cavity. A temperature gradient is established within the cavity such that the polycrystalline SiC is at approximately 2400°C and the seed crystal is at approximately 2200°C. At these temperatures and at reduced pressure (Ar at 200 Pa), SiC sublimes from the source SiC and condenses on the seed crystal. Growth rates of a few mm/h can be achieved. In some boule growth systems, the seed crystal is at the top of the cavity and growth proceeds downward. This eliminates some problems of contamination of the growing boule.

The modified sublimation process has been used to grow both 4H and 6H boules.[17,19] Its successful application to the 3C polytype has not been reported. Techniques for cutting and polishing wafers have been developed and at least one company[11] is now marketing 25-mm-diameter polished 6H-SiC wafers; wafer diameters up to 44 mm have been achieved.

Thin Film Growth on Non-SiC Substrates

Because of the lack of high-quality SiC substrates for many years, efforts were made to grow SiC thin films on non-SiC substrates that might be

suitable for commercial device fabrication. Early in the 1980s, large-area single-crystal 3C-SiC was achieved on (001) Si substrates.[20,21] This created renewed interest in SiC and many research groups began pursuing this growth approach. Unfortunately, the 3C films grown on Si had a high defect density, which included stacking faults, microtwins, and a defect known as inversion domain boundaries (IDBs), also known as antiphase boundaries (APBs).[22] These defects may be caused by the 20% lattice mismatch between the Si and SiC, or perhaps by the nucleation process. Further work demonstrated that the IDBs could be eliminated by using vicinal (001) Si substrates with tilt angles in the range 0.5° to 4°.[23,24] But, this did not eliminate the stacking faults and other defects; hence, devices fabricated from these 3C films have not achieved satisfactory performance.

In order to eliminate the problems caused by a large lattice mismatch, TiC_x (less than 1% mismatch) substrates were investigated.[25] Somewhat improved growth was reported, but great difficulties in producing defect-free single-crystal TiC_x has hindered its use as a substrate for SiC growth.

The remainder of this paper will describe only results achieved using SiC substrates.

Thin Film Growth on 6H-SiC Substrates

Early SiC CVD processes, using Acheson or Lely crystals, typically required temperatures above 1550°C.[25-28] This growth was carried out on the (0001) SiC basal plane, either the Si face or C face. In 1973, it was found that 6H-SiC could be grown on 6H-SiC in the temperature range 1320-1390°C when the growth direction was perpendicular to the [0001] direction.[29] The significance of this "90°-off-axis" was not appreciated until much later. Recently, (1) 3C-SiC films were achieved on the basal planes of 6H-SiC in the range 1350-1550°C,[30-35] and (2) 6H-SiC films were achieved on "off-axis" 6H-SiC substrates that were oriented several degrees off the basal plane.[31-33,36,37] All of the above growth results were achieved on Acheson or Lely crystals. More recently, high quality 6H-SiC films were also grown on "off-axis" 6H-SiC wafers that were produced from sublimation-grown boules.[38]

Epitaxial Growth Models

To explain the success of the 6H CVD at lower temperatures using "off-axis" 6H-SiC substrates, a model was suggested[32,33] whereby the density of atomic-scale steps on a vicinal (0001) 6H substrate determines the polytype of the grown film. Refer to Fig. 3, a schematic cross-sectional view of a vicinal (0001) SiC crystal. The step density increases and the width of terraces

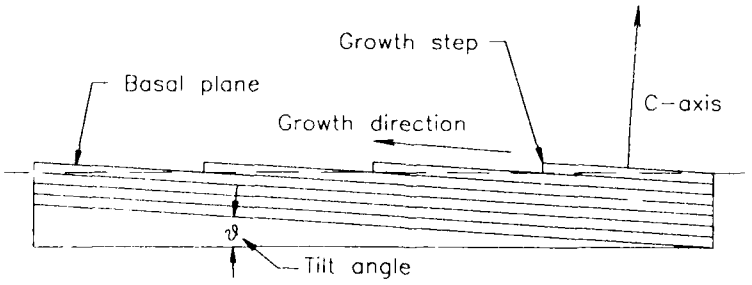


Fig. 3. Vicinal (0001) α-SiC substrate showing surface growth steps.

between steps decreases as the tilt angle of the growth surface increases. According to the model, at tilt angles greater than 1.5°, arriving Si and C atoms can easily migrate to steps where lateral growth occurs parallel to the basal plane. In this case, grown films assume the ABCACB... stacking sequence of the 6H substrate. However, at smaller tilt angles (i.e. < 1.5°), terraces are larger and migration of Si and C atoms to the steps is less likely. Instead, nucleation of 3C occurs on the terraces. Depending on which terrace is the site of nucleation, either the ABC... or the ACB... stacking sequence of the 3C polytype can occur. Coalescence of islands of both sequences create the double positioning boundaries (DPBs) that are commonly seen in 3C films grown on 6H substrates. Also according to the model, 6H films are achieved on the as-grown faces of Lely 6H crystals (very low tilt angles) at 1800°C because surface migration is more active and the Si and C atoms reach the growth steps.

Recent results at NASA Lewis[39] demonstrate that the above model[32,33] is not sufficient to explain the control of polytype in the CVD growth on low-tilt-angle vicinal (0001) 6H-SiC substrates. In these results,[39] 6H films were grown on vicinal (0001) 6H substrates with tilt angles as small as 0.1°. In addition, 3C growth was intentionally produced on the low-tilt-angle substrates by introducing dislocations in the substrates with a diamond scribe. The 3C growth proceeded laterally from the point of intentional nucleation in a direction perpendicular to the growth steps. An essential part of this new result was a pregrowth etch that eliminated all sites of unwanted 3C nucleation. A new growth model[39] that explains the growth of SiC polytypes on vicinal (0001) SiC substrates is as follows. At moderate CVD growth temperatures (1300 to 1500°C), Si and C atoms can migrate to surface steps where lateral growth occurs even at tilt angles as small as 0.1°. In this case, the film will be the same polytype as the substrate. If there are defect sites on the surface (e.g. dislocations, contamination, etc.), then 3C will nucleate at these sites because 3C is the more stable polytype at these lower temperatures. Evidently, atomic steps play the dominant role in controlling polytype formation at larger tilt angles (e.g. > 1.5°), and defects are dominant at smaller angles.

Thin Film Growth on Low-Tilt-Angle Vicinal (0001) 6H-SiC Wafers

Based on the new growth model[39] described in the previous section, 3C films with significantly reduced defect density have been grown on 6H substrates.[39,40] The following is a summary of this process. Vicinal (0001) 6H substrates, with tilt angles in the range 0.1° to 0.5°, were cut from commercial wafers.[11] The surface of the substrates were divided into 1-mm-square mesas with a dicing saw as shown in Fig. 4. The tilt direction was along a diagonal with highest atomic plane at the upper right of each mesa.

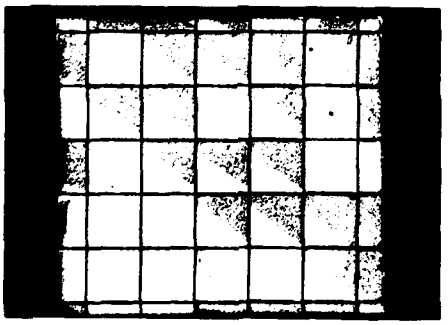


Fig. 4. 6H-SiC substrate (0.5° tilt angle) with 1-mm-square mesas. Dark regions are 3C films; light regions are 6H films.

Prior to growth, the 6H substrates were subjected to an $HCl\backslash H_2$ gaseous etch at 1375°C for 25 min to remove unwanted 3C nucleation sites. The substrates were then removed from the growth chamber and exposed a non-clean laboratory environment. They were then returned to the growth chamber. The SiC films were grown at atmospheric pressure using silane and propane as the sources of Si and C, respectively. The resulting 8-μm-thick film, shown in Fig. 4, was oxidized to distinguish the 3C and 6H regions. Differences in oxidation rates produce contrasting interference colors between 3C and 6H.

A SiC film grew uniformly in thickness on each mesa. Initial growth was mostly 6H. It is presumed that this growth was due to lateral growth from atomic steps on the surface. In many of the mesas, 3C nucleated on the highest atomic plane (upper right in Fig. 4) and then grew laterally over the mesa from 3C steps generated at this point. In this case, the extent of lateral growth was consistent with the amount of vertical growth (8 μm) and the tilt angle of 0.5°. Most of the 3C regions were free of DPBs and had a reduced density of stacking faults compared to previous 3C growth on 6H. As yet, we don't fully understand the 3C nucleation process, but believe that contamination plays a role in this case.

It is hoped that this process will be the basis for producing useful 3C devices.

DEVICE FABRICATION TECHNOLOGY

Much of the technology required to produce working electronic circuits in SiC is directly importable from well-developed silicon processing technologies. Hence, the jump to higher levels of integration should not be exceedingly difficult after individual SiC devices are mastered. Standard techniques for photolithographic pattern definition and material (dielectrics, metals, etc.) deposition are directly applicable to the fabrication of SiC device structures. Doping of 3C and 6H epilayers to achieve *n*- and *p*-type material can be controlled during epitaxial growth, so a variety of device structures can be produced in a relatively straightforward manner.

Patterned doping of SiC can be accomplished through ion implantation, but this is usually carried out at elevated substrate temperatures to achieve proper dopant activation.[41] Diffusion of dopants into SiC is not practical as diffusion coefficients are negligible at temperatures below 1800°C; however, this property is actually an advantage during high-temperature operation because dopants will not redistribute.

The inherent mechanical strength of SiC helps prevent wafer breakage during processing, but its chemical inertness precludes the use of conventional wet etching at room temperature. Satisfactory etching of SiC is accomplished primarily by reactive ion etching (RIE).[42]

BASIC SiC DEVICE STUDIES

6H-SiC appears to be the most attractive polytype for developing useful electronic circuits at this time, but this is simply because current crystal growth techniques produce substantially higher quality 6H material than other SiC polytypes. With unintentional background carrier concentrations in the mid-10^{15} cm^{-3} range being grown,[43] the quality of epitaxial 6H-SiC is sufficient to permit fabrication of discrete devices and small integrated circuits.

A variety of junctions are the fundamental building blocks of any semiconductor technology, especially as it pertains to transistor performance. JFET's (Junction Field Effect Transistors) and BJT's (Bipolar Junction Transistors) rely on *p*-type to *n*-type junctions (i.e., *pn* junctions); MESFET's (Metal Semiconductor Field Effect Transistors) rely on rectifying metal-semiconductor junctions (i.e., Schottky junctions); MOSFET's rely on insulator-semiconductor junctions, and all of these devices require ohmic

contact junctions. It follows that the ultimate performance capabilities of these transistors are largely dependent on the ability to form junctions with desirable characteristics. Although research into the optimization of SiC junction qualities is far from mature, a variety of early experimental 6H-SiC devices have produced some tantalizing results.

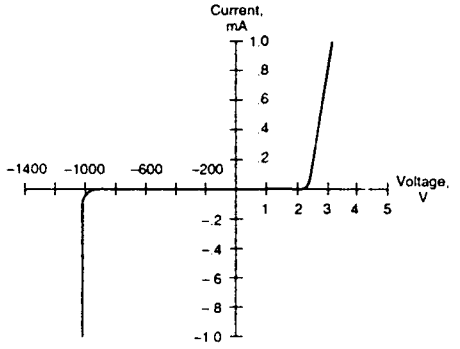


Fig. 5. IV characteristics of 6H-SiC pn junction diode tested at room temperature.

In the case of the pn junction, low leakage currents and high reverse breakdown voltages are desirable in most applications. Figure 5 shows the room-temperature current vs. voltage (I-V) characteristic of a pn junction diode fabricated in epitaxially grown 6H SiC.[44] The $V_{breakdown}$ > 1000 V at the doping level of 2 x 10^{16} cm^{-3} for the diode n-region demonstrates the significantly higher breakdown field enjoyed by 6H-SiC over Si and GaAs (Table I). This 10-fold increase in field strength for SiC theoretically translates into considerable improvements in the characteristics and operating regime of many power semiconductor devices.[45] General semiconductor device physics suggests that the large bandgap (small intrinsic carrier concentration) of SiC should lead to greatly reduced pn junction leakage currents. Gardner et al.[46] have reported 6H-SiC pn junction leakages which are orders of magnitude smaller than leakages reported in similar GaAs structures.

Besides the inherent material properties outlined previously, perhaps one of silicon carbide's biggest assets is its ability to thermally grow a passivating native oxide just like silicon. When SiC is thermally oxidized it produces SiO_2, the same insulator that is produced when pure silicon is thermally oxidized. The importance of this SiC property should not be underestimated as the majority of all integrated circuits (IC's) are based on the Si-SiO_2 MOSFET (Metal Oxide Semiconductor Field Effect Transistor) -- a device which relies on thermally grown silicon dioxide. Unfortunately the SiC MOS devices reported to date suffer from the same major problem that faced silicon MOS devices in the 1960's: interface states. Dangling bonds and surface disorder at the semiconductor-insulator boundary give rise to electrically active defect states. These defect states hinder the ability of the MOSFET to carry current (because of decreased channel carrier mobilities), and cause charge trapping that results in undesirable threshold voltage instability. It should be noted that these interface states also play a role in the characteristics of SiC pn junctions, as Gardner et al.[46] witnessed a substantial change in reverse leakage as a function of sidewall oxide quality.

Early experiments have suggested that SiC devices are inherently more radiation tolerant than comparable silicon devices,[47] but wider ranging radiation tolerance studies are currently being undertaken.

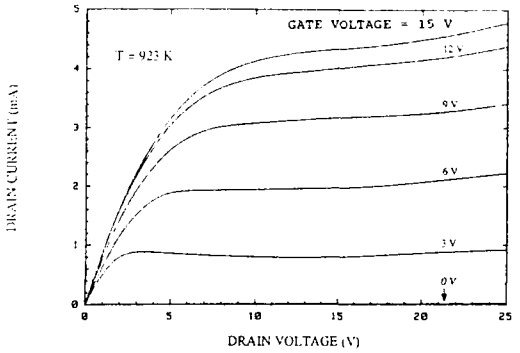


Fig. 6. Drain IV characteristics of an iversion-mode 6H-SiC MOSFET tested at 650°C. (Courtesy of Cree Research Inc.)

SiC TRANSISTORS: CURRENT PERFORMANCE ISSUES

Experimental JFET's, MOSFET's (Fig. 6), MESFET's, and BJT's have been fabricated in single crystal 6H-SiC, and basic operation of these devices at temperatures as high as 650°C has been demonstrated.[48] No other semiconductor material has shown transistor operation at this temperature. However, these devices exhibit several significant shortcomings which point out fundamental challenges that remain to be solved if SiC is to emerge as a truly superior semiconductor for high-temperature, high-radiation, and/or high-power applications.

At 650°C, the operational lifetime of these SiC transistors is typically less than ½ hour. This limitation is strictly due to failure of non-optimized ohmic contact metallizations, and it is not due to any limitations of the SiC semiconductor itself. Reliable contacts to SiC have been demonstrated for 350°C operation, but a crucial area of continued research is to develop ohmic contacts that will remain stable at temperatures approaching 600°C and beyond. The progress that is made in obtaining reliable high-temperature contacts will largely dictate the operational temperature ceiling of SiC electronics. Work is also progressing on reducing parasitic contact resistances (currently above 10^{-5} ohm-cm^2), which could limit the current carrying capability of SiC transistors.

The overall performance of many SiC transistors reported to date (particularly MOSFET's) is also hindered by the non-optimal quality of the SiC-SiO_2 interface discussed previously. If one draws upon the historical parallel with silicon MOS technology, it stands to reason that the performance of SiC MOSFET's should improve substantially when interface state densities are reduced from their current levels of 10^{12-13} cm^{-2} to the 10^{10} cm^{-2} densities found in modern silicon MOSFET's. Substantial progress towards this end has been made very recently, as Brown et. al.[49] reported the first SiC-SiO_2 MOS capacitors with interface state densities of less than 5 x 10^{10} cm^{-2}.

SiC PROSPECTS

Tremendous strides have been made in the development of SiC as a semiconductor for high-temperature, high-radiation, and/or high-power electronic applications. However, some crucial issues remain to be solved before the true performance potential of SiC electronics can be realized. Since wafer size, defect density, and background carrier concentration strongly

influence the scale, yield, and capability of semiconductor circuits and devices, advancements in bulk and epilayer crystal growth will continue to profoundly impact the development of SiC electronics. Clearly, improvements need to be made in the areas of contact metallization and SiC-SiO_2 MOS properties. It is the authors' opinion that the resolution of these key issues and subsequent development of SiC into integrated electronics will be substantially accelerated by the vast knowledge base that has been accumulated in silicon IC technology.

REFERENCES

1. Silicon Carbide, A High Temperature Semiconductor, edited by J. R. O'Connor and J. Smiltens, (Pergamon, New York, 1960).
2. Silicon Carbide-1968, edited by H. K. Henisch and R. Roy, (Pergamon, New York, 1969).
3. Silicon Carbide-1973, edited by R. C. Marshall, J. W. Faust, and C. E. Ryan, (University of South Carolina Press, Columbia, South Carolina, 1974).
4. Amorphous and Crystalline Silicon Carbide, ed. by G. L. Harris and C. Y.-W. Yang, Springer Proceedings in Physics, Vol. 34 (Springer-Verlag Berlin, Heidelberg, 1989).
5. Amorphous and Crystalline Silicon Carbide II, ed. by M. M. Rahmann, C. Y.-W. Yang, and G. L. Harris, Springer Proceedings in Physics, Vol. 43 (Springer-Verlag Berlin, Heidelberg, 1989).
6. R. F. Davis and J. T. Glass, in Advances in Solid-State Chemistry, Vol. 2 (JAI Press Ltd., 1991) pp. 1-111.
7. R. F. Davis, G. Kelner, M. Shur, J. W. Palmour, and J. A. Edmond, Proc. I.E.E.E., **79**(5), 677 (1991).
8. N. W. Jepps and T. F. Page, in Progress in Crystal Growth and Characterization, Vol. 7, ed. by P. Krishna (Pergamon, Oxford, 1983), p. 259.
9. A. Johnson, RCA Review, **26**, 163 (1965).
10. R. W. Keyes, in Silicon Carbide 1973, ed. by R. C. Marshall, J. W. Faust, and C. E. Ryan (University of South Carolina Press, Columbia, South Carolina, 1974), p. 534.
11. Cree Research, Inc., Durham, NC 27713, USA.
12. W. F. Knippenberg, Philips Res. Repts. **18**, 161 (1963).
13. J. A. Lely, Ber. Dt. Keram. Ges. **32**, 229 (1955).
14. Y. M. Tairov and V. F. Tsvetkov, J. Cryst. Growth **43**, 209 (1978).
15. Y. M. Tairov and V. F. Tsvetkov, J. Cryst. Growth **52**, 146 (1981).
16. G. Ziegler, P. Lanig, D. Theis, and C. Weyrich, I.E.E.E. Trans. Electron Devices **ED-30**, 277 (1983).
17. K. Koga, T. Nakata, Y. Ueda, Y. Matsushita, and Y. Fujikawa, in Extended Abstracts of the 1989 Fall Meeting of the Electrochemical Society,(1989), p.689.
18. D. L. Barrett, R. G. Seidensticker, W. Gaida, R. H. Hopkins, and W. J. Choyke, J. Cryst. Growth **109**, 17 (1991).
19. M. Kanaya, J. Takahashi, Y. Fujiwara, and A. Moritani, Appl. Phys. Lett. **58**, 56 (1991).
20. S. Nishino, J. A. Powell, and H. A. Will, Appl. Phys. Lett. **42**, 460 (1983).
21. P. Liaw and R. F. Davis, J. Electrochem. Soc. **132**, 642 (1985).
22. P. Pirouz, C. M. Chorey, and J. A. Powell, Appl. Phys. Lett. **50**, 221 (1987).
23. K. Shibahara, T. Saito, S. Nishino, and H. Matsunami, I.E.E.E. Electron Dev. Lett. **EDL-7**, 692 (1986).
24. J. A. Powell, L. G. Matus, M. A. Kuczmarski, C. M. Chorey, T. Cheng, and P. Pirouz, Appl. Phys. Lett. **51**, 823 (1987).
25. J. D. Parsons, in Proc. Mats. Res. Soc. Symp., Vol 97, 271 (1987).

26. R. B. Campbell and T. L. Chu, J. Electrochem. Soc. **113**, 825 (1966).
27. W. v. Muench and I. Pfaffeneder, Thin Solid Films **31**, 39 (1976).
28. S. Nishino, H. Matsunami, and T. Tanaka, J. Crystal Growth, **45**, 144 (1978).
29. J. A. Powell and H. A. Will, J. Appl. Phys. **44**, 177 (1973).
30. H. S. Kong, J. T. Glass, and R. F. Davis, Appl. Phys. Lett. **49**, 1074 (1986).
31. H. S. Kong, H. J. Kim, J. A. Edmond, J. W. Palmour, J. Ryu, C. H. Carter, Jr., and R. F. Davis, in Materials Research Society Symposium Proceedings, edited by T. Aselage, D. Emin, and C. Wood (Materials Research Society, Pittsburgh, PA, 1987), Vol. 97, p. 233.
32. N. Kuroda, K. Shibahara, W. Yoo, S. Nishino, and H. Matsunami, Extended Abstracts 19th Conf. on Solid State Devices and Materials, Tokyo, 1987, pp. 227.
33. H. Matsunami, K. Shibahara, N. Kuroda, and S. Nishino, in Amorphous and Crystalline Silicon Carbide, ed. by G. L. Harris and C. Y.-W. Yang, Springer Proceedings in Physics, Vol. 34 (Springer-Verlag Berlin, Heidelberg, 1989), pp. 34-39.
34. H. S. Kong, J. T. Glass, and R. F. Davis, J. Mater. Res. **4**, 204 (1989).
35. J. A. Powell, D. J. Larkin, L. G. Matus, W. J. Choyke, J. L. Bradshaw, L. Henderson, M. Yoganathan, J. Yang, and P. Pirouz, Appl. Phys. Lett. **56**, 1353 (1990).
36. H. S. Kong, J. T. Glass, and R. F. Davis, J. Appl. Phys. **64**, 2672 (1988).
37. T. Ueda, H. Nishino, and H. Matsunami, J. Cryst. Growth **104**, 695 (1990).
38. J. A. Powell, D. J. Larkin, L. G. Matus, W. J. Choyke, J. L. Bradshaw, L. Henderson, M. Yoganathan, J. Yang, and P. Pirouz, Appl. Phys. Lett. **56**, 1442 (1990).
39. J. A. Powell, J. B. Petit, J. H. Edgar, I. G. Jenkins, L. G. Matus, J. W. Yang, P. Pirouz, W. J. Choyke, L. Clemen, and M. Yoganathan, Appl. Phys. Lett. **59**, 333 (1991).
40. J. A. Powell, D. J. Larkin, J. B. Petit, and J. H. Edgar, presented at the 4th International Conference on Amorphous and Crystalline Silicon Carbide and Other IV-IV Materials, Santa Clara, CA, 10-11 October 1991 (Proceedings to be published by Springer-Verlag).
41. J. A. Edmond, S. P. Withrow, W. Wadlin, R. F. Davis, in Proc. Mats. Res. Soc. Symp., Vol. 77, 193 (1987).
42. W. S. Pan and A. J. Steckl., J. Electrochem. Soc. **137**, 212 (1990).
43. J. W. Palmour, J. A. Edmond, H. S. Kong, and C. H. Carter, Jr., presented at the 4th International Conference on Amorphous and Crystalline Silicon Carbide and Other IV-IV Materials, Santa Clara, CA, 10-11 October 1991 (Proceedings to be published by Springer-Verlag).
44. L. G. Matus, J. A. Powell, and C. S. Salupo, Appl. Phys. Lett. **59**(14), 1770 (1991).
45. B. J. Baliga, presented at the 4th International Conference on Amorphous and Crystalline Silicon Carbide and Other IV-IV Materials, Santa Clara, CA, 10-11 October 1991 (Proceedings to be published by Springer-Verlag).
46. Gardner, C. T., J. A. Cooper, Jr., M. R. Melloch, J. W. Palmour, and C. H. Carter, Jr., presented at the 4th International Conference on Amorphous and Crystalline Silicon Carbide and Other IV-IV Materials, Santa Clara, CA, 10-11 October 1991 (Proceedings to be published by Springer-Verlag).
47. M. Yoshikawa, H. Itoh, Y. Morita, I. Nashiyama, S. Misawa, H. Okumura, and S. Yoshida, J. Appl. Phys. **70**(3), 1309 (1991).
48. R. F. Davis, G. Kelner, M. Shur, J. W. Palmour, and J. A. Edmond, Proc. IEEE, **79**(5), 677 (1991).
49. D. M. Brown, M. Ghezzo, J. Kretchmer, E. Downey, T. Gorczya, R. Saia, J. Edmond, J. Palmour, C. H. Carter, Jr., G. Gati, S. Dasgupta, J. Pimbley, and P. Chow, presented at the Government Microcircuits Applications Conference, Orlando, FL, 5-7 November 1991.

THE ORIGIN OF POLYTYPES IN SiC AND ZnS

VOLKER HEINE*, C. CHENG+, G.E. ENGEL AND R.J. NEEDS*
*Cavendish Laboratory, Madingley Road, Cambridge CB3 0HE, England
+Now at Physics Department, Cheng-Kung University, Tainan, Taiwan

ABSTRACT

Both SiC and ZnS exist in the cubic diamond-like (zinc blende) structure. A polytype is derived from the cubic stacking of atomic double layers by having a regularly repeated pattern of stacking faults. Dozens of such polytypes are known for SiC and ZnS.

A study with several co-workers has been completed into the origin of this phenomenon. Are the polytypes genuine stable phases frozen in from some higher equilibrium temperature? Or are they inherently metastable structures born of some growth mechanism?

Quantum mechanical calculations have shown that SiC polytypes formed from bands of 2 and 3 cubically stacked layers have a lower energy than other structures, in particular lower than the cubic or wurtzite structures. That already suggests that the polytypes can be stable phases. Further calculations of the phonon free energy and relaxation of the bond lengths rounds out the phase diagram. In this connection it is somewhat surprising that the material normally grows initially in the metastable cubic modification, transforming subsequently to a mixture of polytypes, but the calculations also suggest why this is so.

The answers for ZnS turn out to be different from those for SiC.

1. INTRODUCTION

The purpose of this review is to summarise the results of a lengthy research project by several people [1-23] concerning the origin of polytypes in silicon carbide and to a lesser extent zinc sulphide. It will be assumed that this audience will know what is meant by polytypes and the common notation for them, but a description may be found in several of the main references [7, 11, 12]. Rather fuller reviews than the present one are contained in references [13, 16, 18, 21]: more extensive references will be found there and in the original research articles.

The basic issue is whether polytypes can be regarded as equilibrium structures, i.e. as stable phases at some (presumably) high temperature T from which they have been quenched. In the following we shall confine our remarks to SiC, returning to ZnS in section 5. The structural transformation of SiC is so slow at all but the highest temperatures that no proper phase diagram exists [24, 25 and further references there]. The alternative view is that all the polytypes except one (presumably

the cubic) are only metastable at all T, the result of certain growth processes. Since the existence of a material implies growth of some kind, the question of growth kinetics cannot be left out entirely. But the results of our study are that the cubic (3C) SiC is not the stable phase at any T below the sublimation point at 2500°C. That incidentally raises the interesting question of why it forms so commonly, which will be addressed in section 4. Instead we find that 6H, and probably 4H and 15R, are stable phases at some T, and we suggest a phase diagram (sections 2.1 and 2.2). We can only make some speculative remarks about the higher polytypes (section 2.3) but two features may be susceptible to experimental study. Even if kinetics determine the final outcome of a growth process, the material must presumably be reasonably close to being a stable phase for it to form at all at high T. In section 3 we consider what can be said from our calculations about the physical basis for polytypes and its relation to other properties such as magic angle spinning (MAS) nuclear magnetic resonance (NMR).

Our study used ab initio quantum mechanical calculations of the total energy [6, 7, 9, 12]. We first computed the energy differences of idealised polytypes at T=O with perfect tetrahedral bonding. We then calculated the relaxations from such idealised structures. To obtain the free energies at higher T we needed the phonon spectra which were also derived from such ab initio calculations in the absence of sufficient experimental information [8, 9].

2. RESULTS ON SiC POLYTYPES

2.1 First approximation: energy at T=O

Our calculated relative energies at T=O of the main SiC polytypes 3C, 6H, 4H and 2H are shown in figure 1, with those for Si and ZnS for comparison as discussed in sections 3 and 5. We see that 6H and 4H have the lowest energy, equal within the accuracy of our calculations (~0.5 meV per SiC pair of atoms). The 3C structure has significantly higher energy (~1.5 meV per SiC pair). The 2H energy is much higher, consistent with it being formed only under special conditions in the presence of boron. We first calculated the energies of the idealised structures with perfect tetrahedral bonding and with bond lengths equal to that of the cubic structure [6,7]. We also calculated the relaxation energies of the non-cubic polytypes from the idealised form, involving relaxation of bond angles, bond lengths and lattice constants [12]. The relaxation energies are of order 1 meV and are included in figure 1.

We see already at this level of approximation that one of the polytypes 4H or 6H is the stable structure at T=O and that both may be stable at different ranges of T. The same presumably applies also to 15R and all other polytypes consisting of bands of 2 or 3 cubically stacked

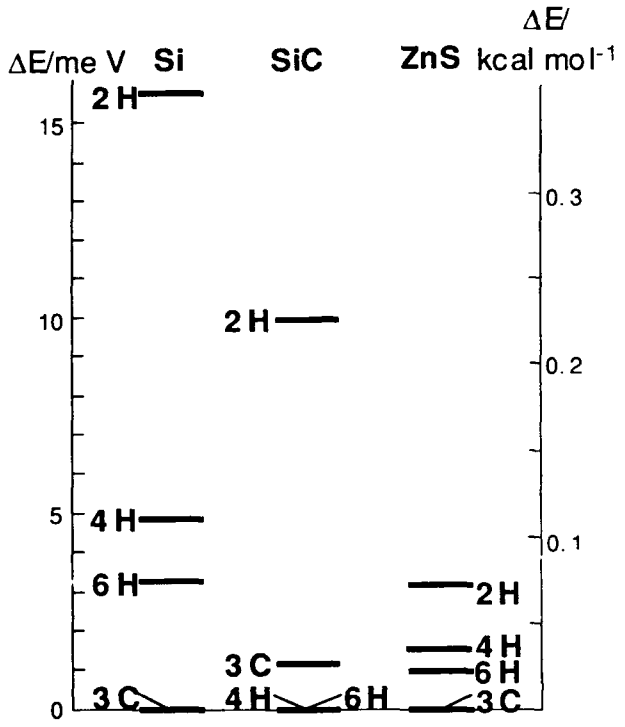


Figure 1. The relative energies of various polytypes as obtained by ab initio calculations at T=O for Si, SiC and ZnS.

layers, since these are intermediate structures between 4H and 6H. At the coarsest level of approximation, this already 'explains' the existence of polytypes and why they consist of 2-layer and 3-layer bands.

2.2 Second approximation: phonon free energies

The phonon spectra of the various polytypes will be different because of the difference in structure. This will result in differences in their phonon free energies, and these differences will vary with temperature, thus opening up the possibility of phase transitions if the total free energy difference changes sign. We write the total free energy difference as

$$G_{4H}(T) - G_{6H}(T) = (E_{4H} - E_{6H}) + (G_{4H} - G_{6H})_{phonon}. \quad (1)$$

where the first bracket on the right is the energy difference at T=O and the second bracket derives from the phonons including the phonon zero-point energy.

Evaluating the phonon free energies was a multi-step process. First a rather complete picture of the phonon spectrum of the cubic structure was obtained by ab initio calculation of the frequencies and phonon eigenvectors at several points in the Brillouin zone [9]. This spectrum was analysed in terms of a shell model known to give good results for other tetrahedrally coordinated semiconductors [8]. The shell model in turn was applied to the various polytypes to give their phonon spectra, from which the phonon free energies were then computed [10, 11].

The main result is that

$$(G_{4H}\text{-}G_{6H})_{phonon} \tag{2}$$

is positive and increasing with T, being of order 0.1 meV per SiC pair at 2100°C. This indicates that 6H will tend to be the stable phase at high T, as is consistent with most experiments [24, 25]. We cannot be more precise because we do not know the value of the first bracket in (1)

$$E_{4H}\text{-}E_{6H}. \tag{3}$$

We know it is zero within the accuracy (~ 0.5 meV per SiC pair) of the ab initio calculations of section 2.1, but need to know it more precisely to construct a phase diagram. Since 4H is the most commonly observed phase after 3C and 6H, and since according to some authors it is more prevalent at lower temperatures [24, 25], we consider it reasonable to suppose that the difference (3) is negative and of magnitude −0.1 meV per SiC pair. Then the free energy difference (1) goes through zero at T_0 = 2100°C, with 4H being stable relative to 6H at temperatures below T_0 and the reverse above T_0 [11]. We can begin to construct a phase diagram as shown in figure 2, but we emphasise that it does depend on our assumption about the precise value of (3).

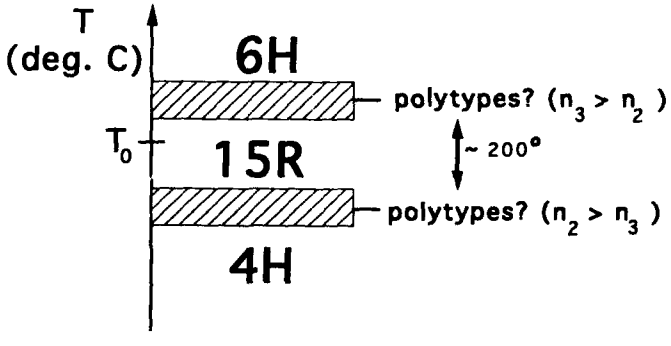


Figure 2. Suggested phase diagram for SiC.

We have also considered the next more complex polytype 15R, or<23> in the Zhdanov notation. Analysis of the ab initio calculated energies of five polytypes [7], plus some theoretical considerations [15], suggest that the energy of 15R is simply a linear interpolation between the energies of 4H and 6H, apart from the small relaxation energies which are a bit more complicated but have also been calculated [12]. We can therefore write down $E_{15R} - E_{6H}$. We have also calculated the phonon free energy of 15R using the shell model already described, and therefore have

$$G_{15R}(T)-G_{6H}(T). \qquad (4)$$

If $G_{15R}(T)$ were simply a linear interpolation between $G_{4H}(T)$ and $G_{6H}(T)$, then (4) would also be zero at T_o and one would have a multiphase degeneracy at T_o. However, it turns out the phonon part is not a linear interpolation, in fact it is negative compared with a linear interpolation, and hence (4) is negative at T_o. Thus on our phase diagram 15R would be a stable intermediate phase around T_o between 4H and 6H as shown in figure 2. In fact we find it would have a surprisingly wide stability region which we estimate to be of order 200 degrees, taking into account both the phonon part [11] and the relaxation effects [12].

There are other temperature effects which we have also considered [10]. In particular one could have thermally activated kinks on the antiphase boundaries between the 2-layer and 3-layer bands of cubic stacking, which the polytypes consist of. The entropy of such kinks is almost certainly responsible for stabilising long period stacking structures in some metallic alloys at high T [26]. However, the activation energy in SiC would be far too high for this mechanism to be significant in our case, nor are such kinks seen in significant numbers on electron micrographs. We were left with the conclusion that the phonon free energy is the factor driving phase stability as a function of temperature [10, 11].

2.3 Speculations about higher polytypes

We cannot make meaningful calculations on polytypes more complex than 15R. However, we can make some speculations, two of which may be susceptible of experimental test, based on some general theory which exists. There exist mathematical models which go through an infinite sequence of stable polytype phases as one varies a parameter such as temperature [26]. Such an infinite sequence is called a devil's staircase. Can that help to explain the observation of so many polytypes?

The first comment is rather simple. We are only considering polytypes (the great majority) consisting of 2-bands and 3-bands, i.e. bands of 2 or 3 cubically stacked atomic double layers. We can count the numbers n_2 and n_3 of 2-bands and 3-bands in one repeat distance. Presumably polytypes like <2333> will tend to be formed as intermediate

phases between 15R (<23>) and 6H (<3>) at the higher temperature phase boundary in figure 2, i.e. those with $n_3 > n_2$. Similarly at the lower phase boundary in figure 2 we expect polytypes with $n_2 > n_3$. We wonder whether careful annealing experiments, with or without stress, may show up some difference like that with temperature.

The second comment is a bit more complicated. A devil's staircase arises from long range, repulsive interactions between the antiphase boundaries between successive bands. Although the devil's staircase has an infinite sequence of phases, this does not mean that 'anything goes': it is a very precisely defined sequence. For example in tables of known polytypes one always finds <232333> but not <233>, although they have the same ratio of n_2 to n_3. This is what would be expected from a phonon free energy mechanism, whereas a relaxation mechanism in the sense of section 2.1 would tend to give the opposite result [16]. This suggests phonon free energy is playing a significant role, but of course there may be another explanation.

Our third comment concerns the possible temperature intervals and free energy differences. The stability range of 15R between 6H and 4H turned out in our calculations to be surprisingly large, namely about 200° (figure 2), though we emphasise that the error bars in this estimate are of order 100% and that the whole picture depends on our choice for the energy difference (3). This wide range arises not because the free energy differences are large but because 4H and 6H are themselves so similar near T_O. Similarly if the higher polytypes are stable phases at the boundaries of 15R with 6H and 4H (figure 2), one may expect significant stability ranges in temperature. But what of the free energy differences between such polytypes? These would be tiny, of order 10^{-6} eV or less per SiC pair of atoms. This is much smaller than k_BT, and people often wonder how it can influence the observed structure. The point is that it is wrong to compare k_BT with the energy differences <u>per atom</u>. For example in aluminium metal the stacking fault energy per atom at the fault is less than k_BT, but the material has no difficulty knowing it has to grow in the fcc structure! The point in SiC is that there are very strong forces in the lateral tetrahedral bonding within one layer. One therefore never has one atom or pair of atoms being misoriented: it has to be a large area of layer. One therefore has to consider the energy to reorient a large area, and compare it with k_BT in the Boltzmann factor. If the area is of order 10^6 atoms, then even a free energy difference of 10^{-6} eV per atom becomes very significant. We therefore see no difficulty of principle in such small free energy differences asserting themselves in observed phase equilibria.

Finally we return to the point in section 1 that we cannot ignore the actual growth or transformation processes. A mechanism for this has been considered, particularly by Pirouz [28, 29]. It is not clear how free energy differences can translate into actual atomic forces driving such a mechanism, but in general terms we suppose that the polytypes would not grow so significantly unless they were at least nearly equilibrium structures.

3. ANALYSIS

So far we have presented our calculations simply in terms of numerical results. We return to the lowest level of polytype energies in section 2.1 and now present some analysis and insight derived from them.

Each successive SiC atomic double layer can be placed in two orientations (conveniently called + and -) on the layers below to build up the structure. The cubic structure would be all + or all - layers. We can analyse the calculated polytype energies in terms of interactions J_n between two layers n apart. I.e. the layers give an energy contribution $-J_n$ if they have the same sign or $+J_n$ if opposite sign.

To get unusual structures, even 4H and 6H, requires interactions J_n that are moderately long ranged up to n=3 and oscillating in their sign. Where do these come from? In metals such oscillatory, long range interactions are standard, the Friedel oscillations. Mott and Jones [27] already pointed out in the 1930's that in some respects the tetrahedrally coordinated semiconductors are not so different from metals. The total band width of the valence band to the centre of the band gap is nearly that of a free electron gas, and half the vertical band gap (the appropriate measure) is only a small fraction of the occupied band width. Our numerical estimates show that the J_n's in SiC are the remnant in the semiconductor of what would be Friedel oscillations in metals, down in magnitude by about an order of magnitude due to the semiconducting character [15].

Analogous effects with similar range can be seen in other properties of the semiconductors including SiC [15]. These include phonons [15], atomic relaxations [12], and electron densities around the antiphase boundaries between bands as seen in MAS-NMR [19, 20].

We can be more specific. Let us ignore J_3 as being quite small. In both Si and SiC, the J_1 is positive and J_2 negative. In that sense there is nothing special about SiC. What is special can be seen from figure 3

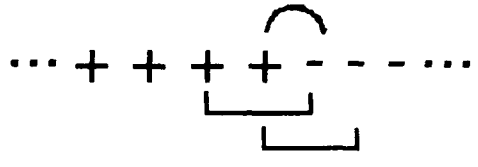


Figure 3. Antiphase boundary between layers of + and - signs. Across the boundary there is one pair of nearest neighbour layers (curved link, above), and two pairs of second neighbours (square link, below).

showing a sequence of layers with + and - orientations with an antiphase boundary in between. The energy of the boundary can be seen to be

$$E_{bound.} = 2(J_1 + 2\ J_2). \tag{5}$$

The reason for the coefficients can be seen from figure 3: across the boundary there is one reversed J_1 interaction (curved link) and two reversed J2 interactions (square link). In SiC the magnitudes of J_1 and J_2 happen to be such that they very nearly cancel in (5) [6, 7]. There does not seem to be any reason why the cancellation should be so good in this case.

4. THE GROWTH OF CUBIC SiC

We return to the issue already mentioned: if SiC is not the stable phase at any temperature, then why does it grow so readily? Indeed there is some evidence that under some conditions producing the 6H polytype, the cubic form crystalises first and then converts fairly quickly to 6H. Of course crystal growth is a non-equilibrium kinetic process so that there is no real contradiction with our results in section 2.1. Nevertheless, all the polytype structures are so similar that one might expect crystallisation to give the thermodynamically stable phase at the temperature of crystallisation.

Some insight can be gained from the analysis of section 3 [17]. The conclusions are tentative because all the calculations so far relate to bulk structures, not to surfaces. The latter are now planned.

Figure 4 shows a sequence of layers of various signs, terminating with a + layer at the surface. We are going to consider an extra layer being added at the surface in the course of crystal growth. It is shown in brackets in figure 4, and we will consider the energy difference between adding it with + or − sign. To be precise, let the energy be $E_0 - J_S$ for adding the new layer with the same sign as the top layer, and $E_0 + J_S$ for adding it with opposite sign. Here E_0 is the average cohesive energy per layer and $\pm J_S$ gives the orientational dependence. We can express J_S in terms of the J_n as before:

$$J_S = J_1 \pm J_2 \tag{6}$$

where the ± depends on the orientation of the next layer down. The point is that the coefficient of the J_2 term is unity in (6), as distinct from 2 in (5). This is clear from figure 4 where we have used curved and square links to denote J_1 and J_2 interactions in the same way as in figure 3. The difference arises because in figure 4 we are at the surface, not in the bulk. Now if (5) is nearly zero as already discussed, with J_1 positive, then J_S in (6) has to be positive, at least of magnitude $\frac{1}{2} J_1$ no matter

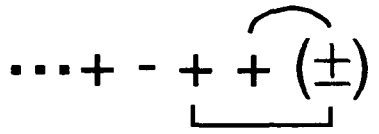


Figure 4. Semi-infinite crystal on the left, with layers of various + and - orientation at the surface. An extra layer, of orientation to be determined and denoted by (±), is being added at the surface.

whether the coefficient of the J_2 term is ±1 in (6). This shows that it is energetically favourable for the new layer to have the same orientation as the preceding top layer. That automatically results in all layers growing with the same sign, i.e. a cubic crystal [17].

We see therefore that the growth of the cubic form of SiC receives a natural explanation in terms of our J_n. Note our implicit assumption, that the new layer goes down into a situation of constrained equilibrium. We assume it goes down with the orientation having the lower energy, but without allowing any rearrangement of lower layers in the crystal to give a global energy minimisation. One presumes that the rate of such larger scale rearrangement would be slow compared with the rate of adding new layers, at least under conditions giving the 3C form.

As already remarked, our scenario of the growth is tentative because it is not valid just to take the J_n values from the bulk and use them at the surface: there are extra surface terms [15].

5. POLYTYPES IN ZnS

The situation in ZnS is different from SiC in two regards. Firstly, the maximal energy difference between the difference between the 2H and 3C polytypes is a factor of five smaller than in Si, a factor of three smaller than in SiC, as shown in figure 1 [22]. Thus all polytypes have more nearly the same energy than in SiC, and this is consistent with there being a large number of observed polytypes with very varied stackings: they are not confined to a special family as the SiC ones are more or less to sets of 2-bands and 3-bands. Secondly there is a reversible transition from the 3C structure at low temperature to the 2H structure above 1024°C. From this and the energy differences of figure 1 we deduce that the temperature-dependent part of the free energy is much larger in ZnS than in SiC, with differences of order 3meV between polytypes instead of 0.1 meV. There has not been any research on whether this free energy is due to phonons or possibly some roughening disorder of the boundaries. The latter is much more efficient at generating entropy differences. In this connection it may be worth noting that a computational study of PbI_2 also ascribes its polytype transition to phonon free energy differences [30]. The fact that the free

energy differences in ZnS are more than in SiC is consistent with the fact that the phase transition between 2H and 3C goes quite easily and is reversible.

We can carry the analysis one step further. The calculations [22] and the way the 6H and 4H energies in figure 1 interpolate linearly between those of 2H and 3C, show that J_1 is non-zero but all other J_n are negligible. If we assume that the temperature-dependent free energy differences, whatever their origin, are also more or less completely confined to J_1, then at the transition at 1024°C we would literally have a multiphase degeneracy with all possible stackings, regular and irregular, having equal free energy. This is a fair summary of what is observed, at least under some conditions [22, 23].

Engel has considered the polytypes observed in ZnS whiskers [23]. These seem to have at their centre a screw dislocation with fairly large Burgers' vector, as shown by the fact that different stacking sequences are observed along one whisker but with the same repeat distance. It has been suggested (see Reference 23 and references there) that in such a whisker, the phase transformation on coming down in T is nucleated at several sites from whence it spreads until the domains collide and overlap. New stacking faults can propagate fast or slow according to whether the corresponding energy change involves J_1 or not. The observed statistical distribution of polytypes can be accounted for very well in this way [23].

REFERENCES

1. J.D.C. McConnell and V. Heine, Explanation of the Polytypes of SiC, Europhys. Conf. Abstracts 6A, (1982) 172.

2. J. Smith, J. Yeomans and V. Heine, in Report of NATO Advanced Study Institute on Modulated Structure Materials, edited by T. Tsakalakos (Martinus Nijhoff Publishers, Dordrecht, 1984) p.95.

3. N. Churcher, K. Kunc and V. Heine, Solid State Comm. 56, 177 (1985).

4. N. Churcher, K. Kunc and V. Heine, J. Phys C: Solid State Phys. 219, 4413 (1986).

5. N. Churcher, K. Kunc and V. Heine, in Phonon 1985: Proceedings of the Second International Conference on Phonon Physics, Budapest 26-30 August 1985, edited by J. Kollar, N. Kroo, N. Menyhard and T. Siklos (World Scientific Publishing Co., Singapore, 1986) p. 956.

6. C. Cheng, R.J. Needs, V. Heine and N.I. Churcher, Europhys. Letters 3, 475 (1987).

7. C. Cheng, R.J. Needs and V. Heine, J. Phys. C: Solid State Phys. 21, 1049 (1988).

8. C. Cheng, K. Kunc and V. Heine, Phys. Rev. B39, 5892 (1989).

9. C. Cheng, K. Kunc and V. Heine, Jrn. de Chimie Physique 86, 881 (1989).

10. C. Cheng, V. Heine and R.J. Needs, Europhys. Letters 12, 69 (1990).

11. C. Cheng, V. Heine and I.L. Jones, J. Phys. Condens. Matter 2, 5097 (1990).

12. C. Cheng, V. Heine and R.J. Needs,. J.Phys. Condens. Matter 1, 5115 (1990).

13. C. Cheng, R.J. Needs,. V. Heine and I.L. Jones. Phase Transitions 16/17, 263 (1989).

14. V. Heine, Phys. Rev. Lett. 64, (Comment) 1178 (1990).

15. J.J.A. Shaw and V. Heine, J.Phys. Condens. Matter 2, 4351 (1990).

16. V. Heine and C. Cheng, in Geometry and Thermodynamics: Common Problems of Quasi-Crystals, Liquid Crystals and Incommensurate Insulators edited by J.C. Toledano (Plenum Press, New York, 1990).

17. V. Heine, C. Cheng and R.J. Needs, J. Am. Ceram. Soc. (1991) to appear.

18. V. Heine in Competing Interactions and Microstructures: Statics and Dynamics. Proceedings of the Workshop, Los Alamos, 5-7 May 1987, edited by R. LeSar (Springer Verlag, Berlin, 1988).

19. A. Qteish, R.J. Needs and V. Heine, Phys. Rev. to appear.

20. A. Qteish, R.J. Needs and V. Heine, Phys Rev. submitted.

21. V. Heine, C. Cheng and R.J. Needs, Materials Science and Engineering B, to appear.

22. G.E. Engel and R.J. Needs,. J.Phys. Condens. Matter 2, 367 (1990).

23. G.E. Engel J. Phys. Condens. Matter 2, 6905 (1990).

24. W.F. Knippenberg, Philips Res. Rep. 18, 161 (1963).

25. N.W. Jepps and T.F Page, J. Cryst. Growth Charact. 7, 259 (1983).

26. J. Yeomans, Solid State Phys. 41, 151 (1988).

27. N.F. Mott and H. Jones, The Theory of Metals and Alloys, (Oxford, Clarendon Press, 1935) p. 159.

28. P. Pirouz, J.W. Young, J.A. Powell and F. Ernst, in Microscopy of Semiconductor Materials 1991, Inst. of Phys. Conference Series 117, edited by A.G. Cullis and N.J. Long, (Institute of Physics, Bristol 1991), p. 149.

29. J.W. Young, T. Suzuki and P. Pirouz, this volume.

30. B. Winkler, M.T. Dove, E. Salje, M. Leslie and B. Palosz, J. Phys. Condens. Matter 3, 539 (1991).

EPITAXIAL MONOCRYSTALLINE SiC FILMS GROWN ON Si BY LOW-PRESSURE CHEMICAL VAPOR DEPOSITION AT 750°C

I. GOLECKI, F. REIDINGER AND J. MARTI
Allied-Signal, Inc., Corporate Research and Technology, P.O.B. 1021, Morristown, NJ 07962

ABSTRACT

Monocrystalline, epitaxial cubic (100) SiC films have been grown on monocrystalline (100) Si substrates at 750°C, the lowest epitaxial growth temperature reported to date. The films were grown by low-pressure chemical vapor deposition, using methylsilane, $SiCH_3H_3$, a single precursor with a Si:C ratio of 1:1, and H_2. The films were characterized by means of transmission electron microscopy, single- and double-crystal X-ray diffraction, infra-red absorption, ellipsometry, thickness measurements, four-point probe measurements, and other methods. Based on X-ray diffractometry, the crystalline quality of our films is equivalent to that of commercial films of similar thickness. We describe the novel growth apparatus used in this study and the properties of the films.

INTRODUCTION

SiC is the leading semiconducting candidate material for use in electronic and opto-electronic devices and circuits designed to operate at 300-700°C and above. SiC is particularly attractive for high power, high frequency and high radiation applications, since its carrier saturation velocity, breakdown electric field, thermal conductivity and tolerance to ionizing radiation are significantly superior to those of Si and GaAs [1]. SiC exists in the cubic, ß phase, as well as in about 170 hexagonal polytypes, commonly grouped under the α phases. Each phase has a somewhat different bandgap and different carrier mobilities. The bandgap of ß-SiC is the lowest: 2.35 eV at room temperature.

Bulk, high-purity and high-quality monocrystalline SiC is not commercially available in sizes greater than 2.5 cm. In addition, the ability to form epitaxial SiC films is desirable in the manufacture of integrated circuits. Thus, there have been efforts to deposit SiC epitaxially on other substrates [2], primarily Si, which is available in sizes up to 20 cm. Epitaxial SiC films have been grown on Si despite the 20% difference in the room-temperature lattice parameters of the two materials: a_o(SiC) = 4.3596 Å, a_o(Si) = 5.4301 Å. Film formation methods have included chemical vapor deposition (CVD), molecular beam epitaxy, sputtering and laser ablation. Most SiC films deposited on Si which have been used for devices were grown by atmospheric pressure CVD at temperatures of 1300-1380°C, using separate precursors for Si and C, e.g., SiH_4 and C_3H_8. Some processes use chlorinated precursors, e.g. $SiHCl_3$ [3], which produce highly corrosive HCl. Such high growth temperatures are undesirable, since they result in high tensile stress and crystalline lattice defects in the SiC film, due to the difference in the coefficients of thermal expansion of SiC (4.63×10^{-6}/°C for the ß phase) and Si (4.16×10^{-6}/°C), averaged between room temperature and 1380°C

[4,5]. Such defects and strain in heteroepitaxial films are known to degrade the carrier mobilities and increase junction leakage currents [6]. In order to fabricate electronic devices in the top ≈0.5 μm region, a SiC film up to 30 μm thick must be grown, requiring a relatively long deposition run of ~30 h. High growth temperatures may also result in increased autodoping and in undesirable smearing of dopant distributions and metal contacts in underlying heteroepitaxial structures. Significantly lower growth temperatures are thus highly desirable. In addition, the use of separate precursors for Si and for C in the growth of SiC thin films may result in small departures from stoichiometry in the films, leading to point defects (interstitials, vacancies, anti-site defects) or even inclusions and precipitates, which further degrade the device characteristics. Many SiC growth procedures also use a surface carbonization step [7] prior to deposition. The lowest reported growth temperature of epitaxial, single-crystalline ß-SiC on Si for device applications is 1000°C [3], where epitaxy was obtained on (111) Si but not on (100) Si.

We have grown single-crystalline, epitaxial cubic (100) SiC films on (100) Si substrates at 750-900°C by low-pressure chemical vapor deposition, using methylsilane, $SiCH_3H_3$, a single gaseous precursor with a Si:C ratio of 1:1, and H_2. These epitaxial growth temperatures are the lowest reported to date. No surface carbonization step was required in our process. The films were grown in a recently built, versatile, cold-wall, high-purity reactor, described below. The films have been characterized by means of transmission electron microscopy (TEM), single- and double-crystal X-ray diffraction, infra-red absorption, ellipsometry, four-point probe measurements, thickness measurements (by optical means, Dektak profilometry and Rutherford backscattering spectrometry), and other methods.

GROWTH APPARATUS

The reactor comprises a water-cooled, electro-polished stainless steel growth chamber, depicted schematically in Fig.1. The chamber is pumped by a chemically-resistant Alcatel 400 l/s turbo-molecular pump (with grease-lubricated bearings), backed by a 190 ft^3/min Edwards Roots blower in series with a 48 ft^3/min Edwards oil-free rotary pump (model DP-80). The base pressure without bakeout is $1x10^{-7}$ Torr. The majority of the vacuum connections are made with Conflat®-type knife-edge flanges. There are eight high-purity mass-flow-controlled gas or vapor delivery lines, built with electropolished stainless-steel tubing and mainly VCR®-type connectors (the balance are Swagelok® stainless-steel fittings). Each line can be evacuated directly to the precursor cylinder valve and on both sides of the mass flow controller with the Edwards pumps and purged with high-purity Ar. The output of every gas line can be directed either to the growth chamber or to the backing pumps (run/vent configuration). A butterfly throttle valve allows control of the pressure in the chamber by varying the flow conductance to the pumps. The vacuum gate and gas valves are electro-pneumatically operated. Safety devices include excess flow valves in the gas lines and an oxidizing furnace connected to the exhaust of the dry pump.

The chamber incorporates a BN-encapsulated, low-mass graphite resistive heater, upon which the substrate is placed. The temperature of the film/substrate is measured in-situ and in real-time through quartz and sapphire windows with a pyrometer operating at 0.8-1.1 μm. The pyrometer readings are calibrated by using Si test wafers having K-type embedded thermocouples (Sensarray, Inc.). The reactor has other features which were not used for the results described here.

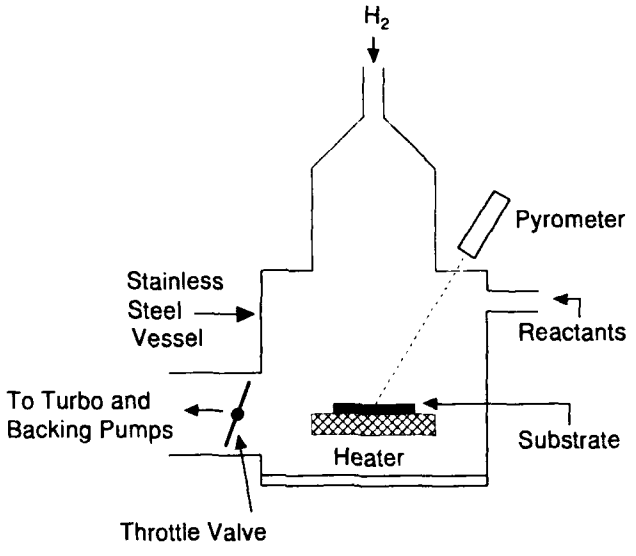


Figure 1. Schematic diagram of the cold-wall growth chamber.

SUBSTRATE PREPARATION AND FILM GROWTH PROCEDURE

The (100) oriented, p-type, 30-70 Ω·cm Si substrates are degreased in an ultrasonic cleaner, dipped in a 10% HF solution and mounted onto the heater. After the deposition chamber is evacuated and purged with Ar, the wafers are heated in flowing H_2 at about 900°C in order to remove any residue of the native surface oxide. The temperature of the substrate is adjusted to the desired value in the range 700-900°C and $SiCH_3H_3$ is admitted into the chamber. The ranges of total pressure in the deposition chamber and total flow rate are 0.1-1 Torr (13-133 Pa) and 100-400 sccm, respectively. The ratio of $SiCH_3H_3$ to H_2 flow rates is in the range 1:(40-1800). At the conclusion of the growth sequence, the precursor flow is diverted to the pump and the wafer is cooled down.

CHARACTERIZATION RESULTS

The films are transparent in the visible and have a refractive index of 2.6 at 0.6328 μm, equal to the tabulated value for cubic SiC [8]. The depth-averaged resistivity measured with a high-sensitivity four-point probe (Four Dimensions, Inc.) is in the range 1-10 Ω·cm at room temperature. The infra-red spectra (see Fig.2) present a single major absorption band centered at 775-790 cm^{-1}, a frequency identical to that reported for bulk SiC [9]. The deposition rates are in the range 0.1-1 μm/h (750-900°C), depending on process conditions, and they increase with temperature. The visual appearance, the resistivity and the infra-red transmission of commercial 0.3 μm thick (100) SiC/(100) Si films are similar to those measured in our films.

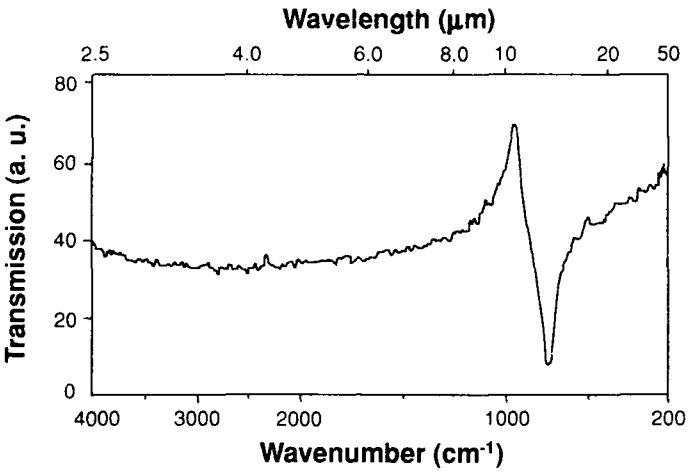


Figure 2. Differential infra-red transmission spectrum of a 0.25 μm thick, epitaxial, (100) ß-SiC / (100) Si sample, grown at 750°C, vs. (100) Si.

Single-crystalline, cubic (100) oriented films are obtained at temperatures as low as 750°C under the present experimental conditions, as evidenced by plan-view TEM studies; see Fig.3. Samples were thinned for TEM by polishing and dimpling the Si side down to about 30 μm, chemical etching in a 5:3:3 solution of HNO_3:HF:CH_3COOH, and Ar ion milling (to perforation) from both sides at 3 keV and 12°. The spots seen in the selected area electron diffraction pattern are indexed to ß-SiC. The contrast seen in the TEM micrograph is associated with (a) mass contrast due to surface roughness (either induced by ion milling during sample preparation for microscopy or already present) and (b) diffraction contrast due to misoriented regions (e.g. possible twinning) surrounding the epitaxial growth. Stacking faults and anti-phase domains could be seen in certain diffraction conditions. There was no clear indication of a well defined dislocation structure, but no attempts were made to characterize the SiC/Si interface, where such a structure could be prevalent.

Standard (θ-2θ) X-ray diffractometer scans, an example of which is given in Fig.4, show only the (200) peaks of cubic SiC and of the Si substrate. There are no peaks at the angles corresponding to the (111) and (220) diffraction lines. These X-ray data signify the films are epitaxial, i.e. have the same orientation as the Si substrate, although such X-ray scans in isolation do not unambiguously prove single-crystallinity. In the present case, however, these X-ray results are consistent with and corroborate the TEM data, which by themselves prove the single-crystalline nature of our films.

X-ray rocking curves were measured with a two circle diffractometer and double-crystal X-ray spectrometer. The full-width-at-half-maximum (FWHM), $\Delta\omega$, of a rocking curve of a monocrystalline film is a semi-quantitative, depth-averaged measure of the concentration of defects and strain in the film. The FWHM usually decreases with increasing film thickness in heteroepitaxial systems, because the defect concentration is highest at the film/substrate interface and decreases with distance away from the interface [10]. The FWHM of the SiC (400) peak of a 0.25 μm thick film grown in this laboratory at 750°C is 0.65°. Similar values in the range 0.65-0.70° were measured



Figure 3. Plan-view TEM image and selected-area diffraction pattern of a 0.25 μm thick, (100) β-SiC film grown on (100) Si at 750°C.

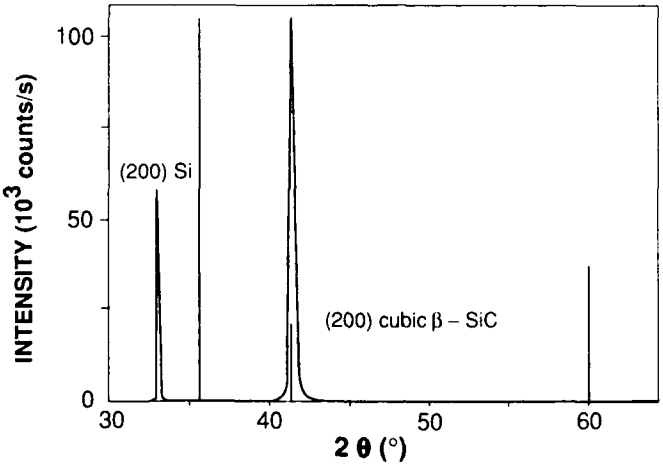


Figure 4. θ-2θ X-ray diffraction scan of a 0.25 μm thick, epitaxial, single crystalline (100) β-SiC film grown on (100) Si at 750°C. The three vertical marker lines indicate, from left to right, the expected positions of the (111), (200) and (220) X-ray lines of β-SiC.

for somewhat thicker, 0.3 μm commercial (100) SiC films grown on (100) Si. An additional benchmark is obtained by comparison with the silicon-on-sapphire (SOS) system, where commercial 0.17 μm and 0.37 μm thick, (100) epitaxial silicon films on(0112) sapphire had $\Delta\omega = 0.7^{o}$ and 0.5°, respectively [10]. SOS films have been and are being used extensively and routinely in integrated circuit technology. Preliminary results indicate that the crystalline quality of our SiC films, as measured by the FWHM of the X-ray rocking curve, is improved by decreasing the flow rate of $SiCH_3H_3$ or increasing the deposition temperature.

SUMMARY

Single-crystalline, epitaxial cubic (100) SiC films have been grown on (100) Si substrates at 750°C by low-pressure chemical vapor deposition, using a single film-forming precursor - methylsilane, and hydrogen. This epitaxial growth temperature is the lowest reported to date. Our study is also the first to report single-crystalline SiC films formed from methylsilane. No surface carbonization step [7] and no halogenated compounds [3] were used in our process, which is therefore much simpler, safer and has a smaller thermal budget than other existing processes for deposition of SiC films. Based on double-crystal X-ray diffractometry measurements, the crystalline quality of our films is equivalent to that of commercial films of similar thickness.

ACKNOWLEDGEMENTS

The encouragement of D. Boudreaux, D. Narasimhan and R.C. Morris is greatly appreciated. We gratefully acknowledge D.K. Pelcher (Rudolph Research, Inc.) for ellipsometry measurements and D. Lie (California Institute of Technology, Pasadena, CA) for Rutherford backscattering measurements of film thicknesses.

References

1. R.J. Trew, J-B. Yan and P.M. Mock, Proc. IEEE **79**, 598 (1991).
2. R.F. Davis, in *The Physics and Chemistry of Carbides, Nitrides and Borides*, R. Freer, ed., (Kluwer Academic Publishers: Dordrecht, the Netherlands, 1990) p.589.
3. Y. Furumura, M. Doki, F. Mieno, T. Eshita, T. Suzuki and M. Maeda, in *Proc. Tenth Intl. Conf. on Chemical Vapor Deposition*, ECS Proc. Vol. **87-8**, G.W. Cullen, ed. (The Electrochemical Society, Inc.: Pennington, NJ, 1987) p.435.
4. Z. Li and R.C. Bradt, J. Amer. Cer. Soc. **70**, 445 (1987).
5. Y.S. Touloukian, R.K. Kirby, R.E. Taylor and T.Y.R. Lee, *Thermophysical Properties of Matter*, Vol **13** (IFI/Plenum: New York, 1977).
6. I. Golecki, in *Proc. Symp. on the Comparison of Thin Film Transistors and SOI Technologies*, Mater. Res. Soc. Symp. Proc. Vol. **33**, 3 (1984).
7. S. Nishino, H. Suhara, H. Ono and H. Matsunami, J. Appl. Phys. **61**, 4889 (1987).
8. W.G. Driscoll and W. Vaughn, ed., *Handbook of Optics* (McGraw-Hill: New York, 1978), p.7-103.
9. W.G. Spitzer, D.A. Kleinman and C.J. Frosch, Phys. Rev. **113**, 133 (1959).
10. I. Golecki, H.L. Glass, G. Kinoshita and T.J. Magee, Applications of Surface Science **9**, 299 (1981).

EVALUATION OF SILICON CARBIDE FORMED WITH A SINGLE PRECURSOR OF Di-tert-BUTYLSILANE

SING-PIN TAY, J.P. ELLUL, SUSAN B. HEWITT*, N.G. TARR*, A.R. BOOTHROYD*
Northern Telecom Electronics Ltd., 185 Corkstown Rd., Nepean, Ontario, Canada K2H 8V4
* Dept. of Electronics, Carleton University, Ottawa, Ontario, Canada.

ABSTRACT

A low temperature process of silicon carbide deposition using the pyrolysis of di-tert-butylsilane has been explored for formation of emitter structures in silicon heterojunction bipolar transistors. Near stoichiometric amorphous silicon carbide films were achieved at 775°C. Doping and annealing of these films resulted in resistivity as low as 0.02 ohm-cm.

INTRODUCTION

Silicon heterojunction bipolar transistors (Si-HBTs) have been investigated for potential application in BiCMOS processes in order to optimize the performance of bipolar transistors and reduce chip power density. This increases *flexibility in utilization of bipolar transistors* beyond I/O circuitry and high-load drivers. Although single-crystalline β-SiC has been useful for wide band-gap emitter formation in Si-HBTs, its epitaxial growth involves reaction of silanes and hydrocarbons at temperatures higher than 1000°C. Such high temperatures are undesirable for BiCMOS processes and in particular for high speed bipolar transistors which have a very thin (about 50 nm) highly doped base. To suppress dopant redistribution in the base during emitter formation, low temperature processes of amorphous and polycrystalline SiC_x deposition have been pursued and reported[1,2]. One such method involves the pyrolysis of di-tert-butylsilane(DTBS)[3]. In this paper we report preliminary results of our DTBS process intended for device quality n^+-SiC HBT emitter formation.

EXPERIMENTAL PROCEDURE

Liquid DTBS has a boiling point of 128°C and a fairly high vapour pressure of 25 Torr at 20°C allowing gas transfer from a 1.2 litre stainless steel ampule into the reaction chamber at room

Mat. Res. Soc. Symp. Proc. Vol. 242. 1992 Materials Research Society

temperature. Vapour flow control was accomplished by use of an MKS Model 1150A controller. A hot-wall LPCVD furnace was used for pyrolysis of DTBS in the pressure range of 0.35 to 1 Torr and temperature from 600 to 800°C. Elimination of residual oxygen in the reaction chamber is critical in the formation of stoichiometric silicon carbide films. This was done by flowing argon, purified by a point-of-use Nanochem system, prior to and during the deposition. To dope the SiC_x emitter with phosphorus we also incorporated tert-butylphosphine(TBP) in the SiC_x deposition process by injecting TBP vapour from a liquid source. TBP has a boiling point of 54°C and a vapour pressure of 141 Torr at 10°C. Both undoped and doped films were deposited on 150mm diameter p-type 8-15 ohm-cm Si(100) wafers as well as on some wafers coated with 300 nm thick silicon dioxide. Some of the films were annealed (RTA) in nitrogen ambient in a rapid thermal reactor in order to examine the film crystallinity as well as resistivity. The experiments carried out are outlined in the following sections:

1. Undoped SiC_x films

Experimental runs were carried out to examine the effect of varying the following process parameters on the deposition rate, stoichiometry, and film quality:

i) Temperature: 550°C -- 800°C
ii) Pressure: 0.25 -- 1 Torr
iii) Argon flow rate: 250 -- 1000 sccm
iv) DTBS flow rate: 250 -- 350 sccm

2. Doped SiC_x films

In these experiments the process conditions were optimized for the best stoichiometric SiC_x films. The deposition temperature was 775°C. and the pressure was 0.35 Torr. The DTBS and argon flow rates were 250 and 500 sccm respectively. Deposition time was adjusted to obtain films with thicknesses around 350 nm. The TBP flow rate varied from 130 to 340 sccm. For film resistivity measurements, some doped films were deposited on a 300 nm thick layer of SiO_2 grown on silicon substrate. These doped films were annealed for 10 sec in N_2 ambient at various temperatures between 900°C and 1200°C.

The SiC_x films were characterized by a number of techniques. Auger electron spectroscopy (AES) and elastic recoil detection (ERD) were used to examine the stoichiometry. The film thickness and refractive index were determined by ellipsometry at wavelengths of 632.8 nm and 800.0 nm, with SEM verification of thickness in most cases. FTIR and Raman spectroscopy were

employed to detect the existence of silicon-silicon, carbon-carbon and silicon-carbon bonds. The crystallinity of the films was examined with TEM and electron diffraction methods. A four-point probe was used to determine the film resistivity.

RESULTS AND DISCUSSIONS

Without the use of Nanochem-purified argon in the process there was always five to ten atomic percent of oxygen in the SiC_x films. Oxygen is known to form generation-recombination centres that can increase junction leakage; therefore every attempt was made to reduce the oxygen content of the films. AES, ERD, and FTIR results indicated the absence of any detectable level of oxygen in the bulk of films that were deposited with the process which incorporates Nanochem-purified argon. Little effect on stoichiometry was seen with argon flow rate varied from 250 to 1000 sccm. The following discussions refer to films without detectable oxygen content achieved in this way.

The SiC film grown at 775°C is nearly stoichiometric as determined by AES. Typical film growth rate at 775°C is 18 nm/min. **Figure 1** indicates that the stoichiometry of these films is heavily dependent on deposition temperature. At temperatures above 775°C, the film is carbon-rich with Si/C ratio being 0.7 at 800°C, while below 775°C the film is silicon-rich with Si/C ratio being 1.9 at 700°C. The stoichiometry does not appear to be significantly dependent on any other variable.

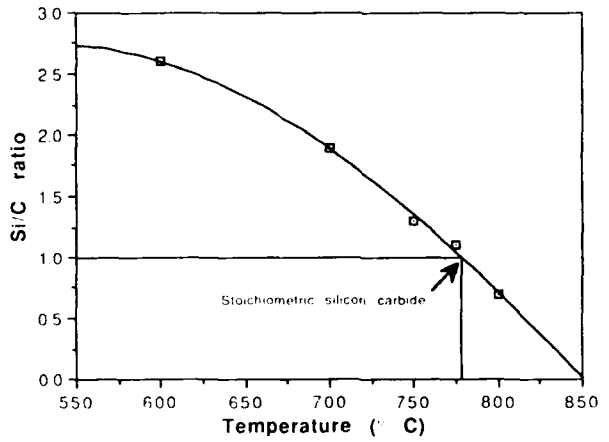


Figure 1. Stoichiometry of undoped SiC_x films versus deposition temperature.

ERD data show that hydrogen content in these films is 2 to 4 percent. Si-C bonding (765 cm^{-1}) was revealed in FTIR spectra for all SiC_x films, whereas Raman spectra indicated that films deposited at temperatures below 750°C were predominantly amorphous silicon.

At wavelengths of 632.8 and 830.0 nm where SiC film may be considered transparent with >40% optical transmission[4], the ellipsometry measurement yielded a refractive index of 2.7 for all SiC_x films deposited at 775°C. This is close to the reported value of 2.64 for monocrystalline SiC [5,6].

The DTBS flow rate is seen to affect the deposition rate only. In general, at constant temperatures, lower DTBS flow rates causes a lowering in the deposition rate (**Figure 2**). The physical quality of the films appears to be dependent on the gas pressure during deposition. While films deposited at pressure from 0.35 to 0.5 Torr adhered well to the substrates, those deposited at 1 Torr were flaky.

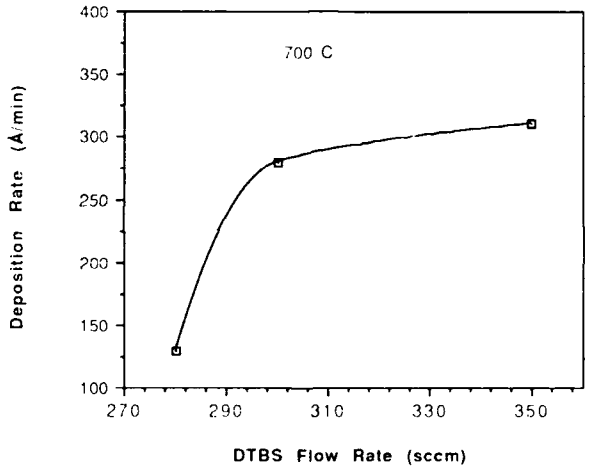


Figure 2. Deposition rate of undoped SiC_x films at 700°C versus DTBS flow rate.

Doped films, 300 -- 370 nm thick, deposited on oxidized silicon substrates, were annealed and exhibited resistivities in the range of 0.02 to 0.34 ohm-cm. The lowest value of 0.02 ohm-cm was achieved for films annealed by RTA at 1100°C. The ratio of resistivities after and before RTA is plotted against the anneal temperature in **Figure 3**. Again, this plot suggests that the most effective anneal temperature is 1100°C for lowering the resistivity of the n$^+$-SiC_x films. At 1200°C, the

resistivity ratio increases rapidly from that for 1100°C. This seems to suggest that the dopant could be evaporating from the surface of the silicon carbide films during the higher temperature anneal. However, since the diffusion coefficient of phosphorus in silicon carbide is very low, it is unlikely that much dopant would reach the film surface and evaporate. It is more probable that the higher temperature anneal caused changes in the structure of the film. TEM of a doped film deposited at 775°C and annealed at 1200°C indicates a polycrystalline grain structure which was identified by electron diffraction as mainly silicon. Diffusion of phosphorus in polysilicon is known to be faster than it is in silicon carbide.

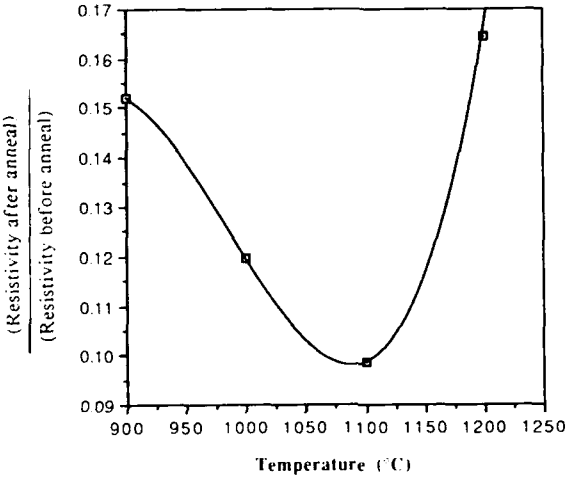


Figure 3. Ratio of resistivities after and before RTA of doped SiC_x vs. anneal temperature.

CONCLUSIONS

Amorphous near-stoichiometric silicon carbide films have been obtained from an LPCVD process using the pyrolysis of di-tert-butylsilane at 775°C. Films in situ doped with phosphorus exhibit resistivities in the 10^{-3} ohm-cm range. This DTBS process may be suitable to produce low thermal budget silicon carbide films intended for device quality n$^+$-SiC HBT emitter formation.

ACKNOWLEDGEMENT

The authors would like to thank their colleagues for their contribution to the work reported in this paper. These include John Boyd, Len Sample, Roger Abbott, Louise Breton, Jody Vlaar, Brian Oliver, Louise Weaver, Lisa MacElwee, and Dave Mayer.

REFERENCES

1. T. Sugii, T. Aoyama, Y Furumura, and T. Ito, Proc. 1st Topical Symp. on Silicon Based Heterostructures, S.S. Iyer et al., ed., Toronto, Canada, Oct 1990, pp. 124.

2. F. Hebert, IEEE Electron Device Lett., vol. EDL-12, no.9, pp.477 (1991).

3. H.J. Boeglin, United States Patent No. 5,053,255, Oct 1, 1991.

4. P. Leung et al., private communication.

5. P.T. Shaffer, R.G. Naum, J. Opt. Soc. Amer., vol. 59, no. 1, pp. 1498 (1970)

6. J.A. Powell, ibid.,vol. 62, no. 3, pp. 341 (1972)

STRESS-INDUCED POLYTYPIC TRANSFORMATION IN SiC

J. W. YANG, T. SUZUKI, P. PIROUZ, J. A. POWELL*, AND T. ISEKI**
Department of Materials Science and Engineering, Case Western Reserve University, Cleveland, OH 44106
*NASA Lewis Research Center, Cleveland, OH 44135
**Department of Inorganic Materials, Tokyo Institute of Technology, Tokyo 152, Japan.

ABSTRACT

Deformation experiments were carried out on 6H-SiC single crystals and the deformed samples were examined by electron-optical techniques to verify any evidence for stress-induced polytypic transformation.

INTRODUCTION

Despite its discovery about 80 years ago [1], polytypism in SiC has still not been satisfactorily explained. A number of attempts have been made to explain the occurrence of polytypism and the mechanism of transformation from one polytype to another [2]. However, none of the mechanisms proposed so far can explain all the experimental observations, and they are often in contradiction with them. Polytypism can be considered in two different ways. Firstly, from a thermodynamic point of view, the stability of each polytype over a certain range of temperature and pressure can be considered. In this respect, great progress has been recently made by means of *ab initio* calculations of the total energy of different polytypes (see Heine in these proceedings [3]). The actual mechanism of polytypic transformation is a kinetic problem and has been considered both as a diffusive process and also as a dislocation process. Recently a dislocation model for polytypic transformation was proposed [4] which is briefly discussed in the following section. It involves the glide of 30° partial dislocations which are assumed to have different activation energies for motion. Thus it implies that the phase transformation depends both on temperature as well as on stress. The assumption of different mobilities of the two 30° partial dislocations is based their different core structures: the core of one of the 30° partials is all carbon atoms (the C(g) partial) while the core of the other partial is all silicon atoms (the Si(g) partial) [5]. The formation of kink pairs and their migration are assumed to be much easier along the Si(g) partial as compared to the C(g) partial [5]. The present paper discusses some experiments designed to check the validity of this model. Before discussing the experimental results, a brief review of the 6H→3C polytypic transformation is given. For more details of the model, see references [4] and [5].

THE 6H→3C TRANSFORMATION

The mechanism of ref. [4] depends on a pinned segment of a screw dislocation which is dissociated on the (0001) plane into a Si(g) and a C(g) 30° partial dislocations. Under an appropriate resolved shear stress, where the Si(g) partial with the higher mobility is the leading partial. it will expand and form a loop on the (0001) plane in a manner similar to the Frank-Read mechanism. On the other hand, the C(g) partial, which has a very low mobility at low temperatures (say below 1500°C), lags behind and cannot form a loop. Hence the loop formed by the Si(g) partial is faulted After the formation of a faulted loop, the leading Si(g) partial approaches the trailing C(g) partial from behind and the screw dislocation cross-slips onto the $(10\bar{1}0)$ prism plane according to the Friedel-Escaig mechanism (see ref. [6]). Subsequent to this, there is a tendency for the screw dislocation to cross-slip back to the basal plane. This can only happen if the screw dislocation can dissociate on the basal plane without violating the stacking sequence, i.e. without forming a high energy *AA* stacking. The sequence of faulted loop formation on the (0001) plane followed by cross-slip on the $(10\bar{1}0)$ plane is shown schematically in Fig.1. On the right hand side of this figure, the stacking sequence of 6H-SiC, i.e. ...*ABCACB*... is shown. Within each faulted loop, the crystal has sheared and the sites change according to $A \rightarrow B$ or $B \rightarrow C$ or $C \rightarrow A$. Thus, as shown in Fig. 1, the final stacking sequence within the loops will be ...*ACB*... and a 6H→3C transformation has taken place.

EXPERIMENTAL PROCEDURE

The material used in the deformation experiments was grown by the Acheson method and supplied by the Taiheiyo Rumdum Co. The crystals are monocrystalline and transparent with a greenish tint which implied the presence of nitrogen impurities. The as-received material was checked by TEM and was found to be quite a perfect single crystal (Fig. 2). No defects are seen in Fig. 2 and the 6H periodicity can be clearly observed. At much lower magnifications in the TEM, and after a thorough search, a low density of stacking faults on the basal planes and inclusions could be found in the specimen.

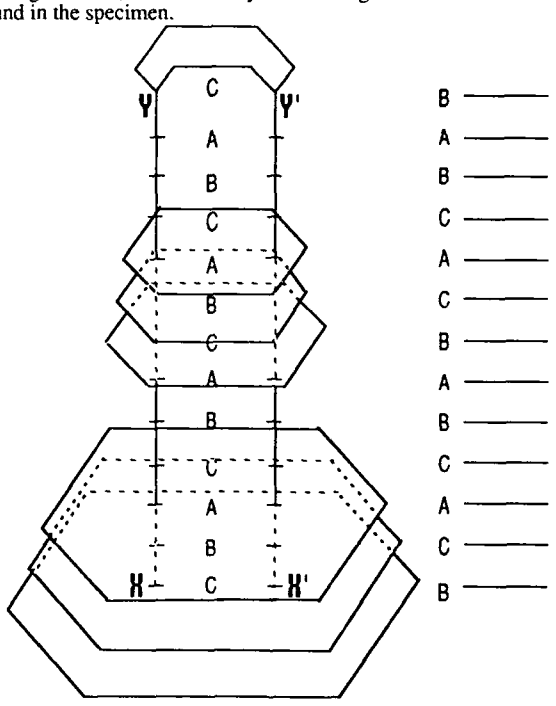


FIG. 1. Schematic of the change in the stacking sequence from 6H to 3C during the 6H→3C polytypic transformation. The scheme follows the model of ref. [4].

The SiC crystals were cut by a diamond saw into parallelepiped-shaped specimens (1x1x3 mm^3) in the orientation shown in Fig.3. The primary glide plane is (0001) and the cross-slip plane is $(10\bar{1}0)$. The resolved shear stress on two of the $\frac{1}{3}<1\bar{2}10>$ dislocations is equal on the basal plane as well as on the corresponding $(10\bar{1}0)$ cross-slip plane. This particular orientation was chosen in order to have a large resolved shear stress both on the basal (0001)

TABLE 1. Deformation conditions

Specimen	Deformation Temperature (°C)	Resolved Shear Stress, τ (*MPa*)	Deformation Time (*hours*)	True Plastic Strain, ε (%)
#1	1400	98	0.5	20.3
#2	1100	22	5.0	17.9
#3	1100	22	0.5	5.1
#4	950	22	5.0	1.0
#5	800	22	24.0	1.1

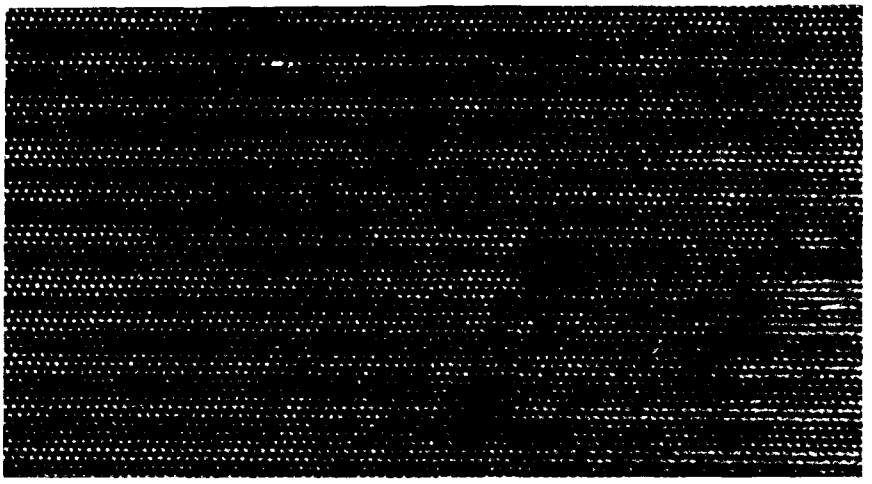


FIG. 2. A HREM Micrograph of the as-received 6H-SiC along a <1120> direction.

plane and also on the $(10\bar{1}0)$ cross-slip plane. Five samples were deformed under the conditions shown in Table 1. Each specimen was pre-loaded by 20 *MPa* and then ramped up to the deformation temperature. Subsequently the applied stress was increased to the desired value and the specimen kept under load for the desired time (see Table 1). After deformation, TEM specimens were prepared with foil normals parallel to [0001] and $[11\bar{2}0]$ directions and examined in JEOL 200CX and JEOL 4000EX microscopes. The latter microscope, with a point-to-point resolution of 0.18 *nm*, was used for HREM.

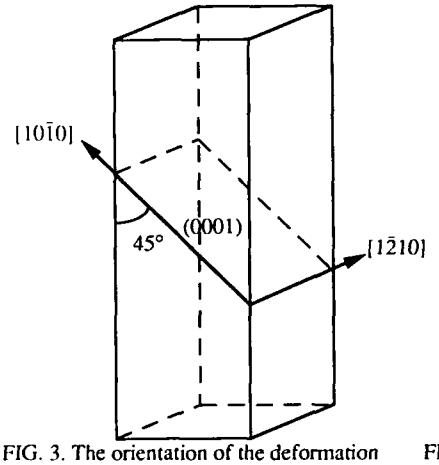


FIG. 3. The orientation of the deformation specimen. The dimensions of the specimen are 1x1x3 mm^3.



FIG. 4. An optical micrograph of the $(1\bar{2}10)$ surface of sample 1 after deformation at 1400°*C* (ε=20.3%).

RESULTS

The plastic strains, ε, undergone by the specimens are shown in Table 1. Samples 1 and 2 underwent a very large plastic strain of ~15-20% while the plastic strain in samples 3 to 5 was lower; in sample 3 ε~5% and for samples 4 and 5 ε~1%. Fig. 4 shows an optical micrograph of

the sample before and after deformation at 1400°C. There is a high density of slip traces which are parallel to the traces of the basal planes. A TEM micrograph of a heavily deformed section of sample 1 compressed at 1400°C is shown in Fig. 5. Note the striped contrast from the different phases. The wide bands in this figure are all 3C. In fact, the predominant phase in this region of the specimen is cubic SiC as shown by the diffraction pattern from this area (see Fig. 5).

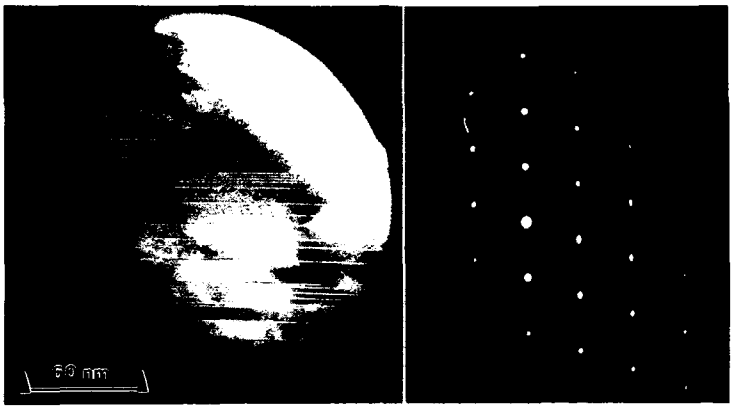


FIG. 5. A TEM micrograph of a heavily deformed section of sample 1 (deformation temperature=1400°C, ε=20.3%). The diffraction pattern from this region is also shown.

Fig. 6 shows an HREM micrograph of a region of Fig. 4 where there is a large density of the 3C phase.

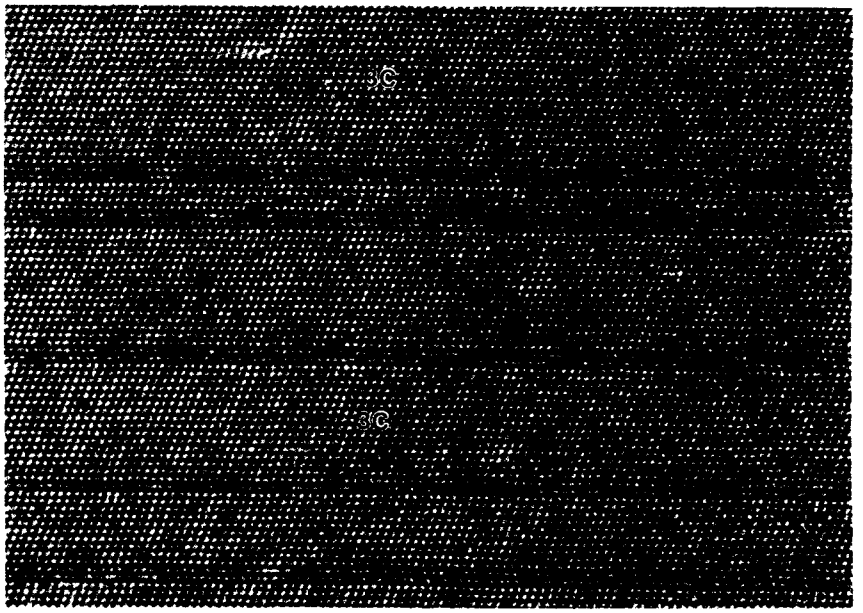


FIG. 6. A HREM micrograph of a region of Fig. 4 where there is a large density of the 3C phase (deformation temperature=1400°C, ε=20.3%).

Fig. 7 shows a HREM micrograph of sample 3 which was deformed at 1100°*C* for 5 *hours*. As may be seen, the region has also been partially transformed to the cubic phase.

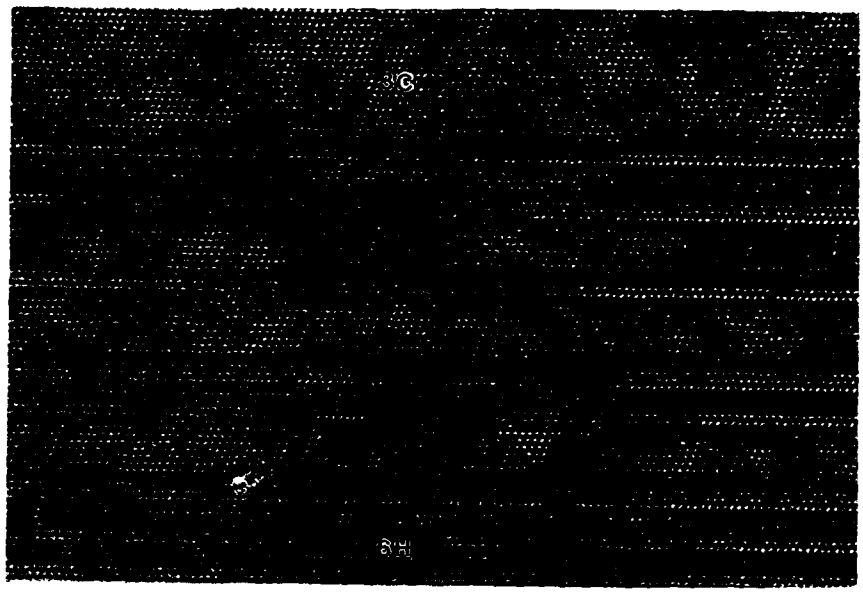


FIG. 7. A HREM micrograph from sample 3 deformed at 1100°*C* for 5 *hours* (ε=17.9%) where there is partial transformation to the 3C phase.

No 6H→3C transformation was observed in samples 4 and 5. However, very wide stacking faults were observed in the specimens deformed below 1000°*C* where ε~1%. An example is shown in the bright-field TEM micrograph of sample 5 in Fig. 8.

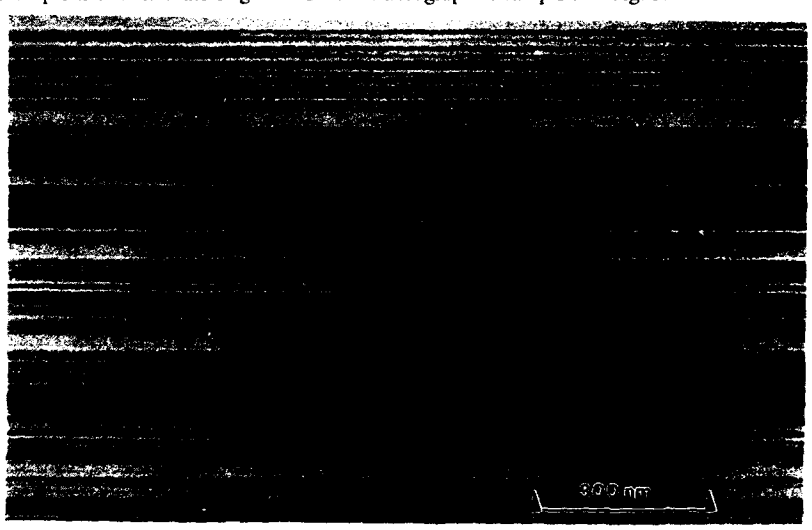


FIG. 8. TEM micrograph of wide stacking faults in sample 5 deformed at 800°*C* (ε=1.1%).

DISCUSSION AND CONCLUSION

According to the model described in ref. [4], there are three requirements for polytypic transformation in SiC: **(i)** A large difference in the mobility of the 30° partial dislocations, **(ii)** A sufficiently large resolved shear stress on the basal plane to form a faulted loop from a pinned segment of the highly mobile 30° Si(g) partial dislocation, and **(iii)** A sufficiently large resolved shear stress on the cross-slip plane to make the screw dislocation cross-slip after it has re-formed. The experiments in this paper were designed to satisfy the above conditions for the 6H→3C polytypic transformation. By choosing relatively low temperatures and low resolved shear stresses, it was intended that the trailing partial dislocation lags far behind the leading partial. In addition, the orientation of the specimen was chosen in such a way that there were roughly equal resolved shear stresses on the primary glide (basal) plane and the cross-slip (prism) plane. From the results of the tests, we can draw the following conclusions:

(a) The large plastic strains in the single crystals of 6H-SiC at these relatively low temperatures (<1500°*C*) and low stresses (<100 *MPa*) occur by the glide of partial dislocations (see also the work of Maeda *et al.* [7]). This is an indirect evidence for the asymmetry of the partials dislocation mobilities and the fact that one of the partial dislocations (presumably the Si(g) partial) can be easily moved even at low temperatures.

b) In samples 1 and 2, there is partial transformation of the 6H polytype to the cubic 3C polytype. These samples correspond to the temperature range 1100-1400°*C* where there is a large plastic strain (~20%). The mobility of the partials is expected to be very different in this temperature range and the results are consistent with the dislocation model proposed in [4].

c) In sample 5, deformed at 800°*C*, there is no 6H→3C transformation despite the very long deformation time (~24 hours). However, the dislocations are very widely dissociated indicating an even larger asymmetry in the mobility of the two partial dislocations as compared to samples 1-4 deformed at higher temperatures. This implies that the asymmetry in the mobility of partials is due to a larger activation energy for the motion of the trailing partial dislocation (presumably the C(g) partial) as compared to the leading partial dislocation (presumably the Si(g) partial) [8]. The absence of polytypic transformation in this sample, and also in samples 3 and 4, may be because of the difficulty of cross-slip under their deformation conditions.

ACKNOWLEDGEMENT

This work was supported by grant number NAG3-758 from NASA.

REFERENCES

[1] H. Baumhauer, Z. Kristal. **50**, 33 (1912).
[2] *Crystal Growth and Characterization of Polytype Structures*, Ed. P. Krishna, in 'Progress in Crystal Growth and Characterization', Volume 7, Pergamon Press (1983).
[3] V. Heine, Mat. Res. Soc. Symp. Proc. **242** (1991). In press.
[4] P. Pirouz, Inst. Phys. Conf. Ser. **104**, 49 (1989).
[5] P. Pirouz, J. W. Yang, J. A. Powell, and F. Ernst, Inst. Phys. Conf. Ser. **117**, 149 (1991).
[6] P. Pirouz and P. M. Hazzledine, Scripta Met. **25**,1167 (1991).
[7] K. Maeda, K. Suzuki, S. Fujita, M. Ichihara, and S. Hyodo, Phil. Mag. **A57**, 573 (1988).
[8] P. Pirouz, Scripta Met. **21**, 1463 (1987).

EFFECT OF CARBONIZATION GAS PRECURSOR ON THE HETEROEPITAXIAL GROWTH OF SiC-ON-Si BY RTCVD

A. J. STECKL AND J. P. LI
Nanoelectronics Laboratory, Department of Electrical and Computer Engineering, University of Cincinnati, Cincinnati, OH 45221-0030

ABSTRACT

A comparison of several simple hydrocarbon gases, with H:C ratios ranging from 1 to 4, as precursors for the carbonization of Si is presented. The growth experiments were performed by RTCVD at reactor pressures of 760 and 5 Torr. For AP-RTCVD, we have found that C_3H_8, C_2H_4 and C_2H_2 have very similar dependence of growth rate on hydrocarbon partial pressure in the chamber. At 1300°C, this involved a maximum in film thickness being obtained at a hydrocarbon flow rate of 8-10 sccm, representing a transition hydrocarbon fraction (in H_2) of ~ $5x10^{-4}$. CH_4 carbonization produces a peak growth rate at a significantly higher fraction, ~ $4x10^{-3}$. For LP-CVD at 5 Torr, the transition carbonization fraction increases by approximately an order of magnitude. The AP-RTCVD carbonization activation energy for C_3H_8, C_2H_4 and C_2H_2 at higher temperatures (~1200-1300°C) has a common value of ~ 0.8 eV, while for lower temperatures it depends on the hydrocarbon.

INTRODUCTION

Silicon carbide is an interesting semiconducting material with many desirable properties: large E_g (2.2 eV for the 3C polytype), high T_m (>2800°C), high E_{br} ($2.5x10^6$V/cm), high thermal conductivity (4 W/cm-°K), high saturated electron drift velocity ($2x10^7$cm/sec), as well as a large degree of physical and chemical stability. These properties are very attractive for many SiC device applications requiring operation under extreme conditions (such as high voltage and/or current, high temperature, etc.) and for heterostructure applications, such as the SiC-Si heterojunction bipolar transistor which requires a large band-gap semiconductor. For heterostructure device fabrication, the epitaxial growth of ß-SiC-on-Si has been accomplished by conventional chemical vapor deposition (CVD) [1-3], by low pressure CVD with simultaneous [4] and alternate supply of Si- and C-bearing gases [5] and by gas-source molecular beam epitaxy [6,7]. We have previously reported the epitaxial growth of ß-SiC films on (100) Si by rapid thermal chemical vapor deposition (RTCVD) at atmospheric [8] and reduced pressures [9]. RTCVD growth is well-suited for the fabrication of thin SiC-on-Si device structures, due to its minimal exposure to high temperature, which is produced by rapidly cycling the substrate temperature. This rapid temperature control is usually provided by Si absorption of the near-IR photoemission of W-halogen lamps. RTCVD growth of SiC-on-Si (100) using C_3H_8 carbonization and/or growth by reaction of C_3H_8 and SiH_4 has been shown [8] to result in monocrystalline (100) SiC thin films.

In this paper we report on a study which compares several simple hydrocarbon gases as precursors for the carbonization growth of SiC-on-Si by RTCVD.

EXPERIMENTAL PROCEDURE

The growth system is a modified RTCVD system from AET/ADDAX. A detailed description of the system and its operation can be found in [8]. The gas precursors used in this study are CH_4, C_3H_8, C_2H_4 and C_2H_2, all diluted to 5% in H_2. The flow rates of each of the hydrocarbon gases referred to later in this paper indicate the rate of flow of the 5% mixture. Hydrogen is also used as the carrier gas. The system pressure was measured by a capacitance manometer and controlled by a throttle valve with a pressure controller. The growth substrates consisted of standard (100) n-type Si wafers with 4-6 ohm-cm resistivity. Prior to being loaded into the chamber, the substrates were dipped in diluted HF and rinsed in DI H_2O. The typical AP-RTCVD process sequence [8] consists of the following steps: (a) pump-down to base

pressure, followed by H_2 flush; (b) in-situ cleaning by exposure to HCl for 2 min at 1200°C; (c) pump-down; (d) establish gas flow and pressure and then ramp-up to carbonization temperature; (e) carbonization and ramp-down to room temperature. The LP-RTCVD process is the same, except for a time delay prior to the initial temperature ramp-up to allow for stabilization of the pressure at the selected level. For preliminary comparisons, we have used the same growth parameters for LP-RTCVD as those obtained for optimized AP-RTCVD growth: growth temperature of 1300°C, temperature ramp rate of 25-50°C/sec, growth time of 60-120 sec.

RESULTS AND DISCUSSION

The fraction of the C-bearing gas in the gas stream (i.e. the ratio of C_xH_y to the total gas flow) was found, for all hydrocarbons investigated, to be extremely important in determining the nucleation process and the structural properties of the resulting SiC film. The SiC average film thickness obtained at atmospheric pressure after 90 sec growth at 1300°C is shown in Fig. 1 as a function of hydrocarbon fraction. For all hydrocarbons, a transition fraction for maximum thickness is observed. For propane, ethylene and acetylene the transition occurs at a fraction of around $5x10^{-4}$. Carbonization with methane yields a substantially higher value of the transition fraction, $4x10^{-3}$, as well as significantly thicker films. The overall characteristic pattern is reproducible, with some variation in the actual value of the transition fraction.

The morphology of films grown by ethylene and acetylene for hydrocarbon fractions less than, equal to, or greater than the transition value is very similar to that observed with propane growth [8] under similar conditions. Since methane appears to behave somewhat differently from the other hydrocarbons, we will concentrate on the morphology of SiC films grown by CH_4 carbonization. The morphology of films grown with selected methane fractions is shown in Fig. 2. At low CH_4 fraction (10^{-3}), dendritic growth occurs, as shown in Fig.2a, because the few nucleation sites present are widely separated and do not interact. At the transition methane fraction (~ $4x10^{-3}$) a uniform and continuous film is observed in Fig. 2d, along with the presence of voids in the underlying Si substrate. At the higher methane fraction of 10^{-2}, the average void size appears to decrease, while the film surface is considerably thinner and markedly smoother. As in the case of propane carbonization [8] at high flow rates, this can be ascribed to the high density of nucleation sites which result in the early formation of a continuous SiC film, thus sealing the surface diffusion path for Si atoms from the substrate and greatly reducing the subsequent growth rate.

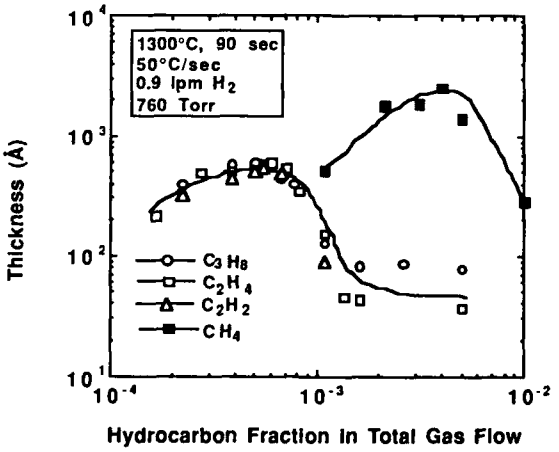


Fig. 1 AP-RTCVD SiC film thickness as a function of hydrocarbon fraction.

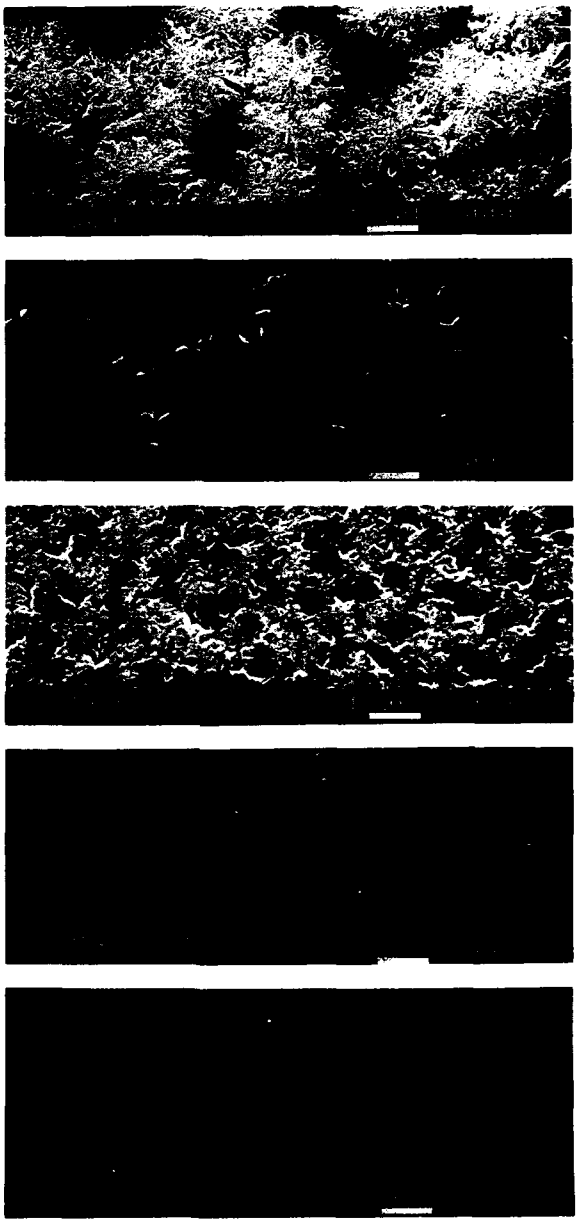


Fig. 2 SiC surface morphology for methane carbonization at several flow rates.

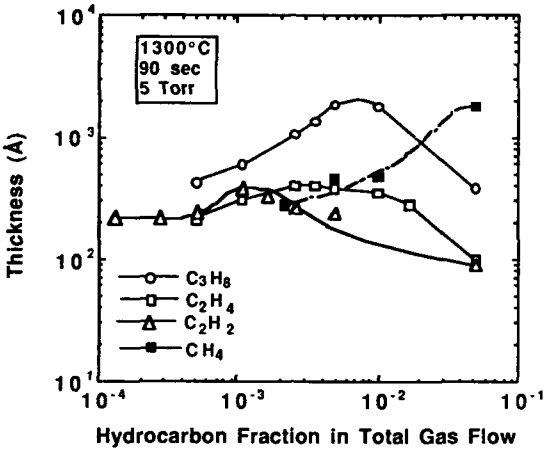


Fig. 3 LP-RTCVD SiC film thickness as a function of hydrocarbon fraction.

In the case of AP-RTCVD growth, the film thickness uniformity is strongly affected by the gas flow pattern inside the reactor. In LP-RTCVD growth, the SiC film thickness is primarily a function of the temperature across the wafer and, therefore, exhibits superior uniformity [9]. The film thickness vs. hydrocarbon fraction was obtained at 5 Torr. As seen in Fig. 3, the overall characteristic is similar to that obtained with films grown at 760 Torr. However, a substantial shift in the values of the transition fraction is observed for all hydrocarbons. This was previously explained [9] for SiC LP-RTCVD with C_3H_8 on the basis that the propane fraction which will provide a density of C atoms on the growth surface at low pressure comparable to that at atmospheric pressure has to be significantly higher to compensate for the lower gas density in the chamber. It is interesting to point out that, while C_3H_8, C_2H_4 and C_2H_2 have roughly the same transition fraction, (~$5x10^{-4}$), for AP-RTCVD, the shift at low pressure is to different transition values: 10^{-3} for acetylene, (3-4)$x10^{-3}$ for ethylene, and (0.5-1)$x10^{-2}$ for propane. The transition fraction for CH_4 at 5 Torr was not reached as it required a methane flow rate higher than that available in the system.

The effect of temperature on the thickness of SiC films grown by AP-RTCVD with the various hydrocarbon precursors is shown in Fig. 4. The flow rate of each precursor is chosen such that it yields the transition value of the hydrocarbon fraction in the total gas flow. For C_3H_8, C_2H_4 and C_2H_2 carbonization, shown in Fig. 4a, two growth regimes are observed. At higher temperatures, the same weak temperature dependence is seen for all three gases, yielding an activation energy of 0.76 eV. The rate-limiting mechanism in this regime is the transport of hydrocarbon reactant to the wafer surface. At lower temperatures the surface reaction rate becomes the rate-limiting mechanism and a different activation energy is associated with each gas: 1.2 eV for C_2H_4, 3.1 eV for C_3H_8, and 3.9 eV for C_2H_2. The transition temperature between the two regimes is around 1175°C. Methane carbonization displays a single growth regime (see Fig. 4b) over the temperature studied, with an activation energy of 2.5 eV.

Preliminary results obtained for the temperature dependence of the thickness at low pressure using carbonization with propane and acetylene are shown in Fig. 5. The respective hydrocarbon transition fraction at 5 Torr is used in each case.

SUMMARY AND ACKNOWLEDGEMENTS

SiC carbonization using RTCVD has been investigated with several hydrocarbon gases: CH_4, C_3H_8, C_2H_4, and C_2H_2. The transition hydrocarbon fraction (for maximum film

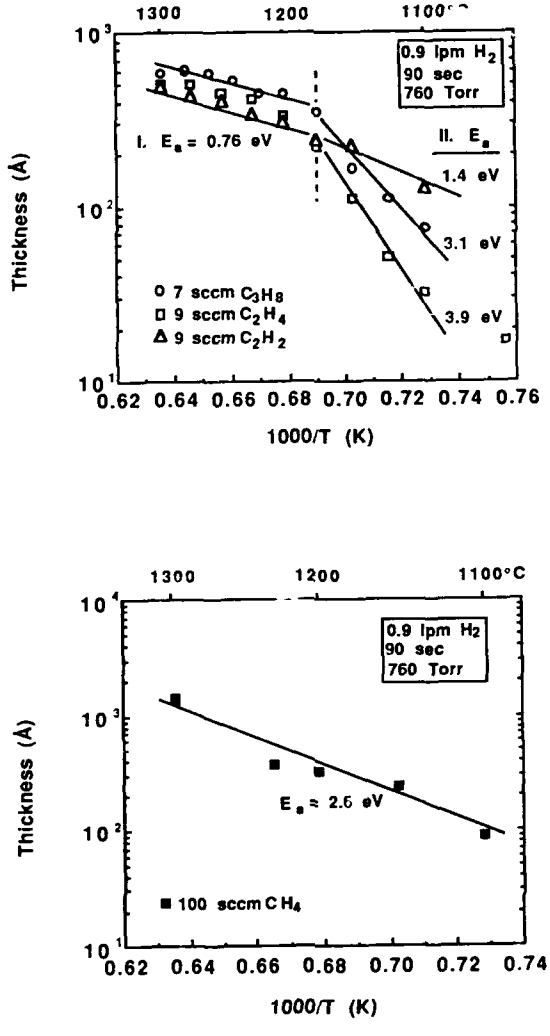


Fig. 4 AP-RTCVD SiC film thickness as a function of temperature: (a) C_3H_8, C_2H_4, C_2H_2; (b) CH_4.

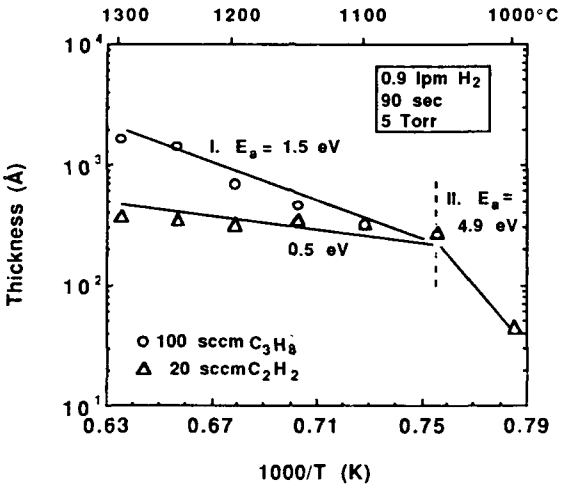


Fig. 5 LP-RTCVD SiC film thickness as a function of temperature.

thickness) for AP-RTCVD is roughly equal for C_3H_8, C_2H_4, and C_2H_2 with a value of $(5\text{-}6)\times10^{-4}$, whereas it is significantly higher for CH_4, namely 4×10^{-3}. For LP-RTCVD at 5 Torr, the transition fractions for all hydrocarbons shift to higher values. Carbonization activation energies were obtained for at 760 and 5 Torr.

The authors acknowledge the support of this work by the Edison Materials Technology Center. Assistance in ellipsometry and other thickness measurements by G. Debrabander, P. H. Yih and J. T. Boyd is greatly appreciated.

REFERENCES

[1] S. Nishino, J. A. Powell, and H. A. Will, "Production of large-area single-crystal wafers of cubic SiC for semiconductor devices", Appl. Phys. Lett., **42**, 460 (1983).

[2] P. Liaw and R. F. Davis, "Epitaxial growth and characterization of ß-SiC thin films", J. Electrochem. Soc., **132**(3), 642 (Mar. 1985).

[3] S. Nishino, H. Suhara, H. Ono and H. Matsunami, "Epitaxial growth and electric characteristics of cubic SiC on silicon", J. Appl. Phys., **61**(10), 4889, (May 1987).

[4] Y. Fujiwara, E. Sakuma, S. Misawa, K. Endo, and S. Yoshida, "Epitaxial growth of 3C-SiC on Si by low-pressure chemical vapor deposition", Appl. Phys. Lett., **49**(7), 388, (1986).

[5] H. Nagasawa and Y. Yamaguchi, "Heteroepitaxial growth of 3C-SiC by LPCVD with alternative gas supply", Proc. of 4th SiC Conference (ICACSC'91), Oct.91, Santa Clara, CA.

[6] T. Sugii, T. Aoyama, and T. Ito, "Low-temperature growth of β-SiC on Si by gas-source MBE", J. Electrochem. Soc., **137**(3), 9890 (1990).

[7] S. Motoyama, N. Morikawa, M. Nasu, and S. Kaneda, "Carbonization process for low-temperature growth of 3C-SiC by the gas-source MBE method", J. Appl. Phys., **68**(1), 101 (1990).

[8] A. J. Steckl and J. P. Li, "Epitaxial growth of β-SiC on Si by RTCVD with C_3H_8 and SiH_4", IEEE Trans. Elec. Dev., **39**(1), 64 (Jan. 1992).

[9] A.J. Steckl and J. P. Li, "Mechanisms in the Low Pressure Growth of SiC-on-Si by RTCVD", Proc. of 4th SiC Conference (ICACSC'91), Oct.91, Santa Clara, CA.

PREPARATION AND CHARACTERIZATION OF 3C-SiC HETEROEPITAXIAL LAYERS ON Si(111)

MITSUGU YAMANAKA and KEIKO IKOMA

Scientific Research Laboratory, Nissan Motor Co., Ltd., 1, Natsushima-cho, Yokosuka 237, Japan

ABSTRACT

3C-SiC layers were grown on Si(111) substrates by chemical vapor deposition (CVD) using SiH_4-CH_3Cl-H_2 gas mixture. 3C-SiC(111) heteroepitaxial layers were obtained with smooth surfaces and reduced warpage. All the epilayers were *n*-type, and the carrier density and Hall mobility were 2.1×10^{16}~2.8×10^{17} cm^{-3} and 120~180 cm^2/Vs at room temperature, respectively. Temperature dependences of the electrical properties of the self-supported 3C-SiC(111) epilayers were measured between 15 and 300 K for the first time. 3C-SiC(111) epilayers showed a similar temperature dependence of carrier density to 3C-SiC(001) heteroepitaxial layer. Hall mobility was maximum (~360 cm^2/Vs) around 100 K.

INTRODUCTION

3C-SiC is a promising semiconductor for electronic devices operating at high temperature, high power, and high frequency because of extreme thermal and chemical stability, wide energy band gap (2.2 eV), high saturated electron velocity (2.5×10^7 cm/s) and high electron mobility (800 cm^2/Vs).

3C-SiC(001) heteroepitaxial layers have been prepared on Si(001) by CVD in recent years [1]. The electrical and optical properties of the epilayers were studied extensively [2,3], and electronic devices were fabricated such as diodes and field effect transistors [4,5]. On the other hand, microcracks were observed in epitaxial 3C-SiC films grown on Si(111), and thermal stress in the 3C-SiC(111) epilayers was calculated to be approximately twice as large as in the 3C-SiC(001) epilayers [6]. Suzuki *et al.* obtained single crystalline 3C-SiC epilayers grown on Si(111) by the formation of 3C-SiC(111) oriented polycrystalline buffer layer using SiH_2Cl_2-C_3H_8-H_2 gas mixture at low temperatures (1273~1373 K), but the epilayers were reported to warp due to the lattice mismatch [7]. Furumura *et al.* reported the growth of 3C-SiC on Si(111) by low pressure CVD using $SiHCl_3$-C_3H_8-H_2 gas mixture without the formation of the buffer layer, and showed single crystalline 3C-SiC layers to be grown on off-axial Si(111) substrates [8]. Tachibana *et al.* reported electrical properties of 3C-SiC(111) epilayers grown by CVD on 6H-SiC(0001) crystals prepared by the Lely process [9]. However, the electrical properties of 3C-SiC(111) heteroepitaxial layers have not been investigated well in comparison to the 3C-SiC(001) epilayers, because of cracks and/or warp of the 3C-SiC(111) epilayers due to the internal stress.

In the present paper, we report the heteroepitaxial growth of 3C-SiC on Si(111) by two-step CVD method to form a carbonized (buffer) layer using methylchloride

(CH_3Cl)-H_2 gas mixture and to grow a 3C-SiC layer using SiH_4-CH_3Cl-H_2 gas mixture. The temperature dependences of the electrical properties of the self-supported 3C-SiC(111) epilayers are presented for the first time.

EXPERIMENTAL PROCEDURE

3C-SiC layers were grown on Si substrates by CVD system with cold-wall type reactor, which was previously evacuated to the pressure of 3×10^{-5} Pa. SiH_4 and CH_3Cl, diluted with H_2, were used as source gases for Si and C, and H_2 purified by Pd-Ag alloy cell and HCl were used as carrier and etching gases, respectively. The flow rates were regulated by mass flow controllers. Substrates were 30 mm × 70 mm × 415 μm Si wafers with just orientation of (111). Si substrates were put on SiC-coated graphite susceptor, $70\times80\times15$ mm^3, which was heated inductively by 200 kHz RF generator. The temperature was measured by a pyrometer viewing through a quartz window.

Prior to the growth, the surface layers of Si substrates were etched by HCl-H_2 gas mixture at 1473 K for 3 min, and carbonized by CH_3Cl-H_2 gas mixture. The substrate temperature was ramped to 1573 K at about 500 K/min, and held at 1573 K for 2 min in the carbonization process. Thereafter, a SiC layer was grown on the carbonized layer using a SiH_4-CH_3Cl-H_2 gas mixture at 1623 K. Typical growth conditions are summarized in Table I. 3C-SiC layers for the evaluation of crystallinity and morphology were grown for 30 min, and those for the measurement of electrical properties and wafer warpage were grown for 180 min.

The surface morphology and thickness of the epilayers were evaluated by means of scanning electron microscope (SEM). The surface roughness and wafer warpage were measured by surface profile measuring system. Reflection high energy electron diffraction (RHEED) was used for the crystallographic analysis.

The electrical properties of the self-supported 3C-SiC(111) epilayers, which were obtained by remoing the Si substrates with a HF-HNO_3-H_2O (7:9:13) solution, were measured using the van der Pauw method at temperatures between 15 and 300 K. Ti electrodes were used for the ohmic contacts without thermal annealing. The temperature of the sample was monitored by Pt resistive thermometer.

Table I. Typical conditions for heteroepitaxial growth of 3C-SiC layer.

Process	Reaction Gas	Flow Rate (sccm)	Temperature (K)
Etching	HCl H_2	95 10000	1473
Carbonization	1%CH_3Cl/H_2 H_2	500 8000	1573
Growth	1%SiH_4/H_2 1%CH_3Cl/H_2 H_2	210 500 8000	1623

RESULTS AND DISCUSSION

Figure 1 shows the SEM image of 3C-SiC layer grown on Si(111) substrate under typical growth condition shown in Table I. The surface of the layer was very smooth (about 5 nm in arithmetic average roughness) and the thickness was about 1 μm according to the SEM image. Figure 2 shows the RHEED patterns of the 3C-SiC layer in the $[1\bar{1}0]$ and $[\bar{1}\bar{1}2]$ incident azimuth. Streak patterns with Kikuchi lines were observed, which indicated that the obtained layer was single crystalline 3C-SiC epitaxially grown on the Si(111) substrate. Reconstructed structure pattern (3×) was clearly recognized in the $[\bar{1}\bar{1}2]$ incident azimuth.

Si substrate warped as a concave surface after heteroepitaxial growth of 3C-SiC(111) layer. Figure 3 shows the wafer warpage, which was measured as a height from the center of the wafer, after the 3C-SiC(111) epilayer 5 μm in thickness was grown under typical growth condition. Furukawa *et al.* reported reduction of wafer warpage of 3C-SiC grown on selectively-etched Si(111) substrate using SiH_4-C_3H_8-H_2 gas mixture [10]. The wafer warpage of our sample was reduced more in comparison to their results. Figure 4 shows SEM and optical micrograph (OM) images of the carbonized layer formed on Si(111) using CH_3Cl-H_2 gas mixture at 1573 K for 2 min. In the carbonization process, voids were formed under the carbonized layer and were observed as the white triangular region in the OM

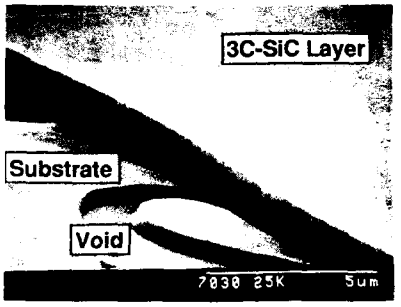


Fig. 1. SEM image of the 3C-SiC layer grown under typical growth condition. Voids are observed under the 3C-SiC layer.

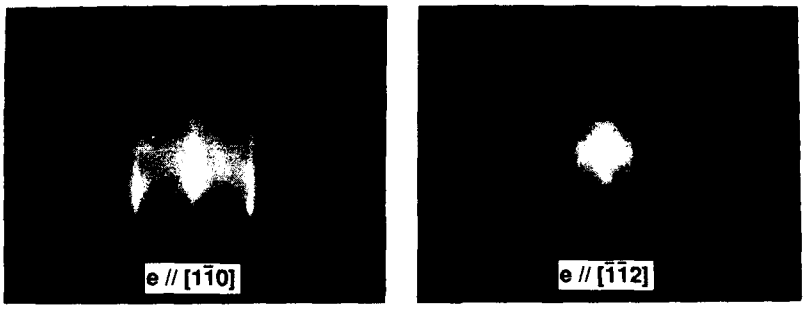


Fig. 2. RHEED patterns of the 3C-SiC layer grown under typical growth condition.

image. The formation of voids reduces the contact area between the epilayer and substrate, which may decrease the internal stress in the epilayer. Therefore, the reduction of wafer warpage is considered to be due to the formation of voids under the epilayer.

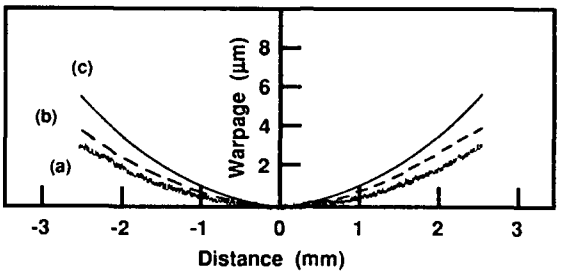


Fig. 3. (a) Wafer warpage after the 3C-SiC epilayer 5 μm in thickness was grown under typical growth condition. (b) and (c) are data obtained for the samples grown on selectively-etched and non-etched Si(111) substrates using SiH_4-C_3H_8-H_2 gas mixture [10].

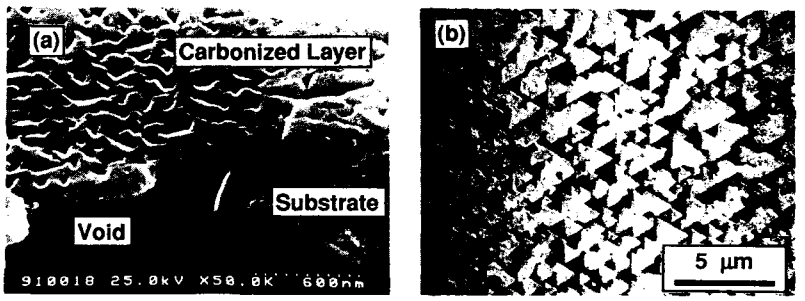


Fig. 4. (a) SEM and (b) optical micrograph images of carbonized layer formed using CH_3Cl-H_2 gas mixture at 1573 K for 2 min. Voids, observed as the white triangular region in (b), were formed under the carbonized layer.

Table II. Electrical properties of the 3C-SiC epilayers grown under several growth conditions.

Sample	Flow Rate of 1%CH_3Cl (sccm) Carbonization	Growth	Thickness (μm)	Carrier Density (cm^{-3})	Hall Mobility (cm^2/Vs)
A	500	500	6.5	2.2×10^{16}	150
B	500	500	4.3	2.8×10^{17}	120
C	1000	500	4.5	1.5×10^{17}	180
D	700	600	6.5	2.6×10^{17}	145
E	700	700	5.7	2.1×10^{17}	26

All the 3C-SiC(111) epilayers showed *n*-type electrical conduction. Table II summarizes carrier density and Hall mobility at room temperature obtained for the epilayers grown under several conditions (flow rate of 1%CH_3Cl/H_2 was varied). The epilayers with high Hall mobility (120~180 cm^2/Vs) were transparent with a light yellow color, but sample E with low mobility (26 cm^2/Vs) was opaque, although the carrier density of sample E (2.1×10^{17} cm^{-3}) was comparable with the others. It seems that a smaller Si/C ratio in the reaction gas than 0.3 is not suitable for the heteroepitaxial growth of 3C-SiC(111) using the present gas mixture.

Figure 5 compares the temperature dependence of carrier density and Hall mobility of the 3C-SiC(111) epilayers with those of the 3C-SiC(001) heteroepitaxial layer grown using SiH_4-C_3H_8-H_2 gas mixture [11]. Since 3C-SiC(111) epilayers showed a similar temperature dependence of carrier density to 3C-SiC(001) epilayer, the activation energy of residual donors may be almost the same as the 20 meV estimated for 3C-SiC(001) epilayer [2]. Therefore, the residual donors in the undoped 3C-SiC(111) epilayer are considered to have the same origin as the 3C-SiC epilayer, and to be highly compensated by residual acceptors.

On the other hand, Hall mobility of 3C-SiC(111) epilayer was lower than that of 3C-SiC(001) epilayer and had a maximum (~360 cm^2/Vs) around 100 K within the present experiment, even though the growth conditions of 3C-SiC(111) epilayers were not optimized yet. Hall mobility seems to be limited by phonon scattering above 200 K and ionized impurity scattering below 80 K, according to the comparison with the temperature dependence of the Hall mobility of 3C-SiC(001) epilayer [2].

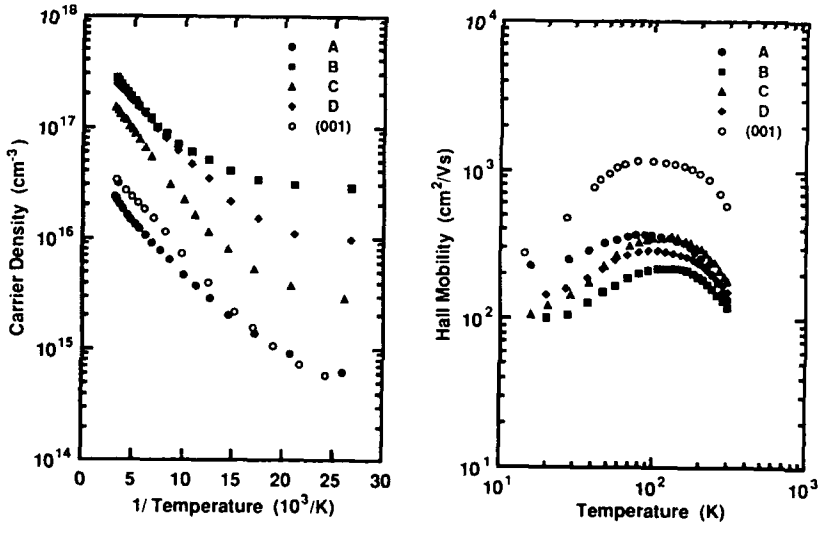


Fig. 5. Temperature dependence of (a) carrier density and (b) Hall mobility of 3C-SiC(111) epilayers. A, B, C, and D denote the samples listed in Table II. Data of 3C-SiC(001) epilayers grown on Si(001) substrate using SiH_4-C_3H_8-H_2 gas mixture [11] are also plotted for comparison.

CONCLUSION

3C-SiC(111) layers were grown on Si(111) substrates by CVD using a SiH_4-CH_3Cl-H_2 gas mixture. 3C-SiC(111) heteroepitaxial films were obtained with smooth surfaces and reduced warpage. All the epilayers were *n*-type, and the carrier density and Hall mobility were 2.1×10^{16}~2.8×10^{17} cm^{-3} and 120~180 cm^2/Vs at room temperature, respectively. 3C-SiC(111) epilayers showed a similar temperature dependence of carrier density to 3C-SiC(001) epilayer. The Hall mobility of 3C-SiC(111) epilayers had a maximum (~360 cm^2/Vs) around 100 K.

In order to investigate the electrical properties of 3C-SiC(111) epilayers further, both optimization of growth condition and high-temperature measurement of electrical properties are required. Estimation of internal stress in the 3C-SiC(111) epilayer is also awaited to discuss the reduction mechanism of wafer warpage in detail.

REFERENCES

1. S.Nishino, A.J.Powell, and H.A.Will, Appl. Phys. Lett. **42**, 460 (1983).
2. M.Yamanaka, H.Daimon, E. Sakuma, S. Misawa, and S. Yoshida, J. Appl. Phys. **61**, 599 (1987).
3. H.Okumura, M.Shinohara, S.Kuroda, K.Endo, E.Sakuma, S.Misawa, and S.Yoshida, Jpn. J. Appl. Phys. **27**, 1712 (1988).
4. K.Furukawa, A.Uemoto, M.Shigeta, A.Suzuki, and S.Nakajima, Appl. Phys. Lett. **48**, 1536 (1986).
5. H.S.Kong, J.W.Palmour, J.T.Glass, and R.F.Davis, Appl. Phys. Lett. **51**, 442 (1988).
6. H.P.Liaw and R.F.Davis, J. Electrochem. Soc. **131**, 3104 (1984).
7. A.Suzuki, K.Furukawa, Y.Higashigaki, S.Harada, S.Nakajima, and T.Inoguchi, J. Cryst. Growth **70**, 287 (1984).
8. Y.Furumura, M.Doki, F.Mieno, T.Eshita, T.Suzuki, and M.Maeda, J. Electrochem. Soc. **135**, 1255 (1988).
9. T.Tachibana, H.S.Kong, Y.C.Wang, and R.F.Davis, J.Appl. Phys. **67**, 6375 (1990).
10. K.Furukawa, A.Uemoto, Y.Fujii, M.Shigeta, A.Suzuki, and S,Nakajima, *Extended Abstract of 19th Conference on Solid State Devices and Materials* 231 (1987).
11. K.Ikoma, M.Yamanaka, H.Yamaguchi, and Y.Shichi, J. Electrochem. Soc. **138**, 3028 (1991).

CHARACTERIZATION OF SILICON CARBIDE THIN FILMS DEPOSITED BY LASER ABLATION ON [001] AND [111] SILICON WAFERS

L. Rimai, R. Ager, E. M. Logothetis, W. H. Weber and J. Hangas.
Ford Motor Co. Research Staff P.O.Box 2053, MD 3028
Dearborn MI 48121-2053

ABSTRACT

Stoichiometric films of 3C SiC, 50 to 1000 nm thick were deposited on Si wafers by laser ablation of ceramic stoichiometric SiC targets. Films grown at substrate temperatures above 1000° C on [001] and above 900° C on [111] show orientation epitaxial to the Si substrate along the film normal. Depending on the deposition conditions, the oriented crystallite dimension along this direction ranges from 20 nm to over 100 nm. The crystallite dimensions in the film plane range from 20 to 70 nm. Raman spectra show the expected TO and LO lines from SiC but indicate that the films sometimes contain other material, for example (30 to 50 Å) graphitic inclusions or small amounts of polycrystalline silicon.

Introduction

Wide gap semiconductors such as SiC are of interest as materials for electronic devices in high temperature and harsh environment applications. The most successful technique so far for the growth of SiC films is that of chemical vapor deposition (CVD). Reaction of SiH_4 with C_3H_8 in a hydrogen flow over a Si substrate held at 1400° C can result in epitaxial growth of a 3C (cubic) SiC film.[1-6] The CVD techniques require very high substrate temperatures for single crystal growth, which can lead to film contamination and hydrogen incorporation. Although oriented crystallite growth of SiC on Si by CVD has been reported at 1150° C [3,4] the development of other lower temperature methods is desirable. Sputtering has produced polycrystalline or amorphous films at lower substrate temperatures, in the absence of hydrogen.[7] Since 1988, laser ablation has been used for the deposition of high-quality, high T_c superconducting oxide films. In this method a high density plume of energetic particles is generated from the target in a very short time interval, reproducing the target's stoichiometry on the film and favoring oriented film growth at relatively low substrate temperatures. Balooch *et al.*[8,9] have reported the preparation of polycrystalline 3C SiC films on a [001] Si substrate at 800° C by laser ablation of a SiC target. In a recent communication we have reported the deposition by laser ablation, at 193 nm, of thin oriented films of SiC on Si wafers at somewhat higher temperatures (1000 to 1070° C).[10] Here we describe the deposition by laser ablation of epitaxial cubic (3C) SiC films on Si wafers at temperatures in the 900 to 1150°C range. These films were characterized by X-ray diffraction, selected area transmission electron diffraction and microscopy and by Raman spectroscopy.

Sample Preparation

The films were deposited inside a stainless steel vacuum system pumped by a turbo-molecular pump to a base pressure of 5×10^{-6} torr. Radiation from an excimer laser of wavelength 193 nm (ArF) or 351 nm (XeF) was focused near the surface of the target where it illuminated a 1×5 mm rectangle with approximately 45° incidence. The pulse energy at the target could be adjusted between 100 and 400 mJ corresponding to fluences from 2 to 8

J/cm^2. Ceramic SiC targets were used. The substrate to target distance was varied between 5 and 7 cm.

The substrates were pre-etched to remove hydrocarbons and native oxide.[10] During deposition the substrate was heated radiatively across a small (~1 mm) gap by a resistive boron nitride coated graphite heater (Union Carbide Boralectric) inside a tantalum radiation shielded furnace. The deposition window was a 2.5 cm square. The substrate temperature was measured with an IR pyrometer, through a sapphire window. Only the initial temperature could be accurately obtained from the pyrometer readings, as optical interference effects in the growing film produce an output from the pyrometer (responding to wavelengths near 1 μm) that oscillates with deposition time. This effect provides a means of gauging the film growth.

The deposited films had elliptical constant thickness contours, as shown by their light interference patterns, with the long axis perpendicular to the large dimension of the illuminated area on the target. Film thicknesses were measured with a stylus profilometer near the edge defined by the (shadow) masking from the front radiation shield. To determine the film thickness near the center of the plume deposition runs were performed with a contact mask made out of tantalum foil yielding a sharp edge in the desired area. Film thicknesses could also be estimated by counting interference fringes from the measured edge. The deposition rates derived from such data will be discussed below.

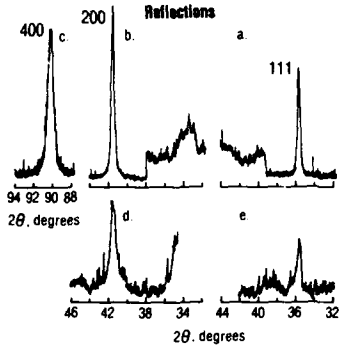


Figure 1 X-ray reflections for (a) [111], (b) and (c) [001] substrates deposited at 1145° C; (d) [001] at 1000° C; (e) [111] at 900° C.

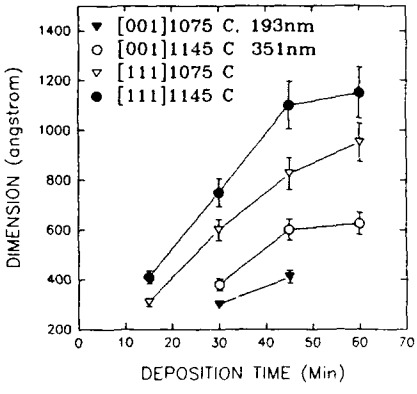


Figure 2. Dependence of crystallite dimension on deposition time and temperature, 200 mJ pulses, 5 Hz.

Film Characterization

Auger spectroscopy showed that target and film had the same stoichiometry. This was verified by testing some non-epitaxial films deposited from non-stoichiometric targets.

Figure 1 shows examples of X-ray diffraction data from "θ-2θ" angular scans such that the wavevector transfer is normal to the plane of the film. The diffraction peaks observed in this scanning geometry are characteristic of spacing between atomic planes parallel to the film. For films deposited on [001] Si, (traces b and c) the lines corresponding to the 200 (2θ = 41.6°, spacing d=2.18 Å) and the 400 (2θ = 90.5°, d=1.09 Å) reflections are visible, whereas

the 111 reflection ($2\theta = 35.7°$, d = 2.52 Å) is absent. The reverse is true for films grown on [111] Si (trace a). This is as expected for epitaxial films of cubic (3C) SiC and is consistent with the fact that the 3C is the stable polytype at these relatively low substrate temperatures. The films that exhibit the sharpest diffraction lines are those deposited at the highest substrate temperatures (above 1050° C for films on [001] Si and 900° C for [111] Si). The diffraction line broadening at the lower temperatures is illustrated by traces d and e in Fig. 1.

From the width of the diffraction lines one can deduce the dimension of the crystallites in the direction normal to the substrate plane. This dimension depends on factors such as deposition time, substrate orientation and temperature as illustrated by the data plotted in Fig. 2. The data in this figure were obtained with a pulse repetition rate of 5 Hz and an approximate pulse energy of 200 mJ at the target. The [001] results at 1075° C were from ablation with 193 nm (ArF) radiation at a target-substrate separation of 5 cm, all others with 351 nm (XeF) radiation and 7 cm target-substrate separation. Under these conditions the deposition rates for comparable substrate temperatures were approximately the same for the two wavelengths. Due to the much larger propagation loss, window and lens transmission loss and beam divergence for the 193 nm radiation, most of the experiments were performed with 351 nm radiation, and no major differences in the results with wavelength change were detected. The larger error bars for the larger crystallite dimensions are a reflection of the larger uncertainty in making the instrumental linewidth correction for the narrower lines.

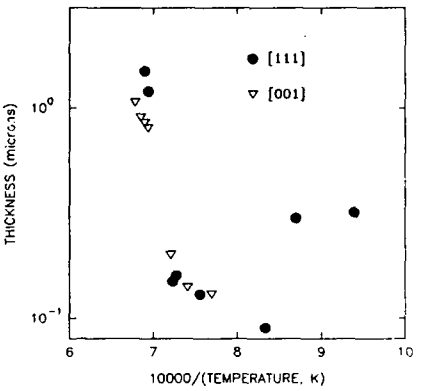


Figure 3. Temperature dependence of film thickness for 60 min. deposition.

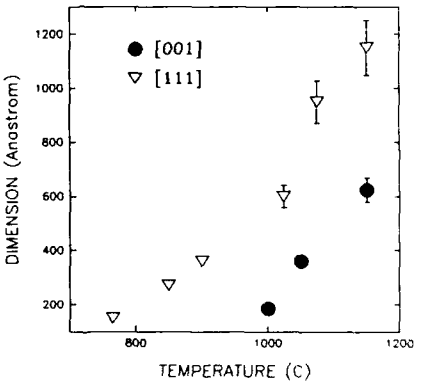


Figure 4. Crystallite size as function of temperature for 60 min. deposition.

Figure 3 shows average film thickness as a function of the inverse of the absolute temperature of the substrate for the same deposition time. It was verified that the film thickness is indeed proportional to deposition time, at least for 200 mJ laser pulses at 5 Hz. Thus the data of Fig. 3 yield deposition rates of 0.05 to 1.0 Å/pulse. Fig. 4 shows the dependence on deposition temperature of the crystallite dimension along the film normal, for a deposition time of 60 min. This same crystallite size is always less than the film thickness, although for the [111] films deposited near 1050° C they are within a factor of 2 of each other. At the highest deposition temperatures the crystallite size for the [111] films reaches 1200Å whereas it only reaches 600Å for the [001] films. The increase in crystallite dimension with deposition time and temperature might be due partly to annealing.

Figure 3 shows that above 1000° C the deposition rate increases rapidly with substrate temperature indicating perhaps the onset of a thermally activated process. For the [111] films

there is a minimum in the deposition rate near 900° C; the decrease in rate with increasing temperature, below 900° C, might be related to reactive reevaporation in the presence of the residual gases in the system (6×10^{-6} to 5×10^{-5} torr). Rate data for [001] films below 1000° C is not shown, as these films did not show any SiC signature in the X-ray scans.

Increased laser fluence above that corresponding to 200 mJ pulses appears to increase crystallite size slightly for the [001] films only, and then only at 193 nm. At 351 nm increased laser energy resulted in roughening of the film surface and eventual local peeling of the film. Lowering the energy below 200 mJ decreased the crystallite dimensions as well as the deposition rate.

Information about crystallinity within the film plane was obtained from transmission electron diffraction on back-thinned specimens prepared by standard procedures. Selected

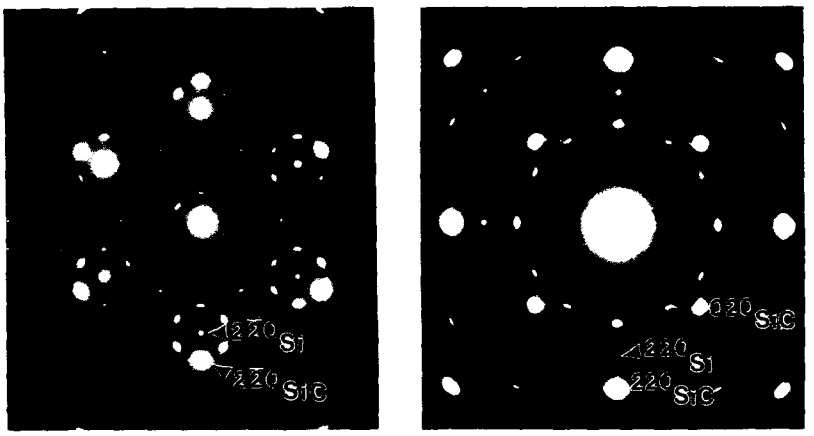


Figure 5 Selected area transmission electron diffraction of SiC on [111] and [001] Si in areas with both film and substrate present.

area diffraction patterns presented in Fig. 5 show that the 3C SiC films grow epitaxially on the Si substrate, the [001] film on the [001] substrate, the [111] film on the [111] substrate, with the {220} planes of the film and substrate parallel to each other. Double diffraction causes satellite spots around 220 reflections in both types of films. Weak reflections due to other orientation variants are present in Fig. 5 and increase in the thinner areas of the [111] films (near the surface). Twins have been identified also in the thin areas of the [001] films. The in-plane grain dimensions are 30 to 70 nm for both films as derived from TEM micrographs.[10]

Further information about these films can be obtained from their Raman spectra.[11,12] For the very thin films grown at low temperatures, the spectra are dominated by the Si substrate. To enhance the SiC contribution from these films, we subtracted from each spectrum a suitably scaled spectrum from the bare substrate.[10] For the films grown at higher temperatures this was not necessary, as shown in Fig. 6 for a film deposited at 1145 °C for 60 min. The top trace (a) in this figure is from the thickest part of the film (d ~ 1 μm) near the edge

of the mask. The SiC TO (796 cm^{-1}) and LO (973 cm^{-1}) modes [11] are clearly seen and there is no significant interference from the Si spectrum. Note the strong, sharp TO line in contrast to the much weaker and broader (~ 50 cm^{-1}) LO line. This broadening may be the result of damping by free carriers, which can substantially affect the LO mode without affecting the TO.[13] The observed LO bands are too weak for detailed shape analysis, but from comparisons with the spectra observed and analyzed for much thicker CVD films we obtain an estimate of 5×10^{18} cm^{-3} for the carrier concentration in the p-type film of Fig. 6.[13]

Spectrum 6(b) is from a spot ~ 1 mm from the edge, where the film is ~ 1500 Å thinner than it is for 6(a). The Si spectrum is clearly enhanced in the thinner region and that from the SiC is depressed. The thin-film interference effects, mentioned above, that produce colored bands in these films when viewed under white light will also lead to a variation in Raman intensity with position. The changes between the (a) and (b) spectra of Fig. 6, however, are not caused solely by this interference effect. The Si F_{2g} peak at 520 cm^{-1} in both (a) and (b) is significantly broader than that from the substrate, shown in Fig. 6 (c). In addition, these lines do not show the same dependence on polarization and sample orientation as does the same line for the substrate. With s-polarized laser light on a [001] surface the F_{2g} mode extinguishes when both the incident and scattered light are polarized along [100], whereas the F_{2g} mode in (a) and (b) does not. We conclude that the SiC film contains some unoriented Si inclusions and that the composition of the film varies with position. From the increased linewidth, the size of the Si inclusions is estimated to be ~ 20-30 Å.[14] In some of the samples (not the one for Fig. 6) we also observed bands near 1360 and 1600 cm^{-1}, indicating the presence of small graphitic inclusions whose size we estimate to be 30-50 Å.[12,15] Similar results were obtained from films grown on [111] substrates.

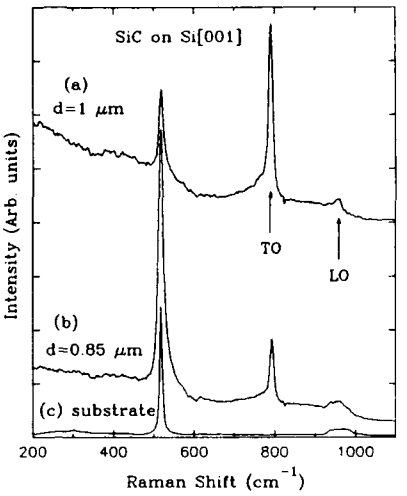


Fig. 6. Raman spectra recorded with 50 mW power of 514.5 nm laser light using a SPEX Triplemate and array detector system. (a) is shifted up by 4 tic marks for clarity. The full scale range is ~ 120 counts/s.

Concluding Comments

Epitaxial films of SiC, with thicknesses in the range of 100 to 1000 nm have been deposited by laser ablation on both [001] and [111] Si substrates. The films grow epitaxially on [111] substrates held at temperatures above 900° C, whereas on [001] substrates they grow epitaxially only above 1000° C. The crystallite size as measured by X-ray diffraction increases with both deposition time and temperature, and tends to be larger for the [111] films. This effect might be a consequence of annealing processes occurring in the already deposited layers and which have lower onset temperature in the [111] crystallographic planes. As in the case of CVD films, the epitaxial deposition rates have a marked temperature dependence, increasing with deposition temperature. In the CVD case this is ascribed to a

thermally activated chemical reaction whereby the volatile Si and C carrier gas molecules decompose at the deposition surface. Such a scheme would not be applicable to deposition by laser ablation, if for no other reason, that the larger molecular fragments that may be part of the ablation plume arrive at the target with very high kinetic energies corresponding to temperatures much higher than that of the substrate. In the present case the explanation has to be sought elsewhere. At the lower temperatures, where the [111] films are polycrystalline, the deposition rate shows a decrease between 800 and 900° C, which might be due to reevaporation of some oxides formed on the growth surface in between laser pulses by reaction with the relatively high pressure of residual gases in the system.

We thank our colleagues, W. Ping for the Auger data, C. Peters for discussions on interpretation of X-ray diffraction data, H. Holloway for discussions on film growth processes and R. Soltis for help with many experimental problems.

REFERENCES

1. J. A. Powell and L. G. Matus in *Amorphous and Crystalline Silicon Carbide and Related Materials*, Springer Proceedings in Physics, Edited by G. L. Harris and C. Y.-W. Yang Vol. 34, p 2, Springer, Berlin, 1989.
2. L. G. Matus and J. A. Powell, in *Amorphous and Crystalline Silicon Carbide and Related Materials*, Springer Proceedings in Physics, Edited by G. L. Harris and C. Y.-W. Yang Vol. 34, p 40, Springer, Berlin, 1989.
3. S. Nishino and J. Saraie, in *Amorphous and Crystalline Silicon Carbide and Related Materials*, Springer Proceedings in Physics, Edited by G. L. Harris and C. Y.-W. Yang Vol. 34, p 45, Springer, Berlin, 1989.
4. M. I. Chaudhry and R. L. Wright, J. Mater. Res. **5**, 1595 (1990).
5. Y. Onuma, F. Nagaune and K. Kamimura in *Amorphous and Crystalline Silicon Carbide and Related Materials*, Springer Proceedings in Physics, Edited by G. L. Harris and C. Y.-W. Yang Vol. 34, p 142, Springer, Berlin, 1989.
6. J. A. Powell, D. J. Larkin, L. G. Matus, W. J. Choyke, J. L. Bradshaw, L. Henderson, M. Yoganathan, J. Yang and P. Pirouz, Appl. Phys. Lett. **56**, 1442 (1990).
7. Y. Inoue, S. Nakashima, A. Mitsuishi, S. Tabata, and S. Tsuboi, Solid State Commun. **48**, 1071 (1983).
8. M. Balooch, R. J. Tench, W. J. Sielhaus, M. J. Allen, A. L. Connor and D. R. Olander, Appl. Phys. Lett. **57**, 1540 (1990).
9. R. J. Tench, M. Balooch, A. L. Connor, L. Bernardez, B. Olson, M. J. Allen, W. J. Siekhaus and D. R. Olander, in Laser Ablation for Materials Synthesis, Edited by D. C. Paine and J. C. Bravman, Mat. Res. Soc. Symposium Proc. Vol 191, p 61, 1990.
10. L. Rimai, R. Ager, E. M. Logothetis, W. H. Weber and J. Hangas, Appl. Phys. Lett. **59**, 2266 (1991).
11. Z. C. Feng, A. J. Mascarenhas, W. J. Choyke and J. A. Powell, J. Appl. Phys. **64**, 3176 (1988)
12. F. Tuinstra and J. L. Koenig, J. Chem. Phys. **53**, 1126 (1970)
13. D. T. Hon and L. Faust, Appl. Phys. **1**, 241 (1973)
14. H. Richter, Z.P. Wang, and L. Ley, Solid State Commun. **39**, 625 (1981).
15. D. S. Knight and W. B. White, J. Mater. Res. **4**, 385 (1989)

HETERO-EPITAXIAL GROWTH OF SiC FILMS BY CVD FROM SILANE, METHANE, PROPANE, AND HYDROGEN MIXTURES

B.Bahavar, M.I.Chaudhry, and R.J.McCluskey, Center for Advanced Materials Processing, Clarkson University, Potsdam, NY

ABSTRACT

Epitaxial silicon carbide films have been produced on Si (100) substrates by CVD with 90% of the carbon supplied by methane and 10% by propane as compared to 100% by propane (or 100% by any carbon source more reactive than methane). This implies a methane to propane mole ratio of thirty. Among possible carbon gases, methane is the purest commercially available hydrocarbon source, But methane has not been commonly used for growth of silicon carbide due to its low chemical reactivity. Our process demonstrates the feasibility of achieving high SiC growth rates while using a carbon source that is predominantly methane. We have established that silicon carbide films grown at 1350 °C in a CVD reactor using the above carbon source ratio results in quality single crystalline films at similar growth rates and lower carrier concentrations than films grown from propane and silane.

The main tools used to characterize the grown films are X-ray and electron diffraction, optical microscopy, surface profilometry, Hall mobility measurements, and thickness measurements.

INTRODUCTION

Silicon carbide (SiC) is a wide band-gap semiconductor material with many attractive features. High thermal conductivity and excellent physical stability favor silicon carbide for applications in high-temperature devices. In particular, β-SiC (cubic or 3C-SiC) seems to be the most suitable for this purpose, owing to its high electron mobility with values up to 800 cm^2/Vs. Preparation of single crystals by chemical vapor deposition (CVD) has been an active research area since the announcement of a "buffer layer" technique [1, 2] which permits the epitaxial growth of β-SiC atop silicon substrates. Briefly, in this two-step β-SiC CVD process, the buffer or initial layer is first deposited by reacting the Si substrate with a hydrocarbon gas. This is accomplished by flowing a dilute mixture of the hydrocarbon in H_2 over the substrate as its temperature is ramped (~40 ^oC /s) from room temperature to the growth temperature (1330–1380 ^oC). The first step is also called the carbonization step where the Si surface layer of the substrate is converted to a β-SiC layer. The second step involves the homo-epitaxy of β-SiC on the initial layer using a dilute mixture of the hydrocarbon and SiH_4 in H_2 . The choices of hydrocarbon include C_3H_8 [1, 3, 4], CH_3Cl [4], and C_2H_4 [5] while CH_4 [6, 7, 8] is observed to produce little if any deposit.

The sucessful use of CH_4 as an alternate source of carbon presents a challenge in understanding the surface chemistry involved in the growth process of β-SiC on Si substrates [8, 9]. In the present paper we report the hetero-epitaxial growth of β-SiC on Si(100) by the two-step CVD method to form the β-SiC buffer layer using the $H_2 - C_3H_8 - SiH_4$ gas system and the growth of β-SiC bulk layer using the $H_2 - CH_4 - C_3H_8 - SiH_4$, $H_2 - CH_4 - SiH_4$, and $H_2 - C_3H_8 - SiH_4$ gas systems.

Mat. Res. Soc. Symp. Proc. Vol. 242. © 1992 Materials Research Society

EXPERIMENTAL

β-SiC films were grown on Si substrates using a cold-wall horizontal CVD reactor, operated at atmospheric pressure. The reactor was a quartz tube with an inside diameter of $50mm$ and an inside length of $500mm$. The Si substrate was placed on an RF-heated SiC-coated graphite susceptor which was held by a quartz support. The temperature was measured by an automatic pyrometer through a quartz window. The difference between the measured and the actual substrate temperature was determined by melting a Si substrate under actual growth conditions. Substrate temperatures in this document were corrected for the difference. Typically, the measured T was 20–30 ^{o}C below the Si melting temperature of 1410±5 ^{o}C .

Substrates were 33 mm × 48 mm × 0.38 mm electronic grade (p-type) single crystal Si with (100) orientation. To prepare the substrates for crystal growth the following sequence was used: (*i*) blowing off the Si particles (produced during cutting) with dry argon, (*ii*) rinsing both sides of the subtrate with methanol (semiconductor grade) and wiping them with a kimwipe to remove extra fine Si particles not seen by the unaided eye, (*iii*) etching the substrate in a %5 HF solution (made from %49 HF stock and D.I. water) for 5 min to remove the native oxide. If liquid drops were detected on the Si substrate upon removing it from the HF solution, then steps (*ii*) and (*iii*) were repeated. There was no degreasing step in the above sequence since the Si wafers and substrates were handled only with a clean kimwipe or tweezers.

CH_4 (99.9995%, MG Industries) and C_3H_8 (99.95%, MG Industries) were used as source gases for carbon. SiH_4 (99.995%, MG Industries) and palladium purified H_2 (99.999%, Air Products) were used as source gas for silicon and carrier gas, respectively. The flow rates were regulated by electronic mass flow controllers (Tylan and Hastings).

After the substrate and susceptor were positioned in the reactor, the native oxide on the Si substrate was removed by heating the substrate at 1200 ^{o}C for 10 min. An epilayer of Si was then grown for 5 min at 1050 ^{o}C . This silicon epilayer of about 0.2 μm thickness was found suitable for subsequent epitaxial growth of β-SiC . Next, the Rf power was turned off and the susceptor and substrate allowed to cool. After cooling for 3 min, the proper gas flows were established for the growth of the β-SiC buffer layer. An additional 1 min was allowed for the new gas mixture to stabilize. The temperature of the susceptor was then ramped to about 1350 ^{o}C (in about 33s) and held at that temperature. After 1 min (time measured from the beginning of the temperature ramp), all gas flows except for H_2 were diverted from the reactor for 1 min in order to prepare the flow conditions for the bulk growth. Temperature was maintained at 1350 ^{o}C during this 1 min purge and proper flow conditions were set for bulk growth. Following the purge period, the stabilized reactant gas flows were directed to the reactor. For samples in which buffer layer growth and bulk growth had identical gas flow conditions, the 1 min purge was omited. After the desired growth time had elapsed, all gas flows except for H_2 were diverted to the exhaust and a 2 min purge period was started. Finally, the RF power was slowly decreased (~100 ^{o}C /min) to zero and the susceptor and the substrate were allowed to cool to near room temperature.

Table I summarizes the experimental conditions for the preparation of β-SiC films. In this table, samples designated BB used C_3H_8 as the sole carbon source, while samples designated with an M used a mixture of CH_4 and C_3H_8 or CH_4 only. The bulk layer growth time was in the range of 5–120 min. Samples having the same growth conditions in Table 1, differ only in their growth time. Growth rates listed in this table are for the center of the samples. Samples

for x-ray evaluation and measurement of electrical properties were grown for 120 min to provide thicknesses greater than 4 μm . The samples grown for 30 min or shorter time periods showed color fringe patters which were indicative of layer thickness and thickness uniformity. The surface morphology of the as-grown β-SiC epi-layers were investigated with a Nomraski microscope. A stylus type profilometer (Dektak IIA, Veeco Instruments) was used to measure surface roughness. Thickness of samples grown for 30 min or shorter were measured by visible light interferometry. Thickness of samples grown for 120 and 240 min were measured by viewing the imbedded layer cross-section under an optical microscope. Structural quality of the crystalline layers was evaluated by x-ray diffraction (Siemens, Model *D500*) and selected area diffraction (*SAD*) using a transmission electron microscope (JEOL, Model JEM-1200EX). The electrical characteristics (Hall mobility and carrier concentration) of the β-SiC layers were determined by making Hall measurements using the van der Pauw technique at room temperature. Ohmic contacts were made by indium soldering of thin gold wires on the layer surface.

Table I. Experimental conditions for epitaxial growth of β-SiC .

Sample	Flow Rates for Buffer Layer (cc/min)				Flow Rates for Bulk Growth (cc/min)				Growth Rate (μm /hr)
	H_2	C_3H_8	CH_4	SiH_4	H_2	C_3H_8	CH_4	SiH_4	
M1	3000	0.00	1.08	0.56	3000	0.00	1.08	0.56	0.0
M2	3000	0.00	1.92	1.00	3000	0.00	1.92	1.00	0.0
M3, M6, M7, M9	3000	0.64	0.00	1.00	3000	.064	1.92	1.00	2.9
M4, M8, M10	3000	0.64	0.00	1.00	3000	0.00	1.92	1.00	3.2
M5	3000	.064	1.92	1.00	3000	.064	1.92	1.00	2.9
BB10, BB13	3000	0.64	0.00	1.00	3000	0.64	0.00	1.00	2.7

RESULTS

Among the five growth conditions for samples M1-M10, only M1 and M2 failed to produce any growth of β-SiC . The surface of the Si substrate in sample M1 was dotted with isolated hazy squares with a side length of about 0.25 mm. Sample M2 also showed hazy squares but with a side length of about 7 mm. Under our experimental conditions, use of CH_4 as the only carbon source during the buffer layer step does not allow SiC formation. Furthermore, sample M5 shows, indirectly, that a small addition of C_3H_8 during the initial thermal ramp results in growth of a β-SiC buffer layer. Visual comparison of samples M3-M10 indicated the superiority of samples (M3, M6, M7, and M9) grown without methane during the buffer layer and with some propane during bulk growth. We will select samples M6 and M7 for comparing β-SiC single crystals grown with 90% of the carbon source as CH_4 with samples BB10 and BB13 grown using C_3H_8 as the only source of carbon.

Figure 1 shows Nomraski photomicrographs for surface morphologies of samples M7 and BB10, both grown for 120 min. The average roughness measured by a stylus profilometer was 130 Å for sample BB10 while that of M7 was 1235 Å. Our profilometer gave an average roughness of 51 Å for the surface of the untreated Si substrate. The crystal quality of samples M7 and BB10 were examined by measuring the full width at half maximum (FWHM) of x-ray rocking curves. Rocking curve measurements for the epitaxial layers were carried out using Cu$K\alpha$ lines at $2\theta = 41.40°$ for (200) peak and $2\theta = 89.90°$ for (400) peak of β-SiC . Table II

shows the FWHM values for the two peaks of β-SiC samples M7 and BB10. These FWHMs were considerably broader than 0.034° from the (400) diffraction peak of the Si substrate with the same instrumental conditions. Thus, the resolution of the x-ray experimental setup was adequate for the analysis of the crystallinity of the grown layer even without a double-crystal diffractometer (DCD). It is clear from Table II that the two samples are almost identical in their overall crystal quality.

The electrical properties of the two samples are summarized in Table III. The Hall measurements resulted in values for Hall mobility, μ_H, layer resistivity, ρ, and carrier concentration, n.

Table II. FWHM of x-ray rocking curves of β-SiC (200) and (400) peaks.

Sample	Thickness (μm)	FWHM of (200) peak	FWHM of (400) peak
M7	5.0	0.114°	0.101°
BB10	5.4	0.113°	0.103°

Table III. Electrical properties of n-type β-SiC layers at room temperature.

Sample	μ_H (cm^2/V.s)	ρ (Ω.cm)	n (cm^{-3})
M7	303	0.43	4.38×10^{16}
BB10	344	0.22	7.61×10^{16}

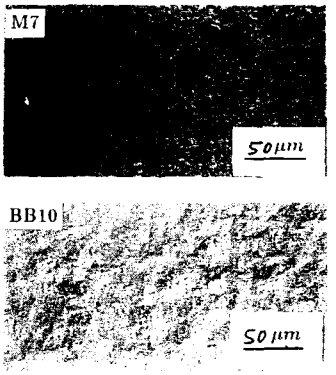


Figure 1. Nomarski microphotographs of the as-grown surfaces of samples M7 and BB10.

For determination of the crystalline state of the two samples we had to use samples BB13 and M6 which had the same growth conditions as BB10 and M7, respectively, but were thinner, making them suitable for transmission electron diffraction analysis of the SAD method. Figure 2 shows the spot patterns for these two samples. It is clear that both samples are single crystalline.

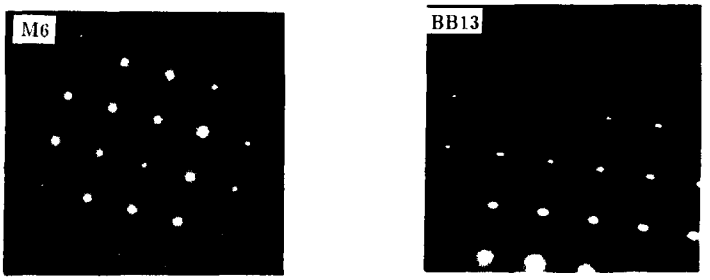


Figure 2. Transmission electron diffraction patterns of samples M6 and BB13. The spot pattern shows the single crystalline nature of the β-SiC films.

DISCUSSION

An important finding of this study is the utilization of CH_4 in the bulk growth of β-SiC layers on a β-SiC surface. An equally important and interesting result is the insight this study provides for the growth mechanism of the buffer layer or the carbonization of the Si surface. These findings can be better understood by considering the bond energies (Table IV) needed for radical species production for the various carbon sources used in the growth of β-SiC on Si substrates [11].

Table IV. Bond energies of several carbon sources used in the growth of β-SiC on Si substrates.

Molecule	Radicals	Bond energy (Kcal/mol)
CH_4	$CH_3 \cdot + H \cdot$	104
CH_3Cl	$CH_3 \cdot + Cl \cdot$	83.5
C_3H_8	$C_2H_5 \cdot + CH_3 \cdot$	85

Stinespring et al., in their experimental and theoretical study of the $H_2 - C_3H_8 - SiH_4$ growth system of β-SiC , determined that the formation of a SiC deposit at low temperatures is critical since it prevents substantial evaporative losses of Si from the substrate [8]. They determined that C_3H_8 produces reactive radical species at about 900 $^\circ C$. Ikoma et al. reported the growth of β-SiC using the $H_2 - CH_3Cl - SiH_4$ system with similar results to that of the $H_2 - C_3H_8 - SiH_4$ system [4]. It is evident from Table IV that both C_3H_8 and CH_3Cl are suitable carbon sources to carbonize the Si substrate at a relatively low temperature. Samples M1 and M2 show that CH_4 fails to carbonize the Si substrate. However, when the buffer layer is formed and the Si out diffusion is capped, the $H_2 - CH_4 - SiH_4$ system by itself is capable of producing β-SiC bulk layers with growth rates comparable to those of the $H_2 - C_3H_8 - SiH_4$ and $H_2 - CH_3Cl - SiH_4$ systems. This agrees with the fact that CH_4 becomes reactive at about 1200 $^\circ C$ [11]. Our preliminary findings, however, suggest that a small addition of C_3H_8 to CH_4 improves the crystal quality of the bulk β-SiC layer. Further studies are needed to investigate other growth parameters, such as gas ratios [5], in the $H_2 - CH_4 - SiH_4$ system in order to make a more accurate conclusions about the crystal quality. Thus, sample M7 reperesents the buffer layer growth by the $H_2 - C_3H_8 - SiH_4$ system and bulk layer growth by $H_2 - CH_4 - C_3H_8 - SiH_4$ system where methane to propane mole ratio is thirty.

The 3-D growth pattern on the surface of sample M7 can be qualitatively explained in terms of surface mobilities. With CH_4 providing 90% of the carbon species for bulk growth, one would expect that potentially different surface moieties (i.e., precursors to the final SiC reaction product) can lead to different sticking coefficients, nucleation, and growth mechanisms [8, 10].

CONCLUSION

β-SiC epitaxial films were grown on Si (100) substrates by the two-step CVD growth where buffer layer is formed by the $H_2 - C_3H_8 - SiH_4$ system, and the bulk layer is formed by the $H_2 - CH_4 - C_3H_8 - SiH_4$ where the methane to propane mole ratio is thirty. It is determined that the small amount of C_3H_8 improves the crystal quality. It may be possible to further decrease the content of C_3H_8 without compromising the crystal quality. The grown layers are single crystalline and have the same overall crystal quality to layers grown by the $H_2 - C_3H_8 - SiH_4$ system in this study. The electrical properties of the layers grown by the two gas systems are

similar. It is determined that methane as the only carbon source is not capable of carbonizing the Si surface. However, methane as the only source of carbon is sufficient for growth of bulk β-SiC layers on a SiC surface. This sensitivity of methane to the surface is explained in terms of the substantial evaporative losses of Si from the Si substrate at temperatures around 1200 ^{o}C where methane may still be a stable molecule and hence not able to cap the Si surface.

ACKNOWLEDGEMENTS

We appreciate the helpful discussions we had with Dr. C.D. Stinespring and Dr. J.A. Powell. This research was supported by The New York State Center for Advanced Materials Processing, Clarkson University, Potsdam, NY.

References

[1] S. Nishino, J.A. Powell, and H.A. Will, Appl. Phys. Lett., 42, 460, (1983).

[2] A. Addamiano and J.A. Sprague, Appl. Phys. Lett., 44 (5), 525-527, (1984).

[3] J.A. Powell, L.G. Matus, and M.A. Kuczmarski, J. Electrochem. Soc., SOLIDSTATE SCIENCE AND TECHNOLOGY, 134 (6), 1558-1565, (1987).

[4] K. Ikoma, M. Yamanaka, H. Yamaguchi, and Y. Shichi, J. Electrochem. Soc., 138 (10), 3028, (1991).

[5] H.S. Kong, J.T. Glass, and R.F. Davis, Appl. Phys. Lett., 49 (17), 1074, (1986).

[6] R.F. Davis (private communication).

[7] J.A. Powell (private communication).

[8] C.D. Stinespring and J.C. Wormhoudt, J. Appl. Phys., 65 (4), 1733-1742, (1989).

[9] R.P.H. Chang and J.M. Poate, MRS Bulletin, XVI (11), 63-65, (1991).

[10] H.S. Kong, J.T. Glass, and R.F. Davis, J. Mater. Res., 4 (1), 204, (1989).

[11] T.W. Graham Solomons, Organic Chemistry, 2nd ed. (John Wiley and Sons, New York, 1980), pp. 129,167.

ELECTRICAL PROPERTIES OF THERMALLY GROWN SiO_2-SiC INTERFACES

NITYA N. SINGH, A. RYS, AND A.U. AHMED
Department of Electrical and Computer Engineering
Kansas State University, Manhattan, KS 66506

ABSTRACT

Fabrication processes of metal-oxide semiconductor (MOS) capacitors on n-type, Si-face, 6H-SiC were studied. The effects of thermal oxidation conditions at temperatures between 1100 and 1250°C on the electrical properties of MOS capacitors were determined. The wafers were annealed under argon to improve the C-V characteristics. C-V characteristics of Al-SiO_2-SiC metal-oxide-semiconductor were measured at high frequency in the dark and under illumination. In the dark inversion does not occur, probably owing to the absence of minority carriers due to the large band gap of 6H-SiC. The accumulation, depletion, and inversion regions were clearly observed when the C-V measurements were made under illumination for both wet and dry thermally grown oxides. The interface trap densities and emission time constants of fast states were determined by ac conductance measurements. From the analysis of data we obtained a total of fixed charges and the slow interface traps, $N_f + N_{ssSlow}$ of 1.5 to 3.3 x 10^{12} cm^{-2}, fast interface trap densities, N_{ssFast} of 0.5 to 1.7 x 10^{11} cm^{-2} eV^{-1} and emission times constant of 0.3 to 1.4 μsec for wet oxidation. For dry oxidation, $N_f + N_{ssSlow}$ of 3.5 to 11.2 x 10^{11} cm^{-2}, N_{ssFast} of 0.7 to 1.25 x 10^{10} cm^{-2} eV^{-1} and emission time constants of 0.6 to 2 μsec were obtained.

INTRODUCTION

Silicon carbide has been known for many years to have excellent physical and electronic properties which should allow production of electronic devices that can operate at significantly higher temperatures compared to devices produced by Si or GaAs. The most important properties are its wide band gap energy (2.9 eV for 6H-SiC at room temperature), chemical stability even at several hundreds of degrees Celsius [1], high thermal conductivity (4.9 W/cm-K) [2], high breakdown electric field (2 x 10^6 V/cm) [3], and high saturated electron drift velocity (2.0 x 10^7 cm/sec) [4]. Due to these electronic and physical properties, silicon carbide will be a useful material for high temperature, high frequency and high power electronic devices [5]. SiC can be used for optoelectronic devices in the visible (blue) and ultra-violet wavelength regions. SiC based electronics have potential aerospace and space applications [6]. The development of SiC electronics has been limited due to the difficulty in growing high-quality, large-area crystals. In the past decade, significant progress has been achieved in the crystal growth techniques such as liquid-phase epitaxy [7], chemical vapor deposition [8-9] and seeded sublimation techniques [10].

The metal-oxide-semiconductor (MOS) structure is the heart of present day electronics. A better understanding of the electrical properties of the SiC MOS structure is of great importance to device operation. Capacitors on both 6H (hexagonal) and 3C (cubic) SiC with thermal oxides have been reported from Kyoto University [11-13]. There is also a report of capacitors on CVD 3C-SiC with wet thermal oxides utilizing mercury-probe contacts [14]. But all these reports dealt with wet oxidation only. This study of MOS capacitors examines both wet and dry oxidation processes and their effect on electrical characteristics. The ac conductance measurement was also used to get accurate information about the interface trap densities and emission time constants.

Thermal oxide layers were grown on n-type, Si-face, 6H-SiC substrates with (0001) orientation and the electron carrier concentration of $\sim 10^{17}$ cm^{-3}. A typical sample size was 0.5 mm in thickness and 1 cm^2 in surface area. Before oxidation, the wafers were cleaned with organic solvents, dipped in HF acid for several minutes to remove the oxide layers initially present, and rinsed in deionized water. The sample was oxidized by both wet and dry oxidation. The dry oxidation was carried out by exposing the SiC to 1 ℓ/min of dry O_2 at 1200-1250°C for 2-5 hours in a horizontal tube. The wet oxidation was conducted at 1100-1250°C for 0.5-3h in an oxygen flow of 1 ℓ/min, which was passed through deionized water at 90°C. After the growth of oxide, all the samples were annealed at the temperature at which oxide was grown for 30 min in an argon flow of 1 ℓ/min. Oxide was etched from a portion of SiC (Si-face) to make ohmic contacts. Selective deposition of Al metal dots with 0.75-1.5 mm diameter were evaporated on both the oxide and the SiC to define field-plates and contacts.

RESULTS AND DISCUSSION

C-V characteristics of the MOS structures were measured at frequencies from 100 Hz to 1 MHz both in the dark and under illumination (275 W Sears sun lamp). However, the capacitance data presented in this paper were taken at 1 MHz because the C-V characteristics showed very small frequency dispersion under light and dark conditions. As can be seen in Fig. 1(a), MOS structures prepared without argon annealing showed an accumulation only during the first C-V measurement under illumination. No accumulation region was observed in these samples during subsequent C-V measurements at 1 MHz, both in the dark and under illumination as shown in Fig. 1(b). Figure 2 and Fig. 3 show the room temperature experimental results measured with 50 mV ac probe signal at 1 MHz for samples prepared by wet and dry oxidation. The measured C-V behavior was corrected for the series resistance [15] of the devices. There was no significant difference between the measured capacitance, C_m, and the corrected capacitance, C_c.

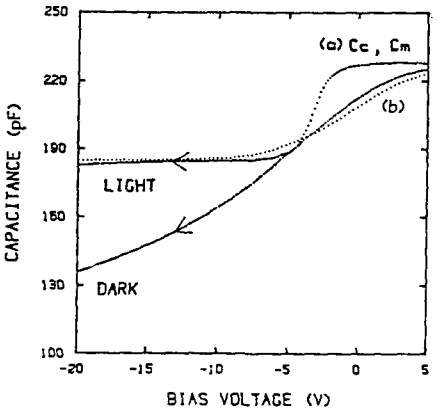


Fig. 1 C-V characteristics of the sample prepared by wet oxidation at 1200°C for 60 minutes without argon annealing (a) First measurement (b) Second measurement. Sweep rate was 10 mV/sec. in Light and 2 mV/sec. in dark.

The C-V curves under illumination clearly showed accumulation, depletion and inversion. In the dark the C-V characteristic in the accumulation and the depletion regions were almost the same as those under illumination. On the other hand, as negative bias increased, the capacitance in the dark continued to decrease even at the bias corresponding to the inversion region under illumination. The theoretical curve under nonequilibrium conditions is generally calculated for the case where minority carriers can't accumulate near the surface even in the bias range corresponding to inversion, so that the depletion layer spreads deeply into the semiconductor bulk [16]. The experimental curve in the dark can

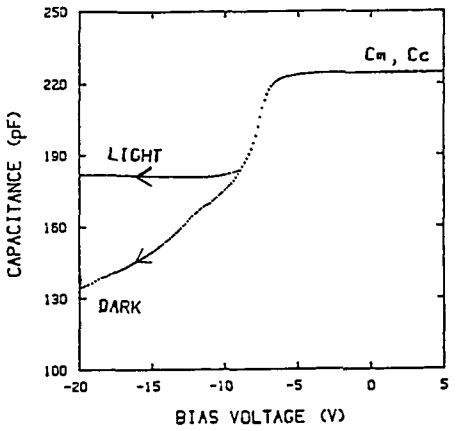


Fig. 2 C-V characteristics of sample prepared by wet oxidation at 1200°C for 1 hour with argon annealing. Measurements were done both in dark and under illumination. Sweep rate was 10 mV/sec. in light and 2 mV/sec. in dark.

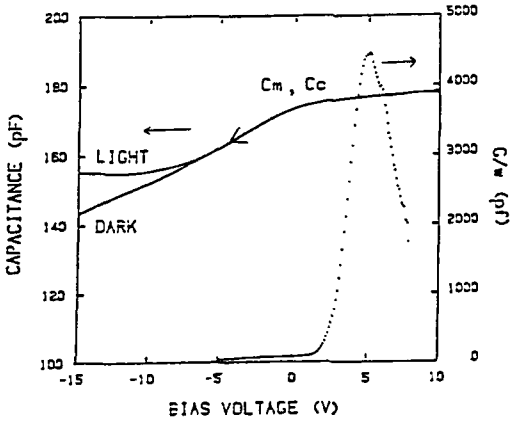


Fig. 3 C-V and G/ω vs. voltage characteristics of sample prepared by dry oxidation at 1250°C for 2 hours with argon annealing. Sweep rate was 10 mV/sec. in light and 2 mV/sec. in dark.

be regarded as the nonequilibrium case, because minority carriers cannot accumulate under dark conditions, since both the minority carrier concentration in the SiC bulk and the thermal generation rate of minority carriers may be extremely small owing to the large band gap (2.9 eV) of 6H-SiC.

The flat-band voltage shift from the center of ideal C-V curves was used to determine the fixed oxide charge density (N_f) and slow interface trap density (N_{ssSlow}). Fast interface trap density (N_{ssFast}) was determined [15] from the G-V plot, as shown in Fig. 3. Thickness of the oxide was calculated from the capacitance at strong accumulation. The uncertainty in this measurement technique is dominated by the error (approx. 10%) in determining the contact diameter. Thickness measured by this technique was in good agreement with the ellipsometer measurements. The emission time constant τ for the fast states was determined from the peak of G_p/ω versus log (ω) plot which occurs at $\omega\tau = 1.98$.

The results of high frequency (1MHz) C-V measurements on MOS capacitors prepared at different temperatures and with different duration by wet and dry oxidations are shown in Tables 1 and 2. An analysis of C-V curves and their corresponding AC conductance peaks indicates that the density of fixed oxide and fast interface states in SiO_2 are strongly dependant on the oxidation temperature and duration of oxidation. It can be seen from Table 1 and Table 2 that the flat-band voltage increases with increase in thickness of SiO_2 and this result is consistent with the theory since oxide thickness is directly proportional to flat-band voltage. Again, the flat-band voltage was negative in wet oxidation whereas it was positive in dry oxidation. This shows that polarity of oxide charges were opposite in wet and dry oxidation. The results from Tables 1 and 2 show that it was not possible to do AC conductance measurements when the oxide layer was thick. For thick oxides, a peak in AC conductance measurement was not observed. This shows the conductance measurement is applicable only in the case of thin insulator layer (< 650 Å).

Table 1
Wet Oxidation

SAMPLE #	OXIDATION TEMP (°C) & TIME (MIN)	T_{ox} (Å) ELLIPSO-METER	T_{ox} (Å) CAPACI-TANCE	ΔV_{fb}(v)	N_f+N_{ssSlow} ($10^{11}cm^{-2}$)	N_{ssFast} ($10^{10}cm^{-2}eV^{-1}$)	Time Const. (μ sec)
1	1150, 30	295	239	-1.75	15.39	5.16	0.87
2	1150, 60	427	351	-2.60	15.57	8.13	0.49
3	1150, 120	598	521	-3.2	15.96	16.42	0.32
4	1150, 180	631	565	-4.6	20.79	--	--
5	1200, 30	461	440	-6.7	33.41	14.6	1.40
6	1200, 60	725	645	-7.1	23.12	--	--
7	1200, 120	985	897	-7.35	24.11	--	--
8	1200, 180	1216	1093	-7.85	15.30	--	--
9	1250,30	791	708	-7.2	21.39	--	--
10	1250, 60	1298	1157	-7.9	14.37	--	--
11	1250, 120	1956	1822	-8.45	9.74	--	--
12	1250, 180	2264	2111	-9.16	9.12	--	--

Wet and dry oxidation growth rates are shown in Fig. 4. Plots on logarithmic scale indicate approximately parabolic oxidation behavior, which indicate a diffusion-limited reaction. These results are in agreement with previously published data on wet oxidation of SiC [12].

Table 2
Dry Oxidation

SAMPLE #	OXIDATION TEMP (°C) & TIME (MIN)	T_{ox} (Å) ELLIPSO -METER	T_{ox} (Å) CAPACI-TANCE	ΔV_{fb}(v)	N_f+N_{mobile} ($10^{11}cm^{-2}$)	$N_{surface}$ ($10^{10}cm^{-2}eV^{-1}$)	Time Const. (μ sec)
1	1200, 120	628	602	1.0	-3.49	0.81	1.57
2	1200, 180	903	837	1.8	-4.52	0.70	1.98
3	1200, 240	1203	1056	2.9	-5.77	–	–
4	1200, 300	1227	1169	3.7	-6.65	–	–
5	1250, 120	1129	1050	5.6	-11.21	0.7	1.57
6	1250, 180	1512	1390	6.45	-9.75	1.25	0.63
7	1250, 240	1956	1800	7.10	-8.10	–	–
8	1250, 300	2342	2222	7.96	-7.50	–	–

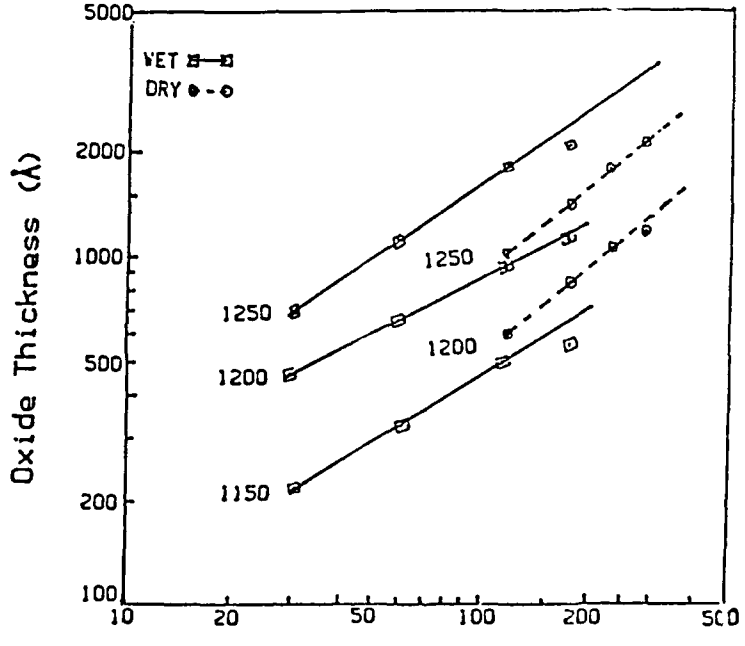


Fig. 4 Wet and dry oxidation growth rate.

CONCLUSIONS

In conclusion we find .hat samples prepared by both dry and wet oxidation show accumulation, depletion and inversion region under illumination. Under dark conditions, inversion did not occur, probably owing to the absence of minority carriers due to the large band gap (2.9 eV) of 6H-SiC. A significant improvement in the C-V characteristics was observed after the oxidized samples were annealed in argon for 30 minutes. The characteristics at the frequencies of 100 Hz - 1MHz were almost the same without any frequency dispersion both in the dark and under illumination. The relation between the oxide thickness and the oxidation time can be expressed by parabolic law which is also used for thermal oxidation of Si. SiO_2 layers grown by wet oxidation process possessed a total positive-fixed charge and slow traps at interface, whereas SiO_2 layers grown by dry oxidation possessed negative combined charge. The slow interface traps have not been directly addressed in this work.

ACKNOWLEDGEMENTS

The authors would like to thank Dr. J.H. Edgar of the Department of Chemical Engineering at KSU for supplying samples for this research and to Dr. L. Matus and Mr. J.B. Petit of NASA Lewis Research Center for valuable advise regarding the ellipsometry measurements and metal contacts formation. This work was supported by the Advanced Manufacturing Institute at KSU under a research project No. 92103.

References

1. R.B. Campbell and H.C. Change, in Semiconductors and Semimetals, edited by R.K. Willardson and A.C. Beer (Academic, New York, 1971), Vol. 7, part-B, Chap. 9, 628.
2. G.A. Slack, J. Appl. Phys. **35**, 3460 (1964).
3. W.V. Muench and I. Pfaffender, J. Appl. Phys **48**, 4831 (1977).
4. W.V. Muench and E. Pettenpaul, J. Appl. Phys **48**, 4823 (1977).
5. Silicon Carbide—1973, edited by R.C. Marshall, J.W. Faust and C.E. Ryan.
6. W.C. Nieberding and J.A. Powell, IEEE Trans. Ind. Electron. **IE-29**, 103-106 (1982).
7. A. Suzuki, M. Ikeda, N. Nagao, H. Matsunami and T. Tanaka, J. Appl. Phys. **47**, 4546 (1976).
8. S. Nishino, Y. Hazuki, H. Matsunami and T. Tanaka, J. Electrochem. Soc., **127**, 2674 (1980).
9. W.V. Muench and P. Hoeck, Solid State Electron. **21**, 479 (1978).
10. L.A. Tang, J.A. Edmond and J.W. Palmour, Extended Abstract of the 176th Electrochem. Soc. Meeting, 705 (1989).
11. A. Suzuki, K. Mameno, N. Furui and H. Matsunami, Appl. Phys. Lett **39**, 89 (1981).
12. A. Suzuki, H. Ashida, N. Furni, K. Mameno and H. Matsunami, Jap. J. of Appl. Phys., **21** (4), 579 (1982)
13. K. Shibahara, S. Nishino and H. Matsunami, Jpn. J. Appl. Phys., **23**, 862 (1984).
14. R.E. Avila, J.J. Kopanski and C.D. Fung, Appl. Phys. Lett., **49**, 334 (1984).
15. E.H. Nicollian and J.R. Brews, MOS Physics and Technology (John Wiley and Son, New York, 1982) 176.
16. S.M. Sze, Physics of Semiconductor Devices (Wiley, New York, 1969), Chap. 9, 425.

ELECTRICAL AND CHEMICAL CHARACTERIZATION OF CONTACTS TO SILICON CARBIDE

JEREMY 3. PETIT* and MARY V. ZELLER**
*Sverdrup Technology, Inc., 2001 Aerospace Parkway, Brook Park, OH 44142
**NASA-Lewis Research Center, 21000 Brookpark Rd., Cleveland, OH 44135

ABSTRACT

Chemical and electrical studies were performed to determine the characteristics of contacts to 6H-SiC. Both elemental metals (Ni, Mo) and silicides ($MoSi_2$, $TaSi_2$, $TiSi_2$) were studied. Chemical analysis by Auger Electron Spectroscopy (AES) was performed to examine interface reactions caused by heat treatment. Electrical measurements (current-voltage and capacitance-voltage) were made during annealing sequences to determine the rectifying or ohmic characteristics of the contacts. Where possible, barrier height and contact resistance values were calculated.

INTRODUCTION

Stable electrical contacts are vital to the realization of the potential high temperature and high power applications of silicon carbide (SiC). Contacts should maintain stable electrical characteristics (specific contact resistance or barrier height) at elevated temperatures for extended periods of time. For power devices, the contact resistance must be small compared to the resistance of the active regions of the device. A specific contact resistance of the order of 10^{-6} $\Omega \cdot cm^2$ or less may be required for many devices[1]. This paper will report on electrical measurements (current-voltage, capacitance-voltage,transmission line method) of contacts on the polar faces of single crystal 6H-SiC. Auger electron spectroscopy (AES) combined with depth profiling was used to examine interfacial reactions as a function of heat treatment and correlate chemical reactions with changes in electrical performance. The contact materials chosen included elemental metals (Ni, Mo) and refractory metal silicides ($MoSi_2$, $TiSi_2$, and $TaSi_2$).

EXPERIMENTAL

All samples were fabricated on sublimation-grown 6H-SiC purchased from Cree Research, Inc. Both C-faced and Si-faced samples were used. The Al contacts were deposited on p-SiC epitaxial films grown in a CVD system with Al doping. All other metals were deposited on as received n-type substrates with carrier concentration in the 10^{17}-10^{18} cm^{-3} range. All depositions were performed by RF sputtering. Prior to deposition, the native oxide was stripped with buffered HF, the samples were cleaned with 1 HF: 1 Methanol: 10 H_2O, rinsed in deionized H_2O, and immersed in methanol until they were blown dry with nitrogen immediately before being placed in the vacuum chamber. The base pressure in the chamber was $<1x10^{-6}$ torr, the Ar pressure was 10 mTorr, and the RF power was 200W except for the $TaSi_2$ and $MoSi_2$ depositions, for which it was 500W. The Ni and Mo depositions were from elemental targets. The $MoSi_2$ and $TaSi_2$ were from stoichiometric compound targets. The $TiSi_2$ contacts consisted of 6 layer Ti/Si structures with the thickness ratio $t_{Si}/t_{Ti} = 2.25$. From atomic density calculations this should yield stoichiometric $TiSi_2$ after annealing. All anneals were performed by a quartz-halogen lamp heated rapid thermal annealer (RTA) in an ambient of 3% H_2 in N_2. The RTA was not equipped to evacuate the chamber prior to annealing. The samples used for AES and those used for electrical studies went through separate annealing runs.

The chemical data for all specimens were obtained by AES with a Perkin-

Elmer 590A Scanning Auger Microprobe equipped with a DEC PDP 11-04 computer system. The base pressure of the spectrometer was $2x10^{-10}$ torr. The AES data were collected by using a 5 kV primary electron beam voltage and 1μA of beam current. The depth profiles were performed by sputter etching with an Argon ion beam at 4 kV and in the continuous sputter mode. The sputtering rate was 30Å/min. as calibrated against Ta_2O_5/Ta standard. All semi-quantitative atomic concentrations were calculated with the Perkin-Elmer MACS VI software sensitivity factors.

The electrical measurements were taken from the circular transmission line test structure shown in figure 1. Photolithography and wet chemical etching were used to define the test structure. $FeCl_3$ was used to etch Ni and Mo. The silicides were etched with $HF:HNO_3$:2-5 H_2O, but this was not effective for $TiSi_2$. Accurate dimensions of this structure were measured by optical microscopy for each sample tested. The electrical data were acquired with Keithely I-V and C-V equipment and software. C-V measurements of rectifying contacts were made with the probes on the central dot and outer field contacts (in this case, the outer field contact functioned as a "large area ohmic contact"). If a contact was found to be ohmic, an attempt was made to calculate the specific contact resistance using the transmission line model (TLM)[2-5]. If one allows for a possible change in the sheet resistance of the SiC under the contact, an "end resistance" measurement is needed to calculate an accurate specific contact resistance value. The end resistance was measured by a method similar to that described in ref[5].

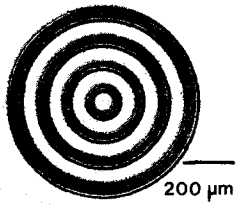


Figure 1: Circular TLM pattern

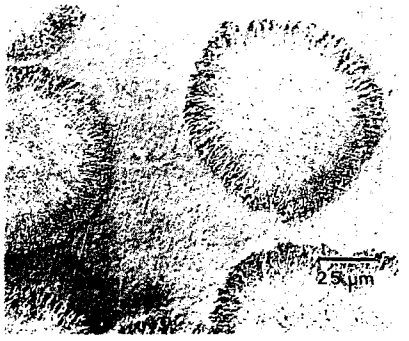


Figure 2: Ni/Mo on Si-face (annealed)

RESULTS AND DISCUSSION

After examination of all specimens by optical microscopy, the chemical composition of the films before and after annealing was obtained using AES. The optical micrographs revealed morphological changes which often assisted in interpreting the AES chemical data.

TaSi2:

The optical micrographs taken before and after RTA treatment showed a smooth surface morphology which suggested that the Ta silicide wetted to the SiC but did not undergo any major chemical reactions with the substrate.

A depth profile recorded after RTA treatment revealed that the contact film remained stoichiometric with a Ta/Si ratio of 1:2. A sharp silicide/SiC interface indicated no major chemical reaction with the substrate. At the interface, the C (KLL) peak shape represented only a trace of metal carbide,

even after annealing. The chemistry of Ta silicide was identical for metallizations on either the Si- or C-face of SiC.

Electrical measurements of as deposited films revealed them to be rectifying with Schottky barrier heights of 1.8 and 1.2 eV on the C- and Si faces respectively. Reverse leakage currents were about 10^{-5} A at -10V. After one anneal at 925°C for 2 min the contacts were too leaky for barrier height measurements, but even after an additional 4 min anneal at 925°C, they were not linear enough for TLM measurements.

MoSi2:

Results similar to Ta silicide were observed by optical microscopy on the Mo silicide metallization of 6H-SiC. Deposition of this silicide on both the Si- and C- faces yielded smooth and visually shiny surfaces, even after annealing.

The depth profiles for the Mo silicide as deposited and after annealing and on both the Si- and C-face of SiC showed no chemical reaction in the bulk silicide film nor at the silicide/SiC interface. All the profiles for Mo silicide on SiC were similar and exhibited sharp interfaces suggesting no diffusion or reaction with the SiC. From the atomic concentration profile, the Mo silicide film contained several atomic % of oxygen which remained in the film after annealing.

After annealing this silicide, a small amount of Mo carbide was detected at the interface when the individual C (KLL) peak shapes, which were recorded during the profile, were examined. The peak shape exhibited a metallic carbide with some spectral overlapping most likely from the carbon in the SiC. The formation of the metal carbide species at the interface could contribute to the adhesion of the Mo silicide to the SiC.

The as deposited contacts were Schottky with a barrier height of 1.0 eV for both polarities. The samples went through an identical annealing sequence as $TaSi_2$ with similar results.

TiSi2:

The surface structure of this silicide after deposition was smooth. After RTA treatment, the surface morphology of the metallization on both the Si- and C-face became rougher.

The depth profile recorded after RTA treatment showed a broader Metal/SiC interface, as compared to the Ta and Mo silicide profiles obtained after annealing. Ti silicide was slightly more reactive. A gradual and steady depletion of Ti started about halfway into the metallization layer and continued through the interface into the substrate. This contact film was Si deficient due to inaccurate control of the thicknesses of the Ti/Si multilayers.

An oxide surface layer, several hundred angstroms thick, was also detected from the depth profile data. From an AES survey scan recorded before sputtering the annealed Ti silicide surface, the major elements identified were Ti and O with only a trace of Si and carbon. Less than 100 angstroms of surface oxide were observed for Ta and Mo silicide. This is explained by the presence of excess elemental Ti in the multilayer structures reacting with residual O_2 in the annealing ambient. In the case of Ta and Mo silicides, the peak position and peak shape of the Si (LVV) AES transitions for the surface Si indicated the presence of a reduced Si species, either elemental Si or silicide, and an oxidized Si species. The single sharp transition for the reduced Si occurred near 90eV and a doublet appeared between 60-80eV for the oxidized Si.

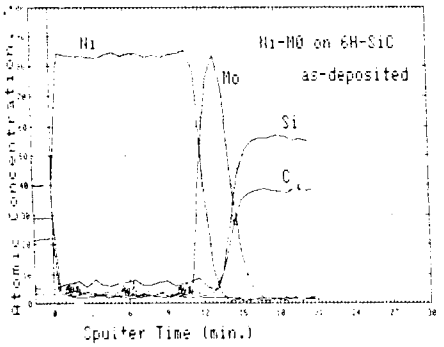
Due to etching difficulties no electrical data was obtained for $TiSi_2$. Future work will rely on reactive ion etching with SF_6.

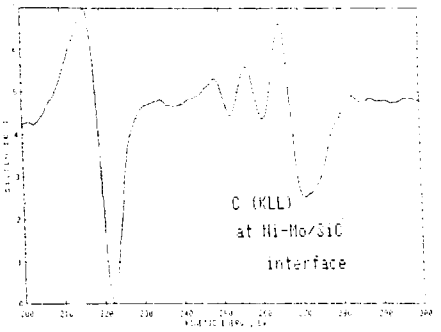
Ni-Mo:

The optical microscopy revealed that the reactivity of the contact material was dependent upon the substrate's crystal orientation. The surface condition of this metallization on the Si-face changed dramatically after annealing from a somewhat grainy structure, to a very blotchy surface with large circular, rough defect sites as shown in Figure 2. The Ni/Mo bilayer film deposited onto the C-face SiC specimen was uniformly rough after annealing, with a texture similar to the circular blotches on the Si-face. No circular features were observed.

The AES data provided considerable chemical information about the contact film both before and after annealing. The as-deposited films showed a similar chemistry which was independent of the crystal face of the SiC substrate. A representative depth profile for the as-deposited Ni-Mo film on 6H-SiC is shown in Figure 3. The Mo/SiC interface was fairly sharp before annealing. A well-defined MoC species was present at the interface. The C peak shape at the interface, shown in Figure 4, was identical to a reference spectrum of MoC [6].

The non-uniformity of the contact film on the Si-face specimen, after





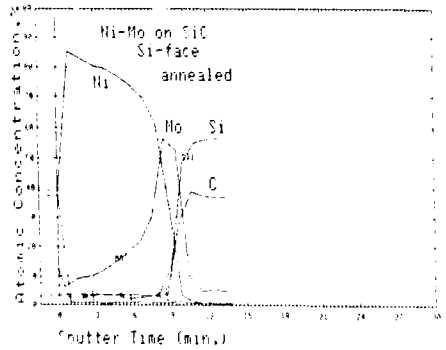


Figure 3: Ni/Mo AES profile(as dep.) (top, left)
Figure 4: C peak at Ni/Mo-SiC interface (top, right)

Figure 5: AES profile of rough Ni/Mo area (bottom, left)

annealing, required the scanning capability of the AES spectrometer. In Figure 5, the depth profile for the grainy areas outside the raised, blotchy circular defect sites, indicated that Mo remained primarily at the interface with some

interface.

The depth profile recorded on a blotchy area of the Si face revealed almost complete degradation of the diffusion barrier layer. A similar reaction, only less severe, was also detected after annealing the contact film deposited onto the C face SiC. In Figure 6, recorded after RTA treatment of the C face specimen, the top 100 angstroms consisted of a Ni_xSi_y species followed by a Mo rich layer several hundred angstroms thick. The bulk of the contact film was composed of Ni, Si, and a neutral C species. The interface between the metallization film and the SiC substrate was very broad.

The as deposited films were rectifying with barrier heights of 1.8 eV on the C-face and 0.9 eV on the Si-face. One pair of samples was annealed initially at 825°C for 2 min and another pair was annealed at 700°C for 2 min. This decreased the barrier height from 1.8 eV on the C-face, to 1.2 and 1.0 eV after the high and low temperature anneals respectively. The high temperature anneal did not effect the barrier height on the Si-face, but after a low temperature anneal the contacts were too leaky to be measured. All of the

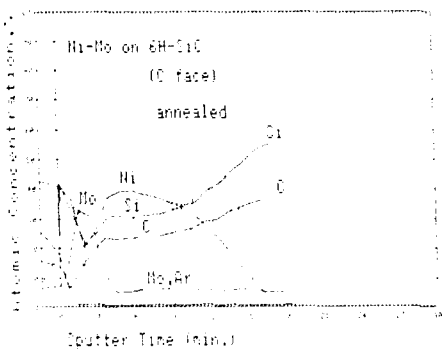


Figure 6: AES profile of Ni/Mo on C-face

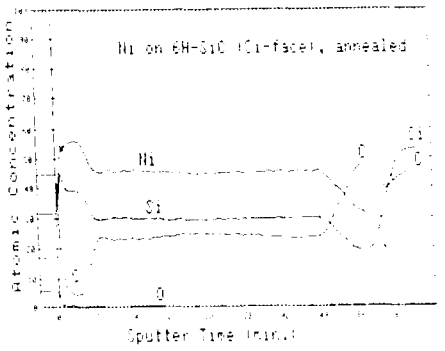


Figure 7: AES profile of Ni film

contacts went through an additional 825°C, 2 min anneal, followed by a 925°C, 2 min anneal. At this point the Si-face samples displayed a linear, ohmic I-V characteristic. Analysis of TLM data by the technique described in ref[4] yielded specific contact resistance values between $2x10^{-3}$ and $7x10^{-4}$ $\Omega \cdot cm^2$ measured with multiple test structures on both samples. No dependence on initial anneal temperature could be detected. It appears that the sheet resistance of the SiC under the contacts has increased, but the spread in the values for end resistance made it difficult to determine the exact amount. Uncertainty in the measurements of end resistance also account for the spread in the specific contact resistance values.

Ni:

The optical microscopy for the as deposited Ni on SiC revealed fairly smooth surfaces, independent of the crystal face. Even after annealing, the resulting surface structure was independent of the crystal face. The texture of both surfaces became grainy after thermal treatment, indicating a chemical reaction with the substrate.

The AES data were similar for Ni on the different SiC faces. The depth profiles for the as-deposited films showed sharp Ni/SiC interfaces. The profiles recorded after annealing revealed extreme reactivity with the substrate. In Figure 7, a NiSi species was detected in the top 100 angstroms

of the annealed metallization film. The bulk film was no longer Ni but a complex mixture of Ni, Si, and a neutral C species. Also at the interface before bulk substrate material was exposed, a large amount of neutral C was present.

The peak shape of this C species was identified as an amorphous, neutral C or a graphitic C species and was similar to that observed in previous studies [7]. The C peak shape for the C species in the bulk, ion-damaged SiC substrate exhibited a weak minimum immediately before the major KLL transition occurring at 274eV as compared to the weak maximum displayed in the amorphous or graphite type C in the upper spectrum.

The contacts were Schottky as deposited, with barrier heights of 2.2 eV on the C-face and 1.5 eV on the Si-face. Annealing was expected to form ohmic contacts, but the contacts were still rectifying after two 2 min anneals at 825°C. Visually the films were dull, grainy, and nonuniform. We believe contamination of the RTA is responsible for this poor result.

SUMMARY AND CONCLUSION

The silicide films appeared to be the most stable, with little reaction on either face. The Ni/Mo films were more stable on the Si-face and formed ohmic contacts more easily on this face. Elemental Ni was unstable on both faces, and reacted to yield a lot of free carbon at the interface. $MoSi_2$ and $TaSi_2$ formed metallic carbides after annealing, as did Ni/Mo on the Si face.

The Schottky barrier heights were higher (1.8-2.2 eV) on the C face than on the Si-face for all contacts except $MoSi_2$. Ni/Mo films formed ohmic contacts after annealing with contact resistances around $1x10^{-3}$. More work is needed to develop stable Schottky and ohmic contacts with good electrical characteristics.

ACKNOWLEDGMENTS

This work was done with internal funding support. The authors wish to thank Carl Salupo for performing depositions and anneals, Phil Neudeck for assistance with I-V and C-V tests, Tony Powell for the p-type samples, and Darwin Boyd for AES trouble shooting.

REFERENCES

1. B.J.Baliga, presented at the 4th ICACSC Conference, Oct. 1991, Santa Clara, CA
2. S.S. Cohen and G.SH. Gildenblatt, Metal-Semiconductor Contacts and Devices, (VLSI Electronics vol. 13, Academic Press, Inc., Orlando, 1986), pp.97-116.
3. G.S. Marlow and M.B. Das, Sol. St. Elect., 25, 91 (1982)
4. G.K. Reeves, Sol. St. Elect., 23, 487 (1980)
5. G.K. Reeves and H.B. Harrison, IEEE Elect. Dev. Lett., EDL-3, 111 (1982)
6. J.T. Grant and T.W. Haas, Surf. Sci.,23, 347 (1970)
7. M.V. Zeller, J. Bellina, N. Saha, J. Filar, J. Hargraeves, and H.A. Will, in Novel Refractory Semiconductors, edited by M. Stavola, S.J. Pearton, and G. Davies (Mater. Res. Proc. 97, Pittsburgh, PA,1987), p.283.

High Temperature Ohmic Contacts for n-type ß-SiC Sensors

J.S. Shor*, R.A. Weber, L.G. Provost, D. Goldstein and A.D. Kurtz

Kulite Semiconductor Products, Inc, Leonia, NJ
**also Columbia University, Microelectronics Sciences Laboratories, NY, NY*

Abstract

In order to fabricate high temperature sensors and other devices, it is necessary to develop ohmic contact metallizations that can withstand elevated temperatures. A variety of ohmic contact metallizations were investigated with contact resistivity measured as a function of anneal time in air. The metallizations were based on Ti and W ohmic contacts, which have contact resistivities as low as 10^{-4} Ω-cm^2. Several of the contact metallizations were stable after 10 hrs. at 650°C, while one system, based on a Ti ohmic contact, was able to withstand > 20 hrs. at 650°C with only a 30-40% increase in contact resistivity.

Introduction

Recently, there has been much interest in semiconducting SiC due to advances in growth techniques and device development [1-3]. SiC exhibits unique properties such as a wide band-gap, high melting point and large thermal conductivity [4], which allow it to operate at high temperatures. In addition, SiC has good mechanical properties at high temperatures [4] and large piezoresistive coefficients [5], making it attractive for high temperature pressure sensors. The research program at Kulite has addressed many of the issues in sensor fabrication including sensor characterization [6], etching [7] and wafer thinning [8]. This paper is the first reporting of our efforts to develop a contact metallization which is useful at elevated temperatures.

Discrete pressure sensors typically have contacts which are much larger than those used in VLSI applications. For example, the silicon devices manufactured at Kulite use contact windows which are 40-150 μm squares [9]. Thus, contact resistivities as high as 10^{-3}-10^{-4} are acceptable for these metallizations. Nevertheless, for high temperature applications, the contacts must be able to withstand elevated temperatures in oxygen rich environments for extended time periods without any major change in the contact resistivity. In addition, the metallization must not lose adhesion to the semiconductor or to oxide layers with which it is in contact. It must also be easily bonded to interconnects, such as Au or Pt wires. Our first goal was to produce metallizations which could fulfill these requirements at 650°C for > 10 hrs. These contacts would be useful for high temperature test measurements, which use sensors whose operating lifetimes are between 10-50 hrs.

There has been a limited amount of research done on metal/SiC contacts. In an early study, Edmond et. al. reported several ohmic contacts on n- and p-type 3C-SiC with contact resistivities as low as 10^{-3} Ω-cm^2 [10]. Bellina, et. al. reported on the reaction of Ti with ß-SiC and found that TiC formed at temperatures as low as 350°C [11]. Furthermore, the formation of TiC was not self limiting unless the SiC layer was carbon rich. On a carbon rich surface, monolayers of TiC could be formed at the Ti/SiC interface, but the Ti would not react further even after 500 hrs. at 800°C. Geib et. al. found that Ta reacted readily at 400°C to form TaC and was not self-limiting, while Mo and W formed very stable Carbides which would not react

significantly at 850°C [12]. Recently, McMullin et. al. examined the durability of metallizations based on Ta, Ti, and W at 600°C in non-oxidizing environments [13].

In this study, several metallizations based on Ti and W were examined. Ti was chosen for its excellent adhesive properties while W has a very close thermal match to SiC and forms a more stable carbide. The room temperature contact resistivity was measured as a function of anneal time in air. In all of the metallizations tested, a thin (300 Å) layer of Au was deposited on top of the conductive layer to make the subsequent ultrasonic bonding process easier.

Experimental

Contact resistivity was measured using the four point probe method developed by Terry and Wilson [14] and modified by Kuphal [15], as shown in Fig. 1. In general, the resistance between two ohmic contacts has three components; (1) the contact resistance, (2) the sheet resistance of the material underneath the layers, and (3) the spreading resistance. When a constant current, I, is applied between the two end contacts, a and d, of a four point measurement (Fig. 1) the voltage drop between the two middle contacts, V_{bc}, is due only to the sheet resistance of the semiconductor. Therefore, the contact resistivity can be measured from the following equation;

$$R_c = A/I_{ad}[V_{ab} - R_s - V_{bc}\{\ln((3s/d) - 1/2)/(2\ln 2)\}]$$

where R_c=contact resistivity, R_s=spreading resistance, d = contact diameter while s is the spacing between the contacts. The logarithmic term that multiplies V_{bc} takes into account the potential drop between two circular contacts. If the contacts are small enough for a given sample thickness, the spreading resistance can be neglected [15]. In these experiments, the spreading resistance term accounted for less than 25% of the measured contact resistivity.

The ß-SiC wafers used in this study were grown at the NASA Lewis research center by previously described means [1]. These unintentionally doped films were 10 μm thick and had resistivities ranging between 0.2-0.8 Ω-cm. The samples were cleaned using the RCA method and were sputtered with a 4000 Å layer of quartz. Contact windows were opened up in the quartz using photolithography and the samples were then degreased and cleaned again by the RCA method. Before the metals were sputtered, the samples were sputter etched to a depth of 200 Å. The background pressure in the sputter system was in the low 10^{-7} Torr range while the Ar pressure used during sputtering was 15 μms. TiN was reactively sputtered from a Ti target in a 20% N_2/Ar atmosphere. The Pt and Au layers were patterned using 10:9:1 H_2O:HCl:HNO_3, while Ti, TiW, and TiN were etched using an EDTA/H_2O_2 solution. The size of the metal pads were several times larger than the contact windows to prevent any etch undercutting from affecting the results. Before the experiments began, several test films were analyzed using AES and XPS to check for film purity. The Ti, TiW, and TiN films were relatively oxygen free, containing < 3% oxygen. Pt and Au films were free of any traceable impurities. The TiN films were bronze colored and had a Ti/N ratio of ≈ 1 based on their XPS lineshapes.

Contact resistivity measurements were taken from a 0.5 cm x 0.5 cm chip with 32 four point probe layouts on it. Contact sizes ranged from 5 μm-30 μm diameters, and the spacing between the contacts was 225 μm. The chips were annealed in air at 650°C and 750°C after

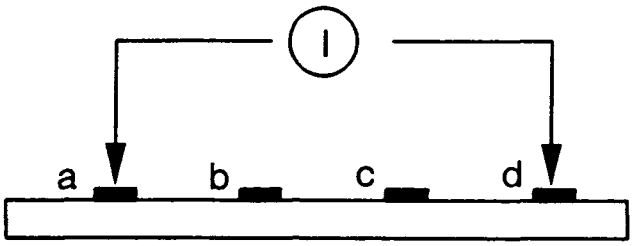


Fig. 1: Four point probe measurement of contact resistivity as suggested by Kuphal [15].

which the room temperature contact resistivity was measured.

Ti/Pt and W/Pt Contacts

The first metallization that was attempted was a thin layer of titanium (400 Å) covered with a thick layer of Pt (6000Å). These contacts were used earlier in a study of ß-SiC strain gauges [6] and operated for several hours at 550°C. However, since Ti and Pt interdiffuse readily at temperatures above 500°C, the contacts eventually peeled off the SiC. Contact resistivities of the 'as deposited' films ranged from $9x10^{-5}$-$2.5x10^{-4}$ Ω-cm^2. A one hour anneal at 650°C caused the contact resistivity to decrease by roughly a factor of two. Linear i-V characteristic of the contacts were observed at 650°C, indicating that they remain ohmic at these high temperatures. After two hours at 650°C, most of the Ti/Pt contacts failed, indicating that this metallization will not fulfill the requirements for high temperature sensors.

W/Pt should provide a more stable contact than Ti/Pt for two reasons: 1) It forms a more stable carbide and 2) W diffuses much less that titanium and in fact has been used as barrier for Ti based metallizations [13]. Fig. 2 shows the contact resistivity of W(1400Å)/Pt(6000Å)/ Au(300Å) films as function of anneal time at 650°C. Unlike the Ti based contacts, there was no sharp initial decrease in the contact resistivity, but rather the contact resistivity decreased by only 7% over the 8 hour time span. This decrease in contact resistivity may be due to a slow carbide formation. The contacts were electrically and mechanically stable after 8 hrs. at 650°C, although some peeling was observed at the edges on the oxide. This peeling may have been an artifact of the metal etch which caused an undercut of the W layer. All of the contacts failed due to loss of adhesion after 15 hours at 650°C or after one hour at 750°C. This failure may due to a) diffusion of the Pt into the W, b) the oxidation of W, or c) a combination of oxidation and diffusion. However, the success of this metallization for 8 hours indicates that it may have some limited usefulness at temperatures between 500-650°C.

ß-SiC/W(1400Å)/Pt(6000Å)/Au(300Å)

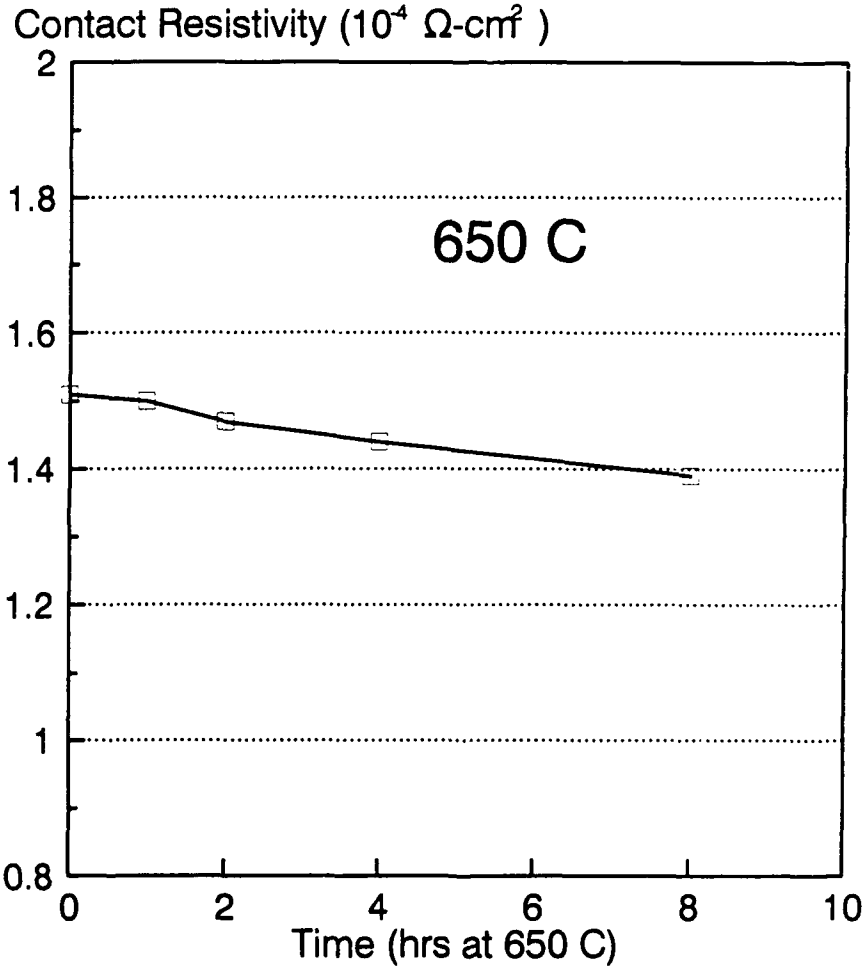


Fig.2: Room temperature contact resistivity of W(1400Å)/Pt(6000Å)/Au(300Å) on n-type ß-SiC as a function of anneal time at 650°C in air.

Diffusion Barriers Between Ti and Pt

In order to improve the contacts, TiW and TiN diffusion barriers were used to prevent the mixing of Ti and Pt layers. TiW is a good diffusion barrier since W is very immobile and the Ti content promotes adhesion. TiN is an amorphous compound, thus eliminating effects such as grain boundary diffusion.

Ti(400Å)/TiW(1400Å)/Pt(6000Å)/Au(300Å) contacts were used in the strain gauge measurements mentioned earlier [6]. These strain gauges were simply thin film rectangular resistors with two contacts and leads at each end. Although this configuration did not allow an exact measurement of the contact resistivity, the failure of the gauges after heat treatment could be attributed to the metallization and thus could act as a measure of the usefulness of the contacts. The strain gauges had resistances ranging between 100-2000 Ω at room temperature. After 3-5 hours at 650°C, the gauge resistance increased rapidly, presumably due to an increase in contact resistivity, which indicates the limitations of this metallization.

Fig. 3 shows the contact resistivity of a Ti(400Å)/TiN(1000Å)/Pt(6000Å)/Au(300Å) metallization as a function of anneal time at 650°C. The contact resistivity showed a similar initial decrease as the Ti/Pt films, after which it increased at a rate of $\approx$ 2%/hr. These contacts were electrically stable after 20 hrs. at 650°C. Most of the contacts became rectifying after 31 hrs. at 650°C, an effect which also occurred after 4 hrs. at 750°C.

SEM photographs of the Ti/TiN/Pt/Au contacts before and after a 20 hr anneal at 650°C are shown in Fig. 4a and 4b. No significant peeling or buckling of the films occurred after the heat treatment, with the exception of a small bubble that is present on the heat treated contact of Fig. 4b. Bubbles of this sort formed sometimes after one hr at 650°C, but did not change with time at this temperature. The bubbles are probably caused by a stress relief effect and not by contamination, since the bubble formation, when it occurred, was very regular within each chip, with exactly one bubble forming on almost all of the larger contacts (15-30 μm) and no bubbles forming on the smaller ones (5-10 μm). The adhesion of the metallization to the oxide layer remained very stable after the anneal. Fig. 4b also shows that some surface roughening occurs, but this does not seem to significantly affect the electrical or mechanical properties of the films. The roughness on the edge of the 'as deposited' contact of Fig. 4a is due to etch undercutting of the thin Au layer.

These results indicate that the Ti/TiN/Pt/Au metallization is both electrically and mechanically stable after > 20 hrs at 650°C and has a low enough contact resistivity to meet the sensor requirements delineated above. Thus, it may be useful for test sensors that operate between 600-700°C or for more reliable instrumentation sensors to operate between 500-550°C. It may be possible to decrease the contact resistivity of this metallization by using a more highly doped SiC layer, enabling it to meet some of the needs of high temperature IC components.

Ti/TiW/Pt/Au films were analyzed using Auger electron spectroscopy to observe carbide formation at the Ti/SiC interface. This interface is shown in Fig. 5, which traces the relative atomic concentration of Ti, Carbon and Si in the 400 Å Ti layer after a 3 hr anneal at 650°C in nitrogen. Pt and W signals were both below the noise level within this layer and thus are not shown. The Ti line closely follows the carbon line which suggests that TiC formed throughout the layer. Previous anneals of Ti/SiC at this temperature had a shifted carbon lineshape which indicates the formation of TiC. Excess Si, caused by the breaking of the Si-C bond may have diffused outward and thus does not appear at the interface. This result gives some insight into the behavior of the Ti based contacts. After one hr. at 650°C, all of these contacts exhibited a sharp drop in contact resistivity, which is probably due to TiC formation. Once the entire Ti layer was consumed, the contact resistivity did not decrease further with temperature.

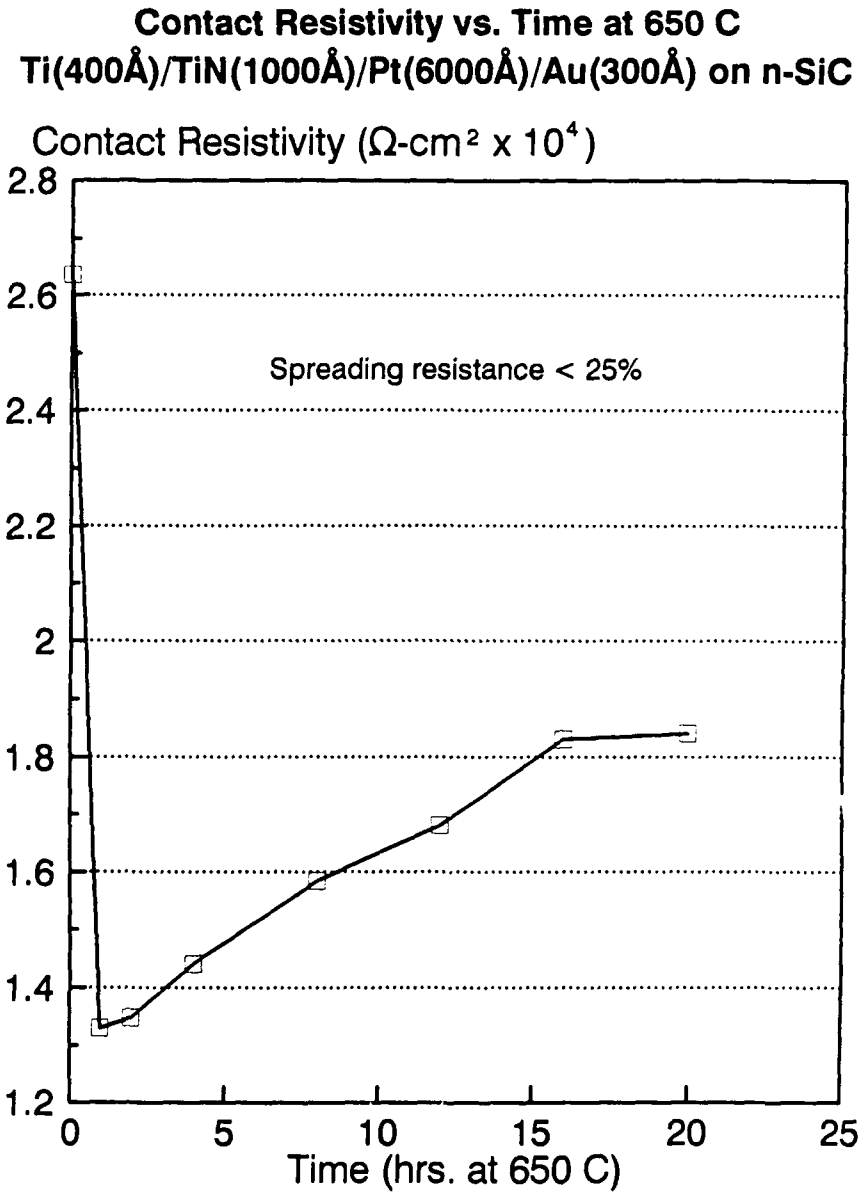


Fig. 3: Room temperature contact resistivity of Ti(400Å)/TiN(1000Å)/Pt(6000Å)/Au(300Å) on n-type ß-SiC as a function of anneal time in air.

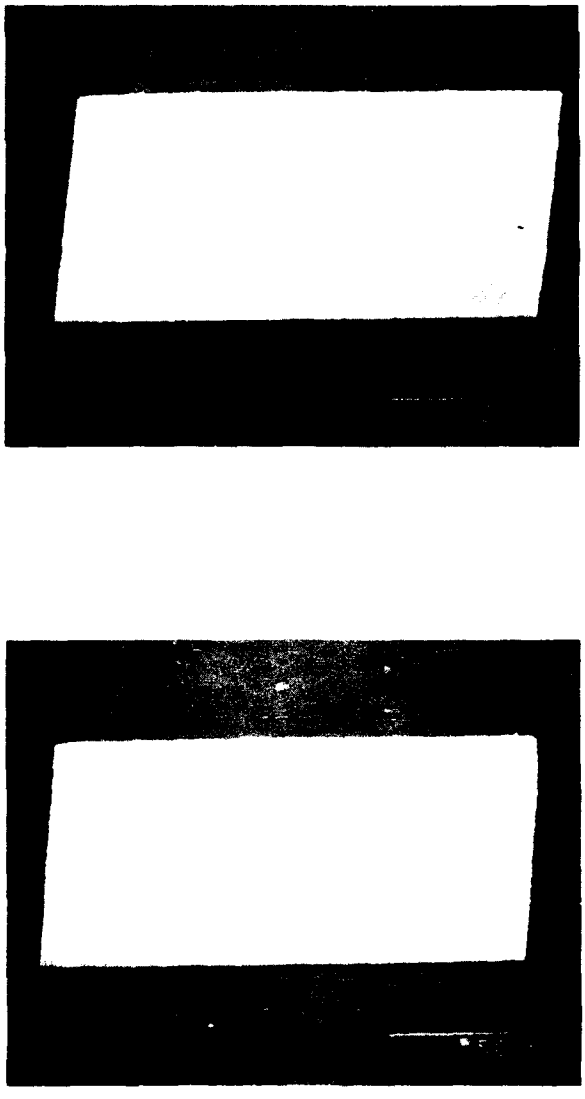


Fig. 4: SEM micrographs of Ti/TiN/Pt/Au contacts on SiC a) as deposited, and b) after 20 hrs. at 650°C in air.

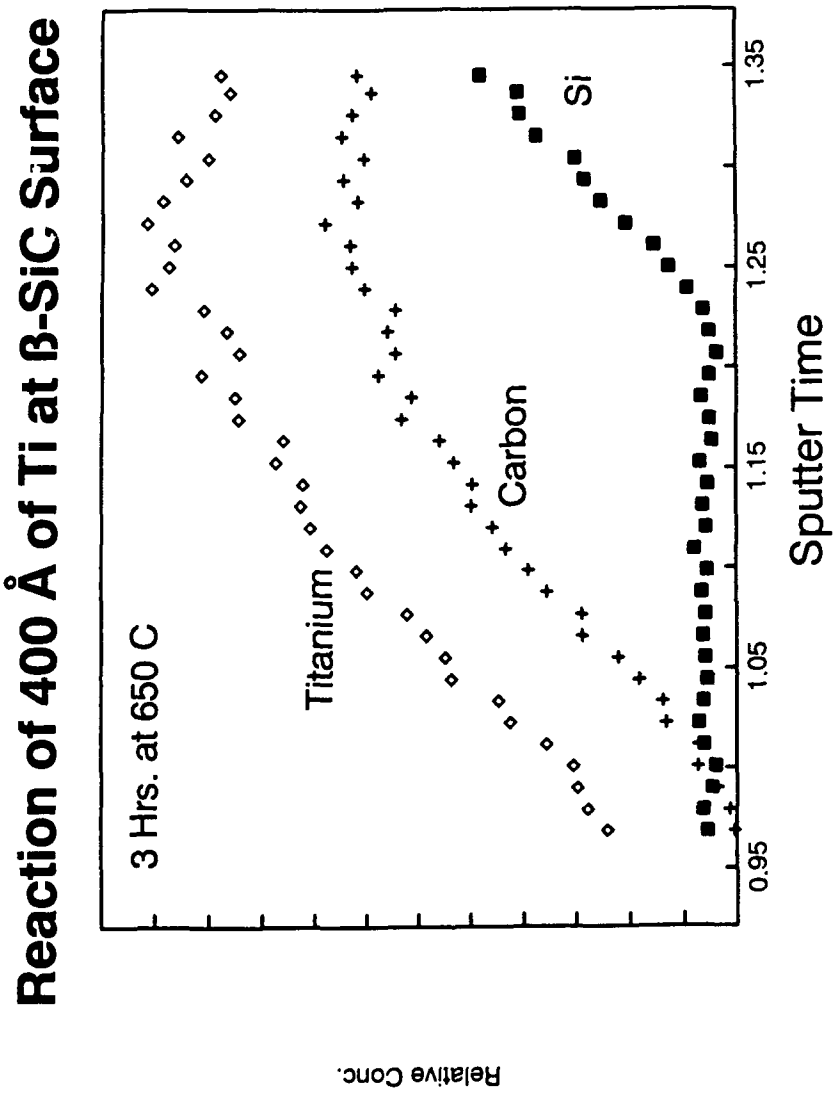


Fig. 5: Auger depth profile of a 400Å Ti film on ß-SiC after 3 hrs. at 650°C in nitrogen.

Conclusion

We have investigated several ohmic contact metallizations on n-type 3C-SiC. Of the metallizations tested, W/Pt/Au was reliable for 8 hrs. at 650°C while Ti/TiN/Pt/Au was able to withstand > 20 hrs. at that temperature without significant deterioration of the electrical or mechanical properties. This work demonstrates that by using the diffusion barrier approach, the lifetime of contact metallizations on SiC may be increased significantly. Extending these concepts to other polytypes and crystal orientations including polar faces of SiC should also be possible.

Acknowledgements

We would like to thank J.A. Powell and L.G. Matus of NASA Lewis for providing the SiC samples and for their useful discussions. We would also like to thank R.M. Osgood of Columbia University for his support.

References

1. J.A. Powell, L.G. Matus, and M.A. Kuczmarski: J. Electrochem. Soc. **134**, 1558 (1987).
2. C. H. Carter, L. Tang, and R.F. Davis, presented at the Fourth National Review Meeting on the Growth and Characterization of SiC, Raleigh, NC, 1987.
3. L.G. Matus, J.A. Powell, C.S. Salupo: Appl. Phys. Lett. **59**, 1770 (1991)
4. " *SiC 1973* " edited by R.C. Marshall, J.W. Faust and C.E. Ryan. Univ. of S. Carolina Press. p. 666.
5. J.S. Shor, D. Goldstein and A.D. Kurtz, in "Amorphous and Crystalline SiC III, to be published by Springer-Verlag.
6. J.S. Shor, D. Goldstein, and A.D. Kurtz in "Transducers 91' Digest of Technical Papers" p. 912-916 (IEEE Press, 1991).
7. J.S. Shor, X.G. Zhang and R.M. Osgood: to be published in J. Electrochem. Soc.
8. J.S. Shor, A.D. Kurtz and R.M. Osgood: to be published in Appl. Phys. Lett.
9. Kulite Semiconductor Products, Inc. Leonia, NJ.
10. J.A. Edmond, J. Ryu, J.T. Glass and R.F. Davis: J. Electrochem. Soc. **135**, 359 (1988).
11. J.J. Bellina and M.V. Zeller: Mat. Res. Soc. Symp. **97**, 265 (1987)
12. K.M. Geib, C. Wilson, R.G. Long, and C.W. Wilmsen: J. Appl. Phys. **68**, 2796 (1990)
13. P.G. McMullin, J.A. Spitznagel, J.R. Szedon and J.A. Costello, to be published in "Amorphous and Crystalline SiC III" Springer-Verlag Press.
14. L.E. Terry and R.W. Wilson: Proc. IEEE **57**, 1580 (1969).
15. E. Kuphal: Solid State Electron. **24**, 69 (1981).

PART VII

Boron Nitride and Other Boron Compounds

HETEROEPITAXIAL GROWTH OF CUBIC BORON NITRIDE ON SILICON

G. L. DOLL[a], T. A. PERRY[a], J. A. SELL[a], C. A. TAYLOR[b], and R. CLARKE[b]
[a]Physics Department, General Motors Research Laboratories, Warren, MI 48090-9055
[b]Harrison B. Randall Laboratory of Physics, Ann Arbor, MI 48109-1120

ABSTRACT

New x-ray diffraction measurements performed on boron nitride films deposited by pulsed excimer laser deposition are presented. The x-ray data, taken with both a molybdenum rotating anode source and synchrotron radiation, indicate that the epitaxial cBN films are $\leq$ 200 Å thick. We also report the successful growth of oriented crystalline diamond on the (001) surface of cBN/Si substrates using the method of pulsed laser deposition. X-ray diffraction measurements indicate that the diamond layer is 200 Å thick with a lattice constant of 3.56 Å. The structures of metastable films (cBN and diamond) are very sensitive to growth conditions: we present evidence that an epitaxial-crystalline to incoherent phase transition occurs when the thickness of the films exceeds a critical value ($\sim$ 200 Å for our present growth conditions).

INTRODUCTION

The development of both cubic boron nitride (cBN) and diamond in thin film form has been pursued vigorously over the last several years. This rapid increase in wide-bandgap semiconductor research can be attributed to the technological impact that these materials would have on electronic and optical devices [1]. Several deposition processes have proven to be successful in the growth of diamond coatings, but the most widely utilized is plasma enhanced chemical vapor deposition (PECVD). It has been shown that under appropriate growth conditions diamond can be grown on a variety of substrates [2]. However, regardless of the deposition technique chosen, the resulting diamond coating is usually polycrystalline and multifaceted with a rough surface. Such films are rarely epitaxial with the substrate except when grown on bulk diamond [3] or cubic boron nitride [4]. Recent work on ion-implanted surfaces reports that epitaxial diamond films may also be grown on copper [5].

In many ways the growth of high quality cBN films has been more elusive than the growth of diamond. While many deposition techniques have been pursued, there exists no single widely used process for the growth of cBN thin films. Deposition techniques such as reactive magnetron sputtering, PECVD, ion beam bombardment, and reactive evaporation result in multiphase, polycrystalline, randomly oriented boron nitride films except when grown on bulk cBN [6] or diamond [7]. As with diamond films, the layers are either of much too poor quality to be useful for electronic device applications or, as is the case with films grown on bulk diamond, they are economically unfeasable to be considered for large

scale production. The only method that has been shown to produce epitaxial cBN films on a substrate other than diamond or bulk cBN, is the method of pulsed excimer laser deposition (PLD) [8]. With this technique, thin epitaxial cBN films can be grown on (001) silicon substrates.

In this paper we present new results on the growth and structural characterization of cubic boron nitride films grown epitaxially on (001) silicon substrates. We also report evidence for the first successful growth of oriented diamond films, deposited by pulsed laser deposition, on the epitaxial cBN.

EXPERIMENTAL

Boron nitride films have been grown on polished, p-type (001) silicon wafers. All substrate preparation procedures and growth conditions for the boron nitride deposition have been described in previous publications [8,9]. The most recent samples prepared by this method typically have a total film thickness of approximately 200 Å of BN, and were grown on one inch diameter silicon wafers.

X-ray diffraction studies were carried out at The University of Michigan using a four-circle diffractometer with a rotating Mo-anode source and graphite crystal monochromater. In addition, high resolution scans have been performed on several cBN/Si films with synchrotron radiation at the National Synchrotron Light Source at Brookhaven National Laboratory.

DISCUSSION AND RESULTS

The crystallinity, composition, and chemical bonding of BN films (total thickness 1000 – 1200 Å) grown by pulsed excimer laser deposition have been investigated previously using TEM [8], x-ray diffraction [8], Auger electron spectroscopy (AES) [9], electron probe microanalysis (EPMA) [10], Rutherford backscattering spectroscopy (RBS) [10], electron energy loss spectroscopy (EELS) [9], spectroscopic ellipsometry [11], and infrared absorption [9]. Taken collectively, these data indicate that a thin ($\lesssim$ 200 Å) epitaxial cBN layer is present at the Si interface with the remainder of the film appearing to be incoherent sp^2-bonded BN.

The high resolution (00ℓ) x-ray diffraction measurements, with the diffraction vector perpendicular to the silicon substrate surface, give no evidence for either elemental boron or hexagonal BN in any of the BN films we have prepared [8]. We have also noted previously that the cBN (004) x-ray peaks (which lie close to the position of the normally forbidden Si(006) reflection) remain instrumentally narrow even for very thin ($\lesssim$ 100 Å) films. This gives evidence that the Si substrate symmetry may, in some way, be contributing to these diffraction peaks. This effect is currently under investigation.

Fig. 1 shows a very weak x-ray diffraction peak taken from a BN film. The position of the peak indexes to the (002) reflection of cBN with a lattice constant a_0 = 3.62 Å. A

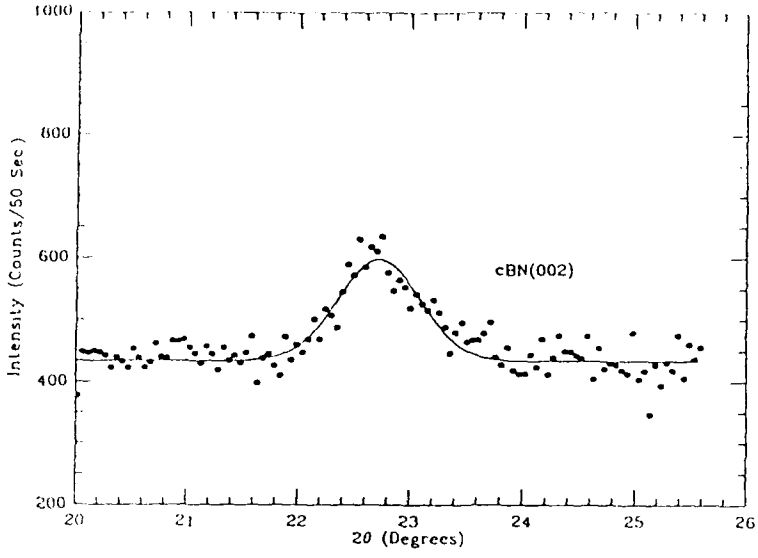


Figure 1: Conventional $\theta - 2\theta$ x-ray diffraction scan of cBN/Si using a Mo rotating anode generator ($\lambda = 0.71$ Å). The position of the peak is consistent with an (002) reflection from a cBN film having a lattice constant of 3.62 Å.

structure factor analysis of the zinc-blende structure indicates that the strongest reflection is the (111), which is $10 - 20$ times more intense than the (002). The cBN (111) reflection has not been observed in (00ℓ) scans on any of the BN films we have grown on (001) Si. This indicates that the cBN is not randomly oriented with the silicon substrate. Using the Debye-Scherrer equation [12], the width of the cBN (002) peak indicates that the cBN film thickness is approximately 100 Å, even though the total film thickness is known to be approximately 700 Å. The inability to resolve the $K\alpha_1$ and $K\alpha_2$ splitting of the cBN (002) peak inhibits an accurate determination of the film thickness. Since the intensity of this peak is nearing the instrumental limit of detection for our rotating anode generator, we have performed synchrotron studies on thin (total thickness $\leq$ 200 Å) films to more accurately determine the thickness of the epitaxial cBN layer. Fig. 2 shows a scan of the synchrotron x-ray intensity with the diffraction vector, $\vec{k}$, normal to the substrate surface. The data is consistent with a cBN (002) diffraction peak from a film approximately 175 Å thick. These x-ray results confirm the conclusions of our previous investigations [8-10]. That is, an epitaxial cBN film $\sim$ 200 Å thick grows initially on the silicon surface, but beyond this thickness the BN film becomes incoherent.

The apparent $\sim$ 200 Å epitaxial film thickness is not well understood at this time;

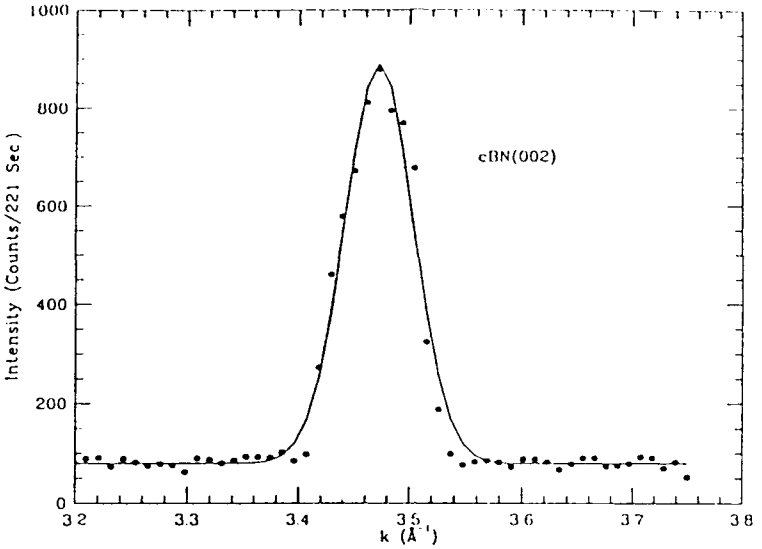


Figure 2: X-ray diffraction (00ℓ) scan of cBN/Si using synchrotron radiation (λ = 1.744 Å). The position and width of the peak is consistent with an (002) reflection from a cBN film having a lattice constant of 3.62 Å, and a thickness of $\sim$ 175 Å.

however, crystalline to incoherent phase transitions have been observed in other epitaxial systems [13,14]. In the growth of homoepitaxial Si, Eaglesham *et al.* [13] have shown that there is an epitaxial thickness, h_{epi}, at which a growing epitaxial layer becomes incoherent (10 to 30 Å for growth on ambient temperature substrates). They attributed the breakdown in epitaxy to a roughening of the growth surface, which causes a nucleation of an incoherent phase. A similar breakdown in epitaxy has been observed [14] in the homoepitaxial growth of GaAs, which among other things depends strongly on composition. This point may be particularly salient to the epitaxial growth of laser deposited cBN. It has been shown [15] that the hBN target experiences melting and undergoes a partial elemental decomposition during the laser deposition process. That is, as a result of the beam-solid interaction, nitrogen is liberated to the gas phase from the melt and the irradiated region of the target condenses to a nitrogen deficient material, $BN_{0.8}$. Subsequent laser pulses on the nitrogen deficient target lead to a nitrogen deficient film. Experimental techniques exist, and are currently being investigated, to increase the thickness of the epitaxial cBN layer [13,14].

Because of the good lattice match (1.4 %), diamond can be grown heteroepitaxially on cBN [4]. We attempted to grow diamond on cBN/Si (with the total BN film thickness less than 100 Å) using the hot-filament CVD technique. These attempts were unsuccessful

because the carbon species generated by the plasma completely etched away the cBN leaving bare silicon. This is not surprising in view of the fact that CH_4/H_2 plasmas are routinely used to etch the surfaces of III-V compounds prior to epitaxial film growth [16].

Recently, we grew laser deposited carbon on some of our cBN/Si samples in hope that the cBN would nucleate the diamond phase. In this experiment, cBN films were first grown on (001) Si substrates following the procedures outlined in the previous section. The substrates were allowed to cool to room temperature in flowing N_2 and the hBN target (used to grow the cBN film) was replaced with pyrolytic graphite. With the substrate at room temperature and the chamber under vacuum (no gases flowing), 100 laser pulses were used to deposit approximately 20 Å of carbon onto the cBN/Si. During the growth of the carbon layer, the KrF laser was pulsed at 5 Hz, and had a fluence of 3.9 J cm^{-2}. The substrate temperature was then elevated to 600 °C and another 1000 pulses of carbon were deposited in approximately 3×10^{-2} torr of flowing H_2. In PECVD diamond growth, H-atoms are believed to selectively etch the sp^2-bonded carbon constituent of the film. Since the plasma generated by the laser-target interaction is believed to have a temperature in excess of 10^4 K [17], sufficient thermal energy exists near the target to dissociate molecular hydrogen. However, it is not known what effect (if any) that the hydrogen has on the carbon species grown in this deposition. Subsequent to deposition, the substrates were allowed to cool to room temperature in flowing H_2, and then removed from the chamber. The films appeared optically smooth, clear in the center and light blue on the edges.

The Raman spectrum of one of the C/cBN/Si samples is shown in Fig. 3. The spectrum has peaks near 960, 1330 and 1604 cm^{-1}. Whereas the peak near 960 cm^{-1} is a second order feature of the Raman-active silicon phonon, the peaks at 1330 and 1604 cm^{-1} are characteristic of sp^2-bonded carbon [18]. Because the Raman scattering efficiency of diamond is much less than that of sp^2-bonded carbon, the Raman spectrum (Fig. 3) is not a sensitive test for diamond in films containing other forms of carbon [18]. Low energy EELS measurements are sensitive to the chemical bonding of the film surface, but provide no information about the remainder of the film. Results of EELS measurements (not shown) performed on a C/cBN/Si sample are also consistent with the spectrum of an sp^2-bonded carbon film.

X-ray diffraction experiments, which are sensitive to the crystallinity of the entire film thickness, were performed on the C/cBN/Si film. The data indicate that the carbon film is not entirely sp^2-bonded carbon. A plot of x-ray intensity *vs.* diffraction angle (2θ) is shown in Fig. 4. Near $2\theta = 47°$, a set of diffraction peaks are present that index to the $K\alpha_1$ and $K\alpha_2$ (004) reflections of diamond ($a_0 = 3.56$ Å). The measured d-spacing from the diffraction peaks is 0.890 ± 0.003 Å, which is in excellent agreement with the (004) d-spacing of diamond (0.892 Å).

We found no evidence in the (00ℓ) x-ray diffraction data for graphite, or other

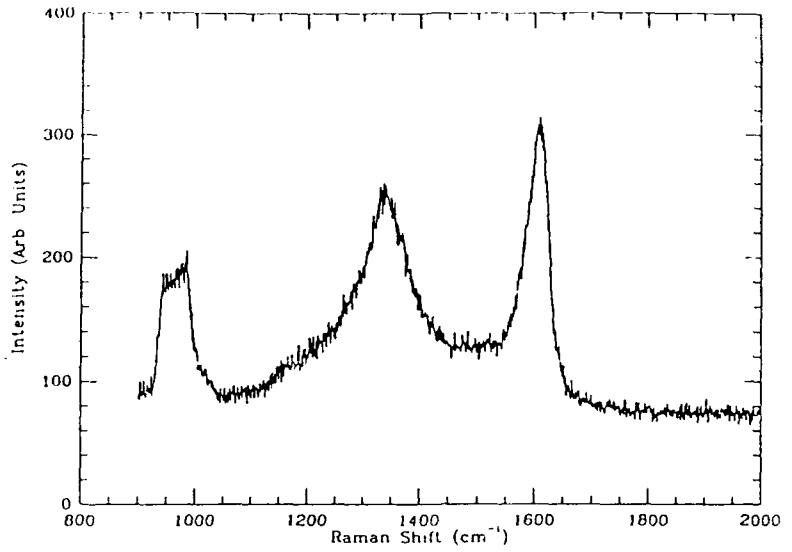


Figure 3: Raman spectrum of a C/cBN/Si film prepared by pulsed laser deposition. The peak at $\sim$ 960 cm^{-1} is a second order excitation of a Si phonon, while the peaks at 1330 and 1604 cm^{-1} are characteristic of disordered graphite.

diamond orientations. The (004) diamond reflection is not coincident with any diffraction peak from graphite, boron nitride, or silicon, and the $K\alpha_1$-$K\alpha_2$ splitting evident in the figure eliminates the possibility of a $\lambda/2$ harmonic from an x-ray peak of the silicon substrate. To our knowledge, this is the first evidence for the growth of crystalline diamond by pulsed laser deposition. Recently, Martin *et al.* [19] have reported that a few layers of hexagonal carbon with some sp^3 bonding can be grown epitaxially on (001) Si by pulsed laser deposition of graphite, but cited no evidence for diamond. Based on the Raman scattering, EELS, and diffraction data, we speculate that the diamond x-ray peaks arise from a thin diamond layer adjacent to the cBN layer, and the remainder of the carbon film is characteristic of sp^2-bonded carbon. Since more intense diamond diffraction peaks (e.g., 111 and 220) were not observed in subsequent (00ℓ) scans, we conclude that the crystalline diamond is oriented with the cBN, and hence the silicon substrate. That is, the [001] direction of the diamond is parallel to the [001] directions of the cBN and Si. The widths of the [004] diamond peaks indicate that the thickness of the diamond layer is approximately 200 Å. The diamond peak intensity is much too weak to enable us to examine the in-plane orientation with our rotating anode source. Diffraction experiments using synchrotron radiation are planned to investigate the possible diamond epitaxy. Given the similarities between cBN and diamond,

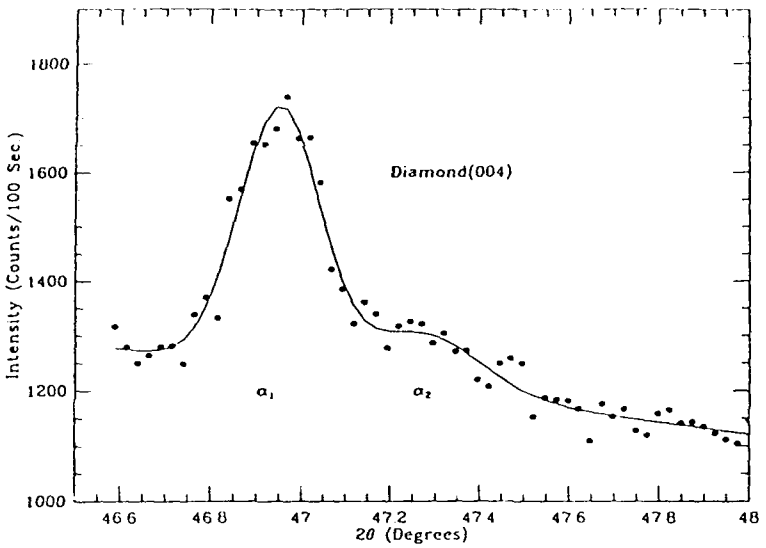


Figure 4: Conventional $\theta - 2\theta$ scan of a C/cBN/Si film using a Mo source ($\lambda = 0.71$ Å). The position of the peaks ($K\alpha_1$ and $K\alpha_2$ wavelength doublet) is consistent with the (004) reflection from a diamond film having a lattice constant of 3.56 Å and a thickness of $\sim$ 200 Å.

it is possible that the diamond may also undergo a crystalline to incoherent phase transition when the thickness of the diamond exceeds $\sim$ 200 Å.

In conclusion, we have shown for the first time, that pulsed laser deposition of carbon can result in a carbon film that contains crystalline diamond, and that the diamond is oriented with the cBN/Si. We have also presented evidence for the existence of an epitaxial-crystalline to incoherent phase transition in the growth of cBN on (001) Si. With our current growth conditions, we believe that an epitaxial thickness of approximately 200 Å can be grown before the onset of this transition.

We thank S. Kidner of U.M., and J. A. Sell, J. P. Heremans, B. K. Fuller, W. J. Meng, and especially D. L. Partin of the Physics Department of GMR for many valuable discussions. We are grateful to S. Schmeig, D. Belton, A. Weiner, and S. Harris of the Physical Chemistry Department of GMR for their XPS measurements and their collaboration in the growth of CVD diamond. We also thank B. G. Demczyk and J. Mansfield of The University of Michigan Electron Microbeam Analysis Laboratory for their assistance with the HRTEM. R. Clarke is supported in part by ONR grant N0014-91-J-1398.

References

[1] J. D. Venables et al., Status and Applications of Diamond and Diamond-like Materials: An Emerging Technology (National Academy Press, Washington, DC 1990).

[2] J. C. Angus and C. C. Hayman, *Science* **241**, 913 (1988).

[3] H. Shiomi, K. Tanabe, Y. Nishibayashi, and N. Fujimori, *Jpn. J. Appl. Phys.* **29**, 34 (1990).

[4] S. A. Grot, C. W. Hatfield, G. Sh. Gildenblat, A. R. Badzian, and T. Badzian, *Appl. Phys. Lett.* **58**, 1542 (1991).

[5] J. F. Prins and H. L. Gaigher, *Proceedings of the Second International Conference on the New Diamond Science and Technology*, Washington, DC (1990); J. Narayan, V. P. Godbole, C. W. White, *Science* **252**, 416 (1991).

[6] O. Mishima, K. Era, J. Tanaka, and S. Yamaoka, *Appl. Phys. Lett.* **53**, 962 (1988).

[7] K. Tsuji, Japanese Patent, 2-192494 (1990).

[8] G. L. Doll, J. A. Sell, C. A. Taylor II, and R. Clarke, *Phys. Rev. B* **43**, 6816 (1991).

[9] G. L. Doll, J. A. Sell, C. A. Taylor II, and R. Clarke, *Proceedings of the Applied Diamond Conference 1991 First International Conference on the Application of Diamond Films and Related Materials.*

[10] G. L. Doll, J. A. Sell, L. Salamanca-Riba, and A. K. Ballal, in *Laser Ablation for Materials Synthesis*, edited by D. C. Paine and J. C. Bravman, Materials Research Society Proceedings Volume 191, Pittsburg, PA, 1990) p. 129.

[11] Songlin Ren, P. C. Eklund, G. L. Doll, *Bull. Am. Phys. Soc.* **36**, 817 (1991).

[12] B. D. Cullity, **Elements of X-ray Diffraction**, second edition, (Addison-Wesley, Reading Massachusetts, 1959), p. 262.

[13] D. J. Eaglesham, H. -J. Gossmann, and M. Cerullo, *Phys. Rev. Lett.* **65**, 1227 (1990).

[14] D. J. Eaglesham, L. N. Pfeiffer, K. W. West, and D. R. Dykaar, *Appl. Phys. Lett.* **58**, 65 (1991).

[15] G. L. Doll, J. A. Sell, and T. A. Perry, in *Surface Chemistry and Beam-Solid Interactions*, edited by H. A. Atwater, F. A. Houle, and D. H. Lowndes, Materials Research Society Proceedings Volume 201, Pittsburg, PA, 1991) p. 207.

[16] B. K. Fuller, *private communication.*

[17] J. T. Cheung and H. Sankur, *CRC Critical Reviews in Solid State and Material Sciences* **15**, 63 (1988).

[18] D. S. Knight and W. B. White, *J. Mater. Res.* **4**, 385 (1989).

[19] J. A. Martin, L. Vazquez, P. Bernard, F. Comin, and S. Ferrer, *Appl. Phys. Lett.* **57**, 1742 (1990).

Pulsed Excimer Laser Ablation Deposition of Boron Nitride on Si (100) Substrates

T. A. Friedmann, K. F. McCarty, E. J. Klaus, D. Boehme, W. M. Clift,
H. A. Johnsen, M. J. Mills, D. K. Ottesen, and R. H. Stulen
Sandia National Laboratories, Livermore CA, 94551

ABSTRACT

We are studying the boron nitride system by using a pulsed excimer laser to ablate from hexagonal BN (hBN) targets to form cubic BN (cBN) films. We are depositing BN films on heated (600°C) silicon (100) surfaces in a flowing (0- 10 sccm) ambient background gas of either NH_3 or N_2 of varying partial pressure (0-100 mTorr). Infrared (IR) reflection spectroscopy indicates the films have short-range hexagonal order. Some films grown at low laser energy densities have shown the cubic phase in IR transmission. Auger electron spectroscopy (AES) indicates the films are nitrogen deficient, which is linked to changes in the target stoichiometry with increasing laser fluence. Raman spectroscopy on the films shows only a strong background luminescence suggesting a high concentration of defects associated with the nitrogen vacancies. Atomic force microscopy (AFM) of the films shows a surface morphology that roughens as the growth rate increases. In order to improve the film stoichiometry it was necessary to actively enhance the nitrogen content of the films. It was found that bombarding films during growth with ions from an ion gun filled with NH_3 gas increased the N/B ratio but did not enhance the cubic phase. RF biasing the substrate gave films which showed both cubic and hexagonal features in IR reflection. High resolution transmission electron microscopy (TEM) confirms the presence of cBN grains of ~200Å size in films grown with an RF bias.

INTRODUCTION

Pulsed laser deposition (PLD) is an emerging technique for synthesis of thin film materials of many different types[1]. In particular, thin films of high temperature superconductors with very high quality have been synthesized by PLD and studied extensively. One of the advantages of PLD is its ability to deposit multicomponent, layered structures by ablating from several different targets during the deposition process. In addition, PLD offers the possibility of depositing metastable phases, such as cubic boron nitride (cBN), which differ in structure from the original target due to the energetics involved in the ablation process. In the intense plume generated during ablation, high energy ions, radicals, and neutrals can be excited allowing for chemical reactions both in the plume and on the substrate surface. In this paper we investigate the possibility of forming cubic boron nitride by ablating from hexagonal boron nitride (hBN) targets.

cBN films are of interest technologically due to their high hardness and high thermal conductivity, much like diamond films. cBN is superior to diamond in several aspects. Electronically, cBN can be doped both p- and n-type, whereas diamond can at present only be doped p-type. In addition, cBN has a larger band gap than diamond[2]. Mechanically, cBN can be used to machine ferrous alloys that graphitize diamond surfaces, and cBN has a higher decomposition temperature than diamond. The major disadvantage of cBN films is that they are harder to synthesize than diamond films, although several groups have reported success growing polycrystalline cBN films[3,4,5]. One group has reported the growth of epitaxial but polycrystalline cBN on silicon (100) surfaces by PLD[6]. The purpose of this paper is to report on a parametric study done to assess the feasibility of synthesizing cBN films through laser ablation of hBN targets.

Mat. Res. Soc. Symp. Proc. Vol. 242. · 1992 Materials Research Society

EXPERIMENTAL METHODS

A schematic diagram of the deposition chamber is shown in Fig. 1. The vacuum chamber is capable of attaining a base pressure of 1 x 10^{-7} Torr. The targets were ablated with a KrF (248 nm) laser (Lambda Physik LPX300) capable of generating 30-ns-duration 1.2-J pulses at a 50 Hz repetition rate. The laser light was focused through a spherical lens with a 30-cm focal length through an AR coated window into the vacuum chamber. The beam hit the rotatable target at a 45° angle forming a rectangular spot with an aspect ratio of ~5:1, varying in area dependent upon the position of the focusing lens. The target-to-substrate distance could be varied but was generally held at ~4 cm. The target was as received pyrolytic boron nitride (Union Carbide). The targets were sanded clean after each exposure to laser light due to the boron enrichment problem described below.

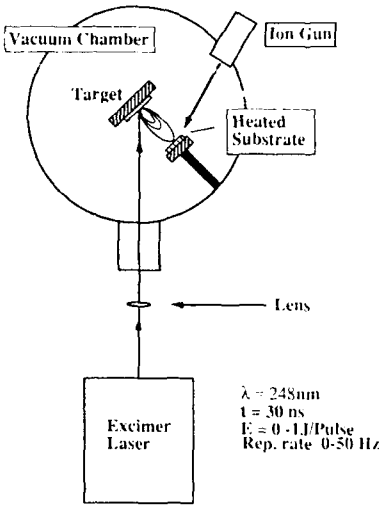


Fig 1. A diagram of the ablation system.

The silicon (100) substrates (p-doped with B to 0.01-0.03 Ωcm) were cleaned to remove the surface oxide layer by a wet dip procedure involving HF and NH_4F that is described elsewhere[7]. In most cases no in situ cleaning of the Si substrates was attempted although some samples were annealed in vacuum at 800°C for five minutes immediately prior to deposition. The Si substrates were resistively heated, and their temperature was measured by a thermocouple pressed directly to their backside. A thickness monitor at room temperature could be moved into position in front of the sample substrate to measure the deposition rate. Depositions were made in in a flowing background of either N_2 or NH_3 gasses (0 - 10 sccm) varying in pressure up to 100 mTorr.

Initially, the laser energy density, film thickness, background gas, and background gas pressure were varied, while the substrate temperature was held at 600°C. The resultant films and exposed targets were examined, as described below, and found to be nitrogen deficient. IR spectroscopy revealed the films to be sp^2 bonded. Consequently, ion bombardment and RF biasing with varying substrate temperature were separately used in an attempt to enhance the nitrogen content of the films and promote growth of the cubic phase. Ions from an ion gun were used to bombard the substrate during growth. The gun was run from 1-5 keV acceleration voltage, using either N_2 or NH_3 gas as a source of ions. For the samples grown in an RF discharge, the effect of the substrate RF bias voltage on sample growth was studied by varying the input power to a N_2/Ar plasma.

Characterization of the samples was accomplished mainly through infrared spectroscopy which serves as a quick screening process to determine bulk film characteristics. For hBN the bonding is sp^2 in nature with two characteristic peaks at 1370 cm^{-1} and 800 cm^{-1} associated with the in-plane B-N bond stretch and out of plane B-N-B bond bend, respectively[8]. The bonding in the cubic material is sp^3 in nature with an IR active TO mode at 1070 cm^{-1}[9]. IR spectroscopy reveals the nature of the bonding in the film but not the long range crystallinity or microstructure. Long range order in the films was assessed using x-ray diffraction (XRD) employing a thin film geometry at an incident angle of 0.5° and a rotating anode source of Cu Kα radiation. AES provided information about the film stoichiometry. TEM was used to probe the microstructure of the films. TEM samples were prepared by scribing the backside of the Si and cleaving small rectangular shaped samples from the larger wafer. These samples were silver pasted to a flap cut in a copper grid such that the film surface could be mounted vertically in the microscope to examine one corner of the film.

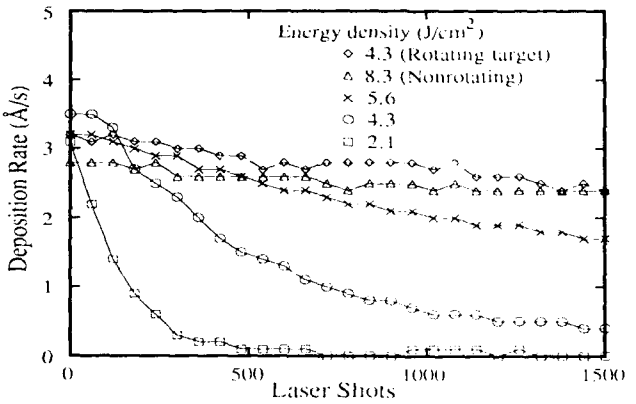


Fig. 2 Deposition rate vs. laser fluence for varying energy density.

RESULTS AND DISCUSSION

In order to study laser-target interactions, the thickness monitor was used to measure the ablation rate as a function of incident laser energy density and fluence for rotating and nonrotating targets. Fig. 2 shows the deposition rate as a function of laser shots for various laser energy densities. It is apparent that for the lower laser energy densities the deposition rate falls off as the number of incident shots increases. For higher energy densities (>6 J/cm^2) the ablation rate is nearly constant. Examination of the exposed targets reveals that at low energy densities the once pristine hexagonal boron nitride has become slightly pitted with dark cones that point toward the incident laser beam. AES of the exposed target shows that these regions are boron rich, as has been reported by others[10]. The decrease in the ablation rate with time may be explained by the preferential liberation of nitrogen from the target leaving boron rich material that has a higher ablation threshold than hBN. The targets exposed to laser energy densities above 6 J/cm^2 show very clean ablation pits with no dark boron rich regions. AFM pictures of films grown at these high energy densities show rough surfaces with large particulates (~1 μm). In contrast, the films grown at lower energy densities do not show these large particulates and are smoother. In order to alleviate the problem of changing target stoichiometry for low laser energy densities, the target is rotated to expose a larger surface area to the incident beam. As can be seen from Fig. 2, this rotation steadies the ablation rate.

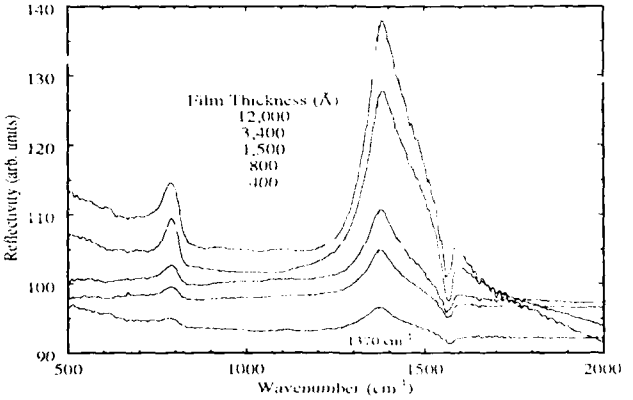


Fig 3. IR reflectance vs. wavenumber for films of varying thickness grown at 4.3 J/cm^2 in 30 μm of N_2 gas with a rotating target. No peaks appear above 2000 wavenumbers.

IR reflection spectroscopy was done on all of our samples to examine the phase composition of the films. Fig. 3 shows a typical set of IR spectra obtained from a series of samples grown at an energy density of 4.3 J/cm^2 in 30 mTorr of flowing nitrogen gas with a rotating target. The samples range in thickness from 400 to 12,000Å. The spectra were ratioed to the spectrum of silicon that was cleaned by the same HF/NH_4F dipping process referenced above[7]. The two peaks at 800 and 1370 cm^{-1} indicative of the hexagonal phase are very prominent in the thicker samples and gradually become less intense as the samples get thinner. The peak at 1065 cm^{-1} indicative of the cubic phase does not appear in these samples.

The background gas pressure was varied up to 100 mTorr in order to determine its effect on sample quality. Films grown in vacuum were thicker and had more particulates than those grown in high pressures of N_2, but the IR spectra of the deposited films did not noticeably change from the spectra shown in Fig. 3. Performing the same study with NH_3 as the background gas revealed no changes in the films, as determined by IR spectroscopy.

Varying the laser energy density from 1 to 8 J/cm^2 in almost all cases gave samples that were hexagonal in phase as determined by IR reflection spectroscopy. Three samples made in 15 mTorr nitrogen gas pressure with a nonrotating target at energy densities of 1, 1.5, and 2 J/cm^2 show the peak at 1065 cm^{-1} in IR transmission indicative of the cubic phase, as can be seen in Fig. 4. (Repeating the measurement in the IR reflection geometry gave the same result.) One sample made at 1 J/cm^2 showed almost entirely cubic phase with the other two samples showing increasing hexagonal phase as the energy density increases. Efforts to reproduce the results of this series of samples have not proven successful, although work is still in progress to do so.

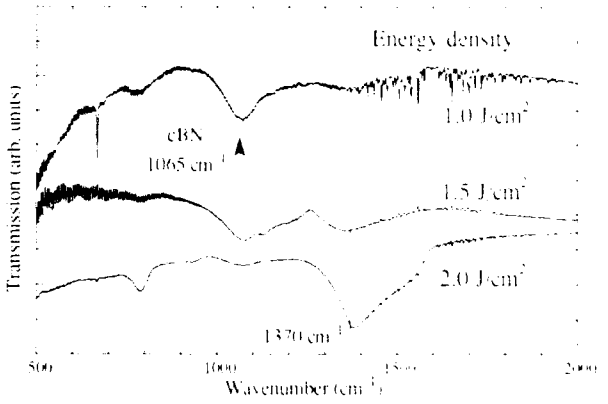


Fig. 4 IR transmission vs. wave number for three samples made at low laser energy density. The IR transmission above 2000 wavenumbers shows no additional peaks.

In general, films produced by PLD without ion enhancement are not stoichiometric BN. Auger analysis of the as-deposited films show that N/B ≈ 0.70. This nitrogen deficiency problem may be linked to the target depletion problem described above. XRD analysis has not shown peaks indicative of either the cubic or hexagonal phases suggesting that the films have either very small crystalline grains or are amorphous. Raman analysis has not shown any peaks but a strong background luminescence possibly associated with the large nitrogen deficiency in these films.

The results above indicate to us that some form of active nitrogen enhancement is necessary in order to produce stoichiometric films and encourage growth of the cubic phase. In order to investigate these possibilities two methods were examined. The first method involved the use of an ion gun to bombard the samples during growth, while the second involved RF biasing the substrate and varying its temperature.

Two series of samples were deposited using the ion gun, one with N_2 and the other with NH_3 gas as the source of ions. The ion energy was varied from 1-5 keV. IR analysis of these samples revealed that the films were hexagonal and that the cubic phase was not enhanced. Auger analysis showed that films deposited with NH_3 as an ion source were closer to stoichiometric with N/B ≈ 0.90. The Auger line shape of the boron peak for these samples was

consistent with the presence of cBN material in the films; however, the presence of surface oxygen impurities incorporated during sample handling made it difficult to state this unambiguously since the B lineshape in B_2O_3 is similar to that of B in cBN.[11] XRD analysis of these films did not show any peaks, indicating the films are either small grained or amorphous. Although ion bombardment shows promise as a means for increasing the nitrogen content of the films, our preliminary results show that we were not able to significantly enhance the cubic phase through this method.

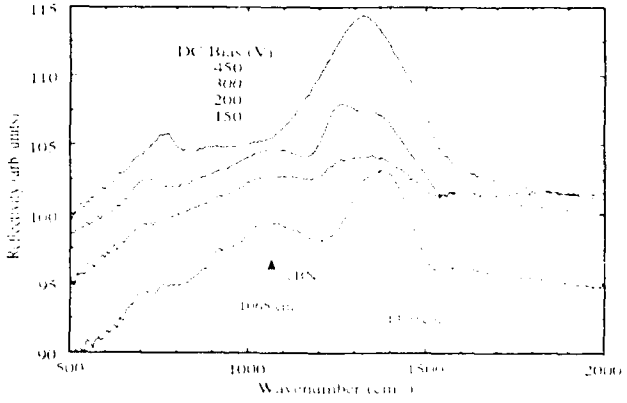
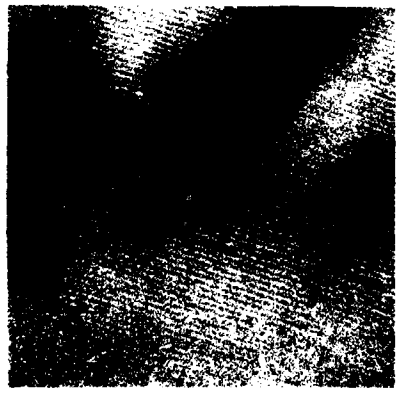


Fig. 5 IR reflection vs. wavenumber for four samples grown in an RF plasma discharge at different DC bias voltages.

Films were grown in an RF plasma discharge, and the RF power to the substrate was varied producing a DC bias between 0 and -450V. The samples were grown at a gas pressure of 15 mTorr in a flowing gas mixture (3.0 sccm) of Ar and N_2 at a ratio of 10:1, respectively. Samples grown with RF biasing show an enhancement in the amount of cubic material. Fig. 5 shows the IR spectra for four samples grown at different bias voltages. Three samples show a



15Å

Fig. 6 TEM micrograph of a BN sample grown at -200V DC bias. The measured row spacing of 1.76Å is consistent with the (200)planes of cBN.

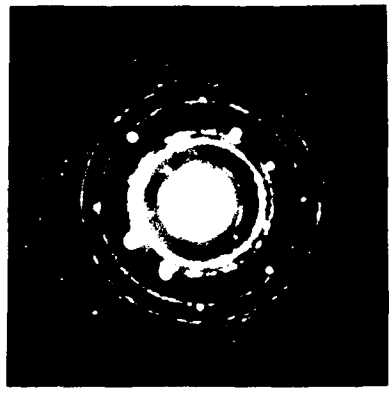


Fig. 7 Electron diffraction pattern of the region shown in Fig. 6. The diameters of the rings are consistent with those of cBN. Silicon Bragg reflections for a [013] zone axis are also seen.

mixture of both cubic and hexagonal phase. The sample grown at -450V bias shows only hexagonal material. It is apparent that at a bias voltage above a certain threshold value between -300V and -450V only hexagonal material appears. Fig. 6 is a TEM micrograph of a sample grown at a bias voltage of -200V. The 1.76Å spacing between the rows of Fig. 6 is consistent with that of the (200) planes of cBN. The positions of the rings for the corresponding electron diffraction pattern in Fig. 7 have been analyzed, verifying the presence of cubic material as can be seen in Table I. The TEM images show grain sizes of ~200Å.

Measured		Standard cBN	
d(hkl)	Intensity	(a = 3.62Å)	hkl
3.150	vw	------	----
2.110	s	2.084	111
1.820	m	1.807	200
1.280	s	1.292	202
1.100	s	1.102	113
1.040	m	1.055	222
0.920	w	0.914	400
0.830	m	0.829	313
0.810	m	0.808	204
0.740	m	0.738	224

Table I. The measured d spacings of Fig. 7 compared to those of standard cBN.

CONCLUSIONS

The hexagonal phase is predominant for the samples we have grown with PLD. Varying the laser energy density has produced some films that show indications of the cubic phase in IR spectroscopy, although we have not been able to reproduce the IR data in other films grown under the same conditions. It has also been shown that it is very difficult to grow samples with the proper stoichiometry; most samples are nitrogen deficient. This is linked to nitrogen depletion in the target with increasing laser fluence making it necessary to supplement the growth procedure by using some activated secondary source of nitrogen. Preliminary efforts to do so with an ion gun run with NH_3 gas show improvements in the N/B ratio, but no indication of the cubic phase in IR spectroscopy. PLD of samples in the presence of an RF discharge has led to films that show mixed phase cubic and hexagonal material in IR spectroscopy. TEM images of these samples show small grained cubic material of ~200Å grain size. Further efforts are under way to increase the fraction of cubic material in the films deposited in an RF discharge.

ACKNOWLEDGMENTS

This work was supported by USDOE-OBES-DMS under the contract DEAC04-76DP00789.

REFERENCES

1. Jeffrey T. Cheung and Haluk Sankur, CRC Crit. Rev. in Solid State and Mat. Sci. 15, 63 (1988).
2. O. Mishima in Synthesis and Properties of Boron Nitride, edited by John J. Pouch and Samuel A. Alterovitz (Trans Tech Publications LTD, Aedermannsdorf, 1990) (Materials Science Forum 54 and 55 (1990) pp. 313-328.)
3. M. Murakawa and S. Watanabe, Surface and Coatings Tech. 43/44, 128 (1990).
4. Akiyoshi Chayahara, Haruki Yokoyama, Takeshi Imura and Yukio Osaka, Jap. J. App. Phys. 26, L1435 (1987).
5. S. Y. Shapoval, V.T. Petrashov, O. A. Popov, A. O. Westner, M. D. Yoder, Jr., and C. K. C. Lok, Appl. Phys. Lett. 57, 1885 (1990).
6. G. L. Doll, J. A. Sell, C. A. Taylor II, and R. Clarke, Phys. Rev. B 43, 6816 (1991).
7. G. S. Higashi, Y. J. Chabal, G. W. Trucks, and Krishnan Raghavachari, Appl. Phys. Lett. 56, 656 (1990).
8. R. Geick, C. H. Penny, and G. Rupprecht, Phys. Rev. 146, 543 (1966).
9. P. J. Gielisse, S. S. Mitra, J. N. Plendl, R. D. Griffis, L. C. Mansur, R. Marshall, and E. A. Pascoe, Phys. Rev. 155, 1039 (1967).
10. G. L. Doll, T. A. Perry, and J. A. Sell at the 1990 Fall Meeting of the Materials Research Society in Boston, Symposium A.
11. D. R. McKenzie, W. G. Sainty, and D. Green in Synthesis and Properties of Boron Nitride, edited by John J. Pouch and Samuel A. Alterovitz (Trans Tech Publications LTD, Aedermannsdorf, 1990) (Materials Science Forum 54 and 55 (1990) pp. 193-206.)

GROWTH OF TETRAHEDRAL PHASES OF BORON NITRIDE THIN FILMS BY REACTIVE SPUTTERING

T.D. Moustakas[a], T. Lei [a], R J. Molnar [a], C. Fountzoulas [a], and E.J. Oles [b]
[a] Molecular Beam Epitaxy Laboratory, Department of Electrical, Computer, and Systems Engineering, Boston University, Boston, Massachusetts, 02215, USA.
[b] Kennametal Inc., USA.

ABSTRACT

Tetrahedrally coordinated phases of boron nitride (c-BN and w-BN) were produced by reactive sputtering. The structure of the films was investigated by XRD and TEM diffraction, and found to be polycrystalline. Films with microhardness up to $3500 kg/mm^2$ were deposited but some degradation over time has been observed. A model for the stabilization of the tetrahedral phases over the graphitic one is proposed.

INTRODUCTION

Bulk boron nitride exists in three allotropic forms; the hexagonal graphite-like form (the thermodynamically stable phase), the zinc-blende and the hexagonal wurtzite-type forms which can be formed under high pressure conditions. Boron nitride thin films have been produced by a variety of deposition methods, such as CVD (1), plasma assisted CVD (2), ion plating (3), electron beam deposition (4), and reactive sputtering (5,6). In general, films produced by ion assisted processes were determined to have a significant cubic component but results from different laboratories are conflicting and there is no consensus as to the underlying cause for the stabilization of c-BN over g-BN under metastable growth conditions.

In this paper, we present data on the growth, structure, chemistry and mechanical properties of BN films produced by reactive sputtering. Evidence is presented that the formation of the tetrahedral phases (c-BN and w-BN) requires the incorporation of defects such as N- or B-vacancies.

EXPERIMENTAL METHODS

The boron nitride films were grown by rf diode sputtering. The boron nitride target, a 12.7 cm diameter and 0.6 cm thick disk, was Carborundum grade AX20 which contains 2% B_2O_3. The substrates (quartz, sapphire, silicon, tungsten carbide, and TiN-coated WC) were held 6 cm below the target and the substrate platform was electrically floated and heated from ambient temperature to 700°C. The deposition system was pumped to a base pressure of 3×10^{-7} Torr and the sputtering was performed in a mixture of Ar and N_2 at a total pressure from 2 to 10 mTorr. The partial pressure of nitrogen was varied from 0% to 100%. The power in the discharge was varied up to 1000 Watts.

The structure of the films was investigated by XRD using a Rigaku diffractometer with parallel beam optics, and TEM diffraction from flakes scraped from various substrates onto a Cu-grid. The platelets of g-BN tend to rest on the grids with their basal planes parallel to the grid planes, and the e-beam is parallel to the c-axis. Under such circumstances, reflections (hkl) with $l \neq 0$ are extinguished and the diffraction patterns from g-BN and c-BN are qualitatively similar. The distinction between the two structures can be made only by careful determination of the ratio of radii of the diffraction rings. Oriented g-BN has a (10.0)

reflection at 2.1693Åand a (11.0) reflection at 1.2521Å. The ratio of the two d-spacings is 1.73 and this should coinside with the ratio of the radii of the two diffraction rings. c-BN has a (111) reflection at 2.088Å and a (220) reflection at 1.2785Å, and the ratio of the radii of the two diffraction rings is expected to be 1.63. w-BN has a (10.0) reflection at 2.211Å, and a (11.0) reflection at 1.277Å, and the ratio between the radii of the two diffraction rings is 1.73. Therefore, based on TEM diffraction alone, one can not distinguish between g-BN and w-BN.

Film composition was determined in a few films by XPS and film microstructure by SEM studies.

EXPERIMENTAL RESULTS AND DISCUSSION

A. Film Deposition Process

The BN-target at the end of a run was found to have a gray color when sputtering took place in pure argon, suggesting that under these conditions the target was reduced and became boron rich. On the contrary, the color of the target remained unchanged when the sputtering discharge contained more than 10% nitrogen. This suggests that nitrogen in the plasma reacts both with the target as well as with the growing BN film.

The film growth rate was found to increase with the power in the discharge, a result which is expected. However, we also found that at a fixed power in the sputtering discharge, the film growth rate increases with the partial pressure of nitrogen in the plasma. This result is illustrated in Fig. 1 for a series of films deposited at 200 Watts forward power and total pressure of $Ar + N_2$ = 5mTorr. The film deposition rate was determined from the thickness of the film divided by the deposition time. Based on the experience of reactive sputtering from elemental targets, one would have expected the opposite result. Reactive gases, in general, carry a significant fraction of the discharge current, but contribute very little to the sputtering rate(7).

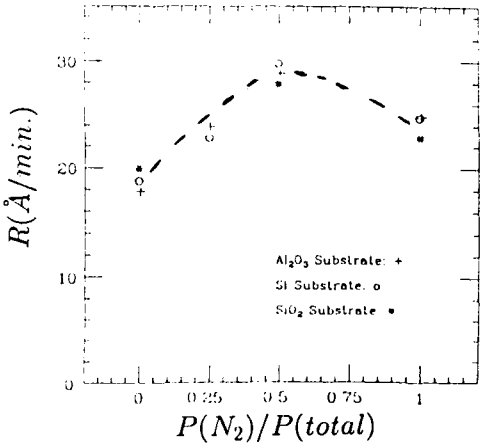


Fig. 1. Deposition rate vs fraction of nitrogen in the discharge

One possible explanation of this result is that the increase in deposition rate is not due

to an increase in the sputtering yield, but it is due to an increase of the thickness of the film because of its structural transformation from the cubic to the graphitic phase. In other words, a material produced in low concentration of nitrogen has the tetrahedrally coordinated structure (denser) while that produced in high concentration of nitrogen acquires the graphitic structure. The mass densities of the two structures ($\rho_{c\ B\text{-}N} = 3.5gr/cm^3$ and $\rho_{g\ B\text{-}N} = 2.2gr/cm^3$) have a ratio of 1.6, in approximate agreement with the observed increase in deposition rate.

B. Film Composition, structure, and microstructure.

The composition of only three films was determined by XPS analysis, and the results are shown in Table I. The oxygen in the films is probably due to the B_2O_3 impurities of the target, and oxygen impurities from the sputtering gases and atmospheric leaks. The carbon could be due to sputtering from the graphite substrate holder.

Table I. Composition of BN Films

Sample	B	N	C	O
BN-207	40.4%	40.8%	7.1%	11.5%
BN-208	39.2%	37.8%	10.7%	12.1%
BN-211	40.6%	36.3%	13.9%	9.0%

The XRD pattern of a BN film produced with 10% N_2 in the sputtering discharge on a tungsten carbide substrate is shown in Fig. 2a. Shown for comparison in Fig.2b is the XRD pattern of the substrate alone. It is obvious that the broad peak at $2\theta \simeq 43°$ is due to the film. However, its identification is not unambiguous.

The most intense reflection from cubic boron nitride occurs at $2\theta = 43.3°$ and corresponds to (111) reflection, whose d-spacing is 2.0872Å(8). However, there are two reports on shock-wave compressed boron nitride, which is reported to have the wurtzite structure with intense reflections in the same 2θ-region. The first type (9) was produced by compression of graphite-like boron nitride up to 550 kbar and its three more intense peaks, in an order of increasing intensity occur at $2\theta = 40.76°, 42.72°, 46.29°$. These peaks correspond to (100), (002), and (101) reflections, whose d-spacings are 2.211Å, 2.114Å, and 1.959Å. The second type (10) was produced by shock-wave compression derived from explosion of a cylindrical charge of 60-150g of hexogene. The XRD data from this material were not indexed. The most intense peaks occur at $2\theta = 14.08°, 23.07°, 27.6°, 33.3°, 40.9°, 43.5°$ and 46.4°, with corresponding d-spacings 6.28Å, 3.85Å, 3.22Å, 2.686Å, 2.201Å, 2.07Å, and 1.955Å. These two results suggest that boron nitride with the wurtzite structure can exist in many polytype forms, due probably to the formation of stacking faults parallel to the (0002) planes (11). The graphitic BN has its most intense peak at $2\theta = 26.75°$, which corresponds to the (0002) reflection (d=3.3281Å) and two much weaker peaks at $2\theta = 41.58°$ and 43.85°, which correspond to the (100) and (101) reflections (12). Finally, it should also be mentioned that elemental boron has one peak in the same 2θ-region. The most intense XRD peaks of boron occur at $2\theta = 20.87°, 21.81°$, and 42.74° and correspond to (003), (101), and (021) reflections of this rhombohedral structure (13).

From the evidence presented in Fig. 2, it appears that the observed peak is due either to BN (cubic or wurtzitic) or to elemental boron. However, the data of Table I suggests that,

to within a few percent, the concentration of boron and nitrogen is the same and thus, it is very unlikely that the observed XRD peak originated from phase separated elemental boron. To differentiate between all of these alternative interpretations regarding the structure of the film we are currently studying the XRD in the 2θ-region smaller than 25^o.

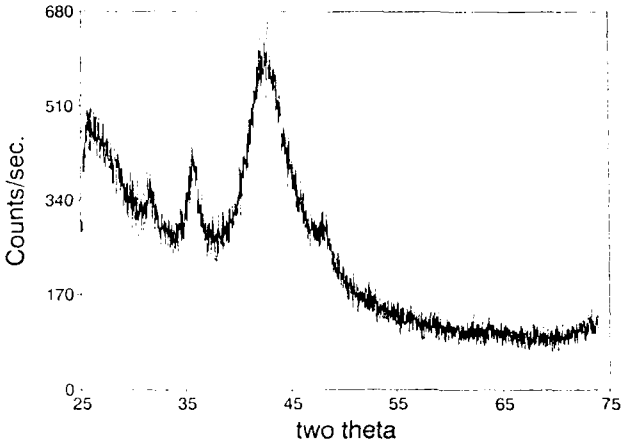


Fig 2a. XRD pattern for a BN-film on a WC substrate

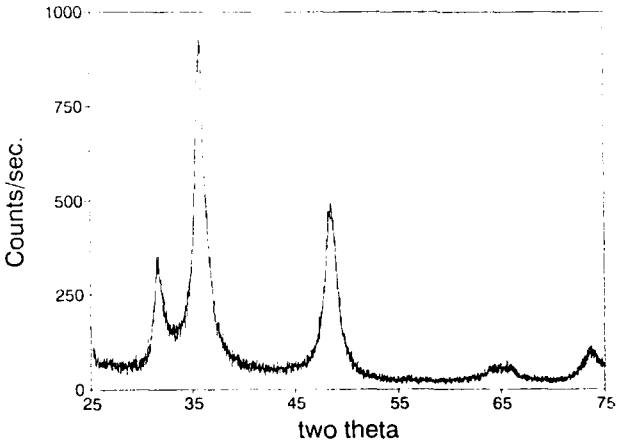
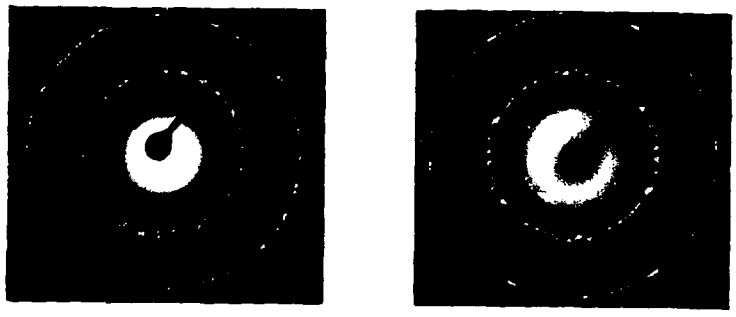


Fig 2b. XRD pattern for the WC substrate

The broadness of the peak at $2\theta \simeq 43^o$ could be either due to the small size of the crystallites or to strain. The later should also cause a shift in the position of the peak. From Debye-Scherrer analysis we find that a crystallite size of about 30Å is required to account for the width of the line.

Figs. 3a and 3b are TEM diffraction patterns for two BN films. These data clearly indicate that the films are polycrstalline with no indication of an amorphous component. A

careful examination of the two patterns indicate that besides the two main rings, pattern 3b has another diffraction ring in the perimeter of the direct beam. This ring is indexed as the (0002) reflection of g-BN whose d-spacing is 3.3281Å. Furthermore, the ratio of the radii of the two outer rings is 1.73. As discussed previously this indicates that this film has either the g-BN or the w-BN structure. The existence of the (0002) reflection suggests that a significant fraction of this film has the g-BN structure. On the contrary, the diffraction pattern of Fig. 3a is consistent with c-BN. The (0002) reflection is not present, and the ratio of the radii of the two diffraction rings is 1.63.



(a) (b)

Fig. 3. TEM diffraction patterns from two BN-films (a) c-BN (b) g-BN

A typical surface murphology and a fractured cross-section for a BN-film with a cubic BN structure is shown in Fig. 4. The surface is smooth and featureless and the cross-section shows no discernible columnar morphology.

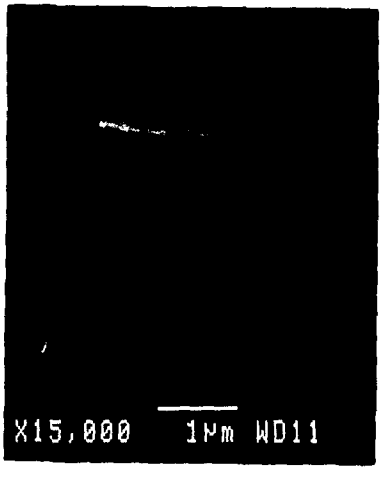


Fig 4 SEM morphology of a c-BN film

C. Film hardness and stability

The microhardness was measured in a large number of samples. A number of them were found to have microhardness of between $2500 kg/mm^2$ to $3500 kg/mm^2$. However, significant degradation in the hardness has been observed over a period of several months from the time of growth. These studies are in progress and are going to be the subject of a future report.

D. Model of growth of the tetrahedrally coordinated phases of BN films.

The theory regarding the growth of c-BN thin films is reported in detail separately (14). In this theory, the incorporation of vacancies (B- or N-vacancies) at the growth face changes the relative binding energy of cubic- versus graphitic-BN so that c-BN can nucleate and grow. ESR measurements reported separately (15) indicate that the films have a concentration of N-vancancies of about 1%. The theory also predicts that off-stoichiometric material is generally unstable to phase separation. Whether the observed degradation in microhardness is the result of such phase separation is currently under study.

CONCLUSIONS

BN films with structures and mechanical properties consistent with the tetrahedrally coordinated phases (c-BN and w-BN) were produced by reactive rf diode sputtering. TEM studies indicate that the films are polycrystalline and XRD studies indicate that the films are either highly strained or have a crystallite size of the order of 30Å. SEM microscopy indicates that the films are dense and featureless. A degradation in microhardness over a period of several months has been observed but the origin of this phenomenon has not been understood yet.

ACKNOWLEDGEMENTS

This research was supported by The National Science Foundation (grant number DMR 9014370), by Boston University, and by Kennametal Corp. The authors are indebted to Dr. R. Koba and Dr. P.E. Jones for numerous discussions.

REFRENCES

1. S.P. Murarka, C.C. Chang, D.N.K. Wang, and T.E. Smith, J. Electrochem. Soc. 126, 1951 (1979).
2. T.H. Yuzuriha and D.W. Hess, Thin Solid Films, 140, 199 (1986).
3. S. Shanfield and R. Wolfson, J. Vac. Sci. Technol., A 1, 323 (1983).
4. E.H. Lee and H. Pooppa, J. Vac. Sci. Technol., 14, 223 (1977).
5. M.D. Wiggins, C.R. Aita and F.S. Hickernell, J. Vac. Sci. Technol., A 2, 322 (1984).
6. M. Mieno and T. Yoshida, Jpn. J. Appl. Phys. Vol 29, L1179 (1990).
7. J.L. Vossen and J.J. Cuomo In "Thin Film Process" (J.L. Vossen and W. Kern eds) Chapter 2, Academic Press, N.Y. (1978).
8. JCPDF 25-1033
9. JCPDF 26-773
10. JCPDF 18-251
11. T.Lei and T.D. Moustakas, This volume
12. JCPDF 9-12
13. JCPDF 12-377
14. Y. Bar-Yam, T. Lei, T.D. Moustakas, D.C. Allan and M.P. Teter, This volume
15. M. Fanciulli and T.D. Moustakas, This volume

EPR Investigation of Defects in Boron Nitride Thin Films

M. FANCIULLI* and T.D. MOUSTAKAS**
*Department of Physics, Boston University, Boston, MA 02215
**Department of Electrical Engineering and Department of Physics, Boston University, Boston MA 02215.

ABSTRACT

Defects in BN thin films, produced by reactive sputtering, were investigated by Electron Paramagnetic Resonance (EPR) measurements. The EPR signals of films produced with up to 10% N_2 in the argon discharge are consistent with films having a cubic structure, and becoming more ordered with nitrogen incorporation in the films. The concentration of spins is in the order of 10^{19} spins/g and they are attributed to nitrogen vacancies with an electron trapped in. Carbon incorporation changes the EPR signal and increases the concentration of spins significantly. This result is consistent with the notion that carbon doping stabilizes the electron in a nitrogen vacancy.

INTRODUCTION

Boron nitride can exists in three allotropic forms: the cubic-BN (zincblende structure), the HCP-BN (wurtzite structure) and the graphitic-BN (graphite structure with different stacking sequence). The first two phases are termodynamically metastable and can be formed by the high temperature and pressure methods [1]. The syntesis of this metastable phases by vapor phase methods has been the subject of an intense interest over the past several year [2]. Such materials are anticipated to find applications as hard coatings, insulators and semiconductors.

In any class of materials defects play a role in determining the mechanical, thermal, optical and electronic properties. It has been proposed recently that defects may also play a role in the stabilization of diamond and cubic BN during the growth of these materials at low pressures and temperatures [3,4] as well as in the stabilization of the cubic phases of these materials during high pressures and temperatures sintering [5,6].

Defects in bulk graphitic BN have been investigated by EPR spectroscopy [5-13, 15-19]. Two types of paramagnetic center were identified [7,8]. One is due to an unpaired electron interacting with a single ^{11}B atom (one boron center) giving rise to a four - line EPR spectrum. The other is due to an unpaired electron interacting with three ^{11}B atoms (three boron center) giving rise to a ten line EPR spectrum. The intensities of the lines for the three boron center are in the ratio 1:3:6:10:12:12:10:6:3:1. The natural abbundance of ^{11}B is 80.2 % and of ^{10}B is 19.8 %. The heavier isotope, which has nuclear spin I=3/2 and nuclear g value $g_N = 1.792424$, determines the EPR spectrum in BN of natural isotopic composition. Khusidman and Neshpor [9,10] suggested that the three boron centers were nitrogen vacancies with an electron trapped in, like F-centers in alkali halides. Romelt [11] suggested also that the unpaired electron stems from oxygen substituting nitrogen atoms.

The role of carbon in the stabilization of the electron in the nitrogen vacancy in graphitic boron nitride was pointed out by several authors [9,10,12-16]. Moore and Singer

[12] concluded that interstitial carbon is responsible for the coloring and paramagnetism in h-BN and that impurity atoms are at least sufficient if not necessary in creating and stabilizing particular defects in the lattice. The decrease in the hyperfine splitting due to the presence of carbon, up to a complete collapse with high carbon concentration, for the three boron centers (F-center) in h-BN was observed by Moore and Singer [12] and by Andrei, Katzir and Suss [15]. This can be explained by a decrease of the degree of delocalization on the boron nuclei of the atoms in the first coordination sphere due to the presence of carbon near the nitrogen vacancy. Theoretical studies on point defects in graphitic BN and the particular problems of substitutional and interstitial carbon were presented by Zunger and Katzir [14]. Carbon is believed to play a similar role in the zincblende and wurtzite boron nitride as suggested by Tikhonenko, Shul'man and Gerasimenko [18].

The EPR spectrum of a polycrystal c-BN consists [6,17 and 19] of a single line with g = 2.0023 and peak to peak linewidth of 20 G, more recently Zhang and Chen [20] obtained a single line with g = 2.00248 and peak to peak linewidth of 27 G.

The wurtzitic boron nitride shows a single resonance line at g = 2.0043 and peak to peak linewidth of 22-25 G [5].

In this paper we report the first EPR studies of defects in BN and carbon doped BN thin films grown by reactive sputtering on silicon substrates.

EXPERIMENTAL METHODS

The BN films used in this study were produced by reactive sputtering from a hexagonal BN target in an atmosphere of argon and nitrogen. The kinetics of growth of BN, as all other III-V compounds, requires that stoichiometric films can only be formed when the flux of group V element (N) is higher than the flux of group III element (B). A set of films was produced by varying the nitrogen partial pressure. In order to investigate the role of carbon impurities in the EPR signals a number of films were also produced in an atmosphere of argon, nitrogen and methane. Films for this study were grown on silicon (100) substrates and self supporting films were obtained by disolving the substrate in a solution containing HF and HNO_3. Details on the growth conditions have been reported in the previous paper [21].

EPR measurements were carried out on an X-band Varian E9 spectrometer at room temperature and using a 100 KHz field modulation. Different modulation amplitudes were used in the atempt to resolve the hyperfine structure. The g-values were evaluated by comparison with a Mn: SrO reference. The absolute number of spins in the samples was obtained by comparison, under the same experimental conditions, with a α,α'-diphenyl-β-picrylhydrazyl (DPPH) reference.

EXPERIMENTAL RESULTS AND DISCUSSION

The EPR signal of the target material, pyrolitic graphitic boron nitride, is shown in figure 1. The g value of the spectrum is 2.0029 $\pm$ 0.0004, the hyperfine interaction constant is A = 8.0 $\pm$ 0.5 Gauss and the resolution parameter is $\Delta H_{ppi}/A = 0.5$, where ΔH_{ppi} is the peak to peak linewidth of a single component. From the isotropic hyperfine interaction constant A we can evaluate $|\psi(0)|^2$ at the boron nuclei of atoms in the first coordination sphere [23]:

$$A = \frac{8\pi}{3} g\beta g_N \beta_N |\psi(0)|^2 \qquad (1)$$

where g, g_N are the electronic and nuclear g values respectively, β, β_N are the electronic

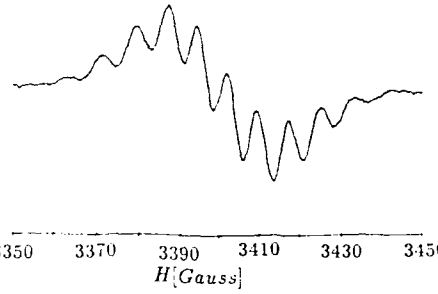


Figure 1: EPR spectrum for the pyrolitic graphitic BN.

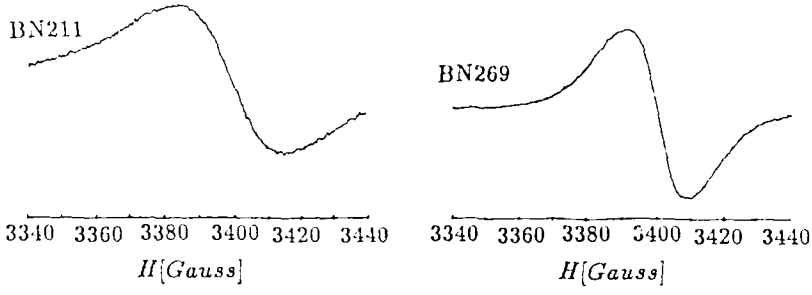


Figure 2: EPR signals from samples grown at different partial N_2 pressure.

and nuclear Bohr magnetons and $\psi(0)$ is the normalized wave function of the F - center electron. We have:

$$|\psi(0)|^2 = 1.05 * 10^{23} cm^{-3} \quad (2)$$

These results are in agreement with those reported earlier [7-10].

EPR studies were conducted on BN films grown at different partial N_2 pressure. Such films are expected to have a variable concentration of nitrogen vacancies which have a significant effect on the structure and properties of the films [21,22]. More specifically, it was found [21] that films produced in less than 10% of N_2 in the sputtering discharge have the cubic structure, while those produced at higher N_2 partial pressure are soft and unstable upon exposure to the atmosphere. The investigated samples and the corresponding EPR results are presented in Table I. The EPR signals for the films produced in pure argon and in 50% argon + 50% nitrogen are presented in figure 2.

Sample	$\%N_2$	g-value	ΔH_{pp} [Gauss]	N_s [spins/g]
BN211	0	2.0024±0.0004	31±1	$4.40 * 10^{19}$
BN222	5	2.0025±0.0004	23±1	$2.04 * 10^{19}$
BN249	10	2.0025±0.0004	21±1	$1.51 * 10^{19}$
BN257	12	2.0029±0.0004	18±1	$1.31 * 10^{19}$
BN269	50	2.0029±0.0004	17±1	$4.04 * 10^{19}$

Table I. Growth condition and experimental results for different $\%N_2$.

The samples grown in less than 10% N_2 show a g value consistent with the results reported on the cubic phase of BN. At higher partial nitrogen pressure the g value is

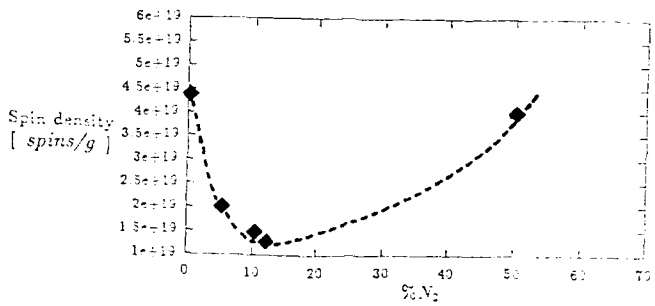


Figure 3: Density of spins as function of partial N_2 pressure.

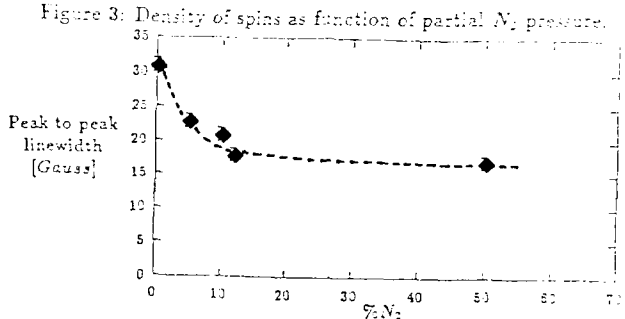


Figure 4: Peak to peak linewidth as function of partial N_2 pressure.

consistent with the results reported on the graphitic BN. The density of paramagnetic defects in the investigated films was found to depend on the partial pressure of nitrogen as indicated in figure 3. The initial decrease of the spin density with the partial pressure of N_2 is consistent with the notion that the defect is a nitrogen vacancy. As discussed in the previous paper [21] the increase in the spin density at higher partial pressure of nitrogen may be related to the structural tranformation from predominantly cubic to predominantly more defective graphitic structure. The decrease of the peak to peak linewidth with the increase of the nitrogen partial pressure, as shown in figure 4, is indicative that the film becomes more ordered with nitrogen incorporation. The g value, the peak to peak linewidth as well as the lack of a resolved hyperfine structure are in general agreement with the results reported for the cubic phase of BN [6,17-20].

As previously pointed out carbon seems to play an important role in the stabilization and/or formation of the paramagnetic center. We invesigated the effect of carbon in BN films by varying the partial pressure of CH_4 in the discharge. The investigated samples and the corresponding EPR results are presented in Table II. The EPR signals for the films produced in 0% methane 5% carbon are presented in figure 5.

Sample	$\%N_2$	$\%CH_4$	g-value	ΔH_{pp} [Gauss]	N_s [spins/g]
BN249	10	0	2.0025±0.0004	21±1	1.51×10^{19}
BN248	10	1	2.0032±0.0004	20±1	3.82×10^{19}
BN258	10	2	2.0031±0.0004	16±1	1.32×10^{20}
BN252	10	5	2.0035±0.0004	7±1	1.85×10^{20}

Table II. Growth conditions and experimental results for different $\%CH_4$.

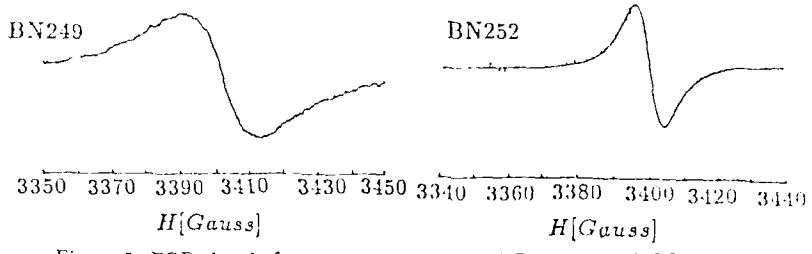


Figure 5: EPR signals from samples grown at different partial CH_4 pressure

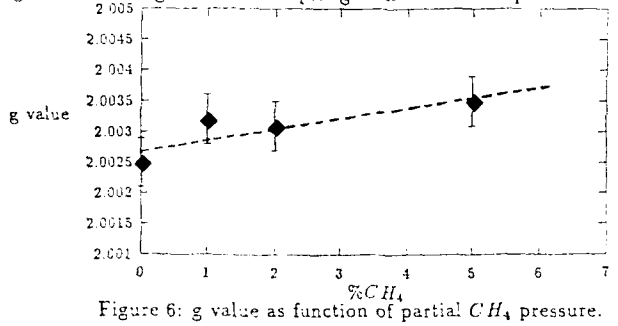


Figure 6: g value as function of partial CH_4 pressure.

We observed an increase in the g value, as shown in fig. 6, which can be explained by the higher spin-orbit interaction due to the presence of carbon. No hyperfine splitting was observed. This can be due to disorder and/or to the mentioned reduction of the electronic delocalization on B neighbors. The collapse of the hyperfine splitting is then the result of rapid electron exchange between the nitrogen vacancies and nearby carbon atom or clusters of carbon atoms.

The density of paramagnetic centers increases as the partial pressure of CH_4 increases as shown in fig. 7. This is in agreement with the interpretation of the role of carbon in stabilyzing the defects. The decrease of the peak to peak linewidth as the partial pressure of CH_4 increases, shown in fig. 8, can be explained by the exchange narrowing due to the increase of the defects concentration [24].

The saturation data for all the samples studied show partial inhomogeneous broadening

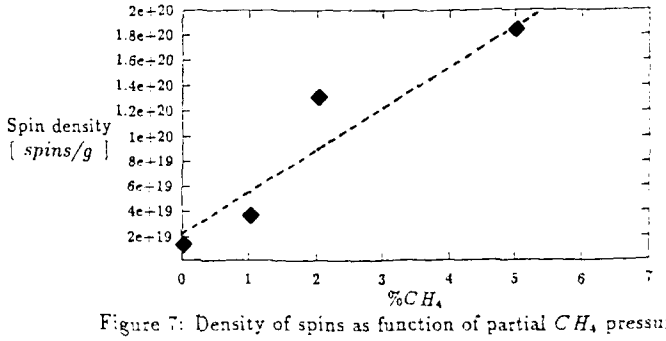


Figure 7: Density of spins as function of partial CH_4 pressure.

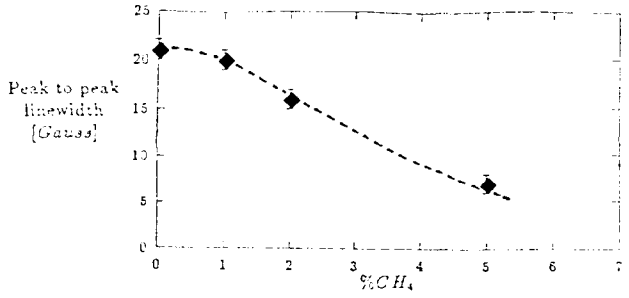


Figure 8: Peak to peak linewidth as function of partial CH_4 pressure.

related to disorder or unresolved hyperfine splitting. This also explained the gaussian character of the resonance signal. A spin-lattice relaxation time T_1 seconds in the order of 10^{-5} was evaluated [25] from the saturation data of both sets of samples. The sample grown at 5% CH_4 has a T_1 one order of magnitude smaller, which is expected due to the larger concentration of defects.

CONCLUSIONS

Defects in BN films, produced by reactive sputtering in an atmosphere containing $Ar+N_2$ as well as $Ar+N_2+CH_4$, were investigated by EPR measurements.

We found that films produced with up to 10% N_2 in the argon discharge have a single line EPR signals with g value and linewidth consistent with what has been observed in high pressure cubic BN. We also observed that the concentration of spin, which are in the order of 10^{19} spins/g, is reduced with increasing the nitrogen pressure in the discharge suggesting that the paramagnetic center is a nitrogen vacancy with an electron trapped in. Additionally, a narrowing of the linewidth with increasing the nitrogen pressure is an indication that the structural order of the films improves with nitrogen incorporation.

Films produced at a nitrogen partial pressure higher than 10% in the argon discharge show an increase in the spin density which is inconsistent with the notion that nitrogen incorporation reduces the number of nitrogen vacancies. Additionally, the g values in this films is 2.0029 which is characteristic of g-BN. Thus, stoiochiometric films, i.e. those produced at high nitrogen partial pressure, have the graphitic structure, in agreement with the conclusions of the previous paper [21]. The higher spin density can be accounted for by the instability of the graphitic films upon exposure to the atmosphere [21].

Doping by carbon increases both the spin density as well as the g value in agreemment with the notion that carbon stabilizes the electron in the nitrogen vacancy. It is important to notice that even in our films which were not intentionally doped with carbon there should be some impurities (i.e. C, O) which stabilize the electron in the nitrogen vacancy.

These findings are consistent with the model that nitrogen vacancies are required to stabilize the cubic phase of this material [3,4].

ACKNOWLEDGMENTS

This research was supported by the National Science Foundation (Grant No. DMR-9014370). We are indebted to Prof. Hans Van Willigen of the University Of Massachusetts for the use of the EPR facilities.

REFERENCES

1. R.H. Wentorf Jr, *J. Chem. Phys.*, 36, 1990 (1961)
2. M. Sokolowky, *J. Crystal Growth*, 46, 136 (1979)
3. Y. Bar-Yam and T.D. Moustakas, *Nature*, 342, 786 (1989)
4. Y. Bar-Yam and T.D. Moustakas, *Mat. Res. Soc. Symp. Proc.*, 162, 201 (1990)
5. M.V. Vlasova, N.G. Kakazei and G.I. Savvakin, *Izv. Akad. Nauk SSSR, Neorg. Mater.*, 16, 2160 (1980)
6. V.B. Shipilo, A.E. Rud', G.V. Leushkina, V.S. Kuz'min and I.I. Ugolev, *Izv. Akad. Nauk SSSR, Neorg. Mater.*, 23, 1993 (1987)
7. D. Geist and G. Romelt, *Solid State Comm.*, 2, 149 (1964)
8. G. Romelt, *Z. Naturforschg.*, 21a, 1970 (1966)
9. M.B. Khusidman and V.S. Neshpor, *Zh. Eksp. Teor. Khim.*, 3, 270 (1967)
10. G. Romelt, in Lattice Defects in semiconductors, Tokyo 407 (1966)
11. M.B. Khusidman and V.S. Neshpor, *Soviet Physics Solid State*, 10, 975 (1968)
12. A.W. Moore and L.S. Singer, *J. Phys. Chem. Solids*, 33, 343 (1972)
13. A. Katzir, J.T. Suss, A. Zunger, A. Halperin, *Phys. Rev. B*, 11, 2370 (1975)
14. A. Zunger and A. Katzir, *Phys. Rev. B*, 11, 2378 (1975)
15. E.Y. Andrei A. Katzir and J.T. Suss, *Phys. Rev. B*, 13, 2831 (1976)
16. D. Geist in Boron and refractory borides, p. 65, Springer (1977)
17. V.B. Shipilo, A.E. Rud', G.V. Leushkina, V.S. Kuz'min and I.I. Ugolev, *Izv. Akad. Nauk SSSR, Neorg. Mater.*, 24, 1303 (1988)
18. K.A. Tikhonenko, L.A. Shul'man and V.K. Gerasimenko, in Effects of High Pressure on Material Properties and Structures (in Russian), *Izd. ISM AN Ukr. SSR*, Kiev 29, (1983)
19. L.A. Shul'man and K.A. Tikhonenko, *Ukr. Fiz. Zh.*, 30, 578 (1985) (in Russian)
20. F. Zhang and G. Chen, This Volume
21. T.D. Moustakas, R. Molnar, T.Lei and E.J. Oles, This volume
22. M.D. Wiggins, C.R. Aita and F.S. Hickernell, *J. Vac. Sci. Technol.*, A2(2), 322 (1984)
23. E. Fermi, *Z. Phys.*, 60, 320 (1930)
24. J.H. Van Vleck, *Phys. Rev.*, 74, 1168 (1948)
25. C.P. Poole, Electron Spin Resonance, John Wiley, (1983 2nd ed.)

ESR CHARACTERISTICS OF CUBIC BORON NITRIDE CRYSTALS

FANGQING ZHANG AND GUANGHUA CHEN
Department of Physics, Lanzhou University, Lanzhou 730001, P.R.China

ABSTRACT

Electron spin resonance (ESR) spectrum have been used to study undoped cubic boron nitride crystals.The results show that the peak-to-peak width of the ESR signal is 27×10^{-4}T and the g-value is 2.00248, the spin density N_S is 2.8×10^{15} cm^{-3},it is considered that the ESR signal is originated from the nitrogen dangling bond. Raman spectrum measurements have been also carried out, the peak positions are at 1054 cm^{-1} and 1306 cm^{-1}.

Introduction

Since the realization of the synthesis of cubic boron nitride (cBN) crystals by Wentorf [1] in 1957, the development of cBN crystals has pursued vigorously in the past few years.Similar to diamond, bonding in cBN have the covalent aspects which provide a tetrahedral-bonding structure--the cubic structure of zinc blende, so this compound was found to be chemically inert, thermally conducting, electrically resistive, and with a hardness second only to that of diamond, it is an attractive material for mechanical, electronic and optical applications.

The use of cBN in electronic devices designed to operate at high temperature is especially noticeable, the high-temperature diode [2] and the ultraviolet-light emiting diode [3] have been already reported. But the high defect density in synthetic cBN have strong influence on the performance of these devices, which obstructs the widespread uses of this kind of material. In this work, electron spin resonance (ESR) and Raman spectra measurements have been carried out to study the defect and microstructure in cBN, and the origination of the defects has been explored.

Experimental

cBN crystals used in this work were prepared by high-pressure, high-temperature method, the grain size was about 2 mm x 1 mm x 0.5 mm. Equilibrium ESR spectrum measurements of these grains have been carried out by using a BRUKER ER 200D-SRC spectrometer in X-band at 300 K. Modulation field was 100 KHz, the microwave power was kept below 2 mW to avoid the saturation of the defect signals, the center magnetic field was 3492×10^{-4}T.

Raman spectrum of cBN was obtained by a SPEX 1403 model Raman spectrometer. A 5145 Å line of an Ar laser was used for the excitation, the incident power was 200 mW.

Results and discussions

A typical ESR spectrum of cBN is shown in Fig.1. As we can see from this figure, the lineshape of the ESR signal is of Lorentz type, the g-value calculated from the ESR spectrum is

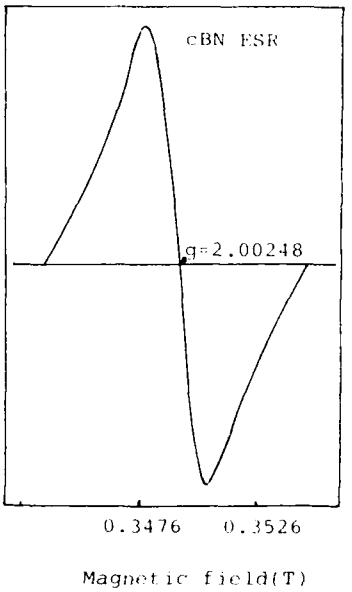


Fig.1. ESR spectrum of cBN crystals at 300 K.

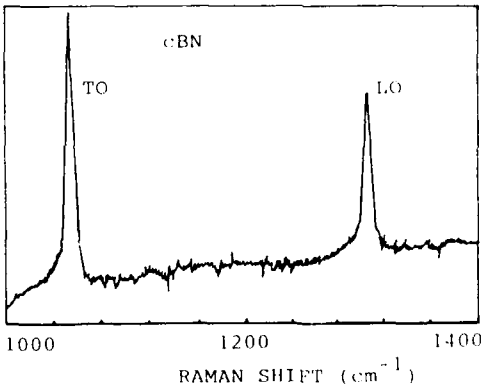


Fig.2. Raman spectrum of cBN crystals.

2.00248, the peak-peak width ΔHpp is 27×10^{-4} T, the spin density is $2.8\times10^{15}cm^{-3}$. The calibrating specimen for the quantitative measurements is Li:F:Li with g= 2.00229, and ΔHpp = 0.6×10^{-4}T. From the g-value we deduced that the ESR signal of the cBN originated from the nitrogen dangling bond.

Shown in Fig.2 is the Raman spectrum of the cBN. Here we can see that,the Raman scattering peak of the TO-mode is at 1045.5cm^{-1} and the LO-mode is at 1306.5 cm^{-1}, the peak intensity ratio of the TO-mode and LO-mode is about 2, this result is consistent with that of Ref.4. Fig.2 also demonstrates that there is a fairly wide scattering band, this indicates that there exists a certain component of disordered phase in the cBN, which is responsible for the high defect density obtained from the ESR measurements.

Acknowledgment

We thank professor I. Inuzuka for the providing of the cBN samples.

References

1. R.H.Wentorf, J. Chem. Phys. 26, (1957) 956.
2. O.Mishima, S.Yamaoka and O.Fukunaga, J.Appl.Phys. 61, (1987) 2822.
3. O.Mishima, K.Era, J.Tanaka and S.Yamaoka, Appl.Phys.Lett. 53, (1988).
4. I.Inuzuka, New Diamond (Japan), Vol.6, No.4, (1990) 5.

THE EFFECTS OF SUBSTRATE BIAS AND Si DOPING ON THE PROPERTIES OF RF SPUTTERED BN FILMS

P.K. BANERJEE, J.S. KIM, B. CHATTERJEE, M. PLATEK AND S.S. MITRA

Thin Film Research Laboratory, Department of Electrical Engineering
University of Rhode Island, Kingston, RI 02881, USA

ABSTRACT

The effect of substrate bias on the properties of rf sputtered boron nitride films on Si and GaAs substrate were investigated. IR transmission and reflectivity of films with different substrate bias were measured with Perkin Elmer 983 IR spectroscopy. From the IR reflectivity data, transverse optical mode(TO) and longitudinal optical mode(LO) frequencies were derived by fitting Kramer-Kronig model. Absorption coefficient was determined from IR transmission data. The resultant TO and LO modes showed that substrate bias caused broadening of reststrahlen band of rf sputtered boron nitride. We also tried to dope boron nitride films with silicon by alternate sputtering of BN and Si targets controlling sputtering time of each target followed by annealing. Electrical resistivity was measured over the temperature range between 175 K to 370 K for both intrinsic and Si-doped boron nitride films. Intrinsic rf sputtered boron nitride showed little change in resistivity (10^9 Ω cm - 10^{11} Ω cm) over the temperature range studied. While Si doped BN showed linear change in resistivity with increasing temperature and its activation energy was about 0.22 eV. The effect of substrate bias was also investigated by monitoring the XPS core level spectra of both B 1s and N 1s peaks, respectively. Substrate bias caused the shift of both B 1s and N 1s peak to higher binding energy. The effect of substrate bias on refractive index was also studied.

1. INTRODUCTION

Boron nitride has many useful properties BN can be prepared several ways, such as sputtering[1-2], chemical vapor deposition[3], ion plating[4], etc. Especially in the sputtered BN films, substrate bias has been known to affect the phase of sputtered BN. Some authors[4] have reported that substrate bias is solely responsible for the formation of cubic phase BN while Seidel et al[2]' data showed slight broadening of IR band on increasing bias. However not much study has been done on the effect of substrate bias on the optical properties of sputtered BN films. Therefore we studied the effect of substrate bias on the optical properties of rf sputtered BN films by monitoring reststrahlen band characteristics of films prepared with various substrate bias voltage. TO and LO modes of resultant films were calculated by Kramer-Kronig model[5] from IR reflectivity data. In addition, XPS spectra of B 1s and N 1s was also taken to see how the substrate bias effect the chemical bonding of sputtered BN. Another important aspect in the study of BN film lies in the electrical doping. Here we attempted to dope BN with Si by alternate sputtering of BN and Si. Electrical resistivity was measured over the temperature range for both intrinsic and Si-doped BN films.

2. EXPERIMENTAL DETAILS

Boron nitride films were sputtered from BN target(99.99%) by MRS 8667 three target sequential rf sputtering unit. Most of films were were deposited in Ar/N_2 mixture. Films were deposited with a rf power of 250 W both at room temperature and at 200°C. Substrates were sputter etched for 30 minutes at 200W just prior to deposition. The partial pressure of nitrogen was kept at 4.0mT - 5.0 mT to make near-stoichiometric BN films as indicated by our earlier experiments. The total pressure of Ar/N_2 mixture was kept fixed at 8 mTorr for all depositions. Substrate bias between -100 V to 0 V was applied during sputtering. Deposition rate of boron nitride films varied from 19 $\sim$ to 28$\AA$/min with substrate bias voltage. For doping with Si, Si was deposited at a power of

Bias voltage(V)	Refractive index
0.0	2.0
-20.0	1.9
-50.0	1.6
-100.0	1.67

Table 1: Refractive index vs. bias voltage.

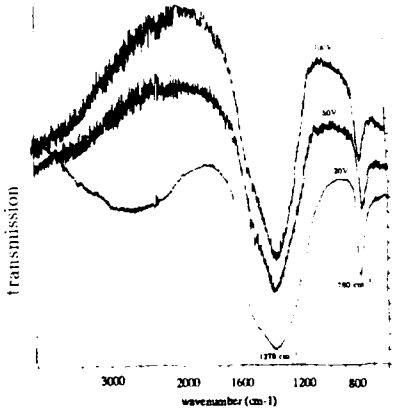


Figure 1: The effect of substrate bias on IR transmission of BN films

100 W in the same environment used to deposit boron nitride. After Si-doped BN was annealed at 500°C for 30 minutes in N_2 atmosphere. X-ray photoelectron spectroscopy was carried out by Physical Electronics PHI 5500 multitechnique surface analyzer. The test chamber was pumped by a sputter ion pump with auxiliary titanium sublimation pump and the base vacuum was about 7 x 10^{-10} Torr. All the measurements were done in the vacuum better than 2 x 10^{-9} Torr. Mg Kα radiation of 1253.6 eV was used as the excitation source. Analyzer energy was 71.55 eV. To avoid the shift of peak by static charging, all peaks were referenced to 1s peak of adventitious carbon at 284.6 eV, measured at an accuracy of 0.1 eV. Infrared transmission and reflectance was studied over the wavenumber of 4000cm^{-1} - 600cm^{-1} by a Perkin Elmer 983 double beam IR spectrophotometer. Refractive index was measured by ellipsometer at a wavelength of 6328$\AA$. Electrical resistivity was measured by four point probe method using two Kiethley 616 electrometer at room temperature. The change in resistivity with temperature increase was monitored by conventional two point probe. Two aluminum contacts separated by the distance of 1.0 mm were deposited on BN films on Al_2O_3 substrates by rf sputtering.

3. RESULTS AND DISCUSSION

The effect of substrate bias on refractive index of BN film is shown in Table 1. Substrate bias seems to reduce refractive index.

Figure 1 shows IR transmission curves of BN films deposited with different bias. For all the films, two absorption peaks characteristic to hexagonal boron nitride are found at 1378 cm^{-1} and 780

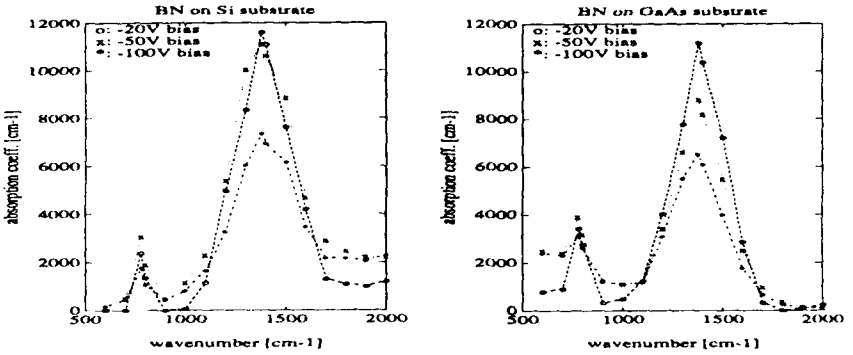


Figure 2: The effect of substrate bias on absorption coefficient of BN films deposited a) Si b) GaAS substrates

cm^{-1}, which is due to B-N stretching and B-N-B bending. Films sputtered with -20V bias, showed two additional peaks at 3400 cm^{-1} and around 2500 cm^{-1} which lacks in the films deposited with higher bias. These peaks are thought to be due to N-H stretching and B-H stretching[6]. Seidel et al[2] reported similar results. Therefore it is possible to say that substrate bias reduces the amount of hydrogen in the films. However, we could not see any shift in both 1378 and 780 cm^{-1} with the change of the substrate bias.

The effect of bias on the absorption coefficient is shown in figure 2. For BN films deposited both on Si and GaAs substrates, the absorption coefficient decreases with the increase of substrate bias. In order to find out TO and LO modes of the films, IR reflectivity data was fitted using Kramer-Kronig relation. Figure 3 exhibits good agreement between measured reflectivity and fitted data by Kamer-Kronig relation for films deposited without bias. Figure 4 shows the effect of bias on the refractive index calculated by Kramer-Kronig relation.

Table 2 lists TO and LO modes of biased and unbiased films. LO and TO modes were obtained from the minima and maxima of modulus of the dielectric constant. As shown in table 2, there is no shift in the position of TO mode with substrate bias. This corroborates the fact that there is no shift in 1380 cm^{-1} in IR transmission. Contrary to TO mode, LO mode showed a shift to higher energy with substrate bias, thereby causing broadening of the reststrahlen band. Based on the IR data we assume that our BN film is amorphous or nanocrystalline hexagonal. However, we have not seen appreciable change in the structure of films except broadening of IR band with substrate bias. Gissler et al[8] reported similar results for BN films by magnetron sputtering.

The effect of substrate heating was also studied. Although substrate heating seems to increase the deposition rate, it has little effect on optical properties. Figure 5 shows the effect of heating on the absorption coefficient.

Figure 6 shows XPS survey spectra of BN films deposited with -50 V substrate bias. Figure 7 shows the effect of substrate bias on XPS core level spectra of B 1s and N 1s. Substrate bias caused the shift of both B 1s and N 1s peak to higher binding energy.

BN is a wide bandgap semiconductor and it is very important to be able to control its electrical properties. We tried to dope BN films with silicon by alternate sputtering of BN and Si targets. Resistivity of intrinsic BN films is in the range of (10^9 Ω cm - 10^{11} Ω cm at room temperature.

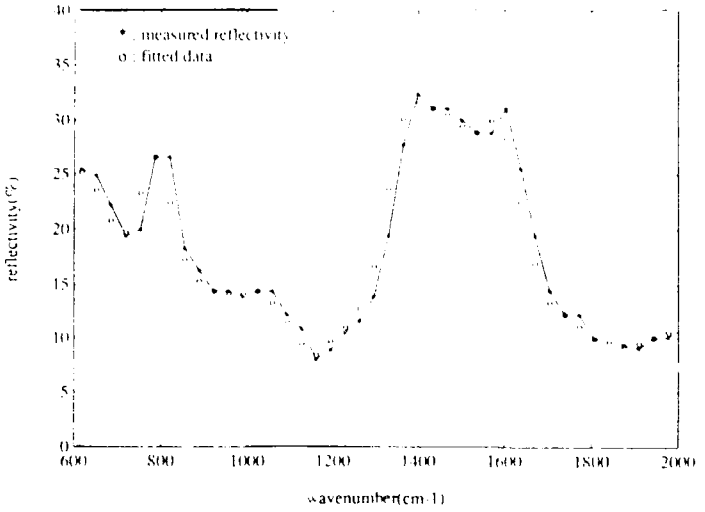


Figure 3: Measured and fitted IR reflectance of BN films prepared with no bias.

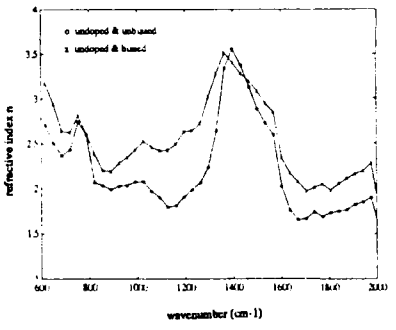


Figure 4. The effect of substrate bias on refractive index of BN films on Si.

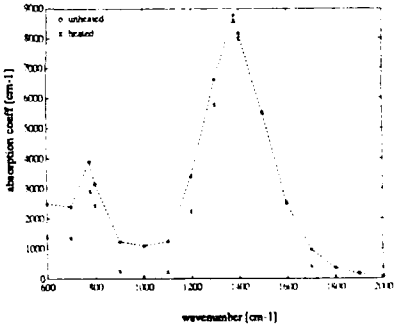


Figure 5. The effect of substrate heating on absorption coefficients of BN films.

Films	LO mode	TO mode
Undoped, unbiased	1728 cm^{-1}	1378 cm^{-1}
Undoped, biased	1741 cm^{-1}	1378 cm^{-1}

Table 2: LO and TO modes of BN films.

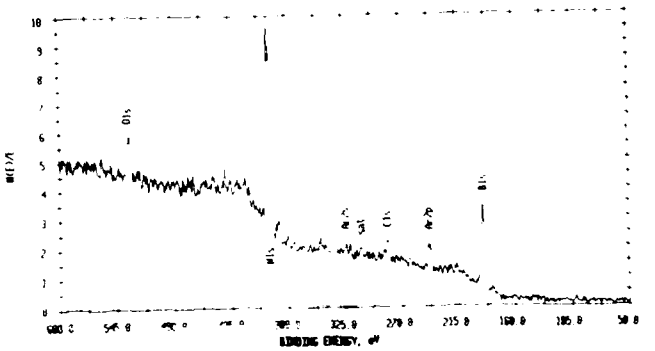


Figure 6: XPS survey spectra of BN films deposited with -50V substrate bias

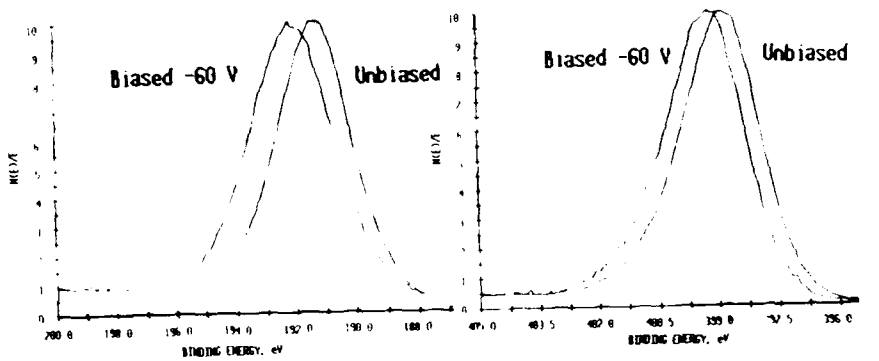


Figure 7: The shift of XPS peaks of a) B 1s b) N 1s for different substrate bias.

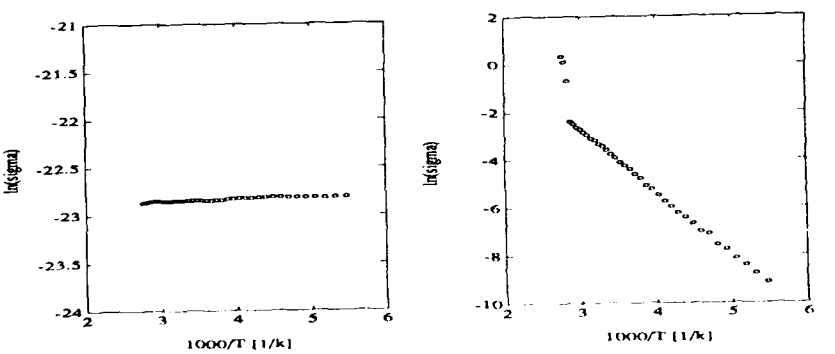


Figure 8: Conductivity as a function of temperature a)intrinsic b) Si doped BN film.

The conductivity of intrinsic BN films as a function of temperature deposited with -50V substrate bias is shown figure 8 a). There is little change in the conductivity over the temperature range studied. The conductivity of Si-doped BN film sputtered under the same condition is shown as a function of temperature in figure 8 b). It shows linear increase in the conductivity with the increase in temperature, which proves that the film is doped. Activation of Si-doped BN films was about 0.22 eV. Mishima[7] reported similar results for Si-doped n type BN films. Detailed discussion of Si-doped BN films will be published elsewhere.

4. CONCLUSIONS

The effects of substrate bias on the propertiers of rf sputtered BN film has been investigated for both undoped and Si-doped BN. Reststrahlen band was calculated using Kramer-Kronig model from IR reflectivity data. Substrate bias is seen to cause broadening of reststrahlen band of rf sputtered BN. It is also shown that doping of BN Si can be achieved by alternate sputtering of BN and Si. Linear increase in the conductivity of Si doped film with temperature increase showed that film is doped. Its activation energy was about 0.22 eV.

REFERENCES

1. M.D. Wiggins, C.R. Aita and F.S. Hickernell, J. Vac. Sci. Technol. A, 2(2), 322(1983)
2. K. Seidel, K. Reichelt, W. Schal and H. Dimigen, Thin Solid Films, 151, 243(1987)
3. J. Kouvetakis, V.V. Patel, C.W. Miller and D.B. Beach, J. Vac. Sci. Technol. A., 8(6), 3929(1990).
4. T. Ikeda, Y. Kawate and Y. Hirai, J. Vac. Sci. Technol. A., 8(4), 3168(1990).
5. P.J. Gielisse, S.S. Mitra, J.N. Plendl, R.D. Griffis and L.C. Mansur, Phys. Rev., 155, 1039(1967).
6. S.P.S. Arya and A. D'amico, Thin Solid Films, 157, 267(1988).
7. O. Mishima, MRS Proceedings, Vol. 162, 543(1990).
8. W. Gissler, J. Haupt, A. Hoffman, P. N. Gibson and G. Rickerby, *Thin Soild Films*, 199, 113(1991).

SUBMILLIMETER OPTICAL PROPERTIES OF HEXAGONAL BORON NITRIDE

A. J. Gatesman, R. H. Giles and J. Waldman
Department of Physics and Applied Physics
University of Massachusetts • Lowell
Lowell, MA 01854

ABSTRACT

The submillimeter optical properties of hot-pressed boron nitride with a hexagonal crystal structure were studied at room temperature from approximately 20 cm^{-1} to 120 cm^{-1} (500μm - 84 μm) with a Fourier Transform Spectrometer. Several grades were studied and probed both parallel and perpendicular to the material's optic axis. The material was found to behave as a negatively uniaxial birefringent crystal. In one case, the birefringence ($\Delta n = n_e - n_o$) was quite large with a value of -0.152. The material's absorption properties were also studied. For certain grades, a modest dichroism was observed. The low absorption ($\alpha < 1$ cm^{-1}) for grade A at frequencies below 38 cm^{-1} suggests the possibility for millimeter/submillimeter wave applications. Results are compared with data by other researchers on related materials.

INTRODUCTION

Boron nitride (BN) has received considerable attention within the last few years due to its favorable mechanical, electrical, optical and chemical properties over a wide range of temperatures. BN crystallizes in two forms; cubic (zinc blende) and hexagonal structures. BN films grown by processes such as CVD and sputtering have the cubic crystal structure (similar to that of GaAs). This material is used in applications such as transmitting substrates for X-ray lithography masks, high quality insulating films for metal-insulator-superconductor (MIS) structures, and coatings to increase the hardness of materials.[1] The material used in this study was hot-pressed BN where the raw material is subjected to a high uniaxial compressive force at an elevated temperature. This results in an orderly arrangement of the boron and nitrogen atoms (a structure similar to that of graphite, see Figure 1). Boron nitride has previously been studied in the ultraviolet, optical, infrared, and microwave frequencies.[2,3,4] Its low absorption coefficient in the microwave has made BN a candidate for window material for gyrotrons, free electron lasers and reentry vehicle communication systems.[4,5] This paper reports the optical properties of hexagonal BN (*h*-BN) in the submillimeter region of the spectrum.

A material with a hexagonal crystal structure is known to be optically anisotropic with a single optic axis coinciding with the axis of crystal symmetry.* In this case, the dielectric constant ε is a 3 x 3 tensor. The dielectric tensor can be shown to be symmetric[7] and the nine components reduce to six where $\varepsilon_{ij} = \varepsilon_{ji}$ for $j \neq i$. Furthermore, there exists an orientation of the cartesian coordinate system where its axes are alined with the material's preferred axes (i.e. in the hexagonal case, one of the cartesian axes alined with the optic axis). This coordinate system is referred to as the principal set of axes and the six components of ε will reduce to three (ε_x, ε_y, ε_z) where the off axis elements are zero.

*Materials with a tetragonal, trigonal or hexagonal crystal structure have a single optic axis and are said to be uniaxial. Orthorhombic, monoclinic and triclinic systems have two optic axes and are said to be biaxial. The remaining crystallographic system, cubic, is optically isotropic.[6]

With the cartesian coordinate system alined along the materials's preferred axes as in Figure 1, ε_y will equal ε_z due to the degree of symmetry inherent in the hexagonal crystal structure. In this case, the x axis is the axis of symmetry (the optic axis) and the planes of atoms are in the y-z plane. This leaves the dielectric constant (or equivalently the complex refractive index, n - ik) to be determined for just *two* cases; (1) the electric field parallel to the x axis and (2) the electric field in the y-z plane.

Hot pressed hexagonal boron nitride was obtained in four grades (A, HP, M, M26) from The Carborundum Co. in Niagara Fall, NY. Two samples per grade were provided; one whose flat surface was parallel to the crystal planes and one whose flat surface was perpendicular to the crystal planes. With a controlled incident linear state of polarization, the response of both parallel and perpendicular directions to the optic axis could be probed.

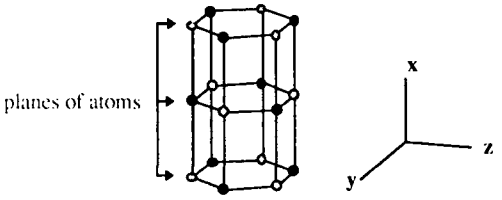


Figure 1 Orientation of the cartesian cooridinate system to coincide with the material's preferred axis and the arrangement of planes of atoms

EXPERIMENTAL

The optic axis of the parallel cut samples is obviously normal to the sample surface. For normally incident radiation, these disks were expected to behave as optically isotropic materials. The optic axis of the perpendicular cut samples lay somewhere along a diameter and had to be located. This direction was determined in the following manner. 513μm radiation from a CO_2 optically pumped submillimeter laser was propagated through a pair of wiregrid polarizers, the wires oriented orthogonally with respect to one another. The BN sample, mounted in a computer controlled rotation stage, was situated between the two wiregrids as shown in Figure 2.

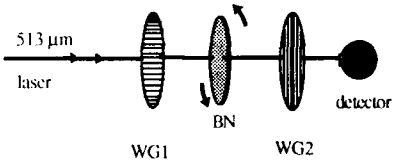


Figure 2 Experiment to determine the location of the optic axis on the perpendicular cut samples

The laser radiation, linearly polarized by WG1, was incident on the BN which was rotated while the detector collected intensity data. In general, the birefringent properties of the perpendicular cut BN depolarized the incident linear state of polarization and WG2 passed a portion of this to the detector. However, when the optic axis of the BN crystal was parallel *or* perpendicular to the wires of WG1, the linear state incident on the BN remained polarized since this state probed only ε_x or ε_y, not a combination of both. For these orientations (obviously four orientations per sample) WG2 reflected all radiation incident upon it and the intensity at the detector was zero. This procedure allowed for the determination of the two orthogonal axes in the plane of each perpendicular cut sample to within two degrees.

In order to distinguish the optic axis, a Fourier Transform Spectrometer was employed from 18 cm^{-1} to 118 cm^{-1}. Our instrument has been optimized for long wavelength data collection by using a liquid helium cooled silicon bolometer with a cooled low-pass filter as the detector. Data was collected with a resolution of 0.1 cm^{-1}. A pair of wiregrid polarizers configured with their wires parallel were positioned in front of the BN to insure a well defined linear state incident on the material. Twelve spectra were collected in total. The first four were grades A, HP, M and M26 in the parallel orientation. The remaining eight were the four grades with the optic axis parallel and perpendicular to the incident linearly polarized radiation. The transmission spectra for grades A and M26 in the perpendicular orientation are shown in Figure 3.

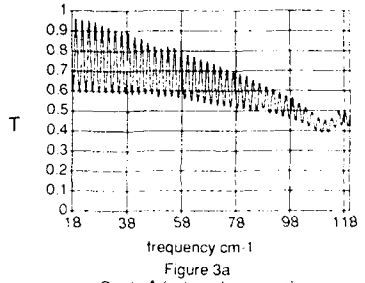


Figure 3a
Grade A (extraordinary axis)

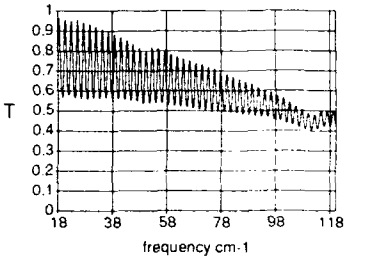


Figure 3b
Grade A (ordinary axis)

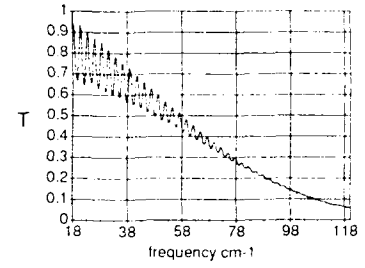


Figure 3c
Grade M26 (extraordinary axis)

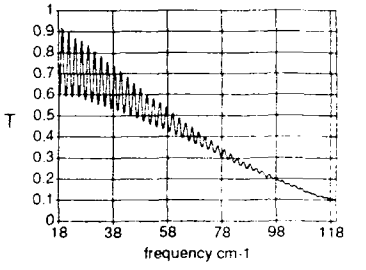


Figure 3d
Grade M26 (ordinary axis)

Spectra for grades HP and M in the perpendicular orientation are similar to (but not identical) to the M26 spectra and are not shown. The spectra of the parallel cut samples are not shown as they were nearly identical to one of the two perpendicular cut samples (as expected) and were useful only in determining which axis was the extraordinary (optic) axis and which one was the ordinary axis. Grade A is interesting because of its lower loss and M26 is interesting because of its dichroic behavior. Both of these points will be returned to later in the Results and Discussion section.

Derivation of the Optical Properties

The material's refractive index n, and absorption coefficient α, were both determined from the transmissivity data. Characteristic of all of the spectra is the rapid oscillation which is caused by the interference between the front and back surfaces of the sample (channel spectra). A transmission maxima occurs when an integral number of wavelengths within the material equals twice the thickness:

$$m \lambda_n = 2t,$$

where λ_n equals λ/n and m = 0, 1, 2, 3,... or written another way: $n = \frac{m}{2 t \nu}$ where ν is the frequency in cm^{-1}. The thickness of the samples were measured with an uncertainty of ±0.0001" (±3μm). With the order number and location in frequency of each of the maxima determined, a value of n could then be associated with each peak of the spectra. Values of n for the extraordinary (optic) axis and perpendicular to it (ordinary axis) are given in Figure 4 and are labelled n_e and n_o respectively. The uncertainty in n is ± 0.006 and is due primarily to the uncertainty in the material's thickness ($\delta t/t \approx 0.003$).

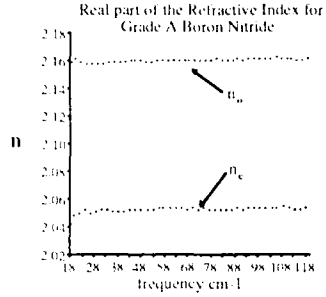


Figure 4a

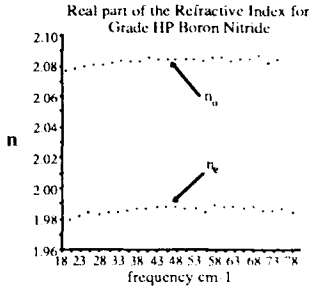


Figure 4b

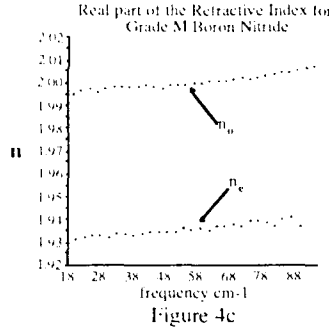


Figure 4c

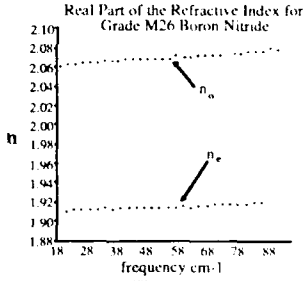


Figure 4d

Calculation of the material's absorption coefficient, α, as a function of frequency was performed in the following way. First realize that the transmissivity T through a homogeneous etalon of uniform thickness is a function of the complex refractive index, thickness and the wavelength:

$$T_{expt} = f(n, k, t, \lambda).$$

For each peak in the spectra, n, t, λ and T_{expt} are known. This leaves the a single unknown, k, to be determined ($\alpha = 4\pi k/\lambda$). A value of k at a given peak is found by increasing k from 0 until a modelled value of the transmissivity (T_{model}) using the appropriate n, t and λ, matches the experimental value. Values of the absorption coefficient α are given for the four grades in Figure 5.

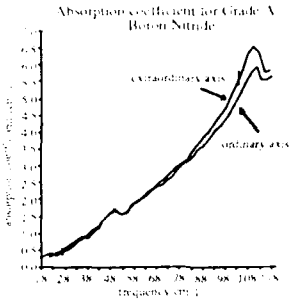


Figure 5a

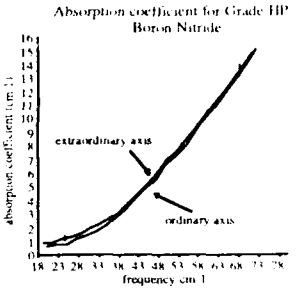


Figure 5b

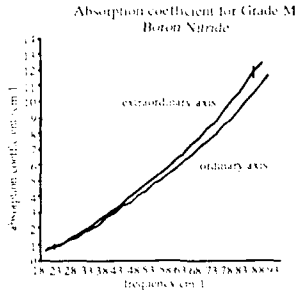


Figure 5c

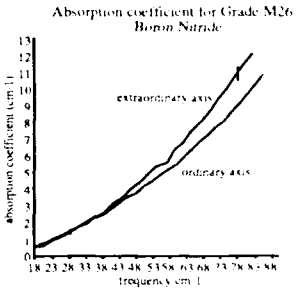


Figure 5d

The uncertainty in α is difficult to calculate because it cannot be solved analytically in terms of T_{expt}, n, λ, and t. However, since the major source of error in α is the uncertainty in T_{expt}, $\delta\alpha$ can be estimated in the following manner. The accuracy of the transmissivity data is ≤ 0.02. After a value of k is found at a particular peak that reproduces the data, it is then varied again (either higher or lower) until $|T_{model} - T_{expt}| > 0.02$. This value of k is called k_{error} and an estimate in the uncertainty in k is given by $|k - k_{error}|$. The corresponding uncertainty in α is indicated by the error bars on two data points in each of the plots. Two bars are given to indicate any slow changes in the uncertainty with frequency.

RESULTS AND DISCUSSION

The birefringence was found to be roughly constant in this frequency range for all of the grades. Values of Δn were -0.108, -0.098, -0.065, and -0.152 for grades A, HP, M and M26 respectively. Optical properties of related ceramics also show a strong birefringence. Aluminum Oxide has a rhombohedral crystal structure and is therefore a uniaxial material. Δn has been measured by Ref. 8 to be 0.36 at 100 cm^{-1}. Beryllium Oxide with a hexagonal crystal structure was found to have a birefringence[9] of 0.144 at 100 cm^{-1}. One difference between these materials and *h*-BN is that *h*-BN exhibits a negative birefringence.

All grades of BN studied were found to exhibit dichroic behavior to some degree as can be seen in Figure 5. In grades A, M, and M26, the dichroism ($\Delta\alpha = \alpha_e - \alpha_o$) is seen to be frequency dependent with increasing values towards shorter wavelengths. Grade HP is the only exception with $\Delta\alpha$ barely larger than the uncertainty at the longest wavelengths studied. In all cases the absorption measured for the electric field parallel to the optic axis was found to be greater than the absorption for the electric field perpendicular to the optic axis and so the dichroism is said to be positive.

For low loss applications in the submillimeter, grade A possesses the most desirable properties. Its refractive index remains roughly constant over the frequency range studied and it exhibits the least absorption of the four grades studied ($\alpha \approx 1$ cm^{-1} at frequencies ≤ 38 cm^{-1}).

CONCLUSION

Hexagonal Boron Nitride, a wide bandgap semiconductor, has received recent attention in the millimeter/submillimeter spectral region due to its many desirable properties. Several grades of *h*-BN were obtained from The Carborundum Company and their room temperature optical properties were studied from 18 cm^{-1} - 118 cm^{-1}. The refractive index n and absorption coefficient α were determined in the submillimeter. The material was found to possess a measurable birefringence, and in some cases, exhibited a slight dichroic behavior. For low loss applications in the submillimeter, grade A appears to be the most desirable with the lowest absorption coefficient of the grades studied.

REFERENCES

1. S.P.S. Arya and A. D'Amico, Thin Solid Films 157, pg. 267-282 (1988)

2. C. Tarrio and S. E. Schnatterly, Phys. Rev B, 40, (11), (1989-I)

3. D. M. Hoffman, G. L. Doll and P. C. Eklund, Phys. Rev B, 30, (10), (1984)

4. H.P.R. Frederikse, A. H. Kahn, and A. L. Dragoo, J. Am Ceram. Soc., 68 (3) 131-135 (1985)

5. J. M. Dutta and C. R. Jones, J. Appl. Phys., 64 (9), 4674 (1988)

6. E. Hecht and A. Zajac, Optics, (Addison-Wesley 1974) Chap. 8

7. M Born and E. Wolf, Principles of Optics, 6th edition, (Pergamon Press 1980), Chap. 14

8. A. S. Barker, Phys. Rev., 132, 1474 (1963)

9. E. Loh, Phys. Rev., 166, 673 (1968)

THERMOELECTRIC PROPERTIES OF BORON AND BORON PHOSPHIDE FILM

Y.KUMASHIRO*, T.YOKOYAMA*, J.NAKAMURA*, K.MATSUDA**, H.YOSHIDA*, AND J.TAKAHASHI***

* Yokohama National University, Tokiwadai 156 Hodogaya-ku, Yokohama, Kanagawa, 240 Japan

** Institute of Industrial Science, University of Tokyo,7-22-1,Roppongi, Minatoku,Tokyo,106 Japan

*** Sumitomo Metal Mining Coorporation, 3-5-3 Nishihara-cho, Niihama, Ehime, 792 Japan

ABSTRACT

This paper describes the thermoelectric properties of amorphous or polycrystalline boron and boron phosphide films prepared using chemical vapor deposition and molecular beam deposition. The temperature dependencies of electrical conductivity of a-B and distorted $B_{13}P_2$ films obey the Mott's rule of $\log\sigma$ vs $T^{-1/4}$, while those of polycrystalline BP films have linear relationship between $\log\sigma$ vs T^{-1}. The a-B and $B_{13}P_2$ films have high electric resistivity and show p-type conductors while BP film shows n-type conductor. The estimated thermoelectric figure of merit of boron phosphide film is compatible to that of sintered specimen, but there remains some problems for a-B to alter.

1.INTRODUCTION

Boron-based semiconductors are refractory semiconductors and are divided into two categories, i.e., boron rich semiconductors derived from four crystalline boron modifications and Ⅲ-Ⅴ compound semiconductors of BP and BAs. One of their common characteristics is high thermoelectric power, which is promising for high temperature thermoelectric devices. The formation of p-n junction is required for thermoelectric device, but there exist some problems.

The undoped boron shows p-type conductor and it is very difficult to prepare n-type boron rich semiconductors by doping [1,2,3]. As for boron phosphide, its single crystalline wafer has high thermoelectric power[4],but the thermal conductivity is also high[5,6] which reduces thermoelectric figure of merit of 1×10^{-8}/K[7]. Then BP single crystalline wafer is not applicable to thermoelectric device. The thermal conductivity of BP sintered polycrystal[8] is smaller than that of single crystslline wafer, which would expect to increase the figure of merit. However thermoelectric power of BP sinterd specimen depends on the purity of starting powder[7]. We have obtained high thermoelectric power and high figure of merit using high purity BP powder prepared by hydroisostatic pressnig[7]. In this case it is very difficult to obtain n-type BP sintered specimen.

Then we have chosen boron film for p-type material and BP polycrystalline film for n-type material as a first step to integrate the thermoelectric device.

The present paper describes such thermoelectric properties as electric conductivity and thermoelectric power of boron and boron phosphide amorphous or polycrystalline films by molecular beam method and by chemical vapor deposition.

2.Experimental Procedure

2.1 The preparation of thin films

The BP thin films were prepared on sapphire substrate by thermal decomposition of a B_2H_6-PH_3 mixture in hydrogen atmosphere[4]. BP film was made at gas flow rates of 20, 500 and 2500 cc/min, for B_2H_6(1% in H_2), PH_3(5% in H_2) and H_2, respectively, in the temperature of 800℃, 900℃ and 1000℃ at a deposition time of 1.5hr. X-ray diffraction pattern of the film grown at 800℃ contains α-B phase, while others show BP single phase with the lattice constant of a_o=4.54 Å. The boron thin films were prepared by molecular beam evaporation method. The schematic diagram of apparatus(Eiko Engineering, EV-10) is shown in Fig.1.

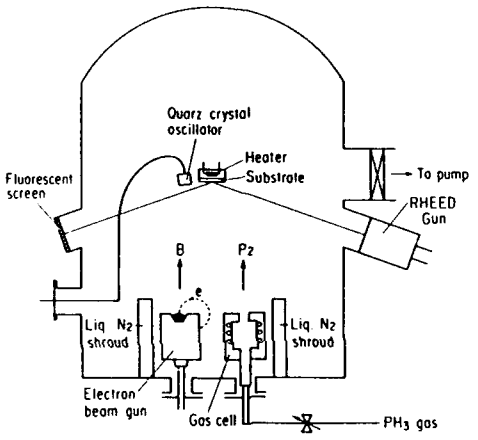


Fig.1 Schematic illustration of molecular beam deposition of boron and boron pnictide films.

The vacuum chamber was evacuated by titanium sublimation pump and an oil diffusion pump systems, and the ultimate pressure was 1×10^{-9} Torr. The sapphire substrate was fixed on sheet heater and was heated up to 800℃. After the substrate was cleaned at 800℃ for 1hr in vacuum of 1×10^{-8}Torr, boron was evaporated by an electron gun in the vacuum of $1\times10^{-7}\sim1\times10^{-8}$ Torr with an incident frequency of $1.50\times10^{16}cm^{-2}\ s^{-1}$.

Boron rod used in the experiment was prepared by zone melting process using halogen-lump image furnace. The analysis of impurities of boron rod is shown in Table 1.

Table 1 Impurity analysis of boron rod used in the experiment(ppm).

Na	Mg	Al	Si	Ca	Cr	Mg	Fe	Ni	Cu	Cd	Sn
<1	<0.1	40	28	0.6	<0.1	<0.1	70	3	0.1	0.2	<0.5

These impurities except for Fe were lost during vacuum evaporation process, which is confirmed by ICP-MS method. Then the obtained film is high purity. RHEED pattern of boron film indicates distorted crystalline pattern but that of X-ray diffraction shows amorphous.

Boron evaporated by an electron beam gun and P_2 molecular flux by cracking of PH_3(20% in hydrogen) were supplied simultaneously on the substrate as shown in Fig.1, and boron phosphide film was deposited on the

sapphire substrate at 800℃. The deposition was performed with the PH_3 flow rate of ~1.0cc/min under the vacuum of ~5×10^{-5}Torr, which is upper limit of the operation of electron beam gun. The composition of films determined using an electron probe microanalyser shows near the composition,$B_{13}P_2$ phase[9] being consistent with X-ray diffraction pattern. However,the RHEED and X-ray diffraction patterns of boron pnictide film indicate distorted crystalline structure.

2.2 Measurement of thermoelectric properties

Ohmic contacts of the films were made by evaporated of Al, followed by annealing in argon at 400℃ for 1hr. Block diagram of the apparatus for thermoelectric measurement is the same as the literature[10]. Electrical conductivity of the films were measured by two terminal method at temperature between room temperature and 600℃ under argon atmosphere. Thermoelectric voltage between hot and cold junctions was measured under constant temperature gradient of 2-3℃.

3. EXPERIMENTAL RESULT AND DISCUSSION

Electrical conductivity of boron film varies from 1×10^{-4} $S\cdot cm^{-1}$ at room temperature to 0.8 $S\cdot cm^{-1}$ at 870K. By applying $\log\sigma$ vs 1/T plot, we obtained Eg=0.6eV, which is much smaller than other amorphous boron film.

On the other hand the present boron film is amorphous, so that the electric condition is expected to be due to hopping condition.

Mott[11] has derived the equation for hopping conduction

$$\sigma = \sigma_0 \exp[-(T_0/T)^{1/4}] \qquad (1)$$

where σ_0 and T_0 are constants. The plots of $\log\sigma$ of a-B film as a function of $T^{-1/4}$ is shown in Fig.2.

The observed values show a good linear relation between $\log\sigma$ and $T^{-1/4}$, and values of $\sigma_0=1.0\times10^{15}$ $S\cdot cm^{-1}$ and $T_0=1.3\times10^9$ K are obtained. T_0 is given as a function of the density of localized states at Fermi level $N(E_F)$

$$T_0 = 16\varepsilon^3 / k\,N(E_F) \qquad (2)$$

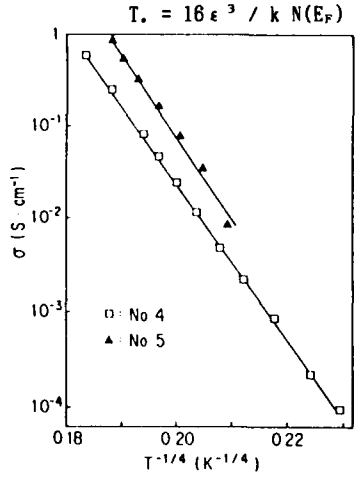


Fig.2 Dependence of conductivity on $T^{-1/4}$, No.4:a-B, No.5:$B_{13}P_2$.

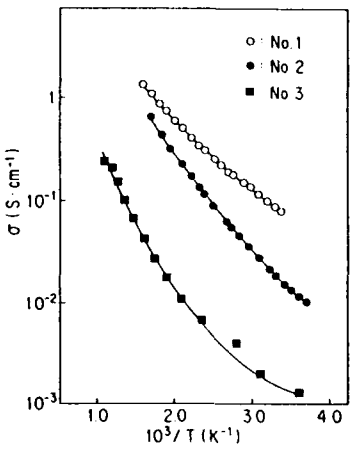


Fig.3 Temperature dependence of conductivity of BP films by CVD process, No.1:Ts=800℃, No.2:Ts= 900℃ No.3:Ts=1000℃.

where ε is the exponential decay factor of localized states ($\varepsilon^{-1} \fallingdotseq 5A$).From the value of T_0 and Eq.(2), $N(E_F)=1.1\times10^{18}$ $cm^{-3}eV^{-1}$ are obtained, which is in good agreement with the value for amorphous boron films 3.8×10^{18} $cm^{-3}\cdot eV^{-1}$[12] and for amorphous boron bulk $\fallingdotseq 10^{18} cm^{-3}\cdot eV^{-1}$ [13]. Also $T_0=6.1\times10^{9}$ K and $N(E_F)=2.4\times10^{18} cm^{-3}\cdot eV^{-1}$ are obtained for distorted $B_{13}P_2$ thin films. The evaporation of phosphorus from the film during growth process would be probable in the present boron pnictide film, which produces the deviation from the composition of $B_{13}P_2$. The Hall measurement of the present boron pnictide film indicates as low mobility of 1.8 $cm^2/s\cdot V$ as a-B film. Then the conduction of the present boron and boron pnictide films could be explained by hopping conduction between icosahedron of boron. Temperature dependencies of conductivity of boron phosphide films are shown in Fig.3. The conductivity of the present BP films are smaller than those of single crystalline BP wafers [4], but the activation energy of conduction are almost same values of 0.18-0.20eV as single crystalline wafers.

Temperature dependences of thermoelectric power for boron and boron phosphide films are shown in Fig.4. The thermoelectric power of boron and boron pnictide films show p-type conduction. They could not be measured below 600K because they were too small in comparison with the electrical noise in these temperature range. The maximum value of 600 $\mu V/K$ for a-B film at 650K decreases rapidly down to the minimum values of 270 $\mu V/K$ at 800K, which indicates the formation of donors. The thermoelectric powers reported for bulk boron[14-16] show a large peak at lower temperature, compared with those for boron film, which would be explained by higher concentrations of impurities or defects in amorphous boron films.

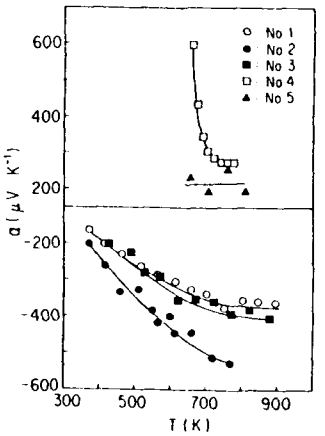


Fig.4 Temperature dependences of thermoelectric power of boron and boron phosphide films, symbols correspond to those in Fig.2 and 3.

Nakamura[12] prepared amorphous boron films containing carbon impurities by pyrolysis of decaborane in molecular flow region and also reported rapid increase of thermoelectric power from 107 $\mu V/K$ at 230℃ to a maximum value of 400 $\mu V/K$ at a 427℃ and gradual decrease to 310 $\mu V/K$ at 730℃. The present boron film is high purity with high resistivity so that such pronounce peak in thermoelectric power would not be observed.

Boron phosphide thin films show n-type conductor, which would be caused by excess phosphorus in BP. The absolute thermoelectric power increases in increasing temperature which behavior is similar to that of single

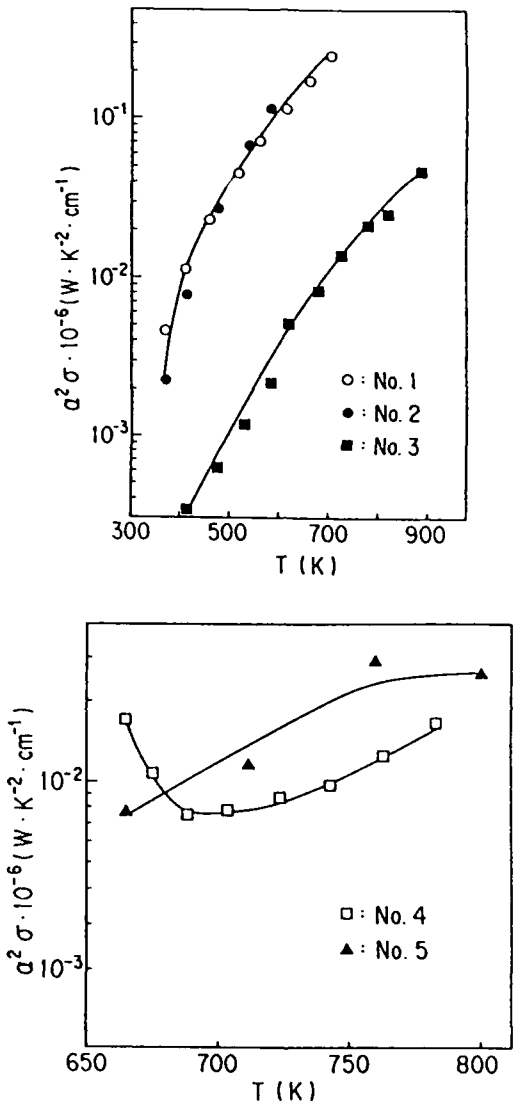


Fig.5 Electric power factor as a function of temperature, symbols correspond to those in Fig.4.

crystalline wafer[4,7]. This is due to the fact that electron concentration ranges impurity region and the Fermi energy lowers by the electron supply from donor level in increasing temperature. This is consistent with the behavior of temperature dependence of electrical conductivity. The thermoelectric power of BP films grown at 800℃ and 1000℃ tend to saturate in increasing temperature. The absolute thermoelectric power of BP film grown at 800℃ is lower than that of grown at 900℃, which would be caused by the compensation of the hole by boron phase. Contrarily, the BP film grown at 1000℃ show single phase, then hole would begin to be thermally excited by inter band transition, which transition temperature to decrease thermoelectric power would be high because of wide bandgap(2.0eV) of BP.

The temperature dependencies of electric power factor, $\alpha^2\sigma$ of these films are shown in Fig.5. The efficiency of energy conversion of thermoelectric device becomes high at larger figure of merit and at high temperature. Figure of merit for material is defined of as

$$Z = \alpha^2 \sigma / \kappa \qquad (3)$$

where κ is the thermal conductivity.

Our previous results on the thermal conductivity of sintered BP[7] indicates almost constant values of ~0.05 W/cm·K at entire temperature up to 800K, which is due to phonon scattering at grain boundary. When we use the thermal conductivity of the present BP films for 0.05W/cm·K, the figure of merit of BP film grown at 800℃ and 900℃ is to be $\sim 1.0\times10^{-5}$/K at high temperature, which is compatible to that of sintered BP specimen [7].

Contrarily, the conductivity of a-B[13] at room temperature spreads from 8×10^{-3} to 3×10^{-5}W/cm·K because of uncertainty of amorphous on the atomic scale and the microstructure such as crack or void, but it increases in raising temperature. The thermal conductivity of amorphous boron is assumed to be 1×10^{-3} W/cm·K, thermoelectric figure of merit in the present a-B film shows the order of 10^{-6}/K being one order smaller than that of BP film. Nakamura [12] found that a-B films containing 0.5~1 carbon at.% vary from 8×10^{-2}S·cm^{-1} at 300K to 30 S·cm^{-1} at 1000K. Then the present a-B film would increase the electrical conductivity by about two order of magnitude without the thermoelectric figure of merit about up to 10^{-5}/K.

4.CONCLUSION

We have prepared p-type amorphous boron and distorted polycrystalline boron pnictide thin films by molecular beam deposition, and n-type polycrystalline BP films by chemical vapor deposition and have measured the thermoelectric properties of these films. The calculated thermoelectric figure of merit for BP film is to be 1×10^{-5}/K, which is compatible to that of BP sintered specimen. The estimated thermoelectric figure of merit for a-B film is smaller than that for BP by one order magnitude,but it would expect to be compatible to BP film by doping carbon.

ACKNOWLEDGEMENT

The authors with to acknowledge Misses H.Yoshizawa and M.Matsumoto for the preparation of BP thin films. This study was performed through Special Coordination Funds of the Science and Technology Agency of the Japanese Government.

REFERENCES

1) J.M.Dusseau and J.L.Robert, J.Less-Common Met., 82, 137(1981).
2) H.Werheit, K.De Groot and W.Malkemper, J.Less-Common Met.,82, 163(1981).
3) G.A.Slack, J.H.Rosolowski, C.Hejna M.Garbauskas and J.S.Kasper, in Proc.9th Int.Symp.Boron, Borides and Related Compounds edited by H.Werheit(Universitat Duisburg Gesamthochschule 1987) pp.132-pp.141.
4) Y.Kumashiro, M.Hirabayashi and T.Koshiro, J.Less-Common Met., 143, 159(1988).
5) Y.Kumashiro, T.Mitsuhashi, S.Okaya, F.Muta, T.Koshiro, Y.Takahashiand M.Hirabayashi, J.Appl.Phys., 65,2147(1989).
6) Y.Kumashiro, T.Mitsuhashi, S.Okaya, F.Muta, T.Koshiro, M.Hirabayashi, and Y.Okaya, High Temp.-High Press. 21, 105(1989).
7) Y.Kumashiro, M.Hirabayashi and S.Takagi, in Mat.Res.Soc.Symp.Proc. Vol.162 edited by J.T.Glass, R.Messier and N.Fujimori (Mat.Res.Soc. 1990) pp.585-594.
8) Y.Kumashiro, M.Hirabayashi, T.Koshiro and Y.Takahashi, in Sintering '87, edited by S.Somiya, M.Shimada, M.Yoshimura and R.Watanabe(Elsevier Appl. Soc. 1987) pp.43-pp.48.
9) M.Takigawa, M.Hirayama and k.Shono, Jpn.J.Appl.Phys., 12, 1504(1973).
10) K.Nakamura, J.Chem. Soc.Jap., Chem.& Indust. Chem., No.5 646(1983).
11) N.F.Mott, J.Non-Cryst.Solids, 1,1(1968).
12) K.Nakamura, J.Electrochem.Soc., 131, 2691(1984).
13) A.A.Berezin, O.A.Golikova, M.M.Kazanin, T.Khomidov, D.N.Mirlin, A.V.Petrov, A.S.Umarov and V.K.Zaitsev, J.Non-Cryst.Solidi, 16, 237(1984).
14) H.Werheit and H.G.Leis, Phys.Status Solidi., 41,247(1970).
15) G.majini and M.Prudenziati, Phys.Status Solidi., A5, K129(1971).
16) J.Cueilleron, J.C.Viala, F.Thevenot, C.Brodhag, Dusseal and A.Elbiach, J.Less-Common Met., 59, 27(1978).
17) D.G.Ca[illegible]ll, H.E.Fisher, S.K.Watson, R.O.Poll and G.A.Slack, Phys.Rev., 40, 3[illegible]4(1989).
18) S.Yugo, T.Sato and T.Kimura, Appl.Phys.Lett., 46, 842(1985).

CHARACTERIZATION OF BORON CARBIDE FILMS FORMED BY PECVD

JOHN MAZUROWSKI*+, SUNWOO LEE*,
G. RAMSEYER+, AND P. A. DOWBEN*
* Department of Physics, Syracuse University, Syracuse, NY.
+ GE Electronics Laboratory, Syracuse, NY.

ABSTRACT

Boron carbide films have been fabricated from pentaborane (B_5H_9) and methane using plasma enhanced chemical vapor deposition (PECVD). Availability of high quality specimens has facilitated analysis of electronic and optical properties. We have undertaken measurements of photoluminescence spectra and infra-red band-edge absorption. Results show that the bandgap is strongly influenced by the ratio of boron to carbon. There is evidence for the existence of shallow trapping levels.

INTRODUCTION

There are many potential applications for boron carbide due to its hardness and temperature stability. Many possible phases have been identified [1,2]. Initial efforts to fabricate boron carbide employed intense heat and pressure, resulting in films stable for 9-20% carbon. More recent experiments using CVD have increased the range of attainable compositions to over 40% carbon [3]. In combining pentaborane(9) with methane at low pressures and temperatures, we have produced some highly uniform films which are suitable for electronic and optical measurements. Using PECVD, we and others have shown that composition of boron carbide films can be controlled over a wide range by adjusting reactant partial pressures [4,5].

EXPERIMENTAL

Deposition of the films was performed in PECVD apparatus described previously [5]. Plate separation was approximately one inch. Temperature, deposition time, total pressure, and microwave power were held constant as the partial pressure ratio of the two reactants was varied over the range of approximately 0.1 to 10. Growth temperatures and pressures were approximately 400°C and 50 mTorr respectively. Two types of substrates were used; silicon and high temperature glass.

Mat. Res. Soc. Symp. Proc. Vol. 242. © 1992 Materials Research Society

Measurements of composition were performed on all of the stable films by Auger electron spectroscopy. The system was calibrated using the boron 179 eV line and the carbon 272 eV line of a B_4C standard. Ar^+ sputtering was used to profile the films. A set of films with measured composition was used for all further experiments.

Most of the films were about one tenth micron thick. Measurements of film thickness were greatly influenced by substrate warp and thickness variations. To reduce this error, Auger profiling was limited by a mask to a 2 mm square. The depth of this sputtered square was measured using a Sloan Dektak profiler. Auger profile data was then calibrated to this measured depth.

Optical absorption spectra for several of the film samples were made using a Cary Model 14 Spectraphotometer, over the wavelength range of 0.4-1.6 μm. The absorption band edge and its shape were used to determine bandgap [6,7].

Photoluminescence measurements were performed using a one meter dual grating spectrometer. Room temperature spectra were done using a 200 mW 514.5 nm laser. Measurements at 12 K were done using a 15 mW 632.8 nm laser. Film compositions for spectra shown were approximately 2% carbon.

RESULTS

Optical absorption data, in the form $(\alpha E)^{1/2}$, was plotted as a function of energy. Here E is energy in units of eV, and α is absorption coefficient in units of 1/μm . Extrapolation of this curve to zero gives the optical gap [6,7]. Figure 1 shows a typical absorption curve for a film with a boron:carbon ratio of approximately 48:1; extrapolation to zero shows that the optical bandgap is 1.77 eV. Using this method for films over our entire composition range indicates that bandgap varies monotonically over a range of 0.8 eV to 1.77 eV, as shown in Figure 2. Films with the least carbon have the highest bandgap.

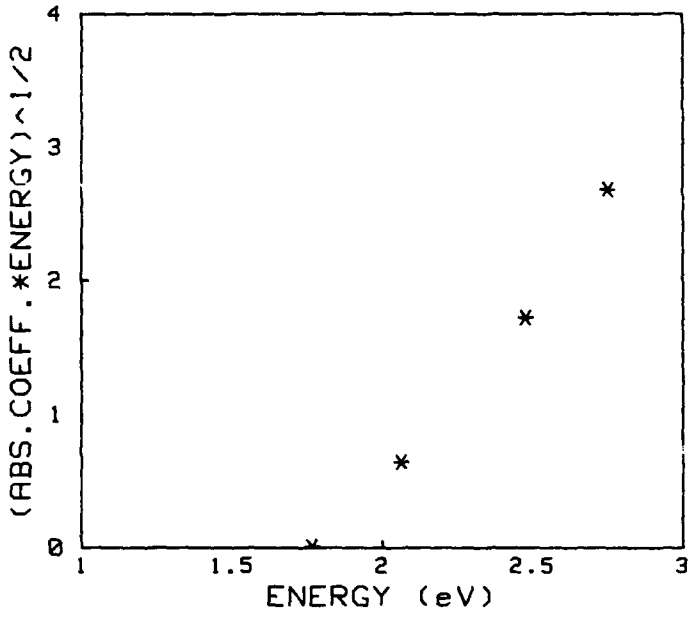


Figure 1. Optical absorption spectrum for a boron carbide film of approximately 2% carbon.

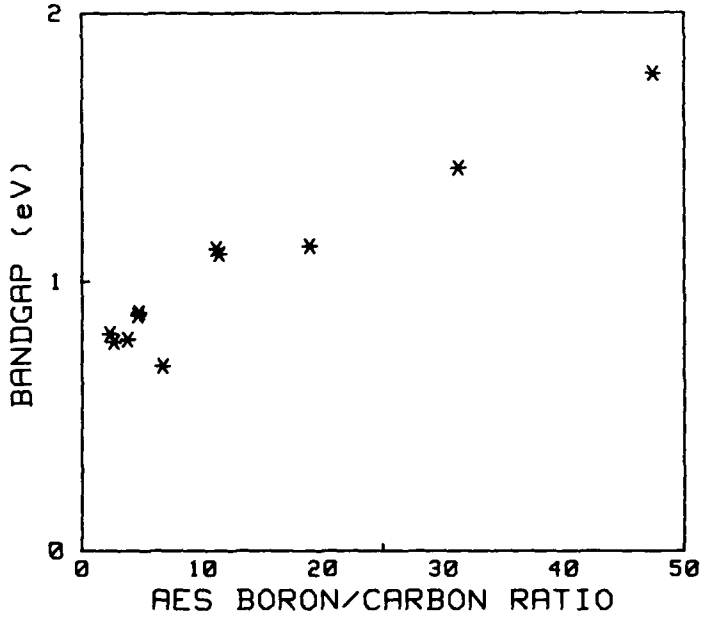


Figure 2. Bandgap, determined by optical absorption at room temperature, compared with composition determined by Auger electron spectroscopy.

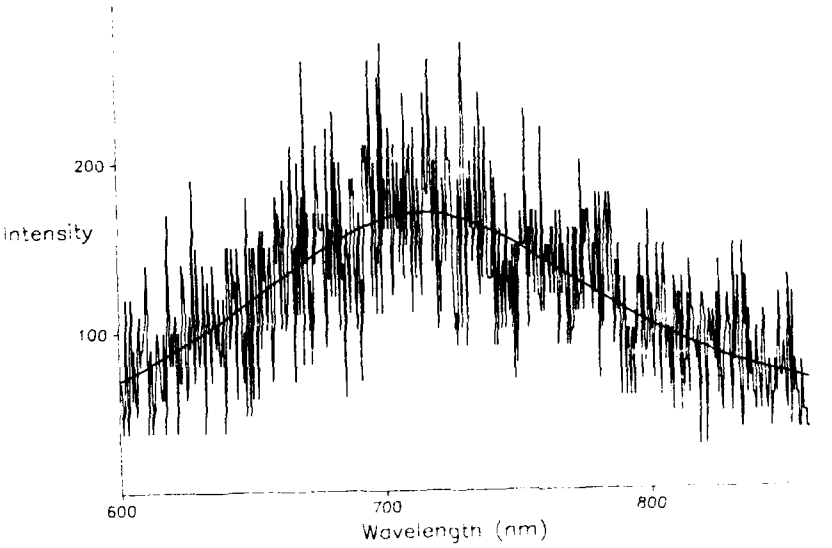


Figure 3. Photoluminescence spectrum taken at 300 K.

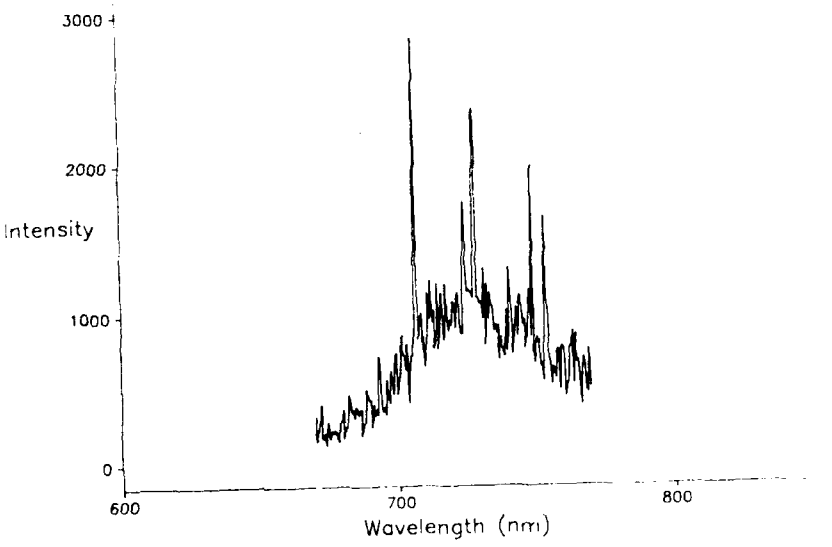


Figure 4. Photoluminescence spectrum taken at 12 K.

Photoluminescence measurements of high bandgap films are shown in Figures 3 and 4. From 300 K to 12 K, FWHM of the photoluminescence peaks changes from 0.39 eV to 0.14 eV. The peak position changes from 1.73 eV to 1.76 eV over the same temperature range. We interpret the photoluminescence data at 12K to indicate that the bandgap is 1.76 eV. Additional sharp features occur at 1.71 eV, 1.70 eV, 1.65 eV, and 1.64 eV.

DISCUSSION

Theories about the structure of boron carbides in the stable 9-20% carbon range are based on twelve atom boron-rich icosahedra with connecting chains of boron and carbon atoms [8]. Most measured conductivities in this composition range are above 1 $(\Omega\text{-cm})^{-1}$ at 300K, which is very high [9]. Electronic transport involves the connecting chains of atoms or substitutional carbon in the icosahedra [9]. It has been suggested that carbon precipitates in substantial quantity dominate DC electronic transport [10]. Conductivity vs composition measurements performed in this work indicate that there may be a heterogeneous population of carriers, but that in all cases conductivities were below 10^{-6} $(\Omega\text{-cm})^{-1}$ [11]. This may be attributable to the presence of a tetragonal phase, about which little is known [12].

Low temperature photoluminescence data for boron rich boron carbide provides a bandgap of 1.76 eV. This is in good agreement with the optical absorption edge measurement data shown in Figure 2. The low temperature photoluminescence spectrum in Figure 4 suggests the presence of additional shallow trapping levels, visible as sharp peaks. The deep acceptor level first suggested in [13] was absent, weak, or non-radiative.

CONCLUSION

We have used PECVD, a novel thin film technology, to fabricate boron carbide films of sufficient quality to undertake electronic and optical measurements of material properties. This method uses PECVD of a carborane cluster combined with methane to yield films whose bandgap depends on composition. Two types of measurements used to provide quantitative bandgap data provide very similar results for one of the films.

ACKNOWLEDGEMENTS

We acknowledge support from the International Society for Hybrid Microelectronics Educational Foundation, and the GE Electronics Laboratory.

REFERENCES

1. Klaus Ploog, J. Crystal Growth 24/25, 197-204 (1974).

2. U. Jansson, J.-O. Carlsson, B. Stridh, S. Soderberg, and M. Olsson, Thin Solid Films 172, 81-93 (1989).

3. D.N. Kevill, T.J. Rissmann, D. Brewe, and C. Wood, J. Crystal Growth 74, 210-216 (1986).

4. V. Cholet, R. Herbin, and L. Vandenbulcke, Thin Solid Films 188, 143-155 (1990).

5. J. Mazurowski, S. Baral-Tosh, G. Ramseyer, J.T. Spencer, Yoon-Gi Kim, and P.A. Dowben in Plasma Processing and Synthesis of Materials, edited by D. Apelian and J. Szekely (Mater. Res. Soc. Proc. 190, Pittsburgh, PA 1991) pp. 101-106.

6. G.D. Cody, B. Abeles, C.R. Wronski, B. Brooks, and W.A. Lanford, J. Non-Crystalline Solids 35/36, 463-468 (1980).

7. J. Tauc, in Optical Properties of Solids, edited by F. Abeles (North Holland, Amsterdam, 1972), pp. 279-313.

8. T.L. Aselage and D. Emin in Boron Rich Solids, edited by D. Emin, T.L. Aselage, A.C. Switendick, B. Morosin, and C.L. Beckel (American Institute of Physics, New York, 1991) pp. 177-185.

9. D. Emin in Boron Rich Solids, edited by D. Emin, T.L. Aselage, A.C. Switendick, B. Morosin, and C.L. Beckel (American Institute of Physics, New York, 1991) pp. 65-76.

10. A.K. Bandyopadhyay, F. Beuneu, L. Zuppiroli, and M. Beauvy, J. Phys. Chem. Solids 45(2), 207-214 (1984).

11. J. Mazurowski, (in preparation).

12. U. Jansson and J.-O. Carlsson, Thin Solid Films 124, 101-107 (1985).

13. G.W. Samsonov and G.W. Sinelkova, Ukr. Fiz. Zh. 6, 687 (1961).

MODELING OF THE FORMATION OF BORON CARBIDE PARTICLES IN AN AEROSOL FLOW REACTOR

Yun Xiong*, Sotiris E. Pratsinis* and Alan W. Weimer**
*Center for Aerosol Processes, Department of Chemical Engineering, University of Cincinnati, Cincinnati, OH 45221
**Ceramics and Advanced Materials Research, Dow Chemical U.S.A , Midland, MI 48674

ABSTRACT

The formation of submicron crystals of boron carbide (B_4C) by rapid carbothermal reduction of intimately mixed carbon-boron oxide precursor powders in an aerosol flow reactor at temperatures above the boiling point of boron oxide is investigated. The employed high heating rates (10^5 K/s) of the process force release of gaseous boron oxide and suboxides and rupture of the precursor particles resulting in formation of boron carbide molecular clusters that grow to macroscopic particles by coagulation. Consequently, the formation and growth of B_4C particles is described by simultaneous interparticle collision and coalescence using a two-dimensional distribution model that traces the evolution of both size and shape characteristics of the particles through their volume and surface area. Here, in addition to the coagulation term, the governing population balance equation includes a coalescence contribution based on B_4C sintering law. The predicted evolution of the two-dimensional particle size distribution leads to a direct characterization of morphology as well as the average size and polydispersity of the powders. Furthermore, model predictions of the volume and surface area of boron carbide particles can be directly compared with experimental data of B_4C specific surface area and grain size.

INTRODUCTION

There is substantial interest in the manufacture of boron carbide (B_4C) due to its high hardness and various desirable chemical and electrical properties [1]. Conventional methods for manufacturing boron carbide involve the reduction of boron oxide with carbon in a batch electric arc furnace [2]. These processes are characterized by slow, nonuniform heating, chemical impurities, and subsequent processing complications. Recently, Weimer et al. [1] described a rapid carbothermal reduction process in a flow reactor configuration for continuously manufacturing submicron crystals of boron carbide. A uniform solid mixture of calcined corn starch (carbon "soot") and boron oxide is milled to particles of less than 45 μm. These particles are suspended in argon gas and fed into a 0.14 m I.D. x 1.68 m long graphite flow reactor which is maintained at approximately 2200 K [1]. Additional argon gas is fed around the particle inlet to mitigate deposits to reactor walls. The precursor particles contain carbon and boron oxide in stoichiometric amounts that convert to boron carbide according to:

$$7C(s) + 2B_2O_3(l, g) = B_4C(s) + 6CO(g) \quad (1)$$

As the particles enter the reactor they are heated to a temperature which is below the boiling point of carbon but above the boiling point of boron oxide, 2133 K [3]. The reactor temperature is also above the temperature, 1733 K, at which liquid boron oxide is reduced to gaseous boron oxide in the presence of carbon [4]. As a result, rapid heating (10^5 K/s [5]) promotes rapid volatilization of B_2O_3 and release of CO from the precursor particles, forcing particle rupture in a similar fashion to the breakup of coal particles in pulverized coal combustion [6].

Assuming instantaneous breakup of precursor particles and formation of boron carbide clusters, particle formation and growth can be modeled by simultaneous coagulation and coalescence. This paper studies formation and growth of boron carbide particles by the rapid carbothermal reduction process using a two-dimensional size distribution model. The predicted B_4C grain (crystallite) sizes are compared with experimental data.

THEORY

A two-dimensional particle size distribution function is defined as $n_t(v,a)$ where $n_t(v,a)dadv$ is the number density of particles having volume between v and v + dv and surface area in the range a to a + da at time t. For an aerosol that is rapidly formed by gas phase reaction at high temperatures, the rate of change in $n_t(v,a)$ is given by the rate of simultaneous coagulation and coalescence among aerosol particles. The two-dimensional population balance equation can be written in a continuous form as [7, 8]:

$$\frac{\partial n_t(v,a)}{\partial t} = \frac{1}{2}\int_0^v \theta\left(a > \left(\frac{\bar{v}}{v_o}\right)^{2/3}a_o + \left(\frac{v-\bar{v}}{v_o}\right)^{2/3}a_o\right)\int_{\left(\frac{\bar{v}}{v_o}\right)^{2/3}a_o}^{\frac{\bar{v}}{v_o}a_o} \beta_{\bar{v},v-\bar{v}}(\bar{a},a-\bar{a})n_t(\bar{v},\bar{a})n_t(v-\bar{v},a-\bar{a})d\bar{a}d\bar{v}$$

$$- n_t(v,a)\int_0^\infty \int_{\left(\frac{\bar{v}}{v_o}\right)^{2/3}a_o}^{\frac{\bar{v}}{v_o}a_o} \beta_{v,\bar{v}}(a,\bar{a})n_t(\bar{v},\bar{a})d\bar{a}d\bar{v} \quad \frac{\partial n_t(v,a)}{\partial t} + \frac{1}{\tau_f}\frac{\partial}{\partial a}\left([a - \left(\frac{v}{v_o}\right)^{2/3}a_o]n_t(v,a)\right) \qquad (2)$$

where v_o and a_o are the volume and surface area respectively, of a primary spherical particle. An agglomerate of volume v is thus composed of v/v_o primary particles. Its surface area lies between that of a perfect sphere when complete coalescence has taken place, $(v/v_o)^{2/3}a_o$, and that of an aggregate of primary particles just touching one another, $(v/v_o)a_o$.

The first right-hand-side (RHS) term of Eqn. 2 accounts for the gain of particles of volume v and surface area a by coagulation of smaller particles. The step function θ is introduced because a particle of volume v produced by collision between particles of volume $\bar{v}$ and $v - \bar{v}$ cannot have upon contact surface area less than the sum of the surface area of the two particles. Only coalescence can reduce the resulting particle surface area to the theoretical minimum, i.e. that of a sphere of volume v. The second RHS term in Eqn. 2 accounts for the loss of particles of volume v and surface area a by coagulation with all particulate entities. β, the coagulation coefficient, is a function of the particle volume and surface area of the colliding particles. In this study, Fuchs expression for the Brownian coagulation coefficient covering the whole size regime [9, 10] is used with corrections taking into account the variable cross sectional area [8].

The third RHS term in Eqn. 2 is the sintering contribution related through the continuity equation to a linear approximation of the sintering law as expressed by the surface area reduction rate [7]. The characteristic sintering time, τ_f, depends on the B_4C sintering mechanism. Boron carbide and other covalently-bonded solids such as SiC and Si_3N_4 sinter by solid-state diffusional processes [11]. For solid-state diffusion, the characteristic sintering time of two equal-sized grains of diameter d_g is given by [12]:

$$\tau_f \propto \frac{k_B T}{D^* \Omega \gamma} d_g^3 \qquad (3)$$

where D^* is the self-diffusion coefficient for the mobile species, Ω is the atomic volume of the diffusing material, and γ is the surface energy. There is little data on pressureless sintering of boron carbide in the absence of additives and to the best of the authors' knowledge, the D^* and

γ of B_4C have not been reported in the literature. Excess carbon enhances self-diffusion in both SiC and B_4C. van Rijswijk and Shanefield [13] showed that in a carbon-rich atmosphere, the bulk-diffusion rate of silicon substantially increases such that carbon self-diffusion becomes slower and, as a result, rate controlling. This results in an 100-fold increase in the overall self-diffusion rate of SiC. If excess carbon has the same effect on boron carbide self-diffusion, the silicon carbide self-diffusion coefficient in a carbon-rich atmosphere can be used as a first approximation in describing the B_4C sintering. From Fig. 1 of [13], an expression for the B_4C self-diffusion coefficient is deduced as:

$$D^* = 0.3\exp\left[-\frac{53{,}648}{T}\right] \tag{4}$$

The carbon vacancy volume Ω is calculated as 3.64×10^{-23} cm^3.

The surface energy of B_4C also needs to be estimated from related compounds, preferably covalent carbides such as SiC and TiC. Livey and Murray [14] found that the surface energies of the carbides of Zr, U, Ti and Ta show a linear relationship with the heat of formation of these carbides. They reported the surface energy of TiC at 1373 K as 1190 ± 350 dyne/cm. Assuming that B_4C and SiC also follow approximately the same relationship, then their surface energies can be estimated from their heat of formation and the surface energy and heat of formation of the refractory monocarbides. Dean [15] gives the heat of formation values for B_4C, SiC and TiC as -17, -17.5, -44.0 kcal/mole, respectively. According to the above reasoning, B_4C and SiC should have about the same surface energy: ~ 1000 dyne/cm. Using these estimated values of D^* and γ, a quantitative expression of the characteristic sintering time for B_4C is obtained:

$$\tau_f = 97 T d_g^3 \exp\left[-\frac{53{,}648}{T}\right] \tag{5}$$

where a constant 5/80 is used to equate Eqn. 3 [12]. The average grain size within an agglomerate of volume v and surface area a can be obtained from:

$$d_g = \frac{6v}{a} \tag{6}$$

Equation 2 is a two-dimensional partial integro-differential equation that needs to be solved numerically. A one-dimensional sectional method [16, 17] is extended to include the surface area dimension [8]. This results in a set of ordinary differential equations (ODEs) that are solved using an efficient ODEs solver, subroutine IVPAG [18].

RESULTS AND DISCUSSION

Tables I and II of Weimer et al. [1] list the experimental runs made at reactor temperatures above the boiling point of boron oxide (~2133 K). From the measured specific surface area an experimentally determined average grain size of the product B_4C powders can be obtained:

$$d_g = \frac{6}{\rho_p A} \tag{7}$$

where the particle density ρ_p is 2.52 g/cm^3 for B_4C and A is the measured specific surface area.

Since the powder feeding rate was kept constant, the average size and morphology of product B_4C powders are affected by the argon feeding rate and reactor temperature. A higher argon flow rate means a shorter reactor residence time period, resulting in smaller average product particle sizes. While increasing temperature enhances the coagulation rate ($\beta \alpha T^{1/2}$), it decreases the residence time more profoundly ($t \alpha T^{-1}$). Consequently, for a given argon flow rate, the agglomerate particle size decreases with increasing temperature. With respect to particle morphology, increasing both the reactor residence time and temperature promotes coalescence and subsequently increases the grain/crystallite size of the final product.

Figure 1 shows two snapshots of the number density of B_4C agglomerates in the two-dimensional space of particle volume and surface area at 2173 K and residence times 0.2 s and 1.12 s (product), respectively. The number of agglomerate B_4C particles is reduced by coagulation and consequently the average agglomerate size increases as the residence time increases from 0.2 to 1.12 s. It is worth noting that coagulation greatly depletes the small particles but does very little in increasing the size of the large ones over this time period. The two-dimensional distribution is bound by the two heavy solid lines. The diagonal line corresponds to aggregates consisting of B_4C primary particles just touching one another upon collision without sintering (the collision line). The line on the left corresponds to fully coalesced B_4C particles (the coalescence line). Therefore, the grain size of B_4C agglomerates increases from the collision to the coalescence line as the initially aggregated clusters are progressively densified by sintering of the primary particles in the cluster.

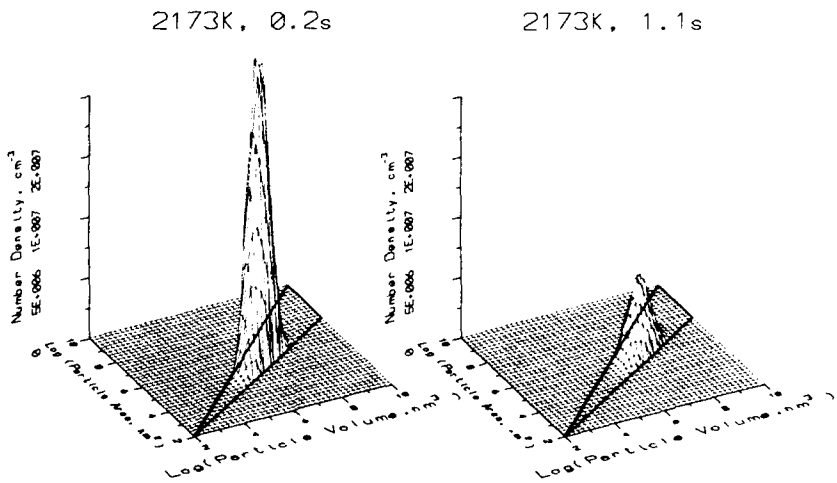


Figure 1. Number density of B_4C agglomerates at 2173 K and residence times 0.2 s and 1.12 s, respectively, in the two-dimensional space of particle volume and surface area.

Temperature has a much stronger effect on the particle coalescence rate than on the particle collision rate as indicated by the exponential temperature dependence of the characteristic sintering time of B_4C (Eqn. 5). The two-dimensional particle size distribution shifts towards the coalescence line as temperature increases indicating more progressed particle sintering at high temperatures. For agglomerates of the same volume, there are relatively more particles having low surface area (large grains, Eqn. 6) at high temperatures. If favorable sintering conditions are sustained, the agglomerates eventually approach a spherical geometry and their surface area becomes proportional to $v^{2/3}$ (coalescence line). Indeed, the simulations show that the average B_4C grain size is $d_g \approx 0.06$ μm at 2173 K and 1.12 s while at 2373 K and 0.71 s

d_g = 0.09 μm. In contrast, the corresponding mean solid sphere diameter of the agglomerate particles is 0.44 μm at 2173 K and 0.37 μm at 2373 K at the above residence times. This model prediction is in qualitative agreement with micrographs of B_4C powders made at the above temperatures [1].

Figure 2 compares model predictions of the B_4C average grain size as a function of temperature with experimental data [1]. Clearly, the equivalent solid sphere diameter of the agglomerate particles is much larger than the grain size. The two-dimensional model (triangles) predicts correctly the grain growth trend. Quantitative agreement with experimental data is excellent, in view of the estimated B_4C sintering rates (diffusivity and surface energy). When the sintering rate is increased by a factor of 10, model predictions (squares) match the experimental data (stars). Thus, the present two-dimensional particle size distribution model can be used to infer effective sintering rates from experimental measurements. This is particularly valuable for ceramic materials whose sintering rate expressions are often unavailable.

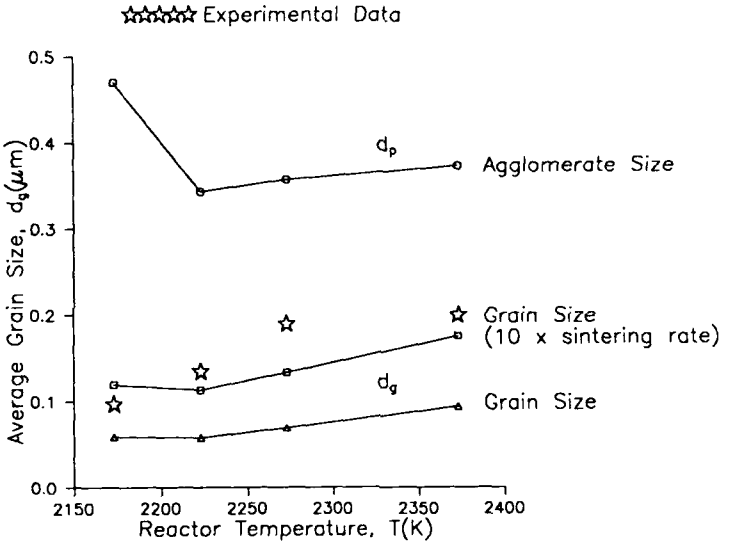


Figure 2. Comparison of model predicted average grain size of the B_4C powders with experimental data.

CONCLUSIONS

The formation of submicron crystals of boron carbide by the rapid carbothermal reduction of solid precursors in an aerosol flow reactor is investigated. At temperatures above the boiling point of boron oxide (2133 K) and high heating rates (10^5 K/s), B_4C molecular clusters are formed instantaneously and they grow to macroscopic particles by coagulation and coalescence. This formation and growth process is modeled by a two-dimensional aerosol distribution model that traces the evolution of both size and shape characteristics of particles through their volume and surface area. Model predictions for the average volume and

grain/crystallite size of the product B_4C powders are in excellent agreement with experimental micrographs and specific surface area data. The effect of temperature and residence time on particle size and morphology is also adequately represented by the model. In fact, it is the first time that a model of both sound theoretical background and numerical feasibility has been developed and used to predict the grain/crystallite size growth during gas phase particulate manufacture.

ACKNOWLEDGEMENT

This research was supported by the National Science Foundation Grant CTS-8957042. Computer time and the IMSL software were provided by the Ohio Supercomputer Center.

REFERENCES

1. A. W. Weimer, W. G. Moore, R. P. Roach, C. N. Haney and W. Rafaniello, AIChE J. 37, 759 (1991).
2. A. Lipp,Tech. Rundschau, 28 (14), 33 (1965).
3. R. C. Weast, M. J. Astle and W. H. Beyer, CRC Handbook of Chemistry and Physics, 6th ed. (CRC Press, Florida, 1986).
4. R. H. Lamoreaux, D. L. Hildenbrand and L. Brewer, J. Phys. Chem. Ref. Data 16 (3), 419 (1987).
5. A. W. Weimer, W. G. Moore, R. P. Roach, J. E. Hitt, R. S. Dixit and S. E. Pratsinis, to be submitted to the Journal of the American Ceramic Society (1991).
6. I. Celik, T. J. O'Brien and D. B. Godbole, Chem. Eng. Sci. 45 (1), 65 (1990).
7. W. Koch and S. K. Friedlander, J. Colloid Interf. Sci. 140 (2), 419 (1990).
8. Y. Xiong and S. E. Pratsinis, to be submitted to the Journal of Aerosol Science (1991).
9. N. A. Fuchs, The Mechanics of Aerosols (Pergamon Press, New York, 1964).
10. J. H. Seinfeld, Atmospheric Chemistry and Physics of Air Pollution (Wiley, New York, 1986), Table 10.1.
11. C. Greskovich and J. H. Rosolowski, J. Am. Ceram. Soc. 59 (8), 336 (1976).
12. W. D. Kingery, H. K. Bowen and D. R. Uhlmann, Introduction to Ceramics (Wiley, New York, 1976).
13. W. van Rijswijk and D. J. Shanefield, J. Am. Ceram. Soc. 73 (1), 148 (1990).
14. D. T. Livey and P. Murray, J. Am. Ceram. Soc. 39 (11), 363 (1956).
15. J. A. Dean, Lange's Handbook of Chemistry, 13th ed. (McGraw-Hill, New York, 1985).
16. F. Gelbard, Y. Tambour and J. H. Seinfeld, J. Colloid Interf. Sci. 76 (2), 541 (1980).
17. Y. Xiong and S. E. Pratsinis, J. Aerosol Sci. 22 (5), 637 (1991).
18. IMSL, User's Manual (IMSL Math / Library, Vol. 2, Version 1.1, Houston, 1989).

PART VIII

Amorphous and Micro-crystalline Semiconductors

AMORPHOUS AND MICROCRYSTALLINE SiC AS NEW SYNTHETIC WIDE GAP SEMICONDUCTORS

Y.Hamakawa and H.Okamoto

Faculty of engineering Science, Osaka University, Toyonaka, Osaka, Japan 560.

ABSTRACT

A review is given on recent progress in amorphous and microcrystalline silicon-carbide (a-SiC, μc-SiC) semiconductors and their technological applications to optoelectronic functional devices. Firstly, some significant properties in this alloy as a new synthetic material are pointed out with recent advances of thin film technologies, such as plasma CVD, ECR-CVD and ion-beam CVD etc. There exists an energy gap controllability from 1.7eV to 3.6 eV with retaining the valency electron control from n-type through i- to p-type semiconductors. While its conductivity can also be controlled more than ten order of magnitudes, e.g., from 10^{-9} to 10^{2} Scm^{-1} by controlling the impurity doping and preparation conditions.

Secondly, a series of technical data on the electronic and optoelectronic properties of a-$Si_{1-x}C_x$ and μc-SiC are demonstrated from recent achievements. In the final part of the paper, current state of the art in the field of optoelectronic applications from live technologies on amorphous silicon solar cells, a-SiC visible light LED and EL devices are reviewed. A technological evolution from "***microelectronics***" to "***macroelectronics***" will be discussed

INTRODUCTION

Since the recent success of valency electron control in the glow discharge-produced amorphous silicon carbon alloy (a-SiC:H) in 1981 [1], a new age in amorphous silicon alloys has opened up, and a group of new materials such as amorphous silicon-germanium (a-SiGe:H), amorphous silicon-nitride (a-SiN:H) and amorphous silicon-tin (a-SiSn:H) have been successively developed in the past few years. The significance of this material innovation is that one can control electrical, optical and also opto-electronic properties by controlling atomic compositions in the mixed alloys. Therefore, a wide variety of application fields has also been developed with these new electronic materials. In fact, a-SiC:H/a-Si:H heterojunction solar cells [2], a-Si:H/a-SiGe:H stacked solar cells [3], superlattice devices [4], a-Si:H/a-SiN:H thin film transistors [5], photo-receptors [6], X-ray sensor [7], color sensors [8], etc. have been developed, and some of them are already being marketed.

In the recent few years,an intensive effort has been made to realize a-SiC:H TFLED (Thin Film Light Emitting Diode) and TFEL (Thin Film Electroluminescence) devices, which would have a number of attractive advantages such as low power dissipation, capability of large-area multi-color emission, and completely solid state flat panel modular display. As a result, a visible light injection type EL device has been developed with the cell structure of a-SiC:H p-i-n junction, and the emission colors of red, orange, yellow and green are obtained by controlling the carbon content in a-SiC:H [9], [10]. Recently, Toyama et al have succeeded in obtaining blue color emission with a thin-film intrinsic EL structure of TCO/Y_2O_3/a-C:H (amorphous carbon)/a-Si_xN_{1-x}:H/Y_2O_3/Al with luminance intensity of more than 30 cd/m^2 at $180V_{rms}$, 10kHz [11]. In this paper, recent advances in the a-SiC and μc-SiC film technologies are reviewed from material preparation technologies to their applications to optoelectronic functional devices.

Mat. Res. Soc. Symp. Proc. Vol. 242. © 1992 Materials Research Society

TOPICS OF THE MATERIAL PREPARATION TECHNOLOGY

As the preparation technology for a-SiC alloy, the plasma CVD is now widely utilized everywhere. While ECR CVD and Ion-beam CVD (IB-CVD) are intensively investigated in a recent few years.

Figure 1(a) shows a schematic illustration of the ECR CVD apparatus. Microwave power at 2.45 GHz is introduced into the ECR plasma excitation chamber through a rectangular wave guide through a window made of fused quarts plate. The ECR excitation chamber forms a cylindrical resonator of $TE1_{13}$ mode of the introduced microwave. In the system, the magnetic flux required for satisfying the electron cyclotron resonance condition is about 875 Gauss at the center of the magnetic coil. The generated ECR plasma is extracted from the ECR excitation chamber into the deposition chamber along with the gradient of dispersed magnetic field as shown in Fig.1(b). The extracted ECR plasma interacts with the reaction gas introduced into the deposition chamber and decomposes them ,that is, produces active species for film growth.

The unique advantage of the ECR CVD is that the growing surface receives almost no bombardment damages by electrons and/or other heavy species soft landing having an energy of several tens of eV [12] . This effect might result not only in prevention of weak bonds from being introduced into the network but also suppression of the diffusion of long-lifetime radical species due to the raised surface temperature. It is expected that films with dense network and low defect density are formed.

For the deposition of a-SiC and μc-SiC, hydrogen is used as an ECR plasma excitation gas, and a mixture of SiH_4, CH_4 and B_2H_6 or PH_3 are usually employed as a reac-

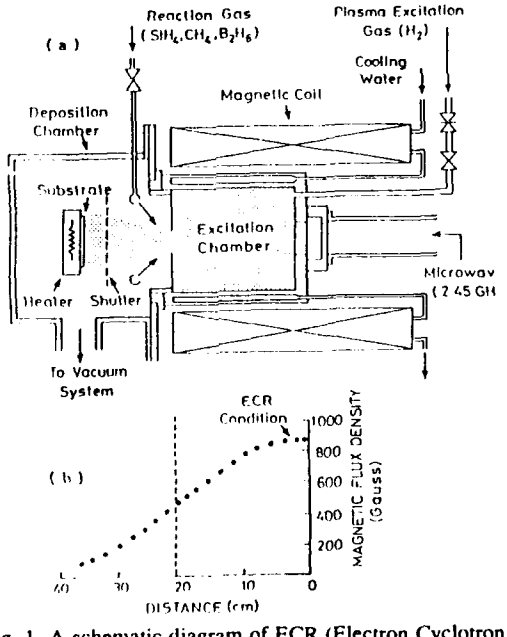


Fig. 1 A schematic diagram of ECR (Electron Cyclotron Resonance) plasma CVD system (a) and the profile of the magnetic field for the extraction of the plasma from the excitation chamber into the deposition chamber (b).

tion gas for the growth of p- and n-type SiC:H. Details of the preparation conditions are summarized in Table 1. Since the operation pressure is in the range of 10^{-3} and 10^{-4} Torr, the lifetime of chemically active hydrogen radicals is quite long, so that a large amount of hydrogen radicals will reach the growing surface and play an important role in determining the properties of growing films. Therefore, the dependence of the material properties on the hydrogen dilution ratio in the reaction gas has been investigated. Figure 2 shows the dependence of the optical energy gap and dark conductivity of the samples on the H_2 dilution ratio. As the ratio increases, the optical gap (E_o) and also the dark-conductivity (σ_d) of both p- and n-type films increase.

Table I. Preparation conditions of p-type amorphous and microcrystal SiC in ECR plasma CVD.

Substrate Temperature	: R.T. - 400°C
Microwave Power	: 150 - 400 W
Total Gas Pressure	: 10^{-3} - 10^{-4} Torr
Plasma excitation Gas (flow rate)	: H_2 (10 - 100 sccm)
Reaction Gas (Flow rate)	: SiH_4 (10 - 50 sccm) : CH_4 (10 - 50 sccm)
	: B_2H_6 (40 - 100 sccm)
Microwave Frequency	: 2.45 GHz
Magnetic Flux Density	: 875 gauss

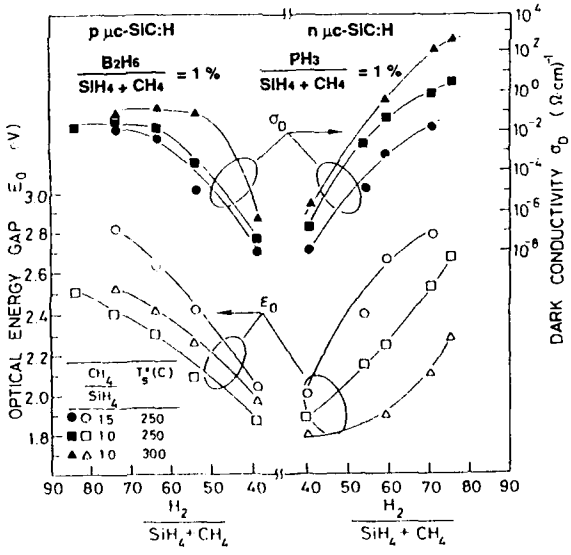


Fig. 2 Dependence of the optical energy gap and dark conductivities of p- and n-type μc-SiC:H on the hydrogen dilution ratio in the reaction gas in ECR CVD.

As can be seen from Fig.2, there are two main factors which determine the optical energy gap; one is the composition ratio of Si:C:H corresponding to the source gas ratio CH_4/SiH_4, and the other is the grade of H_2 dilution which might be related to the details of the network structure. The film properties are strongly dependent not only on the substrate temperature and microwave power but also on the ratio of hydrogen to reaction gases ($H_2/(CH_4+SiH_4)$ during deposition. Although the optical energy gap increases with the flow rate of CH_4, the effect is not as remarkable as the dependence of hydrogen dilution. Hydrogen dilution has the effect of reducing the hydrogen content in the film, and also of enhancing the degree of microcrystallinity.

The formation of Si and SiC microcrystallites is confirmed by Raman spectra as mentioned in the original work [12]. The Raman spectrum of the films prepared at microwave powers higher than 250 Watts exhibits distinct structures at around 520 and 740 cm^{-1}, which correspond to TO phonon modes of crystalline Si and SiC clusters.

The conductivity of μc-SiC:H can also be controlled by adjusting the flow ratio of dopant gas to host reaction gas. Figure 3 shows the dependence of the optical energy gap and dark conductivity of μc-SiC:H prepared by ECR CVD on the flow ratio of B_2H_6 p-type doping gas. Here, the hydrogen dilution ratio is kept constant at 74. The data for p a-SiC:H prepared by RF plasma CVD are also shown for comparison. The carbon content x in both the cases is about 0.3. It is clear that the total doping efficiency in p μc-SiC:H is higher than that in p a-SiC:H by several orders of magnitude.

Figure 4 summarizes the relation between the dark conductivity and the optical energy gap of p- and n-type a-SiC:H prepared by conventional RF plasma CVD and p- and n-type μc-SiC:H prepared by ECR plasma CVD. As the optical energy gap in-

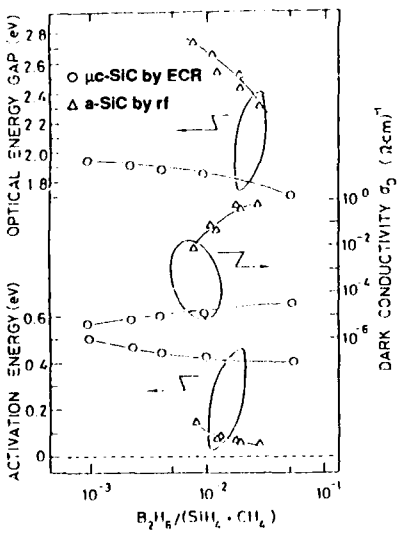


Fig. 3 Dependence of dark conductivity, activation energy and optical energy gap on the dopant gas ratio in the reaction gases for p-type μc-SiC:H.

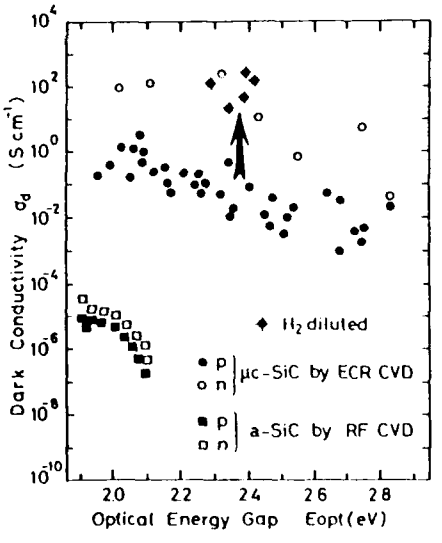


Fig. 4 Relationship between dark-conductivity and optical energy gap of amorphous and microcrystalline SiC:H prepared by RF and ECR plasma CVD.

creases, the dark conductivity of the films prepared by the RF plasma CVD rapidly decreases, while that of the films prepared by the ECR plasma CVD remains higher than 10^{-1} Scm^{-1} even when the optical energy gap exceeds 2.5 eV. In the figure, the star marked highly H_2 diluted p-type μc-SiC:H film has more than 3×10^{19} cm^{-3} hole concentrations with 24 cm^2/Vs mobility which are identified by Hall measurements [12].

Another topics in the material preparation technology field is the IBD (Ion Beam Deposition) method [13]. A high stability film against the light induced degradation with high deposition rate is still important key issue in the field. To conquer these problems, tremendous R&D efforts have been in progress by the wide varieties of approaches, e.g.; the Chemical Annealing Treatment (CAT) [14], Intense Xenon Light Pulse Assisted Plasma CVD [15], IBD and so on. Among these, IBD method is a unique challenge in views of a wide range controllability on both hydrogen content and decomposed species ion energy.

Figure 5 shows a schematic illustration of the IBD system. A typical a-Si film growth condition in this system is: the ion acceleration voltage V_{acc}=100-300V, ionic current I_e, with voltage V_e are 0.8A at 400V, and substrate temperature T_s=100-300°C, while chamber base pressure is 10^{-6} Torr or less.

As the preliminary experiment, a systematic investigations on the undoped a-Si film deposition has been made by a series of deposition parameters. The result shows a considerably good film quality having 10^4-10^6 photo- to dark-conductivity ratio σ_{ph}/σ_d with optical energy gaps of 1.7-1.8 eV. A noticeable feature of IBD produced film is a better stability against light exposure. Figure 6 shows a comparison of changes in the photoconductivity σ_{ph} with AM1 light illumination for IBD produced film and conventional plasma CVD produced film [13]. As a summary of this section, Fig.7 shows plots of recent results of dark σ_d and photoconductivity σ_{ph} of a-Si alloys with their optical energy gap.

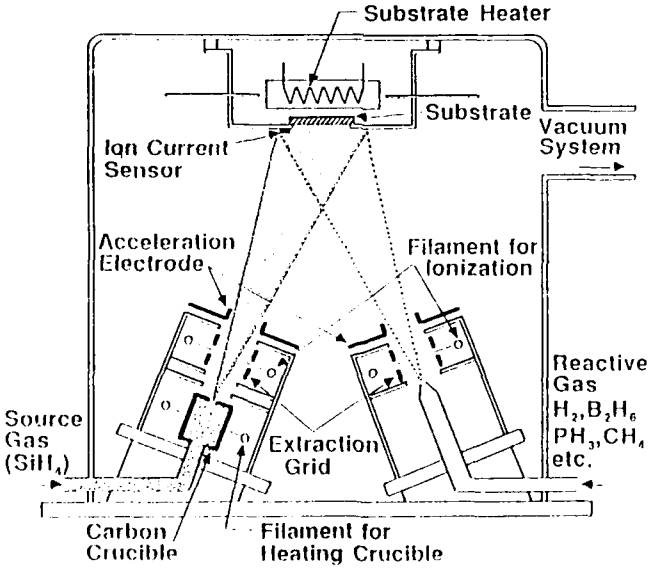


Fig. 5 A schematic representation of IBD (Ion Beam Deposition) system.

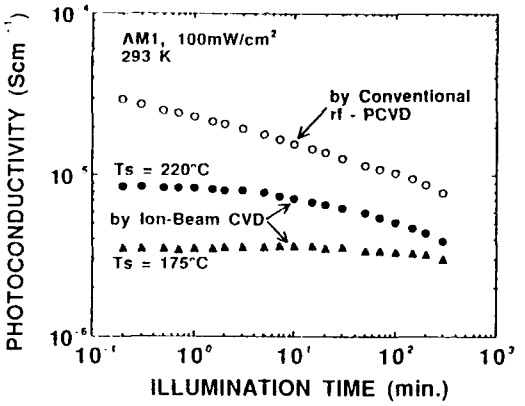


Fig. 6 Change in the photoconductivity with illumination time in IBD produced a-Si:H and PCVD produced a-Si:H films.

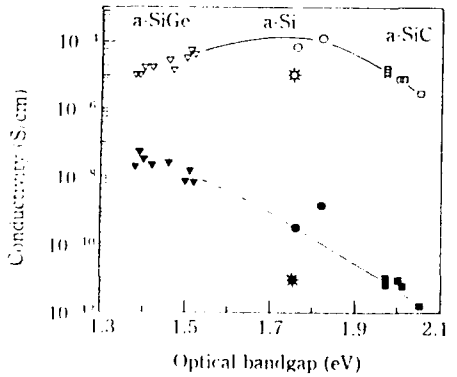


Fig. 7 Dark and photo-conductivities of a-SiGe:H (triangles), a-Si:H (circles), a-SiC:H (squares) versus optical gap. Star mark ✡ and ✱ show the property of IBD produced film.

APPLICATION TO a-Si SOLAR CELL TECHNOLOGY

An improvement in cell efficiency is of prime importance, which is directly connected to cost-reduction in photovoltaic systems. A wide variety of R & D efforts have been in progress from the field of material preparation technology to device structure, and also to PV system engineering. Among these, a remarkable advances has been seen in the technology of the wide gap windows heterojunction, graded band profiling, d doping, superlattice, BSF treatment and also the stacked junctions with new materials such as a-SiC, μc-SiC alloys [1,2,3]. As the results, amorphous silicon solar cell efficiency is being improved day by day. Present day, a utilization of a-SiC as the wide gap window has become the routine technology for high efficiency solar cells. According to a recent histogram of several thousands modules mass-production data [16], the In-line efficiency has reached to 9%, and several institutes reported more than 10% efficiency

for the 100cm² or more area as the top data in recent few years. While, the laboratory phase efficiencies are more than 12% with a-SiC/a-Si heterojunction.

As it has been reported elsewhere [17] that the amount of percentage light induced degradation increase with increasing i-layer thickness. The reason is that the volume recombination of the photo-generated carriers become relatively large with decreasing the lowest electric field in the i-layer. For the purpose of suppressing this effect, the tandem type solar cell has been recommended as a more reliable a-Si solar cell. Figure 8 shows light induced change in the conversion efficiencies of a-Si single, a-Si/a-Si tandem and a-SiC/a-Si/a-SiGe triple tandem solar cells [18].

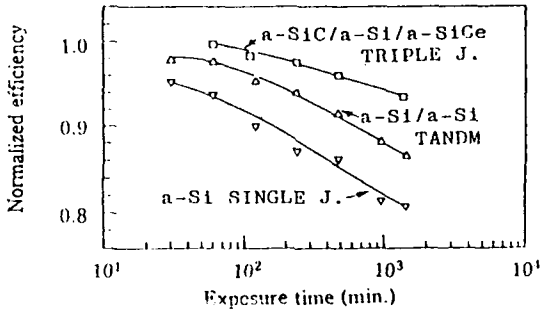


Fig. 8 Light-induced change in conventional efficiencies of single, tandem, and triple a-Si solar cells which is normalized to initial values. (inverted triangles: a-Si single cell, triangles: a-Si/a-Si tandem cell, squares: a-Si/a-Si/a-SiGe triple cell).

Recently, a concept of the band profiling design has been initiated as an optimum design of the ambipolar carrier transport in i-layer of the multi-band gap junction. As an example of result, band profile of the a-SiC/a-Si/a-SiGe triple band gap tandem solar cell is illustrated in Fig.9 with its photovoltaic performance [18]. At the present stage of investigation on a-Si/poly Si tandem junctions, a conversion efficiency of 15.04% with V_{oc}=1.478V, J_{sc}=16.17mA/cm² and FF=63% has been obtained on a two-teminal cell of

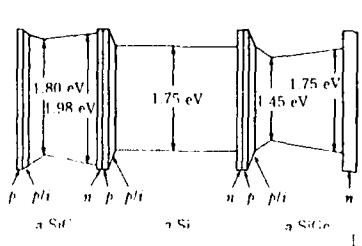
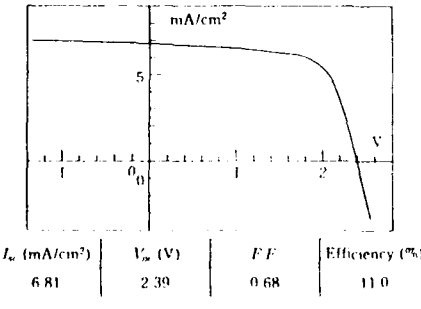


Fig. 9 (a) Bandgap profile of a-SiC/a-Si/a-SiGe multi-bandgap stacked solar cell.



I_{sc} (mA/cm²)	V_{oc} (V)	FF	Efficiency (%)
6.81	2.39	0.68	11.0

Fig. 9 (b) Voltage-current and solar cell characteristics of a-SiC/a-Si/a-SiGe multi-bandgap stacked solar cell.

sensitive area 5x6mm2 under AM1 illumination. Quite recently, by the same combination on four-terminal cell 19.1% efficiency has been obtained by Ma Wen et al. as shown in Fig.10 [19].

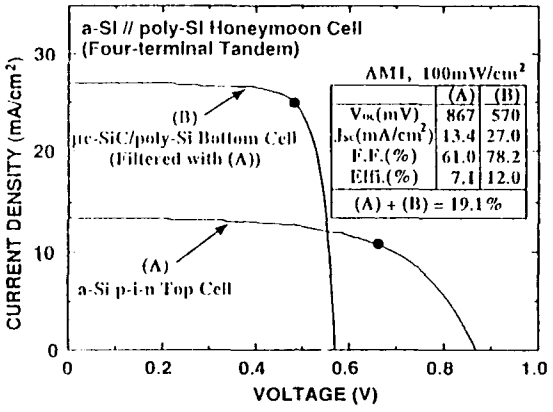


Fig. 10 Output characteristics of a-Si//poly-Si four-terminal tandem solar cell: top a-Si transparent solar cell and bottom μc-SiC/poly-Si heterojunction solar cell (filtered by top cell).

PROGRESS IN TFLED's PERFORMANCE

Full use of the significances of the wide area producibility with a wide band gap controllability and also the valency electron controllability in a-SiC alloys, thin film visible color light emitting diode (TFLED) has been developed in the recent few years [10]. Figure 11 shows a typical junction structure of the TFLED.

An injection type electroluminescence occurs under the forward biased condition, as it does in crystalline LED's. The thicknesses of p-type and n-type a-SiC:H carrier injector layers are usually set at 150Å and 300Å, respectively. Due to the limitation of the valency electron controllability of high band gap a-SiC:H, the optical band gap of the p and n injection layers has to be kept as low as 2 eV, while for a visible emission the optical band gap of the i-layer shouid be larger than about 2.5eV. This implies the existence of notch barriers at the p/i (ΔE_v) and i/n (ΔE_c) interfaces. These band disconti-

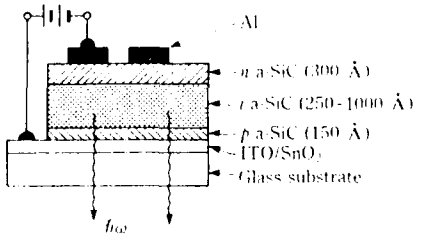


Fig. 11 Schematic illustration of p a-SiC:H/i a-SiC:H/n a-SiC:H thin film LED formed on glass/ITO/SnO_2 substrate.

nuities have been estimated from the results of internal photoemission measurement [20]. For instance, for E_0 of i layer = 2.58eV and E_0 of p-, n- layer = 2.00eV, the conduction band discontinuity of ΔE_c at the i/n interface and the valence band discontinuity ΔE_v at the p/i interface are 0.19 eV and 0.48 eV, respectively.

Figure 12 shows logarithmic plots of the J-V characteristics measured at room temperature for various optical gaps of i-layers (2.58, 2.68, 2.97 and 3.25 eV.). In these samples, the thickness of the i-layer was set at 500Å. As can be seen in the data, even though a-SiC:H is employed as the i-layer, the rectification ratio of more than 10^3 is obtained at 8 V for the sample with E_0 = 2.58 eV. However, it should be noted that when the optical gap - in other words, the carbon content - of the i-layer increases, the threshold voltage which is here defined as the voltage required to give a current of 10^{-7} A/cm² increases markedly. This may be partly due to the increase of series resistance in the i-layer itself and to the increase of the barrier height at both p/i and i/n interfaces.

An attempt has been made to improve the carrier injection efficiency by two approaches. One is to utilize wide-gap with highly-conductive p type μc (microcrystalline)-SiC:H as an injector; this was produced by Electron Cyclotron Resonance (ECR) plasma CVD. The result shows that as the optical energy gap of p-layer increases, the EL spectrum shifts towards a shorter wavelength and the emitting color changes drastically from red to orange and then to yellow. The highest luminance of a yellow-emission LED achieved so far on this device structure was about 10 cd/m², with an injection current density of 100mA/cm² and bias voltage of 10V.

Another approach to the improvement of LED performance is a use of hot carrier tunneling injection (HIT) through an insulating (wide band gap) layer at either the p/i or i/n interface, or at both the interfaces [20, 21]. For the a-SiC material, a wide band gap a-SiC:H (E_0 = 3.5eV) and a near-stoichiometric a-SiN:H (E_0 = 5eV) can be utilized profita-

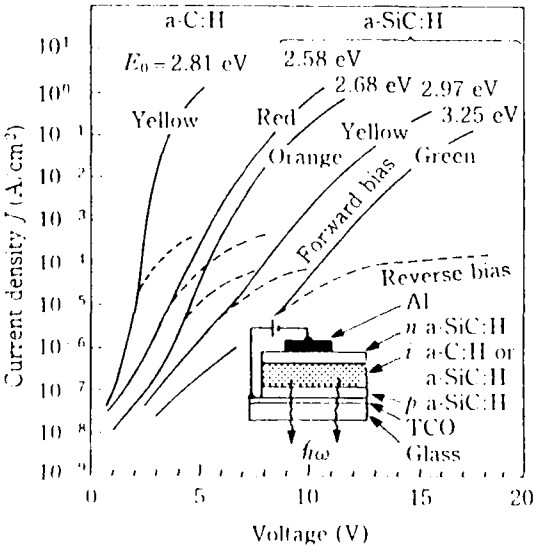


Fig. 12 Current-voltage (J-V) characteristics of LEDs consisting of a-SiC:H and a-C:H luminescent i layers.

bly as the insulating layer. The silicon nitride layer was formed by the conventional plasma CVD with the use of a 1:9 SiH4-NH_4 gas mixture. When an electric field is applied to LED provided with such insulation layers, the electric field will be mainly applied across the thin insulating layers. This high electric field accelerates carriers, then, increases the concentration of carriers injected into the conduction or valence band of the i-layer; we thereby call the insulating layers hot-carrier tunneling injector (HTI) layers. Moreover, a decrease in the electric field in the i-layer due to the presence of HTI layers would result in the reduction of field-quenching effects of radiative recombination, and eventually a significant improvement of the LED performance could be expected with the utilization of HTI layers.

Figure 13 demonstrates the luminance in LEDs with the HTI structure. The parameter in the figure - for example, 100/300/100 - shows that the thickness of the a-SiC:H HTI layer at the p/i interface is 100 Å, that of the luminescent i-layer, 300Å, and that of the HTI layer at the i/n interface, 100Å. As can be seen in the figure, the luminance of the LEDs based on the HTI structure is higher than that of a conventional type by more than one order of magnitude. With this novel structure, the luminance was improved to about 20cd/cm² with injection current density of about 600 mA/cm² for a yellow-emission LED. An essentially similar result has been obtained with the use of HTI layers based upon near-stoichiometric a-SiN:H, although the optimum thickness is about half of that in the case of a-SiC HTI layer, presumably due to the wider band gap. By combing a new preparation technology such as ECR microcrystalline SiC, with new device structures - e.g., superlattice i-layer and stacked p-i-n/p-i-n etc.[21, 22] we hope that the final goal of the luminance for practical use of more than 50 cd/m2 can be achieved in the near future.

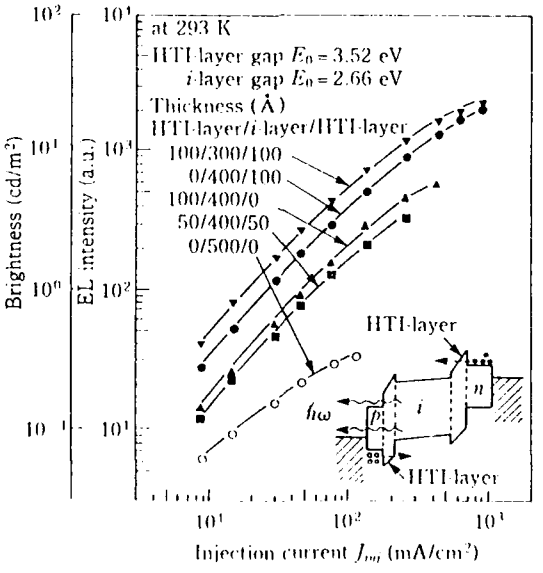


Fig. 13 Improvement of the luminance by utilizing a-SiC HTI structures in the LEDs.

a-C:H TFEL DEVICE

Another interesting device developed by a-SiC alloys is an ac driven Thin Film Electroluminescent (TFEL) cell. The device is constructed with multilayers of glass/ITO/ SnO_2/Y_2O_3 (3000Å)/a-SiC:H or a-C:H (2.8-3.0eV, 1000Å)/a-SiN:H (500Å)/Y_2O_3 (3000Å)/ Al. Semi-insulating Y_2O_3 layers were deposited by electron beam evaporation. Dielectric constants for Y_2O_3 and a-SiN:H are roughly estimated to be 16 and 8, respectively. In this multilayer cell configuration, a blue light emission in a-C:H active layer has been observed [11]. Figure 14 shows the luminance-voltage characteristics of a-C:H TFEL devices under operation with a 10kHz sinusoidal ac voltage with a photograph demonstration. The blue-emission cell shows the maximum luminance of 30cd/m² with an efficiency in excess of 10^{-1}lm/W. A series of material selection trials on insulator layers shows that Y_2O_3 layer may play an important role in injecting excess electrons (more than 10^{-6}C/cm² at 10kHz operation) into the active luminescent a-C:H layer. An insertion of a-SiN:H is also essential for the blue shift of the emission spectrum [23].

Comparing the EL performances of a-C:H cells with that of a-SiC:H cells, the a-C:H devices has about one order of magnitude higher emission with higher EL peak energy by 0.36 eV. That is, the emission color of whitish orange in a-SiC:H cells shifts to blue in a-C:H cells. Moreover, the a-C:H EL device has a threshold voltage lower by 40 V_{rms} than that of the a-SiC:H EL device. This may be due to a lower dielectric constant of a-C:H (about 2.2); a greater electric field is distributed across the luminescent layer before the onset of emission.

The emission spectrum of the a-C:H TFEL device is compared with the PL spectrum in Fig. 15. The EL spectrum has several structures, in sharp contrast to featureless PL spectrum. The peak positions have no unique dependence on the total device thickness or on details of the multi-layered structure, excluding optical interference from possible interpretations. The dominant EL peak energy lies at 2.4 eV, which is very close to the PL peak energy. This peak corresponds to greenish blue, while total emission color identified by the naked eye is a purer blue, presumably due to the contribution from higher energy subpeaks in the EL spectrum.

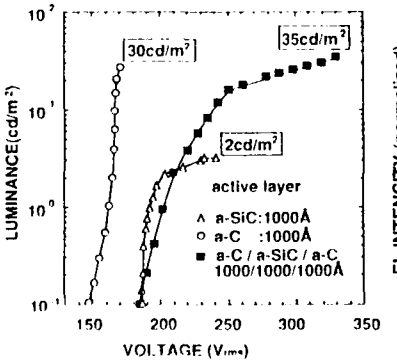


Fig. 14 Luminance-voltage characteristics of intrinsic EL devices based on a-C:H and a-SiC:H luminescent layers.

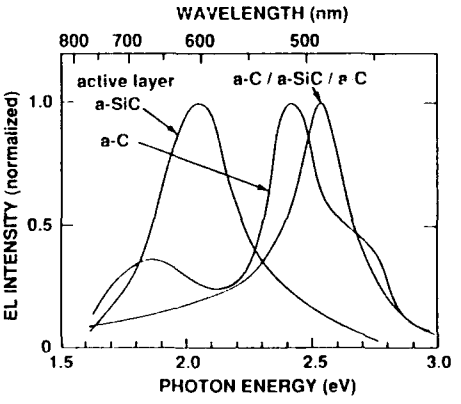


Fig. 15 Emission spectra of EL devices utilizing a-C:H and a-SiC:H luminescent layers.

As it has been discussed in the former sections, the significance of amorphous semiconductors is that they are free from difficulty in epitaxial growth, which is indispensble for growth of crystalline materals. Therefore, these new materials can be deposited easily with uniform on a wide surface of any foreign material, facilitating processing and mass production. Amorphous silicon alloys have enabled us to produce large area integrated solar cells even 40cmx120cm "NEDO" size module and also manufacture of large area TFT matrixes for driving liquid crystal TV units. The TFLED and TFEL devices might be a promising candidate for solid state display panel for HDTV.

Overviewing these advancement of material Innovation, a new kind of evolution has been going on in the field of semiconductor electronics. Stated simply, these developments point to the emergence of a new technology which could be called "***macroelectronics***", as opposed to "***microelectronics***". In response to this new trend, a technological innovation has taken place in semiconductor material science from the "***bulk crystalline age***" to that of high-quality "***multilayered thin film age***". In the near future, this innovation will be spread not only to fields in semiconductors, but also in those related to all functional materials of dielectrics, thin-film superconductors, etc. As precursors of technological innovations in the 21st century, new "waves" in these and other fields are well worth watching. How big and what kinds of new flowers and fruits will bloom on new trees? It will be great fun to watch.

REFERENCES

[1] Y. Hamakawa and Y. Tawada: Int. J. Solar Energy, **1** (1982) 251.
[2] Y. Tawada, M. Kondo, H. Okamoto and Y. Hamakawa: Solar Energy Mat., **6** (1982) 299.
[3] S.R. Ovshinsky: MRS 1985 Spring Meeting, San Francisco (1985) 251.
[4] S. Tsuda, H. Tatui, T. Matsuyama, H. Haku, K. Watanabe, Y. Nakashima, S. Nakano and Y. Kuwano: Proc. 2nd Int. Photovoltaic Science and Engineering Conf., *Beijing (1986)* 409.
[5] for example, JARECT, ed. by Y. Hamakawa (Ohm-Sha & North-Holland, Tokyo and Amsterdam, 1983) **6**, p.252.
[6] I. Shimizu: J. Non-Cryst. Solids, **77&78** (1985) 1363.
[7] Wei Gunag-Pu, H. Okamoto and Y. Hamakawa: Jpn. J. Appl. Phys., **24** (1985) 1105.
[8] S. Nakano, T. Fukatsu, M. Takeuc'i, S. Nakajima and Y. Kuwano: Proc. 3rd Sensor Symposium, Tsukuba (1983) 97.
[9] D. Kruangam, T. Endo, H. Okamoto and Y. Hamakawa: Jpn. J. Appl. Phys., **24** (1985) L806.
[10] Y. Hamakawa, D. Kruangam, T. Yoyama , M. Yoshimi, S.M. Paasche and H. Okamoto: Int. J. Optoelectronics Devices and Technology, **4** (1989) 281.
[11] Y. Hamakawa, T. Toyama and H. Okamoto: Proc. 1st Int. Conf. on Amorphous Semiconductor Technology, Ashevill (1989) 180.
[12] Y. Hamakawa, Y. Matsumoto, G. Hirata and H. Okamoto: MRS Proc., **164** (1990) 291.
[13] Y. Hamakawa, K. Hattori and H. Okamoto: a-Si Solar Cell Contractors Meeting, Sunshine Project, MITI, May 8-10 (1990).
[14] H. Shirai, D. Das, J. Hanna and I. Shimizu: Tech. Digest of PVSEC-5, Kyoto (1990) 59.
[15] Y. Tawada and H. Yamagishi: a-Si Solar Cell Contractors Meeting, Sunshine Project, MITI, May 8-10 (1990)
[16] for example, S. Tsuda, N. Nakamura, K. Watanabe, T. Takahama, H. Nishiwaki, M. Ohnishi and Y. Kuwano: Solar Cells, **9** (1983) 25.
[17] Y. Hamakawa: Proc. Euroforum - New Energy Congress -, **1**, Saarbrucken (1988) 194.
[18] Y. Nakata, H. Sannomiya, S. Moriuchi, Y. Inoue, K. Komoto, A. Yokota, M. Itoh and T. Tsuji: Int. J. Optoelectronics Devices and Technology, **5** (1990) 209.
[19] W. Ma, T. Horiuchi, M. Yoshimi, K. Hattori, H. Okamoto and Y. Hamakawa: Proc. 22nd IEEE PVSC (tobe published)
[20] D. Kruangam, M. Deguchi, T. Toyama, H. Okamoto and Y. Hamakawa: IEEE Trans. Electron Devices, **ED-35** (1988) 957.
[21] S. Paasche, T. Toyama, H. Okamoto and Y. Hamakawa: IEEE Trans. Electron Devices, **ED-36** (1989) 2895.
[22] D. Kruangam, M. Deguchi, T. Endo, H. Okamoto and Y. Hamakawa: Extended Abstracts of 18th Int. Conf. Solid State Devices and Materials, Tokyo (1986) 683.
[23] H. Shimizu, M. Yoshimi, K. Hattori, H. Okamoto and Y. Hamakawa: Proc. 14th ICAS, Garmisch-Partenkirchen (1991) (to be published)

HIGH-QUALITY AMORPHOUS SILICON CARBIDE PREPARED BY A NEW FABRICATION METHOD FOR A WINDOW P-LAYER OF SOLAR CELLS

K.Ninomiya, H.Haku, H.Tarui, N.Nakamura, M.Tanaka, K.Wakisaka
S.Tsuda, H.Nishiwaki, S.Nakano and Y.Kuwano

Sanyo Electric Co.,Ltd., Functional Materials Research Center
1-18-13, Hashiridani, Hirakata, Osaka, 573, Japan

ABSTRACT

A total area conversion efficiency of 11.1% has been achieved for a 10cm×10cm integrated-type single-junction a-Si solar cell submodule using a high-quality wide-bandgap p-layer doped with $B(CH_3)_3$ and other advanced techniques. This is the highest conversion efficiency ever reported for an a-Si solar cell with an area of $100cm^2$. As for a multi-junction solar cell, 12.1% was obtained for a $1cm^2$ cell with a high-quality wide-bandgap a-Si i-layer. The layer was fabricated by a hydrogen dilution method at a low substrate temperature for a front active layer of an a-Si/a-Si/a-SiGe stacked solar cell.

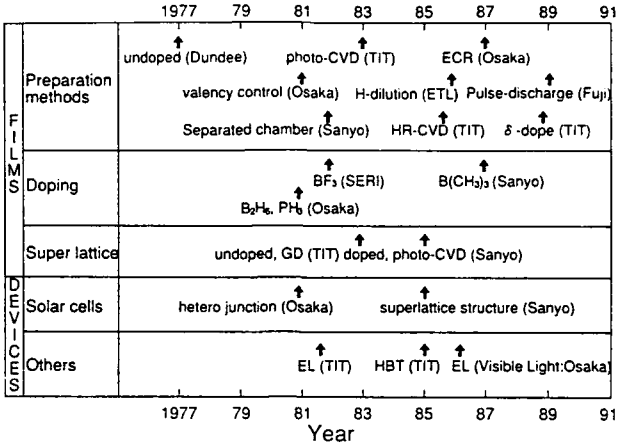
For further improvement in conversion efficiency, a wider-bandgap a-SiC was developed using a novel plasma CVD method, called the CPM (Controlled Plasma Magnetron) method. From XPS and IR measurements, the resultant films were found to have high Si-C bond density and low Si-H bond density. p-type a-SiC was fabricated using the post-doping technique, and dark conductivity more than $10^{-5}(\Omega \cdot cm)^{-1}$ was obtained ($Eopt_3 \geqq 2eV$; $Eopt_2 \geqq 2.2eV$), whereas that of conventional p-type a-SiC is less than $10^{-6}(\Omega \cdot cm)^{-1}$. These properties are very promising for application to the p-layers of advanced a-Si solar cells.

INTRODUCTION

It is necessary for us to establish a clean energy system that will not destroy the global environment. Solar cells, therefore, are receiving much attention as a clean energy source. Amorphous silicon (a-Si) solar cells have many attractive features, such as low fabrication cost and large area availability. Thus, intensive research efforts have been concentrated on developing a-Si solar cells, especially on improvements in conversion efficiency. For this purpose, the development of a high-quality wide-bandgap material is very important, because it is used as the window layer of an a-Si solar cell or the front active layer of a multi-junction solar cell. Consequently, many investigations have been performed in this area.

In 1981, a p-type a-SiC/i/n a-Si solar cell was first proposed by the Hamakawa group, resulting in a considerable increase in conversion efficiency[1]. Since then, much research has been performed to obtain high-quality p-type a-SiC for high-performance a-Si solar cells and other devices as shown in Table 1. p-type a-SiC doped with $B(CH_3)_3$ has excellent properties for the window layer of a-Si solar cell[2]. Recently, we achieved the highest conversion efficiency of 11.1% for a 10cm×10cm integrated-type single-junction a-Si solar cell submodule using p-type a-SiC doped with $B(CH_3)_3$ and other advanced techniques including:(1) the "Super Chamber" method; (2) a highly-textured TCO; (3) an ultra-thin

Table 1 History of a-SiC and related devices



interface layer; and (4) a low-damage laser patterning process.

For further improvement in conversion efficiency, multi-junction solar cells have been investigated. Usually, a-Si or a-SiC are used as a front active layer in multi-junction solar cells. However, there is the problem that film properties deteriorate with increasing optical bandgap. Recently, high-quality a-SiC alloys were reported[3], but their opto-electric properties were still inferior to those of a-Si. Therefore, wide-bandgap high-quality a-Si films without carbon were studied using the hydrogen dilution method at a low substrate temperature [4]. Through this method and other advanced technologies, a conversion efficiency of 12.1% was obtained for a $1cm^2$ a-Si/a-Si/a-SiGe stacked solar cell.

For further improvement in conversion efficiency, wider-bandgap materials were also developed. A more transparent and conductive p-layer was fabricated using a novel plasma CVD method, called the CPM (Controlled Plasma Magnetron) method[5] and a post-doping technique. IR (infrared) measurements and XPS (X-ray Photoelectron Spectroscopy) studies showed that these films have a high Si-C bond density and a low Si-H bond density. The absorption coefficients of these films were about one order of magnitude lower than those of conventional a-SiC, and a dark conductivity of $1.4\times10^{-4}(\Omega\cdot cm)^{-1}$ was obtained.

In this paper, we propose some useful techniques for obtaining high-quality wide-bandgap a-SiC or a-Si. First, several excellent properties of p-type a-SiC doped with $B(CH_3)_3$ are described. Second, high-quality wide-bandgap a-Si fabricated by the hydrogen dilution method at a low substrate temperature is discussed. Finally, we propose a carbon-rich a-SiC prepared by the CPM method for higher-efficiency a-Si solar cells.

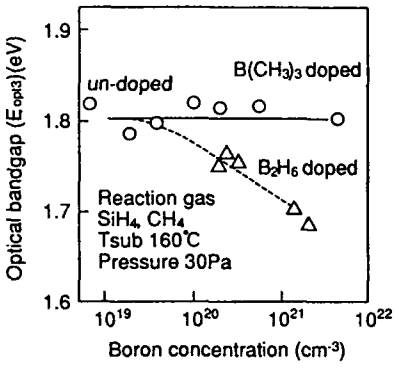


Fig.1 Optical bandgap ($Eopt_3$) of p-type a-SiC as a function of boron concentration

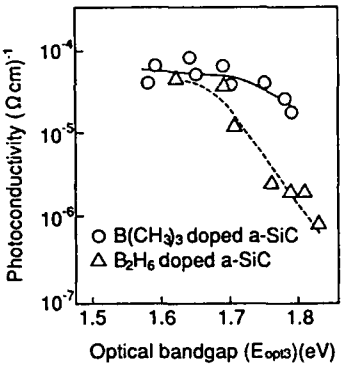


Fig.2 Photoconductivity of p-type a-SiC films as a function of optical bandgap($Eopt_3$)

HIGH-EFFICIENCY A-SI SOLAR CELLS

Approaches to obtain high-quality window layers for high-efficiency solar cells

p-type a-SiC is conventionally used for the p-layer of a-Si solar cells. Usually, B_2H_6 is used as a p-type doping gas, but B-B and B-H bonds included in B_2H_6 are thought to remain easily in a-SiC films, resulting in high defect densities. Therefore, $B(CH_3)_3$, which has no B-B and B-H bonds, was studied instead of B_2H_6.

Conventional a-SiC films doped with B_2H_6 have the problem of bandgap narrowing in the highly doped region. The change in optical bandgap ($Eopt_3$) of p-type a-SiC is shown in Fig.1 as a function of boron concentration. The optical bandgap was determined from the $h\nu$ vs $(\alpha h\nu)^{1/3}$ plot using the T/(1-R) method [6]. This method has good linearity in the low energy region compared with the conventional Tauc's plot ($h\nu$ vs $(\alpha h\nu)^{1/2}$ plot), especially in the case of a-Si related alloys, as described later. The optical bandgap of a-SiC doped with B_2H_6 decreased as the boron concentration increased. In contrast, that of a-SiC doped with $B(CH_3)_3$ was almost constant ($Eopt_3$~1.8eV). Since carbon content of a-SiC doped with $B(CH_3)_3$ was found to be almost constant in this region, it was determined that bandgap narrowing could be avoided by using $B(CH_3)_3$.

Fig.2 shows the relationship between photoconductivity and optical bandgap. As shown in this figure, the photoconductivity of a-SiC films was improved about one order of magnitude by using $B(CH_3)_3$. From the SIMS (Secondary Ion Mass Spectroscopy) measurement, the ratio of B-B bonds/B atoms in a-SiC doped with $B(CH_3)_3$ was about ten times smaller than that of a-SiC doped with B_2H_6. Thus, it is considered that the higher doping efficiency and the higher photoconductivity of a-SiC doped with $B(CH_3)_3$ is depend

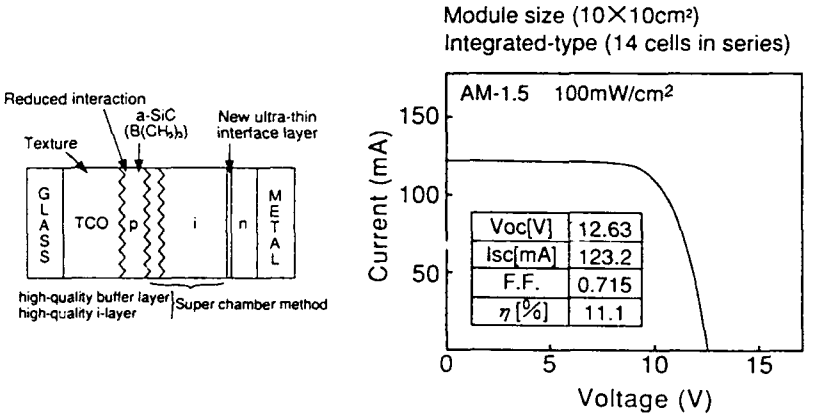


Fig.3 Structure and illuminated I-V characteristic of an integrated-type a-Si solar cell submodule

on low defect density due to low densities of B-B and B-H bonds.

Various advanced techniques, including the use of $B(CH_3)_3$, have led us to the world's highest conversion efficiency of 11.1% (total area efficiency) for a 10cm × 10cm integrated-type single-junction a-Si solar cell submodule, as shown in Fig.3. Successful techniques developed to improve a-Si solar cell efficiency include:

(1) A high-quality i-layer and p/i buffer layer using a separated ultra-high vacuum reaction chamber apparatus called the "Super Chamber"[7]. Using this chamber, the defect density in the i-layer and p/i buffer layer can be reduced, leading to improved output characteristics for a-Si solar cells.
(2) A high-quality and low absorption coefficient p-layer of a-SiC doped with $B(CH_3)_3$, improves photosensitivity in the short wavelength region.
(3) A highly-textured TCO with a high haze ratio and gentle slope in the grains yields a more uniform p-layer, which can improve photo-sensitivity in the long wavelength region.
(4) A new type of ultra-thin interface layer between the i- and n-layers has been developed. This new interface layer can reduce the defect density of n-layer.
(5) A new laser patterning technique, called the "Ablation Oriented Laser Patterning" method, which can make integrated-type a-Si solar cell submodules with very low damage. It has led to improvement of the effective area and short circuit current.

All of these improvements were introduced for the fabrication of integrated-type single-junction a-Si solar cell submodules. The resultant cell had an open circuit voltage of 12.63V, short circuit current of 123.2mA, fill factor of 0.715 and a conversion efficiency of 11.1%.

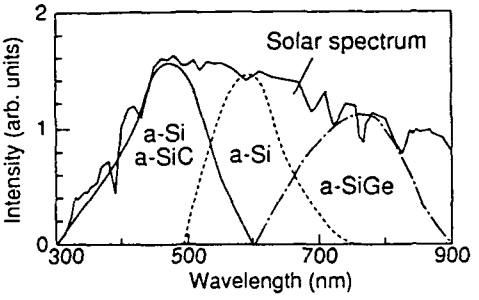


Fig.4 Photo-response spectra of a-Si and related alloys

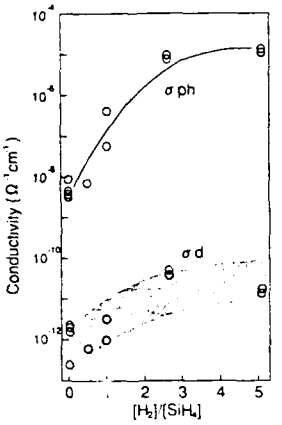


Fig.5 Conductivity of a-Si as a function of the hydrogen flow ratio

High-quality a-Si i-layer for high-efficiency multi-junction solar cells

For further improvement in conversion efficiency, high-quality wide-bandgap a-Si was investigated from the viewpoint of the front active layers of multi-junction solar cells, as shown in Fig.4. Although it is well known that deposition at low substrate temperatures results in wide-bandgap a-Si, the quality was very poor when conventional deposition parameters were used. Therefore, hydrogen dilution of the source gas and optimization of the deposition parameters was investigated. Typical experimental results for a-Si fabricated at a low substrate temperature are shown in Fig.5. Although, the photoconductivity of the a-Si film was less than $10^{-8}(\Omega \cdot cm)^{-1}$ when pure SiH_4 was used, it increased rapidly as the SiH_4 was diluted with hydrogen. When $[H_2]/[SiH_4]=5$, the photoconductivity was improved to more than $10^{-5}(\Omega \cdot cm)^{-1}$, and the photosensitivity rose as high as 10^6, at a low substrate temperature of 80℃. These values are comparable to those obtained in conventional device-quality films deposited at 200℃. Concerning the optical bandgap (Eopt) of these films, $Eopt_2$ was around 2.0eV when the $h\nu$ vs $(\alpha h\nu)^{1/2}$ plot (Tauc's plot) was used, and around 1.7eV when the $h\nu$ vs $(\alpha h\nu)^{1/3}$ plot ($Eopt_3$) was used. The Eopt were higher than those for conventional a-Si films fabricated at 200℃ by 100~150meV. In addition, the thermal stability of this wide-bandgap a-Si was examined using annealing experiments.

Fig.6 shows the characteristics of a-Si solar cells whose i-layer was prepared by the hydrogen dilution method at a low substrate temperature. As shown in this figure, the open circuit voltage (Voc) is as high as 0.95V. The increase in Voc is attributed to the increased built-in potential of the solar cell, which is due to the wide-bandgap of i-layer. The conversion efficiency of 9% was even obtained for a ~1500Å thick i-layer. By using this high-quality wide-bandgap a-Si as the front active layer for a $1cm^2$ a-Si/a-Si/a-SiGe stacked solar cell, conversion efficiency of 12.1% was

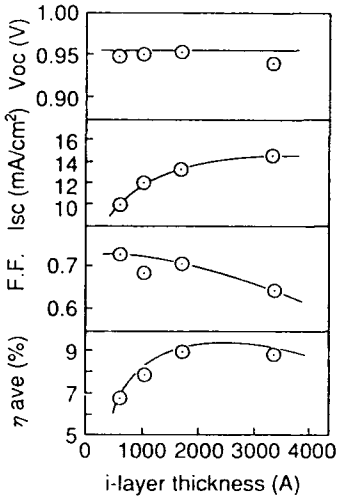


Fig.6 Characteristics of a-Si solar cells as a function of the i-layer thickness. i-layers were wide-bandgap a-Si prepared by the hydrogen dilution method at a low substrate temperature

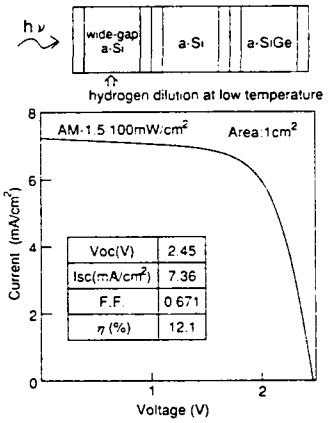


Fig.7 Illuminated I-V characteristics of a 3-stacked solar cell whose front cell was fabricated by the hydrogen dilution method at a low substrate temperature

obtained, as shown in Fig.7.

WIDER-BANDGAP A-SICPREPARED BY THE CPM (CONTROLLED PLASMA MAGNETRON) METHOD

Although high-quality wide-bandgap a-Si can be fabricated by the hydrogen dilution method at low substrate temperatures, as mentioned in the last section, it is difficult to raise $Eopt_3$ above 2.0eV. Therefore, carbon-rich a-SiC was investigated. It is well known that film quality deteriorates as the carbon content increases. This is thought to be caused by the existence of $C-H_3$ bonds in films in large quantities[8]. Therefore, we investigated the possibility of increasing the number of Si-C bonds, instead of $C-H_3$ bonds, with a novel plasma CVD method, called the CPM (Controlled Plasma Magnetron) method[5].

The CPM (Controlled Plasma Magnetron) method

A schematic diagram of the CPM method is shown in Fig.8. This method is basically a capacitively coupled RF glow discharge plasma CVD method. Electromagnets are positioned under the RF electrode to generate a magnetic field in the plasma, and thus the plasma can be confined near the RF electrode. Therefore, a high electron density

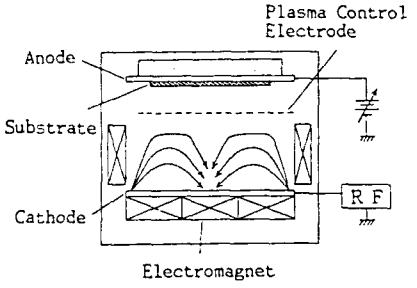


Fig.8 Schematic diagram of the CPM method

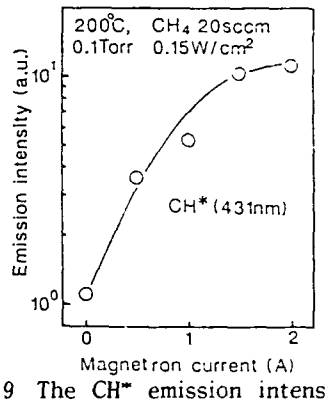


Fig.9 The CH* emission intensity near the RF electrode as a function of Img

plasma can be easily obtained and plasma damage to the substrate decrease.

The strength of the magnetic field is controlled by the magnetron current (Img) through the electromagnet. 100 gauss of magnetic field can be obtained at Img=2A near the center of the RF electrode. Fig.9 shows the emission intensity of CH*(431nm) near the RF electrode in a CH_4 plasma measured by the OES (Optical Emission Spectroscopy) method as a function of Img. CH* emission intensity increased with Img, and became about 1 order of magnitude larger than that with conventional method (Img=0A) in the case of Img=2A. Then the CH_4 was found to be effectively decomposed by the CPM method. This indicates carbon-rich a-SiC films can be easily obtained by the CPM method. When a magnetic field was applied to the plasma, optical emission could not be observed near the substrate. In contrast, plasma emission is almost constant between the substrate and the RF electrode in the conventional RF plasma CVD method. Therefore, plasma damage to the substrate in the CPM method is thought to be small compared with that in the conventional method.

The specifications of this reaction chamber are almost equivalent to those for the super chamber. The background pressure is below 4×10^{-6}Pa, even at a substrate temperature of 400℃, so undesirable impurities, such as oxygen or nitrogen, can be reduced below $5\times10^{18}cm^{-3}$.

Undoped a-SiC films prepared by the CPM method

Undoped a-SiC was prepared using the CPM method. The depositon conditions are shown in Table 2. The gases were SiH_4(100%) and CH_4(diluted to 10% in H_2). The total pressure was 13.3Pa. The magnetic field, which was controlled by the magnetron current (Img), was 0 to 100 Gauss (Img=0~2A).

The substrates were glass (Corning 7059) and single crystalline silicon (c-Si:>1000Ω·cm). Both the transmittance(T) and reflectance(R) of a-SiC on glass was measured, and then the absorption coefficient was calculated by the T/(1-R) method[5]. From

the IR spectra, hydrogen contents were estimated using the absorbance of the Si-H stretching mode (~2050cm^{-1}). The XPS spectra were characterized by fitting Gaussian curves to the peaks. Conductivity was determined using a coplanar Al electrode.

Fig.10 shows the absorption coefficient (α) of a-SiC films prepared by the conventional plasma CVD method and the CPM method. The α decreases as the magnetic field increases, and the α with 2A of Img is about one order of magnitude lower than that of conventional a-SiC. Although the α of conventional a-SiC at a photon energy of 3eV is 2×10^5cm^{-1}, that of a-SiC prepared by the CPM method is 2×10^4cm^{-1}. Figs.11 and 12 show the plot of $h\nu$ vs $(\alpha h\nu)^{1/2}$ (Tauc's plot) and $h\nu$ vs $(\alpha h\nu)^{1/3}$. Tauc's plot is often used to determine the optical bandgap($Eopt_2$) of a-Si and related alloys such as a-SiC and a-SiGe, but it significantly deviates from a linear relationship in the low energy region, especially in the case of a-Si related alloys. Therefore other ways of determining optical bandgap ($h\nu$ vs $(\alpha h\nu)^{1/3}$) have been attempted and good

Table 2 Deposition conditions

Tsub (℃)	400
Gas flow rate (SCCM)	SiH_4 : 1 CH_4*: 100 B_2H_6**: 0~100
RF power density (W/cm^2)	0.15
Pressure (Pa)	13.3
Magnetic field (Gauss)	0~100
Magnet current (A)	0~2

*CH_4 : 10%CH_4/H_2
**B_2H_6 : 0.1%B_2H_6/H_2

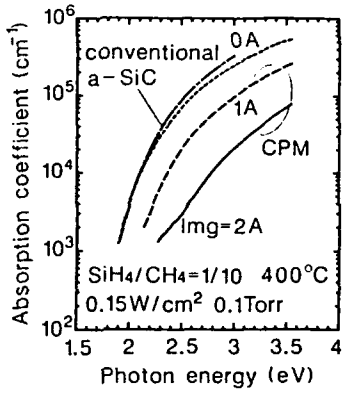


Fig.10 The α of a-SiC by the CPM method and conventional method

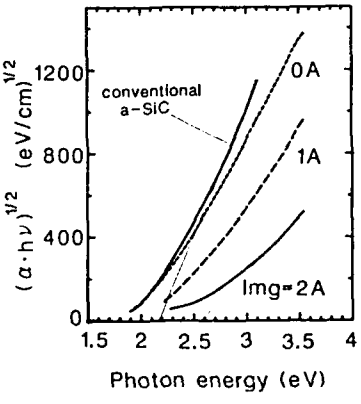


Fig.11 $h\nu$ vs $(\alpha h\nu)^{1/2}$ plots of a-SiC (Tauc's plot)

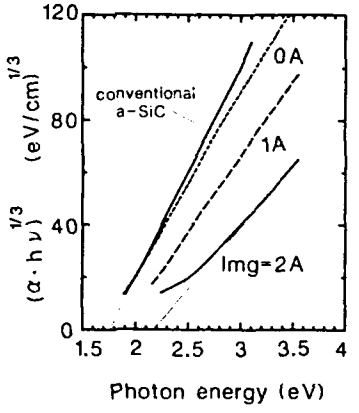


Fig.12 $h\nu$ vs $(\alpha h\nu)^{1/3}$ plots of a-SiC

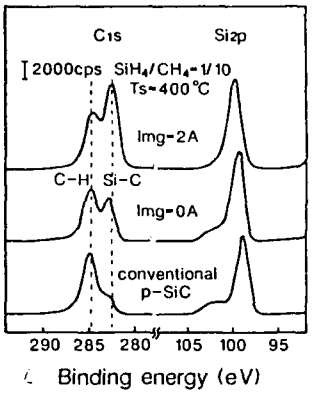


Fig.13 The XPS spectra of a-SiC prepraed by the CPM method

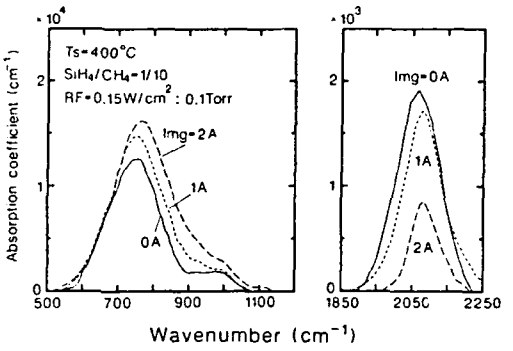


Fig.14 The IR absorption spectra of a-SiC prepared by the CPM method

linearity was found[6]. Indeed, the linearity of Fig.12 is better than that of Fig.11. This indicates that the $h\nu$ vs $(\alpha h\nu)^{1/3}$ plot is useful to determine the optical bandgap ($Eopt_3$). The $Eopt_3$ of a-SiC by the CPM method was about 2.2eV ($Eopt_2$=2.5eV), which was about 0.4eV higher than that of conventional a-SiC. Since a higher optical bandgap is desirable for the window layer of a-Si solar cells, this a-SiC was expected to be effective for improving conversion efficiency.

XPS and AES (Auger Electron Spectroscopy) measurements were used to analyse the carbon content of films quantitatively. The XPS spectra are shown in Fig.13. Carbon bonded as Si-C at a binding energy of ~282eV was found to drastically increase as Img increased. The ratio of Si-C bonds to Si was estimated by fitting these spectra to Gaussian curves, using the reference XPS spectra of crystalline (stoichiometric) SiC. Although the ratio of Si-C to Si in conventional a-SiC was about 0.15, that of a-SiC by the CPM method was 0.6. These results indicate that a-SiC films with a high Si-C bond density can be easily produced using the CPM method. The AES was used to estimate the film composition, and the x value in $a\text{-}Si_{1-x}C_x$ was found to increase 0.3 (conventional a-SiC) to 0.55 (Img=2A). This indicates that the a-SiC with Img=2A is nearly stoichiometric. Fig.14 shows the IR spectra of these films. As the magnetic field increased, the absorption coefficient of Si-C bonds increased as same as the XPS results. However, Si-H bond density was found to decrease about 1/4. The hydrogen content bonded to Si was estimated to be 30% (Img=0A) and 8% (Img=2A), when the A factor was equal to that of a-Si ($A=1.4\times10^{20}cm^2$). From the XPS and IR measurements, a-SiC films prepared by the CPM method were found to have many Si-C bonds and low Si-H bond density.

p-type a-SiC films

As mentioned above, wide-bandgap ($Eopt_3 \geqq 2.0eV$) a-SiC could be

fabricated by the CPM method. Thus, boron doping of such films was investigated.

Usually, p-type a-SiC is deposited by the decomposition of a mixture gases, including SiH_4, CH_4 and B_2H_6. Using this method, however, highly transparent and highly conductive p-type a-SiC could not be obtained in this experiment. Thus, we adopted another doping method, called the post doping method. Undoped a-SiC was first deposited on the substrate, and then it was exposed to the B_2H_6 plasma, as shown in the left part of Fig.15.

The right part of Fig.15 shows the boron profile of a post doped film measured by SIMS to estimate the effective depth for the p-layer. Post doping was performed for 10min. on 2000Å thick a-SiC. The conditions included an RF power of 0.05 W/cm^2, Img of 0A, a gas flow late of 100sccm and a pressure of 13.3Pa. As shown in Fig.15, the effective depth as a p-layer was estimated about 200Å, in which the boron concentration was about 1/e compared with that at the surface. This thickness is sufficient for the p-layer of a-Si solar cells. Fig.16 shows the dark conductivity (σ d) of p-type a-SiC prepared by these two methods. The dark conductivity was measured for a-SiC with a thickness of 200Å in the case of post doping. As for the conventional method, σ d of 10% of B_2H_6 to SiH_4 is $3\times10^{-7}(\Omega\cdot cm)^{-1}$ and lower than that of p-type a-SiC. By using the post-doping method, σ d increased to $1.4\times10^{-4}(\Omega\cdot cm)^{-1}$, which is higher than that of conventional p-type a-SiC. Therefore, the post-doping method was found to be effective for obtaining highly-conductive p-type a-SiC in the case of doping such carbon-rich films.

Fig.17 shows α of p-type a-SiC films prepared by the CPM method and conventional method. Since α can not be determined accurately for a thin film, the post-doped films was fabricated by the 5 cycle repetition of deposition and post doping ((120Å +post doping 5min.)×5times). The dark conductivity of these films was almost same ($3\times10^{-7}(\Omega\cdot cm)^{-1}$). Although the α of p-type a-SiC was higher than that of undoped a-SiC, that prepared by the CPM method was lower than that prepared by the conventional method. The post-doped film was found to have the lowest α, especially in the short wavelength region. Although α of conventional film was $2\times10^5cm^{-1}$ at 400nm, that of film prepared by the CPM method was $5\times10^4cm^{-1}$. This means that the absorbance in a 100Å thick p-layer

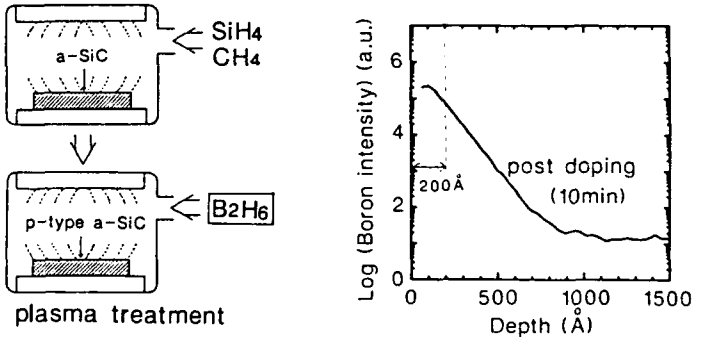


Fig.15 Post-doping method and boron depth profile of p-type a-SiC doped by this method

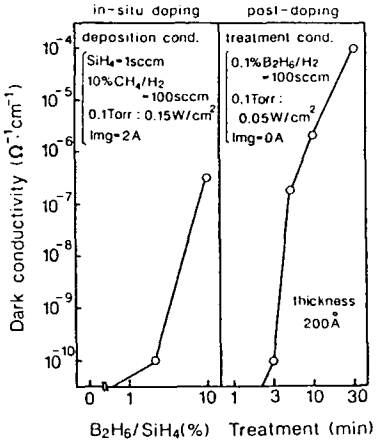


Fig.16 The σ d of p-type a-SiC by the CPM method using the post-doping technique and conventional method

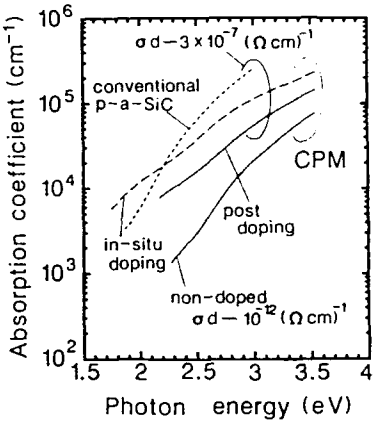


Fig.17 The α of p-type a-SiC with the σ d of 3×10^{-7} $(\Omega\cdot cm)^{-1}$

Table 3 Film properties of p-type a-SiC prepared by the CPM method using the post-doping technique

		CPM	Conventional
Un-doped	Carbon content (from AES)	~0.5	<0.2
	XPS peak ratio C_{1s} (Si-C)/Si_{2p}	~0.6	~0.15
	Hydrogen content (Si-Hx)	<10 at.%	~30 at.%
	Absorp. coeff. at 400nm	6×10^{4}~2×10^{5} cm^{-1}	$>2\times10^{5}cm^{-1}$
p-type	$Eopt_3$ ($Eopt_2$)	>2.0 (2.2) eV	<1.7 (1.9) eV
	Dark conductivity	3×10^{-7}~1×10^{-4} $(\Omega cm)^{-1}$	~10^{-6} $(\Omega cm)^{-1}$

can be decreased from 20 to 5% using the CPM method. By using this wider bandgap ($Eopt_3$: 2.0eV) and highly conductive (σ d : 10^{-5} $(\Omega\cdot cm)^{-1}$) p-type a-SiC as a window layer, the conversion efficiency of a-Si solar cells is expected to be improved furthermore. Table 3 shows a summary of film properties prepared by the CPM method.

CONCLUSIONS

High-quality wide-bandgap materials were developed to improve

the conversion efficiency of a-Si solar cells. A total area conversion efficiency of 11.1% was achieved for a 10cm×10cm integrated-type a-Si solar cell submodule, using p-type a-SiC doped with $B(CH_3)_3$ and other advanced techniques.

High-quality wide-bandgap a-Si was obtained by the hydrogen dilution method at a low substrate temperature. By using this wide-bandgap a-Si as the front active layer in a-Si/a-Si/a-SiGe stacked solar cells, a conversion efficiency of 12.1% was obtained for a $1cm^2$ cell.

For further improvement in conversion efficiency, wider-bandgap ($Eopt_3 \geqq 2.0eV$) a-SiC was prepared by the CPM method, which can decompose material gases effectively. The obtained film has a high Si-C bond density and low Si-H bond density. The absorption coefficient of these films was about 1 order of magnitude lower than that of conventional a-SiC. Post doping technique was adopted to this carbon-rich a-SiC to prepare p-type a-SiC, and highly conductive ($\sigma d \geqq 10^{-5}(\Omega \cdot cm)^{-1}$) and wide-bandgap ($Eopt_3 \geqq 2.0eV$) films were obtained. These film properties promise higher efficiency a-Si solar cells.

ACKNOWLEDGEMENT

This work is supported by NEDO as a part of the Sunshine Project under the Ministry of International Trade and Industry.

References

[1] Y.Tawada, M.Kondo, H.Okamoto and Y.Hamakawa, J.Appl.Phys., 53, 5273(1982)
[2] H.Tarui, T.Matsuyama, N.Nakamura, S.Tsuda, S. [illegible] and Y.Kuwano, Jpn.J.Appl.Phys., 28, 2436(1989)
[3] A.Matsuda and K.Tanaka, J. Non-Cryst. Solids, 97&98, 1367(1987)
[4] Y.Hishikawa, S.Tsuda, S.Nakano and Y.Kuwano, J.Appl.Phys., 69, 508(1991)
[5] M.Ohnishi, M.Tanaka, K.Ninomiya, N.Nakamura, S.Tsuda, S.Nakano and Y.Kuwano, Jpn.J.Appl.Phys., 27, 40(1988)
[6] Y.Hishikawa, N.Nakamura, S.Tsuda, S.Nakano and Y.Kuwano, 30, 1008(1991)
[7] S.Tsuda and Y.Kuwano, Jpn.J.Appl.Phys., 26, 33(1987)
[8] W.Beyer, J.Non-Cryst. Solids, 77&78, 857(1985)

DOPED AMORPHOUS AND MICROCRYSTALLINE SILICON CARBIDE AS WIDE BAND-GAP MATERIAL

F. Demichelis*, C.F. Pirri*, E. Tresso* and P. Rava*

* Dipartimento di Fisica, Politecnico - C. so Duca degli Abruzzi 24, 10129 Torino (Italy)
* Elettrorava S.p.A., 10040 Savonera Torino (Italy)

Amorphous and microcrystalline silicon carbide, undoped and doped, are promising materials as wide band gap semiconductors (E_g > 2 eV). In the present work results on hydrogenated and fluorinated a SiC and μc-SiC films intrinsic , B or P doped are reported. Energy gap higher than 2 eV are obtained together with electrical dark conductivities in the range 10^{-12} - 10^{-2} $\Omega^{-1}cm^{-1}$.

INTRODUCTION

Anderson and Spear (1) first reported results on hydrogenated amorphous silicon carbide (a-SiC:H) films, deposited by the glow-discharge method, and showed that the optical band-gap of the films increases continuously with increasing carbon content. In recent years there has been a great interest to control the electrical conductivity of wide band-gap a-SiC:H thin films for application in devices such as heterojunction bipolar transistors (2) and photovoltaic cells (3). So a number of investigations have been made on a-SiC:H and related materials. Fundamental changes in the electro-optical characteristics of a-SiC:H occur with doping.

Boron doped a-SiC:H (p-type) is widely used as a window layer for heterojunction amorphous silicon solar cells resulting in significant improvement in efficiency (4). However B doping degrades some properties of a-SiC:H in fact, as the boron concentration increases defects are introduced in the pseudo-gap, decreasing the energy gap.

Phosphorus doped a-SiC:H (n-type) films show good optical properties and high band gap even at high dopant concentration, but they do not reach high electrical conductivity (5).

In fluorinated amorphous silicon carbide, a-SiC:H,F, the optical gap increases with fluorine content up to values as high as 3.1 eV (6). Using suitable deposition conditions excellent films having large optical gap and high photoconductivity have been obtained (7).

Recently Hattori et al. (8) have deduced from Raman experiments that samples composed of Si microcrystals embedded in an amorphous SiC matrix show optical transparency and good electrical conductivity. A further improvement in the conductivity without changes in the high optical gap can be obtained by doping the microcrystalline samples (9,10).

In order to establish how silicon carbide alloys could provide wide band gap material as well as a good control of electrical properties we investigated the optical and electrical properties of undoped and doped amorphous and microcrystalline silicon carbide alloys. Optical gap higher than 2 eV together with conductivity in the range 10^{-12} - 10^{-2} $\Omega^{-1}cm^{-1}$ have been obtained.

TABLE I
Deposition conditions

	SiH_4 (sccm)	CH_4 (sccm)	H_2 (sccm)	PH_3 - B_2H_6 (vppm)	T_d (°C)	p (Pa)	P (W)
PECVD a-SiC:H	50-100	0-150	0-70	0-3 10^3	200	40	50
PECVD μc-SiC:H	3-13	0-10	180-200	0-1 10^4	200	30-40	150

	SiH_4 (sccm)	CF_4 (sccm)	H_2 (sccm)	T_d (°C)	p (Pa)	P (W)
PECVD μc-SiC:H,F	4	0.5-2	200	200	30	150
	Ar (sccm)	CF_4 (sccm)	H_2 (sccm)	T_d (°C)	p (Pa)	P (W)
SPUTT. a-SiC:H,F	100	1.5-11	7-17	250	0.4-0.7	300

EXPERIMENTAL

Films of a-SiC:H and μc - SiC:H were deposited by Plasma Enhanced Chemical Vapour Deposition (PECVD) of SiH_4-CH_4-(H_2) mixtures with controlled addition of B_2H_6 or PH_3.

The a-SiC:H,F films were prepared by R.F. sputtering of a silicon target in Ar+H_2+CF_4 mixture.

The μc-SiC:H,F films were deposited by PECVD in SiH_4-CF_4-H_2 mixtures.

The deposition conditions of the films are listed in Table I. The cristallinity of the films was verified by IR and Raman spectroscopies and Transmission Electron Microscopy (TEM).

Optical transmittance and reflectance were measured by a Perkin Elmer UV-visible-NIR Lambda 9 spectrophotometer in the wavelength region 200-2500 nm. D.C. electrical conductivity was measured in coplanar configuration under vacuum with a Hewlett Packard 4329 A High Resistance Meter.

RESULTS AND DISCUSSION

The absorption coefficient as deduced from direct optical and PDS measurements is shown in Fig. 1 for undoped, p doped and n doped a-SiC:H typical samples and in Fig. 2 for undoped and doped μc -SiC:H samples. It can be observed that in a SiC:H the undoped films show an absorption coefficient vs. photon energy typical of semiconductors with energy gaps higher than 2 eV. As dopant atoms are incorporated the optical properties degrade and the energy gap decreases, more strongly for boron doped than for phosphorus doped amorphous films. For μc SiC:H films the optical properties are only slightly affected by doping and all the

samples show energy gaps higher than 2 eV.

In order to compare our results with those published by other authors, the optical gap Eg was deduced using Tauc's definition, even if its applicability to microcrystalline films, to doped amorphous semiconductors and carbon-rich materials is questionable (11,12). Moreover also the E_{04} gap defined as the energy corresponding to $\alpha = 10^4\ cm^{-1}$ was deduced. Both E_g and E_{04} for the different sets of samples are summarized in Table II. In undoped a-SiC:H, E_g is included in the range 1.9 - 2.5 eV, depending on carbon contents. In amorphous samples a narrowing in E_g can be observed as the doping concentration increases, higher in boron than in phosphorus doped films. This fact can be explained for boron doped samples by the decrease of H content and an increase of defects as B_2H_6 partial pressure increases. In phosphorus doped films H decrease was not observed and the narrowing of the band-gap is probably only due to dopant induced defects (5).

Microcrystalline undoped SiC:H films, investigated by TEM, have shown crystalline fraction lower than 50% and crystalline size of about 200 Å. Values of E_g are around 1.9 - 2.2 eV independently from microcrystal fraction and size and with carbon and hydrogen percentage ranging from 5 to 15% and from 5 to 20% respectively. In phosphorus doped microcrystalline films an enhancement in microcrystallinity has been observed (13) and the optical properties are practically independent from P content (10). It is known that boron inhibits microcrystal formation (14), so only slightly doped films are microcrystalline and have energy gap higher than 2 eV. As the boron content increases the microcrystal fraction and size decreases and the optical properties of the films follow the trend of p-doped a-SiC:H.

A particular interest must be devoted to fluorinated silicon carbide samples. Both amorphous and microcrystalline SiC:H,F show high values of E_g (as it can be observed in Fig.3-4). In a-SiC:H,F samples prepared by sputtering energy gap from 2.0 up to 3.1 eV have been obtained. In samples prepared by PECVD the values of E_g are included in the range 2.25-2.45 eV. Probably the fluorine incorporation gives rise to the removal of localized states near the band edges increasing the energy gap (6,15).

The dark conductivity σ_d for the different samples is reported in Table II. It can be seen that the conductivity of a-SiC:H is very low and it increases about 7 orders of magnitude in boron doped samples and about 5 orders of magnitude in phosphorus doped ones.

A remarkable improvement in conductivity is obtained in uc-SiC:H. From values included in the range 10^{-5} - $10^{-8}\ \Omega^{-1}\ cm^{-1}$ for undoped samples, values as high as $10^{-3}\ \Omega^{-1}\ cm^{-1}$ and $10^{-2}\ \Omega^{-1}\ cm^{-1}$ for boron and phosphorus doped respectively can be achieved.

The high optical gap together with the high conductivity is attributed to the change in the network structure, i.e. the microcrystallization. As far as the a-SiC:H,F films are concerned it can be observed that the fluorine incorporation widens drastically the gap whereas the conductivity is only one order of magnitude higher than that of a-SiC:H (6).

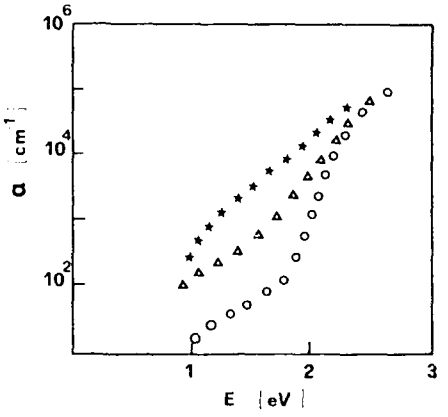


Fig. 1 - Absorption coefficient vs. energy for device-quality a-SiC:H with 10 at% of C: (●) undoped, (Δ) P doped with 4200 vppm of PH_3 and (★) B doped with 4200 vppm of B_2H_6.

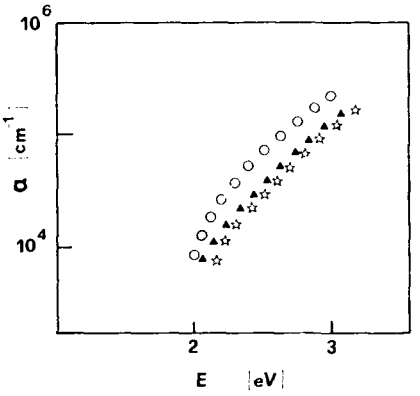


Fig. 2 - Absorption coefficient vs. energy for μc-SiC:H with 5 at% of C: (☆) undoped, (▲) P doped with 2200 vppm of PH_3 and (⊙) B doped with 5000 vppm of B_2H_6.

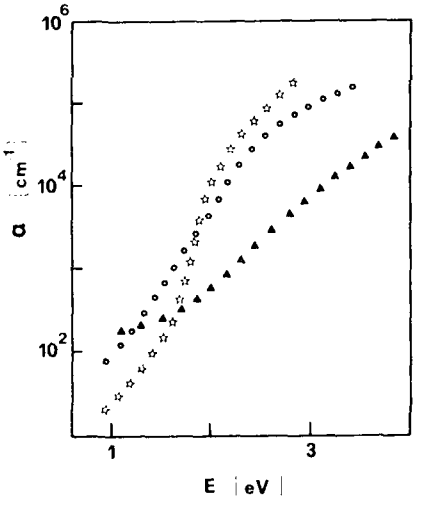


Fig. 3 - Absorption coefficient vs. energy for undoped a-SiC:H,F produced by sputtering with different CF_4 partial pressure: (☆) 8 mPa, (○) 23 mPa, (▲) 51 mPa.

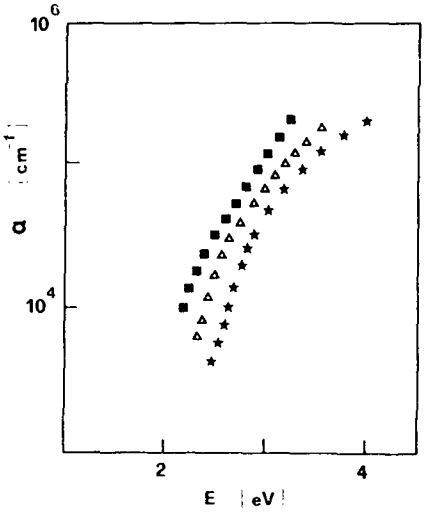


Fig. 4 - Absorption coefficient vs. energy for PECVD undoped μc-SiC:H,F with different CF_4 partial pressure: (■) 75 mPa, (▲) 225 mPa, (★) 375 mPa.

TABLE II
Band-gap and electrical conductivity

	E_g (eV)	E_{04} (eV)	σ_d ($\Omega^{-1}cm^{-1}$)
PECVD a-SiC:H undoped	1.9-2.5	2.0-2.7	10^{-10}-10^{-13}
PECVD a-SiC:H B-doped	1.6-1.9	1.8-2.1	10^{-5}-10^{-9}
PECVD a-SiC:H P-doped	1.9-2.1	2.0-2.2	10^{-7}-10^{-10}
PECVD μc-SiC:H undoped	1.9-2.2	2.1-2.2	10^{-5}-10^{-9}
PECVD μc-SiC:H B-doped	1.9-2.2	1.9-2.2	10^{-3}-10^{-7}
PECVD μc-SiC:H P-doped	1.9-2.2	2.1-2.2	10^{-2}-10^{-5}
PECVD μc-SiC:H,F undoped	2.0-2.4	2.1-2.6	10^{-7}-10^{-9}
SPUTT. a-SiC:H undoped	2.0-2.6	2.0-2.7	10^{-9}-10^{-10}
SPUTT. a-SiC:H,F undoped	2.0-3.1	2.0-3.1	10^{-9}-10^{-11}

CONCLUSIONS

As a conclusion it can be deduced that in silicon-carbon alloys high optical band-gap can be achieved both in amorphous and in microcrystalline films. In amorphous films the high band-gap is coupled to a difficulty to control electrical properties. In doped films the electrical conductivity ranges from 10^{-12} to 10^{-5} $\Omega^{-1}cm^{-1}$ with a decrease of optical gap from 2.1 to 1.6 eV.

In microcrystalline SiC:H films energy gaps in the range 2 - 2.25 eV have been obtained with dark electrical conductivity from 10^{-9} to 10^{-2} $\Omega^{-1}cm^{-1}$.

In fluorinated undoped SiC:H,F films energy gaps up to 3.1 eV for amorphous and 2.4 for microcrystalline films have been optained. In such films the conductivity is of the order of 10^{-9} $\Omega^{-1}cm^{-1}$.

REFERENCES

(1) D.A. Anderson and W.E. Spear - Phil. Mag. 35, 1 (1977)

(2) K. Sasaki, S. Furukawa and M.M. Ratiman - 1985 Int. Electron Devices Meeting - Washington D.C. Tech. Dig., p.294

(3) Y. Hamakawa and Y. Tawada - Int. J. Solar Energy 1, 125 (1982)

(4) Y. Tawada, M. Kondo, H. Okamoto and Y. Hamakawa - Proc. 15th IEEE Photovoltaic Specialist Conference, Florida (IEEE New York, 1981) p.245

(5) F. Demichelis, C.F. Pirri, E. Tresso, G. Della Mea, V. Rigato and P. Rava - Semicond. Sci. and Technol. 6 (1991 in press)

(6) F. Demichelis, C.F. Pirri, E. Tresso and T. Stapinski - Journ. Appl. Phys. (submitted)

(7) N. Saito Phil. Mag. B 55, 615 (1987)

(8) Y. Hattori, D. Kruangam, T. Toyama, H. Okamoto and Y. Hamakawa - Journ. Non-Cryst. Solids 97-98, 1079 (1987)

(9) F. Demichelis, C.F. Pirri and E. Tresso - Phil. Mag. B (in press)

(10) F. Demichelis, C.F. Pirri, E. Tresso, G. della Mea, V. Rigato and P. Rava - Mat. Res. Soc. Symp. Proc., vol. 219, p. 793 (1991)

(11) B. Goldstein, C.R. Dickson, P.M. Fauchet - Appl.Phys. Lett. 52, 2672 (1988)

(12) D. DasGupta, F. Demichelis, C.F. Pirri, A. Tagliaferro Phys. Rev B 43, 2131, (1991)

(13) A. Matsuda, S. Yamasaki, K. Nakagawa, H. Okushi, K. Tanaka, S. Izima, M. Matsuda and H. Yamamoto - Jap. J. Appl. Phys. 19, 1305 (1980)

(14) J.L. Guimaraes, R. Martins, F. Fortunato, I. Ferreira, M. Santos, N. Carvalho - Mat. Res. Soc. Symp. Proc., vol. 118, p. 617 (1988)

(15) F. Demichelis, C.F. Pirri, E. Tresso, P. Rava, I. Boarino, T. Stapinski - Proc. 10th E.C. Photov. Solar En. Conf. (Lisbona, 1991) p. 121

WIDE-GAP POLYSILANE PRODUCED BY PLASMA-ENHANCED CVD AT CRYOGENIC TEMPERATURES

S. Miyazaki, H. Shin, K. Okamoto and M. Hirose
Department of Electrical Engineering, Hiroshima University
Higashi-Hiroshima 724, Japan

ABSTRACT

Polysilane thin films have been grown by the rf glow discharge decomposition of SiH_4 at substrate temperatures ranging from -84 to -110°C. The infrared absorption spectra have shown that polysilane chains $(SiH_2)_n$ are predominantly incorporated in the matrix together with SiH_3 which terminates the chain. Also, the infrared absorption band at 2120~2140 cm^{-1} and a distinct Raman peak at ~430 cm^{-1} indicates that fairly long chains $(SiH_2)_n$ with n>11 are produced. Polysilane prepared at -110°C has an optical bandgap of about 3.1 eV and exhibits a visible luminescence around 2.75 eV at 100 K.

INTRODUCTION

The physical properties of binary Si:H materials are tightly connected with the hydrogen contents and the Si-H bonding configurations. As is well known device-quality hydrogenated amorphous silicon with an optical bandgap of 1.7~1.8 eV contains about 10~15 at.% hydrogen in the form of monohydride when it is prepared at temperatures from 200 to 300°C by the plasma enhanced CVD using SiH_4. Wide-optical-gap (2.4~2.55 eV) binary Si:H alloys consisting of a significant amount of polysilane $(SiH_2)_n$ groups have been grown at -53 °C by the disilane glow discharge decomposition [1] or at room temperature by the homogeneous chemical vapor deposition (HOMOCVD) of silane[2]. Despite a number of work on hydrogen-rich Si:H alloys, very little is known on the specific feature of vibrational spectra and on an optical bandgap value for ideal polysilane.

In this paper, we describe the procedure of fabricating long chain polysilane from an SiH_4 discharge at cryogenic temperatures. The optical characterization of the deposited films has been carried out to confirm the existence of long polysilane chains and a wide optical bandgap formation.

EXPERIMENTAL

Binary Si:H films were deposited on quartz, Al and c-Si substrates by the rf glow discharge decomposition of 3% SiH_4 diluted with H_2 in a capacitively coupled reactor[3]. The substrate temperature was changed in the range -57 to -110°C by controlling liquid nitrogen flow rate. The total gas pressure and the rf power density were maintained at 0.2 Torr and 0.44 W/cm^2, respectively.

RESULTS AND DISCUSSION

Film Growth and Structural Analysis

The film growth rate is kept constant at about 0.3 Å/sec in the temperature range from -57 to -81 °C, while it is abruptly increased up to about 2 Å/sec below -84°C as shown in Fig. 1. The growth rate enhancement could be attributed to an increase in

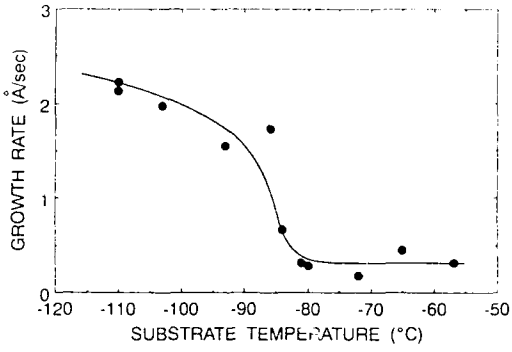


Fig. 1 Si:H film growth rate as a function of substrate temperature.

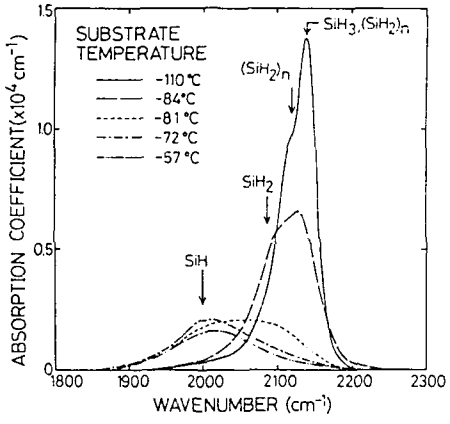


Fig. 2 Infrared absorption spectra of the SiHx stretching modes for binary Si:H films grown at different substrate temperatures.

the effective sticking probability of gas phase products or the increased surface residence-time of major film precursors. Also, the etching reaction promoted by hydrogen radicals might be effectively quenched at such low temperatures[4]. Further discussion on the film growth rate should be done in connection with incorporated hydrogen bonds.

The infrared absorption spectra for films grown at temperatures below -84°C exhibit the predominant incorporation of polysilane chains $(SiH_2)_n$ whose vibrational bands appear at 2120 and 2140 cm^{-1} [5] as represented in Fig. 2. An appreciable amount of SiH_3 units, which give rise to the absorption at 2140 cm^{-1} and terminate the $(SiH_2)_n$ chains, are also incorporated in the matrix. At temperatures above -81°C, the isolated SiH_2 bond absorption at 2090 cm^{-1} or the SiH bond absorption at 2000 cm^{-1} is predominant as in the case of hydrogenated amorphous silicon grown at 200~300°C. The hydrogen content estimated by the integrated absorption intensity of the stretching mode using a proportional constant of 1.4×10^{20} cm^{-2} [6] rapidly decreases with increasing the substrate temperature, being about 28 at.% for a sample prepared at -57°C. The proportional constant can not be used for the case of

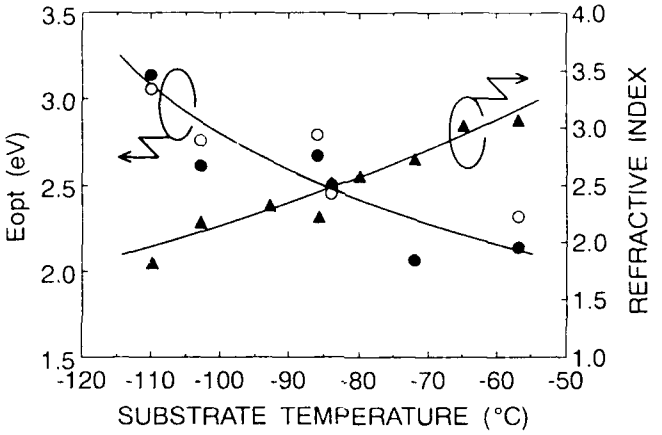


Fig. 3 Optical bandgap E_{opt} and refractive index as a function of substrate temperature. Open circles denote E_{opt} determined from the photon energy at which the absorption coefficient becomes equal to 10^4 cm^{-1}.

polysilane. The polysilane chain length is evaluated from the absorption peak shift of the stretching mode or the infrared absorption intensity ratio of 845 cm^{-1} (bend-scissors) band to 890 cm^{-1} (wagging) [8], indicating that the value of n for $(SiH_2)_n$ is larger than 11 for films grown at substrate temperatures below -84°C. From these results it is likely that the growth rate enhancement at temperatures below -84°C and corresponding long-chain polysilane formation are caused by a higher condensation rate of gas phase products and their polymerization reactions on the surface without any hydrogen radial etching. Note that the gas phase polymerization reaction is negligible in the present experimental conditions because a silane partial pressure is as low as 6 mTorr.

Optical Properties

The optical bandgap was determined by the Tauc plot and also by the photon energy at which the absorption coefficient reaches 10^4 cm^{-1} as shown in Fig. 3. The measured optical bandgap is 3.1~3.2 eV for films deposited at a substrate temperature of -110°C, being in consistence with a theoretical value (3.1 eV) predicted for an ideal linear-chained polysilane[7]. Gradual decrease of the refractive index with lowering the substrate temperature is basically explained by the increase of the optical bandgap. This implies that the growth rate enhancement at low substrate temperatures is not due to a decrease in the film density.

The Raman spectrum taken for polysilane grown on an Al plate at -84°C provides additional information on the material structure. A distinct peak with a full width at half maximum of ~25 cm^{-1} appears at ~430 cm^{-1}, being very different from a broad peak at 480 cm^{-1} that originates from the Si-Si TO mode in conventional a-Si:H with a hydrogen content of 12 at.% as compared in Fig. 4. The fairly sharp ~430 cm^{-1} peak has been assigned as the LO mode of Si skeleton for long-chain polysilane[5,9]. This is consistent with the chain length n>11 estimated by the infrared absorption.

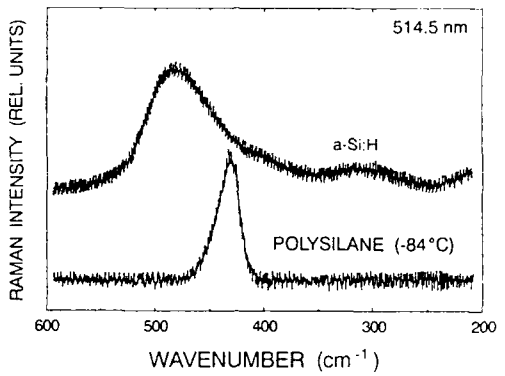


Fig. 4 Raman spectra for polysilane grown at -84°C and conventional a-Si:H prepared at 300°C. An Ar^+ ion laser was used as an excitation source.

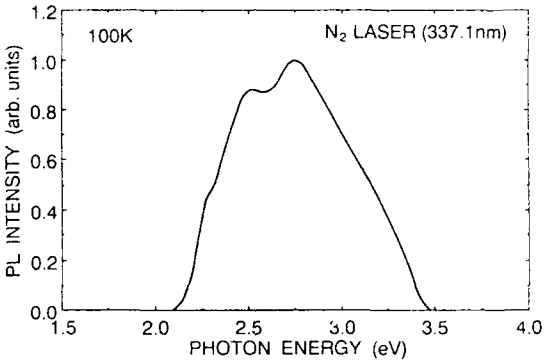


Fig. 5 Photoluminescence spectrum obtained at 100 K for polysilane grown at -110°C. A 337.1 nm line from an N_2 laser is utilized as an excitation source.

The polysilane film prepared at -110°C, whose optical bandgap is 3.1 eV, exhibits a visible photoluminescence at 2.75 eV with a full width at half maximum of 0.8 eV at 100 K for the excitation with a 337.1 nm light from an N_2 laser as shown in Fig. 5. Although an infinitely chained polysilane $(SiH_2)_n$ has a direct allowed gap at the Γ point as predicted by the calculation using the Slater-Koster LCAO method [10], the origin of this luminescence band is still unknown and might be due to the band-tail transition with strong phonon coupling or defect related bound-exciton rather than the interband transition.

Structural Stability

The result of the gas-evolution measurement for polysilane grown at -84 C is shown in Fig. 6. The evolution spectrum for conventional a-Si:H prepared at 300°C is also shown for comparison. In a-Si:H the hydrogen evolution peak appears around 400°C, while in the polysilane the evolution maximum for molecular

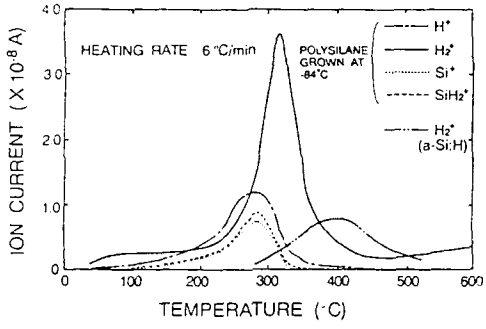


Fig. 6 Gas-evolution intensity for polysilane grown at -84 °C and conventional a-Si:H prepared at 300 °C. Samples were heated at a constant heating rate of 6 °C/min.

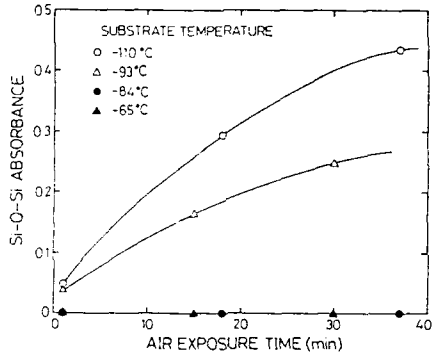


Fig. 7 Infrared absorbance of the Si-O-Si stretching mode at ~1050 cm^{-1} as a function of air exposure time for films grown at different temperatures.

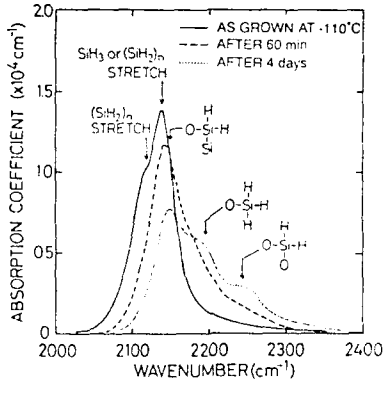


Fig. 8 Infrared absorption spectra for polysilane grown at -110 °C for different air exposure times.

hydrogen is shifted down to 320 C because of the absence of three dimensional Si network. It is interesting to note that the evolution of SiH_x molecular units arising from the thermal dissociation of the $(SiH_2)_n$ chain is observable at about 280 C. This is a possible cause of polysilane surface oxidation at room temperature. The IR absorption at ~1050 cm^{-1} due to the Si-O-Si stretching mode is measured as a function of air exposure time for films grown at different temperatures (Fig. 7). Polysilane deposited at temperatures below -93 C contains a significant amount of SiH_3 units and the film is easily oxidized. The oxidation starts from the backbond of SiH_3 in the film as shown in Fig. 8, where polysilane uptakes oxygen to produce $OSiH_2$ (~2160 cm^{-1}), $OSiH_3$ (~2180 cm^{-1}) and O_2SiH_2 (~2230 cm^{-1}) units[11]. The Si-Si bond connected with SiH_3 which is located at the edge of polysilane chain is more reactive than that of the Si skeleton in the $(SiH_2)_n$ chain because of a little high electronegativity of H compared to that of Si. Oxygen molecule preferentially attacks the backbond of SiH_3 and the incorporation of highly electronegative oxygen causes the further oxidation of the Si skeleton. On the other hand, no oxidation proceeds for polysilane grown at temperatures above -84 C because of less amount of SiH_3.

CONCLUSIONS

We have demonstrated that wide-bandgap (~3.1 eV) binary Si:H films consisting of long-chained $(SiH_2)_n$ ($n>11$) units can be deposited at temperatures below -84 C by plasma enhanced CVD and that polysilane grown at -110 C exhibits visible photoluminescence band around 2.75 eV at 100K. It is also shown that polysilane which contains an appreciable amount of SiH_3 units tends to be oxidized.

ACKNOWLEDGEMENTS

The authors would like to thank K. Nakanishi and M. Takakura for their help on the photoluminescence and gas-evolution measurements. This work was supported in part by the Grant-in-Aid for Scientific Research and Development Program in Sunshine Project from the Ministry of International Trade and Industry, the Japanese Government.

REFERENCES

[1] S. Furukawa and N. Matsumoto, Phys. Rev. B, 31, 2114 (1985).
[2] D. J. Wolford, J. A. Reimer and B. A. Scott, Appl. Phys. Lett. 42, 369 (1983).
[3] H. Shin, S. Miyazaki, H. Ichihashi and M. Hirose, Proc. of the Intern. Seminar on Reactive Plasmas, edited by T. Goto (Organizing Committee of the Intern. Seminar on Reactive Plasmas, Nagoya, 1991), p. 201.
[4] S. Miyazaki, Y. Kiriki, Y. Inoue and M. Hirose, Jpn. J. Appl. Phys. 30, 1539 (1991).
[5] W. B. Pollard and G. Lucovsky, Phys. Rev. B, 26, 3172 (1982).
[6] C. J. Fang, K. J. Gruntz, L. Ley and M. Cardona, J. Non-Cryst. Solids 35 & 36, 255 (1980).
[7] K. Takeda, M. Matsumoto and M. Fukuchi, Phys. Rev. B, 30, 5871 (1984).
[8] S. Furukawa and N. Matsumoto, Phys. Rev. B, 31, 2114 (1985).
[9] P. Vora, S. A. Solin and P. John, Phys. Rev. B, 29, 3423 (1984).
[10] N. Matsumoto, S. Furukawa and K. Takada, Solid State Commun. 53, 881 (1985).
[11] G. Lucovsky, Solid State commun. 29, 571 (1979).

OPTICALLY INDUCED PARAMAGNETISM IN AMORPHOUS HYDROGENATED SILICON NITRIDE THIN FILMS

W. L. WARREN[1], J. KANICKI[2], F. C. RONG[3], W. R. BUCHWALD[3], and M. HARMATZ[3]
[1]Sandia National Laboratories, Albuquerque, NM 87185
[2]IBM T.J. Watson Research Center, Yorktown Heights, NY 10598
[3]Electronics Technology and Devices Lab, Ft. Monmouth, NJ 07703

ABSTRACT

The creation mechanisms of Si and N dangling bond defect centers in amorphous hydrogenated silicon nitride thin films by ultra-violet (UV) illumination are investigated. The creation efficiency and density of Si centers in the N-rich films are independent of illumination temperature, strongly suggesting that the creation mechanism of the spins is electronic in nature, i.e., a charge transfer mechanism. However, our results suggest that the creation of the Si dangling bond in the Si-rich films are different. Last, we find that the creation of the N dangling-bond in N-rich films can be fit to a stretched exponential time dependence, which is characteristic of dispersive charge transport.

INTRODUCTION

Amorphous hydrogenated silicon nitride (a-SiN_x:H) is a rather unique material due to its use in a wide variety of applications. For instance, a-SiN_x:H is extensively used in non-volatile memories because of its excellent charge trapping properties, or as the primary dielectric for thin film transistors. In order to fabricate higher quality films, much effort has been employed in understanding the origin and nature of paramagnetic and diamagnetic defects in this material [1-6]; interesting enough, these defects appear to be an intrinsic part of the material [6].

It has been known for quite some time that optical illumination creates paramagnetic defects in a-SiN_x:H thin films [2,3,5,6] as is the case for several amorphous materials, i.e., a-Si [1,7], a-Se, a-As_2Se_3, a-As [8], etc. Typically the only paramagnetic defect observed in UV-illuminated as-deposited a-SiN_x:H is the Si dangling bond (db) [1-3,5,6]. However, after annealing N-rich films at temperatures exceeding the substrate temperature (T_s), the N db becomes the dominant defect center generated by UV illumination [6,9]. In order to further understand the mechanism(s) by which the intrinsic diamagnetic defect sites are brought to their neutral paramagnetic state, we have employed electron paramagnetic resonance (EPR), optical illumination at different temperatures, and differing processing conditions in this study.

EXPERIMENTAL CONDITIONS

The a-SiN_x:H thin films were deposited by plasma enhanced chemical vapor deposition (PECVD) on fused silica substrates to a thickness of approximately 1 micron at T_s of 250 or 400°C. The stoichiometry, determined by an electron microprobe technique, was changed by varying the NH_3 to SiH_4 ratio [9-11].

The EPR measurements were made using non-saturating microwave power conditions. The density of Si and N dbs were determined by using a TE_{104} microwave cavity and a weak pitch spin standard. UV-illumination (hv < 5.5 eV) was performed using an Oriel 100W Hg lamp at either room temperature or 100 K. Monochromatic illumination was obtained by filtering the broadband light with appropriate narrow-band (10 nm) interference filters.

RESULTS AND DISCUSSION

Fig. 1 illustrates the variation of the Si db densities with film stoichiometry (x) for as-deposited and broad-band UV-illuminated a-SiN_x:H thin films. The variation of the Si db with x have been reported for as-deposited films by a number of investigators [10,11]. Some general features of the EPR spectra are the zero-crossing g-value and the peak-to-peak derivative linewidth of the Si db varies from g = 2.005 and ΔH_{pp} = 7 G in a-Si to g = 2.0028 and ΔH_{pp} = 13.6 G, respectively, for both the as-deposited and UV-illuminated a-SiN_x:H films. The broadening has been attributed to spin delocalization on the N neighbors as the N content increases [6,12]. As shown in Fig. 1, the Si db concentrations for both the as-deposited and UV-illuminated films are dependent on film stoichiometry; they are the lowest for N-rich and a-Si:H films [3,10,11]. (3) The as-deposited Si db density is dependent on substrate temperature [3,10]; however, the UV-induced spin density is not [3].

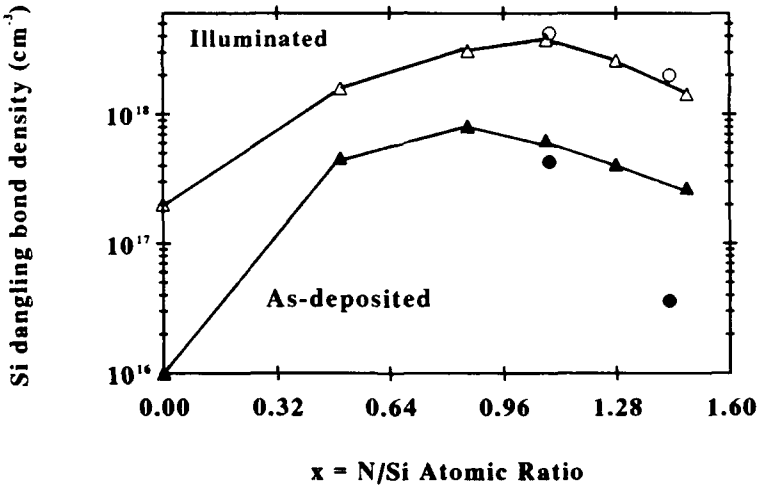


Fig. 1 Si db concentration for as-deposited and UV-illuminated a-SiN_x:H films. The triangles are for films deposited at T_s = 250°C and the circles are for films deposited at T_s = 400°C. The Si spin densities for a-Si:H were obtained from ref. 7.

It is very important to note that the time needed to saturate the Si db density is dependent on film stoichiometry as illustrated in Fig. 2. The samples in Fig. 2 were all deposited at T_s = 250°C and the UV-illumination was performed at room

temperature using broad-band illumination. The spin saturation time in the N-rich films is extremely short compared to the spin saturation time in the Si-rich films. We believe that this may be a clue to the spin creation mechanism in these films. For example, the short times needed to create the spins in the N-rich films may suggest that the creation mechanism is electronic in nature. Meanwhile, for the Si-rich films the time dependence approaches that observed for creating Si dbs in a-Si:H, where breaking of weak Si-Si bonds is believed to be the spin creation mechanism [7]. From a chemical standpoint, this appears reasonable since to first order one would anticipate significantly more weak Si-Si bonds in the Si-rich films [13].

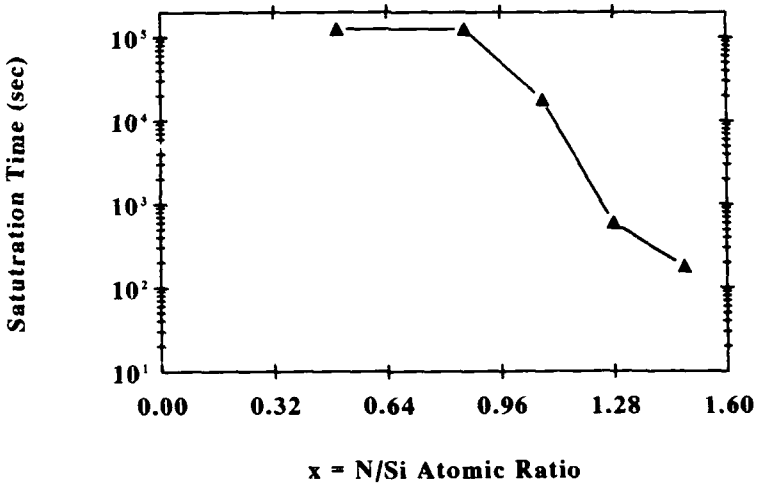


Fig. 2 Saturation time to create the Si dangling bonds in nitride films with different stoichiometries. The films were illuminated at room temperature using a broad-band UV lamp.

Of course, it is possible that the various saturation times, and saturation densities, result from different absorption coefficients of the films to the broad-band UV light [3]. To see if this is the case, the films were illuminated with monochromatic light corresponding to an absorption coefficient of 10^4 cm^{-1} for the different films, this ensured that the light is absorbed uniformly throughout the films; the power density was kept constant for all of the films using appropriate neutral density filters. We find that the extrapolated saturation times are still significantly longer in the Si-rich films than for the N-rich films. For example, the time to saturate the spin density for the x = 1.48 films was 240 min.; it was over 4000 min. for the x = 1.08 films, and over 7000 min. for the x = 0.86 films. This result indicates that a different mechanism must be responsible for Si db creation in the N-rich and the Si-rich films.

There appears to be a fair amount of evidence that the creation of Si dangling bonds in the N-rich nitride films is electronic in nature; it simply involves a change of spin and charge state of pre-existing diamagnetic positively ($^{+}$Si) and negatively ($^{-}$Si) charged Si sites [2,3,5,6]. To further

elucidate the creation mechanism, we have measured the Si db concentration as a function of illumination time at different temperatures as illustrated in Fig. 3. The N-rich films (x = 1.48) were illuminated *in situ* in the EPR cavity at 300 and 100 K using a 5.17 eV narrow-band interference filter. The creation kinetics are temperature independent.

We believe that this temperature independence is consistent with the notion that neutral Si db centers are created by the photo-excitation of electrons from $^{-}$Si sites [3]; the emitted electrons are subsequent captured by $^{+}$Si sites to also create neutral Si dbs. On the other hand, if the annihilation of excitons [14], diffusion of atomic hydrogen [7], or bond breaking events [1,13] were involved in the creation of Si dbs for the N-rich films, a temperature dependence would have been expected.

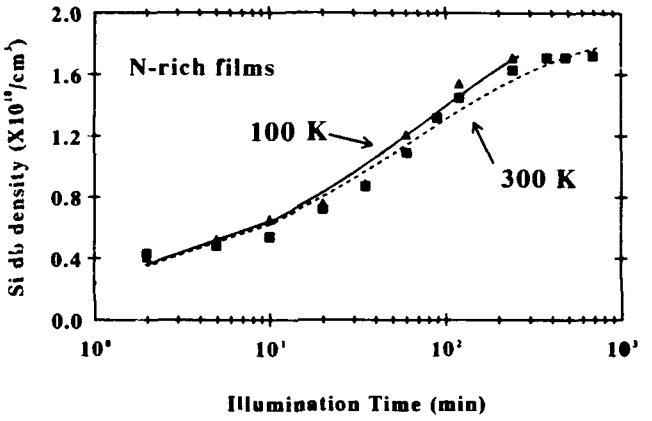


Fig. 3 Creation kinetics of Si dbs in N-rich a-$SiN_{1.48}$:H films at 300 K and 100 K using monochromatic (5.17 eV) light. The lines were plotted using eqn. (1).

As first observed by Kanicki et al. [5], we also find that the illumination time dependence for creating Si dbs can be fit by a stretched exponential function both at 100 and 300 K as illustrated in Fig. 3. The function can be expressed as:

$$N(t) = N_S\{1 - \exp[-(t/\tau)^{\beta}]\} \qquad (1)$$

where N(t) is either the Si or N db density at time t, N_S is the saturated Si or N db spin density, τ is the time constant and β is a characteristic stretching parameter related to dispersive carrier transport. Earlier works have shown that carrier transport is dispersive in a-$SiN_{1.48}$:H [15]. Dispersive charge transport leads to a stretched exponential function, common to many amorphous materials [16]. The values for the stretched exponential at 300 K are 0.48 and 3900 sec for β and τ, respectively, and are 0.48 and 5000 sec for β and τ, respectively at 100 K. Generally, β can be related to the

transport of electrons (or holes) by drift or diffusion. A larger ß value indicates that the mechanism is less dispersive. This stretched exponential formalism further agrees with the assertation that the creation of spins in a-$SiN_{1.48}$:H is electronic in nature.

As mentioned earlier, the N db has also been observed in N-rich a-SiN_x:*H* films. The N db is not observed in Si-rich nitrides because it falls into the valence band [9]. To create the N dbs a two step process is generally needed [17]: (1) the N-rich films are annealed above T_s, and (2) subsequently illuminated with UV-light. The density of N dbs is dependent on the films' initial hydrogen concentration suggesting that the creation involves the evolution of hydrogen from an N-H site.

Recently, it was suggested that once the hydrogen evolves from an N-H group, N-charged sites are left behind that become paramagnetic upon exposure to UV-light [17]. If the UV-light does change the spin state and charge state of diamagnetic N-charged sites: an analog to the creation of neutral paramagnetic Si dbs in the N-rich films, except that now the precursors are charged diamagnetic N sites, one might anticipate that the creation kinetics of the paramagnetic neutral N dbs should be similar to that observed for the Si dbs. Fig. 4 shows that this is roughly the case. (The samples used in Fig. 4 were annealed at 650°C for 15 min, followed by *in situ* UV-illumination in the EPR cavity using broad-band UV light.) Not only are the shapes of Figs. 3 and 4 similar, but the creation of both paramagnetic centers is relatively temperature independent.

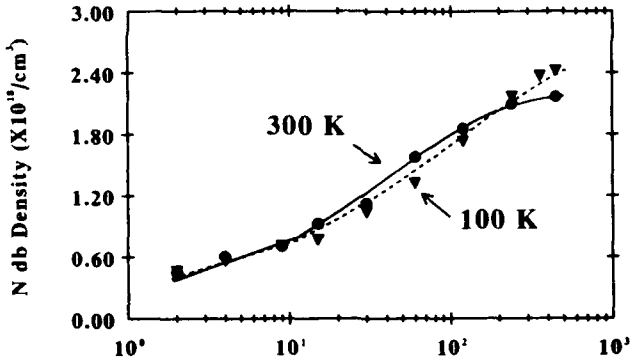


Fig. 4 Creation kinetics of N dbs in N-rich a-$SiN_{1.48}$:H films at 300 K and 100 K using broad-band UV-light. The lines were plotted using eqn. (1). Before UV-illumination, the films were annealed at 650°C for 15 min.

Last, we find that the illumination time dependence for the creation of N dbs can also be fit by a stretched exponential function as shown in Fig. 4. The values for the stretched exponential at 300 K are 0.61 and 2500 sec for ß and τ, respectively, and are 0.49 and 6500 sec for ß and τ,

respectively at 100 K. Hence, these results (stretched exponential and temperature independence for creating the spins) lend support for the aforementioned N dangling bond creation mechanism.

CONCLUSIONS

In summary, we have explored the creation mechanisms of Si and N dangling bonds in a-SiN_x:H thin films by UV-light. We find evidence that the creation of Si and N dangling bonds in N-rich films is a charge transfer mechanism, and that charged diamagnetic sites are most likely the precursors to the neutral EPR active sites. For the Si-rich compositions, the results are consistent with the Si dangling bond being created by a different mechanism; breaking weak Si-Si bonds appears most reasonable.

ACKNOWLEDGEMENTS

It is a pleasure to thank J. Robertson (National Power, UK), C. H. Seager (Sandia), and E. H. Poindexter (U.S. Army ETDL) for many helpful suggestions and discussions during the course of this work.

REFERENCES

1)T. Shimizu, H. Kidoh, A. Morimoto, and M. Kumeda, Jpn. J. Appl. Phys., 28, 586 (1989).
2)P.M. Lenahan, D.T. Krick, and J. Kanicki, Appl. Surf. Sci., 39, 392 (1989).
3)J. Kanicki, W.L. Warren, C.H. Seager, M.S. Crowder and P.M. Lenahan, J. Non-Cryst. Solids, in press.
4)J. Robertson, Phil. Mag B63, 47 (1991).
5)J. Kanicki, M. Sankaran, A. Gelatos, M.S. Crowder, and E.D. Tober, Appl. Phys. Lett., 57, 698 (1990).
6)W.L. Warren, J. Kanicki, F.C. Rong, and E.H. Poindexter, J. Electrochem. Soc., (1992) in press.
7)M. Stutzmann, W.B. Jackson, and C.C. Tsai, Phys. Rev. B32, 23 (1985).
8)S.G. Bishop, U. Strom, and P.C. Taylor, Phys. Rev. B15, 2278 (1977).
9)W.L. Warren, J. Kanicki, J. Robertson, and P.M. Lenahan, Appl. Phys. Lett., 59, 1699 (1991).
10)D. Jousse, J. Kanicki, D.T. Krick and P.M. Lenahan, Appl Phys. Lett., 52, 445 (1988).
11)S. Hasegawa, M. Matsuda, and Y. Kurata, Appl. Phys. Lett., 58, 741 (1991).
12)N. Ishii, S. Oozora, M. Kumeda, and T. Shimizu, Phys. Status Solidi B114, K111 (1982).
13)Z. Yin and F.W. Smith, Phys. Rev. B42, 3666 (1990).
14)A.N. Trukhin, Phys. Status Solidi B98, 541 (1980).
15)D. Jousse, and J. Kanicki, Appl. Phys. Lett., 55, 1112 (1989).
16)J. Kakalios, R.A. Street, and W.B. Jackson, Phys. Rev. Lett., 59, 1037 (1987).
17)W.L. Warren, P.M. Lenahan, and J. Kanicki, J. Appl. Phys., 70, 2220 (1991).

STRUCTURE, CHARACTERISTICS, AND THE APPLICATION OF PHOSPHORUS DOPED HYDROGENATED MICROCRYSTALLINE SILICON

S. J. Jeng, D. E. Kotecki, J. Kanicki*, C. C. Parks, and J. Tien
IBM, Semiconductor Development Laboratory, Hopewell Junction, NY 12533
*IBM, T. J. Watson Research Center, Yorktown Heights, NY 10598

ABSTRACT

The microstructure, electrical, and optical properties of *in situ* phosphorus doped hydrogenated microcrystalline silicon (μc-Si:H:P) films are strongly affected by deposition parameters and subsequent thermal processes. μc-Si:H:P films with thickness ranging from 200 to 1000Å have been deposited on Si and SiO_2 substrates. The μc-Si:H:P film is best deposited at 200°C in terms of structure, and H and P content. In this film, microcrystallites are embedded in an amorphous matrix and have a volume fraction of $\simeq$85%. The band-gap of the film is 1.8 eV. In this paper, the materials and processing issues of μc-Si:H:P deposited in a parallel plate RF plasma and in a downstream RF plasma chemical deposition reactor have been studied using HRTEM, SIMS, electrical, and optical measurements.

INTRODUCTION

The concept of using a wide band-gap emitter or a narrow band-gap base in a heterojunction bipolar transistors (HBT) to improve the transistor performance was introduced by Shockley and Kroemer in 1950s [1]. This idea has been realized later using the more advanced epitaxial growth and thin film deposition technologies. Recently, hydrogenated amorphous silicon (a-Si:H) [2], hydrogenated microcrystalline silicon (μc-Si:H) [3], and hydrogenated amorphous silioen carbide (a-SiC:H) [4] have been used as emitter contacts in HBTs to suppress minority carrier injection and improve the current gain. Nevertheless, the resistivity, thermal stability, stress, and the reproducibility of these materials still need to be optimized and controlled. In this paper, the correlations between structural, chemical, electrical, and optical characteristics of μc-Si:H:P grown by plasma enhanced chemical vapor deposition (PECVD) have been studied. The effects of thermal processing on the structure and properties of μc-Si:H:P are reported. The use of a silicon nitride cap prior to anneal is shown to limit crystallization during RTA. It has also been demonstrated that polysilicon can be deposited by low pressure chemical vapor deposition (LPCVD) at 630°C on top of a thick μc-Si:H film without changing the structure of the μc-Si:H film.

EXPERIMENTAL

μc-Si:H:P films were deposited on Si and SiO_2 substrates in a parallel plate RF powered reactor with the gas mixture of 1% PH_3 in SiH_4 and 100% H_2. Before deposition, Si substrate were cleaned by the RCA procedure [5], then 10:1 HF dip, and immediately loaded into the process chamber and pumped down to a base pressure of 2×10^{-6} Torr. Films with a thickness of 200Å to 0.1μm were deposited at different substrate temperatures and gas dilutions (% of (1% PH_3/SiH_4) in H_2). RF power density, total pres-

sure, and the flow rate of 1% PH_3 in SiH_4 was 0.1 W-cm^{-2}, 1.0 Torr, and 10 sccm, respectively. Table I summarizes the deposition parameters, the structure, resistivity, and H and P content of the films.

μc-Si:H:P films with and without a silicon nitride cap were then rapid thermal annealed at a temperature between 600 and 1000°C in N_2 for 10-30 sec. Polysilicon was deposited on thick μc-Si:H films at 630°C in a conventional LPCVD batch reactor from silane.

Temperature (°C)	Gas Dilution (%)	Structure	Dep. Rate (Å/min)	Avg. Grain (Å)	Resistivity (Ω-cm) (1 μm thick)	H Content (cm^{-3})	P Content (cm^{-3})
100	1	M	36	25	-	1.3×10^{22}	1.5×10^{20}
100	10	A	120	-	-	1.3×10^{22}	4.7×10^{20}
200	1	M	48	30	0.28	1.3×10^{22}	2.0×10^{20}
200	2	M	74	30	-	9.9×10^{21}	4.0×10^{19}
200	5	M	91	30	-	9.9×10^{21}	5.0×10^{19}
200	10	M	103	30	-	1.2×10^{22}	4.7×10^{20}
200	∞	A	245	-	-	1.1×10^{22}	5.0×10^{19}
300	1	M	48	35	0.21	8.1×10^{21}	3.3×10^{20}
300	10	M	97	35	-	5.6×10^{21}	4.3×10^{20}
400	1	M	91	40	0.13	1.4×10^{21}	2.4×10^{20}
400	10	M	143	40	-	9.9×10^{20}	3.1×10^{20}
500	1	M	52	50	0.05	8.0×10^{19}	1.0×10^{20}
500	10	M	119	50	-	-	-

Table I. The deposition conditions and the corresponding structure (either amorphous (A) or microcrystalline (M)), deposition rate, average grain size, resistivity, and the H, P contents in the films.

RESULTS AND DISCUSSION

From Table I, the film deposition rate decreases with increasing H_2 flow because the atomic H produced in the plasma enhances a competing etching process. This reverse etching process can be promoted by the addition of H will also preferentially eliminate the energetically unfavorable amorphous structure. Hence, microcrystallinity can be promoted by gas dilution [6]. The microcrystalline film shown in Figure 1 was obtained at a substrate temperature of 100°C by using a 1% dilution of (1% PH_3/SiH_4) in H_2, while those films deposited with 10% dilution are entirely amorphous at this temperature. In Fig. 1, microcrystallites with average size of 25Å are embedded in the amorphous matrix and have the volume fraction of ~85%. The μc-Si:H:P/c-Si interface is clean without visible residual oxide.

At a constant growth temperature, the film resistivity decreases as the film thickness is increased because the crystallite grain size is larger in the thicker film [7], and also because more P atoms activated with a larger crystallite size. At a constant film thickness, the crystallites size increases with increasing growth temperature, while the film resistivity decreases as shown in Table I. At a higher temperature, the adsorbed surface species (SiH_x and PH_x) are more mobile and can migrate to lower energy sites. Therefore, Si atoms can be incorporated into an ordered crystalline structure thereby increasing the crystallite size and activating more P atoms. From the electrical and compositional measurements, approximately 10% of the P is activated in the μc-Si:H:P film, and the rest of the P is likely segregated at grain boundaries or in the amorphous phase.



Figure 1. A high resolution lattice image of a 350Å -thick μc-Si:H:P film deposited at 100°C and with 1% of (1% PH_3/SiH_4) in H_2. The arrows indicate the clean μc-Si:H:P/c-Si interface.



Figure 2. Cross-sectional lattice image of a 260Å μc-Si:H:P film after a 900°C, 30 sec RTA without an a-Si_xN_y:H capping layer. The μc-Si:H:P film is totally recrystallized, and the original μc-Si:H:P/crystalline Si interface is indicated by the arrows.



Figure 3. Cross-sectional lattice image of a 260Å μc-Si:H:P film after a 900 C, 30 sec RTA with a 5000Å a-Si_xN_y:H capping layer. The original μc-Si:H:P/crystalline Si interface is indicated by the arrows.

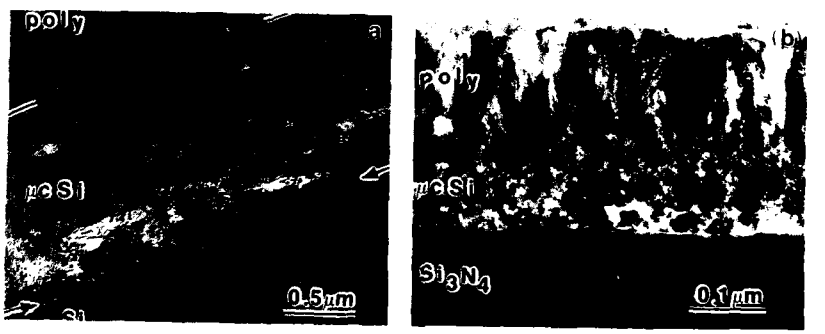


Figure 4. Cross-sectional images of the test structure (a) polysilicon/μc-Si:H:P/c-Si and (b) polysilicon/μc-Si:H:P/Si_3N_4. The structure of the μc-Si:H:P remains unchanged after a 630°C, 5 min polysilicon deposition.

The structure, electrical, and optical characteristics of μc Si:H:P are strongly affected by thermal process. To limit recrystallization during RTA, a 0.5μm-thick nitrogen-rich hydrogenated silicon nitride (a-SiN_x:H) capping layer was deposited onto μc-Si:H:P before RTA. The lattice images of a 260Å μc-Si:H:P film after a RTA at 900°C for 30 sec without and with a 0.5μm a-SiN_x:H capping layer, respectively, are shown in Figs. 2 and 3.

Without the capping layer (Fig. 2), the microcrystalline film is found to totally recrystallize and align with the the substrate. Voids are also observed in the film which are believed to be trapped H_2 bubbles, which lead to surface roughness. SIMS measurements show that the H concentration decreases after a RTA. The optical band-gap decreases with increasing RTA temperatures, and it was measured to be approximately 1.8 eV, 1.33 eV, and 1.15 eV, respectively, after a 600°C, 700°C, and 900°C, 10 sec RTA.

With an a-SiN_x:H capping layer (Fig. 3) the structure consists of a 40Å recrystallized layer at the μc-Si:H:P/crystalline silicon interface and a 220Å layer of polycrystalline silicon with an average grain size of ~ 40Å. Thus, an a-SiN_x:H layer has been shown to inhibit recrystallization of μc-Si:H:P film, limit formation of H_2 bubbles, and hence prevent surface roughening.

Polysilicon films were deposited onto the μc-Si:H:P films to test the thermal stability of the μc-Si:H:P films. First, a μc-Si:H:P film was deposited on a Si substrate or on top of a Si_3N_4 layer by PECVD at 200°C. Subsequently, a polysilicon film was deposited on these structures by LPCVD at 630°C. The μc-Si:H:P film structure on both Si substrate and Si_3N_4 is unchanged after the 630°C, 5 min polysilicon deposition.

CONCLUSIONS

In conclusion, μc-Si:H:P is best deposited at 200-300°C by PECVD in terms of microstructure, H and P content, and dopant activation.

1. The microstructure and optical band-gap of μc-Si:H:P films was found to be stable if subsequent thermal cycle is kept below 650°C.

2. An a-SiN_x:H capping layer is deposited prior to the anneal has been found to suppress H evolution and inhibit the recrystallization of μc-Si:H:P film during higher temperature RTA. This a-SiN_x:H cap can be easily removed by wet etching in 10:1 HF or H_3PO_4.

3. It has been shown that polysilicon can be deposited by LPCVD at 630°C on top of microcrystalline silicon without altering the structure of the microcrystalline film.

REFERENCES

1. H. Kroemer, Proc. IRE, 45 1535 (1957).
2. R. Mertens, J. Nijs, J. Symons, K. Baerf, and M. Ghannam, *Solid State Devices* Proceedings of the 17th European Solid State Device Research Conference in 1987 (North-Holland, Amsterdam, Netherlands, 1988), pp.697-701.
3. Hiroshi Fujioka, and Kanetake Takasaki, Fujitsu Sci. Tech. J., 24 391 (1988).
4. T. Sugii, T. Yamazaki, Z. Suzuki, and T. Ito, IEDM Tech. Dig. 89, pp.659-662, 1989.
5. W. Kern and D. A. Puotinen, RCA Rev. 31 187 (1970).
6. N. M. Johnson, J. Walker, C. M. Doland, K. Winer, and R. A. Street, Appl. Phys. Lett., 54 1872 (1989).
7. J. Kanicki, E. Hasan, J. Griffith, T. Takamori, and J. C. Tsang, Mater. Res. Soc. Symp., 149 239 (1989).

ELECTRICAL AND OPTICAL PROPERTIES OF OXYGENATED MICROCRYSTALLINE SILICON (mc-Si:O:H)

M.TARAJI*, SUNIL GOKHALE*, S.M.CHAUDHARI*, M.G.TAKWALE*, AND S.V.GHAISAS**
* School of Energy Studies, Dept. of Physics, University of Poona
** Department of Electrical Science, University of Poona, Pune 411007 INDIA

ABSTRACT

Hydrogenated microcrystalline silicon with oxygen(mc-Si:O:H) is grown using radio frequency glow discharge method. Oxygen is introduced during growth by varying it's partial pressure in the growth chamber. The crystalline volume fraction 'f' and the crystallite size 'δ' are found to vary with the oxygen content. Results indicate that oxygen can etch the silicon surface when present in low amount while it forms a-SiO_{2-x} with increasing contents. Optical absorption studies in the range of 2 to 3 eV suggest that the absorption coefficient 'α' lies in between the values of c-Si and a-Si:H, being closer to a-Si:H. The Hall mobility measurements for these samples indicate that for optimum oxygen contents the mobility as high as 35 cm^2V^{-1} sec^{-1} can be obtained. Results on I-V characteristics for *p-i-n* structure are presented.

INTRODUCTION

Role of oxygen in silicon as an n-type dopant impurity was recognized by Kaiser[1], and the exact mechanism for such a behaviour is still not well understood. It is well established however that oxygen alters the electrical behaviour in c-Si depending on it's concentration and shows reproducible results for annealing behaviour[2]. The hydrogenated microcrystalline silicon is studied over last decade, both as a potential application material in devices [3,4,5,6] and to understand growth of silicon from a silane plasma [7]. So far effect of oxygen incorporation in mc-Si:H, on it's electrical and optical behaviour has not been reported. In this paper we report, effect of intentional oxygen incorporation on f, δ, optical absorption α, Hall mobility μ_H, and the conductivity σ of mc-Si:H. Oxygen containing mc-Si:H will be referred as mc-Si:O:H.

EXPERIMENTAL

The films were deposited under the 13.56 MHz r.f. glow discharge in an Anelva (Japan) made systeme. The deposition conditions were: SiH_4 and H_2 flow rates-0.5 and 100sccm respectively, substrate temperature- 300°C, the r.f power density-0.47W/cm^2 and the pressure during deposition- 0.2Torr. The background pressure in the system was less than 10^{-7} T. The films were deposited on 7059 corning and (100) oriented Si wafers after following standard cleaning procedures. The X-ray diffraction measurements were carried out on a Seaman-Bohlin arrangement, model Rotaflex .200B, by Rigaku, Japan. The X-ray diffraction was measured with incident angles in the range of 0.2 to 7°. Volume fraction was determined from the area under (111) plane diffraction peak, as the relative intensity for all other planes in different samples was within experimental errors. δ was determined from FWHM measurements of (111) difraction peaks using Debye Sherrer formula[8]. Infrared (I.R.) absorption measurements were carried out on a Perkin-Elmer I.R. spectrometer (model 783). The O_2 partial pressure was adjusted using a precision leak valve before introducing SiH_4 and H_2. The partial pressure was varied from 2×10^{-7} to 5×10^{-3} Torr. However beyond 5×10^{-6} Torr, the

microcrystallanity was lost. Hence, results are presented in the oxygen partial pressure range of 2×10^{-7} to 5×10^{-6} Torr. The estimated pumping speed at the chamber is 70 ltr/sec. Optical transmission and reflectance measurements are carried out in the UV-visible-NIR wavelength region using a Hitachi-330 spectrometer. The optical gap was found from the extrapolated line intrcepts from the high absorption ($\alpha \sim 10^{4} cm^{-1}$) region in $(\alpha h\nu)^{1/2}$ Vs $(h\nu)$ plots for each sample. The Hall measurements were carried out on the films deposited on 7059 corning glass substrates having film dimensions ,3 mm width ,15 mm length and ears for electrode placement. The measurements were carried out in dark with constant ambient temperature. The Hall voltage was measured on a Keithley electrometer (model 614). Typically time required for a stable reading varied from 1 to 4 hours. The conductivity measurements were performed usng Van der Paw as well as 2 point probe method.

RESULTS AND DISCUSSIONS

Effect on the film morphology

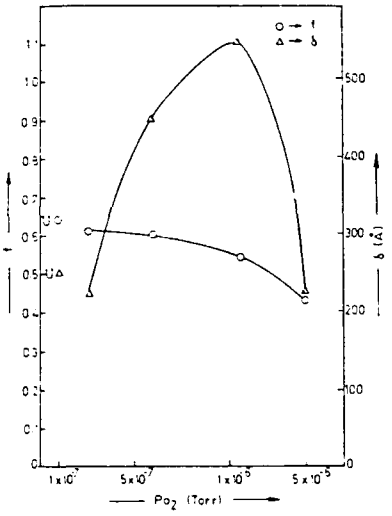


Figure 1- Variation of volume fraction f and crystallite size δ as a function of oxygen partial pressure p_{02}. The continuous line is only as a guide to the eye.

Fig. 1 shows variation of f and δ as a function of the oxygen partial pressure p_{02}. A maximum for δ (550 ± 50 A^{o}) is obtained around $1.6 \cdot 10^{-6}$ T of p_{02}. Similar value is obtained in mc Si:H prepared by photo-CVD method ,while by r. f. glow discharge to be around 400A^{o} [9,10]. Since the only parameter varied is p_{02} ,the variation in δ can be related to the presence of nescent oxygen in the plasma. The sample without intentional oxygen incorporation (here after referred as sample U) has the highest f value (0.64). With increasing p_{02} f decreases down to 0.43. The relative O_2 contents of these films is obtained from the I.R. absorption measurements. As can be seen from the Fig. 2, the Si-O-Si stretching mode lies in between 1000 to 1100 cm^{-1}, with a tendancy towards 1100 cm^{-1} as p_{02} increases. In fact we could clearly identify SiO_2 at high enough p_{02} ($p_{02} \sim 10^{-2}$T). Hence the oxygen related stoichiometry in the films is like SiO_{2-x}. The growth rate is observed to be 1.1 A^{o}/sec for sample U, while it is less than 0.8 A^{o}/sec for films in the presence of intentional oxygen. δ increases with p_{02} untill 1.6×10^{-6} T (Fig. 1). Larger value of δ indicates smaller value of surface nuclei during growth. Hence ,increasing δ while simultaneously decreasing growth rate with p_{02} indicates that oxygen from plasma is etching the surface during the growth. This behaviour of oxygen is different compared to that of hydrogen, which is shown to influence the growth of microcrystallanity via mechanisms other than etching[7].

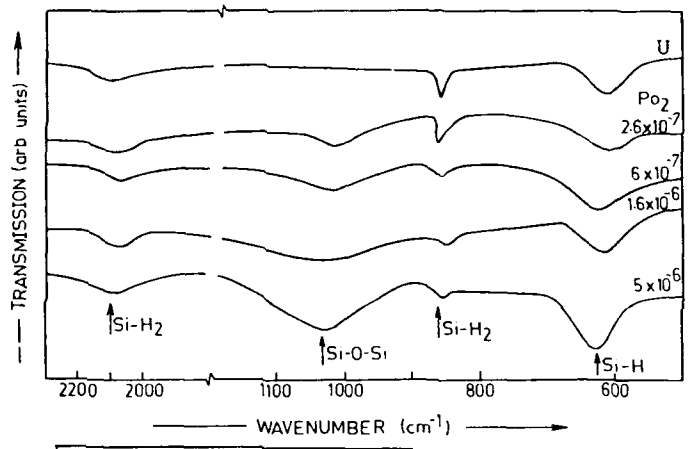


Figure 2- I.R. absorption spectra for microcrystalline films deposited with different oxygen partial pressures.

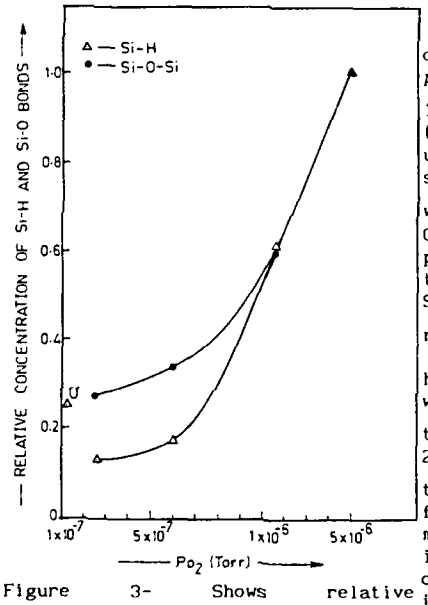


Figure 3- Shows relative concentration of Si-H and Si-O bonds as calculated from the area of the absorption coefficient Vs wave number curves. The absolute content of the hydrogen can be obtained by multiplying the relative concentration by $1.24 \times 10^{22} cm^{-3}$. The area for hydrogen is considered only under the wagging mode at 640 cm^{-1}.

Fig.3 shows that the oxygen contents in the films increases with p_{O_2}. For pressures exceeding $2.\cdot 10^{-6}$ T, both , δ and f decrease (Fig.1). From the shift and the area under the I.R. spectra in Fig.2, it is seen that SiO_{2-x} content is increasing with a concomitant shift of x towards 0. This indicates that under high enough pressure , oxygen atoms cluster around the adsorbed Si atoms forming stable SiO_2 nuclei, that help build amorphous network around it.

Fig.3 also shows that relative hydrogen content in the film increases with p_{O_2}. The hydrogen content is 6 % in the sample U, where as it increases to 20 % at $p_{O_2}=5 \times 10^{-6}$ T. Thus oxygen in the film, damps the hydrogen removal from the film during growth. We expect most of the hydrogen and oxygen to be incorporated in the amorphous regions of the films that form the intergranular regions between different microrystallites. Indeed, the films get passivated as can be seen from the electical measurements discussed in the next part of the paper.

Electrical and optical properties

We show absorption coefficient α in Fig.4 in the range of 2 to 3 eV. For comparison , α for c-Si and that for a-Si:H (bandgap=1.6 eV) is also shown. All these films show absorption higher by an order of magnitude than c-Si above 2.2 eV. However α rapidly decreases near 2 eV. The bandgap from the Tauc plots for these films is estimated to be around 1.8 eV while it is

close to 2.0 eV for the sample U.

Fig.5 shows σ (a), μ_H and n (b), as a function of p_{O2}. Thermal gradient test shows that all these films are n-type. For the sample U, n is of the order of $10^{17} cm^{-3}$ while μ_H is ~ 1 $cm^2 V^{-1} sec^{-1}$ [3]. Increasing the oxygen (and hydrogen) content increases the mobility, simultaneously decreases the carrier density untill $p_{O2} = 1.6 \times 10^{-6}$. We speculate that the carriers in the sample U are contributed from the defect complexes in the intergranular region of the microcrystallites. On addition of oxygen and hydrogen, these donor states alongwith trap states associated with these complexes are removed, rendering high mobility. The maximum mobility is about 40 $cm^2 V^{-1} sec^{-1}$, which is comparable to the one obtained for polycrystalline samples

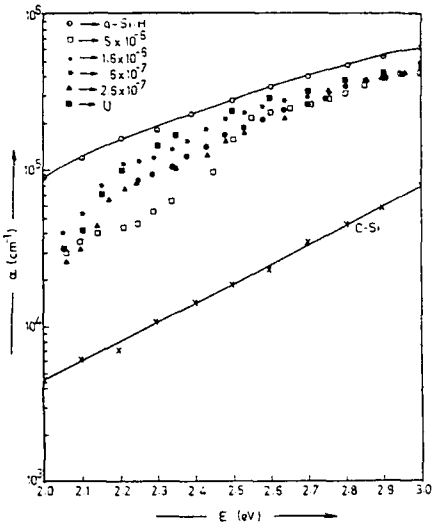


Figure 4- Shows the variation of the optical absorption coefficient α in the photon energy range of 2 to 3 eV for various p_{O2}. Corresponding plots for c-Si and a-Si:H are also given for comparison.

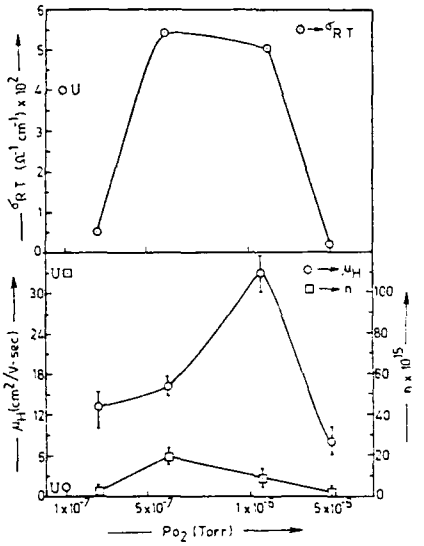


Figure 5- (a) Variation of room temperature conductivity σ and (b) that of Hall mobility μ_H and carrier density n, with p_{O2}.

having grain size ~ 300 A^o [11]. Thus clearly a passivation effect is observed, when we compare the μ_H values of mc-Si:H films grown by r.f. discharge methods where for 400 A^o grain size the value does not exceed 2 $cm^2 V^{-1} sec^{-1}$ [12]. On increasing p_{O2} to 5×10^{-6} T, μ_H decreases to 8 $cm^2 V^{-1} sec^{-1}$. Correspondigly, the δ value decreases to 120 A^o. We find that the μ_H varies sensitively with the oxygen content. It increases with δ but is insensitive to f. Effect of oxygen on the mobility can be understood qualitatively using an expression for μ_{eff} based on phenomenological considerations for polycrystalline semiconducting materials having grain size ≤ 600 A^o [13].

$$\mu_{eff} = \mu_g / \left((1 - n_t t / N_d d) + \exp(q V_b / KT) \times (2 m^* \pi K T)^{1/2} \mu_g / s q d\right)^{-1} \qquad (1)$$

where, μ_g is mobility in the grain, n_t is the filled trap density, t is the thickness of the grain boundary, N_d is the dopant concentration, d is the average size of the grain, q is electonic charge, s is a correction parameter, and V_b is grain boundary potential.

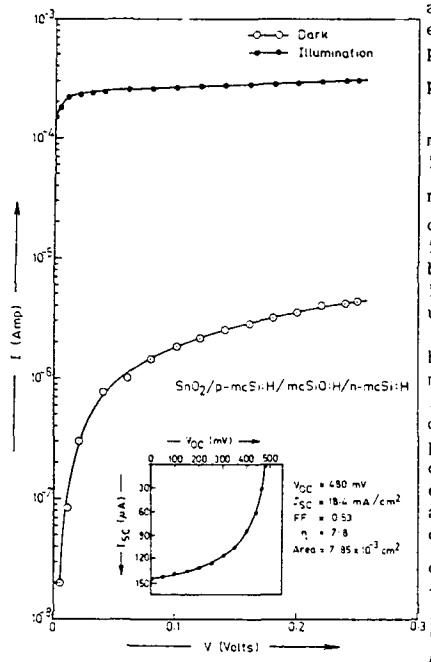


Figure 6- I-V characteristics for the sructure SnO_2\ *p*- a- Si:H (40 A^o)*p*- mc-Si:H (300 A^o)\mc -Si:O:H (3000 A^o)*n* -mc- Si:H (180 A^o)\Ag , with and without illumination under reverse bias conditions. The inset shows the forward characteristics for solar cell operation.

The increase in μ_H observed in the mc-Si:O:H samples is attributable to increase in d, decrease in V_b and n_t. Thus removal of trap states on oxygen and associated hydrogen incorporation and increase in δ seem to be the main effects responsible for the increased mobility, within the model used in expression (1).

Since mobility for mc-Si:O:H is higher than mc-Si:H by an order of magnitude, the product $\mu\tau$, where τ is the lifetime of the photo-generated carriers, is also large. It's absorption properties in the 2 to 3 eV range are comparable with a-Si:H. Hence it is expected to favourably response as an active *i* layer in a *p-i-n* type solar cell. We have deposited on SnO_2 deposited glass substrates (resistance ~ 10 Ω/□) following sequence of *layers. a-Si:H (p - type)* 40 A^o *:mc-* Si:H (*p* - type) 300 A^o:mc - Si:O:H 3000 A^o:mc - Si:H (*n* - type) 180 A^o.: metallisation with Ag. Fig. 6 shows the I-V plots for this configuration with and without illumination under reverse bias. Clearly a current gain on illumination ~ 10^4 indicates that the photo conducting properties of this material are reasonable compared to a-Si:H. The inset shows the forward bias characteristics for the solar cell application. Over 1 mm^2 area a fill factor around 0.53 and an efficiency of 7.5 % could be obtained. I_{SC} values up to 22 mA/cm^2 are observed. The V_{OC} is however relatively low (~ 0.5 V). We have measured the capacitance for this structure as a function of reverse and forward voltage. The $1/C^2$ Vs V plots are linear and indicate a value 1.05 V for the barrier potential V_{bi} from the intercept on the V axis. It is possible that relatively highier series resistance, and the recombinations at the junctions are reducing the V_{OC}. With appropriet deposition conditions it can be improved. Further work is in progress in that direction. These results suggest that mc-Si:O:H can be a potential material in the photo-voltaic devices.

CONCLUSION

Intentional inclusion of the oxygen in the r.f. plasma during the growth of mc-Si:H, affects the morphology of the film as well as it's elctrical and optical properties. Effects on the morphology are manifested mainly in terms of changes in δ and f. The variation of δ and f with p_{02} suggest that the oxygen on the surface introduces two competing reactions; one is etching of the adsorbed Si atoms when oxygen concentration is less while other is formation of SiO_{2-x} at higher concentration that presumably leads to amorphous network around it.

On optimum oxygen incorporation, elctron mobility can be improved above 30 $cm^2 V^{-1} sec^{-1}$ in mc-Si:O:H. It shows comparable absorption in the 2.2 to 3.0 eV photon energy range to that of a-Si:H. The unintentional n-type dopant density in this case is ~ 10^{15} cm^{-3}. Results on *p-i-n* structure demonstrate that the material has potential for photo-voltaic devices.

ACKNOWLEDGEMENTS

Authors gratefully acknowledge useful discussions with Prof. V.G. Bhide and Dr. S.V. Rajarshi. One of us (MF) gratefully acknowledges the financial support given by Department of Non Conventional Energy Sources, Government of India, during this work.

REFERENCES

1. W. Kaiser, Phys. Rev., 105, 1751 (1957).
2. V.P. Markevich, L.F. Mkarenko and L.L. Murin, in Materials Sciencs Forum, Vol. 38-41, (1989), pp 589-594, (Proceedings from International Conference on Defects in Semiconductors (ICDS-15), Budapest, Hungary, Aug 22-26, 1988).
3. J.I. Pancove, in Hydrogenated Amorphous Silicon Part D Devices and Applications, Semiconductors and Semi Metals Vol.21 eds. R.K. Willardson and A.C. Beer. (Academic Press Inc , Orlando, 1984)439.
4. T.D. Monstakes, H.P. Matsuka and R. Friedman, J. Appl. Phys. 58 983 (1985).
5. M. Faraji, S. Babras, S. Mirzapur, C. Agashe, S. Rajarshi, R. Dusane, and S.V. Ghaisas, Japanese J. Appl. Phys., 29 2080 (1989).
6. Y. Hamakawa and H. Okameto, in Amorphous Semiconductors Technology and Devices Vol16, edited by Y. Hamakawa, (OHM publication, North Holland) chapter 5
7. A. Asano, Appl. Phys. Lett. 56 533 (1990).
8. B.D. Cullity, Elements of X-Ray Diffraction (Addison-Wesley Publishing company, 1956).
9. A. Matsuda, J. Non-crystalline Solids, 59/60, 767 (1983).
10. J. Datta, A.L. Unaogu, Swati Ray and A.K. Barua, J. Appl. Phys., 66, 4709 (1989).
11. J.Y.W. Seto, J. Appl. Phys. 46, 5247 (1975).
12. G. Lucovsky and W.B. Pollard in The Physics of Hydrogenated Amorphous Silicon II Vol.56, edited by, J.D. Joannopoulous and G. Lucovsky (Springer-Verlag, New York, 1984) chapter 7.
13. S.N. Singh, B.K. Das, R.C. Narula and S.C. Jain in Photo Voltaic Materials and Devices, edited by, B.K. Das and S.N. Singh (Wiley Eastern Limited 1985)chapter 2.

PART IX

Chalcopyrites, Oxides, and Halides

LATTICE-MATCHED HETEROEPITAXY OF WIDE GAP TERNARY COMPOUND SEMICONDUCTORS

KLAUS J. BACHMANN

Department of Materials Science and Engineering and Department of Chemical Engineering, North Carolina State University, Raleigh, North Carolina 27695-7914

ABSTRACT

A variety of applications are identified for heteroepitaxial structures of wide gap I-III-VI_2 and II-IV-V_2 semiconductors, and are assessed in comparison with ternary III-V alloys and other wide gap materials. Non-linear optical applications of the I-III-VI_2 and II-IV-V_2 compound heterostructures are discussed, which require the growth of thick epitaxial layers imposing stringent requirements on the conditions of heteroepitaxy. In particular, recent results concerning the MOCVD growth of $ZnSi_xGe_{1-x}P_2$ alloys lattice-matching Si or GaP substrates are reviewed. Also, heterostructures of $Cu_zAg_{1-z}GaS_2$ alloys that lattice-match Si, Ge, GaP or GaAs substrates are considered in the context of optoelectronic devices operating in the blue wavelength regime. Since under the conditions of MOCVD, metastable alloys of the II-IV-V_2 compounds and group IV elements are realized, II-IV-V_2 alloys may also serve as interlayers in the integration of silicon and germanium with exactly lattice-matched tetrahedrally coordinated compound semiconductors, e.g. $ZnSi_xGe_{1-x}P_2$.

1. PRINCIPLES OF WIDE BANDGAP MATERIALS SELECTION

Wide bandgap semiconductors, i.e. semiconductors with bandgaps ≥2 eV, are associated with high chemical stability as well as low intrinsic carrier concentrations, and consequently large built-in voltage/small leakage current across electrical junctions. Therefore, they may be operated at elevated temperature and represent valuable supplements to conventional semiconductors that have smaller bandgaps, i.e. Si and GaAs, in specialized applications that expose the electronic circuits to hostile corrosive, radiative or thermal environments. Another possibly advantageous use of wide bandgap materials is in the construction of microwave transistors having high Johnson figure of merit

$$[P_m Z]^{1/2} F_t = \frac{\mathcal{E}_b v_s}{2\pi}. \qquad (1)$$

Mat. Res. Soc. Symp. Proc. Vol. 242. © 1992 Materials Research Society

However, the large gains in the Johnson figure of merit, that have been reported in the literature as an incentive for research and development [1], refer to break-down fields $\mathcal{E}_b$ in the limit of very small ionized dopant concentrations. This implies larger impedance Z than for the less depleted junctions in conventional semiconductors and thus translates into less dramatic improvements in the maximum power P_m and cut-off frequency F_t than in the figure of merit. Controlled complementary doping and low resistivity ohmic contacts are important topics of the experimental evaluation of the performance and reliability of microwave devices built from wide gap materials which, in time, will reveal their true potential. The engineering of appropriate doping profiles at electrical junctions is a particular problem of wide gap materials because of the difficulties in identifying shallow dopants and in controlling their stoichiometry within narrow tolerances. The latter is important because of the role of native point defects in the formation of DX and recombination centers degrading the control of the conduc-

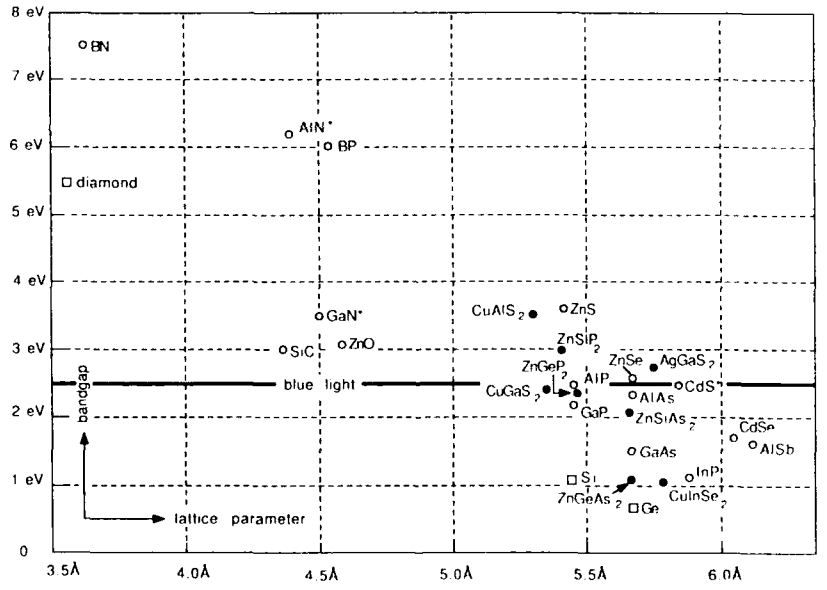


Figure 1. A Selection of semiconductors ordered by their bandgaps and a-axis lattice parameters. Open diamonds: group IV elements; open circles: III-V compounds; filled circles: II-IV-V_2 compounds; open squares: II-VI compounds; filled squares: I-III-VI_2 compounds. The asterisk denotes the wurzite structure. In this case, $\sqrt{2}$xa(wurzite) is used for the plot.

tivity and carrier lifetime [2,3]. Also, within a given class of materials, larger bandgaps correspond generally to larger effective masses. Therefore, it is prudent to select for a specific optoelectronic applications a suitable material with minimum required bandgap.

Figure 1 shows a selection of semiconductors ordered by their bandgaps and a-axis lattice parameters. Diamond holds a unique position among these materials because of its high thermal conductivity $\sigma = 20$ W/cmK and saturation velocity $v_s = 2.7 \times 10^7$ cm/s that may provide for potential gains with regard to the power dissipation and possibly also reduced delay in future microelectronic circuits made from diamond as suggested by its relatively high Keyes figure of merit $\sigma(v_s/\varepsilon_1)^{1/2}$ [1]. The III-V compounds with bandgaps ≥6 eV, e.g. BN, BP and AlN, have thermal conductivities σ < 1W/cmK. Consequently they are not a match to the potential of diamond with regard to replacing conventional semiconductors in future microelectronic circuits. However, they may become useful as nearly lattice-matched dielectrics for the realization of diamond and silicon carbide MIS transistors. Another field of applications, where ternary alloys and compounds can make an impact, is optical electronics. In principle, nearly lattice matched BN/diamond, and exactly lattice-matched BN_yP_{1-y}/GaN and slightly mismatched $Al_xGa_{1-x}N$/SiC and $Al_xGa_{1-x}N$/GaN heterostructures could become useful materials combinations for the fabrication of uv emission and detection devices if the problem of controlling their electrical properties can be solved. In spite of the long time of R&D on SiC and GaN light emitting devices, laser emission has not been achieved in these materials thus far. Considerable progress has been made with respect to $Al_xGa_{1-x}N$/GaN heterostructures in the past decade, but the doping of Al-rich alloys still remains to be a serious problem, as is the lattice-mismatch of AlN and GaN. Therefore, a closer look at alternative materials is in order. There exist several semiconductors that have direct bandgaps in the range $2.5 \leq E_g \leq 3.5$ eV and a-axis lattice parameters ≥5Å. Semiconductors with even lower energy gaps are appropriate for use as low gap components in the engineering of quantum wells, wires and boxes, where above band gap optical transitions in the blue wavelength regime are made possible by confinement effects. At least some of these materials systems exactly lattice-match readily available substrate wafers of excellent mechanical and thermal properties, e.g. Si, which adds further credence to their exploration.

All compounds of interest in this context represent normal tetrahedral structures obeying the Grimm-Sommerfeld rule [4] and are related by cation substitutions as illustrated in fig.2. The lowering of the symmetry from Fd3m for diamond to $F\bar{4}3m$ for the zb structures II-VI and III-V compounds to $I\bar{4}2d$ for the cp structure II-IV-V_2 and I-III-VI_2 compounds, in conjunction with spin orbit splitting, completely lifts the valence band degeneracy at the zone center for the cp structure materials with potential advantages to their use in the construction of spin polarized electron photoemitters. Also, the

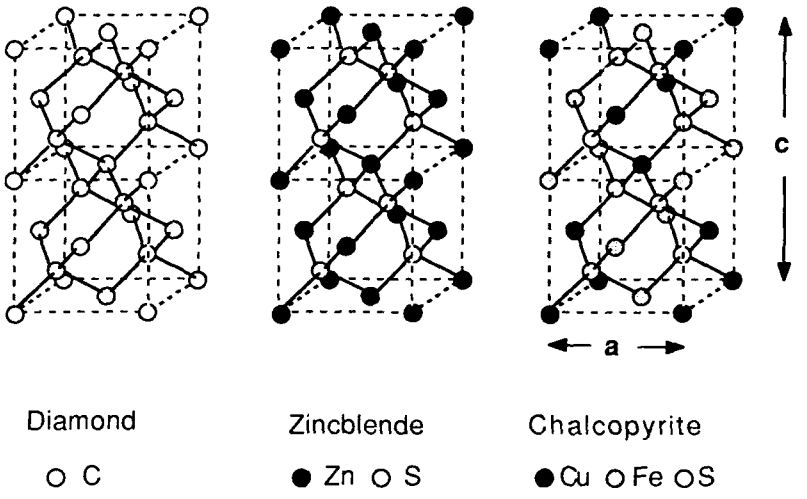


Figure2. Schematic representation of the diamond, zincblende and chalcopyrite structures.

smaller first Brillouin zones, associated with the larger unit cells of the cp structure materials as compared to their zb structure parent compounds, cause certain vectors,that are fractions of a reciprocal lattice vector in the zb structure, to become full reciprocal lattice vectors in the cp structure which results in a remapping of several high symmetry points from the zone boundary into the zone center, e.g. X_{zb} maps into Γ_{cp}. Thus indirect bandgaps in the zb structure may become direct in the cp structure, as for example in the case $ZnGeP_2$ which is the II-IV-V_2 analog to GaP. However, the bond length differences, established in the bonding of the anions to the two different cations in the cp structure, result in a displacement of the anions from the ideal zb structure sublattice positions and cause ratios of the c- and a-axis lattice parameters $c/a \neq 2$, which is not recognized by zone folding schemes.

First principles band structure calculations for the I-III-VI and II-IV-V semiconductors have been carried out [5] that incorporate the contributions of the outer d-electrons of the group I and group II elements to the bonding and account for the tetragonal distortions. They show that in the I-III-VI_2 compounds, the group I d-electrons contribute substantially to the charge density in the upper valence band which is corroborated by the sulfur K-edge features observed in x-ray absorption near edge fine structure measurements [6]. The hybridization of the group I d-electrons with the chalcogen p-electrons in the upper valence band has a pronounced effect onto the band gap accounting for about half of the band gap narrowing in the I-III-VI_2 semicon-ductors as compared to their II-VI parent compounds. For this reason, $CuGaS_2$ has a substantially

smaller bandgap ZnS (see fig.1). On the one hand, this places $CuGaS_2$ outside the range of compounds that can be used for the fabrication of blue light emitting diodes, but on the other hand, it implies significantly lower tendency to self-compensation than for ZnS. The bandgap depression is less for the silver containing I-III-VI_2 compounds, as illustrated by the higher bandgap of $AgGaS_2$ as compared to providing the opportunity for blue emission from alloys on the pseudobinary $CuGaS_2$-$AgGaS_2$. Another suitable cp structure materials system is the $ZnGeP_2$-$ZnSiP_2$ system. Both systems provide readily for p-type conductivity and exactly lattice-match GaP or Si substrates. Also, $ZnGeP_2$ and $AgGaS_2$ exhibit substantial birefringence and are thus suitable choices for phase-matched non-linear optical applications. Therefore, we focus in part 3 of this paper onto heteroepitaxial structures of cp structure materials. since the ordering of ternary III-V alloys of composition ABC_2 observed under the conditions of MOCVD and molecular beam epitaxy (MBE) [6-17], established an additional tie of the III-V alloys to the cp structure materials, and considerable knowledge has been gained in the heteroepitaxy of III-V systems that pertains to the heteroepitaxial growth of the cp structure materials, a few remarks are added in the following part 2 of this paper on ternary III-V heterostructures.

2. HETROSTRUCTURES EMPLOYING TERNARY III-V ALLOYS

There exists a substantial body of knowledge regarding the heteroepitaxial growth of nearly lattice-matched III-V alloys on silicon and germanium that gives valuable insights into critical steps during the nucleation stage and into interdifusion/autodoping during growth:

1. Lattice-matching is not necessarily a guaranty for high quality epitaxial growth, i.e. appropriate in-situ surface cleaning is essential. For example, the relatively close lattice matching of GaP to Si resulted only recently in superior defect structure in GaP/Si heterostructures as compared to substantially mismatched GaAs/Si heterostructures which was clearly related to improvements in the surface cleaning [18].

2. Even at the relatively low substrate temperatures of MOCVD growth, interdiffusion/autodoping can be substantial and requires the development of growth methods that proceed at low temperature. Figure 3 shows the SIMS profiles of the Ge doping profile at the interfaces of nearly lattice-matched $Al_xGa_{1-x}As$/Ge heterostructures grown by MOCVD grown at selected temperatures without any intentional introduction of Ge into the vapor phase. The enhanced interfacial recombination associated with enhanced Ge doping in the interfacial region at the higher growth temperature forces, in this case, a compromise between low interfacial recombination velocity at low growth temperature and high bulk lifetime of minority carriers in $Al_xGa_{1-x}As$ epilayers grown at high substrate temperature [19].

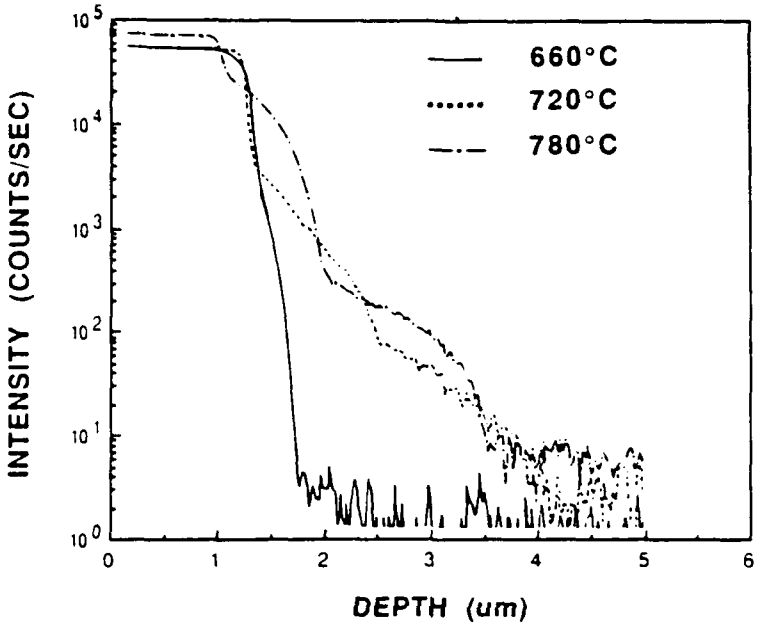


Figure 3. SIMS profile of Ge at the interface of $Al_{0.08}Ga_{0.92}As$ epilayers grown by MOCVD on Ge at selected growth temperatures.

3. In the same study [19], microscopic APBs were observed at the Al_xGaAs_{1-x}/Ge interface that terminated upon a short period of growth. The mechanism for the termination process is not known at present, and remains to be an important research topic since microscopic APBs at interfaces could have significant effects on the performance and reliability of heterostructure devices. The cause for the formation of localized APBs could very well be related to the break-up of double steps on vicinal surfaces of Si and Ge into single steps at kinks as revealed by STM [20]. Since the production of discontinuities in surface steps by impurities is also well known, this enhances the above stated importance of an effective in-situ surface cleaning step as part of the epitaxial growth sequence.

The growth temperature of MOCVD can be lowered, and the interdiffusion/autodoping problem can thus be reduced, by either an atomic layer epitaxy (ALE) approach, which makes use of sequential chemisorption / reaction cycles [21], or enhancement of the growth rate at a low temperature by plasma/light excitation of the precursor molecules [22]. The former two approaches work well for small layer thickness because they are inherently very slow. This is tolerable in the construction of thin confined hete-rostructures, but is prohibitive in cases where thick epilayers must be

produced. For reasons discussed below, this is necessary for non-linear optical applications of heterostructures of the cp structure materials. Plasma enhanced MOCVD has been used by us for surface cleaning of silicon substrates prior to GaP growth and for the in-situ generation of phoshine and highly reactive fragments thereof from solid red phosphorus in a remote helium-hydrogen plasma [23]. Extreme caution is required in such a process since the semiconductor surface may be easily damaged by energetic particles extracted from the plasma. Thus light enhanced MOCVD appears to be the most favorable approach in the context of the desired heterostructures in particular since such a process can be carried out in an ALE mode with alternating chemisorption / illumination-reaction cycles, if so desired in the context of confined heterostructures.

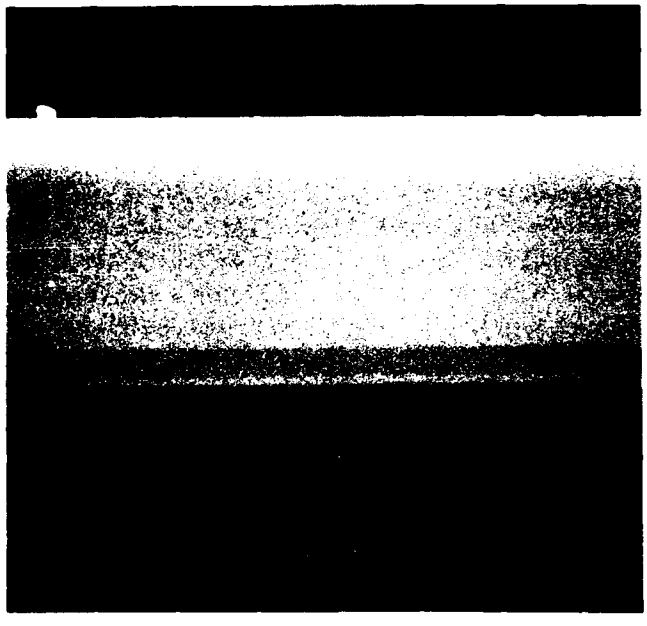
The ordering of ternary III-V alloys of composition ABC_2 in the CuPt, CuAu-I or cp structures has been reported for a variety of systems [6-17]. Although initially theoretical predictions characterized the ordering as an equilibrium phenomenon, more recently, these predictions have been revised to support the conclusion that the excess free energy is positive for all mismatched systems and nearly zero for the lattice matched systems considered [24]. Possible exception are $AlInP_2$ and $AlInAs_2$ for which first principles calculations result in a negative bulk formation enthalpy [25] which is at variance with the results of the empirical tight binding calculations of reference [24]. In view of difficulties with accounting for entropy effects in the temperature dependence of the free energy and the very small values for the excess enthalpy, theoretical approaches presently cannot explain the experimentally observed ordering, which may be related to surface energetics that could stabilize ordering [26] in conjunction with kinetic hindrances that prevent the rearrangement of atoms, once ordered, into the thermodynamic equilibrium configuration. Under certain conditions of epitaxy, the ordering may be entirely controlled by kinetics, i.e. the modification of the energy barrier to the addition of a new layer of cations, A or B, on polar surfaces may be affected by the backbonding of the anions C to the next subsurface layer of cations, B or A, which generally possess different electronegativities and sizes. This principle, in conjunction with the choice of ligands on the precursor molecules for growth, may favor the alternative addition of A and B atomic layers even though a disordered bulk lattice is energetically favored. However, regardless of the mechanism of ordering, the prospect of subsequent disordering and concomitant bandgap changes in the presence of fast diffusing impurities [27] or of radiation enhanced diffusion in the volume filled by laser light of relatively high energy, the lack of thermodynamic equilibrium is of concern in the context of device reliability. Therefore, in opinion of the author, the thermodynamically stable II-IV-V_2 and I-III-VI_2 semiconductors are superior to metastable ordered epitaxial structures, such as ordered III-V layers, in all applications that require a non-cubic component in a heterostructure, e.g. non-linear optical applications that require birefringence for phase-matching.

3. HETEROSTRUCTURES OF CHALCOPYRITE STRUCTURE SEMICONDUCTORS

Both positive and negative values of the birefringence are realized in cp structure semiconductors [28] so that type I as well as type II phase matching may be realized in frequency mixing, harmonic generation and other non-linear optical applications of single crystals of these materials. Second harmonic generation (SHG) with 3% conversion efficiency for Q-switched CO laser light has been reported in $ZnGeP_2$ bulk single crystals of ~1 cm size [29]. Also, a remarkable 49% external conversion efficiency (80% internal conversion efficiency) was achieved for SHG with pulsed CO_2 laser radiation of up to 1GW/cm^2 power density and 2ns pulse width [29]. Since the CO_2 laser is one of the most powerful sources of coherent radiation known to date, the extension of its use to shorter wavelengths with high conversion efficiency is an impotant accomplishment that should stimulate more research in this field of application. A critical impediment to the optimization of frequency mixing and harmonic generation in cp materials is the residual absorption within their transparency ranges which reduces the conversion efficiency and contributes to the laser damage threshold affecting thus critically the reliability of the non-linear optical components. It is due to both impurities and native point defects requiring extraordinary care under the conditions of bulk crystal growth to achieve the needed level of control of the purity and stoichiometry of the compound. High pressure methods of crystal growth are helpful in this regard, but thus far is not capable of producing large crystals [30].

An additional problem of the growth of large bulk single crystals of congruently melting cp structure materials from the melt is cracking during cooling to room temperature because of the disordering of the cations at elevated temperature, due to the larger entropy of the disordered zb phase. Fortunately the transition temperatures for the II-IV-V_2 and I-III-VI_2 compounds represent large fractions of their melting temperatures so that this problem is eliminated at the relatively low substrate temperatures employed in heteroepitaxial growth. Also, the lower processing temperature of heteroepitaxial structures provides for better purity [31] and allows the growth of cp structure epilayers for materials that melt incongruently. For example $CdSnP_2$ forms in a peritectic reaction from tin and CdP_2 at 585°C and has been produced in the form of epitaxial films on InP by liquid phase epitaxy from Sn solutions below the peritectic temperature [32]. However, the habit of the nuclei of the epilayer in the form of platelets with slowest growth on the (112) plane and substrate dissolution control make the growth of homogeneous epilayers for optical applications by LPE very difficult, thus favoring vapor phase deposition.

High quality epitaxial films of $ZnGeAs_2$ [33] and $ZnGeP_2$ [34,35] have been grown by atmospheric pressure MOCVD on GaAs and GaP substrate wafers, respectively, utilizing dimethylzinc, germane, phosphine and arsine as source materials. Figures 4



|----------|
2μm

Figure 4. XTEM image of a GaP/$ZnGeP_2$/GaP double heterostructure. Courtesy of Dr. G.-C. Xing, North Carolina State University [34].

shows a cross sectional transmission electron microscopy (XTEM) image of a (001)-GaP/$ZnGeP_2$/GaP double heterostructure [34]. Also, multiple heterostructures GaP/$ZnGeP_2$/GaP/$ZnGeP_2$/... have been grown. The perfectly smooth interface morphology of double and multiple heterostructure makes MOCVD suitable for the growth of confined heterostructures combining zb and cp structure materials and to utilize double heterostructures of cp and zb materials for the guiding of light and carrier confinement in conventional optoelectronic device structures. APBs have been observed for $ZnGeAs_2$ epilayer on (001) GaAs substrates, but are not observed under the conditions of OMVCD growth of $ZnGeP_2$ on GaP [36]. The reasons for this difference in behavior is presently not understood. In-plane phase matched SHG with CO-laser light should be possible for (111)-GaP/(112)-$ZnGeP_2$/(111)-GaP double heterostructures [35]. In view of the availability of large III-V and group IV substrate crystals of excellent mechanical strength and perfection, heteroepitaxy could provide for substantially

longer beam path than achievable with bulk crystal growth technology for cp structure materials, i.e. ~7.5 cm with currently available technology for the heteroepitaxial growth on III-V substrates. However a substantial development effort will be required to generate films of uniform properties over a thickness of tens of micrometer which is needed for SHG using infrared radiation in the 2 to 10 μm wavelength range.

Extended ranges of metastable solid solutions have been discovered recently in the investigation of the OMCVD of $ZnGeP_2$ on GaP where an excess of at least 15% Ge can be incorporated into the lattice of the $ZnGeP_2$ at a substrate temperature of 585°C without any sign of precipitation [34,35]. This is in contrast to the behavior $ZnGeP_2$ crystals grown from the melt where even a small excess of Ge is precipitated. The excess Ge is incorporated into both the cation and anion sublattices, so that with increasing Ge concentration the alloys gradually approach the diamond structure of pure Ge. In contrast to melt-grown single crystals of $ZnGeP_2$ that have high resistivity, the $ZnGeP_2$:Ge alloys are low resistivity p-type. Recently epitaxial films of diluted pseudoternary alloys in the system Ge-$ZnGeP_2$-$ZnSiP_2$ have been produced by OMCVD [34,35] with net acceptor concentrations at much lower levels than encountered in the $ZnGeP_2$:Ge alloys. Therefore, these alloys are better suited for the fabrication of pn-junction or Schottky barrier devices than the highly resistive $ZnGeP_2$ bulk crystals and

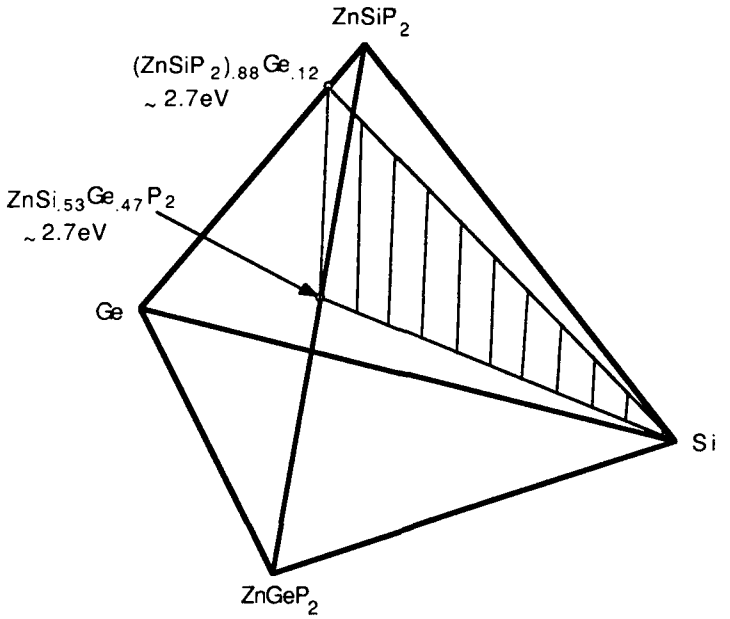


Figure 5. Composition tetrahedron $ZnSiP_2$-$ZnGeP_2$-Si-Ge showing the plane of exactly lattice-matched compositions to silicon at 300K.

the highly conductive $ZnGeP_2$: Ge alloys. Since there may be a continuous range of pseudoquaternary alloys in the system $ZnSiP_2$-$ZnGeP_2$-Si-Ge as illustrated in figure 5, and II-IV-V_2-rich alloys have been produced by us already in this system, it may become useful for the continuous grading from the diamond structure of pure silicon into the cp structure maintaining exact lattice matching through the entire graded layer.

The heteroepitaxial growth of $CuGaS_2$ on GaP substrates by MOCVD has been demonstrated utilizing triethylphosphine-cyclopentadienyl copper(I), triethylgallium and diethylsulfide or hydrogensulfide as source materials [37]. Since both $CuGaS_2$ and AgGaS can be produced with p-type conductivity, up to 20 Ωcm for $CuGaS_2$ and much lower values for $AgGaS_2$, there exists an excellent chance to produce lightly doped p-type $CuGaS_2$-$AgGaS_2$ alloy epilayers on p^+-GaP (or p^+-Si) or p^+-GaAs (or p^+-Ge) substrates. Preferred device structures employing these alloys would be Schottky barriers for broad band uv detection and hetero-structures employing n^+-$Zn_xCd_{1-x}S$ or n^+-ZnS_ySe_y front layers for near uv detection and blue light emission. The lattice matching alloy compositions are $Zn_xCd_{1-x}S/Cu_zAg_{1-z}GaS_2$/Si, $Zn_xCd_{1-x}S/Cu_zAg_{1-z}GaS_2$/GaP, $Zn_xCd_{1-x}S/Cu_zAg_{1-z}Ga$/Ge and $Zn_xCd_{1-x}S/Cu_zAg_{1-z}Ga$/Ge, respectively. Unknown factors in the realization of such heterostructure devices are the possible formation of APBs and the chemical stability of the I-III-VI/IV interface. For III-V substrates, the formation of volatile group III subsulfides upon exposure to H_2S could be utilized as an efficient in-situ cleaning method [38]. Because of the chemical matching at the interface also the direct growth of p-$Cu_xAg_{1-x}GaS$ on n-ZnS substrates represents an interesting option.

In summary, a variety of interesting applications for heteroepitaxial structures of wide gap I-III-VI_2 and II-IV-V_2 semiconductors have been identified, e.g partially solar blind uv detectors, blue light emitting diodes and possibly lasers as well as non-linear optical applications of I-III-VI_2 and II-IV-V_2, which require the growth of thick epitaxial layers imposing stringent requirements on the conditions of heteroepitaxy. MOCVD growth of $ZnGeP_2$ and $CuGaS_2$ as well as $ZnSi_xGe_{1-x}P_2$ alloys has been achieved with encouraging surface and bulk properties. $Cu_zAg_{1-z}GaS_2$ alloys lattice-matching Si, Ge, GaP or GaAs substrates may have utility in the context of optoelectronic devices operating in the blue wavelength regime. Since under the conditions of MOCVD, metastable alloys of the II-IV-V_2 compounds and group IV elements are realized, II-IV-V_2 alloys may also serve as interlayers in the integration of silicon and germanium with exactly lattice-matched tetrahedrally coordinated compound semiconductors.

ACKNOWLEDGEMENTS

This work has been supported by NASA grant NAG 1-1100.

REFERENCES

1. K.E. Spear, J. Am. Ceram. Soc. 72, 171 (1989)
2. D.V. Lang in Deep Centers in Semiconductors, edited by S.T. Pantelides, (Gordon and Breach, New York 1985) p. 489
3. J.M. Sallese, D.K. Maude, M.L. Fille, U. Willke, J.C. Portal and P. Gibart , Chemical Shifts of DX Centers, in Non- Stoichiometry in Semiconductors, edited by K.J. Bachmann, H.-L. Hwang and C. Schwab, (Elsevier Publishing Company, Amsterdam 1992, in print); J.M. Spaeth, M. Fockele and K. Krambrock, OMDR of Stoichiometry Defects in III-V Semiconductors, ibid. 1992, in print
4. E. Parthe, Crystal Chemistry Of Tetrahedral Structures. (Gordon and Breach, New York, 1964)
5. J.E. Jaffe and A. Zunger, Phys Rev B, 28, 5822 (1983); Phys. Rev B, **29**: 1882 (1984); Phys. Rev. B, 30: 741-756 (1984)
6. P. Saintctavit, J. Petiau and A.M Flank , Physica B, 158: 623 (1989)
7. T.S. Kuan, T.F. Kuench, W.I. Wang and E.L. Wilkie, Phys. Rev. Lett. 54, 201 (1985)
8. Y, Matsui, H. Hayashi and K. Yoshida, Appl. Phys. Lett. 48, 1060 (1986)
9. H.R. Jen, M.J. Cherng and G.B. Stringfellow Appl. Phys. Lett. 48, 1603 (1986)
10. T.S. Kuan, W.I. Wang and E.L. Wilkie, Appl. Phys. Lett. 51, 51(1987)
11. M.A. Shahid, S. Mahajan, D.E. Laughlin and H.M. Cox, Phys. Rev. Lett. 58, 2567 (1987)
12. A. Gomyo, T. Suzuki, K. Kobayashi, S. Kawata, I. Hino and T. Yuasa, Appl. Phys. Lett. 50, 673, (1987)
13. O. Ueda, M. Takikawa, J. Komeno and I. Umebu, Jpn. J. Appl. Phys. 26, L1824 (1987)
14. S. Yasunami, C. Nozaki and Y. Ohba, Appl. Phys. Lett. 52, 2031 (1988)
15. A. Gomyo, T. Suzuki, and S. Iijima, Phys. Rev. Lett. 60, 2645 (1988)
16. P. Bellon, J.P. Chevalier, G.P. Martin, E. Dupont-Nevet, C. Thiebaut and J.P. Andre, Appl. Phys. Lett. 52, 567 (1988)
17. M. Kondow, H. Kakibayashi and S. Minagawa, J. Cryst. Growth 88, 291 (1988)
18. A.E. Blakeslee, M.M. Al-Jassim, J.M. Olson and K.M. Jones, (MRS Symp. Proc. 116 Heteroepitaxy on Silicon: Fundamentals, Structure and Devices, edited by H.K. Choi, R. Hull, H. Ishiwara and R.J. Nemanich, Pittsburgh 1988) pp.313-318; K. Uchida, K. Komaha, M. Tajima, T. Soga, T. Jimbo and M. Umeno, ibid. pp.319-322
19. S.W. Choi, K.J. Bachmann, T. Colpitts, J.B. Posthill and M.L. Timmons, J. Electrochem. Soc. (1991) in print
20. J.E. Griffith, J.A. Kuby, P.E. Wierenga, R.S. Becker and J.S. Vickers, J. Vac. Sci. Technol. A6, 493 (1988)
21. M.A. Tischler and S.M. Bedair, J. Crystal Growth 77, 89 (1986)
22. A.D. Huelsman and R. Reif, J Electron. Mater. 18, 91 (1989); J. Vac. Sci. Technol. A7, 2554 (1989)
23. S.W. Choi, G. Lucovsky and K.J. Bachmann, *unpublished results*
24. C.-Y. Yeh, A.-B. Chen and A. Sher, Phys. Rev. B. 43, 9138 (1991)
25. J.E. Bernard, R.G. Dandrea, L.G. Fereira, S. Froyen, S.-H. Wei and A. Zunger, Bull. Am. Phys. Soc. 35, 667 (1990)
26. R.G. Dandrea, J.E. Bernard, S.-H. Wei and A. Zunger, Phys. Rev. Lett. 64, 36 (1990)
27. W.D. Laidig, N. Holonyak, M.D. Camras, K. Hess, J.J. Coleman, P.D. Daphys and J. Bardeen, Appl. Phys. Lett. 38, 776 (1981)
27. R.L. Byer, in Quantum Electronics, edited by H. Rabin and C.L. Tang, Vol. I, Part B, (Academic Press, Inc., New York, 1978) pp. 587-702

28. Yu.M. Andreev, A.D. Belykh, V.G. Voevodin, P.P. Geiko, A.I. Gribenyukov, V.A. Gurashvili and S.M. Izyumov, Sov. J. Quantum Electron. 17: 490(1987); Yu.M. Andreev, V.Yu. Baranov , V.G. Voevodin, P.P. Geiko, A.I. Gribenyukov,S.V. Izyumov, S.M. Kosochkin, V.D. Pis'mennyi, Yu.A. Satov and B. Strel'tsov, ibid. 17: 1435-1436 (1987)
30. G.-C. Xing, K.J. Bachmann, J.B. Posthill, Appl. Phys. Lett. 56: 271 (1990)
31. G.C. Xing, K.J. Bachmann, J.B. Posthill, G.S. Solomon and M.L. Timmons in Heteroepitaxial Approaches in Semiconductors: Lattice Mismatch and its Consequences, edited by A.T. Macrander, and T.J. Drummond (The Electrochemical Society, Pennington, 1989) pp.132-135
32. K.J. Bachmann, E. Buehler, J.L. Shay and G.K. Kammlott, J. Electron. Mater. 3, 451 (1974)
33. G.S. Solomon, M.L. Timmons and J.B. Posthill, J. Appl. Phys. 65, 1952 (1989)
34. G.C. Xing, Growth and characterization of $ZnGeP_2$/GaP heterostructure by MOCVD and $ZnGeP_2$ bulk single crystals, Thesis. North Carolina State University, Raleigh, North Carolina
35. G.C. Xing, K.J. Bachmann, G.S. Solomon, J.B. Posthill and M.L. Timmons, J Crystal Growth 94: 381-386 (1989); G.-C. Xing, K.J. Bachmann, J.B. Posthill and M.L. Timmons in Diamond, Boron Nitride, Silicon Carbide and Related Wide Gap Compound Semiconductors, edited by J.T.Glass, R. Messier and N. Fujimori, MRS Symp. Proc. 162, Pittsburgh, PA 1989) pb. 615-619; J. Crystal Growth 113, 113 (1991)
36. J.B. Posthill, G.S. Solomon, M.L. Timmons, G.-C. Xing and K.J. Bachmann (Proc. 47th Ann. Meeting of the Electron Microscopy Society of America 1989) p. 582-586
37. Hara K, Kojima T, Kukimoto H, Jpn. J. Appl. Phys. 26: L1107 (1987)
38. M. Bettini, K. J. Bachmann and J. L. Shay, CdS/InP and CdS/GaAs Solar Cells, J. Appl. Phys. 49, 865 (1978).

OBSERVATION OF GAS FLOW PATTERNS IN A CVD REACTOR FOR WIDE BAND GAP SEMICONDUCTOR THIN FILM DEPOSITION

KINYA ATSUMI*, YOSHIKI UENO*, TADASHI HATTORI*
and YOSHIHIRO HAMAKAWA**
*Research Laboratories, Nippondenso Co.,Ltd. Nissin-cho, Aichi 470-01, JAPAN
**Faculty of Engineering Science, Osaka University, 1-1 Machikaneyama, Toyonaka, Osaka 560, JAPAN

ABSTRACT

A new method for the direct observation of two-dimensional gas flow patterns in a CVD reactor has been developed by combining a laser scanning technique with generating micron-sized TiO_2 particles. With this specially developed technology, the size of generated TiO_2 particles are quite uniform, and of high density by the use of hydrolysis of Ti-alkoxide in the ceramic honeycomb at the top inlet of the model chamber. In this system, vertical cross sections of the gas flow patterns can be visualized by illuminated TiO_2 particles in a He-Ne laser light sheet. Using this technique, detailed gas flow patterns can be clearly identified in the reaction chamber. Changes in the gas flow patterns with the various growth conditions, such as gas flow rate and pressure, have been measured. In this presentation, GaAs thin film growth by the MOCVD method will be reported as an example.

This gas flow visualization method could be a useful tool to identify the mechanism of CVD reactions to give better understanding about carrier gas transport and thin film growth for wide band gap semiconductors such as GaN, a-SiC, SiNx, etc.

INTRODUCTION

In the last decade, remarkable progress has been seen in thin film deposition technologies over the wide varieties of materials in metals, semiconductors and dielectrics. These growth technologies have made it possible to synthesize electrical, optical and optoelectronic properties of compound semiconductors by controlling atomic composition in the mixed alloys [1,2] and also by controlling the epitaxial growth process even at the monolayer level [3,4,5]. With these growth technologies, e.g. metal organic chemical vapor deposition (MOCVD), molecular beam epitaxy (MBE), plasma assisted chemical vapor deposition (plasma CVD), etc., there exists a possibility to develop a new type of multilayered functional device such as three-dimensional integrated circuits (3DIC's), optoelectronics integrated circuits (OEIC's) and super lattice devices.

Among these, the growth mechanisms in the CVD processes are very complex because they contain the mass transport phenomena with various chemical reactions in the gas phase. Especially in the MOCVD process, the epitaxially grown film quality, which directly affects thickness, composition and impurity doping profile, is strongly dependent on gas flow dynamics in the reactor because this process is operated at atmospheric or slightly reduced pressure ($\sim$0.1 atm) conditions. Thus, a basic understanding of gas flow patterns inside the reactor is a key issue to produce highly uniform epitaxial thin films in a reproducible method on a large scale.

Recently, much attention has been given to the area of gas flow motions in the vertical and horizontal MOCVD reactors through flow visualization studies

using laser light and through numerical simulation studies via a supercomputer. In past studies of flow visualization, interference holography of gas density variations [6,7] and scattering of a laser light sheet using micron-sized TiO_2 particles as a gas tracer [8,9,10] have been attempted in the reactor. Flow visualization by means of a laser light sheet is an excellent method because of the ability to see cross sections of gas flow structures. However, there still remains problems caused by the non-uniformity of the TiO_2 particles. This includes their size and smoke density based upon a very active reaction of particle generation. We have paid particular attention to this point, and started a series of systematic investigations on the production of fine and uniform micron-sized TiO_2 particles without disturbing the gas flow in the reactor. In this paper, we will present a new flow visualization technique and discuss the influence of recirculating vortexes over the GaAs substrate in the MOCVD reactor chamber.

EXPERIMENTAL PROCEDURE

1. Epitaxial Growth of GaAs and AlAs

A vertical MOCVD reactor which we employed in our experiment is shown in Fig.1. It consists of a vertical tapered quartz tube and a rf-heated susceptor with diameters of 100mm and 80mm respectively. The graphite susceptor does not rotate. The carrier and source gases are introduced into the reactor at the top inlet through a stainless steel pipe with a diameter of 6.45mm.

Triethylgallium (TEG), trimethylaluminum (TMA) and 10% AsH_3 as the source materials and H_2 as a carrier gas are used for GaAs/AlAs heteroepitaxy. A 2-inch GaAs substrate was used to measure the distribution of the film thickness as observed in SEM cross-sections. The epitaxial growth was performed at a susceptor temperature of 670℃, with two different reactor pressures and total flow rate conditions. One is maintained at 10Torr and 1slm (standard liter per minute), the other, at 100Torr and 3slm respectively.

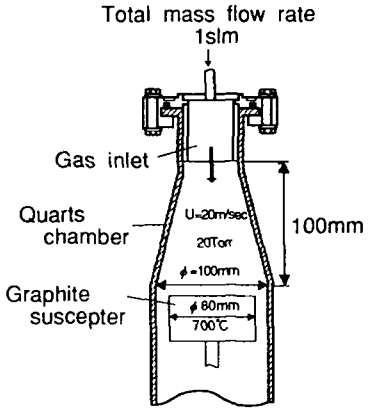


Fig.1 A schematic diagram of the vertical MOCVD reactor. The source materials and carrier gas are introduced into the reactor at the top inlet through a stainless steel pipe.

Fig.2 shows the distribution profiles of GaAs epitaxial film thickness under the two growth conditions. In the latter condition, that is 100Torr and 3slm, we obtained a thickness uniformity of ±5% distribution even without rotating the susceptor and produced a good surface morphology. However, the former condition showed a peculiar distribution profile whose shape was like the letter "W" over the 2-inch substrate. In addition, the morphology was very poor especially at the thick distributed film area. But this "W" shape indicates that the gas flows axisymmetrically over the substrate in the reactor chamber.

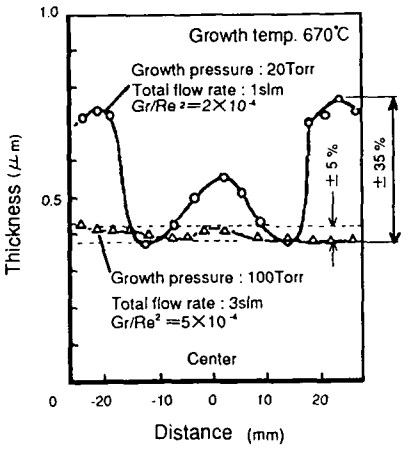


Fig.2 Distribution profiles of GaAs epitaxial film thickness over a 2-inch GaAs substrate under two growth conditions.

2. Flow Visualization

In the MOCVD process, the gas flow behavior is governed by H_2 carrier gas because the concentration of the source materials is very small. The typical dimensionless numbers whose magnitude determine the fluid characteristics are shown in Table I. In this MOCVD process, when we take a characteristic length at the gas inlet of the reactor, the Reynolds (Re) number is very small (=50). The flows are laminar. Moreover, the Mach (Ma) number and the Knudsen (Kn) number are also very small. Thus we treat the flows as an incompressible and viscous fluid. The ratio of the buoyancy force, which is generated by a temperature difference between the susceptor and the introduced gas, to the inertial force of jet gas (Grashof number (Gr) / Re^2) is very small in this case. The fluid is considered as a forced convection flow.

Fig.3 shows an experimental apparatus for flow visualization studies. This apparatus consists of a model chamber, a system for generating TiO_2 smoke particles and a He-Ne laser. To examine the detailed gas flow patterns over the susceptor, we constructed a rectangular model chamber twice as large as the genuine MOCVD reactor. It is made of acrylic plates. The flow visualization studies applied the similarity law and were performed under atmospheric pressure by adjusting to the value of the Reynolds number. The operating conditions in the flow visualization are shown in Table II. The gas velocity at the inlet part of the reactor was 20m/sec in the growing conditions (pressure: 20Torr, gas flow rate of H_2 : 1slm). However corresponding to the Reynolds number under atmospheric pressure by the use of N_2 carrier gas in place of H_2, the gas velocity will become extremely slow (about 50mm/sec) in the flow visualization model chamber.

TABLE I. Typical dimensionless numbers and fluid characteristics in the growth conditions at 20Torr and 1slm.

Dimensionless number	1slm 20Torr670℃	Critical value	Condition
$Re=\frac{\rho \cdot u \cdot d}{\mu}$	50	<2000	Laminar flow
$Kn=\frac{\lambda}{d}$	7×10^{-4}	<0.01	Viscous flow
$M=\frac{u}{c}$	1.5×10^{-2}	$<<1$	Incompressible
$\frac{Gr}{Re^2}=\frac{g\cdot\beta\cdot d\cdot\Delta T}{u^2}$	2×10^{-4}	$<<1$	Forced convection

ρ :Gas density
u :Gas velocity
d :Characteristic length
μ :Coefficient of viscosity
λ :Mean free path
C :Velocity of sound wave
g :Gravitational acceleration
β :Thermal expansion coefficient
ΔT :Temperature difference
Re :Reynolds number
Kn :Knudsen number
M :Mach number
Gr :Grashof number

$$Gr=\frac{\rho^2\cdot g\cdot\beta\cdot d^3\cdot\Delta T}{\mu^2}$$

In addition, we can estimate the susceptor temperature in the model chamber which is related to the temperature difference between the susceptor and the inlet gas (ΔT℃) by fixing the value of Gr/Re^2. As a result, it became very small (less than 0.01℃). Hence, the susceptor must be kept at room temperature.

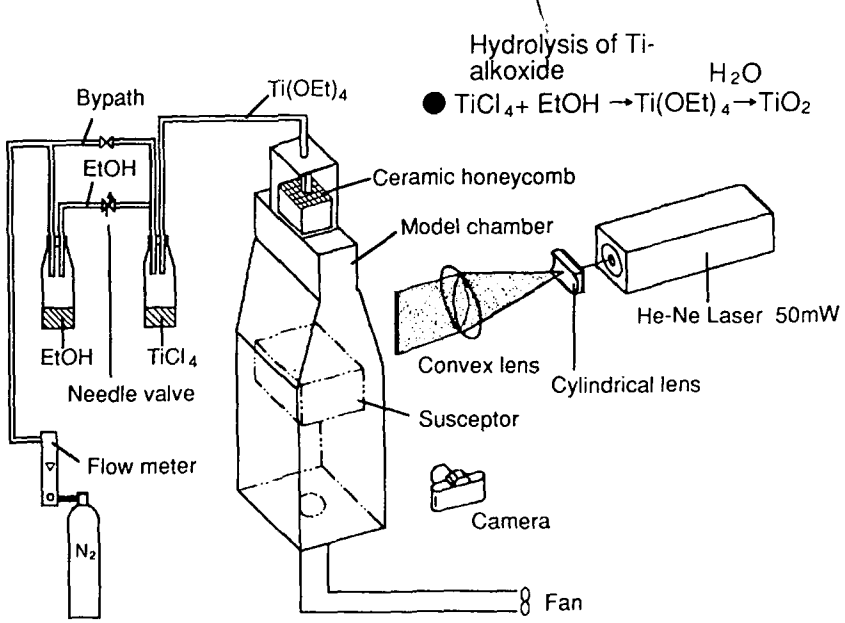


Fig.3 A schematic diagram of the experimental apparatus used for flow visualization. The micron-sized TiO_2 particles are generated without disturbing the gas flow patterns.

A special feature of this flow visualization apparatus exists in the process of generating micron-sized TiO_2 particles which are highly uniform in size and smoke density. That is, N_2 carrier gas containing ethyl alcohol vapor comes into contact with $TiCl_4$ just on the surface of the $TiCl_4$ liquid. $TiCl_4$ will change into Ti-alkoxide ($Ti(OCH_2CH_3)_4$), which is a colorless and clear gas, through a reaction with ethyl alcohol. Then the carrier gas with the Ti-alkoxide is passed through an Al_2O_3-made ceramic honeycomb which is mounted at the top inlet of the model chamber. The interior walls of the ceramic honeycomb are extremely porous, so a large amount of water is adsorbed. Ti-alkoxide gas will turn into micron-sized TiO_2 particles through a hydrolytic reaction with the adsorbed water. The TiO_2 particles are generated via a 2-step reaction of $TiCl_4$. Furthermore, the concentration of smoke can be adjusted by a needle valve which is set up in the pathway between ethyl alcohol and $TiCl_4$. Moreover, the ceramic honeycomb plays another important role, that is rectifying the inlet gas flow direction by the use of rectifier grids. In the flow visualization, a He-Ne laser light beam is spread out to the shape of a sheet through a cylindrical lens and illuminate TiO_2 particles in the gas flow field. The gas flow patterns are recorded on films by a camera in front of the model chamber.

TABLE II. Operating conditions for flow visualization.

×2 Model chamber

	H_2,20Torr	N_2,760Torr
Re	50	
Q SLM	1	0.4
U m/s	20	0.05 → Extremely slow
P Torr	20	760
Gr/Re^2	2×10^{-4}	
ΔT ℃	650	0.01

$$\Delta T = \frac{U^2}{g \cdot \beta \cdot l} \left(\frac{Gr}{Re^2}\right)$$

It is very difficult to visualize the gas flow at an extremely low velocity because it can be easily influenced by the disturbance of external conditions. For instance, when ethyl alcohol or $TiCl_4$ are bubbled by the carrier gas, we will obtain pulsative flows by small changes in pressure. Utilizing the high vapor pressure of ethyl alcohol, this problem has been avoided. If we do not use rectifier grids we will not be able to make the gas flow straight toward the susceptor from the gas inlet which is 300mm away. In addition, if we illuminated the particles with a tungsten lamp as a source of light instead of a laser light, non-axisymmetric flows will occur instantly by increasing the temperature at the model chamber's side wall. Our system has solved all of these problems.

RESULTS AND DISCUSSION

Adopting these new flow visualization techniques, TiO_2 particles can be generated in a smooth and thick fashion. As a result, we were able to observe the vertical cross sections of detailed gas flow patterns on the susceptor

precisely, clearly and continuously since these reactions were very stable.



(a) Impinging jet (b) Stable flow



(c) Diffusion (d) Lack of hydrolytic reaction

Fig.4 The photographs of the flow visualization.

The photographs of the flow visualization are shown in Fig.4. From these photographs, we could see that the introduced gas from the top inlet of the reactor was a jet. The width of the jet was not well developed between the top inlet and the susceptor. The moment the initial introduced jet gas impinged on the substrate and created vortexes was captured in (Fig.4-a). This was because the gas around the jet was quiescent at the first stage in the model chamber. These vortexes reached the reactor's side wall and disappeared. Then the flow induced by the jet is axisymmetric near the substrate and becomes stable (Fig.4-b). After approximately 30 minutes, the diffusion of gas in the reactor was also observed (Fig.4-c). Fig.4-c shows that the environmental gas is also moving and generating vortexes. The shortage of adsorbed water in the ceramic honeycomb could not show a hydrolytic reaction inside the flux of the jet gas. Consequently TiO_2 particles could not be

generated with high density (Fig.4-d). This happened when the TiO_2 particles had become attached to the interior walls of the ceramic honeycomb.

The gas flow states in Fig.4-b have been investigated in more detail. It has been shown that the injected gas, which impinges the substrate perpendicularly, flows radially outward along the substrate surface, separates and then forms recirculating cells under the susceptor edge. The cells then move onto the substrate and stop. It seems that the cells are balanced with the momentum of the flux. Fig.4-b does not show vortexes but the vortexes are always located between the jet and where the flow separated (see Fig4-c).

Fig.5 shows the recirculating cells which rotate clockwise and counterclockwise on the right and the left respectively. The main stream can be separated from the substrate by the existence of the recirculating cells. When we increase the gas flow rate, the gas flow velocity will increase as well. This causes the cells to move outward to another position where the momentum is balanced on the substrate. These phenomena are very interesting. The reasons why these phenomena exist are thought to be caused by the interaction between the following effects. (1) The shape of the susceptor edge. (2) The distance between the susceptor and the reactor's side wall. (3) The total gas flow rate (i.e.the velocity of the jet gas).

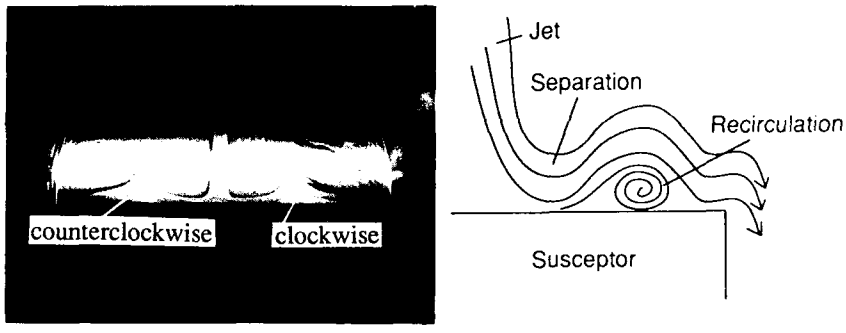


Fig.5 The recirculating cells and the flow separations on the substrate.

The result of the film thickness distribution profile at the conditions of 20 Torr and 1slm and that of flow visualization under atmospheric pressure being adjusted to the Reynolds number are compared. The result is shown in Fig.6. The position where the film is thick correspnds to the flow separation point. The presence of the vortexes on the substrate strongly affects the film quality. When the material species are entered into the recirculating cells once, they will not be able to get out except by diffusion. Thus fresh gas supply cannot be sufficient to the substrate surface under the recirculating cells. It decreases the partial pressure of AsH_3 and as a result, the epitaxial growth is not well done.

The Reynolds number is independent of reactor pressure when the gas flow rate is fixed, because the gas velocity changes at an inverse proportional rate to those of the reactor pressure. On the other hand the gas density is directly proportional to the pressure ($Re \propto \rho \cdot u$). Further, increasing the total gas flow rate implies increasing the Reynolds number. Fig.7 shows the photographs taken when total gas flow rates are increased. As total gas flow rates are increased, the cells are moved outward.

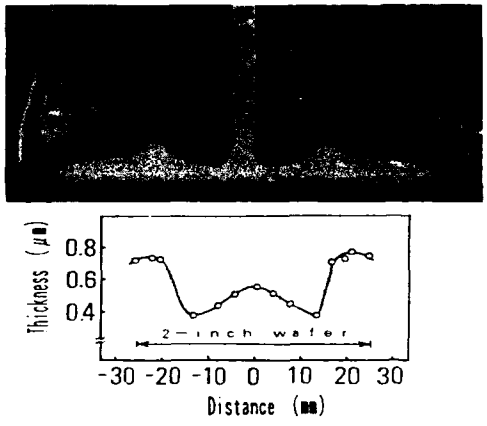


Fig.6 The distribution of the epitaxial film (10Torr, 1slm) and the gas flow pattern. The position where the film is thick corresponds to that of the flow separation point.



(a) Total gas flow rate= 0.6 l/min.



(c) Total gas flow rate= 1.9 l/min. (d) Total gas flow rate= 2.5 l/min.

Fig.7 Flow visualization photographs when total gas flow rates are increased. As total gas flow rates are increased, the cells are moved outward.

The gas flow pattern of the epitaxial growth conditions which are 100 Torr and 3 slm is visualized in Fig.8. The position of the recirculating cells are moved to the substrate edge and good epitaxial growth is achieved with a good uniform film thickness. According to these results, three times the total gas flow rate will be necessary to move the recirculating cells outside of the 2-inch substrate.

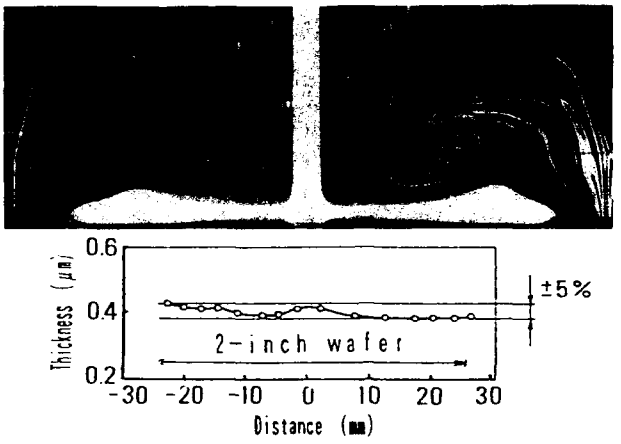


Fig.8 The distribution profile of the epitaxial film (100Torr, 3slm) and the gas flow pattern. The position of the recirculating cells is moved to the substrate edge. As a result, the film thickness uniformity was ±5% distribution.

Fig.9 summarizes the relationship between the total flow rates (= the Reynolds number) and the distance of the two recirculating cells (= the gas separations) in the flow visualization model chamber. The position of the cells is in proportion to the total gas flow rates. Thus the gas flow behavior is strongly influenced by the total gas flow rates.

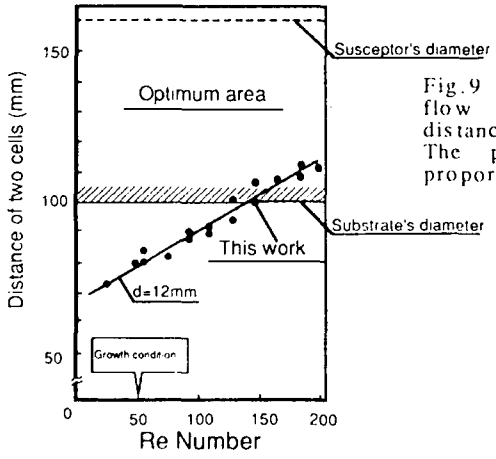


Fig.9 Relationship between the total flow rates(=Re number) and the distance of the two recirculating cells. The position of the cells is in proportion to the total gas flow rates.

CONCLUSION

A new flow visualization method has been developed and applied to study gas flow patterns in a MOCVD vertical reactor. Employing this method, the vertical cross sections of detailed gas flow patterns on the susceptor can be observed precisely, clearly and furthermore continuously without disturbing the genuine gas stream. In this study, we found a good agreement between the film thickness distributions and the gas flow patterns. The gas flow separations which are caused by the recirculating cells are moved by changing the total gas flow rates. The existence of these separations and cells prevent fresh gas being supplied to the substrate and consequently epitaxial growth is not well done. Thus, the total gas flow rates severely affect the gas flow patterns.

This flow visualization technique is of wide application to the CVD process in the region of being governed by viscous fluid. It might be a useful tool to identify the mechanism of CVD reactions to give better understanding about carrier gas transport and thin film growth for wide band gap semiconductors.

REFERENCES

1. Y.Hamakawa and Y.Tawada, Int.J.Solar Energy, 1 (1982) 251
2. Y.Hattori, D.Kruangam, K.Katoh, Y.Nitta, H.Okamoto and Y.Hamakawa, Proc. 19th IEEE Photovoltatic Specialists Conference, (1987) 689
3. J.Nishizawa, H.Abe and T.Kurabayashi, J.Electrochem. Soc, 132 (1985) 1197
4. A.Doi, Y.Aoyagi and S.Namba, Appl.Phys.Lett, 48 (1986) 1787
5. Y.Horikoshi, M. Kawashima and H.Yamaguchi, Jpn.J.Appl.Phys, 25 (1986) L868
6. L.J.Giling, J.Electrochem.Soc, 129 (1982) 634
7. J. E.Williams and R.W.Peterson, J.Cryst.Growth, 77 (1986) 128
8. C.A.Wang, S.H.Groves, S.C.Palmateer, D.W.Weyburne and R.A.Brown, J.Cryst.Growth, 77 (1986) 136
9. D.I.Fotiadis, A.M.Kremer, D.R. McKenna and K.F.Jensen, J.Cryst.Growth, 85 (1987) 154
10. M.D.Keijser, C.V.Opdorp and C.Weber, J.Cryst.Growth 92 (1988) 33

ELECTRONIC TRANSITION-RELATED OPTICAL ABSORPTION IN VANADIA FILMS

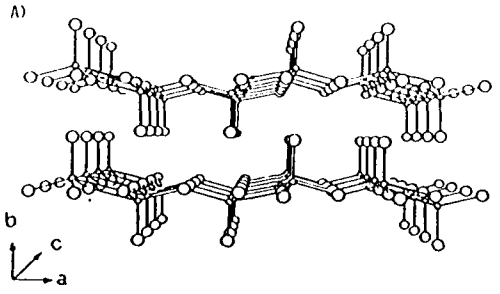
NADA M. ABUHADBA AND CAROLYN R. AITA
Materials Department, University of Wisconsin-Milwaukee, P.O. Box 784, Milwaukee, Wisconsin 53201

ABSTRACT

Vanadium pentoxide (vanadia) is a wide band gap semiconductor. Its layered orthorhombic structure consists of alternating sublayers of V+O atoms and O atoms (vanadyl O) alone aligned perpendicular to the b-axis. This unique structure makes vanadia a useful host for alkali atom intercalation for electrochromic applications, and therefore, an understanding of its optical properties is important. Here, we study the optical absorption characteristics of vanadia in the incident photon energy range E=2.5-6.0 eV (λ=490-200 nm). The material is in the form of 0.1μm thick films sputter deposited in Ne/O_2 discharges. Two types of films were studied: single-oriented films with the b-axis perpendicular to the substrate, and amorphous films with an oxygen deficiency. The optical absorption coefficient, α(E), was determined and interpreted in terms of the structure of the V 3d conduction band. Amorphous, O-deficient vanadia were examined for room temperature aging and were found to oxidize and increase in transmittance in the photon energy range studied.

INTRODUCTION

Vanadia, V_2O_5, is a wide band gap semiconductor at room temperature. It crystallizes in the orthorhombic crystal structure with bulk parameters a=11.519 Å, b=4.373 Å, and c=3.564 Å [1-6]. The crystal structure is shown in Fig. 1a [7]. Perpendicular to the b crystal axis, i.e., in the {010} plane, vanadia has a layered structure consisting of alternating rows of V+O atoms and O atoms alone. In vanadia, a central V atom is bonded to six O atoms in a distorted octahedral symmetry. Four O atoms are coplanar, a fifth O lies 1.59 Å above the central V atom and is referred to as the vanadyl O, and a sixth O atom lies 2.78 Å below the central V. Figure 1b shows the local atomic arrangement. Bonding perpendicular to the layer is weak because of the large seperation between a central V atom and the vanadyl O of an adjacent layer.



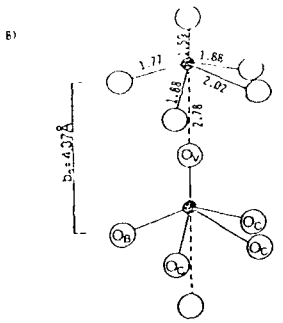


Fig. 1: a) Perspective drawing of the vanadia lattice, with small circles indicating V and larger circles indicating O [from Ref.7]. b) The local arrangement around a central V atom in distorted octahedral coordination with six O [O_V=vanadyl O, O_C =chain O, O_b=bridge O]

Interest in the optical properties of vanadia originated as a result of a better understanding of the catalytic process of hydrocarbon oxidation [7-11]. The oxygen molecule dissociates at the surface of nonstoichiometric vanadia by trapping an oxygen atom at a vacant vanadyl oxygen site. Optical-related studies showed presence of a broad infrared band centered at about 1μm, the intensity of which increased or decreased upon reduction or oxidation of vanadia respectively [9,11]. The band was attributed to electronic transitions within occupied V^{+4} 3d band (i.e $3d^1$--->$3d^1$).

The wide interlayer spacing allows intercalation of alkali atoms within the vandia lattice, and that, in turn resulted in the interest in thin films of vanadia in solid state batteries [12] and electrochromic devices for smart windows [13-16]. Intercalation and de-intercalation are associated with reduction and oxidation of the material, and hence the IR band in thin film vanadia has repeatedly been investigated [13,16,18]. However, there have been few studies of optical behavior at energy greater than the band gap, i.e. in the ultraviolet spectral region, which is the subject of the present paper. Aita et al. [17-21] have been studying the effect of various sputter deposition parameters on the vanadia films structural and optical properties grown in Ar/O_2 discharges.

We report here the optical properties of single (010) orientation vanadia and amorphous vanadia films for incident photon energy, E=2.5-6.0 eV (wavelength λ=490-200 nm). Films are grown by radio frequency reactive sputter deposition in Ne/O_2 discharges. The effect of using Ne/O_2 discharges on the films' structural properties is discussed in Ref. 27. Optical absorption characteristics in the ultraviolet region are related to the structure of the vanadia conduction band. The effect of room temperature aging of the amorphous films is discussed in terms of film oxidation.

EXPERIMENT

Film Growth

A liquid N_2-cold trapped, hot-oil diffusion pumped, rf-excited planar diode sputter deposition system was used to grow the films. The target was a 12.7 cm-diam, 99.7% V disc bonded to a water-cooled cathode. The substrates were pyrex glass slides and fused silica placed on a water-cooled Cu anode. The anode-cathode spacing was 5 cm.

The chamber was evacuated to 6.65 x 10^{-6} pa (5x10^{-7} torr) before backfilling with sputtering gas. The total gas pressure was measured with a capacitance manometer and kept constant at 1.33 Pa (1x10^{-2} torr). 99.999% pure Ne and 99.997% pure O_2 were used. Each component was introduced separately into the sputtering chamber. Ne:O_2 ratios were

established using an MKS Baratron Series 260 control system, Model 258 flow transducers, and Model 248A solenoid control valves. With a shutter covering the substrates, a two-step pre-sputter procedure was carried out in which the target was sputtered in Ne for 45 minutes, and then for an additional 45 minutes in the Ne/O_2 gas mixture used for the actual deposition, after which the shutter was opened. Peak-to-peak cathode voltage, V_c, was -1.6 kV. Specific deposition conditions are recorded in Table 1.

Ne gas was used as the sputtering rare gas instead of the commonly used Ar for several reasons. A well-known characteristic of reactive sputter deposition from an elemental target is that compound formation at the target surface above a critical reactive gas content, for example oxygen content [21-22]. In that 'mode' of the target, the flux of species sputtered off the target and arriving at the substrate is almost totally in molecular form. It is also known that metastable Ne (Ne^m= 16.62 and 16.71 eV) can Penning ionize ground state O_2 molecules (ionization potential E_i =12.1 eV) whereas Ar metastables (Ar^m =11.55 and 11.72 eV) cannot [23-25]. The product of Penning ionization ($Ne^m + O_2$ -----> $O_2^+ + Ne^o + 1e$) is a positively-charged oxygen species which is readily attracted to the negatively biased target, enhancing target oxidation. The target surface no longer getters all oxygen from the plasma, making it available for reaction with metal or suboxide species at the substrate. While that property of Ne is unattractive for forming metal suboxides by reactive sputtering, it is very convenient for forming high valence metal oxides. In addition, the low mass of Ne^+ results in a lower sputtering yield and hence lower deposition rate. The mobility of species at the substarte is not only temperature dependent but also time dependent. For both of these reasons, crystalline growth is in general enhanced (disordered or amorphous growth is minimized) when Ne rather than Ar is used as the rare gas component of the discharge, aiding at the formation of highly orientated uniepitaxial films (i.e. polycrystalline with sharp fiber texture) [26-27].

Film Characterization

Film thickness was determined using a Tencor Alpha Step Model 200 profilometer to measure the height of a step produced by masking a region of the substrate during deposition. Growth rate was determined by dividing thickness by deposition time.

Crystallography was determined by double-angle x-ray diffraction (XRD) using Cu Kα radiation (λ = 1.5418 Å) for films grown on glass slides. Peak position (2Θ), intensity, and full width at one-half of the maximum intensity (FWHM) were measured. The diffractometer was calibrated using the {01.1} diffraction peak of a quartz standard at $2\Theta=26.66\pm0.02^o$ whose width is 0.25^o. The interplanar spacing, d{hkl} was calculated using the Bragg equation for n^{th} order diffraction: $d\{hkl\}=n\lambda/2\sin\Theta$.

A Perkin-Elmer Model 330 UV-Visible-Near IR double beam spectrophotometer with a specular reflection attachment was used to measure the transmittance and reflection of near normal incidence radiation in the 200-650 nm range for films on fused silica. Measurements were performed immediately after deposition and then again after a period of nine months. In the transmittance regime, a bare fused silica substrate was placed in the path of the reference beam so that the recorded transmittance is due to the transmission through the film alone. Reflectance measurements were made relative to an Al mirror. No sample was placed in the reference beam path. In the energy region studied here, which is near and above the band gap, the film is highly absorbing so that reflection of the incident beam at the film-substrate interface is minimized, thus allowing the use of Eq. (1) for absorption coefficient calculations [28]:

$$T=[(1-R)^2 \exp(-\alpha x)]/[1-R^2\exp(-2\alpha x)]. \quad (1)$$

T is transmittance, R is reflectance, x is film thickness, and α is the absorption coefficient calculated as a function of wavelength.

RESULTS

Film thickness, growth rate, and x-ray diffraction results are given in Table I. Films that showed no x-ray diffraction peaks were green in color and are referred to here as amorphous vanadia . Crystalline films showed two x-ray diffraction peaks attributed to first and second order diffraction of (010) planes of orthorhombic vanadia.

Table I: Film designation, sputtering gas O_2 content ($\%O_2$), film thickness (T), growth rate (G), crystal structure (CS), and interlayer spacing (B).

Film	$\%O_2$	T (Å)	G(Å /min)	CS	B(Å)
A	2	1300	11	Amorphous	---
B	4	840	14	Amorphous	---
C	10	890	7	(010) ortho-rhombic	4.405
D	25	1300	11	(010) ortho-rhombic	4.398

Figure 2 shows the absorption coefficient calculated using Eq. 1 as a function of incident photon energy for Films A, C, and D. The transmittance through as-deposited amorphous Films A and B is compared to that after a period of nine months of aging to test for film stability. The results are shown in Fig. 3.

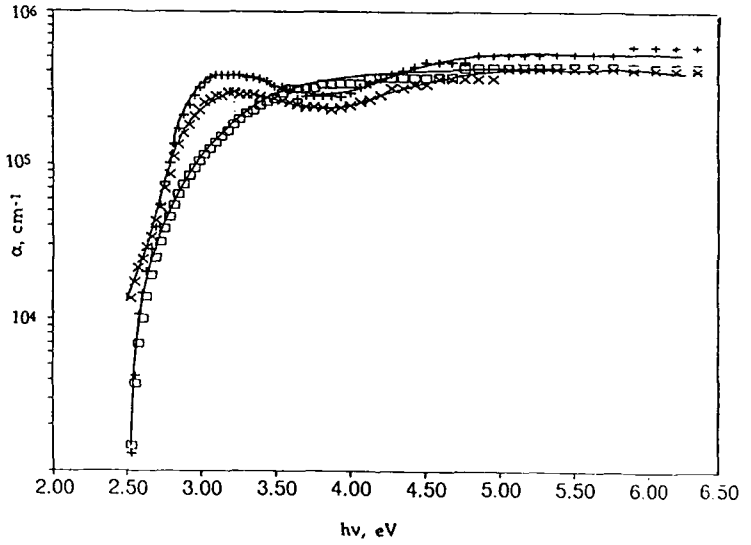


Fig. 2: Absorption coefficient as a function of incident photon energy for crystalline vanadia Film C (+) and Film D (x) and amorphous vanadia Film A (□).

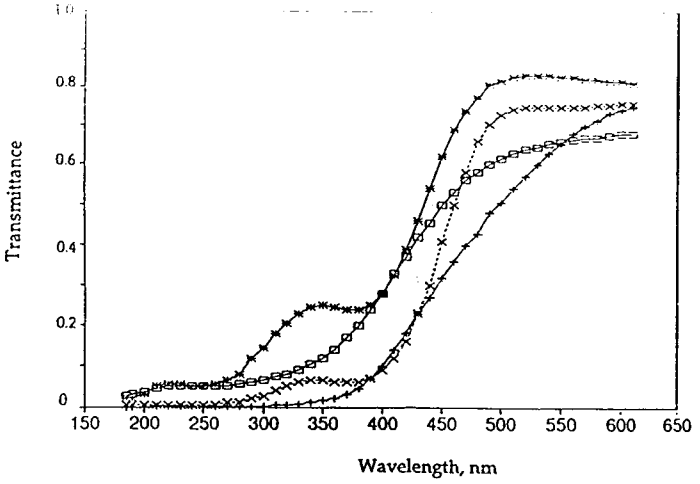


Fig.3: Transmittance through Film A (+), and Film B (□) in as deposited state. In the aged state, Films A and B are designated by (x) and (*) respectively.

DISCUSSION

Vanadia films grown in discharges of O_2 content greater than 4% and at cathode voltage of 1.6kV had a solely <010> orientation, i.e the films are uniepitaxial, with the b axis lying perpendicular to the substrate. The interlayer spacing was always greater than the bulk value (4.373Å). No long range order was detected in films grown in O_2 content less than 4%. It was previously reported that the critical O_2 content needed to produce crystalline vanadia in Ne/O_2 discharges decreased with increasing cathode voltage [27], and is less than the critical O_2 content found in Ar/O_2 discharges at 1.6 kV, consistent with the previous discussion of Penning ionization of O_2.

A comparison of the absorption behavior of crystalline vanadia Films C and D and amorphous vanadia Film A in Fig. 2 reveals two main differences:

1) an absorption band with an onset at 2.5 eV and centered at 3.2 eV present only in crystalline vanadia, followed by another broader band, the onset of which is at 3.8 eV.

2) a shift in the absorption edge for hν > 2.8 eV toward higher energy in amorphous vanadia .

The structure of the optical absorption curve of crystalline vanadia can be explained as follows. The valance band in vanadia has an O 2p nature. The conduction band consists of two split-off V 3d bands, a feature characteristic of the symmetry of crystalline vanadia. The lower V 3d band was first calculated by Bullet to be 0.4 eV wide, and separated by 0.3 eV from the upper and broader V 3d band [29]. The onset of absorption at 2.5 eV is therefore attributed to electronic transitions from the O 2p to the lower V 3d band. The broader, higher energy band whose onset is 3.8 eV, is attributed to transitions from the O 2p to the upper V 3d band. The first spectroscopic measurements on single crystal V_2O_5 to reveal such a band structure was performed by Mokerov et al. [30]. In the real part, n, and imaginary part, k, of the complex refractive index, a band with a maximum at 2.5 eV and 0.4 eV wide, followed

by a stronger band centered at 2.92 eV for polarized light with E ll a, and at 3.15 eV for E ll c was reported.

The split-off V 3d bands lose resolution in as-deposited amorphous vanadia films, accompanied by a shift in the absorption edge to higher energy. The latter effect has previously been observed to occur in nanocrystalline vanadia thin films after Li^+ intercalation to produce V^{+4} sites [16], consistent with the substoichiometric nature of the amorphous films. Crystalline films do not age at room temperature, whereas amorphous films do. We attribute this aging to oxidation which annhilates V^{+4} defects. A similar result was previously reported for substoichiometric vanadia on sapphire [17].

REFERENCES

1. ASTM Joint Commission on Powder Diffraction Standards File No. 9-387, (1974). b and c are reversed in this reference from the manner in which they appear throughout the literature.
2. H. G. Bachmann, F.R. Ahmed, and W.H. Barnes, Z. Kristal. 115, S.11 (1961).
3. L. Fiermans and J. Vennik, Surf. Sci. 9, 187 (1968).
4. E. Gillis and E. Boesman, Phys. Status Solidi 14, 337 (1966).
5. P. Clauws and J. Vennik, Phys. Status Solidi B 66, 553 (1974).
6. W. Lambrecht, B. Djafari-Rouhani, and J. Vennik, J. Phys. C 19, 369 (1986).
7. R.Ramirez, B. Casal, L. Utera, and E. Ruiz-Hitzky , J. Chem. Phys. in press.
8. L. Fiermans, P. Clauws, W. Lambrecht, L. Vandenbrouche, and J. Vennik, Phys. Status Solidi A 59, 495 (1980).
9. L. Fiermans, L. Vandenbrouche, R. Vandenberge, J. Vennik, and G. Dalmai, J. Microsc. Spectros. Electron. 4, 543 (1979).
10. J.H. Perlstein, J. Solid State Chem. 3 , 217 (1971).
11. J. Bullot, P. Cordier, O. Gallais, M. Gauthier, and F. Babonneau, J. Non-cryst. Sol. 68, 135 (1984).
12. J.B. Bates, N.J. Dudney, C.F. Luck, and L. Klatt, Ceramic Transactions 11, 35 (1990).
13. S.F. Cogan, N.M. Nguyen, S.J. Perrotti, and R. D. Rauh in Optical Materials Technology for Energy Efficiency and Solar Energy Conversion VII (SPIE, 1016,1988) pp. 57-62.
14. S.F. Cogan, N.M Nguyen, S. J. Perrotti, and R. D. Rauh: J. Appl. Phys. 66, 1989, 1333.
15. A. Talledo, A.M. Andersson, C.G. Granqvist: J. Mater. Res. 5, 1253 (1990).
16. A. Talledo, A.M. Andersson, and C.G. Granqvist, J. Appl. Physics, 69, 3261 (1991).
17. S.D. Hansen and C.R. Aita: J. Vac. Sci. Technol. A 3, 660 (1985).
18. C.R.Aita , Y.-L. Liu, M.L. Kao, and S.D. Hansen, J. Appl. Phys. 60, 749 (1986).
19. C.R.Aita, C.-K. Kwok, and M.L. Kao, Mat. Res. Soc. Proc .82, 435 (1987).
20. C.R. Aita and M.L. Kao, J. Vac. Sci. Technol. A 5, 2714 (1987).
21. C.R. Aita, L.-J. Liou, C-K. Kwok, R.C. Lee, and E. Kolawa, Thin Solid Films 193-4, 18 (1991).
22. R.C. Lee and C.R. Aita, J. Appl. Phys. 70, 2094 (1991).
23. C.R. Aita and Ngoc C. Tran, J. Appl Phys. 56, 958 (1984).
24. J.W.Coburn and E. Kay, Appl. Phys. Lett. 18,435 (1971).
25. C.R. Aita and M.E. Marhic, J. Vac. Sci. Technol. A, 1(1), 69 (1983).
26. N.M. Abuhadba and C.R. Aita, J. Appl. Phys. 71, xxx (1992).
27. N.M. Abuhadba and C.R. Aita, Mater. Sci. Technol. xxx (1991).
28. J.I. Pankove, Optical Processes in Semiconductors (Prentice-Hill, Englewood Cliffs, NJ, 1971), p. 93.
29. D.W. Bullet, J.Phys. C.Solid St. Phys. 13, L595 (1980).
30. V.G. Mokerov, V.L. Makarov, V.B. Tulvinski, and A.R. Begishev, Opt. Spectrosc., 40, 58 (1976).

PHASE MAPPING SPUTTER DEPOSITED WIDE BAND-GAP METAL OXIDES

C.R. AITA,* R.C. LEE,* C.-K.KWOK,* AND E.A. KOLAWA**
*Materials Department, University of Wisconsin-Milwaukee, P.O. Box 784, Milwaukee, WI 53201
**Department of Electrical Engineering, California Institute of Technology, Pasadena, CA 91125

ABSTRACT

Reactive sputter deposition is a widely-used process for growing films of high melting point materials near room temperature and desirable metastable structures not attainable in material grown under conditions of thermodynamic equilibrium. Both categories include wide band-gap metal oxides. A first step towards reproducible growth is to develop a "phase map" for the metal-oxygen system of interest. The map graphically relates independent sputter deposition process parameters, the growth environment, and the metallurgical phase(s) formed in the film. This paper shows how phase maps are constructed and used to observe general trends in oxide phase formation sequence, with examples from the Nb-O, Y-O, and Zr-O systems.

INTRODUCTION

In this study, metal oxide films were grown on unheated substrates by sputtering a metal target in radio frequency (rf)-excited rare gas-O_2 discharges. Optical emission spectrometry was used for *in situ* sputtering discharge diagnostics. Characterization for metallurgical phase identification included x-ray diffraction, infrared absorption, Rutherford backscattering, optical spectrophotometry, and electrical resistivity measurements. From these data, a "phase map" was constructed, interrelating independent process parameters, the growth environment, and metallurgical phases present in the films.

Sputter deposition is governed by kinetics. The process parameters onto which phase regions and growth environment characteristics are mapped are not analogous to the thermodynamic variables used to describe overlayers [1]. The scientific motivation for constructing a phase map is to understand the phase formation sequence in terms of a changing growth environment - a first step towards modeling metal oxide growth by reactive sputter deposition. An important technological outcome is that another investigator, using the information about the equivalence of process parameters shown on the phase map, can make educated decisions when designing an experiment to obtain specific film properties, even when no means of *in situ* discharge diagnostics is available.

Sputter deposition is a low pressure, glow discharge process carried out in a set-up shown in Fig. 1 [2]. The high negative cathode potential drops to ground across the Crookes dark space. The potential rises in the plasma to a small positive value. The anode surface floats at a small negative potential. Positive ions from the plasma accelerate across the Crookes dark space and strike the target surface. Material is ejected (sputtered) by momentum transfer. Most of the ejected target species are uncharged, move randomly between the electrodes, become thermalized, and condense on any surface in their path, i.e. the substrate. A metal oxide film is grown here by sputtering a metal target in a rare gas-O_2 discharge. For a fixed machine geometry, independent process parameters include total gas pressure, nominal sputtering gas O_2 content, rare gas type, and cathode voltage. Combinations of these parameters determine deposition rate, rf power, and substrate surface temperature.

A continuous oxide layer forms at the target surface once the nominal gas O_2 content exceeds a critical value, O_2*. For $O_2 > O_2$*, the target material effectively being bombarded is an oxide. O_2* strongly depends on cathode voltage and rare gas type. For a given rare gas

type and cathode voltage, there is another important value of gas O_2 content, O_2**, at which oxygen species first appear in the plasma and are available for reaction at the substrate. At O_2**, the target surface is no longer able to getter all oxygen from the plasma. Metal oxide molecules can be sputtered intact from the target surface. However, the sputtering process can also dissociate the target surface oxide. *Therefore, for any set of process parameters, the sputtered flux can consist of both metal atoms and metal oxide molecules.* Three questions will be addressed below: 1) what phases are present in the films; 2) what is the nature of the sputtered flux as a function of process parameter; 3) how is the phase formation sequence affected by the nature of the sputtered flux and the availability of oxygen?

EXPERIMENTAL

Films were grown in an rf diode apparatus operated at 13.56 Mhz by sputtering a 13-cm diam, metal (M=Nb,Y,Zr) target bonded to a water-cooled Cu cathode [3-10]. Suprasil fused silica, <111>-cut Si, and carbon foil substrates were placed on a water-cooled M-coated Cu pallet covering the anode. The anode-cathode spacing was 6 cm. The sputtering gas, O_2 (99.99%) and a rare gas, Ne (99.996%), Ar (9°.999%), or Kr (99.9995%) was at a total pressure of 0.01 Torr. Cathode voltage, sputtering gas O_2 content, and rare gas type were varied.

Optical emission spectrometry was used for *in situ* discharge diagnostics [11]. Radiation of wavelength λ emitted between the anode and cathode was sampled through an optical window, as shown in Fig. 1. The optical emission intensity, $I(\lambda)$, of radiative electronic transitions of excited neutral metal atoms to ground state [12] were monitored at the following wavelengths: for Nb, λ= 4059, 4101, 5079, and 5344 Å; for Y, λ=3621, 4128, 4143, 4236, 6191, and 6793Å; for Zr, λ=3520, 3548, and 3601 Å. *Applying the condition of an optically thin plasma in local thermal equilibrium,* $I(\lambda)$ is proportional to the number of ground state M atoms in the discharge [13]. In addition, emission from excited neutral O atoms was monitored, at λ=5331, 6157, 7772-5 Å [14,15]. For a given rare gas type and cathode voltage, these data were used to directly determine: 1) the gas O_2 content at which a continuous oxide layer formed at the target surface, i.e. O_2* [$I(\lambda)$ from M atoms disappears or sharply deceases], and 2) the inability of the oxidized target surface to getter all oxygen from the plasma, i.e. O_2** [$I(\lambda)$ from O atoms appears].

Furthermore, assuming unity sticking coefficient, the fractional flux of M atoms, f(M), and M-oxide molecules, f(M-oxide), incident on the substrate during deposition were calculated from the following equations [3]:

$$f(M)=\{Rel.I(\lambda)/[G'\rho(M\text{-}oxide)_S/\rho(M)_S]\} \quad (1)$$

$$f(M\text{-}oxide)=1-\{Rel.I(\lambda)/[G'\rho(M\text{-}oxide)_S/\rho(M)_S]\}, \quad (2)$$

where f(M)+f(M-oxide)=1. G' is growth rate relative to its value in a pure rare gas discharge operated at the same cathode voltage, and $\rho(M\text{-}oxide)_S/\rho(M)_S$ is the bulk atomic density of the condensed M-oxide phase relative the density of the pure metal phase. The exact form of the gas phase M-oxide(s) species is unknown, but mass spectrometry data [2] show that for many oxide systems, the prevalent form is the metal monoxide, MO.

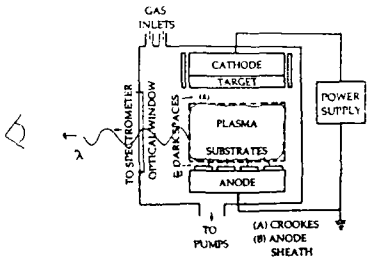


Fig. 1: An rf diode sputter deposition set-up.

Post-deposition, film thickness was measured with a profilometer from a step produced by masking part of the substrate during deposition. Growth rate was determined by dividing thickness by length of deposition. Crystallography was determined by double-angle x-ray diffraction (XRD). Rutherford backscattering spectrometry (RBS) was used to measure the M:O atomic concentration. Fast-fourier transform infrared spectrometry was used to determine optical absorption due to lattice vibrations, yielding data about short range M-O atomic order. Resistivity was measured with a four point probe. Optical transmission and reflection were measured by double-beam spectrophotometry as a function of incident photon wavelength. The refractive index and the optical absorption coefficient was determined from these measurements. The optical absorption edge structure is related to the joint density of electronic states near the valence and conduction band edges, which is sensitive to structural and chemical disorder.

PHASE MAPS

To construct a phase map, first, metallurgical phase boundaries are graphed onto process parameter space. The process parameter-phase diagram is then overlayed with values of the growth environment parameters which are: 1) the fractional M or M-oxide flux to the substrate, 2) formation of a continuous target surface oxide layer, i.e. at O_2* , and 3) the appearance of oxygen in the plasma available for reaction at the substrate, either with M metal or with a suboxide, i.e. at O_2**.

Figures 2-4 show the phases present in Nb-O, Y-O, and Zr-O films graphed onto process parameter space. These figures were developed on the basis of XRD, RBS, IR and optical spectrometry, and electrical measurements. See Refs. 3-10 for specific values of film properties. Values of f(M) and f(M-oxide) calculated from Eqs.(1-2), as well as the position of O_2* and O_2** are shown on Figs 2-4.

The phase formation sequence in the stable, bulk, room temperature Nb-O system is as follows: Nb (bcc)→NbO (fcc, NaCl structure)→NbO_2 (tetragonal)→Nb_2O_{5-x} with $0 \le x \le 0.2$ (related forms collectively called "niobia", based on building blocks of the ReO_3-type lattice) [16]. Figure 2 shows that bcc Nb, NbO, NbO_2, and crystalline niobia phases are also formed in sputter deposited films. Nb films have a strong preferred or sole {110} orientation. Ar-O_2 discharges produce Nb+NbO and NbO+NbO_2 biphasic structures. Individual metal and/or suboxide XRD peaks are not resolvable in films grown in Kr-O_2 discharges; these structures are denoted "Nb-suboxide". Crystalline niobia forms only when a high cathode voltage, Ne-50% O_2 discharge is used. Throughout most of the niobia phase field, films have no long range crystallographic order, and are called "a-niobia". All crystalline and a-niobia films are transparent and insulating [3,4]. In addition, an amorphous, semitransparent phase, "x-niobia", with a finite resistivity but with an IR absorption spectrum that has a strong a-niobia component, is sometimes formed at the Nb-suboxide/a-niobia phase boundary.

The growth environment and Nb-O phase formation are related as follows:

1) a- and crystalline niobia are formed when f(Nb-oxide) is large (often unity) and the target surface is oxidized, thereby unable to getter all oxygen from the discharge, making it available for reaction at the substrate.

2) Nb, Nb-suboxides, and biphasic structures are formed when f(Nb) is large and the target surface is not fully oxidized, thereby able to getter oxygen from the discharge, making it unavailable for reaction at the substrate. Phase separation, the type of growth expected under theromdynamic equilibrium conditions occurs in Ar-O_2 and is absent in Kr-O_2 discharges. f(Nb) is larger when Kr rather than Ar is used. To form a well-ordered suboxide phase (NbO or NbO_2), these free Nb atoms must react with oxygen before their surface mobility is quenched by the subsequent arriving flux. There is always an overpressure of neutral rare gas atoms on the substrate, characteristic of the sputter deposition environment. Kr, with an atomic diameter of 2.06 Å, compared to Ar, with a diameter of 1.76 Å, is more effective at blocking the diffusion of a Nb or oxygen species along the substrate. In other words, more Nb atoms must react at the substrate and more severe limitations on their surface mobility make it more difficult for these atoms to find a reaction partner when Kr, rather than Ar is used. The deposition rate in Kr-O_2 and Ar-O_2 is approximately the same for a given set of

process parameters [4], hence the rate of arriving flux capable of quenching a reaction, is not a factor.

3) x-niobia forms when f(Nb-oxide) is large, the target surface is oxidized, but no oxygen is available for reaction at the substrate. As in the case of ZrO discussed below, this initially-formed target surface oxide (for example, NbO) may getter oxygen from the discharge. The result is a deficit in the amount of oxygen required to complete oxidation at the substrate to form a-niobia.

There are two stable STP phases of the bulk Y-O system: hcp Y and Y_2O_3 with a bcc bixbyite structure (c-yttria) [17]. Figure 3 shows that only these two phases are present in films sputter deposited in Ar-O_2 discharges, with c-yttria having a sole {111} orientation over much of the yttria phase field. Two additional phases with no long range crystallographic order detectable by XRD form in films grown in Ne-O_2 discharges: metallic a-Y and insulating a-yttria. The IR absorption spectrum of a-yttria [10] is the same as that of bulk c-yttria [18,19], indicating that the *average* Y-O short range order is the same.

The growth environment and Y-O phase formation are related as follows:

1) Y films are grown from a high Y flux and a target whose surface does not have a continuous oxide layer.

2) Yttria films are grown from an oxidized target surface. However, in contrast to the Nb-O system, it can be seen from Fig. 3a that an oxidized target surface is associated with a large Y, as well as a large Y-oxide flux. Although both conditions produce c-yttria, important

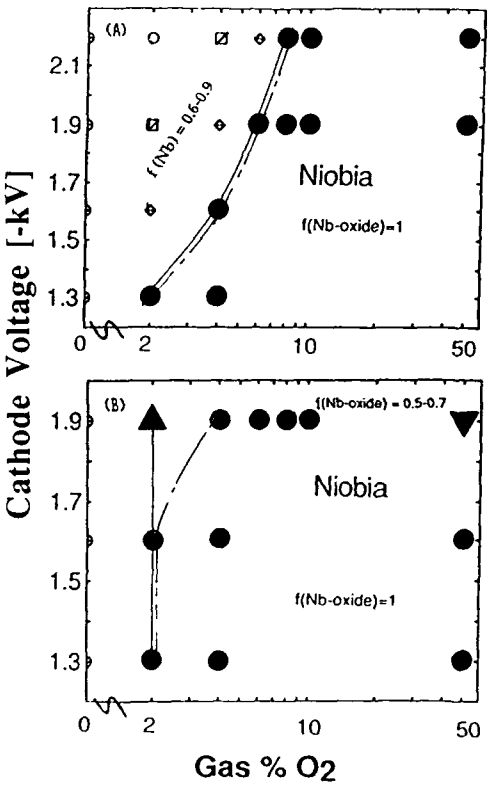


Fig. 2:

A phase map for the Nb-O system.

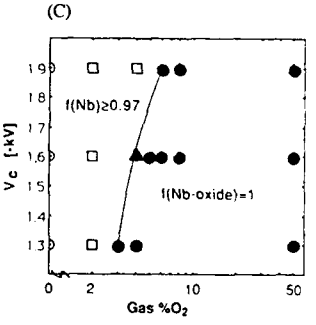
Rare gas: a) Ar, b) Ne, c) Kr.

O_2* ———

O_2**— - - —

Phases present:

- ○ -Nb or Nb(O)
- ▨ -Nb+NbO
- ◇ -NbO+NbO_2
- □ -Nb-suboxide
- ▲ -x-niobia
- ● -a-niobia
- ▼ -crystalline niobia



differences occur in the shape of the fundamental optical absorption edge [8-10]. A large Y-oxide flux results in c-yttria whose optical absorption edge consists of two direct interband transitions (at 5.07 and 5.73 eV) in agreement with bulk single crystal data [21] and a recent theoretical calculation [22]. A large atomic Y flux results in c-yttria with a "disordered" optical absorption edge, i.e. the two direct transitions cannot be resolved. We proposed [10] that this optical disorder arises from a disorder in the placement of Y at its two nonequivalent positions within the yttria unit cell [17].

3) A Y target sputtered in Ne-≥2% O_2 discharges has a completely oxidized surface. However, dissociation of the sputtered Y-oxide molecule in the plasma volume results in a large Y flux to the substrate [8]. However, local thermal equilibrium does not hold, and so Eqs. (1-2) cannot be used to calculate f(Y). Films grown in Ne-O_2 discharges are c-yttria with a disordered fundamental optical absorption edge or a-yttria.

There are two stable STP phases of the bulk Zr-O system: hcp Zr and monoclinic (m-) ZrO_2 [23]. Fig. 4 shows that in general, the following phase sequence occurs in sputter deposited films: hcp Zr→ ZrO→a-ZrO_2→m+t-ZrO_2→m-ZrO_2. Zirconia (ZrO_2) takes three forms: 1) monoclinic (m-) zirconia with a single {11$\bar{1}$} orientation parallel to the substrate plane, 2) a mixture of m-zirconia and tetragonal (t-) zirconia, a high temperature polymorph, and 3) a-zirconia with no long range order detectable by XRD. m- and t-zirconia coexist in bulk material when the crystallite diameter is small, a consequence of the dominance of the surface energy contribution to the Gibbs free energy of formation. The critical diameter below which t-zirconia is stabilized in the films is ~130 Å [6,7], in good agreement with bulk nanocrystalline zirconia.

Growth environment data was taken only for -1.9 kV discharges. That data show that f(Zr-oxide) is large for gas O_2 content ≥ 2% for all rare gas types and cathode voltage. Unlike

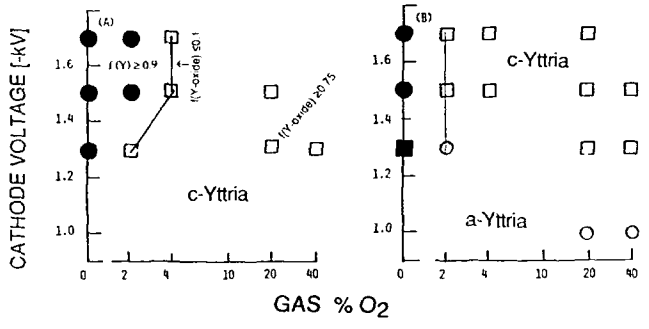
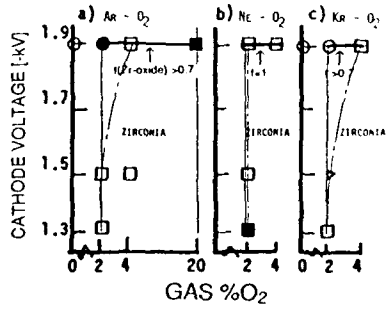


Fig. 3: A phase map for the Y-O system. Rare gas: a) Ar, b) Ne.——O_2*=O_2**.
Phases present: ● -hcp Y and Y(O); □ c-yttria; ■ -a-Y; ○ -a-yttria.

Fig. 4:

A phase map for the Zr-O system.
——O_2*; - - - - - - - O_2**.
Phases present:
○ - Zr and Zr(O); ● - ZrO;
▷ - a-zirconia; □ - m+t-zirconia;
■ - m-zirconia.



yttria formation in the Y-O system, a high Zr-oxide flux to the substrate is not only associated with zirconia formation, but with ZrO and Zr doped with O as well. Furthermore, similar to the Nb-O system, O_2* and O_2** are not always coincident. We proposed [5] that the first oxide to be formed at the target, and sputtered intact, is ZrO (at O_2*). Not until ZrO_2 is formed at the target surface and the target no longer getters all oxygen from the plasma (at O_2**) is ZrO_2 formed in the film.

SUMMARY AND CONCLUSIONS

Phase maps for sputter deposited M-oxides (M=Nb, Y, Zr) in the growth regime of near room temperature, low surface diffusion, and unity sticking coefficient are presented above. We conclude:

1) A high M-oxide fractional flux and oxygen in the plasma available for reaction at the substrate results in high valency oxide growth [niobia, yttria, zirconia].

2) A high M fractional flux and oxygen in the plasma available for reaction at the substrate also produces a high valency oxide, but with possible subtle structural disorder, evidenced by disorder in the joint density of electronic states near the valence and conduction band edges [yttria].

3) A high M-oxide fractional flux but no oxygen in the plasma available for reaction at the substrate results in oxygen-doped metal [Zr(O)] and suboxide [x-niobia, ZrO] growth.

4) A low M-oxide fractional flux and no oxygen in the plasma available for reaction at the substrate results in oxygen-doped metal and suboxide [NbO, NbO_2, Nb-suboxide] growth.

Acknowledgements

This work was supported under US ARO Grant No. DAAL-03-89-K-0022 and by a gift from Johnson Controls, Inc. to the Wisconsin Distinguished Professorship of CRA.

REFERENCES

1. See, for example: M.G. Lagally, Y.-W. Mo, R. Kariotis, B.S. Swartzentruber, and M. B. Webb, in Kinetics of Ordering and Growth at Surfaces (edited by M.G. Lagally, Plenum, NY, NY, 1990) pp. 145-150.
2. C.R. Aita: J. Vac. Sci. Technol., A 3, 625 (1985).
3. R.C. Lee and C.R. Aita, J. Appl. Phys. 70, 2094 (1991).
4. R.C. Lee and C.R. Aita, J. Vac. Sci. Technol. A 10, xxx (1992).
5. C.-K. Kwok and C.R. Aita: J. Vac. Sci. Technol. A 7, 1235 (1989).
6. C.-K. Kwok and C.R. Aita, J. Appl. Phys. 66, 2756 (1989).
7. C.-K. Kwok and C.R. Aita, J. Vac. Sci. Technol. A 8, 3345 (1990).
8. C.-K. Kwok, C.R. Aita, and E. Kolawa, J. Vac. Sci. Technol. A 8, 1330 (1990).
9. C.-K. Kwok, C.R. Aita, and E. Kolawa, J. Appl. Phys. 68, 2945 (1990).
10. C.R. Aita and C.-K. Kwok. J. Am. Ceram. Soc. 73, 3209 (1990).
11. J.E. Greene, J. Vac. Sci. Technol. 15, 1718 (1978).
12. C. Candler, Atomic Spectra and the Vector Model, Van Nostrand, Princeton, NJ, 1964)
13. H.G. Kuhn, Atomic Spectra, (Academic, New York, NY, 1963) pp. 79-83.
14. C.R. Aita and M.E. Marhic, J. Appl. Phys. 52, 6584 (1981).
15. C.R. Aita and M.E. Marhic, J. Vac. Sci. Technol. A 1, 69 (1983).
16. L. Eyring: in Nonstoichiometric Oxides, (edited by. O.T. Sorensen, Academic Press, New York, NY, 1981) pp. 366-372.
17. R.C. Anderson, in High Temperature Oxides (Edited by A.M. Alper, Academic, New York, NY, 1970) Ch. 1.
18. Y. Nigara, Jpn. J. Appl. Phys. 7, 404 (1968).
19. N.T. McDevitt and W.L. Baun, Spectrochima Acta 20, 799 (1964).
20. V.N. Abramov and A.I. Kuznetsov: Soc. Phys. Solid State, 20, 1978, 399.
21. W.-Y. Ching, private communication.
22. H.J. Goldschmidt, *op. cit.* pp. 352-7f.
23. See, for a recent review: M. Ruhle, J. Vac. Sci. Technol. A 3, 749 (1985).

CHEMICAL VAPOR DEPOSITION OF HIGHLY TRANSPARENT AND CONDUCTIVE BORON DOPED ZINC OXIDE THIN FILMS

JIANHUA HU AND ROY G. GORDON
Department of Chemistry, Harvard University, Cambridge, MA 02138

ABSTRACT

Boron doped zinc oxide films have been successfully deposited from a gas mixture of 0.05% diethyl zinc, 2.3% ethanol and various diborane concentrations in the temperature range 300°C to 430°C in an atmospheric pressure chemical vapor deposition reactor. The dopant diborane was found to decrease the film growth rate. The crystallite sizes of doped films were smaller than those of undoped films. Hall coefficient and resistance measurements at room temperatures gave conductivities between 250 and 1700 Ω^{-1}, electron densities between 1.4×10^{20} and 6.7×10^{20} cm^{-3}, and mobilities between 7 and 23 $cm^2/V\text{-}s$. Optical measurements showed that a film with a sheet resistance of 8.8 Ω/square has an average visible absorption of about 8% and maximum infrared reflectance close to 85%. The ratio of conductivity to absorption coefficient is between 0.05 Ω^{-1} and 0.55 Ω^{-1}. The band gap of doped film was widened and followed the Burstein-Moss relation.

INTRODUCTION

Highly conductive and transparent zinc oxide films have recently been studied extensively because of their potential applications in liquid crystal displays, energy-efficient windows and solar cell technology [1-3]. The most common transparent and conductive oxide films in use are indium tin oxide and fluorine doped tin oxide films. The fabrication process of optoelectronic devices such as amorphous silicon solar cells uses plasma-enhanced chemical vapor deposition to deposit an *a*-Si:H film. In this deposition process, the oxide films must be exposed to a hydrogen plasma, which will reduce the oxide to metals, resulting in a loss of transparency in the visible region [4]. This degradation process occurs even at low temperature and low plasma power density [5]. Zinc oxide films, however, are more stable than indium tin oxide and fluorine doped tin oxide films in the presence of a hydrogen plasma [5]. Zinc is also cheaper than indium or tin. Therefore, it may be advantageous to use highly conductive and transparent zinc oxide films rather than indium tin oxide or fluorine doped tin oxide films in the mass production of low cost optoelectronic devices such as photovoltaic cells.

Zinc oxide is an n-type semiconductor and has a band gap about 3.2 eV. Pure zinc oxide film has high visible transmittance and also high resistivity. Although non-stoichiometric zinc oxide films can be made to be both highly transparent and highly conductive, they are not very stable at high temperatures. Doped zinc oxide films, on the other hand, can be made to have very stable electrical and optical properties. Zinc oxide films doped with fluorine [6, 7], boron [8], aluminum [1, 5], gallium [9] and indium [10] have high dc conductivity, high visible transmittance and high infrared reflectance.

The deposition of zinc oxide films has been achieved by metalorganic chemical vapor deposition (MOCVD), rf magnetron sputtering, reactive sputtering, ion beam sputtering, and spray pyrolysis. Metalorganic chemical vapor deposition is especially useful for large scale coatings at high growth rates. The most commonly used organometallic zinc precursors are diethyl zinc (DEZ) [6, 11] and dimethyl zinc (DMZ) [7, 12]. The oxidant can be pure oxygen, water, alcohol or even some oxygen-containing cyclic compound such as tetrahydrofuran. Since the reaction between oxygen and diethyl zinc is fast and the upstream reaction in a flow reactor makes film cover only very small areas, it is impractical to use pure oxygen to react with diethyl zinc to deposit zinc oxide films over large areas. The reaction between diethyl zinc and alcohol depends on the alcohol used and on the deposition temperature; good film coverage on the substrate can be obtained by choosing different alcohols at different deposition temperatures.

In this paper we report the deposition of boron doped zinc oxide films from diethyl zinc, ethanol and diborane in an atmospheric pressure chemical vapor deposition reactor. Also discussed is the influence of the dopant concentration and deposition temperature on the film growth rate, structure, electrical and optical properties.

EXPERIMENTAL

Zinc oxide deposition was carried out in an atmospheric pressure laminar flow rectangular nickel reactor which has been described previously [6]. High purity helium was used as the carrier gas for both diethyl zinc and ethanol. The dopant was 2.2% diborane in high purity helium. Small amounts of water in the ethanol were removed by distillation from magnesium turnings. The DEZ bubbler temperature was maintained at 25°C and the DEZ vapor pressure at this temperature is about 16.1torr. Diborane was mixed with DEZ and this mixture was diluted by helium before flowing into the reactor. The ethanol bubbler was kept in an oven at 50°C to obtain a high vapor pressure of 214 torr. The total gas flow rate was 12.0 l/min through a cross section of 0.6x12.0 cm^2. The reactor was heated from the bottom by a hot plate and its temperature was determined by thermocouples inserted in holes in the side of the reactor. The reactor nozzle was insulated from the heated block by a cold zone of width 3.5 cm and its temperature was maintained at about 150°C lower than that of the central part of the reactor. This cold zone ensures the establishment of laminar flow before the gas reaches the substrate. The soda lime glass substrates were cleaned with a low sodium detergent and then rinsed with deionized water.

The film thickness was determined mainly with an Alpha-Step 200 profilometer and a Metricon PC-2000 prism coupler. The sheet resistance R was measured with a Veeco FPP-100 Four Point Probe. Assuming that the film was homogeneous in the direction perpendicular to the substrate plane, the film bulk resistivity ρ follows the simple relation $\rho=Rt$, where t is the film thickness. To measure Hall coefficients, the film was covered by a Scotch tape 0.5 inch wide and the remainder of the film was etched away by immersing the sample into 4 M hydrochloric acid. The transverse voltage in the presence of a dc current was measured in a constant perpendicular magnetic field by using a Varian V-2300-A electric magnet, which was calibrated by a Gaussmeter to have an intensity of 10.0 kG. The measurement was repeated after reversing the direction of magnetic field. These two measurements usually gave voltages with very similar magnitudes and opposite sign, indicating that the hysteresis effect was negligible. Zinc oxide crystallite sizes were obtained with a JEOL JSM-6400 scanning electron microscope.

The near normal infrared reflectance was measured with a Nicolet Model 7199 Fourier Transform spectrometer with a relative reflection attachment. A gold mirror with a known reflectance was used as the reflectance standard in the wavelength range from 2.0 to 20 μm [13]. The near ultraviolet, visible and near infrared spectra were obtained with a Varian 2390 spectrophotometer using an integrating sphere detector which could measure both the total and diffuse components of the reflectance and transmittance. The reflectance standard was a barium sulphate plate and its reflectance was taken as 100.0% between 0.2 μm and 2.2 μm.

RESULTS AND DISCUSSION

Deposition of doped zinc oxide films was carried out at several temperatures with 0.05% diethyl zinc, 2.3% ethanol and different diborane concentrations. The ethanol concentration of 2.3% was found to give a maximum film growth rate for a diethyl zinc concentration of 0.05%. The film thickness was not uniform along the gas flow direction and there was a peak growth rate on the substrate. The position of the peak growth rate varies with the dopant gas flow and the deposition temperature for constant diethyl zinc and ethanol concentrations. Fig. 1 shows that the peak growth rate decreases with the dopant concentration.

The film growth rate strongly depends on the deposition temperature. Fig. 2 shows that the film peak growth rate first increases with deposition temperature and then becomes constant at temperatures above 400°C. The constant peak growth rate at high temperature indicates that the gas

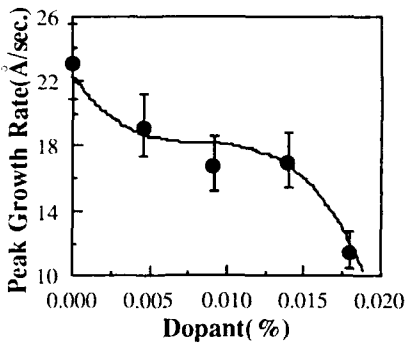


Fig. 1. Peak growth rate dependence on the dopant concentration (DEZ, 0.05%; ethanol, 2.3%; T=375°C).

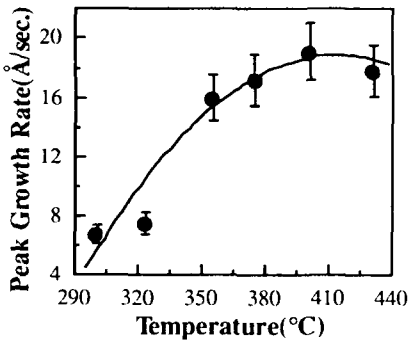


Fig. 2. Peak growth rate dependence on the deposition temperature (DEZ, 0.05%; ethanol, 2.3%; diborane, 0.014%).

phase reactions are fast and the growth rate is controlled by the diffusion of the film precursors to the substrate.

The film morphology and crystallite sizes were determined by scanning electron microscopy (SEM). Fig. 3 A shows the electron micrograph of an undoped zinc oxide sample deposited at 355°C. It has a thickness of 0.64 μm and is composed of disklike structures with disk diameters between 200 nm and 800 nm. Fig. 3 B shows the corresponding electron micrograph of a doped sample deposited by introducing 0.014% diborane into the gas phase. The doped film with a thickness of 0.77 μm has crystallite sizes about 100 nm. The dopant reduces the crystallite sizes.

The crystallite sizes also depend on the temperature and the film thickness. The film deposited at 375°C from 0.05% diethyl zinc, 2.3% ethanol and 0.014% diborane with a thickness of 225 nm has crystallite sizes below 100 nm. The film deposited with the same conditions but with a thickness of 995 nm has crystallite sizes of about 150 nm. Increasing the deposition temperature usually increases the crystallite sizes and changes the film morphology.

Boron is an n-type dopant for zinc oxide. A boron atom replaces a zinc atom in the crystallite or occupies an interstitial position. The electron density calculated from the measured Hall coefficient increases with dopant concentration. Fig. 4. shows the electron density dependence on the dopant concentration. The electron density first increases rapidly with diborane concentration and then levels off at high diborane concentrations. The dependence of film conductivity σ and mobility μ on the dopant concentration is given in Fig. 5.

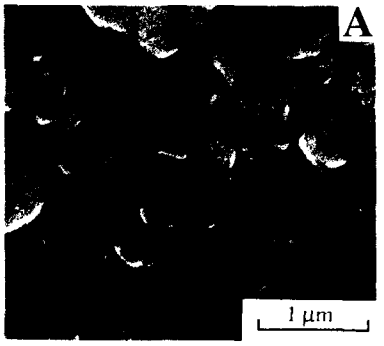


Fig. 3A. Electron micrograph of an undoped zinc oxide film (DEZ, 0.05%; ethanol, 2.3%; T=355°C).



Fig. 3B. Electron micrograph of a doped ZnO film (DEZ, 0.05%; ethanol, 2.3%; diborane, 0.014%; T=355°C).

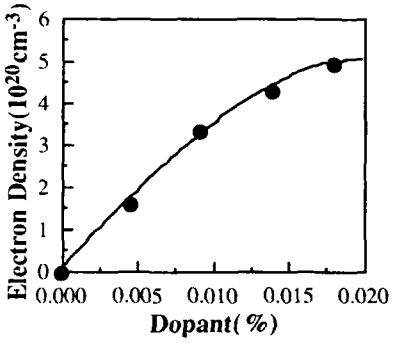


Fig. 4. Electron density dependence on the dopant concentration (DEZ, 0.05%; ethanol, 2.3%; T=375°C).

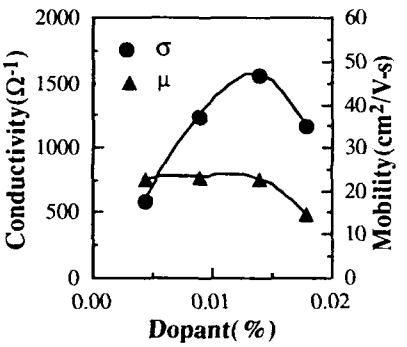


Fig. 5. Conductivity and mobility dependence on the dopant concentration (DEZ, 0.05%; ethanol, 2.3%; T=375°C).

The films are the same as those used in Fig. 4. According to Drude theory [14], the conductivity σ is proportional to the free electron density N_e following the relation $\sigma=(N_e e^2)/(m^*\gamma)$, where e is the electron charge, m* is the effective mass of the conduction electrons, and γ is the scattering frequency. The Hall mobility μ_H is related to the scattering frequency γ by $\mu_H=e/(m^*\gamma)$. Grain boundary scattering is determined by the size of the crystallites. Impurity scattering, on the other hand, increases with dopant concentration. In the low dopant concentration range, the important contribution to scattering comes from grain boundary scattering, which is the same for films with the same crystallite sizes. The film mobility is therefore independent of dopant concentration. Since the electron density increases with dopant concentration, the film conductivity increases with dopant concentration. In the high dopant concentration range, the role of impurity scattering exceeds that of grain boundary scattering. The increase in the electron density can not compensate for the increase in the impurity scattering frequency. Therefore, the conductivity and mobility both decrease at high dopant concentrations.

The dependence of film conductivity and mobility on film thickness is shown in Fig. 6. Both conductivity and mobility first increase rapidly with film thickness and then become constant. When the films are very thin, the crystallite sizes are small and grain boundary scattering is dominant, limiting film conductivity and mobility. As the films become thicker, the influence from grain boundary scattering decreases and impurity scattering is the main factor limiting film mobility

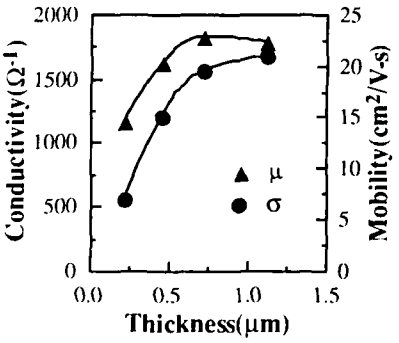


Fig. 6. Conductivity and mobility dependence on the film thickness (DEZ, 0.05%; ethanol, 2.3%; diborane, 0.014%; T=375°C).

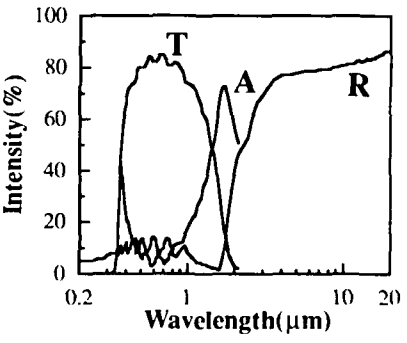


Fig. 7. Reflectance, transmittance and Absorbance of a ZnO:B sample (DEZ, 0.05%; ethanol, 2.3%; diborane, 0.014%; T=375°C).

Table I. Film deposition temperature T_d, thickness t, electron density N_e, conductivity σ, electron mobility μ, band gap E_g and Figure of Merit FM. The diethyl zinc, ethanol and diborane concentrations in the gas phase are 0.05%, 2.3% and 0.014%, respectively.

Sample	T_d ℃	t μm	N_e $10^{20}cm^{-3}$	σ $(\Omega cm)^{-1}$	μ $cm^2/V\text{-}s$	E_g eV	FM Ω^{-1}
2257	300	0.60	1.4	253	11	3.40	0.06
2254	325	0.53	3.9	751	12	3.46	0.20
2252	355	0.77	3.3	1063	20	3.45	0.40
2260	375	0.72	4.3	1563	23	3.55	0.53
2266	400	0.69	5.4	1698	20	3.64	0.54
2267	430	0.64	6.7	1366	13	3.70	0.41

and conductivity. Therefore, for film with thickness above 0.8 μm, its conductivity and mobility will not vary with its thickness.

The electron density, conductivity and mobility dependence on the deposition temperature are given in Table I. The electron density increases with deposition temperature, indicating more electronically active boron atoms were incorporated into the film. Therefore, the ionized impurity scattering is more important for films deposited at higher temperatures than for those deposited at lower temperatures. However, higher deposition temperature also leads to larger crystallite sizes and therefore less grain boundary scattering. In the low temperature range, grain boundary scattering is dominant over ionized impurity scattering, and the film mobility and conductivity increase with deposition temperature. At high temperatures, ionized impurity scattering is more important than grain boundary scattering. The increase of the electron density with temperature can not compensate for the increase of the scattering, and so the conductivity and mobility both decrease at temperatures above 400°C.

The film's optical properties were modified by doping. The doped films behave like metals in the infrared and have high reflectance. In the visible region, the doped films behave like dielectrics and have high transmittance. The transition between these behaviors is at the plasma wavelength, which moves to a shorter wavelength as the electron density in the film increases. The undoped films usually have their plasma wavelengths in the infrared; while the boron doped films have their plasma wavelengths in the near infrared. Fig. 7 shows the reflectance, transmittance and absorbance of a boron doped zinc oxide sample. The film has a thickness of 0.72 μm, electron density of $4.3x10^{20}$ cm^{-3}, mobility of 23 $cm^2/V\text{-}s$, plasma wavelength of about 1.55 μm, maximum infrared reflectance of 85%, and average visible absorption of 8%.

The performance of doped zinc oxide films as transparent conductors may be ranked by a quantity called the Figure of Merit which is the ratio of film conductivity σ to average visible absorption coefficient α, $\sigma/\alpha=-1/(R\ln T)$, where R is the sheet resistance in Ω/square, T is the

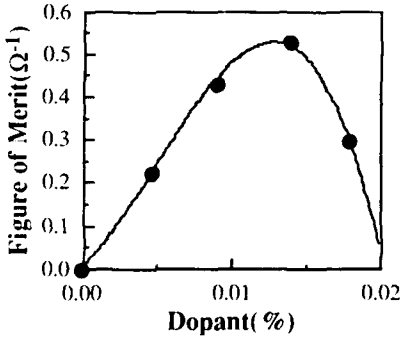


Fig. 8. Figure of Merit dependence on the dopant concentration (DEZ, 0.05%; ethanol, 2.3%; T=375°C).

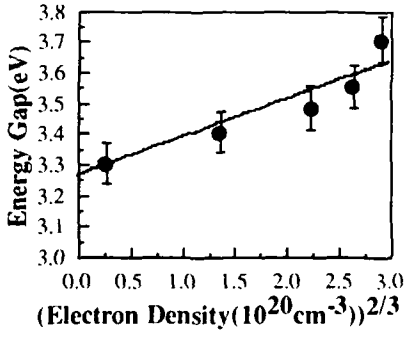


Fig. 9. Band gap as a function of $Ne^{2/3}$ for films deposited with different diborane concentrations (DEZ, 0.05%; ethanol, 2.3%; T=375°C).

average fractional visible transmittance. Fig. 8. shows that the Figure of Merit first increases with dopant concentration and then decreases at high dopant concentrations. Table I shows that the Figure of Merit dependence on the deposition temperature.

The optical absorption coefficient α of a direct band gap semiconductor near the absorption edge, for photon energy hv greater than the band gap energy E_g of the semiconductor, is given by $\alpha = A(hv - E_g)^{1/2}$ [14], where A is a constant. In heavily doped zinc oxide films, the lowest states in the conduction band are occupied by free electrons and so the valence electrons require more energy to be excited to higher energy states in the conduction band. Therefore, the band gaps of doped zinc oxide films are wider than those of undoped zinc oxide films. The Burstein-Moss theory predicates that the band gap widening is proportional to $N_e^{2/3}$, where N_e is the electron density. Fig. 9. gives the band gap as a function of $N_e^{2/3}$ for films deposited at 375°C.

CONCLUSIONS

Boron doped zinc oxide films have been successfully deposited from diethyl zinc, ethanol and diborane in the temperature range 300°C to 430°C in an atmospheric pressure chemical vapor deposition reactor. The films were crystalline, and the crystallite sizes depended on the deposition temperature, dopant concentration and film thickness. The resistance and Hall coefficient measurements showed that the films have high conductivity, high electron density and high mobility. The optical measurements showed that the films are highly transparent in the visible and highly reflectant in the infrared. The band gap of the film increases with electron density and approximately follows the Burstein-Moss relation.

ACKNOWLEDGEMENTS

This work was supported by Solar Energy Research Institute (now the National Renewable Energy Laboratory). Instruments of Harvard University Materials Research Laboratory, supported by the National Science Foundation, were also used. We would like to thank Yuan Z. Lu and David Carter for their assistance in some film characterizations. The Watkins-Johnson Company donated the gas dispersion nozzle.

REFERENCES

1. Z.-C. Jin, I. Hamberg, and C. G. Granqvist, J. Appl. Phys. 64, 5117 (1988).
2. R. E. I. Schropp and A. Madan, J. Appl. Phys. 66, 2027 (1989).
3. J. B. Yoo, A. L. Fahrenbruch, and R. H. Bube, J. Appl. Phys. 68, 4694 (1990).
4. R. Banerjee, S. Ray, N. Basu, A. K. Batabyal, and A. K. Barua, J. Appl. Phys. 62, 912 (1987).
5. T. Minami, H. Sato, H. Nanto, and S. Takata, Thin Solid Films 176, 277 (1989).
6. J. Hu and R. G. Gordon, Solar Cells 30, 437 (1991).
7. J. Hu and R. G. Gordon, Mater. Res. Soc. Symp. Proc. 202, 457 (1991).
8. W. W. Wenas, A. Yamada, M. Konagai, and K. Takahashi, Jpn. J. Appl. Phys. 30, 1441 (1991).
9. B. H. Choi, H. B. Im, J. S. Song and K. H. Yoon, Thin Solid Films 194, 712 (1990).
10. S. N. Qiu, C. X. Qiu and I. Shih, Solar Energy Mater. 15, 261 (1987).
11. S. Oda, H. Tokunaga, N. Kitajima, J. Hanna, I. Shimizu, and H. Kokado, Jpn. J. Appl. Phys. 24, 1607 (1985).
12. F. T. J. Smith, Appl. Phys. Lett. 43, 1108 (1983).
13. D. A. Strickler, Ph. D. thesis, Harvard University, 1989.
14. I. Hamberg and C. G. Granqvist, J. Appl. Phys. 60, R123 (1986).

ZnO ON Si_3N_4 BIMORPHS WITH LARGE DEFLECTIONS

WAI-SHING CHOI AND JAN G. SMITS
Sensors, Actuators and Micromechanics Laboratories, Boston University, 44 Cummington Street, Boston MA 02215

ABSTRACT

Piezoelectric bimorphs and piezoelectric strain sensors based on sputtered ZnO films were fabricated on Si_3N_4 cantilever beams to form tactile sensors. The sensors were used to determine object positions. Deflections of the bimorphs showed a quadratic dependence on the applied voltages. Deflection as large as 1166 μm were registered for a bimorph of 2980 μm long. The apparent d_{31} of ZnO under a bias of -4 volts was - 103×10^{-12} m/V, which was approximately 20 times larger than the previously reported values of -5.12×10^{-12} m/V. The large deflections of the bimorphs were due to the quadratic effect under strong electric field.

INTRODUCTION

The design of a tactile sensor combines the functions of piezoelectric bimorphs and piezoelectric strain sensors. Piezoelectric bimorphs were first reported by C. Baldwin Sawyer [1]. They were made by joining two pieces of piezoelectric elements together to form a composite cantilever beam. However, the actuation function of the homogeneous piezoelectric bimorph can be realized by a heterogeneous piezoelectric bimorph, which is constructed by depositing a single layer of piezoelectric material on a layer of non-piezoelectric material. The response of such heterogeneous bimorphs has been investigated by Steel et al. [2] and Smits et al. [3]. Numerous applications of heterogeneous bimorphs using piezoelectric materials such as PLZT, PZT, PVF and ZnO had been reported. The applications include telephone receivers [4], thickness extensional mode resonators [5], PI_FET accelerometers [6], resonant diaphragm pressure sensors [7], resonant force sensors [8], monolithic band-pass filters made of cantilevers [9], dampers in vibration control of beams [10 - 13] and regulators of vibration modes of rectangular plates to control sound radiation [14]. Circular bimorphs are used in integrated micropumps built on silicon wafers [15].

FABRICATION

A (100) Si wafer is oxidized in dry oxygen at 1150°C to obtain 0.5 μm of masking oxide. By means of photolithography, an array of 3.11 mm x 0.96 mm rectangular windows are patterned onto the wafer. SiO_2 inside the windows is then etched away in Buffered Oxide Etch (BOE). A sacrificial layer of Zinc Oxide (ZnO) of 1.0 μm thick is deposited onto the wafer by magnetron sputtering. The ZnO film outside the rectangular windows is etched away in a mixture of Phosphoric acid, Acetic acid and water (1:50:50). A layer of Si_3N_4 of 1 μm thick is then sputtered onto the wafer. A layer of Chromium-Gold is evaporated on top of the Si_3N_4 to define the bottom electrodes. Piezoelectric ZnO of 1 μm thick is then sputtered and patterned on top of the bottom electrodes. A second layer of Chromium-Gold is evaporated onto the wafer to define the top electrodes. This step completes the construction of the critical components of the tactile sensor. The device

Mat. Res. Soc. Symp. Proc. Vol. 242. ©1992 Materials Research Society

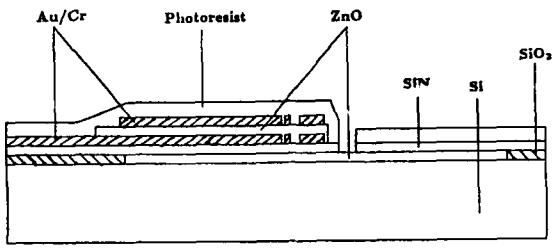


Figure 1. Cross-section of the bimorph with the moat opened to expose the sacrificial ZnO for the final etching.

is now ready to be etched free. Photoresist is spin-coated onto the wafer and patterned with a mask that exposes the necessary areas of the Si_3N_4 needed to be etched in order to reveal the cantilever beam structure of the device. The Si_3N_4 is etched in BOE until the sacrificial ZnO is reached, as shown in Figure 1. With the same photoresist still in position, the sacrificial ZnO underneath the Si_3N_4 is etched in a mixture of Acetic acid, Phosphoric acid and water till the cantilever beams are free from the Si substrate.

RESULTS

Sensors were successfully fabricated on three Si wafers, and around a hundred of them were produced. Half of the fabricated devices were 2980 μm long, while the other half were 1688 μm long. The cantilever beams all curved upwards. The curvature was due to the mismatch of thermal expansion coefficients between the materials, and the existence of residual stresses in the sputtered films. A SEM picture of the cross-section of the bimorph is shown in Figure 2.

DEVICE CHARACTERIZATION

Around thirty of the tactile sensors were tested under a probe station, which is equipped with a 30× optical microscope and a reticle with a resolution of 33.3 μm per unit on the eye-piece. A DC voltage was applied across bender electrode areas via the bonding pads. In order to observe any hysteresis effects, the bending voltage was applied in a particular sequence. The bending voltage was lowered first from 0 V to -6.5 V uni-directionally with small increments. From -6.5 V, the voltage was raised uni-directionally back to 0 V. From 0 V, the voltage was increased to 6.5 V and then decreased back to 0V. All the devices tested behaved in a similar fashion.

The position of the free tip of the sensor was read off from the reticle at the input voltages. The deflection of the free end due to an input voltage was obtained as the difference between the position of the free end at the input voltage and the initial position at zero input voltage.

DISCUSSION

The result of the deflection versus DC voltage of a typical bimorph is presented in Figure 3.

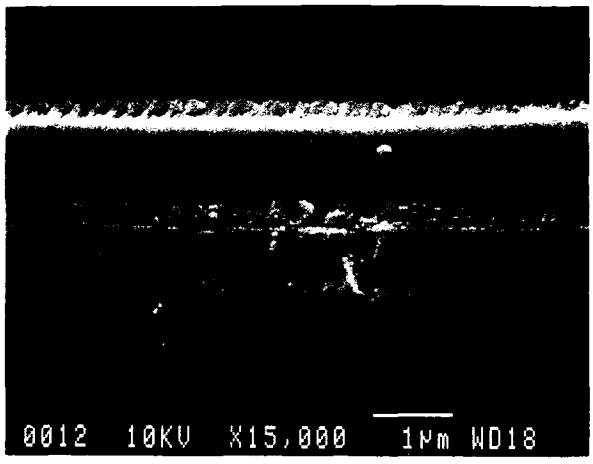


Figure 2. A SEM picture showing the cross-section of the bimorph. The layer with a granular under-surface is the sputtered Si_3N_4 film, which is about 1 μm thick. On top of the Si_3N_4 film are layers of Cr/Au of 0.5 μm, sputtered ZnO of 1 μm thick and Cr/Au of 0.2 μm thick.

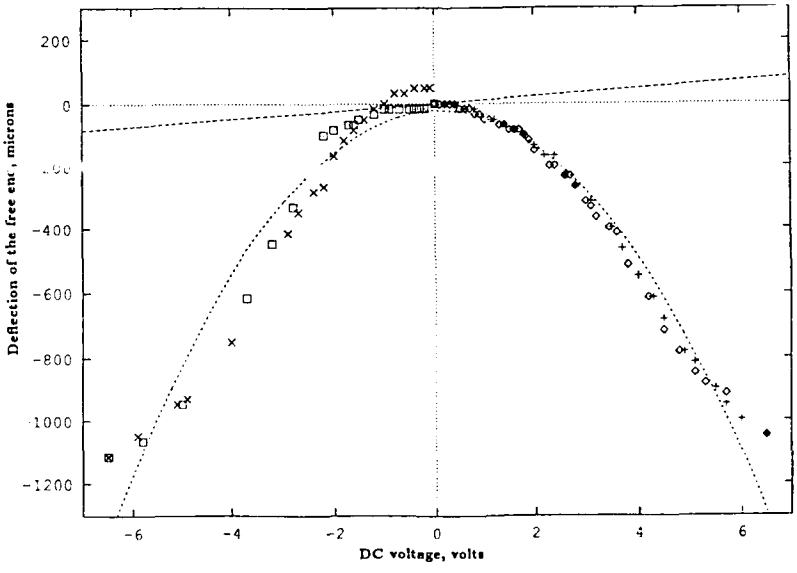


Figure 3. Deflection of the free end as a function of the DC bending voltage.

The parabolic shape of the plot indicated that the heterogeneous bimorph responded strongly to the amplitude, but not the polarity, of the applied voltages. We could divide the deflection dependence on voltage amplitudes into two regions : from 0 V to 1.7 V, a weak-field region and from 1.7 V to 6.6 V, a strong-field region. Saturation in deflection was observed at voltage amplitude above 6 V.

Smits and Choi [3] had derived the constituent equations for a heterogeneous bimorph, in which the deflection of the bimorph due to an external voltage was given as

$$\delta = \frac{3d_{31}ABL^2}{K}V \tag{1}$$

where

$$A = s_{11}^{si}s_{11}^{p}(s_{11}^{p}h_{si} + s_{11}^{si}h_p) \qquad B = \frac{h_{si}(h_{si} + h_p)}{(s_{11}^{p}h_{si} + s_{11}^{si}h_p)}$$

$$\begin{aligned} K = {} & (s_{11}^{si})^2(hp)^4 + 4s_{11}^{si}s_{11}^{p}h_{si}(h_p)^3 \\ & + 6s_{11}^{si}s_{11}^{p}(h_{si})^2(h_p)^2 + 4s_{11}^{si}s_{11}^{p}h_p(h_{si})^3 \\ & + (s_{11}^{p})^2(h_{si})^4 \end{aligned}$$

s_{11}^{si} and s_{11}^{p} are the elastic compliances of the Si_3N_4 and ZnO respectively, and h_{si} and h_p are the thickness of Si_3N_4 and ZnO respectively. d_{31} is the piezoelectric constant of ZnO and L is the length of the bender.

For the tactile sensor under testing, h_{si}, h_p, s_{11}^{si}, s_{11}^{p}, L and d_{31} assume respectively the following values: 1.0 μm, 1.0 μm, 17.8×10^{-12} m^2/N [16], 8.1×10^{-12} m^2/N [17], 2583 μm and -5.12×10^{-12} m/V [18]. Using these values, the deflection according (1) becomes

$$\delta(V) = 12 \times 10^{-6}\,V \tag{2}$$

Equation (2) is plotted in Figure 3 as the dotted line through the origin. The piezoelectric effect represented by this line is not sufficient to explain the measured data. The best straight line through the data points in the left branch gives a slope value of 243 μm/V at a bias of -4V. The value of the slope implies that an 'effective' piezoelectric coefficient d_{31}^{eff} can be found as -103.7×10^{-12} m/V, which is around 20 times larger than the previously reported value of -5.12×10^{-12} m/V.

A least-squares fit is performed to the data in Figure 3 with a second order polynomial in V, and the following coefficients from the fitting are obtained

$$\delta(V) = -21.255 \times 10^{-6} + 6.377 \times 10^{-6}V - 30.933 \times 10^{-6}V^2 \tag{3}$$

From equation (3), it is observed that the second order term has a more dominant effect on the deflections of the bimorph than the linear piezoelectric term. Such strong quadratic dependence on voltage suggests that the electrostrictive effect, which is a quadratic function of the electric field, is responsible for the deflections in the high field regions. Electrostrictive effects which occur under high electric field, had been reported in piezoelectric ceramics by Mason [19].

CONCLUSION

ZnO on Si_3N_4 bimorphs were fabricated as the actuation components of the tactile sensors. Deflections of the bimorph in the range of 1000 μm can be achieved with a voltage of 6V. Deflections of the bimorphs were observed to have a strong square dependence on the applied voltage. An effective d_{31} of 103×10^{-12} was found for the ZnO films. The large deflections were due to the contribution from electrostriction. This was the first time that a large effective piezoelectric coefficient as a result of biasing into the electrostrictive regime was reported in piezoelectric ZnO films.

REFERENCES

[1] C. B. Sawyer, Proceedings Institute of Radio Engineers 19 (11), 2020-2029 (Nov 1931).

[2] M. R. Steel, F. Harrison and P. G. Harper, J. Phys. D: Appl. Phys. 11, 979-989 (1978).

[3] J. G. Smits and W. Choi, IEEE Transactions on Ultrasonics, Ferroelectrics, and Frequency Control, 38 (3), 256-270 (1991).

[4] W. J. Denkmann, R. E. Nickell, and D. C. Stickler, IEEE Transactions on Audio and Electroacoustics AU-21 (4), 317-324 (1973).

[5] K. Nakamura,H. Sasaki,and H. Shimizu, Electronics Letters 17 (14), 507-509 (1981)

[6] P. L. Chen, R. S. Muller, R. D. Jolly, G. L. Halac, R. M. White, A. P. Andrews, T. C. Lim, and M. E. Motamedi, IEEE Transactions on Electron Devices, ED-29 (1), 27-33 (1982).

[7] J. G. Smits, in Proceedings of the Symposium on Force, Displacement, Pressure and Flow Sensors, 135-151 (Sep. 1982).

[8] F. R. Blom, Ph.D. Thesis, Twente University, 1989.

[9] A. P. Andrews, United States Patent No. 4 517 486 (14 May 1985).

[10] T. Bailey and J. E. Hubbard Jr., J. Guidance 8 (5), 605-611 (1985).

[11] D. Ricketts, J. Acoust. Soc. Am. 80 (3), 723-726 (1986).

[12] A. Baz and S. Poh, J. Sound and Vibration 126 (2), 327-343 (1988).

[13] H. S. Tzou and M. Gadre, AIAA 26 (8), 1014-1017 (1988).

[14] C. R. Fuller, C. H. Hansen and S. D. Snyder, Journal of Sound and Vibration 150 (2), 179-190 (1991).

[15] J. G. Smits, Sensors and Actuators A21 – 23, pp.203-206 (1990).

[16] C. T. Lynch, Practical Handbook of Materials Science (CRC Press, Inc., 1989), pp. 321-322.

[17] M. J. Weber, Handbook of Laser Science and Technolgy IV, part 2, (CRC Press Inc., 1986), pp. 64-65.

[18] K. H. Hellwege and A. M. Hellwege, Landolt – Börnstein, Vol. 11 – III (Springer-Verlag Berlin-Heidelberg, Germany, 1979). p.370.

[19] W. P. Mason, Physical Review 74 (9), pp. 1134-1147 (1948).

INFLUENCE OF SUBSTRATE TEMPERATURE ON TIN OXIDE THIN FILMS DEPOSITED BY ELECTRON BEAM EVAPORATION TECHNIQUE

S.M. Rozati, S. Mirzapour, M.G.Takwale, B.R.Marathe and V.G. Bhide

School of Energy Studies, Department of Physics, University of Poona, Pune 411 007, India.

Abstract

Transparent conducting tin oxide films were prepared by an electron beam evaporation technique. As-deposited films were amorphous or polycrystalline depending on the substrate temperature and the time of deposition. In order to get transparent and conducting thin films of SnO_2, as-deposited films were subjected to further heat-treatment in air at 650^oC for 2 hours. Physical properties of as-deposited and annealed films are discussed with reference to substrate temperature and deposition time.

1. Introduction

SnO_2 thin films have received high technological importance because of their electrical, optical and structural properties. These films are extensively used as solar cell windows [1], heat-mirrors [2], sensors [3] etc. Different deposition techniques, namely sputtering [4], spray pyrolysis [5], chemical vapour deposition [6], evaporation [7] etc. are used for deposition of these films. SnO_2 thin films in this work, have been prepared by evaporation of high purity SnO_2 pellets on Corning 7059 glass substrate. SnO_2 molecules decompose in the gaseous state when heated in a vacuum and deposit as amorphous structure or suboxides depending on substrate temperature and time of deposition. The suboxides are oxygen deficient Sn-O films formed by partial loss of oxygen during evaporation. In order to get transparent and conducting films of SnO_2, post-deposition heat-treatment in air at 650^oC for 2 hours has been performed. It is observed that the physical properties of these films depend strongly on substrate temperature, time of deposition and annealing treatment. The properties of SnO_2 thin films can be varied by changing process parameters of the deposition technique [8].

2. Experimental

The experimental set-up for the deposition of the films consists of a stainless steel vacuum chamber connected to an oil diffusion pump with LN_2 trap. The vacuum system is able

to evacuate the chamber to a pressure of 10^{-6} Torr. The electron beam gun is basically a diode having a cathode in the form of a filament and a grounded anode. SnO_2 powder (supplied by Aldrich) was pressed into pellets and evaporated using an electron beam with a power of 3 KW. The pellets were initialy degassed with the shutter closed for about 10 minutes by applying a low power electron beam. The distance between the gun and the substrate holder was kept around 18 cm. As-deposited and annealed films were studied by using grazing angle X-ray diffractometer (Rigaku, $Ru_{200}B$), Hitachi optical spectrophotometer and Hall coefficient measuring equipment. Hall measurement has been carried out at room temperature using van der Pauw geometry.

3. Results and Discussion

A) Effect of Substrate Temperature on Hall Mobility :

Fig.(1) shows the variation in n, μ and resistivity with substrate temperature. There is a decrease in mobility (μ) as the substrate temperature is increased from 50°C to 200°C. Above 200°C there is a higher increase in the mobility. The orientation of the films deposited at different substrate temperatures is shown in Fig.2. The low value of mobility appears to be due to the presence of [110] orientation. This [110] orientation has trap density of 9.4×10^{14} Sn at./cm^2 [9], while [101] orientation has trap density of 2.54×10^{14} Sn at./cm^2 [10]. The lesser trap density along [101] orientation appears to be responsible for the higher value of mobility for [101] oriented films (see Fig.2).

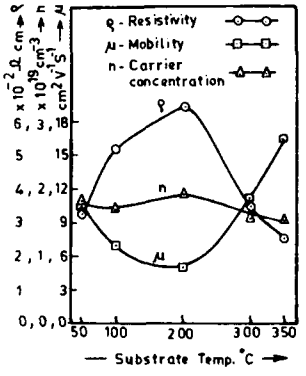


Fig.1. Variation of resistivity carrier concentration & mobility with substrate temperature.

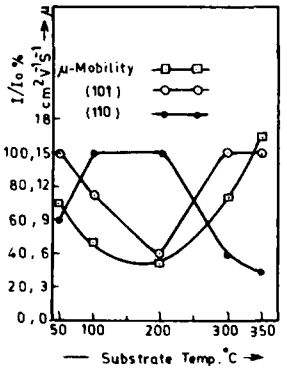


Fig.2. The variation of mobility and (I/I_o) for planes (101) & (110) with substrate temp.

B) The Effect of Time of Deposition on SnO_2 Films :

Fig. 3(a-c) shows the XRD patterns of as-deposited SnO_2 films deposited at different duration of time at a deposition rate of 2 A^o/S. All depositions were performed at substrate temperature of 350°C. Fig. 3(a) shows an amorphous structure for as-deposited SnO_2 films deposited for 10 minutes, while XRD patterns 3(b) and 3(c) are for polycrystalline suboxides of SnO_2 films deposited for 20 and 30 minutes respectively. The extension of the deposition time helps the transition of amorphous to polycrystalline structure. Fig.(4) shows XRD patterns of the same films (as in Fig.3) after post-deposition heat-treatment, viz. 650°C for 2 hours in air. This heat-treatment was carried out to improve the transparency of the films. The high conductivity of undoped SnO_2 films has been attributed to oxygen vacancies [10]. Fig. 4(b) and 4(c) show the complete transformation of as-deposited films to SnO_2 structure.

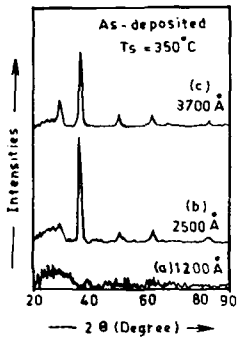


Fig.3. As deposited films of SnO_2
a) 10 minutes
b) 20 minutes
c) 30 minutes

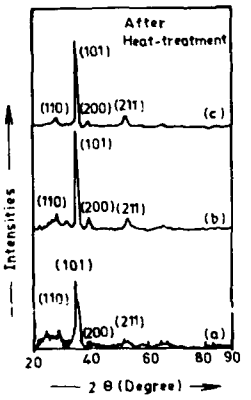


Fig.4. Post deposition heat treatment of SnO_2
a) 10 minutes
b) 20 minutes
c) 30 minutes

C) Optical Properties :

Fig. (5) shows tne room temperature transmission curve of as-deposited and annealed samples of tin oxide thin films deposited at 350°C for 20 minutes at a rate of 2A^o/S. As shown in Fig.(6), the square of absorption coefficient was found to be linearly proportional to photon energy, which suggests that direct allowed transition occurs in this film [11]. From the dependence of the absorption coefficient on photon energy and extrapolating the linear region to zero, the band gap was found to be 2.57 eV before annealing and 3.42 eV after annealing.

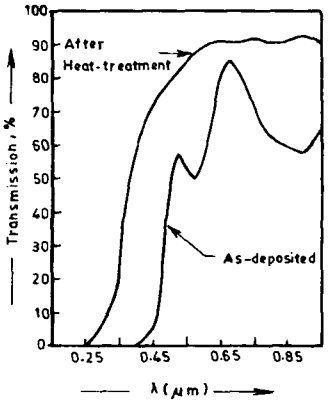


Fig.5. Spectral transmittance of as-deposited and air annealed films of SnO_2 deposited at 350°C

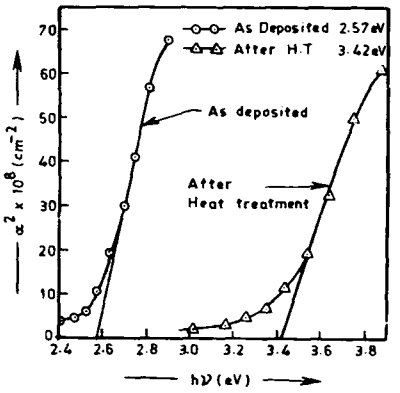


Fig.6. Squred of absorption coefficient for as-deposited and heat-treated films.

4. CONCLUSION

In this work, it is observed that in order to get better physical properties of SnO_2, such as better structure one should extend the deposition time. Lower deposition time results in amorphous films. The films become polycrystalline when deposition time is increased. However, these films have only SnO phase. After annealing at 650°C for 2 hours, the SnO phase changes to SnO_2. It is also observed that films which are oriented along [101] show better electrical properties. Subsequently films of random orientation having trap density of 9.4×10^{14} Sn at/cm^2, show lower mobility and higher resistivity. It is also observed that the band gap of as-deposited films increases by subsequent heat treatment from a value of 2.57 eV to 3.42 eV resulting in high visible transparency.

ACKNOWLEDGEMENTS

This work was supported by Department of Science and technology and Department of Non-Conventional Energy Sources of Government of India. We would like to express our heartly thanks to Dr. S.M. Choudhary and Mr. Gulab Chavan for their help in XRD spectrophotometer and thickness measurements.

REFERENCES

1. S. Ray, J. Dutta, A.K. Barua, S.K. Deb, Thin Solid Films 119, 201 (1991).
2. C.M. Lampert, Sol. Energy Mat. 6, 1 (1981).
3. Y.K. Fang and J.J. Lee, Thin Solid Films, 169, 51 (1989).
4. B. Stjerna and C.G. Granqvist, Sol. Energy Mat. 20, 225 (1990).
5. S. Mirzapour, S.M. Rozati, M.G.Takwale, B.R.Marathe and V.G.Bhide, J. of Mat er. lett. (To be published)
6. T. Maruyama and K. Fukui, Thin Solid Films 203, 297 (1991).
7. I. Hamberg and C.G. Granqvist, J. Appl. Phys. 60, R123 (1986).
8. V. Vasu and A. Subrahmanyam, Thin Solid Films 202, 283 (1991).
9. D. Belanger, J.P. Dodelet, B.A. Lombos, J.I. Dickson, J. of Elec. Chem. Soc. 132, 1398 (1985).
10. C. Agashe, M.G. Takwale, B.R. Marathe and V.G.Bhide, J. of Mat. Sci. 24, 2628 (1989).
11. R.L. Weiher and R.P. Ley, J. of Appl. Phys. 37, 299 (1966).

NANOMETER SIZE LEAD IODIDE PARTICLES

VIVEK MEHROTRA, ERIC RODEGHIERO, JENS W. OTTO AND EMMANUEL P. GIANNELIS, Department of Materials Science and Engineering, Cornell University, Ithaca, NY 14853.

ABSTRACT

Nanometer size lead iodide particles have been synthesized in the porous network of a cross-linked polymer matrix. The optical band gap of the nanocrystals is shifted towards higher energy as compared to the bulk value. This shift is attributed to the quantum size effect on excitons. Intercalation with aniline leads to a further shift in the band gap which depends on the dipole moment of the intercalated guest species. Differential scanning calorimetry and high temperature x-ray diffraction have been used to analyze the ferroelectric transition in PbI_2.

INTRODUCTION

Semiconductor nanocrystallites (or quantum dots) are a subject of extensive research [1-5]. These efforts are directed towards an understanding of the effect of size and dimension on the electronic and optical properties of materials. Size quantization effects occur when the Bohr radius of the exciton (or electron) is comparable to the crystallite dimensions and leads to new phenomena and applications. For example, a shift in interband absorption or luminescence peak, and a non-linear optical effect are a manifestation of the quantum size effect in semiconducting nanocrystals. The non-linear optical effects have potential applications in ultrafast optical devices. Effective-mass models and empirical pseudopotential methods have been employed to explain these effects [5].

Lead iodide (PbI_2) is a direct band gap semiconductor and has a layered lattice structure. Its use has been demonstrated in holography, photocapacitive devices, and radiation detection [6,7]. Recently, it has been shown that PbI_2 exhibits ferroelectricity with a Curie temperature of about 573 K [8]. The combination of semiconducting and ferroelectric properties raise the possibility of photoferroelectric phenomena in PbI_2. Furthermore, PbI_2 nanocrystallites offer an opportunity to study the effect of particle size on the ferroelectric phase transition. Small ferroelectric particles are expected to show different dielectric properties as compared to bulk crystals [9,10].

The structural repeat unit in PbI_2 consists of three planes of strongly bonded atoms: a plane of lead atoms sandwiched between two layers of iodine atoms. These structural units are separated by weak van der Waals forces. As a result, foreign guest species can be introduced (intercalated) within the van der Waals gap. This leads to an expansion of the unit cell, depending on the size of the guest molecules. In addition, the properties of the intercalated material are dramatically

Mat. Res. Soc. Symp. Proc. Vol. 242. © 1992 Materials Research Society

altered. For example, it was recently shown that the optical band gap of PbI_2 thin film shifts by about 0.5 eV upon intercalation with aniline ($C_6H_5NH_2$) and the shift depends on the dipole moment of the intercalated guest species [11].

In this paper, we report a new approach for the synthesis of nanometer size lead iodide particles in the pores of a polymer matrix. This technique was recently used for the preparation of nanometer size magnetic particles [12]. The optical band gap of PbI_2 is blue shifted due to small particle size. Intercalation with aniline leads to a further shift in the band gap. Thus, the optical band gap of PbI_2 can be fine-tuned by varying the size of the nanocrystals and by a proper choice of the guest molecule. Preliminary results on the effect of particle size on the ferroelectric transition are also discussed.

The polymer matrix used is a strongly acidic, cation-exchange resin containing sulfonate functional groups. It consists of cross-linked sulfonated polystyrene divinyl benzene matrix leading to a porous network. The degree of cross-linking determines the exchange capacity and the porosity of the resin. We used 50X8-200 resin (Dowex®) which is composed of an 8% cross-linked matrix yielding a medium porosity. The resin exists in the form of uniform spherical beads, approximately 150 μm in diameter.

EXPERIMENTAL

The synthesis steps are similar to those described in reference 12. The washed beads were exposed to an aqueous solution of lead nitrate for about three hours followed by thorough washings to remove any excess physisorbed lead ions. During this treatment, two protons were exchanged for one Pb^{2+}. The Pb^{2+}-exchanged beads were then exposed to an aqueous solution of sodium iodide. The product was finally washed with deionized water and dried at 60°C. Intercalation of nanoscale PbI_2 particles with aniline was achieved by exposing the nanocomposite beads to aniline vapors in an evacuated chamber ($\approx 10^{-2}$ Torr).

X-ray diffraction patterns were obtained using a Scintag diffractometer (CuKα radiation). A high temperature attachment, operating in a dynamic vacuum of 10^{-2} Torr, was used to perform x-ray diffraction as a function of temperature. Transmission electron micrographs were obtained on JEOL 1200EX (at 120kV). A microtome was used to prepare thin specimens. A heating/cooling rate of 20°C/min was used in the DSC scans.

Optical transmission measurements were performed on a single PbI_2-polymer composite bead using a xenon arc lamp. Two different gratings were used for the ultraviolet and visible region. A sapphire single crystal was used for mounting the beads. The light from the lamp was monochromated and focussed to a 20 μm spot on the center of the spherical bead. The transmitted light was collected and refocussed onto the detector by a sapphire lens. A thermoelectrically cooled GaAs photomultiplier tube was used as the detector. A normalization spectrum was taken using a dried, pristine polymer bead.

RESULTS AND DISCUSSION

The x-ray diffraction pattern of the nanocomposite is shown in Figure 1(a). Upon intercalation with aniline, the (001) diffraction peak shifts from about 6.98 Å to 10.74 Å, Figure 1(b). Intercalation leads to an increased separation between the *interlayer* iodine atomic planes. The pristine beads were x-ray amorphous.

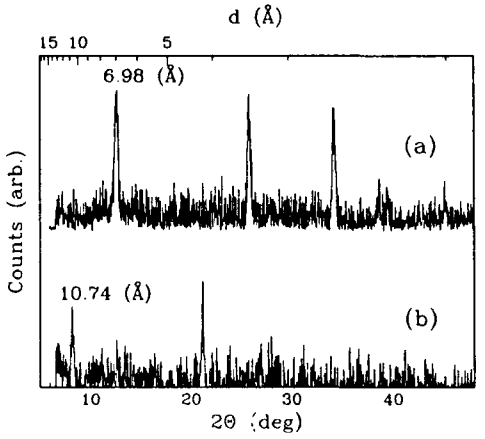


Figure 1. XRD pattern of (a) pristine and (b) aniline intercalated PbI_2 nano-composites.

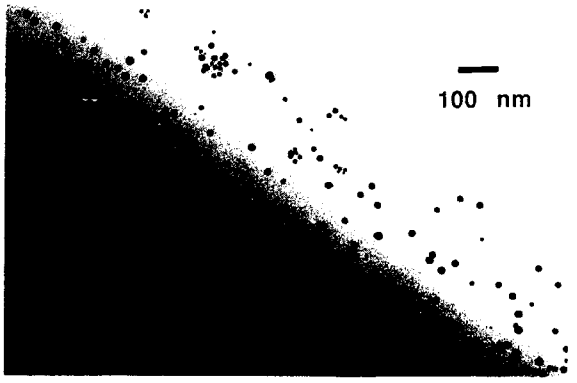


Figure 2. Transmission electron micrograph showing nanometer size PbI_2 particles in the polymer matrix.

Transmission electron microscopy shows that the PbI_2 particles are spherical with a mean diameter of 190 Å (Figure 2). The particle size distribution is Gaussian with a standard deviation of about 40 Å. A small fraction of the particles have a mean diameter of about 110 Å. Because of the melting of the polymer from

electron-beam damage, the particles tend to aggregate upon prolonged exposure to the beam.

The optical absorption spectrum of the nanocomposite containing PbI_2 particles is shown in Figure 3. The absorption edge appears at about 3.25 eV. This is a blue-shift of 0.75 eV from the optical band gap of bulk PbI_2 (=2.5 eV, [11]). This shift towards higher energy due to small particle size is attributed to quantum confinement of excitons and is a well known phenomenon [1-5]. The optical absorption spectrum of the same composite after intercalation with aniline is shown in Figure 4. The absorption edge appears at about 4.1 eV indicating an additional shift of 0.85 eV. This shift is due not only to the weakened interaction between the interlayer iodine planes, but also to the guest-host interaction. The former originates from an increased separation between the interlayer iodine planes upon intercalation, and causes a flattening of the bands, thereby increasing the band-gap. The latter is due to the polar $-NH_2$ group of aniline electrostatically interacting with the iodine $5p_z$ electron, thereby increasing its binding energy [11]. This electrostatic attraction depends on the dipole moment of the intercalated guest species. The larger the dipole moment, the stronger is this effect and hence a larger shift in the band gap is expected.

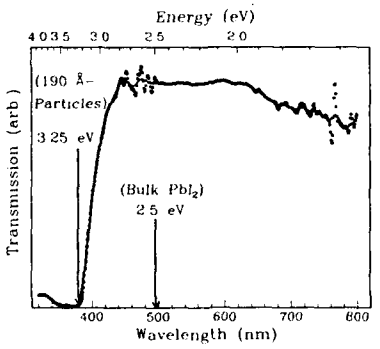


Figure 3. Optical absorption spectrum of a single PbI_2-polymer bead. The oscillations at certain wavelengths are due to the xenon lamp.

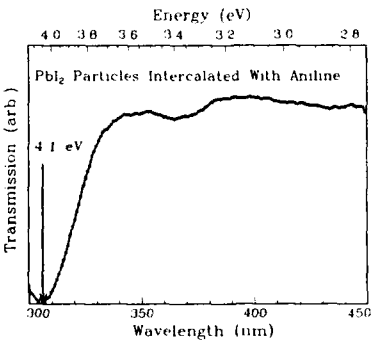


Figure 4. Optical absorption spectrum of aniline intercalated PbI_2-polymer bead.

It was recently shown by capacitance measurements that PbI_2 undergoes a ferroelectric transition at about 573 K [8]. Since PbI_2 belongs to one of the ferroelectric space groups, P3m1, ferroelectricity is expected in this compound [13]. Polytypic phase transitions are well known in this material [14]. In order to examine the effect of particle size on the ferroelectric transition, the transition in the bulk material must be understood. We have investigated the phase transitions in bulk PbI_2 by means of differential scanning calorimetry and x-ray diffraction.

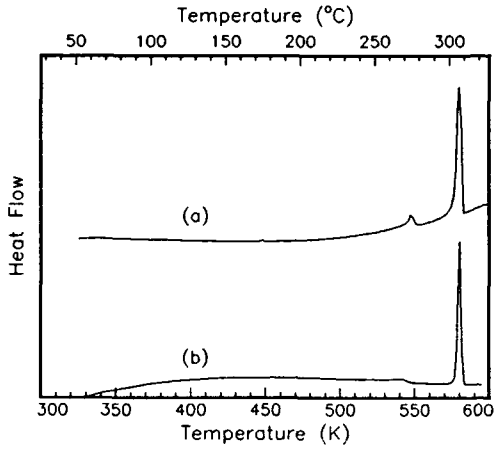


Figure 5. DSC spectra of bulk PbI_2 with (a) no prior annealing and (b) annealing at 595 K for 1h.

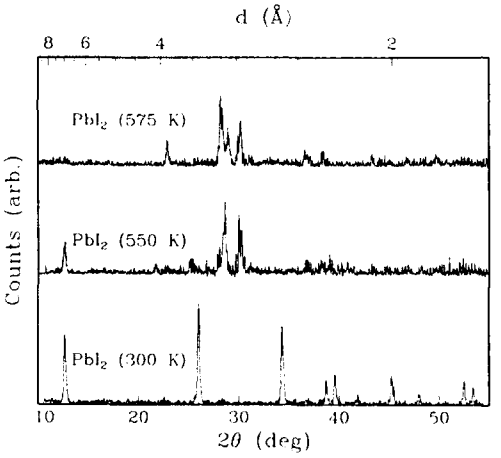


Figure 6. X-ray diffraction patterns of bulk PbI_2 at 300 K, 550 K and 575 K.

The DSC spectrum of bulk PbI_2, precipitated by adding an aqueous solution of sodium iodide to the lead nitrate solution, is shown in Figure 5(a). The particle size of the precipitated PbI_2 crystals was approximately 1 μm. Three successive heating and cooling DSC scans were taken. Two main transitions are evident at 548 K and 580 K. The transition at 580 K is broad during the first heating cycle, but becomes sharper and more prominent during successive cooling and heating cycles. A minor transition at 448 K, observed during the second and third heating cycles, is attributed to a polytypic phase transition [14]. On annealing PbI_2 at 595 K for one hour prior to the DSC experiment, the transition at 580 K becomes dominant, Figure 5(b). The transitions in the range 575-581 K, depending on the thermal history, represent the ferroelectric transition in PbI_2.

Figure 6 summarizes the results of high temperature x-ray diffraction. The first traces of a new phase appear at about 550 K. A mixed phase exists in this temperature region. At temperatures greater than 575 K, the phase transition is complete. This transition is attributed to the ferroelectric transition in PbI_2. The structure of the new phase as well as the effect of particle size on the ferroelectric transition is under investigation. A preliminary DSC analysis of the PbI_2 containing nanocomposites show the absence of any phase transition attributable to PbI_2 particles. However, this does not unequivocally

demonstrate a lack of ferroelectric transition due to small particle effects. A further investigation using Raman spectroscopy and high temperature x-ray diffraction is in progress.

CONCLUSIONS

Lead iodide particles with nanometer dimensions have been synthesized in the pores of a polymer matrix. The band gap of PbI_2 can be tailored by varying the size of the nanocrystals and by intercalating a guest species of appropriate dipole moment. For particles approximately 190 Å in diameter an absorption edge at about 3.25 eV is observed. The absorption edge shifts to 4.1 eV upon intercalation with aniline. Bulk PbI_2 undergoes a ferroelectric transition at about 573 K. Current work is directed towards correlating the particle size with the ferroelectric transition.

ACKNOWLEDGMENTS

This work supported by the National Science Foundation (DMR-8818558) through the Materials Science Center at Cornell. We thank Professor Arthur L. Ruoff for the use of the optical absorption system.

REFERENCES

1. L.E. Brus, J. Chem. Phys. 80, 4403 (1984).
2. C.J. Sandroff, D.M. Hwang, and W.M. Chung, Phys. Rev. B 33 5953 (1986).
3. S.V. Nair, S. Sinha, and K.C. Rustagi, Phys. Rev. B 35, 4098 (1987).
4. Y. Kayanuma, Phys. Rev. B 38, 9797 (1988).
5. M.V. Rama Krishna and R.A. Friesner, Phys. Rev. Lett. 67, 629 (1991).
6. M.R. Tubbs, Phys. Status Solidi B 67, 11 (1975).
7. J.C. Lund, L.P. Moy, M.R. Squillante, F. Sinclair, K.S. Shah, and G. Entine, Nucl. Instrum. Methods A 283, 299 (1989).
8. S.H.L. Oakey, J. Mat. Sc. Lett. 8, 957 (1989).
9. K. Ishikawa, K. Yoshikawa, and N. Okada, Phys. Rev. B 37, 5852 (1988).
10. P. Würfel and I.P. Batra, Ferroelectrics 12, 55 (1976).
11. V. Mehrotra, S. Lombardo, M.O. Thompson, and E.P. Giannelis, Phys. Rev. B 44, 5786 (1991).
12. J.K. Vassiliou, V. Mehrotra, M.W. Russell, and E.P. Giannelis in Clusters and Clusters-Assembled Materials, edited by R.S. Averback, J. Bernholc, and D.L. Nelson (Mater. Res. Soc. Proc. 206, Pittsburgh, PA 1991) pp. 561-566.
13. D.B. Litvin, Acta Cryst. A 42, 44 (1986).
14. E. Salje, B. Palosz, and B. Wruck, in Structural and Magnetic Phase Transitions in Minerals, edited by S. Ghose, J.M.D. Coey, and E. Salje (Springer Verlag, New York, 1988) p. 217.

EFFECTS OF CONTACT MATERIALS ON THE THERMALLY STIMULATED CURRENT SPECTRA OF MERCURIC IODIDE

X.J. BAO*, T.E. SCHLESINGER*, R.B. JAMES**, A.Y. CHENG***, C. ORTALE*** AND L. VAN DEN BERG***
*Carnegie Mellon University, Department of Electrical and Computer Engineering, Pittsburgh, PA 15213
**Sandia National Laboratories, Advanced Materials Division, Livermore, CA 94450
***EG&G Energy Measurements, Inc., Goleta, CA 93116

ABSTRACT

Mercuric iodide (HgI_2) single crystals deposited with transparent indium-tin-oxide (ITO), and semitransparent gold and nickel contacts were investigated by thermally stimulated current spectroscopy (TSC). The differences in the TSC spectra from these samples indicate that the defect structure in HgI_2 may be modified by the contact material. These defects act as carrier traps and have strong implications in the application of HgI_2 nuclear detectors. A method of numerical analysis was developed to extract information such as carrier trap activation energy, capture cross-section, and trap concentration-lifetime product from the TSC measurements.

INTRODUCTION

Mercuric iodide is one of the two leading candidates (the other being cadmium telluride) for use as room temperature semiconductor X-ray and gamma-ray detectors [1]. Compared with conventional semiconductor nuclear detectors such as lithium-drifted silicon, lithium-drifted germanium or high-purity germanium detectors, HgI_2 nuclear detectors have the advantages of a large bandgap (2.1 eV at room temperature), high resistivity ($\rho \approx 10^{13}$ Ωcm in the dark at room temperature), and large atomic numbers (80 and 53 for Hg and I, respectively). The large bandgap and high resistivity ensure that HgI_2 detectors have very small dark current at room temperature. Therefore, unlike Si and Ge based detectors, no cryogenic cooling is needed for HgI_2 detectors. The large atomic numbers make HgI_2 many times more efficient than Si or Ge based detectors in stopping the incident X-ray or gamma-ray photons to be detected, since the photoelectric effect is roughly proportional to the fifth power of the atomic number.

At present, HgI_2 spectrometers have resolutions comparable to that of Si detectors for X-rays of moderate energy (e.g. 5.9 keV Mn K_α line) [2]. One of the issues of concern in the further development of HgI_2 detectors has been the low manufacturing yield of about 20% [3]. This is believed to be caused by defects introduced during crystal growth and device fabrication. These defects act as recombination centers and carrier traps, thus decreasing the carrier lifetime, causing polarization effect, and resulting in incomplete charge collection, all of which are detrimental to detector performance. In addition, carrier trapping is also the main culprit in degrading the performance of HgI_2 detectors in the higher photon energy range (above 100 keV) where the resolution of HgI_2 detectors is considerably inferior to that of Ge detectors.

HgI_2 is a soft and reactive material. It undergoes a phase transition at 127 ^{0}C from red tetragonal (α-phase) to yellow orthorhombic (β-phase) crystal structure and melts at 259 ^{0}C. Previous studies have shown that defects can easily be introduced during processing [4]. The deposition of electrical contacts on HgI_2 is a major and crucial step in the fabrication of HgI_2 detectors. Studies of various contact materials on HgI_2 by low temperature photo-

luminescence spectroscopy (PL) have shown that recombination centers may be introduced in the interfacial region between contact layer and HgI_2 substrate [5, 6]. In this study, we have employed TSC methods to study the effects of the indium-tin-oxide, gold, and nickel electrical contacts on the carrier traps in HgI_2.

EXPERIMENTAL AND NUMERICAL

The HgI_2 single crystals were grown from vapor phase at EG&G Energy Measurements, Inc. Slices of 1 cm x 1 cm with thickness of about 0.05 cm were cut from these crystals by sawing with a thread dipped in a KI solution. Each sample was chemically etched in a 10% (by weight) KI aqueous solution prior to contact deposition. The ITO was deposited by sputtering and was transparent. Au and Ni were deposited by thermal evaporation and were semitransparent with a transparency of about 50% in the visible light region. Transparent and semitransparent contacts were necessary to make the TSC measurements. These deposited conducting layers formed the front contacts. Painted colloidal carbon was used as back contacts in all samples. Each sample was then mounted onto an alumina substrate with the transparent or semitransparent electrode facing up. TSC measurements were performed between 78 and 278 K. The sample was first cooled to 78 K in the dark and then illuminated through the front contact for 5 minutes with a 20 mW argon ion laser beam (operated at 4880 Å). Current was measured as a function of temperature as the sample was heated in the dark by a resistive heater. A DC bias of 12 V was applied to the sample all the time. The rate of the temperature change was also recorded as a function of temperature.

Many methods exist for analyzing TSC data to obtain trap activation energy, and sometimes also carrier capture cross-section and trap concentration-lifetime product [7]. The most commonly used method is to measure several TSC spectra with different heating rates. For each heating rate β, a current maximum T_m can be obtained. From a plot of $\ln(\frac{T_m^2}{\beta(T_m)})$ vs. $\frac{1}{kT_m}$ (α is a constant), the activation energy can be obtained. Under certain assumptions, either the carrier capture cross-section or the trap concentration-lifetime product may also be obtained. Several disadvantages are associated with this method: (1) several TSC spectra have to be taken from each sample, (2) for each TSC spectrum, only the TSC current maximum temperature T_m is used for information extraction, (3) quite a large range of heating rates have to be used, this is difficult to achieve since at high heating rate, there may be a large temperature gradient between the sample and the temperature sensor and also the sample itself may not be uniformly heated. In this study, we have developed a numerical method to analyze TSC data using only one TSC spectrum to obtain activation energy, carrier cross-section, and trap concentration-lifetime product.

Under the assumption that traps only interact with their respective bands but not with each other, and that $|\frac{dn}{dt}| \ll |\frac{n}{\tau_n}|$ (electron traps are considered here), the TSC process is described by the following equations,

$$n = \frac{\tau_n N_c \sigma_i v_{th} exp(-\frac{E_i}{kT}) n_i}{1 + \frac{\tau_n}{\tau_r}(1 - \frac{n_t}{N_t})},$$

and

$$\frac{dn_i}{dt} = -\frac{N_c \sigma_i v_{th} exp(-\frac{E_i}{kT}) n_i}{1 + \frac{\tau_n}{\tau_r}(1 - \frac{n_t}{N_t})},$$

where n_i is the concentration of electrons trapped in the ith trap, n is the concentration of free electrons, N_c is the effective density of states in the conduction band, τ_n is the steady state lifetime of electrons in the conduction band, σ_i is the electron capture cross-section of the ith trap, v_{th} is the thermal velocity of the conduction band electrons, N_t is the total

concentration of the *ith* trap, $\tau_i = \frac{1}{N_i \sigma_i v_{th}}$ is the retrapping time, and E_i is the activation energy of the *ith* trap.

It can be shown that the shape of the TSC spectrum resulting from the above equations is determined by four parameters: heating rate $\beta(T) = \frac{dT}{dt}$, trap activation energy E_i, carrier capture cross-section σ_i, and trap concentration-lifetime product $N_i\tau_n$. For each experimentally obtained TSC spectrum, $\beta(T)$ is also recorded, so that it can be treated as known and used for the numerical analysis. A numerical integration subroutine using the Runge-Kutta method[8] was written to solve the TSC rate equations and obtain a calculated TSC spectrum for any given set of σ_i, E_i, and $N_i\tau_n$. From each calculated spectrum, the temperatures at which the TSC current reaches maximum (labeled T_m^c) and half-maximum on the low and high temperature side of T_m^c (labeled T_-^c and T_+^c, respectively) were noted. Thus these temperatures as a function of σ_i, E_i, and $N_i\tau_n$ can be numerically obtained.

$$T_-^c = T_-^c(\sigma_i, E_i, N_i\tau_n), \quad T_m^c = T_m^c(\sigma_i, E_i, N_i\tau_n), \quad T_+^c = T_+^c(\sigma_i, E_i, N_i\tau_n).$$

From the measured TSC spectrum, temperatures at which the TSC current is maximum and half maximum can also obtained and are labeled as T_-^m, T_m^m, and T_+^m. With these values, a three dimensional root finding problem is set up, with three unknowns: σ_i, E_i, and $N_i\tau_n$. The three equations are,

$$\begin{cases} T_-^c(\sigma_i, E_i, N_i\tau_n) - T_-^m = 0 \\ T_m^c(\sigma_i, E_i, N_i\tau_n) - T_m^m = 0 \\ T_+^c(\sigma_i, E_i, N_i\tau_n) - T_+^m = 0. \end{cases}$$

A subroutine was written to solve the above problem using Newton-Raphson method [8]. Therefore, for each measured TSC curve, using the above numerical method, the carrier capture cross-section, activation energy, and trap concentration-lifetime product can be extracted.

RESULTS AND DISCUSSIONS

Many researchers have performed TSC measurements on HgI_2. Some of them have tentatively related TSC peaks they have observed to stoichiometry [9], energy resolution [10], polarization effect [11], and structural imperfection such as dislocations [12]. These results have been summarized in Ref. 13, where TSC peaks of various workers were categorized into eleven peaks, labeled as T_1 to T_{11}.

Fig. 1 shows the measured TSC spectrum (dotted line) from a sample contacted with an ITO electrode. Five peaks were observed and were labeled according to Ref. 13. The dominant peak is T_6 and is analyzed with the numerical method we have developed. The continuous line is a calculated fit to this peak. Fig. 2 shows a measured (dotted line) and a calculated (continuous line) TSC spectrum for a Au-contacted sample. Only one broad peak (T_8) was observed. In Fig. 3 are measured (dotted line) and calculated (continuous line) TSC spectra for a Ni-contacted sample. Three peaks were observed. T_1 and T_5 were analyzed with the numerical method. T_6 was not clearly resolved and was fitted with parameters obtained from the ITO-contacted sample. For all three samples, the measured T_m, and extracted values of carrier capture cross-section, activation energy, trap concentration-lifetime product were summarized in Table I.

ITO has been used as an electrode material on HgI_2 to fabricate photodetectors. These detectors, in conjunction with a scintillator material such as CsI(Tl), NaI(Tl) or BGO, were used as nuclear spectrometers in a different approach [14]. Instead of detecting the incident radiation directly, HgI_2 photodetectors detect the visible light generated by

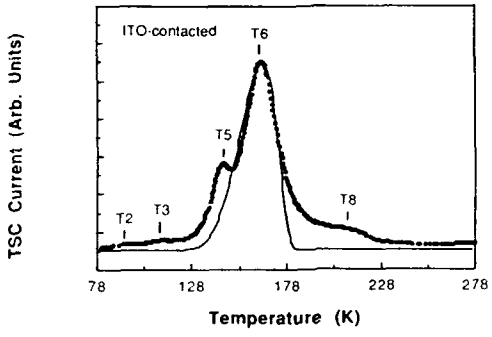


Figure 1: TSC spectra from a sample contacted with a transparent indium-tin-oxide electrical contact. The dots represent the measured spectrum, the continuous curve represents the calculated spectrum.

the radiation in the scintillators. This approach takes advantage of the high gamma-ray stopping power of the scintillators and also avoids the carrier trapping problem associated with HgI_2 nuclear detectors when detecting gamma-rays. ITO contacts have been shown to work better in terms of photoresponse and long-term stability than several alternative transparent and semitransparent contacts, even though recombination centers related to the deposition of the film were found to degrade the uniformity of the photoresponse [15]. The TSC spectra from ITO-contacted samples resembles those from Pd-contacted samples in that the dominant peak is T_6 [6]. Since Pd is the most commonly used contact materials, it seems that this trap is not detrimental to the device performance.

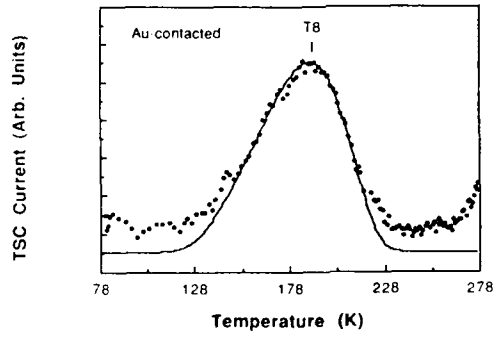


Figure 2: TSC spectra from a sample contacted with a semitransparent gold electrical contact. The dots represent the measured spectrum, the continuous curve represents the calculated spectrum.

Au has also been used as a contact material for HgI_2 detectors [16], but not as widely

as Pd. The TSC spectrum shown in Fig. 2 is quite different from that of Fig. 1. Due to the large width of the peak T_8, a relatively small activation energy of 0.20 eV was obtained. Previous study has shown that the deposition of Au on HgI_2 has very little effect on the PL spectra and does not introduce any new recombination centers [13]. It seems that Au should still be a candidate in the search for the "best" contact material for HgI_2 nuclear detectors. Optimization of deposition conditions and different deposition methods should be further investigated.

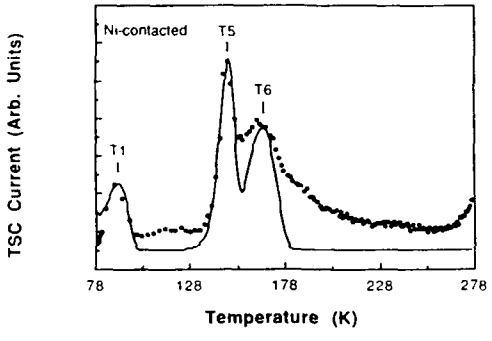


Figure 3: TSC spectra from a sample contacted with a semitransparent nickel electrical contact. The dots represent the measured spectrum, the continuous curve represents the calculated spectrum.

Ni has never been tried as a contact material for HgI_2 detectors. The dominant TSC peak in Ni-contacted samples was a narrow T_5. This peak has been related to mechanical damages due to cleaving [12]. Cleaving has been abandoned in the HgI_2 device fabrication because it was believed to be harmful. Another peak at 89 K (T_1) has been related to iodine deficiency [9]. This trap is also undesirable since iodine deficiency in the sample has been reported to be related to poor crystal quality and poor detector performance[16]. These results seem to agree with PL studies of Ni-contacted samples. Extensive study of the correlation between PL spectra and HgI_2 device performance has shown that one recombination center called band 3 in PL spectra was detrimental to detector performance [13]. The origin of this defect is still being studied but preliminary results indicate that Ni is one of the suspects. It seems that nickel is not likely to become a useful contact material for HgI_2 detectors.

CONCLUSIONS

ITO, Au, and Ni contacts on HgI_2 were investigated by TSC in the context of nuclear detector applications. A numerical method was developed to analyze the experimentally obtained TSC spectra. This study suggested that the defect structure in HgI_2 is strongly affected by the contact material.

ACKNOWLEDGEMENTS

We would like to thank the U.S. Department of Energy for financial support.

Table 1: Summary of TSC results for samples contacted with ITO, Au, and Ni electrodes.

	T_1	T_2	T_3	T_5	T_6	T_8
T_m (K) (ITO)		95	113	144	165	213
σ_i (cm^2)					1E-15	
E_t (eV)					0.38	
$N_t\tau_n$ (cm^{-3}s)					1E+9	
T_m (K) (Au)						193
σ_i (cm^2)						5E-22
E_t (eV)						0.20
$N_t\tau_n$ (cm^{-3}s)						9E+15
T_m (K) (Ni)	89			147	166	202
σ_i (cm^2)	3E-14			2E-11		
E_t (eV)	0.19			0.48		
$N_t\tau_n$ (cm^{-3}s)	1E+9			1E+3		

REFERENCES

1. See articles in Nucl. Instr. Meth. Phys. Res. A283 (1989).
2. A.J. Dabrowski, W.M. Szymczyki, J.S. Iwanczyk, J.H. Kusmiss, W. Drummond, and L. Ames, Nucl. Instr. Meth. 213, 89 (1983).
3. N.L. Skinner, C. Ortale, M.M. Schieber, and L. van den Berg, Nucl. Instr. Meth. Phys. Res. A283, 119 (1989).
4. X.J. Bao, T.E. Schlesinger, R.B. James, R.H. Stallen, C. Ortale, and A. Y. Cheng, J. Appl. Phys. 68, 86 (1990).
5. R.B. James, X.J. Bao, T.E. Schlesinger, C. Ortale, and A.Y. Cheng, J. Appl. Phys. 67, 2571 (1990).
6. X.J. Bao, T.E. Schlesinger, R.B. James, G.L. Gentry, A.Y. Cheng, and C. Ortale, J. Appl. Phys. 69, 4247 (1991).
7. A.G. Milnes, Deep Impurities in Semiconductors, (Wiley, New York, 1973).
8. W.H. Press, B.P. Flannery, S.A. Teukolsky, and W.T. Vetterling, Numerical Recipes in C, (Cambridge University Press, New York, 1988).
9. R.C. Whited, and L. van den Berg, IEEE Trans. Nucl. Sci. NS-24, 156 (1977).
10. T. Mohammed-Brahim, Phys. Stat. Sol. (a) 65, K1 (1981).
11. A. Tadjine, D. Gosselin, J.M. Koebel, and P. Siffert, Mat. Res. Soc. Symp. Proc. 16, 217 (1983).
12. R. Stuck, J.C. Muller, J.P. Ponpon, C. Scharager, C. Schwab, and P. Siffert, J. Appl. Phys. 47, 1549 (1976).
13. X.J. Bao, Ph.D. Thesis (Dept. of ECE, Carnegie Mellon University, 1991).
14. J. Markakis, C. Ortale, W. Schnepple, J. Iwanczyk, and A. Dabrowski, IEEE Trans. Nucl. Sci. NS-32, 559 (1985).
15. R.B. James, X.J. Bao, T.E. Schlesinger, J.M. Markakis, A.Y. Cheng, and C. Ortale, J. Appl. Phys. 66, 2578 (1989).
16. J. Howes, and J. Walting, Mat. Res. Symp. Proc. 16, 207 (1983).
17. J.L. Merz, Z.L. Wu, L. van den Berg, and W.F. Schnepple, Nucl. Instr. Meth. 213, 51 (1983).

OPTICAL AND MAGNETIC RESONANCE INVESTIGATIONS OF MERCURIC IODIDE CRYSTALS

B.K. MEYER, D.M. HOFMANN, J. ECKSTEIN[+] and K.W. BENZ[+]
Physik-Department E 16, TU Munich, James-Franck Str., 8046 Garching, Germany
[+] Kristallographisches Institut, University Freiburg, Hebelstr. 25, 7800 Freiburg, Germany

ABSTRACT

The optical properties of the red modification of mercuric iodide (HgJ_2) were studied by optical absorption, magnetic circular dichroism, photoluminescence and optically detected magnetic resonance investigations. The experiments demonstrate the involvment of acceptors with energy levels at E_V + 0.14 ± 0.01 eV and 0.15 ± 0.01 eV in the absorption and recombination at 2.2 eV. The g - values are 0.85 and 0.74, respectively.

1. INTRODUCTION

The red modification of mercuric iodide, a wide band gap compound semiconductor (E_g=2.37 eV at 4.2 K) with a high atomic number, could be a promising candidate for room temperature, low noise nuclear radiation detectors. The detector quality is however severely influenced by the presence of stoichiometric defects (interstitials, cation and anion vacancies) and dislocations. The analysis of defect structures is quite different from cubic III-V or II-VI compound semiconductors, because HgJ_2 is an anisotropic layered material with tetragonal crystal structure. In the tetragonal unit cell alternating layers of Hg and I are present. I-I interlayers have a Van der Waals bonds, whereas Hg-Hg and Hg-I are covalent bonded [1].
For a characterization and a correlation between defects and the detector properties of HgJ_2 one needs to know the atomic and electronic structure and the energy level position of the relevant point defects. In principle these informations can be obtained from electron spin resonance (ESR) using optically detection (ODESR). The technique, originally applied for the study of colour centres in alkali halides [2] and recently successfully applied for the study of intrinsic defects in III-V semiconductors [3,4,5], is based on the magnetic circular dichroism of the absorption (MCD). A first application to study defects in HgJ_2 will be presented.

2. EXPERIMENTAL DETAILS

2.1 Optical measurements

The MCD and absorption measurements were performed in a magneto-optical system in Faraday configuration at Helium temperatures (4.2 K or pumped Helium 1.6 K). The magnetic fields up to 4 Tesla were provided by a superconducting split coil magnet. Light from a halogen lamp was dispersed by a grating monochromator (Spex, 1681). The transmitted light was detected by a fast Germanium detector (North Coast) using lock-in techniques. The circularly polarized light was generated by a stress modulator (HINDS)

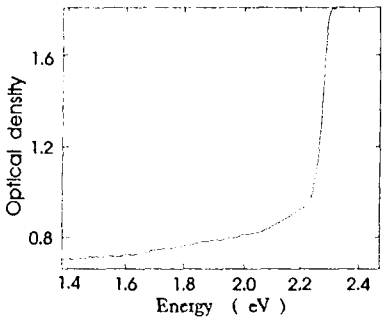


Fig.1 :
Optical absorption spectrum of HgJ_2 at T=1.5 K

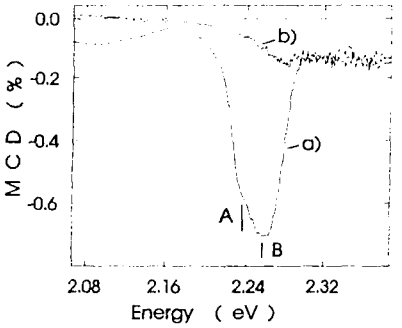


Fig.2 :
Magnetic circular dichroism (MCD) for two different magnetic fields a) B=2 T, T=1.5 K; b) B=0, T=1.5 K

working at 44 kHz in combination with a Glan Thompson linear polarizer. For the optically detected spin resonance experiments (ODESR) the samples were mounted in a cylindrical cavity (TE_{011}) with wide optical access having a loaded Q of 5000. Approximately 1 W of microwave power at 24 GHz could be delivered by a Gunn diode amplified by a travelling wave tube (Hughes).
In the luminescence measurements the sample was excited by the 514 nm Ar^+ ion laser line and the emitted light detected by a Si-pin diode or cooled photomultiplier with Si response. The emission light was analysed by a high resolution monochromator (Jarell Ash 25-100) with the sample in superfluid Helium (< 2K). The excitation power was normally 100 mW in an unfocussed beam.

2.2 Crystal growth

HgJ_2 crystals have been grown by using the Piper-Polish technique in a vertical arrangement. Prior to growth the ampoule was submersed into a silicon oil bath (T=125 ± 0.2 °C). After temperature homogeneization the ampoule with its self-seeding conepart was pulled out of the oil bath through a heater with a transport rate of 1 mm per day. The heater temperature was kept at 120 ± 0.2 °C, which is below the HgJ_2 phase transition temperature of 127 °C. When the spike of the cone was 10 mm above the oil surface, a seed crystal was formed. The central cone of the ingot was single crystal capped either with one or several mirror like facets.
A successful crystal growth needs high purity starting materials. 100 g dried HgJ_2 powder was placed in quartz glas tube and evacuated at 60 °C for 12 h. This procedure was followed by a fourfold sublimation in a seperate quartzglas tube, which was fixed to the growth ampoule. About 50 g of purified HgJ_2 was transported into the growth ampoule, which was seperated from the tube by sealing. A deviation from stoichiometry was measured by wet chemical analysis. Typical composition range for HgJ_2 was between 1.986 and 1.992, depending on the purification and growth conditions.

3 EXPERIMENTAL RESULTS

3.1 Absorption and MCD

In fig 1 the optical absorption spectrum measured at 1.5 K is shown. The absorption below band gap is smoothly varying. There are no indications

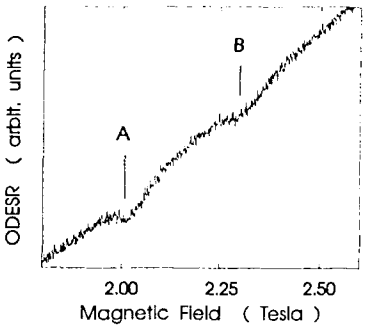


Fig.3 :
Optically detected magnetic resonance (ODESR) recorded at the E=2.2 eV MCD band, 24 GHz, 100 mW, T=1.5 K

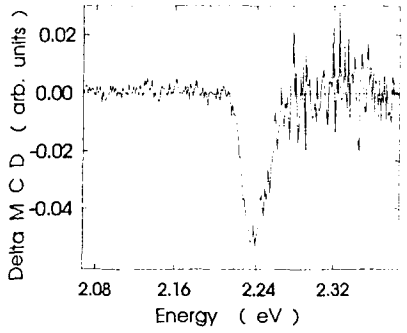


Fig.4 :
ODESR excitation spectrum by monitoring the 2020 mT ODESR line

of absorption bands in the range from 2 eV to 1.4 eV. We note, however, that the absorption spectrum rapidly increases at 2.2 eV and has a high optical density of 1.8 already at 2.3 eV, whereas the band gap energy is 2.37 eV. This could indicate that defects which have their transitions close to the band gap energy might be present in a considerable amount.
The MCD measures the difference of the left and right circularly polarized absorption in the magnetic field. For a paramagnetic defect the MCD intensity is field and temperature dependent [2]. Clearly an absorption band is seen in the MCD spectrum measured at 2 T and 1.5 K (fig.2.a). The lineshape is asymmetric and seems to be a superposition of two bands peaking at the energies of 2.235 eV (A) and 2.250 eV (B) indicated by arrows in fig. 2.
The total MCD starting at 2.16 eV is paramagnetic (measurement at 0 Tesla, fig. 2b). The intensity is also reduced by raising the temperature, i.e. it is at half of its value for 4.2 K and 2 T, thus showing the Boltzmann population difference in the ground state. This opens the possibilty to perform optically detected magnetic resonance.

3.2 ODESR and ODESR excitation

The ODESR is measured by setting the monochromator to the maximum of the MCD band at 2.26 eV and sweeping the magnetic field under continous irradiation with 24 GHz microwaves. The observed two resonances (see fig.3) occur as decreases in the magnetic field dependent increase of the MCD. Their field positions are at 2020 mT (A) and 2320 mT (B). Neither at lower nor at higher fields (< 4 T) we observe additional resonances. The signals could only be measured for a crystal orientation parallel to the c-axis due to the birefringence caused by the tetragonal crystal structure (field- and temperature-independent dichroism).
The spectra of the MCD bands giving rise to the signals, e. g. resonance A at 2020 mT, are measured by a low frequency on/off modulation of the microwaves and scanning the optical excitation energy. This ODESR excitation spectrum is shown in fig.4. In comparison to the total MCD lineshape (fig. 2a) it can be seen that the defect responsible for the A resonance absorbs only in the low energy part of the total MCD. The low energy onset of the ODESR excitation spectrum of resonance A is at 2.22 eV, which will be the basis of the energy level determination.

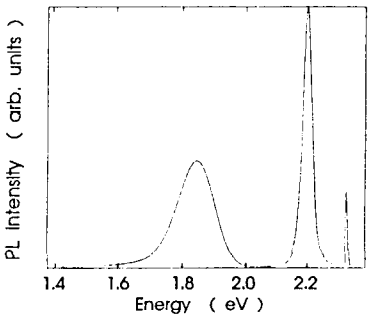


Fig.5 :
Photoluminescence spectrum for HgJ_2 at T=1.6 K for Ar^+ ion laser excitation (5145 A)

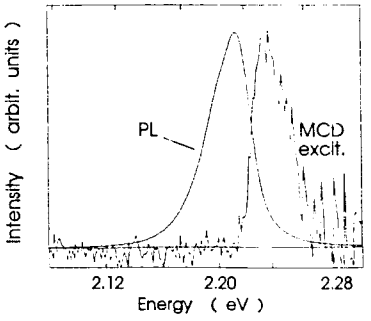


Fig.6 :
Comparison of the photoluminescence and MCD spectra of the 2.2 eV transition

In a similar way it can be shown that the high energy part of the MCD (maximum at 2.26 eV) is caused by the defect responsible for resonance B. Its energy onset is at 2.30 eV.

3.3 Photoluminescence

In the low temperature PL measurements three luminescence bands show up (fig.5). The one close to the band gap at 2.33 eV is believed to be due to an exitonic transition [6]. The luminescence at 2.2 eV with a half width of 50 meV dominates in all of our samples cut from different regions of the boule. At 1.84 eV (HW=120 meV) a third emission band is located. By changing the excitation power over more than three decades (P_{max}=800 mW) the emission bands at 2.33 eV and 2.2 eV increase linearily in intensity without any indications of saturation. Both showed a strong sublinear behaviour. The 2.33 eV band has a slope of 0.7 ± 0.05 and the band at 2.2 eV a slope of 0.55 ± 0.05. For donor-acceptor and band-acceptor (e^0A^0) transitions slopes of the order of 1 are usually found. The remarkable deviations from 1 are indications of strong non-radiative processes. We observe a clear shift of the maximum of the 2.2 eV band to higher energies when increasing the excitation power. This behaviour indicates a donor-acceptor pair recombination. With respect to the 2.2 eV band, which is of prime interest here, we can state, that the PL results give strong evidence for donor-acceptor pair recombination. From a comparison of the PL and MCD bands we will show that in both cases the same acceptor is involved.

4. INTERPRETATION AND DISCUSSION

4.1 MCD

We observe the ESR tagged MCD band just below the band gap energy. The symmetries of the ground and the excited state are important for the MCD line shape. Assuming an ionisation transition to the conduction band as the origin of the MCD we have a state with T_2 symmetry as the ground state (acceptor) whereas the conduction band has A_1 symmetry. For a T_2 to A_1 transition we expect a single MCD band with a Gaussian line shape for moderate electron phonon coupling. Indeed the MCD shape found is very similar to the bound to free ionisation transition of the Mn^{2+} ($Mn^+ \cdots Mn^{3+}$ +

e_{cb}) acceptor in GaAs [3], the EK2 double acceptor in GaAs and the intrinsic Ga_{Sb} cation antisite defect in GaSb, also acting as double acceptors [4,5]. In all cases the sharp low energy threshold could be used to determine the binding energy to be $E_{gap} - E_{tr} = E_a$. From the onsets of the ODESR excitation bands which we attribute to the electron ionisation transitions of the acceptors $A^- \rightarrow A^o + e_{cb}$ a binding energy of 140 ± 10 meV and 150 ± 10 meV can be inferred.

In order to observe a paramagnetic MCD in an ionisation transition to the conduction band the acceptor must be a double acceptor with two levels in the gap. Single acceptors giving rise to a transition $A^- \rightarrow A^o + e_{cb}$ have a non-paramagnetic ground state. This considerably narrows the possibilties of which chemical origin the acceptor is. Those could be the group V elements (N, P, As,..) on the Iodine side. With respect to the Hg side, a IIb element, no extrinsic impurity can act as a double acceptor. Although HgJ_2 is a very impure semiconductor (impurity content 10^{18} cm^{-3}), electrically active traps are found only in the range 10^{14} to 10^{15} cm^{-3}, implying that most impurities are not electronically active. Nonmetallic impurities such as C, Cl and Br are present in the 1-100 ppm range, more important in the 10-50 ppm range are the metallic ones such as Na, K, Ca, Al and Fe. Na and K are single acceptors, Fe could act as a donor and an acceptor, but should have completely different optical and magnetic properties [7]. The best candidate is an intrinsic defect acting as an acceptor.

The problem which defects are present in non-stoichiometric HgJ_2 is still under discussion. Frenkel as well as Schottky disorder on the iodine defficient, i.e. Hg rich side, would produce Hg_i and/or V_I interstitials, both supposed to act as donors. V_{Hg} are expected to dominate on the iodine rich side (we neglect for the moment antistructure disorder for which sofar no experimental evidence is presented). For the slight deviations from the stoichiometric composition of 2, as found in our crystals, V_{Hg} can still be present. The observation of two ODESR resonances with slightly different excitation spectra would be in line with the two possible sites of the V_{Hg} in the tetragonal crystal structure of HgJ_2.

The presence of negatively charged Hg vacancies in HgJ_2 is also inferred from positron annihilation studies [8].

4.2 Photoluminescence

The PL experiments indicate donor-acceptor recombination for the 2.2 eV emission band. In fig.6 we compare the spectral positions of the PL band with the ESR tagged MCD band (bound to free transition). We note that the maximum of the PL band coincides with the onset of the MCD band. This could imply for a D-A recombination that the shallow donor binding energy is very small. For a comparison with the experiments we calculated within the effective mass theory, (EMT), both the shallow donor and shallow acceptor binding energies.

For the shallow EMT acceptor we obtained E_A=34.6 meV, for the donor binding energy 10.7 meV [9].

For a D-A recombination the peak position of the PL band (neglecting coulombic effects $e^2/\epsilon R$) is given by $E_{PL} = E_{gap} - E_D - E_A$. The PL band of the effective mass donors and acceptors should be at 2.325 eV. For the luminescence at 2.22 eV we calculate with E_D=10.7 meV an acceptor binding energy of 140 meV. Compared to the EMT value of 34 meV, the intrinsic acceptor is in between an shallow and deep level defect.

4.3 ODESR

Reflection measurements and their group theoretical interpretation gave for HgJ_2 the ordering of the valence subbands Γ_7^-, Γ_6^- (separated by the crystal field energy of 0.19 eV)[10]. We thus have to asign the resonance taking place within the Γ_7^- state. For a pure J=1/2 state (L=1, S=1/2) we get the Lande g-value of 2/3=0.66. Experimentally we find our g-values at 0.85 and 0.74 not far above that value. The absence of any hyperfine interactions (hf) with neighbouring nuclei (iodine has I=5/2) is in line with the shallow nature of the defect (delocalised wavefunction). For a deep, highly localised defect state we expect the g-values around 2 and resolved hf interactions.

CONCLUSION

Optical absorption, magnetic circular dichroism, photoluminescence and optically detected magnetic resonance investigations have been performed to study the absorption and recombination of the 2.2. eV band in HgJ_2. They show the presence of an acceptor levels at E_v + 0.14 eV and E_v + 0.15 eV. In the MCD spectrum the bound to free transition ($A^- \rightarrow A^0 + e_{cb}$) is monitored, the photoluminescence is consistent with a shallow donor - acceptor recombination. Based on the magnetic properties of the defect, the paramagnetism of the ground state as well as the spin resonance data we conclude that most probably a Hg vacancy is involved.

REFERENCES

[1] S. B. Hyder, J. of Appl. Phys., 48, 313 (1977)
[2] L. F. Mollenauer and S. Pan, Phys. Rev. B6, 772 (1972)
[3] M. Baeumler, B.K. Meyer, U. Kaufmann, and J. Schneider, Materials Science Forum Vols. 38 - 41, 797 (1989)
[4] G. Roos, A. Schoner, G. Pensl, J. Wagner, B.K. Meyer, and R.C. Newman, J. Appl. Phys. 69, 1454 (1991)
[5] E. Diwo, Diplomarbeit, Paderborn, Germany, 1988
[6] I. K. Akopyan, B. V. Bondarenko, B. A. Kazennov, and B. V. Novikov, Sov. Phys. Solid State, 29, 238 (1987), (transl. Fiz. Tverd. Tela, 29, 419 (1987))
[7] A. Zunger, in Solid State Physics, Vol. 39, Ed. H. Ehrenreich and D. Turnbull (Academic Press, New York), p.276 (1986)
[8] S. Gits, Nuclear Instruments and Methods Vol. 213, 43 (1983)
[9] B. K. Meyer, Al. L. Efros unpublished
[10] I. Akopyan, B. Novikov, S. Permogorov, A. Selkin and V. Travnikov, Phys. Stat. Sol. (b) 70, (1975)

EFFECTS OF REACTIVE SPUTTERING PARAMETERS ON THE GROWTH AND PROPERTIES OF ACOUSTOOPTIC ZnO FILMS

E. JACOBSOHN AND D. SHECHTMAN
Technion, Department of Materials Engineering, Haifa 32000, Israel

Abstract

1 μm ZnO films were deposited on SiO_2 by reactive sputtering using a D.C. magnetron gun. The microstructure, orientation and chemistry of the deposited layers were examined. It is shown that the oxygen partial pressure plays an important role in the structure of the layer through a mechanism of surface diffusion.

INTRODUCTION

Zinc Oxide films have aroused increasing interest in recent years due to their potential use in acousto and electro-optic device technology. The integration of surface acoustic wave (SAW) devices and silicon technology requires the deposition of a piezoelectric material, such as ZnO, on oxidized silicon wafers. The advantage of ZnO relative to other piezoelectric materials stems from it's low price and from the possibility of depositing it on many kinds of substrates. More important, ZnO has the strongest piezoelectric coupling effect of any ferroelectric material.

Several models were developed to predict the effect of the sputtering parameters (pressure and temperature) on the film structure. The best known are those of Thornton [1] and Mazor et. al. [2]. These models do not apply in the case of sputtering in a reactive atmosphere at relatively low deposition rate ($\approx 0.3\mu m/h$), conditions which are mostly used for the sputtering of piezoelectric Zinc oxide films [3].

The purpose of the study reported here is to find the effect of the deposition parameters on the stoichiometry, morphology, and crystallography of the growing layer. The structure of ZnO sputtered layers was studied by: Transmission Electron Microscopy (TEM), Scanning Electron Microscopy (SEM), X-Ray Diffraction (XRD) and Auger Electron Spectroscopy (AES).

EXPERIMENTAL PROCEDURE

Sample preparation and characterization

ZnO films were deposited by reactive sputtering on (100)Si substrates coated with 1000Å of SiO_2, using a high purity Zn plate (99.999%) as a target and a gas mixture of Ar-O_2 (20-80 *vol.*%) at 7.5*mtorr*. Both gases were 99.999% pure and the desired oxygen partial pressure in each experiment was monitored by a mass flow controller. The growth rate was measured by an Inficon thickness monitor.

A d.c. magnetron gun was used for the depositions in a discharge power range between 100W and 250W.

The sputtering chamber was pumped down to $5 \cdot 10^{-7}$ torr before the O_2/Ar gas mixture was introduced. The target was presputtered for about 20min. prior to the deposition.

The ZnO film thickness was measured by an α-step gage. Subsequently, a thin Al film (2000 Å) was deposited by sputtering on the ZnO layer and interdigital electrodes were then made by conventional photolithography, on the samples that were found to be well c-axis oriented with a close structure and smooth surface.

The stoichiometry of the ZnO layers were studied by Auger spectroscopy and compared to a standard ZnO sample.

Cross-section and edge-on samples were examined using TEM in order to resolve the grain structure and orientation. In addition an X-ray diffractometer (CuKα-radiation) and SEM were used for this purpose.

Electrical measurements

The resonant system of the interdigital transducer (IDT) had the following parameters: IDT period (equal to the wavelength of surface Rayleigh waves) $\lambda = 60\mu m$; electrode width $d = \lambda/4 = 15\mu m$; acoustic aperture: $u = 50\lambda = 3mm$; IDT length $l = m\lambda = 12mm$; and the number of the electrode pairs was $m = 200$.

Return loss response of our resonator was measured with a spectrum analyzer. The frequency spectrum reveals a clear resonant shape due to the piezoelectric properties of ZnO. The main resonant frequency was $\nu_r = 78.96$MHz and corresponds to the acoustic wave velocity $v = \lambda\nu_r = 4.7 \cdot 10^5$ cm/s. The last value is close to the calculated one for Rayleigh surface waves at given parameter q [4, 5].

EXPERIMENTAL RESULTS

a. Stoichiometry

Fig. 1 shows the AES compositional depth profile for a sample that was deposited using sputtering power discharge of 100W in an atmosphere of 20% vol.O_2. The concentrations were calibrated using a standard ZnO powder. Since the composition through the thickness is constant the measurement was stopped before the interface was reached. It can be seen that the obtained film is relatively free of impurities. The O/Zn ratio was calculated and was found to be 0.8. Further enlargement of the discharge power to 150W increased the O/Zn ratio to 1.0.

The stoichiometric composition of the ZnO was maintained even with further increases of the discharge power up to 250W. In other words, above a certain power all films have stoichiometric composition which is independent of the gas compositions.

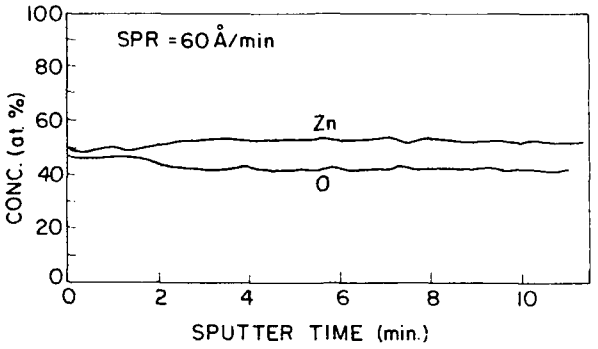


Figure 1: AES compositional depth profile for a sample sputtered at 20%*vol.* O_2 and discharge power of 100W

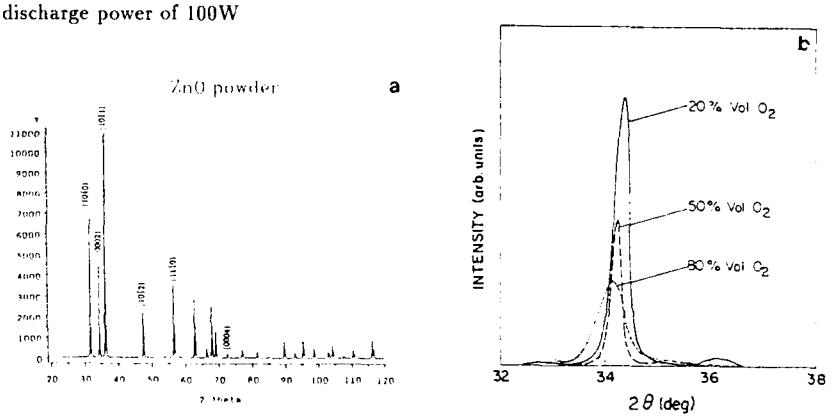


Figure 2: X-ray diffraction spectra from: a. bulk ZnO powder b. from ZnO films sputtered at 150W at different oxygen concentrations

b. Orientation

ZnO has the structure of wurtzite - hcp structure in which half of the tetrahedral intersti tials sites are occupied. In order to receive high piezoelectric effect (high coupling factor) the film must grow highly oriented with it's c-axis perpendicular to the substrate.

Fig. 2a shows X-ray diffraction spectra using Cu-K_α radiation of bulk ZnO powder (99%).

In our ZnO sputtered film the (0002) peak was the strongest peak and in most cases the only one (In such cases (0004) was also detected). Fig. 2b shows the effect of oxygen concentration at constant total pressure and at 150W, on the orientation of the grown layer.

It can be seen that for oxygen concentrations above 20%*vol.* both peaks of (10$\bar{1}$1) and (10$\bar{1}$1) do not exist. At 20%*vol.* O_2 a weak peak of (10$\bar{1}$0) plane was detected.

Such X-ray measurements were done with all the samples.

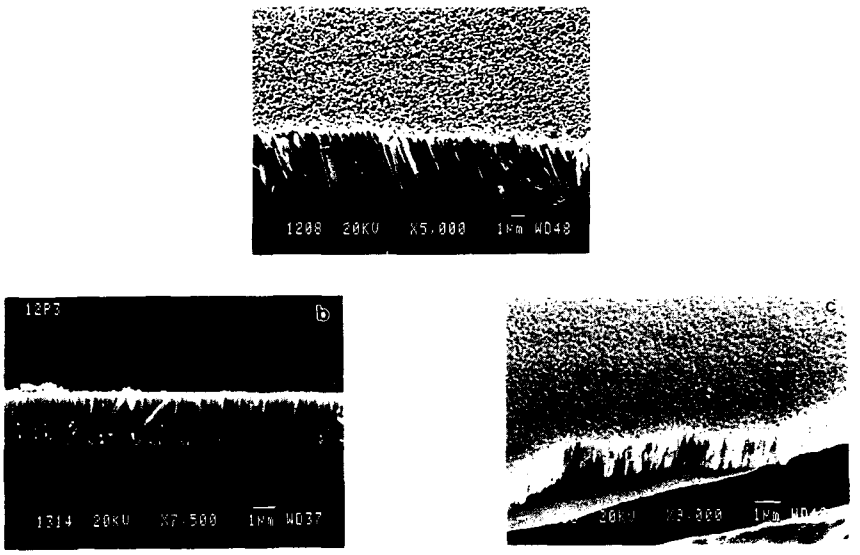


Figure 3: The influence of the O_2 concentration on the structure: a. 20%*vol.* O_2 b. 50%*vol.* O_2 c. 80%*vol.* O_2.

The results showed that highly oriented films were obtained above 20% *vol.*O_2 at discharge power range 100–200W. A partial volume of 80%*vol.* O_2 was needed at the power of 250W to obtain a well oriented film.

c. Structure

The SEM investigation of cross-sectioned samples revealed that the films grew in a columnar structure, with the columns perpendicular to the substrate surface.

Fig. 3 shows the effect of the O_2 concentration on the resultant structure at a given discharge power of 200W. When 20%*vol.* of oxygen (fig. 3a) was used the resultant structure consisted of columns with an open structure. As the concentration was raised a denser structure was resulted (fig. 3b, 3c). This type of behavior was observed at all other discharge powers. At 250W, however, the resultant film was covered with flakes that were analysed by AES to be ZnO. The flakes originated from the material deposited on the gun shield .This phenomena was reported by Maniv [6]. The column width was 0.2 0.5 μm. A denser structure leads to a smoother surface which is essential for SAW devices.

TEM investigation of cross-sectioned specimens revealed that the columnar grains do not grow directly on the substrate (fig. 4). An intermediate layer of equiaxed grains grows on the substrate and columnar grains develop on it.

Fig. 4 is an example of this behavior, it appears that as the oxygen concentration is raised the thinner this equiaxed grains layer is. When this area is inspected closely (higher magnifications) one can see that rotational Moiré patterns occurred between many pairs of grains. This implies that there is only a slight angular rotation between the orientations of the grains. Selected Area Diffraction (SAD) taken from this layer showed the existence

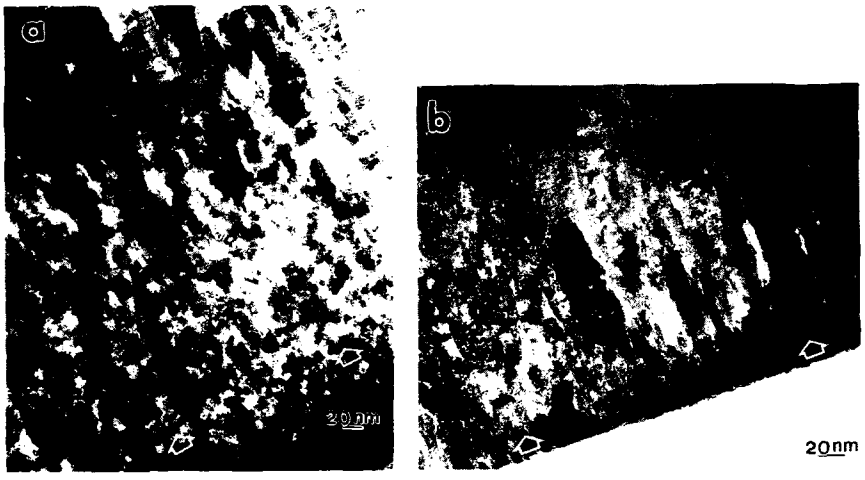


Figure 4: TEM image of cross sectioned sample sputtered at 100W: a. $20\%O_2 vol.$ b. $50\%O_2 vol.$ (the arrows point the directions of growth)

of preferred orientation.

During the deposition a large concentration of planar defects were formed (the SAD pattern taken from this area had verified that). The columnar grain width measured from the TEM images was found to be 40- 200nm. The big differences between this measurement and that of column width (Fig. 3) suggests that each column consist of several grains.

DISCUSSION

The results of this study show that the microstructure and crystallographic orientation of reactively sputtered ZnO films depends on the oxygen partial pressure and on the discharge power.

The AES results have demonstrated that in order to obtain stoichiometric ZnO a discharge power grater than 100W is needed. This effect of the discharge power on the O/Zn ratio was observed by Brett et al. [7]. They explained the enhanced film oxidation as a result of increased discharge power, through a mechanisms of preferential resputtering and evaporating of Zn, and by activation of oxygen species.

The oxygen partial pressure plays an important role in governing the deposition rate. By increasing the oxygen partial pressure from 20% *vol.* to 30% *vol.* at discharge power of 150W for instance, a decrease in the deposition rate from $25nm\ min$ to $3nm\ min$ was observed (these changes in deposition rate were approximately three times larger than the changes in the film density). At higher oxygen content the rate decreases and remains almost constant beyond 50% *vol.* The reduction in the deposition rate as oxygen is added may be due to the formation of negative oxygen ions which trap electrons, thereby producing

higher plasma impedance, low ion current and hence lower sputtering rate. Furthermore, the negative ions do not contribute to the sputtering yield [8].

There are two main factors which govern the structure of a sputtered thin film: a) geometrical shadowing of the incident beam by protruding parts of a growing surface; b) surface diffusion [9]. It was argued qualitatively [1] that the shadowing dictates a morphology of low-density columnar grains. Introducing surface diffusion allows the development of wider, smoother uniform columnar grains.

During the entire experiment the substrates were cooled to room temperature. However, in sputtering, the arriving species acquire enough kinetic energy for surface diffusion to occur. It is suggested that at high deposition rates there is not enough time for the atoms to diffuse on the surface. In such a case a structure of low-density tapered columns with domed tops is obtained (fig. 3).

When the deposition rate is lowered by increasing the O_2 content the surface diffusion becomes more effective and smoother and wider columnar grains are formed.

The lack of surface diffusion explains the phenomena of equiaxed grains layer (fig. 4). When the diffusion rate is relatively low it takes a longer time for the atoms to arrange in an energetically favorable way (c-axis perpendicular to the surface) which will lead to the growth of columnar grains. Thus whenever there is enough time for surface diffusion to occur, this equiaxed grain layer is relatively thin (fig. 4b). The thinner this layer is, the better the orientation is and the XRD results have verified that.

In the case of reactive sputtering at relatively low deposition rates the oxygen partial pressure plays the role of the temperature in the zone model of Movchan and Demchishin [10] by governing the surface diffusion.

Acknowledements: The Louis Edelstein center at the Technion is gratefuly acknowledged for the support of this study.

References

[1] J. A. Thornton, Ann. Mater. Sci. 7, 239 (1977).

[2] D.J. Srolovitz, A. Mazor and B.G. Bukiet, J. Vac. Technol.A 6 (4),2371 (1988).

[3] F.S. Hickernell, AWE Transactions on Sonics and Ultrasonics SU-32 5, 621 (1985).

[4] F.S. Hickernell, J.Appl.Phys. 44, 1061 (1973).

[5] G. Kino, R.S. Wagers, J.Appl.Phys.44, 1480 (1973).

[6] S. Maniv, Vacuum 33, 215 (1983).

[7] M.J. Brett and R.R. Parsons, J. Vac. Sci. Technol. A(3) ,423 (1986).

[8] K.B. Sundaram and B.K. Garside, J. Phys. D 17 [illegible] 47 (1984).

[9] G.S. Bales et. all., Science 249, 264 (1990).

[10] B.A. Movchan and A.V. Demchishin, Phys. Met. Metallogr. USSR 28, 83 (1969).

Author Index

Abuhadba, Nada M., 731
Ager, R., 549
Ahlgren, W.L., 273
Ahmed, A.U., 561
Aita, Carolyn R., 731, 737
Akasaki, I., 383
Akram, S., 261
Allan, D.C., 335
Amano, H., 383
Anderson, Gregory C., 171
Anderson, Timothy J., 215, 281
Antonelli, A., 323
Atsumi, Kinya, 721
Audurier, V., 475

Bachmann, Klaus J., 707
Badzian, A.R., 145
Bahavar, B., 555
Banerjee, P.K., 617
Bao, X.J., 767
Bar-Yam, Y., 335
Belogorokhov, A.I., 299, 303
Benz, K.W., 209, 773
Bernholc, J., 323
Bhat, I.B., 237, 261
Bhide, V.G., 755
Biegelsen, D.K., 191
Bird, Thomas, 481
Boehme, D., 593
Boemare, Claude, 267
Boothroyd, A.R., 525
Bretschneider, Eric, 215, 281
Bringans, R.D., 191
Brown, S.W., 127
Bryden, W.A., 409, 441
Buchwald, W.R., 687
Buckle, K., 31
Budai, J.D., 243
Butler, James E., 37

Carmo, M.C., 287
Chakoumakos, B.C., 243
Chang, C.C., 255
Chatterjee, B., 617
Chaudhari, S.M., 699
Chaudhry, M.I., 555
Chen, Guanghua, 613
Chen, Hsiung, 133
Chen, Yunliang, 227
Cheng, A.Y., 767
Cheng, C., 507
Cheng, Y.T., 469
Choi, Wai-Shing, 749
Chu, C.H., 361
Clark, H.R., 13
Clarke, R., 585
Clift, W.M., 593
Cui, Jie, 227

Davidson, J.L., 165
De, Badal, 373, 377
DeMattei, R.C., 293
Demenet, J.L., 475
Demichelis, F., 675
Dillon, R.O., 133
Ding, J., 203
Ditizio, R.A., 145
Doll, G.L., 585
Doverspike, Kathleen, 37, 139
Dowben, P.A., 637
Drory, M.D., 121

Ecelberger, S.A., 409, 441
Eckert, Hellmut, 249
Eckstein, J., 773
Edgar, J.H., 421, 463
Eddy Jr., C.R., 427
Edwards, L.M., 165
Efros, Al.L., 209
Egan, R.J., 395
Ehsani, H., 261
Ellis, C., 69
Ellul, J.P., 525
Engel, G.E., 507
Erwin, S.C., 3
Estreicher, S.K., 355, 361

Fanciulli, M., 605
Fang, J., 215
Faraji, M., 699
Feigelson, R.S., 293
Fonash, S.J., 145
Fountzoulas, C., 599
Freedman, Andrew, 109
Freitas, Jr., Jaime A., 37, 139
Friedmann, T.A., 593
Fujimori, Naoji, 115

Gatesman, A.J., 623
Geis, M.W., 13
Ghaisas, S.V., 699
Ghandhi, S.K., 261
Ghatak, Kamakhya P., 373, 377
Giannelis, Emmanuel P., 761
Gier, Thurman E., 249
Gilbert, D., 31
Gildenblat, G.Sh., 145
Giles, R.H., 623
Glesener, John W., 57, 161
Gokhale, Sunil, 699
Goldstein, D., 573
Golecki, I., 519
Gordon, Roy G., 445, 743
Graham, R.J., 97
Green, David M., 281
Grillo, D.C., 203, 221
Grot, S.A., 145
Gunshor, R.L., 203, 221
Gustafson, T.K., 457

Hagstrom, Stig B., 43, 51
Haku, H., 663
Hamakawa, Yoshihiro, 651, 721
Hangas, J., 549
Harmatz, M., 687
Harris, J.H., 451
Harrison, William T.A., 249
Hattori, Tadashi, 721
Heine, Volker, 507
Heremans, J., 469
Hewitt, Susan B., 525
Hirose, M., 681
Hoffman, A., 63
Hoffman, David M., 445
Hofmann, D.M., 209, 773
Holloway, P.H., 31, 215
Hu, Jinhua, 743
Hua, G.C., 203, 221
Hudson, G.C., 23
Humphreys, T.P., 23

Iacoponi, J., 237
Ikoma, Keiko, 543
Imai, Takahiro, 115
Iseki, T., 531

Jackson, K.A., 3
Jacobsohn, E., 779
James, R.B., 767
Jeng, S.J., 693
Jeon, H., 203
Johnsen, H.A., 593
Johnson, S.M., 273
Johnston, Peter N., 171
Johs, B., 237
Jones, K.S., 215

Kajihara, S.A., 323
Kajimoto, Atsushi, 487
Kanicki, J., 687, 693
Kapoor, Sanjiv, 43, 51
Kelly, Michael A., 43, 51
Khar'kovsky, A.Yu., 299
Kim, J.S., 617
Kistenmacher, T.J., 409, 441
Klaus, E.J., 593
Koba, R., 31
Kobayashi, M., 203, 221
Kolawa, E.A., 737
Konkel, W.H., 273
Kotecki, D.E., 693
Kumashiro, Y., 629
Kurtz, A.D., 573
Kuwano, Y., 663
Kwok, C.-K., 737

Laks, David B., 311, 349
Lambrecht, W.R.L., 367
Lee, R.C., 737
Lee, Sunwoo, 637
Lei, T., 335, 427, 433, 599
Lenef, A., 127
Li, J.P., 537
Liu, Y., 127
Logothetis, E.M., 549
Lowndes, D.H., 243
Lu, Z., 255

Malta, D.P., 23
Manory, R., 63
Marathe, B.R., 755
Marks, C.M., 139
Markunas, R.J., 23
Marti, J., 519
Matsuda, K., 629
Matsunami, Hiroyuki, 487
Matus, L.G., 495
Mazurowski, John, 637
McCamy, J.W., 243
McCarty, K.F., 593
McCluskey, R.J., 555
Mehrotra, Vivek, 761
Meng, W.J., 469
Menon, G., 427
Meyer, B.K., 209, 773
Mills, M.J., 593
Mirzapour, S., 755
Mitra, S.S., 617
Miyazaki, S., 681
Molnar, R.J., 427, 599
Moran, Kelly L., 249
Morgan, J.S., 409
Morrish, Arthur A., 57, 161
Moustakas, T.D., 335, 427, 433, 599, 605

Nakamura, J., 629
Nakamura, N., 663
Nakano, S., 663
Nazare, M.H., 267
Needs, R.J., 507
Nemanich, R.J., 23
Neudeck, P.G., 495
Neumark, G.F., 255
Ninomiya, K., 663
Nishibayashi, Yoshiki, 115
Nishiwaki, H., 663
Nishizawa, Jun-Ichi, 179
Nurmikko, A.V., 203

Ochoa, R., 31
Oettinger, K., 209
Okamoto, H., 651
Okamoto, K., 681
Oles, E.J., 599
Olson, Darin S., 43, 51
Ortale, C., 767
Otsuka, N., 203, 221
Ott, Andrew W., 249
Ottesen, D.K., 593
Otto, Jens W., 761
Oyama, Yutaka, 179

Padmapani, Nallan C., 255
Parks, C.C., 693
Paterson, P.J.K., 63
Pathangey, B., 215
Pederson, M.R., 3
Pehrsson, Pehr E., 57
Perry, T.A., 469, 585
Petit, Jeremy B., 495, 567

Pickett, W.E., 3
Pirouz, P., 531
Pirri, C.F., 675
Platek, M., 617
Poehler, T.O., 409
Ponce, F.A., 191
Pong, Chungdee, 293
Posthill, J.B., 23
Powell, J.A., 495, 531
Pratsinis, Sotiris E., 643
Prawer, Steven, 63, 171
Provost, L.G., 573
Pryor, R.W., 13

Rabier, J., 475
Ramesham, R., 69
Ramseyer, G., 637
Rand, S.C., 127
Rava, P., 675
Redman, D.A., 127
Rees, Jr., William S., 281
Reidinger, F., 519
Riaz, Umar, 445
Rimai, L., 549
Roberson, M.A., 355, 361
Robinson, Gary N., 109
Rodeghiero, Eric, 761
Rodgers, J., 31
Rong, F.C., 687
Ross, J., 457
Rozati, S.M., 755
Rubin, M., 457
Rudder, R.A., 23
Ruth, R.P., 273
Rys, A., 561

Sahaida, Scott R., 151
Salk, M., 209
Satoh, S., 127
Schlesinger, T.E., 767
Segall, B., 367
Sell, J.A., 585
Sen, S., 273
Shechtman, D., 779
Shen, Aidong, 227
Shen, Yuhua, 227
Shin, H., 681
Shor, J.S., 573
Shu, Q., 127
Simmons, J.H., 31
Singh, Nitya N., 561
Singh, Rajiv K., 31, 79
Smits, Jan G., 749
Snail, K.A., 139, 161
Snyder, Paul G., 481
Soares, M.J., 287
Solinsky, J., 361
Speck, J.S., 121
Stadler, W., 209
Stair, Kathleen, 481
Steckl, A.J., 537
Stinespring, Charter D., 109
Strom, U., 139
Stuart, S-A., 63
Stucky, Galen D., 249
Stulen, R.H., 593

Suto, Ken, 179
Suzuki, T., 531
Swartz, L.-E., 191
Sywe, B.S., 421, 463

Takahashi, J., 629
Takwale, M.G., 699, 755
Tamargo, M.C., 255
Tanaka, M., 663
Tansley, T.L., 395
Tarr, N.G., 525
Tarui, H., 663
Tay, Sing-Pin, 525
Taylor, C.A., 585
Tellshow, R., 31
Teter, M.P., 335
Thomas, R.E., 23
Thompson, Dale G., 151
Tien, J., 693
Tramontana, J.C., 191
Tresso, E., 675
Tsuda, S., 663
Tsuji, K., 127
Tsuji, Tsuzumi, 487
Tsuno, Takashi, 115

Ueno, Yoshiki, 721

Van de Walle, Chris G., 311, 349
Van den Berg, L., 767
Vavilov, Victor S., 87
Viatella, John, 79
Vigil, J.A., 273

Wakisaka, K., 663
Waldman, J., 623
Wang, Hailong, 227
Warren, W.L., 687
Weber, R.A., 573
Weber, W.H., 549
Weimer, Alan W., 643
Weiser, Paul S., 63
Whitaker, J., 127
Williams, K.E., 121
Woollam, J.A., 237

Xie, W., 203, 221
Xiong, Yun, 643
Xu, Liang, 227

Yamanaka, Mitsugu, 543
Yang, J.W., 531
Yao, Huade, 481
Yazu, S., 127
Yi, G.-J., 255
Yokoyama, T., 629
Yoshida, H., 629
Yoshimoto, Masahiro, 487
Youngman, R.A., 451
Yu, J.E., 215
Yu, Z.J., 421, 463

Zeiler, Mary V., 567
Zhang, Fangqing, 613
Zuhr, R.A., 243

Subject Index

abrasion resistance, 171
acoustooptic, 779
aluminum
  arsenide (AlAs), 481
  gallium nitride (AlGaN), 383
  nitride (AlN), 367, 395, 451, 463, 469, 475
  phosphide (AlP), 361
annealing, 287
apex of silicon pyramids, 69
atomic
  force microscopy (AFM), 133
  layer epitaxy (ALE), 109
auger electron spectroscopy (AES), 567

bandgap, 367, 637
band structure, 367
barriers, 3
  diffusion, 63
  Schottky junction, 3, 161
bimorphs, 749
boron, 613, 629
  carbide (BC), 637, 643
  nitride (BN), 367, 599, 605, 623
    cubic, 585, 599, 605
    hexagonal, 593, 605
  phosphide, 629
Burstein-Moss shift, 373

cadmium zinc telluride (CdZnTe), 209
carbon, 57
  chemistry, 3
  electrical properties, 133
  sp^2, 57
carbonization, 543
carbothermal reduction, 643
carrier traps, 767
cathodoluminescence, 97, 179, 273
chemical vapor deposition (CVD), 97, 267, 445, 543, 555, 743
  combustion assisted (CACVD), 139
  electron cyclotron resonance (ECR-CVD), 651
  ion-beam (IBCVD), 651
  metal organic (MOCVD), 215, 273, 293, 421, 463, 707, 721
  plasma
    assisted (PACVD), 23
    enhanced (PECVD), 121, 637, 681, 693
  rapid thermal (RTCVD), 537
coagulation, 643
coalescence, 643
contacts
  ohmics, 573
  Schottky, 151
covalent ceramics, 475
crystal growth, 495

dangling bonds, 687
defects, 97, 605
Dektak profilometry, 519
diamond, 43, 51, 57, 102, 161, 171, 585
  (001), 115
  crystals, 69, 139
  CVD, 13, 63, 127
  doping, 323
  films, 97, 121, 165
  growth, 23, 37
  in solid state devices, 87
  interfaces, 3
  /nickel, 3
  surface chemistry, 3
  thin films, 31
dimer, 115
diode
  blue and blue/green laser, 203
  high temperature, 613
  light emitting, 203
    a-SiC visible light, 651
    UV/blue, 383, 613
  ZnSe/ZnCdSe structures, 221
di-tert-butylsilane, 525
doping
  carbon boron nitride, 605
  efficiencies, 323, 349
  nitrogen, 281
  n-type, 323
  problems, 311
  p-type, 281

Einstein relation, 377
electrical conductivity, 629
electroluminescence, 215
electron
  channeling pattern, 421
  cyclotron resonance (ECR), 31
    technique, 31, 145
  paramagnetic resonance (EPR), 605, 687
electronic
  device, 145
  states, 127
  structure, 361
epitaxial
  films, 115
    homoepitaxial diamond film, 13, 145
    zinc sulfide (ZnS) thin films, 243
  growth, 537
excimer laser melting, 255

ferroelectric transition, 761
first-principle calculations, 349
fluorine, 3

gallium
  arsenide (GaAs), 191, 261, 457, 721
  nitride (GaN), 367, 383, 395, 457
    thin films, 445
  phosphide (GaP), 487

growth
  heteroepitaxial, 409, 441, 543
  mechanisms, 51
  sequence, 121

heat flow equation, 79
heteroepitaxy, 191, 457, 555
heterostructures, 707
  CdS/CdTe, 267
  multi, 383
hydrogen, 43

implantation, 87, 171
indium nitride (InN), 395, 409, 441
infrared spectra, 303, 681
intercalation, 761
interface energies, 3
interfacial layer, 121
interstitial
  hydrogen, 355
  oxygen, 361
iron (Fe), 63

laminar flame conduction, 139
Landau levels, 377
laser
  ablation, 549, 593
  irradiation, 79
  solid interaction, 79
lattice mismatch, 221
lead iodide particles, 761
linear muffin tin orbital (LMTO), 367
local density approximation (LDA), 367
lower energy electron diffraction (LEED), 109
luminescence, donor-acceptor pair, 209

magnetic resonance, 773
mass analysis, 299
mercuric iodide (HgI), 767, 773
metal(-)
  organic
    (MOMBE), 487
    (MOVPE), 281
  oxide, 737
    semiconductor (MOS), 561
methane, 637
molecular beam epitaxy (MBE), 191, 203, 221, 227, 255, 561
morphology, 115, 441
mosaic film, 13

native-defect compensation, 311
nucleation, 57
  density, 69
  detectors, 767

optical absorption, 249, 731, 773
organic-metal vapor phase epitaxy, 231, 261, 487
oxidation, 561
oxy-acetylene, 37

patterning, 165
pentaborane, 637
phase map, 737
photo-darkening, 451
photoenhancement, 487
photo-induced absorption, 451
photoluminescence, 209, 267, 637, 681, 773
piezoelectric, 749
plasma effect, 299
p-n junction, 179
point defects, 171
polysilane, 681
polytypes, 507
polytypism, 531
potential energy surfaces, 361
pulsed nanosecond lasers, 79

quantizing magnetic field, 377
quantum
  dots, 373
  size effect, 383, 761
  wires (QWS), 373

radiation-induced centers, 127
Raman scattering, 31, 469, 681
relative stability, 361
remote plasma, 31
RF biasing, 593
rocking curves, x-ray, 221
Rutherford backscattering, 519

sapphire, 441
scanning tunneling microscopy, 115
selective nucleation, 69
self-compensation, 311, 349
semiconductor, 109, 299, 303
  compound, 475, 555
  impurities in, 349
  semiconductor grade diamond substrates, 13
  silicon carbide, 495
  wide-band gap semiconductors, 221, 227, 303, 311, 373, 377, 555, 675, 707, 721
sensors, 573
sequential deposition chamber, 43
sharp edges, 69
silicides, 567
silicon (Si), 361, 593, 663
  carbide (SiC), 355, 361, 367, 463, 507, 525, 531, 537, 543, 549, 555, 561, 567, 573, 651, 663, 675
  hydrogenated microcrystalline, 693, 699
  mesa structure, 69
sintering law, 643
sodalite analogues, 237
solidification velocities, 79
solubilities, 349
  solubility limits, 311
spectroscopic ellipsometry, 237, 481
spectroscopy, 127, 303
  auger, 121
  infrared reflection (IR), 593
  optical, 127
  Rutherford backscattering (RBS), 171
  thermally stimulated current, 767

sputtered carbon, 51
sputtering, 441
  deposition, 469, 731, 737
  magnetron, 151, 409, 457
  reactive, 779
stoichiometry, 179, 287
strained layer superlattice, 227, 293
submillimeter optical properties, 623
surface
  acoustic wave (SAW), 779
  chemistry, 109
  diffusion, 779
  modification, 79

tantalum, 151
TDM-CVP, 179
terahertz, 127
tert-butylphosphine, 525
thermoelectric device, 629
titanium nitride (TiN), 63
transistors, heterojunction bipolar, 525
transmission electron microscopy (TEM), 215, 475
twinning, 255

vandadia, 731
vapor transport, 273

wear, 171
wurtzite, 355, 367

zinc
  amide, 281
  cadmium selenide (ZnCdSe), 237
  chalcogenides, 249
  oxide, 743, 749, 779
  selendie (ZnSe), 179, 191, 203, 237, 255, 261, 273, 281, 293, 311, 349
  sulfide (ZnS), 215, 243, 507
zincblende, 355, 367